

業績論文リスト

分野名	論文
分子神経生物学分野(1)	Kato T, Abe Y, Hirokawa S, Iwakura Y, Mizuno M, Namba H, Nawa H. Neurobehavioral Differences Between Mice Receiving Distinct Neuregulin Variants as Neonates; Impact on Sensitivity to MK-801. <i>Current Molecular Medicine</i> 2015, 15, 222-236
分子神経生物学分野(2)	Sakai M, Watanabe Y, Someya T, Araki K, Shibuya M, Niizato K, Oshima K, Kunii Y, Yabe H, Matsumoto J, Wada A, Hino M, Hashimoto T, Hishimoto A, Kitamura N, Iritani S, Shirakawa O, Maeda K, Miyashita A, Niwa S, Takahashi H, Kakita A, Kuwano R, Nawa H. Assessment of copy number variations in the brain genome of schizophrenia patients. Sakai et al. <i>Molecular Cytogenetics</i> (2015) 8:46 DOI 10.1186/s13039-015-0144-5
細胞神経生物学分野(1)	Watanabe-Iida I, Konno K, Akashi K, Abe M, Natsume R, Watanabe M, Sakimura K. Determination of kainate receptor subunit ratios in mouse brain using novel chimeric protein standards. <i>J Neurochem.</i> 2015 Oct 8. doi: 10.1111/jnc.13384.
細胞神経生物学分野(2)	Kakegawa W, Mitakidis N, Miura E, Abe M, Matsuda K, Takeo YH, Kohda K, Motohashi J, Takahashi A, Nagao S, Muramatsu S, Watanabe M, Sakimura K, Aricescu AR, Yuzaki M. Anterograde c1ql1 signaling is required in order to determine and maintain a single-winner climbing fiber in the mouse cerebellum. <i>Neuron.</i> 2015 Jan 21;85(2):316-29. doi: 10.1016/j.neuron.2014.12.020.
細胞神経生物学分野(3)	Ageta-Ishihara N, Yamazaki M, Konno K, Nakayama H, Abe M, Hashimoto K, Nishioka T, Kaibuchi K, Hattori S, Miyakawa T, Tanaka K, Huda F, Hirai H, Hashimoto K, Watanabe M, Sakimura K, Kinoshita M. A CDC42EP4/septin-based perisynaptic glial scaffold facilitates glutamate clearance. <i>Nat Commun.</i> 2015 Dec 10;6:10090. doi: 10.1038/ncomms10090.
システム脳生理学分野(1)	Watanabe T, Sasaki M, Komagata S, Tsukano H, Hishida R, Kohno T, Baba H, Shibuki K, Spinal mechanisms underlying potentiation of hindpaw responses observed after transient hindpaw ischemia in mice. <i>Scientific Reports</i> 5, 11191, 2015.
システム脳生理学分野(2)	Tsukano H, Horie M, Bo T, Uchimura A, Hishida R, Kudoh M, Takahashi K, Takebayashi H, Shibuki K, Delineation of a frequency-organized region isolated from the mouse primary auditory cortex. <i>J. Neurophysiol.</i> 113, 2900-2920, 2015.
システム脳生理学分野(3)	Meguro R, Hishida R, Tsukano H, Yoshitake K, Imamura R, Tohmi M, Kitsukawa T, Hirabayashi T, Yagi T, Takebayashi H, Shibuki K, Impaired clustered protocadherin-a (cPcdh-a) leads to aggregated retinogeniculate terminals and impaired visual acuity in mice. <i>J. Neurochem.</i> 133, 66-72, 2015.
病理学分野/デジタル医学分野/脳疾患標本資源解析学分野(1)	Nakashima M, Saitsu H, Tohyama J, Kato M, Shiina M, Takei N, Kitaura H, Shirozu H, Masuda H, Watanabe K, Ohba C, Tsurusaki Y, Miyake N, Takebayashi H, Ogata K, Kameyama S, Kakita A*, Matsumoto N* (*: co-last authors). Somatic mutations in the MTOR gene cause focal cortical dysplasia type IIb. <i>Annals of Neurology.</i> 78(3): 375-386, 2015
病理学分野/デジタル医学分野/脳疾患標本資源解析学分野(2)	Ogura R, Tsukamoto Y, Natsumeda M, Isogawa M, Aoki H, Kobayashi T, Yoshida S, Okamoto K, Takahashi H, Fujii Y, Kakita A. Immunohistochemical profiles of IDH1, MGMT and P53: practical significance for prognostication of patients with diffuse gliomas. <i>Neuropathology.</i> 35(4): 324-335, 2015
病理学分野/デジタル医学分野/脳疾患標本資源解析学分野(3)	Kimura T, Kitaura H, Masuda H, Kameyama S, Saito Y, Sugai K, Otsuki T, Nakazawa A, Morota N, Yamamoto T, Iida K, Nakagawa M, Mizuno T, Takahashi H, Kakita A. Characteristic expression of p57/Kip2 in balloon cells in focal cortical dysplasia. <i>Neuropathology.</i> 35(5): 401-409, 2015
分子病態学(客員)分野(1)	Tanji K, Odagiri S, Miki Y, Maruyama A, Nikaido Y, Mimura J, Mori F, Warabi E, Yanagawa T, Ueno S, Itoh K, Wakabayashi K. p62 deficiency enhances α -synuclein pathology in mice. <i>Brain Pathol</i> 25: 552-564, 2015
分子病態学(客員)分野(2)	Nakamura K, Mori F, Kon T, Tanji K, Miki Y, Tomiyama M, Kurotaki H, Toyoshima Y, Kakita A, Takahashi H, Yamada M, Wakabayashi K. Filamentous aggregations of phosphorylated α -synuclein in Schwann cells (Schwann cell cytoplasmic inclusions) in multiple system atrophy. <i>Acta Neuropathol Comm</i> 3: 29, 2015
分子病態学(客員)分野(3)	Mori F, Miki Y, Tanji K, Kakita A, Takahashi H, Utsumi J, Sasaki H, Wakabayashi K. Sortilin-related receptor CNS expressed 2 (SorCS2) localizes in Bunina bodies in amyotrophic lateral sclerosis. <i>Neurosci Lett</i> 608: 6-11, 2015

分野名	論文
脳神経外科学分野(1)	Fukuda M, Takao T, Hiraishi T, Aoki H, Ogura R, Sato Y, Fujii Y. Cortico-cortical activity between the primary and supplementary motor cortex: An intraoperative near-infrared spectroscopy study. <i>Surg Neurol Int</i> 6: 44, 2015. DOI: 10.4103/2152-7806.153872.
脳神経外科学分野(2)	Ogura R, Tsukamoto Y, Natsumeda M, Isogawa M, Aoki H, Kobayashi T, Yoshida S, Okamoto K, Takahashi H, Fujii Y, Kakita A. Immunohistochemical profiles of IDH1, MGMT and P53: practical significance for prognostication of patients with diffuse gliomas. <i>Neuropathology</i> . 35(4): 324-335, 2015
脳神経外科学分野(3)	Nishiyama K, Yoshimura J, Fujii Y. Limitations of neuroendoscopic treatment for pediatric hydrocephalus and considerations from future perspectives. <i>Neurol Med Chir</i> 2015 (doi: 10.2176/nmc.ra.2014-0433)
神経内科学分野(1)	Kanazawa M, Kawamura K, Takahashi T, Miura M, Tanaka Y, Koyama M, Toriyabe M, Igarashi H, Nakada T, Nishihara M, Nishizawa M, Shimohata T. Multiple therapeutic effects of progranulin on experimental acute ischaemic stroke. <i>Brain</i> 2015;138:1932-1948.
神経内科学分野(2)	Hokari M, Yokoseki A, Arakawa M, Saji E, Yanagawa K, Yanagimura F, Toyoshima Y, Okamoto K, Ueki S, Hatase T, Ohashi R, Fukuchi T, Akazawa K, Yamada M, Kakita A, Takahashi H, Nishizawa M, Kawachi I. Clinicopathological features in anterior visual pathway in neuromyelitis optica. <i>Annals of Neurology</i> 2016;79(4):605-624. doi: 10.1002/ana.24608. PMID: 26836302.
神経内科学分野(3)	Ikeda T, Takahashi T, Tsujita M, Kanazawa M, Toriyabe M, Koyama M, Itoh K, Nakada T, Nishizawa M, Shimohata T. Effects of Alda-1, an Aldehyde Dehydrogenase-2 Agonist, on Hypoglycemic Neuronal Death. <i>PLOS ONE</i> 2015;10:e0128844.
統合脳機能研究センター(1)	Suzuki Y, Nakamura Y, Yamada K, Igarashi H, Kasuga K, Yokoyama Y, Ikeuchi T, Nishizawa M, Kwee IL, Nakada T. Reduced CSF Water Influx in Alzheimer's Disease Supporting the β -Amyloid Clearance Hypothesis. <i>PLoS One</i> . 10(5):e0123708, 2015.
統合脳機能研究センター(2)	Nakada T. The Molecular Mechanisms of Neural Flow Coupling: A New Concept. <i>J Neuroimaging</i> . 25(6):861-5, 2015.
統合脳機能研究センター(3)	Igarashi H, Suzuki Y, Huber VJ, Ida M, Nakada T. N-acetylaspartate Decrease in Acute Stage of Ischemic Stroke: A Perspective from Experimental and Clinical Studies. <i>Magn Reson Med Sci</i> . 14(1):13-24, 2014.
遺伝子機能解析学分野/ 生命情報工学分野(1)	Sato Y, Bernier F, Yamanaka Y, Aoshima K, Oda Y, Ingelsson M, Lannfelt L, Miyashita A, Kuwano R, Ikeuchi T. Reduced plasma desmosterol-to-cholesterol ratio and longitudinal cognitive decline in Alzheimer's disease. <i>Alzheimer's & Dementia: Diagnosis, Assessment & Disease Monitoring</i> 1:67-74, 2015
遺伝子機能解析学分野/ 生命情報工学分野(2)	Kasuga K, Kikuchi M, Tokutake T, Nakaya A, Tezuka T, Tsukie T, Hara N, Miyashita A, Kuwano R, Ikeuchi T. Systematic review and meta-analysis of Japanese familial Alzheimer's disease and FTDP-17. <i>Journal of Human Genetics</i> 60:281-283, 2015
遺伝子機能解析学分野/ 生命情報工学分野(3)	Yajima R, Tokutake T, Koyama A, Kasuga K, Tezuka T, Nishizawa M, Ikeuchi T. ApoE-isoform-dependent cellular uptake of amyloid- β is mediated by lipoprotein receptor LR11/SorLA. <i>Biochemical Biophysical Research Communications</i> 456:482-488, 2015
動物資源開発研究分野(1)	Chiken S, Sato A, Ohta C, Kurokawa M, Arai S, Maeshima J, Sunayama-Morita T, Sasaoka T, Nambu A. Dopamine D1 receptor-mediated transmission maintains information flow through the cortico-striato-entopeduncular direct pathway to release movements. <i>Cerebral Cortex</i> 2015 Dec; Vol.25 No.12:4885-97. doi:
動物資源開発研究分野(2)	Nakamura T, Sato A, Kitsukawa T, Sasaoka T, Yamamori T. Expression pattern of immediate early genes in the cerebellum of D1R KO, D2R and wild type KO mice under various conditions. <i>Frontiers in Cell and Developmental Biology</i> . Vol.3, Article 38, June 2015 doi: 10.3389/fcell.2015.00038
動物資源開発研究分野(3)	Hayashiji N, Yuasa S, Miyagoe-Suzuki Y, Hara M, Ito N, Hashimoto H, Kusumoto D, Seki T, Tohyama S, Kodaira M, Kunitomi A, Kashimura S, Takei M, Saito Y, Okata S, Egashira T, Endo J, Sasaoka T, Takeda S and Fukuda K. G-CSF supports long-term muscle regeneration in mouse models of muscular dystrophy. <i>Nature Communications</i> 2015
プロジェクト研究分野(1)	Natsumeda M, Maitani K, Liu Y, Miyahara H, Kaur H, Chu Q, Zhang H, Kahlert U, Eberhart CG. Targeting Notch Signaling and Autophagy Increases Cytotoxicity in Glioblastoma Neurospheres. <i>Brain Pathol</i> . 2015 Nov 27. p 1-11

※論文は出版元の転載許可を受けています。

2. 業績論文（抜粋）

論文は出版元の転載許可を受けています

Neurobehavioral Differences Between Mice Receiving Distinct Neuregulin Variants as Neonates; Impact on Sensitivity to MK-801

T. Kato¹, Y. Abe¹, S. Hirokawa², Y. Iwakura¹, M. Mizuno¹, H. Namba¹ and H. Nawa^{*,1}

¹Department of Molecular Neurobiology, Brain Research Institute, Niigata University, Niigata 951-8585, Japan

²Department of Molecular Genetics, Niigata University Graduate School of Medical and Dental Sciences, Niigata 951-8510, Japan

Abstract: Neuregulin-1 (NRG1) is a well-recognized risk gene for schizophrenia and is often implicated in the neurodevelopmental hypothesis of this illness. Alternative splicing and proteolytic processing of the *NRG1* gene produce more than 30 structural variants; however, the neuropathological roles of individual variants remain to be characterized. On the basis of the neurodevelopmental hypothesis of schizophrenia, we administered eNRG1 (0.1~1.0 µg/g), a core epidermal growth factor-like (EGF) domain common for all splicing NRG1 variants, to neonatal mice and compared their behavioral performance with mice challenged with a full mature form of type 1 NRG1 variant. During the neonatal stage, recombinant eNRG1 protein administered from the periphery passed the blood-brain barrier and activated its receptor (ErbB4) in the brain. In adults, the mice receiving the highest dose exhibited lower locomotor activity and deficits in prepulse inhibition and tone-dependent fear learning, although the hearing reduction of the eNRG1-treated mice may explain these behavioral deficits. Neonatal eNRG1 treatment also significantly potentiated MK-801-driven locomotor activity in an eNRG1 dose-dependent manner. In parallel eNRG1 treatment enhanced MK-801-driven c-Fos induction and decreased immunoreactivity for NMDA receptor subunits in adult brain. In contrast, mice that had been treated with the same molar dose of a full mature form of type 1 NRG1 as neonates did not exhibit hypersensitivity to MK-801. However, both animal models exhibited similar hypersensitivity to methamphetamine. Collectively, our findings suggest that aberrant peripheral NRG1 signals during neurodevelopment alter later behavioral traits and auditory functions in the NRG1 subtype-dependent manner.

Keywords: Behavior, MK-801, Neuregulin-1, NMDA receptor, hearing, schizophrenia.

INTRODUCTION

Genetic polymorphism of neuregulin-1 (*NRG1*) is suggested to associate with vulnerability to psychiatric diseases such as schizophrenia and bipolar disorder [1-3]. The genetic association of *NRG1* with schizophrenia was first demonstrated with the haplotype block called HAPICE that is located in the 5'-end of the gene and consists of three single nucleotide polymorphisms (SNPs) and two microsatellites [1]. This initial finding has been replicated in multiple samples, but not in all populations [1-3]. Alternative splicing or promoter usage of the *NRG1* gene produces multiple isoforms of *NRG1* precursor proteins (type I-VI) [4-6]. The posttranslational processing of the *NRG1* precursors further modifies the protein structures of these isoforms to alter their biological activity [7]. However, the pathological contribution of each *NRG1* isoform is not fully understood. Genetic mutant mice that lack the isoform-specific exon(s) or overexpress a specific isoform of *NRG1* exhibit distinct behavioral abnormalities relevant to schizophrenia endophenotypes, potentially suggesting the divergence of the

isoforms' functions *in vivo* [8-12]. These experiments were often performed by independent researchers and did not allow us to accurately compare the behavioral consequences of the individual isoforms' manipulations. To test the functional difference of the *NRG1* isoforms, here, we investigated and compared the behavioral traits of the mice treated with type1 *NRG1* (T1-*NRG1*) and those with its processing product; an epidermal growth factor (EGF) domain peptide (eNRG1). These *NRG1* derivatives are potentially induced or recruited in the prenatal and perinatal immune inflammatory processes that are implicated in schizophrenia etiology [13,14].

We have been testing the neurodevelopmental hypothesis of schizophrenia, assessing the neurobehavioral impact of neonatal exposure to T1-*NRG1* [15]. In addition to T1-*NRG1*, here, we challenged mouse neonates with eNRG1 to compare the neurobehavioral effects of the two *NRG1* variants, eNRG1 and T1-*NRG1*. Although there are multiple isoforms of *NRG1* precursor proteins (type I-VI), which are generated by alternative splicing or promoter usage of the *NRG1* gene, but all *NRG1* isoforms carry this core active domain (i.e., eNRG1) for their receptor binding [5,6]. Moreover, eNRG1 is naturally produced by proteolytic processing of T1-*NRG1* with a protease, neuropsin, and suggested to exert a distinct action in

*Address correspondence to this author at the Department of Molecular Neurobiology, Brain Research Institute, Niigata University, 1-757 Asahimachi-dori, Niigata 951-8585, Japan; E-mail: hnawa@bri.niigata-u.ac.jp

hippocampal synaptic plasticity [7]. We assessed basal behavioral traits to evaluate the relevancy of eNRG1-injected mice to an animal model for schizophrenia, comparing the previous results from the mice exposed to T1-NRG1 [15]. As NRG1 signals are known to regulate NMDA receptor expression and function in the brain [16-19]. Thus, we investigated the sensitivity of eNRG1-treated mice to the NMDA receptor antagonist MK-801 as well as the expression of NMDA receptor subunits in these mice [17,18].

MATERIALS AND METHODS

Ethics Statement

All of the animal experiments described were approved by the Animal Use and Care Committee of Niigata University and performed in accordance with the guidelines of NIH (USA).

Animals

C57BL/6NCrj mouse dams of late pregnancy were purchased from Nihon Charles River (Yokohama, Japan) and their pups were used for experiments. Mice were housed with their dam in polypropylene cages (24L × 17W × 12H cm) in temperature-controlled colony room maintained under a 12-h light-dark cycle (light on 8:00 h) with free access to food and water. At postnatal day (PND) 25-28, pups were weaned and separated into cage (three or four animals per cage). Both male and female mice were subjected to behavioral tests during PND 56-70 [15]. Behavioral tests were performed during the light-cycle.

Reagents

Recombinant epidermal growth factor domain of human NRG 1 β 1/hereregulin 1 β 1 was purchased from PeproTech EC (London, UK). This NRG1 peptide is sufficient for activation of the ErbB4 receptor tyrosine kinase. We will refer to it simply as "eNRG1". Alternatively, we used the full mature form of recombinant type-1 NRG1 β 1 protein (T1-NRG1; MW 25400 Da) [15]. (+)-MK-801 (dizocilpine) was purchased from Tocris Cookson Ltd (Ellisville, MO, USA).

NRG1-Treatment and Psychotomimetic Challenge

eNRG1 or T1-NRG1 was administered subcutaneously (s.c.) to individual litters during postnatal days PND 2-10 at the nape of the neck at a dose of 0.1, 0.3, or 1.0 μ g/g body weight (injection volume 15 μ l/g). The experimental design and procedures were based on our previous studies of the EGF model for schizophrenia [20]. Control littermates received a phosphate-buffered saline (PBS; vehicle) injection of the same volume. MK-801 (0.3 μ g/g; 10 μ l/g) and methamphetamine (1.0 μ g/g; 10 μ l/g) dissolved in saline were administered intraperitoneally (i.p.) to adult mice (PND 56-70) [15,21].

Immunoprecipitation

Protein extracts were prepared from whole brains of eNRG1-treated or vehicle-treated control mice on PND2 [15]. Each brain was homogenized in a RIPA lysis buffer [50 mM Tris-HCl buffer (pH 7.4) with 1% TritonX-100, 1% sodium deoxycholate, 0.1% sodium dodecyl sulfate (SDS), 150 mM NaCl, 5 mM EDTA, 1 mM Na₃VO₄, and 1 mM NaF) plus a protease inhibitor cocktail (Complete Mini; Roche, Mannheim, Germany). After centrifugation, supernatants were harvested and protein content was determined using a Micro BCA kit (Pierce Chemical, Rockland, IL, USA). Each brain lysate (2 mg protein) was then incubated with 2 μ g of anti-ErbB4 antibody (Santa Cruz Biotechnology, Santa Cruz, CA, USA) overnight and mixed with Protein G Sepharose beads (20 μ l; GE Healthcare Bio-Science AB, Uppsala, Sweden) for 3 h. Sepharose beads were washed with RIPA buffer, and denatured with 100 μ l of 2 × SDS sample buffer (125 mM Tris-HCl pH 6.8, 4% SDS, 10% 2-mercaptoethanol). The specificity of the anti-ErbB4 antibody was ascertained by immunoblotting of cell lysates containing individual ErbB1-4 proteins (HN, unpublished data). Immunoprecipitates were then analyzed by gel electrophoresis as described below.

Immunoblotting

Brain tissues were homogenized in the sample lysis buffer (62.5 mM Tris-HCl pH 6.8, 2 % SDS, 0.5 % NP-40, 5 mM EDTA) plus the protease inhibitor cocktail (Roche). Protein samples (15-30 μ g/lane) were separated by SDS-polyacrylamide gel electrophoresis and transferred to nitrocellulose membranes. Membranes were probed with antibodies directed against phosphotyrosine (1:1000, Millipore, Bedford, MA, USA), ErbB4 (1:1000, Santa Cruz Biotechnology). Alternatively, immunoblots were probed with antibodies directed against excitatory and inhibitory neuronal markers [GluA1 (1:500, Millipore), GluA2/3 (1:1000, Millipore), GluA4 (1:1000, Millipore), GluN1 (1:1000, Millipore), GluN2A (1:500, Millipore), GluN2B (1: 500, Millipore), GluN2C (1:500, Millipore), GluN2D (1:1000, Santa Cruz Biotechnology), GAD65/67 (1:1000, Millipore), parvalbumin (1:3000, Abcam, Cambridge UK), tyrosine hydroxylase (1:1000, Millipore) neuregulin-1 (1:300, RandD Systems, Minneapolis, MN), and β -actin (1:2000, Millipore)]. Immunoreactivity on membranes was detected by peroxidase-conjugated anti-immunoglobulin antibodies followed by chemiluminescence reaction (ECL kit, GE Healthcare) and film exposure. The intensity of an immunoreactive band, whose size matched the authentic molecular weight, was measured by an image processing software, GENETOOLS (Syngene, Cambridge, UK).

Auditory Brain-Stem Evoked Response

The lowest level, at which an auditory brain-stem evoked response (ABR) pattern is recognized, was

determined in each mouse [15]. Mice were anesthetized with an intramuscular injection of ketamine (75 mg/kg) and xylazine (7.5 mg/kg), and placed in a close acoustic room [15]. A stainless-steel electrode was inserted subcutaneously into the vertex (positive pole), retroauricular region (negative pole), and opposite retroauricular region (background). Acoustic stimuli, consisting of a tone burst (0.1 ms rise and fall no plateau) at a frequency of 10 kHz, were presented to each mouse with a sound stimulator (DPS-725, Diamedical System, Tokyo, Japan) and speaker (PT-R9, Pioneer, Tokyo, Japan) in an open field. For each time point, 500 responses for each mouse were recorded and filtered for band widths of 100–3000 Hz. The Neuropac μ (Nihonkoden, Tokyo, Japan) was used to analyze the ABR response.

c-Fos Immunohistochemistry

Levels of c-Fos expression were assessed by counting the number of c-Fos-immunoreactive cells [22]. Mice were deeply anesthetized with halothane (Takeda Pharmaceutical Co, Osaka, Japan) 3 h after the single injection of MK-801 (0.3 μ g/g) and perfused intracardially with PBS, followed by 4% paraformaldehyde in 0.1 M phosphate-buffer (pH 7.2). Coronal sections (40 μ m) were made by a cryostat and incubated with a blocking solution containing PBS, 5% nonfat milk and 0.25% TritonX-100 for 2 h and incubated with rabbit anti-c-Fos antibody (1:20000; PC-38, Calbiochem, La Jolla, CA, USA) in the blocking solution 48 h at 4°C, followed by biotinylated anti-rabbit immunoglobulin antibody (1:200; BA-1000, Vector Laboratories). Sections were washed and processed with the avidin-biotinylated horseradish peroxidase complex (Vector ABC kit Vector Laboratories, Burlingame, CA, USA). Immunoreactivity was visualized with the chromogen 3, 3'-diaminobenzidine. To quantify the number of c-Fos positive cells in the brain, we used an all-in-one microscope (BZ-9000, Keyence, Osaka, Japan) and a BZ-Analyzer (Keyence) to scan the sections, and quantified the cell numbers from the digital images using NIH Image (ver. 1.61) cell-counting system [23].

Behavioral Testing

Acoustic startle response and prepulse inhibition (PPI) were measured as fully described previously [10,15]. Test paradigm of context- and tone-dependent fear learning, locomotor measurement, resident-intruder assessment [24] and further procedural details of individual behavioral tests, see Supplementary Information. Three independent cohorts of mice were made for each NRG1 subtypes and each doses and assigned to the following three types of experiments; basal behavioral tests (locomotor assessment, sound startle test, and fear conditioning in the less stressful order), the MK-801 experiments, and the resident-intruder test (see below).

Statistical Analysis

Data are presented as mean \pm SEM. Computation was carried out using the SPSS 11.0 for Windows (Tokyo, Japan). Behavioral or immunohistochemical data were first subjected to the Shapiro-Wilk test (for the fitting to Gesian distribution) and Levene's test (for the equality of standard deviations) and then either one-way analysis of variance (ANOVA) or Student's t-test. ANOVA adopts NRG1-treatment as a between-subject factor, NRG1-treatment as a between-subject factor and time as a within-subject factor, or eNRG1/T1-NRG1 treatment and drug injection as between-subject factors. ABR data were subjected to two-way ANOVA with eNRG1-treatment as a between-subject factor and frequency of auditory stimulus as a within-subject factor. Other data stem from experimental groups were subjected to Student's t-test. Some of the data in the frequency of c-fos, startle responses and PPI scores had showed biased distributions or difference in deviations among groups, suggesting the risk of type 1 errors in ANOVA (Supplemental Table S1). Subsequently, a Tukey HSD test was applied to the data carrying equal deviations as a *post hoc* test. Alternatively, a Scheffe's test was applied to the data having non-equal deviations to validate the initial ANOVA assessment. When there was significant interaction between eNRG1-treatment and drug, data were analyzed separately to avoid the interaction for the final analysis. A *p* value < 0.05 was regarded as statistically significant.

RESULTS

eNRG1 Penetration into the Brain

Since the blood-brain barrier of neonatal mice is immature, peripherally administered cytokines can reach the brain [15,25]. To confirm that eNRG1 in circulation penetrates the blood-brain barrier and activates intracerebral NRG1 receptors, we subcutaneously administered eNRG1 (1.0 μ g/g) to mouse pups (PND2) and examined eNRG1 immunoreactivity and the phosphorylation of ErbB4 in the cerebrum. Immunoblotting revealed that there was eNRG1 immunoreactivity in the cerebrum of the eNRG1-injected mice but not in that of saline-injected controls (Fig. 1A). Peripheral injection of eNRG1 also significantly increased phosphorylation levels of ErbB4 [$F(4,11) = 11.4$, $p < 0.01$]. The increase persisted between 1-6 h after the injection with a peak of ErbB4 phosphorylation at 3 h (Fig. 1B, C). Thus, a peripheral injection of eNRG1 to mouse pups can produce hyper-signaling of NRG1/ErbB4 in the neonatal mouse brain.

Exploratory Activity in Novel Environment

We administered various concentrations (vehicle alone, 0.1, 0.3, and 1.0 μ g/g) of eNRG1 repeatedly to mouse neonates. We monitored several parameters of

mouse development; tooth eruption, eyelid opening, and body weight gain (Table 1). NRG1, which belongs to the EGF polypeptide family, promotes tooth eruption and eyelid opening [15,26]. A one-way ANOVA revealed that repeated eNRG1 injections significantly stimulated eyelid opening [dose: $F(3,56) = 90.31$, $p < 0.001$] and tooth eruption [dose: $F(3,56) = 35.54$,

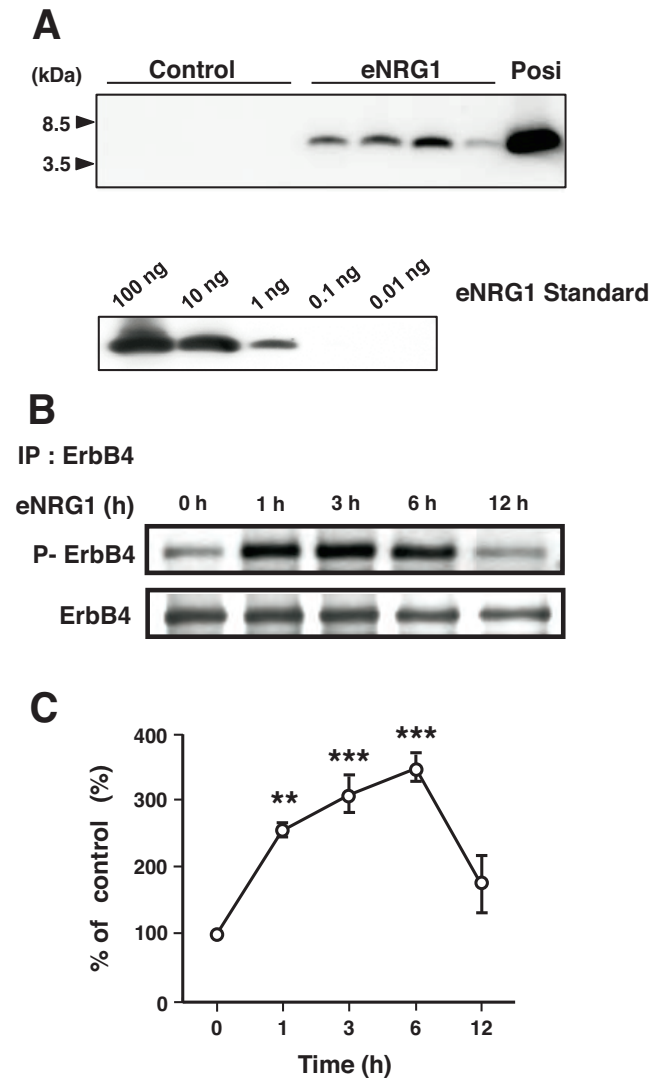


Fig. (1). ErbB4 activation and eNRG1 immunoreactivity in the brain following peripheral eNRG1 injection. **(A)** Neonatal mice (PND2) were subcutaneously challenged with eNRG1 (1.0 $\mu\text{g/g}$) and intracardially perfused with PBS 3 h after eNRG1 injection. Brain lysates (200 $\mu\text{g/lane}$) were subjected to SDS polyacrylamide electrophoresis with the authentic eNRG1 protein (1 ng; Posi). The presence of eNRG1 protein in the brain was examined by immunoblotting ($n = 4$ mice per group). **(B)** Whole brain lysates were prepared 0, 1, 3, 6, and 12 h after subcutaneous injection of eNRG1 (1.0 $\mu\text{g/g}$) to neonatal mice (PND2). ErbB4 phosphorylation levels were examined using immunoblotting for phosphotyrosine combined with ErbB4 immunoprecipitation. **(C)** Relative levels of ErbB4 phosphorylation in the brains of eNRG1-injected mice are presented (% of 0 time; mean \pm SEM, $n = 3$ per each time points). * $p < 0.05$ compared with 0 time by Tukey HSD.

$p < 0.001$] in a dose-dependent manner. These results verified the physiological activity of injected eNRG1 *in vivo*. In addition, injections with higher doses of eNRG1 (i.e. 0.3 $\mu\text{g/g}$ and 1.0 $\mu\text{g/g}$), produced a 10-20% decrease in body weight gain that persisted until adulthood (Table 1).

At the young adult stage (PND54-70), we assessed the locomotor activity of eNRG1-treated mice in a novel environment. A one-way ANOVA yielded a significant difference among eNRG1 doses [$F(3,36) = 4.6$, $p < 0.01$]. *Post hoc* comparisons revealed that the mice treated with the highest dose (1.0 $\mu\text{g/g}$) of eNRG1 displayed significantly fewer horizontal movements compared with the other three groups ($p < 0.05$) (Fig. 2A), whereas stereotypic behaviors of these mice were similar among the groups [dose: $F(3,36) = 0.7$, $p = 0.54$] (Fig. 2B). There were no significant differences in the above indices between males and females [gender \times dose: $F(3,32) = 1.23$, $p = 0.31$ for horizontal movements; gender \times dose: $F(3,32) = 0.27$, $p = 0.85$ for stereotypic movements], although stereotypic movements fundamentally differed between males and females [gender: $F(3,32) = 1.23$, $p < 0.01$].

Effects of Neonatal eNRG1-Treatment on Other Behavioral Traits

Using the mice treated with 1.0 and 0.3 $\mu\text{g/g}$ doses of eNRG1, we further analyzed other behaviors of these animals in adulthood (PND56-70) such as fear learning ability, sensorimotor gating and social behavioral traits. The mice treated with the 1.0 $\mu\text{g/g}$ dose of eNRG1 as neonates exhibited a marked reduction of PPI [eNRG1: $F(1,49) = 61.3$, $p < 0.001$, repeated ANOVA for 4 prepulses] (Table 2). There were no significant differences in eNRG1 effects between males and females [gender \times eNRG1: $F(1,47) = 2.26$, $p = 0.14$]. These mice also showed a reduction in tone-dependent learning scores but did not alter context-dependent learning scores [$F(1,39) = 0.004$, $p = 0.95$ for context-dependent learning; $F(1,39) = 23.8$, $p < 0.001$ for tone-dependent learning, both repeated ANOVA for 5 bins]. There was no significant difference in shock sensitivity [$F(1,39) = 0.005$, $p = 0.95$] (Table 2). There were no significant differences between males and females in eNRG1 effects on the above indices, either [gender \times eNRG1: $F(1,37) = 1.20$, $p = 0.28$ for conditioning; gender \times eNRG1: $F(1,37) = 0.41$, $p = 0.53$ for context-dependent learning; gender \times eNRG1: $F(1,37) = 1.87$, $p = 0.18$ for tone-dependent learning]. Similar behavioral alterations were observed when we administered the lower dose of eNRG1 (0.3 $\mu\text{g/g}$) to mouse pups (Supplemental Fig. S1). This dose (0.3 $\mu\text{g/g}$) was approximately 40 pmol per gram body weight and equivalent to the molar dose of T1-NRG1 that had been given to mouse pups in our previous study [15].

To investigate the impact of neonatal eNRG1-treatment on social behaviors in adulthood, we used a resident-intruder behavioral assay. In this assay, a group-housed male mouse (intruder) was placed in another home cage where a resident male mouse had

Table 1. Summary of physical development.

Dose	Vehicle		eNRG1	
Tooth Eruption (PND)				
0.1 µg/g	11.6 ± 0.2		10.4 ± 0.2***	
0.3 µg/g	11.6 ± 0.2		10.2 ± 0.2***	
1.0 µg/g	10.9 ± 0.2		9.4 ± 0.2***	
Eyelid Opening (PND)				
0.1 µg/g	13.9 ± 0.1		11.5 ± 0.2***	
0.3 µg/g	13.7 ± 0.2		10.8 ± 0.1***	
1.0 µg/g	13.1 ± 0.2		10.5 ± 0.2***	
Body Growth; P11				
0.1 µg/g	5.72 ± 0.13		5.52 ± 0.07	
0.3 µg/g	6.18 ± 0.20		5.62 ± 0.14*	
1.0 µg/g	6.05 ± 0.17		5.08 ± 0.22**	
Body Growth; P56	Male	Female	Male	Female
0.1 µg/g	24.2 ± 0.6	20.2 ± 0.3	23.8 ± 0.2	19.3 ± 0.3
0.3 µg/g	24.2 ± 0.6	20.3 ± 0.4	21.4 ± 0.3**	18.4 ± 0.5*
1.0 µg/g	19.4 ± 0.3	16.6 ± 0.3	17.6 ± 0.4**	14.3 ± 0.6**

eNRG1 or vehicle was administered (s.c.) daily to neonatal mice during PND2-10. During and after treatment, we monitored eyelid opening, tooth eruption and body weight of all mice. Data are expressed as mean ± SEM ($n = 10$ per group). P -values, compared between eNRG1-treated and vehicle-treated groups by unpaired two-tailed t -test. * $p < 0.05$, ** $p < 0.01$, *** $p < 0.001$.

been housed alone until the test day (Table 2). eNRG1-treated mice exhibited decreased sniffing duration compared with vehicle-treated controls ($p < 0.05$, unpaired t -test), whereas no significant difference between groups was found with sniffing counts or fighting counts (Table 2). The lower frequency of aggressive behaviors of the present mice can be ascribed to the mouse strain used in the present study (i.e., C57BL/6N) [27,28].

Effects of Neonatal eNRG1-Treatment on MK-801-Driven-Locomotor Activity

Sensitivity to psychostimulants, such as NMDA receptor antagonists, have often been evaluated in animal models to assess their relevancy to a schizophrenia model. To test whether neonatal eNRG1-treatment (0.1, 0.3, and 1.0 µg/g) alters acute responsiveness to an NMDA receptor antagonist, MK-801, in adulthood, mice were first acclimated to a novel environment to minimize the substantial difference of exploratory activity and/or motivation between groups. After one hour acclimation, mice were challenged with a 0.3 µg/g dose of MK-801 (Fig. 3). The given dose of MK-801 was the minimum dose that can induce hyperlocomotion in mice [29]. MK-801 markedly increased the locomotor activity of mice for approximately 2 h in both the eNRG1-treated and control groups [drug: $F(1,36) = 29.7$, $p < 0.001$]. However, the magnitude of

MK-801-induced locomotor activity was significantly higher in the eNRG1-treated group than in the control group [eNRG1-treatment: $F(1,36) = 5.2$, $p < 0.05$; eNRG1 × drug: $F(1,36) = 6.0$, $p < 0.05$] (Fig. 3A). The sensitivity appeared to depend on the dose of eNRG1 [eNRG1 dose: $F(1,36) = 3.2$, $p < 0.05$] (Fig. 3C). Thus, these results indicate that neonatal exposure to eNRG1 enhances behavioral sensitivity to MK-801 in a dose-dependent manner. However, there was no significant difference in MK-801-triggered stereotypic scores between eNRG1-treated and vehicle-treated control mice at any dose of eNRG1 [eNRG1 dose: $F(3,36) = 1.2$, $p = 0.34$] (Fig. 3B, D).

Effects of Neonatal eNRG1-Treatment on c-Fos-Expression in the Brain

The NMDA antagonist MK-801 increases both dopamine and glutamate efflux primarily in the forebrain regions [30,31] and induces the gene expression of c-Fos through MK-801-evoked glutamatergic neurotransmission and subsequent MAP kinase/AP-1 activation [22]. Employing c-Fos expression as a marker of neuronal activity, we examined the effects of neonatal eNRG1 treatment on MK-801-induced c-Fos expression and attempted to confirm the above observation; the higher sensitivity of eNRG1-treated mice to MK-801. We counted the number of c-Fos positive cells in the medial prefrontal cortex (mPFC), nucleus accumbens (NAc), piriform cortex, and

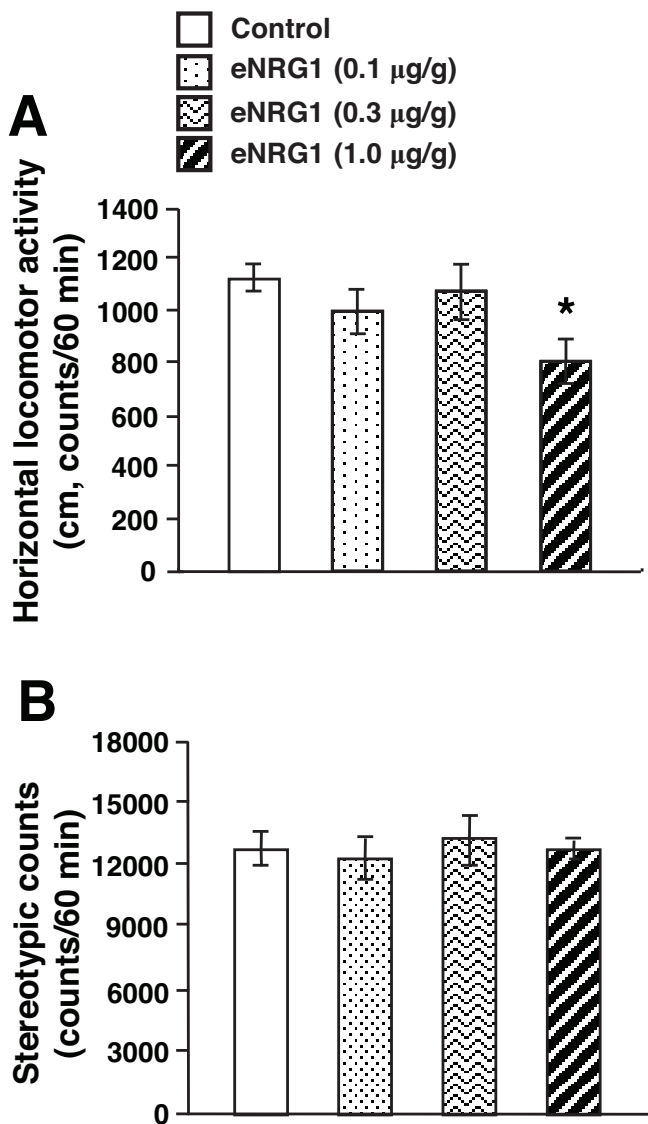


Fig. (2). Baseline locomotor activity and stereotypic behavior in a novel environment. **(A)** Total locomotor activity and **(B)** stereotypic behavior counts of eNRG1 (0.1, 0.3 and 1.0 µg/g)-treated and vehicle-treated control mice for 60 min ($n = 10$ mice per group). Data is expressed as mean \pm SEM. * $p < 0.05$ compared with control mice by Tukey HSD.

striatum. MK-801 challenge significantly increased the number of c-Fos-positive cells in these regions in both control and eNRG1-treated mice [drug: $F(1,12) = 384.1$, $p < 0.001$ for mPFC; $F(1,12) = 139$, $p < 0.001$ for NAc; $F(1,12) = 69.6$, $p < 0.001$ for piriform cortex]. In the mPFC and NAc, however, we found significant statistical interactions between MK-801 challenge and eNRG treatment [eNRG1 \times drug: $F(1,12) = 8.5$, $p < 0.05$ for mPFC, $F(1,12) = 12.4$, $p < 0.01$ for NAc]. The interactions indicate that MK-801-triggered increases in the number of c-Fos-positive cells were greater in eNRG1-treated mice than in control mice (Fig. 4A-H). In contrast, the number of c-Fos positive cells in the piriform cortex was indistinguishable in control and eNRG1-treated mice following MK-801 challenges [eNRG1-treatment: $F(1,12) = 1.4$, $p = 0.27$, eNRG1-treatment \times drug $F(1,12) = 0.6$, $p = 0.45$] (Fig. 4I). As

compared between control and eNRG1-treated mice in the saline challenged-groups, however, there was a significant difference in the basal frequency of c-Fos-positive cells in the mPFC ($p < 0.001$). In the striatum, we found no detectable increase in c-Fos expression following MK-801 challenge [drug: $F(1,12) = 0.1$, $p = 0.79$] (Fig. 4I).

Table 2. Summary of behavioral traits.

	Vehicle	eNRG1
Prepulse inhibition (% inhibition)		
73dB	20.5 \pm 3.2	-2.5 \pm 3.9***
76dB	38.5 \pm 3.5	4.7 \pm 4.8***
79dB	47.2 \pm 3.3	3.7 \pm 5.3***
82dB	57.6 \pm 3.2	8.7 \pm 4.9***
Learning (% freezing)		
Shock sensitivity	61.3 \pm 3.4	60.0 \pm 4.7
Context-dependent	66.5 \pm 1.5	65.7 \pm 2.1
Tone-dependent	66.0 \pm 1.3	41.5 \pm 3.2***
Resident-intruder test		
Sniffing Duration (sec)	178.3 \pm 8.9	145.8 \pm 8.1*
Sniffing Counts (times)	9.7 \pm 0.8	8.1 \pm 0.7
Aggression (frequency)	2.28 \pm 0.14	3.61 \pm 0.23

Neonatal mice were treated with eNRG1 (1.0 µg/g) or vehicle (control) as described in the Materials and Methods. In adulthood, PPI levels (%) were measured with 73, 76, 79 and 82 dB prepulse stimuli ($n = 25-26$ mice per group) and a main pulse of 120 dB. eNRG1-treated and vehicle-treated mice were also subjected to context-tone-foot shock pairs to evaluate their fear learning. Mean freezing rates (%) were measured for 150 sec (30 sec/bin) during conditioning or during the same context exposure and during tone exposure in the test paradigm ($n = 20-21$ mice per group). In the resident-intruder assay, we measured the total time duration of sniffing behaviors and frequency of sniffing and fighting behaviors of the resident males over a 10-min period ($n = 18$ mice per group). Data are expressed as mean \pm SEM. * $p < 0.05$, *** $p < 0.001$ by Tukey HSD or Student's t-test.

NMDA Receptor-Like Immunoreactivity in eNRG1-Treated Mice

Alterations in brain expression of NMDA receptors are often implicated in the behavioral sensitivity to the NMDA receptor blockers MK-801, phencyclidine, and ketamine [24,32]. We aimed to elucidate the molecular phenotypes underlying the hypersensitivity of eNRG1 (1.0 µg/g eNRG1)-treated mice to MK-801. Using Western blot techniques, we estimated protein levels for NMDA receptor subunits (GluN1, GluN2A-2D) and AMPA receptor subunits (GluA1-A4) in the frontal cortex, hippocampus, and striatum plus NAc (Fig. 5A). In addition to these receptors, we also examined molecular markers for GABAergic and dopaminergic neurons. Among the receptors examined, there were significant decreases in hippocampal levels of GluN2C-like immunoreactivity and frontal cortex levels of GluN2D-like immunoreactivity in eNRG1-treated mice compared with those of control mice (Fig. 5B). In addition, there was a decrease in GAD67-like

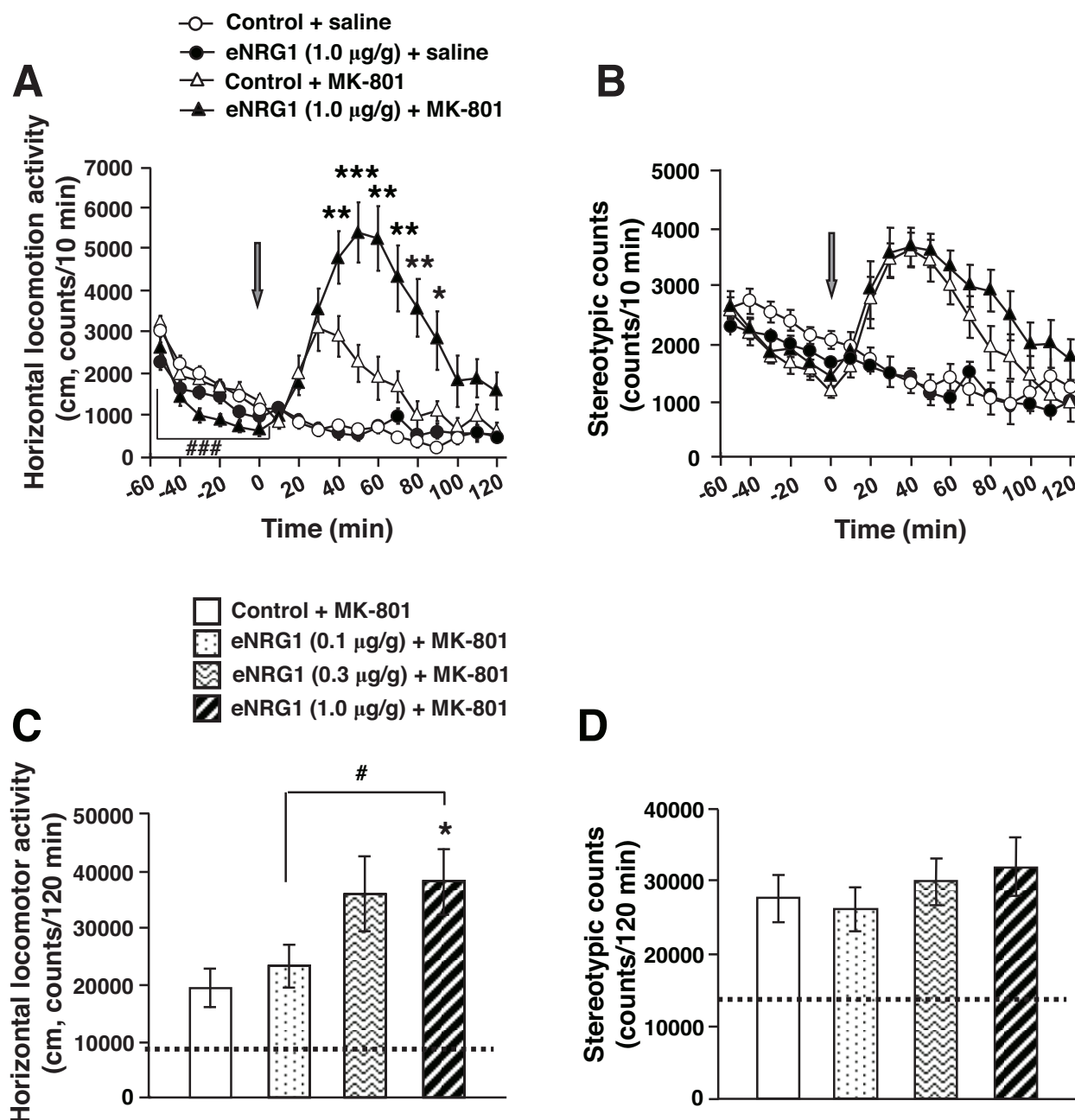


Fig. (3). Hyper-locomotor activity and stereotypic behavior induced by MK-801. **(A, C)** Horizontal locomotor activity and **(B, D)** stereotypic behavior of eNRG1 (0.1, 0.3 and 1.0 $\mu\text{g/g}$)-treated and vehicle-treated control mice were monitored before and after MK-801 (0.3 $\mu\text{g/g}$, i.p.) or saline challenge every 10 min. Prior to MK-801 challenge, mice were acclimated to a test chamber to minimize their exploratory movement. Total locomotor activity and stereotypic counts of eNRG1-treated and vehicle-treated control mice were calculated and presented ($n = 10$ mice per group). Data is expressed as mean \pm SEM. Arrows mark the timing of MK-801 challenge. * $p < 0.05$, ** $p < 0.01$ and *** $p < 0.001$ compared with vehicle-treated control mice challenged by MK-801 and # $p < 0.05$ compared between marked groups by Tukey HSD. Note; There was a significant main effect of eNRG1 treatment on total locomotor activity during the acclimation period of the four groups of mice; $F(1, 36) = 19.3$, ### $p < 0.001$ for eNRG1, $F(1,36) = 0.46$, $p = 0.503$ for MK-801, $F(1,36) = 1.46$, $p = 0.234$ for eNRG1 \times MK-801.

immunoreactivity in eNRG1-treated mice. As we performed multiple comparisons here, we attempted to compensate the statistics with a Bonferroni's method. However, the differences in GluN2C-like and GluN2D-like immunoreactivities still remained to be significant. There were no significant differences in other receptors and other GABAergic/dopaminergic markers between groups after compensation.

Distinct Sensitivity of eNRG1-Treated and T1-NRG1-Treated Mice to MK-801 But Not to Methamphetamine

Recently, we reported that neonatal exposure to full length T1-NRG1 results in behavioral impairments and hypersensitivity to methamphetamine in mice [15]. To compare the *in vivo* effects of eNRG1 and T1-NRG1,

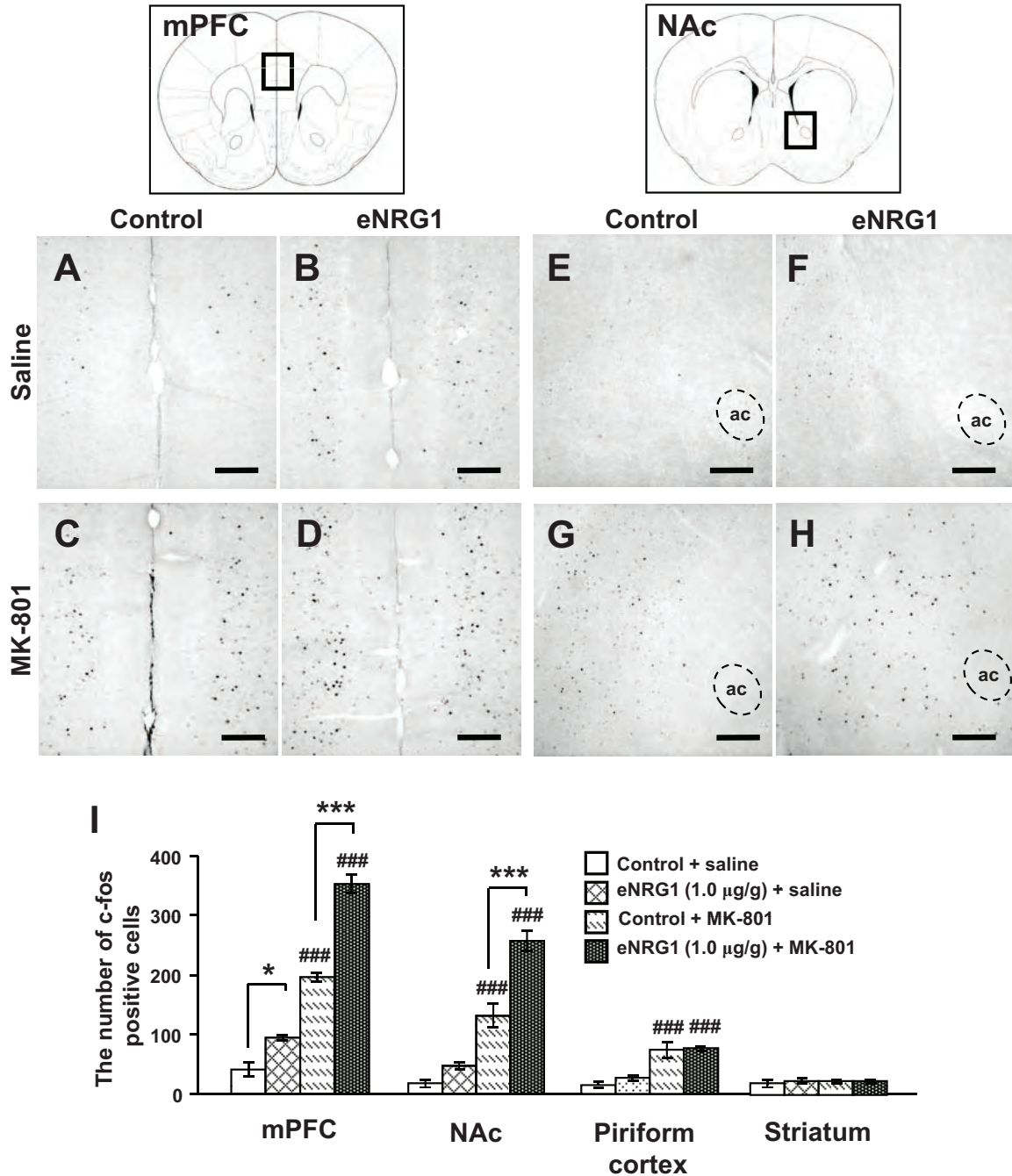
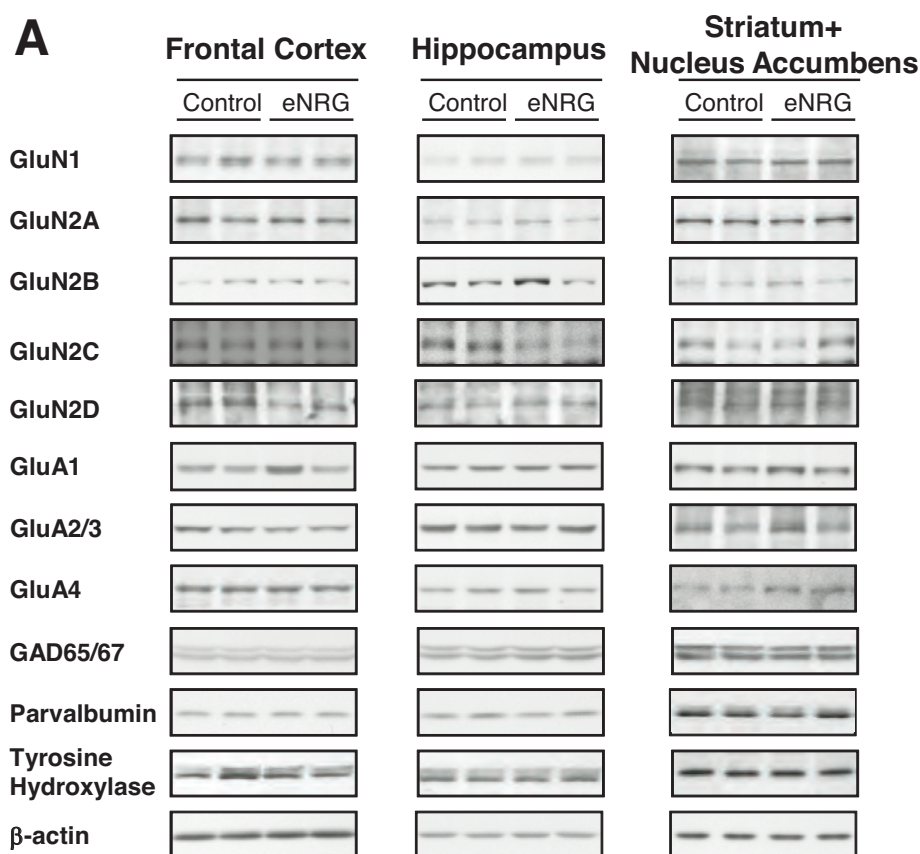


Fig. (4). Neonatal exposure to eNRG1 enhances c-Fos expression following MK-801-challenge. In adulthood, vehicle-treated mice (**A, C, E, G**) and eNRG1-treated mice (**B, D, F, H**) were subjected to c-Fos immunohistochemistry 2 h after saline (**A, B, E, F**) or MK-801 (**C, D, G, H**) challenge. Representative pictures of mPFC (prelimbic cortex; **A - D**) and NAc (**E - H**) are shown. Scale bar, 100 µm. (**I**) The number of c-Fos-positive cells in the microscopic field (725 × 965 µm) was counted bilaterally using five to seven sections of mPFC (+1.70 ~ +1.98 mm from Bregma), NAc, and striatum (+1.18 ~ +1.54 mm from Bregma), piriform cortex (+1.18 ~ +1.98 mm from Bregma), averaged for each mouse, and subjected to statistical analysis (*n* = 4 mice per group). Values are expressed as mean ± SEM. **p* < 0.05, ****p* < 0.001 compared between marked groups. ###*p* < 0.001 compared with saline-challenged groups by Scheffe's test.

we measured the sensitivity of T1-NRG1-treated and eNRG1-treated mice to the NMDA receptor antagonist and methamphetamine (Figs. 6, 7). We prepared both types of mouse models by daily administering the same molar dose of T1-NRG1 (1.0 µg/g body weight) and eNRG1 (0.3 µg/g body weight) to mouse pups, allowed

them to reach 2 months of age, and challenged with MK-801 or saline. This dose was approximately 40 pmol per gram body weight and equivalent to the molar dose of T1-NRG1 that had been given to mouse pups in our previous study [15].

**B**

	Frontal Cortex (% of control)	Hippocampus (% of control)	Striatum + Nucleus Accumbens (% of control)
GluN1 #	93 ± 4	105 ± 15	99 ± 5
GluN2A	88 ± 11	111 ± 12	99 ± 8
GluN2B #	100 ± 6	110 ± 17	98 ± 13
GluN2C	103 ± 17	50 ± 7**	79 ± 11
GluN2D #	58 ± 7**	124 ± 16	96 ± 10
GluA1 #	121 ± 13	96 ± 7	104 ± 6
GluA2/3	107 ± 3	80 ± 11	105 ± 14
GluA4 #	99 ± 2	92 ± 7	109 ± 12
GAD65	92 ± 3	116 ± 3	94 ± 3
GAD67	84 ± 3*	99 ± 2	90 ± 8
Parvalbumin	104 ± 8	96 ± 6	96 ± 7
TH	92 ± 3	80 ± 5	90 ± 7
β -actin (n=5-6)	101 ± 6	98 ± 10	97 ± 9
(n=9-10) #	104 ± 3	99 ± 5	98 ± 4

Fig. (5). Influences of neonatal eNRG1 treatment on the immunoreactivity of glutamate receptors, GABAergic and dopaminergic markers. Protein extracts were prepared from the frontal cortex, hippocampus, and striatum plus NAc of vehicle-treated and eNRG1 (1.0 μ g/g)-treated mice ($n = 4-5$ mice per group) at the adult stage (PND70-80) and subjected to immunoblotting with the antibodies directed against NMDA receptors (GluN1, GluN2A, GluN2B, GluN2C, GluN2D), AMPA receptors (GluA1, GluA2/3 and GluA4), GABAergic markers (glutamic acid decarboxylase; GAD65/67 and parvalbumin), a dopaminergic marker (TH; tyrosine hydroxylase), and a loading control (β -actin). **(A)** Typical signals of two samples in each brain region are displayed. **(B)** The intensity of the immunoreactivity appearing at the authentic size(s) was measured by densitometric analysis and subjected to an unpaired two-tailed t -test. * $p < 0.05$, ** $p < 0.01$ without Bonferroni's compensation. #) The number of samples was increased to 9 or 10 when the values of SEM from 4-5 mice had been larger than 20%; GluN1, GluN2B, GluA1, GluA4, and β -actin. Relative levels of the markers in eNRG1-treated mice are presented (% of control; mean \pm SEM; $n = 4-5$ or $n = 9-10$ for #).

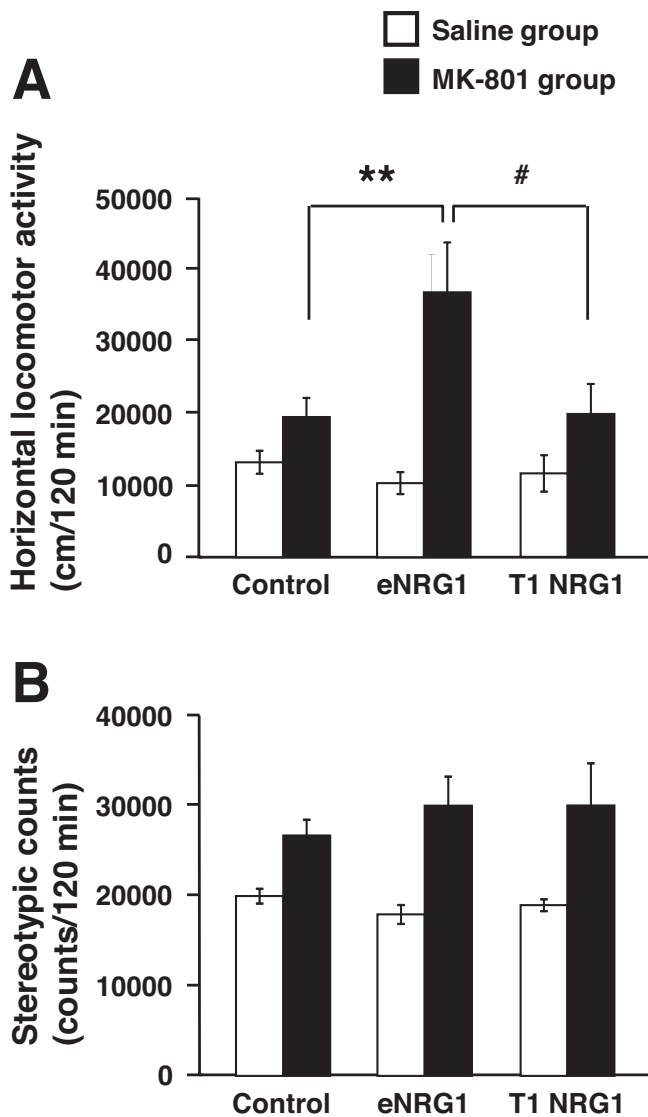


Fig. (6). Difference of eNRG1-treated and T1-NRG1-treated mice in MK-801-driven locomotor activity and stereotypic behaviors. eNRG1 (0.3 $\mu\text{g/g}$)-treated, T1-NRG1 (1.0 $\mu\text{g/g}$)-treated and vehicle-treated mice (control) as neonates were challenged with MK-801 (0.3 $\mu\text{g/g}$; black boxes) or saline (white boxes) and their horizontal locomotor activity (**A**) and stereotypic behavior (**B**) were compared. Total horizontal activity and stereotypic score of mice were measured for the 120 min period after challenge and presented with the scales of cm/120 min and counts/120 min, respectively ($n = 10-23$ mice per group). Data is expressed as mean \pm SEM. ** $p < 0.01$, compared between control and eNRG1-treated mice challenged with MK-801 and # $p < 0.05$ compared between eNRG1-treated mice challenged with MK-801 and T1-NRG1-treated mice challenged with MK-801 by Tukey HSD.

An initial 2-way ANOVA on horizontal locomotor activity, using the subject factors of NRG1 isoform and MK-801, revealed a main effect of MK-801 [$F(1,74) = 23.57$, $p < 0.001$] and a significant interaction between NRG1 isoform and MK-801 [$F(2,74) = 5.17$, $p < 0.01$]. We then stratified on MK-801 treatment (MK-801-challenged and saline-challenged groups; Fig. 6A). In the saline-challenged control groups, there was no

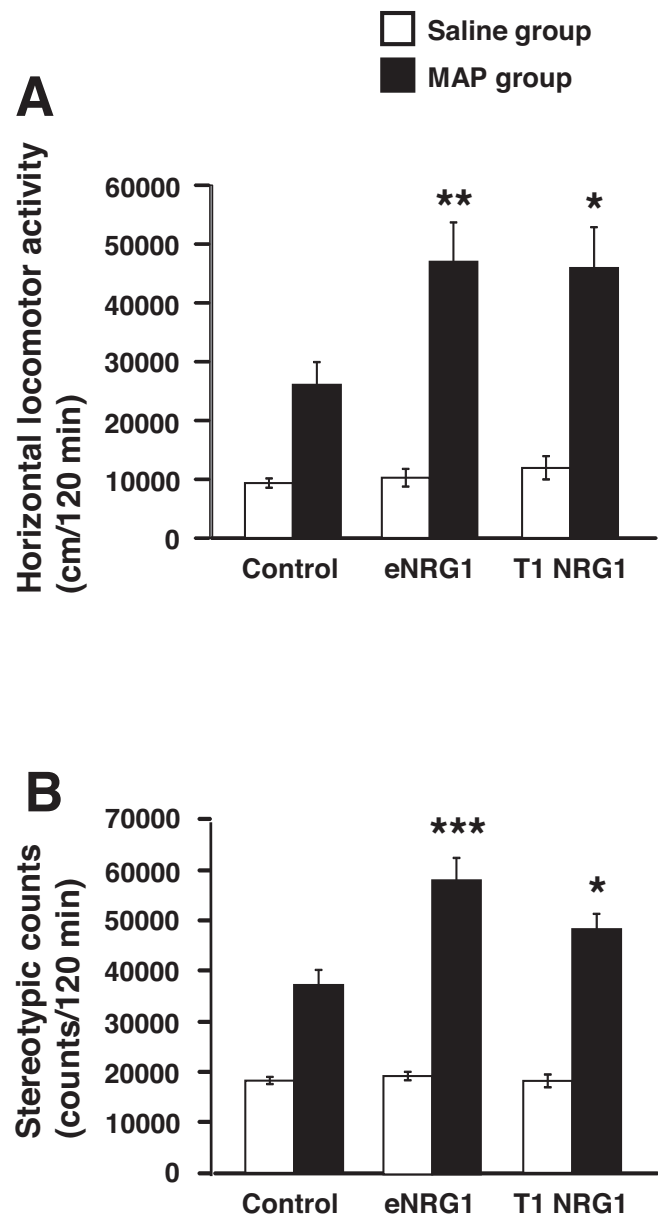


Fig. (7). Similar enhancement of eNRG1-treated and T1-NRG1-treated mice in methamphetamine-driven locomotor activity and stereotypic behaviors. eNRG1 (0.3 $\mu\text{g/g}$)-treated, T1-NRG1 (1.0 $\mu\text{g/g}$)-treated and vehicle-treated mice (control) as neonates were challenged with methamphetamine (MAP; 1.0 $\mu\text{g/g}$ black boxes) or saline (white boxes) and their horizontal locomotor activity (**A**) and stereotypic behavior (**B**) were compared. Data is expressed as mean \pm SEM. * $p < 0.05$, ** $p < 0.01$ between control and eNRG1-treated or T1-NRG1 treated mice challenged with MAP by Tukey HSD.

difference in basal locomotor activity among T1-NRG1-treated, eNRG1-treated and control mice [NRG1 isoform : $F(2,37) = 0.70$, $p = 0.50$]. A one-way ANOVA for the MK-801-challenged group revealed a significant effect of isoform [$F(2,37) = 4.80$, $p < 0.05$]. *Post-hoc* analyses suggest that MK-801-driven horizontal locomotor activity of T1-NRG1-treated mice was indistinguishable from that of control mice receiving

MK-801 whereas eNRG1-treated mice displayed a larger locomotor response to MK-801 than control mice. A two-way ANOVA for stereotypic movement revealed no significant effect of NRG1 isoform or no interaction between NRG1 isoform and MK-801 [NRG1 isoform: $F(2,74) = 0.15$, $p = 0.86$; NRG1 isoform \times MK-801: $F(2,74) = 0.99$, $p = 0.37$] (Fig. 6B). The results from the horizontal activity test revealed a significant difference in behavioral sensitivity to the NMDA receptor antagonist between T1-NRG1-treated and eNRG1-treated mice.

We also compared the magnitude of methamphetamine effects on locomotor activity. An initial 2-way ANOVA on horizontal movement, with between subject factors of NRG1 isoform and methamphetamine, revealed a main effect of methamphetamine [$F(1,92) = 60.2$, $p < 0.001$] and an interaction between NRG1 isoform and methamphetamine [$F(2,92) = 5.19$, $p < 0.01$]. We then stratified on methamphetamine treatment (methamphetamine-challenged and saline-challenged groups; Fig. 7A). In the saline-challenged groups, there were no significant differences among eNRG1-treated, T1-NRG1-treated, and control groups [$F(2,46) = 0.60$, $p = 0.56$]. A one-way ANOVA for the methamphetamine-challenged groups revealed a significant effect of NRG1 isoform [$F(2,46) = 5.68$, $p < 0.01$]. *Post-hoc* analyses detected a significant difference between eNRG1-treated and control groups and between T1-NRG1-treated and control groups, but not between eNRG1-treated and T1-NRG1-treated groups. These results suggest that neonatal treatments with eNRG1 and T1-NRG1 similarly enhance methamphetamine-induced horizontal locomotion. We analyzed the effects of NRG1 isoform on stereotypic movements in a similar manner (Fig. 7B). There was a main effect of methamphetamine [$F(1,92) = 101$, $p < 0.001$] and an interaction between NRG1 isoform and methamphetamine [$F(2,92) = 4.74$, $p < 0.05$]. Thus, we stratified on methamphetamine treatment. In the saline-challenged groups, there were no significant differences among groups [$F(2,46) = 0.0064$, $p = 0.99$]. In the methamphetamine-challenged groups, however, there was a significant effect of NRG1 isoform [$F(2,46) = 5.19$, $p < 0.01$]. *Post-hoc* tests detected a significant difference between eNRG1-treated and control groups and between T1-NRG1-treated and control groups, but not between eNRG1-treated and T1-NRG1-treated groups. These analyses suggest that neonatal treatments with eNRG1 and T1-NRG1 similarly enhance methamphetamine-triggered stereotypic movements.

Auditory Perception of eNRG1-Treated Mice

NRG1 signaling is involved in the survival of cochlear sensory neurons; thus, we tested sound startle responses of the mice treated with eNRG1 (0.3 and 1.0 $\mu\text{g/g}$) to increasing noises and also measured the auditory stimulus thresholds in different tone frequencies. In the sound startle response test, the lower dose of eNRG1-treated mice exhibited a marked increase in startle responses to 110-dB and 120-dB tones, compared with control mice [eNRG1 \times pulse:

$F(6,114) = 30.6$, $p < 0.001$] (Fig. 8A). Conversely, the eNRG1-treated mice exhibited marked increases in the auditory stimulus thresholds at all stimulus frequencies at the ABR test [eNRG1 \times stimulus frequencies: $F(5,90) = 11.2$, $p < 0.001$] (Fig. 8B). The mice treated with the higher dose of eNRG1 (1.0 $\mu\text{g/g}$) similarly exhibited the increases in startle responses and the auditory stimulus thresholds [eNRG1 \times pulse: $F(6,114) = 21.4$, $p < 0.001$ for startle responses; eNRG1 \times stimulus frequencies: $F(5,90) = 13.4$, $p < 0.001$ for auditory stimulus thresholds] (Fig. 8A, B). The results from the ABR test suggest deterioration in hearing of eNRG1-treated mice. We speculate that, in the sound startle response test, the saturated levels of tone stimuli appear to produce higher startle responses in burst-noise-naïve eNRG1-treated mice with deterioration in hearing.

DISCUSSION

In our preceding study, mice pups were treated with T1-NRG1 and their behavioral consequences were analyzed with respect to the relevancy to an animal model for schizophrenia [15]. The T1-NRG1-treated animals exhibit various behavioral abnormalities in PPI and social traits but their gross learning performance and hearing ability are normal [15]. In addition to the isoform of T1-NRG1, here mouse pups were challenged with eNRG1, the core domain peptide that is produced by the neuropsin-dependent processing of T1-NRG1 [7]. In agreement with the preceding results from T1-NRG1-treated mice, transient exposure of eNRG1 during the neonatal stage similarly altered adult behavioral traits in PPI and resident-intruder test. Even though the mice were treated with the same molar dose of NRG1, eNRG1-treated mice exhibited additional behavioral deficits in tone-dependent fear learning, sound-startle responses and sensitivity to the NMDA receptor antagonist MK-801.

We also found that eNRG1-treated mice have a hearing disability. This finding is consistent with the previous report that ErbB4 signals regulate the development of hair follicles in the inner ear and that the manipulation of NRG1 signals indeed impair hearing in mice [33,34]. In this context, we can suggest that the deficits in prepulse inhibition, sound-startle responses, and tone-dependent learning of eNRG1-treated mice are, in part, due to the deterioration in hearing.

The decrease of 1.0 $\mu\text{g/g}$ eNRG1-treated mice in exploratory movement is also noteworthy. In contrast to the basal locomotor reduction, these mice rather exhibited the higher locomotor responses following MK-801 challenge. Although the lower basal movement might reflect the elevation of their anxiety levels, we do not rule out the possibility that these behavioral features of eNRG1-treated mice might be indirectly influenced by their deterioration in hearing as well.

In the present study, we additionally prepared the animal treated with the full soluble type 1 isoform of T1-NRG1 at the same molar dose of eNRG1 and

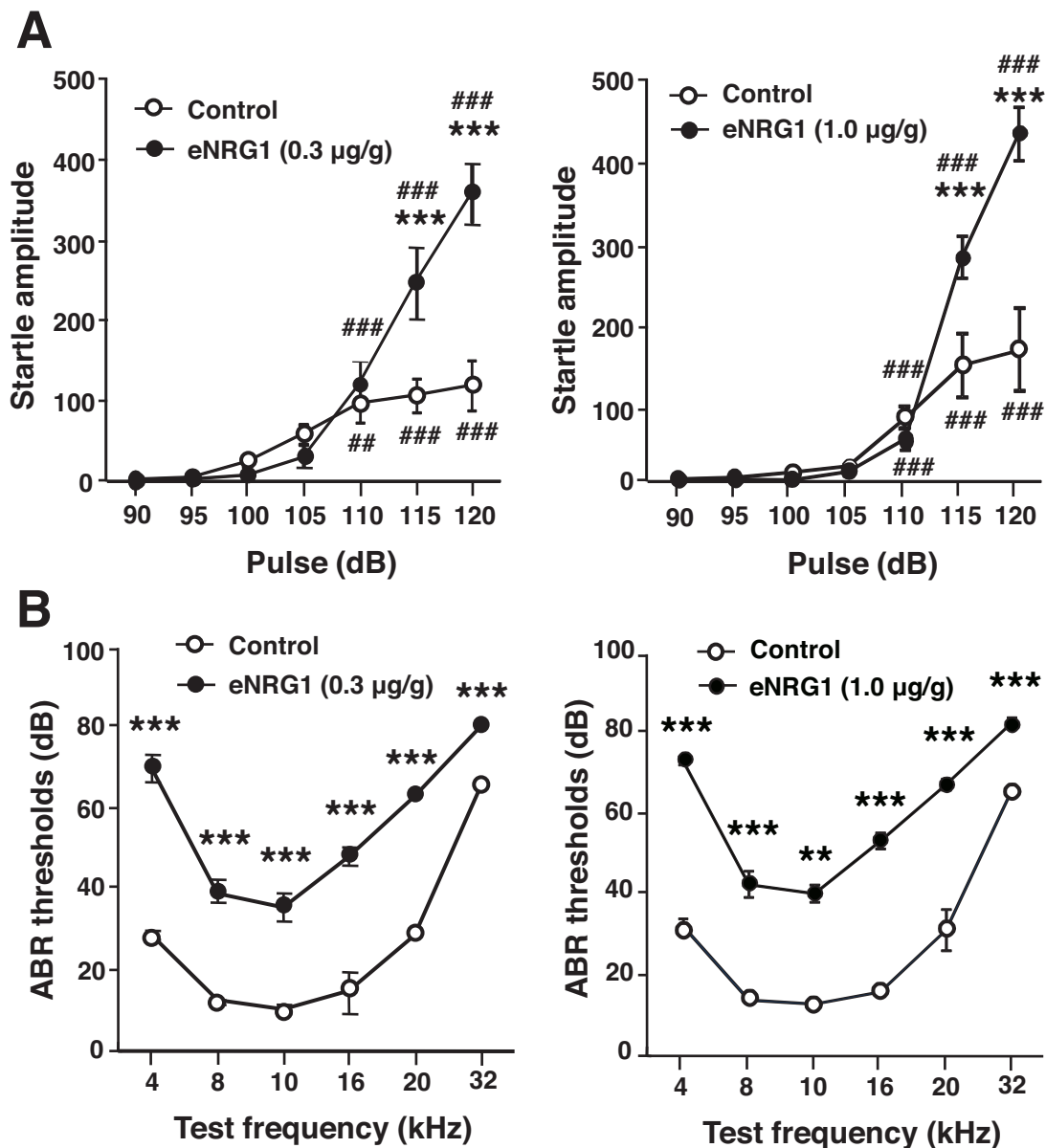


Fig. (8). Auditory responses of eNRG1-treated mice as adults. **(A)** Relative amplitudes of startle responses of eNRG1 (left; 0.3 µg/g and right; 1.0 µg/g)-treated and vehicle-treated mice (control) were monitored with 90 – 120 dB tones ($n = 10$ mice per group). Data is expressed as mean \pm SEM. *** $p < 0.001$ compared between groups. # $p < 0.01$ and ### $p < 0.001$ compared with startle levels at 90 dB by Tukey HSD. **(B)** ABR thresholds of eNRG1 (left; 0.3 µg/g and right; 1.0 µg/g)-treated and vehicle-treated mice were determined with specific auditory stimuli (4, 8, 10, 16, 20, and 32 kHz) by varying the sound pressure levels ($n = 9-11$ mice per group). Data is expressed as mean \pm SEM. ** $p < 0.01$ and *** $p < 0.001$ compared between groups by Scheffe's test.

compared the sensitivities of eNRG1-treated and T1-NRG1-treated mice to two psychotomimetics, MK-801 and methamphetamine. The MK-801-driven locomotor enhancement was larger in mice treated with eNRG1 as neonates, compared with T1-NRG1-treated mice, even though the given molar concentration of T1-NRG1 was nearly equal to the dose of eNRG1. The hypersensitivity of the eNRG1-treated mice to MK-801 was also apparent in the magnitude of c-Fos induction in the brain. Following MK-801 challenge, eNRG1-treated mice contained a higher number of c-Fos-positive cells in the mPFC as well as in the NAC than control mice receiving MK-801. Both brain regions are

implicated as target regions of MK-801 [35]. In contrast to the responses to MK-801, there were no significant difference in methamphetamine-triggered locomotor enhancement between T1-NRG1-treated and eNRG1-treated mice. The behavioral difference of T1-NRG1-treated and eNRG1-treated mice might reflect qualitative differences in *in vivo* activities of eNRG1 and T1-NRG1. Alternatively, the quantitative difference in the efficacy of blood-brain barrier permeability or in metabolic rates in the brain might underly the behavioral difference between these NRG1 variants. However, the magnitude and peak time of ErbB4 phosphorylation appeared to be similar between

eNRG1 and T1-NRG1 (i.e. both ~3-fold increases three hours after injection of their 1.0 µg/g dose) [15].

Several reports indicate the activity difference among NRG1 splicing variants. Major splicing variants of NRG1 (type 1; NDF, type 2; GGF, and type 3; SMDF) exhibit distinct interactions to individual ErbB1-4 receptor subtypes, presumably leading to distinct biological effects in the brain [35,36]. NRG1 isoforms exhibit qualitative differences due to their specific structures such as an immunoglobulin-like domain. This domain, which is found in T1-NRG1 but not eNRG1, carries a heparin binding activity and regulates tissue distribution and receptor interactions of the ligand [7,37,38].

eNRG1 is produced from T1-NRG1 as well as potentially from the type2 isoform of NRG1 through the neuroprotease-dependent proteolytic processing [7]. The protease neuroprotease recognizes and cleaves the immunoglobulin-like domain of the NRG1 precursors and liberate their carboxyl terminal domain; eNRG1. Tamura *et al.* [7] demonstrate the biological implication of the neuroprotease-dependent NRG1 processing in hippocampal synapse plasticity. As the molar dose of eNRG1 was adjusted to that of T1-NRG1 in some of the present experiments, their dose difference cannot illustrate the behavioral differences between T1-NRG1-treated and eNRG1-treated mice. Nonetheless, the present results demonstrate that the biological actions of individual NRG1 variants significantly differ *in vivo* and result in distinct behavioral consequences. Corroborating our findings, mice deficient in type 3 NRG1 exhibit distinct behavioral deficits from type 1 NRG1-knockout mice [8,9,11]. However, it remains to be explored whether the present behavioral differences of T1-NRG1-treated and eNRG1-treated mice are ascribed to the unique activity of the immunoglobulin-like domain or that of the neuroprotease-cleaving product eNRG1 [7,38].

To elucidate the molecular underpinnings of the given hypersensitivity to the NMDA receptor antagonist, we assessed the neurochemical influences of eNRG1 in adulthood, focusing on NMDA-type and AMPA-type glutamate receptors. There were reductions in NMDA receptor-like immunoreactivities (i.e. GluN2C and GluN2D) in the frontal cortex and hippocampus of eNRG1-treated mice, which can be involved in the hypersensitivity to MK-801. The specificity of the anti-GluN2D antibody, but not that for the anti-GluN2C antibody, has been verified with the use of knockout mice [39,40] Although the molecular nature of the present GluN2C-like immunoreactivity required further validation, the above arguments are in agreement with the observation that NMDA receptor-hypomorphic mutant mice show hypersensitivity to an NMDA receptor blocker [24,41]. Recently, Belforte *et al.* (2010) also provide supportive evidence that the psychometric activity of MK-801 is ascribed to a decrease in the NMDA receptor sensitivity of parvalbumin-positive GABA neurons during postnatal development [42]. As parvalbumin-positive GABA neurons are enriched with ErbB4 receptors for NRG1,

the expression of NMDA receptors in this cell population might be affected by excess eNRG1 in the present model [43-46]. However, we do not rule out the possibility that the eNRG1-driven hypersensitivity to MK-801 may involve glutamatergic, dopaminergic, or cholinergic brain circuits as suggested previously [47].

NRG1 is one of the most promising candidate genes for schizophrenia. Most of the single nucleotide polymorphisms (SNPs) associating with schizophrenia are located in the genomic promoter region and introns of the 5'-side of the *NRG1* gene [4,48,49]. Although the functional effects of these polymorphisms on gene transcription or alternative splicing of NRG1 isoforms are largely speculative, postmortem studies indicate that schizophrenic alterations of NRG1 mRNA levels are isoform-specific [3,50,51]. In agreement, the individual SNPs in human *NRG1* are differentially implicated in psychotic symptoms, spatial working memory capacity, and white matter density and integrity [52,53]. In addition to schizophrenia, the genetic and neuropathologic association with NRG1 is implicated in several other psychiatric disease major depression, and bipolar disorder as well although several controversies still remain [54,55]. The differential expression of NRG1 processing enzymes is reported in schizophrenia and bipolar disorder [56]. Thus differential processing of NRG1 protein may contribute to the disease specificity as well.

The present results indicate that the composition of NRG1 isoforms might influence behavioral or cognitive traits in humans as well. Future studies should investigate the biological or pathological actions of individual NRG1 splicing isoforms underlying the SNP-dependent cognitive and anatomical traits in normal subjects and/or patients with schizophrenia.

ABBREVIATIONS

ABR	= Auditory brain-stem evoked response
ANOVA	= Analysis of variance
EGF	= Epidermal growth factor
eNRG1	= An epidermal growth factor domain peptide of neuregulin-1
mPFC	= Medial prefrontal cortex
NAc	= Nucleus accumbens
NRG1	= Neuregulin-1
PBS	= Phosphate-buffered saline
PND	= Postnatal day
PPI	= Prepulse inhibition
SNP	= Single nucleotide polymorphisms
T1-NRG1	= Type1 neuregulin-1

CONFLICT OF INTEREST

The authors confirm that this article content has not conflicts of interest.

ACKNOWLEDGEMENTS

The authors are grateful to Minoru Tanaka and Michisuke Yokoyama for their assistance with mouse breeding. This work was supported by MEXT KAKENHI (No.24116010), JSPS KAKENHI (No. 22300107), and a grant for Promotion of Niigata University Research Projects.

SUPPLEMENTARY MATERIAL

Supplementary material is available on the publisher's web site along with the published article.

REFERENCES

- [1] Stefansson H, Sigurdsson E, Steinthorsdottir V, *et al.* Neuregulin 1 and susceptibility to schizophrenia. *Am J Hum Genet* 2002; 71(4): 877-92.
- [2] Green EK, Raybould R, Macgregor S, *et al.* Operation of the schizophrenia susceptibility gene, neuregulin 1, across traditional diagnostic boundaries to increase risk for bipolar disorder. *Arch Gen Psychiatry* 2005; 62(6): 642-8.
- [3] Chong VZ, Thompson M, Beltaifa S, Webster MJ, Law AJ, Weickert CS. Elevated neuregulin-1 and ErbB4 protein in the prefrontal cortex of schizophrenic patients. *Schizophr Res* 2008; 100(1-3): 270-80.
- [4] Steinthorsdottir V, Stefansson H, Ghosh S, *et al.* Multiple novel transcription initiation sites for NRG1. *Gene* 2004; 342(1): 97-105.
- [5] Mei L, Xiong WC. Neuregulin 1 in neural development, synaptic plasticity and schizophrenia. *Nat Rev Neurosci* 2008; 9(6): 437-52.
- [6] Shamir A, Buonanno A. Molecular and cellular characterization of Neuregulin-1 type IV isoforms. *J Neurochem* 2010; 113(5): 1163-76.
- [7] Tamura H, Kawata M, Hamaguchi S, Ishikawa Y, Shiosaka S. Processing of neuregulin-1 by neuropsin regulates GABAergic neuron to control neural plasticity of the mouse hippocampus. *J Neurosci* 2012; 32(37): 12657-72.
- [8] Chen YJ, Johnson MA, Lieberman MD, *et al.* Type III neuregulin-1 is required for normal sensorimotor gating, memory-related behaviors, and corticostriatal circuit components. *J Neurosci* 2008; 28(27): 6872-83.
- [9] Rimer M, Barrett DW, Maldonado MA, Vock VM, Gonzalez-Lima F. Neuregulin-1 immunoglobulin-like domain mutant mice: clozapine sensitivity and impaired latent inhibition. *Neuroreport* 2005; 16(3): 271-5.
- [10] Kato T, Kasai A, Mizuno M, *et al.* Phenotypic characterization of transgenic mice overexpressing neuregulin-1. *PLoS One* 2010; 5(12): e14185.
- [11] Karl T, Burne TH, Van den Buuse M, Chesworth R. Do transmembrane domain neuregulin 1 mutant mice exhibit a reliable sensorimotor gating deficit? *Behav Brain Res* 2011; 223(2): 336-41.
- [12] Yin DM, Chen YJ, Lu YS, *et al.* Reversal of behavioral deficits and synaptic dysfunction in mice overexpressing neuregulin 1. *Neuron* 2013; 78(4): 644-57.
- [13] Meyer U. Developmental neuroinflammation and schizophrenia. *Prog Neuropsychopharmacol Biol Psychiatry* 2013; 42: 20-34.
- [14] Iwakura Y, Nawa H. ErbB1-4-dependent EGF/neuregulin signals and their cross talk in the central nervous system: pathological implications in schizophrenia and Parkinson's disease. *Front Cell Neurosci* 2013; 7: 4.
- [15] Kato T, Abe Y, Sotoyama H, *et al.* Transient exposure of neonatal mice to neuregulin-1 results in hyperdopaminergic states in adulthood: implication in neurodevelopmental hypothesis for schizophrenia. *Mol Psychiatry* 2011; 16(3): 307-20.
- [16] Ozaki M, Sasner M, Yano R, Lu HS, Buonanno A. Neuregulin-beta induces expression of an NMDA-receptor subunit. *Nature* 1997; 390(6661): 691-4.
- [17] Gu Z, Jiang Q, Fu AK, Ip NY, Yan Z. Regulation of NMDA receptors by neuregulin signaling in prefrontal cortex. *J Neurosci* 2005; 25(20): 4974-84.
- [18] Hahn CG, Wang HY, Cho DS, *et al.* Altered neuregulin 1-erbB4 signaling contributes to NMDA receptor hypofunction in schizophrenia. *Nat Med* 2006; 12(7): 824-8.
- [19] Pitcher GM, Kalia LV, Ng D, *et al.* Schizophrenia susceptibility pathway neuregulin 1-ErbB4 suppresses Src upregulation of NMDA receptors. *Nat Med* 2011; 17(4): 470-8.
- [20] Futamura T, Kakita A, Tohmi M, Sotoyama H, Takahashi H, Nawa H. Neonatal perturbation of neurotrophic signaling results in abnormal sensorimotor gating and social interaction in adults: implication for epidermal growth factor in cognitive development. *Mol Psychiatry* 2003; 8: 19-29.
- [21] Savonenko AV, Melnikova T, Laird FM, Stewart KA, Price DL, Wong PC. Alteration of BACE1-dependent NRG1/ErbB4 signaling and schizophrenia-like phenotypes in BACE1-null mice. *Proc Natl Acad Sci U S A* 2008; 105(14): 5585-90.
- [22] Chartoff EH, Heusner CL, Palmiter RD. Dopamine is not required for the hyperlocomotor response to NMDA receptor antagonists. *Neuropsychopharmacology* 2005; 30(7): 1324-33.
- [23] Brown HE, Garcia MM, Harlan RE. A two focal plane method for digital quantification of nuclear immunoreactivity in large brain areas using NIH-image software. *Brain Res Protoc* 1998; 2(4): 264-72.
- [24] Mohn AR, Gainetdinov RR, Caron MG, Koller BH. Mice with reduced NMDA receptor expression display behaviors related to schizophrenia. *Cell* 1999; 98(4): 427-36.
- [25] Tohmi M, Tsuda N, Zheng Y, *et al.* The cellular and behavioral consequences of interleukin-1 alpha penetration through the blood-brain barrier of neonatal rats: a critical period for efficacy. *Neuroscience* 2007; 150(1): 234-50.
- [26] Tohmi M, Tsuda N, Mizuno M, Takei N, Frankland PW, Nawa H. Distinct influences of neonatal epidermal growth factor challenge on adult neurobehavioral traits in four mouse strains. *Behav Genet* 2005; 35(5): 615-29.
- [27] Abramov U, Puussaar T, Raud S, Kurrikoff K, Vasar E. Behavioural differences between C57BL/6 and 129S6/SvEv strains are reinforced by environmental enrichment. *Neurosci Lett* 2008; 443(3): 223-7.
- [28] Parmigiani S, Palanza P, Rogers J, Ferrari PF. Selection, evolution of behavior and animal models in behavioral neuroscience. *Neurosci Biobehav Rev* 1999; 23(7): 957-69.
- [29] Liljequist S, Ossowska K, Grabowska-Andén M, Andén NE. Effect of the NMDA receptor antagonist, MK-801, on locomotor activity and on the metabolism of dopamine in various brain areas of mice. *Eur J Pharmacol* 1991; 195(1): 55-61.
- [30] Krystal JH, Karper LP, Seibyl JP, *et al.* Subanesthetic effects of the noncompetitive NMDA antagonist, ketamine, in humans. Psychotomimetic, perceptual, cognitive, and neuroendocrine responses. *Arch Gen Psychiatry* 1994; 51(3): 199-214.
- [31] Lahti AC, Koffel B, LaPorte D, Tamminga CA. Subanesthetic doses of ketamine stimulate psychosis in schizophrenia. *Neuropsychopharmacology* 1995; 13(1): 9-19.
- [32] Hagino Y, Kasai S, Han W, *et al.* Essential role of NMDA receptor channel $\epsilon 4$ subunit (GluN2D) in the effects of phencyclidine, but not methamphetamine. *PLoS One* 2010; 5(10): e13722.
- [33] Stankovic K, Rio C, Xia A, *et al.* Survival of adult spiral ganglion neurons requires erbB receptor signaling in the inner ear. *J Neurosci* 2004; 24(40): 8651-61.
- [34] Morris JK, Maklad A, Hansen LA, *et al.* A disorganized innervation of the inner ear persists in the absence of ErbB2. *Brain Res* 2006; 1091(1): 186-99.
- [35] Bakshi VP, Geyer MA. Multiple limbic regions mediate the disruption of prepulse inhibition produced in rats by the noncompetitive NMDA antagonist dizocilpine. *J Neurosci* 1998; 18(20): 8394-401.
- [36] Osheroff PL, Tsai SP, Chiang NY, *et al.* Receptor binding and biological activity of mammalian expressed sensory and

- motor neuron-derived factor (SMDF). *Growth Factors* 1999; 16(3): 241-53.
- [37] O'Tuathaigh CM, Babovic D, O'Sullivan GJ, *et al.* Phenotypic characterization of spatial cognition and social behavior in mice with 'knockout' of the schizophrenia risk gene neuregulin 1. *Neuroscience* 2007; 147(1): 18-27.
- [38] Pankonin MS, Gallagher JT, Loeb JA. Specific structural features of heparan sulfate proteoglycans potentiate neuregulin-1 signaling. *J Biol Chem* 2005; 280(1): 383-8.
- [39] Obiang P, Macrez R, Jullienne A, *et al.* GluN2D subunit-containing NMDA receptors control tissue plasminogen activator-mediated spatial memory. *J Neurosci* 2012; 32(37): 12726-34.
- [40] Bai N, Aida T, Yanagisawa M, *et al.* NMDA receptor subunits have different roles in NMDA-induced neurotoxicity in the retina. *Mol Brain* 2013; 6: 34.
- [41] Duncan GE, Moy SS, Perez A, *et al.* Deficits in sensorimotor gating and tests of social behavior in a genetic model of reduced NMDA receptor function. *Behav Brain Res* 2004; 153(2): 507-19.
- [42] Belforte JE, Zsiros V, Sklar ER, *et al.* Postnatal NMDA receptor ablation in corticolimbic interneurons confers schizophrenia-like phenotypes. *Nat Neurosci* 2010; 13(1): 76-83.
- [43] Vullhorst D, Neddens J, Karavanova I, *et al.* Selective expression of ErbB4 in interneurons, but not pyramidal cells, of the rodent hippocampus. *J Neurosci* 2009; 29(39): 12255-64.
- [44] Abe Y, Namba H, Kato T, Iwakura Y, Nawa H. Neuregulin-1 signals from the periphery regulate AMPA receptor sensitivity and expression in GABAergic interneurons in developing neocortex. *J Neurosci* 2011; 31(15): 5699-709.
- [45] Ting AK, Chen Y, Wen L, *et al.* Neuregulin 1 promotes excitatory synapse development and function in GABAergic interneurons. *J Neurosci* 2011; 31(1): 15-25.
- [46] Shamir A, Kwon OB, Karavanova I, *et al.* The importance of the NRG-1/ErbB4 pathway for synaptic plasticity and behaviors associated with psychiatric disorders. *J Neurosci* 2012; 32(9): 2988-97.
- [47] Jentsch JD, Roth RH. The neuropsychopharmacology of phencyclidine: from NMDA receptor hypofunction to the dopamine hypothesis of schizophrenia. *Neuropsychopharmacology* 1999; 20(3): 201-25.
- [48] Munafò MR, Thiselton DL, Clark TG, Flint J. Association of the NRG1 gene and schizophrenia: a meta-analysis. *Mol Psychiatry* 2006; 11(6): 539-46.
- [49] Li D, Collier DA, He L. Meta-analysis shows strong positive association of the neuregulin 1 (NRG1) gene with schizophrenia. *Hum Mol Genet* 2006; 15(12): 1995-2002.
- [50] Hashimoto R, Straub RE, Weickert CS, Hyde TM, Kleinman JE, Weinberger DR. Expression analysis of neuregulin-1 in the dorsolateral prefrontal cortex in schizophrenia. *Mol Psychiatry* 2004; 9(3): 299-307.
- [51] Law AJ, Lipska BK, Weickert CS, *et al.* Neuregulin 1 transcripts are differentially expressed in schizophrenia and regulated by 5' SNPs associated with the disease. *Proc Natl Acad Sci U S A* 2006; 103(17): 6747-52.
- [52] Hall J, Whalley HC, Job DE, *et al.* A neuregulin 1 variant associated with abnormal cortical function and psychotic symptoms. *Nat Neurosci* 2006; 9(12): 1477-8.
- [53] McIntosh AM, Moorhead TW, Job D, *et al.* The effects of a neuregulin 1 variant on white matter density and integrity. *Mol Psychiatry* 2008; 13(11): 1054-9.
- [54] Thomson PA, Christoforou A, Morris SW, *et al.* Association of Neuregulin 1 with schizophrenia and bipolar disorder in a second cohort from the Scottish population. *Mol Psychiatry* 2007; 12(1): 94-104.
- [55] Bousman CA, Potiradis M, Everall IP, Gunn JM. Effects of neuregulin-1 genetic variation and depression symptom severity on longitudinal patterns of psychotic symptoms in primary care attendees. *Am J Med Genet B Neuropsychiatr Genet* 2014; 165B(1): 62-7.
- [56] Marballi K, Cruz D, Thompson P, Walss-Bass C. Differential neuregulin 1 cleavage in the prefrontal cortex and hippocampus in schizophrenia and bipolar disorder: preliminary findings. *PLoS One* 2012; 7(5): e36431.

RESEARCH

Open Access



Assessment of copy number variations in the brain genome of schizophrenia patients

Miwako Sakai^{1,2}, Yuichiro Watanabe², Toshiyuki Someya², Kazuaki Araki¹, Masako Shibuya², Kazuhiro Niizato³, Kenichi Oshima³, Yasuto Kunii⁴, Hirooki Yabe⁴, Junya Matsumoto⁴, Akira Wada⁴, Mizuki Hino⁴, Takeshi Hashimoto⁵, Akitoyo Hishimoto⁵, Noboru Kitamura⁵, Shuji Iritani^{3,6}, Osamu Shirakawa^{5,7}, Kiyoshi Maeda^{5,8}, Akinori Miyashita⁹, Shin-ichi Niwa⁴, Hitoshi Takahashi¹⁰, Akiyoshi Kakita¹⁰, Ryozo Kuwano⁹ and Hiroyuki Nawa^{1*}

Abstract

Background: Cytogenomic mutations and chromosomal abnormality are implicated in the neuropathology of several brain diseases. Cell heterogeneity of brain tissues makes their detection and validation difficult, however. In the present study, we analyzed gene dosage alterations in brain DNA of schizophrenia patients and compared those with the copy number variations (CNVs) identified in schizophrenia patients as well as with those in Asian lymphocyte DNA and attempted to obtain hints at the pathological contribution of cytogenomic instability to schizophrenia.

Results: Brain DNA was extracted from postmortem striatum of schizophrenia patients and control subjects ($n = 48$ each) and subjected to the direct two color microarray analysis that limits technical data variations. Disease-associated biases of relative DNA doses were statistically analyzed with Bonferroni's compensation on the premise of brain cell mosaicism. We found that the relative gene dosage of 85 regions significantly varied among a million of probe sites. In the candidate CNV regions, 26 regions had no overlaps with the common CNVs found in Asian populations and included the genes (i.e., ANTXRL, CHST9, DNM3, NDST3, SDK1, STRC, SKY) that are associated with schizophrenia and/or other psychiatric diseases. The majority of these candidate CNVs exhibited high statistical probabilities but their signal differences in gene dosage were less than 1.5-fold. For test evaluation, we rather selected the 10 candidate CNV regions that exhibited higher aberration scores or larger global effects and were thus confirmable by PCR. Quantitative PCR verified the loss of gene dosage at two loci (1p36.21 and 1p13.3) and confirmed the global variation of the copy number distributions at two loci (11p15.4 and 13q21.1), both indicating the utility of the present strategy. These test loci, however, exhibited the same somatic CNV patterns in the other brain region.

Conclusions: The present study lists the candidate regions potentially representing cytogenomic CNVs in the brain of schizophrenia patients, although the significant but modest alterations in their brain genome doses largely remain to be characterized further.

Keywords: CNV, Caudate, Genome instability, Schizophrenia, Somatic mutation

Background

Copy number variation (CNV) is defined as a deletion or duplication/multiplication of a genomic fragment spanning more than 1 kb when compared to a reference genome [1–3]. Approximately 37,000 sites of common CNVs have been identified in the human genome and they occupy 12 % of the entire genome [4, 5]. The genome-wide

association studies (GWAS) on schizophrenia analyzed DNA which was isolated from peripheral lymphocytes and have identified risk CNV sites, some of which are not present in the patients' parents [6–9].

Somatic mosaicism of genome sequences and structures have recently drawn particular attention [10–12]. Nearly 30 % of developing brain cells in human are reported to harbor aberrant chromosomal compositions [13, 14]. In addition, there are significant genomic differences in somatic cells between monozygotic twins and among tissues [15–18]. Accordingly, aberrant cytogenomic variations in

* Correspondence: hnawa@bri.niigata-u.ac.jp

¹Department of Molecular Neurobiology, Brain Research Institute, Niigata University, 1-757, Asahimachi-dori, 951-8585 Niigata, Japan
Full list of author information is available at the end of the article



© 2015 Sakai et al. This is an Open Access article distributed under the terms of the Creative Commons Attribution License (<http://creativecommons.org/licenses/by/4.0/>), which permits unrestricted use, distribution, and reproduction in any medium, provided the original work is properly credited. The Creative Commons Public Domain Dedication waiver (<http://creativecommons.org/publicdomain/zero/1.0/>) applies to the data made available in this article, unless otherwise stated.

human brain are implicated in neurodegenerative and neurodevelopmental disorders such as Alzheimer's disease, amyotrophic lateral sclerosis, and Huntington's diseases [19–25]. It is an open question whether the brain-specific somatic mutation or CNV might also contribute to the etiology or neuropathology of schizophrenia [26–28].

To obtain hints at the above question, we prepared DNA from the brain tissue of 48 schizophrenia patients and 48 control subjects. Labeling brain DNA samples, we directly applied those to Agilent 1 M comparative genomic hybridization (CGH) arrays to measure relative gene doses without the use of reference genome. This direct comparison through the case–control pairing reduces technical data deviations and enhances the statistical power of detection [29, 30]. With the potential genomic mosaicism of heterogeneous brain cell mixtures, we expected that the target genome could be diluted with normal DNA from the off-target cells and thus assumed non-integer values of CNVs in this analysis [31]. Technical limitations of this approach are further discussed below.

Results

The striatum contain neural stem cells that proliferate throughout human life and carries somatic mutation in its mitochondrial genome [32, 33]. Therefore, we hypothesized that the striatum may be a potential candidate region that would exhibit somatic mosaicism in brain genome structures. DNA was extracted from postmortem striatum of patients with chronic schizophrenia (n = 48) and age-matched controls who had no history of neuropsychiatric disorders (n = 48) (Additional file 1: Table S1). Although there were significant differences in postmortem intervals (PMIs) between groups, there was no detectable difference in DNA quality (data not shown). All other indices were indistinguishable between schizophrenia patients and control subjects. A DNA sample was randomly picked from each group, paired to a sample in the other group, and subjected to two-color competitive CGH analysis with 1 M SurePrint G3 Human CGH Microarrays.

We applied the ADM-2 algorithm to the CGH signals of individual microarray probes (nearly 1 million) and searched for the primary candidate CNV loci associated with schizophrenia. A flowchart of the present study design is shown in Additional file 1: Figure S1. We chose 1381 chromosomal loci that exhibited large group differences in gain/loss calls (Selection 1). In each probe site located on the primary candidate loci, we plotted the distribution of log₂ signal ratios from 48 sets of microarray analyses and tested the null hypothesis that the mean log₂ signal ratios was zero, indicating that the two groups were indistinguishable (Selection 2). We calculated total probabilities and averaged log₂ signal ratios for individual candidate loci and judged their statistical significance with Bonferroni's correction. The number of the candidate loci maintaining the

statistical significance through Selection 2 was reduced to 85 (Details in Additional file 1: Table S2).

Positive CNV loci were found in almost all chromosomes except chromosome 17 and 21 (Fig. 1). Individual loci covered 1–746 probe sites (3–2200 kb) and exhibited average log₂ ratios of –1.46 to +0.63 (i.e., odds ratio (OR) = 0.36–1.55). A majority of the average log₂ ratios were between –0.59 to +0.59 (i.e., < 1.5-fold differences) and only 4 loci showed more than 1.5-fold differences in array CGH signals. A genomic region spanning from 6p22.2 to 6p21.32 contained six CNV loci and included genes for the major histocompatibility complex that is highly associated with schizophrenia in GWAS [34]. Among the 85 CNV loci in Selection 2, 59 loci were reported and 26 loci were not reported in the CNV study on leukocyte DNA samples of Asian populations (Additional file 1: Table S2) [2].

To validate the authenticity of the present procedure, we attempted to verify the above genome dosage changes of several candidate loci using quantitative polymerase chain reaction (qPCR). According to the following two criteria, we selected the test loci whose signal differences were larger between groups and could be detectable with the given accuracy of qPCR; (i) those exhibiting the large and consistent gain/loss calls across the limited sample pairs (from Selection 1) and (ii) the loci represented larger global effects shared in most of the schizophrenia samples (from Selection 2).

In the former category, the gene dosage of Hs03385437 (1p13.3), CC70L1J (1p36.21), Hs03318079 (Chr18:q22.1), Hs04794356 (4q24), Hs05080419 (9q22.2), and Hs07134106 (19p12) produced exclusive gain/loss calls in not less than four sample pairs. No discrepant calls were detected in any sample pairs. Using the same DNA pairs showing the difference in the penetrance call (Selection 1), we determined and confirmed the gene dosage of those DNA samples using qPCR. ANOVA detected significant gene dose differences at two loci (Hs03385437 and CC70L1J) between patient and control groups (Fig. 2).

In this measurement, we used *RNaseP* gene as an internal DNA dose control. Measured genome doses of the above regions appeared not to be integer levels in several control samples, potentially reflecting the cell mosaicism of the original tissues. We also extracted DNA from the prefrontal cortex of the same subjects of both groups and compared the genome doses of the above loci (Hs03385437 and CC70L1J). We calculated the copy number ratio of the patient' DNA dosage to that of the control subject' dosage and compared these ratios between the brain regions. At both loci, almost all the copy number ratios were markedly lower than 1.0 except the C26:S34 pair, supporting our primary observation that the absolute gene dosages of these loci were decreased in the schizophrenia samples. However, copy number ratios did not significantly differ

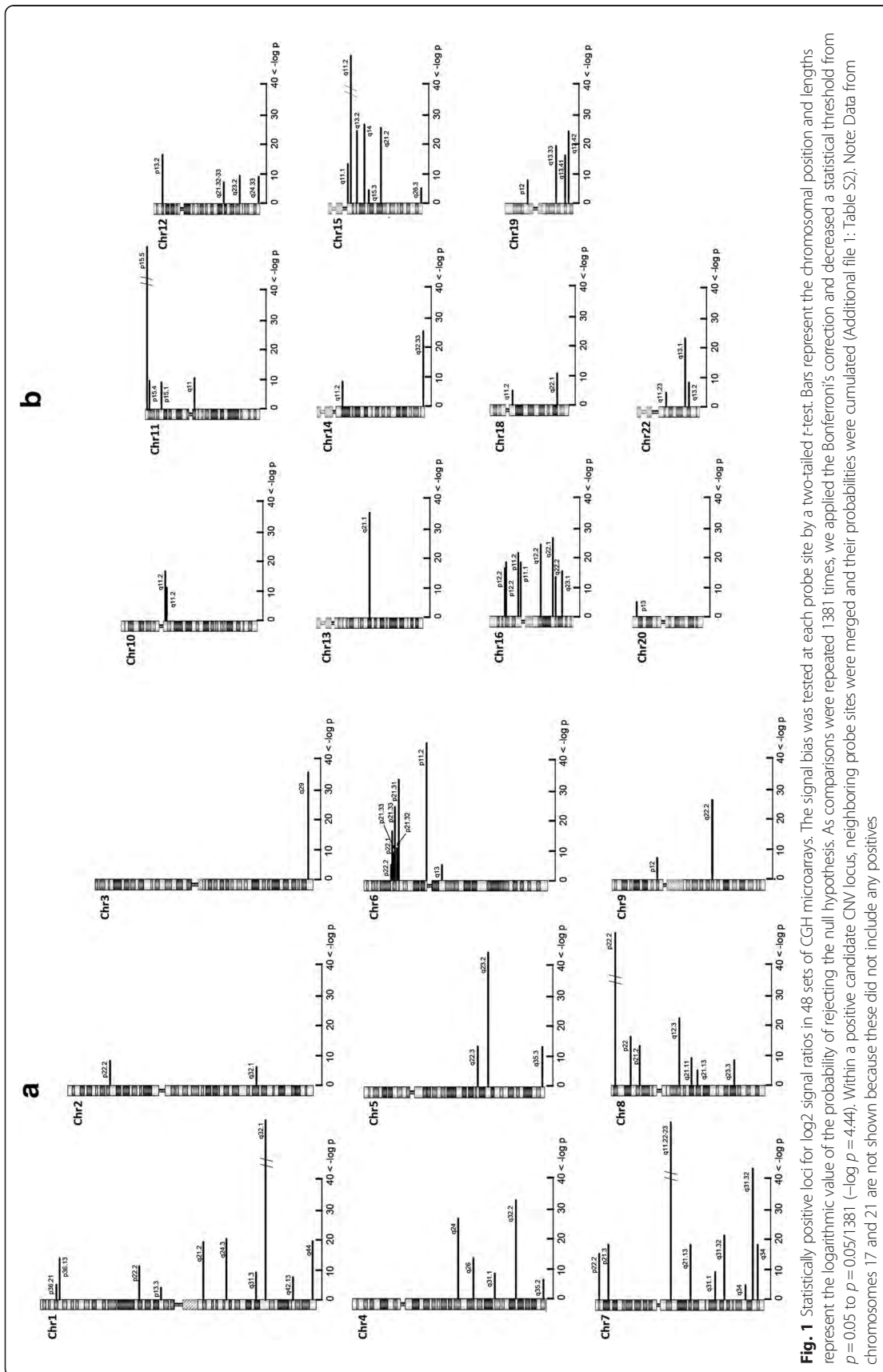
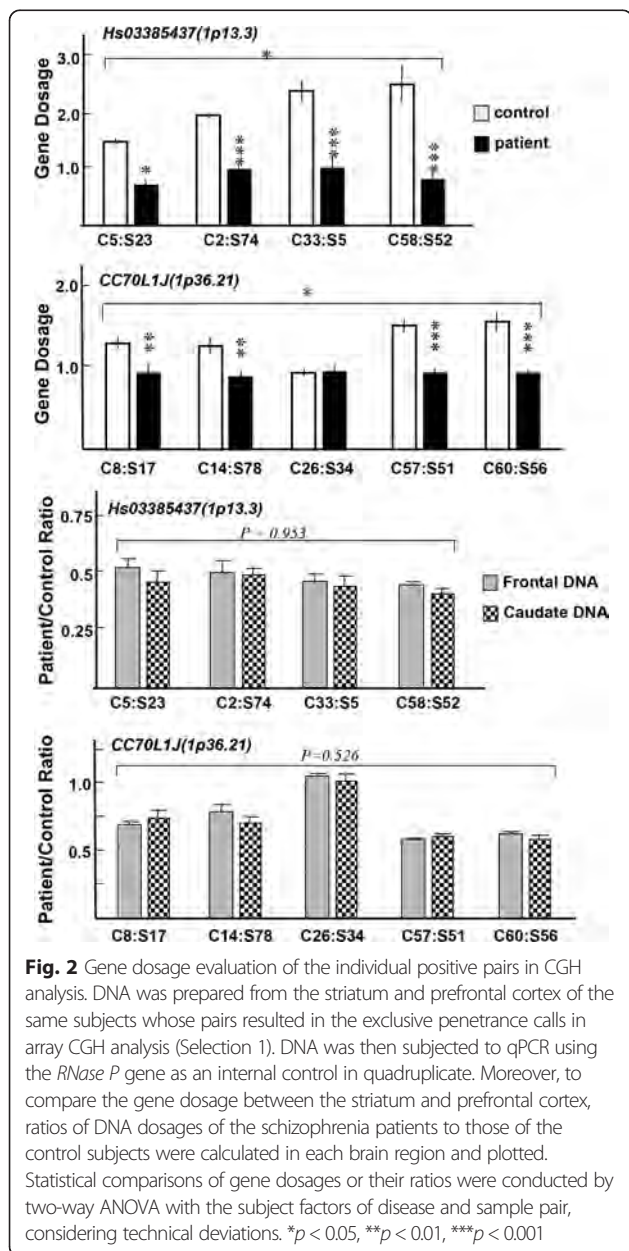


Fig. 1 Statistically positive loci for \log_2 signal ratios in 48 sets of CGH microarrays. The signal bias was tested at each probe site by a two-tailed t -test. Bars represent the chromosomal position and lengths represent the logarithmic value of the probability of rejecting the null hypothesis. As comparisons were repeated 1381 times, we applied the Bonferroni's correction and decreased a statistical threshold from $p = 0.05$ to $p = 0.05/1381$ ($-\log p = 4.44$). Within a positive candidate CNV locus, neighboring probe sites were merged and their probabilities were cumulated (Additional file 1: Table S2). Note: Data from chromosomes 17 and 21 are not shown because these did not include any positives



between these brain regions in any of the sample pairs (Fig. 2). At least at these two candidate loci, we failed to find evidence for a gene dosage difference between these brain regions.

In the latter category, Hs0358779 (6p22.1), Hs03265736 (7p21.3), Hs03765933 (11p15.4), and Hs03298358 (q21.1) exhibited higher \log_2 signal ratios and were thus subjected to the test evaluation. Gene dosage of these four loci were determined by qPCR using all the DNA samples in control and schizophrenia groups ($n = 48$ each). Differences in gene dosages were replicated by qPCR for Hs03765933 and Hs03298358 (Fig. 3). In contrast to the data distributions of Fig. 2, almost all the values of the gene doses were located

at the levels of integers but with several exceptions. These candidate CNVs appear to reflect the gene dosage differences of germinal origin.

Discussion

Several recent reports have indicated the neuropathological contribution of somatic CNV or DNA instability of the brain genome [19–28, 35–40]. In accordance with these findings, a small proportion few percent of brain cells are known to exhibit aneuploidy and carry large CNVs [13, 14, 41]. Aneuploidy is detected by fluorescence *in situ* hybridization (FISH) and appears to be increased by the onset of Alzheimer's disease [20, 22]. The aneuploidy of chromosome 1, 18 and X was also identified in the brain of schizophrenia patients [21, 41]. Despite its advantages, FISH cannot be employed in exploratory investigations, unless the specific genome region of the CNV of interest is identified. Since bonafide genome structures from off-target cells could dilute the abnormal genome DNA population, more sensitive technologies remain to be developed, which detect low quantities of CNV in heterogeneous cell mixtures of the brain tissue [42, 43]. In the present study, we attempted to evaluate the efficacy of the CGH microarray technique to extract somatic CNVs in the postmortem brains of schizophrenia patients [42, 43].

With given semi-quantitative nature of the microarray technique, we applied statistics to the 1 M array CGH results from 48 sample pairs. Using the high density CGH array and statistical approach, we found 85 candidate CNV loci in the present study; 59 CNV loci are overlapped with the common CNV regions and the remaining 26 loci are not reported in peripheral leukocyte-derived DNA of Asian people [2, 44]. Of note, the 26 candidate regions encode the seven genes that are associated with or implicated in schizophrenia or other psychiatric diseases; ANTXRL, CHST9, DNM3, NDST3, SDK1, STRC, and SKY (Additional file 1: Table S2). DNM3 in the candidate region of 1q24.3 is disruptively mutated in some of schizophrenia patients [45]. ANTXRL and CHST9 are located in the CNV regions associated with bipolar disorder and autism [46, 47]. NDST3 and STRC are the risk genes for schizophrenia and hearing impairment that are identified by GWAS, respectively [48, 49]. SDK1 and SKY are the genes whose expression levels are markedly altered in the brain of schizophrenia patients [50, 51]. Accordingly, the present listing of the candidate brain CNVs is informative for future cytogenomic studies on schizophrenia [21, 41].

It was difficult for us to validate most of the above-mentioned 85 candidate loci with qPCR analysis with the given small signal differences between groups (i.e., less than 1.5-fold). Therefore, we selected the best 10 test loci that exhibited relatively large and/or wide effects on gene dosage. The six loci were chosen from Selection 1 as putative rare CNVs, which exhibited exclusive gain/loss calls in the

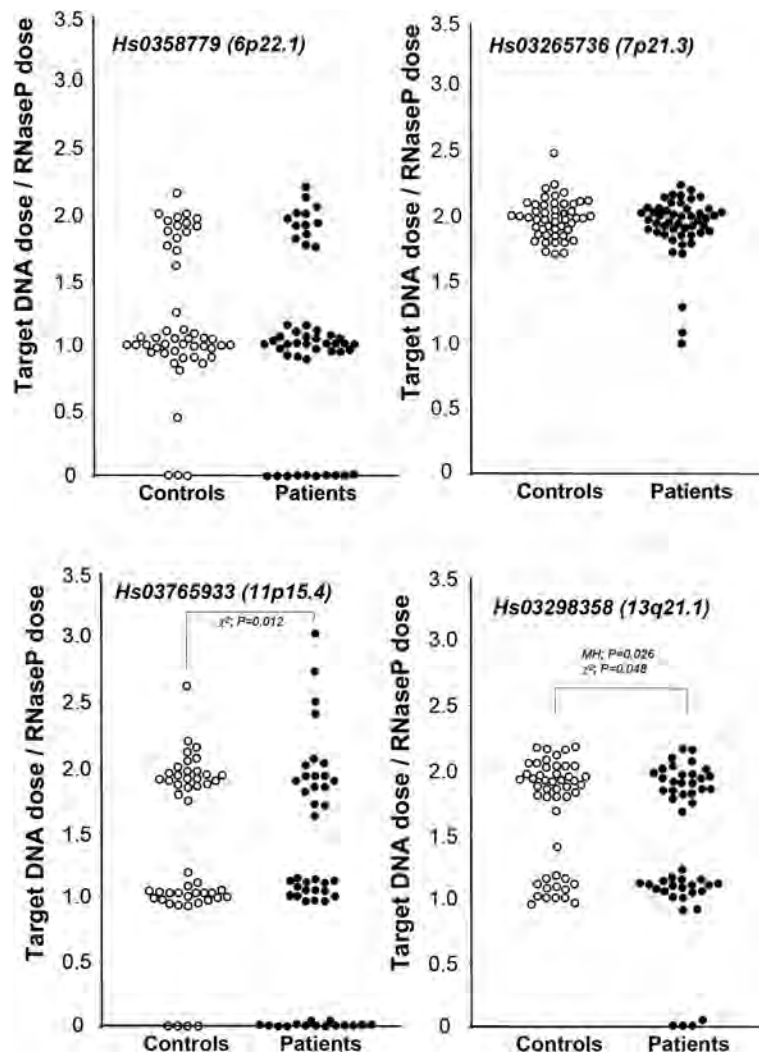


Fig. 3 qPCR evaluations of candidate CNV loci from Selection 2. Gene dosages of the candidate loci 6p22.1, 7p21.3, 11p15.4, 13q21.1, and the *RNase P* (internal control) were determined by qPCR using all sample DNAs and TaqMan probes (Additional file 1: Table S3). Individual gene dosages of 48 patients' or 48 controls' DNAs were plotted and compared between groups using the Chi-square and Mann-Whitney U tests

limited number of samples. From Selection 2, the four loci were chosen as provisional common variants, which showed large effects and higher probability levels in the above parametric analysis. The qPCR analysis confirmed the schizophrenia-associated gene dosage differences at nearly half of the candidate CNV loci, suggesting the validity of the present strategy.

Unfortunately we had neither stored peripheral tissues nor information about these CNVs in peripheral DNA of the same subjects. To estimate the contribution of somatic CNVs to the present CNV listing, therefore, we were compelled to compare the gene dosages between the two brain regions or to search for their absence in the databases of Asian CNVs of leukocyte origin [2,44]. In the test PCR, however, we could not detect significant differences in gene dosages between the striatum and prefrontal cortex, at least,

at these test CNV loci. If somatic CNVs were produced prior to neuroectodermal differentiation, there should be no difference between these two neural tissues, suggesting that the present comparison between these brain regions was inappropriate. Therefore, a comparative analysis of DNA from germinal cells of the same subjects will warrant this definitive conclusion [45].

Among the CNV candidate regions in Fig. 1, 26 candidate regions are not reported as the common CNVs of Asian populations [2, 44]. The majority of these loci exhibited high statistical significance with the probabilities of less than 10^{-100} , such as 4q35.2, 6p11.2, 7q11-12, 11p15.4-15.5, and 15q11.2. In contrast, their CGH signal differences between patients and controls were markedly smaller (OR = 0.988-1.055). As discussed above, these candidate CNV loci include the peculiar genes that are

implicated in schizophrenia [45–51]. These regions, which exhibited small signal differences, might represent more promising candidates of somatic CNV sites because the genome aberration of target cells is presumably diluted in the brain and should result in smaller ORs. However, such small differences in gene dosage should make the conventional qPCR verification more challenging with the given technical deviations [52]. To avoid target DNA dilution with cell mosaicism, single cell qPCR or FISH may be more beneficial in theory [20–22, 43]. However, it would be difficult to independently perform microdissection of hundreds of cells and perform single-cell analysis unless the target cell population is identified with molecular markers and its sensitivity of gene detection is high enough. FISH also requires properly fixed and processed brain tissues of the same subjects. With the given technical difficulties, therefore, we have been unable to verify these small variations.

Conclusion

The present CGH analysis lists the potential candidate regions of somatic CNVs associated with schizophrenia, although most of those exhibited the modest but highly significant alterations in brain genome doses. Future studies aim to develop more elaborate techniques for somatic genome mosaicism and to verify the schizophrenia-associated cytogenomic instability in the above CNV candidates [53–56].

Methods

Ethical approval

The study was approved by Niigata University Medical Ethics Committee (No. 683). The use of postmortem brain tissues was authorized by the Matsuzawa Hospital Ethics Committee, Kobe University Medical Ethics Committee, Fukushima Medical University Ethics Committee, and Niigata University Medical Ethics Committee. The families of the control and schizophrenia patients provided written informed consent to allow the use of brain tissues for pathological investigations.

Brain tissue

Postmortem brain tissue was collected from patients with chronic schizophrenia (30 men, 18 women; mean age, 64.5 ± 12.5 years old) and from age-matched control subjects (30 men, 18 women; mean age, 64.2 ± 12.0 years old), with no history of neuropsychiatric disorders (Additional file 1: Table S1). The diagnosis of schizophrenia was confirmed by examining the patient's report according to DSM-III or DSM-IV categories (American Psychiatric Association). Postmortem brains of schizophrenia patients were collected at Matsuzawa Hospital, Kobe University, Fukushima Medical University and Niigata University, while those of control subjects were collected at Niigata

University. In brief, the left cerebral hemisphere was fixed in formalin for diagnostic examination and the right hemisphere was frozen at -80°C . Tissue samples were taken from postmortem brains that did not exhibit neurodegenerative abnormalities by conventional pathological staining (data not shown). The striatum (caudate) was identified in frozen coronal slices according to a human brain atlas. All tissues were collected and stored according to the principles of the Declaration of Helsinki, and tissue use was in compliance with the Human Tissue Act 2004.

DNA extraction

High molecular weight DNA was extracted by the guanidinium – phenol procedure (Gentra Pure Gene Tissue Kit, Qiagen, Tokyo, Japan) according to the manufacturer's protocol. Extracted DNA was quantified by spectrophotometry using a Nanodrop ND-2000[®] (Thermo Scientific Wilmington, DE, USA). Samples with absorbance ratios of A260/280 ~ 1.80 and A260/230 > 1.90 , respectively, were regarded as sufficiently pure and suitable for CGH analysis. Some DNA samples were subjected to 1.0 % agarose gel electrophoresis for quality control. Evidence of DNA degradation was not detected in randomly-picked DNA samples from patient or control groups (data not shown).

Comparative genomic hybridization (CGH)

Array-based CGH was performed by the manufacturer Takara Bio Dragon Genomics Center (Seta, Shiga, Japan). In brief, DNA (2 micro g) was fluorescently labeled by random priming DNA synthesis in the presence of Cy3-dUTP (control group) or Cy5-dUTP (patient group) (Genomic DNA Enzymatic Labeling Kit; Agilent Technologies, Hachioji, Tokyo, Japan). DNA labeling efficiency was estimated by spectrophotometry (Nanodrop ND-2000[®]) measuring optical absorbance at 260 nm for DNA, at 550 nm for Cy5, and at 649 nm for Cy3. Cy5- and Cy3-labeled DNAs were randomly paired, mixed, and hybridized to SurePrint G3 Human CGH Microarrays (1 M) in the presence of human Cot-1 DNA (Oligo aCGH/ChIP-on-chip Hybridization Kit, Agilent Technologies). Following hybridization for 24 h, microarray slides were washed according to the manufacturer's instructions and immediately scanned on a DNA Microarray Scanner (Agilent Technologies). With the given limitation of the sample number, we took an advantage of the above direct comparison between case and control samples [57]. This approach allowed us to determine relative ratios of their gene dosages but not their absolute gene dosages. However this procedure decreased data deviations, compared with the CGH analysis utilizing two microarrays and reference genome DNA [30].

Quantitative polymerase chain reaction (qPCR)

To validate the results from the microarray experiments, we performed qPCR using TaqMan probes (Applied Biosystems, Foster City, CA) as described previously [32]. Gene dosages of the following genomic regions of interest were measured for the sample pair sets that exhibited the exclusive positive penetrance call with the Aberration Detection Method 2 (ADM-2) algorithm; CC70LIJ (1p13.3), Hs03385437 (1p36.21), Hs04794356 (4q24), Hs05080419 (9q22.2), Hs03318079 (18q21.1), and Hs07134106 (19p12). Using all the samples, we also determined the gene dosages of the candidate CNV loci that exhibited lower probability scores by the global *t*-test analysis; Hs03587795 (6p22.1), Hs03265736 (7p21.3), Hs03765933 (11p15.4), and Hs03298358 (13q21.1). DNA sequences of TaqMan probes and PCR primers are shown in the Additional file 1. We obtained cycle threshold (CT) values for the region of interest for each sample with FAM[™]-labeled probes, simultaneously monitoring those for *RNaseP* gene (an internal control) with its VIC[®]-labeled probe (ABI PRISM 7900HT Sequence Detection System and SDS v2.3 software, both Applied Biosystems). These CT values of the target gene and *RNaseP* gene were obtained for all the DNA samples. Copy number of the target gene was estimated from CT values by CopyCaller v1.0 software (Applied Biosystems).

Statistics

The ADM-2 algorithm prompted by Genomic Workbench software (edition 5.0.14, Agilent Technologies, 2010) was used to identify individual and common aberrations for 48 microarray data sets. This algorithm identifies all aberrant intervals with consistently high or low log ratios based on the statistical score. The algorithm searches for intervals where a statistical score based on the average quality-weighted log ratio of the sample and reference channels exceed a user-specified threshold. For the primary screening (Selection 1), we applied the following filtering options to the human genome assembly hg19 (excluding sex chromosomes): sensitivity threshold = 6, fuzzy zero = On, bin size = 10, and centralization threshold = 6. We then selected the primary candidate loci of somatic CNVs which exhibited ≥ 4 difference in gain/loss calls in the whole penetrance summary.

To calculate mean signal OR and the probability of CNVs between groups, we plotted individual log₂ signal ratios at all the probe sites within the above candidate loci. The Kolmogorov–Smirnov test revealed that log₂ signal ratios were judged to fit into the Gaussian distribution at more than 80 % of probe sites. Assuming their Gaussian distribution, we analyzed their statistical biases against log₂ = 0 (i.e., the null hypothesis of equal signal intensities between patients and controls) by two tailed *t*-test at each probe position. Within a candidate CNV

locus containing multiple probe sites, their log₂ signal ratios were averaged and probabilities were summed and then subjected to Bonferroni's correction (Selection 2). Statistical difference of qPCR results between individual sample pairs was determined with ANOVA or two tailed *t*-test, incorporating technical errors into account. Alternatively, group differences of qPCR results from individual samples were estimated by the chi-square and Mann–Whitney U tests. Statistical analyses were performed using SPSS software (IBM Japan, Tokyo, Japan).

Additional file

Additional file 1: Figure S1. A flowchart of the study design. **Table S1.** Autopsy and clinical information of the subjects used. **Table S2.** List of candidate CNV regions and their statistical details. **Table S3.** Custom Taqman PCR primers and probes used.

Abbreviations

ADM: Aberration detection method; ANOVA: Analysis of variance; CGH: Comparative genomic hybridization; CNV: Copy number variation; CT: Cycle threshold; FISH: Fluorescent in situ hybridization; OR: Odds ratio; PMI: Postmortem interval; qPCR: Quantitative polymerase chain reaction.

Competing interests

The authors have no conflicts of interest to declare except OS; The author received honoraria from Otsuka Pharmaceutical; Shionogi; GlaxoSmithKline; Eli Lilly; and Tanabe Mitsubishi Pharma, and donations for research from the Otsuka Pharmaceutical Corporation.

Authors' contributions

TS, RK, and HN designed the experiments and wrote the manuscript; M. Sakai, YW, KA, M. Shibuya, AM, and HN performed the experiments; KN, KO, YK, HY, JM, AW, MH, TH, AH NK, SI, OS, KM, SN, HT, and AK collected and examined postmortem tissues. All authors read and approved the final manuscript.

Acknowledgments

This work was supported by Grant-in-Aids for Scientific Research on Innovative Areas (No. 24116010) and for Challenging Exploratory Research (No. 21659273) and a grant for Promotion of Niigata University Research Projects.

Author details

¹Department of Molecular Neurobiology, Brain Research Institute, Niigata University, 1-757, Asahimachi-dori, 951-8585 Niigata, Japan. ²Department of Psychiatry, Graduate School of Medical and Dental Sciences, Niigata University, 1-757, Asahimachi-dori, 951-8510 Niigata, Japan. ³Matsuzawa Hospital, Setagaya-ku, 156-0057 Tokyo, Japan. ⁴Departments of Neuropsychiatry, Fukushima Medical University School of Medicine, 960-1295 Fukushima, Japan. ⁵Division of Psychiatry and Neurology, Kobe University Graduate School of Medicine, 650-0017 Kobe, Hyogo, Japan. ⁶Department of Mental Health, Nagoya University Graduate School of Medicine, 466-8550 Nagoya, Aichi, Japan. ⁷Department of Neuropsychiatry, Kinki University Faculty of Medicine, 589-8511 Osaka-Sayama, Osaka, Japan. ⁸Department of Social Rehabilitation, Kobe University School of Medicine, 654-0142 Hyogo, Japan. ⁹Department of Molecular Genetics, Brain Research Institute, Niigata University, 951-8585 Niigata, Japan. ¹⁰Pathology and Brain Disease Research Center, Brain Research Institute, Niigata University, 951-8585 Niigata, Japan.

Received: 9 March 2015 Accepted: 12 May 2015

Published online: 01 July 2015

References

1. Conrad DF, Pinto D, Redon R, Feuk L, Gokcumen O, Zhang Y, et al. Origins and functional impact of copy number variation in the human genome. *Nature*. 2010;464:704–12.

2. Park H, Kim JI, Ju YS, Gokcumen O, Mills RE, Kim S, et al. Discovery of common Asian copy number variants using integrated high-resolution array CGH and massively parallel DNA sequencing. *Nat Genet.* 2010;42:400–5.
3. Girirajan S, Campbell CD, Eichle EE. Human copy number variation and complex genetic disease. *Ann Rev Genetics.* 2011;45:203–26.
4. Zhang F, Gu W, Hurler ME, Lupski JR. Copy number variation in human health, disease, and evolution. *Annu Rev Genomics Hum Genet.* 2009;10:451–81.
5. Malhotra D, Sebat J. CNVs: harbingers of a rare variant revolution in psychiatric genetics. *Cell.* 2012;148:1223–41.
6. Xu B, Roos JL, Levy S, van Rensburg EJ, Gogos JA, Karayiorgou M. Strong association of de novo copy number mutations with sporadic schizophrenia. *Nat Genet.* 2008;40:880–5.
7. Malhotra D, McCarthy S, Michaelson JJ, Vacic V, Burdick KE, Yoon S, et al. High frequencies of de novo CNVs in bipolar disorder and schizophrenia. *Neuron.* 2011;72:951–63.
8. Rees E, Moskvina V, Owen MJ, O'Donovan MC, Kirov G. De novo rates and selection of schizophrenia-associated copy number variants. *Biol Psychiatry.* 2011;70:1109–14.
9. Kirov G, Pocklington AJ, Holmans P, Ivanov D, Ikeda M, Ruderfer D, et al. De novo CNV analysis implicates specific abnormalities of postsynaptic signalling complexes in the pathogenesis of schizophrenia. *Mol Psychiatry.* 2012;17:142–53.
10. Iourov IY, Vorsanova SG, Yurov YB. Molecular cytogenetics and cytogenomics of brain diseases. *Curr Genomics.* 2008;9:452–65.
11. Erickson RP. Somatic gene mutation and human disease other than cancer: an update. *Mutat Res.* 2010;705:96–106.
12. Iourov IY, Vorsanova SG, Yurov YB. Somatic cell genomics of brain disorders: a new opportunity to clarify genetic-environmental interactions. *Cytogenet Genome Res.* 2013;139:181–8.
13. Yurov YB, Iourov IY, Vorsanova SG, Liehr T, Kolotii AD, Kutsev SI, et al. Aneuploidy and confined chromosomal mosaicism in the developing human brain. *PLoS One.* 2007;2:e558.
14. Yang AH, Kaushal D, Rehen SK, Kriedt K, Kingsbury MA, McConnell MJ, et al. Chromosome segregation defects contribute to aneuploidy in normal neural progenitor cells. *J Neurosci.* 2003;23:10454–62.
15. Piotrowski A, Bruder CE, Andersson R, Diaz de Ståhl T, Menzel U, et al. Somatic mosaicism for copy number variation in differentiated human tissues. *Hum Mutat.* 2008;29:1118–24.
16. De S. Somatic mosaicism in healthy human tissues. *Trends Genet.* 2011;27:217–23.
17. Lindhurst MJ, Parker VE, Payne F, Sapp JC, Rudge S, Harris J, et al. Mosaic overgrowth with fibroadipose hyperplasia is caused by somatic activating mutations in PIK3CA. *Nat Genet.* 2012;44:928–33.
18. Bloom RJ, Kähler AK, Collins AL, Chen G, Cannon TD, Hultman C, et al. Comprehensive analysis of copy number variation in monozygotic twins discordant for bipolar disorder or schizophrenia. *Schizophr Res.* 2013;146:289–90.
19. Yurov YB, Vorsanova SG, Iourov IY, Demidova IA, Beresheva AK, Kravetz VS, et al. Unexplained autism is frequently associated with low-level mosaic aneuploidy. *J Med Genet.* 2007;44:521–5.
20. Mosch B, Morawski M, Mittag A, Lenz D, Tarnok A, Arendt T. Aneuploidy and DNA replication in the normal human brain and Alzheimer's disease. *J Neurosci.* 2007;27:6859–67.
21. Yurov YB, Iourov IY, Vorsanova SG, Demidova IA, Kravetz VS, Beresheva AK, et al. The schizophrenia brain exhibits low-level aneuploidy involving chromosome. *Schizophr Res.* 2008;98:139–47.
22. Iourov IY, Vorsanova SG, Liehr T, Yurov YB. Aneuploidy in the normal, Alzheimer's disease and ataxia-telangiectasia brain: differential expression and pathological meaning. *Neurobiol Dis.* 2009;34:212–20.
23. Iourov IY, Vorsanova SG, Liehr T, Kolotii AD, Yurov YB. Increased chromosome instability dramatically disrupts neural genome integrity and mediates cerebellar degeneration in the ataxia-telangiectasia brain. *Hum Mol Genet.* 2009;18:2656–69.
24. Lee JM, Zhang J, Su AI, Walker JR, Wiltshire T, Kang K, et al. A novel approach to investigate tissue-specific trinucleotide repeat instability. *BMC Syst Biol.* 2010;4:29.
25. Pamphlett R, Morahan JM, Luquin N, Yu B. Looking for differences in copy number between blood and brain in sporadic amyotrophic lateral sclerosis. *Muscle Nerve.* 2011;44:492–8.
26. Chen J, Cohen ML, Lerner AJ, Yang Y, Herrup K. DNA damage and cell cycle events implicate cerebellar dentate nucleus neurons as targets of Alzheimer's disease. *Mol Neurodegener.* 2010;5:60.
27. Arendt T, Brückner MK, Mosch B, Lösche A. Selective cell death of hyperploid neurons in Alzheimer's disease. *Am J Pathol.* 2010;177:15–20.
28. Ye T, Lipska BK, Tao R, Hyde TM, Wang L, Li C, et al. Analysis of copy number variations in brain DNA from patients with schizophrenia and other psychiatric disorders. *Biol Psychiatry.* 2012;72:651–4.
29. Shalon D, Smith SJ, Brown PO. A DNA microarray system for analyzing complex DNA samples using two-color fluorescent probe hybridization. *Genome Res.* 1996;6:639–45.
30. Yang YH, Speed T. Design issues for cDNA microarray experiments. *Nat Rev Genet.* 2002;3:579–88.
31. Zhang D, Qian Y, Akula N, Alliey-Rodriguez N, Tang J, Bipolar Genome Study, et al. Accuracy of CNV detection from GWAS data. *PLoS One.* 2011;6:e14511.
32. Ernst A, Alkass K, Bernard S, Salehpour M, Perl S, Tisdale J, et al. Neurogenesis in the striatum of the adult human brain. *Cell.* 2014;156:1072–83.
33. Williams SL, Mash DC, Züchner S, Moraes SC. Somatic mtDNA mutation spectra in the aging human putamen. *PLoS Genet.* 2013;9:10.
34. International Schizophrenia Consortium, Purcell SM, Wray NR, Stone JL, Visscher PM, O'Donovan MC, et al. Common polygenic variation contributes to risk of schizophrenia and bipolar disorder. *Nature.* 2009;460:748–52.
35. Filho AB, Souza J, Faucz FR, Sotomaior VS, Dupont B, Bartel F, et al. Somatic/gonadal mosaicism in a syndromic form of ectrodactyly, including eye abnormalities, documented through array-based comparative genomic hybridization. *Am J Med Genet A.* 2011;155A:1152–6.
36. Etheridge SP, Bowles NE, Arrington CB, Pilcher T, Rope A, Wilde AA, et al. Somatic mosaicism contributes to phenotypic variation in Timothy syndrome. *Am J Med Genet A.* 2011;155A:2578–83.
37. Terracciano A, Specchio N, Darra F, Sferra A, Bernardina BD, Vigeveno F, et al. Somatic mosaicism of PCDH19 mutation in a family with low-penetrance EFMR. *Neurogenetics.* 2012;13:341–5.
38. Bundo M, Toyoshima M, Okada Y, Akamatsu W, Ueda J, Nemoto-Miyauchi T, et al. Increased I1 retrotransposition in the neuronal genome in schizophrenia. *Neuron.* 2014;81:306–13.
39. Singer T, McConnell MJ, Marchetto MC, Coufal NG, Gage FH. LINE-1 retrotransposons: mediators of somatic variation in neuronal genomes? *Trends Neurosci.* 2010;33:345–54.
40. Peterson SE, Yang AH, Bushman DM, Westra JW, Yung YC, Barral S, et al. Aneuploid cells are differentially susceptible to caspase-mediated death during embryonic cerebral cortical development. *J Neurosci.* 2012;32:16213–22.
41. Yurov YB, Vostrikov VM, Vorsanova SG, Monakhov VV, Iourov IY. Multicolor fluorescent in situ hybridization on postmortem brain in schizophrenia as an approach for identification of low-level chromosomal aneuploidy in neuropsychiatric diseases. *Brain Dev.* 2001;23:S186–90.
42. Mkrtchyan H, Gross M, Hinreiner S, Polytko A, Manvelyan M, Mrasek K, et al. The human genome puzzle - the role of copy number variation in somatic mosaicism. *Curr Genomics.* 2010;11:426–31.
43. Iourov IY, Vorsanova SG, Yurov YB. Single cell genomics of the brain: focus on neuronal diversity and neuropsychiatric diseases. *Curr Genomics.* 2012;13:477–88.
44. Xu H, Poh WT, Sim X, Ong RT, Suo C, Tay WT, et al. SgD-CNV, a database for common and rare copy number variants in three Asian populations. *Hum Mutat.* 2011;32:1341–9.
45. Purcell SM, Moran JL, Fromer M, Ruderfer D, Solovieff N, Roussos P, et al. A polygenic burden of rare disruptive mutations in schizophrenia. *Nature.* 2014;506:185–90.
46. Priebe L, Degenhardt FA, Herms S, Haenisch B, Mattheisen M, Nieratschker V, et al. Genome-wide survey implicates the influence of copy number variants (CNVs) in the development of early-onset bipolar disorder. *Mol Psychiatry.* 2012;17:421–32.
47. Krumm N, O'Roak BJ, Karakoc E, Mohajeri K, Nelson B, Vives L, et al. Transmission disequilibrium of small CNVs in simplex autism. *Am J Hum Genet.* 2013;93:595–606.
48. Lencz T, Guha S, Liu C, Rosenfeld J, Mukherjee S, DeRosse P, et al. Genome-wide association study implicates NDST3 in schizophrenia and bipolar disorder. *Nat Commun.* 2013;4:2739.
49. Francey LJ, Conlin LK, Kadesch HE, Clark D, Berrodin D, Sun Y, et al. Genome-wide SNP genotyping identifies the Stereocilin (STRC) gene as a major contributor to pediatric bilateral sensorineural hearing impairment. *Am J Med Genet A.* 2012;158A:298–308.

50. Pidsley R, Viana J, Hannon E, Spiers HH, Troakes C, Al-Saraj S, et al. Methyloomic profiling of human brain tissue supports a neurodevelopmental origin for schizophrenia. *Genome Biol.* 2014;15:483.
51. Huang KC, Yang KC, Lin H, Tsao Tsun-Hui T, Lee WK, Lee SA, et al. Analysis of schizophrenia and hepatocellular carcinoma genetic network with corresponding modularity and pathways: novel insights to the immune system. *BMC Genomics.* 2013;14 Suppl 5:S10.
52. Shanmuganathan A, Black MB. Researchgate. 2014. http://www.researchgate.net/post/What_is_the_fold_change_value_correlation_between_microarray_and_qPCR_experiments
53. Tsubahara M, Hayashi Y, Nijima S, Yamamoto M, Kamijo T, Murata Y, et al. Isolated growth hormone deficiency in two siblings because of paternal mosaicism for a mutation in the GH1 gene. *Clin Endocrinol (Oxf).* 2012;76:420–4.
54. Kurek KC, Luks VL, Ayturk UM, Alomari AI, Fishman SJ, Spencer SA, et al. Somatic mosaic activating mutations in PIK3CA cause CLOVES syndrome. *Am J Hum Genet.* 2012;90:1108–15.
55. Abyzov A, Mariani J, Palejev D, Zhang Y, Haney MS, Tomasini L, et al. Somatic copy number mosaicism in human skin revealed by induced pluripotent stem cells. *Nature.* 2012;492:438–42.
56. Whale AS, Huggett JF, Cowen S, Zhang Y, Haney MS, Tomasini L, et al. Comparison of microfluidic digital PCR and conventional quantitative PCR for measuring copy number variation. *Nucleic Acids Res.* 2012;40:e82.
57. Watanabe Y, Nunokawa A, Kaneko N, Someya T. A case–control study and meta-analysis of association between a common copy number variation of the glutathione S-transferase mu 1 (GSTM1) gene and schizophrenia. *Schizophr Res.* 2010;124:236–7.

**Submit your next manuscript to BioMed Central
and take full advantage of:**

- Convenient online submission
- Thorough peer review
- No space constraints or color figure charges
- Immediate publication on acceptance
- Inclusion in PubMed, CAS, Scopus and Google Scholar
- Research which is freely available for redistribution

Submit your manuscript at
www.biomedcentral.com/submit



ORIGINAL
ARTICLE

Determination of kainate receptor subunit ratios in mouse brain using novel chimeric protein standards

Izumi Watanabe-Iida,^{*,†} Kohtarou Konno,^{†,‡} Kaori Akashi,^{*,†} Manabu Abe,^{*,†} Rie Natsume,^{*,†} Masahiko Watanabe^{†,‡} and Kenji Sakimura^{*,†}^{*}Department of Cellular Neurobiology, Brain Research Institute, Niigata University, Niigata, Japan[†]CREST, Japan Science and Technology Agency, Chiyoda-ku, Japan[‡]Department of Anatomy, Hokkaido University School of Medicine, Sapporo, Japan**Abstract**

Kainate-type glutamate receptors (KARs) are tetrameric channels assembled from GluK1–5. GluK1–3 are low-affinity subunits that form homomeric and heteromeric KARs, while GluK4 and GluK5 are high-affinity subunits that require co-assembly with GluK1–3 for functional expression. Although the subunit composition is thought to be highly heterogeneous in the brain, the distribution of KAR subunits at the protein level and their relative abundance in given regions of the brain remain largely unknown. In the present study, we titrated C-terminal antibodies to each KAR subunit using chimeric GluA2–GluK fusion proteins, and measured their relative abundance in the P2 and post-synaptic density (PSD) fractions of the adult mouse hippocampus and cerebellum. Analytical western blots showed that GluK2 and GluK3 were the major KAR subunits, with additional expression of GluK5 in the hippocampus and cerebellum. In both regions, GluK4 was

very low and GluK1 was below the detection threshold. The relative amount of low-affinity subunits (GluK2 plus GluK3) was several times higher than that of high-affinity subunits (GluK4 plus GluK5) in both regions. Of note, the highest ratio of high-affinity subunits to low-affinity subunits was found in the hippocampal PSD fraction (0.32), suggesting that heteromeric receptors consisting of high- and low-affinity subunits highly accumulate at hippocampal synapses. In comparison, this ratio was decreased to 0.15 in the cerebellar PSD fraction, suggesting that KARs consisting of low-affinity subunits are more prevalent in the cerebellum. Therefore, low-affinity KAR subunits are predominant in the brain, with distinct subunit combinations between the hippocampus and cerebellum.

Keywords: antibody, GluK2, GluK3, kainate receptor, quantification, western blot.

J. Neurochem. (2016) **136**, 295–305.

A kainate type of the ionotropic glutamate receptor family (KAR) is widely expressed in the central nervous system and involved in neurotransmission (Lerma 2003, 2006; Pinheiro and Mulle 2006; Contractor *et al.* 2011). There are five members of KAR subunits, GluK1–GluK5, which significantly differ in spatio-temporal patterns of expressions in the brain (Wisden and Seeburg 1993). KAR subunits are grouped into low-affinity subunits GluK1–GluK3, and high-affinity subunits GluK4 and GluK5 (Bettler *et al.* 1992). When expressed in cell lines or *Xenopus* oocytes, low-affinity subunits can form functional homomeric KAR channels (Bettler *et al.* 1990, 1992; Egebjerg *et al.* 1991), while high-affinity subunits require any of GluK1–GluK3 to form functional KAR channels (Herb *et al.* 1992; Sakimura *et al.* 1992). KAR subunits are expressed in various neurons, such as pyramidal neurons, granule cells, and inhibitory interneurons in the hippocampus (Bahn *et al.* 1994; Bureau

et al. 1999) and Purkinje cells, granule cells, and inhibitory interneurons in the cerebellum (Wisden and Seeburg 1993).

KAR-mediated responses are recorded in cerebellar neurons (Renard *et al.* 1995; Savidge *et al.* 1999; Bureau *et al.* 2000), where GluK2 and GluK3 are mainly expressed

Received July 2, 2015; revised manuscript received September 4, 2015; accepted October 1, 2015.

Address correspondence and reprint requests to Kenji Sakimura, Department of Cellular Neurobiology, Brain Research Institute, Niigata University, Niigata 951-8585, Japan. E-mail: sakimura@bri.niigata-u.ac.jp

Abbreviations used: AMPAR, AMPA-type glutamate receptor; DG, dentate gyrus; DIG, digoxigenin; KAR, kainate-type glutamate receptor; KO, knockout; NBT/BCIP, nitro-blue tetrazolium and 5-bromo-4-chloro-3'-indolylphosphate; NMDAR, NMDA-type glutamate receptor; PB, phosphate buffer; PFA, paraformaldehyde; PSD, post-synaptic density; SDS, sodium dodecyl sulfate; TNT, Tris-NaCl-Tween.

(Gallyas *et al.* 2003). KAR-mediated excitatory post-synaptic currents (EPSCs) are detectable at mossy fiber-CA3 synapses in the hippocampus, but are lost in GluK4/GluK5-double knockout mice (Fernandes *et al.* 2009), suggesting that low-affinity subunits alone are insufficient, and co-expression of high-affinity subunits are essential, to form functional KARs at this hippocampal synapse. Thus, the composition of low-affinity and high-affinity KAR subunits and their functional contribution appear to be differentially regulated depending on the brain regions. Despite the wealth of knowledge on expressions at the transcription level (Wisden and Seeburg 1993), the distribution of KAR subunits at the protein level and their relative abundance in given regions of the brain remain largely unknown.

In the present study, we undertook this issue by testing the specificity and standardizing the titer of C-terminal antibodies to each KAR subunit using chimeric GluA2-GluK fusion proteins. With this novel method, we studied the relative abundance of KAR subunits in the adult mouse hippocampus and cerebellum, and found that low-affinity subunits are predominantly expressed in both regions.

Materials and methods

Animal experiments

All animal experiments were carried out in accordance with the guidelines laid down by the animal welfare committees and the ethics committees of Niigata University.

Fixation and sections

Under deep pentobarbital anesthesia (100 mg/kg body weight, ip.), mice were fixed by transcardial perfusion with 4% paraformaldehyde in 0.1 M phosphate buffer (pH 7.2) for chromogenic *in situ* hybridization. After excision from the skull, brains were further post-fixed for 3 days at 20°C and cryoprotected with 30% sucrose in 0.1 M phosphate buffer, and cryosections (30 µm) were prepared on a cryostat (CM1900; Leica Microsystems, Wetzlar, Germany).

In situ hybridization

Mouse cDNA fragments of GluK1 (nucleotides 46–850 bp; GenBank accession number, NM_146072), GluK2 (42–788, NM_001111268), GluK3 (24–798, NM_001081097), GluK4 (59–889, NM_175481), and GluK5 (11–894, NM_008168) were subcloned into pBluescript II plasmid vector. Digoxigenin-labeled cRNA probes were transcribed *in vitro* (Yamasaki *et al.* 2010). Fragmentation of riboprobes by alkaline digestion was omitted to increase the sensitivity and specificity. The chromogenic *in situ* hybridization was carried out as reported previously (Konno *et al.* 2014).

KAR-knockout mice

GluK2, GluK3, GluK4, and GluK5-knockout (KO) mice were generated using ES cell line RENKA derived from C57BL/6N (Mishina and Sakimura 2007). Detailed characterization of GluK2-KO, GluK3-KO, and GluK5-KO mice was described in Figure S1.

Production of GluK4-KO mice was previously reported (Akashi *et al.* 2009).

Antibody

We produced anti-GluK1 antibody in the guinea pig against C-terminal 36 amino acid (aa) residues of mouse anti-GluK1 (898–934, NM_146072) and anti-GluK3 antibody in the rabbit against C-terminal 17 aa residues of mouse GluK3 (903–919, NM_001081097). We also used rabbit polyclonal antibodies to anti-GluK2 (Synaptic Systems, Goettingen, Germany), anti-GluK4 (Akashi *et al.* 2009), and anti-GluK5 (Millipore Corporation, Bedford, MA, USA), which were raised against the C-terminal 55 aa residues of rat GluK2 (844–908, NM_019309), C-terminal 91 aa of mouse GluK4 (866–896, NM_175481) and C-terminal 21 aa of rat GluK5 (960–979, NM_031508).

RT-PCR

Total RNA was isolated from whole brains of adult and post-natal day 3 (P3) mice using TRIzol LS Reagent (Thermo Fisher Scientific Inc., Waltham, MA, USA) following the protocol of the manufacturer. Semiquantitative reverse transcription (RT)-PCR was performed using an RT-PCR kit from Clontech (Takara, Tokyo, Japan). Briefly, 1 µg of total RNA was reverse transcribed using random hexamer primers for 1 h at 42°C. The resulting cDNA was appropriately diluted, and amplified using the following primers: GluK1 (exon 10–12), sense, 5'-TCGCTTGCCTAGGAGTCAGT-3'; antisense, 5'-GGGTGAAAAACCACCATATTC-3'; glyceraldehyde-3-phosphate dehydrogenase, sense, 5'-AGGTCGGTGTGAACGGATTG-3'; antisense, 5'-TGTAGACCATGTAGTTGAGGTCA-3'. Amplified products were electrophoresed and visualized by ethidium bromide staining. The relative expression of GluK1 was measured after scanning the bands with a CS Analyzer ver.3.0 (ATTO, Tokyo, Japan).

Construction of chimeric proteins

To standardize the titer of each C-terminal antibody, we generated standard chimeric proteins consisting of mouse GluA2 subunit (1–833 aa, NM_013540) in the N-terminal side and mouse KAR subunits (GluK1, 841–934; GluK2, 841–908; GluK3, 842–919; GluK4, 826–952; GluK5, 825–979) in the C-terminal side (Fig. 3a). cDNAs for these chimeric proteins were subcloned into the pEF-BOS vector (Mizushima and Nagata 1990). Plasmid vectors were transiently transfected into COS-7 cells and/or HEK293 cells using the Plus Reagent and Lipofectamine Reagent (Invitrogen, Carlsbad, CA, USA) grown in the Dulbecco's Modified Eagle Medium containing 10% fetal bovine serum at 37°C in 5% CO₂. 24 h after transfection, cells were lysed at 4°C in the sodium dodecyl sulfate (SDS) sample buffer (2% SDS, 3.3% glycerol, 125 mM Tris-HCl, pH 7.4). The extract was centrifuged at 10 000g for 10–20 min to remove cell debris, and the supernatant was used for SDS-Polyacrylamide Gel Electrophoresis (SDS-PAGE) experiments.

Preparation of brain samples

C57BL/6N mice were purchased from Charles River Laboratories Japan (Yokohama, Japan), and were decapitated by cervical dislocation. Whole brains from P3 and adulthood (7–12 weeks of age) were homogenized in the homogenate buffer (0.32 M sucrose,

5 mM EDTA, 5 mM HEPES-NaOH, pH 7.4, complete protease inhibitor cocktail tablet; Roche, Mannheim, Germany). After measuring the total protein concentration by the bicinchoninic acid (BCA) Protein Assay Reagent (ThermoFisher Scientific Inc.), the whole brain lysates were recovered in the SDS sample buffer and used for western blot analysis. Fractionated protein samples were prepared from the hippocampus and cerebellum of adult male C57BL/6N mice and of adult male GluK2-KO, GluK3-KO, GluK4-KO, and GluK5-KO mice. Preparation of fractionated protein samples and western blot was performed as previously described (Abe *et al.* 2004; Fukaya *et al.* 2006; Yamazaki *et al.* 2010). Brain tissues were excised and homogenized in the homogenate buffer and centrifuged at 1000g for 10 min. The resulting supernatants were then centrifuged at 10 000g for 10 min to obtain P2 fractions. The pellets were resuspended with homogenate buffer and aliquoted for P2 fraction, and the remaining samples were further separated on a sucrose density gradient (0.32, 0.8 and 1.2 M sucrose) by ultracentrifugation at 90 000g for 2 h at 2°C to obtain synaptosomal fractions. Triton X-100 was added to the aliquot samples to a final concentration of 1% and incubated at 2°C for 30 min and centrifuged at 10 000g for 10 min at 2°C to obtain P2 fractions. To prepare PSD fraction, the synaptosomal fraction was further solubilized with 0.5% Triton X-100 and then centrifuged at 200 000g for 1 h. The resulting pellet (PSD fraction) was suspended in 1% SDS, 40 mM Tris-HCl, pH 8.0 and diluted in SDS sample buffer. Protein sample of each fraction was heated at 100°C for 5 min in the presence of 2-mercaptoethanol and 0.002% Bromophenol blue and subjected to SDS-PAGE for western blot.

Western blot

Protein samples were separated by 8% SDS-PAGE under reducing conditions and electrophoretically transferred to a nitrocellulose membrane (Amersham, Buckinghamshire, UK). Membranes were blocked with 5% non-fat milk with Tris-buffered saline-Tween 20 (TBS-T) (137 mM NaCl, 0.1% Tween 20, 20 mM Tris-HCl, pH 7.6) for 1 h at 20°C. After washing for 30 min with three changes of TBS-T, membranes were incubated with each primary antibody (1 µg/mL) in TBS-T for 3–4 h at 20°C. After three washes with TBS-T, the membranes were incubated with horseradish peroxidase-conjugated secondary antibody for 1 h at 20°C in TBS-T. After three washes with TBS-T, proteins were visualized with enhanced chemiluminescence (ECL) (GE Healthcare, Piscataway Township, NJ, USA and EZ capture MG; ATTO, Tokyo, Japan) using a medical X-ray film (FUJIFILM Corporation, Tokyo, Japan) and a luminescence image analyzer with an electronically cooled charge-coupled device camera (LAS-4000 mini; GE Healthcare).

Quantitative analysis of western blot

Signal intensities of immunoreacted bands were determined by densitometric measurement using ImageJ software (available from the US National Institutes of Health), imageQuant TL (GE Healthcare) and CS Analyzer ver.3.0 (ATTO).

Statistical analysis

All data are presented as mean ± SE. Groups were compared using the two-tailed, unpaired Student's *t*-test. Statistical significance is indicated as follows: ****p* < 0.001.

Results

GluK1–5 mRNA expressions in the mouse brain

Distinct regional expression patterns of mRNAs for five GluK subunits have been reported in the rat brain (Wisden and Seeburg 1993; Bahn *et al.* 1994). In this study, we performed *in situ* hybridization for GluK1–5 mRNAs in the adult mouse brain using Digoxigenin-labeled cRNA probes, with special interest in the hippocampus and cerebellum (Fig. 1). Expression levels were generally low for GluK1 mRNA, but the hybridizing signals were selective to interneurons in the hippocampus and Purkinje cells in the cerebellum (Fig. 1a,f,k and p). GluK2 mRNA was widely expressed, with intense signals in the olfactory bulb, striatum, hippocampus, and cerebellum (Fig. 1b). In the hippocampus, GluK2 mRNA was expressed in both principal neurons (i.e., pyramidal and granule cells) and interneurons, which were identified as cells forming compact pyramidal cell and granule cell layers or cells dispersed inside and outside the layers respectively. The intensity of GluK2 mRNA expression was in the order of the dentate gyrus > CA3 > CA1 (Fig. 1g). In the cerebellum, granule cells expressed GluK2 mRNA intensely (Fig. 1l and q). GluK3 mRNA was moderately expressed in the cerebral cortex, hippocampus and cerebellum (Fig. 1c). GluK3 mRNA was detected in granule cells in the dentate gyrus, interneurons in the hippocampal Ammon's horn, and interneurons in the cerebellum; cerebellar interneurons were identified as cells dispersed in the molecular and granular layers (Fig. 1h,m and r). Expression levels were generally low for GluK4 mRNA, but intense signals were noted in pyramidal cells in the hippocampal CA3, granule cells in the dentate gyrus, and Purkinje cells in the cerebellum (Fig. 1d,i, n and s). Strong signals for GluK5 mRNA were found in the whole brain, especially in pyramidal cells in the hippocampal CA1–CA3, granule cells in the dentate gyrus, and interneurons and granule cells in the cerebellum (Fig. 1e,j,o and t). These distinct regional and cellular expressions in the adult mouse brain were consistent with those in the adult rat brain (Wisden and Seeburg 1993). We then examined how the distinct regional expressions of respective GluK subunits were reflected at the protein level.

Specificity of GluK antibodies

We checked the specificity of GluK2–5 antibodies with western blot analysis using hippocampal extracts from wild-type and GluK-defective mutant mice (Fig. 2a). Each of GluK2–5 antibodies recognized protein bands at expected molecular weights in the hippocampus of wild-type mice: GluK2, 102 kDa; GluK3, 104 kDa; GluK4, 107 kDa; GluK5, 109 kDa. No such bands were detected in the hippocampus of mutant mice lacking the corresponding GluK subunits. These results verify the specificity of these GluK2–5 antibodies and further indicate their applicability to quantitative western blot analysis.

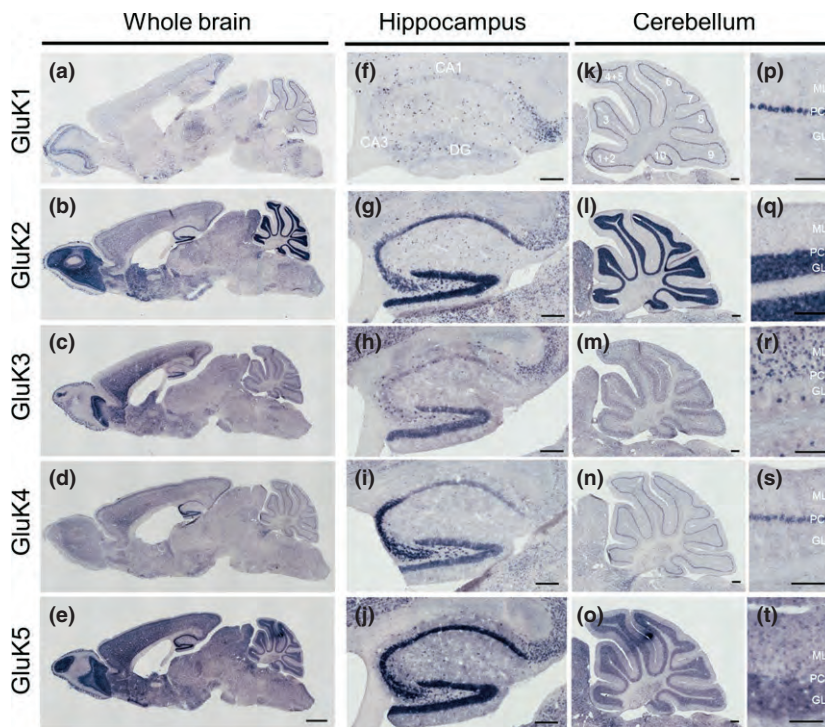


Fig. 1 Expression of kainate-type glutamate receptor (KAR) subunit mRNAs in mouse brain. *In situ* hybridization with specific RNA probes for KAR subunits: (a) GluK1 (b) GluK2 (c) GluK3 (d) GluK4 (e) GluK5, in C57BL/6N mouse whole brain. High power images of hippocampal and cerebellar layer structures; (f, k, p) GluK1, (g, l, q) GluK2, (h, m, r) GluK3, (i, n, s) GluK4, (j, o, t) GluK5, in C57BL/6N mouse whole brain. CA1-3, CA1-3 regions of the Ammon's horn; DG, dentate gyrus; GL, granular layer; ML, molecular layer; PCL, Purkinje cell layer. Arabic numerals indicate cerebellar lobules. Scale bars: a-e, 1 mm; f-j, 200 μ m; k-o, 100 μ m; p-t, 100 μ m.

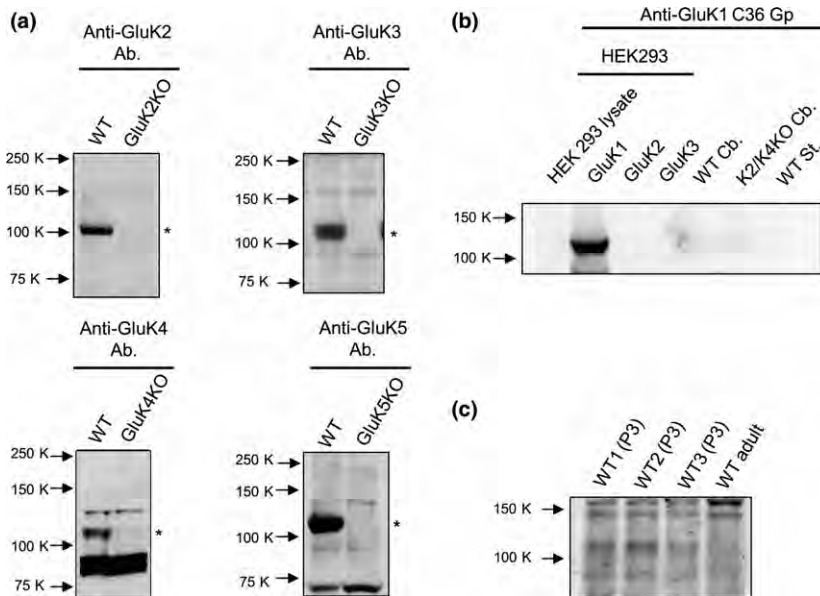


Fig. 2 Characterization of each anti-GluK subunit antibody. (a) Hippocampal lysate (30–40 μ g) of wild type and GluK2, GluK3, GluK4, and GluK5-knockout (KO) mice were examined by western blot analyses with anti-GluK2 (Synaptic systems), anti-GluK3, anti-GluK4 (ours), and anti-GluK5 (Millipore) antibodies. Asterisks show correct bands of GluK2, GluK3, GluK4, and GluK5. (b) Characterization of guinea pig anti-GluK1 C36 antibody with recombinant GluK1-GluK3 proteins and brain P2 fractions prepared from cerebellum (Cb.) and striatum (St.), indicating no cross-reactivity to GluK2 and GluK3. (c) Whole brain lysates (50 μ g) from juvenile (P3) (WT pool 1, pool 2, pool 3) and adult mice were loaded and detected with our anti-GluK1 C36 antibody.

Because commercially available GluK1 antibody was found to cross-react to GluK2 (Figure S2), we produced GluK1 antibody in the guinea pig. To test the specificity of guinea pig GluK1 antibody, we used lysates of COS-7 and HEK293 cells transfected with GluK1-3 cDNAs, and found selective protein band in GluK1-transfected lysates (Fig. 2b). However, no protein bands were observed in the extracts from adult wild-type cerebellum and striatum. Because transcription levels of GluK1 were transiently increased

during the perinatal period (Bettler *et al.* 1990; Bahn *et al.* 1994; Figure S3), we examined brain lysates prepared from post-natal day 3 (P3) and adult mice. A putative GluK1 protein band just above 100 kDa was faintly detected in brains at P3, but not in adulthood (Fig. 2c). This indicates that the amount of GluK1 proteins is below the detection threshold in adult brains when using this GluK1 antibody. Thus, we measured GluK2-5 protein levels in the subsequent analyses.

Titration of GluK antibodies

We titrated GluK2-5 antibodies using GluA2-KAR chimeric proteins, in which the C-terminal sequence of GluA2 (downstream to the M4 domain) was replaced with that of GluK2-5 (Fig. 3a). Because all of the GluK2-5 antibodies were raised against the C-terminal regions, the titer of GluK2-5 antibodies could be standardized by using GluA2 antibody raised against the N-terminal domain (Fig. 3b). The densitometric measurement of protein bands for different loads of chimeric proteins showed linear dose-intensity plots for each of GluK2-5 and GluA2 antibodies (Fig. 3c). Since an extreme difference in the intensities

between chimeric protein bands detected by GluA2 and GluK2-5 antibodies failed to stabilize their titer ratio, we used each of their signal intensities from the same range and generated standard curves (Fig. 3c). From these plots, the titer ratios of GluK2-5 antibodies were calculated to be 8.0, 2.4, 30.5, and 24.6 times that of GluA2 antibody.

Relative amounts of GluK in hippocampus and cerebellum

Using the titer ratios, we estimated the relative amount of GluK2-5 proteins in the P2 and PSD fractions prepared from the hippocampus and cerebellum (Figs 4 and 5). The

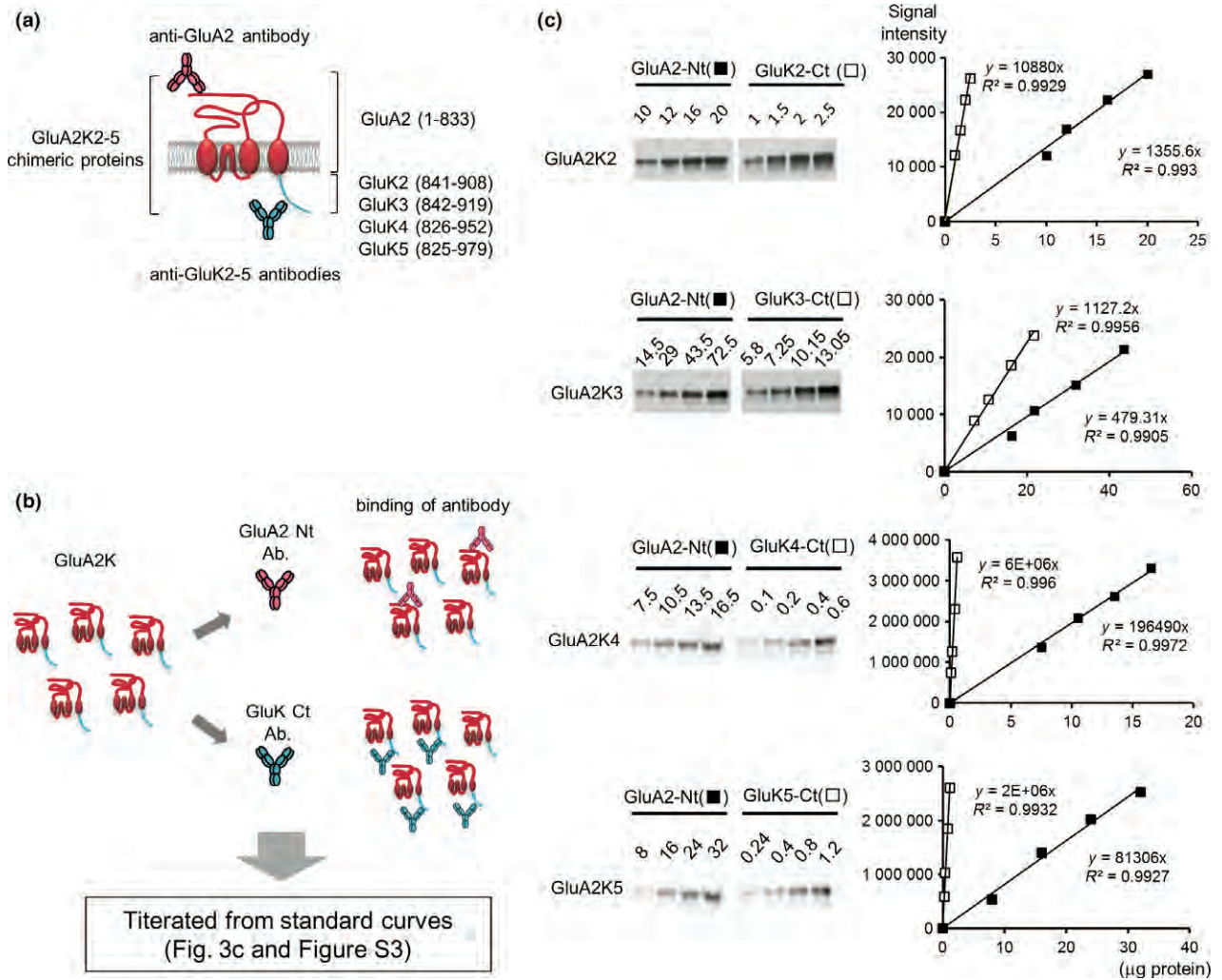


Fig. 3 Unique method of GluK subunits determination by western blot. (a) Scheme of a chimeric protein of GluA2K2-GluA2K5 used for quantification analysis whose N-terminal GluA2 was fused with four C-terminal GluK2-5. Each titer was corrected by the titer of anti-GluA2 N-terminal antibody, and used for quantitative analysis of the four GluK subunits. (b) Chimeric proteins prepared from COS-7 cells or HEK293 cells were used for determining the ratio of antibody titers. Each antibody binds to chimeric protein depending on each affinity titer, and this reaction can be seen as western blot band signals. (c) Western

blot for determination of each titer of GluK2-5 antibodies with chimeric GluA2K2-5 proteins detected by GluA2 antibody and GluK2-5 antibodies. Each number of loaded samples of transfected cell lysates represents protein amount (μg). Examples of standard curves of GluA2K2-5 signal intensities detected by anti-GluA2 antibody (black square) and anti-GluK2-5 antibodies (white square) are shown. The ratios of anti-GluK2-5 antibody titers to anti-GluA2 antibody were determined by using GluA2K2-5 intensities.

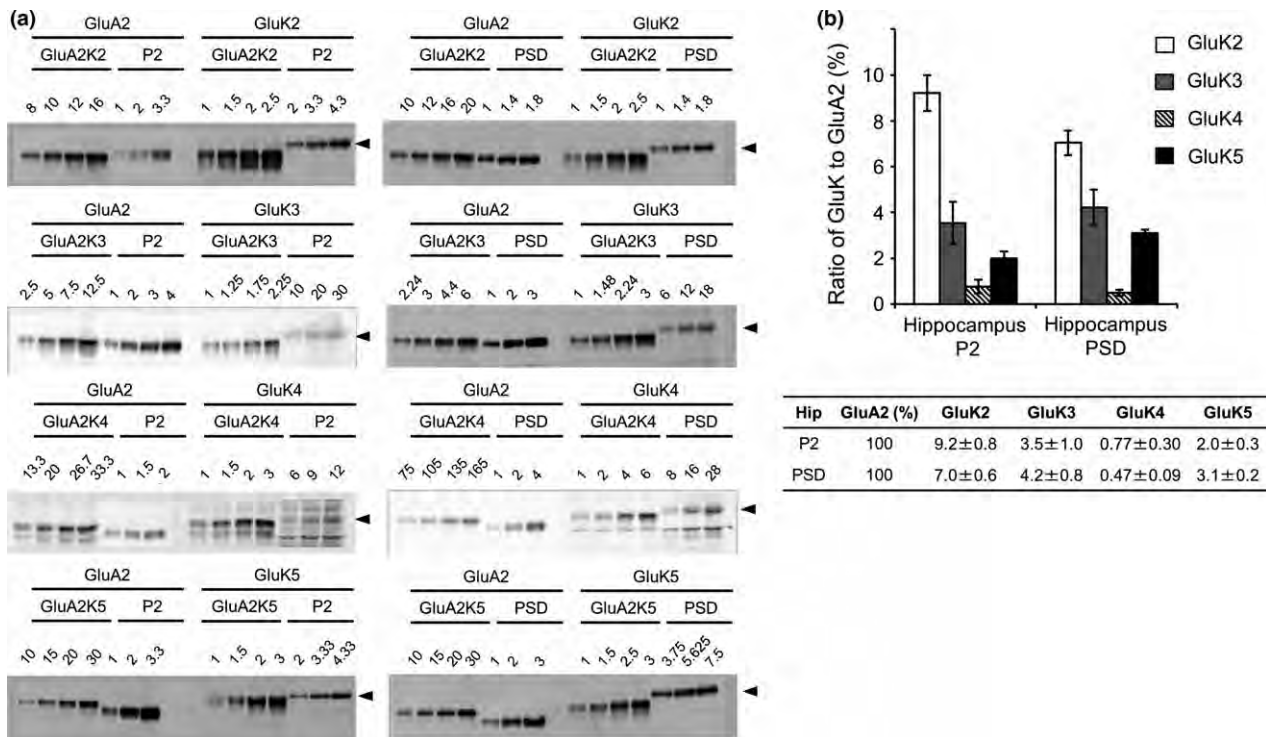


Fig. 4 Determination of GluK subunits in hippocampus. (a) Analytical western blots of GluK subunits in P2 and post-synaptic density (PSD) fractions of hippocampus. Graded dilutions of hippocampal P2 and PSD fractions and each of chimeric GluA2K were subjected to analytical western blot. In order to simplify the picture, loaded protein amounts are indicated with relative one (see Table S1). The molecular weights are growing larger, in the order of GluA2 < GluA2K2-

amounts of loaded protein samples on western blots were changed according to the titer of each antibody and subunit content in each fraction, as summarized in Table S1. We generated standard curves of chimeric proteins and endogenous proteins (GluA2, GluK2-5) in every experiments ($n = 3$). A representative example is shown in Figure S4, where we made four standard curves of GluA2K2 detected by GluA2 antibody, GluA2K2 detected by GluK2 antibody, GluA2 in hippocampal PSD fraction, and GluK2 in hippocampal PSD fraction in the same intensity range (< 30000 (intensity), see vertical axis in Figure S4). Using these standard curves, we titrated their titer ratio and determined the ratio of GluK2 to GluA2. The western blot images (Figs 4a and 5a) are of one of those experiments determining GluK2-GluK5. We averaged the amounts of GluK2-5 proteins relative to GluA2 protein in each experiment (GluK2-GluK5, $n = 3$, respectively), as shown in the graph and table (Figs 4b and 5b).

In the hippocampus, GluK2, GluK3, GluK4, and GluK5 amounted to $9.2 \pm 0.8\%$, $3.5 \pm 1.0\%$, $0.77 \pm 0.30\%$, and $2.0 \pm 0.3\%$, respectively, of GluA2 in the P2 fraction ($n = 3$ for each), and to $7.0 \pm 0.6\%$, $4.2 \pm 0.8\%$, $0.47 \pm 0.09\%$, and $3.1 \pm 0.2\%$, respectively, of GluA2 in the PSD fraction

($n = 3$ for each) (Fig. 4b). In the cerebellum, GluK2, GluK3, GluK4, and GluK5 amounted to $22 \pm 2\%$, $17 \pm 4\%$, $1.9 \pm 0.4\%$, and $2.8 \pm 0.5\%$, respectively, of GluA2 in the P2 fraction ($n = 3$ for each), and to $9.9 \pm 2.4\%$, $7.3 \pm 1.0\%$, $1.1 \pm 0.1\%$, and $1.4 \pm 0.2\%$, respectively, of GluA2 in the PSD fraction ($n = 3$ for each) (Fig. 5b). These data show that the composition of GluK2-5 subunits is different depending on the brain regions and biochemical fractions, with GluK2 being the major component in the hippocampus and cerebellum.

By setting the relative amount of GluK2 in each fraction as 1.00, we compared the ratio of four GluK subunits among the four hippocampal and cerebellar fractions (Fig. 6a). In all fractions, the relative abundance of GluK2-5 subunits was in the order of GluK2 > GluK3 > GluK5 > GluK4, with relative enrichment of GluK3 in the cerebellar fractions and of GluK5 in the hippocampal PSD fraction (Fig. 6a). To simplify the understanding of composition of GluK subunits in each fraction, we also set GluK2 in the hippocampus P2 fraction as 1.00 and compared the ratio between the P2 and PSD fractions in the hippocampus and cerebellum (Fig. 6b). When collectively calculating low-affinity subunits (GluK2 plus GluK3) as 1.00, the ratio of high-affinity subunits

($n = 3$ for each) (Fig. 4b). In the cerebellum, GluK2, GluK3, GluK4, and GluK5 amounted to $22 \pm 2\%$, $17 \pm 4\%$, $1.9 \pm 0.4\%$, and $2.8 \pm 0.5\%$, respectively, of GluA2 in the P2 fraction ($n = 3$ for each), and to $9.9 \pm 2.4\%$, $7.3 \pm 1.0\%$, $1.1 \pm 0.1\%$, and $1.4 \pm 0.2\%$, respectively, of GluA2 in the PSD fraction ($n = 3$ for each) (Fig. 5b). These data show that the composition of GluK2-5 subunits is different depending on the brain regions and biochemical fractions, with GluK2 being the major component in the hippocampus and cerebellum.

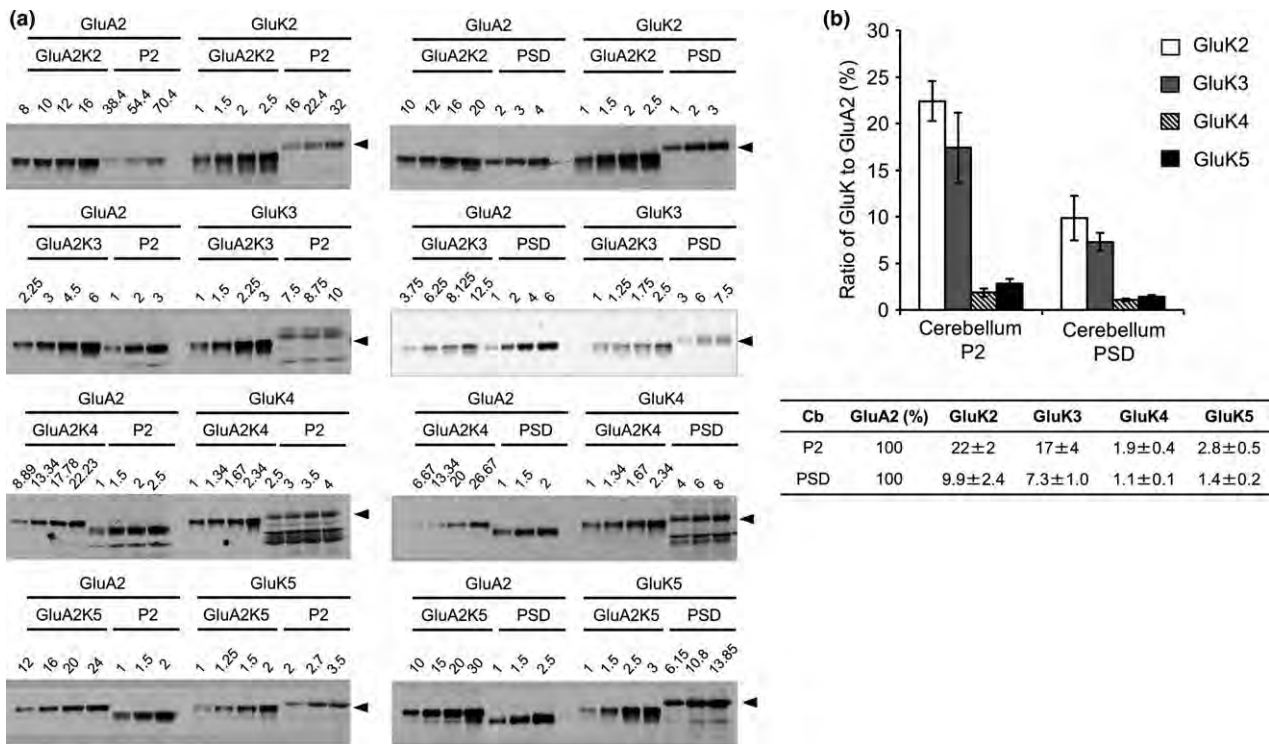


Fig. 5 Determination of GluK subunits in cerebellum. (a) Analytical western blots of GluK subunits in P2 and post-synaptic density (PSD) fractions of cerebellum. Detailed explanation is as shown in Fig. 4. (b) Ratios of kainate-type glutamate receptor subunits in cerebellum P2

and PSD fractions are shown in the table and the bar graphs. The ratios of GluK2 (white), GluK3 (gray), GluK4 (stripe), and GluK5 (black) are normalized by the amount of GluA2 in each brain region and fraction. Error bars represent SEM.

(GluK4 plus GluK5) was higher in the hippocampus (0.22 in the P2 and 0.32 in the PSD fraction) than in the cerebellum (0.12, and 0.15 respectively). By setting the relative amount in the P2 fraction as 1.00 in each region, each GluK subunit showed 3–5-fold enrichment in the PSD fraction of the hippocampus and cerebellum (Table 1).

Discussion

In the present study, the relative amount of KAR subunits was compared by standardizing the titer of KAR subunit antibodies using chimeric GluA2-GluK fusion proteins. Based on the titrated antibodies, we examined the relative amount of each KAR subunit in biochemical fractions prepared from the adult mouse hippocampus and cerebellum.

This method enabled the assessment of the amount of KAR subunits relative to GluA2 subunit in the same biochemical fractions. Compared to standardized immunoblot analysis using endogenous standard proteins, such as actin, this method is advantageous in that it is applicable to the comparison of relative amounts of multiple subunits using different antibodies. Although its low sensitivity such as inability of GluK1 detection in the adult mouse brain is to be further improved, the reliability of the present comparison for GluK2–5 subunits was ensured by specific detection of GluK2–5 protein bands,

as demonstrates by using GluK2–5 defective mice as negative controls, and by linear dose-intensity plots using chimeric GluA2-KAR protein standards. Here, we have shown that low-affinity KAR subunits are predominantly expressed in the adult mouse brain, where the relative amount of GluK2 plus GluK3 was several times higher than that of GluK4 plus GluK5 in the hippocampus and cerebellum.

Native KARs are thought to be heteromeric receptors composed of various combinations of subunits. When expressed in HEK293 cells and *Xenopus* oocytes, GluK4 and GluK5 subunits associate with GluK1–3 subunits to form heteromeric receptors with pharmacological properties distinct from homomeric receptors consisting of the low-affinity subunits. Moreover, the amplitude of channel activity of GluK2/GluK5 heteromeric receptors is several times larger than that of GluK2 homomeric receptors (Sakimura *et al.* 1992). Immunoprecipitated analysis has revealed that GluK5 is co-immunoprecipitated with GluK2 in CA3 pyramidal cells (Wenthold *et al.* 1994). A single molecule imaging of fluorescence-tagged GluK2 and GluK5 subunits revealed that they assemble with a 2 : 2 stoichiometry (Reiner *et al.* 2012). Crystal structure analysis has shown that the N-terminal domains of GluK2 and GluK5 subunits preferentially co-assemble as heterodimers rather than as homodimers (Kumar *et al.* 2011). In the hippocampus of GluK4/GluK5-double

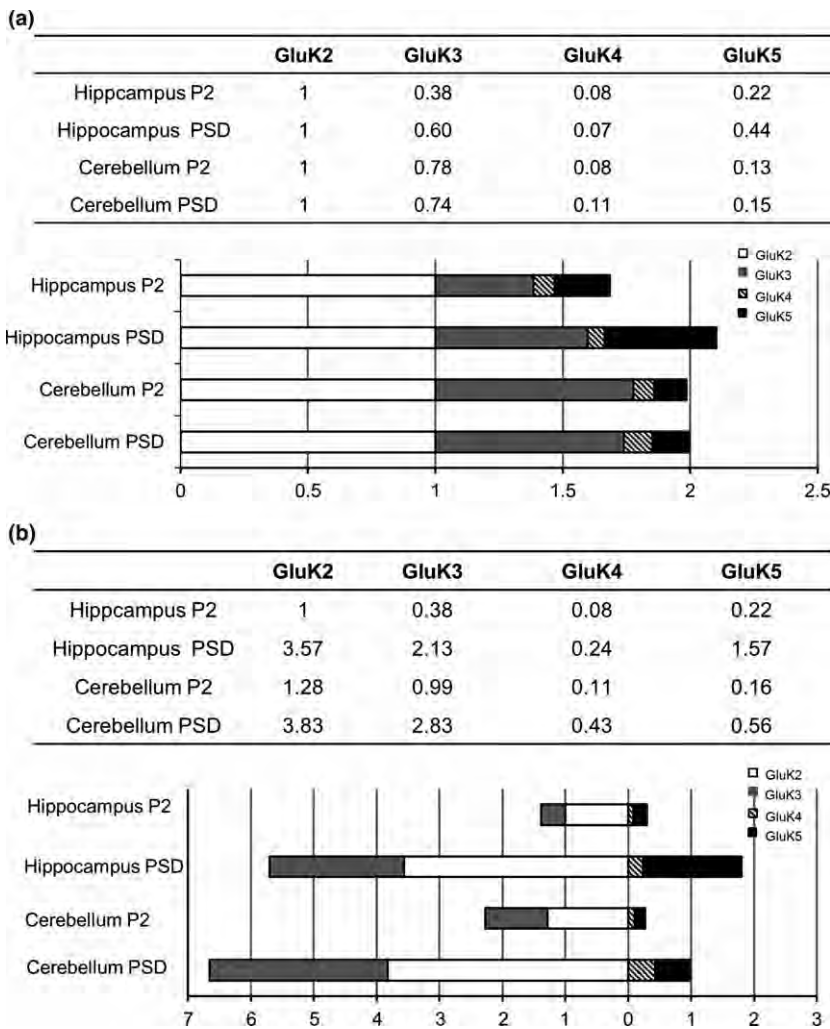


Fig. 6 Composition of kainate-type glutamate receptor (KAR) subunits in hippocampus and cerebellum. (a) Relative ratios of KAR subunits in hippocampal P2, post-synaptic density (PSD) and cerebellar P2, PSD are shown in the table and the bar graph. The ratios of GluK3 (gray), GluK4 (stripe), and GluK5 (black) are normalized by the amount of GluK2 (white) in the brain regions respectively. (b) Relative amounts of KAR subunits normalized by the amount of GluK2 in hippocampus P2 fraction are shown in the table and the bar graph. Low-affinity GluK2 and GluK3 are described in the left side of position 0, and high affinity GluK4 and GluK5 are described in the right side.

knockout mice, detectable KAR-mediated EPSCs are lost at mossy fiber-CA3 synapses (Fernandes *et al.* 2009). These findings indicate that one form of functional KARs in the brain is heteromeric receptors consisting of high- and low-affinity subunits. GluK4 and GluK5 subunits in hippocampal and cerebellar fractions are likely to represent, mostly if not all, such heteromeric receptors. The highest GluK5-to-GluK2 ratio and its marked increment from the P2 fraction (0.22) to the PSD fraction (0.44) in the hippocampus further suggest that heteromeric receptors consisting of high- and low-affinity subunits highly accumulate at hippocampal synapses.

Another form of functional KARs in the brain is homomeric and heteromeric receptors consisting of only low-affinity KAR subunits. Application of kainate and glutamate elicits current responses in HEK293 cells expressing GluK1 (Q), GluK2(Q/R), GluK1/GluK2, GluK3a, and GluK3b (Sommer *et al.* 1992; Coussen *et al.* 2005). GluK1 and GluK2 subunits co-assemble to generate recombinant receptors with novel functional properties (Cui and Mayer 1999). Two splice variants of GluK2 subunit (GluK2a and GluK2b)

also co-assemble to regulate KAR trafficking and function (Coussen *et al.* 2005). The ratio of low-affinity (GluK2 plus GluK3) to high-affinity (GluK4 plus GluK5) was higher in the cerebellum (8.5 in the P2 fraction and 6.7 in the PSD fraction) than in the hippocampus (4.6 and 3.1, respectively), suggesting that KARs consisting of low-affinity subunits are more prevalent in the cerebellum. There have been many studies on KAR-mediated synaptic transmission focusing on hippocampus CA3-dentate gyrus synapses, reporting loss of GluK4 and GluK5 showed no detectable KAR-EPSCs in hippocampus. In this study, it is reasonable to expect that GluK2 homomer in cerebellum granule cells would not show KAR-EPSCs. Indeed, cerebellar granule cells in wild type showed no KAR-mediated synaptic transmission, but loss of AMPAR activity increased GluK5 expression and GluK2/5-containing KAR-mediated synaptic transmission (Yan *et al.* 2013). KAR activity is possibly regulated by an increase in GluK4 or GluK5 expression, when AMPAR activity decreased.

Expression patterns of five KAR subunits by *in situ* hybridization are quite similar between rat and mouse brains.

Table 1 Enrichment of GluK subunits in the post-synaptic density (PSD) fraction of the hippocampus and cerebellum

	GluK2	GluK3	GluK4	GluK5
Hippocampus P2	1	1	1	1
Hippocampus PSD	3.57	5.56	2.84	7.24
Cerebellum P2	1	1	1	1
Cerebellum PSD	2.99	2.83	4.00	3.46

These values are calculated from Fig. 6b.

In both species, GluK5 mRNA is prominently expressed in various brain regions, including the hippocampus and cerebellum (Wisden and Seeburg 1993; this study). It was thus unexpected to find predominant protein contents of low-affinity KAR subunits over high-affinity ones in the adult brain. This was particularly prominent in the cerebellum, where GluK4 and GluK5 mRNAs are highly expressed, but their protein contents were less than one-tenth of that of GluK2. This discrepancy raises the possibility that the predominant low-affinity subunit expression is constructed mainly at the post-transcriptional level. Considering that high-affinity subunits cannot form functional homomeric KARs (Bettler *et al.* 1990, 1992; Egebjerg *et al.* 1991; Herb *et al.* 1992; Sakimura *et al.* 1992), homomeric receptors consisting of high-affinity subunits alone might be unstable and prone to be degraded, even if they are constructed in neurons. In NMDARs, heteromeric subunit configuration is essential for channel function and synaptic expression. Without GluN2 subunits, GluN1 subunit is unable to accumulate on the post-synaptic membrane and its turnover rate is accelerated (Abe *et al.* 2004). Without GluN1 subunit, GluN2 subunits are retained in the ER for degradation (McIlhinney *et al.* 1996; Fukaya *et al.* 2003). In KAR, GluK5 also has an ER retention motif and enables recruiting the membrane when co-assembled with GluK1, GluK2, and GluK3 (Gallyas *et al.* 2003). Without them, GluK5 was also heavily retained in the ER and lost its current in heterologous cells (Hayes *et al.* 2003; Ren *et al.* 2003). We also found that the amount of GluK5 is less enriched in PSD fraction of cerebellum than that of hippocampus (Table 1), indicating the trafficking of GluK subunit to the post-synaptic plasma membrane may be differentially regulated in these regions. Perhaps its turnover rate is maintained depending on the brain region. Overall, this discrepancy of the amount of GluK5 at mRNA and protein level remains to be investigated.

In this study, we noticed the importance of low-affinity subunits as major KAR subunits, although their main roles have not been understood so far. In our data, GluK2-GluK5 showed positive concentration efficiency to PSD fractions from P2 fractions. The fractionation procedure was performed as previously described (Abe *et al.* 2004; Fukaya *et al.* 2006; Yamazaki *et al.* 2010; see method section). In

hippocampus, concentration levels of both GluK2 and GluK3 are fourfold higher in PSD fractions than in P2 fraction. The proportions of AMPAR and KAR subunits in enriched synaptic membrane fractions in rat cortex with synaptic purification technique (Phillips *et al.* 2001; Pinheiro *et al.* 2003, 2005) showed that GluK2/3 was predominantly present in PSD fractions (about 70–80%) with much lower levels of pre-synaptic and non-synaptic synaptosomal protein fractions (about 20–30%) (Feligioni *et al.* 2006), which are consistent with our data as mentioned above. On the other hand, GluA1 and GluA2 were not predominantly present in PSD fraction (40–60%) compared with GluK2/3. Biochemical distribution and protein solubility of other glutamate receptors showed that many NMDA-type glutamate receptors were in the insoluble membrane fractions, while AMPARs were in the insoluble membrane fractions and the soluble fractions (Fukaya *et al.* 2006; Inamura *et al.* 2006), suggesting that the distribution of KAR at ultrasympaptic fraction may be different from that of AMPAR. These data might elucidate the controversy of subcellular localization of KAR including pre- and/or post-synapse, and point to a hidden role of the post-synaptic afferent in the neuron. Future study will provide an insight into whether low-affinity KAR subunits mediate neurotransmission signal at post-synaptic sites.

Acknowledgments and conflict of interest disclosure

We thank C. Nakamoto, H. Azechi and Y. Suzuki for technical assistance and advice. We also thank M. Kawamura and H. Uchida for the valuable discussion. This study was supported by CREST and Grants-in-aid for Scientific Research from the Ministry of Education, Culture, Sports, Science and Technology of Japan (21300118, 24650195, 24240048 to K.S.). We have no conflict of interest to declare.

All experiments were conducted in compliance with the ARRIVE guidelines.

Supporting information

Additional supporting information may be found in the online version of this article at the publisher's web-site:

Figure S1. (a) To construct a *Grik2* targeting vector, a 770 bp DNA fragment carrying exon 14 of the *Grik2* was amplified by PCR, and inserted to the targeting vector as described previously (Akashi *et al.* 2009). In this clone, a DNA fragment of pgk promoter-driven Neo-poly(A) flanked by two *flp* sites (*Neo cassette*) and *loxP* sequence was located at the site 311 bp upstream of the exon 14, while the other *loxP* sequence was placed at the site 241 bp downstream of the exon 14. It contained a 6.83 kb *Grik2* at the 5' side and 3.79 kb *Grik2* at the 3' side, followed by an MC1 promoter-driven diphtheria toxin (DT) gene. (b) To construct a *Grik3* targeting vector, a 817 bp DNA fragment carrying exon 12 of the *Grik3* was amplified by PCR, and inserted to the *SacI* sites of the middle entry clone (pDME-1). In this clone, a DNA fragment of *Neo cassette* and

loxP sequence was located at the site 428 bp upstream of the exon 12, while the other *loxP* sequence was placed at the site 270 bp downstream of the exon 12. The 5.07 kb upstream and 5.24 kb downstream homologous genomic DNA fragments were retrieved from the BAC clone (RP23-131M1), and then subcloned to 5' entry clone (pD3UE-2) and 3' entry clone (pD5DE-2) respectively. For targeting vector assembly, the three entry clones were recombined to a destination vector plasmid (pDEST-DT; containing a cytomegalovirus enhancer/chicken actin (CAG) promoter-driven DT gene by using a MultiSite Gateway Three-fragment Vector construction Kit (Invitrogen) (Sasaki *et al.* 2004). (c) To construct a *Grik5* targeting vector, a 770 bp DNA fragment carrying exon 13, 14, and 15 of the *Grik5* was amplified by PCR, and inserted to the targeting vector as described previously (Akashi *et al.* 2009). In this clone, a DNA fragment of *Neo cassette* and *loxP* sequence was located at the site 411 bp upstream of the exon 13, while the other *loxP* sequence was placed at the site 96 bp downstream of the exon 15. It contained a 6.53 kb *Grik5* at the 5' side and 3.13 kb *Grik5* at the 3' side, followed by an MC1 promoter-driven DT gene. Each targeting vector introduced into C57BL/6N ES cell line RENKA and recombinant clones were identified by Southern blot. To produce germline chimeras, recombinant ES clones were microinjected into eight cell stage embryos of CD1 mouse strain. To generate *Grik2*, *Grik3* and *Grik5*-null mice, each flowed mouse was crossed with the telencephalin-Cre mice (Nakamura *et al.* 2001).

Figure S2. Specificity of GluK1 antibody (Upstate) was checked with western blot analysis of COS-7 cell lysates transfected with each cDNA of GluK1-GluK3. Cross reactivity of GluK1 antibodies between GluK1 and GluK2 was tested using the brain extracts, hippocampal P2 fractions, derived from wild type and GluK2-KO mice. A detected GluK1 band of the GluK1 antibody in the wild type disappeared in GluK2-KO mice.

Figure S3. (a) RT-PCR was performed using primers spanning exon 10–12 with whole brain of adult wild type (C57BL/6N), GluK3^{flox/flox} mice and post-natal day 3 (P3) GluK3^{flox/flox} mice. Amplification of glyceraldehyde-3-phosphate dehydrogenase gene was used as a positive control for the RT reaction (bottom panel). P3 GluK3^{flox/flox} mice were used instead of wild type mice. (b) GluK1 transcript was decreased in adult mice, compared to P3 mice (top panel). The expression level of adult mice GluK1 transcript was normalized by that of P3 mice. Error bars represent SEM. Student's *t*-test was used for statistical analysis.

Figure S4. (a) Determination of GluK2 ratio to GluA2 examined by chimeric protein and hippocampus PSD sample is shown as an example of the determination method. Amounts of loaded COS-7 cells lysate expressing GluA2K2 and hippocampal PSD sample are shown as a relative value. (b) Standard curves of GluA2K2 (left) and hippocampus PSD sample (right) were detected by GluA2 antibody (black square and circle) and GluK2 antibody (white square and circle). The protein ratio of GluK2 to GluA2 in hippocampus PSD was quantified by correcting titer ratio of GluK2 antibody to GluA2 antibody. (c) The titer of GluK2 antibody to GluA2 antibody was obtained from calculation using the slopes of GluA2K2 standard curves (b, left). The relative ratio of GluK2 protein to GluA2 protein was also calculated by using the slopes of GluK2 and GluA2 standard curves (b, right) and GluK2 titer ratio mentioned above.

Table S1. The amount (mg) of loaded protein samples of hippocampus and cerebellum.

References

- Abe M., Fukaya M., Yagi T., Mishina M., Watanabe M. and Sakimura K. (2004) NMDA receptor GluRepsilon/NR2 subunits are essential for postsynaptic localization and protein stability of GluRzeta1/NR1 subunit. *J. Neurosci.* **24**, 7292–7304.
- Akashi K., Kakizaki T., Kamiya H., Fukaya M., Yamasaki M., Abe M., Natsume R., Watanabe M. and Sakimura K. (2009) NMDA receptor GluN2B (GluR epsilon 2/NR2B) subunit is crucial for channel function, postsynaptic macromolecular organization, and actin cytoskeleton at hippocampal CA3 synapses. *J. Neurosci.* **29**, 10869–10882.
- Bahn S., Volk B. and Wisden W. (1994) Kainate receptor gene expression in the developing rat brain. *J. Neurosci.* **14**, 5525–5547.
- Bettler B., Boulter J., Hermans-Borgmeyer I., O'Shea-Greenfield A., Deneris E. S., Moll C., Borgmeyer U., Hollmann M. and Heinemann S. (1990) Cloning of a novel glutamate receptor subunit, GluR5: Expression in the nervous system during development. *Neuron* **5**, 583–595.
- Bettler B., Egebjerg J., Sharma G., Pecht G., Hermans-Borgmeyer I., Moll C., Stevens C. F. and Heinemann S. (1992) Cloning of a putative glutamate receptor: a low affinity kainate-binding subunit. *Neuron* **8**, 257–265.
- Bureau I., Bischoff S., Heinemann S. F. and Mulle C. (1999) Kainate receptor-mediated responses in the CA1 field of wild-type and GluR6-deficient mice. *J. Neurosci.* **19**, 653–663.
- Bureau I., Dieudonne S., Coussen F. and Mulle C. (2000) Kainate receptor-mediated synaptic currents in cerebellar Golgi cells are not shaped by diffusion of glutamate. *Proc. Natl Acad. Sci. USA* **97**, 6838–6843.
- Contractor A., Mulle C. and Swanson G. T. (2011) Kainate receptors coming of age: milestones of two decades of research. *Trends Neurosci.* **34**, 154–163.
- Coussen F., Perrais D., Jaskolski F., Sachidhanandam S., Normand E., Bockaert J., Marin P. and Mulle C. (2005) Co-assembly of two GluR6 kainate receptor splice variants within a functional protein complex. *Neuron* **47**, 555–566.
- Cui C. and Mayer M. L. (1999) Heteromeric kainate receptors formed by the coassembly of GluR5, GluR6, and GluR7. *J. Neurosci.* **19**, 8281–8291.
- Egebjerg J., Bettler B., Hermans-Borgmeyer I. and Heinemann S. (1991) Cloning of a cDNA for a glutamate receptor subunit activated by kainate but not AMPA. *Nature* **351**, 745–748.
- Feligioni M., Holman D., Haglerod C., Davanger S. and Henley J. M. (2006) Ultrastructural localisation and differential agonist-induced regulation of AMPA and kainate receptors present at the presynaptic active zone and postsynaptic density. *J. Neurochem.* **99**, 549–560.
- Fernandes H. B., Catches J. S., Petralia R. S., Copits B. A., Xu J., Russell T. A., Swanson G. T. and Contractor A. (2009) High-affinity kainate receptor subunits are necessary for ionotropic but not metabotropic signaling. *Neuron* **63**, 818–829.
- Fukaya M., Kato A., Lovett C., Tonegawa S. and Watanabe M. (2003) Retention of NMDA receptor NR2 subunits in the lumen of endoplasmic reticulum in targeted NR1 knockout mice. *Proc. Natl Acad. Sci. USA* **100**, 4855–4860.
- Fukaya M., Tsujita M., Yamazaki M., Kushiya E., Abe M., Akashi K., Natsume R., Kano M., Kamiya H., Watanabe M. and Sakimura K. (2006) Abundant distribution of TARP gamma-8 in synaptic and extrasynaptic surface of hippocampal neurons and its major role in AMPA receptor expression on spines and dendrites. *Eur. J. Neurosci.* **24**, 2177–2190.
- Gallyas F., Ball S. M. and Molnar E. (2003) Assembly and cell surface expression of KA-2 subunit-containing kainate receptors. *J. Neurochem.* **86**, 1414–1427.

- Hayes D. M., Braud S., Hurtado D. E., McCallum J., Standley S., Isaac J. T. R. and Roche K. W. (2003) Trafficking and surface expression of the glutamate receptor subunit, KA2. *Biochem. Biophys. Res. Commun.* **310**, 8–13.
- Herb A., Burnashev N., Werner P., Sakmann B., Wisden W. and Seeburg P. H. (1992) The KA-2 subunit of excitatory amino acid receptors shows widespread expression in brain and forms ion channels with distantly related subunits. *Neuron* **8**, 775–785.
- Inamura M., Itakura M., Okamoto H., Hoka S., Mizoguchi A., Fukazawa Y., Shigemoto R., Yamamori S. and Takahashi M. (2006) Differential localization and regulation of stargazin-like protein, gamma-8 and stargazin in the plasma membrane of hippocampal and cortical neurons. *Neurosci. Res.* **55**, 45–53.
- Konno K., Matsuda K., Nakamoto C., Uchigashima M., Miyazaki T., Yamasaki M., Sakimura K., Yuzaki M. and Watanabe M. (2014) Enriched expression of GluD1 in higher brain regions and its involvement in parallel fiber-interneuron synapse formation in the cerebellum. *J. Neurosci.* **34**, 7412–7424.
- Kumar J., Schuck P. and Mayer M. L. (2011) Structure and assembly mechanism for heteromeric kainate receptors. *Neuron* **71**, 319–331.
- Lerma J. (2003) Roles and rules of kainate receptors in synaptic transmission. *Nat. Rev. Neurosci.* **4**, 481–495.
- Lerma J. (2006) Kainate receptor physiology. *Curr. Opin. Pharmacol.* **6**, 89–97.
- McIlhinney R. A. J., Molnár E., Atack J. R. and Whiting P. J. (1996) Cell surface expression of the human N-methyl-D-aspartate receptor subunit 1a requires the co-expression of the NR2A subunit in transfected cells. *Neuroscience* **70**, 989–997.
- Mishina M. and Sakimura K. (2007) Conditional gene targeting on the pure C57BL/6 genetic background. *Neurosci. Res.* **58**, 105–112.
- Mizushima S. and Nagata S. (1990) pEF-BOS, a powerful mammalian expression vector. *Nucleic Acids Res.* **18**, 5322.
- Nakamura K., Manabe T., Watanabe M., *et al.* (2001) Enhancement of hippocampal LTP, reference memory and sensorimotor gating in mutant mice lacking a telencephalon-specific cell adhesion molecule. *Eur. J. Neurosci.* **13**, 179–189.
- Phillips G. R., Huang J. K., Wang Y., Tanaka H., Shapiro L., Zhang W., Shan W. S. *et al.* (2001) The presynaptic particle web: ultrastructure, composition, dissolution, and reconstitution. *Neuron* **32**, 63–77.
- Pinheiro P. and Mulle C. (2006) Kainate receptors. *Cell Tissue Res.* **326**, 457–482.
- Pinheiro P. S., Rodrigues R. J., Silva A. P., Cunha R. A., Oliveira C. R. and Malva J. O. (2003) Solubilization and immunological identification of presynaptic α -amino-3-hydroxy-5-methyl-4-isoxazolepropionic acid receptors in the rat hippocampus. *Neurosci. Lett.* **336**, 97–100.
- Pinheiro P. S., Rodrigues R. J., Rebola N., Xapelli S., Oliveira C. R. and Malva J. O. (2005) Presynaptic kainate receptors are localized close to release sites in rat hippocampal synapses. *Neurochem. Int.* **47**, 309–316.
- Reiner A., Arant R. J. and Isacoff E. Y. (2012) Assembly stoichiometry of the GluK2/GluK5 kainate receptor complex. *Cell Rep.* **1**, 234–240.
- Ren Z., Riley N. J., Garcia E. P., Sanders J. M., Swanson G. T. and Marshall J. (2003) Multiple trafficking signals regulate kainate receptor KA2 subunit surface expression. *J. Neurosci.* **23**, 6608–6616.
- Renard A., Crépel F. and Audinat E. (1995) Evidence for two types of non-NMDA receptors in rat cerebellar Purkinje cells maintained in slice cultures. *Neuropharmacology* **34**, 335–346.
- Sakimura K., Morita T., Kushiya E. and Mishina M. (1992) Primary structure and expression of the γ 2 subunit of the glutamate receptor channel selective for kainate. *Neuron* **8**, 267–274.
- Sasaki Y., Sone T., Yoshida S., Yahata K., Hotta J., Chesnut J. D., Honda T. and Imamoto F. (2004) Evidence for high specificity and efficiency of multiple recombination signals in mixed DNA cloning by the Multisite Gateway system. *J. Biotechnol.* **107**, 233–243.
- Savidge J. R., Sturgess N. C., Bristow D. R. and Lock E. A. (1999) Characterisation of kainate receptor mediated whole-cell currents in rat cultured cerebellar granule cells. *Neuropharmacology* **38**, 375–382.
- Sommer B., Burnashev N., Verdoorn T. A., Keinänen K., Sakmann B. and Seeburg P. H. (1992) A glutamate receptor channel with high affinity for domoate and kainate. *EMBO J.* **11**, 1651–1656.
- Wentholt R. J., Trumpy V. A., Zhu W. S. and Petralia R. S. (1994) Biochemical and assembly properties of GluR6 and KA2, two members of the kainate receptor family, determined with subunit-specific antibodies. *J. Biol. Chem.* **269**, 1332–1339.
- Wisden W. and Seeburg P. H. (1993) A complex mosaic of high-affinity kainate receptors in rat brain. *J. Neurosci.* **13**, 3582–3598.
- Yamasaki M., Matsui M. and Watanabe M. (2010) Preferential localization of muscarinic M1 receptor on dendritic shaft and spine of cortical pyramidal cells and its anatomical evidence for volume transmission. *J. Neurosci.* **30**, 4408–4418.
- Yamazaki M., Fukaya M., Hashimoto K., Yamasaki M., Tsujita M., Itakura M., Abe M. *et al.* (2010) TARPs gamma-2 and gamma-7 are essential for AMPA receptor expression in the cerebellum. *Eur. J. Neurosci.* **31**, 2204–2220.
- Yan D., Yamasaki M., Straub C., Watanabe M. and Tomita S. (2013) Homeostatic control of synaptic transmission by distinct glutamate receptors. *Neuron* **78**, 687–699.

Anterograde C1ql1 Signaling Is Required in Order to Determine and Maintain a Single-Winner Climbing Fiber in the Mouse Cerebellum

Wataru Kakegawa,^{1,2} Nikolaos Mitakidis,³ Eriko Miura,^{1,2} Manabu Abe,^{2,4} Keiko Matsuda,^{1,2} Yukari H. Takeo,^{1,2} Kazuhisa Kohda,^{1,2} Junko Motohashi,^{1,2} Akiyo Takahashi,^{1,2} Soichi Nagao,⁵ Shin-ichi Muramatsu,⁶ Masahiko Watanabe,^{2,7} Kenji Sakimura,^{2,4} A. Radu Aricescu,³ and Michisuke Yuzaki^{1,2,*}

¹Department of Physiology, Keio University School of Medicine, Tokyo 160-8582, Japan

²Core Research for Evolutional Science and Technology (CREST), Japan Science and Technology Agency (JST), Tokyo 102-0075, Japan

³Division of Structural Biology, Wellcome Trust Centre for Human Genetics, University of Oxford, Oxford OX3 7BN, UK

⁴Department of Cellular Neurobiology, Brain Research Institute, Niigata University, Niigata 951-8585, Japan

⁵Laboratory for Motor Learning Control, RIKEN Brain Science Institute, Saitama 351-0198, Japan

⁶Division of Neurology, Jichi Medical University, Tochigi 329-0498, Japan

⁷Department of Anatomy, Graduate School of Medicine, Hokkaido University, Sapporo 060-8638, Japan

*Correspondence: myuzaki@a5.keio.jp

<http://dx.doi.org/10.1016/j.neuron.2014.12.020>

SUMMARY

Neuronal networks are dynamically modified by selective synapse pruning during development and adulthood. However, how certain connections win the competition with others and are subsequently maintained is not fully understood. Here, we show that C1ql1, a member of the C1q family of proteins, is provided by climbing fibers (CFs) and serves as a crucial anterograde signal to determine and maintain the single-winner CF in the mouse cerebellum throughout development and adulthood. C1ql1 specifically binds to the brain-specific angiogenesis inhibitor 3 (Bai3), which is a member of the cell-adhesion G-protein-coupled receptor family and expressed on postsynaptic Purkinje cells. C1ql1-Bai3 signaling is required for motor learning but not for gross motor performance or coordination. Because related family members of C1ql1 and Bai3 are expressed in various brain regions, the mechanism described here likely applies to synapse formation, maintenance, and function in multiple neuronal circuits essential for important brain functions.

INTRODUCTION

In mammals, precise neuronal network formation is generally achieved by selective synapse pruning: a few inputs are strengthened by increasing the number of their synaptic contacts, while weak inputs are physically removed. As a model of activity-dependent synapse refinement in the central nervous system (CNS), postnatal pruning of supernumerary synapses between climbing fibers (CFs, axons of inferior olivary [IO] neurons) and Purkinje cells in the cerebellum has been extensively studied (Cesa and Strata, 2009; Kano and Hashimoto, 2009; Lohof et al.,

1996; Watanabe and Kano, 2011). Multiple CFs initially innervate a single Purkinje cell soma, but a single CF becomes dominant in a postsynaptic, voltage-dependent Ca^{2+} channel activity-dependent manner during postnatal days (P) 3–7 in mice (Kano and Hashimoto, 2009; Watanabe and Kano, 2011). The “single-winner” CF translocates to the Purkinje cell dendrites around P9, and the rest of the CFs remaining on the soma are eventually eliminated by P21 (Hashimoto et al., 2009). CF pruning is reportedly regulated by activities in Purkinje cells mediated by parallel-fiber (PF, an axon of a granule cell) inputs through metabotropic glutamate receptor 1 (mGluR1), as well as inhibitory inputs through γ -aminobutyric acid (GABA) receptors (Kano and Hashimoto, 2009; Watanabe and Kano, 2011). Although a recent live-imaging study indicated that translocation of CF synapses to dendrites may provide a competitive advantage to the winner CF (Carrillo et al., 2013), how a selected CF is strengthened remains unclear. Furthermore, although brain-derived neurotrophic factor and insulin-like growth factor are suggested to be involved in strengthening CF synapses, the site of synaptic expression and action remains largely elusive (Watanabe and Kano, 2011). In addition, while CF synapses further undergo activity-dependent expansion or retraction throughout adulthood (Cesa and Strata, 2009), how the winner CF is maintained is unknown.

C1q, which is a member of the innate immune system, recognizes various targets via its C-terminal globular domain (gC1q). Recently, C1q released from neurons has been shown to regulate postnatal elimination of inactive synapses between retinal ganglion cells and the lateral geniculate nucleus *in vivo* (Stevens et al., 2007). The group of proteins containing the gC1q domain is referred to as the C1q family. Like adiponectin, which is released from adipose tissues and regulates glucose and lipid metabolism in muscle and liver, most C1q family members are secreted and involved in various signaling pathways (Kishore et al., 2004; Yuzaki, 2008). In the cerebellum, Cbln1, a cerebellin family of C1q homologous, is released from granule cells and plays a crucial role in the formation and maintenance of PF-Purkinje cell synapses by binding to its postsynaptic receptor, the delta2 glutamate

receptor (GluD2) (Matsuda et al., 2010). C1q-like family members (C1q1–C1q4) are also expressed in the CNS (Iijima et al., 2010; Shimono et al., 2010) and are implicated in synapse formation or elimination in cultured hippocampal neurons in vitro (Bolliger et al., 2011). It is interesting that C1q1 mRNA is selectively and highly expressed in IO neurons (Iijima et al., 2010) during development and throughout adulthood. Here, we examined the hypothesis that C1q1 provided by CFs may regulate CF synapse formation, elimination, and maintenance in vivo. We found that C1q1 plays a crucial role in strengthening and maintaining single-winner CFs by binding to brain-specific angiogenesis inhibitor 3 (Bai3), a cell-adhesion G protein-coupled receptor (GPCR) that is constitutively expressed in Purkinje cells. Furthermore, our in vivo results demonstrate that C1q1–Bai3 signaling is essential for CFs to mediate normal motor learning but not gross motor coordination.

RESULTS

C1q1 Is Required to Win CF Competition

We first investigated the localization of endogenous C1q1 proteins in the wild-type (WT) mouse cerebellum. Immunohistochemical (IHC) analysis revealed punctate C1q1 immunoreactivity in the molecular layer of the cerebellum along the proximal dendrites of Purkinje cells (Figure 1A). The C1q1-immunopositive puncta were mostly located at the edge of CF terminals ($74\% \pm 4\%$, $n = 1,195$ puncta from 10 slices), which were immunopositive for vesicular glutamate transporter 2 (vGluT2). Similarly, postembedding immunogold electron microscopy (EM) analysis revealed high levels of C1q1 immunoreactivity at presynaptic sites and CF synaptic clefts (Figure 1B). These results suggest that, like Cbln1 at PF synapses, the C1q1 protein provided by CFs localizes at CF synapses.

To investigate the physiological functions of C1q1, we generated mice in which the *C1q1* gene was disrupted (Figures S1A and S1B available online). IHC and immunogold EM analyses revealed essentially no C1q1 immunoreactivity (Figures 1A, 1B, and S1C) in *C1q1*-null cerebellum. The cerebella of *C1q1*-null mice exhibited normal foliation and laminated cortical structures (Figure S1D). IHC analysis of adult cerebellar slices (Figure 1C) revealed that the number of vGluT2-positive puncta was significantly reduced in *C1q1*-null cerebella (76 ± 2 , $n = 10$ slices) compared to WT (243 ± 6 , $n = 10$ slices, $p < 0.001$; Figure 1D). Although CF terminals translocated to dendrites and penetrated $85\% \pm 1\%$ ($n = 10$ slices) of the molecular layer thickness in adult WT cerebella, the depth reached by most distal CF terminals was significantly smaller in *C1q1*-null cerebella ($68\% \pm 1\%$, $n = 10$ slices, $p < 0.001$; Figure 1E). The reductions in CF terminal number and height were not observed in *C1q1*-null cerebella at P9 but became increasingly evident during development (Figures 1D and 1E). In contrast, although PF and inhibitory inputs to Purkinje cells are reported to affect CF synapse elimination processes (Kano and Hashimoto, 2009; Watanabe and Kano, 2011), no changes were observed in the number or distribution of vesicular glutamate transporter 1 (vGluT1, a marker for PF terminals; Figure S1E) or vesicular GABA transporter (vGAT, a marker for inhibitory fiber terminals; Figure S1F). These results indicate that CF

refinement processes at stages later than P9 were specifically impaired in *C1q1*-null cerebella.

Next, we evaluated CF synapse function by assessing CF-evoked excitatory postsynaptic currents (CF-EPSCs) in Purkinje cells with whole-cell patch-clamp recordings. The number of functional CF synapses on single Purkinje cells was estimated by varying the stimulus intensity because a single CF input has a single threshold for excitation. At P4–P6, both WT and *C1q1*-null Purkinje cells were innervated by a similar number (from three to nine) of CFs ($p = 0.15$; Figures 1F and 1G). Among these CF inputs, a single CF-EPSC was already dominant in both WT (disparity index = SD/mean of CF-EPSC amplitudes; 0.67 ± 0.05 , $n = 24$) and *C1q1*-null (0.65 ± 0.05 , $n = 26$) Purkinje cells ($p = 0.70$). In contrast, although single CF-EPSCs were elicited in 89% of WT Purkinje cells by P22–P28, only 57% of the Purkinje cells attained a one-to-one relationship with CFs in *C1q1*-null mice ($p < 0.01$; Figure 1G). Furthermore, while the amplitude of the largest CF-EPSCs steadily increased during development in WT mice, it remained constant after P7–P9 in *C1q1*-null mice (Figure 1H). Finally, voltage-dependent Ca^{2+} channel currents, which reportedly regulate the initial functional differentiation of multiple CF inputs during P3–P7 (Hashimoto et al., 2011), were similar between WT and *C1q1*-null cerebella (Figure S2). These results suggest that the winning CFs, which were selected during the initial functional differentiation stage by P7, were not further strengthened in the absence of C1q1.

To examine causal relationships between C1q1 expression and determination of the winner CFs, we expressed C1q1 together with enhanced GFP in WT IO neurons at P0–P1 with lentivirus vectors (Figure 2A). GFP expression was detected in essentially all CF terminals surrounding the observed Purkinje cell soma by P5 (Figure 2B). At P7–P8, Purkinje cells were innervated by multiple CFs overexpressing C1q1, with a dominant CF producing the largest EPSC in a manner similar to that of GFP-only-expressing Purkinje cells (Figure 2C). It is interesting that the amplitudes of the strongest CF-EPSC and also of the weaker CF-EPSCs were increased by C1q1 overexpression in CFs (Figure 2D). Thus, C1q1, at least when overexpressed in IO neurons, could enhance synaptic connectivity between CF and Purkinje cells, regardless of the original synaptic strength.

Unexpectedly, at P14–P15, 79% of Purkinje cells had already attained a one-to-one relationship when C1q1 was overexpressed in CFs, compared to only 57% of control Purkinje cells innervated by single CFs ($p < 0.05$; Figures 2E and 2F). The amplitude of the dominant CF-EPSCs was significantly larger in Purkinje cells innervated by CFs overexpressing C1q1 at all developmental stages (Figure 2G). Thus, although synaptic connections at less dominant CFs were enhanced by C1q1 overexpression, their elimination was also facilitated. These results indicate that C1q1 has dual functions: strengthening existing CF synapses and inducing the elimination of inactive synapses (see Discussion).

Purkinje-Cell-Specific Bai3-Null Mice Phenocopy C1q1-Null Mice

Recently, affinity chromatography identified C1q proteins as ligands for Bai3, a member of the cell-adhesion GPCR family (Bolliger et al., 2011). Although Bai3 was reported to regulate

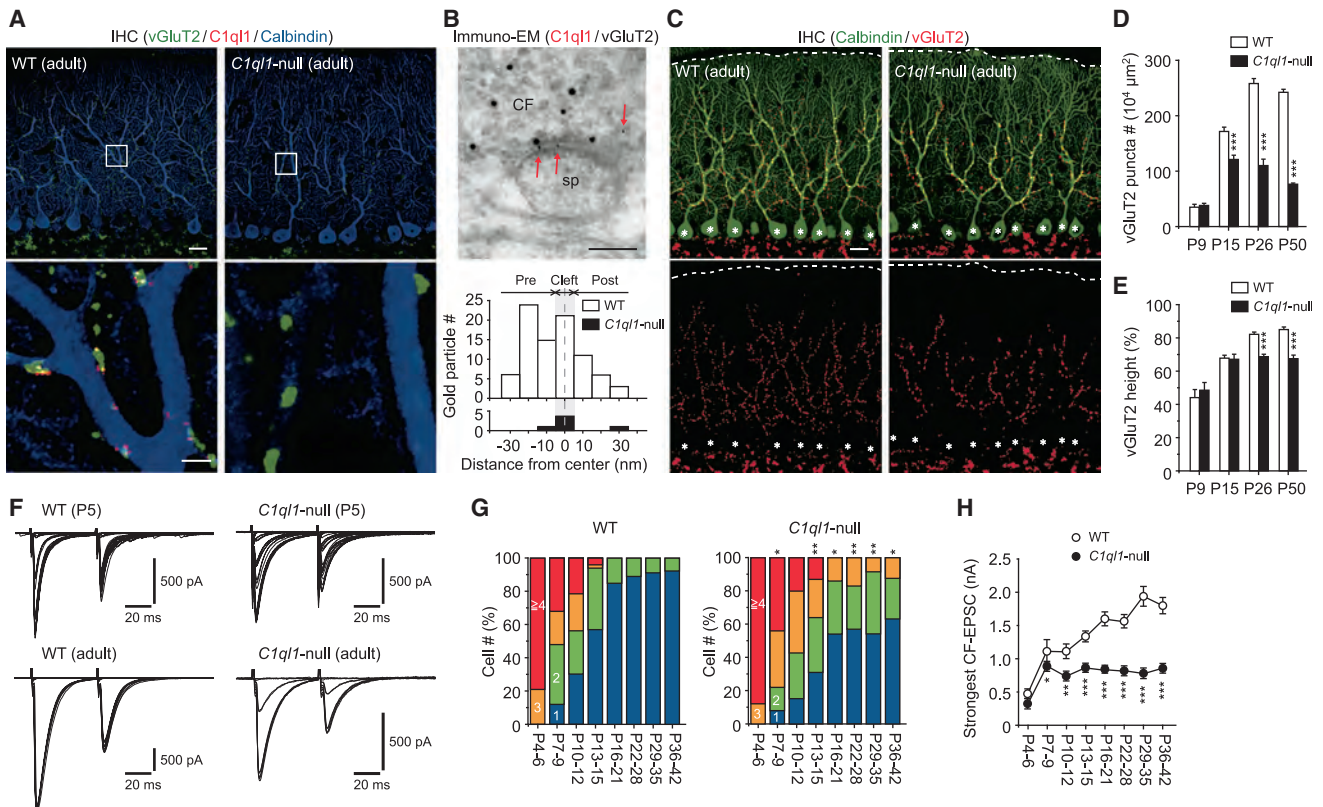


Figure 1. C1q1 Is Localized at CF Synapses during Their Formation and Maturation

(A) IHC images of endogenous C1q1 in adult WT (left) and *C1q1*-null (right) mouse cerebella. Areas surrounded by white squares are magnified in the lower panels. Scale bars in upper and lower panels, 20 μ m and 3 μ m, respectively.

(B) Postembedding immunogold EM images of endogenous C1q1 in adult WT mouse cerebellum. C1q1 and vGluT2 (a marker for CF terminals) were immunolabeled with 10 nm and 20 nm gold particles, respectively. sp, Purkinje cell spine. Red arrows indicate gold particles labeling C1q1 around CF synapses. Scale bar, 200 nm. Histogram shows the vertical distribution of C1q1-positive particles around CF synapses. Distances were measured from the midline (dotted line) of the synaptic cleft to the center of immunogold particles. On the x axis, negative and positive numbers represent presynaptic or postsynaptic side, respectively, from the midline.

(C) IHC images of vGluT2 in adult WT (left) and *C1q1*-null (right) mouse cerebella. Dotted lines and asterisks represent pial surface and Purkinje cell soma, respectively. Scale bar, 20 μ m.

(D) Developmental changes in the density of vGluT2 puncta.

(E) Developmental changes in the localization of vGluT2 puncta. The relative height is represented as a percentage, where 100% is at the top of Purkinje cell distal dendrites and 0% is at the Purkinje cell soma.

(F) CF-EPSC traces evoked by the paired-pulse stimulation (50 ms interstimulus interval) in various intensities in P5 (top) and adult (bottom) WT (left) and *C1q1*-null (right) mice.

(G and H) Developmental changes in the percentage of the number of CFs innervating single Purkinje cells (G) and the strongest CF-EPSC amplitudes (H).

* $p < 0.05$, ** $p < 0.01$, *** $p < 0.001$ by two-way factorial ANOVA followed by Bonferroni post hoc test in (D), (E), and (H). * $p < 0.05$, ** $p < 0.01$ by Mann-Whitney U test in (G). Data are represented as mean \pm SEM. See also Figures S1 and S2.

synapse formation or elimination in cultured hippocampal neurons in vitro (Bolliger et al., 2011) and affect dendrite morphogenesis (Lanoue et al., 2013), its in vivo localization and synaptic functions have not been established. We first examined endogenous Bai3 in the cerebellum. IHC analysis revealed that, like C1q1, Bai3 immunoreactivity was mostly located adjacent to vGluT2-positive CF terminals in WT mice (69% \pm 5%, $n = 1,003$ puncta from 10 slices; Figure 3A). Superresolution microscopic analysis also revealed that, although C1q1 and Bai3 immunoreactivities were mostly colocalized, Bai3 was located in more peripheral regions along vGluT2 (Figure 3B). Similarly,

postembedding immunogold EM analysis revealed that Bai3 immunoreactivity was highly abundant at postsynaptic sites and in CF synaptic clefts (Figure 3C). These results support the view that, like GluD2 for Cbln1 at PF synapses, Bai3 may serve as a postsynaptic receptor for C1q1 at CF synapses.

To examine whether C1q1 serves as an endogenous ligand for Bai3, we generated mice in which the *Bai3* gene was specifically disrupted in Purkinje cells (*PC-Bai3*-null mice; Figures S3A and S3B). IHC and immunogold EM analyses detected essentially no Bai3 immunoreactivity in *PC-Bai3*-null cerebellum (Figures 3A, 3C, and S3C), indicating that, indeed, Bai3 was

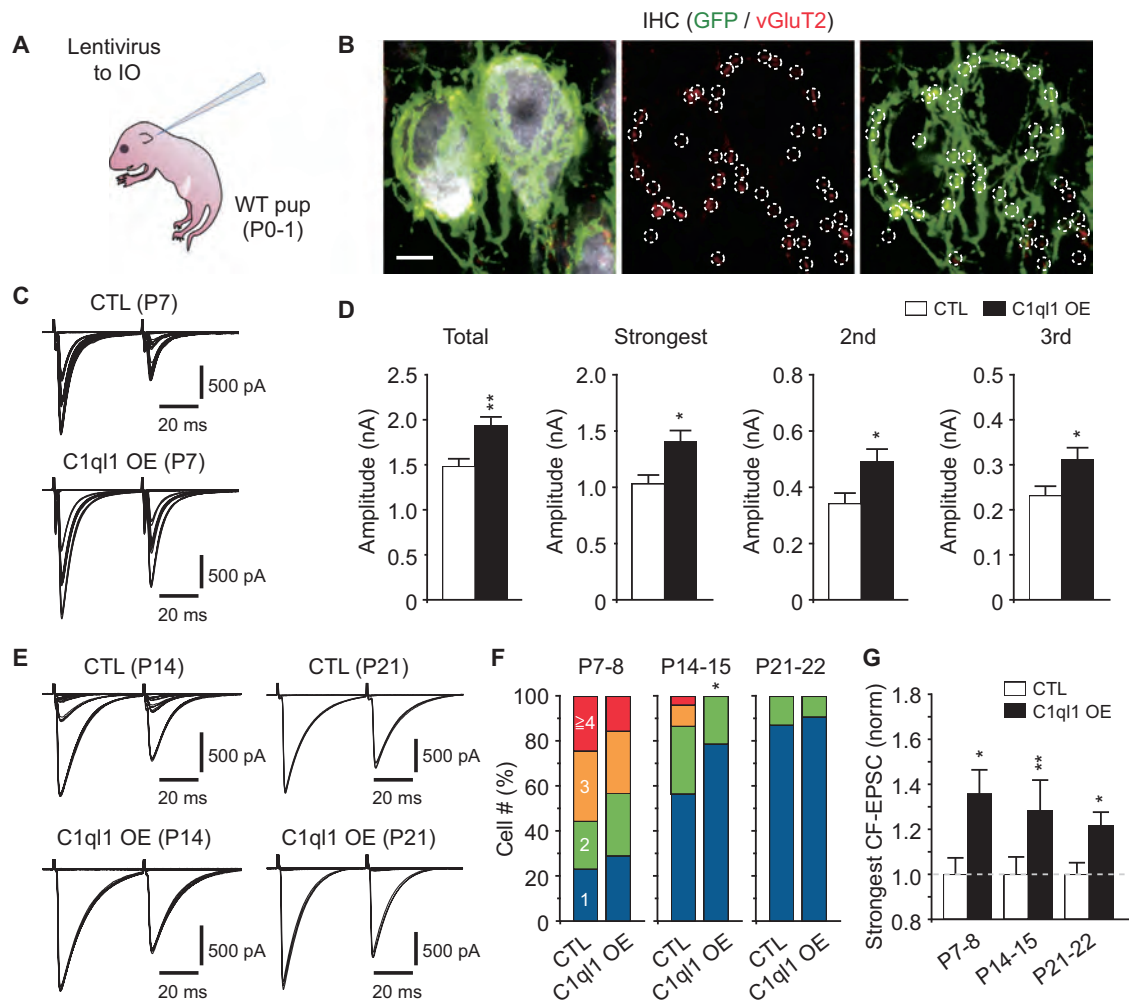


Figure 2. C1q1 Promotes CF Synapse Refinement during Development

(A) Cartoon showing the lentivirus injection into IOs in WT mouse pup (P0–P1) for the expression of C1q1.

(B) IHC images of vGluT2 (red in dashed circles) expression along GFP-positive CFs surrounding Purkinje cell soma at P5. Purkinje cells were immunostained for calbindin (white). Scale bar, 5 μ m.

(C) CF-EPSCs evoked by various stimulus intensities from P7 WT cerebellar slices, in which CFs expressed GFP only (CTL, top) or GFP plus C1q1 (C1q1 OE, bottom).

(D) Histograms showing total CF-EPSC amplitude (Total) and the mean amplitudes of CF-EPSCs evoked by the strongest, second strongest (2nd), or third strongest (3rd) CF activation.

(E) CF-EPSCs recorded from P14 (left) and P21 (right) cerebellar slices.

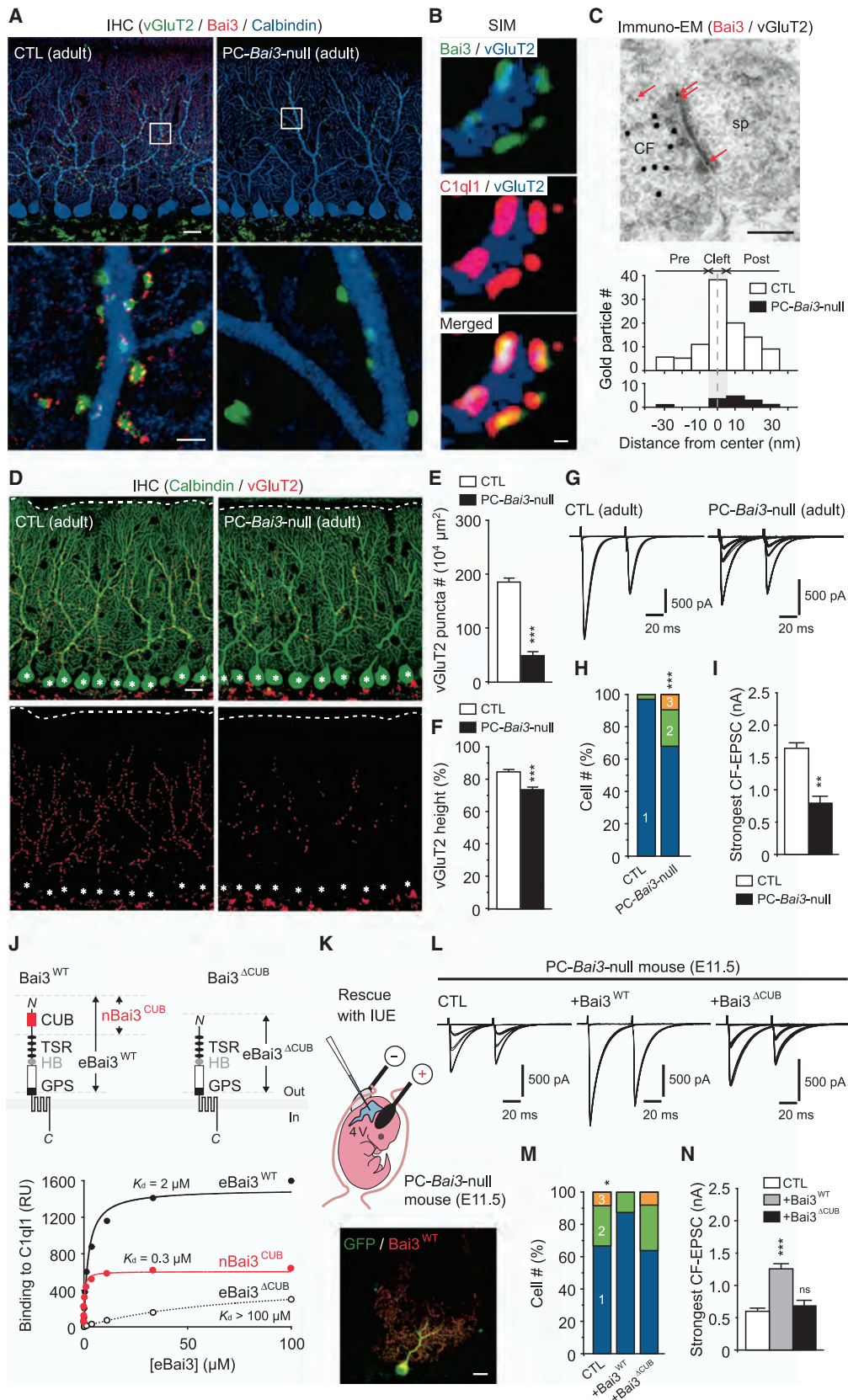
(F and G) Developmental changes in the percentage of the number of CFs innervating single Purkinje cells (F) and the strongest CF-EPSC amplitudes (normalized by the amplitude in CTL, G).

* $p < 0.05$, ** $p < 0.01$ by Mann-Whitney U test. Data are represented as mean \pm SEM.

postsynaptically located at CF synapses. Although PC-*Bai3*-null mice had normal cerebellar structure (Figure S3D) and immunoreactivities for vGluT1 and vGAT in cerebellar slices (Figures S3E and S3F), the numbers of vGluT2-positive puncta were significantly reduced in adult PC-*Bai3*-null cerebella (47 ± 5 , $n = 10$ slices) compared to control littermate (185 ± 8 , $n = 10$ slices; $p < 0.001$; Figures 3D and 3E). In addition, the depth of the molecular layer thickness reached by the most distal CF terminals was significantly less in PC-*Bai3*-null ($74\% \pm 1\%$, $n = 10$ slices) than in control ($84\% \pm 1\%$, $n = 10$ slices) cerebella

($p < 0.001$; Figure 3F). Whole-cell patch-clamp recordings from adult PC-*Bai3*-null cerebellar slices revealed that only 68% of Purkinje cells attained a one-to-one relationship with CFs ($p < 0.001$ versus control; Figures 3G and 3H). Furthermore, the amplitudes of the strongest CF-EPSCs were significantly smaller in PC-*Bai3*-null Purkinje cells ($p < 0.01$ versus control; Figure 3I). Together, these results indicate that PC-*Bai3*-null mice phenocopied C1q1-null mice.

To further examine whether the function of *Bai3* was mediated by C1q1 binding, we next designed a *Bai3* mutant that could not



(legend on next page)

bind C1q1. Surface plasmon resonance (SPR) assays revealed that the extracellular domain of Bai3 (eBai3^{WT}) bound to C1q1 with a dissociation constant (K_D) of 2 μ M; this interaction was significantly reduced by deleting the N-terminal CUB (complement C1r/C1s, Uegf, Bmp1) domain (eBai3 ^{Δ CUB}; $K_D > 100 \mu$ M; Figures 3J, S4A, and S4B). Conversely, the short N-terminal region of Bai3 containing the CUB domain (nBai3^{CUB}) was sufficient for C1q1 binding ($K_D = 0.3 \mu$ M; Figures 3J and S4C). Similarly, C1q1 proteins strongly bound to heterologous cells expressing full-length Bai3 (Bai3^{WT}) but not to cells expressing Bai1, Bai2, or Bai3 lacking the CUB domain (Bai3 ^{Δ CUB}) (Figures S4F and S4G). We introduced cDNAs encoding GFP only, GFP plus Bai3^{WT}, or GFP plus Bai3 ^{Δ CUB} into PC-Bai3-null Purkinje cells by in utero electroporation (IUE) at embryonic day (E) 11.5 (Figure 3K). Whole-cell patch-clamp recordings revealed that, although expression of Bai3^{WT} in PC-Bai3-null Purkinje cells restored a one-to-one relationship with CFs, expression of Bai3 ^{Δ CUB} or GFP alone was insufficient ($p < 0.05$; Figures 3L and 3M). Furthermore, the amplitudes of the strongest CF-EPSCs were significantly increased in PC-Bai3-null Purkinje cells expressing Bai3^{WT} compared to cells expressing Bai3 ^{Δ CUB} or GFP alone ($p < 0.001$; Figures 3L and 3N). Because Bai2, a closely related cell-adhesion GPCR that shares similar domain structures (Stephenson et al., 2014), is reportedly expressed on Purkinje cells along with Bai3 (Selimi et al., 2009), we generated mice in which the *Bai2* gene was disrupted specifically in Purkinje cells (PC-Bai2-null mice; Figures S5A and S5B). In contrast to PC-Bai3-null mice, PC-Bai2-null cerebellum showed no changes in the amount or distribution of vGluT2 immunoreactivity (Figures S5C–S5E). Together, these results indicate that the function of Bai3 at CF synapses is mediated by the CUB domain, which C1q1 directly binds.

C1q1–Bai3 Triggers Pruning of Surplus CFs in Adult Mice

Although synaptic pruning could occur throughout adulthood (Cesa and Strata, 2009; Holtmaat and Svoboda, 2009), it is un-

clear whether the molecules involved in developmental pruning exert their functions in the adult brain. To address this question, we next expressed C1q1 (C1q1^{WT}) in adult *C1q1*-null IO neurons with adenoassociated virus (AAV) vectors (Figure 4A). Whole-cell patch-clamp recordings showed that, although 38% of Purkinje cells remained innervated by multiple CFs in the adult *C1q1*-null cerebellum, 84% of Purkinje cells attained a one-to-one relationship with CFs by expressing C1q1^{WT} ($p < 0.05$; Figures 4B and 4C). Furthermore, the amplitudes of the strongest CF-EPSCs were significantly increased by C1q1^{WT} expression in adult *C1q1*-null mice ($p < 0.001$; Figure 4D). Although it is difficult to rule out the possibility that CFs in *C1q1*-null mice are in a state of permanent immaturity, these results indicate that C1q1 can strengthen CF synapses and promote CF pruning to determine a single-winner CF, even at the adult stage in *C1q1*-null mice.

To test whether the function of C1q1 in adult synaptic pruning was mediated by Bai3 as observed during development, we next designed a mutant C1q1 that did not bind Bai3. Because the C-terminal globular C1q domain of C1q1 (gC1q1; Figure 4E) was sufficient for binding to Bai3 (Figure S4D), we solved the crystal structure of gC1q1 (Figure 4F; Table 1). Based on this structure, we designed a “glycan wedge” mutant by introducing two *N*-linked glycosylation sites in each subunit of the trimeric gC1q1 domain (C1q1^{GW}; Figures 4E and 4F); the attachment of a bulky *N*-glycan moiety to Asn residues has been shown to prevent specific protein-protein interactions (Luo et al., 2003; Rondard et al., 2008). Indeed, SPR assays demonstrated that C1q1^{GW} did not retain any binding to Bai3 (Figures 4E and S4E). Similarly, C1q1^{GW} proteins did not bind to cells expressing full-length Bai3 (Figures S4F and S4G). C1q1^{WT} and C1q1^{GW} were similarly expressed in vGluT2-positive CF terminals (Figure S6A), indicating that binding of Bai3 was likely to be nonessential for localizing C1q1 at CF terminals. Whole-cell patch-clamp recordings showed that, unlike C1q1^{WT}, expression of C1q1^{GW} in CFs did not restore the normal process of CF synapse elimination in *C1q1*-null mice (Figures 4B and 4C).

Figure 3. C1q1 Is an Endogenous Ligand for Bai3 to Win the CF Competition

(A and B) Confocal (A) and superresolution structured illumination (SIM; B) microscopic images of endogenous Bai3 (red in A and green in B), C1q1 (red in B), and vGluT2 (green in A and blue in B) immunoreactivities in the molecular layer of adult WT and *C1q1*-null cerebella. Purkinje cells were immunostained for calbindin (blue in A). Scale bars, 20 μ m and 3 μ m in the upper and lower left panels, respectively, in (A) and 200 nm in (B).

(C) Postembedding immunogold EM images of endogenous Bai3 in adult WT mouse cerebellum. Bai3 and vGluT2 (a marker for CF terminals) were immunolabeled with 10 nm and 20 nm gold particles, respectively. sp, Purkinje cell spine. Red arrows indicate gold particles labeling Bai3 around CF synapses. Scale bar, 200 nm. Histogram shows the vertical distribution of Bai3-positive particles around CF synapses.

(D) IHC images of vGluT2 in adult PC-Bai3-null (right) and its control littermate (CTL, left) mouse cerebella. Dotted lines and asterisks represent pial surface and Purkinje cell soma, respectively. Scale bar, 20 μ m.

(E and F) Quantification of the density (E) and the height (F) of vGluT2 puncta in the molecular layer of each mouse.

(G) CF-EPSCs evoked by various stimulus intensities in adult PC-Bai3-null (right) and CTL (left) mice.

(H and I) Histograms showing the percentage of the number of CFs innervating single Purkinje cells (H) and the strongest CF-EPSC amplitudes (I).

(J) Diagrams of a full-length Bai3 (Bai3^{WT}, top left) and a Bai3 lacking CUB domain (Bai3 ^{Δ CUB}, top right) and the equilibrium SPR data (bottom) of the C1q1 binding to the extracellular region of Bai3^{WT} (eBai3^{WT}), N-terminal region containing CUB domain (nBai3^{CUB}), and extracellular region of Bai3 ^{Δ CUB} (eBai3 ^{Δ CUB}). TSR, thrombospondin repeats; HB, hormone-binding domain; GPS, GPCR proteolysis sequence.

(K) Cartoon showing IUE to PC-Bai3-null embryo at E11.5. cDNA solution was loaded into the fourth cerebral ventricle (4V) to perform IUE.

(L) CF-EPSCs recorded from adult PC-Bai3-null Purkinje cells expressing Bai3^{WT} (center), Bai3 ^{Δ CUB} (right), and empty vector (CTL, left).

(M and N) Histograms showing the percentage of the number of CFs innervating single Purkinje cells (M) and the strongest CF-EPSC amplitudes (N) in each condition.

** $p < 0.01$, *** $p < 0.001$ by Mann-Whitney U test in (E), (F), (H), and (I). * $p < 0.05$, *** $p < 0.001$ by Kruskal-Wallis test followed by Steel post hoc test in (M) and (N). ns, no significance. Data are represented as mean \pm SEM.

See also Figures S3–S6.

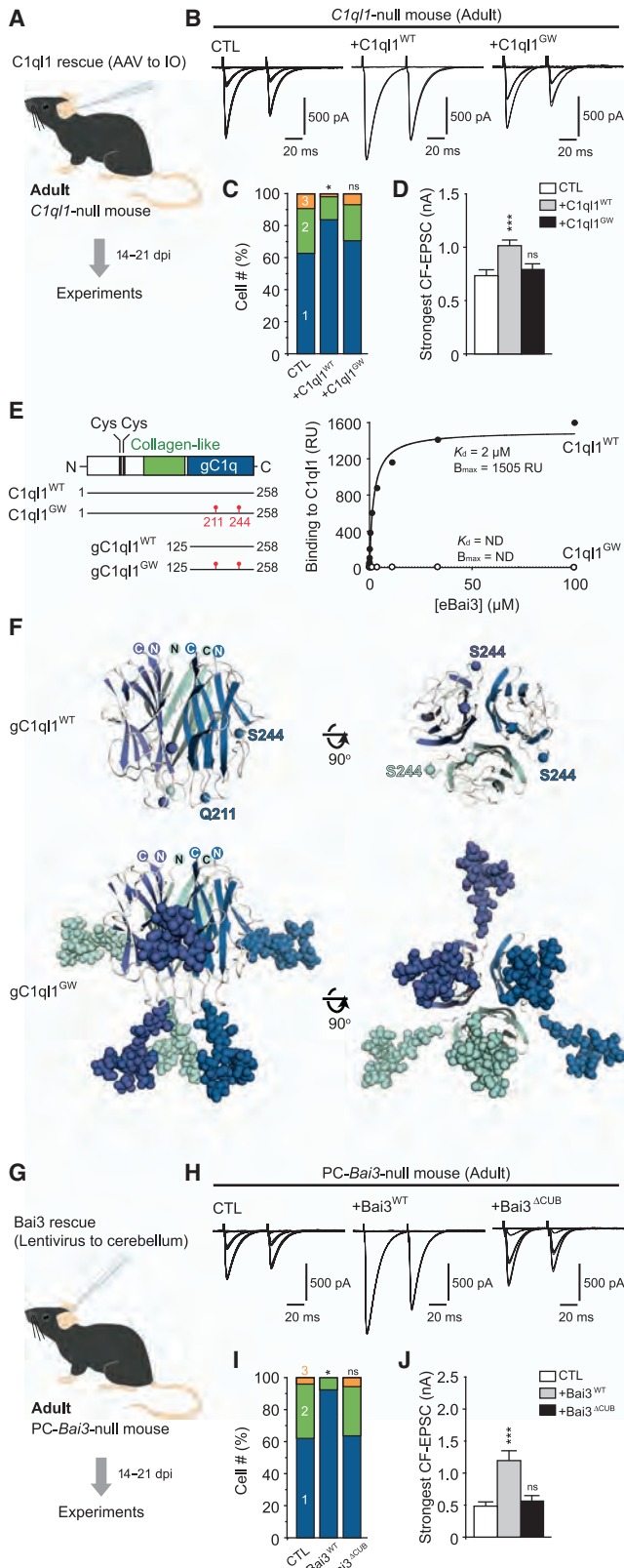


Figure 4. C1q1-Bai3 Signaling Triggers Surplus CF Synapse Elimination in Adult Mutant Mice

(A) Cartoon showing the AAV injection into adult *C1q1*-null mouse IO for the expression of C1q1. Experiments were performed at 14–21 days postinfection (dpi). (B) CF-EPSCs recorded from adult *C1q1*-null Purkinje cells innervated by CFs expressing WT C1q1 (C1q1^{WT}, center), C1q1^{GW} (right), and empty vector (CTL, left). (C and D) Histograms showing the percentage of the number of CFs innervating single Purkinje cells (C) and the strongest CF-EPSC amplitudes (D) in each condition. (E) Diagrams (left) for C1q1^{WT}, C1q1^{GW}, and their globular domains (gC1q1^{WT} and gC1q1^{GW}, respectively), and the equilibrium SPR data of each C1q1 binding to eBai3 (right). RU, resonance unit. (F) Cartoon representation of the gC1q1^{WT} (top) and gC1q1^{GW} (bottom) trimeric structures. Individual monomers are separately colored. Glycosylation sites introduced by mutagenesis (original residues were Q211 and S244) are indicated by spheres in C1q1^{WT}. The gC1q1^{GW} trimeric structure is shown with modeled Man9GlcNAc2 glycans (atoms in sphere representation). (G) Cartoon showing the lentivirus injection into adult PC-*Bai3*-null mouse cerebellum for the expression of Bai3. Experiments were performed at 14–21 dpi. (H) CF-EPSCs recorded from adult PC-*Bai3*-null Purkinje cells expressing WT Bai3 (Bai3^{WT}, center), Bai3^{ΔCUB} (right), and empty vector (CTL, left). (I and J) Histograms showing the percentage of the number of CFs innervating single Purkinje cells (I) and the strongest CF-EPSC amplitudes (J) in each condition. **p* < 0.05, ****p* < 0.001 by Kruskal-Wallis test followed by Steel post hoc test. ns, no significance. Data are represented as mean ± SEM. See also Figures S4 and S6 and Table 1.

Furthermore, the amplitudes of the strongest CF-EPSCs were not increased by C1q1^{GW} expression in adult *C1q1*-null mice (Figures 4B and 4D). These results indicate that the function of C1q1 in determining a single-winner CF in the adult brain is mediated by an interface used for Bai3 binding.

Finally, to examine whether expression of Bai3 in adult PC-*Bai3*-null Purkinje cells could also restore CF phenotypes, we used lentiviral vectors to express Bai3^{WT} or Bai3^{ΔCUB} in Purkinje cells (Figure 4G). Bai3^{WT} and Bai3^{ΔCUB} were similarly expressed in dendritic spines of Purkinje cells (Figure S6B), indicating that binding of C1q1 was likely to be nonessential for localizing Bai3 at postsynaptic sites. Whole-cell patch-clamp recordings showed that Bai3^{WT}, but not Bai3^{ΔCUB} or empty vector, restored the normal process of CF synapse elimination in PC-*Bai3*-null mice (*p* < 0.05; Figures 4H and 4I). Similarly, the amplitudes of the strongest CF-EPSCs were increased by Bai3^{WT} expression but not Bai3^{ΔCUB} or empty vector in adult PC-*Bai3*-null mice (*p* < 0.001; Figures 4H and 4J). These results indicate that C1q1 provided by CFs and Bai3 in Purkinje cells likely act together to trigger signaling pathways necessary for determining single-winner CFs, even in the adult cerebellum.

The C1q1-Bai3 Interaction Is Required to Maintain CF Synapses

C1q1 and Bai3 continue to be expressed in the adult brain (Iijima et al., 2010; Lanoue et al., 2013). To examine the functions of C1q1-Bai3 signaling in adults, we knocked down C1q1 in the IO neurons of adult WT mice by infecting them with an AAV that contained an engineered microRNA targeting C1q1 plus the *GFP* gene (miR-*C1q1*) (Figure 5A). Expression of miR-

Table 1. Crystallographic Data Collection and Structure Refinement Statistics

Statistics	gC1q1
Data Collection	
Space group	H3
Cell dimensions: a, b, c (Å)	68.08, 68.08, 65.91
Cell angles: α , β , γ (°)	90.00, 90.00, 120.00
Resolution (Å)	43.94–1.44 (1.48–1.44)
Total reflections	155,787 (11,142)
Unique reflections	20,630 (1,532)
Completeness (%)	100.0 (99.9)
R_{merge}	0.067 (0.875)
R_{pim}	0.028 (0.378)
$I/\sigma I$	16.9 (2.1)
Redundancy	7.6 (7.3)
Wilson B factor (Å ²)	11.55
Refinement Statistics	
Resolution range (Å)	34.04–1.44 (1.51–1.44)
Number of reflections	20,628 (2,956)
R_{work}	0.140 (0.205)
R_{free}^a	0.169 (0.255)
Number of atoms	1,121
Protein	1,029
Ligands (Cd, Ni, Mg, Cl)	7 (2, 2, 1, 2)
Water molecules	85
RMSD bonds (Å)	0.006
RMSD angles (°)	1.096
Average B factors (Å ²)	
Protein main/side chains	14.43/18.92
Cd/Ni/Mg/Cl	13.16/10.00/28.39/45.39
Water	31.01

This structure was determined from one crystal. Numbers in parentheses refer to the highest resolution shell. Ramachandran statistics and Molpro probability scores are included in the [Supplemental Experimental Procedures](#). RMSD, root-mean-square deviation.

^a R_{free} was calculated as per R_{work} for a 5% subset of reflections that was not used in the crystallographic refinement.

C1q1 significantly reduced C1q1 immunoreactivities in GFP-expressing IO neurons (17% ± 6% of IO neurons expressing scrambled microRNA [miR-SCR], $p < 0.05$; [Figure 5B](#)). IHC analysis of cerebellar slices revealed that the number of vGluT2-positive puncta was significantly reduced in mice expressing miR-*C1q1* (110 ± 9, $n = 10$ slices; [Figures 5C and 5D](#)) compared to mice expressing miR-SCR (180 ± 6, $n = 10$ slices; $p < 0.001$; [Figures 5C and 5D](#)). In addition, the depth of the molecular layer thickness reached by the most distal CF terminals was reduced in mice expressing miR-*C1q1* (80% ± 1%, $n = 10$ slices; [Figures 5C and 5E](#)) compared to mice expressing miR-SCR (84% ± 1%, $n = 10$ slices, $p < 0.05$; [Figures 5C and 5E](#)). In contrast, whole-cell patch-clamp recordings from adult cerebellar slices revealed that similar percentages of Purkinje cells were innervated by single CFs in mice expressing miR-*C1q1* (83%; [Figures 5F and 5G](#)) and miR-SCR (89%, $p = 0.51$; [Figures 5F and 5G](#)). Nevertheless,

the amplitudes of the strongest CF-EPSCs were significantly smaller in mice expressing miR-*C1q1* ($p < 0.001$ versus miR-SCR; [Figures 5F and 5H](#)). The reduced amplitudes of CF-EPSCs due to miR-*C1q1* expression were restored by coexpression of the miR-*C1q1*-resistant form of C1q1^{WT} (rC1q1^{WT}; $p < 0.001$ versus miR-*C1q1*) but not the resistant form of C1q1^{GW} (rC1q1^{GW}; $p = 0.64$ versus miR-*C1q1*; [Figures 5F and 5H](#)). We also knocked down Bai3 by infecting adult WT Purkinje cells with a lentivirus containing an engineered microRNA targeting Bai3 plus the GFP gene (miR-*Bai3*; [Figure S7](#)). We obtained essentially the same results as those with miR-*C1q1*. It is important to note that the reduced CF-EPSC amplitudes observed with miR-*Bai3* were restored by coexpression of the miR-*Bai3*-resistant form of Bai3^{WT} but not Bai3^{ΔCUB} ([Figure S7](#)). Together, these results indicate that, even after a single final winner CF was selected, C1q1-Bai3 signaling was necessary to maintain the winner CF synapses on Purkinje cell dendrites.

C1q1-Bai3 Signaling in Motor Learning

To understand the consequences of abnormal CF synapses in vivo, we examined the behaviors of *C1q1*-null and PC-*Bai3*-null mice. Unexpectedly, these mice showed no ataxia and could walk along a straight line with regular steps ([Movie S1](#)). They showed normal motor coordination on the rotor-rod test ([Figures S8A and S8B](#)). Nystagmus, which is characteristic of *GluD2*-null humans ([Hills et al., 2013](#)) and mice ([Yoshida et al., 2004](#)), was absent in the *C1q1*-null and PC-*Bai3*-null mice ([Figures S8C–S8E](#)). These results indicate that innervation of Purkinje cells by multiple CFs does not necessarily manifest as gross motor discoordination or nystagmus.

To further clarify the role of C1q1-Bai3 signaling in the cerebellum, we next examined adaptation of the horizontal optokinetic response (hOKR), a motor learning paradigm shown to be dependent on the cerebellum ([Ito, 2006](#)). Continuous oscillation of a screen around a stationary animal increases the hOKR gain in WT mice ([Figures 6A and 6B](#)). Although the hOKR was similarly observed in all genotypes before the training ([Figure 6B](#); [Movie S2](#)), the gain did not increase in *C1q1*-null and PC-*Bai3*-null mice ([Figures 6C and 6D](#); [Movie S2](#)), indicating that motor learning was severely impaired in these mice.

According to the Marr-Albus-Ito theory, the activities of CFs encode retinal slip errors that serve as a teacher signal to induce long-term depression (LTD) of synaptic transmission at concomitantly activated PF synapses, leading to hOKR adaptation ([Ito, 2013](#)). To test this hypothesis, we examined whether LTD could be induced in cerebellar slices prepared from *C1q1*-null and PC-*Bai3*-null mice by simultaneously activating PFs and CFs for 2 min at 1 Hz in the current-clamp mode ([Figure 6E](#)). This protocol robustly induced LTD of PF-evoked EPSCs (PF-EPSCs) in WT, but not *C1q1*-null ($p < 0.001$; [Figures 6F and 6G](#)) or PC-*Bai3*-null ($p < 0.001$ versus control; [Figures 6F and 6H](#)), Purkinje cells. Activation of CF input triggers dendritic spikes and a burst of somatic spikes known as complex spikes in WT Purkinje cells ([Eccles et al., 1966](#)). The occurrence of the complex spike was significantly reduced in Purkinje cells from *C1q1*-null (53 ± 9 in 120 trials, $n = 22$ versus WT [118 ± 2 in 120 trials, $n = 22$]; $p < 0.001$ by Mann-Whitney U test) and PC-*Bai3*-null mice (64 ± 8 in 120 trials, $n = 24$ versus

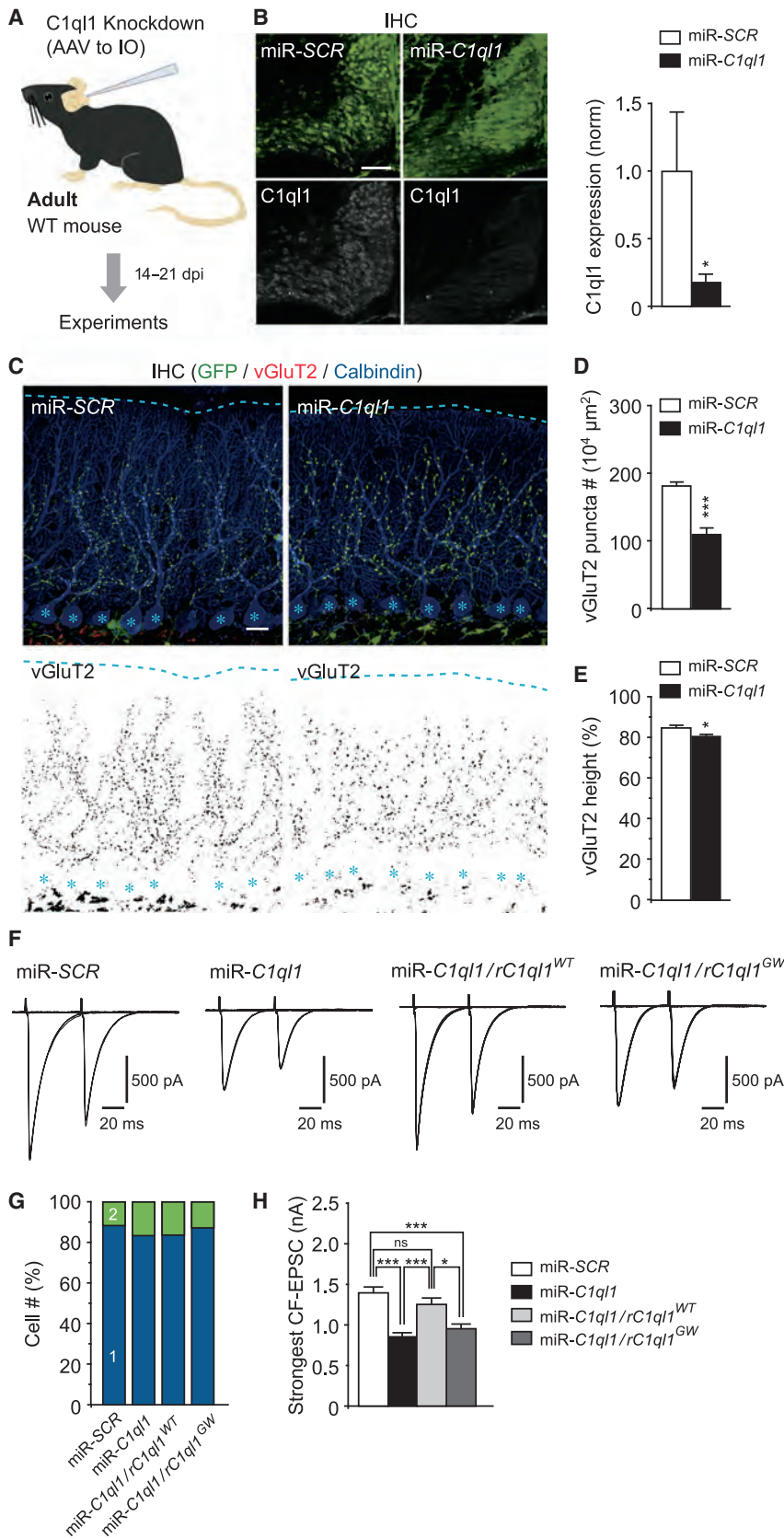


Figure 5. C1ql1-Bai3 Interaction Is Essential for the Maintenance of CF Synapse in Adults

(A) Cartoon showing the AAV injection into adult WT mouse IO for the introduction of miR-C1ql1 or miR-SCR. Experiments were performed at 14–21 dpi. (B) IHC images (left) and the quantitative data (right) showing C1ql1 is knocked down by miR-C1ql1 (right) but not miR-SCR (left) in GFP-expressing IO neurons. Scale bar, 100 μm . (C) IHC images of vGluT2 in adult WT mouse cerebella with CFs expressing GFP plus miR-SCR (left) or miR-C1ql1 (right). vGluT2 immunoreactivities are binarized in the bottom. Dotted lines and asterisks represent pial surface of the molecular layer and Purkinje cell soma, respectively. Scale bar, 20 μm . (D and E) Quantification of the density (D) and the height (E) of vGluT2 puncta on the molecular layer of each condition. (F) CF-EPSCs evoked by various stimulus intensities in adult WT cerebellar slices with CFs introducing miR-SCR, miR-C1ql1, miR-C1ql1 plus a resistant form of C1ql1 (*rC1ql1^{WT}*) or miR-C1ql1 plus a *rC1ql1^{GW}*. (G and H) Histograms showing the percentage of the number of CFs innervating single Purkinje cells (G) and the strongest CF-EPSC amplitudes (H) in each condition. * $p < 0.05$, *** $p < 0.001$ by Mann-Whitney U test in (B), (D), and (E). * $p < 0.05$, *** $p < 0.001$ by Kruskal-Wallis test followed by Scheffé post hoc test in (H). ns, no significance. Data are represented as mean \pm SEM. See also Figure S7.

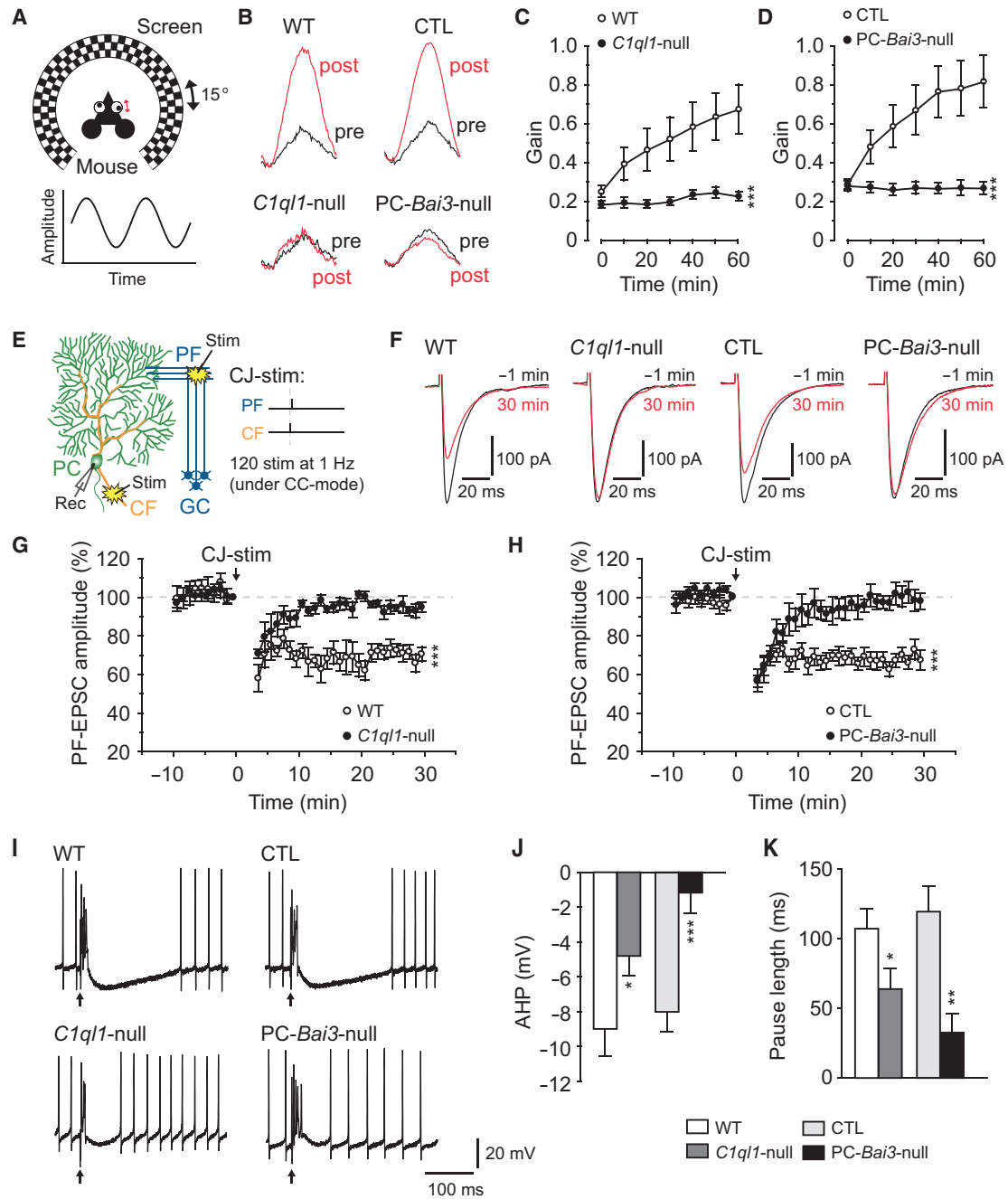


Figure 6. Abnormal CF Synapses Impair Synaptic Plasticity and Motor Learning in Adult Mutant Mice

(A) Cartoon showing hOKR system. The mouse was mounted on a table surrounded by a checked-pattern screen with its head fixed. Eye movements during sinusoidal oscillation of the screen (15°) were monitored.

(B–D) Representative hOKR waveforms before (pre) and 60 min after (post) training (B) and the data of hOKR acquisition for 60 min in WT versus *C1q1*-null (C) mice and *PC-Bai3*-null versus its control littermate *Bai3^{fllox}* (CTL, D).

(E) An orientation of stimulus and recording electrodes (left) and the stimulus protocol (CJ-stim, right) to induce LTD at PF synapses.

(F–H) PF-EPSCs just before (black) and 30 min after (red) CJ-stim (F) and the data of LTD recordings in WT versus *C1q1*-null mice (G) and *PC-Bai3*-null versus CTL mice (H).

(I–K) Complex spike waveforms recorded from each mouse (I) and the quantification of the amplitude of afterhyperpolarization (AHP, J) and the pause length of spontaneous spikes (K) after the complex spike.

****p* < 0.001 by two-way repeated-measures ANOVA in (C) and (D). **p* < 0.05, ***p* < 0.01, ****p* < 0.001 by Mann-Whitney U test in (G), (H), (J), and (K). Data are represented as mean ± SEM.

See also [Figure S8](#) and [Movies S1](#) and [S2](#).

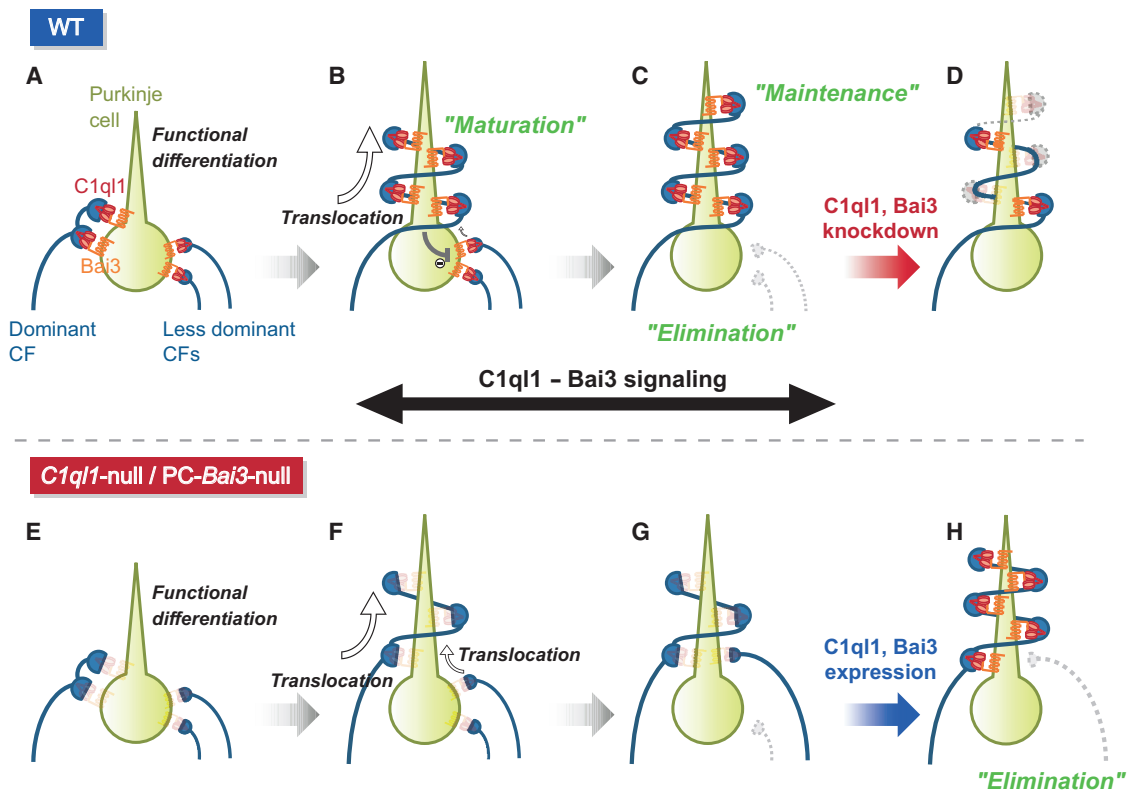


Figure 7. A Model for C1q1-Bai3 Signaling in Synaptic Competition at CF Synapses

(A and E) The disparity is formed among multiple CFs innervating a single Purkinje cell soma by P7 in both WT (A) and *C1q1*-null or *PC-Bai3*-null (E) cerebellum. (B) Although the C1q1-Bai3 signaling promotes maturation of all CFs, the winning CF may trigger a signaling pathway to eliminate less dominant synapses. The winning CF may occupy the postsynaptic region close to proximal dendrites and prevent translocation of somatic synapses formed by less dominant CFs to proximal dendrites.

(C) CFs remaining on the Purkinje cell soma are eventually eliminated.

(D) Knockdown of C1q1 or Bai3 revealed that the C1q1-Bai3 signaling is required to maintain the winner CF in adult.

(F) In the absence of C1q1-Bai3 signaling, the dominant CF cannot be strengthened enough to prevent the translocation of synapses formed by less dominant CFs.

(G) Weak CF synapses translocated to proximal dendrites escape from the elimination process at soma.

(H) Expression of C1q1 or Bai3 in adult *C1q1*-null or *PC-Bai3*-null Purkinje cells determines the single-winner CF by promoting the maturation of the dominant CF and eliminating less dominant CFs.

control [120 in 120 trials, $n = 30$]; $p < 0.001$ by Mann-Whitney U test). Furthermore, dendritic spikes reportedly convey additional signals by triggering a pause in firing following the complex spike in WT Purkinje cells (Davie et al., 2008). Such CF-evoked afterhyperpolarization (Figures 6I and 6J) and suppression of the spontaneous spikes (Figures 6I and 6K) were significantly reduced in Purkinje cells from *C1q1*-null (both $ps < 0.05$ versus WT) and *PC-Bai3*-null mice ($p < 0.001$ and $p < 0.01$ versus control, respectively). These findings indicate that C1q1-Bai3 signaling is required for normal CF functions, such as complex spikes and CF-evoked afterhyperpolarization, which are necessary for LTD and motor learning in the adult cerebellum.

DISCUSSION

In the present study, we demonstrated that C1q1 from CFs plays crucial roles in determining a single-winner CF during

development by binding to its postsynaptic receptor Bai3 in Purkinje cells. CF synapse competition during development is divided into at least three stages: selection of functionally dominant CFs by P7 (Figure 7A), further strengthening and translocation of the dominant CF to Purkinje cell dendrites (Figure 7B), and elimination of weak CFs remaining on the soma while maintaining a single-winner CF (Figure 7C). We propose that C1q1-Bai3 signaling is required for the second and third stages; in the absence of C1q1-Bai3 signaling, the dominant CF cannot be strengthened enough to prevent the translocation of synapses formed by less dominant CFs (Figure 7F), which escape from the later elimination process (Figure 7G). These phenotypes could be rescued by expression of C1q1 and Bai3 in adult *C1q1*-null and *PC-Bai3*-null mice, respectively (Figure 7H). Conversely, maintenance of the winner CF requires C1q1-Bai3 signaling throughout adulthood (Figure 7D). Furthermore, C1q1 and Bai3 were essential for CFs to mediate cerebellar synaptic plasticity necessary for motor learning. Therefore,

C1ql1-Bai3 signaling represents a new mechanism that regulates the selection and maintenance of functional winner inputs by an anterograde signal supplied by the input neuron itself.

Dual C1ql1-Bai3 Signaling in CF Synapse Formation and Elimination

The P/Q-type Ca^{2+} channel is the major Ca^{2+} channel in Purkinje cells and reportedly regulates developmental CF pruning (Kano and Hashimoto, 2009; Watanabe and Kano, 2011). Ca^{2+} channel activities are thought to mediate the selective enhancement of a single strong CF input by inducing long-term potentiation (LTP) (Bosman et al., 2008) and activating Sema3A signaling in Purkinje cells (Uesaka et al., 2014). Ca^{2+} channel activities also reportedly induce synapse elimination by activating the Arc/Arg3.1 pathway in Purkinje cells (Mikuni et al., 2013). GABAergic inputs also likely regulate CF elimination by controlling Ca^{2+} channel activities in Purkinje cells (Nakayama et al., 2012; Watanabe and Kano, 2011). Indeed, mice lacking functional P/Q-type Ca^{2+} channels do not exhibit disparity among multiple CF inputs by P7, and Purkinje cells in adult mice remain innervated by multiple CFs (Hashimoto et al., 2011; Miyazaki et al., 2004). In contrast, disparity is normally formed among CF inputs in *C1ql1*-null mice by P7, which is consistent with the normal Ca^{2+} channel activities in these mice (Figure S2). The CF-EPSC amplitudes in Purkinje cells lacking P/Q-type Ca^{2+} channels (Hashimoto et al., 2011) or GABAergic inputs (Nakayama et al., 2012) increased at later developmental stages to a level similar to that in WT mice. By contrast, the amplitude of the largest CF-EPSCs remained constant after P7–P9 in *C1ql1*-null mice (Figure 1H). These findings indicate that C1ql1 does not simply mediate signaling downstream of Ca^{2+} channels.

Another major pathway that reportedly mediates CF elimination in the later developmental stage (approximately the P12 stage in mice) is mGluR1 and its downstream signaling in Purkinje cells, which involves molecules such as $\text{G}\alpha_q$, phospholipase C β_4 , protein kinase $\text{C}\gamma$ (PKC γ) (Kano and Hashimoto, 2009; Uesaka et al., 2014; Watanabe and Kano, 2011), and Sema7A (Uesaka et al., 2014). In mice lacking one of these mGluR1 signaling pathway components, Purkinje cells remain innervated by multiple CFs, even in adulthood. Because mGluR1 is activated mainly by PF inputs, innervation of Purkinje cells by multiple CFs in *GluD2*-null or *Cbln1*-null mice is thought to be caused by impaired PF synapse formation (Watanabe and Kano, 2011). However, unlike in *C1ql1*-null or *PC-Bai3*-null mice, the numbers and heights of the CF terminals are unaffected in mGluR1 knockout mice (Hashimoto et al., 2001). Similarly, CF-EPSC amplitudes were also unaffected in Sema7A knocked-down Purkinje cells (Uesaka et al., 2014), indicating that signaling pathways downstream of mGluR1 are distinct from C1ql1-Bai3.

If this is the case, then what is the function of C1ql1-Bai3 signaling? C1ql1 enhanced the amplitudes of the strongest CF-EPSC and the weaker CF-EPSCs when it was overexpressed in all CFs at P0–P1 (Figure 2D). In addition, when C1ql1 or Bai3 was knocked down in adult WT mice, the CF-EPSC amplitudes and the number of CF synapses decreased (Figures 5 and S7). Similarly, the number of CF terminals was reduced in *C1ql1*-null and *PC-Bai3*-null cerebella (Figures 1

and 3). These results indicate that the primary function of C1ql1-Bai3 signaling is to promote CF synapse maturation regardless of their synaptic strength. Synapse maturation could be caused by enhanced formation or/and reduced removal of synapses. Because the height of the CF synapses were significantly reduced in the absence of C1ql1-Bai3 signaling (Figures 1, 3, 5, and S7), CFs are likely more dependent on C1ql1-Bai3 signaling to form and maintain synapses at distal regions of Purkinje cell dendritic shafts.

C1ql1-Bai3 signaling exerts an apparently opposite function on loser CFs: while overexpression of C1ql1 at P0–P1 strengthened winner CFs, it promoted early elimination of loser CFs at P14–P15 (Figure 2). Similarly, reintroduction of C1ql1 or Bai3 in mice deficient in the corresponding molecule induced the elimination of weak CF inputs in the adult cerebellum (Figure 4). C1ql1-Bai3 signaling may simply promote maturation of the dominant CF to the level where it could trigger signaling pathways, such as Ca^{2+} spikes and Arc/Arg3.1, to eliminate weaker CF inputs, whereas the winner CFs with strong C1ql1-Bai3 signaling may be resistant to the elimination process. The auto-proteolysis domain of Bai3 may also serve as a bistable switch to distinguish the winner from losing synapses (Araç et al., 2012). Alternatively, C1ql1-Bai3 signaling may trigger a pathway, which is independent of maturation of a winner CF, to eliminate weak CF inputs. For example, Bai1, a relative of Bai3, reportedly interacts with Elmo1/Dock180 (Park et al., 2007) or Par3/Tiam1 (Duman et al., 2013) to control the activity of the small GTPase Rac, a powerful regulator of actin cytoskeletal organization. Indeed, Bai3 was shown to interact with Elmo1 in vitro (Lanoue et al., 2013). Further studies are clearly warranted to clarify how C1ql1-Bai3 signaling is regulated and functions at CF synapses.

The Purkinje cell dendrites consist of two domains, a proximal one innervated by single CFs and a distal one on which many PF synapses are formed. These two domains are dynamically established and maintained by competition between PFs and CFs (Cesa and Strata, 2009; Watanabe and Kano, 2011). For example, when PF synapses are reduced in *Cbln1*-null (Hirai et al., 2005) or *GluD2*-null (Hashimoto et al., 2001) mice, CFs form synapses on distal dendrites of Purkinje cells. Conversely, when CF synaptic activity was pharmacologically inhibited or IO neurons were lesioned, CF synapses were lost and PFs formed synapses on proximal Purkinje cell dendrites (Cesa and Strata, 2009; Watanabe and Kano, 2011). Similarly, PFs invaded CF territories in P/Q-type Ca^{2+} channel-deficient Purkinje cells (Miyazaki et al., 2004). Notably, although CF synaptic inputs were reduced, PF synapses did not form on proximal dendrites of *C1ql1*-null or *PC-Bai3*-null Purkinje cells (Figures S1E and S3E). These findings indicate that, although changes in C1ql1-Bai3 signaling may be involved in the dynamic regulation of CF territories, its deficiency was not sufficient to allow PFs to form synapses on the proximal domain of Purkinje cell dendrites. PF synapse formation requires Cbln1 released from PFs to bind to GluD2 (Matsuda et al., 2010). Because GluD2 clustering is destabilized by Ca^{2+} channel activities (Hirai, 2001), reduction of Ca^{2+} channel activities may be a prerequisite for PFs to form synapses on the proximal dendritic domain of Purkinje cells.

C1q Family Proteins and Synaptic Functions

Based on the behavioral phenotypes of ataxic mutant mice lacking mGluR1, PKC γ , and GluD2, monoinnervation of Purkinje cells by CFs was thought to be required for motor coordination (Chen and Tonegawa, 1997). In contrast, although *C1ql1*-null and *PC-Bai3*-null Purkinje cells remain innervated by multiple CF inputs, these mice have normal gaits without significant impairment in beam or rotor-rod tests (Figure S8; Movie S1). However, motor learning, as measured by hOKR, was severely impaired in these mice (Figure 6). Recently, mGluR1 β -rescue mice, in which the splice variant of mGluR1 is expressed in *mGluR1*-null Purkinje cells, were shown to display normal motor coordination, even though their Purkinje cells were innervated by multiple CFs. These mice showed impaired LTD and eyeblink conditioning, another form of cerebellum-dependent motor learning (Ohtani et al., 2014). Similarly, a single injection of recombinant *Cbln1* restored LTD and eyeblink conditioning in adult *Cbln1*-null mice without significantly affecting the CF innervation pattern or LTP at PF-Purkinje cell synapses (Emi et al., 2013). Furthermore, GluD2^{ACT7}-rescue mice, in which GluD2 lacking seven C-terminal amino acids was expressed in *GluD2*-null Purkinje cells, displayed impaired LTD and eyeblink conditioning despite morphologically normal PF and CF synapses (Kakegawa et al., 2008). These findings indicate that LTD, rather than monoinnervation of Purkinje cells by CFs, is likely linked to motor learning in the cerebellum and indicate that C1ql1-Bai3 signaling is required for normal CF functions, such as complex spikes and CF-evoked afterhyperpolarization, which are necessary for LTD.

Family members of C1ql1 (C1ql2–C1ql4) are expressed in various brain regions (Iijima et al., 2010). Bai3 and its related members Bai1 and Bai2 are also widely expressed (Kee et al., 2004) and have been implicated in psychiatric disorders, such as schizophrenia and bipolar disorders (Lanoue et al., 2013). Thus, signaling mechanisms similar to the one mediated by C1ql1 and Bai3 in the cerebellum likely regulate synaptic competition and maintenance in various neuronal circuits essential for brain functions. In the hippocampus, C1ql2 and C1ql3 are highly expressed in adult dentate gyrus granule cells, and their mossy fiber afferents make dynamic branched axon-type synapses like CFs. Notably, mossy fiber synapses reportedly display learning-induced structural plasticity related to the precision of learning in adult mice (Ruediger et al., 2011). Therefore, future studies should assess whether and how C1ql proteins mediate activity-dependent structural plasticity essential for memory and learning.

EXPERIMENTAL PROCEDURES

All procedures related to animal care and treatment were performed in accordance with the guidelines set down by the Animal Resource Committee of Keio University. *C1ql1*-null, *PC-Bai2*-null, and *PC-Bai3*-null mice were generated and maintained on C57BL/6N backgrounds. As controls, WT mice were used for *C1ql1*-null mice and *Bai2*^{flox}, and *Bai3*^{flox} mice were used for *PC-Bai2*-null and *PC-Bai3*-null mice. For the behavioral analyses, littermates were used as controls. Experimental details of mouse generation as well as electrophysiological, anatomical, biochemical, structural, and behavioral analyses are described in the Supplemental Experimental Procedures. Data are

represented as mean \pm SEM. Statistical analyses were performed using the Excel statistics 2012 add-in software (Social Survey Research Information), and significant differences were defined as * $p < 0.05$, ** $p < 0.01$, and *** $p < 0.001$.

ACCESSION NUMBERS

The coordinates and structure factors for the reported crystal structure are deposited in the Protein Data Bank (PDB) under PDB ID 4d7y.

SUPPLEMENTAL INFORMATION

Supplemental Information includes Supplemental Experimental Procedures, eight figures, and two movies and can be found with this article online at <http://dx.doi.org/10.1016/j.neuron.2014.12.020>.

AUTHOR CONTRIBUTIONS

W.K. designed the project, carried out the electrophysiological and behavioral works, analyzed the data, and wrote the paper. N.M. and A.R.A. performed structural and SPR analyses and designed mutant constructs. E.M. performed the anatomical experiments and the IUE approach. M.A. and K.S. designed and generated mutant mice. K.M. performed the cell binding assays. Y.H.T. designed and prepared the microRNA constructs. K.K., A.T., J.M., and S.M. designed and prepared the recombinant viruses. S.N. supervised the hOKR experiment. M.W. generated essential antibodies. M.Y. designed and supervised the project and wrote the paper.

ACKNOWLEDGMENTS

We thank S. Narumi and S. Otsuka for their technical assistance and S. Matsuda and K.F. Tanaka for their useful comments. We also thank T. Miyazaki and K. Konno for their support on anatomical experiments, H. Okado for lentivirus production, H. Sakuma and T. Watanabe (Zeiss) for their support on superresolution microscopy analysis, and the staff at Diamond beamline I04 for synchrotron assistance. This work was supported by a grant-in-aid for scientific research from the Ministry of Education, Culture, Sports, Science and Technology of Japan and the Japan Society for the Promotion of Science (W.K. and M.Y.); the CREST from the Japan Science and Technology Agency (M.Y.); the Kanae Foundation (W.K.); the Nakajima Foundation (W.K.); the Keio Gijuku Fukuzawa Memorial Fund for the Advancement of Education and Research (W.K.); the Takeda Science Foundation (W.K. and M.Y.); the UK Medical Research Council (MRC) (A.R.A.); and a Wellcome Trust PhD studentship (N.M.). Further support from the Wellcome Trust Core Award 090532/Z/09/Z is acknowledged. A.R.A. is an MRC Senior Research Fellow.

Accepted: November 26, 2014

Published: January 21, 2015

REFERENCES

- Araç, D., Boucard, A.A., Bolliger, M.F., Nguyen, J., Soltis, S.M., Südhof, T.C., and Brunger, A.T. (2012). A novel evolutionarily conserved domain of cell-adhesion GPCRs mediates autolysis. *EMBO J.* 31, 1364–1378.
- Bolliger, M.F., Martinelli, D.C., and Südhof, T.C. (2011). The cell-adhesion G protein-coupled receptor BAI3 is a high-affinity receptor for C1q-like proteins. *Proc. Natl. Acad. Sci. USA* 108, 2534–2539.
- Bosman, L.W., Takechi, H., Hartmann, J., Eilers, J., and Konnerth, A. (2008). Homosynaptic long-term synaptic potentiation of the “winner” climbing fiber synapse in developing Purkinje cells. *J. Neurosci.* 28, 798–807.
- Carrillo, J., Nishiyama, N., and Nishiyama, H. (2013). Dendritic translocation establishes the winner in cerebellar climbing fiber synapse elimination. *J. Neurosci.* 33, 7641–7653.
- Cesa, R., and Strata, P. (2009). Axonal competition in the synaptic wiring of the cerebellar cortex during development and in the mature cerebellum. *Neuroscience* 162, 624–632.

- Chen, C., and Tonegawa, S. (1997). Molecular genetic analysis of synaptic plasticity, activity-dependent neural development, learning, and memory in the mammalian brain. *Annu. Rev. Neurosci.* *20*, 157–184.
- Davie, J.T., Clark, B.A., and Häusser, M. (2008). The origin of the complex spike in cerebellar Purkinje cells. *J. Neurosci.* *28*, 7599–7609.
- Duman, J.G., Tzeng, C.P., Tu, Y.K., Munjal, T., Schwedter, B., Ho, T.S., and Toliás, K.F. (2013). The adhesion-GPCR BAI1 regulates synaptogenesis by controlling the recruitment of the Par3/Tiam1 polarity complex to synaptic sites. *J. Neurosci.* *33*, 6964–6978.
- Eccles, J.C., Llinás, R., and Sasaki, K. (1966). The excitatory synaptic action of climbing fibres on the Purkinje cells of the cerebellum. *J. Physiol.* *182*, 268–296.
- Emi, K., Kakegawa, W., Miura, E., Ito-Ishida, A., Kohda, K., and Yuzaki, M. (2013). Reevaluation of the role of parallel fiber synapses in delay eyeblink conditioning in mice using Cbln1 as a tool. *Front. Neural Circuits* *7*, 180, <http://dx.doi.org/10.3389/fncir.2013.00180>.
- Hashimoto, K., Ichikawa, R., Takechi, H., Inoue, Y., Aiba, A., Sakimura, K., Mishina, M., Hashikawa, T., Konnerth, A., Watanabe, M., and Kano, M. (2001). Roles of glutamate receptor $\delta 2$ subunit (GluRdelta2) and metabotropic glutamate receptor subtype 1 (mGluR1) in climbing fiber synapse elimination during postnatal cerebellar development. *J. Neurosci.* *21*, 9701–9712.
- Hashimoto, K., Ichikawa, R., Kitamura, K., Watanabe, M., and Kano, M. (2009). Translocation of a “winner” climbing fiber to the Purkinje cell dendrite and subsequent elimination of “losers” from the soma in developing cerebellum. *Neuron* *63*, 106–118.
- Hashimoto, K., Tsujita, M., Miyazaki, T., Kitamura, K., Yamazaki, M., Shin, H.S., Watanabe, M., Sakimura, K., and Kano, M. (2011). Postsynaptic P/Q-type Ca^{2+} channel in Purkinje cell mediates synaptic competition and elimination in developing cerebellum. *Proc. Natl. Acad. Sci. USA* *108*, 9987–9992.
- Hills, L.B., Masri, A., Konno, K., Kakegawa, W., Lam, A.T., Lim-Melia, E., Chandry, N., Hill, R.S., Partlow, J.N., Al-Saffar, M., et al. (2013). Deletions in *GRID2* lead to a recessive syndrome of cerebellar ataxia and tonic upgaze in humans. *Neurology* *81*, 1378–1386.
- Hirai, H. (2001). Ca^{2+} -dependent regulation of synaptic $\delta 2$ glutamate receptor density in cultured rat Purkinje neurons. *Eur. J. Neurosci.* *14*, 73–82.
- Hirai, H., Pang, Z., Bao, D., Miyazaki, T., Li, L., Miura, E., Parris, J., Rong, Y., Watanabe, M., Yuzaki, M., and Morgan, J.I. (2005). Cbln1 is essential for synaptic integrity and plasticity in the cerebellum. *Nat. Neurosci.* *8*, 1534–1541.
- Holtmaat, A., and Svoboda, K. (2009). Experience-dependent structural synaptic plasticity in the mammalian brain. *Nat. Rev. Neurosci.* *10*, 647–658.
- Iijima, T., Miura, E., Watanabe, M., and Yuzaki, M. (2010). Distinct expression of C1q-like family mRNAs in mouse brain and biochemical characterization of their encoded proteins. *Eur. J. Neurosci.* *31*, 1606–1615.
- Ito, M. (2006). Cerebellar circuitry as a neuronal machine. *Prog. Neurobiol.* *78*, 272–303.
- Ito, M. (2013). Error detection and representation in the olivo-cerebellar system. *Front. Neural Circuits* *7*, 1, <http://dx.doi.org/10.3389/fncir.2013.00001>.
- Kakegawa, W., Miyazaki, T., Emi, K., Matsuda, K., Kohda, K., Motohashi, J., Mishina, M., Kawahara, S., Watanabe, M., and Yuzaki, M. (2008). Differential regulation of synaptic plasticity and cerebellar motor learning by the C-terminal PDZ-binding motif of GluRdelta2. *J. Neurosci.* *28*, 1460–1468.
- Kano, M., and Hashimoto, K. (2009). Synapse elimination in the central nervous system. *Curr. Opin. Neurobiol.* *19*, 154–161.
- Kee, H.J., Ahn, K.Y., Choi, K.C., Won Song, J., Heo, T., Jung, S., Kim, J.K., Bae, C.S., and Kim, K.K. (2004). Expression of brain-specific angiogenesis inhibitor 3 (BAI3) in normal brain and implications for BAI3 in ischemia-induced brain angiogenesis and malignant glioma. *FEBS Lett.* *569*, 307–316.
- Kishore, U., Gaboriaud, C., Waters, P., Shrive, A.K., Greenhough, T.J., Reid, K.B., Sim, R.B., and Arlaud, G.J. (2004). C1q and tumor necrosis factor superfamily: modularity and versatility. *Trends Immunol.* *25*, 551–561.
- Lanoue, V., Usardi, A., Sigoillot, S.M., Talleur, M., Iyer, K., Mariani, J., Isope, P., Vojdani, G., Heintz, N., and Selimi, F. (2013). The adhesion-GPCR BAI3, a gene linked to psychiatric disorders, regulates dendrite morphogenesis in neurons. *Mol. Psychiatry* *18*, 943–950.
- Lohof, A.M., Delhaye-Bouchaud, N., and Mariani, J. (1996). Synapse elimination in the central nervous system: functional significance and cellular mechanisms. *Rev. Neurosci.* *7*, 85–101.
- Luo, B.H., Springer, T.A., and Takagi, J. (2003). Stabilizing the open conformation of the integrin headpiece with a glycan wedge increases affinity for ligand. *Proc. Natl. Acad. Sci. USA* *100*, 2403–2408.
- Matsuda, K., Miura, E., Miyazaki, T., Kakegawa, W., Emi, K., Narumi, S., Fukazawa, Y., Ito-Ishida, A., Kondo, T., Shigemoto, R., et al. (2010). Cbln1 is a ligand for an orphan glutamate receptor $\delta 2$, a bidirectional synapse organizer. *Science* *328*, 363–368.
- Mikuni, T., Uesaka, N., Okuno, H., Hirai, H., Deisseroth, K., Bito, H., and Kano, M. (2013). Arc/Arg3.1 is a postsynaptic mediator of activity-dependent synapse elimination in the developing cerebellum. *Neuron* *78*, 1024–1035.
- Miyazaki, T., Hashimoto, K., Shin, H.S., Kano, M., and Watanabe, M. (2004). P/Q-type Ca^{2+} channel $\alpha 1A$ regulates synaptic competition on developing cerebellar Purkinje cells. *J. Neurosci.* *24*, 1734–1743.
- Nakayama, H., Miyazaki, T., Kitamura, K., Hashimoto, K., Yanagawa, Y., Obata, K., Sakimura, K., Watanabe, M., and Kano, M. (2012). GABAergic inhibition regulates developmental synapse elimination in the cerebellum. *Neuron* *74*, 384–396.
- Ohtani, Y., Miyata, M., Hashimoto, K., Tabata, T., Kishimoto, Y., Fukaya, M., Kase, D., Kassai, H., Nakao, K., Hirata, T., et al. (2014). The synaptic targeting of mGluR1 by its carboxyl-terminal domain is crucial for cerebellar function. *J. Neurosci.* *34*, 2702–2712.
- Park, D., Tosello-Tramont, A.-C.C., Elliott, M.R., Lu, M., Haney, L.B., Ma, Z., Klibanov, A.L., Mandell, J.W., and Ravichandran, K.S. (2007). BAI1 is an engulfment receptor for apoptotic cells upstream of the ELMO/Dock180/Rac module. *Nature* *450*, 430–434.
- Rondard, P., Huang, S., Monnier, C., Tu, H., Blanchard, B., Oueslati, N., Malhaire, F., Li, Y., Trinquet, E., Labesse, G., et al. (2008). Functioning of the dimeric GABA_B receptor extracellular domain revealed by glycan wedge scanning. *EMBO J.* *27*, 1321–1332.
- Ruediger, S., Vittori, C., Bednarek, E., Genoud, C., Strata, P., Sacchetti, B., and Caroni, P. (2011). Learning-related feedforward inhibitory connectivity growth required for memory precision. *Nature* *473*, 514–518.
- Selimi, F., Cristea, I.M., Heller, E., Chait, B.T., and Heintz, N. (2009). Proteomic studies of a single CNS synapse type: the parallel fiber/purkinje cell synapse. *PLoS Biol.* *7*, e83.
- Shimono, C., Manabe, R., Yamada, T., Fukuda, S., Kawai, J., Furutani, Y., Tsutsui, K., Ikenaka, K., Hayashizaki, Y., and Sekiguchi, K. (2010). Identification and characterization of nCLP2, a novel C1q family protein expressed in the central nervous system. *J. Biochem.* *147*, 565–579.
- Stephenson, J.R., Purcell, R.H., and Hall, R.A. (2014). The BAI subfamily of adhesion GPCRs: synaptic regulation and beyond. *Trends Pharmacol. Sci.* *35*, 208–215.
- Stevens, B., Allen, N.J., Vazquez, L.E., Howell, G.R., Christopherson, K.S., Nouri, N., Micheva, K.D., Mehalow, A.K., Huberman, A.D., Stafford, B., et al. (2007). The classical complement cascade mediates CNS synapse elimination. *Cell* *131*, 1164–1178.
- Uesaka, N., Uchigashima, M., Mikuni, T., Nakazawa, T., Nakao, H., Hirai, H., Aiba, A., Watanabe, M., and Kano, M. (2014). Retrograde semaphorin signaling regulates synapse elimination in the developing mouse brain. *Science* *344*, 1020–1023.
- Watanabe, M., and Kano, M. (2011). Climbing fiber synapse elimination in cerebellar Purkinje cells. *Eur. J. Neurosci.* *34*, 1697–1710.
- Yoshida, T., Katoh, A., Ohtsuki, G., Mishina, M., and Hirano, T. (2004). Oscillating Purkinje neuron activity causing involuntary eye movement in a mutant mouse deficient in the glutamate receptor $\delta 2$ subunit. *J. Neurosci.* *24*, 2440–2448.
- Yuzaki, M. (2008). Cbln and C1q family proteins: new transneuronal cytokines. *Cell. Mol. Life Sci.* *65*, 1698–1705.

ARTICLE

Received 19 Sep 2015 | Accepted 30 Oct 2015 | Published 10 Dec 2015

DOI: 10.1038/ncomms10090

OPEN

A CDC42EP4/septin-based perisynaptic glial scaffold facilitates glutamate clearance

Natsumi Ageta-Ishihara¹, Maya Yamazaki², Kohtarou Konno³, Hisako Nakayama⁴, Manabu Abe², Kenji Hashimoto⁵, Tomoki Nishioka⁶, Kozo Kaibuchi⁶, Satoko Hattori⁷, Tsuyoshi Miyakawa^{7,8}, Kohichi Tanaka⁹, Fathul Huda¹⁰, Hirokazu Hirai¹⁰, Kouichi Hashimoto⁴, Masahiko Watanabe³, Kenji Sakimura² & Makoto Kinoshita¹

The small GTPase-effector proteins CDC42EP1-5/BORG1-5 interact reciprocally with CDC42 or the septin cytoskeleton. Here we show that, in the cerebellum, CDC42EP4 is exclusively expressed in Bergmann glia and localizes beneath specific membrane domains enwrapping dendritic spines of Purkinje cells. CDC42EP4 forms complexes with septin hetero-oligomers, which interact with a subset of glutamate transporter GLAST/EAAT1. In *Cdc42ep4*^{-/-} mice, GLAST is dissociated from septins and is delocalized away from the parallel fibre-Purkinje cell synapses. The excitatory postsynaptic current exhibits a protracted decay time constant, reduced sensitivity to a competitive inhibitor of the AMPA-type glutamate receptors (γ DGG) and excessive baseline inward current in response to a subthreshold dose of a nonselective inhibitor of the glutamate transporters/EAAT1-5 (DL-TBOA). Insufficient glutamate-buffering/clearance capacity in these mice manifests as motor coordination/learning defects, which are aggravated with subthreshold DL-TBOA. We propose that the CDC42EP4/septin-based glial scaffold facilitates perisynaptic localization of GLAST and optimizes the efficiency of glutamate-buffering and clearance.

¹ Division of Biological Sciences, Department of Molecular Biology, Nagoya University Graduate School of Science, Nagoya 464-8602, Japan. ² Department of Cellular Neurobiology, Brain Research Institute, Niigata University, Niigata 951-8585, Japan. ³ Department of Anatomy, Hokkaido University Graduate School of Medicine, Sapporo 060-8638, Japan. ⁴ Department of Neurophysiology, Graduate School of Biomedical and Health Sciences, Hiroshima University, Hiroshima 734-8551, Japan. ⁵ Division of Clinical Neuroscience, Chiba University Center for Forensic Mental Health, Chiba 260-8670, Japan. ⁶ Department of Cell Pharmacology, Nagoya University Graduate School of Medicine, Showa, Nagoya 466-8560, Japan. ⁷ Division of Systems Medical Science, Institute for Comprehensive Medical Science, Fujita Health University, Toyoake 470-1192, Japan. ⁸ Center for Genetic Analysis of Behavior, National Institute for Physiological Sciences, Okazaki 444-8585, Japan. ⁹ Laboratory of Molecular Neuroscience, Medical Research Institute, Tokyo Medical and Dental University, Tokyo 113-8510, Japan. ¹⁰ Department of Neurophysiology and Neural Repair, Gunma University Graduate School of Medicine, Maebashi, Gunma 371-8511, Japan. Correspondence and requests for materials should be addressed to M.K. (email: kinoshita.makoto@c.mbox.nagoya-u.ac.jp).

Glutamate transporters (Excitatory Amino Acid Transporter 1–5/EAAT1–5) are membrane-bound solute carrier proteins that terminate glutamatergic neurotransmission and maintain the glutamate homeostasis by the symport of extracellular glutamate and Na^+/H^+ into the glial and neuronal cytoplasm¹. The extracellular glutamate concentration surges to 160–250 μM near perisynaptic domains of Bergmann glia in the cerebellum, which is rapidly buffered and cleared by binding to and reuptake through EAATs^{2,3}. When the glutamate-buffering/clearance capacity falls short of glutamate-release activities, glutamate pervades the extracellular space. Excessive external glutamate entails protracted activation of glutamate receptors in the nearest synaptic and extrasynaptic membranes, and in the neighbouring synapses, and of glial responses. In the cerebellar molecular layer, GLAST/EAAT1/SLC1A3 is highly concentrated along perisynaptic Bergmann glial membranes⁴ and plays a major role in the clearance of glutamate released from the parallel fibres (PFs, from granule cells in the cerebellar granule cell layer) and climbing fibres (CFs, from neurons in the inferior olivary nuclei) to Purkinje cells (PCs), while GLT-1/EAAT2, the major glial transporter in the forebrain, and neuronal EAAT4 play relatively minor roles⁵. Genetic loss of GLAST results in anomalous CF–PC innervations and defective motor coordination/learning⁶, attesting its central role in Bergmann glia-mediated glutamate homeostasis in the cerebellum.

Despite the developmental and physiological significance of GLAST, and the linkage to human episodic ataxia and schizophrenia^{7–9}, little is known about the post-translational regulation. Physical interactions with beta-III spectrin/GTRAP41 and ARHGEF11/GTRAP48 were reported to facilitate the anchorage and activity of EAAT4 (ref. 10). However, physiological significance of these findings from heterologous cells, and whether these proteins modulate the localization and/or activity of GLAST, remains unknown. Previous studies demonstrated a physical interaction between GLAST and septins (a family of polymerizing GTPases that constitute the membrane skeleton) *in vitro* and in heterologous cells, and their partial co-localization in Bergmann glia^{11,12}. However, hypothetical septin dependence of the perisynaptic targeting and activity of GLAST has never been directly tested *in vivo*, partly because of the redundancy among the septin family (see Discussion).

Another line of biochemical and cell biological studies showed that a family of CRIB-domain proteins CDC42EPs/BORGs binds to septin hetero-oligomers or CDC42 (a signalling small GTPase that controls cytoskeleton and cell morphogenesis) in a mutually exclusive manner. The major determinant of the binding preference of CDC42EPs is the status of CDC42-bound nucleotide; $\text{GTP-CDC42} > \text{septins} > \text{GDP-CDC42}$ (refs 13–15). However, again, *in vivo* relevance of the hypothetical CDC42–CDC42EP–septin pathway remains unclear.

Given the above background, genetic deletion of the dominant CDC42EP species in Bergmann glia is a rational approach to address the two open issues: physiological roles of the CDC42–CDC42EP–septin pathway and of the septin–GLAST interaction in the brain. We find robust co-expression and co-localization of CDC42EP4 and septins in Bergmann glia, generate CDC42EP4-null mice and conduct biochemical, fine morphological, electrophysiological, pharmacological and behavioural analyses. The unique and systematic approach reveals the requirement of CDC42EP4 in Bergmann glia for the septin-mediated perisynaptic localization of GLAST, and for the efficient buffering and clearance of glutamate from around synapses towards PCs.

Results

Selective expression of CDC42EP4 in Bergmann glia. We conducted immunoblot (IB) for the expression profiling of the CDC42EP4 protein in the whole brain, two brain subregions (cerebellum and hippocampus) and seven non-neural tissues from adult C57BL/6N mice (Fig. 1a). The major band of ~ 39 kDa, which fits the calculated molecular mass of 37,980, was the most abundant in the cerebellum (Fig. 1b and Supplementary Fig. 15) as predicted from public gene expression databases including National Center for Biotechnology Information.

Fluorescence *in situ* hybridization (FISH) for *Cdc42ep4* mRNA highlighted the PC layer in the cerebellum (Fig. 1c, left), which is consistent with the data in the Allen Mouse Brain Atlas #71723875 (Allen Institute for Brain Science). Double-label FISH showed complementary distribution of mRNAs for CDC42EP4 and calbindin (PC marker) and overlap between mRNAs for CDC42EP4 and GLAST (Bergmann glia marker; Fig. 1c, right), demonstrating highly Bergmann glia-selective expression of the *Cdc42ep4* gene.

Clustering of CDC42EP4 in perisynaptic glial processes. Consistently, double-label immunofluorescence (IF) for CDC42EP4 and calbindin, respectively, highlighted Bergmann glia and PCs in a mutually exclusive manner (Fig. 1d). At a higher magnification with a lower gain level, CDC42EP4 immunoreactivity appeared as ‘hotspots’, which were interspersed along PC dendrites and tightly apposed to dendritic spines (Fig. 1d, right). CDC42EP4 was far more concentrated in the processes of Bergmann glia than in the cell bodies (Fig. 1e).

To analyse the subcellular distribution of CDC42EP4 at higher resolutions, we conducted silver-enhanced immunoelectron microscopy. Bergmann glial processes thoroughly ensheathed dendritic spines of PCs, except for synaptic contact sites with axon terminals. Gold particles for CDC42EP4 were commonly found as submembranous clusters in Bergmann glial processes that surrounded dendritic spines, particularly around the spine neck (Fig. 1f). Quantitative analysis demonstrated a gradient of CDC42EP4 from the base (neck) to the apex (head) of spines (Fig. 1g). These data indicate that CDC42EP4 in Bergmann glia is localized beneath specific membrane domains that are facing dendritic spines of PCs. The characteristic distribution of CDC42EP4 is reminiscent of those of septin subunits, SEPT4/H5 (ref. 16), SEPT7/hCDC10 (ref. 16) and SEPT2/Nedd5 (ref. 11), whose physiological role has been unknown.

Generation of *Cdc42ep4*-floxed and -null mice. To explore physiological roles of *Cdc42ep4* using a reverse genetic approach, we generated a line of C57BL/6N mice harbouring a floxed allele, which was subsequently converted to a null allele by crossing with another line that ubiquitously expresses Cre recombinase (Fig. 2a–c). Analyses of *Cdc42ep4*^{−/−} offspring demonstrated the total absence of CDC42EP4 in IB and IF (Fig. 2d,e and Supplementary Fig. 15). For the following analyses, we consistently compared *Cdc42ep4*^{−/−} (knockout; KO) and *Cdc42ep4*^{fl/fl} (wild type; WT) male littermates generated from *Cdc42ep4*^{fl/−} (heterozygous) parents. There was no difference by genotype in the gross appearance, body weight and fertility (Supplementary Fig. 1).

Normal architecture of the *Cdc42ep4*^{−/−} cerebellum. We conducted IF with specific markers for the four major neuronal and glial components (PFs, CFs, PCs and Bergmann glia), which did not show obvious anomaly in the cerebellar cortex of KO mice (Figs 3a and 5b). Transmission electron microscopy (TEM) images showed no recognizable ultrastructural defects in the

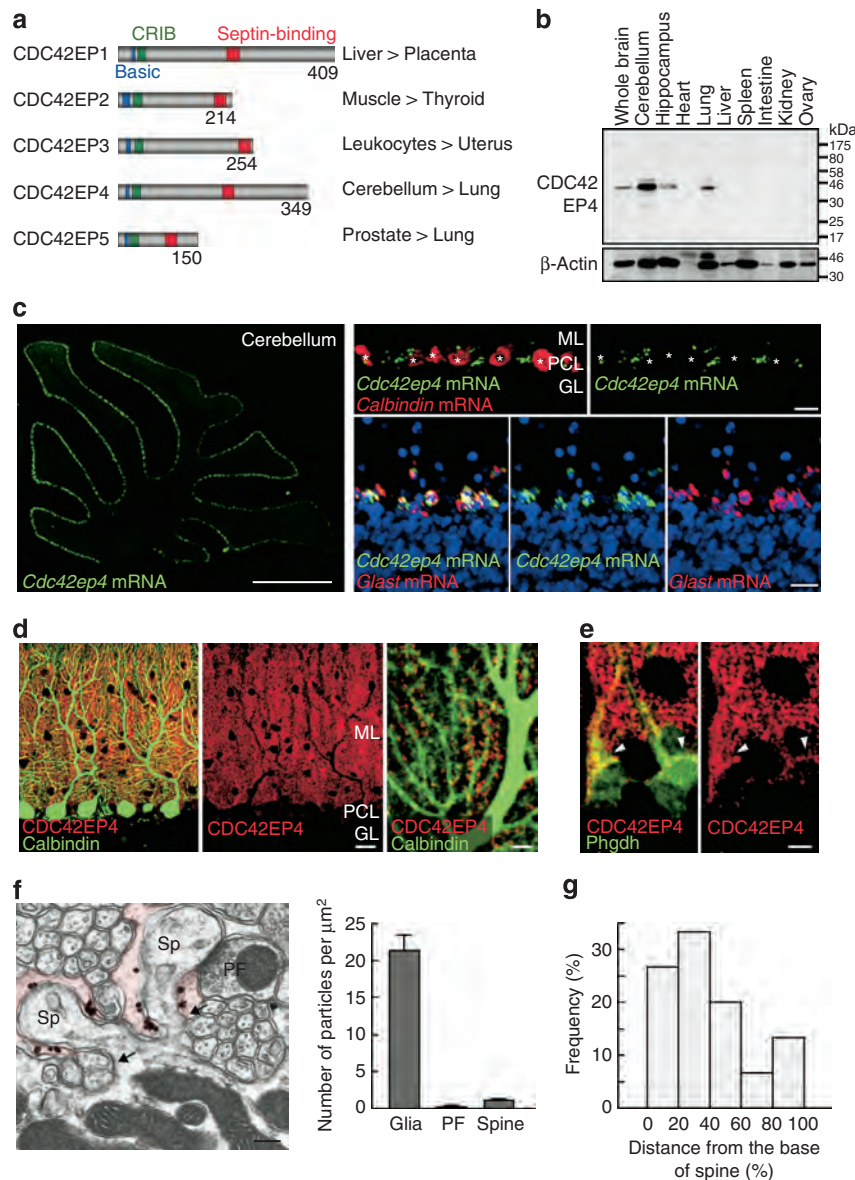


Figure 1 | Bergmann glia-selective expression and unique perisynaptic localization of CDC42EP4. (a) The CDC42EP/BORG family and gene expression pattern in the mouse. Each CDC42EP contains a set of basic-CRIB-BD domains. Anti-CDC42EP4 antibody was raised against a region between the CRIB and BD3 (septin-binding) domains. The numbers denote amino-acid residues. CDC42EP1/2/3/4/5, respectively, corresponds to BORG5/1/2/4/3. (b) Lysates from adult mouse tissues (50 μg total protein per lane) were immunoblotted for CDC42EP4 and were reprobed for β -actin as a loading control. The major ~39-kDa band was most abundant in the cerebellum. (c) FISH for *Cdc42ep4* mRNA in the adult mouse cerebellum. (Left) Labels for *Cdc42ep4* (green) highlighted the PC layer in a parasagittal section. (Top) Double-label FISH for mRNAs for *Cdc42ep4* and a PC marker calbindin (red). *Cdc42ep4* mRNA was excluded from PCs (*). (Bottom) Double-label FISH for *Cdc42ep4* and *Glast* (red) mRNAs, and TOTO-3 stain for DNA (blue). The two mRNA signals overlapped in all ($n = 115$) Bergmann glial cells identified in a representative section. Scale bars, 1 mm and 20 μm . (d) (Left and centre) Double-label IF for CDC42EP4 (red) and calbindin (green) in the cerebellar cortex. The diffuse granular signals for CDC42EP4 distributed throughout the molecular layer and in the PC layer, which were excluded from PCs and the granule cell layer. (Right) At a higher magnification, CDC42EP4-positive puncta were interspersed and aligned along PC dendrites. (e) Double-label IF for CDC42EP4 (red) and a Bergmann glial marker Phgdh (green). The limited overlap in Bergmann glial cell bodies (arrowheads) indicated selective localization of CDC42EP4 in glial processes. Scale bar, 5 μm . (f) (Left) Immunoelectron microscopy image for CDC42EP4 in the molecular layer. Gold particles for CDC42EP4 were found as submembranous clusters in terminal processes of Bergmann glia (tinted), each surrounding a dendritic spine (Sp) of a PC. PF, parallel fibre terminal. Scale bar, 200 nm. (Right) Quantification of glia-selective localization of CDC42EP4. Data represented as mean \pm s.e.m. (g) Histogram showing a gradient of CDC42EP4 signals relative to the geometry of dendritic spines of PCs; higher in regions facing spine base (arrows in f) than in regions facing the spine head.

molecular layer (Fig. 3b), including the lengths of the post-synaptic density (PSD) in PF-PC synapses (Fig. 3c). Four major proteins at glutamatergic synapses, GluA1, GluA2, GluA4 and PSD-95, did not show quantitative differences by genotype (Fig. 3d and Supplementary Fig. 15). These data indicate that CDC42EP4 is dispensable for the morphological development of

the major neuronal and glial components, and synapse architecture in the cerebellar cortex.

Septin oligomers as the major binding partners of CDC42EP4.

For unbiased identification of physiological binding partners of CDC42EP4 in Bergmann glia, we conducted proteomic analysis

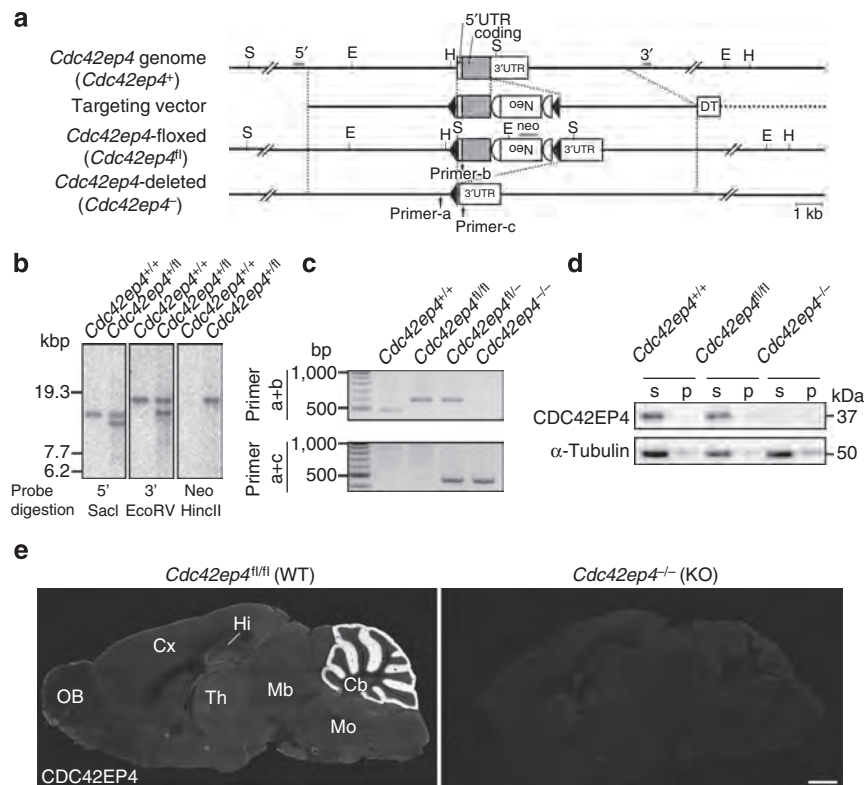


Figure 2 | Generation of *Cdc42ep4*^{-/-} mice and morphology of the major neuronal components. (a) The KO strategy of the *Cdc42ep4* gene. A schematic diagram showing the wild-type (*Cdc42ep4*⁺), floxed (*Cdc42ep4*^{fl/fl}) and null (*Cdc42ep4*^{-/-}) alleles, and the targeting vector. Note that Cre-mediated loxP recombination leaves no coding exon. The restriction sites for Sac I (S), EcoRV (E) and Hinc II (H), three probes (grey bars) used for Southern blot analysis and three PCR primer sites are indicated. Signs; coding region (grey box), untranslated region (open box), loxP (black triangle), frt (open half-circle), neomycin resistance cassette (Neo), diphtheria toxin A-chain cassette (DT). (b) Southern blot analysis. Genomic DNAs purified from WT and the chimera (*Cdc42ep4*^{+/+}; *Cdc42ep4*^{fl/+}) mice were digested with the restriction enzymes and hybridized with the probes as indicated. The band patterns, as seen in preceding Southern blot analysis of ES cell clones, reconfirmed successful homologous recombination of the clone. See Methods for details. (c) PCR genotyping. Two sets of primers discriminated genomic DNAs from *Cdc42ep4*^{+/+}, *Cdc42ep4*^{fl/fl} (WT), *Cdc42ep4*^{fl/+} and *Cdc42ep4*^{-/-} (KO) mice. (d) Expression and extractability of CDC42EP4 in the adult mouse cerebellum. The pellet/supernatant assay showed that CDC42EP4 is partitioned mostly to the detergent-extractable, supernatant (s) fraction but not to the inextractable, pellet (p) fraction. CDC42EP4 was absent from KO tissues. α -Tubulin was used as a loading control. (e) IF for CDC42EP4 on parasagittal brain sections of adult male littermate WT and KO mice. The molecular layer of the WT cerebellum (Cb) was intensely labelled for CDC42EP4, which was absent from the KO brain. The faint, diffuse labelling of the entire brain is attributed to astrocytes. These results are consistent with the immunoblot data (Figs 1b and 2d) and warrant the specificity (high signal-to-noise ratio) of the antibody. Scale bar, 1 mm. UTR, untranslated repeat.

of cerebellar lysates. Immunoaffinity chromatography for CDC42EP4 followed by mass spectrometry identified CDC42EP4, nine septin subunits (SEPT2/3/4/5/6/7/8/10/11) and a few other cytoskeletal proteins including Myosin-10 (nonmuscle myosin heavy chain IIB) and α -II/ β -II spectrins (Table 1). The minimal background noises in the three negative control experiments (for example, anti-CDC42EP4 IgG captured no peptides from KO samples) reconfirmed the absence of CDC42EP4 in the KO cerebellum and the antibody specificity. Intriguingly, however, CDC42 and Tc10/RhoQ (another small GTPase that can bind to CDC42EPs *in vitro*¹³) were not detected (Table 1 and Supplementary Fig. 13). Thus, the major physiological binding partners of CDC42EP4 in the adult mouse cerebellum are not small GTPases, but hetero-oligomers of septins.

Physiological network of CDC42EP4, septins and GLAST. Previous studies with recombinant proteins separately demonstrated direct interactions between CDC42EP5/BORG3 and septin hetero-oligomers (for example, SEPT6/7 and SEPT2/6/7, but not individual subunits)^{14,15}, and between SEPT2 and GLAST¹¹. However, higher-order molecular network composed of

CDC42EPs, septin hetero-oligomers and GLAST has never been tested. We addressed this with their co-immunoprecipitation (co-IP) from cerebellar lysate (Fig. 4a and Supplementary Figs 13–15), and double-label IF that showed their partial overlap in Bergmann glia (Fig. 4e). These data, along with the previous studies and our proteomic and IF findings, indicate physiological molecular network that contains CDC42EP4, septin hetero-oligomers and a subset of GLAST.

Loss of CDC42EP4 diminishes septin-GLAST interaction. To validate the significance of CDC42EP4 in the molecular network, we compared the status with or without CDC42EP4. Pellet/supernatant assay of cerebellar lysates showed that the amount and solubility of SEPT7, SEPT4 and GLAST were unaffected by the loss of CDC42EP4 (Fig. 4b–d and Supplementary Fig. 15). Their distribution patterns assessed using IF showed no recognizable difference by genotype (Fig. 5b). Intriguingly, however, a co-IP/IB assay revealed a significant reduction (Δ 50%) of GLAST that was pulled down with SEPT4 (a Bergmann glia-selective septin subunit) from the *Cdc42ep4*^{-/-} cerebellum, when the interactions with two other major septin subunits in Bergmann

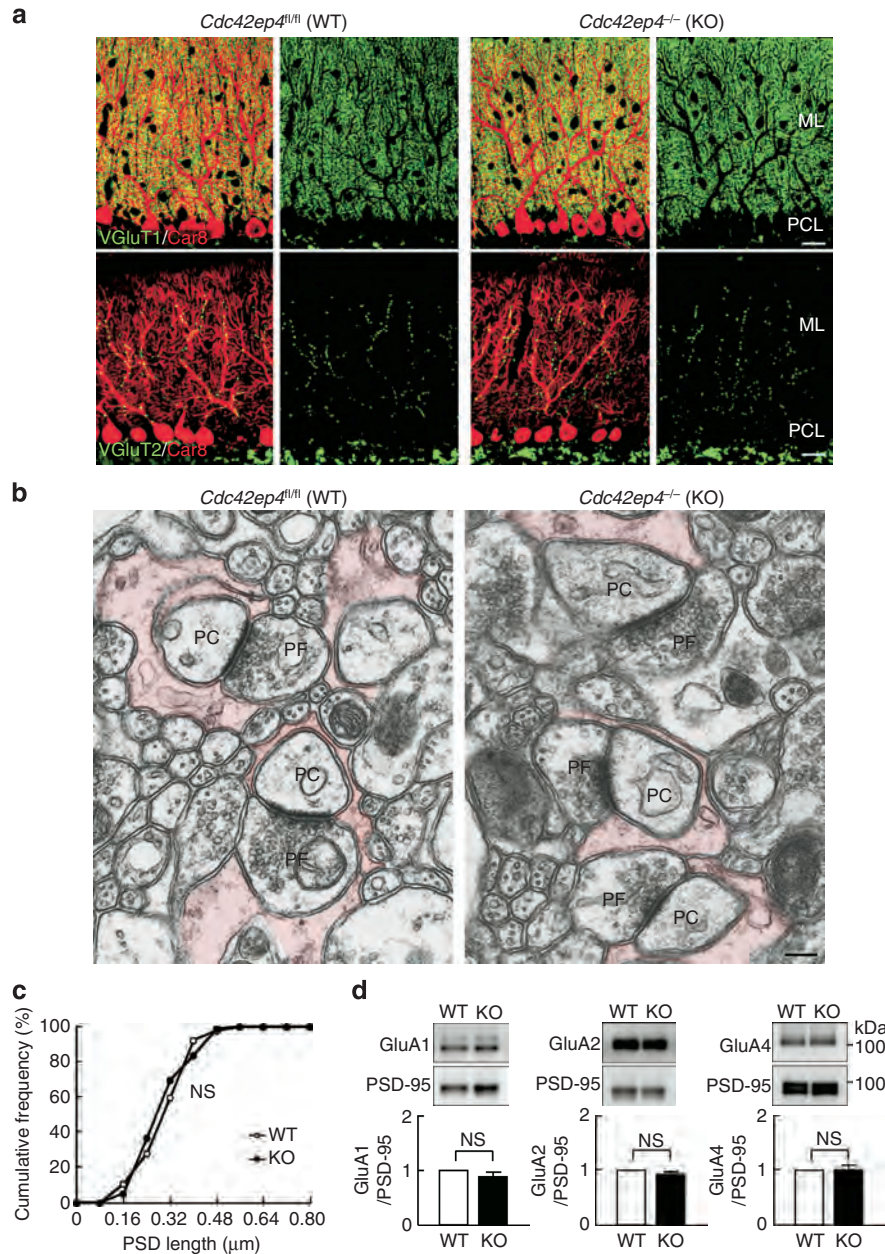


Figure 3 | Morphological analysis of the neuronal and glial components in *Cdc42ep4^{fl/fl}* and *Cdc42ep4^{-/-}* cerebellar cortices. (a) Double-label IF of WT and KO cerebellar cortices for a Purkinje cell marker Car8 (red) and a parallel fibre (that is, granule cell) marker VGLuT1 (top, green) or a climbing fibre marker VGLuT2 (bottom, green). No obvious morphological anomaly, including aberrant CF-PC innervation, was found in the major neuronal components of KO-derived samples. Scale bar, 20 μm. **(b)** Transmission electron microscopy images of WT and KO molecular layers. No obvious ultrastructural difference was found between the genotypes. PF, parallel fibre terminal or bouton. PC, dendritic spine of Purkinje cell. Bergmann glial processes are tinted. Scale bar, 200 nm. **(c)** Cumulative histogram of PSD length of the PF-PC synapses, showing no significant difference between the genotypes ($n = 92$ synapses from two littermates for each genotype, NS, $P > 0.05$ by Kolmogorov-Smirnov test). **(d)** Quantitative immunoblot of WT and KO cerebellar PSD fractions for GluA1, GluA2 and GluA4 (the major subunits of the AMPARs), each normalized with PSD-95. There was no significant quantitative difference by genotype ($n = 3$, NS, $P > 0.05$ by t -test).

glia (SEPT2 and SEPT7) were unaffected (Fig. 5a and Supplementary Fig. 15). The significant dissociation of GLAST from septin hetero-oligomers by the loss of CDC42EP4 indicates a role for CDC42EP4 as a stabilizer and/or an adapter for the association between GLAST and septin hetero-oligomers.

GLAST delocalizes away from perisynapse without CDC42EP4. Previous fluorescence recovery after photobleaching assay showed that septin depletion via RNA interference augmented diffusional mobility of green fluorescent protein-tagged GLAST on the

plasma membrane, while septin filament stabilization gave the opposite effect, indicating a role for septins as submembranous scaffold and/or diffusion barrier for GLAST¹². To assess whether the dissociation from septins by the loss of CDC42EP4 could alter the distribution of GLAST, we conducted quantitative mapping of GLAST in Bergmann glia by postembedding immunoelectron microscopy technique (Fig. 5c–e). As expected, gold particles for GLAST were distributed along Bergmann glia membrane enveloping pre- and postsynaptic elements of PF-PC synapses, whereas neuronal membranes were

Table 1 | Proteomic analysis for the binding partners of CDC42EP4 in the cerebellum.

Identified proteins (69)	Peptide number				Sequence coverage (%)			
	KO IgG	KO ep4	WT IgG	WT ep4	KO IgG	KO ep4	WT IgG	WT ep4
CDC42EP4				20				63
SEPT7			1	21			2.1	45
SEPT4			1	19			1.9	43
SEPT11				14				34
SEPT5				12				42
SEPT2				11				47
α -II spectrin			8	18			4.7	9.1
SEPT3				7				22
Myosin-10	2		1	10	1.3		0.81	6.7
SEPT8				6				24
SEPT10				5				16
SEPT6				5				26
β -II spectrin			1	4			0.8	2.8

List of proteins purified from WT cerebellar lysate with CDC42EP4-immunoaffinity column and identified LC-MS/MS analysis (rightmost columns). The numbers denote the count of peptides assigned to each protein (left) and the sequence coverage (right). The blank columns are zero. The specificity of the counts is corroborated by few false-positive counts in the controls (three left columns, that is, KO lysate captured with nonimmune IgG or anti-CDC42EP4 antibody, and WT lysate captured with nonimmune IgG). Another co-IP method used for the immunoblot analyses detected GLAST (peptide number = 2, sequence coverage = 6.45), but not CDC42. Co-IP, Co-immunoprecipitation; KO, knockout; WT, wild type.

scarcely labelled. The distribution and density of immunogold particles were comparable between WT and KO mice (Fig. 5d). Intriguingly, however, the distance from perisynaptic GLAST signals to the nearest PSD edge (arrowheads, Fig. 5c) was significantly longer in KO mice than that in WT mice (Fig. 5e). Together, the biochemical and fine morphometric data consistently indicate that CDC42EP4 in Bergmann glia is required for GLAST to interact with septins and to localize along perisynaptic membrane domains enwrapping PF-PC synapses.

Cdc42ep4^{-/-} mice exhibit insufficient glutamate clearance.

To explore whether the anomalies of GLAST (that is, dissociation from septins and delocalization from synapses) in *Cdc42ep4*^{-/-} mice affect glutamatergic neurotransmissions, we assessed electrophysiological properties of the major glutamatergic synapses in cerebellar slices. We first examined the CF-PC synapse by stimulating CFs in the granule cell layer and recording the evoked excitatory postsynaptic currents (EPSCs) with a whole-cell voltage clamp configuration (Fig. 6a). Most PCs in 7-week-old WT ($n = 16/18$, 89%) and KO ($n = 17/21$, 81%) mice elicited a single large EPSC in an all-or-none manner as stimulus intensity gradually increased (Fig. 6a, left). The number of steps, which reflects the number of CFs innervating a given PC^{17,18}, was comparable between WT and KO mice (Fig. 6a, right), indicating that CDC42EP4 is dispensable for the postnatal establishment of CF-PC monoinnervation. The major parameters of CF-EPSC kinetics (that is, amplitude, 10–90% rise time and decay time constant) were also comparable (Supplementary Table 1). These data indicate that properties of the CF-mediated synaptic transmission are normal in young adult KO mice.

Given the major role for GLAST in glutamate clearance from extracellular space around PF-PC synapses⁵, the delocalization of GLAST away from PSD (Fig. 5e) might affect PF-EPSC kinetics in KO mice. To test this, we measured the decay time constant of PF-EPSC, which is known to protract as glutamate reuptake delays^{19–22}. The PF-EPSCs elicited by the stimulation in the molecular layer of KO mice showed normal paired-pulse facilitation (Fig. 6b and Supplementary Table 1), indicating that the presynaptic functions were largely unaffected. As previous studies showed that desensitization of the AMPA receptors (AMPA receptors) masks the effects of GLAST insufficiency on PF-PC synapses²⁰, we also employed cyclothiazide (CTZ) to block

desensitization of AMPARs. While bath application of CTZ prolonged the decay time constant of PF-EPSCs in both genotypes, it was significantly longer in KO than in WT ($P = 0.010$, Fig. 6c). These data suggest a recognizable delay in the glutamate clearance from PF-PC synapses in KO mice.

To corroborate the above findings, we compared glutamate transients in PF-PC synapses using a low-affinity competitive inhibitor of the AMPARs, γ -D-glutamylglycine (γ DGG). γ DGG is a rapidly unbinding competitive antagonist that is readily displaced from AMPARs by released glutamate²³. Therefore, the degree of inhibition of the EPSC roughly reflects the relative size and kinetics of the glutamate transient in the synaptic cleft. Bath application of 1 mM γ DGG inhibited the PF-EPSC amplitude to $\sim 50\%$ of the basal level in WT, while only to $\sim 80\%$ in KO, suggesting that the size of glutamate transient at PF-PC synapses was significantly higher in KO than in WT (WT versus KO, $51.5 \pm 2.2/79.1 \pm 4.2\%$, $n = 7$, $P < 0.001$, Fig. 6d).

The above findings, in conjunction with the molecular-level anomalies, suggest that PF-PC synapses in KO mice have hotspots around active zones with subnormal glutamate-buffering capacity. Since the density of AMPARs is the highest in postsynaptic active zones, we hypothesized that KO mice are sensitive to subthreshold doses of glutamate clearance inhibitors. To test this, we applied 50 μ M DL-TBOA, which nonselectively inhibits glutamate transporters (EAAT1–5) but only partially as the half-maximal inhibitory concentration for EAAT1/GLAST is 70 μ M. The treatment with the low-dose DL-TBOA in addition to CTZ elicited a significantly larger baseline inward current in KO PCs (WT versus KO, $310 \pm 26/864 \pm 185$ pA, $n = 11/12$, $P < 0.001$, Fig. 6e, trace 3). The aberrant baseline inward current of KO mice was abolished by additional application of an AMPAR antagonist, NBQX (from 895 ± 260 to 367 ± 84 pA, $n = 7$, $P = 0.016$, Fig. 6e, trace 4). Thus, the large baseline inward current in KO PCs is generated by AMPARs exposed to excessive external glutamate. A previous study showed that 200 μ M DL-TBOA augmented AMPAR-mediated inward current of PCs in WT mice¹⁹, while KO PCs were sensitive enough to react to 50 μ M DL-TBOA. These results further support the compromised glutamate-buffering/clearance in KO mice, which may be due to the delocalization of GLAST from PF-PC synapse active zones (Fig. 5e), and/or their dissociation from the perisynaptic clusters of septins and CDC42EP4 (Fig. 5a).

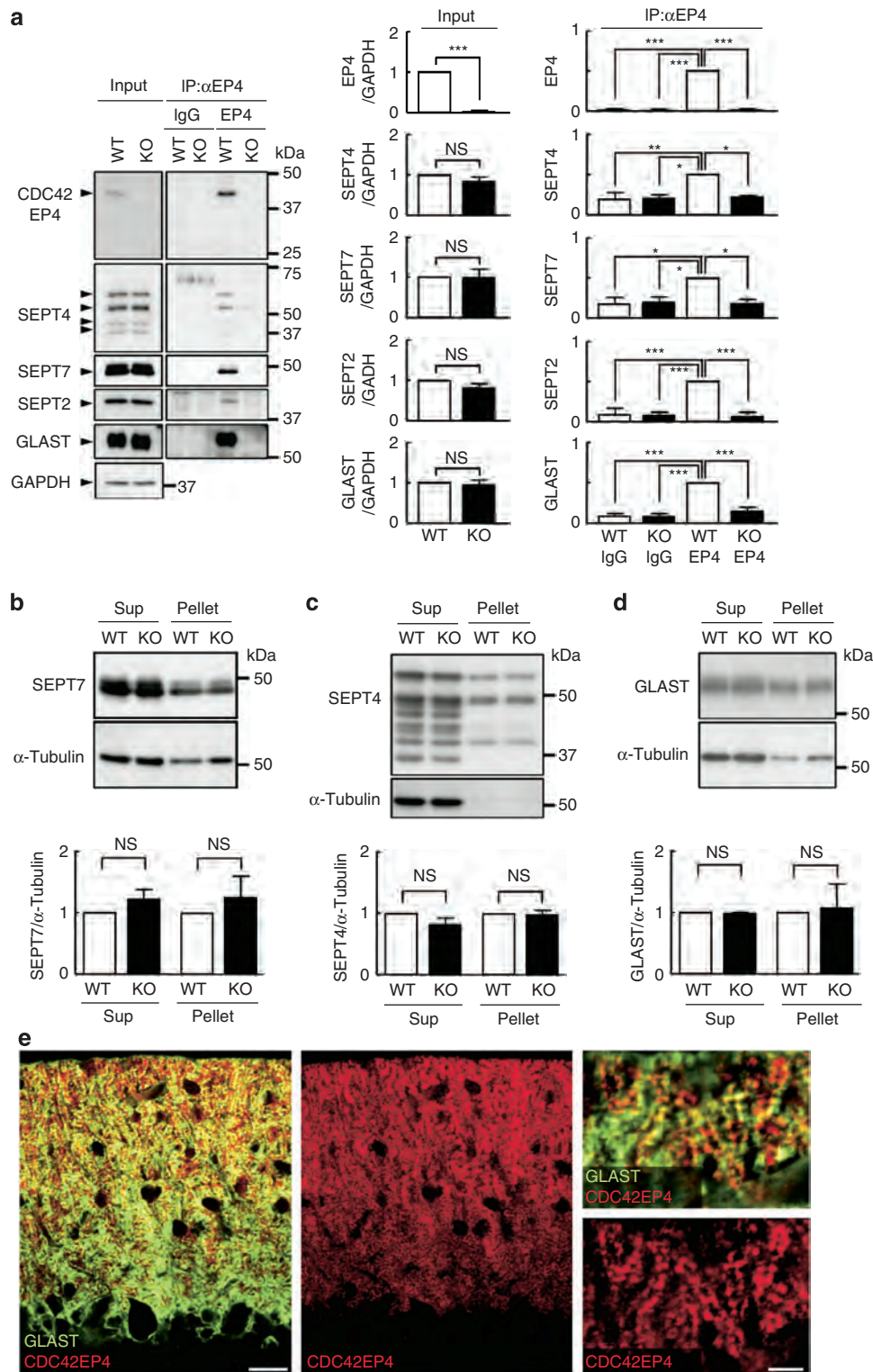


Figure 4 | Biochemical analysis of binding partners of CDC42EP4 in *Cdc42ep4^{fl/fl}* and *Cdc42ep4^{-/-}* cerebella. (a) Co-IP/IB assay of CDC42EP4 with representative septin subunits and GLAST from WT and KO cerebellar lysates. (Input) IB for SEPT4, SEPT7, SEPT2 and GLAST, respectively, detected a quadruplet of 54, 52, 48 and 44 kDa, a doublet of 51 and 48 kDa, a single 42 kDa band and a broad 55 kDa band in the cerebellar lysate. (IP) Anti-CDC42EP4 antibody pulled down SEPT4, SEPT7, SEPT2 and GLAST only from WT cerebellar lysate. The graphs show densitometric quantification of the yield ($n=3$, $*P<0.001$, $**P<0.01$, $*P<0.05$, NS, $P>0.05$ by one-way ANOVA with *post hoc* Tukey test). (Note: the extraction condition including the lysis buffer composition was optimized to detect GLAST, which was distinct from the one used mainly for the proteomic analysis (Table 1). See Methods.) (b-d) Pellet/supernatant assay results on the quantity and extractability of SEPT7, SEPT4 and GLAST in WT and KO cerebella. There was no significant difference in their amount and partitioning by genotype ($n=3$, NS, $P>0.05$ by *t*-test). The same membranes were reprobbed for α -tubulin as a loading control, which was used for normalization. (e) Double-label IF for GLAST (green) and CDC42EP4 (red) in WT cerebellar cortex showing their partial co-localization in Bergmann glial processes. Scale bars, 20 and 5 μ m.**

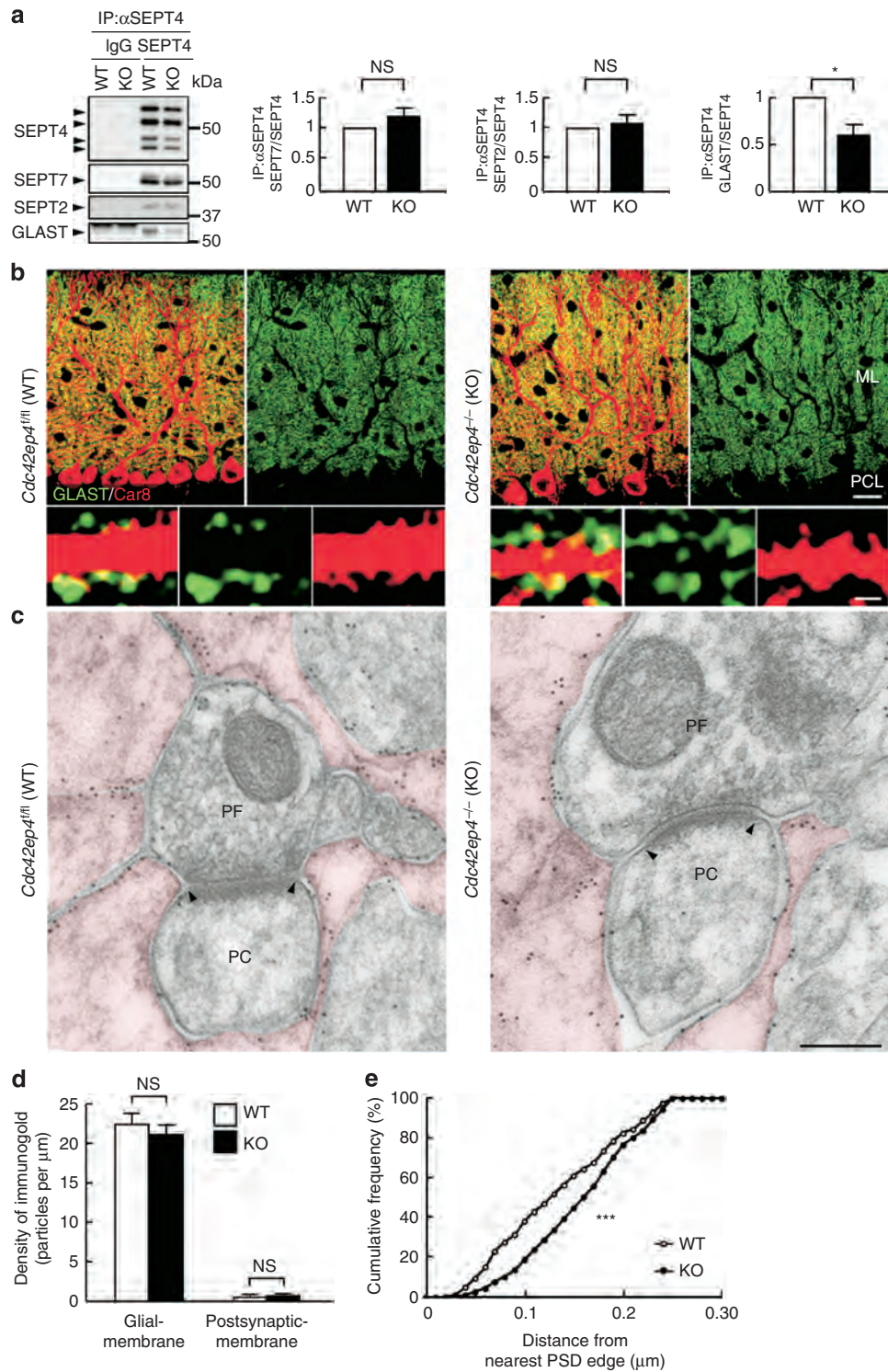


Figure 5 | Loss of CDC42EP4 dissociates the GLAST-septin interaction and delocalizes GLAST away from synapses. (a) Quantitative co-IP/IB assay between SEPT4 and SEPT7, SEPT2 or GLAST in WT and KO cerebellar lysates. While the interaction among the septin subunits did not differ, the relative amount of GLAST pulled down with SEPT4 from KO lysate was significantly less than that from WT ($n = 3$, $*P < 0.05$, NS, $P > 0.05$ by t -test), indicating that septin-GLAST interaction depends on CDC42EP4. See Fig. 4a-d for the comparable amount and solubility of these proteins in WT and KO cerebella. (b) Double-label IF for GLAST (green) and a Purkinje cell marker Car8 (red) in WT and KO cerebellar cortices. Genetic loss of CDC42EP4 caused no recognizable difference in the distribution of GLAST up to the resolution. Scale bars, 20 and 1 μ m. (c) Immunoelectron microscopy images for GLAST in WT and KO molecular layers. PF, parallel fibre terminal or bouton. PC, dendritic spine of Purkinje cell. Bergmann glial processes are tinted. The pattern of GLAST distribution appears comparable to that of a previous study⁴. Scale bar, 200 nm. (d) Quantitative analysis of immunoelectron microscopy data. Bergmann glia selectivity and labelling density of GLAST were comparable between WT and KO mice: Bergmann glia; 22.4 \pm 1.3/21.1 \pm 1.2 particles per μ m ($n = 519/467$ particles from two littermate pairs, NS, $P > 0.05$ by Mann-Whitney U -test). Postsynaptic membrane; 0.50 \pm 0.21/0.68 \pm 0.24 particles per μ m ($n = 5/8$ particles, $P = 0.68$ by Mann-Whitney U -test; cf. Figs 4d and 5a-c). (e) Cumulative histogram of the distance of GLAST measured from the nearest PSD edge (for example, arrowheads in c). A significant right shift of the curve for KO mice demonstrates delocalization of GLAST away from PSDs of PF-PC synapses (median, WT = 0.27 μ m, KO = 0.31 μ m from the nearest edge of PSD; $n = 22/19$ synapses from two littermates for each genotype, $***P < 0.001$ by Kolmogorov-Smirnov test).

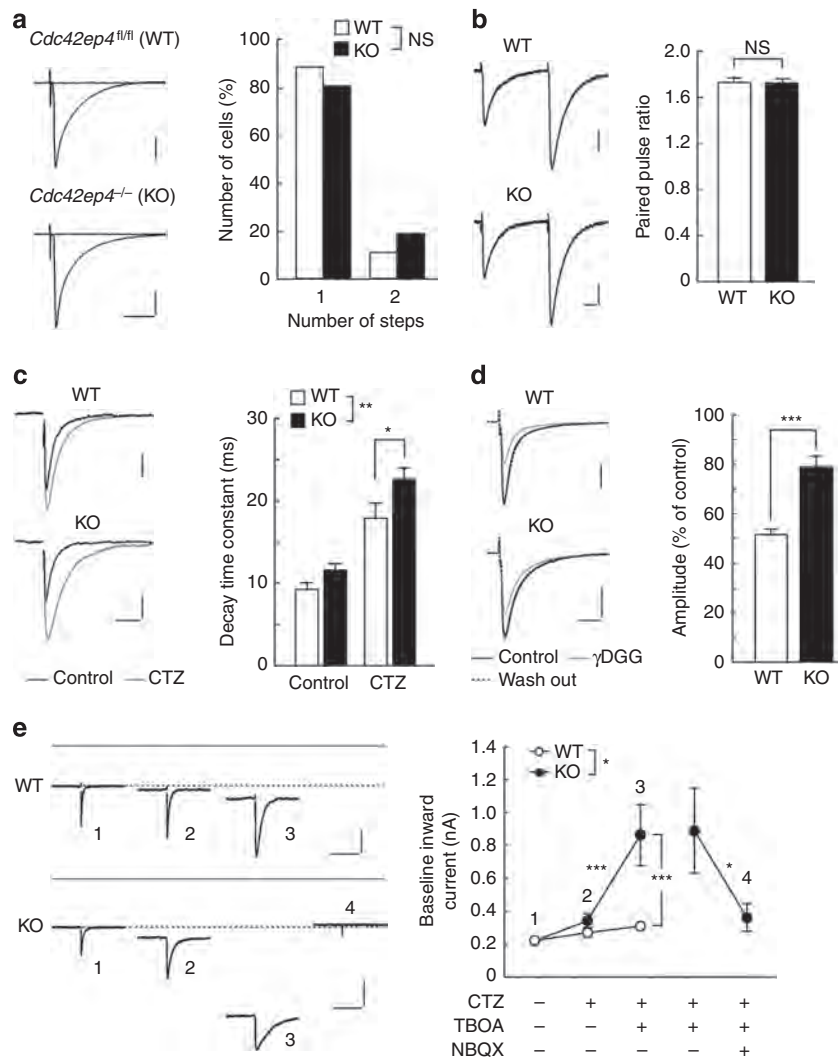


Figure 6 | *Cdc42ep4^{-/-}* mice exhibit insufficient glutamate-buffering/clearance capacity. (a; Left) Sample traces of CF-EPSCs. Two to three traces were superimposed. Scale bars, 10 ms and 500 pA. (Right) Summary histogram showing the number of CF-EPSC steps ($n = 21/18$, $P = 0.513$ by Mann-Whitney U -test). Holding potential was -10 mV in **a** and -70 mV in **b-e**. (b; Left) PF-EPSCs in response to paired stimuli at 50 ms intervals. Scale bars, 10 ms and 100 pA. (Right) Summary graph of the paired-pulse ratio ($n = 22/19$, $P = 0.824$ by Mann-Whitney U -test). (c; Left) Sample traces of PF-EPSCs with (grey) or without (black) 100 μ M CTZ in a WT and a KO mice. Scale bars, 25 ms and 50 pA. (Right) The decay time constant of PF-EPSCs. Although CTZ prolonged the decay time constant both in WT and KO ($n = 11/17$, WT, from 9.3 ± 0.8 to 17.9 ± 1.8 ms, $***P < 0.001$; KO, from 11.6 ± 0.8 to 22.6 ± 1.3 ms; $***P < 0.001$), the effect was significantly larger in KO than in WT ($**P = 0.006$ by two-way ANOVA with *post hoc* Tukey test), which resulted in more protracted postsynaptic response in KO PCs ($*P = 0.010$). (d; Left) PF-EPSCs before (black), in the presence of 1 mM γ DGG (grey), and after washout (dashed). Scale bars, 10 ms and 200 pA. (Right) Summary histogram showing the effects of γ DGG. KO PF-EPSCs were significantly more insensitive to γ DGG than WT ones ($n = 7/7$, $***P < 0.001$ by Mann-Whitney U -test). (e; Left) Sample traces of PF-EPSCs in a WT and a KO mice in control ACSF (1), in the presence of CTZ (2), CTZ plus 50 μ M TBOA (3), CTZ, TBOA plus 10 μ M NBQX (4). Grey and dashed lines, respectively, indicate the zero offset level and baseline holding current level in the control ACSF. Scale bars, 200 ms and 100 pA. (Right) The summary graph showing the holding current. The effects of CTZ plus TBOA was significantly larger on KO than on WT ($n = 11/12$, $***P < 0.001$ by two-way repeated measures ANOVA with *post hoc* Tukey test). (Two right plots) Additional application of NBQX significantly diminished the inward current by TBOA ($n = 7$, $*P = 0.016$ by Wilcoxon signed-rank test).

In addition, the content of glutamate, glutamine and related amino acids and monoamines in cerebellar tissues from WT and KO mice was comparable, as assessed using high-performance liquid chromatography (Table 2). Thus, the total amount of the glutamate/glutamine shuttle components, and other major neurotransmitters and metabolites, are unaffected by the loss of CDC42EP4.

Impaired motor coordination/learning in *Cdc42ep4^{-/-}* mice.

As a means of unbiased screening for neural dysfunctions, a cohort of WT and KO littermates were subjected to a systematic

battery of behavioural tests. In 14 behavioural test paradigms including the rotating rod (rota-rod) test, WT and KO mice performed almost comparably (Table 3 and Supplementary Figs 1–12). Given the robust compensatory potential of the motor control circuitry, and the molecular and electrophysiological endophenotype of KO mice, we assessed their motor coordination and motor learning with the balance beam test, which is superior to the rota-rod test in detection sensitivity²⁴. While the moving speed of 12-week-old KO mice on the initial trial (the intercept) was normal, the slopes of their learning curves were significantly flatter than those of WT mice

Table 2 | The bulk content of representative neurotransmitters and metabolites in the cerebella of *Cdc42ep4^{fl/fl}* and *Cdc42ep4^{-/-}* littermate mice.

Neurotransmitters and metabolites (per mg tissue)		
	WT	KO
Glu (nmol)	8.07 ± 0.521	7.97 ± 0.253
Gln (nmol)	5.54 ± 0.459	5.25 ± 0.128
Gly (nmol)	0.66 ± 0.065	0.81 ± 0.13
GABA (nmol)	1.43 ± 0.102	1.48 ± 0.133
L-Ser (nmol)	0.40 ± 0.028	0.40 ± 0.028
D-Ser (nmol)	0.003 ± 0.0001	0.003 ± 0.0000
5-HT (ng)	0.16 ± 0.021	0.16 ± 0.013
5-HIAA (ng)	0.09 ± 0.01	0.11 ± 0.007
NE (ng)	0.35 ± 0.037	0.39 ± 0.013
MHPG (ng)	0.12 ± 0.062	0.07 ± 0.0006
HVA (ng)	0.005 ± 0.003	0.008 ± 0.002
DA (ng)	0.004 ± 0.001	0.005 ± 0.003
DOPAC (ng)	0.006 ± 0.002	0.008 ± 0.004

The amount of glutamate, glutamine and other substances extracted from WT and KO cerebellar tissues ($n = 3, 3$). There was no significant difference. KO, knockout; WT, wild type.

($n = 13/13$, $P = 0.0003$ and 0.0004 , respectively, for the beam diameters of 28 and 11 mm; Fig. 7a). In a follow-up of the same cohort at 24 weeks of age, the learning curve of KO mice was consistently lower than that of WT mice ($n = 12/12$, $P = 0.018$ and 0.014 ; Fig. 7a).

To test whether the persistent underperformance is caused by the insufficient glutamate-buffering/clearance capacity in Bergmann glia, and not by the loss of extracerebellar astrocytic CDC42EP4 (Fig. 2e), we attempted the partial inhibition of EAATs with DL-TBOA. Direct subpial injection of 100 μ M DL-TBOA with CTZ above lobule VI of the cerebellar cortex did not affect the motor performance of WT mice, whereas the pharmacological decompensation elicited significant and transient motor incoordination in KO mice, as was obvious now in the rota-rod test ($n = 5/4$, $P = 0.0011$, Fig. 7b). The remarkable hypersensitivity to the subthreshold DL-TBOA recapitulated *in vivo* has corroborated the insufficient glutamate-buffering/clearance capacity in KO mice.

Discussion

Previous studies indicated that CDC42EPs bind to small GTPases (CDC42, RhoQ/Tc10) and septins in a mutually exclusive manner^{13,14}, and that interaction of CDC42EP1/BORG5 with CDC42 and atypical protein kinase C is required for cell motility in early mouse embryo²⁵. A recent study revealed defective angiogenesis in *Cdc42ep1^{-/-}* mice, which is due partly to septin/actomyosin dysregulation that affects migration of vascular endothelial cells²⁶. In contrast, CDC42EP4 in Bergmann glia is mainly in complex with septins and GLAST, and is dispensable for developmental cell migration and post-developmental morphological integrity. The distinct binding partners and physiological roles of CDC42EPs may reflect their distinct primary structure and/or expression pattern. Since *Cdc42ep1* mRNA is also expressed in Bergmann glia (Allen Mouse Brain Atlas #68342384), *Cdc42ep1^{-/-}* mice and *Cdc42ep1^{-/-}*; *Cdc42ep4^{-/-}* double-mutant mice would exhibit intriguing cerebellar phenotypes.

Genetic loss of a vital septin subunit (that is, SEPT7, SEPT9 or SEPT11) causes embryonic lethality²⁷⁻²⁹, whereas obvious brain anomaly or motor incoordination has never been reported in mice that lack one or two other septin subunits (that is, SEPT3, SEPT4, SEPT5, SEPT6, SEPT3 and SEPT5, or SEPT4 and SEPT6),

despite their abundance in the cerebellum and other brain regions³⁰⁻³⁴. In contrast, *GLAST^{-/-}* mice exhibit protracted glutamate transient, multiple CF-PC innervations and failure in the rota-rod test^{6,21}.

The present study demonstrated that *Cdc42ep4^{-/-}* mice develop CF-PC innervations with largely normal wiring pattern and electrophysiological properties (Figs 3a and 6a), and pass the rotating rod (rota-rod) test (Table 3). However, pharmacological decompensation with inhibitors of AMPAR, AMPAR desensitization or EAATs consistently indicated their insufficient glutamate-buffering/clearance capacity in electrophysiological analyses (Fig. 6c-e), and caused failure in the rota-rod test (Fig. 7b). Thus, the severity of cerebellar phenotypes is ranked *GLAST^{-/-}* > *Cdc42ep4^{-/-}* > septin-null mice, which would justify an interpretation of the phenotype of *Cdc42ep4^{-/-}* mice as a mild insufficiency of GLAST function, rather than as a partial loss of septin function. Since *Sept4^{-/-}* mice and Bergmann glia-selective *Sept7^{-/-}* mice exhibit subnormal motor coordination only in infancy (Kinoshita, Ageta-Ishihara *et al.*, unpublished), the pharmacological decompensation technique may help differentiate these and other septin mutant mice from WT littermates.

Glutamate released from PF boutons/terminals not only depolarizes PCs via AMPARs; however, the spillover fraction evokes Ca^{2+} responses in the perisynaptic compartments ('microdomains') of lamellar Bergmann glial processes mainly via mGluR1 (refs 35,36). A subdomain in such a compartment tightly wraps a PF-PC synapse, where GLAST outnumbers other EAATs^{4,37}. While EAAT4 is localized to PC spines for slow glutamate clearance²⁰, GLAST is concentrated along perisynaptic processes of Bergmann glia and contributes to the fast and efficient limitation/termination of glutamate neurotransmission and spillover^{1,5,20}. However, the molecular basis to target and concentrate GLAST to the proximity of synaptic gap remains unclear.

Physical and functional interactions of the cytoplasmic tail of GLAST with submembranous septins have been consistently demonstrated *in vitro*, in tissue culture cell cortex and Bergmann glial processes^{11,12}. The interaction with submembranous septins has been hypothesized to provide membrane-bound GLAST trimers with scaffolds, limit their lateral diffusion and/or augment their transport activity, which collectively contribute to perisynaptic concentration of glutamate clearance activity. However, the hypothesis has never been tested *in vivo* partly because of the aforementioned redundancy problem in septin reverse genetics.

This study demonstrated that CDC42EP4 clusters beneath Bergmann glial membrane subdomains wrapping dendritic spines where septins and GLAST abound^{4,11,16}. In the absence of CDC42EP4, GLAST is dissociated from septins (Fig. 5a) and delocalized away from synapses (Fig. 5e). These findings support the above hypothesis of septins as scaffold/barrier for GLAST, and may further implicate subtle alterations in tripartite synapse geometry, for example, retraction of glial components from synaptic clefts, with or without secondary remodelling of neuronal components.

The distribution of GLAST visualized with IF and immunoelectron microscopy appears more diffuse along Bergmann glial membranes than that of CDC42EP4 (Figs 1f, 4e and 5c), which corresponds to the IP/IB data that only a subset of GLAST is pulled down with CDC42EP4 and/or septins. These data suggest other membrane-proximal proteins that contribute to perisynaptic localization of GLAST. One such candidate is NHERF1 (Na⁺/H⁺-exchange regulatory factor-1) whose PDZ domain interacts with the cytoplasmic tail of GLAST^{12,38}. So far, however, neither GLAST-related phenotype for *Nherf1^{-/-}* mice³⁹ nor

Table 3 | Systematic behavioural test results of *Cdc42ep4^{fl/fl}* and *Cdc42ep4^{-/-}* littermate mice.

Tests	Mental/physical activities	Indices measured (inexhaustive)	Alteration from wild-type <i>Cdc42ep4^{-/-}</i>	Related figures*
General health and neurological screening	General health	Body weight	→	1
		Rectal temperature	→	
		Grip strength	→	
		Hanging persistence	→	
Light/dark transition test	Exploratory activity	Distance travelled in the light chamber	→	2
		Light avoidance	Distance travelled in the dark chamber	
	Latency to the first entry to the light chamber		→	
	Time stayed in the light chamber		→	
	Number of transitions between chambers		→	
	Open field test	Exploratory activity Avoidance from open space Anxiety-like behaviour	Distance travelled	
Centre time			→	
Vertical activity			→	
Stereotypical movements			→	
Elevated plus maze test	Exploratory activity Height avoidance	Distance travelled	→	4
		Entries into open arms	→	
		Number of entries	→	
		Time stayed on open arms	→	
Acoustic startle response	Startle reflex to loudness	Amplitude of body motion	→	5a
		Decrement of startle amplitude	→	
Prepulse inhibition (PPI) test	Sensorimotor gating	Latency to immobility	→	5b
Porsolt forced swim test	Despair-like behaviour	Activity level (distance travelled)	→	6
Home cage monitoring	Diurnal cycle of locomotor activity	Mean number of particles	→	7
		Distance travelled	→	
Social interaction test (one-chamber, stranger pair)	Social behaviour Social behaviour, anxiety-like behaviour	Number of contacts	→	8
		Total duration of active contacts	→	
		Mean contact duration	→	
		Total duration of contacts	→	
		Time spent with novel stranger	→	
		Distance travelled	→	
Social interaction test (three chambers, one to two caged strangers)	Social behaviour, anxiety-like behaviour	Time spent with novel stranger	→	9
		Distance travelled	→	
Rota-rod test	Motor coordination/learning	Latency to fall	→ (↓ with CTZ + TBOA)	Fig. 7b, 10
Tail suspension test	Behavioural despair	Latency to immobility	→	11
Barnes maze test	Spatial memory	Time spent around target hole	→	12
Balance beam test	Motor coordination/learning	Moving speed	↓	Fig. 7a

Comparative table of the results of systematic behavioural tests with WT and KO littermate mice (C57BL/6, male, $n = 13\text{-}8/13\text{-}9$ (the dropouts are due to failed data acquisition or spontaneous deaths)). Symbols (KO phenotype relative to WT): →, no significant difference; ↑/↓, statistically significant increase/decrease ($P < 0.05$). *See Figs. 7a,b and Supplementary Figs 1-12 for details.

expression and localization NHERF1 in Bergmann glia has been reported. Thus, the unique phenotype of *Cdc42ep4^{-/-}* mice provides the first *in vivo* evidence for the significance of perisynaptic concentration of GLAST by submembranous scaffold and/or diffusion barrier.

GLAST abounds near PF-PC synapses and the buffering/clearance capacity far surpasses the level of glutamate release, which confers remarkable tolerance to EAAT inhibitors. Our electrophysiological analysis with pharmacological interventions revealed insufficient glutamate-buffering/clearance capacity in *Cdc42ep4^{-/-}* PF-PC synapses. The decay time constant of EPSC, which reflects the retention of extracellular glutamate, was mildly protracted on inhibition of AMPAR desensitization with CTZ (Fig. 6c). Additional inhibition of EAATs with subthreshold DL-TBOA significantly augmented AMPAR-mediated inward current only in the *Cdc42ep4^{-/-}* cerebellum (Fig. 6d,e). Further, a low-affinity glutamate analogue γ DGG was less effective in the inhibition of EPSC (Fig. 6d). These data concordantly indicate

higher extracellular glutamate level in the mutant. Given the properties of EAATs and their distribution around glutamatergic synapses to PCs^{5,20,37}, and unaltered expression of the major AMPAR subunits in the *Cdc42ep4^{-/-}* cerebellum (Fig. 3d), the phenotype is attributed principally, if not all, to the insufficiency of GLAST function. As the total amounts of glutamate and GLAST are unaltered in the *Cdc42ep4^{-/-}* cerebellum, the delocalization of GLAST from perisynaptic glial processes (Fig. 5e), with or without altered transporter activity due to the dissociation from CDC42EP/septins, appears to be the major cause of the glutamate intolerance.

Overall, the unique phenotype of *Cdc42ep4^{-/-}* mice provided the first *in vivo* evidence for submembranous molecular network that is required for the perisynaptic concentration and efficiency of GLAST. This study illuminated the spatial regulation of GLAST by the CDC42EP4/septin-based scaffold beneath perisynaptic glial membranes, which ensures optimal buffering/clearance of extracellular glutamate from around synapses. Since CDC42EPs

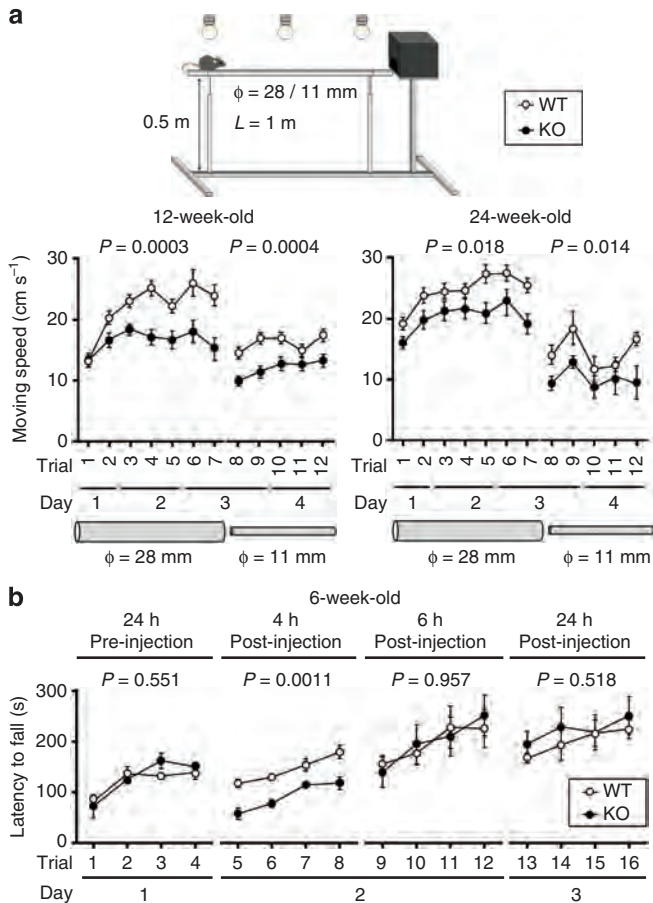


Figure 7 | Motor coordination and motor learning defects in *Cdc42ep4*^{-/-} mice. (a) (Top) Set-up for the balance beam test. The height (0.5 m above the floor) and illumination (100 lux) motivate mice to escape by traversing along a horizontal rod (1 m \times 28 or 11 mm) into a dark box. (Bottom) The learning curves of a cohort of WT and KO mice measured at 3 and 6 months of age. The moving speeds are plotted for seven trials with a 28-mm rod and subsequent five trials with an 11-mm rod over 4 days. The motor coordination defects in KO mice remained uncompensated up to 6 months of age ($n = 13/13$ and $12/12$, $P = 0.0003$, 0.0004 , 0.018 , 0.014 by two-way repeated measures ANOVA). (b) The learning curves of 6-week-old WT and KO littermate mice assessed by the rota-rod test before and after direct cerebellar cortical injection of CTZ plus DL-TBOA (100 μM each per 10 μl). The local inhibition of EAATs with the subthreshold dose of DL-TBOA elicited a significant motor coordination defects transiently (around 4 h post-injection) and only in KO mice ($n = 5/4$, $P = 0.551$, 0.0011 , 0.957 , 0.518 by two-way repeated measures ANOVA). The aberrant hypersensitivity of KO mice indicates their glutamate clearance deficit that is adaptively compensated.

and septins, as with GLAST, are implicated in human neurological and psychiatric disorders including schizophrenia by unbiased proteomic and genome-wide association studies^{8,9,40–43}, whether relevant mechanisms underlie the pathophysiology in other brain regions is to be tested in future studies.

Methods

Animal experiments. Animal experiments had been approved by the institutional review committees and conducted in accordance with the regulations for the care and use of animals at Nagoya University, Niigata University, Hokkaido University, Hiroshima University, Fujita Health University and Gunma University. We consistently compared male littermates raised in the same cages unless otherwise noted.

Antibodies. We raised rabbit polyclonal antibodies against seven antigens and consistently used one (#2) against a recombinant polypeptide Arg⁵⁸-Met¹⁰⁰ from

CDC42EP4 that gave the best signal/noise ratio in IB and IF analyses. The specificity was warranted by the absence of the signals in *Cdc42ep4*^{-/-} tissues (Fig. 2d,e). We used antibodies for septins, SEPT2 (1:2,000), SEPT4 (1:3,000) and SEPT7 (1:4,000) as previously described^{33,44}, GLAST⁴⁵, 3-phosphoglycerate dehydrogenase (Phgdh)⁴⁶, calbindin⁴⁷, carbonic anhydrase 8 (Car8)⁴⁸, VGLUT1, 2 (ref. 49) and commercial antibodies for GluR1, 2 (Alomone Labs, AGC-004, 1:200, AGC-005, 1:150), GLAST (Frontier Institute, Rb-Af660, 1:2,000), PSD-95 (Cell Signaling, 3450, 1:1,000), CDC42 (Santa Cruz, L0809, 1:100), β -actin (Sigma, A5441, 1:5,000) and α -Tubulin (Sigma, T9026, 1:10,000). For secondary antibodies, we used Alexa 488-, Cy3- or horseradish peroxidase-conjugated IgGs from rabbit, goat or guinea pig (Jackson ImmunoResearch, 706-545-148, 711-165-152, 111-035-003) diluted at 1:200–1,000. Histidine-tagged recombinant CDC42 (Cytoskeleton) was used to quantify endogenous CDC42.

Biochemical fractionation and IB analysis. Each tissue was dissected, weighed and homogenized by sonication in 3 ml g^{-1} of buffer A (10 mM Tris-HCl at pH 7.6, 0.15 M NaCl, 1% Triton X-100, protease inhibitors). The supernatant after centrifugation at 20,400g at 4 $^{\circ}\text{C}$ for 0.5 h was labelled as soluble fraction. The pellet was dissolved with sonication in 1 ml g^{-1} buffer B (3% SDS, 5% 2-mercaptoethanol), which was termed pellet fraction. The samples were resolved by 10%PAGE (SDS-PAGE), transferred to reinforced nitrocellulose or PVDF membranes and subjected to IB analysis using a blocking buffer containing 5% skim milk in TBST (0.1 M Tris-HCl at pH 7.4, 0.15 M NaCl, 0.05% Tween 20). Chemiluminescence detection and densitometry were performed with horseradish peroxidase-conjugated secondary antibodies, ECL-Plus reagent (PerkinElmer), TrueBlot (Rockland) and an image analyser LAS-3000mini with MultiGauge software (Fuji). Uncropped version of each image is shown in Supplementary Fig. 15.

Immunoprecipitation. For IP/IB experiments, whole cerebella were lysed with buffer A' (0.2 M Tris-HCl at pH 7.35, 0.3 M NaCl, 0.2% SDS, 0.2% Triton X-100, 0.2% sodium deoxycholate, 20 mM 2-mercaptoethanol and protease inhibitors), centrifuged and the supernatant was mixed with protein A Sepharose CL-4B (GE Healthcare) or Affi-Prep Protein A Support (Bio-Rad) that had been pre-incubated with anti-CDC42EP4, anti-SEPT4 or nonimmune rabbit IgG (as a negative control). After washing the beads with the same buffer, bound proteins were lysed for IB. For IP/MS experiments, we used buffer C (20 mM Tris-HCl at pH 8.0, 0.15 M NaCl, 1 mM EDTA, 1% NP-40 and protease inhibitors) with more stringent wash condition⁵⁰.

Mass spectrometry and peptide mass fingerprinting. After IP, bead-bound proteins were eluted with solution (7 M guanidine, 50 mM Tris-HCl at pH 8.0), reduced with 5 mM dithiothreitol for 0.5 h, alkylated with 10 mM iodoacetamide for 1 h in the dark, demineralized and concentrated by methanol/chloroform precipitation and digested (0.5 μg trypsin in 1.2 M urea and 50 mM Tris-HCl at pH 8.5).

Mass spectrometric analysis (LC-MS/MS) was carried out as previously described⁵⁰. Briefly, we used an LTQ Orbitrap XL mass spectrometer (Thermo Scientific) connected to an HTC-PAL autosampler and a Paradigm MS4 HPLC with a C18 reversed-phase column and ADVANCE Plug and Play Nano Source (Michrom Bioresources). The reversed-phase chromatography condition was a linear gradient (0 min, 5% B; 70 min, 100% B) of solvent A (2% CH_3CN with 0.1% trifluoroacetic acid (TFA)) and solvent B (98% CH_3CN with 0.1% TFA) at a flow rate of 500 nl min^{-1} . The mass spectrometer was operated in the data-dependent MS2 mode. Peak lists were generated and calibrated by using the Mascot software (Matrix Science), and validation of the MS/MS-based peptide and protein identifications was made with the Scaffold programme (ver. 3, Proteome Software). The peptide probability by Mascot was used for the Scaffold Local FDR algorithm. Peptide identification was approved by the presence of at least two peptides that exceeded the probability of 95%. Proteins that contained similar peptides and could not be differentiated by MS/MS data alone were grouped to satisfy the principle of parsimony.

Measurement of neurotransmitters and metabolites. We used previously described methods for the extraction and measurement of amino acids, amines and metabolites^{51–54}. Briefly, cerebellar hemispheres dissected on ice were frozen in liquid N_2 and stored at -80 $^{\circ}\text{C}$ until extraction. For measurement of amino acids, each sample was weighed, homogenized in 1.5 ml CH_3OH on ice, centrifuged at 3,000g for 6 min at 4 $^{\circ}\text{C}$ and 20 μl of the supernatant was dried by evaporation at 40 $^{\circ}\text{C}$. The residue was dissolved with 20 μl water, 20 μl 0.1 M borate buffer at pH 8.0 and 60 μl 50 mM 4-fluoro-7-nitro-2,1,3-benzoxadiazole (NBD-F; Tokyo Kasei Kogyo) in CH_3CN , reacted at 60 $^{\circ}\text{C}$ for 2 min and stopped by adding 100 μl 0.1% TFA and 10% CH_3CN in water. Total D-/L-serine levels were measured using a column-switching HPLC system (SCL-10A VP, Shimadzu)⁵¹. Glutamate, glutamine, glycine and GABA were measured using an HPLC system (LC-20AT, Shimadzu)⁵². Fluorescence emission at 530 nm was measured with an excitation at 470 nm. For monoamines and their metabolites, tissue samples were homogenized in 0.2 M HClO_4 containing 0.1 mM EDTA and 100 $\mu\text{g l}^{-1}$ isoproterenol (internal standard), and centrifuged at 20,000g for 15 min at 4 $^{\circ}\text{C}$. Supernatants were filtered

through 0.45- μm pore membranes (Millex-LH, Millipore). We used a reversed-phase column (SC-50DS) and an electrochemical detector (ECD-300) in an HPLC system (EP-300, DG-300 and EPC-300, all from Eicom) with the mobile phase containing 0.1 M acetate-citric acid buffer at pH 3.5, 16% CH_3OH , 5 mg l^{-1} EDTA and 0.19 g l^{-1} sodium octyl sulfate.

Tissue preparation for histochemistry. Under deep pentobarbital anaesthesia (0.1 mg per g of body weight), mice were fixed transcardially with 4% paraformaldehyde in 0.1 M phosphate buffer (PB) at pH 7.2 for IF and immunoelectron microscopy, or with 4% paraformaldehyde/0.1% glutaraldehyde in PB for TEM. After excision from the skull, brains for immunohistochemistry were immersed in the same fixative for 2 h. In IF for CDC42EP4, fixed brains were sliced at 50 μm with a microslicer (VT1000S, Leica) and subjected to free-floating incubation, while 4- μm -thick paraffin sections with a sliding microtome (SM1000R, Leica) were used for Car8, GLAST, VGluT1 and VGluT2. Brains for FISH were removed under deep pentobarbital anaesthesia and immediately frozen in powdered dry ice, cut at 20 μm with the cryostat and mounted on silane-coated glass slides.

FISH. Mouse cDNA fragments for *Cdc42ep4* (nucleotide 331–1,118, GenBank BC003857), calbindin (37–1,071, BC016421), GLAST (1,620–2,576, BC066154) and Phgdh (1–1,799, BC110673) were subcloned into the pBluescript II plasmid vector. Digoxigenin (DIG)- or fluorescein-labelled cRNA probes were transcribed *in vitro*⁵⁵.

Sections were processed as follows: acetylation with 0.25% acetic anhydride in 0.1 M triethanolamine-HCl at pH 8.0 for 10 min and prehybridization for 1 h in buffer A (50% formamide, 50 mM Tris-HCl at pH 7.5, 0.6 M NaCl, 0.02% Ficoll, 0.02% polyvinylpyrrolidone, 0.02% bovine serum albumin, 200 mg l^{-1} tRNA, 1 mM EDTA and 10% dextran sulfate). Hybridization with cRNA probes was performed in buffer A at 63.5 °C for 12 h, and then sections were washed at 61 °C with 5 \times standard sodium citrate (SSC) for 0.5 h, 4 \times SSC containing 50% formamide for 0.7 h, 2 \times SSC containing 50% formamide for 0.7 h and 0.1 \times SSC for 0.5 h. Sections were incubated successively in NTE buffer (0.5 M NaCl, 0.01 M Tris-HCl at pH 7.5, 5 mM EDTA), 20 mM iodoacetamide in NTE buffer and TNT buffer (0.1 M Tris-HCl at pH 7.5, 0.15 M NaCl), each for 0.3 h at room temperature.

For double-labelling FISH, sections were reacted with peroxidase-conjugated anti-fluorescein antibody (Invitrogen, A21253, 1:1,500) and incubated with the FITC-TSA plus amplification kit (PerkinElmer). After inactivation of residual peroxidase activities with 3% H_2O_2 , the sections were incubated successively with DIG-labelled cRNA probe, the peroxidase-conjugated anti-DIG IgG (Roche, 11 207 733 910, 1:1,000) and the Cy3-TSA plus reagents (PerkinElmer), and then counterstained with TOTO-3 (Invitrogen, T3604, final 0.2 μM) in PBS.

Immunohistochemistry. For immunohistochemistry, 4- μm -thick paraffin sections were incubated with 10% normal donkey serum for 20 min, a mixture of primary antibodies (1 mg l^{-1}) overnight and a mixture of Alexa 488- or Cy3-labelled species-specific secondary antibodies for 2 h at a dilution of 1:200. Fluorescence imaging was conducted using scanning laser confocal microscopes IX81/FV1000 (Olympus) with a $\times 40$ objective lens (numerical aperture (NA) 1.0) and LSM-780 (Zeiss) with $\times 40$ (NA 1.1) and $\times 63$ (NA 1.4) objective lenses, and wide-field microscopes (BZ-9000, Keyence or BX-60, Olympus) with $\times 40$ and $\times 20$ objective lenses (NA 1.3, Nikon or NA 0.7, Olympus).

Electron microscopy. Conventional electron microscopy, pre-embedding silver-enhanced immunoelectron microscopy and postembedding immunogold electron microscopy were conducted as described previously^{56,57}. Briefly, pre-embedding immunoelectron microscopy was conducted by incubation in blocking solution for goat gold conjugates (Aurion, Electron Microscopy Sciences) for 0.5 h, and then with CDC42EP4 antibody (1 mg l^{-1}) diluted with 1% BSA and 0.004% saponin in PBS overnight. Anti-rabbit IgG linked to 1.4 nm gold particles (1:100, Nanogold labelling reagents, Nanoprobes, #2003) were incubated for 2 h, and gold particles were intensified using a silver enhancement kit (R-Gent SE-EM, Aurion). In post-embedding immunogold, 80-nm-thick sections were cut with an ultramicrotome (Ultracut, Leica), incubated overnight with rabbit GLAST antibody (20 mg l^{-1}) and then with colloidal gold (10 nm)-conjugated anti-rabbit or anti-guinea pig IgG (British Biocell, EM.GAR10, 1:100) for 2 h. The samples were mounted on grids and stained with 2% uranyl acetate for 20 min, and observed with a TEM (H-7100, Hitachi).

Electrophysiology. We prepared 250- μm -thick cerebellar slices as described previously^{58,59}. In brief, 5–7-week-old mice deeply anaesthetized with CO_2 were decapitated. The cerebella were quickly cut parasagittally with a microslicer (VT1200S, Leica) in a chilled cutting solution ((in mM) 120 choline-Cl, 3 KCl, 1.25 NaH_2PO_4 , 28 NaHCO_3 , 8 MgCl_2 and 25 glucose), incubated in normal ACSF (artificial cerebrospinal fluid; 125 NaCl, 2.5 KCl, 2 CaCl_2 , 1 MgSO_4 , 1.25 NaH_2PO_4 , 26 NaHCO_3 and 20 glucose, bubbled with 95% O_2 and 5% CO_2) at 36 °C for 0.5 h and then kept at room temperature. All recordings were performed at 32–34 °C. Whole-cell recordings were made from visually identified PCs under an upright microscope (BX51WI, Olympus). Pipette solution contained (55 CsCl, 10 Cs D-gluconate, 20 TEA-Cl, 20 BAPTA, 4 MgCl_2 , 4 ATP, 0.4 GTP, 5 QX314-Cl and

30 HEPES at pH 7.3, adjusted with CsOH). To block inhibitory synaptic transmission, 10 μM bicuculline was consistently supplemented to the normal ACSF. All the drugs were obtained from Tocris Bioscience. Stimulation pipettes ($\sim 5 \mu\text{m}$ tip diameter) filled with the normal ACSF were used to apply square pulses for focal stimulation (duration, 0.1 ms; amplitude, 0–90 V). PFs were stimulated in the molecular layer. CFs were stimulated in the granular layer around the PC soma under investigation. The stimulation was given at 0.2 Hz (Fig. 6a,b) or 0.05 Hz (Fig. 6c–e). The number of CFs innervating the recorded PC was estimated by the number of discrete CF-EPSC steps in response to a gradual rise in the stimulus intensity. The stimulation pipette was systematically moved around each PC soma. Ionic currents were recorded with a patch clamp amplifier (EPC10, HEKA Elektronik). The pipette access resistance was compensated by 70–80%. Online data acquisition and offline data analysis were conducted with software, PATCHMASTER and FITMASTER (HEKA).

Generation of *Cdc42ep4*-floxed and null mice. The targeting strategy is illustrated in Fig. 2a. We constructed the targeting vector using the MultiSite Gateway Three-Fragment Vector Construction kit (Invitrogen) and BAC Subcloning Kit (Gene Bridges) with some modifications. Briefly, a DNA fragment carrying the loxP sequence and *pgk*-promoter-driven neomycin-resistance (Neo) cassette flanked by two F1p recognition target sites was inserted in reverse orientation directly downstream of the sole coding exon of *Cdc42ep4* isolated from a C57BL/6 mouse genomic BAC clone RP23-366j17. The other loxP site was inserted into the intron directly upstream of the coding exon. The resulting targeting vector, which consisted of 5' and 3' homology arms, the floxed coding region with the Neo cassette and diphtheria toxin gene (DT) for negative selection, was linearized and electroporated into the C57BL/6N mouse embryonic stem (ES) cell line, RENKA⁶⁰. Genomic DNA from neomycin/G418-resistant ES cell clones were analysed with Southern blot analysis, and positive clones with proper homologous recombination were microinjected to host embryos as described previously⁶¹. The null allele (*Cdc42ep4*^{-/-}) was created by crossing heterozygous floxed (*Cdc42ep4*^{fl/+}) mice with CAG-Cre transgenic mice⁶². For Southern blot analysis, genomic DNA was digested with Sac I, EcoR V and Hinc II, and hybridized with 5', 3' and neo probes, respectively. The predicted fragment sizes for the WT and floxed alleles for each probe, 13/11.3, 16.4/12.7 and N.A./16.1 (kb), respectively, were confirmed. We thereafter conducted genotyping using PCR with the following primers: (a) 5'-TGCTTCAGTACCTTCGGAC-3', (b) 5'-TTCGAGTTCACAGAGCTGGA-3' and (c) 5'-TCATAGAGAAGGTGGCAGC-3' to distinguish the WT, floxed and null alleles by 490-bp (with primers a + b), 580-bp (a + b) and 480-bp (a + c) products, respectively. After confirming germline transmission and Mendelian inheritance of the *Cdc42ep4*^{fl} and *Cdc42ep4*^{-/-} alleles, the lines have been deposited to RIKEN Bioresource Center (RBRC04894 and RBRC09539, respectively).

Balance beam and rota-rod tests. All systematic behavioural tests were conducted on male littermates (10–38 weeks old) as described previously^{33,63}. In the balance beam test, the motor coordination was quantitatively assessed by the performance on the first trial, the moving speed and the numbers of pauses and slips along a 1-m-long rod (diameter, 28 mm). After six trials on Days 1–3, five trials with a thinner rod (diameter, 11 mm) were conducted on Days 3–4. The increment in the moving speed and decrements in the numbers of pauses and slips were quantified as indices of motor learning. In the rota-rod test, we measured the latency to fall from a rotating rod (diameter, 30 mm) that was accelerated from 4 to 40 r.p.m. over 5 min per trial. For pharmacological experiment (see below), each mouse was subjected to four sessions (four trials per session) at 24 h before injection, and 4, 6 and 24 h after injection.

Direct cerebellar cortical injection. We applied a method established for viral delivery⁶⁴ with minor modifications. Briefly, 6-week-old mice (WT, 4F + 1M; KO, 3F + 1M) anaesthetized with ketamine (100 mg kg^{-1}) and xylazine (16 mg kg^{-1}) were mounted in a stereotaxic frame, and the occipital bone was drilled at 5 mm caudal to the bregma. A blunt-ended Hamilton syringe tip (33 G) attached to a micropump and a controller (UltramicroPump II, Micro4; World Precision Instrument) was placed beneath the pia mater above lobule VI. The mixture of CTZ and DL-threo- β -benzyloxyaspartic acid (DL-TBOA; 100 μM each in 10 μl) was injected at a rate of 333 nl min^{-1} . After suturing the scalp, and recovery from anaesthesia on a warm pad, the mice were returned to home cages.

Systematic behavioural analysis. We applied our standard protocols^{63,65,66} to a cohort of male littermates ($n = 13, 13$) reared in the same cages: behavioural testing was conducted between 9 a.m. and 6 p.m. except for the continuous home cage monitoring. Each apparatus was cleaned with sodium hypochlorite solution to minimize odour after use. We conducted tests in the following order: general health and neurological screening (including body weight and temperature measurements, grip strength test, righting test, whisker touch test and ear twitch reflexes, wire hang test), light/dark transition test, open field test, elevated plus maze test, one-chamber social interaction test, rota-rod test, three-chamber sociability and preference for social novelty test, prepulse inhibition test of acoustic startle response, Porsolt forced swim test, Barnes maze test, tail suspension test and long-term monitoring of locomotion and social interaction in home cage. Intervals between tests were > 24 h.

Neuromuscular strength tests. Neuromuscular strength was assessed with the forelimb grip strength test and wire hang test. Forelimb grip strength was measured by pulling a mouse in the tail while its forepaws hung on to a wire grid attached to a spring balance. The tensile force (N) when the mouse released the grid was measured three times, and the greatest value was analysed. In the wire hang test, a wire mesh with a mouse on top was slowly inverted and the latency to fall was measured.

Light/dark transition test. The apparatus had a pair of differentially illuminated (390 versus 2 lux) chambers ($21 \times 41 \times 25$ cm) connected with a door in the middle. Each mouse was released in the dark chamber, and image data were acquired from the top with a CCD (charge-coupled device) camera for 10 min. The latency until the first entry into the light chamber, the time spent in each chamber, the number of transitions and the total distance travelled were automatically measured using ImageLD software (see Image analysis).

Open field test. Voluntary locomotor activity was measured in an open field test. Each mouse was placed in the centre of the open field apparatus ($40 \times 40 \times 30$ cm; Accuscan Instruments) illuminated at 100 lux. The following indices were monitored for 120 min: total distance travelled, time spent in the centre area of 20×20 cm, number of rearing and beam-breaks were automatically measured by counting interruptions of infrared beams.

Elevated plus maze test. The apparatus had two open arms (25×5 cm, with 3-mm-high plastic ledges) and two closed arms (25×5 cm, with 15-cm-high transparent walls) interconnected via a central crossing (5×5 cm), which was set at 55 cm height and illuminated at 100 lux. The numbers of entries into, and the time spent in the open and enclosed arms, were recorded for 10 min. Image data were acquired from the top with a CCD camera, and the number of entries into and the time spent in the open/closed arms, and total distance travelled, were measured automatically using the ImageEP software (see Image analysis).

Acoustic startle response and prepulse inhibition test. A mouse restrained in a cylinder was placed in the chamber of a startle reflex measurement system (O'Hara & Co.) with 70-dB background white noise. After 10 min, the mouse's startle response to a startle stimulus (110 or 120 dB white noise for 40 ms) was measured by a motion sensor for 140 ms. A test session was a random sequence of four trials each with a prepulse stimulus (74 or 78 dB white noise for 20 ms that preceded the startle stimulus by 100 ms) and two without. Six blocks of six trials were presented in a pseudorandom order with the average intertrial interval of 15 s.

Porsolt forced swim test. Each mouse was released in 7.5-cm-deep water at 23°C in an acrylic cylinder (10 cm in diameter), and the duration of the motion for evacuation was measured up to 10 min automatically using the ImageTS/PS software (see Image analysis).

Social interaction and voluntary activity in the home cage. The position of each mouse housed alone in a cage was monitored from the top continuously for a week. The distance travelled along the diurnal cycle was measured automatically using the ImageHA software (see Image analysis). Two mice of the same genotype that had been separately reared were housed together in a home cage and their two-dimensional (2D) images from the top were captured at 1 fps for a week. Their physical contact and separation were represented, respectively, as one and two particles, and their locomotor activity was quantified by the differentials of pixels between successive frames by using the ImageHA software (see Image analysis).

One-chamber social interaction test. The positions of two mice placed in a novel chamber ($40 \times 40 \times 30$ cm) were monitored from the top at three frame s^{-1} . Their horizontal distance travelled and the number of contacts were measured automatically using the ImageSI software (see Image analysis).

Three-chamber test for sociability and social novelty. The apparatus for Crawley's test had three chambers ($20 \times 40 \times 22$ cm) separated by two transparent partitions each with an opening (5×3 cm) and a lid with an infrared CCD camera. A male mouse (9-week old, C57BL/6J, termed Stranger 1) that had no prior contact with the subject mice was enclosed in a cylinder cage (9 cm in diameter, set in the left chamber) that allowed nose contacts. Each subject mouse was released in the middle chamber and allowed to explore for 10 min, while the time spent in each chamber and within 5 cm from each cage was measured automatically using the ImageCSI software (see Image analysis). Subsequently, another unfamiliar mouse (Stranger 2) was placed in another cylinder cage (in the right chamber) and monitored likewise for another 10 min.

Rota-rod test. For the initial screening, each mouse was subjected to nine trials over 3 days. See Balance beam and rota-rod tests for details.

Tail suspension test. The movement of each mouse suspended by the tail at a height of 30 cm was recorded for 10 min and analysed by using the ImageTS/PS software (see Image analysis).

Barnes maze test. The apparatus consisted of a blight (800 lux), white circular platform (diameter, 1 m) with 12 holes along the perimeter, 0.75 m above the floor, and a dark escape box (containing cage bedding) set under one of the holes ('target'). Following habituation sessions on the day before, each mouse was consistently trained to learn a randomly assigned target position (1–3 trials per day \times 6 days). The platform was turned 90° per day to minimize the influence from local cues. The distance travelled, time spent and number of errors from the centre to the target hole were measured from time-lapse images with a video-tracking software, ImageBM. One day (24 h) after the last training session, the first probe test was carried out without escape box to exclude local cue-dependent navigation, when mice were allowed to explore for 3 min and the time spent around each hole was measured. The probe test was followed by a training session with the target. To assess long-term spatial memory retention, the mice were again subjected to the probe test 1 month later.

Image analysis. The application programmes for behavioural data acquisition and analysis (ImageLD, EP, SI, CSI, TS/PS, BM, HA) were created on the ImageJ (<http://rsb.info.nih.gov/ij/>). ImageLD and EP are freely available from <http://www.mouse-phenotype.org/software.html>.

Statistical analysis. Quantitative data are represented as mean \pm s.e.m. Prism 4.0 (GraphPad Software), Stat View (SAS Institute) or Sigma Plot (SYSTAT), Excel (Microsoft) were used for statistical analyses. Behavioural data were analysed by analysis of variance (ANOVA; one-way and two-way repeated measures), unless otherwise noted. For the other data, t -test, Mann–Whitney U -test, Wilcoxon signed-rank test (two rightmost plots in Fig. 6e) and two-way (Fig. 6c) or two-way repeated measures ANOVA (Fig. 6e) followed by Tukey's *post hoc* comparisons were applied. For behavioural tests, either one-way ANOVA or two-way repeated measures ANOVA was applied for statistical analyses unless otherwise noted.

References

1. Tzingounis, A. V. & Wadiche, J. I. Glutamate transporters: confining runaway excitation by shaping synaptic transmission. *Nat. Rev. Neurosci.* **8**, 935–947 (2007).
2. Bergles, D. E., Dzubay, J. A. & Jahr, C. E. Glutamate transporter currents in bergmann glial cells follow the time course of extrasynaptic glutamate. *Proc. Natl Acad. Sci. USA* **94**, 14821–14825 (1997).
3. Dzubay, J. A. & Jahr, C. E. The concentration of synaptically released glutamate outside of the climbing fiber–Purkinje cell synaptic cleft. *J. Neurosci.* **19**, 5265–5274 (1999).
4. Chaudhry, F. A. *et al.* Glutamate transporters in glial plasma membranes: highly differentiated localizations revealed by quantitative ultrastructural immunocytochemistry. *Neuron* **15**, 711–720 (1995).
5. Takayasu, Y., Iino, M., Takatsuru, Y., Tanaka, K. & Ozawa, S. Functions of glutamate transporters in cerebellar Purkinje cell synapses. *Acta Physiol.* **197**, 1–12 (2009).
6. Watase, K. *et al.* Motor discoordination and increased susceptibility to cerebellar injury in GLAST mutant mice. *Eur. J. Neurosci.* **10**, 976–988 (1998).
7. Maragakis, N. J. & Rothstein, J. D. Glutamate transporters: animal models to neurologic disease. *Neurobiol. Dis.* **15**, 461–473 (2004).
8. Walsh, T. *et al.* Rare structural variants disrupt multiple genes in neurodevelopmental pathways in schizophrenia. *Science* **320**, 539–543 (2008).
9. McCullumsmith, R. E. & Sanacora, G. Regulation of extrasynaptic glutamate levels as a pathophysiological mechanism in disorders of motivation and addiction. *Neuropsychopharmacology* **40**, 254–255 (2015).
10. Jackson, M. *et al.* Modulation of the neuronal glutamate transporter EAAT4 by two interacting proteins. *Nature* **410**, 89–93 (2001).
11. Kinoshita, N. *et al.* Mammalian septin Sept2 modulates the activity of GLAST, a glutamate transporter in astrocytes. *Genes Cells* **9**, 1–14 (2004).
12. Hagiwara, A. *et al.* Submembranous septins as relatively stable components of actin-based membrane skeleton. *Cytoskeleton* **68**, 512–525 (2011).
13. Joberty, G., Perlungher, R. R. & Macara, I. G. The Borgs, a new family of Cdc42 and TC10 GTPase-interacting proteins. *Mol. Cell Biol.* **19**, 6585–6597 (1999).
14. Joberty, G. *et al.* Borg proteins control septin organization and are negatively regulated by Cdc42. *Nat. Cell Biol.* **3**, 861–866 (2001).
15. Sheffield, P. J. *et al.* Borg/septin interactions and the assembly of mammalian septin heterodimers, trimers, and filaments. *J. Biol. Chem.* **278**, 3483–3488 (2003).
16. Kinoshita, A., Noda, M. & Kinoshita, M. Differential localization of septins in the mouse brain. *J. Comp. Neurol.* **428**, 223–239 (2000).
17. Hashimoto, K. & Kano, M. Functional differentiation of multiple climbing fiber inputs during synapse elimination in the developing cerebellum. *Neuron* **38**, 785–796 (2003).

18. Nakayama, H. *et al.* GABAergic inhibition regulates developmental synapse elimination in the cerebellum. *Neuron* **74**, 384–396 (2012).
19. Takayasu, Y., Iino, M. & Ozawa, S. Roles of glutamate transporters in shaping excitatory synaptic currents in cerebellar Purkinje cells. *Eur. J. Neurosci.* **19**, 1285–1295 (2004).
20. Takayasu, Y. *et al.* Differential roles of glial and neuronal glutamate transporters in Purkinje cell synapses. *J. Neurosci.* **25**, 8788–8793 (2005).
21. Takatsuru, Y. *et al.* Roles of glial glutamate transporters in shaping EPSCs at the climbing fiber-Purkinje cell synapses. *Neurosci. Res.* **54**, 140–148 (2006).
22. Takatsuru, Y., Iino, M., Tanaka, K. & Ozawa, S. Contribution of glutamate transporter GLT-1 to removal of synaptically released glutamate at climbing fiber-Purkinje cell synapses. *Neurosci. Lett.* **420**, 85–89 (2007).
23. Wadiche, J. I. & Jahr, C. E. Multivesicular release at climbing fiber-Purkinje cell synapses. *Neuron* **32**, 301–313 (2001).
24. Stanley, J. L. *et al.* The mouse beam walking assay offers improved sensitivity over the mouse rotarod in determining motor coordination deficits induced by benzodiazepines. *J. Psychopharmacol.* **19**, 221–227 (2005).
25. Vong, Q. P. *et al.* A role for *borg5* during trophoctoderm differentiation. *Stem Cells* **28**, 1030–1038 (2010).
26. Liu, Z., Vong, Q. P., Liu, C. & Zheng, Y. *Borg5* is required for angiogenesis by regulating persistent directional migration of the cardiac microvascular endothelial cells. *Mol. Biol. Cell* **25**, 841–851 (2014).
27. Fuchtbauer, A. *et al.* Septin9 is involved in septin filament formation and cellular stability. *Biol. Chem.* **392**, 769–777 (2011).
28. Roseler, S. *et al.* Lethal phenotype of mice carrying a Sept11 null mutation. *Biol. Chem.* **392**, 779–781 (2011).
29. Menon, M. B. *et al.* Genetic deletion of SEPT7 reveals a cell type-specific role of septins in microtubule destabilization for the completion of cytokinesis. *PLoS Genet.* **10**, e1004558 (2014).
30. Peng, X. R., Jia, Z., Zhang, Y., Ware, J. & Trimble, W. S. The septin CDCrel-1 is dispensable for normal development and neurotransmitter release. *Mol. Cell Biol.* **22**, 378–387 (2002).
31. Ono, R. *et al.* Disruption of Sept6, a fusion partner gene of MLL, does not affect ontogeny, leukemogenesis induced by MLL-SEPT6, or phenotype induced by the loss of Sept4. *Mol. Cell Biol.* **25**, 10965–10978 (2005).
32. Fujishima, K., Kiyonari, H., Kurisu, J., Hirano, T. & Kengaku, M. Targeted disruption of Sept3, a heteromeric assembly partner of Sept5 and Sept7 in axons, has no effect on developing CNS neurons. *J. Neurochem.* **102**, 77–92 (2007).
33. Ihara, M. *et al.* Sept4, a component of presynaptic scaffold and Lewy bodies, is required for the suppression of alpha-synuclein neurotoxicity. *Neuron* **53**, 519–533 (2007).
34. Tsang, C. W. *et al.* Superfluous role of mammalian septins 3 and 5 in neuronal development and synaptic transmission. *Mol. Cell Biol.* **28**, 7012–7029 (2008).
35. Grosche, J. *et al.* Microdomains for neuron-glia interaction: parallel fiber signaling to Bergmann glial cells. *Nat. Neurosci.* **2**, 139–143 (1999).
36. Beierlein, M. & Regehr, W. G. Brief bursts of parallel fiber activity trigger calcium signals in bergmann glia. *J. Neurosci.* **26**, 6958–6967 (2006).
37. Lehre, K. P. & Danbolt, N. C. The number of glutamate transporter subtype molecules at glutamatergic synapses: chemical and stereological quantification in young adult rat brain. *J. Neurosci.* **18**, 8751–8757 (1998).
38. Lee, A. *et al.* Na⁺-H⁺ exchanger regulatory factor 1 is a PDZ scaffold for the astroglial glutamate transporter GLAST. *Glia* **55**, 119–129 (2007).
39. Shenolikar, S., Voltz, J. W., Minkoff, C. M., Wade, J. B. & Weinman, E. J. Targeted disruption of the mouse NHERF-1 gene promotes internalization of proximal tubule sodium-phosphate cotransporter type IIa and renal phosphate wasting. *Proc. Natl Acad. Sci. USA* **99**, 11470–11475 (2002).
40. Pennington, K. *et al.* Prominent synaptic and metabolic abnormalities revealed by proteomic analysis of the dorsolateral prefrontal cortex in schizophrenia and bipolar disorder. *Mol. Psychiatry* **13**, 1102–1117 (2008).
41. Datta, D., Arion, D., Corradi, J. P. & Lewis, D. A. Altered Expression of CDC42 Signaling Pathway Components in Cortical Layer 3 Pyramidal Cells in Schizophrenia. *Biol. Psychiatry* **78**, 775–85 (2015).
42. Furney, S. J. *et al.* Genome-wide association with MRI atrophy measures as a quantitative trait locus for Alzheimer's disease. *Mol. Psychiatry* **16**, 1130–1138 (2011).
43. Schizophrenia Working Group of the Psychiatric Genomics Consortium. Genetic insights from 108 schizophrenia-associated genetic loci. *Nature* **511**, 421–427 (2014).
44. Ageta-Ishihara, N. *et al.* Septins promote dendrite and axon development by negatively regulating microtubule stability via HDAC6-mediated deacetylation. *Nat. Commun.* **4**, 2532 (2013).
45. Shibata, T. *et al.* Glutamate transporter GLAST is expressed in the radial glia-astrocyte lineage of developing mouse spinal cord. *J. Neurosci.* **17**, 9212–9219 (1997).
46. Yamasaki, M. *et al.* 3-Phosphoglycerate dehydrogenase, a key enzyme for L-serine biosynthesis, is preferentially expressed in the radial glia/astrocyte lineage and olfactory ensheathing glia in the mouse brain. *J. Neurosci.* **21**, 7691–7704 (2001).
47. Nakagawa, S., Watanabe, M., Isobe, T., Kondo, H. & Inoue, Y. Cytological compartmentalization in the staggerer cerebellum, as revealed by calbindin immunohistochemistry for Purkinje cells. *J. Comp. Neurol.* **395**, 112–120 (1998).
48. Patrizi, A. *et al.* Synapse formation and clustering of neuroligin-2 in the absence of GABAA receptors. *Proc. Natl Acad. Sci. USA* **105**, 13151–13156 (2008).
49. Miyazaki, T., Fukaya, M., Shimizu, H. & Watanabe, M. Subtype switching of vesicular glutamate transporters at parallel fibre-Purkinje cell synapses in developing mouse cerebellum. *Eur. J. Neurosci.* **17**, 2563–2572 (2003).
50. Amano, M. *et al.* A proteomic approach for comprehensively screening substrates of protein kinases such as Rho-kinase. *PLoS ONE* **5**, e8704 (2010).
51. Fukushima, T., Kawai, J., Imai, K. & Toyooka, T. Simultaneous determination of D- and L-serine in rat brain microdialysis sample using a column-switching HPLC with fluorimetric detection. *Biomed. Chromatogr.* **18**, 813–819 (2004).
52. Aoyama, C. *et al.* A fully automated amino acid analyzer using NBD-F as a fluorescent derivatization reagent. *Biomed. Chromatogr.* **18**, 630–636 (2004).
53. Horio, M. *et al.* Levels of D-serine in the brain and peripheral organs of serine racemase (*Srr*) knock-out mice. *Neurochem. Int.* **59**, 853–859 (2011).
54. Chen, H. *et al.* Protective effects of the antioxidant sulforaphane on behavioral changes and neurotoxicity in mice after the administration of methamphetamine. *Psychopharmacology (Berl)* **222**, 37–45 (2012).
55. Yamasaki, M., Matsui, M. & Watanabe, M. Preferential localization of muscarinic M1 receptor on dendritic shaft and spine of cortical pyramidal cells and its anatomical evidence for volume transmission. *J. Neurosci.* **30**, 4408–4418 (2010).
56. Fukaya, M. & Watanabe, M. Improved immunohistochemical detection of postsynaptically located PSD-95/SAP90 protein family by protease section pretreatment: a study in the adult mouse brain. *J. Comp. Neurol.* **426**, 572–586 (2000).
57. Abe, M. *et al.* NMDA receptor GluRepsilon/NR2 subunits are essential for postsynaptic localization and protein stability of GluRzeta1/NR1 subunit. *J. Neurosci.* **24**, 7292–7304 (2004).
58. Aiba, A. *et al.* Deficient cerebellar long-term depression and impaired motor learning in mGluR1 mutant mice. *Cell* **79**, 377–388 (1994).
59. Kano, M. *et al.* Impaired synapse elimination during cerebellar development in PKC gamma mutant mice. *Cell* **83**, 1223–1231 (1995).
60. Mishina, M. & Sakimura, K. Conditional gene targeting on the pure C57BL/6 genetic background. *Neurosci. Res.* **58**, 105–112 (2007).
61. Fukaya, M. *et al.* Abundant distribution of TARP gamma-8 in synaptic and extrasynaptic surface of hippocampal neurons and its major role in AMPA receptor expression on spines and dendrites. *Eur. J. Neurosci.* **24**, 2177–2190 (2006).
62. Sakai, K. & Miyazaki, J. A transgenic mouse line that retains Cre recombinase activity in mature oocytes irrespective of the cre transgene transmission. *Biochem. Biophys. Res. Commun.* **237**, 318–324 (1997).
63. Ageta-Ishihara, N. *et al.* Chronic overload of SEPT4, a parkin substrate that aggregates in Parkinson's disease, causes behavioral alterations but not neurodegeneration in mice. *Mol. Brain* **6**, 35 (2013).
64. Huda, F. *et al.* Distinct transduction profiles in the CNS via three injection routes of AAV9 and the application to generation of a neurodegenerative mouse model. *Mol. Ther. Methods Clin. Dev.* **1**, 14032 (2014).
65. Watanabe, S. *et al.* SIRT1 overexpression ameliorates a mouse model of SOD1-linked amyotrophic lateral sclerosis via HSF1/HSP70i chaperone system. *Mol. Brain* **7**, 62 (2014).
66. Takao, K. *et al.* Impaired long-term memory retention and working memory in *sdv* mutant mice with a deletion in *Dtnbp1*, a susceptibility gene for schizophrenia. *Mol. Brain* **1**, 11 (2008).

Acknowledgements

We thank C. Oshima (Nagoya University) and M. Yanagisawa (Tokyo Medical and Dental University) for the technical help, T. Miyazaki (Osaka University) for CAG-Cre transgenic mice and M. Itakura (Kitasato University) for GluA4 antibody, and the Mochida Memorial Foundation and Hori Science Foundation for financial aids. This work was supported in part by Grant-in-Aid for Scientific Research, Grant-in-Aid for Young Investigator, Grants-in-Aid for Scientific Research on Innovative Areas 'Synapse pathology', 'Microscopy pathology', 'Neural Diversity and Neocortical Organization', 'Glial Assembly' and 'Adaptive Circuit Shift', Technical Supports for Fluorescent Probes and Imaging, for Behavioural Analysis and for Antibody Production from Comprehensive Brain Science Network, and the Strategic Research Program for Brain Sciences (Integrated Research on Neuropsychiatric disorders) each from the MEXT of Japan.

Author contributions

M.Y., M.A. and K.S. established the *Cdc42ep4^{fl}* line; N.A.-I., K.Ko. and M.W. conducted the biochemical and morphological analyses; H.N. and Ko.H. conducted electrophysiological analyses, Ke.H. supervised transmitter measurement; T.N. and K.Ka. conducted mass spectrometric analysis, K.T. provided reagents and critical suggestions for GLAST experiments; S.H. and T.M. supervised the behavioural tests; F.H. and H.H. designed and conducted drug injection surgery; and M.K. designed the study and wrote the manuscript with W.M. and Ko.H. All authors read and approved the final manuscript.

Additional information

Supplementary Information accompanies this paper at <http://www.nature.com/naturecommunications>

Competing financial interests: The authors declare no competing financial interests.

Reprints and permission information is available online at <http://npg.nature.com/reprintsandpermissions/>

How to cite this article: Ageta-Ishihara, N. *et al.* A CDC42EP4/septin-based perisynaptic glial scaffold facilitates glutamate clearance. *Nat. Commun.* 6:10090 doi: 10.1038/ncomms10090 (2015).



This work is licensed under a Creative Commons Attribution 4.0 International License. The images or other third party material in this article are included in the article's Creative Commons license, unless indicated otherwise in the credit line; if the material is not included under the Creative Commons license, users will need to obtain permission from the license holder to reproduce the material. To view a copy of this license, visit <http://creativecommons.org/licenses/by/4.0/>

SCIENTIFIC REPORTS



OPEN

Spinal mechanisms underlying potentiation of hindpaw responses observed after transient hindpaw ischemia in mice

Received: 18 March 2015

Accepted: 23 April 2015

Published: 13 July 2015

Tatsunori Watanabe^{1,2}, Mika Sasaki², Seiji Komagata¹, Hiroaki Tsukano¹, Ryuichi Hishida¹, Tatsuro Kohno², Hiroshi Baba² & Katsuei Shibuki¹

Transient ischemia produces postischemic tingling sensation. Ischemia also produces nerve conduction block that may modulate spinal neural circuits. In the present study, reduced mechanical thresholds for hindpaw-withdrawal reflex were found in mice after transient hindpaw ischemia, which was produced by a high pressure applied around the hindpaw for 30 min. The reduction in the threshold was blocked by spinal application of LY354740, a specific agonist of group II metabotropic glutamate receptors. Neural activities in the spinal cord and the primary somatosensory cortex (S1) were investigated using activity-dependent changes in endogenous fluorescence derived from mitochondrial flavoproteins. Ischemic treatment induced potentiation of the ipsilateral spinal and contralateral S1 responses to hindpaw stimulation. Both types of potentiation were blocked by spinal application of LY354740. The contralateral S1 responses, abolished by lesioning the ipsilateral dorsal column, reappeared after ischemic treatment, indicating that postischemic tingling sensation reflects a sensory modality shift from tactile sensation to nociception in the spinal cord. Changes in neural responses were investigated during ischemic treatment in the contralateral spinal cord and the ipsilateral S1. Potentiation already appeared during ischemic treatment for 30 min. The present findings suggest that the postischemic potentiation shares spinal mechanisms, at least in part, with neuropathic pain.

The mechanism of postischemic tingling sensation has been attributed to enhanced excitability of peripheral nerves during recovery from ischemic conduction block^{1,2}. However, nerve conduction block is known to quickly induce plasticity in the central nervous system in experimental animals³ and humans⁴⁻⁶. Cessation of low frequency spontaneous firing of A β tactile afferents after partial denervation produces potentiation of neural responses in the primary somatosensory cortex (S1) elicited via the remaining nerves⁷. Reduction in the mechanical thresholds for paw-withdrawal reflex is observed at the same time⁷. This reduction in mechanical thresholds can be inhibited by spinal application of LY354740⁷, a specific antagonist of group II metabotropic glutamate receptors (mGluRs)⁸. If similar spinal mechanisms are also responsible for postischemic tingling sensation, this should be abolished by spinal application of LY354740. In the present study, we reproduced postischemic mechanical allodynia in mice, and tested roles of spinal mechanisms using this model.

Neuropathic pain is produced by nerve injury in animal models⁹⁻¹¹, and the resulting pain is usually evaluated using behavioral tests more than 24 h after the injury to allow the recovery of animals from surgical injury. Therefore, the findings obtained from behavioral tests are affected by complex cascades

¹Department of Neurophysiology, Brain Research Institute, Niigata University, 1-757 Asahi-machi, Chuo-ku, Niigata 951-8585, Japan. ²Department of Anesthesiology, School of Medicine, Niigata University, 1-757 Asahi-machi, Chuo-ku, Niigata 951-8510, Japan. Correspondence and requests for materials should be addressed to K.S. (email: shibuki@bri.niigata-u.ac.jp)

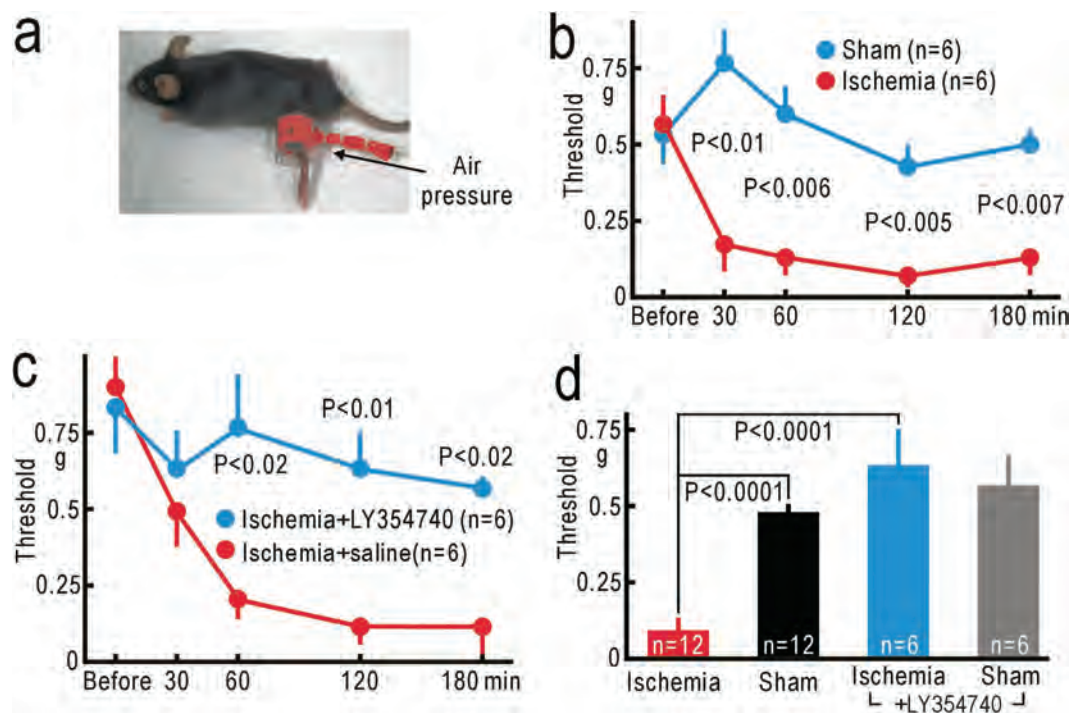


Figure 1. Reduced mechanical thresholds for hindpaw-withdrawal reflex. (a) Application of high pressure (250 mm Hg) to the left thigh. (b) Mechanical thresholds for left hindpaw-withdrawal reflex before and after ischemic or sham treatment applied to the left thigh. Mean \pm SEM are shown. (c) Mechanical thresholds for hindpaw-withdrawal reflex after hindpaw ischemia in mice with spinal application of LY354740 (10 nM, 5 μ l) or saline alone. (d) Comparison of the thresholds for the left hindpaw-withdrawal reflex at 2 h after ischemic or sham treatment, with or without spinal application of LY354740. In the ischemia group, data were mixed in mice with or without spinal application of saline. In the sham-treated group, data were mixed in mice with sham treatment to the left thigh or to the right thigh.

of inflammation and gene expression during the recovery period^{12–14}. However, postischemic mechanical allodynia is induced very quickly after transient hindpaw ischemia. Thus, if neural changes reflecting postischemic tingling sensation are found, these changes may be useful for investigating the neural mechanisms that trigger neuropathic pain. Activity-dependent flavoprotein fluorescence signals reflect aerobic energy metabolism in mitochondria¹⁵, and are useful for investigating fine neural activities and plasticity^{16–18}. Flavoprotein signals are resistant to and spontaneously recover from photobleaching¹⁹, and quantitatively reflect neural activities^{20,21}. Spinal activities elicited by peripheral stimulation have been visualized using flavoprotein fluorescence signals²². An initial phase of neuropathic pain after partial denervation is observed as long-lasting potentiation of flavoprotein fluorescence signals in S1⁷. Furthermore, a modality shift from tactile sensation to nociception can be visualized as reappearance of S1 responses to tactile stimulation in mice with ipsilateral dorsal column lesioning⁷. It is because the tactile sensation is mediated via the ipsilateral dorsal column to the contralateral S1²³, while nociception is mediated via the contralateral spinothalamic tract²⁴. In the present study, we confirmed that such a modality shift from tactile sensation to nociception was produced within 30 min after ischemic treatment.

Results

Reduced mechanical thresholds for paw-withdrawal reflex after ischemic treatment. Because unpleasant postischemic tingling sensation is exacerbated by external mechanical forces, we measured the thresholds for hindpaw-withdrawal reflex using von Frey filaments²⁵. The thresholds before hindpaw ischemia were 0.57 ± 0.10 g (mean \pm SEM, $n = 6$). Mice were transiently anesthetized with 1% isoflurane, and a pressure of 250 mmHg was applied for 30 min to a rubber cuff set around the thigh (Fig. 1a). At 30 min after the ischemic treatment was finished, the mechanical thresholds were significantly reduced compared with the corresponding data in sham-treated mice with no pressure application ($P < 0.01$, Fig. 1b). The thresholds reached the minimal values of 0.07 ± 0.02 g ($n = 6$) at 2 h after the ischemic treatment (Fig. 1b), and were clearly and significantly smaller than the corresponding values in sham-treated mice ($P < 0.005$). Isoflurane anesthesia alone produced no reduction in the threshold in sham-treated mice (Fig. 1b).

Next, we tested whether the reduction in the thresholds was sensitive to spinal application of 10 nM LY354740 (Fig. 1c), which can block the initial phase of neuropathic pain after partial denervation⁷.

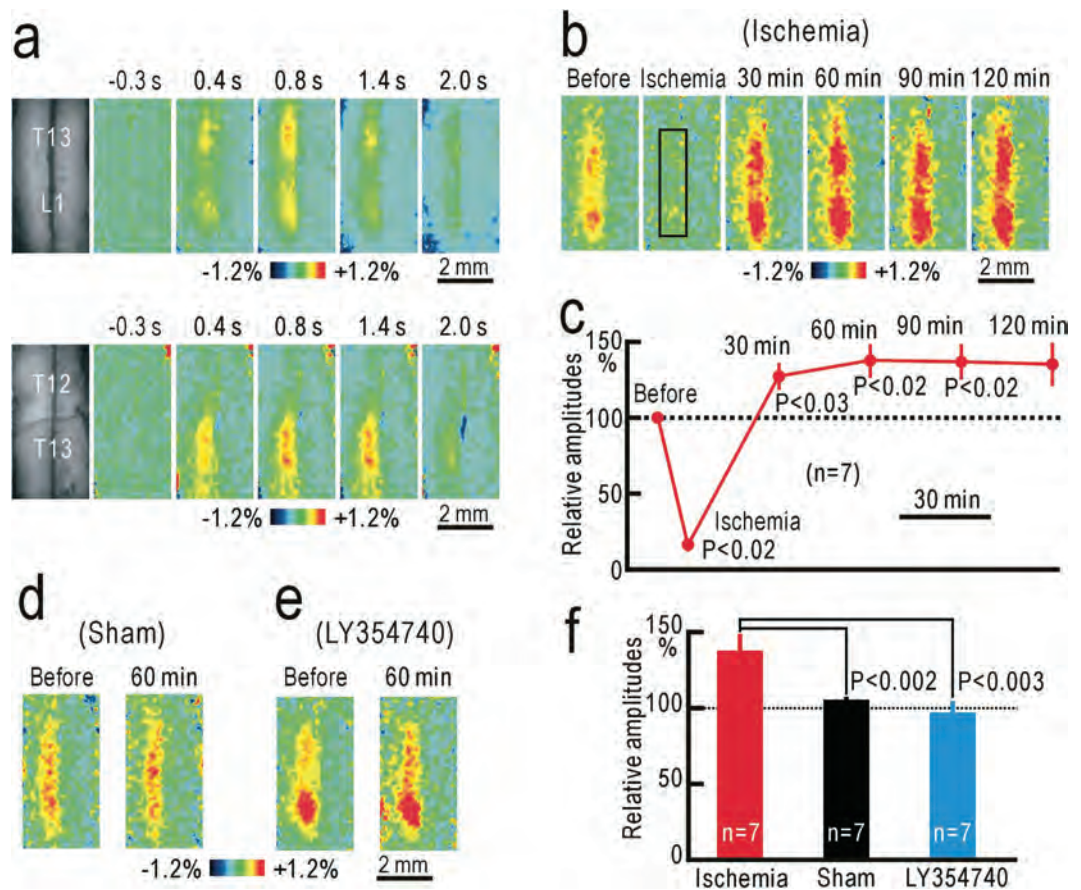


Figure 2. Potentiation of the spinal responses after hindpaw ischemia. (a) Example of ipsilateral spinal responses elicited by vibratory stimulation applied to the left hindpaw at T13 and L1 level (upper panels). The left-most panels are original fluorescence images, and others are pseudocolor images of response magnitudes in $\Delta F/F_0$ recorded at the time before and after the stimulus onset shown on each image. Another example of ipsilateral spinal responses elicited by vibratory stimulation applied to the left hindpaw at T12 and T13 level (lower panels). (b) Example of spinal responses recorded in the same mouse before, during, and 30–120 min after ischemic treatment applied to the left thigh for 30 min. The response amplitudes were measured in the square window of 100×25 pixels shown in the second panel. (c) Relative amplitudes of spinal responses during and after ischemic treatment. The amplitudes were normalized by those recorded before hindpaw ischemia. (d) Example of spinal responses recorded before and at 60 min after sham treatment. (e) Example of spinal responses recorded before and at 60 min after hindpaw ischemia in a mouse with spinal application of 10 nM LY354740. (f) Comparison of the normalized response amplitudes in mice at 60 min after hindpaw ischemia, sham treatment, or hindpaw ischemia with spinal application of 10 nM LY354740.

When the ischemic treatment was applied to the mice that received spinal application of LY354740, the thresholds at 2 h after hindpaw ischemia were 0.63 ± 0.12 g ($n = 6$). In contrast, the thresholds were 0.12 ± 0.06 g ($n = 6$) in mice that received spinal application of saline alone (Fig. 1c). The difference at 2 h after hindpaw ischemia or sham-treatment was statistically significant ($P < 0.01$). We confirmed that spinal application of LY354740 alone had no apparent effect on the mechanical thresholds for paw-withdrawal reflex (Fig. 1d). Interestingly, a slight but significant reduction in the threshold was observed in the right hindpaw (Supplementary Fig. S1), suggesting that transient hindpaw ischemia might also have some effects on the contralateral spinal cord.

Flavoprotein fluorescence responses in the spinal cord. Because the behavioral test data suggested the presence of some spinal plasticity, we recorded ipsilateral spinal responses elicited by vibratory hindpaw stimulation using flavoprotein fluorescence imaging. Hindpaw stimulation produced an increase in fluorescence on the dorsal surface of the ipsilateral spinal cord corresponding to the dorsal horn at the T13 and L1 level (Fig. 2a). Because minimal response was found at T12, the fluorescence changes were attributed mainly to localized activities in the dorsal horn but not to ascending afferent activities mediated via the dorsal column. The responses started at 0.2 s after the onset of the stimulation,

and peaked at approximately 1% in $\Delta F/F_0$ at 0.6–0.8 s after the stimulus onset. Although these properties were similar to those recorded in cortical areas^{7,26}, the decay was slower than that of the cortical responses, as the hemodynamic responses were not marked in the spinal cord (Supplementary Figs S2).

The spinal responses to vibratory hindpaw stimulation were abolished by a pressure of 250 mmHg applied to the thigh, indicating that ischemic conduction block was successfully produced at 250 mmHg (Fig. 2b). The responses reappeared within 30 min after hindpaw ischemia, and the magnitude of the responses estimated at 30 min after hindpaw ischemia was slightly but significantly potentiated ($P < 0.03$, Fig. 2b,c). At 1 h after hindpaw ischemia, the response amplitudes reached maximal values, and were potentiated to $138 \pm 11\%$ ($n = 7$) compared with those before hindpaw ischemia (Fig. 2c). No clear potentiation was observed in sham-treated mice, and the difference between the two groups was statistically significant ($P < 0.002$, Fig. 2d,f).

Next, we applied 10 nM LY354740 on the surface of the spinal cord during imaging experiments. Application of LY354740 had no immediate effect on the spinal responses to vibratory hindpaw stimulation (Fig. 2e). However, the spinal responses were not clearly potentiated after hindpaw ischemia, and the relative amplitudes at 1 h after hindpaw ischemia were significantly smaller than those in mice with no LY354740 ($P < 0.003$, Fig. 2e,f). These data suggest that transient hindpaw ischemia produced spinal potentiation, and the reduction in mechanical thresholds for paw-withdrawal reflex, likely via similar spinal mechanisms sensitive to LY354740.

The spinal responses occasionally appeared in separated segments (for example, Fig. 2a), which might reflect the presence of functional units. Therefore, we tested the fine somatotopic maps in the spinal responses elicited by vibratory stimulation applied to each toe. The spinal responses to stimulation of each toe appeared in small areas that were different each other (Supplementary Fig. S2). The responsive areas were arranged almost linearly (Supplementary Figs S2). These results were compatible with a previous morphological study on spinal distribution of afferent fibers from each digit²⁷. Therefore, the apparent segments in the spinal responses likely reflected strong stimulation of the skin convexes by the brush used for hindpaw stimulation.

Flavoprotein fluorescence responses in S1. Flavoprotein fluorescence responses elicited by hindpaw stimulation appeared in the contralateral S1 (Fig. 3a). The initial time course of S1 responses elicited by hindpaw stimulation was similar to that of spinal responses, while hemodynamic responses obscured the later phase of the responses (Supplementary Figs S3). Although neural responses in S1 are arranged according to somatotopic maps over a large scale^{26,28,29}, the responses elicited by stimulation of each toe were not clearly separated, and no fine somatotopic map was found (Supplementary Figs S3). When a pressure of 250 mmHg was applied to the thigh, S1 responses were almost completely abolished (Fig. 3b). However, the responses reappeared and were potentiated after hindpaw ischemia (Fig. 3b,c). The potentiation was maintained up to 3 h after hindpaw ischemia. The relative amplitudes at 1 h after hindpaw ischemia ($165 \pm 18\%$, $n = 13$) were significantly larger than those in sham-treated mice ($99 \pm 4\%$, $n = 8$, $P < 0.003$, Fig. 3d,g). Potentiation of S1 responses after ischemic treatment was almost completely abolished by spinal application of 10 nM LY354740 (Fig. 3e,f). The relative amplitudes of S1 responses in mice with spinal application with LY354740 were $105 \pm 6\%$ ($n = 9$) at 1 h after hindpaw ischemia, and were significantly smaller than those in mice with spinal application of saline alone ($150 \pm 16\%$, $n = 8$, $P < 0.007$, Fig. 3g). Therefore, the suppression of S1 potentiation is likely attributable to the pharmacological effects of LY354740, but not to non-specific spinal injury caused by the drug application.

Modality shift from tactile sensation to nociception induced by hindpaw ischemia. Potentiation in S1 after ischemic treatment may be produced by a modality shift from tactile sensation to nociception, as observed after partial denervation⁷. When we disrupted the ipsilateral dorsal column at the T11 level (Fig. 4a), S1 responses elicited by hindpaw stimulation were abolished (Fig. 4b). However, S1 responses reappeared at 30 and 60 min after ischemic treatment applied to the hindpaw (Fig. 4b). As no such response was observed in sham-treated mice (Fig. 4c), the reappearing S1 responses cannot be attributed to spontaneous recovery from the injury caused by dorsal column lesioning. The difference in S1 responses in the operated mice was statistically significant at 30 and 60 min after hindpaw ischemia or sham treatment ($P < 0.01$ for both, Fig. 4d). The reappearing S1 responses suggest that the modality shift from tactile sensation to nociception was induced within 30 min after ischemic treatment.

Potentiation in the contralateral spinal cord and the ipsilateral S1 during hindpaw ischemia. Changes in neural responses were not observable during ischemic treatment in the ipsilateral spinal cord or in the contralateral S1 because of conduction block of the peripheral nerves. However, we found that the spinal responses elicited by vibratory stimulation applied to the hindpaw contralateral to the ischemic treatment were significantly potentiated during ischemic treatment (Fig. 5a,b). The potentiation was maintained for at least 60 min after hindpaw ischemia. Cortical responses in S1 ipsilateral to the ischemic treatment were similarly potentiated during and after hindpaw ischemia (Fig. 5c,d), indicating that spinal and cortical potentiation had already been initiated during ischemic treatment. Comparison of the potentiation at 60 min after hindpaw ischemia in the spinal cord (ipsilateral: $138 \pm 11\%$, $n = 7$; contralateral: $140 \pm 6\%$, $n = 5$) and S1 (contralateral: $165 \pm 18\%$, $n = 13$; ipsilateral: $171 \pm 14\%$, $n = 14$) revealed that the neural changes in the contralateral spinal cord and the ipsilateral

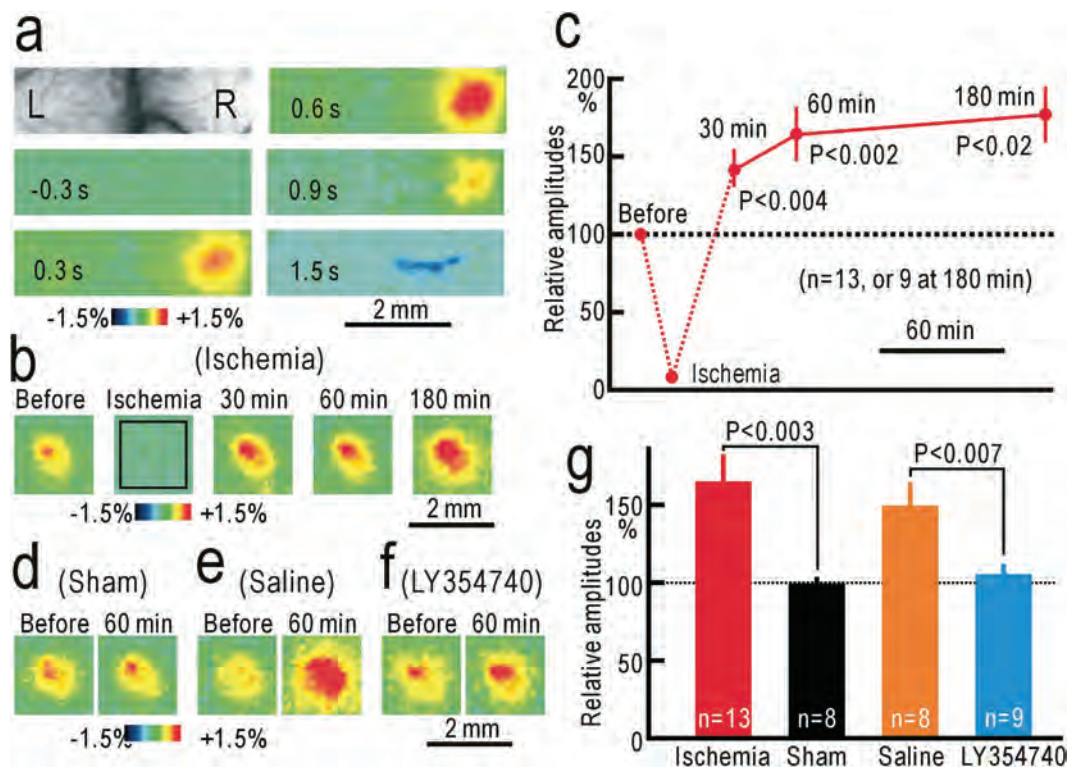


Figure 3. Potentiation of the S1 responses after ischemic treatment. (a) Example of contralateral S1 responses elicited by vibratory stimulation applied to the left hindpaw. (b) Example of S1 responses recorded in the same mouse before, during, and 30–180 min after ischemia applied to the left thigh for 30 min. The response amplitudes were measured in the square window of 60×60 pixels shown in the second panel. (c) Relative amplitudes of S1 responses during and after hindpaw ischemia. (d) Example of S1 responses recorded before and at 60 min after sham treatment. (e) Example of S1 responses recorded before and at 60 min after hindpaw ischemia in a mouse with spinal application of saline alone. (f) Example of S1 responses recorded before and at 60 min after hindpaw ischemia in a mouse with spinal application of 10 nM LY354740. (g) Comparison of the normalized response amplitudes in mice at 60 min after hindpaw ischemia, sham treatment, hindpaw ischemia with spinal application of saline alone, or hindpaw ischemia with spinal application of 10 nM LY354740.

S1 were comparable to those in the opposite sides. These results suggest that reduction in the mechanical thresholds of the right hindpaw-withdrawal reflex could be observed after ischemic treatment applied to the left thigh. In accordance with these results, a slight but significant reduction in the mechanical threshold ($P < 0.02$) was observed in the right hindpaw withdrawal reflex at 3 h after ischemia applied to the hindpaw. However, S1 responses to forepaw stimulation were not clearly affected by ischemia applied to the hindpaw (Supplementary Figs S4).

Discussion

Postischemic mechanical allodynia produced by spinal mechanisms in mice. In the present study, we found that mechanical thresholds for hindpaw-withdrawal reflex were reduced after ischemic treatment. Previous studies also reported that hyperalgesia³⁰ or mechanical allodynia³¹ is observed after hindpaw ischemia in animal experiments. However, it is difficult to differentiate between tingling sensation (or dysesthesia) and hyperalgesia or mechanical allodynia using behavioral tests, because all of these symptoms produce reduced mechanical thresholds. The reduced mechanical thresholds after ischemic treatment in the present study can be regarded as dysesthesia, because tingling sensation rather than pain is frequently experienced by human subjects after reversible hindpaw ischemia. Usually, postischemic dysesthesia due to hyperexcitability of peripheral nerves continues for approximately 5 min after ischemic treatment¹, while use of a tourniquet to prevent bleeding for more than 2 h can produce long-lasting dysesthesia³².

The reduced mechanical thresholds were accompanied by potentiation in the spinal cord and S1. These three changes after ischemic treatment were abolished by spinal application of LY354740. Spinal and S1 responses to the right hindpaw stimulation were also potentiated during ischemia applied to the left hindpaw. Although long lasting-ischemia and reperfusion produce peroxides and resulting cytokine-mediated adverse pathophysiological effects on peripheral tissues^{33,34}, potentiation in the

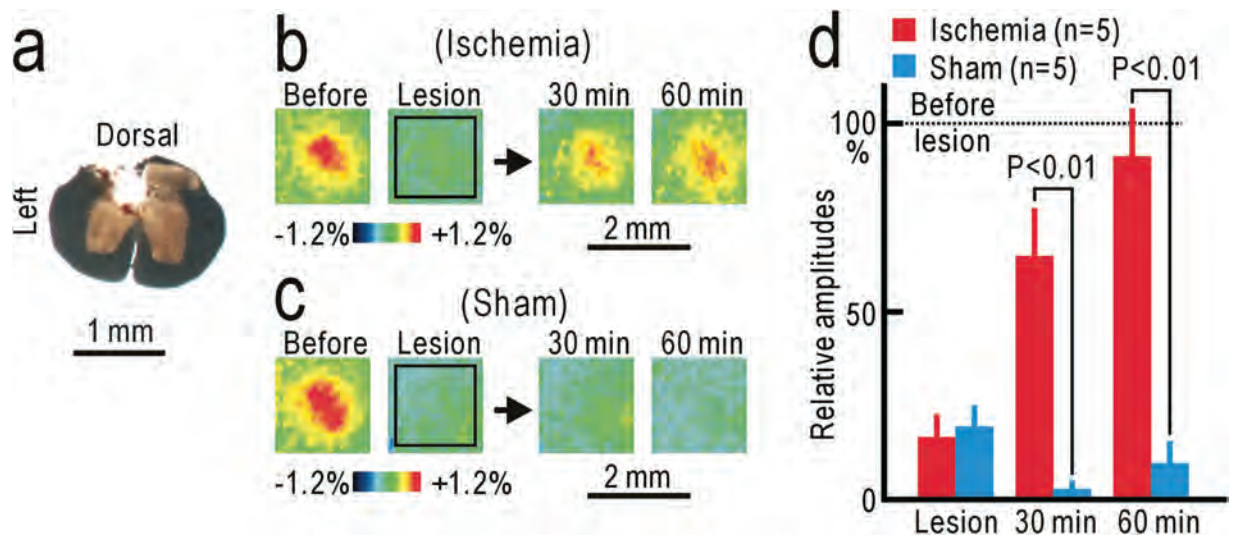


Figure 4. Sensory modality shift induced by ischemic treatment. (a) Lesion in the left dorsal column at T11 level. (b) Example of the right S1 responses modified by the left column lesioning and ischemic treatment applied to the left thigh. (c) Example of the right S1 responses modified by the left column lesioning and sham treatment applied to the left thigh. (d) Response amplitudes immediately after dorsal column lesioning, and at 30 min and 60 min after ischemic or sham treatment.

contralateral spinal cord or in the ipsilateral S1 was observed before reperfusion was started, and S1 responses to forepaw stimulation were not affected by ischemia applied to the hindpaw. Taken together, these data suggest that posts ischemic tingling sensation was produced by localized spinal mechanisms in our mouse model.

Spinal neural circuits and mechanisms producing posts ischemic plasticity. Neural imaging is useful for investigating mechanisms underlying posts ischemic tingling sensation. We used endogenous fluorescence signals derived from the mitochondrial flavoproteins¹⁵. Because flavoproteins are endogenous proteins of the electron transfer system in the mitochondria, it is very unlikely that flavoproteins work as a calcium chelator and have some artificial effects on the calcium dynamics, which play essential roles in induction of synaptic plasticity. We have successfully recorded various types of neural plasticity using this imaging method^{16,17,20,35}. Flavoprotein fluorescence responses are mainly derived from synaptically-driven neuronal activity²¹, and no clear fluorescence response was found from the ipsilateral dorsal column that mediates tactile sensory information during hindpaw stimulation. Therefore, the spinal flavoprotein fluorescence responses were presumably derived from dorsal parts of the dorsal horn, which is composed of lamina I–VI³⁶. Of these, tactile inputs mediated by A β fibers are terminated mainly in lamina III–V. Lamina II, or the substantial gelatinosa, has a critical role in neuropathic pain^{37,38}, and receives nociceptive inputs mediated mainly by C fibers³⁹. Group II mGluRs are located in the substantial gelatinosa⁴⁰. Taken together, the spinal fluorescence responses elicited by tactile stimuli to the hindpaw are likely derived from neuronal activity in lamina III–V, and the potentiation observed after ischemic treatment likely reflects the recruitment of neuronal activity in the substantial gelatinosa.

An initial phase of neuropathic pain after partial denervation is abolished by spinal application of LY354740⁷, and this compound and similar group II mGluR agonists alleviate neuropathic pain^{8,41}. Because the potentiation in the present study was also susceptible to spinal application of LY354740, these two types of potentiation may share similar mechanisms, at least in part, with neuropathic pain (Fig. 6a). Activation of postsynaptic group II mGluRs reduces presynaptic transmitter release⁴², produces membrane hyperpolarization by opening inward rectifier K⁺ channels^{43,44}, and modulates spontaneous Ca²⁺ spikes⁴⁵. Therefore, failure of group II mGluR activation during conduction block of peripheral nerve activities may increase the excitability and intracellular Ca²⁺ concentration of postsynaptic neurons. These changes induce down-regulation of the neuron-specific KCl cotransporter (KCC2) in dorsal horn neurons and a resulting reduced neuronal Cl⁻ gradient^{46–48}. Nociceptive spinal neurons are dynamically regulated by inhibition from various sources^{49,50}, and modulation of the Cl⁻ gradient can explain the increased responsiveness of spinothalamic tract neurons to innocuous mechanical stimuli in animals with neuropathic pain^{48,51}. The spinal potentiation is induced not only in the ipsilateral site that fails to receive basal afferent firing, but also in the contralateral site or nearby site after partial nerve cutting. Because stimulation of different skin areas produces separate spinal responses (for example, Fig. 3), the potentiation in nearby spinal sites may have been induced by diffusible mediators produced in spinal neurons that failed to receive basal afferent firing (Fig. 6b). It is suggested that hindpaw ischemia produced

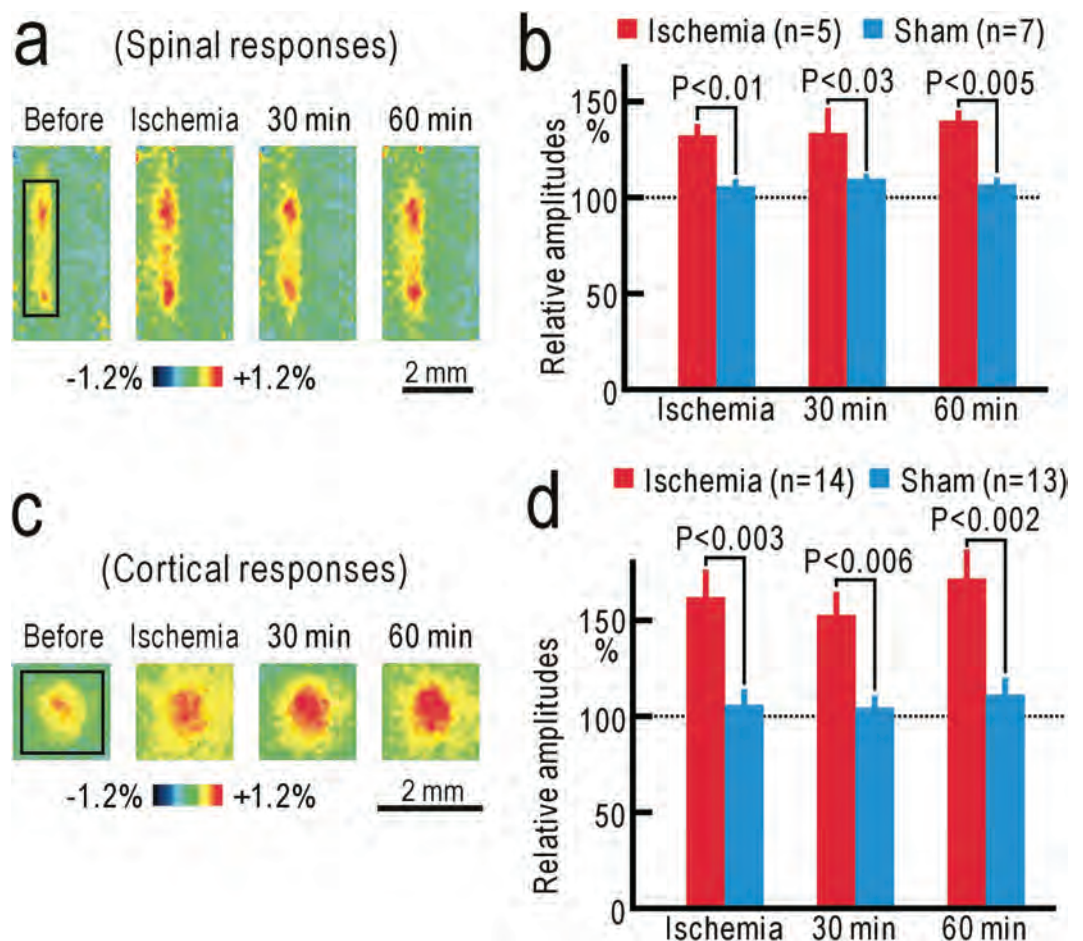


Figure 5. Responses to peripheral stimulation contralateral to hindpaw ischemia. (a) Example of spinal responses to left hindpaw stimulation before, during, and at 30 min and 60 min after ischemic treatment applied to the right hindpaw. (b) Relative amplitudes of the responses to left hindpaw stimulation before, during, and at 30 min and 60 min after ischemic or sham treatment applied to the right hindpaw. Responses were normalized by those recorded before ischemic or sham treatment. (c) Example of S1 responses to left hindpaw stimulation before, during, and after ischemic treatment applied to the right hindpaw. (d) Relative amplitudes of the responses to left hindpaw stimulation.

some diffusible mediators that produced not only potentiation of contralateral hindpaw responses but also contralateral mechanical allodynia. Diffusible mediators may also play a role in potentiation of spinal responses ipsilateral to ischemic treatment. In accordance with this concept, neuropathic pain was reported to be facilitated by a number of diffusible mediators such as nitric oxide⁵² and ATP/cytokines⁵³. The mechanical allodynia observed after hindpaw ischemia seemed to be more clearly observed in mice compared with similar phenomena in humans. Furthermore, humans do not clearly exhibit tingling sensation contralateral to the ischemic side or after partial nerve cutting. This difference may be attributed to the small size of spinal circuits in mice, in which diffusible messengers such as nitric oxide can be very effective. Another important consideration is that the potentiation observed during ischemic treatment in the present study could not be induced by repetitive activity in peripheral nerves, another condition known to induce spinal potentiation^{54,55}.

Postischemic changes as an experimental model for investigating neuropathic pain. Neuropathic pain is usually induced by peripheral nerve injury in animal models^{9–11}. It is produced by a complex cascade of inflammation and gene expression, and not only neurons but also glial cells in the spinal cord have important roles in neuropathic pain^{12–14}. We have reported that an initial phase of neuropathic pain is observed at a few hours after partial denervation⁷. However, postischemic tingling sensation and plasticity, which share similar spinal mechanisms with neuropathic pain, were observed at 30 min after reversible hindpaw ischemia. Furthermore, potentiation of spinal responses contralateral to the ischemic side appeared within 30 min of ischemic treatment. Regardless of the species difference, the very early onset of neural plasticity during reversible hindpaw ischemia or transient functional deafferentation in mice make them useful as an experimental model for observing and

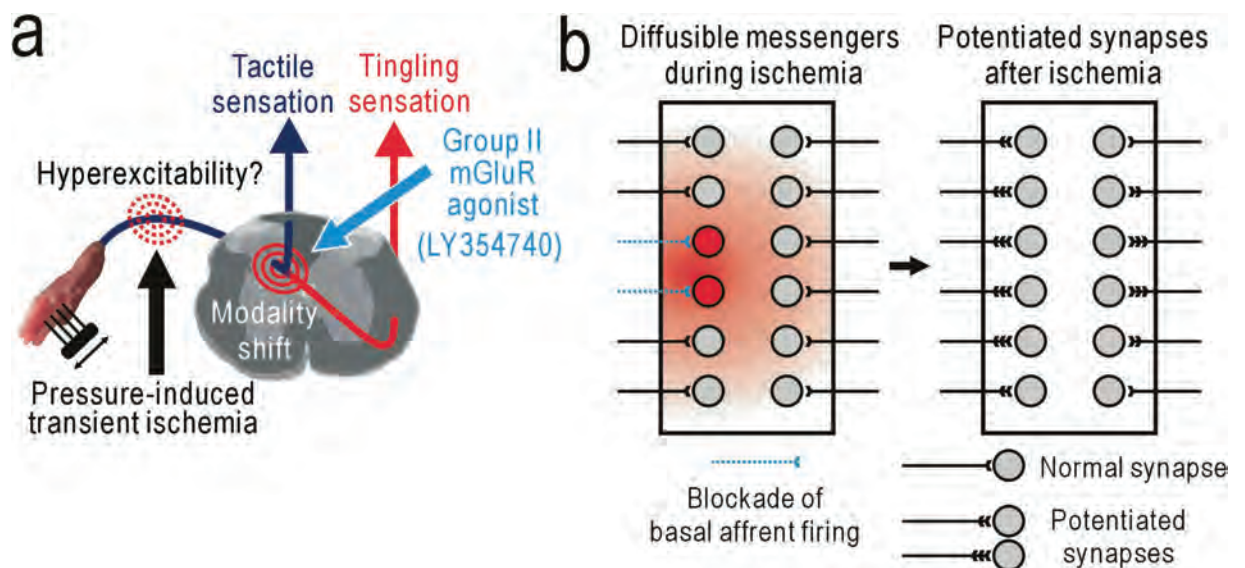


Figure 6. Mechanisms underlying postischemic plasticity. (a) Sensory modality shift from tactile to tingling sensation at the spinal cord level. (b) Schematic drawings of spinal potentiation ipsilateral and contralateral to ischemic treatment. Expected spinal potentiation induced after partial nerve cutting may also be induced by similar mechanisms.

investigating the detailed cellular and molecular cascades that trigger human neuropathic pain. However, further studies on neuronal and glial activities in the spinal cord are required for establishing a new preclinical model of early neuropathic pain based on the present studies.

Materials and methods

The experiments in the present study were approved by the ethics committee of animal experiments in Niigata University (approved number: 233-4), and were carried out in accordance with the approved guidelines. Male C57BL/6 mice between 7 and 10 weeks old, purchased from Charles River Japan (Tokyo, Japan), were used in the present study.

Estimation of mechanical thresholds for hindpaw-withdrawal reflex. The mechanical thresholds for hindpaw-withdrawal reflex were measured using von Frey filaments²⁵. The forces produced by von Frey filaments were between 0.008 and 1.4 g (respective sizes: between 1.65 and 4.17). Mice were separately placed into a transparent plastic box with a mesh floor, and accustomed to the state for 30 min. The thresholds were determined from the minimal force at which hindpaw withdrawal reflex was induced more than twice in eight trials. Transient ischemia was applied to the left hindpaw of mice lightly anesthetized with 1% isoflurane. Urethane anesthesia (1.65 g/kg, i.p.) was also used for imaging experiments. A small rubber cuff was set around the left thigh, and covered with a hard plastic tube (Fig. 1a). Air pressure at 250 mmHg was applied for 30 min to the tubing connected to the cuff using a mercury manometer. The pressure was directed to the thigh, because inflation of the rubber cuff was limited by the hard plastic tube. We confirmed that this treatment was sufficient to produce transient ischemia of the hindpaw, as neural responses elicited by vibratory stimulation to the hindpaw were blocked by this manipulation (for example, Figs 2c,4b). No apparent impairment except reduced threshold of paw-withdrawal reflex was found in the left leg after the mice recovered from isoflurane anesthesia.

Imaging experiments. The surgical procedures were performed as described previously⁷. Mice were anesthetized with urethane (1.65 g/kg, i.p.), and a tracheotomy was performed for facilitating spontaneous respiration. During the experiments, body temperature was monitored using a rectal probe and maintained at 38°C using a silicon rubber heater. These surgical operations were usually finished within 60 min. Recordings were started at 30 min after the surgical operations. Additional doses of urethane (0.1–0.2 g/kg, s.c.) were administered when necessary. When spinal responses to hindpaw stimulation were investigated, the vertebral arch was removed at the T13 and L1 level, and the dorsal surface of the spinal cord with the intact dura mater was exposed. The surface was cleaned with saline, and covered with 2% agarose to prevent spinal movement. The surface of the agarose gel was covered with a mixture of petroleum jelly and liquid paraffin to prevent drying. The spinal cord was fixed under a microscope using a clamp (STS-A; Narishige, Tokyo, Japan). Spontaneous respiration was maintained during the imaging experiment, because the movement of the spinal cord caused by respiration was minimal.

Flavoprotein fluorescence imaging was performed as described previously⁷. Endogenous green fluorescence ($\lambda = 500\text{--}550\text{ nm}$) was recorded in blue light ($\lambda = 450\text{--}490\text{ nm}$). Images (128×168 pixels) of the spinal cord or S1 were recorded at 9 frames/s using a cooled charge coupled device camera (ORCA-R2; Hamamatsu Photonics, Hamamatsu, Japan). The camera was attached to a binocular epifluorescence microscope (M165 FC; Leica Microsystems, Wetzlar, Germany) with a 75-W xenon light source and a $1\times$ objective lens. Serial images were taken in recording sessions repeated at 50 s intervals. Brush vibration (amplitude: 0.2 mm; frequency: 50 Hz) was applied for 600 ms to the sole of the hindpaw using a mechanical stimulator (DPS-290; Dia Medical, Tokyo, Japan). When fine somatotopic maps were investigated in the spinal cord or S1, brush vibration was applied to each toe. Fluorescence changes elicited by the stimulation were averaged over 24 trials. Because it took approximately 20 min to obtain data from 24 trials, the recording time of the averaged data was defined as the middle point of the recording period. Spatial averaging in 5×5 pixels and temporal averaging in three consecutive frames were used for smoothing and improving the image quality. The images were normalized, pixel by pixel, with respect to a reference image, which was obtained by averaging five images taken immediately before the stimulation. In the figures, parts of the normalized images are shown in a pseudocolor scale representing the fractional fluorescence changes ($\Delta F/F_0$). The response amplitude was evaluated as values of $\Delta F/F_0$ in a square window of 100×25 pixels or $3.84 \times 0.96\text{ mm}$. The location of the window was adjusted to maximize the response amplitude in $\Delta F/F_0$. After the recordings, mice were euthanized with an overdose of pentobarbital (300 mg/kg, i.p.).

For investigating the S1 responses to hindpaw stimulation, the disinfected head skin was incised, and the skull over the right S1 was exposed. The surface of the skull was cleaned with sterile saline, and a small piece of metal was attached to the skull with dental acrylic resin (Super Bond; Sun Medical, Shiga, Japan) to fix the head under a microscope. The surface of the skull was covered with a mixture of petroleum jelly and liquid paraffin to keep the skull transparent. The response amplitude was evaluated as values of $\Delta F/F_0$ in a square window of 60×60 pixels or $1.55 \times 1.55\text{ mm}$.

Dorsal column lesioning. The left dorsal column was disrupted using an ultrasonic cutter (NE87; NSK, Kanuma, Japan) at the T11 level, as described previously⁷. To verify the lesion, the spinal cord was isolated after the recording experiments and fixed with 10% paraformaldehyde. Serial spinal cord sections of 100- μm thickness were cut using a microslicer (PRO-7; Dosaka, Kyoto, Japan), and the translucent images were observed.

Spinal application of LY354740 to the spinal cord. In behavioral experiments, LY354740 (10 nM, 5 μl), obtained from Santa Cruz Biotechnology (Santa Cruz, USA), was applied to the spinal cord with intrathecal injection before hindpaw ischemia. In imaging experiments of the spinal responses, epidural application and infiltration of 10 nM LY354740 for at least 30 min was performed before the epidural surface was covered with 2% agarose. Epidural application and infiltration of saline alone was naturally performed in other imaging experiments of the spinal responses. In imaging experiments of S1 responses, the epidural application and infiltration of 10 nM LY354740 or saline alone was performed at the T13–L1 level.

Statistics. Statistical significance in data was analyzed using StatView software (SAS Institute Inc., Cary, USA). Unpaired data obtained from different mice were evaluated by the Mann Whitney U-test. Paired data obtained from the same mice were evaluated by the Wilcoxon signed rank test. Only P values less than 0.05 are shown.

References

- Ochoa, J. L. & Torebjork, H. E. Paraesthesiae from ectopic impulse generation in human sensory nerves. *Brain* **103**, 835–853 (1980).
- Mogyoros, I., Bostock, H. & Burke, D. Mechanisms of paresthesias arising from healthy axons. *Muscle Nerve* **23**, 310–320 (2000).
- Calford, M. B. & Tweedale, R. Immediate and chronic changes in responses of somatosensory cortex in adult flying-fox after digit amputation. *Nature* **332**, 446–448 (1988).
- Tinazzi, M. *et al.* Transient deafferentation in humans induces rapid modulation of primary sensory cortex not associated with subcortical changes: a somatosensory evoked potential study. *Neurosci. Lett.* **223**, 21–24 (1997).
- Werhahn, K. J., Mortensen, J., Kaelin-Lang, A., Boroojerdi, B. & Cohen, L. G. Cortical excitability changes induced by deafferentation of the contralateral hemisphere. *Brain* **125**, 1402–1413 (2002).
- Bjorkman, A., Weibull, A., Rosen, B., Svensson, J. & Lundborg, G. Rapid cortical reorganisation and improved sensitivity of the hand following cutaneous anaesthesia of the forearm. *Eur. J. Neurosci.* **29**, 837–844 (2009).
- Komagata, S. *et al.* Initial phase of neuropathic pain within a few hours after nerve injury in mice. *J. Neurosci.* **31**, 4896–4905 (2011).
- Simmons, R. M., Webster, A. A., Kalra, A. B. & Iyengar, S. Group II mGluR receptor agonists are effective in persistent and neuropathic pain models in rats. *Pharmacol. Biochem. Behav.* **73**, 419–427 (2002).
- Bennett, G. J. & Xie, Y. K. A peripheral mononeuropathy in rat that produces disorders of pain sensation like those seen in man. *Pain* **33**, 87–107 (1988).
- Kim, S. H. & Chung, J. M. An experimental model for peripheral neuropathy produced by segmental spinal nerve ligation in the rat. *Pain* **50**, 355–363 (1992).
- Decosterd, I. & Woolf, C. J. Spared nerve injury: an animal model of persistent peripheral neuropathic pain. *Pain* **87**, 149–158 (2000).
- Tsuda, M. *et al.* P2 \times 4 receptors induced in spinal microglia gate tactile allodynia after nerve injury. *Nature* **424**, 778–783 (2003).

13. Campbell, J. N. & Meyer, R. A. Mechanisms of neuropathic pain. *Neuron* **52**, 77–92 (2006).
14. Basbaum, A. I., Bautista, D. M., Scherrer, G. & Julius, D. Cellular and molecular mechanisms of pain. *Cell* **139**, 267–284 (2009).
15. Shibuki, K. *et al.* Dynamic imaging of somatosensory cortical activity in the rat visualized by flavoprotein autofluorescence. *J. Physiol.* **549**, 919–927 (2003).
16. Yamashita, H. *et al.* Restoration of contralateral representation in the mouse somatosensory cortex after crossing nerve transfer. *PLoS One* **7**, e35676 (2012).
17. Yoshitake, K. *et al.* Visual map shifts based on whisker-guided cues in the young mouse visual cortex. *Cell Rep.* **5**, 1365–1374 (2013).
18. Tohmi, M., Meguro, R., Tsukano, H., Hishida, R. & Shibuki, K. The extrageniculate visual pathway generates distinct response properties in the higher visual areas of mice. *Curr. Biol.* **24**, 587–597 (2014).
19. Kubota, Y. *et al.* Transcranial photo-inactivation of neural activities in the mouse auditory cortex. *Neurosci. Res.* **60**, 422–430 (2008).
20. Tohmi, M., Kitaura, H., Komagata, S., Kudoh, M. & Shibuki, K. Enduring critical period plasticity visualized by transcranial flavoprotein imaging in mouse primary visual cortex. *J. Neurosci.* **26**, 11775–11785 (2006).
21. Llano, D. A., Theyel, B. B., Mallik, A. K., Sherman, S. M. & Issa, N. P. Rapid and sensitive mapping of long-range connections *in vitro* using flavoprotein autofluorescence imaging combined with laser photostimulation. *J. Neurophysiol.* **101**, 3325–3340 (2009).
22. Jongen, J. L. *et al.* Autofluorescent flavoprotein imaging of spinal nociceptive activity. *J. Neurosci.* **30**, 4081–4087 (2010).
23. Jain, N., Florence, S. L. & Kaas, J. H. Limits on plasticity in somatosensory cortex of adult rats: hindlimb cortex is not reactivated after dorsal column section. *J. Neurophysiol.* **73**, 1537–1546 (1995).
24. Peschanski, M., Briand, A., Gautron, M. & Guilbaud, G. Electrophysiological evidence for a role of the anterolateral quadrant of the spinal cord in the transmission of noxious messages to the thalamic ventrobasal complex in the rat. *Brain Res.* **342**, 77–84 (1985).
25. Amaya, F., Samad, T. A., Barrett, L., Broom, D. C. & Woolf, C. J. Perianglionic inflammation elicits a distally radiating pain hypersensitivity by promoting COX-2 induction in the dorsal root ganglion. *Pain* **142**, 59–67 (2009).
26. Kitaura, H., Hishida, R. & Shibuki, K. Transcranial imaging of somatotopic map plasticity after tail cut in mice. *Brain Res.* **1319**, 54–59 (2010).
27. Takahashi, Y. *et al.* Organization of cutaneous ventrodorsal and rostrocaudal axial lines in the rat hindlimb and trunk in the dorsal horn of the spinal cord. *J. Comp. Neurol.* **445**, 133–144 (2002).
28. Woolsey, T. A. & Van der Loos, H. The structural organization of layer IV in the somatosensory region (SI) of mouse cerebral cortex. The description of a cortical field composed of discrete cytoarchitectonic units. *Brain Res.* **17**, 205–242 (1970).
29. Nelson, R. J., Sur, M., Felleman, D. J. & Kaas, J. H. Representations of the body surface in postcentral parietal cortex of Macaca fascicularis. *J. Comp. Neurol.* **192**, 611–643 (1980).
30. Gelgor, L., Phillips, S. & Mitchell, D. Hyperalgesia following ischaemia of the rat's tail. *Pain* **24**, 251–257 (1986).
31. Coderre, T. J., Xanthos, D. N., Francis, L. & Bennett, G. J. Chronic post-ischemia pain (CPIP): a novel animal model of complex regional pain syndrome-type I (CRPS-I; reflex sympathetic dystrophy) produced by prolonged hindpaw ischemia and reperfusion in the rat. *Pain* **112**, 94–105 (2004).
32. Horlocker, T. T. *et al.* Anesthetic, patient, and surgical risk factors for neurologic complications after prolonged total tourniquet time during total knee arthroplasty. *Anesth. Analg.* **102**, 950–955 (2006).
33. Welbourn, R. *et al.* Role of neutrophil adherence receptors (CD 18) in lung permeability following lower torso ischemia. *Circ. Res.* **71**, 82–86 (1992).
34. Germann, G., Drucke, D. & Steinau, H. U. Adhesion receptors and cytokine profiles in controlled tourniquet ischaemia in the upper extremity. *J. Hand. Surg. Br.* **22**, 778–782 (1997).
35. Takahashi, K. *et al.* Transcranial fluorescence imaging of auditory cortical plasticity regulated by acoustic environments in mice. *Eur. J. Neurosci.* **23**, 1365–1376 (2006).
36. Rexed, B. A cytoarchitectonic atlas of the spinal cord in the cat. *J. Comp. Neurol.* **100**, 297–379 (1954).
37. Moore, K. A. *et al.* Partial peripheral nerve injury promotes a selective loss of GABAergic inhibition in the superficial dorsal horn of the spinal cord. *J. Neurosci.* **22**, 6724–6731 (2002).
38. Terashima, Y. *et al.* Changes in synaptic transmission of substantia gelatinosa neurons in a rat model of lumbar radicular pain revealed by *in vivo* patch-clamp recording. *Pain* **152**, 1024–1032 (2011).
39. Woolf, C. J. & Fitzgerald, M. The properties of neurones recorded in the superficial dorsal horn of the rat spinal cord. *J. Comp. Neurol.* **221**, 313–328 (1983).
40. Jia, H., Rustioni, A. & Valtschanoff, J. G. Metabotropic glutamate receptors in superficial laminae of the rat dorsal horn. *J. Comp. Neurol.* **410**, 627–642 (1999).
41. Jones, C. K., Eberle, E. L., Peters, S. C., Monn, J. A. & Shannon, H. E. Analgesic effects of the selective group II (mGlu2/3) metabotropic glutamate receptor agonists LY379268 and LY389795 in persistent and inflammatory pain models after acute and repeated dosing. *Neuropharmacology* **49 Suppl 1**, 206–218 (2005).
42. Goudet, C. *et al.* Metabotropic receptors for glutamate and GABA in pain. *Brain Res. Rev.* **60**, 43–56 (2009).
43. Irie, T., Fukui, I. & Ohmori, H. Activation of GIRK channels by muscarinic receptors and group II metabotropic glutamate receptors suppresses Golgi cell activity in the cochlear nucleus of mice. *J. Neurophysiol.* **96**, 2633–2644 (2006).
44. Lee, C. C. & Sherman, S. M. Topography and physiology of ascending streams in the auditory tectothalamic pathway. *Proc. Natl. Acad. Sci. U. S. A.* **107**, 372–377 (2010).
45. Koga, K., Iwahori, Y., Ozaki, S. & Ohta, H. Regulation of spontaneous Ca(2+) spikes by metabotropic glutamate receptors in primary cultures of rat cortical neurons. *J. Neurosci. Res.* **88**, 2252–2262 (2010).
46. Coull, J. A. *et al.* Trans-synaptic shift in anion gradient in spinal lamina I neurons as a mechanism of neuropathic pain. *Nature* **424**, 938–942 (2003).
47. Wake, H. *et al.* Early changes in KCC2 phosphorylation in response to neuronal stress result in functional downregulation. *J. Neurosci.* **27**, 1642–1650 (2007).
48. Lavertu, G., Cote, S. L. & De Koninck, Y. Enhancing K-Cl co-transport restores normal spinothalamic sensory coding in a neuropathic pain model. *Brain* **137**, 724–738 (2014).
49. Melzack, R. & Wall, P. D. Pain mechanisms: a new theory. *Science* **150**, 971–979 (1965).
50. Daniele, C. A. & MacDermott, A. B. Low-threshold primary afferent drive onto GABAergic interneurons in the superficial dorsal horn of the mouse. *J. Neurosci.* **29**, 686–695 (2009).
51. Palecek, J. *et al.* Responses of spinothalamic tract neurons to mechanical and thermal stimuli in an experimental model of peripheral neuropathy in primates. *J. Neurophysiol.* **68**, 1951–1966 (1992).
52. Schmidtke, A., Tegeder, I. & Geisslinger, G. No NO, no pain? The role of nitric oxide and cGMP in spinal pain processing. *Trends Neurosci.* **32**, 339–346 (2009).
53. Inoue, K. The function of microglia through purinergic receptors: neuropathic pain and cytokine release. *Pharmacol. Ther.* **109**, 210–226 (2006).

54. Ikeda, H., Heinke, B., Ruscheweyh, R. & Sandkuhler, J. Synaptic plasticity in spinal lamina I projection neurons that mediate hyperalgesia. *Science* **299**, 1237–1240 (2003).
55. Ikeda, H., Kiritoshi, T. & Murase, K. Synaptic plasticity in the spinal dorsal horn. *Neurosci. Res.* **64**, 133–136 (2009).

Acknowledgements

We thank S. Maruyama and A. Matsushima for their technical assistance. This work was supported by a Grant-in-Aid for Scientific Research (No. 22115011) and Core Research for Evolutional Science and Technology program (CREST) from the Japanese Government.

Author Contributions

T.W., M.S., S.K., and K.S. designed the experiments; T.W., M.S. and H.T. conducted experiments; T.W., H.T., R.H., T.K., H.B. and K.S. analyzed the data; T.K. and H.B. provided materials; T.W., and K.S. wrote the manuscript.

Additional Information

Supplementary information accompanies this paper at <http://www.nature.com/srep>

Competing financial interests: The authors declare no competing financial interests.

How to cite this article: Watanabe, T. *et al.* Spinal mechanisms underlying potentiation of hindpaw responses observed after transient hindpaw ischemia in mice. *Sci. Rep.* **5**, 11191; doi: 10.1038/srep11191 (2015).



This work is licensed under a Creative Commons Attribution 4.0 International License. The images or other third party material in this article are included in the article's Creative Commons license, unless indicated otherwise in the credit line; if the material is not included under the Creative Commons license, users will need to obtain permission from the license holder to reproduce the material. To view a copy of this license, visit <http://creativecommons.org/licenses/by/4.0/>

Delineation of a frequency-organized region isolated from the mouse primary auditory cortex

◎ Hiroaki Tsukano,¹ Masao Horie,² Takeshi Bo,¹ Arikuni Uchimura,³ Ryuichi Hishida,¹ Masaharu Kudoh,⁴ Kuniyuki Takahashi,⁵ Hirohide Takebayashi,² and Katsuei Shibuki¹

¹Department of Neurophysiology, Brain Research Institute, Niigata University, Niigata, Japan; ²Division of Neurobiology and Anatomy, Graduate School of Medicine and Dental Sciences, Niigata University, Niigata, Japan; ³KOKORO-Biology Group, Laboratories for Integrated Biology, Graduate School of Frontier Biosciences, Osaka University, Osaka, Japan; ⁴Department of Physiology, Teikyo University School of Medicine, Tokyo, Japan; and ⁵Department of Otolaryngology, Graduate School of Medicine and Dental Sciences, Niigata University, Niigata, Japan

Submitted 21 November 2014; accepted in final form 17 February 2015

Tsukano H, Horie M, Bo T, Uchimura A, Hishida R, Kudoh M, Takahashi K, Takebayashi H, Shibuki K. Delineation of a frequency-organized region isolated from the mouse primary auditory cortex. *J Neurophysiol* 113: 2900–2920, 2015. First published February 18, 2015; doi:10.1152/jn.00932.2014.—The primary auditory cortex (AI) is the representative recipient of information from the ears in the mammalian cortex. However, the delineation of the AI is still controversial in a mouse. Recently, it was reported, using optical imaging, that two distinct areas of the AI, located ventrally and dorsally, are activated by high-frequency tones, whereas only one area is activated by low-frequency tones. Here, we show that the dorsal high-frequency area is an independent region that is separated from the rest of the AI. We could visualize the two distinct high-frequency areas using flavoprotein fluorescence imaging, as reported previously. SMI-32 immunolabeling revealed that the dorsal region had a different cytoarchitectural pattern from the rest of the AI. Specifically, the ratio of SMI-32-positive pyramidal neurons to nonpyramidal neurons was larger in the dorsal high-frequency area than the rest of the AI. We named this new region the dorsomedial field (DM). Retrograde tracing showed that neurons projecting to the DM were localized in the rostral part of the ventral division of the medial geniculate body with a distinct frequency organization, where few neurons projected to the AI. Furthermore, the responses of the DM to ultrasonic courtship songs presented by males were significantly greater in females than in males; in contrast, there was no sex difference in response to artificial pure tones. Our findings offer a basic outline on the processing of ultrasonic vocal information on the basis of the precisely subdivided, multiple frequency-organized auditory cortex map in mice.

auditory cortex; mapping; multiple frequency organization; courtship song; mice

THE PRIMARY SENSORY CORTEX of the mammalian brain is widely known to receive the first thalamic inputs that convey peripheral sensory information, such as hearing and vision. In the auditory cortex, the primary auditory cortex (AI) is the main recipient of information from the ears into the cortex and transfers this information to higher-order auditory cortical regions (Kaas and Hackett 2000). The AI is important in terms of being both the receiver and the relay point in hierarchical auditory processing and has been studied using various animals, including mice.

Address for reprint requests and other correspondence: H. Tsukano, Dept. of Neurophysiology, Brain Research Institute, Niigata Univ., 1-757 Asahimachidori, Chuo-ku, Niigata 951-8585, Japan (e-mail: tsukano-nii@umin.ac.jp).

The mouse is widely used in auditory physiological research because of its merits as an animal model in auditory cortical studies involving two-photon Ca²⁺ imaging (Bandyopadhyay et al. 2010; Bathellier et al. 2012; Honma et al. 2013; Issa et al. 2014; Rothschild et al. 2010), voltage-sensitive imaging (Sawatari et al. 2011; Takahashi et al. 2006), anatomical studies (Barkat et al. 2011; Hackett et al. 2011; Hofstetter and Ehret 1992; Horie et al. 2013; Llano and Sherman 2008; Oviedo et al. 2010), genetic manipulation (Barkat et al. 2011; Rotschafer and Razak 2013; Xiong et al. 2012), and behavioral analysis (Tsukano et al. 2011). Accordingly, the attainment of precise knowledge of the AI in mice is essential. However, the delineation of the map of the mouse auditory cortex is under debate, as maps obtained by electrophysiology have been amended in recent studies using optical imaging.

The classical mouse auditory cortex map was drawn using unit recording. The anterior auditory field (AAF) and AI with clear frequency gradients are placed at the center as the core and are surrounded by the belt region, considered the higher-order region, including the secondary auditory field (AII), the ultrasonic field (UF), and the dorsoposterior field (DP) (Stiebler et al. 1997). The AAF and AI have frequency-organized arrangements covering the frequencies up to 40 kHz; neurons with characteristic frequency over 50 kHz are localized in the UF (Fig. 1A). A subsequent study indicated that a distinct UF region does not exist, with the AAF and AI having the full range of frequency organization, processing sounds from 4 kHz up to 64 kHz (Guo et al. 2012). The term “UF” has thus been redefined as subparts within the AAF and AI that process high-frequency sounds (Fig. 1B). Recently, however, Issa et al. (2014) have reported elegantly that the AI is divided into two rostral areas that process high-frequency tones, despite only one caudal area being activated by low-frequency tones. This leads to the generation of forked, dual-frequency gradients inside of the AI (Issa et al. 2014). The larger dorsal branch of the fork-shaped frequency gradients travels toward the high-frequency area of the AI, referred to as the UF, as reported by Guo et al. (2012), whereas the smaller ventral division has an axis of the frequency organization toward the AII (Fig. 1C) (Issa et al. 2014). This new map was obtained using optical imaging. Moreover, they clearly revealed that the direction of the frequency organization of the AAF was present and is directed from the dorsorostral to ventrocaudal direction. Their study used transgenic mice, in which the calcium-

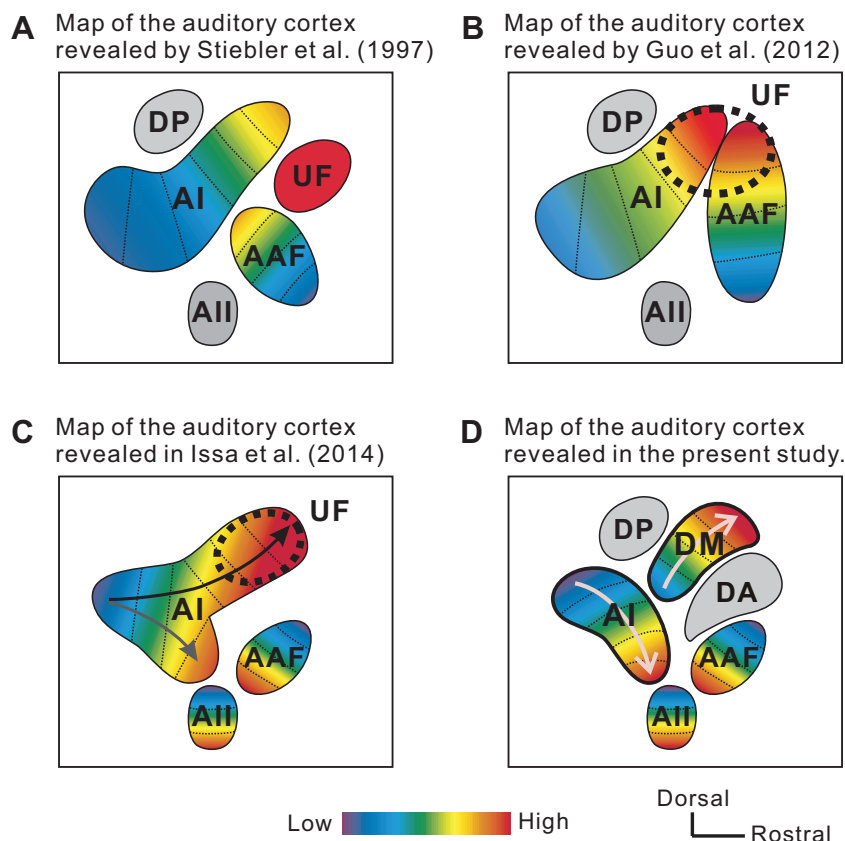


Fig. 1. Schematic maps of the mouse auditory cortex in previous studies and the present study. *A*: schematic map of the auditory cortex in Stiebler et al. (1997). Frequency gradients of the anterior auditory field (AAF) and primary auditory cortex (AI) included neurons with characteristic frequencies up to 40 kHz, and neurons with characteristic frequencies higher than 50 kHz are located in the distinct ultrasonic field (UF). *B*: map of the auditory cortex in Guo et al. (2012). The AAF and AI had ultrasonic bands higher than 50 kHz. The UF was interpreted to be high-frequency subparts in the high-frequency area of the AAF and AI but not a distinct region. *A* and *B*: these maps were drawn according to the results obtained by unit recording. *C*: map of the auditory cortex in Issa et al. (2014), showing 2 streams of frequency gradients inside of the AI. The major gradient runs toward the dorsal part, including the UF area, whereas the minor gradient runs toward the secondary auditory field (AII). The direction of the frequency organization of the AAF is drawn along the ventrocaudal axis, consistent with the data reported by Horie et al. (2013). *D*: map of the auditory cortex reported in the present study. Newly delineated, distinct region dorsomedial field (DM) was isolated from the AI high-frequency area. The direction of the frequency organization of the AI is the one traveling toward AII. The direction of the frequency organization of the AAF matches that reported in the previous studies (Horie et al. 2013; Issa et al. 2014). The region that Stiebler et al. (1997) defined as UF [referred to as dorsoanterior field (DA)] responds to slow-frequency modulation (FM) components, regardless of tonal frequency range. *C* and *D*: these maps were drawn according to the results obtained by optical imaging. DP, dorsoposterior field.

sensitive protein GCaMP3 was initially expressed uniformly, offering much better spatial resolution regarding the auditory cortical surface than that achieved by unit recording. Principally, however, previous anatomical studies reported that frequency-organized maps in the AAF and AI reflect distinct topological projections from frequency-organized maps in the medial and lateral parts, respectively, of the ventral division of the medial geniculate body (MGv; MGB) in mice as well (Horie et al. 2013; Takemoto et al. 2014). Moreover, various mammals have multiple frequency-organized regions with distinct, unique frequency direction (Higgins et al. 2010; Kalatsky et al. 2005; Kanold et al. 2014); spectral, temporal, and spatial sensitivities (Bizley et al. 2009; Imaizumi et al. 2004; Polley et al. 2007); and thalamocortical projections (Lee et al. 2004; Storace et al. 2010, 2012) without redundancy. The mouse AI, therefore, would be exceptional if the fork-shaped frequency gradients existed inside of a single region.

In this study, we tried to clarify whether the frequency gradient inside of the AI proceeds in a straight line or shows a forked shape. For this purpose, we used a combination of flavoprotein autofluorescence imaging and anatomical techniques. Flavoproteins are endogenous fluorescent proteins in mitochondria, and fluorescence imaging of these proteins has been used to map precisely the auditory cortex (Honma et al. 2013; Horie et al. 2013; Kubota et al. 2008; Ohshima et al. 2010; Takahashi et al. 2006), visual cortex (Andermann et al. 2011; Tohmi et al. 2009, 2014; Yoshitake et al. 2013), somatosensory cortex (Komagata et al. 2011), and insular cortex (Gogolla et al. 2014). With the use of this technique, we reproduced the finding that the mouse AI is divided into two areas in response to high-frequency tones

(Issa et al. 2014; Tsukano et al. 2013a). Additionally, we used SMI-32 immunolabeling, which has been used to partition various cortical regions (Boire et al. 2005; Budinger et al. 2000; Mellott et al. 2010; Ouda et al. 2012; Paxinos et al. 2009; Rothschild et al. 2010; van der Gucht et al. 2001; Wong and Kaas 2009) to investigate the cytoarchitecture in the two AI high-frequency areas. We found that the dorsal part of the AI high-frequency area is a different region from the rest of the AI, including the low-frequency area and the ventral high-frequency area, and the posterior frequency-organized region, which is referred to as the AI, is restricted to the low-frequency area and the ventral high-frequency area that has been considered as a supplemental AI area in the study by Issa et al. (2014) (Fig. 1*D*). Existence of multiple frequency organizations in the mouse auditory cortex may unify the auditory cortical maps of mice and other mammals.

METHODS

Animals. The Committee for Animal Care at Niigata University approved the experimental protocols used in this study. We used 5- to 7-wk-old C57BL/6 mice ($n = 197$; Charles River Japan, Yokohama, Japan), 7- to 9-wk-old Balb/c mice ($n = 3$; Charles River Japan), and 7- to 9-wk-old CBA/CaJ mice ($n = 3$; The Jackson Laboratory, Bar Harbor, ME). The animals were housed in cages with ad libitum access to food pellets and water and were kept on a 12-h light/dark cycle. Male and female mice used in the experiments (see Fig. 14) were 6-wk-old C57BL/6 mice, produced in our institute, and they were not housed with mice of the opposite sex after weaning at 3 wk old.

In vivo flavoprotein fluorescence imaging. In vivo flavoprotein fluorescence imaging was performed, as described in our previous studies (Takahashi et al. 2006; Tsukano et al. 2013b). Mice were

deeply anesthetized with urethane (1.7 g/kg ip; Wako, Osaka, Japan), and their rectal temperatures were maintained at 37°C. After local anesthesia using bupivacaine, the skin and temporal muscle over the right auditory cortex were incised. A piece of metal was attached to the skull with dental resin, and the head was fixed by screwing the metal piece onto a manipulator. The skull over the auditory cortex was removed in mice used for some experiments (see Figs. 2B, 3, 4, 6, 8, 12, and 13) to compare response patterns of the auditory cortex or further tracer-injection experiments. Transcranial imaging was performed in the other experiments. The right auditory cortex was observed unless otherwise noted. The exposed surface of the intact skull was covered with liquid paraffin (Wako) to keep the skull transparent in transcranial imaging. Cortical images (128 × 168 pixels after binning) of endogenous green fluorescence ($\lambda = 500\text{--}550$ nm) in blue light ($\lambda = 470\text{--}490$ nm) were recorded using a cooled charge-coupled device (CCD) camera system (AQUACOSMOS with ORCA-R2 camera; Hamamatsu Photonics, Hamamatsu, Japan). Images were taken at 9.7 Hz [54 Hz in some experiments (see Figs. 11 and 14, C–E)]. Images were averaged over 20 trials unless otherwise noted. Spatial averaging of 5 × 5 pixels was applied. Images were calculated as fluorescence change (ΔF)/baseline intensity (F_0), where $\Delta F = F - F_0$. The F_0 was obtained by averaging the intensity values during the prestimulus period (~500 ms). The response amplitude was evaluated as $\Delta F/F_0$ in a circle window with a diameter of 20 pixels. When the frequency organization was evaluated (see Figs. 5 and 7), a circle window with a diameter of 15 pixels was chosen to give the largest response amplitude, and the location of the center pixel was considered to be the frequency-specific response peak.

In vivo two-photon calcium imaging. Calcium imaging was performed using a two-photon microscope (TCS SP5 MP; Leica Microsystems, Wetzlar, Germany) with a hybrid detector (HyD; Leica Microsystems) and a Ti:Sapphire mode-locked femto second laser (Chameleon Vision; Coherent, Santa Clara, CA), as described in our previous studies (Honma et al. 2013; Tohmi et al. 2014; Yoshitake et al. 2013). Calcium-sensitive dye was prepared by dissolving Fura-2 AM (Invitrogen Life Technologies, Boston, MA) in 20% (w/v) Pluronic F-127 in DMSO (Invitrogen Life Technologies) and diluted with Ringer solution containing sulforhodamine 101 (SR-101; Invitrogen Life Technologies). After anesthetic induction with urethane (1.9 g/kg ip), craniotomy, and localization using flavoprotein fluorescence imaging, a solution of calcium-sensitive dye was pressure injected (5–20 kPa) for 5–10 min into *layer II/III* using glass pipettes (tip diameter: 2–4 μm). Astrocytes were distinguished from neurons using SR-101. After injection, the pipette was withdrawn, and the craniotomy was covered with 2% agarose (1-B; Sigma-Aldrich, St. Louis, MO) and a thin cover glass (thickness <0.15 mm; Matsunami, Osaka, Japan), which was fixed to the skull with dental cement (Sun Medical, Shiga, Japan). Excitation wavelength for Fura-2 was 800 nm, and that for SR-101 was 900–950 nm. Images (256 × 256 pixels) were recorded at 3.7 Hz in a 260 × 260- μm region.

The data were realigned using AQUACOSMOS and MATLAB software (MathWorks, Natick, MA). Data from five to six trials of the same stimulation were averaged. Size-matched regions of interest (ROIs) were chosen. Data were calculated as $\Delta F/F_0$, where $\Delta F = F - F_0$. The F_0 was obtained by averaging the intensity values during the prestimulus period (~3 s). The response of each neuron was defined as the maximum value in poststimulus observation windows (~5 s). Neurons were defined as responsive when the response peak was >4 SD above the baselines during the prestimulus period to minimize errors by baseline fluctuations. The best frequency (BF) of a neuron was defined as the frequency to which the neuron had the greatest response. We examined the correlation between frequency and location and computed a regression line. The direction of the frequency organization was defined so as to make the correlation coefficient as large as possible. Then, we examined the residuals as a measure of deviation from the frequency organization. The bandwidth of tuning curves was defined as the logarithmic ratio of minimum and maxi-

um frequencies that resulted in a response >75% of the peak amplitude.

Auditory stimuli. Tones were made by a computer using a custom-written LabVIEW program (National Instruments, Austin, TX) at a sampling rate of 500 kHz. Courtship songs of a male mouse, emitted when he was placed with a familiar female mouse in estrous in the same cage, were recorded using the recording software Avisoft-RECORDER (Avisoft Bioacoustics, Glienicke, Germany) at a sampling frequency of 250 kHz, with a microphone (CM16/CPMA; Avisoft Bioacoustics) and a preamplifier (UltraSoundGate 116; Avisoft Bioacoustics). Sounds were low-pass filtered at 150 kHz (3624; NF, Kanagawa, Japan). Pure tones at frequencies of 5–80 kHz were amplitude modulated by 20 Hz sine wave. A speaker for 5–40 kHz (SRS-3050A; Stax, Saitama, Japan) or 50–80 kHz (ES105A; Murata, Kyoto, Japan) was set 10 cm in front of the mice. Sound intensity was calibrated using the microphone (types 4135 and 2669; Brüel & Kjær, Nærum, Denmark) and the sound level meter (type 2610; Brüel & Kjær). The sound intensity was 60 dB sound pressure level (SPL) for flavoprotein fluorescence imaging and 80 dB SPL for two-photon imaging. The sound duration was 500 ms with a rise/fall time of 10 ms. The desired sound spectrum was determined using a digital spectrum analyzer (R9211A; Advantest, Tokyo, Japan) or the custom-written LabVIEW program. When the UF and DP (Stiebler et al. 1997) were activated specifically, frequency modulation (FM) direction-reversal stimulation (24 kHz/s) was used (Honma et al. 2013). The sound intensity was set to 60 dB SPL, and the band frequency was between 5 and 11 kHz.

Acoustic exposure. For acoustic exposure experiments (see Figs. 9 and 10), home cages were placed in the sound-shielded chamber and exposed to a 5- or 35-kHz sound stimulus through a speaker (SRS-3050A; Stax) placed above the cage. The exposure sound consisted of an amplitude-modulated tone with a carrier frequency of 5 or 35 kHz and modulation frequency of 20 Hz. Duration of the tones was 500 ms, and a rise/fall time was 10 ms. The sound intensity was adjusted to 70 dB SPL at the floor of the cage. This tonal stimulus was repeated at 1 Hz throughout the exposing periods (P7–P35). Mice of normal groups were reared in the normal cages. Mice of quiet groups were reared in the chamber but not exposed to any tones. Flavoprotein fluorescence imaging was performed within 1 wk after exposure was finished. When a circular window was put on the response of the dorsomedial field (DM) to evaluate response amplitudes, a window was put to make the response amplitude maximum, kept >22 pixels apart dorsal to the AI response peak, according to the data (see Fig. 2E).

Retrograde tracer experiments. To visualize neurons in the MGB projecting to each cortical region, a neural tracer was injected into the center of each region identified by flavoprotein fluorescence imaging (Horie et al. 2013). A glass capillary (tip diameter 20–30 μm) filled with tracer solution and a platinum wire was introduced into the center of the subregion of the right auditory cortex to ~500 μm below the surface. Alexa Fluor 488- or 555-conjugated cholera toxin subunit B (CTB; Molecular Probes, Eugene, OR) was used in injections (see Fig. 13). Fluorescein and Texas Red (Molecular Probes) were used in some animals, but the results were the same. Fluorescent CTB solution (0.5% in phosphate buffer) was injected iontophoretically by a 5- μA pulse current (5 s on; 5 s off) for 15 min. In some experiments (see Figs. 8 and 12), biotinylated dextran amine (BDA; molecular weight 3,000; Molecular Probes) was injected iontophoretically by a 5- μA pulse current (7 s on; 7 s off) for 15 min. Survival of 3 days for fluorescent CTB or 7 days for BDA was ensured until perfusion. After anesthetizing mice deeply with pentobarbital (1.0 g/kg ip), the brains were dissected and immersed in 4% paraformaldehyde overnight, and a consecutive series of 40- μm -thick coronal or horizontal sections was cut using a sliding cryotome. To observe fluorescent tracers, sections were mounted on glass slides and covered with Fluoromount (Cosmo Bio, Tokyo, Japan).

To visualize BDA, sections were rinsed initially in 20 mM PBS and incubated in PBS containing 3% hydrogen peroxide and 0.1% Triton X-100 for 15 min at room temperature. After rinsing in 20 mM PBS containing 0.1% Triton X-100 (PBST), the sections were incubated for 40 min in 20 mM PBST containing avidin-biotin peroxidase complex (Vectastain ABC kit; Vector Laboratories, Burlingame, CA). Sections were rinsed in 20 mM PBS, and BDA was visualized in a solution comprising 0.05% diaminobenzidine tetrahydrochloride and 0.003% hydrogen peroxide in 50 mM Tris-HCl buffer (pH 7.4) for 20 min. All sections were finally, thoroughly rinsed in 50 mM Tris-HCl buffer and mounted onto gelatin-coated slides. Adjacent sections were counterstained using 0.1% cresyl violet (Chroma Gesellschaft, Kongen, Germany). After the mounted sections had dried, they were dehydrated in a graded ethanol series, cleared in xylene, and coverslipped using the covering reagent Bioleat (Okenshoji, Tokyo, Japan).

The borders of the MGB subdivisions were delineated, according to the SMI-32 immunolabeling pattern (Honma et al. 2013; Horie et al. 2013; LeDoux et al. 1985, 1987) and an atlas (Paxinos 2003; Paxinos and Franklin 2001; Paxinos et al. 2009). The immunohistochemistry of SMI-32 reacts with a nonphosphorylated epitope in neurofilament M and H (NNF). Sections were rinsed and incubated in PBST containing 3% hydrogen peroxide, as described for BDA visualization. After rinsing in 20 mM PBS, the sections were incubated overnight at room temperature with the monoclonal antibody (MAb) SMI-32 (1:2,000; Covance Research Products, Berkeley, CA) (Sternberger and Sternberger 1983), diluted with 20 mM PBS containing 0.5% skim milk. Sections were then incubated in anti-mouse IgG (1:100; MBL, Nagoya, Japan) at room temperature for 2 h. The sections were rinsed in 20 mM PBS, and the immunoreactions were visualized in a Tris-HCl buffer containing 0.05% diaminobenzidine tetrahydrochloride and 0.003% hydrogen peroxide for 5 min at room temperature. After visualization, the sections were coverslipped. All sections were observed under the light microscope (Eclipse Ni; Nikon, Tokyo, Japan) and a CCD camera (DS-Fi2; Nikon). The drawings and images were prepared using CorelDRAW (E Frontier, Tokyo, Japan), Illustrator (Adobe Systems, San Jose, CA), and Photoshop (Adobe Systems) software.

AAV injection to investigate interhemispheric connectivity. To confirm that the corresponding subareas have interhemispheric connections with each other via the corpus callosum, adeno-associated virus (AAV) vector for GCaMP3 expression (Penn Vector Core, Philadelphia, PA) was injected into an area of the right AI after functional identification, which stains the axonal branches reaching the contralateral auditory cortex (see Fig. 3). A glass capillary (tip diameter: 20–30 μm) filled with AAV solution (500 μL) was introduced to a depth of 500 μm from the surface and slowly pressure injected for 30 min by a custom-made pump. After injection, the hole in the skull was covered with 2% agarose (1-B; Sigma-Aldrich), and the skin was sutured. Mice were recovered from anesthesia in their home cages. Two weeks after the injection, the left auditory cortex was observed using an epifluorescence microscope [excitation (Ex), 470–490 nm; emission (Em), 500–550 nm] and a two-photon microscope (Ex, 900 nm; Em, 500–550 nm).

Statistics. The Mann-Whitney U-test or Wilcoxon signed-rank test was used to evaluate differences between unpaired or paired data from two groups, respectively. When data from three groups were compared, Tukey-Kramer test was used as a post hoc test after ANOVA. The correlation coefficients and the *P* values were calculated using Spearman rank correlation test. When the difference between two slopes was evaluated, the slope test was performed. The χ^2 test was used to evaluate the difference between two percentages. These tests were performed using SPSS (IBM, Tokyo, Japan) or MATLAB software. All of the data in the text and graphs are presented as means \pm SE.

RESULTS

Finding the new, distinct region identified from the AI. Prior imaging studies have identified distinct auditory cortical regions based on response magnitudes to tones and the topographic organization of tone-frequency responses (cochleotopy) (Harel et al. 2000; Horie et al. 2013; Kubota et al. 2008; Sawatari et al. 2011; Takahashi et al. 2006). In this study, we try to confirm frequency organizations by demonstrating distinct response magnitude peaks and mirror-reversed frequency organization in the AAF and AI using flavoprotein fluorescence imaging. In addition, we try to observe flavoprotein fluorescence responses precisely within a cortical region, typically defined as the AI in mice, according to the Paxinos anatomic atlas (Paxinos and Franklin 2001). First, we observed neural responses in the right auditory cortex of C57BL/6 mice in a 5- to 70-kHz range after craniotomy (Fig. 2A). The frequency-organized map of the AI was arranged in a caudal-rostral direction. Although only one area was activated in response to a 5-kHz tone, the AI responses to a 40-kHz tone were observed in two different areas, which were dorsoventrally separated from each other, as reported previously (Fig. 2B) (Issa et al. 2014; Tsukano et al. 2013a). We also confirmed that the AI high-frequency area showed two different response peaks when stimulated by high-frequency tones using transcranial flavoprotein fluorescence imaging (Fig. 2C). Significantly separated double peaks in $\Delta F/F_0$ were found by positioning serial ROIs across both dorsal and ventral AI high-frequency areas (Fig. 2E; $P < 0.01$ between ROI 6 vs. 11; $P < 0.05$ between ROI 11 vs. 20). These data confirmed the presence of apparently separated AI high-frequency areas in mice. The regions overlapped to the places where Stiebler et al. (1997) drew the UF and DP in their auditory cortical map, hereby referred to as Stiebler's UF and DP in this report, were confirmed by several studies (Honma et al. 2013; Joachimsthaller et al. 2014; Stiebler et al. 1997), and both areas are known to be activated by directional changes of slow FM sounds (Honma et al. 2013; Tsukano et al. 2013b). Moreover, cortical responses to ultrasonic sounds are not specific enough to divide the broad area into specific subareas. Therefore, we verified whether the dorsal high-frequency area of the AI overlaps Stiebler's UF or DP using FM directional changes. The dorsal area of the AI mapped between Stiebler's UF and DP (Fig. 2D). To evaluate these data quantitatively, we positioned ROIs across Stiebler's UF and DP, and the same ROIs were placed onto the image of the responses to a 35-kHz tone obtained from the same mouse (Fig. 2F). The response peaks of the dorsal area of the AI did not overlap Stiebler's UF or DP (Fig. 2F; $P < 0.05$ at ROI 9; $P < 0.05$ at ROI 21; $P < 0.05$ at ROI 31). The observation that the AI was divided into two areas in the response to high-frequency tones was also made in the left auditory cortex (data not shown). We visualized the auditory cortex in CBA/CAJ and Balb/c mice as well. The structures of responses of the AAF, AI, and AII were the same among three strains, and the AI was divided into two areas in response to high-frequency tones (data not shown). These results, along with prior studies, suggest that intrinsic response peaks identify functionally distinct regions in the auditory cortex (Kalatsky et al. 2005).

It remains unclear how auditory cortical regions, defined according to sound-response magnitudes, align with traditional

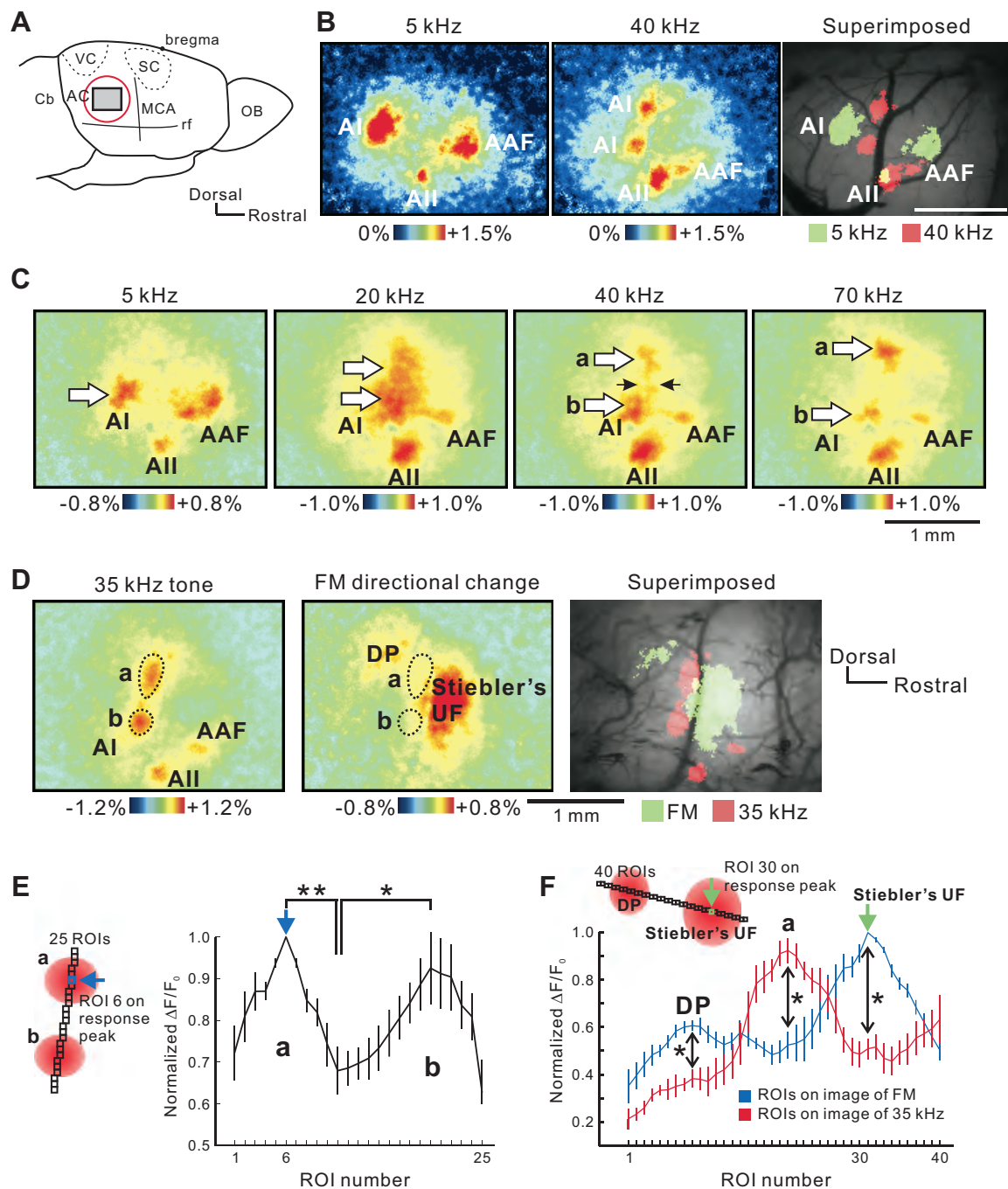


Fig. 2. Two distinct responses to high-frequency tones in the AI. *A*: schematic drawing of the mouse auditory cortex. Auditory cortex (AC); cerebellum (Cb); medial cerebral artery (MCA); olfactory bulb (OB); rhinal fissure (rf); somatosensory cortex (SC); visual cortex (VC). *B*: neural responses to a 5- or 40-kHz tone obtained by flavoprotein fluorescence imaging in a mouse with craniotomy. The AI in response to a 40-kHz tone area was divided into 2 parts. Three images were obtained from the same mouse. Scale bar, 1 mm. *C*: neural responses to 5–70 kHz tones revealed by transcranial flavoprotein fluorescence imaging. The caudal AI low-frequency area was clearly activated. When 20–70 kHz tones were presented, the AI high-frequency area was divided into 2 parts: the dorsal part (a) and the ventral part (b), indicated by white arrows. Four images were obtained from the same mouse. *D*: positional relationship between the dorsal part of the AI high-frequency area and Stiebler's UF and DP. Stiebler's UF and DP were activated by slow FM directional changes (Honma et al. 2013). Three images were obtained from the same mouse. *E*: quantitative analysis of response slopes by a 35-kHz tone. Regions of interest (ROIs) were placed across the 2 highest peaks in the AI high-frequency areas, and the significant double peaks in fluorescence change (ΔF)/baseline intensity (F_0) were drawn ($*P < 0.05$; $**P < 0.01$; Wilcoxon signed-rank test, 10 mice). Each value was normalized as percent of the peak value at ROI 6, which was put on the response peak of the dorsal AI high-frequency area and used as a landmark to register across individuals. Sites a and b are equivalent to those shown in *C*. *F*: quantitative analysis of response slopes on the response in the experiment shown in *D*. ROIs were placed across the peaks in Stiebler's UF and DP, and the same ROIs were placed onto the image of the responses to a 35-kHz tone obtained from the same mouse (inset). The red line was obtained from the response to a 35-kHz tone, and the blue line was obtained from the response to FM directional changes in the same mouse. The red line peak derived from the dorsal AI high-frequency area was placed in the middle of Stiebler's UF and DP ($*P < 0.05$; Wilcoxon signed-rank test, 6 mice). Each value was normalized as percent of the peak value at ROI 30, which was put on the response peak of Stiebler's UF and used as a landmark to register across individuals. Transcranial imaging was performed in experiments C–F.

cytoarchitectonic partitions. To address this problem, we investigated the cytoarchitectural pattern of the AI low-frequency area, the ventral AI high-frequency area, and the dorsal AI high-frequency area (see Fig. 4A) after identifying the regions by flavoprotein optical imaging. We characterized these areas histologically by immunolabeling NNF using MAb SMI-32, which is widely used to partition and identify various cortical and brain regions, including the auditory cortex (Budinger et al. 2000; Mellott et al. 2010; Ouda et al. 2012; Rothschild et al. 2010), MGB (Honma et al. 2013; Horie et al. 2013; Paxinos et al. 2009), visual cortex (Boire et al. 2005; van der Gucht et al. 2001; Wong and Kaas 2009), and other regions. To perform this analysis, it is necessary to determine the low- and high-frequency areas of the AI on slice sections. However, mouse monoclonal SMI-32 immunolabeling using mouse IgG as a secondary antibody gave high-background staining after marking the identified area with injection of fluorescent beads, dye, or ink. Therefore, we injected BDA into an identified area of the AI in the right hemisphere in vivo and then observed NNF cytoarchitecture in the left AI on slice sections guided by axonal branches stained with BDA projecting from neurons in the right AI. It is widely known that the corresponding areas have interhemispheric projections via the corpus callosum in mammalian brains (Budinger et al. 2000; Oviedo et al. 2010; Rouiller et al. 1991; Xiong et al. 2012), as shown in the schema of Fig. 3A. We confirmed this fact in the present study as well (Fig. 3). After we identified the precise location of the subregions in the right auditory cortex using flavoprotein fluorescence imaging, we injected AAV-GCaMP3 solution into the AI 5-kHz area (Fig. 3, B–D). This technique visualizes the axon terminals originating from the injected subarea in vivo (Glickfeld et al. 2013; Oh et al. 2014). Two weeks after injection of AAV-GCaMP3 into the AI 5-kHz area in the right hemisphere, the fluorescent axon terminals were observed in the contralateral left AI 5-kHz area (Fig. 3E). GCaMP3-positive axon terminals were visualized using a two-photon microscopy in the place where an intense signal was observed in Fig. 3E (Fig. 3F), whereas no GCaMP3-positive terminals were observed outside of the AI (Fig. 3G). The large calcium responses to a 5-kHz tone derived from GCaMP3-positive terminals were observed in the left AI 5-kHz area (Fig. 3H), and the responses of the AAF and AII were close to those observed in a naïve mouse (Fig. 3D). These data confirm that it is possible to observe the NNF pattern of the identified area in the contralateral auditory cortex on slice sections, guided by axon terminals, stained by BDA injected into the right auditory cortex.

The NNF immunolabeling pattern appeared much denser in the dorsal part than in the ventral part of the AI high-frequency area or the AI low-frequency area, whereas the weak NNF immunolabeling pattern appeared in the latter two areas (Fig. 4B). Moreover, the dorsal part of the AI high-frequency area appeared to have the particular laminar pattern of immunolabeling. To analyze quantitatively the difference in NNF immunolabeling patterns, we first counted the number of NNF-positive neurons in each area. However, labeled neurons were not significantly different in number among the three areas (Fig. 4C). NNF immunolabeling clearly distinguished pyramidal from nonpyramidal neurons, the two most common neuron types. Pyramidal neurons had NNF-positive apical dendrites, reaching the superficial layer, and a densely labeled large soma

(Fig. 4D). Conversely, nonpyramidal neurons had few NNF-positive apical and basal dendrites, and their soma was labeled weakly. Therefore, the difference in the ratios of NNF-positive pyramidal neurons to nonpyramidal neurons could account for the apparent density difference with the NNF immunolabeling patterns. In layers II, III, and IV, the ratio of NNF-positive pyramidal/nonpyramidal neurons did not differ noticeably, and nonpyramidal neurons were dominant in all three areas (Fig. 4E). However, the deeper layers V and VI in the dorsal AI high-frequency area were almost fully occupied by NNF-positive pyramidal neurons. The ratio of NNF-positive pyramidal/nonpyramidal neurons was significantly higher than that observed in the other two areas [Fig. 4F; $P < 0.05$ (area a vs. c); $P < 0.05$ (area b vs. c)] when compared in layers V, VI, and II–VI, whereas there was no significant difference between areas a and b in any layer. Thus the presence of numerous NNF-positive pyramidal neurons in the deeper layers could explain the dense NNF immunolabeling pattern in the dorsal AI high-frequency area, since these neurons have thick NNF-positive basal dendrites and apical dendrites that reach superficial layers. These data (Figs. 2 and 4) strongly suggest that the dorsal AI high-frequency area, located between Stiebler's UF and DP, is likely a newly defined region with a different cytoarchitectural pattern. We tentatively refer to this new area as the DM (Fig. 1D).

Frequency organizations of the AI and DM. We next re-evaluated the precise frequency organizations of the auditory cortex based on the finding that the dorsal AI high-frequency area is a newly defined region. We investigated frequency gradients by plotting the response peaks using flavoprotein fluorescence imaging described in our previous study (Fig. 5) (Honma et al. 2013). The posterior frequency-organized region labeled as the "AI," has a low-to-high (5–80 kHz) tone-frequency response axis directed from the dorsocaudal to the ventrorostral temporal cortex (Fig. 5, A and B). The frequency gradient of the AI ran in a mild clockwise direction. The corresponding frequency gradient for the newly identified DM was directed from ventrocaudal to dorsorostral anatomic axis (Fig. 5, A and C). Similar maps were obtained using other sound-intensity levels (for example, at 40 dB SPL; data not shown). The slopes of the AI and DM frequency gradients were not significantly different ($P > 0.9$) using comparison of regression coefficients. Both the AI and DM have high-frequency bands inside of their frequency gradients. The ratios of the response amplitudes of the DM and AI were plotted against the stimulus frequency to investigate whether the response property was similar in these two regions (Fig. 5, D and E). Although the AI is responsive to ultrasonic sounds, the DM is more responsive to ultrasonic sounds over 40 kHz than is the AI (Fig. 5E). These data suggest that the DM and AI have distinct frequency gradient directions for tone-response topographies and that the DM responds more vigorously to high-frequency sounds than the AI.

Differences in robustness of frequency gradients between regions have been confirmed using two-photon imaging (Issa et al. 2014). We have shown that the DM and AI have a robust, frequency-organized structure using flavoprotein fluorescence imaging. To evaluate the extent of heterogeneity in the frequency organization at the high-resolution scale, we performed in vivo two-photon imaging to determine the properties of neurons in the supragranular layers in the AI and DM (Fig. 6),

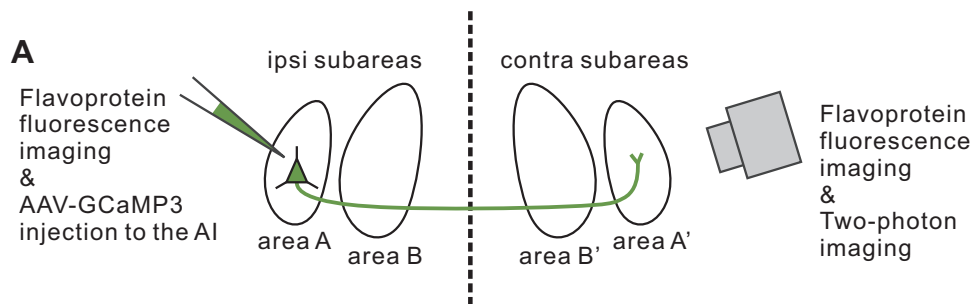
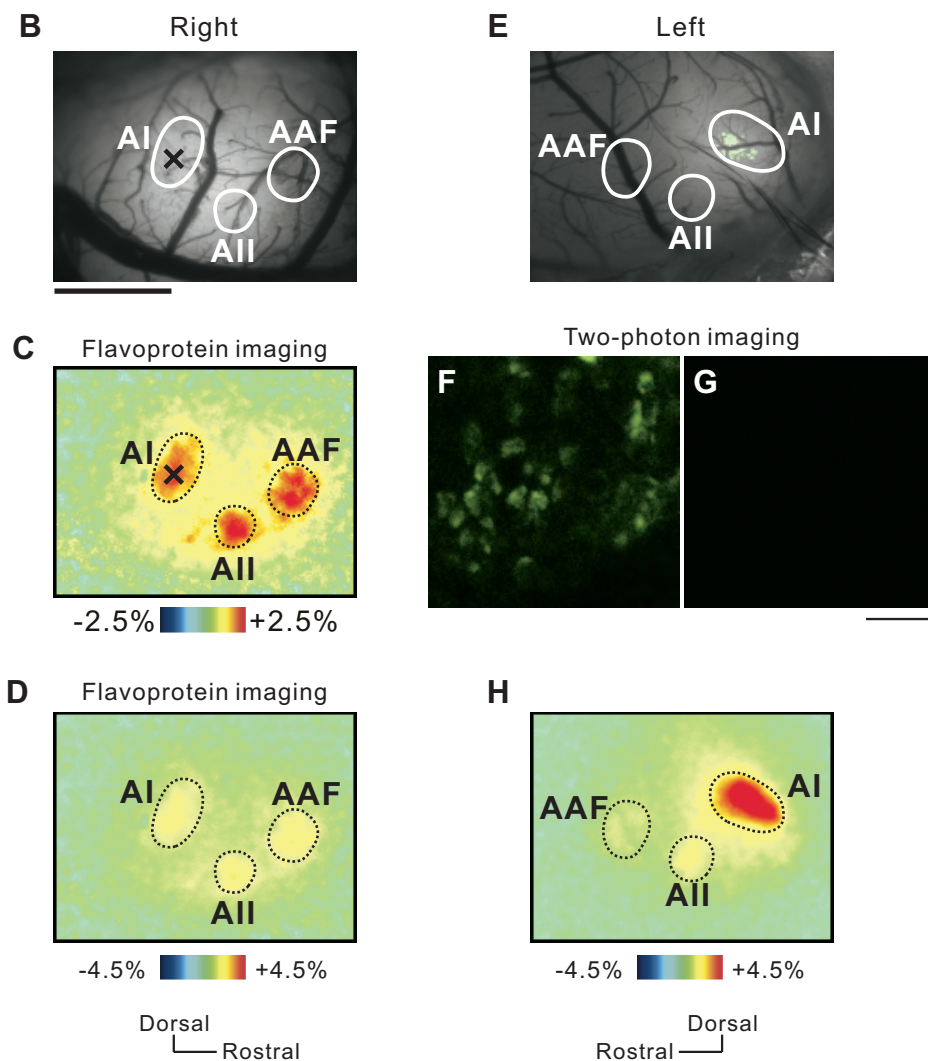


Fig. 3. Interhemispheric projection between the auditory cortices. *A*: schematic drawing showing that a neuron in the subarea in the auditory cortex projects to the equivalent contralateral subarea. *B–D*: injection site of adeno-associated virus (AAV)-GCaMP3 in the right auditory cortex. The areal borders were drawn according to the flavoprotein fluorescence response to a 5-kHz tone (*C*). *C* and *D*: the images shown are the same except for the color range. \times , injection site. *E*: GCaMP3-positive axon terminals in the AI 5-kHz area in the left auditory cortex observed using a stereoscopic microscope. The top 10% pixels in intensity are colored green. *F*: GCaMP3-positive axon terminals visualized using a 2-photon microscopy in the place where an intense signal was observed in *E*. *G*: no GCaMP3-positive terminals found outside of the AI 5-kHz area. *H*: the large calcium responses to a 5-kHz tone derived from GCaMP3-positive terminals in the left AI. This response was obtained using an epifluorescent microscope under the same experimental condition as that to perform usual flavoprotein fluorescence imaging. Only the AI showed a much larger response in *H* due to GCaMP-stained terminals. Flavoprotein fluorescence responses, which were small compared with GCaMP signals, were observed in the 5-kHz area in the AAF and AII. Scale bars, 1 mm (*B*); 10 μ m (*F* and *G*).



since the regional characteristic obtained by low-resolution imaging reflects an ensemble of the single neuronal properties in *layers II/III* (Andermann et al. 2011; Marshel et al. 2011; Tohmi et al. 2014). After identifying the precise location of the AI or DM using flavoprotein fluorescence imaging (Fig. 6*A*), we injected Fura-2 solution to observe the calcium responses in each neuron (Fig. 6*B*). The frequency at which the response amplitude reached the maximum in a given neuron was defined as the BF (Fig. 6*C*). Although the overall frequency gradients in the DM and AI had the same directions as those defined using flavoprotein fluorescence imaging, the frequency gradient in the DM neurons was less variable than that in the AI (Fig. 6, *D* and *E*). The degree of the frequency organization of

the microscopic structures was evaluated using residuals between each neuron and the regression line. The value of residuals was greater in the AI than in the DM (Fig. 6*F*; $P < 0.001$), implying that neuronal responses in *layers II/III* of the AI were more complex than those in the DM.

The DM was less sensitive to low-frequency tones than the AI in flavoprotein fluorescence imaging (Fig. 5*E*). This was explained by the neuronal distribution revealed by two-photon imaging; there were few neurons in the DM with BF < 20 kHz (Fig. 6, *G* and *H*). In contrast, the bandwidth of the neurons in the DM and AI was similar (Fig. 6*I*). A tendency that bandwidth values obtained in two-photon studies, including this study, are smaller than those in electrophysiological study

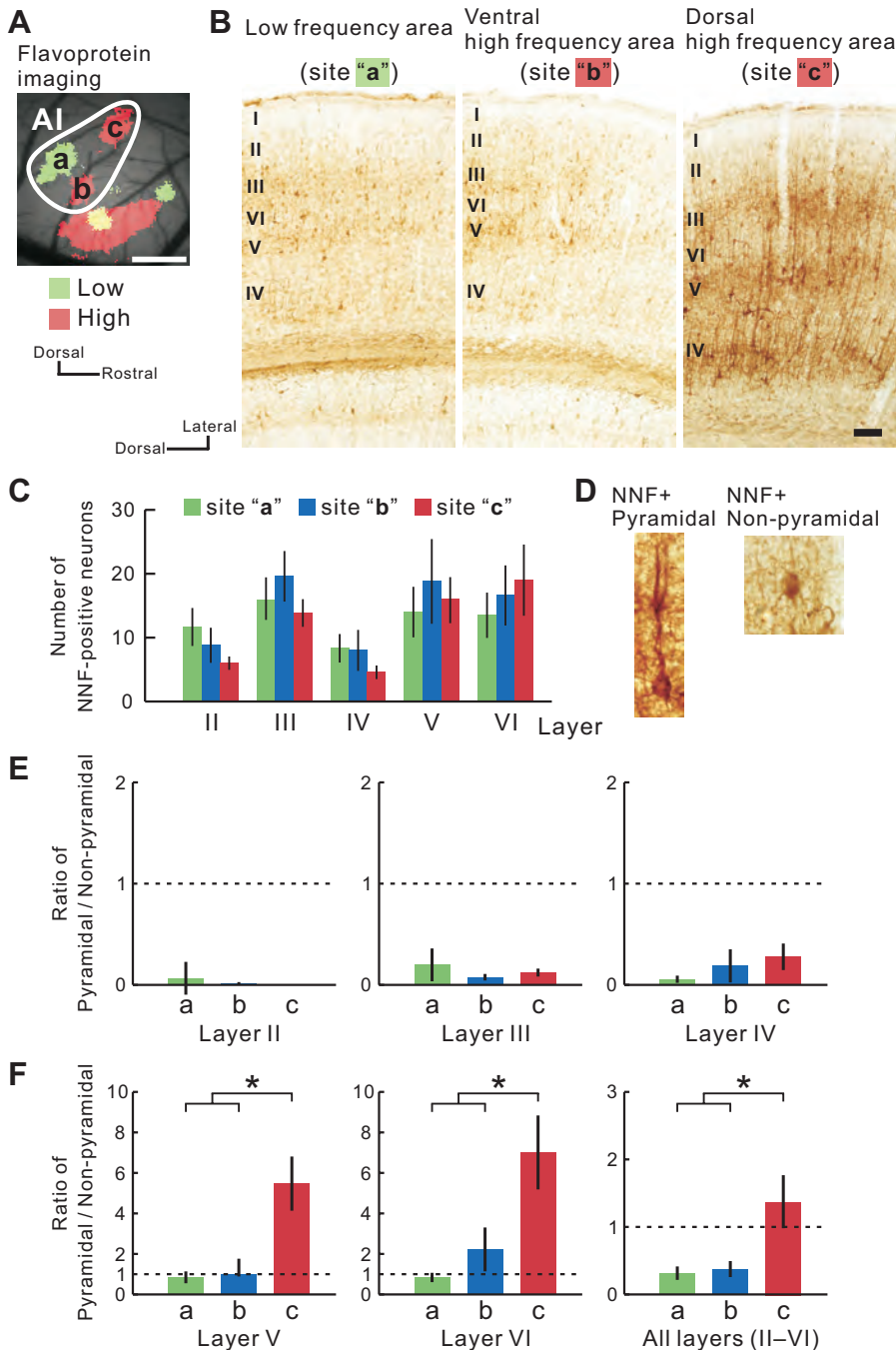


Fig. 4. Histological properties of the new region different from the AI in SMI-32 immunolabeling. *A*: functional location of the AI obtained using flavoprotein fluorescence imaging. Scale bar, 500 μm . *B*: sample images of SMI-32 immunolabeling patterns. We observed nonphosphorylated neurofilament (NNF) at sites a, b, and c, indicated in *A*. Scale bar, 100 μm . *C*: number of NNF-positive neurons in each area of the AI. Layers were identified based on Nissl staining in an adjacent section. *D*: typical images of an NNF-positive pyramidal and nonpyramidal neuron. *E*: ratio of the number of NNF-positive pyramidal/nonpyramidal neurons in the superficial layers (II, III, and IV). *F*: ratio of the number of NNF-positive pyramidal/nonpyramidal neurons in the deep layers (V and VI) and all of the layers (II–VI). * $P < 0.05$, Tukey-Kramer's test. Site a, $n = 6$; site b, $n = 6$; site c, $n = 7$. NNF and biotinylated dextran amine (BDA) were visualized in the adjacent tissue sections.

(Guo et al. 2012) might be attributed to the property of a calcium-sensitive dye in detecting spikes.

Frequency organizations of the AAF. We also found the presence of the precise frequency organization in the AAF (Fig. 7). The neural response to a 5-kHz tone was placed at the most rostral part of the AAF. When mice heard tones at 5–80 kHz, neural responses to higher tones shifted to the ventrocaudal direction. No clear response was found near Stiebler's UF indicated by the white arrow (Fig. 7*A*, inset). The plotting of response peaks elicited by tones at 5–80 kHz also confirmed the presence of the precise octave-based frequency organization in the AAF (Fig. 7, *B* and *C*), as reported previously (Horie et al. 2013; Issa et al. 2014). Therefore, the low-high and high-low mirror-imaged frequency organizations between the

AAF and AI, reported in other species, were preserved in mice as well.

There is a discrepancy in the direction of the frequency organization of the AAF between studies using optical imaging (Fig. 7) (Honma et al. 2013; Issa et al. 2014) and studies using electrophysiology (Guo et al. 2012). The latest mapping study using electrophysiology considered the whole area, which was composed of the AAF, Stiebler's UF, and the DM in this study as a single region of the AAF, as shown by the schema in Fig. 8*A* (Guo et al. 2012), and the direction of the frequency organization of the AAF was drawn dorsocaudally (Fig. 1*C*). Therefore, we investigated NNF immunolabeling patterns and anatomical properties in the AAF, Stiebler's UF, and the DM (Fig. 8, *B–E*) to confirm our physiological mapping shown in Fig. 7.

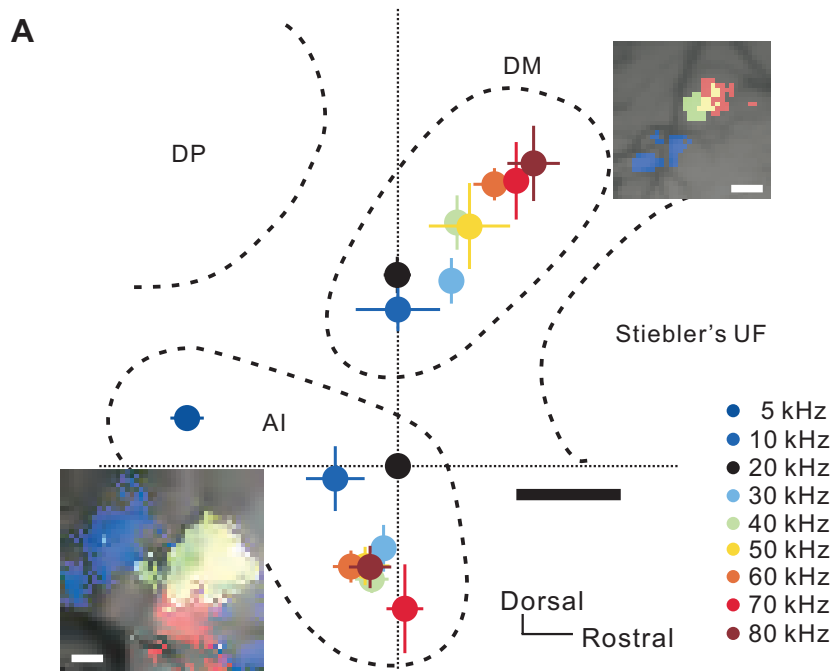
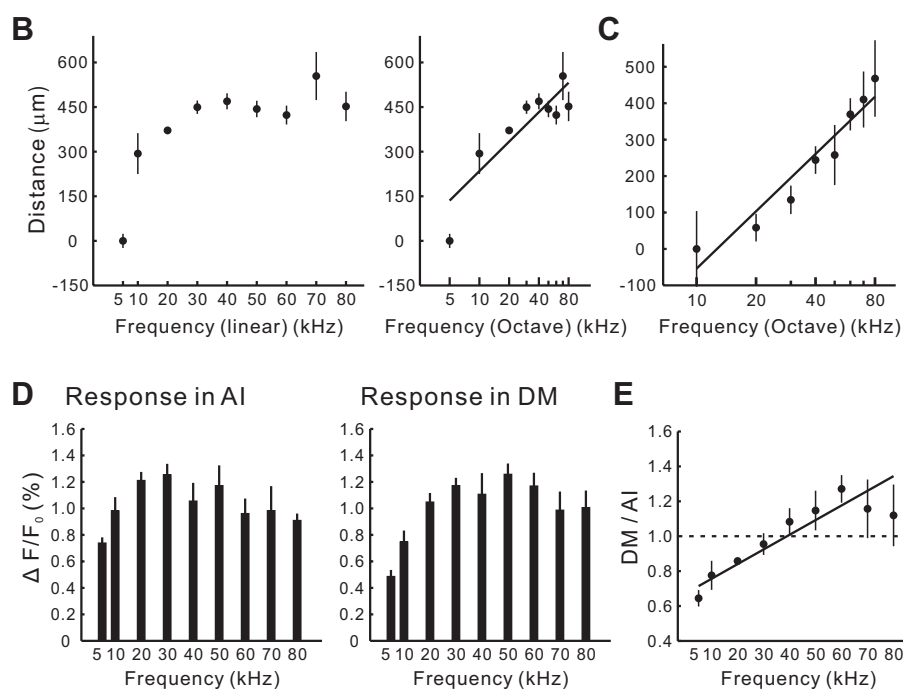


Fig. 5. Frequency organizations of the AI and DM revealed by flavoprotein fluorescence imaging. *A*: 2 frequency gradients for 5–80 kHz sounds in the AI and newly identified DM revealed by flavoprotein fluorescence imaging. The location of the 20-kHz response peak in the AI was used as the origin of coordinates on which data from several animals were superimposed. Black scale bar, 200 μm . See color-coding key on right. *Top inset*: response peak shifts in DM. Blue, 40 kHz; green, 60 kHz; red, 80 kHz; yellow, overlap between 60 and 80 kHz. White scale bar, 100 μm . *Bottom inset*: blue, 5 kHz; green, 10 kHz; yellow, 20 kHz; red, 50 kHz. White scale bar, 100 μm . *B*: a frequency gradient of the linear (*left*) and the log scales (*right*) in the AI. The horizontal axis is a line connecting points of 5 and 80 kHz ($r = 0.85$; $P < 0.001$, Spearman's rank correlation test). The slope in the octave axis was 1.01 octave/125 μm . *C*: a frequency gradient in the DM ($r = 0.69$; $P < 0.001$, Spearman's rank correlation test). The slope was 1.17 octave/125 μm . *D*: response amplitudes against each frequency in the AI (*left*) and DM (*right*). *E*: ratio of amplitudes of the DM to AI by each stimulus frequency ($r = 0.63$, $P < 0.001$, Spearman's rank correlation test). 5 kHz, $n = 15$; 10 kHz, $n = 5$; 20 kHz, $n = 15$; 30 kHz, $n = 8$; 40 kHz, $n = 6$; 50 kHz, $n = 7$; 60 kHz, $n = 8$; 70 kHz, $n = 3$; 80 kHz, $n = 3$.



First, NNF immunolabeling patterns of the AAF and Stiebler's UF were totally different (Fig. 8C); apparently, the gross immunolabeling pattern of Stiebler's UF was much weaker than that of the AAF (Fig. 8C). Although there was no difference in number of total NNF-positive neurons between the AAF and Stiebler's UF (Fig. 8D), Stiebler's UF lacked NNF-positive neurons in the *layer VI* (Fig. 8E), and the density of NNF immunolabeling within somas and dendrites per se was much weaker in Stiebler's UF, especially in the *layer III*, shown in Fig. 8C. Furthermore, the density of NNF immunolabeling in the DM was denser than that in the AAF (Figs. 4B and 8C), which is because the DM contained more than twice

as many NNF-positive neurons as did the AAF and Stiebler's UF (Fig. 8D). These data indicate that the area that was defined as the AAF in the past study (Guo et al. 2012) (Fig. 8A) includes three subregions with a distinct immunolabeling pattern.

The Stiebler's UF is more responsive to slow FM stimuli than to tones and does not have any frequency-organized structure (Honma et al. 2013; Stiebler et al. 1997), suggesting that the Stiebler's UF belongs to the belt region that receives thalamic inputs from the dorsal division of the MGB (MGd) (Winer and Schreiner 2011). Therefore, we investigated from which division of the MGB the Stiebler's UF receives dense

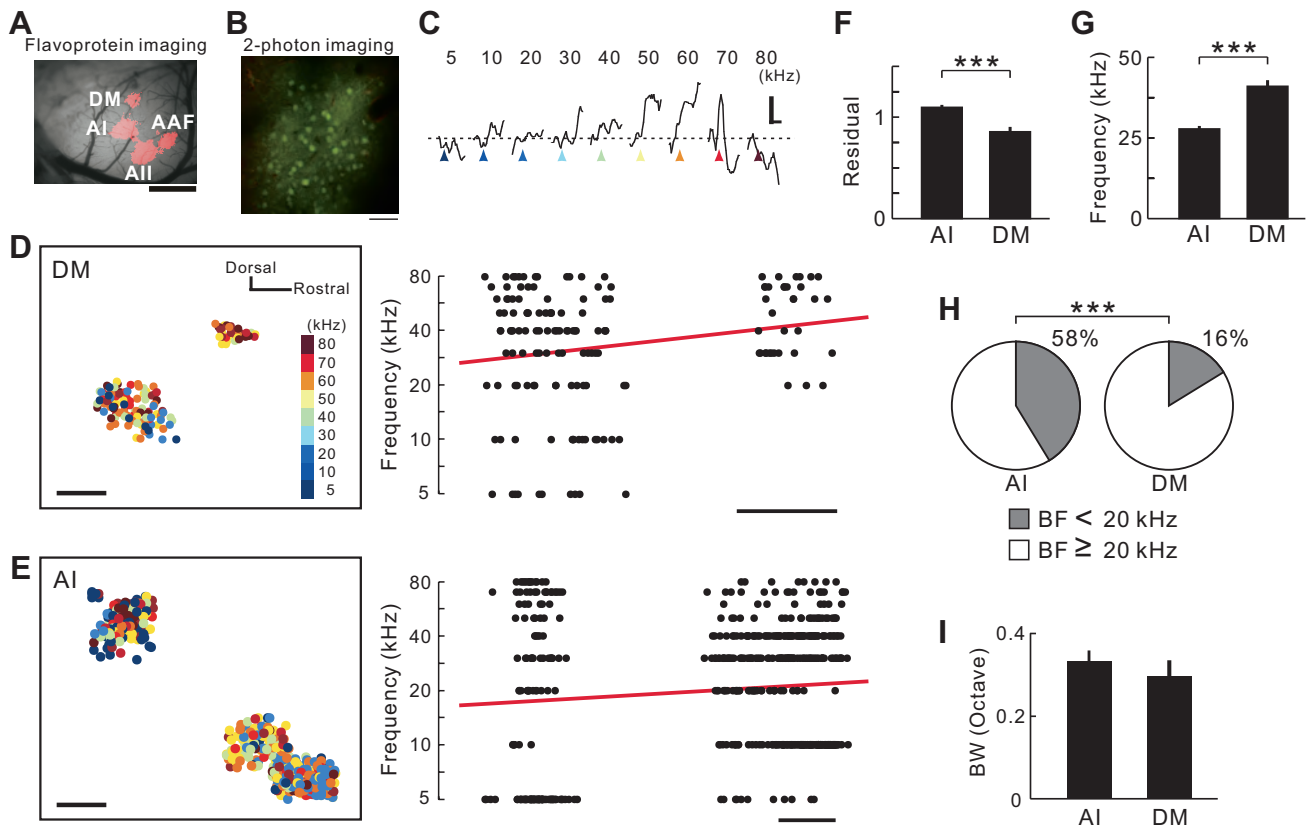


Fig. 6. Frequency organizations of the AI and DM revealed by 2-photon imaging. *A*: identification of subregions in the auditory cortex using flavoprotein fluorescence imaging. The image was obtained using a 35-kHz tone. Scale bar, 1 mm. *B*: example of staining with Fura-2 and sulforhodamine 101 in the auditory cortex. Scale bar, 50 μ m. *C*: sample traces of calcium response in a neuron with a best frequency (BF) of 60 kHz. Horizontal scale, 3 s; vertical scale, 2%; triangles, timing when a tone was given. A series of sounds at 80 dB sound pressure level was presented to a mouse. *D*: distribution of neurons in the DM. Data were obtained from 3 animals, and images were superimposed on the location of a 5-kHz response peak in the AI as the origin of coordinates obtained using flavoprotein fluorescence imaging. Color of each plot represents its BF. A significant, progressive increase in frequency was observed ($P < 0.05$, Spearman's rank correlation test; 163 neurons). Scale bar, 200 μ m. *E*: distribution of neurons in the AI. Data were obtained from 4 animals and reconstructed. A significant, progressive increase in frequency was observed ($P < 0.0001$, Spearman's rank correlation test; 598 neurons). Scale bar, 200 μ m. *F*: comparison of the degree of the frequency organization between the AI and DM. The extent of disorder was evaluated using the distances of each neuron from the regression line ($***P < 0.001$, Mann-Whitney U-test). *G*: averages of BFs ($***P < 0.001$, Mann-Whitney U-test). *H*: percentages of neurons with BF ≤ 10 kHz ($***P < 0.0001$, χ^2 test). *I*: comparison of neuron bandwidths (BW) between the AI and DM, defined as the logarithmic ratio of minimum and maximum frequencies that resulted in a response $>75\%$ ($P > 0.2$, Mann-Whitney U-test) of the peak amplitude.

projections (Fig. 8*F*). We injected BDA solution into the Stiebler's UF as a retrograde tracer after identifying the region, according to the response to FM reversal stimuli (Fig. 2*D*), and evaluated neuronal distribution using coronal sections between 2.8 and 3.4 mm posterior to the bregma. The MGv and MGd were partitioned according to the SMI-32 immunolabeling patterns (Honma et al. 2013; Horie et al. 2013; LeDoux et al. 1985, 1987) and an atlas (Paxinos 2003; Paxinos and Franklin 2001; Paxinos et al. 2009). Whereas 64.6% neurons of BDA-stained neurons were placed in the MGv, as much as 35.4% neurons were placed in the MGd (Fig. 8*F*). These data are clearly consistent with the results reported by Hofstetter and Ehret (1992), showing that the Stiebler's UF received robust thalamic projections from both MGd and MGv. In contrast, as for the region referred to as the AAF in the present study, 90% of the thalamic inputs originated from the MGv, and only 10% originated from the MGd (Fig. 8*F*), which is consistent with the fact that the AAF is one of the lemniscal core regions. Furthermore, we injected BDA solution into the DM to clarify the origin of the thalamic input. The DM presumably receives thalamic information from the MGv but not from the MGd,

because the DM has the clear frequency organization shown in Fig. 5. As expected, it was revealed that as much as 97% neurons projecting to the DM were localized in the MGv, and remaining 3% neurons were located in the MGd (Fig. 8*F*). Overall, these data indicate that the AAF, Stiebler's UF, and DM are not combined into a single region but three different regions with distinct histological and anatomical properties. Hence, these data support our physiological mapping that reveals that the frequency gradient of the AAF travels ventro-caudally (Fig. 7).

Comparison of the effects of acoustic exposures between the AI and DM. The number of cortical neurons with a particular characteristic frequency increases after animals are passively exposed for a long time to the tonal stimuli at the same frequency (de Villers-Sidani et al. 2007; Nakahara et al. 2004; Zhang et al. 2001). This plastic change can be observed, as response amplitude increases when observed by flavoprotein fluorescence imaging (Takahashi et al. 2006; Tohmi et al. 2009). The potentiation induced by the passive acoustic exposure exhibits regional and tonal specificity. Whereas the AAF is relatively insensitive to the passive acoustic exposure (Taka-

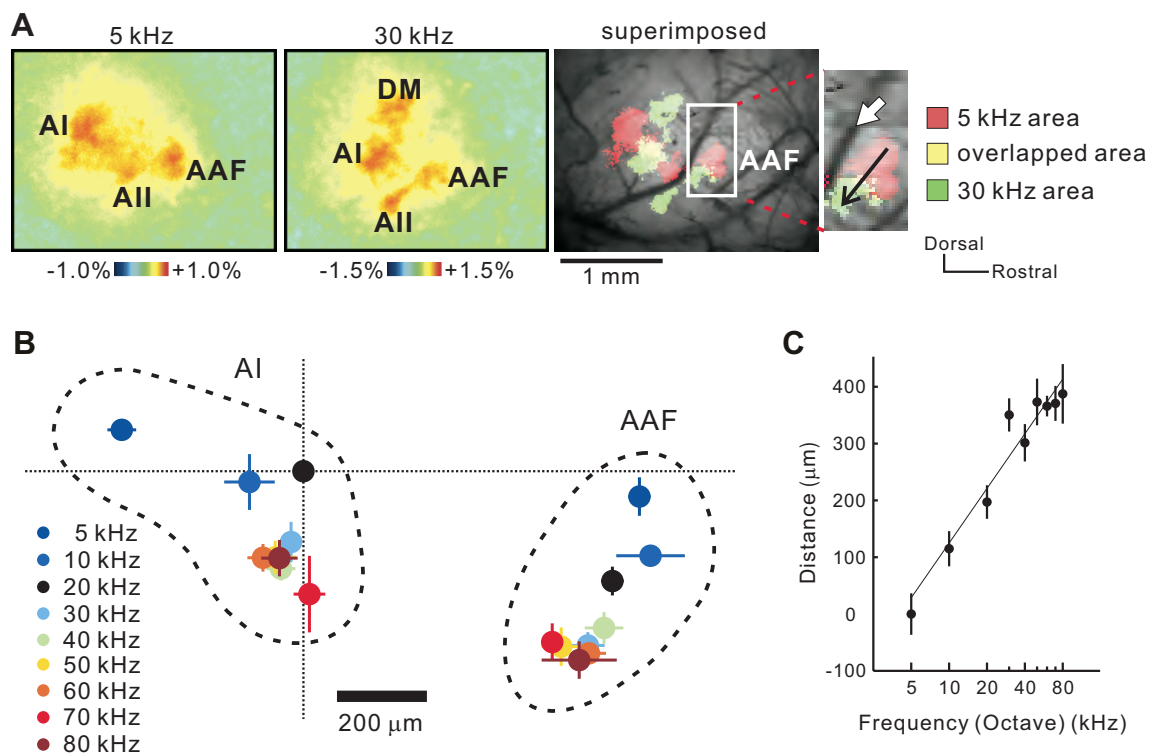


Fig. 7. Frequency organization of the AAF and AI. *A*: images of responses to a 5 (*left*)- and 30 (*middle*)-kHz tone and a superimposed image of these 2 images (*right*). The white arrow indicates the region defined as the high-frequency area of AAF in Guo et al. (2012). *B*: frequency-organized maps of the AI and AAF to 5–80 kHz sounds revealed by flavoprotein fluorescence imaging. The response peak of AI to 20 kHz is used as the origin of coordinates to superimpose the data in several animals. *C*: frequency gradient of the AAF. The horizontal axis is a line connecting points of 5 and 80 kHz (5 kHz, $n = 15$; 10 kHz, $n = 5$; 20 kHz, $n = 15$; 30 kHz, $n = 8$; 40 kHz, $n = 6$; 50 kHz, $n = 7$; 60 kHz, $n = 8$; 70 kHz, $n = 3$; 80 kHz, $n = 3$; $P < 0.001$).

hashi et al. 2006), the AI responses are clearly potentiated by the exposure (de Villers-Sidani et al. 2007; Nakahara et al. 2004; Zhang et al. 2001). We tested whether the plastic change to acoustic exposure was observed in the DM, which is expected to have different properties from those in the AI. We observed that when mice were reared under 5 kHz tone exposure from P7 to P35 (Fig. 9A), significant potentiation of neural responses to a 5-kHz tone occurred only in the AI ($\Delta F/F_0$ in normal environment, $0.68 \pm 0.06\%$, $n = 10$; quiet environment, $0.64 \pm 0.05\%$, $n = 6$; exposed, $0.87 \pm 0.04\%$, $n = 14$), and such potentiation was not found in the AAF or AII (Fig. 9, *B* and *C*). In the AAF, AI, AII, and DM, the responses to a 35-kHz tone were not clearly potentiated after exposure to a 5-kHz tone because of the frequency specificity in the potentiation (Fig. 10A), as reported previously (Takahashi et al. 2006). When mice were exposed to a 35-kHz tone, significant potentiation was observed only in the AI (normal environment, $0.95 \pm 0.08\%$, $n = 10$; quiet environment, $0.95 \pm 0.05\%$, $n = 6$; exposed, $1.09 \pm 0.03\%$, $n = 14$), whereas no potentiation was observed in the DM as in the AAF or AII (Fig. 9, *D* and *E*). Although the size of responsive areas after the plasticity occurred seemed to be expanded in an experience-dependent manner, the location of the AI peak was not shifted by the plasticity. Therefore, it is unlikely that the AI and DM have merged by the plasticity. The neural responses were not potentiated in all three areas to a 5-kHz tone (Fig. 10B). Flavoprotein fluorescence imaging showed that responses of the DM to a 5-kHz tone were very weak and diffused and did not show robust, clear peaks in re-

sponse to a 5-kHz tone (Fig. 2B). Moreover, single neuronal analysis showed that there were few low-frequency neurons in the DM (Fig. 6). Therefore, reliable analysis was not possible regarding DM responses to a 5-kHz tone, and we used only a 35-kHz tone to evaluate the effect of acoustic exposures. Overall, the resistance to plasticity of the DM indicates that the DM is a functionally distinct region from the AI.

Thalamocortical projections from the MGB to the DM. Auditory cortical regions have different latencies to auditory stimuli across species. In previous studies, neurons in the AAF were activated with shorter latencies than those in the AI (Kubota et al. 2008; Linden et al. 2003; Sawatari et al. 2011). We verified the latency of the neural response to a 35-kHz tone in the DM using flavoprotein fluorescence imaging (Fig. 11). The latency was evaluated as the time until the fluorescence signal reached 25% or 50% maximum of the peak. The latency of the AAF response to a 35-kHz tone was shorter than that of the AI, as we described previously (Fig. 11A) (Kubota et al. 2008), which is consistent with the results obtained by voltage-sensitive dye imaging (Sawatari et al. 2011). The latency of the DM was also shorter than that of the AI and comparable with that in the AAF (Fig. 11A). The latencies to reach 25% maximum were 122.2 ± 5.4 ms in the AAF, 120.2 ± 4.5 ms in the DM, 142.0 ± 4.7 ms in the AI, and 146.0 ± 5.8 ms in the AII ($n = 18$, each; Fig. 11B). The latencies to reach 50% maximum were 185 ± 4.7 ms in the AAF, 189.3 ± 5.6 ms in the DM, 212.5 ± 6.5 ms in the AI, and 215.6 ± 7.5 ms in the AII ($n = 18$, each; Fig. 11B). The latencies to reach 25% and

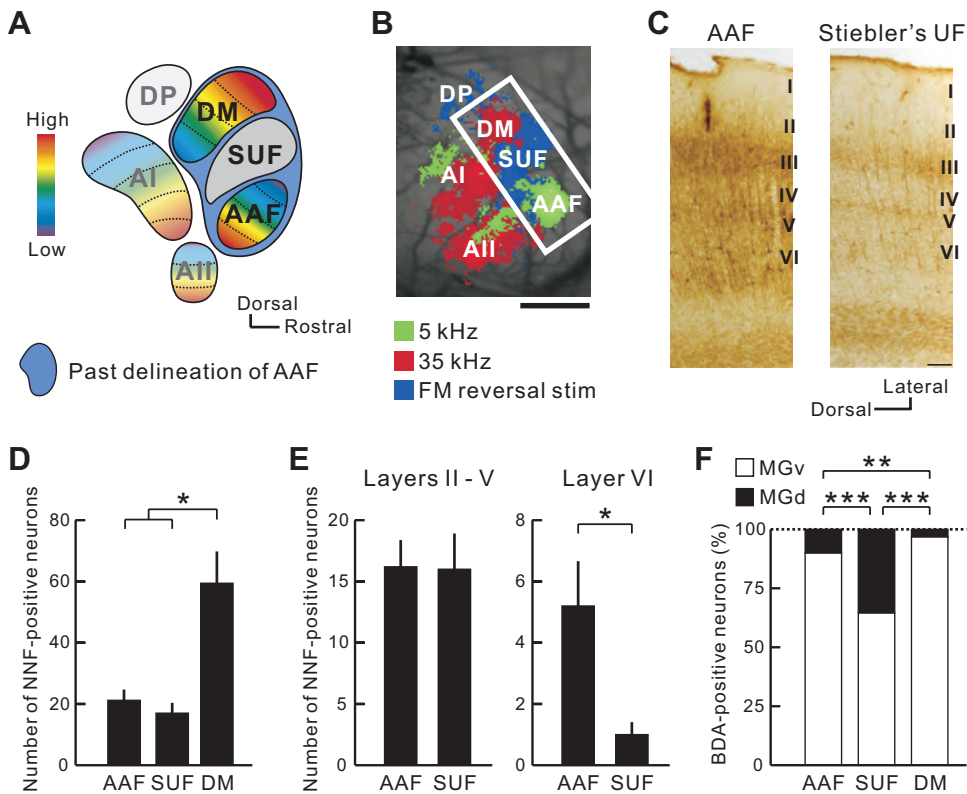


Fig. 8. Difference in histological and anatomical properties among the AAF, Stiebler's UF, and DM. *A*: schematic drawing of the auditory cortical map. The area enclosed by the blue oval was the definition of the AAF proposed by Guo et al. (2012). SUF, Stiebler's UF. *B*: auditory cortical map revealed by flavoprotein fluorescence responses. The area enclosed by the white rectangle is equivalent to that in the blue oval in *A*. Scale bar, 500 μ m. *C*: sample images of SMI-32 immunolabeling patterns in the AAF and Stiebler's UF. Scale bar, 100 μ m. *D*: number of NNF-positive neurons in the AAF, Stiebler's UF, and DM. $*P < 0.05$, Tukey-Kramer's test; AAF, $n = 5$; Stiebler's UF, $n = 4$; DM, $n = 7$. *E*: number of NNF-positive neurons in the layer VI and the others of the AAF and Stiebler's UF. $*P < 0.05$, Mann-Whitney U-test; AAF, $n = 5$; Stiebler's UF, $n = 4$; DM, $n = 7$. *F*: percentage of neuronal distribution in the medial geniculate body [MGB; the ventral division of MGB (MGv) or the dorsal division of MGB (MGd)] by their cortical target. $**P < 0.01$; $***P < 0.000001$, χ^2 test after Bonferroni correction; to AAF, $n = 150$ neurons from 3 mice; to Stiebler's UF, $n = 144$ neurons from 6 mice; to DM, $n = 316$ neurons from 7 mice.

50% maximum had the same tendency. The latencies of the AAF and DM were significantly shorter than those of the AI and AII, and there were no significant differences between the AAF and DM or the AI and AII (Fig. 11C). These data also support the fact that the DM receives thalamocortical projections directly from the MGv but not via the AAF or AI.

The mouse MGv is composed of several compartments that topographically project to their corresponding subregions in the auditory cortex (Horie et al. 2013; Takemoto et al. 2014). The region that projects to the AAF or AI is localized in the middle part of the MGv. On these bases, we tried to identify the region that projected to the DM. First, we injected BDA into the AI or DM after identification, and we evaluated the locations of neurons that project to the AI or DM using coronal sections (Fig. 12). Neurons projecting to the DM were found in the ventral half of the MGv, and those projecting to the ventral AI high-frequency area were observed in a neighboring region located at the same ventrodorsal level (Fig. 12). However, we found that neurons projecting to the DM were located rostral to those projecting to the AI as a whole. Therefore, we prepared horizontal sections to evaluate the relative rostrocaudal location of neurons projecting to the DM and AI (Fig. 13). We injected Alexa Fluor-conjugated CTB into the ventral AI high-frequency area or the DM, identified using a tone at 40 kHz (Fig. 13, *A* and *B*). In horizontal sections of the MGv, the neurons projecting to the DM were located more rostrally than the neurons projecting to the AI (Fig. 13, *C–F*). The relative location of the neuronal population projecting to the DM was measured in reference to the averaged coordinates of neurons projecting to the AI (Fig. 13*J*). The neurons projecting to the DM were located significantly more rostral and more medial compared with those projecting to the AI ($P < 0.001$, for both).

Next, we tested whether the frequency organization in the DM reflects the distinct frequency organization in a single region within the MGv or partly overlapped regions projecting to the AI and DM, as suggested by the fork-shaped, frequency-organized map proposed by Issa et al. (2014) (Fig. 1C). We injected fluorescent CTB into the low- and high-frequency regions of the DM. Results clearly indicated that the frequency organization in the MGv projecting to the DM was structured along a single latero-medial axis within a single compartment of the MGv (Fig. 13, *G–I*). The quantitative distribution map showed a significant place shift in location between the areas projecting to the low- and high-frequency areas of the DM (Fig. 13*K*; $P < 0.001$). These data indicate that neurons projecting to the DM are localized in the rostral part of the MGv with a distinct frequency organization along the latero-medial axis, and no fewer than four compartments were independent from each other within the MGv (Fig. 13*L*).

Vocalization processing in the auditory cortex. Although the frequency gradient in the AI also includes ultrasonic bands, the responses of the DM to ultrasonic tones were larger than those of the AI (Fig. 5E). Therefore, we verified the possibility that the DM may be involved in ultrasonic courtship songs produced by male mice for females (Fig. 14A). Although this courtship vocalization produced by male mice is one of the representative ultrasonic, communication-related sounds (Asaba et al. 2014; Hammerschmidt et al. 2009; Holy and Guo 2005), as well as isolation calls produced by pups (Ehret and Haack 1982; Thornton et al. 2005; Uematsu et al. 2007), no research has been performed about central processing of courtship songs, although several studies about pup isolation calls have been reported (Galindo-Leon et al. 2009). The courtship songs produced by male mice include characteristic features,

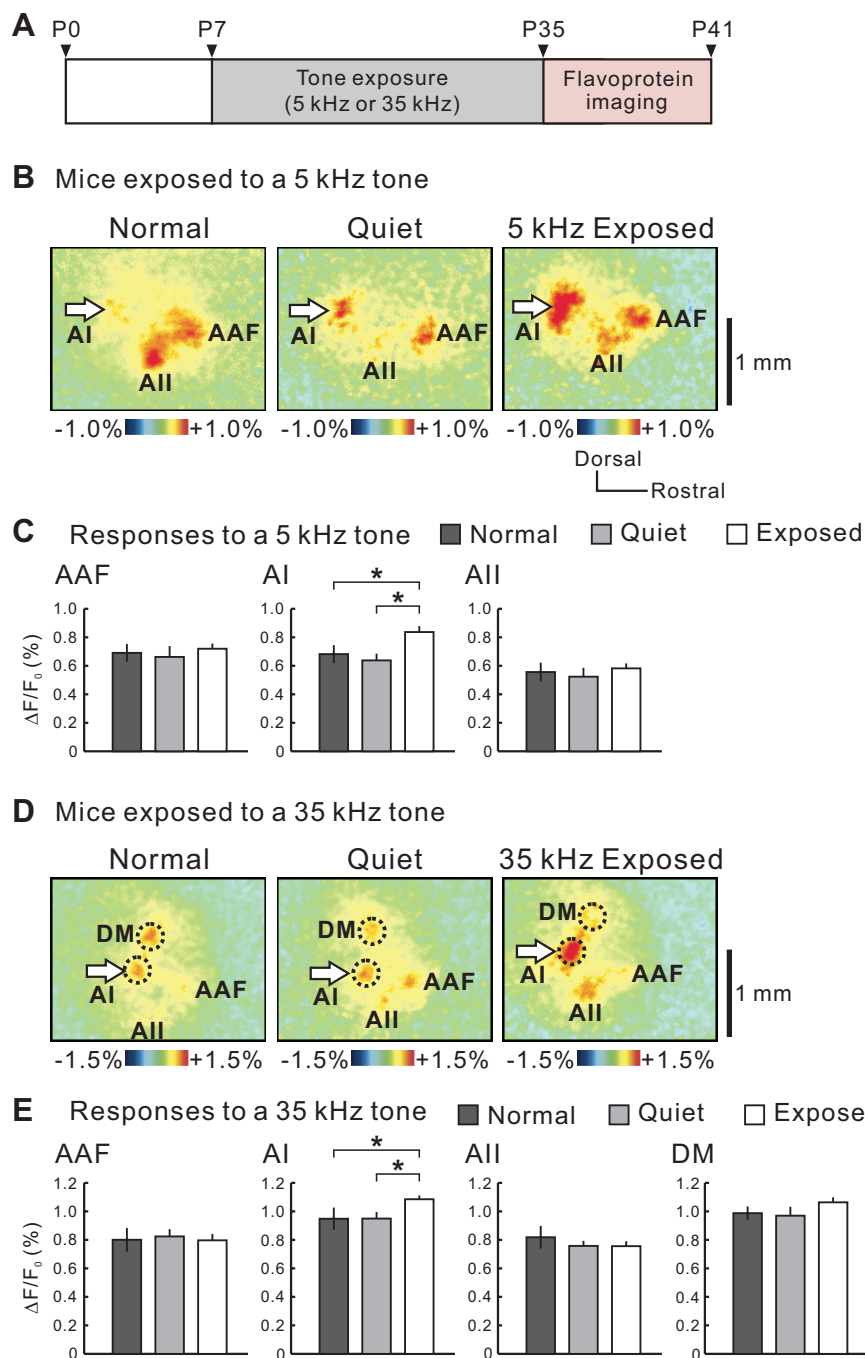


Fig. 9. Plasticity after acoustic exposure in the AI and DM. *A*: schedule of experiments. Imaging was performed within 1 wk after cessation of acoustic exposure. *P*, period. *B* and *C*: response amplitudes to a 5-kHz tone in mice exposed to a 5-kHz tone ($*P < 0.05$, Mann-Whitney U-test; normal, $n = 10$; quiet, $n = 6$; exposed, $n = 14$). Mice rearing in a normal home cage (Normal), in the chamber without presentation of any tones (Quiet), or in the chamber with acoustic exposure (Exposed). *D* and *E*: response amplitudes to a 35-kHz tone in mice exposed to a 35-kHz tone ($*P < 0.05$, Mann-Whitney U-test; normal, $n = 10$; quiet, $n = 6$; exposed, $n = 14$).

such as a high-frequency band over 50 kHz, fast FM, pitch jumps, and intermittent rhythms (Fischer and Hammerschmidt 2011; Lahvis et al. 2011). The AAF, AI, AII, and DM in both sexes were clearly activated by stimulation with songs produced by males (Fig. 14*B*). Interestingly, the temporal order of the rising phase of neural responses to a male's courtship song was different from that of an artificial tone (Fig. 14, *C* and *D*). The DM was activated first, followed by simultaneous activation of the AAF and AI, and the AII was activated last. The latency to reach 25% maximum was 143 ± 6.2 ms in the DM, 170 ± 9.4 ms in the AAF, 181 ± 7.4 ms in the AI, and 208 ± 13.7 ms in the AII (Fig. 14*E*), and the latency to reach 50% maximum was 243 ± 6.5 ms in the DM, 279 ± 8.7 ms in the

AAF, 291 ± 9.3 ms in the AI, and 340 ± 11.9 ms in the AII ($n = 20$ in total; male, $n = 7$; female, $n = 13$; Fig. 14*E*). As for the latency, there were no differences between male and female mice in all of the regions. These data indicate that vocalization is similarly processed in the DM of both male and female mice regarding the latency of the DM responses to a male's courtship song. In contrast, the amplitudes of the response to a male's song were significantly larger in females than in males in the DM alone (Fig. 14*F*; male, $1.61 \pm 0.10\%$, $n = 15$; female, $2.0 \pm 0.19\%$, $n = 16$; $P < 0.05$). The response amplitudes in the AAF, AI, and AII were slightly larger in females than in males, although there were no significant differences between the sexes (AAF, $P > 0.6$; AI, $P > 0.8$;

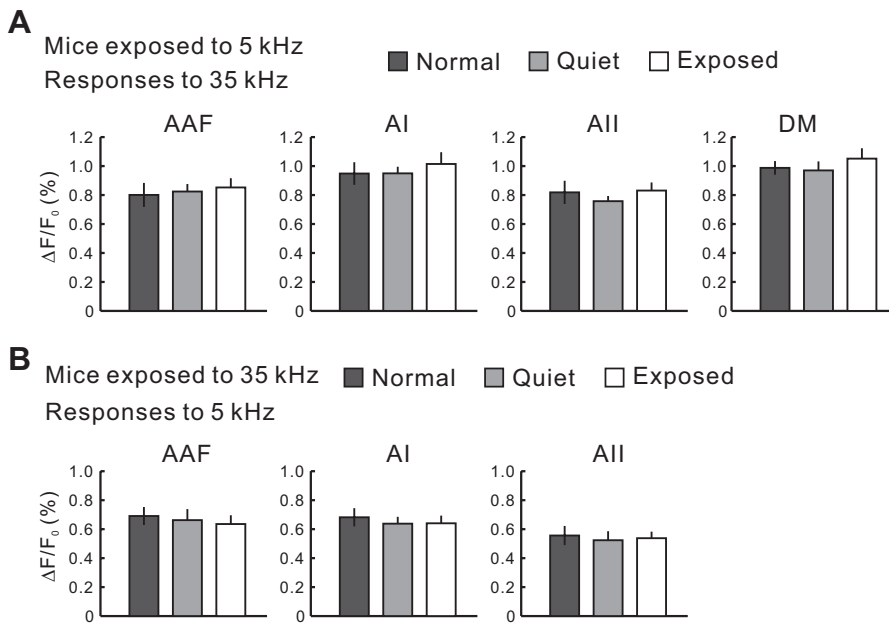


Fig. 10. . Frequency specificity in plasticity after acoustic exposure. *A*: the response amplitudes to a 35-kHz tone in mice exposed to a 5-kHz tone. There was no significant difference between normal and exposed or quiet and exposed mice. Normal, $n = 10$; quiet, $n = 6$; exposed, $n = 14$. *B*: the response amplitudes to a 5-kHz tone in mice exposed to 35-kHz. There was no significant difference between normal and exposed or quiet and exposed mice. Normal, $n = 10$; quiet, $n = 6$; exposed, $n = 14$.

AII, $P > 0.5$). The slight difference in the AAF, AI, and AII might be attributed to the significant difference in the DM, as it was reported that neural responses in a downstream region with a longer latency are affected by neural responses in an upstream region with a shorter latency in the auditory cortex (Kubota et al. 2008). As expected from this idea, there was no

difference between the sexes in response to a 70-kHz artificial tone (Fig. 14G). These data imply that ultrasonic courtship songs produced by males, mediated via a distinct rostral compartment of the MGv, reach the DM first and are processed further through pathways from the DM to other cortical regions in mice.

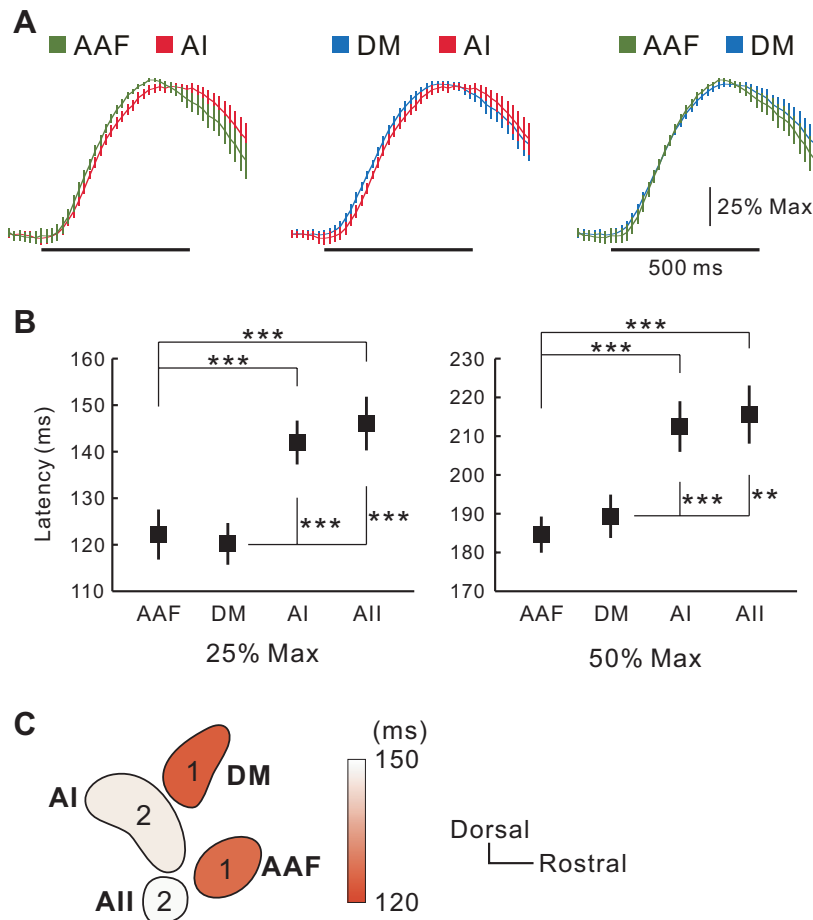


Fig. 11. Responses in the DM and AAF faster than those in the AI and AII. *A*: temporal profiles of $\Delta F/F_0$ in the AAF, AI, and DM in response to a 35-kHz tone. Frame rate was set at 54 Hz. Horizontal black bars indicate the stimulus period. *B*: times required to reach 25% (left) and 50% (right) of the maximal $\Delta F/F_0$ after the stimulus onset in the AAF, DM, AI, and AII ($***P < 0.001$, $**P < 0.01$, 1-way repeated-measures ANOVA; $n = 18$ each). *C*: schema of latencies reaching 25% maximum by color. The numbers indicate the order of response.

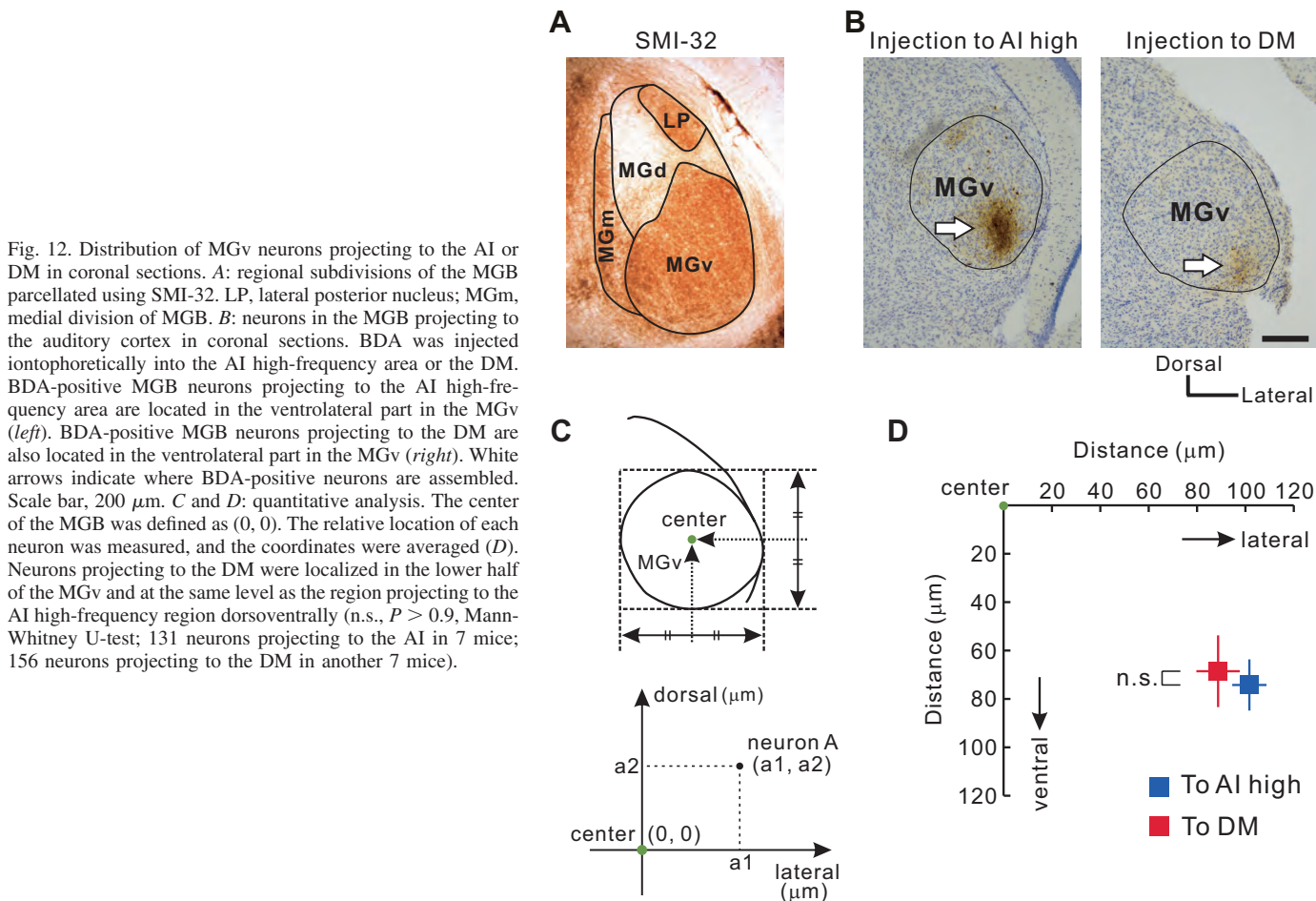


Fig. 12. Distribution of MGv neurons projecting to the AI or DM in coronal sections. *A*: regional subdivisions of the MGB parcellated using SMI-32. LP, lateral posterior nucleus; MGm, medial division of MGB. *B*: neurons in the MGB projecting to the auditory cortex in coronal sections. BDA was injected iontophoretically into the AI high-frequency area or the DM. BDA-positive MGB neurons projecting to the AI high-frequency area are located in the ventrolateral part in the MGv (*left*). BDA-positive MGB neurons projecting to the DM are also located in the ventrolateral part in the MGv (*right*). White arrows indicate where BDA-positive neurons are assembled. Scale bar, 200 μm . *C* and *D*: quantitative analysis. The center of the MGB was defined as (0, 0). The relative location of each neuron was measured, and the coordinates were averaged (*D*). Neurons projecting to the DM were localized in the lower half of the MGv and at the same level as the region projecting to the AI high-frequency region dorsoventrally (n.s., $P > 0.9$, Mann-Whitney U-test; 131 neurons projecting to the AI in 7 mice; 156 neurons projecting to the DM in another 7 mice).

DISCUSSION

In the present study, we observed the regional characteristics in the mouse auditory cortex using flavoprotein fluorescence imaging, two-photon calcium imaging, immunohistochemistry, and tracer experiments. The regional borders of the AI were re-delineated by isolating the DM, which has been reported to be a part of the AI, specialized for processing high-frequency sound signals in mice (Guo et al. 2012; Issa et al. 2014; Joachimsthaler et al. 2014; Sawatari et al. 2011; Stiebler et al. 1997). In the present study, we identified the DM as the fifth frequency-organized region in the cortex, in addition to the three frequency-organized regions—the AAF, AI, and AII—in the auditory cortex (Issa et al. 2014; Kubota et al. 2008) and the insular auditory field (IAF) in the insular cortex (Gogolla et al. 2014; Sawatari et al. 2011; Takemoto et al. 2014). We demonstrated that the frequency gradient of the AI ran from the dorsocaudal to ventrorostral direction, whereas the frequency gradient in the DM ran from the ventrocaudal to dorsorostral direction. The direction of the frequency organization of the AAF was from dorsostral to ventrocaudal, consistent with recent reports (Horie et al. 2013; Issa et al. 2014; Kubota et al. 2008). The DM responses to a courtship song by males were significantly larger in female mice, which is the first evidence to suggest that the gender-specific biological importance of courtship songs might be reflected in the properties of the mouse auditory system.

Technical merits of using flavoprotein fluorescence imaging to investigate cortical functions in mice. There were several technical advantages in the present study to localize the newly found DM region. First, we used flavoprotein autofluorescence imaging to visualize the mouse auditory cortex. Flavoprotein fluorescence imaging gave us very similar results to those obtained in GCaMP3-expressing mice (Issa et al. 2014) regarding the regional borders between the DM and surrounding regions. This method detects neural activity based on activity-dependent oxygen metabolism; therefore, there is no need to stain neurons using dye solutions, thus allowing uniform observability on the cortical surface (Llano et al. 2009; Shibuki et al. 2003, 2006) and allowing the delineation of regional borders, as in our previous studies (Honma et al. 2013; Kubota et al. 2008; Ohshima et al. 2010). Because of the merits of intrinsic fluorescence imaging, we were able to find a small trough in neuronal activity between the AI and DM (Fig. 2), as seen in GCaMP3-expressing mice (Issa et al. 2014). A critical requirement for delineating small cortical regions is the uniform distribution of fluorophores in the brain, which was based on endogenous flavoproteins or homogeneously expressed GCaMP3. In contrast, unit recording requires the insertion of an electrode into the cortex, and therefore, the recording sites must be set at some intervals. Therefore, the regional border, such as that between the AAF and AI, must be defined as a result of the assumption that the border corresponds to the frequency-gradient reversal line based on unit recording de-

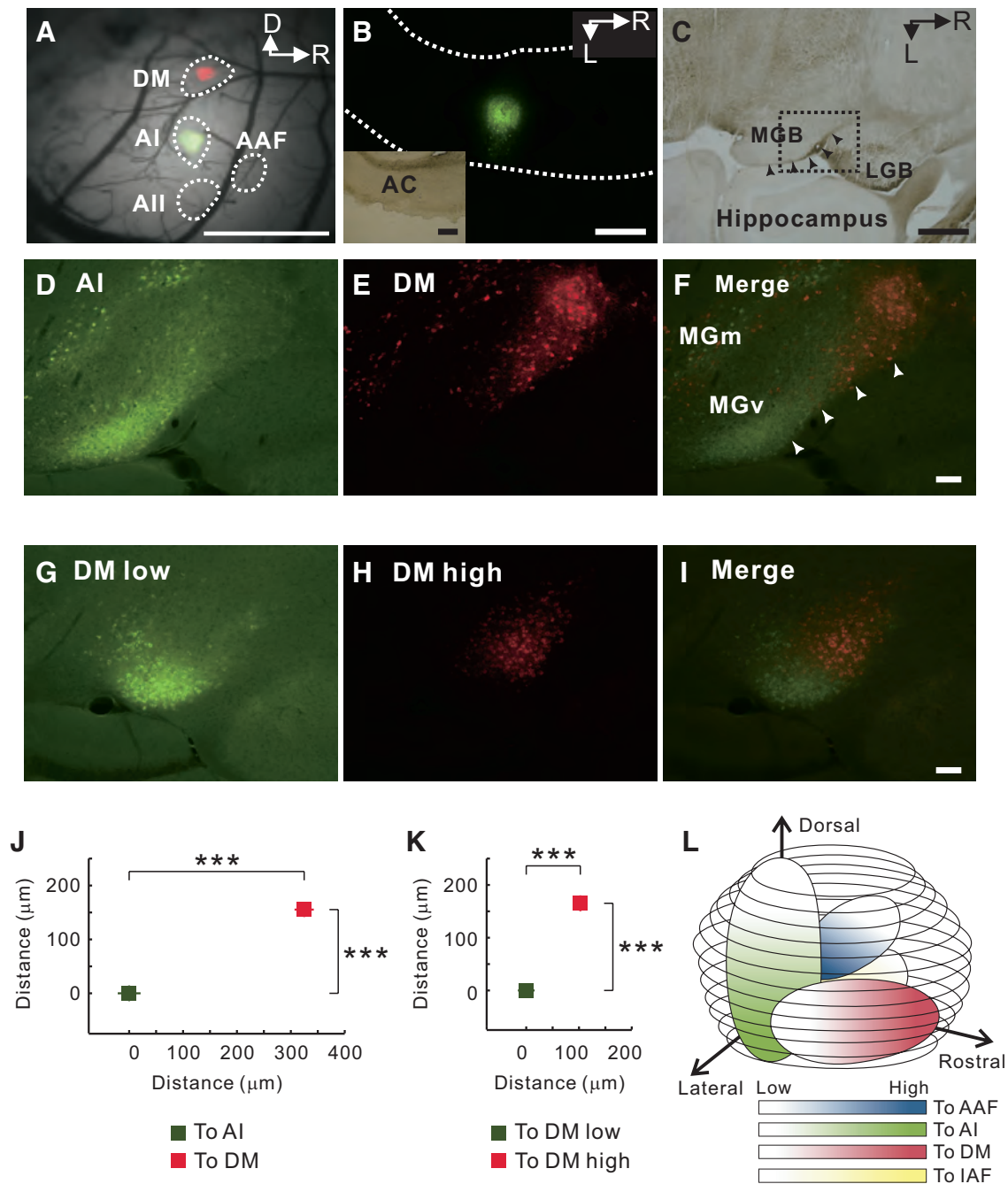


Fig. 13. Distribution of MGv neurons projecting to the DM in horizontal sections. *A*: injection sites in the AI and DM. Image of the brain surface and merged images obtained through a green or a red filter. The dotted lines indicate the outlines of responses to a 40-kHz tone. Scale bar, 1 mm. D, dorsal; R, rostral. *B*: injection site after a horizontal slice was prepared. The dotted lines indicate the outlines of the auditory cortex. *Inset*: the same image observed under bright-field microscopy. Scale bars, 500 μm . L, lateral. *C*: bright-field view of the MGB in a horizontal slice. The dotted rectangle represents the window containing images of *D–F*. Scale bar, 500 μm . LGB, lateral geniculate body. *D–F*: neurons projecting to the AI ventral high-frequency area and DM (*F*). The arrowheads indicate the lateral edge of the MGv as shown in *C*. Scale bar, 100 μm . *G–I*: neurons projecting to the low- and high-frequency areas of the DM (*I*). Scale bar, 100 μm . *J*: the relative coordinates of neurons projecting to the DM vs. the AI. The average of the coordinates of neurons projecting to the AI was set as the origin. In 6 mice, 71 neurons projecting to the AI and 103 neurons projecting to the DM were found. $***P < 0.001$, Mann-Whitney U-test. *K*: the relative coordinates of neurons projecting to a low-frequency area vs. high-frequency (60 kHz) area in the DM. The average of the coordinates of neurons projecting to a low-frequency area was set as the origin. In 3 mice, 33 neurons projecting to the low-frequency area of the DM and 28 neurons projecting to the high-frequency area were found. $***P < 0.001$, Mann-Whitney U-test. *L*: 3-dimensional schematic view of the relative locations of 4 compartments within MGv. The schema of the compartment projecting to the insular auditory field (IAF), AAF, or AI was compensated, according to the elegant study by Takemoto et al. (2014) and, in part, the study by Horie et al. (2013).

scribed in previous studies. Thus it is no wonder that the small trough between the DM and the ventral AI high-frequency area was not found in previous studies using unit recording. The DM is sensitive to ultrasonic sounds over 40 kHz, and the

response of the AI is somewhat weaker than that of the DM. These factors might have led to the conclusion that a single frequency gradient extended from the AI low-frequency area to the DM in previous electrophysiological experiments (Guo et

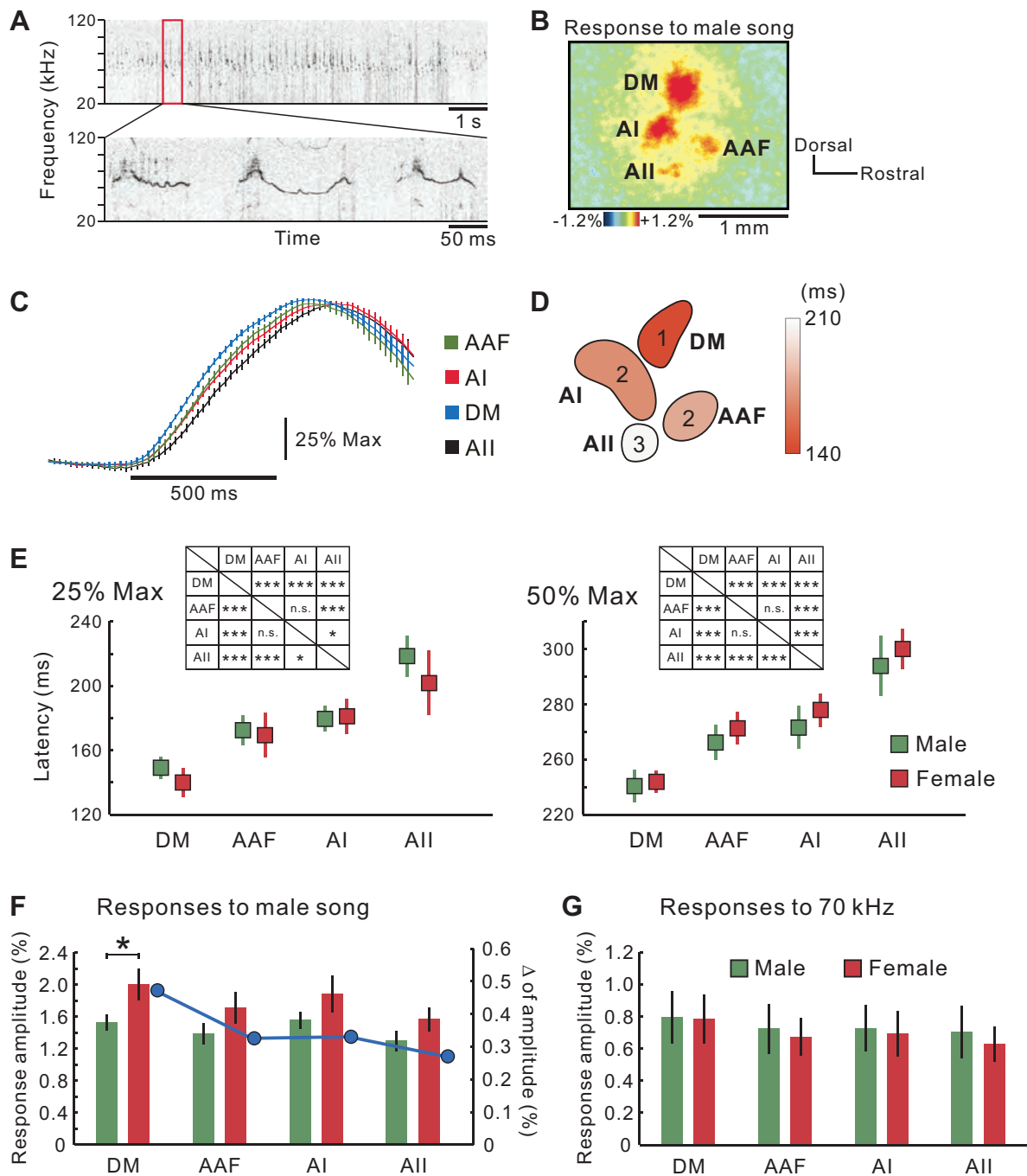


Fig. 14. Auditory responses to courtship male songs. *A*: recorded spectrogram of a courtship song produced by a male C57BL/6 mouse when approaching a female (*top*). The red box indicates the segment used in this study as a stimulus (*bottom*). *B*: the typical image of the response in the auditory cortex to the male's song. The dorsal anterior "UF" region identified by Stiebler et al. (1997) was not activated, probably because this region is responsive to slow FM sweeps, ~ 24 kHz/s, which were not included in the male's songs. The DM was identified based on the responses to a 70-kHz tone, as performed in the previous sections. The response peaks of the DM to a 70-kHz tone and a courtship song did not shift significantly. *C*: temporal profiles of $\Delta F/F_0$ in each region in response to the male's song ($n = 20$). Images were obtained at 54 Hz. *D*: schema showing the latency of responses to reach 25% maximum. *E*: the time required to reach 25% (*left*) or 50% maximum (*right*); male, $n = 7$; female, $n = 13$. *Insets*: statistical significance of pair-wise comparisons between regions with respect to latency required to reach 25% maximum (*left*) and 50% maximum (*right*) of the response peak to a male's song. The sexes were mixed, because there was no difference between them. *** $P < 0.001$, * $P < 0.05$, 1-way repeated-measures ANOVA; $n = 20$. *F*: response amplitudes to a male's song (*left* axis). The blue plots indicate the difference in averaged amplitudes between females and males (*right* axis); male, $n = 15$; female, $n = 16$. * $P < 0.05$, Mann-Whitney U-test. *G*: response amplitudes to a 70-kHz ultrasonic tone; male, $n = 15$; female, $n = 16$.

al. 2012) or that the strong frequency gradient traveled across these two different regions (Issa et al. 2014).

Another benefit of flavoprotein fluorescence imaging is that variability of the signal amplitudes in $\Delta F/F_0$ is very small in

each mouse, especially when transcranial imaging is performed. Because the skull of a mouse is transparent, and flavoproteins exist originally in neurons, we can observe the same pattern of responses transcranially without craniotomy,

which might confound the results. Moreover, as flavoproteins are an endogenous protein in the mitochondrial electron transport chain, it is very unlikely that flavoproteins work as a calcium chelator and have some artificial effects on the calcium dynamics, which is essential for the induction of cortical plasticity (Zucker 1999).

Finally, we were able to combine flavoprotein fluorescence imaging with anatomical techniques using fluorescent tracers, because the flavoprotein signals were much weaker than those from the fluorescent tracers. The combination of flavoprotein fluorescence imaging and microinjection of a retrograde fluorescent tracer could reveal multiple compartments in the MGv. Because the MGv is located deep within the brain, it is difficult to perform precise MGv experiments without anatomical studies. Direct optical imaging to observe responses in the MGv has not been reported. Although functional MRI (fMRI) imaging can be used to observe activities deep within the brain, the spatial resolution is too low to find multiple compartments in the mouse MGv. Without the fine spatial resolution achieved by anatomical studies, the precise multicompartments with a distinct frequency gradient (Fig. 13L) could not be visualized, because the general concept of one frequency organization in one region is also applicable in mice. The combination of optical imaging and localized tracer injection into functionally identified, small cortical regions is expected to be greatly advantageous for detecting fine topological organization in other sensory cortices other than the auditory cortex.

New definition of regions included in the mouse auditory cortex. Our findings suggest that the term UF might not be appropriate. Stiebler et al. (1997) defined the UF as a distinct, frequency-unorganized region, where neurons have a characteristic frequency over 50 kHz (Fig. 1A). Then, UF as a distinct region was denied, and the term UF has also been used to indicate the high-frequency area of the AAF and AI (Fig. 1B) (Guo et al. 2012) or only the dorsal AI high-frequency area (Fig. 1C) (Issa et al. 2014). However, optical imaging revealed that frequency direction of the AAF runs ventrocaudally (Issa et al. 2014) and that the AII has the distinct frequency organization (Issa et al. 2014; Kubota et al. 2008). By delineating the DM, we have identified the four distinct frequency-organized regions of the AAF, AI, DM, and AII, in total, each of which has its own high-frequency area (up to 80 kHz) corresponding to the UF. Optical imaging also revealed that a vacant region insensitive to pure tones containing vocalization-specific neurons is located between the AAF and AI dorsal high-frequency area (Issa et al. 2014), and we have already reported that the region between the AAF and DM is responsive to slow FM components, regardless of tonal frequency range (Fig. 1D) (Honma et al. 2013; Tsukano et al. 2013b). These facts indicate that the distinct FM-sensitive region exists in this area in the mouse auditory cortex, similar to that observed in bats (Suga and Jen 1976). Actually, there is a possibility that Stiebler et al. (1997) might perform recordings without distinguishing between the DM and frequency-unorganized, FM-sensitive region. They mentioned in their paper that neurons observed in the rostral part of the UF were FM sensitive but not tone sensitive (Stiebler et al. 1997). The confusion of two different regions might obscure a frequency-organized structure and lead to the misconception that UF was not frequency organized (Stiebler et al. 1997). Overall, we propose to subdivide the dorsal part of the auditory cortex

precisely and to assign new, anatomical names: the dorsoanterior field (DA) to the FM-sensitive region just dorsal to the AAF and the DM to the region newly identified in the present study (Fig. 1D), in addition to the classical DP named previously (Stiebler et al. 1997).

Multiple frequency organizations have been found in various mammals. By identifying the DM with a distinct frequency gradient using flavoprotein fluorescence imaging, multiple frequency organizations were revealed in the mouse auditory cortex in the present study. In primates, frequency-organized structures exist in the belt region besides the core region. With the use of fMRI, it was revealed that the caudal-medial (CM) field in macaques, which belongs to the belt, has stronger frequency gradient than do fields in the core, and other belt fields also have a frequency gradient (Petkov et al. 2006). Moreover, multiple frequency-organized structures were also found in rodents, such as guinea pigs (Nishimura et al. 2007), ferrets (Bizley and King 2009), chinchillas (Harel et al. 2000), and rats (Higgins et al. 2010; Kalatsky et al. 2005) using optical imaging. Especially the auditory cortical maps revealed in rats (Higgins et al. 2010; Kalatsky et al. 2005) are quite similar to those we revealed in mice. Several imaging studies have revealed that the AII is frequency organized in mice (Issa et al. 2014; Kubota et al. 2008). The IAF in the mouse insular cortex anterior to the auditory cortex is also frequency organized (Sawatari et al. 2011; Takemoto et al. 2014). Hence, at least five frequency-organized regions exist inside and near the auditory cortex in mice. Each frequency-organized region receives distinct thalamic information from equivalent compartments with a distinct frequency organization in the MGv (Fig. 13L) (Horie et al. 2013; Takemoto et al. 2014), and the sound responses are presumably conveyed through the course of the hierarchical, inter-regional processing in the auditory cortex (Fig. 14) (Kaas and Hackett 2000; Kubota et al. 2005).

The basic concept of “core and belt” prevails in the auditory cortex across species (Winer and Schreiner 2011). The core region contains the AAF and AI, which receive dense projections from the frequency-organized MGv and process lemniscal information from the cochlea. The belt region surrounding the core receives nonlemniscal information from the frequency-unorganized MGd across species basically (Winer and Schreiner 2011). Although the DM in mice is located dorsal to the AAF and AI and should be considered as the belt (Fig. 1D), the DM has a clear frequency gradient and receives topographic thalamic inputs directly from the MGv (Fig. 13). In rats, the ventral auditory field, which is frequency organized and placed ventral to the AAF and AI, also receives dense thalamic projections from the caudal part of the MGv (Storace et al. 2010). These findings suggest that the belt regions in rodents receive frequency-organized, lemniscal-thalamic information directly. In contrast, the belt fields with a frequency organization, including the CM, receive thalamic inputs from the frequency-unorganized MGd in marmosets (de la Mothe et al. 2012), suggesting that the frequency representation in the belt may derive from the core after intracortical interactions in primates. Although these present and prior observations suggest that rodents and primates have multiple frequency-organized belt auditory fields, it remains to be seen to what degree these fields are functionally homologous or analogous between rodents and primates.

Many animal species use ultrasonic frequencies for navigation or communication with others. Actually, rodents communicate with each other using ultrasonic frequency vocalization over 50 kHz. Ultrasonic songs produced by male mice induce exploratory behaviors in female mice (Hammerschmidt et al. 2009; Holy and Guo 2005), and isolated pups attempt to communicate with their mother by producing isolation calls (Ehret 2005; Hahn and Schanz 2005). Therefore, it is critical for mice to receive and process ultrasonic sounds. The DM has fewer neurons with low BFs and responds well to ultrasonic sounds compared with the AI (Figs. 5, D and E, and 6). Moreover, strong plasticity is not induced in the DM by acoustic exposure (Fig. 9). The degree of variability in the frequency organization in cellular resolution recording is less marked in the DM than in the AI (Fig. 6). These data imply that the DM is not dynamically regulated by learning; instead, the DM is dedicated for processing some congenitally important sounds, such as courtship chirps, as shown in Fig. 14.

The DM may play a role of recipient and relay point for processing of courtship songs. The thalamocortical auditory pathway comprises parallel pathways, and each region in the auditory cortex receives a topological projection from the corresponding subregion in the MGv (Horie et al. 2013; Takemoto et al. 2014). The DM receives dense projections directly from the rostral part of the MGv (Fig. 13) and is the first region to be activated in both sexes by a male courtship song. These data imply that the MGv determines the region of the auditory cortex to which song information will be sent. A characteristic waveform and frequency included in voices emitted under a specific condition (Hammerschmidt et al. 2009; Holy and Guo 2005; Insel et al. 1986) may selectively activate gating channels in the thalamus (Schiff et al. 2013) to choose a specific recipient in the auditory cortex. Furthermore, there was a significant difference in response amplitudes of a male courtship song in the DM between sexes (Fig. 14F), which may reflect the results of previous behavioral studies that female mice respond specifically to male courtship songs (Hammerschmidt et al. 2009). The auditory cortex is required for fear conditioning using complex sounds (Letzkus et al. 2011). Therefore, subregions of the auditory cortex may themselves have roles for evaluating the biological meanings attached to natural sounds.

ACKNOWLEDGMENTS

The authors thank S. Maruyama for technical assistance and A. Matsushima for mouse breeding and maintenance.

GRANTS

Support for this study was provided by the Japan Society for the Promotion of Science KAKENHI (Grant Number 24700320; to H. Tsukano).

DISCLOSURES

The authors declare no competing interests.

AUTHOR CONTRIBUTIONS

Author contributions: H. Tsukano, R.H., M.K., K.T., H. Takebayashi, and K.S. conception and design of research; H. Tsukano, M.H., T.B., and A.U. performed experiments; H. Tsukano, M.H., T.B., and A.U. analyzed data; H. Tsukano, M.H., and K.S. interpreted results of experiments; H. Tsukano prepared figures; H. Tsukano drafted manuscript; H. Tsukano, M.K., H.

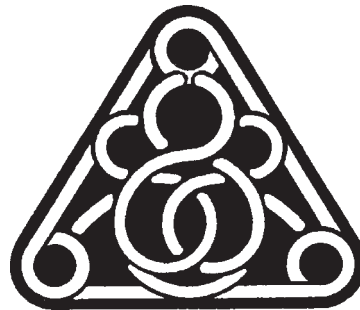
Takebayashi, and K.S. edited and revised manuscript; H. Tsukano, M.H., T.B., R.H., M.K., K.T., H. Takebayashi, and K.S. approved final version of manuscript.

REFERENCES

- Andermann ML, Kerlin AM, Roumis DK, Glickfeld LL, Reid RC. Functional specialization of mouse higher visual cortical areas. *Neuron* 72: 1025–1039, 2011.
- Asaba A, Okabe S, Nagasawa M, Kato M, Koshida N, Osakada T, Mogi K, Kikusui T. Developmental social environment imprints female preference for male song in mice. *PLoS One* 9: e87186, 2014.
- Bandyopadhyay S, Shamma SA, Kanold PO. Dichotomy of functional organization in the mouse auditory cortex. *Nat Neurosci* 13: 361–368, 2010.
- Barkat TR, Polley DB, Hensch TK. A critical period for auditory thalamocortical connectivity. *Nat Neurosci* 14: 1189–1194, 2011.
- Bathellier B, Ushakova L, Rumpel S. Discrete neocortical dynamics predict behavioral categorization of sounds. *Neuron* 76: 435–449, 2012.
- Bizley JK, King AJ. Visual influences on ferret auditory cortex. *Hear Res* 258: 55–63, 2009.
- Bizley JK, Walker KM, Silverman BW, King AJ, Schnupp JW. Interdependent encoding of pitch, timbre, and spatial location in auditory cortex. *J Neurosci* 29: 2064–2075, 2009.
- Boire D, Desgent S, Matteau I, Ptitto M. Regional analysis of neurofilament protein immunoreactivity in the hamster's cortex. *J Chem Neuroanat* 29: 193–208, 2005.
- Budinger E, Heil P, Scheich H. Functional organization of auditory cortex in the Mongolian gerbil (*Meriones unguiculatus*). III. Anatomical subdivisions and corticocortical connections. *Eur J Neurosci* 12: 2425–2451, 2000.
- de la Mothe LA, Blumell S, Kajikawa Y, Hackett TA. Thalamic connections of auditory cortex in marmoset monkeys: lateral belt and parabelt regions. *Anat Rec (Hoboken)* 295: 822–836, 2012.
- de Villers-Sidani E, Chang EF, Bao S, Merzenich MM. Critical period window for spectral tuning defined in the primary auditory cortex (A1) in the rat. *J Neurosci* 27: 180–189, 2007.
- Ehret G. Infant rodent ultrasounds—a gate to the understanding of sound communication. *Behav Genet* 35: 19–29, 2005.
- Ehret G, Haack B. Ultrasound recognition in house mice: key stimulus configuration and recognition mechanisms. *J Comp Physiol A* 148: 245–251, 1982.
- Fischer J, Hammerschmidt K. Ultrasonic vocalizations in mouse models for speech and socio-cognitive disorders: insights into the evolution of vocal communication. *Genes Brain Behav* 10: 17–27, 2011.
- Galindo-Leon EE, Lin FG, Liu RC. Inhibitory plasticity in a lateral band improves cortical detection of natural vocalizations. *Neuron* 62: 705–716, 2009.
- Glickfeld LL, Andermann ML, Bonin V, Reid RC. Cortico-cortical projections in mouse visual cortex are functionally target specific. *Nat Neurosci* 16: 219–226, 2013.
- Gogolla N, Takesian AE, Feng G, Fagiolini M, Hensch TK. Sensory integration in mouse insular cortex reflects GABA circuit maturation. *Neuron* 83: 894–905, 2014.
- Guo W, Chambers AR, Darrow KN, Hancock KE, Shinn-Cunningham BG, Polley DB. Robustness of cortical topography across fields, laminae, anesthetic states, and neurophysiological signal types. *J Neurosci* 32: 9159–9172, 2012.
- Hackett TA, Barkat TR, O'Brien BM, Hensch TK, Polley DB. Linking topography to tonotopy in the mouse auditory thalamocortical circuit. *J Neurosci* 31: 2983–2995, 2011.
- Hahn ME, Schanz N. The effects of cold, rotation, and genotype on the production of ultrasonic calls in infant mice. *Behav Genet* 32, 267–273, 2005.
- Hammerschmidt K, Radyushkin K, Ehrenreich H, Fischer J. Female mice respond to male ultrasonic 'songs' with approach behaviour. *Biol Lett* 5: 589–592, 2009.
- Harel N, Mori N, Sawada S, Mount RJ, Harrison RV. Three distinct auditory areas of cortex (AI, AII, and AAF) defined by optical imaging of intrinsic signals. *Neuroimage* 11: 302–312, 2000.
- Higgins NC, Storace DA, Escabi MA, Read HL. Specialization of binaural responses in ventral auditory cortices. *J Neurosci* 30: 14522–14532, 2010.
- Hofstetter KM, Ehret G. The auditory cortex of the mouse: connections of the ultrasonic field. *J Comp Neurol* 323: 370–386, 1992.
- Holy TE, Guo Z. Ultrasonic songs of male mice. *PLoS Biol* 3: e386, 2005.

- Honma Y, Tsukano H, Horie M, Ohshima S, Tohmi M, Kubota Y, Takahashi K, Hishida R, Takahashi S, Shibuki K. Auditory cortical areas activated by slow frequency-modulated sounds in mice. *PLoS One* 8: e68113, 2013.
- Horie M, Tsukano H, Hishida R, Takebayashi H, Shibuki K. Dual compartments of the ventral division of the medial geniculate body projecting to the core region of the auditory cortex in C57BL/6 mice. *Neurosci Res* 76: 207–212, 2013.
- Imaizumi K, Priebe NJ, Crum PA, Bedenbaugh PH, Cheung SW, Schreiner CE. Modular functional organization of cat anterior auditory field. *J Neurophysiol* 92: 444–457, 2004.
- Insel TR, Hill JL, Mayor RB. Rat pup ultrasonic isolation calls: possible mediation by the benzodiazepine receptor complex. *Pharmacol Biochem Behav* 24: 1263–1267, 1986.
- Issa JB, Haeffele BD, Agarwal A, Bergles DE, Young ED, Yue DT. Multiscale optical Ca²⁺ imaging of tonal organization in mouse auditory cortex. *Neuron* 83: 944–959, 2014.
- Joachimsthaler B, Uhlmann M, Miller F, Ehret G, Kurt S. Quantitative analysis of neuronal response properties in primary and higher-order auditory cortical fields of awake house mice (*Mus musculus*). *Eur J Neurosci* 39: 904–918, 2014.
- Kaas JH, Hackett TA. Subdivisions of auditory cortex and processing streams in primates. *Proc Natl Acad Sci USA* 97: 11793–11799, 2000.
- Kalatsky VA, Polley DB, Merzenich MM, Schreiner CE, Stryker MP. Fine functional organization of auditory cortex revealed by Fourier optical imaging. *Proc Natl Acad Sci USA* 102: 13325–13330, 2005.
- Kanold PO, Nelken I, Polley DB. Local versus global scales of organization in auditory cortex. *Trends Neurosci* 37: 502–510, 2014.
- Komagata S, Chen S, Suzuki A, Yamashita H, Hishida R, Maeda T, Shibata M, Shibuki K. Initial phase of neuropathic pain within a few hours after nerve injury in mice. *J Neurosci* 31: 4896–4905, 2011.
- Kubota Y, Kamatani D, Tsukano H, Ohshima S, Takahashi K, Hishida R, Kudoh M, Takahashi S, Shibuki K. Transcranial photo-inactivation of neural activities in the mouse auditory cortex. *Neurosci Res* 60: 422–430, 2008.
- Lahvis GP, Alleva E, Scattoni ML. Translating mouse vocalizations: prosody and frequency modulation. *Genes Brain Behav* 10: 4–16, 2011.
- LeDoux JE, Ruggiero DA, Forest R, Stornetta R, Reis DJ. Topographic organization of convergent projections to the thalamus from the inferior colliculus and spinal cord in the rat. *J Comp Neurol* 264: 123–146, 1987.
- LeDoux JE, Ruggiero DA, Reis DJ. Projections to the subcortical forebrain from anatomically defined regions of the medial geniculate body in the rat. *J Comp Neurol* 242: 182–213, 1985.
- Lee CC, Schreiner CE, Imaizumi K, Winer JA. Tonotopic and heterotopic projection systems in physiologically defined auditory cortex. *Neuroscience* 128: 871–887, 2004.
- Letzkus JJ, Wolff SB, Meyer EM, Tovote P, Courtin J, Herry C, Lüthi A. A disinhibitory microcircuit for associative fear learning in the auditory cortex. *Nature* 480: 331–335, 2011.
- Linden JF, Liu RC, Sahani M, Schreiner CE, Merzenich MM. Spectrotemporal structure of receptive fields in areas AI and AAF of mouse auditory cortex. *J Neurophysiol* 90: 2660–2675, 2003.
- Llano DA, Sherman SM. Evidence for nonreciprocal organization of the mouse auditory thalamocortical-corticothalamic projection systems. *J Comp Neurol* 507: 1209–1227, 2008.
- Llano DA, Theyel BB, Mallik AK, Sherman SM, Issa NP. Rapid and sensitive mapping of long-range connections in vitro using flavoprotein autofluorescence imaging combined with laser photostimulation. *J Neurophysiol* 101: 3325–3340, 2009.
- Marshall JH, Garrett ME, Nauhaus I, Callaway EM. Functional specialization of seven mouse visual cortical areas. *Neuron* 72: 1040–1054, 2011.
- Mellott JG, Van der Gucht E, Lee CC, Carrasco A, Winer JA, Lomber SG. Areas of cat auditory cortex as defined by neurofilament proteins expressing SMI-32. *Hear Res* 267: 119–136, 2010.
- Nakahara H, Zhang LI, Merzenich MM. Specialization of primary auditory cortex processing by sound exposure in the “critical period”. *Proc Natl Acad Sci USA* 101: 7170–7174, 2004.
- Nishimura M, Shirasawa H, Kaizo H, Song WJ. New field with tonotopic organization in guinea pig auditory cortex. *J Neurophysiol* 97: 927–932, 2007.
- Oh SW, Harris JA, Ng L, Winslow B, Cain N, Mihalas S, Wang Q, Lau C, Kuan L, Henry AM, Mortrud MT, Ouellette B, Nguyen TN, Sorensen SA, Slaughterbeck CR, Wakeman W, Li Y, Feng D, Ho A, Nicholas E, Hirokawa KE, Bohn P, Joines KM, Peng H, Hawrylycz MJ, Phillips JW, Hohmann JG, Wahnoutka P, Gerfen CR, Koch C, Bernard A, Dang C, Jones AR, Zeng H. A mesoscale connectome of the mouse brain. *Nature* 508: 207–214, 2014.
- Ohshima S, Tsukano H, Kubota Y, Takahashi K, Hishida R, Takahashi S, Shibuki K. Cortical depression in the mouse auditory cortex after sound discrimination learning. *Neurosci Res* 67: 51–58, 2010.
- Ouda L, Druga R, Syka J. Distribution of SMI-32-immunoreactive neurons in the central auditory system of the rat. *Brain Struct Funct* 217: 19–36, 2012.
- Oviedo HV, Bureau I, Svoboda K, Zador AM. The functional asymmetry of auditory cortex is reflected in the organization of local cortical circuits. *Nat Neurosci* 13: 1413–1420, 2010.
- Paxinos G. (editor). *The Rat Nervous System*, 3rd ed. San Diego: Academic, 2003.
- Paxinos G, Franklin KBJ. *The Mouse Brain in Stereotaxic Coordinates*, 2nd ed. San Diego: Academic, 2001.
- Paxinos G, Watson C, Carrive P, Kirkcaldie M, Ashwell KW. *Chemoarchitectonic Atlas of the Rat Brain*, 2nd ed. San Diego: Academic, 2009.
- Petkov CI, Kayser C, Augath M, Logothetis NK. Functional imaging reveals numerous fields in the monkey auditory cortex. *PLoS Biol* 4: e215, 2006.
- Polley DB, Read HL, Storace DA, Merzenich MM. Multiparametric auditory receptive field organization across five cortical fields in the albino rat. *J Neurophysiol* 97: 3621–3638, 2007.
- Rothschild G, Nelken I, Mizrahi A. Functional organization and population dynamics in the mouse primary auditory cortex. *Nat Neurosci* 13: 353–360, 2010.
- Rotschafer S, Razak K. Altered auditory processing in a mouse model of fragile X syndrome. *Brain Res* 1506: 12–24, 2013.
- Rouiller EM, Simm GM, Villa AE, de Ribaupierre Y, de Ribaupierre F. Auditory corticocortical interconnections in the cat: evidence for parallel and hierarchical arrangement of the auditory cortical areas. *Exp Brain Res* 86: 483–505, 1991.
- Sawatari H, Tanaka Y, Takemoto M, Nishimura M, Hasegawa K, Saitoh K, Song WJ. Identification and characterization of an insular auditory field in mice. *Eur J Neurosci* 34: 1944–1952, 2011.
- Schiff ND, Shah SA, Hudson AE, Nauvel T, Kalik SF, Purpura KP. Gating of attentional effort through the central thalamus. *J Neurophysiol* 109: 1152–1163, 2013.
- Shibuki K, Hishida R, Murakami H, Kudoh M, Kawaguchi T, Watanabe M, Watanabe S, Kouuchi T, Tanaka R. Dynamic imaging of somatosensory cortical activity in the rat visualized by flavoprotein autofluorescence. *J Physiol* 549: 919–927, 2003.
- Shibuki K, Ono K, Hishida R, Kudoh M. Endogenous fluorescence imaging of somatosensory cortical activities after discrimination learning in rats. *Neuroimage* 30: 735–744, 2006.
- Sternberger LA, Sternberger NH. Monoclonal antibodies distinguish phosphorylated and nonphosphorylated forms of neurofilaments in situ. *Proc Natl Acad Sci USA* 80: 6126–6130, 1983.
- Stiebler I, Neulist R, Fichtel I, Ehret G. The auditory cortex of the house mouse: left-right differences, tonotopic organization and quantitative analysis of frequency representation. *J Comp Physiol A* 181: 559–571, 1997.
- Storace DA, Higgins NC, Chikar JA, Oliver DL, Read HL. Gene expression identifies distinct ascending glutamatergic pathways to frequency-organized auditory cortex in the rat brain. *J Neurosci* 32: 15759–15768, 2012.
- Storace DA, Higgins NC, Read HL. Thalamic label patterns suggest primary and ventral auditory fields are distinct core regions. *J Comp Neurol* 518: 1630–1646, 2010.
- Suga N, Jen PH. Disproportionate tonotopic representation for processing CF-FM sonar signals in the mustache bat auditory cortex. *Science* 194: 542–544, 1976.
- Takahashi K, Hishida R, Kubota Y, Kudoh M, Takahashi S, Shibuki K. Transcranial fluorescence imaging of auditory cortical plasticity regulated by acoustic environments in mice. *Eur J Neurosci* 23: 1365–1376, 2006.
- Takemoto M, Hasegawa K, Nishimura M, Song WJ. The insular auditory field receives input from the lemniscal subdivision of the auditory thalamus in mice. *J Comp Neurol* 522: 1373–1389, 2014.
- Thornton LM, Hahn ME, Schanz N. Genetic and developmental influences on infant mouse ultrasonic calling. III. Patterns of inheritance in the calls of mice 3–9 days of age. *Behav Genet* 35: 73–83, 2005.
- Tohmi M, Meguro R, Tsukano H, Hishida R, Shibuki K. The extrageniculate visual pathway generates distinct response properties in the higher visual areas of mice. *Curr Biol* 24: 587–597, 2014.

- Tohmi M, Takahashi K, Kubota Y, Hishida R, Shibuki K.** Transcranial flavoprotein fluorescence imaging of mouse cortical activity and plasticity. *J Neurochem* 109, Suppl 1: 3–9, 2009.
- Tsukano H, Hishida R, Shibuki K.** Detection of virtual pitch up to 5 kHz by mice. *Neurosci Res* 71: 140–144, 2011.
- Tsukano H, Horie M, Hishida R, Shibuki K.** New subarea in the rostradorsal part of the primary auditory cortex in mice. *J Physiol Sci* 63: S205, 2013a.
- Tsukano H, Horie M, Honma Y, Ohga S, Hishida R, Takebayashi H, Takahashi S, Shibuki K.** Age-related deterioration of cortical responses to slow FM sounds in the auditory belt region of adult C57BL/6 mice. *Neurosci Lett* 556: 204–209, 2013b.
- Uematsu A, Kikusui T, Kihara T, Harada T, Kato M, Nakano K, Murakami O, Koshida N, Takeuchi Y, Mori Y.** Maternal approaches to pup ultrasonic vocalizations produced by a nanocrystalline silicon thermoacoustic emitter. *Brain Res* 1163: 91–99, 2007.
- van der Gucht E, Vandesande F, Arckens L.** Neurofilament protein: a selective marker for the architectonic parcellation of the visual cortex in adult cat brain. *J Comp Neurol* 441: 345–368, 2001.
- Winer JA, Schreiner CE. (editors).** *The Auditory Cortex*. New York: Springer, 2011.
- Wong P, Kaas JH.** An architectonic study of the neocortex of the short-tailed opossum (*Monodelphis domestica*). *Brain Behav Evol* 73: 206–228, 2009.
- Xiong Q, Oviedo HV, Trotman LC, Zador AM.** PTEN regulation of local and long-range connections in mouse auditory cortex. *J Neurosci* 32: 1643–1652, 2012.
- Yoshitake K, Tsukano H, Tohmi M, Komagata S, Hishida R, Yagi T, Shibuki K.** Visual map shifts based on whisker-guided cues in the young mouse visual cortex. *Cell Rep* 5: 1365–1374, 2013.
- Zhang LI, Bao S, Merzenich MM.** Persistent and specific influences of early acoustic environments on primary auditory cortex. *Nat Neurosci* 4: 1123–1130, 2001.
- Zucker RS.** Calcium- and activity-dependent synaptic plasticity. *Curr Opin Neurobiol* 9: 305–313, 1999.



ORIGINAL
ARTICLEImpaired clustered protocadherin- α leads to aggregated retinogeniculate terminals and impaired visual acuity in mice

Reiko Meguro,* Ryuichi Hishida,† Hiroaki Tsukano,† Kohei Yoshitake,†‡
Ryota Imamura,† Manavu Tohmi,† Takashi Kitsukawa,‡§
Takahiro Hirabayashi,‡§ Takeshi Yagi,‡§ Hirohide Takebayashi* and
Katsuei Shibuki†‡

*Division of Neurobiology and Anatomy, Graduate School of Medical and Dental Sciences, Niigata University, Niigata, Japan

†Department of Neurophysiology, Brain Research Institute, Niigata University, Niigata, Japan

‡Japan Science and Technology Agency-Core Research for Evolutional Science and Technology (CREST), Osaka University, Suita, Japan

§KOKORO-Biology Group, Graduate School of Frontier Biosciences, Osaka University, Osaka, Japan

Abstract

Clustered protocadherins (cPcdhs) comprising cPcdh- α , - β , and - γ , encode a large family of cadherin-like cell-adhesion molecules specific to neurons. Impairment of cPcdh- α results in abnormal neuronal projection patterns in specific brain areas. To elucidate the role of cPcdh- α in retinogeniculate projections, we investigated the morphological patterns of retinogeniculate terminals in the lateral geniculate (LG) nucleus of mice with impaired cPcdh- α . We found huge aggregated retinogeniculate terminals in the dorsal LG nucleus, whereas no such aggregated terminals derived from the retina were observed in the olivary pretectal nucleus and the ventral LG nucleus. These

aggregated terminals appeared between P10 and P14, just before eye opening and at the beginning of the refinement stage of the retinogeniculate projections. Reduced visual acuity was observed in adult mice with impaired cPcdh- α , whereas the orientation selectivity and direction selectivity of neurons in the primary visual cortex were apparently normal. These findings suggest that cPcdh- α is required for adequate spacing of retinogeniculate projections, which may be essential for normal development of visual acuity.

Keywords: aggregated terminals, lateral geniculate nucleus, protocadherin, retinal terminals, visual acuity.

J. Neurochem. (2015) **133**, 66–72.

Clustered protocadherins (cPcdhs) are the largest subgroup of the cadherin superfamily of neuronal adhesion molecules (Kohmura *et al.* 1998; Junghans *et al.* 2005; Shapiro *et al.* 2007; Yagi 2012). Mammalian cPcdh genes consist of three families, cPcdh- α , - β , and - γ , each of which has a clustered structure in a small genome locus on a single chromosome (Wu 2005). In normal mice, olfactory sensory neurons expressing the same odorant receptor project their axons into a specific glomerulus in the main olfactory bulb (Mori and Sakano 2011). However, these projection patterns are abnormal in cPcdh- α knockout (KO) mice, in which the constant region of cPcdh- α is deleted (Hasegawa *et al.* 2008). Furthermore, abnormal aggregation of serotonergic axons is observed in cPcdh- α KO mice (Katori *et al.* 2009), suggesting that cPcdh- α is important for the normal development of axonal projection patterns derived from specific types of neurons.

In the visual system of mice, cPcdh- α is expressed in the optic nerve fibers, in the lateral geniculate nucleus (LG), and in the primary visual cortex (V1) for 2 weeks after birth (Morishita *et al.* 2004). This period before eye opening is very important for eye-specific segregation of the retinogeniculate fibers (Jaubert-Miazza *et al.* 2005; Guido 2008), the

Received November 22, 2014; revised manuscript received January 16, 2015; accepted January 26, 2015.

Correspondence and present address: Reiko Meguro, School of Health Sciences, Faculty of Medicine, Niigata University, 2-746 Asahi-machi, Chuo-ku, Niigata 951-8518, Japan. E-mail: meguror@clg.niigata-u.ac.jp

Abbreviations used: BDA, biotinylated dextran amine; cPcdh, clustered protocadherin; CTb, cholera toxin β subunit; DAB, diaminobenzidine; IGL, intergeniculate leaflet; LG, lateral geniculate nucleus; LGd, dorsal LG; LGv, ventral LG; OPT, olivary pretectal nucleus; PBS, phosphate-buffered saline; V1, primary visual cortex.

refinement of retinogeniculate synapses (Chen and Regehr 2000; Hooks and Chen 2006, 2008; Liu and Chen 2008), and the maturation of inhibitory neurons (Golding *et al.* 2014) in the dorsal LG (LGd). In the present study, we thus investigated the morphology of retinogeniculate terminals in cPcdh- α KO mice and found abnormally aggregated terminals mainly in LGd. These aggregated terminals found in adults were also observed at P14 but not until P10. The abnormal aggregation can result in impaired transmission of visual information through LGd. As expected, we found significantly deteriorated visual acuity in cPcdh- α KO mice, which was determined using a behavioral test (Prusky *et al.* 2000), whereas the orientation tuning of V1 neurons was apparently normal in cPcdh- α KO mice.

Materials and methods

Animal experiments

We used male and female mice of cPcdh- α -KO (Hasegawa *et al.* 2008) and C57BL/6J strain obtained from Charles River Japan (Tokyo, Japan). All experiments were performed in accordance with the guide for the Care and Use of Laboratory Animals of the Science Council of Japan, and were approved by the Animal Experiment Committee of Niigata University.

Neural tracing experiments

Five wild type (WT) mice and five cPcdh- α KO mice of aged 8–10 weeks were anesthetized intraperitoneally with a mixture of ketamine (300 mg/kg; Daiichi-Sankyo, Tokyo, Japan) and xylazine (30 mg/mL; Bayer, Leverkusen, Germany). The cholera toxin β subunit (CTb, 5 ng in 1 μ L of saline; List Biological Laboratories, Campbell, CA, USA), an anterograde neural tracer, was injected into the left eye using a glass pipette. Five days after the injection, the mice were anesthetized with an overdose of pentobarbital (100 mg/kg, i.p.) and perfused with phosphate-buffered saline, followed by 4% paraformaldehyde in 0.1 M phosphate buffer (pH 7.2). For the developmental study, two WT and two cPcdh- α KO mice at each of P10, P14, and P19 were tested in a similar manner with a minimum survival time of 48 h for CTb transportation (Wu *et al.* 2000). The transported CTb in LG was visualized as described previously (Horie *et al.* 2013). Briefly, 50 μ m coronal sections, prepared using a cryostat, were incubated with a goat polyclonal anti-CTb antibody (1 : 8000 dilution; List Biological Laboratories) overnight, followed by incubation with a biotinylated anti-goat IgG antibody (1 : 200 dilution; Jackson, West Grove, PA, USA) for 2 h. The sections were further incubated with an avidin–biotin complex (1 : 100 dilution; Vector Laboratories, Burlingame, CA, USA) and the CTb immunoreactivity was visualized with oxidized diaminobenzidine. The reacted sections were mounted on gelatin-coated glass slides and air-dried. Some serial CTb-labeled sections were counter-stained with cresyl violet. Sections were observed using a microscope (BX-50; Olympus, Tokyo, Japan) and images were acquired using a CCD camera (CS-600; Olympus). The terminal size measurement was taken using a program based on Matlab (Mathworks, Natick, MA, USA). To visualize the corticogeniculate fibers in two of the each WT and cPcdh- α mice, biotinylated dextran amine (BDA-3000;

Invitrogen, Carlsbad, CA, USA) was injected into V1, as described previously (Horie *et al.* 2013; Tohmi *et al.* 2014).

Two-photon calcium imaging of V1 neurons

Orientation selectivity and direction selectivity in V1 neurons were tested using two-photon calcium imaging in five WT and five cPcdh- α KO mice. The two-photon calcium imaging was performed as described previously (Honma *et al.* 2013; Yoshitake *et al.* 2013; Tohmi *et al.* 2014). Briefly, V1 was identified using flavoprotein fluorescence imaging in mice anesthetized with urethane (1.75 g/kg, i.p.). After removing the skull above V1, a glass pipette filled with the cocktail of fura-2 AM (Invitrogen) and sulforhodamine 101 (SR-101; Invitrogen) was inserted at the center of V1 and was advanced into the supragranular layers, down to a depth of 200–300 μ m from the surface. The cocktail was injected using a pressure of 4–15 kPa for 5–10 min, so that the cells in the area located 200–300 μ m from the tip of the pipette were labeled with fura-2. Astrocytes labeled with SR-101 were excluded from further analysis. After the mice were set under a two-photon microscope (TCS SP5 MP; Leica Microsystems, Wetzlar, Germany), grating patterns moving in eight directions (from 0° to 315° in 45° steps) were administered to the mice and V1 neuronal responses were analyzed, as described previously (Honma *et al.* 2013; Yoshitake *et al.* 2013).

Behavioral assessment of visual acuity

Visual acuity of mice was measured via a visual water maze task developed by Prusky and coworkers (Prusky *et al.* 2000; Prusky and Douglas 2004). Ten WT and nine cPcdh- α KO mice (aged 7–12 weeks) were trained and tested in the visual water maze task in 32 trials every day to assess their visual acuity. During the training phase, they were trained to choose a sine-wave vertical grating pattern at a low spatial frequency (0.14 cycles/degree) from a homogeneous gray pattern with the same averaged luminous intensity. In the subsequent testing phase, the limit of their discriminatory ability was assessed at spatial frequencies higher than 0.14 cycles/degree. A preliminary grating threshold was established at which the mice achieved 70% correct choices. The spatial frequencies around the threshold were retested and the average performance was calculated to plot a frequency-of-seeing curve. The point at 70% accuracy was determined from the curve and was defined as the visual acuity.

Statistical tests

The Kormogorv–Smirnov test was used to evaluate the differences in the cumulative distributions of terminal area sizes between WT and cPcdh- α mice. For group comparisons, the Mann–Whitney *U* test was used.

Results

Abnormal aggregation of retinogeniculate terminals in cPcdh- α KO mice

The gross anatomical features of the thalamus and the tectum were checked in WT (Fig. 1a) and cPcdh- α KO (Fig. 1b) mice aged 8–10 weeks. The distribution of CTb-positive terminals originating from the contralateral eye was apparently similar between the two types of mice. At a higher magnification,

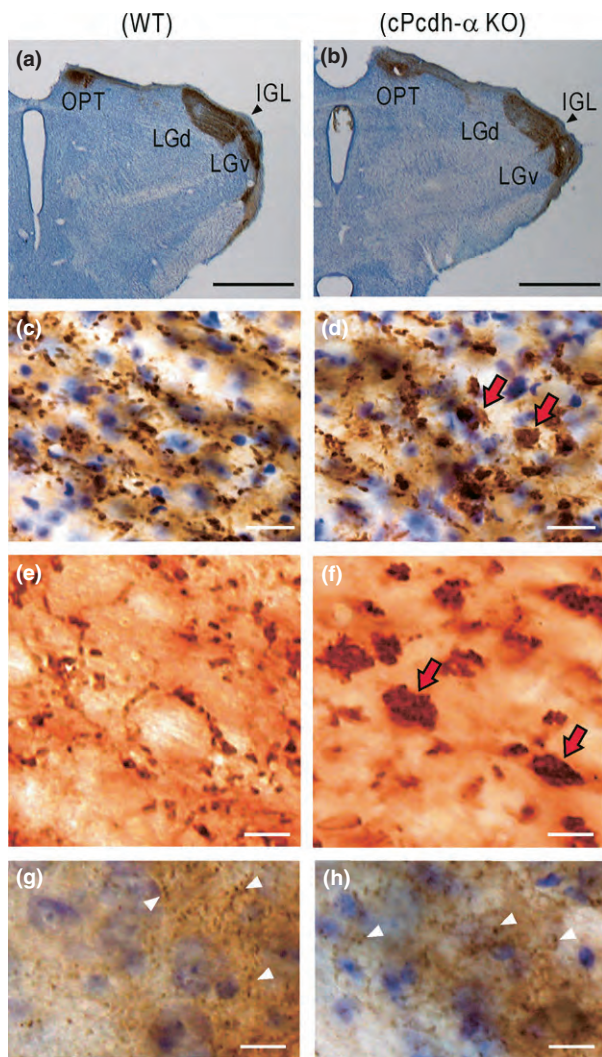


Fig. 1 Retinogeniculate axon terminals in cPcdh- α KO mice. (a and b) Gross distribution patterns of cholera toxin β subunit (CTb)-positive brown terminals derived from the contralateral eye in olivary pretectal nucleus (OPT), dorsal LG (LGd), intergeniculate leaflet (IGL; arrow head), and ventral LG (LGv) of a WT (a) and a cPcdh- α KO (b) mouse, aged 8–10 weeks. Sections were processed by Nissl staining. (c and d) Higher magnification of LGd shown in a (c) and b (d). Many aggregated terminals (arrows) were scattered in the LGd of cPcdh- α KO mice (d). (e and f) Other images of CTb-positive terminals at a higher magnification in a WT (e) and a cPcdh- α (f) mouse. These sections were not counter-stained. (g and h) Corticogeniculate terminals in LGd (arrowheads) labeled after biotinylated dextran amine (BDA) injection into the primary visual cortex (V1) of a WT (g) and a cPcdh- α KO (h) mouse. No aggregated terminals were found. Scale bars, 1 mm in (a and b), 20 μ m in (c and d), and 10 μ m in (e–h).

however, many aggregated terminals were found in LGd of cPcdh- α KO mice (Fig. 1d and f) but not in WT mice (Fig. 1c and e). Some aggregated terminals (arrows in Fig. 1d) were comparable in size to the soma of Nissl-stained LGd neurons. The abnormally aggregated terminals were intermingled with

apparently normal terminals in the LGd of cPcdh- α KO mice. Such abnormal terminals were also observed in the ipsilateral retinogeniculate projection, within the other side of LGd. Some aggregated terminals were also found in the intergeniculate leaflet, whereas few were observed in the olivary pretectal nucleus and in the ventral LG (LGv) in cPcdh- α KO and WT mice (data not shown). As a control, we tested the distribution pattern of corticogeniculate terminals, which represent another main input into the LGd. BDA-positive terminals in LGd, labeled after BDA injection into V1, were not aggregated, and were apparently similar between a WT (Fig. 1g) and a cPcdh- α (Fig. 1h) mouse.

Quantitative analysis of isolated retinogeniculate terminals in cPcdh- α -KO mice

We arbitrarily categorized the aggregated retinogeniculate terminals into three types on the basis of their approximate sizes: large ($\geq 100 \mu\text{m}^2$), medium (< 100 and $> 40 \mu\text{m}^2$), and small ($\leq 40 \mu\text{m}^2$) types. The large type was distributed all over the LGd in cPcdh- α KO mice, except the area receiving CTb-negative terminals from the ipsilateral eye (Fig. 2b). In WT mice, only a few terminals of the large type appeared near the lateral surface of the LGd (Fig. 2a). The medium terminals were observed throughout the LGd in both types of mice (Fig. 2a and b), and the small terminals were as well (data not shown). A quantitative analysis of size distribution in the isolated terminals with or without aggregation revealed a significant difference between WT and cPcdh- α KO mice ($p < 0.001$, Fig. 2c). The mean size of the isolated terminals was $13.1 \mu\text{m}^2$ in WT mice and $27.7 \mu\text{m}^2$ in cPcdh- α KO mice. This difference was statistically significant ($p < 0.005$, Fig. 2d). Fine terminals ($< 13.1 \mu\text{m}^2$) occupied 71% of isolated terminals in WT mice and 56% of those in cPcdh- α KO mice. The density of fine terminals in cPcdh- α KO mice was 62.5% of that observed in WT mice; this difference was also statistically significant ($p < 0.005$, Fig. 2e).

Appearance of the aggregated retinogeniculate terminals at P14 in cPcdh- α KO mice

We examined the post-natal development of retinogeniculate terminals in cPcdh- α KO mice. Gross distribution patterns were similar between WT and cPcdh- α KO mice at all stages after P10, including the normal completion of eye-specific segregation patterns up to P10 (data not shown). In WT mice, the retinogeniculate terminals did not change much in shape and size between P10 and P19, whereas their densities were reduced between P10 and P19 (Fig. 3a, c, and e). In cPcdh- α mice, the aggregated retinogeniculate terminals, which were not present at P10, were observed at P14, at the day of eye opening (Fig. 3b and d). Dark rearing had no effect on these results (data not shown), suggesting that visual experience is not required for aggregation. At P19, the aggregated terminals increased in size and were as large as those

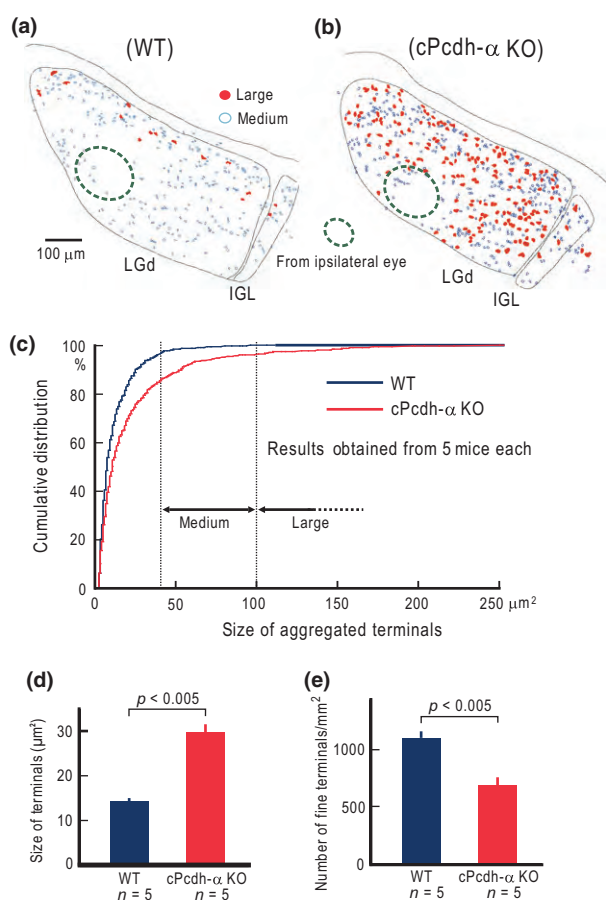


Fig. 2 Quantitative analysis of isolated retinogeniculate terminals. (a and b) Typical schematic distribution of retinal terminals at the center level of dorsal LG (LGd), including the area that receives inputs from the ipsilateral eye. Aggregated terminals were arbitrarily categorized into large ($\geq 100 \mu\text{m}^2$), medium (< 100 and $> 40 \mu\text{m}^2$), and small ($\leq 40 \mu\text{m}^2$) types. Only the large and medium types are shown. The areas surrounded by a dotted line received inputs from the ipsilateral eye. (c) Cumulative distribution of area sizes. The isolated aggregated terminal size measurement was taken on the binarized digital images of cholera toxin β subunit (CTb)-stained sections. (d) Sizes of isolated retinogeniculate terminals. (e) Number of fine type isolated retinogeniculate terminals ($< 13.1 \mu\text{m}^2$) per mm^2 in LGd sections. In the analyses shown in (c–e), the areas that received inputs from the ipsilateral eye were omitted.

observed in adult mice aged 8–10 weeks (Fig. 3f). The mean size of the isolated terminals were 11.72, 12.58, 14.63 μm^2 in two WT mice and 16.57, 20.63, 25.39 μm^2 in two cPcdh- α KO mice, at P10, P14, and P19, respectively.

Deteriorated visual acuity in cPcdh- α KO mice

The presence of the aggregated retinogeniculate terminals suggests abnormal visual functions in cPcdh- α KO mice. Therefore, we performed two-photon calcium imaging of the V1 neurons. However, the orientation selectivity and direction selectivity were apparently similar between WT and cPcdh- α

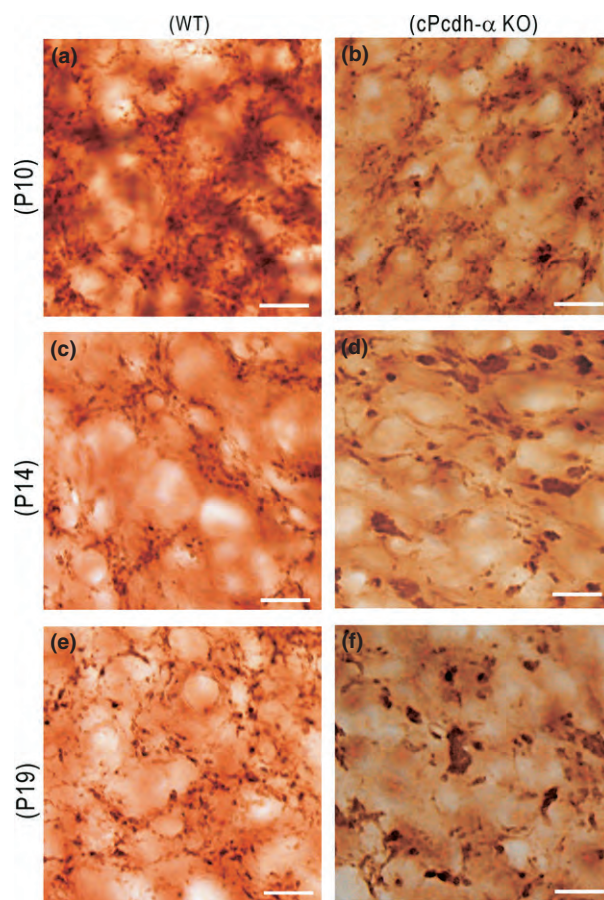


Fig. 3 Ontogenetic observation of retinogeniculate terminals. (a, c, and e) Retinogeniculate terminals at P10 (a), P14 (c), and P19 (e) in WT mice. (b, d, and f) Retinogeniculate terminals at P10 (b), P14 (d), and P19 (f) in cPcdh- α KO mice. Scale bars, 20 μm in (a–f).

KO mice (Fig. 4a and b), as reported previously (Yoshitake *et al.* 2013). We further tested the visual acuity of mice using a behavioral test (Prusky *et al.* 2000), and compared the results between WT and cPcdh- α KO mice (Fig. 4c). WT and cPcdh- α KO mice similarly performed low-frequency tasks at 0.14 cycles/degree during the training phase. The visual acuity of WT mice [0.56 ± 0.01 cycles/degree (mean \pm SEM), $n = 10$] was comparable to the values reported previously (Prusky *et al.* 2000; Prusky and Douglas 2004). However, the visual acuity of cPcdh- α KO mice (0.41 ± 0.01 cycles/degree, $n = 9$) was significantly deteriorated compared with that observed in WT mice ($p < 0.0003$; Fig. 4d and e).

Discussion

Mechanisms underlying terminal aggregation in cPcdh- α KO mice

In the present study, we found abnormal terminal aggregation in the LGd of cPcdh- α KO mice. Impairment of cPcdh- α results in abnormal projection patterns from olfactory sensory neurons expressing a given odorant receptor onto a

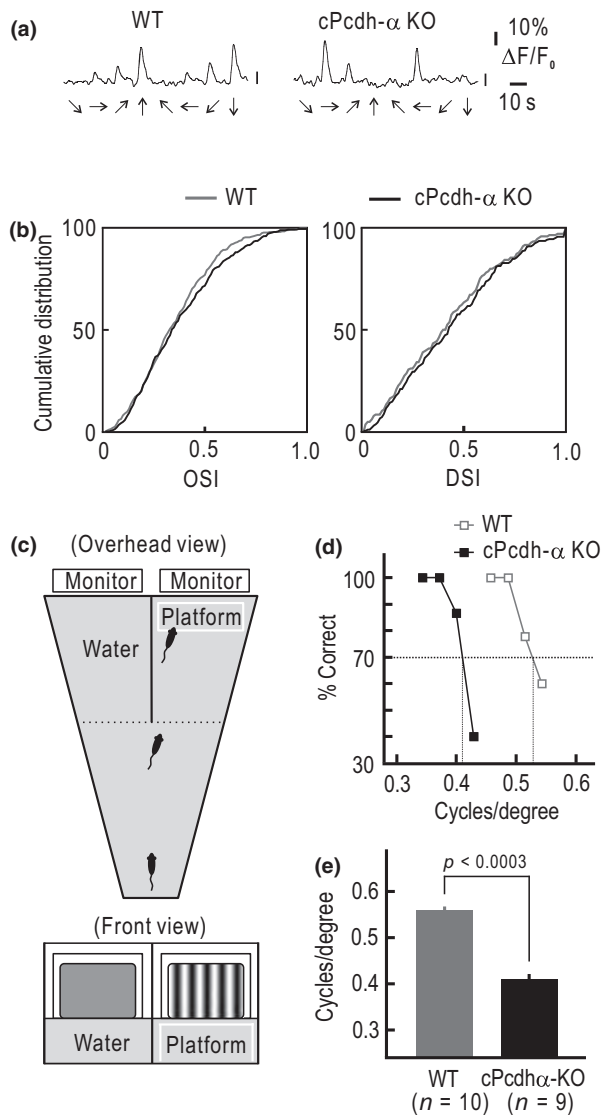


Fig. 4 Reduced visual acuity in cPcdh- α KO mice. (a) Sample traces of neuronal calcium response to moving grating patterns (from 0° to 315° in 45° steps) in a WT mouse (left) and a cPcdh- α KO mouse (right). (b) Cumulative distributions of the orientation selectivity index (OSI) of 481 neurons in WT mice and 423 neurons in cPcdh- α KO mice (left). The distribution of the direction selectivity index (DSI) of 197 neurons in WT mice and 164 neurons in cPcdh- α KO mice is also shown (right). DSI was estimated in neurons with an OSI > 0.4. (c) Schematic drawing of the Prusky water maze used to estimate visual acuity. (d) Examples of the results obtained for a WT and a cPcdh- α KO mouse. (e) Visual acuity in 10 WT and nine cPcdh- α KO mice.

single glomerulus in the olfactory bulb (Hasegawa *et al.* 2008). Abnormal aggregation of serotonergic fibers is also found in cPcdh- α mice (Katori *et al.* 2009). The corticocortical pathways connecting the primary somatosensory cortices in both hemispheres are also impaired in cPcdh- α KO mice (Yamashita *et al.* 2012). These findings indicate that cPcdh- α is required for normal development of axonal

projection patterns derived from specific types of neurons. Although cPcdh- α is expressed in most neurons, impairment of cPcdh- α has dominant effects exclusively in specific types of neurons or synapses. The retinal fiber innervating areas, such as LGd, LGv, and the superior colliculus, also express cPcdh- α , and almost all the optic tract fibers contain cPcdh- α protein during the early post-natal stage, with abnormality appearing in the LGv and the superior colliculus. These findings suggest that other cPcdhs or cell-adhesion molecules might replace cPcdh- α in other neurons or synapses.

Distinct subsets of the cPcdh cluster are expressed differentially in individual neurons, and enormous cell surface diversity may result from their combinatorial expression (Kohmura *et al.* 1998; Wang *et al.* 2002a; Esumi *et al.* 2005; Kaneko *et al.* 2006). The cell surface diversity attributed to cPcdhs assists the formation of specific synapses between neurons expressing similar sets of cPcdhs (Shapiro and Colman 1999; Phillips *et al.* 2003; Yagi 2012). Alternatively, cPcdh- γ supposedly plays a role in self-avoidance between neurites that express the same sets of cPcdh- γ (Lefebvre *et al.* 2012; Zipursky and Grueber 2013). The abnormal terminal aggregation observed in the LGd of cPcdh- α KO mice can be explained by either of the following mechanisms: it may be attributed to non-specific synapse formation between a single LGd neuron and many retinal ganglion cells, or the failure of avoidance between retinogeniculate terminals, which avoid one another in WT mice.

In cPcdh- α KO mice, terminal aggregation was not observed at P10, and appeared just before normal eye opening at P14; thus, cPcdh- α is likely to play an important role in the refinement process of retinogeniculate terminals between P10 and P14 (Chen and Regehr 2000; Hooks and Chen 2006, 2008; Liu and Chen 2008). The slight mean size difference of retinogeniculate terminals already appeared at P10, the starting point of the refinement process with lots of excess terminals to be eliminated. cPcdh- α might have some effects on the size of immature terminals. In contrast, cPcdh- γ is required for neuronal survival and for preparing appropriate synapses in the early development of the spinal cord (Wang *et al.* 2002b; Prasad *et al.* 2008; Prasad and Weiner 2011; Chen *et al.* 2012). Moreover, cPcdh- γ -deleted mutant mice lack voluntary movements and reflexes and die shortly after birth (Wang *et al.* 2002b; Chen *et al.* 2012). Therefore, cPcdh- α and cPcdh- γ may play distinct roles in the neural circuit formation at different developmental stages.

Relationship between terminal aggregation and impaired visual acuity in cPcdh- α KO mice

In the present study, we observed aggregation of retinogeniculate terminals and impaired visual acuity in cPcdh- α KO mice. However, the relationship between the two phenomena remains unclear, because there could be other abnormalities in retinal circuits, in which cPcdh- γ plays an important role (Lefebvre *et al.* 2012), or in circuits higher than LGd, such

as geniculocortical projections, intracortical circuits in V1 or higher visual areas. To date, orientation selectivity, direction selectivity, and ocular dominance plasticity in V1 are apparently normal in cPcdh- α KO mice (Fig. 4 and Yoshitake *et al.* 2013). The estimation of visual acuity required visual discrimination learning, in which no apparent difference was found between WT and cPcdh- α KO mice when a grating pattern of 0.14 cycles/degree was used. However, V1 plasticity induced by spatial mismatches between whisker and visual inputs is impaired in cPcdh- α KO mice, suggesting the presence of some abnormalities in higher areas of these mice (Yoshitake *et al.* 2013). The possibility of retinal circuit and geniculocortical circuit abnormality also needs to be considered. However, an important finding in the present study is that the magnitude of impaired visual acuity in cPcdh- α KO mice was comparable to that of the aggregated retinthalamic terminals. We investigated visual acuity in the present study, since the aggregated retinogeniculate terminals had suggested impaired visual acuity in cPcdh- α KO mice. However, we cannot exclude the possibility that other parameters such as the size of receptive field are abnormal in cPcdh- α KO mice.

Normal retinogeniculate synapses are highly efficient in signal transmission (Budisantoso *et al.* 2012), and aggregation of terminals is unlikely to further assist signal transmission. Instead, non-specific mixing of the information conveyed by each retinal ganglion axon at the aggregated terminals probably impairs signal transmission. Therefore, the fine spatial information conveyed through LGd may be mediated mainly via fine terminals ($< 13.1 \mu\text{m}^2$). The density of fine terminals in LGd was reduced to 62.5% in cPcdh- α KO mice compared with WT mice. Assuming that retinogeniculate terminals with spatial information were distributed in the grid, the visual acuity discriminating two vertical (or horizontal) lines are inversely proportional to the grid intervals, or proportional to the square root of the terminal density. When the visual acuity determined using grating patterns would be proportional to the square root of the fine-terminal density, it would deteriorate to 79% in cPcdh- α KO mice. Because the visual acuity observed in WT mice was 0.56 cycles/degree, the expected visual acuity in cPcdh- α KO mice could be 0.44 cycles/degree. This expected value is very close to 0.41 cycles/degree, which was the value obtained in behavioral experiments. This simplified argument suggests that the aggregation of retinogeniculate terminals in cPcdh- α KO mice explains a considerable part of the deteriorated visual acuity in cPcdh- α KO mice, although the possibility that other abnormalities may contribute to the observed visual impairment cannot be excluded (Katori *et al.* 2009; Lefebvre *et al.* 2012; Yoshitake *et al.* 2013). Therefore, morphological and functional studies on the retinogeniculate synapses in mice with genetically manipulated cPcdhs may be useful for elucidating the functions of cPcdhs in the future.

Acknowledgments and conflict of interest disclosure

This work was supported by JSPS KAKENHI Grant Number 23659091 and JST-CREST. The authors declare no competing financial interests.

All experiments were conducted in compliance with the ARRIVE guidelines.

References

- Budisantoso T., Matsui K., Kamasawa N., Fukazawa Y. and Shigemoto R. (2012) Mechanisms underlying signal filtering at a multisynapse contact. *J. Neurosci.* **32**, 2357–2376.
- Chen C. and Regehr W. G. (2000) Developmental remodeling of the retinogeniculate synapse. *Neuron* **28**, 955–966.
- Chen W. V., Alvarez F. J., Lefebvre J. L. *et al.* (2012) Functional significance of isoform diversification in the protocadherin gamma gene cluster. *Neuron* **75**, 402–409.
- Esumi S., Kakazu N., Taguchi Y., Hirayama T., Sasaki A., Hirabayashi T., Koide T., Kitsukawa T., Hamada S. and Yagi T. (2005) Monoallelic yet combinatorial expression of variable exons of the protocadherin-alpha gene cluster in single neurons. *Nat. Genet.* **37**, 171–176.
- Golding B., Pouchelon G., Bellone C. *et al.* (2014) Retinal input directs the recruitment of inhibitory interneurons into thalamic visual circuits. *Neuron* **81**, 1057–1069.
- Guido W. (2008) Refinement of the retinogeniculate pathway. *J. Physiol.* **586**, 4357–4362.
- Hasegawa S., Hamada S., Kumode Y., Esumi S., Katori S., Fukuda E., Uchiyama Y., Hirabayashi T., Mombaerts P. and Yagi T. (2008) The protocadherin-alpha family is involved in axonal coalescence of olfactory sensory neurons into glomeruli of the olfactory bulb in mouse. *Mol. Cell Neurosci.* **38**, 66–79.
- Honma Y., Tsukano H., Horie M., Ohshima S., Tohmi M., Kubota Y., Takahashi K., Hishida R., Takahashi S. and Shibuki K. (2013) Auditory cortical areas activated by slow frequency-modulated sounds in mice. *PLoS ONE* **8**, e68113.
- Hooks B. M. and Chen C. (2006) Distinct roles for spontaneous and visual activity in remodeling of the retinogeniculate synapse. *Neuron* **52**, 281–291.
- Hooks B. M. and Chen C. (2008) Vision triggers an experience-dependent sensitive period at the retinogeniculate synapse. *J. Neurosci.* **28**, 4807–4817.
- Horie M., Meguro R., Hoshino K., Ishida N. and Norita M. (2013) Neuroanatomical study on the tecto-supragenulate-dorsal auditory cortex pathway in the rat. *Neuroscience* **228**, 382–394.
- Jaubert-Miazza L., Green E., Lo F. S., Bui K., Mills J. and Guido W. (2005) Structural and functional composition of the developing retinogeniculate pathway in the mouse. *Vis. Neurosci.* **22**, 661–676.
- Junghans D., Haas I. G. and Kemler R. (2005) Mammalian cadherins and protocadherins: about cell death, synapses and processing. *Curr. Opin. Cell Biol.* **17**, 446–452.
- Kaneko R., Kato H., Kawamura Y., Esumi S., Hirayama T., Hirabayashi T. and Yagi T. (2006) Allelic Gene Regulation of Pcdh- α and Pcdh- γ Clusters Involving Both Monoallelic and Biallelic Expression in Single Purkinje Cells. *J. Biol. Chem.* **281**, 30551–30560.
- Katori S., Hamada S., Noguchi Y., Fukuda E., Yamamoto T., Yamamoto H., Hasegawa S. and Yagi T. (2009) Protocadherin-alpha family is required for serotonergic projections to appropriately innervate target brain areas. *J. Neurosci.* **29**, 9137–9147.

- Kohmura N., Senzaki K., Hamada S., Kai N., Yasuda R., Watanabe M., Ishii H., Yasuda M., Mishina M. and Yagi T. (1998) Diversity revealed by a novel family of cadherins expressed in neurons at a synaptic complex. *Neuron* **20**, 1137–1151.
- Lefebvre J. L., Kostadinov D., Chen W. V., Maniatis T. and Sanes J. R. (2012) Protocadherins mediate dendritic self-avoidance in the mammalian nervous system. *Nature* **488**, 517–521.
- Liu X. and Chen C. (2008) Different roles for AMPA and NMDA receptors in transmission at the immature retinogeniculate synapse. *J. Neurophysiol.* **99**, 629–643.
- Mori K. and Sakano H. (2011) How is the olfactory map formed and interpreted in the mammalian brain? *Annu. Rev. Neurosci.* **34**, 467–499.
- Morishita H., Murata Y., Esumi S., Hamada S. and Yagi T. (2004) CNR/Pcdhalpha family in subplate neurons, and developing cortical connectivity. *NeuroReport* **15**, 2595–2599.
- Phillips G. R., Tanaka H., Frank M., Elste A., Fidler L., Benson D. L. and Colman D. R. (2003) γ -Protocadherins are targeted to subsets of synapses and intracellular organelles in neurons. *J. Neurosci.* **23**, 5096–5104.
- Prasad T. and Weiner J. A. (2011) Direct and Indirect Regulation of Spinal Cord Ia Afferent Terminal Formation by the γ -Protocadherins. *Front. Mol. Neurosci.* **4**, 54.
- Prasad T., Wang X., Gray P. A. and Weiner J. A. (2008) A differential developmental pattern of spinal interneuron apoptosis during synaptogenesis: insights from genetic analyses of the protocadherin-gamma gene cluster. *Development* **135**, 4153–4164.
- Prusky G. T. and Douglas R. M. (2004) Characterization of mouse cortical spatial vision. *Vision. Res.* **44**, 3411–3418.
- Prusky G. T., West P. W. and Douglas R. M. (2000) Behavioral assessment of visual acuity in mice and rats. *Vision. Res.* **40**, 2201–2209.
- Shapiro L. and Colman D. R. (1999) The diversity of cadherins and implications for a synaptic adhesive code in the CNS. *Neuron* **23**, 427–430.
- Shapiro L., Love J. and Colman D. R. (2007) Adhesion molecules in the nervous system: structural insights into function and diversity. *Annu. Rev. Neurosci.* **30**, 451–474.
- Tohmi M., Meguro R., Tsukano H., Hishida R. and Shibuki K. (2014) The extrageniculate visual pathway generates distinct response properties in the higher visual areas of mice. *Curr. Biol.* **24**, 587–597.
- Wang X., Su H. and Bradley A. (2002a) Molecular mechanisms governing Pcdh-gamma gene expression: evidence for a multiple promoter and cis-alternative splicing model. *Genes Dev.* **16**, 1890–1905.
- Wang X., Weiner J. A., Levi S., Craig A. M., Bradley A. and Sanes J. R. (2002b) Gamma protocadherins are required for survival of spinal interneurons. *Neuron* **36**, 843–854.
- Wu Q. (2005) Comparative genomics and diversifying selection of the clustered vertebrate protocadherin genes. *Genetics* **169**, 2179–2188.
- Wu H. H., Cork R. J. and Mize R. R. (2000) Normal development of the ipsilateral retinocollicular pathway and its disruption in double endothelial and neuronal nitric oxide synthase gene knockout mice. *J. Comp. Neurol.* **426**, 651–665.
- Yagi T. (2012) Molecular codes for neuronal individuality and cell assembly in the brain. *Front. Mol. Neurosci.* **5**, 45.
- Yamashita H., Chen S., Komagata S., Hishida R., Iwasato T., Itoharu S., Yagi T., Endo N., Shibata M. and Shibuki K. (2012) Restoration of contralateral representation in the mouse somatosensory cortex after crossing nerve transfer. *PLoS ONE* **7**, e35676.
- Yoshitake K., Tsukano H., Tohmi M., Komagata S., Hishida R., Yagi T. and Shibuki K. (2013) Visual map shifts based on whisker-guided cues in the young mouse visual cortex. *Cell Rep.* **5**, 1365–1374.
- Zipursky S. L. and Grueber W. B. (2013) The molecular basis of self-avoidance. *Annu. Rev. Neurosci.* **36**, 547–568.

Somatic Mutations in the *MTOR* Gene Cause Focal Cortical Dysplasia Type IIb

Mitsuko Nakashima, MD, PhD,^{1a} Hirotomo Saitsu, MD, PhD,^{1a}
 Nobuyuki Takei, PhD,² Jun Tohyama, MD, PhD,³ Mitsuhiro Kato, MD, PhD,⁴
 Hiroki Kitaura, DDS, PhD,⁵ Masaaki Shiina, MD, PhD,⁶ Hiroshi Shirozu, MD, PhD,⁷
 Hiroshi Masuda, MD,⁷ Keisuke Watanabe, PhD,⁸ Chihiro Ohba, MD, PhD,¹
 Yoshinori Tsurusaki, PhD,¹ Noriko Miyake, MD, PhD,¹ Yingjun Zheng, MD, PhD,⁵
 Tatsuhiro Sato, PhD,⁹ Hirohide Takebayashi, MD, PhD,⁸
 Kazuhiro Ogata, MD, PhD,⁶ Shigeki Kameyama, MD, PhD,⁷
 Akiyoshi Kakita, MD, PhD,^{5b} and Naomichi Matsumoto, MD, PhD^{1b}

Objective: Focal cortical dysplasia (FCD) type IIb is a cortical malformation characterized by cortical architectural abnormalities, dysmorphic neurons, and balloon cells. It has been suggested that FCDs are caused by somatic mutations in cells in the developing brain. Here, we explore the possible involvement of somatic mutations in FCD type IIb.

Methods: We collected a total of 24 blood-brain paired samples with FCD, including 13 individuals with FCD type IIb, 5 with type IIa, and 6 with type I. We performed whole-exome sequencing using paired samples from 9 of the FCD type IIb subjects. Somatic *MTOR* mutations were identified and further investigated using all 24 paired samples by deep sequencing of the entire gene's coding region. Somatic *MTOR* mutations were confirmed by droplet digital polymerase chain reaction. The effect of *MTOR* mutations on mammalian target of rapamycin (mTOR) kinase signaling was evaluated by immunohistochemistry and Western blotting analyses of brain samples and by *in vitro* transfection experiments.

Results: We identified four lesion-specific somatic *MTOR* mutations in 6 of 13 (46%) individuals with FCD type IIb showing mutant allele rates of 1.11% to 9.31%. Functional analyses showed that phosphorylation of ribosomal protein S6 in FCD type IIb brain tissues with *MTOR* mutations was clearly elevated, compared to control samples. Transfection of any of the four *MTOR* mutants into HEK293T cells led to elevated phosphorylation of 4EBP, the direct target of mTOR kinase.

Interpretation: We found low-prevalence somatic mutations in *MTOR* in FCD type IIb, indicating that activating somatic mutations in *MTOR* cause FCD type IIb.

ANN NEUROL 2015;78:375–386

Focal cortical dysplasia (FCD) is a cortical malformation frequently associated with drug-resistant epilepsy that requires surgical treatment.^{1,2} FCD can be classified

into three types (I, II, and III) based on its clinicopathological features.³ Type I refers to abnormalities in cortical architecture without cellular anomalies,³ whereas type III

View this article online at wileyonlinelibrary.com. DOI: 10.1002/ana.24444

Received Oct 8, 2014, and in revised form May 26, 2015. Accepted for publication May 26, 2015.

^aThese authors contributed equally to this work.

^bThese are co-last authors.

Address correspondence to Dr Naomichi Matsumoto, Department of Human Genetics, Yokohama City University Graduate School of Medicine, 3-9 Fukuura, Kanazawa-ku, Yokohama 236-0004, Japan. E-mail: naomat@yokohama-cu.ac.jp

From the ¹Department of Human Genetics, Yokohama City University Graduate School of Medicine, Yokohama, Japan; ²Department of Molecular Neurobiology, Brain Research Institute, Niigata University, Niigata, Japan; ³Department of Child Neurology, Nishi-Niigata Chuo National Hospital, Niigata, Japan; ⁴Department of Pediatrics, Showa University School of Medicine, Tokyo, Japan; ⁵Department of Pathology, Brain Research Institute, University of Niigata, Niigata, Japan; ⁶Department of Biochemistry, Yokohama City University Graduate School of Medicine, Yokohama, Japan; and ⁷Department of Functional Neurosurgery, Epilepsy Center, Nishi-Niigata Chuo National Hospital, Niigata, Japan; ⁸Division of Neurobiology and Anatomy, Graduate School of Medical and Dental Sciences, Niigata University, Niigata, Japan; and ⁹Division of Biochemistry, School of Pharmaceutical Sciences, Kitasato University, Tokyo, Japan.

Additional Supporting Information can be found in the online version of this article.

involves cortical lamination abnormalities associated with a principal lesion, which are usually adjacent and affect the same cortical area or lobes.³ FCD type II is characterized by severe architectural abnormalities and dysmorphic neurons and can be further subdivided into types IIb (with balloon cells) and IIa (without balloon cells).^{3,4}

It has been suggested that FCDs are likely to arise from somatic mutations in cells in the developing brain, but that the molecular basis of the three types of FCD can differ.^{2,4} Several studies have demonstrated that the phosphatidylinositol 3-kinase (PI3K)/AKT3/mechanistic target of rapamycin (mTOR)-signaling pathway is activated in FCD type IIb.^{5–11} This pathway regulates cell proliferation, metabolism, autophagy, and apoptosis in developing cerebral cells. Furthermore, some cortical malformations are demonstrated to possess somatic mutations in genes of the PI3K/AKT3/mTOR-signaling pathway.^{12–19} In this study, we analyzed paired brain lesions and blood leukocytes (or saliva) from individuals with FCDs who underwent surgery to evaluate the possible involvement of somatic mutations in the disease.

Subjects and Methods

Study Subjects and Samples

Thirteen individuals with FCD type IIb, 5 with type IIa, and 6 with type I were investigated in this study. All participants underwent preoperative clinical evaluations, including seizure charts, electroencephalography, and neuroimaging with magnetic resonance imaging (MRI), followed by surgical treatment. Subjects or their families provided us with written informed consent for participation in this study. The institutional review boards of Yokohama City University, Nishi-Niigata Chuo National Hospital, Yamagata University, and the University of Niigata approved this study. Surgically operated brain tissues (lesions) and peripheral blood leukocytes (or saliva) (normal tissues) were obtained from all participants. Fresh surgical specimens were immediately cut into 5-mm blocks in the operating room, and some of the blocks were fixed with 20% buffered formalin and embedded in paraffin wax. Serial 4- μ m-thick sections were then cut and stained with hematoxylin-eosin or Klüver-Barrera stain. Histopathological diagnosis was performed according to the recent classification system.³ As controls for immunohistochemistry (IHC) and Western blotting analyses, we selected 6 subjects (ID/age [years]/sex = 15473/18/M, 15732/38/F, 15294/26/M, 16080/43/M, 16312/12/M, and 16337/12/M) who had suffered from localized neocortical seizures for years and underwent surgery to treat epilepsy. In all cases, histopathological evaluation of resected brain lesions revealed none of the obvious abnormalities in cortical layering that are required for a diagnosis of FCD type I.³ These cases could thus be regarded as mild malformations of cortical development.³

DNA Preparation

Fresh frozen brain tissues were dissolved in sodium dodecyl sulfate (SDS)/sodium chloride-based lysis solution with proteinase K and incubated at 55°C for 1 hour, then 37°C overnight. Genomic DNA was extracted from peripheral blood leukocytes and saliva using QuickGene-610L (Fujifilm, Tokyo, Japan) and Oragene (DNA Genotek Inc., Kanata, Ontario, Canada), respectively, according to the manufacturer's instructions.

Somatic Variant Calling Using Paired Whole Exome Sequencing Data

Paired brain lesions and blood leukocytes (or saliva) from nine individuals with FCD Type IIb were analyzed by whole-exome sequencing (WES). DNA was captured using a SureSelect Human All Exon V5 Kit (Agilent Technologies, Santa Clara, CA) and sequenced on an Illumina HiSeq 2500 (Illumina, San Diego, CA) with 101-bp paired-end reads. Read bases below the Phred quality score of 20 were trimmed from the 3' end of reads. These cleaned reads were aligned to the human reference genome sequence (UCSC hg19, NCBI build 37) using Novoa-align (Novocraft Technologies, Petaling Jaya, Malaysia). Paired WES data (from brain and blood/saliva) were analyzed by MuTect²⁰ and VarScan 2²¹ to detect de novo somatic single-nucleotide variants (SNVs) in brain tissues. For MuTect, we carefully examined both filter-passed and -rejected variants to avoid false-negative results, considering the cellular complexity in brain tissues. For Varscan 2, minimum read depth for somatic variant calls in normal and tumor samples was set to 12. Exclusion criteria were: (1) variants on mutant alleles with <2 reads in the brain and \geq 2 reads in leukocytes (or saliva); (2) variants registered in dbSNP 137, except for clinically associated single-nucleotide polymorphisms (flagged); (3) variants registered in 6,500 exomes of the National Heart, Lung, and Blood Institute Exome Sequencing Project Exome Variant Server and the 1000 Genomes database^{22,23}; (4) variants observed in our 575 in-house control exomes; and (5) synonymous variants. Called variants were annotated using ANNOVAR software.²⁴

Validation of Candidate Somatic Variants

Candidate somatic variants extracted from WES data were validated by polymerase chain reaction (PCR)-based deep sequencing using specific primers. Sequencing libraries were prepared using the SureSelect XT Library Prep Kit (Agilent Technologies) and sequenced on a MiSeq (Illumina) with 150-bp paired-end reads. Trimming and alignment of reads were performed as described above. Allele counting was performed using Integrative Genomics Viewer software (IGV).²⁵

Somatic Mutation Screening of MTOR

A total of 16 primer sets covering the entire coding region and intron-exon boundaries of *MTOR* (MIM 601231; RefSeq accession number: NM_004958.3) were used to amplify DNA from brain lesions and blood leukocytes (or saliva). Sequence libraries were prepared with the Nextera DNA Sample Preparation Kit (Illumina). An Agilent DNA 1000 Kit (Agilent Technologies)

and KAPA Library Quantification Kits (Kapa Biosystems, Wilmington, MA) were used to check size distribution and DNA concentration of the libraries, respectively. Libraries were sequenced on an MiSeq (Illumina). Trimming and alignment of reads were performed as described above. Variants were called by MuTect. All mutations were visually reviewed by IGV.

Droplet Digital PCR

Somatic *MTOR* mutations were confirmed by droplet digital PCR (ddPCR). Custom locked nucleic acid probes for each wild-type (WT) and mutant allele- and region-specific primers were purchased from Integrated DNA Technology (Coralville, IA). A 20- μ l assay mix containing 50ng of genomic DNA, ddPCR Supermix for Probes (No dUTP; Bio-Rad, Hercules, CA), 250nM of WT and mutant probes, and 900nM of PCR primers were emulsified into \sim 20,000 droplets using a QX100 Droplet Generator (Bio-Rad). Target-specific primers and probes are shown in Supporting Table 1. In preliminary experiments, appropriate T_m values and thresholds were examined for each WT and mutant allele using cloned DNAs to minimize background. These experiments revealed that virtually no false-positive droplets were observed in the optimized experimental conditions. We tested six paired samples with *MTOR* mutations using mutation-specific primers and probes sets. PCR was performed using the following cycles: 10 minutes at 95°C; 40 cycles of 30 seconds at 94°C and 2 minutes at 59°C (c.6644C>A, c.6644C>T) or 53°C (c.4376C>A, c.4379T>C); and 10 minutes at 98°C. Droplet reading and data analysis were performed using QX200 Droplet Reader and QuantaSoft software (Bio-Rad), respectively.

Statistical Analysis of Correlation Between MTOR Mutations and Clinical Features

We assessed the relevance between *MTOR* mutations and clinical features, including seizure onset age, seizure frequency, neurological findings, IQ at pre- or postsurgery, and lesion volume, by Wilcoxon rank-sum or Fisher exact test ($p < 0.05$ was considered as significant). Lesion volume in each subject was calculated from MRI proton density weighted images (PDWIs) using OsiriX MD (Pixmeo, Geneva, Switzerland). In brief, the margin of high-intensity signals in PDWIs, which indicates FCD, obtained just before surgery was delineated manually as a region of interest (ROI) area in both axial and coronal views, and the ROI area in each slice was calculated. Then, the volume of the lesion was automatically calculated based on each area and slice thickness. In subjects 14434, 17424, and 11683, lesion volume was manually calculated. All analyses were performed using R software (version 3.1.0; R Foundation for Statistical Computing, Vienna, Austria).

Immunohistochemistry

Paraffin-embedded sections were immunostained with rabbit polyclonal antibody against the ribosomal protein, phospho-S6 (Ser235/236; diluted 1:1,000; Cell Signaling Technologies, Danvers, MA), as previously described.²⁶

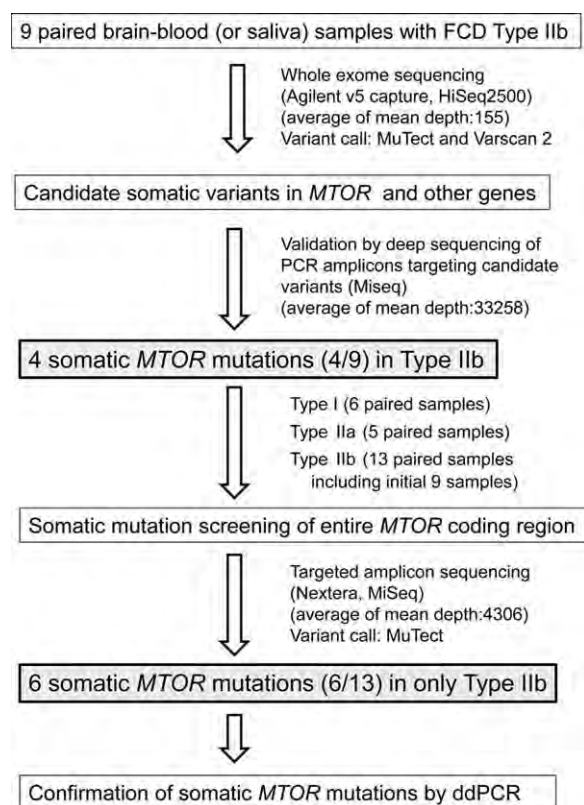


FIGURE 1: Flow chart of somatic mutation analysis in subjects with focal cortical dysplasia (FCD). The flow of analysis in this study is outlined. ddPCR = droplet digital polymerase chain reaction; PCR = polymerase chain reaction.

Structural Analysis of mTOR

FoldX software (version 3.0 β 3) was used to calculate free energy changes after mutation using the mTOR crystal structure (amino acids [aa] 1,376–2,549)/mLST8 complex (Protein Data Bank [PDB] 4JSN).²⁷ The calculation was repeated three times, and the resultant data are presented as an average value with a standard deviation.

Western Blotting Analysis

Fresh-frozen tissues of surgical specimens taken from the 5 subjects with *MTOR* mutations (ID: 16964, 17424, 11683, 14434, and 16578) and the six controls (described above). Fresh-frozen tissues of a patient with an *MTOR* mutation (ID: 15622) were not available for Western blotting. These were lysed with SDS sample buffer containing protease (Complete; Roche Diagnostics, Mannheim, Germany) and phosphatase inhibitor cocktails (PhosSTOP; Roche Diagnostics). Protein concentration was determined using BCA protein assay reagent (Thermo Fisher Scientific, Waltham, MA). Equal amounts of protein (40 μ g/lane for phospho and total S6 and 2 μ g/lane for actin) were separated by SDS polyacrylamide gel electrophoresis (PAGE) and analyzed by Western blotting with rabbit polyclonal antibodies against total S6 (Cell Signaling Technologies) and phospho-S6 (Ser235/236), and with a mouse monoclonal antibody against actin (Merck Millipore, Billerica, MA).

TABLE 1. Summary of Whole-Exome Sequencing in Individuals with FCD Type IIb (n = 9)

Subject	Mean Depth ^b (Brain/Blood)	%_bases_above_ 20× (Brain/Blood)	Program	<i>De novo</i> SNV Call (Filter Passed)	Common Variants in Two Programs	Candidate Gene(s) Common in Two or More Cases
11683	193.7/178.4	95.0/94.3	MuTect	422 (13)	13	<i>UNC79</i>
			Varscan 2	35		
15035 ^a	192.9/194.5	94.9/94.7	MuTect	446 (6)	25	
			Varscan 2	74		
15622	146.3/121.3	95.6/94.6	MuTect	428 (10)	11	<i>NME5</i>
			Varscan 2	28		
16129	109.2/67.37	93.8/88.4	MuTect	318 (10)	30	<i>NME5</i>
			Varscan 2	148		
16578	117.8/143.2	94.5/95.4	MuTect	357 (12)	56	<i>NBPF8, UNC79, MTOR, KAT6B</i>
			Varscan 2	232		
17562	158.2/166.2	95.8/95.8	MuTect	348 (8)	20	<i>NBPF8</i>
			Varscan 2	79		
14434	154.2/259.4	92.8/95.5	MuTect	376 (9)	102	<i>MTOR, KAT6B, CES4A</i>
			Varscan 2	706		
15381	127.5/108.6	94.8/93.7	MuTect	460 (10)	23	
			Varscan 2	43		
16325	131.0/141.2	93.7/94.0	MuTect	319 (6)	22	<i>NBPF8, CES4A</i>
			Varscan 2	68		

^aDNA from saliva instead of blood was used.

^bAgainst protein coding sequences of RefSeq genes.

FCD = focal cortical dysplasia; SNV = single-nucleotide variant.

Human WT *MTOR* complementary DNA (cDNA; NM_004958.3) and mutant *MTOR* cDNA (p.Ala1459Asp, p.Leu1460Pro, p.Ser2215Phe and p.Ser2215Tyr) were cloned in pEF-BOS-FLAG vector.²⁸ Human *EIF4EBP1* (NM_004095.3) was introduced into pCMV-FLAG.²⁹ HEK293T cells were cultured in Dulbecco's modified Eagle's medium supplemented with 10% fetal bovine serum and penicillin/streptomycin at 37°C in an atmosphere of 5% CO₂. HEK293T cells were cotransfected with FLAG-4EBP and WT or mutant *MTOR* plasmids using Eugene6 (Roche Diagnostics), according to the manufacturer's instructions. To assess the activity of *MTOR* mutants, cells were starved for serum and amino acids in Hank's balanced salt solution for 1 hour. Cells were then lysed and incubated with anti-DYKDDDDK antibody beads (WAKO, Osaka, Japan) at 4°C for 4 hours. Immunoprecipitates were analyzed by SDS-PAGE and Western blotting with anti-phospho-4EBP (Thr37/46; Cell Signaling Technologies) or anti-DYKDDDDK (WAKO), as previously described.³⁰

Results

Somatic Mutation Screening and Validation

A flow chart of our analysis is illustrated in Figure 1. Using MuTect²⁰ and VarScan 2,²¹ we detected a number of possible somatic variants in WES data of nine paired samples (Table 1). To quickly narrow down candidate variants, we first searched for those variants commonly detected by the two programs, then focused on candidate genes whose variants were found in two or more cases (Table 1). Among six candidate genes, *MTOR* is of interest. It encodes the serine/threonine kinase mTOR, a key regulator of the PI3K/AKT3/mTOR-signaling pathway,^{31,32} and an *MTOR* somatic mutation has been reported in hemimegalencephaly.¹³ Considering the possible involvement of the mTOR pathway in FCD, we investigated variants in candidate genes involved in the mTOR pathway (Supporting Table 2). We only detected

TABLE 2. Summary of Deep Sequencing of MTOR in Individuals With FCD

Subject	Type	Variant in MTOR by MuTect	Whole-Exome Sequencing				Variant-Targeted Deep Sequencing ^c (Validation)				MTOR-Targeted Deep Sequencing ^c			
			Brain		Blood		Brain		Blood		Brain		Blood	
			Mut/Ref Counts (% ^b)	Mut/Ref Counts (% ^b)	Mutation	Mut/Ref Counts (% ^b)	Mut/Ref Counts (% ^b)	Mutation	Mut/Ref Counts (% ^b)	Mut/Ref Counts (% ^b)	Mutation	Mut/Ref Counts (% ^b)	Mut/Ref Counts (% ^b)	
11683	IIb	c.6644C>A (p.Ser2215Tyr)	4/357 (1.11)	0/318 (0.00)	True	406/28,719 (1.39)	9/31,396 (0.03)	1,968/1,335	c.6644C>A (p.Ser2215Tyr)	382/2,426 (1.54)	0/1,242 (0.00)			
15035 ^a	IIb	—	—	—	—	—	—	1,619/1,189	—	—	—			
15622	IIb	c.4376C>A (p.Ala1459Asp)	3/221 (1.34)	0/187 (0.00)	True	406/28,605 (1.40)	18/38,815 (0.05)	860/3,017	c.4376C>A (p.Ala1459Asp)	331/1,970 (1.65)	6/10,394 (0.06)			
16129	IIb	c.1897T>C (p.Ser633Pro)	2/67 (2.90)	0/97 (0.00)	False	24/26,447 (0.09)	29/35,285 (0.08)	2,546/2,611	—	—	—			
16578	IIb	c.4379T>C (p.Leu1460Pro)	4/199 (1.97)	0/174 (0.00)	True	623/28,382 (2.15)	52/103,377 (0.05)	3,195/15,181	c.4379T>C (p.Leu1460Pro)	150/9,303 (1.59)	26/42,551 (0.06)			
17562	IIb	—	—	—	—	—	—	2,198/2,851	—	—	—			
14434	IIb	c.6644C>T (p.Ser2215Phe)	6/314 (1.88)	0/502 (0.00)	True	160/6,876 (2.27)	1/17,069 (0.01)	1,148/3,373	c.6644C>T (p.Ser2215Phe)	24/747 (3.11)	0/2,556 (0.00)			
15381	IIb	—	—	—	—	—	—	2478/2,215	—	—	—			
16325	IIb	c.1820C>T (p.Ala607Val)	2/59 (3.28)	0/59 (0.00)	False	20/11,990 (0.17)	74/42,140 (0.17)	1,224/1,422	—	—	—			
15524	IIb	ND	ND	ND	ND	ND	ND	3,168/5,350	—	—	—			
16964	IIb	ND	ND	ND	ND	ND	ND	2,606/6,393	c.4379T>C (p.Leu1460Pro)	111/2,167 (4.87)	4/8,255 (0.05)			
17424 ^a	IIb	ND	ND	ND	ND	ND	ND	1,483/4,723	c.6644C>A (p.Ser2215Tyr)	74/721 (9.31)	3/3,665 (0.08)			
18437	IIb	ND	ND	ND	ND	ND	ND	2,003/1,9375	—	—	—			

^aDNA from saliva instead of blood was used.

^bPercent of mutant allele was calculated by mutant allele reads/(mutant allele reads + reference allele reads).

^cVariants were called by MuTect, and reads were manually counted by Integrative Genomics Viewer software (IGV).

^dAgainst protein coding sequences of MTOR.

FCD = focal cortical dysplasia; Mut = mutant allele; N.D. = whole-exome sequencing and variant-targeted sequencing were not performed; Ref = reference allele.

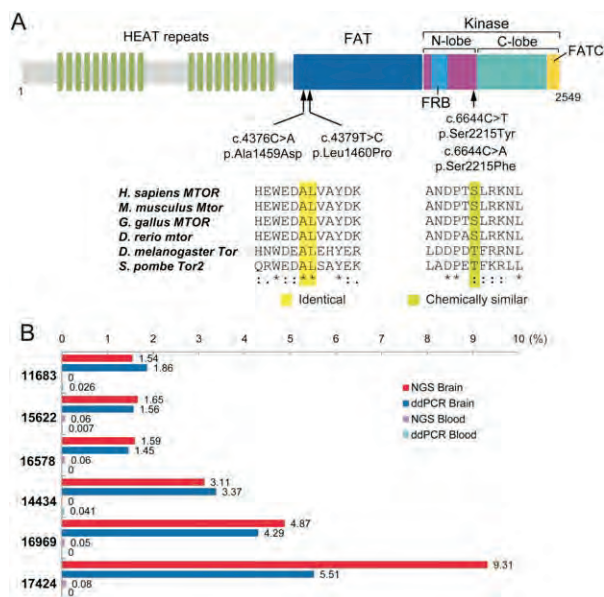


FIGURE 2: Somatic *MTOR* mutations in individuals with focal cortical dysplasia (FCD) type IIb. (A) Schematic of the mammalian target of rapamycin (mTOR) protein with HEAT repeats, FAT domain, kinase domain comprising N- and C-lobes, FRB domain, and FATC domain. All four identified missense mutations occurred at evolutionarily conserved amino acids in the FAT domain ($n = 2$; Ala1459 and Leu1460) or N-lobe of the kinase domain ($n = 2$; Ser2215). Multiple amino acid sequences of mTOR proteins were aligned with tools available on the CLUSTALW website (<http://www.genome.jp/tools/clustalw/>). (B) Percentage of mutant alleles of *MTOR* in blood leukocytes and brain lesions in FCD type IIb. All samples showed both results analyzed by targeted amplicon deep sequencing (NGS) and ddPCR. ddPCR = droplet digital polymerase chain reaction; NGS = next-generation sequencing.

variants in six mTOR-related genes (*MTOR*, *AKT3*, *TSC1*, *TSC2*, *PIK3*, and *P TEN*) by MuTect and subsequently examined by targeted deep sequencing. Four *MTOR* mutations were validated: c.4376C>A (p.Ala1459Asp); c.4379T>C (p.Leu1460Pro); c.6644C>A (p.Ser2215Tyr); and c.6644C>T (p.Ser2215Phe; Table 2). No variants in other genes were validated because they were absent in targeted deep sequencing, suggesting that they were false positive. We also examined germline or somatic mutations in candidate genes involved in the mTOR pathway (Supporting Table 2) using nonbrain Varscan 2 data, but we could not detect any pathogenic variants in these genes.

We then screened the entire *MTOR* coding region using deep sequencing of PCR amplicons from 13 individuals with FCD type IIb, including the 9 analyzed by WES. In addition, to explore possible involvement of somatic *MTOR* mutations in other types of FCD, we also screened 5 subjects with FCD type IIa and 6 with type I. We identified two recurrent mutations (c.4379T>C and c.6644C>A) in an additional two individuals with FCD type IIb. A total of four lesion-specific

somatic *MTOR* mutations were verified in 6 individuals with FCD type IIb (6 of 13 [46%]; Fig 2A; Table 2). No candidate mutations were identified in individuals with FCD type I or IIa (Supporting Table 3). Mutant allele frequencies in brain lesions were very low (range, 1.54–9.31%; average, 3.67%) but were clearly higher than those in blood leukocytes or saliva (all <0.1%; Table 2), excluding possible PCR or sequencing errors. Furthermore, we verified the mutant allele frequencies by ddPCR. Fractional abundance in each sample was nearly consistent with mutant allele frequencies from the deep

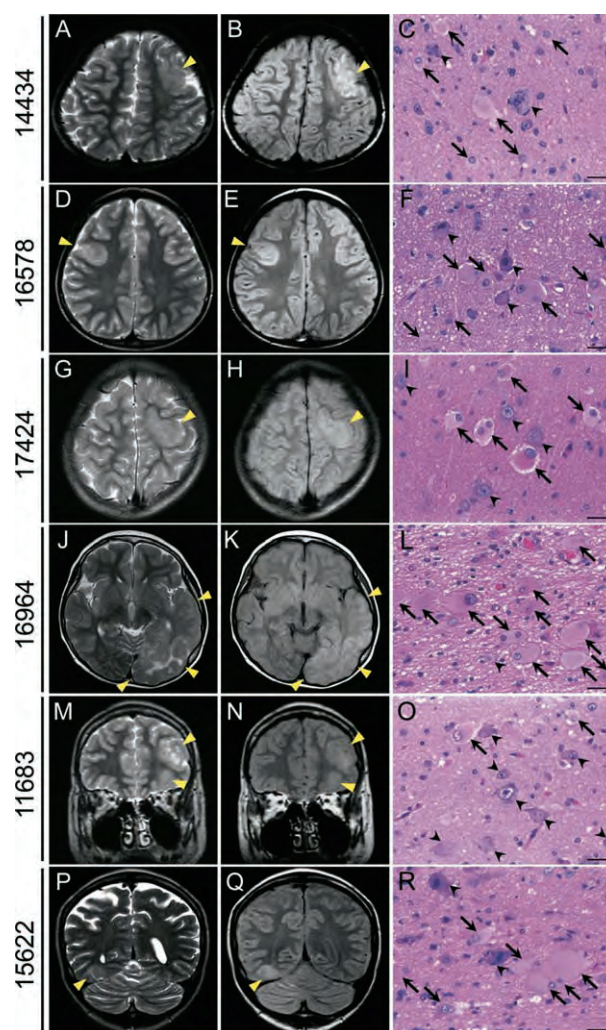


FIGURE 3: Brain magnetic resonance imaging (MRI) and histopathological features of subjects with somatic *MTOR* mutations. Coronal or axial brain MRI of subjects with somatic *MTOR* mutations. T2-weighted (A, D, G, J, M, P) and proton-density-weighted (B, E, H, K, N, Q) images show abnormal configurations of cerebral gyri and high signal, respectively. Yellow arrowheads indicate focal cortical dysplasia (FCD) lesions. Photomicrographs of hematoxylin-eosin-stained histology sections (C, F, I, L, O, R) demonstrating characteristic dysplastic features with dysmorphic neurons (arrowheads) and balloon cells (arrows) in surgical specimens taken from 6 individuals with somatic *MTOR* mutations. Bar = 20 μ m.

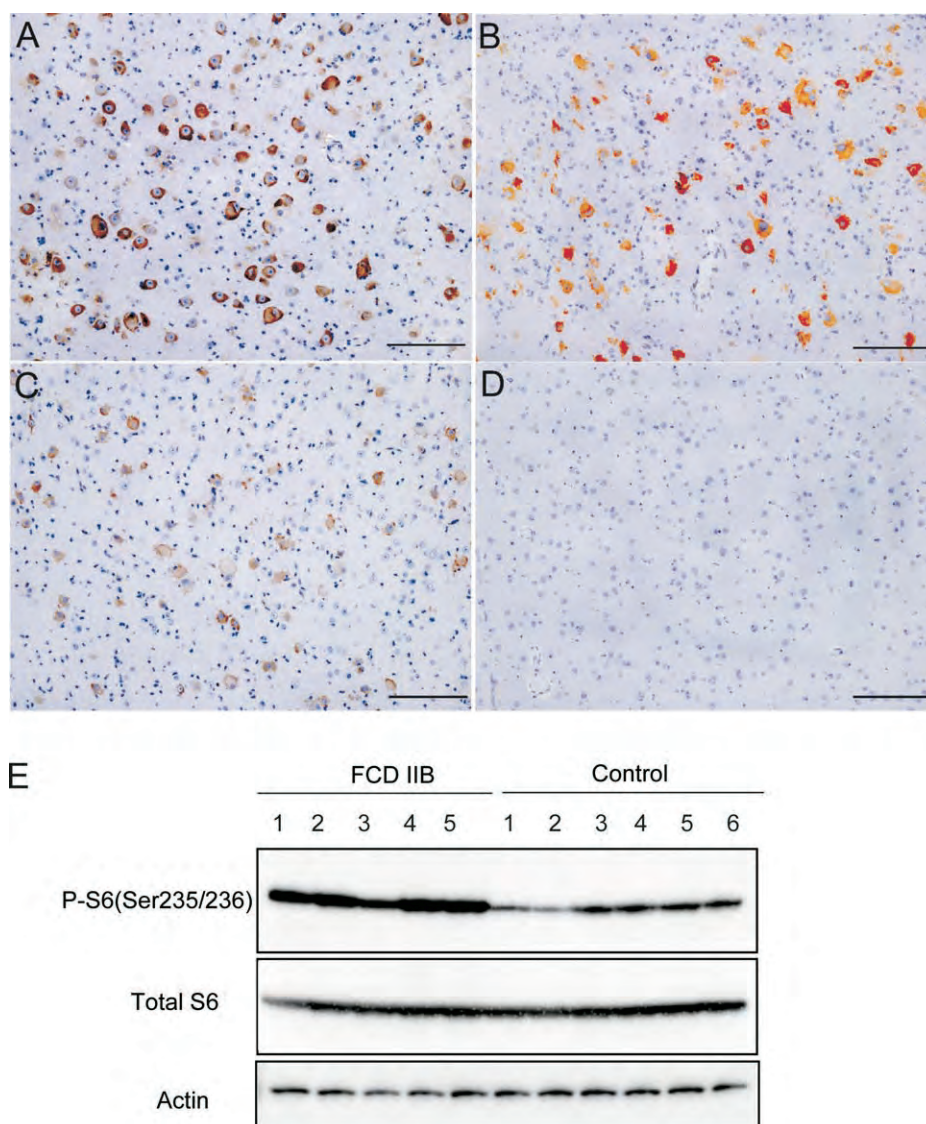


FIGURE 4: Expression of phospho-S6 in focal cortical dysplasia (FCD) type IIb. Immunohistochemical features (A–D) and Western blotting (E) for phospho-S6 in brain tissues taken from subjects with FCD type IIb and controls. (A–C) Many dysmorphic neurons and balloon cells in an FCD type IIb brain section with an *MTOR* mutation (A: 16578, B: 15622; Table 2 and Supporting Table 3) and without a mutation (C: 15381; Table 2 and Supporting Table 3) showed intense immunoreactivity to phospho-S6. (D) Neurons in the control (#16080) showed no or very faint reactivity. Bar = 120 μ m. (E) Expression of phospho-S6 (Ser235/236), total S6 protein, and actin are depicted in the upper, middle, and lower panel, respectively. Western blotting showed a larger amount of phosphorylated S6 in brain tissues of FCD type IIb (lanes 1–5: 16964, 17424, 11683, 14434, and 16578, respectively), compared to controls (lanes 1–6: 15473, 15732, 15294, 16080, 16312, and 16337, respectively). Equal amounts of protein (40 μ g/lane for phospho and total S6 and 2 μ g/lane for actin) were applied.

sequencing data (Fig 2B). Fractional abundance in blood was extremely low or zero (0–0.034%; Fig 2B), being equivalent to no-template control. Low-prevalence mosaic rates for all mutations were reproducible by ddPCR.

Correlation Between *MTOR* Mutations and Clinical Features

Correlation of *MTOR* mutations with clinical phenotypes was statistically analyzed. Clinical features of the 13 individuals with FCD type IIb are described in detail (Sup-

porting Table 4). Brain MRI showed severe architectural abnormalities in 6 individuals with somatic *MTOR* mutations (Fig 3), as well as in 7 without *MTOR* mutations (data not shown). We found no statistical difference for any clinical feature between mutation-positive and -negative groups.

Phosphorylation of Ribosomal Protein S6 in FCD Samples

At primary histopathological examination, all specimens with FCD type IIb (Table 2 and Supporting Table 4)

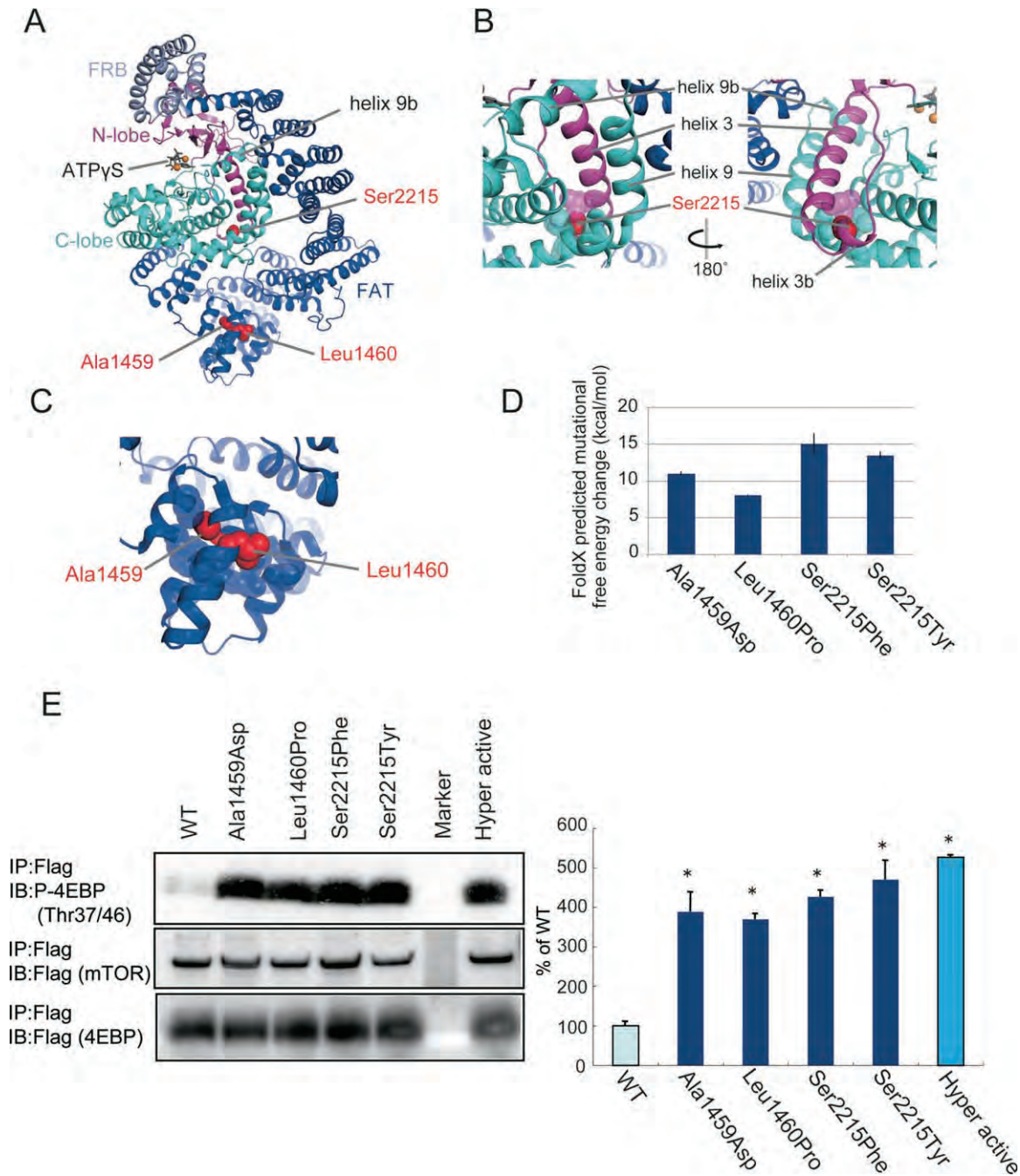


FIGURE 5: Mammalian target of rapamycin (mTOR) signaling activation by *MTOR* mutations. Structural consideration of the four mutations. (A) Crystal structure of mTOR (residues 1,376–2,549) in complex with mLST8, ATP γ S, and magnesium ions (Protein Data Bank [PDB] code 4JSP). FAT domain, N- and C-lobes of the kinase domain, and the FRB domain in the N-lobe are colored blue, magenta, cyan, and light blue, respectively. Nonhydrolyzed ATP analog, ATP γ S, and magnesium ions are shown as gray sticks and orange balls, respectively. Residues at mutation sites are shown as van der Waals spheres in red. The secondary structure assignment is according to published nomenclature. (B and C) Close-up of regions around the mutation sites from the front and back. Side chains of some residues near the mutation sites are represented as transparent van der Waals spheres. (D) Free energy change upon amino acid mutations, estimated from calculations using FoldX software. (E) HEK293T cells were transfected with FLAG-MTOR or pcDNA3.1-MTOR hyperactive mutant and FLAG-4EBP plasmids. Cell lysates were immunoprecipitated with anti-Flag antibody beads and then probed with anti-phospho-4EBP (Thr36/47; left, upper panel), anti-Flag for mTOR (left, middle panel), and 4EBP (left, lower panel). Three separate experiments were performed. Transfection efficacy was almost the same in each transfection. Note that all the mutants found in this study led to significant activation of the mTOR pathway, and the mutants are comparable with the hyperactive mutant (right panel). $n = 3$ for WT and mutants. $*p < 0.0001$ by analysis of variance. Western blotting were quantified by densitometric analysis using ImageJ software (NIH, Bethesda, MD). Bars represent means \pm standard error of the mean. ATP = adenosine triphosphate; FCD = focal cortical dysplasia.

TABLE 3. Prediction of Somatic *MTOR* Mutation Pathogenicity

Subject	Mutation	SIFT	PolyPhen2	Mutation Taster
11683 and 17424	c.6644C>A (p.Ser2215Tyr)	0	Possibly damaging (0.876)	Disease-causing (0.999)
15622	c.4376C>A (p.Ala1459Asp)	0	Benign (0.133)	Disease-causing (0.999)
16578 and 16964	c.4379T>C (p.Leu1460Pro)	0	Benign (0.352)	Disease-causing (0.999)
14434	c.6644C>T (p.Ser2215Phe)	0	Possibly damaging (0.824)	Disease-causing (0.999)

SIFT (<http://sift.jcvi.org/>): scores of less than 0.05% indicate substitutions that are predicted as intolerant. PolyPhen-2 (<http://genetics.bwh.harvard.edu/pph2/>): HumVar scores are evaluated as 0.000 (most probably benign) to 0.999 (most probably damaging). Mutation Taster (<http://www.mutationtaster.org/>): rapid evaluation of DNA sequence alterations. Alterations are classified as disease-causing or polymorphisms.

showed numerous dysmorphic neurons and balloon cells regardless of the presence or absence of mutations (Fig 3C, F, I, L, O, R). We then examined the activation of the mTOR pathway in FCD type I, IIa, and IIb using IHC for phospho-S6, which is a downstream phosphorylated protein in the mTOR pathway. In FCD type IIb specimens with or without *MTOR* mutations, almost all dysmorphic neurons and balloon cells were distributed in both the cortex and subcortical white matter and showed intense reactivity for phospho-S6 (Fig 4A–C). A small proportion of normal-looking pyramidal neurons distributed in the cortex also showed a variable intensity of reactivity for phospho-S6. On the other hand, neurons showed no or faint reactivity for phospho-S6 in all control specimens (Fig 4D). We also confirmed the expression level of phospho-S6 by Western blotting of proteins extracted from lesion-specific brain sections. The ratio of phosphorylation (the ratio of intensities of phospho-S6/total-S6) in each FCD type IIb individual with an *MTOR* mutation (range, 0.72–1.24; average = 1.17) was much higher than that in the control specimens (range, 0.22–0.63; average = 0.51; Fig 4E). Note that the lowest ratio (0.72) in FCD type IIb was still greater than the highest ratio (0.63) in the control. These results indicated that mTOR signaling was increased in FCD type IIb cases of *MTOR* mutations.

MTOR Mutations Activate the mTOR Pathway

mTOR (aa 1,376–2,549) consists of Huntingtin, elongation factor 3, a subunit of protein phosphatase 2A, and TOR1 (HEAT) repeats, a FRAP, ATM, and TRAP (FAT) domain, a kinase domain comprising N- and C-lobes that form a catalytic cleft, a FKBP12/rapamycin binding (FRB) domain, and a FRAP, ATM, TRRAP, and C-terminal (FATC) domain (Figs 2A and 5A).³¹ The neighboring p.Leu1460Pro and p.Ala1459Asp mutations are located in the FAT domain, whereas p.Ser2215Tyr and p.Ser2215Phe are at the same residue within the

kinase domain (Figs 2A and 5A). All altered amino acids are evolutionarily well conserved (Fig 2A), and the mutations were predicted to be deleterious by at least two online programs (Table 3). To evaluate the effects of missense mutations on mTOR function from a structural viewpoint, we mapped their location on the mTOR crystal structure (aa 1,376–2,549) in complex with mLST8, ATP γ S, and magnesium ions.³¹ The FRB domain in the N-lobe and helix 9b in the C-lobe hinder substrate access to the active site, negatively regulating mTOR kinase activity.^{33–35} Because residues at sites Ala1459 and Leu1460 are located in an N-terminal helix of the FAT domain and are involved in a hydrophobic core (Fig 5A, C), mutations here would destabilize the local structure of the FAT domain and impair its interaction with the kinase domain. This could release it from the restriction of active site accessibility, thereby hyperactivating mTOR kinase activity as reported previously.³³ Ser2215 is located in helix 3b, which is adjacent to the structural frame involving closely located helices 3, 9, and 9b (Fig 5A, B). Thus, mutations of Ser2215 to Tyr and Phe are likely to destabilize the structural frame and affect helix 9b conformation, restricting active site accessibility, and leading to mTOR kinase hyperactivation. Thus, all four somatic *MTOR* mutations were predicted to induce mTOR pathway hyperactivation. The free energy change calculated by FoldX software revealed a remarkable increase after all mutations, supporting our structural predictions (Fig 5D). Moreover, the *MTOR* mutations found in FCD type IIb were analyzed in cultured cells (in vitro). Plasmids carrying WT and mutant *MTOR*s (p.Ala1459Asp, p.Leu1460Pro, p.Ser2215Phe, and p.Ser2215Tyr) were transfected into HEK293T cells together with FLAG-4EBP, the best-known substrate for mTOR complex 1 (mTORC1). Mutant *MTOR*-transfected cells exhibited significantly strong phosphorylation of 4EBP, compared to WT *MTOR*-transfected cells, indicating that all *MTOR* mutants are constitutively active

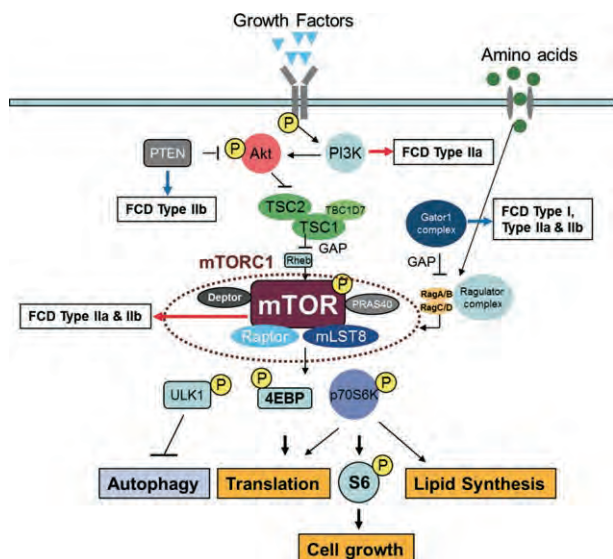


FIGURE 6: Schematic presentation of the mammalian target of rapamycin (mTOR)-signaling pathway. Upstream regulators of mTOR complex 1 (mTORC1), after stimulation with growth factors, are PI3K, Akt, TSC1/2, and Rheb. PTEN suppresses Akt activity. Another regulatory pathway that is activated by amino acids is Rags/Ragulator signaling. Gator1 suppresses mTORC1 activity. Activated mTORC1 directly phosphorylates 4EBP, p70S6K, and ULK1. Focal cortical dysplasia is caused by gain-of-function mutations (red arrows) or loss-of-function mutations (blue arrows) in mTOR-related genes. Black arrows and cross-end bars indicate activation of phosphorylation and inhibition of phosphorylation, respectively.

(Fig 5E). Signal intensities of all *MTOR* mutants were comparable with that of the plasmid carrying a hyperactive mutation of rat mTOR, which was used as a positive control.³⁴

Discussion

We found that the low-prevalence somatic *MTOR* mutations in 6 of 13 individuals with FCD type IIb (46%; Table 2 and Supporting Table 4). While this article was being reviewed, Lim et al also reported that somatic *MTOR* mutations caused FCD type IIb.³⁶ These results corroborated that low-prevalence somatic *MTOR* mutation is one of the genetic causes in FCD type IIb. However, there may be mutations in up- or downstream genes in the mTOR cascade in the other subjects having no *MTOR* mutation (Fig 6). Indeed, somatic mutations in *PTEN* and germline mutations in *DEPDC5*, encoding a component of Gator1, were reported in FCD type IIb.^{16–18,37} *PTEN* is one of the tumor-suppressor genes, encoding plasma membrane lipid phosphatase, which antagonizes PI3K-Akt signaling.³⁸ Gator1 has GTPase-activating activity for RagA/B and thus suppresses mTORC1 activity in static and low-amino-acid conditions.³⁹ Therefore, loss of function in *PTEN* and Gator1

may cause mTOR activation. Similarly, mutations in other genes involved in the mTOR cascade are involved in tuberous sclerosis (with mutations in *TSC1* and *TSC2*) and hemimegalencephaly (with mutations in *AKT3*, *DEPDC5*, *MTOR*, *PIK3CA*, and *PTEN*), which share histopathological similarities.^{12–17,19,37} These findings strongly suggest that unidentified mutations in related molecules of the mTOR pathway may possibly be the pathogenesis of FCD type IIb.

Somatic *MTOR* mutations in FCD type IIb are likely to cause hyperactivation of the mTOR-signaling pathway, which is involved in growth, migration, and the maturation of neurons and glial cells.⁸ All individuals with *MTOR* mutations showed distinctive balloon cells in their brain tissues (Fig 3 C, F, I, L, O, R). Such cells are also observed in tuberous sclerosis and hemimegalencephaly, in which the mTOR-signaling pathway is activated,^{2,8,10,13,32} raising the possibility that they are markers of aberrant mTOR signaling. Our IHC and Western blotting results clearly demonstrated high levels of phospho-S6, the well-known hallmark of mTOR cascade activation, in FCD type IIb lesions with *MTOR* mutations, specifically in dysmorphic neurons and balloon cells (Fig 4A, B, E). We failed to detect apparent differences on IHC expression of phospho-S6 between FCD type IIb with and without mutations (Fig 4A–C). In both cases, a large proportion of the abnormal cells (dysmorphic neurons and balloon cells) were phospho-S6-positive. Furthermore, we found no clinical differences between FCD type IIb individuals with or without *MTOR* mutations. These findings supported the hypothesis that *MTOR*-mutation-negative subjects may have mutations in other molecular members of the pathway, which lead to net activation of the mTOR signaling.¹⁹

We also investigated *MTOR* mutations in limited numbers of brain samples with FCD type I and IIa (six in type I and five in type IIa) and found no associated variants (Supporting Table 3). IHC examination of FCD type IIa revealed that many dysmorphic neurons showed phospho-S6-immunoreactivity as those noted in FCD type IIb (data not shown). In our series of FCD type IIa, both the number of dysmorphic neurons and intensities of phospho-S6-immunopositivity differed markedly among cases. Interestingly, Lim et al also reported somatic *MTOR* mutations in FCD type IIa.³⁶ Therefore, a further study with a large number of FCD type IIa cases would be necessary for better understanding of the molecular profiles and precise pathomechanisms underlying FCD type IIa. In control neocortical tissues, we found no dysmorphic neurons, balloon cells, or apparent cytoarchitectural abnormalities without any trace of aberrant mTOR signaling (Fig 4D, E). Consistent with this,

we observed no apparent phospho-S6 immunoreactivity in FCD type I (data not shown). mTOR activity is controlled by various extracellular cues, such as nutrients and growth factors in the brain.⁸ In a culture system, all of the mutants found in this study were constitutively active (Fig 5E), regardless of any extracellular stimuli. Therefore, these somatic mutations could induce dysregulation of growth of neurons and glia, or presumably of their progenitors during brain development. A large number of somatic mutations in cancer cells are clustered in the FAT domains or the kinase domains, and most activate the mTOR-signaling pathway.^{6,33} The mTOR protein can form two distinct complexes—mTORC1 and mTOR complex 2 (mTORC2)—and involvement of these different complexes results in divergence of the signaling pathway into two distinct channels. mTORC1 is composed of mTOR, mLST8, and Raptor and phosphorylates the downstream proteins, S6K1 and 4EBP, which regulate cell growth, proliferation, ribosome biogenesis, and autophagy (Fig 6).^{32,40} mTORC2 is composed of mTOR, mLST8, Rictor, and mSin1 and phosphorylates Akt, PKC, and SGK, which are involved in cell cycle, cell survival, and actin organization and morphology.^{32,40,41} Rapamycin, an allosteric inhibitor of mTOR, binds to mTOR with FKBP12 and inhibits kinase activity of mTORC1. mTORC1 is known to play a pivotal role in cerebral cortical development, though little is known about mTORC2.^{8,9} The mutations, p.Ser2215Tyr and p.Leu1460Pro, lead to the constitutive activation of mTORC1 signaling, but not that of mTORC2, and both mutations are sensitive to rapamycin.^{6,42} These findings imply that mTOR inhibitors would be able to alleviate intractable epilepsy in FCD type IIb.

Acknowledgments

This work was supported by grants from the Ministry of Health, Labor and Welfare of Japan; a Grant-in-Aid for Scientific Research (A), (B), and (C); a Grant-in-Aid for Exploratory Research from the Japan Society for the Promotion of Science; the Takeda Science Foundation; the fund for Creation of Innovation Centers for Advanced Interdisciplinary Research Areas Program in the Project for Developing Innovation Systems from the Japan Science and Technology Agency; the Strategic Research Program for Brain Sciences; and the Collaborative Research Project of the Brain Research Institute, the University of Niigata, and a Grant-in-Aid for Scientific Research on Innovative Areas (Transcription Cycle) from the Ministry of Education, Culture, Sports, Science and Technology of Japan.

We thank the patients and their families for participating in this work. We also thank N. Watanabe, M. Sato,

K. Takabe, and S. Nigorikawa for their excellent technical assistance. The plasmids of pCMV-FLAG and hyperactive mTOR mutant were kindly gifted by Dr K. Yonezawa and Dr T. Maeda, respectively.

Authorship

M.K., A.K., and N.Ma. conceived the study. M.N., H.Sa., and N.Ma. designed and performed analyses. M.N., Y.T., N.Mi., and H.Sa. performed exome sequencing. M.N. and C.O. performed targeted amplicon sequencing. M.N. performed statistical analysis and ddPCR. M.S. and K.O. performed protein structural analyses. J.T., M.K., H.Sh., H.M., and S.K. evaluated patients and provided samples. H.K., K.W., H.T., Y.Z., and A.K. processed tissue samples and performed pathological evaluation. N.T. and T.S. validated mTORC1 signaling. M.N., H.Sa., N.T., A.K., and N.Ma. wrote the manuscript. M.K., A.K., and N.Ma. obtained research funding.

Potential Conflicts of Interest

Nothing to report.

References

1. Taylor DC, Falconer MA, Bruton CJ, Corsellis JA. Focal dysplasia of the cerebral cortex in epilepsy. *J Neurol Neurosurg Psychiatry* 1971;34:369–387.
2. Marin-Valencia I, Guerrini R, Gleeson JG. Pathogenetic mechanisms of focal cortical dysplasia. *Epilepsia* 2014;55:970–978.
3. Blumcke I, Thom M, Aronica E, et al. The clinicopathologic spectrum of focal cortical dysplasias: a consensus classification proposed by an ad hoc Task Force of the ILAE Diagnostic Methods Commission. *Epilepsia* 2011;52:158–174.
4. Sisodiya SM, Fauser S, Cross JH, Thom M. Focal cortical dysplasia type II: biological features and clinical perspectives. *Lancet Neurol* 2009;8:830–843.
5. Baybis M, Yu J, Lee A, et al. mTOR cascade activation distinguishes tubers from focal cortical dysplasia. *Ann Neurol* 2004;56:478–487.
6. Sato T, Nakashima A, Guo L, Coffman K, Tamanoi F. Single amino-acid changes that confer constitutive activation of mTOR are discovered in human cancer. *Oncogene* 2010;29:2746–2752.
7. Ljungberg MC, Bhattacharjee MB, Lu Y, et al. Activation of mammalian target of rapamycin in cytomegalic neurons of human cortical dysplasia. *Ann Neurol* 2006;60:420–429.
8. Takei N, Nawa H. mTOR signaling and its roles in normal and abnormal brain development. *Front Mol Neurosci* 2014;7:28.
9. Crino PB. mTOR: a pathogenic signaling pathway in developmental brain malformations. *Trends Mol Med* 2011;17:734–742.
10. Poduri A, Evrony GD, Cai X, Walsh CA. Somatic mutation, genomic variation, and neurological disease. *Science* 2013;341:1237758.
11. Schick V, Majores M, Koch A, et al. Alterations of phosphatidylinositol 3-kinase pathway components in epilepsy-associated glioneuronal lesions. *Epilepsia* 2007;48(Suppl 5):65–73.

12. Riviere JB, Mirzaa GM, O'Roak BJ, et al. De novo germline and postzygotic mutations in AKT3, PIK3R2 and PIK3CA cause a spectrum of related megalencephaly syndromes. *Nat Genet* 2012;44:934–940.
13. Lee JH, Huynh M, Silhavy JL, et al. De novo somatic mutations in components of the PI3K-AKT3-mTOR pathway cause hemimegalencephaly. *Nat Genet* 2012;44:941–945.
14. Lindhurst MJ, Sapp JC, Teer JK, et al. A mosaic activating mutation in AKT1 associated with the Proteus syndrome. *N Engl J Med* 2011;365:611–619.
15. Poduri A, Evrony GD, Cai X, et al. Somatic activation of AKT3 causes hemispheric developmental brain malformations. *Neuron* 2012;74:41–48.
16. D'Gama AM, Geng Y, Couto JA, et al. Mammalian target of rapamycin pathway mutations cause hemimegalencephaly and focal cortical dysplasia. *Ann Neurol*. 2015;77:720–725.
17. Baulac S, Ishida S, Marsan E, et al. Familial focal epilepsy with focal cortical dysplasia due to DEPDC5 mutations. *Ann Neurol* 2015;77:675–683.
18. Schick V, Majores M, Engels G, et al. Activation of Akt independent of PTEN and CTMP tumor-suppressor gene mutations in epilepsy-associated Taylor-type focal cortical dysplasias. *Acta Neuropathol* 2006;112:715–725.
19. Jansen LA, Mirzaa GM, Ishak GE, et al. PI3K/AKT pathway mutations cause a spectrum of brain malformations from megalencephaly to focal cortical dysplasia. *Brain* 2015;138(Pt 6):1613–1628.
20. Cibulskis K, Lawrence MS, Carter SL, et al. Sensitive detection of somatic point mutations in impure and heterogeneous cancer samples. *Nat Biotechnol* 2013;31:213–219.
21. Koboldt DC, Zhang Q, Larson DE, et al. VarScan 2: somatic mutation and copy number alteration discovery in cancer by exome sequencing. *Genome Res* 2012;22:568–576.
22. Genomes Project C, Abecasis GR, Altshuler D, et al. A map of human genome variation from population-scale sequencing. *Nature* 2010;467:1061–1073.
23. Genomes Project C, Abecasis GR, Auton A, et al. An integrated map of genetic variation from 1,092 human genomes. *Nature* 2012;491:56–65.
24. Wang K, Li M, Hakonarson H. ANNOVAR: functional annotation of genetic variants from high-throughput sequencing data. *Nucleic Acids Res* 2010;38:e164.
25. Thorvaldsdottir H, Robinson JT, Mesirov JP. Integrative Genomics Viewer (IGV): high-performance genomics data visualization and exploration. *Brief Bioinform* 2013;14:178–192.
26. Miyahara H, Natsumeda M, Shiga A, et al. Suppressed expression of autophagosomal protein LC3 in cortical tubers of tuberous sclerosis complex. *Brain Pathol* 2013;23:254–262.
27. Guerois R, Nielsen JE, Serrano L. Predicting changes in the stability of proteins and protein complexes: a study of more than 1000 mutations. *J Mol Biol* 2002;320:369–387.
28. Mizushima S, Nagata S. pEF-BOS, a powerful mammalian expression vector. *Nucleic Acids Res* 1990;18:5322.
29. Eguchi S, Tokunaga C, Hidayat S, et al. Different roles for the TOS and RAIP motifs of the translational regulator protein 4E-BP1 in the association with raptor and phosphorylation by mTOR in the regulation of cell size. *Genes Cells* 2006;11:757–766.
30. Takei N, Inamura N, Kawamura M, et al. Brain-derived neurotrophic factor induces mammalian target of rapamycin-dependent local activation of translation machinery and protein synthesis in neuronal dendrites. *J Neurosci* 2004;24:9760–9769.
31. Yang H, Rudge DG, Koos JD, et al. mTOR kinase structure, mechanism and regulation. *Nature* 2013;497:217–223.
32. Laplante M, Sabatini DM. mTOR signaling in growth control and disease. *Cell* 2012;149:274–293.
33. Urano J, Sato T, Matsuo T, et al. Point mutations in TOR confer Rheb-independent growth in fission yeast and nutrient-independent mammalian TOR signaling in mammalian cells. *Proc Natl Acad Sci U S A* 2007;104:3514–3519.
34. Ohne Y, Takahara T, Hatakeyama R, et al. Isolation of hyperactive mutants of mammalian target of rapamycin. *J Biol Chem* 2008;283:31861–31870.
35. Reinke A, Chen JC, Aronova S, Powers T. Caffeine targets TOR complex I and provides evidence for a regulatory link between the FRB and kinase domains of Tor1p. *J Biol Chem* 2006;281:31616–31626.
36. Lim JS, Kim WI, Kang HC, et al. Brain somatic mutations in MTOR cause focal cortical dysplasia type II leading to intractable epilepsy. *Nat Med* 2015;21:395–400.
37. Scheffer IE, Heron SE, Regan BM, et al. Mutations in mammalian target of rapamycin regulator DEPDC5 cause focal epilepsy with brain malformations. *Ann Neurol* 2014;75:782–787.
38. Salmena L, Carracedo A, Pandolfi PP. Tenets of PTEN tumor suppression. *Cell* 2008;133:403–414.
39. Bar-Peled L, Chantranupong L, Cherniack AD, et al. A Tumor suppressor complex with GAP activity for the Rag GTPases that signal amino acid sufficiency to mTORC1. *Science* 2013;340:1100–1106.
40. Zoncu R, Efeyan A, Sabatini DM. mTOR: from growth signal integration to cancer, diabetes and ageing. *Nat Rev Mol Cell Biol* 2011;12:21–35.
41. Loewith R, Jacinto E, Wullschlegel S, et al. Two TOR complexes, only one of which is rapamycin sensitive, have distinct roles in cell growth control. *Mol Cell* 2002;10:457–468.
42. Grabiner BC, Nardi V, Birsoy K, et al. A diverse array of cancer-associated MTOR mutations are hyperactivating and can predict rapamycin sensitivity. *Cancer Discov* 2014;4:554–563.

Original Article

Immunohistochemical profiles of IDH1, MGMT and P53: Practical significance for prognostication of patients with diffuse gliomas

Ryosuke Ogura,² Yoshihiro Tsukamoto,² Manabu Natsumeda,¹ Mizuho Isogawa,¹ Hiroshi Aoki,¹ Tsutomu Kobayashi,¹ Seiichi Yoshida,¹ Kouichiro Okamoto,¹ Hitoshi Takahashi,² Yukihiro Fujii¹ and Akiyoshi Kakita²

Departments of ¹Neurosurgery and ²Pathology, Brain Research Institute, University of Niigata, Niigata, Japan

Genetic and epigenetic status, including mutations of isocitrate dehydrogenase (*IDH*) and *TP53* and methylation of O⁶-methylguanine-DNA methyltransferase (*MGMT*), are associated with the development of various types of glioma and are useful for prognostication. Here, using routinely available histology sections from 312 patients with diffuse gliomas, we performed immunohistochemistry using antibodies specific for IDH1 mutation, MGMT methylation status, and aberrant p53 expression to evaluate the possible prognostic significance of these features. With regard to overall survival (OS), univariate analysis indicated that an IDH1-positive profile in patients with glioblastoma (GBM), anaplastic astrocytoma (AA), anaplastic oligoastrocytoma and oligodendroglioma, or a MGMT-negative profile in patients with GBM and AA were significantly associated with a favorable outcome. Multivariate analysis revealed that both profiles were independent factors influencing prognosis. The OS of patients with IDH1-positive/MGMT-negative profiles was significantly longer than that of patients with negative/negative and negative/positive profiles. A p53 profile was not an independent prognostic factor. However, for GBM/AA patients with IDH1-negative/MGMT-negative profiles, p53 overexpression was significantly associated with an unfavorable outcome. Thus, the immunohistochemical profiles of IDH1 and MGMT are of considerable significance in gliomas, and a combination of IDH1, MGMT and p53 profiles may be useful for prognostication of GBM/AA.

Key words: glioma, IDH1, immunohistochemistry, MGMT, p53.

INTRODUCTION

Glioma is the most common type of primary brain tumor. Recent molecular studies of various histopathological types of glioma¹ have revealed several genetic pathways critical for the development of astrocytic and oligodendroglial tumors.^{2,3} For prognostication of patients with diffuse gliomas, it has been shown that the molecular profiles of isocitrate dehydrogenase 1/2 (*IDH1/2*) mutation, O⁶-methylguanine-DNA methyltransferase (*MGMT*) promoter methylation, 1p19q co-deletion, and glioma CpG island methylator phenotype (G-CIMP) are possible factors, whereas the impact of *TP53* and *EGFR* mutation has remained unclear.⁴ Moreover, a recent genetic and epigenetic study has revealed that a combination of *IDH1* mutation and *MGMT* methylation status outperforms information about either *IDH1* or *MGMT* alone in predicting the survival of patients with glioblastoma (GBM).⁵ Thus, in clinical practice, it is important to have information on these molecular profiles. However, identification of molecular profiles by DNA sequencing requires intensive laboratory work by trained personnel using specialized equipment, and therefore the methodology is not always available for daily clinical use at every medical center.

On the other hand, immunohistochemistry is a technique that can be applied to routinely available histology sections. For detection of *IDH1* mutations, an IDH1-R132H mutation-specific antibody is available, and the results show concordance with DNA sequencing without any cross-reactivity with the wild-type or other mutant IDH1 proteins.^{6,7} Moreover, immunohistochemistry with a monoclonal antibody MT3.1 against MGMT protein has been

Correspondence: Akiyoshi Kakita, MD, PhD, Department of Pathology, Brain Research Institute, University of Niigata, 1-757 Asahimachi, Chuo-ku, Niigata 951-8585, Japan. Email: kakita@bri.niigata-u.ac.jp

Received 21 October 2014; revised 21 December 2014 and accepted 22 December 2014; published online 6 May 2015.

Table 1 Clinical profiles of patients in each group

Group	Grade IV	Grade III		Grade II	
	GBM	AA	AOA/AOD	DA	OA/OD
No. of patients	165	61	40	19	27
Age (years)					
Median	64	58	59	38	45
Range	18–85	24–89	22–81	24–67	25–74
Age (years), <i>n</i> (%)					
<50	25 (15.1)	23 (37.7)	8 (20)	12 (63.2)	15 (55.6)
50–59 years	26 (15.8)	10 (16.4)	11 (27.5)	5 (26.3)	4 (14.8)
60–69 years	60 (36.4)	7 (11.5)	10 (25.0)	2 (10.5)	6 (22.2)
≥70	54 (32.7)	21 (34.4)	11 (27.5)	0	2 (7.4)
Gender, <i>n</i> (%)					
Male	93 (56.3)	33 (54.1)	26 (65)	9 (47.4)	14 (51.9)
Female	72 (43.6)	28 (45.9)	14 (35)	10 (52.6)	13 (48.1)
KPS, <i>n</i> (%)					
100	4 (2.4)	11 (18.0)	4 (10.0)	12 (63.2)	9 (33.3)
70–90	95 (57.6)	32 (52.5)	19 (47.5)	7 (36.8)	17 (63.0)
<70	66 (40.0)	18 (29.5)	17 (42.5)	0	1 (3.7)
Surgery, <i>n</i> (%)					
Total/Subtotal	72 (43.6)	12 (19.6)	21 (52.5)	12 (63.2)	17 (63.0)
Partial	53 (32.1)	27 (44.3)	19 (47.5)	7 (36.8)	9 (33.3)
Stereo biopsy	38 (23.0)	19 (31.2)	0	0	1 (3.7)
Others	2 (1.2)	3 (4.9)	0	0	0
Initial treatment, <i>n</i> (%)					
None	8 (4.8)	2 (3.3)	0	12 (63.2)	11 (40.7)
RT alone	61 (37.0)	21 (34.4)	8 (20.0)	7 (36.8)	16 (59.3)
CRT	95 (57.6)	36 (59.0)	32 (80.0)	0	0
Others	1 (0.6)	2 (3.3)	0	0	0

GBM, glioblastoma; AA, anaplastic astrocytoma; AOA, anaplastic oligoastrocytoma; AOD, anaplastic oligodendroglioma; DA, diffuse astrocytoma; OA, oligoastrocytoma; OD, oligodendroglioma; KPS, Karnofsky performance status; RT, radiotherapy; CRT, chemoradiotherapy.

employed to assess *in vivo* MGMT methylation status, and a significant negative association of MGMT with survival has been detected in patients with WHO grades II and IV astrocytomas.⁸ Furthermore, immunohistochemical detection of overall p53 protein expression may be an independent indicator of shorter survival in patients with astrocytic tumors, even though overexpression of p53 is not always associated with point mutations in the *TP53* gene.⁹ In the present study, we performed immunohistochemistry using antibodies specific for IDH1 mutation, MGMT status, and aberrant p53 expression in order to evaluate the possible prognostic significance of these features and their combinations in patients with diffuse gliomas.

MATERIALS AND METHODS

Patients

We reviewed the medical records of 312 consecutive patients (175 male, 137 female; age at surgery, mean ± SD = 58.4 ± 15.6 years) who were admitted to the University of Niigata Hospital, Japan, between 2000 and 2013, and were diagnosed pathologically as having diffuse gliomas, including diffuse astrocytoma (DA), oligodendroglioma (OD), oligoastrocytoma (OA), anaplastic astrocytoma

(AA), anaplastic oligodendroglioma (AOD), anaplastic oligoastrocytoma (AOA) and GBM. The study was approved by the hospital Ethics Committee, and written informed consent to use resected tissues for research purposes was obtained from all patients. First, in accordance with the histopathological diagnosis of diffuse gliomas,¹ the patients were divided into five groups: GBM, AA, AOA/AOD, DA and OA/OD. Table 1 summarizes the clinical profiles of the patients in each of these histologically defined groups.

Histology and immunohistochemistry

The surgical specimens were fixed with 20% buffered formalin and embedded in paraffin. Histopathological examination was performed on 4-μm-thick sections stained with HE. The paraffin-embedded sections were processed for immunohistochemistry using methods previously described.¹⁰ Primary monoclonal antibodies against the following antigens were used: human IDH1 R132H (clone H09; Dianova, Hamburg, Germany; dilution 1:100), MGMT (clone MT3.1; Chemicon International, Temecula, CA, USA; 1:50), and human p53 (clone DO-7; Dako, Glostrup, Denmark; 1:50). Immunohistochemical features were evaluated by two persons (RO and YT)

independently without information on the patients' profiles or histological grades, and then were confirmed by a pathologist (AK).

IDH1 mutations: direct DNA sequencing and immunohistochemical evaluation

Genomic DNA was extracted from paraffin-embedded sections, as described previously,¹¹ and PCR amplification was performed using primer sets (forward: 5'-CGGTCTTCAGAGAAGCCATT-3'; and reverse: 5'-TTCATACC TTGCTTAATGGGTGT-3') for exon 4 of the *IDH1* gene around the R132 residue. The PCR products were then sequenced on a 3130xl Genetic Analyzer (Applied Biosystems, Foster City, CA, USA) with a Big Dye Terminator v1.1 Cycle Sequencing Kit (Applied Biosystems) in accordance with the manufacturer's instructions.

IDH1 immunoreactivity was judged as "positive" when a large proportion of tumor cells showed strong cytoplasmic reactivity (Fig. 1A), whereas it was regarded as "negative" if weak or no reactivity was observed (Fig. 1B). Labeling of macrophages was ignored.

To compare the results of both direct DNA sequencing and immunohistochemistry, we preliminarily applied both methods to specimens taken from 37 patients with GBM. All four patients with an IDH1-immunopositive profile showed an identical heterozygous mutation in *IDH1* (CGT→CAT) (Fig. 1C) resulting in an Arg→His (R132H) amino acid substitution. The other 33 patients with an IDH1-immunonegative profile showed the wild-type *IDH1* gene. Furthermore, direct DNA sequencing using samples taken from areas with sparsely infiltrating tumor cells failed to detect the mutation, although in one patient with anaplastic astrocytoma immunohistochemistry demonstrated a small number of positive cells in this type of area (Fig. 1C). Thus, application of immunohistochemistry for detection of IDH1 R132H mutation was shown to be reliable and of practical use.

Evaluation of MGMT and p53

MGMT immunoreactivity was evaluated in representative areas of the tumors showing the characteristic features defining their histological grades.¹ Individual tumor nuclei were regarded as positive when they showed an intensity similar to that of vascular endothelial cells used as an internal positive control (Fig. 1D,E). In accordance with a previous report,¹² we determined percentages of MGMT-positive tumor cells in individual cases by continuously counting over 400 nuclei observed in high-magnification views. We carefully excluded possible positive staining of non-neoplastic cells, including oligodendrocytes and infiltrating inflammatory cells.^{13,14} For individual cases, when the proportion of labeled nuclei/all tumor nuclei was 30%

or more, the case was regarded as "positive", whereas a case was considered "negative" when the proportion was less than 30% (Fig. 1D,E). Indeed, there was a clear difference between the numbers of "negative" and "positive" cases (Fig. 1F), which enabled us to judge with confidence. Immunonegativity for MGMT may represent the methylation status of the MGMT gene, and is positively linked to the response of a tumor to chemotherapy.¹⁵

Evaluation of p53 expression was performed in a semi-quantitative manner by continuously counting over 1000 tumor cells in the areas of highest expression. According to the percentage of tumor cells showing reactivity, we distinguished four groups: many (>50%), several (10–50%), rare (<10%), or no cells positive (Fig. 1G–J).¹⁶ In accordance with previous reports,^{9,17} we considered cases in the many and several groups as "positive" and those in the rare and negative groups as "negative".

Statistical analysis

Data analysis was carried out using the SPSS ver17.0 software package (SPSS Inc., Chicago, IL, USA) and GraphPad Prism 5.0 statistical software (<http://graphpad-prism.software.informer.com/5.0/>). Overall survival (OS) and progression-free survival (PFS) were calculated from the time of surgery until death, disease progression, or last follow-up according to the Kaplan-Meier method with log-rank test for comparison between groups. Univariate and multivariate analysis with the Cox proportional hazards model was used to assess prognostic factors. Results are expressed as relative risk with the 95% confidence interval (95% CI).

RESULTS

Significance of immunohistochemical profiles of IDH1, MGMT and p53

Tables 2 and 3 summarize the immunohistochemical profiles and their prognostic values in terms of OS and PFS for patients included in each of the histologically defined groups. Figure 2 shows the Kaplan-Meier curves of the OS rate and median OS (mOS) for patients with grades III/IV malignant astrocytomas (AA/GBM).

The numbers of patients with IDH1-positive profiles were significantly higher and lower than those of patients with IDH1-negative profiles for grade II (DA, $P = 0.003$; OA/OD, $P = 0.004$) and grades III (AA, $P = 0.007$)/IV (GBM, $P < 0.001$) gliomas, respectively, and there were no significant differences in the numbers of patients with both profiles in the AOA/AOD group ($P = 0.114$). The numbers of patients with MGMT-negative profiles in the oligodendroglial tumor groups (OA/OD, $P = 0.001$; AOA/AOD,

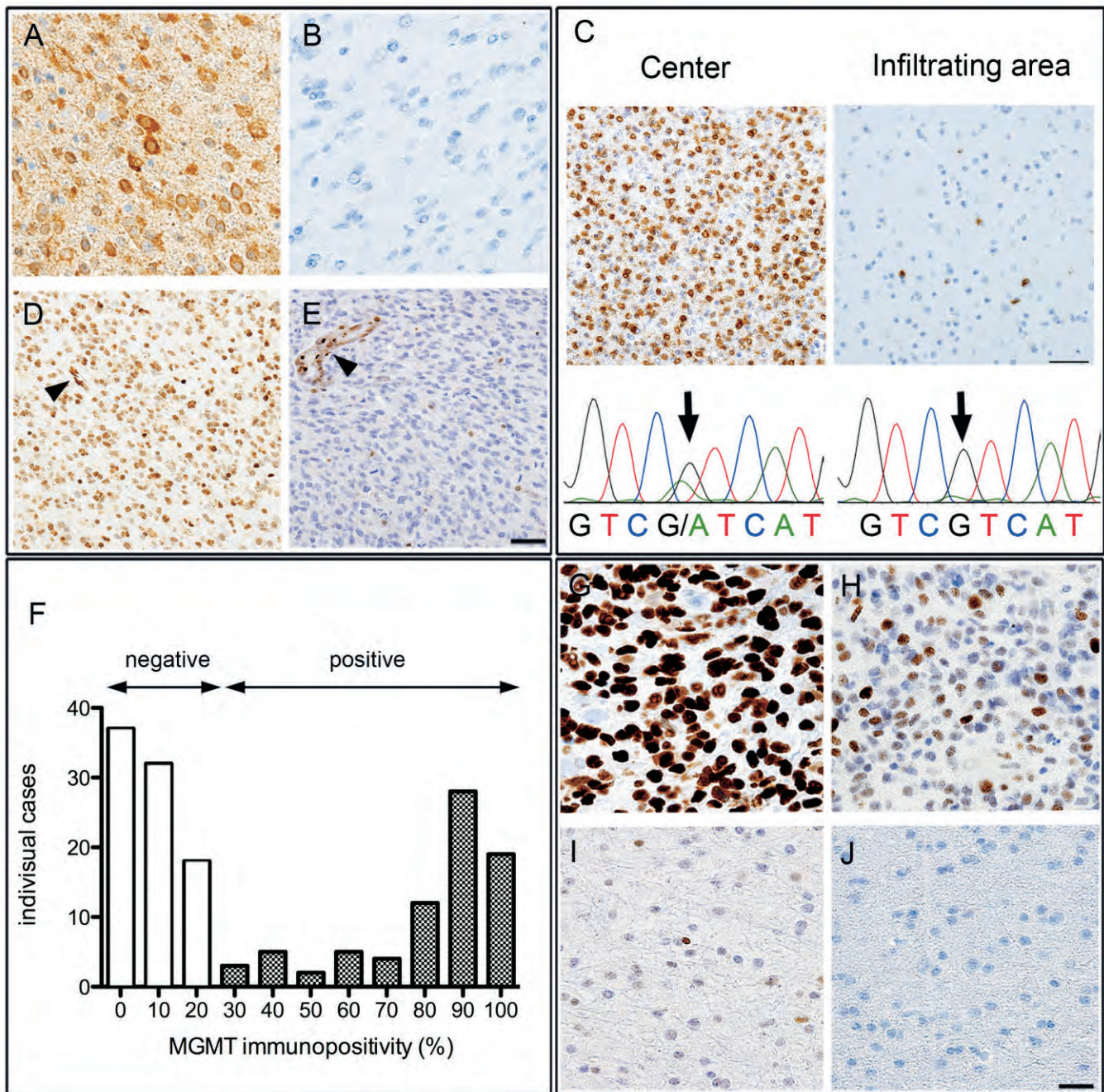


Fig. 1 Evaluation of isocitrate dehydrogenase 1 (IDH1), O⁶-methylguanine-DNA methyltransferase (MGMT) and p53 status. Immunohistochemistry for IDH1 (A, B), MGMT (D, E), and p53 (G–J). Examples of IDH1 positivity (A), IDH1 negativity (B), MGMT positivity (D), and MGMT negativity (E). Arrowheads in D and E indicate endothelial cells used as an internal positive control. Examples of p53 many (G), several (H), rare (I), and no (J) cells positive. (C) Demonstration of IDH1 immunohistochemistry and direct DNA sequencing of *IDH1* in a patient with anaplastic astrocytoma. In the tumor center (left panels), many IDH1-positive cells and heterozygous mutation of *IDH1* R132H (arrow) are evident, whereas in the infiltrating area (right panels), scattered IDH1-positive cells but no mutations are demonstrated. (F) A histogram showing the proportion of the MGMT-labeled nuclei/all tumor nuclei for all 165 cases of glioblastoma. A clear numerical distinction is evident between less than 30% (regarded as “negative”) and 30% and more (“positive”). Scale bars = 50 μm.

Table 2 Prognostic value of mOS and mPFS of patients included in each histologically defined group, in accordance with immunohistochemical profiles of IDH1, MGMT and p53 of the gliomas

Group	Total	IDH1			MGMT			p53	
		Positive	Negative	<i>P</i> value	Negative	Positive	<i>P</i> value	Negative	<i>P</i> value
GBM									
No. of patients (%)	165	6 (4)	159 (96)	<0.001	89 (54)	76 (46)	0.312	62 (38)	0.001
mOS (months)	14	66	14	0.006	18	12	<0.001	13	0.921
mPFS (months)	5	59	4	0.005	7	3	<0.001	5	0.671
AA									
No. of patients (%)	61	20 (33)	41 (67)	0.007	33 (54)	28 (46)	0.522	28 (46)	0.522
mOS (months)	22	46	15	0.013	30	15	0.009	18	0.967
mPFS (months)	5	22	4	0.002	11	3	<0.001	6	0.847
AOA/AOD									
No. of patients (%)	40	15 (38)	25 (62)	0.114	32 (80)	8 (20)	<0.001	19 (47)	0.752
mOS (months)	80	NR	25	0.025	80	21	0.206	25	0.522
mPFS (months)	24	NR	10	0.001	28	7	0.160	20	0.470
DA									
No. of patients (%)	19	16 (84)	3 (16)	0.003	11 (58)	8 (42)	0.491	14 (74)	0.039
mOS (months)	NR	NR	ND	–	NR	ND	–	ND	–
mPFS (months)	NR	NR	51	–	44	NR	–	51	–
OA/OD									
No. of patients (%)	27	22 (81)	5 (19)	0.004	21 (78)	6 (22)	0.001	23 (85)	<0.001
mOS (months)	NR	NR	40	0.100	NR	NR	0.381	NR	0.021
mPFS (months)	NR	NR	19	0.080	NR	19	0.142	NR	0.031

P-values were calculated by the log-rank test and Chi-square test.

mOS, median overall survival; mPFS, median progression free survival; NR, not reached; ND, not determined. GBM, glioblastoma; AA, anaplastic astrocytoma; AOA, anaplastic oligoastrocytoma; AOD, anaplastic oligodendroglioma; DA, diffuse astrocytoma; OA, oligoastrocytoma; OD, oligodendroglioma

$P < 0.001$) were significantly higher than those of patients with MGMT-positive profiles, whereas the numbers of patients with either profile in the astrocytic tumor groups (DA, $P = 0.491$; AA, $P = 0.522$; GBM, $P = 0.312$) were almost equal. The proportion of patients with a p53-positive profile in each histologically defined group appeared to increase in accordance with malignancy grading (OA/OD 15%, DA 26%, AOA/AOD 53%, AA 54% and GBM 62%). The number of patients with p53-positive profiles was significantly higher than that of patients with p53-negative profiles for grade IV (GBM, $P = 0.001$) only.

With regard to OS and PFS, univariate analysis indicated that either an IDH1-positive profile for patients with GBM (OS and PFS: $P = 0.014$ and $P = 0.015$, respectively), AA ($P = 0.020$ and $P = 0.004$) (Fig. 2A for GBM/AA) and AOA/AOD ($P = 0.035$ and $P = 0.003$), or a MGMT-negative profile for patients with GBM (both $P < 0.001$) and AA ($P = 0.016$ and $P = 0.006$) (Fig. 2B for GBM/AA) was significantly associated with a favorable outcome. Multivariate analysis revealed that both an IDH1-positive profile ($P = 0.031$ and $P = 0.013$) and a MGMT-negative profile (both $P < 0.001$) were independent factors affecting prognosis for patients with GBM (Table 3). For patients with grade II gliomas (DA and OA/OD), the prognostic value of IDH1 and MGMT status was less significant.

On the basis of the IDH1 and MGMT profiles, a total of 226 patients with grades III/IV malignant astrocytomas (165 and 61 patients with GBM and AA, respectively) were divided into four groups. The mOS of patients with IDH1-positive/MGMT-negative ($n = 18$), positive/positive ($n = 8$), negative/negative ($n = 104$), and negative/positive ($n = 96$) profiles was 56, 22, 17 and 12 months, respectively (Fig. 2C). The mOS of patients with positive/negative profiles was significantly longer than that of patients with negative/negative ($P = 0.002$) and negative/positive ($P < 0.001$) profiles. Similarly, the mOS of patients with positive/positive and negative/negative profiles was significantly longer ($P = 0.008$ and $P < 0.001$, respectively) than that of patients with a negative/positive profile. Thus, a combination of both IDH1 and MGMT profiles was able to accurately predict outcome in patients with malignant astrocytomas.

On the other hand, a p53 positive/negative profile was not an independent factor affecting prognosis for patients with malignant astrocytomas (Table 3) when we defined the many and several groups ($p53 > 10\%$) (Fig. 2D) or the many group only ($p53 > 50\%$) (Fig. 2E) as “positive”. Next, we examined the effects of combinations of the IDH1, MGMT and p53 profiles (Fig. 2F–I). For patients with IDH1-positive profiles (Fig. 2F,G), neither $p53 > 10\%$ (Fig. 2F) nor $p53 > 50\%$ (Fig. 2G) were a prognostic factor. Similarly, for patients with IDH1-negative profiles

Table 3 Prognostic univariate and multivariate Cox regression analyses of patients included in each histologically defined group

Univariate		OS			PFS		
		HR	95% CI	P-value	HR	95% CI	P-value
GBM							
IDH1	Pos vs. neg	0.230	0.071–0.742	0.014	0.228	0.069–0.751	0.015
MGMT	Neg vs. pos	0.463	0.323–0.665	<0.001	0.503	0.347–0.729	<0.001
p53	Pos vs. neg	1.014	0.711–1.445	0.940	1.073	0.740–1.556	0.709
KPS	≥70 vs. <70	0.614	0.431–0.876	0.007	0.717	0.493–1.043	0.082
Age	≥65 vs. <65	1.632	1.142–2.332	0.007	1.226	0.848–1.774	0.278
Total/subtotal	Yes vs. no	0.530	0.367–0.765	0.001	0.605	0.420–0.872	0.007
CRT	Yes vs. no	0.446	0.313–0.638	<0.001	0.585	0.400–0.854	0.005
AA							
IDH1	Pos vs. neg	0.459	0.239–0.884	0.020	0.373	0.189–0.736	0.004
MGMT	Neg vs. pos	0.473	0.257–0.872	0.016	0.416	0.221–0.780	0.006
p53	Pos vs. neg	1.066	0.583–1.951	0.835	0.987	0.530–1.839	0.968
KPS	≥70 vs. <70	0.334	0.169–0.660	0.002	0.413	0.204–0.835	0.014
Age	≥60 vs. <60	3.120	1.651–5.898	<0.001	1.964	1.001–3.850	0.050
Total/subtotal	Yes vs. no	0.382	0.173–0.844	0.017	0.370	0.160–0.858	0.021
CRT	Yes vs. no	0.565	0.305–1.046	0.069	0.883	0.461–1.692	0.707
AOA/AOD							
IDH1	Pos vs. neg	0.291	0.092–0.916	0.035	0.238	0.093–0.611	0.003
MGMT	Neg vs. pos	0.521	0.184–1.474	0.219	0.529	0.212–1.320	0.172
p53	Pos vs. neg	0.742	0.294–1.874	0.528	0.760	0.356–1.622	0.477
KPS	≥70 vs. <70	0.339	0.122–0.945	0.039	0.394	0.173–0.896	0.026
Age	≥60 vs. <60	2.067	0.777–5.501	0.146	3.267	1.407–7.584	0.006
Total/subtotal	Yes vs. no	0.260	0.092–0.737	0.011	0.399	0.184–0.866	0.020
CRT	Yes vs. no	0.560	0.198–1.578	0.272	0.836	0.333–2.096	0.702
DA							
IDH1	Pos vs. neg	NR			1.014	0.117–8.774	0.990
MGMT	Neg vs. pos	NR			2.276	0.384–13.497	0.365
p53	Pos vs. neg	6.329	0.569–70.412	0.133	0.645	0.075–5.544	0.690
Age	≥45 vs. <45	2.171	0.131–35.996	0.588	0.400	0.046–3.451	0.405
Total/subtotal	Yes vs. no	0.812	0.066–9.975	0.871	0.714	0.140–3.643	0.685
RT	Yes vs. no	NR			1.290	0.255–6.525	0.758
OA/OD							
IDH1	Pos vs. neg	0.246	0.040–1.498	0.128	0.306	0.075–1.239	0.097
MGMT	Neg vs. pos	0.458	0.076–2.746	0.393	0.399	0.112–1.420	0.156
p53	Pos vs. neg	6.407	1.052–39.020	0.044	4.155	1.025–16.839	0.046
Age	≥45 vs. <45	1.504	0.251–9.006	0.655	2.299	0.547–9.657	0.255
Total/subtotal	Yes vs. no	0.345	0.058–2.068	0.244	0.321	0.076–1.348	0.121
RT	Yes vs. no	1.829	0.204–16.389	0.589	3.236	0.397–26.349	0.272
Multivariate							
		OS			PFS		
		HR	95% CI	P-value	HR	95% CI	P-value
GBM							
IDH1	Pos vs. neg	0.265	0.079–0.886	0.031	0.209	0.061–0.715	0.013
MGMT	Neg vs. pos	0.457	0.315–0.663	<0.001	0.483	0.329–0.710	<0.001
KPS	≥70 vs. <70	0.694	0.481–1.002	0.051	0.667	0.454–0.980	0.039
Age	≥65 vs. <65	1.207	0.814–1.791	0.349	0.982	0.657–1.469	0.931
Total/subtotal	Yes vs. no	0.582	0.402–0.841	0.004	0.618	0.427–0.895	0.011
CRT	Yes vs. no	0.580	0.390–0.864	0.007	0.675	0.446–1.023	0.064

P values were calculated by Cox proportional hazard models.

CI, confidence interval; HR, hazard ratio; neg, negative; pos, positive; GBM, glioblastoma; AA, anaplastic astrocytoma; AOA, anaplastic oligoastrocytoma; AOD, anaplastic oligodendroglioma; DA, diffuse astrocytoma; OA, oligoastrocytoma; OD, oligodendroglioma; KPS, Karnofsky performance status; RT, radiotherapy; CRT, chemoradiotherapy

(Fig. 2H,I), p53 >10% (Fig. 2H) was not a prognostic factor, and a MGMT-negative profile appeared to operate as a favorable factor. However, the OS of patients with p53 >50% who were MGMT-negative ($n = 28$) was significantly shorter than that of patients with p53 ≤50%/MGMT-

negative profiles ($n = 76$, $P = 0.044$) (Fig. 2I). Thus, for patients with IDH1-negative/MGMT-negative profiles, p53 >50% was associated with a poor outcome.

Based on combinations of the IDH1, MGMT and p53 profiles, three groups of patients with malignant

astrocytomas were distinguishable in terms of outcome (Figs 2J and 3). Group C ($n = 124$) showed significantly the poorest outcome (mOS = 12 m) relative to Group B ($n = 76$, mOS = 18 m, $P < 0.001$) and Group A ($n = 18$, mOS = 56 m, $P < 0.001$). Group B also showed a poorer outcome than Group A ($P = 0.005$).

Clinical factors and prognosis

For patients with malignant astrocytomas, several clinical characteristics, including Karnofsky performance status score, age, total/subtotal removal of the tumor, and use of chemoradiotherapy (CRT: yes vs. no, $n = 131$ vs. 95; Fig. 2K) showed a significant relationship with OS (Table 3). Multivariate analysis indicated that total/subtotal removal of the tumor and use of CRT were independent factors significantly associated with a favorable outcome (Table 3).

For patients with malignant astrocytomas who received CRT ($n = 131$; Fig. 2L), the mOS of those with a MGMT-negative profile ($n = 77$, 24 months) was significantly ($P < 0.001$) longer than that of patients with a MGMT-positive profile ($n = 54$, 15 months).

DISCUSSION

Recent molecular analyses of glioma tissue have revealed that several profiles, including *IDH1/2* mutation, *TP53* mutation, *TERT* promoter mutation, *ATRX* mutation, 1p/19q co-deletion, and *MGMT* methylation status, are associated with the development of various histological types of glioma. In the present study, we performed immunohistochemistry to evaluate subsets of these molecular profiles using routinely available histology sections (Fig. 1). This revealed that the significance of the profiles differed in accordance with the histopathological classification of the gliomas, and that combination of the profiles was of prognostic value (Tables 2 and 3, and Figs 2 and 3).

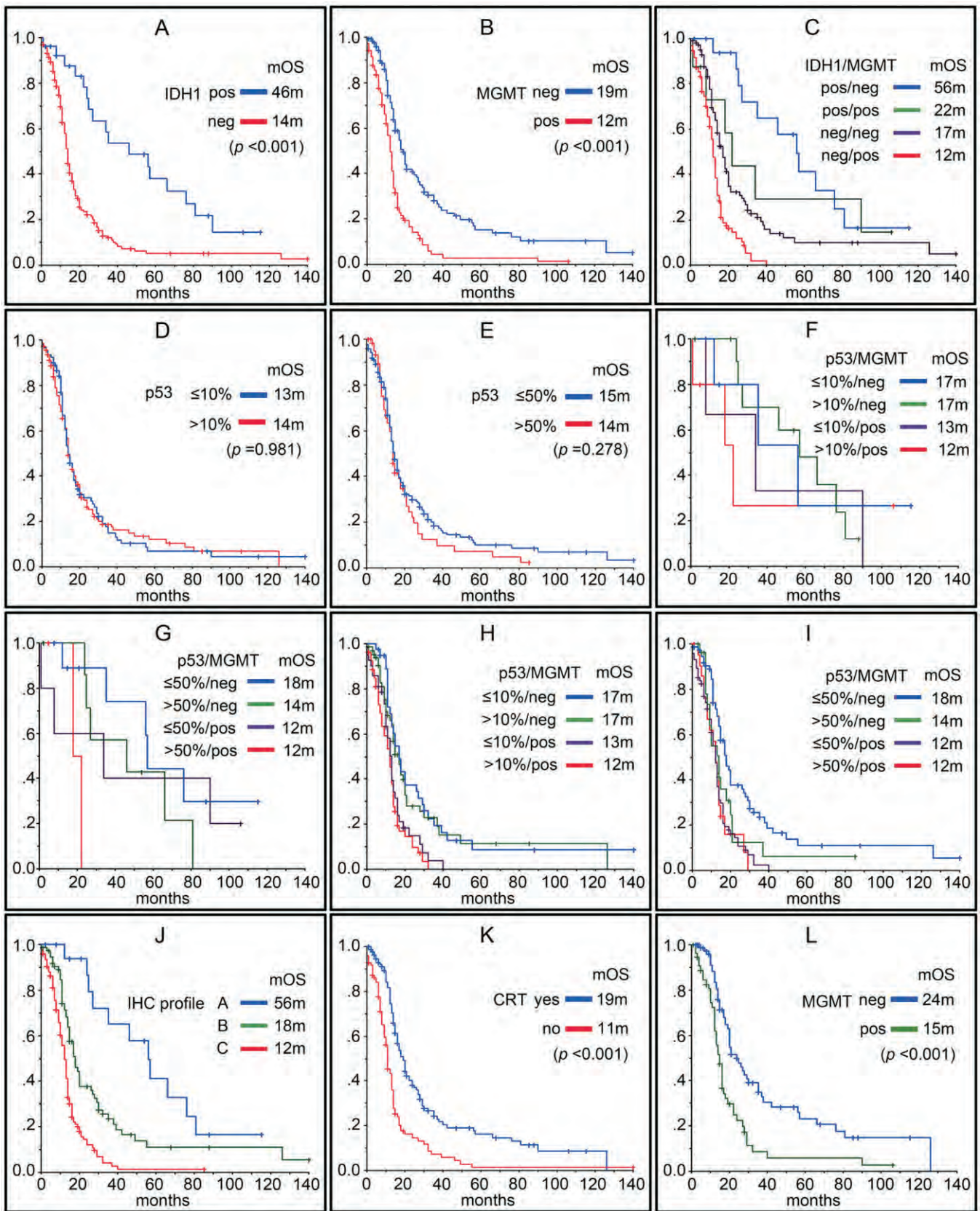
Patients with *IDH1*-mutated malignant glioma may survive longer than those with wild-type *IDH1* glioma.^{18–20} Recently, a genetic and epigenetic study has indicated a possible mechanism underlying this phenomenon, in which *IDH1* mutations induce the CpG island methylator

phenotype, a factor associated with biologically benign behavior of the glioma cells.²¹ Therefore, in clinical practice, detection of *IDH1* mutations is important, and for this purpose direct DNA sequencing is frequently employed. However, tissue samples from diffuse gliomas are usually an admixture of tumor cells and pre-existing brain parenchyma; therefore the sensitivity of this method for detection of a mutant sequence within wild-type sequences depends on the ratio of the two tissue components, and is estimated to be 20% or more.²² Pyrosequencing analysis is a much more sensitive method, capable of detecting a minimum of 5% mutant alleles.^{22,23} Moreover, the use of BEAMing (beads, emulsion, amplification, magnetics) PCR and droplet digital PCR can detect a mutant allele in a tissue sample with a sensitivity of 0.01%.²⁴ Thus, advances in methodology have improved the sensitivity of mutation detection; on the other hand, these techniques require specific equipment and skill, and as a consequence they are sometimes unavailable in a standard clinical laboratory. Immunohistochemistry is a technique that can be performed simultaneously with practical histopathological diagnosis of tumors. This method has apparently high sensitivity for detection of *IDH1* mutations.⁷ Consistent with this, our preliminary attempt to perform both immunohistochemistry and direct DNA sequencing on tissues showing glioma infiltration showed that mutation was detectable by immunohistochemistry only (Fig. 1C).

Immunohistochemistry with the *IDH1*-R132H antibody is highly specific for detecting the most common mutation in the gene.⁷ The sensitivity of this method is estimated to be 94%,²⁵ but other *IDH1* mutations, including R132C, R132S, R132G, R132L, R132V and R132P,^{6,7,20,26–30} or *IDH2* mutations³¹ are not recognized by this antibody. Therefore, even though such *IDH1/2* mutations are rare in practice, for *IDH1*-immunonegative cases, direct DNA sequencing for *IDH1/2* may provide more detailed information on the genes.^{32–34}

The frequencies of patients with *IDH1*-immunopositive profiles in the present study (Table 2) were similar to those reported previously, where direct DNA sequencing identified *IDH1* mutations in 70%–80% of diffuse gliomas, including DA (72.51%), OD (77.81%), OA (81.43%), AA (48.71%), AOA (66.40%), AOD (32.79%) and primary

Fig. 2 Kaplan-Meier curves. Overall survival rate (OS) for patients with grades III/IV malignant astrocytomas (anaplastic astrocytoma and glioblastoma) (A–J). Median OS (months: *m*) for patients with (A) isocitrate dehydrogenase 1 (*IDH1*), (B) O⁶-methylguanine-DNA methyltransferase (*MGMT*), (C) the *IDH1*/*MGMT* combination, (D) p53 (>10%: many and several groups, or ≤10%), (E) p53 (>50%: many groups only, or ≤50%), (F) in patients with *IDH1* positivity, combination of p53 (>≤10%)/*MGMT*, (G) in patients with *IDH1* positivity, combination of p53 (>≤50%)/*MGMT*, (H) in patients with *IDH1* negativity, combination of p53 (>≤10%)/*MGMT*, and (I) in patients with *IDH1* negativity, combination of p53 (>≤50%)-immunopositive (*pos*) or negative (*neg*) profiles are described. (J) OS for patients in Groups A, B and C. The groups were defined as depicted in Figure 3. (K) OS for patients with (*yes*) or without (*no*) chemoradiotherapy (CRT). (L) For the patients with CRT, a *MGMT*-negative profile was significantly associated with a favorable outcome. *P*-values were calculated by the log-rank test.



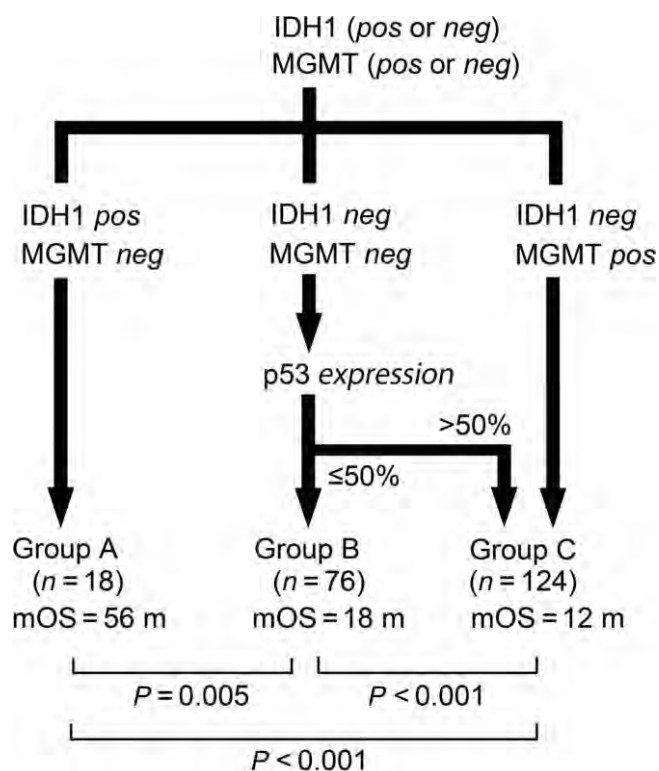


Fig. 3 Schematic representation of Groups A, B and C distinguishable on the basis of combinations of the isocitrate dehydrogenase 1 (IDH1), O⁶-methylguanine-DNA methyltransferase (MGMT) and p53 immunoprofiles. The median overall survival (mOSs) of the three groups differ significantly. Eight patients with IDH1-positive and MGMT-positive profiles were excluded. Note that for the patients with IDH1-negative and MGMT-negative profiles, the p53 profile (> or ≤50%) was a useful factor for prognostication.

GBM (4.43%).³¹ In grade II gliomas, it is still unclear whether *IDH1* mutations influence outcome.^{35–38} In the present study, IDH1 immunoprofiles showed no significant association with the outcome of patients with grade II gliomas (Tables 2 and 3). On the other hand, for patients who were diagnosed histopathologically as having grade III or IV glioma, IDH1 positivity was a factor significantly predictive of a favorable outcome (Tables 2 and 3).

At present, *MGMT* status is recognized to be a prognostic factor and a powerful predictor of the response to temozolomide in patients with GBM.¹⁵ Based on several clinical studies involving patients with GBM, it has been shown that *MGMT* promoter methylation assessed by methylation-specific PCR or pyrosequencing is a favorable prognostic factor.^{12,39,40} *MGMT* status can be regulated by several mechanisms, including histone modification^{41–43} and post-transcriptional regulation with miRNA,⁴⁴ and for this reason *MGMT* status is not always identical at the DNA, RNA and protein levels. For example, it has been shown that mRNA expression is transcriptionally regulated,

resulting in a low level in approximately 20% of patients, in whom the *MGMT* promoter is unmethylated.^{45,46} Moreover, it has been demonstrated that variation in *MGMT* promoter methylation can occur within the same tumor after treatment.⁴⁷ Furthermore, a previous study employing multivariate analysis has indicated that expression of *MGMT* protein, rather than *MGMT* status, was correlated with the survival of patients with GBM.⁴⁸ Thus, immunohistochemical evaluation of *MGMT* protein status in glioma tissue may provide useful prognostic information.

Recent molecular studies have provided more details of the complex mechanisms that determine *MGMT* methylation status. For example, it seems plausible that *IDH* mutations can lead to *MGMT* methylation, as gliomas with *IDH* mutation show a reduction of α -ketoglutarate and accumulation of 2-hydroxyglutarate, resulting in genome-wide histone and DNA methylation.⁴⁹ Moreover, *TP53* mutation may also influence *MGMT* methylation status, in association with TNF- α -induced NF- κ B activation and chronic inflammation, which can induce DNA methylation.^{50–52} Thus, *IDH1* and *TP53* mutations may alter *MGMT* methylation status.

There are some technical issues concerning *MGMT*-immunohistochemistry, including intra- and inter-observer variability in the assessment of immunoreactivity,^{8,12,53} the need for exclusion of non-neoplastic cells,¹³ variability among antigen retrieval methods, the antibodies employed, and the cutoff values adopted.⁵³ According to our criteria for judgment of *MGMT* positivity or negativity (Fig. 1D–F), we found that a *MGMT*-negative profile was associated with a favorable outcome for patients with malignant astrocytomas (Tables 2 and 3, and Fig. 2B). Consistent with this evidence, a recent study of both protein expression and DNA methylation found that patients with high protein expression had a poor outcome, even though the promoter was methylated,⁴¹ and that patients with low protein expression and a methylated promoter had a favorable outcome.^{54,55}

We therefore evaluated the association between CRT and *MGMT* profiles and survival in patients with malignant astrocytomas, and found that a *MGMT*-negative profile predicted a favorable outcome for patients who received CRT (Fig. 2L), suggesting that glioma cells with low *MGMT* expression may be much more sensitive to CRT. The proportions of patients with *MGMT*-negative profiles in the oligodendroglial (OA/OD and AOA/AOD) groups were high (Table 2). This seems to reflect the fact that *MGMT* promoter methylation is frequently evident in oligodendroglial tumors.⁵⁶

It has been recognized that the p53 pathway plays a role in the pathogenesis of gliomas. However, at present it remains controversial whether *TP53* mutation can be regarded as a true prognostic factor. Immunoreactivity of

p53 may be associated with *TP53* mutation, LOH of *TP53*, and aberrant expression of various p53-regulatory genes, including MDM2 and p14^{ARF}.^{1,3,57–59} In the present study, as the grade of malignancy increased, the proportion of patients with p53-positive profiles tended to increase; however, expression of p53 in patients with any tumor grade showed no significant association with outcome (Tables 2 and 3).

In the present study, we found that a combination of both IDH1 and MGMT profiles would be useful for prognostication (Fig. 2C). Therefore, after diagnosis of GBM and AA, on the basis of immunohistochemistry for both IDH1 and MGMT, it would be possible to estimate the mOS of the patients. Moreover, if patients were found to have a MGMT-negative profile, CRT could be considered. Consistent with this, a recent molecular study has revealed that the combination of *IDH1* mutation and *MGMT* methylation status outperforms information on either *IDH1* or *MGMT* alone for predicting the survival of patients with GBM: patients with IDH1 mutations/*MGMT* methylation survived longer, whereas those with no IDH1 mutations/no *MGMT* methylation showed shorter survival.⁵

Furthermore, we found that p53 overexpression in patients with IDH1-negative and MGMT-negative profiles could be a useful prognostic factor (Fig. 2I). Therefore, based on a combination of the IDH1, MGMT and p53 profiles, three groups were distinguishable, and their mOSs differed significantly (Figs 2J and 3). Clinicopathologically, these findings appear to have potential importance for predicting the outcome of patients with malignant astrocytomas.

In conclusion, the immunohistochemical profiles of IDH1, MGMT and p53 are of significant importance for prognostication in patients with malignant astrocytomas. A combination of IDH1 positivity and MGMT negativity may indicate a favorable prognosis, whereas a combination of IDH1 negativity and MGMT positivity may be unfavorable. For patients with IDH1 negativity and MGMT negativity, the p53 profile may have a crucial prognostic impact, overexpression conferring an unfavorable prognosis. If information on these profiles were immediately available following histopathological diagnosis, it would be useful for prompt and accurate decision-making with regard to treatment.

ACKNOWLEDGMENTS

We thank Professor Kouhei Akazawa, Department of Medical Informatics, University of Niigata, for statistical analysis. This work was supported by a Grant-in-Aid for Scientific Research (no. 25250008) from the Ministry of Education, Culture, Sports, Science, and Technology, Japan,

and a grant (24-7) for Nervous and Mental Disorders from the Ministry of Health, Labor and Welfare, Japan.

REFERENCES

1. Louis DN, Ohgaki H, Wiestler OD, Cavenee WK, eds. *WHO Classification of Tumours of the Central Nervous System*, 4th edn. Lyon: IARC, 2007.
2. Arita H, Narita Y, Fukushima S *et al.* Upregulating mutations in the *TERT* promoter commonly occur in adult malignant gliomas and are strongly associated with total 1p19q loss. *Acta Neuropathol* 2013; **126**: 267–276.
3. Cancer Genome Atlas Research Network. Comprehensive genomic characterization defines human glioblastoma genes and core pathways. *Nature* 2008; **455**: 1061–1068.
4. Weller M, Stupp R, Hegi ME *et al.* Personalized care in neuro-oncology coming of age: why we need MGMT and 1p/19q testing for malignant glioma patients in clinical practice. *Neuro Oncol* 2012; **14** (Suppl 4): 100–108.
5. Molenaar RJ, Verbaan D, Lamba S *et al.* The combination of IDH1 mutations and MGMT methylation status predicts survival in glioblastoma better than either IDH1 or MGMT alone. *Neuro Oncol* 2014; **16**: 1263–1273.
6. Agarwal S, Sharma MC, Jha P *et al.* Comparative study of IDH1 mutations in gliomas by immunohistochemistry and DNA sequencing. *Neuro Oncol* 2013; **15**: 718–726.
7. Capper D, Weissert S, Balss J *et al.* Characterization of R132H mutation-specific IDH1 antibody binding in brain tumors. *Brain Pathol* 2010; **20**: 245–254.
8. Capper D, Mittelbronn M, Meyermann R, Schittenhelm J. Pitfalls in the assessment of MGMT expression and its correlation with survival in diffuse astrocytomas: proposal of feasible immunohistochemical approach. *Acta Neuropathol* 2008; **115**: 249–259.
9. Pardo FS, Hsu DW, Zeheb R, Efrid JT, Okunieff PG, Malkin DM. Mutant, wild type, or overall p53 expression: freedom from clinical progression in tumours of astrocytic lineage. *Br J Cancer* 2004; **91**: 1678–1686.
10. Ogura R, Aoki H, Natsumeda M *et al.* Epstein-Barr virus-associated primary central nervous system cytotoxic T-cell lymphoma. *Neuropathology* 2013; **33**: 436–441.
11. Nobusawa S, Lachuer J, Wierinckx A *et al.* Intratumoral patterns of genomic imbalance in glioblastomas. *Brain Pathol* 2010; **20**: 936–944.
12. Quillien V, Lavenu A, Karayan-Tapon L *et al.* Comparative assessment of 5 methods (methylation-specific polymerase chain reaction, MethyLight,

- pyrosequencing, methylation-sensitive high-resolution melting, and immunohistochemistry) to analyze O⁶-methylguanine-DNA-methyltransferase in a series of 100 glioblastoma patients. *Cancer* 2012; **118**: 4201–4211.
13. Sasai K, Nodagashira M, Nishihara H *et al.* Careful exclusion of non-neoplastic brain components is required for an appropriate evaluation of O⁶-methylguanine-DNA methyltransferase status in glioma: relationship between immunohistochemistry and methylation analysis. *Am J Surg Pathol* 2008; **32**: 1220–1227.
 14. Nakasu S, Fukami T, Baba K, Matsuda M. Immunohistochemical study for O⁶-methylguanine-DNA methyltransferase in the non-neoplastic and neoplastic components of gliomas. *J Neurooncol* 2004; **70**: 333–340.
 15. Hegi ME, Diserens AC, Gorlia T *et al.* MGMT gene silencing and benefit from temozolomide in glioblastoma. *N Engl J Med* 2005; **352**: 997–1003.
 16. Rodriguez FJ, Scheithauer BW, Burger PC, Jenkins S, Giannini C. Anaplasia in pilocytic astrocytoma predicts aggressive behavior. *Am J Surg Pathol* 2010; **34**: 147–160.
 17. Takami H, Yoshida A, Fukushima S *et al.* Revisiting TP53 mutations and immunohistochemistry – a comparative study in 157 diffuse gliomas. *Brain Pathol* 2014. doi: 10.1111/bpa.12173 (Epub ahead of print).
 18. van den Bent MJ, Dubbink HJ, Marie Y *et al.* IDH1 and IDH2 mutations are prognostic but not predictive for outcome in anaplastic oligodendroglial tumors: a report of the European Organization for Research and Treatment of Cancer Brain Tumor Group. *Clin Cancer Res* 2010; **16**: 1597–1604.
 19. Weller M, Felsberg J, Hartmann C *et al.* Molecular predictors of progression-free and overall survival in patients with newly diagnosed glioblastoma: a prospective translational study of the German Glioma Network. *J Clin Oncol* 2009; **27**: 5743–5750.
 20. Yan H, Parsons DW, Jin G *et al.* IDH1 and IDH2 mutations in gliomas. *N Engl J Med* 2009; **360**: 765–773.
 21. Turcan S, Rohle D, Goenka A *et al.* IDH1 mutation is sufficient to establish the glioma hypermethylator phenotype. *Nature* 2012; **483**: 479–483.
 22. Arita H, Nairta Y, Matsushita Y *et al.* Development of a robust and sensitive pyrosequencing assay for the detection of IDH1/2 mutations in gliomas. *Brain Tumor Pathol* 2015; **32**: 22–30 (in press).
 23. Felsberg J, Wolter M, Seul H *et al.* Rapid and sensitive assessment of the IDH1 and IDH2 mutation status in cerebral gliomas based on DNA pyrosequencing. *Acta Neuropathol* 2010; **119**: 501–507.
 24. Chen WW, Balaj L, Liao LM *et al.* BEAMing and Droplet Digital PCR Analysis of Mutant IDH1 mRNA in Glioma Patient Serum and Cerebrospinal Fluid Extracellular Vesicles. *Mol Ther Nucleic Acids* 2013; **2**: e109. doi: 10.1038/mtna.2013.28.
 25. Loussouarn D, Le Loupp AG, Frenel JS *et al.* Comparison of immunohistochemistry, DNA sequencing and allele-specific PCR for the detection of IDH1 mutations in gliomas. *Int J Oncol* 2012; **40**: 2058–2062.
 26. Bleeker FE, Lamba S, Leenstra S *et al.* IDH1 mutations at residue p.R132(IDH1(R132)) occur frequently in high-grade gliomas but not in other solid tumors. *Hum Mutat* 2009; **30**: 7–11.
 27. Horbinski C, Kofler J, Kelly LM *et al.* Diagnostic use of IDH1/2 mutation analysis in routine clinical testing of formalin-fixed, paraffin-embedded glioma tissues. *J Neuropathol Exp Neurol* 2009; **268**: 1597–1604.
 28. Ichimura K, Pearson DM, Kocalkowski S *et al.* IDH1 mutations are present in the majority of common adult gliomas but rare in primary glioblastomas. *Neuro Oncol* 2009; **11**: 341–347.
 29. Parsons DW, Jones S, Zhang X *et al.* An integrated genomic analysis of human glioblastoma multiforme. *Science* 2008; **321**: 1807–1812.
 30. Sonoda Y, Kumabe T, Nakamura T *et al.* Analysis of IDH1 and IDH2 mutations in Japanese glioma patients. *Cancer Sci* 2009; **100**: 1996–1998.
 31. Zhang C, Moore LM, Yung WK, Zhang W. IDH1/2 mutations target a key hallmark of cancer by deregulating cellular metabolism in glioma. *Neuro Oncol* 2013; **15**: 1114–1126.
 32. Figarella-Branger D, Maues de Paula A, Colin C, Bouvier C. Histomolecular classification of adult diffuse gliomas: the diagnostic value of immunohistochemical markers. *Rev Neurol (Paris)* 2011; **167**: 683–690.
 33. Figarella-Branger D, Bouvier C, de Paula AM *et al.* Molecular genetics of adult grade II gliomas: towards a comprehensive tumor classification system. *J Neurooncol* 2012; **110**: 205–213.
 34. Gupta R, Webb-Myers R, Flanagan S, Buckland ME. Isocitrate dehydrogenase mutations in diffuse gliomas: clinical and aetiological implications. *J Clin Pathol* 2011; **64**: 835–844.
 35. Dubbink HJ, Taal W, van Marion R *et al.* IDH1 mutations in low-grade astrocytomas predict survival but not response to temozolomide. *Neurology* 2009; **73**: 1792–1795.
 36. Houillier C, Wang X, Kaloshi G *et al.* IDH1 or IDH2 mutations predict longer survival and response to temozolomide in low-grade gliomas. *Neurology* 2010; **75**: 1560–1566.

37. Mellai M, Piazzini A, Caldera V *et al.* IDH1 and IDH2 mutations, immunohistochemistry and associations in a series of brain tumors. *J Neurooncol* 2011; **105**: 345–357.
38. Sanson M, Marie Y, Paris S *et al.* Isocitrate dehydrogenase 1 codon 132 mutation is an important prognostic biomarker in gliomas. *J Clin Oncol* 2009; **27**: 4150–4154.
39. Weller M, Stupp R, Reifenberger G *et al.* MGMT promoter methylation in malignant gliomas: ready for personalized medicine? *Nature Rev Neurol* 2010; **6**: 39–51.
40. Wick W, Hartmann C, Engel C *et al.* NOA-04 randomized phase III trial of sequential radiochemotherapy of anaplastic glioma with procarbazine, lomustine, and vincristine or temozolomide. *J Clin Oncol* 2009; **27**: 5874–5880.
41. Kitange GJ, Mladek AC, Carlson BL *et al.* Inhibition of histone deacetylation potentiates the evolution of acquired temozolomide resistance linked to MGMT upregulation in glioblastoma xenografts. *Clin Cancer Res* 2012; **18**: 4070–4079.
42. Nakagawachi T, Soejima H, Urano T *et al.* Silencing effect of CpG island hypermethylation and histone modifications on O⁶-methylguanine-DNA methyltransferase (MGMT) gene expression in human cancer. *Oncogene* 2003; **22**: 8835–8844.
43. Zhao W, Soejima H, Higashimoto K *et al.* The essential role of histone H3 Lys9 di-methylation and MeCP2 binding in MGMT silencing with poor DNA methylation of the promoter CpG island. *J Biochem* 2005; **137**: 431–440.
44. Kreth S, Limbeck E, Hinske LC *et al.* In human glioblastomas transcript elongation by alternative polyadenylation and miRNA targeting is a potent mechanism of MGMT silencing. *Acta Neuropathol* 2013; **125**: 671–681.
45. Everhard S, Tost J, El Abdalaoui H *et al.* Identification of regions correlating MGMT promoter methylation and gene expression in glioblastomas. *Neuro Oncol* 2009; **11**: 348–356.
46. Ramakrishnan V, Kushwaha D, Koay DC *et al.* Post-transcriptional regulation of O⁶-methylguanine-DNA methyltransferase MGMT in glioblastomas. *Cancer Biomark* 2011; **10**: 185–193.
47. Parkinson JF, Wheeler HR, Clarkson A *et al.* Variation of O(6)-methylguanine-DNA methyltransferase (MGMT) promoter methylation in serial samples in glioblastoma. *J Neurooncol* 2008; **87**: 71–78.
48. Spiegl-Kreinecker S, Pirker C, Filipits M *et al.* O⁶-Methylguanine DNA methyltransferase protein expression in tumor cells predicts outcome of temozolomide therapy in glioblastoma patients. *Neuro Oncol* 2010; **12**: 28–36.
49. Xu W, Yang H, Liu Y *et al.* Oncometabolite 2-hydroxyglutarate is a competitive inhibitor of α -ketoglutarate-dependent dioxygenases. *Cancer Cell* 2011; **19**: 17–30.
50. Cooks T, Pateras IS, Tarcic O *et al.* Mutant p53 prolongs NF- κ B activation and promotes chronic inflammation and inflammation associated colorectal cancer. *Cancer Cell* 2013; **23**: 634–646.
51. Issa JP, Ahuja N, Toyota M, Bronner MP, Brentnall TA. Accelerated age-related CpG island methylation in ulcerative colitis. *Cancer Res* 2001; **61**: 3573–3577.
52. Hsieh CJ, Klump B, Holzmann K, Borchard F, Gregor M, Porschen R. Hypermethylation of the p16INK4a promoter in colectomy specimens of patients with long-standing and extensive ulcerative colitis. *Cancer Res* 1998; **58**: 3942–3945.
53. Preusser M, Charles Janzer R, Felsberg J, Reifenberger G, Hamou MF, Diserens AC. Anti-O⁶-methylguanine-methyltransferase (MGMT) immunohistochemistry in glioblastoma multiforme: observer variability and lack of association with patient survival impede its use as clinical biomarker. *Brain Pathol* 2008; **18**: 520–532.
54. Cao VT, Jung TY, Jung S *et al.* The correlation and prognostic significance of MGMT promoter methylation and MGMT protein in glioblastomas. *Neurosurgery* 2009; **65**: 866–875.
55. Lalezari S, Chou AP, Tran A *et al.* Combined analysis of O⁶-methylguanine-DNA methyltransferase protein expression and promoter methylation provides optimized prognostication of glioblastoma outcome. *Neuro Oncol* 2013; **15**: 370–381.
56. Kuo LT, Tsai SY, Chang CC *et al.* Genetic and epigenetic alterations in primary-progressive paired oligodendroglial tumors. *PLoS ONE* 2009; **24**: e67139.
57. Momota H, Narita Y, Matsushita Y, Miyakita Y, Shibui S. p53 abnormality and tumor invasion in patients with malignant astrocytoma. *Brain Tumor Pathol* 2010; **27**: 95–101.
58. Peraud A, Kreth FW, Wiestler OD, Kleihues P, Reulen HJ. Prognostic impact of TP53 mutations and p53 protein overexpression in supratentorial WHO grade II astrocytomas and oligoastrocytomas. *Clin Cancer Res* 2002; **8**: 1117–1124.
59. Reifenberger J, Ring GU, Gies U *et al.* Analysis of p53 mutation and epidermal growth factor receptor amplification in recurrent gliomas with malignant progression. *J Neuropathol Exp Neurol* 1996; **55**: 822–831.

Original Article

Characteristic expression of p57/Kip2 in balloon cells in focal cortical dysplasia

Tadashi Kimura,^{1,7} Hiroki Kitaura,¹ Hiroshi Masuda,² Shigeki Kameyama,² Yuko Saito,³ Kenji Sugai,³ Taisuke Otsuki,³ Atsuko Nakazawa,⁴ Nobuhito Morota,⁴ Takamichi Yamamoto,⁵ Kouji Iida,⁶ Masanori Nakagawa,⁷ Toshiki Mizuno,⁷ Hitoshi Takahashi¹ and Akiyoshi Kakita¹

¹Department of Pathology, Brain Research Institute, University of Niigata, ²Department of Functional Neurosurgery, Epilepsy Center, Nishi-Niigata Chuo National Hospital, Niigata, ³National Center of Neurology and Psychiatry, ⁴National Medical Center for Children and Mothers, National Center for Child Health and Development, Tokyo, ⁵Comprehensive Epilepsy Center, Seirei Hamamatsu General Hospital, Hamamatsu, ⁶Department of Neurosurgery, University of Hiroshima, Hiroshima and ⁷Department of Neurology, Graduate School of Medical Science, Kyoto Prefectural University of Medicine, Kyoto, Japan

Balloon cells are a pathognomonic cellular feature of various cortical malformations, including focal cortical dysplasia type IIb (FCD IIb), cortical tubers of tuberous sclerosis (TSC) and hemimegalencephaly (HME). In the present study, we investigated the immunohistochemical expression of p57/Kip2, a member of the Cip/Kip family of cyclin-dependent kinase inhibitory proteins, in balloon cells in surgical specimens taken from 26, 17 and six patients with FCD IIb, TSC and HME, respectively. Characteristic dot-like reactivity with a faint, intense, reticular and process-like pattern was confined to the proximal portion of the cytoplasmic processes of the cells. Immunoelectron microscopy revealed the p57/Kip2 reactivity on intermediate filaments in the proximal portion of the processes. The immunohistochemical profile appeared similar to that of CD34; however, a double immunofluorescence study demonstrated that no cells showed reactivity for both p57/Kip2 and CD34. The frequencies of the p57/Kip2-positive cells in FCD IIb and HME were significantly higher than those in TSC, suggesting that the balloon cells may be heterogeneous. These findings suggest some functional significance of the protein

on the cytoplasmic processes of balloon cells and appear consistent with the notion that the cells are abnormally differentiated progenitor cells.

Key words: balloon cell, focal cortical dysplasia, hemimegalencephaly, p57/Kip2, tuberous sclerosis.

INTRODUCTION

Balloon cells are a pathognomonic cellular feature of various cortical malformations, including focal cortical dysplasia type IIb (FCD IIb),¹ cortical tubers of tuberous sclerosis (TSC)² and hemimegalencephaly (HME).³ Patients with these malformations often suffer intractable epilepsy requiring surgical resection of the lesions. The origin and identity of these cells are uncertain. However, a large number of studies have indicated that subsets of balloon cells express various proteins characteristic of glial, neuronal and stem cell/progenitor cells, including GFAP, vimentin, nestin,^{4,5} neurofilament, neuronal specific nuclear protein (NeuN), microtubule associated protein 2 (MAP2),⁶ class III beta-tubulin (TuJ1),⁷ glutamate receptor,⁸ CD133, CD34,⁹ and minichromosome maintenance complex component 2 (Mcm2).¹⁰ With regard to the origin of balloon cells, an *in vitro* study of isolated balloon cells taken from patients with FCD IIb and TSC has indicated that such cells are abnormal stem cells that contribute to the pathogenesis of these disorders.¹¹ Furthermore, an immunohistochemical study using a panel of several antibodies specific for certain progenitor cell types, including brain lipid-binding protein (BLBP), Otx1, GFAP- δ and Pax6, has indicated that balloon cells are derived from radial glial progenitor cells.⁵ Another morphological and electrophysiological study of FCD IIb

Correspondence: Akiyoshi Kakita, MD, PhD, Department of Pathology, Brain Research Institute, University of Niigata, 1-757 Asahimachi, Chuo-ku, Niigata 951-8585, Japan. Email: kakita@bri.niigata-u.ac.jp

Sources of financial support: This work was supported by a Grant-in-Aid for Scientific Research (no. 25250008) and Exploratory Research (no. 25640027) from the Ministry of Education, Culture, Sports, Science, and Technology, Japan, and a grant (24-7) for Nervous and Mental Disorders and a Health Labour Sciences Research Grant (H26-052) from the Ministry of Health, Labor and Welfare, Japan.

Received 22 December 2014; revised 18 January 2015 and accepted 19 January 2015; published online 7 May 2015.

has also proposed that balloon cells represent radial glial cells that have failed to undergo postnatal degeneration.¹² Moreover, an immunohistochemical study examining the expression of cell cycle proteins, including non-phosphorylated retinoblastoma protein, cdk4 and p53, in balloon cells in FCD IIb has hypothesized that these cells are the remnants of early cortical cells, which have failed to undergo differentiation or elimination during development and have undergone cell cycle arrest.¹³ Thus, dysregulation of cell cycle proteins may be a pivotal mechanism underlying the dysplastic features of balloon cells, including abnormal cell fate determination, cell immaturity, and subsequent abnormal morphology.

In the present study, we examined the immunohistochemical expression of p57/Kip2 and p27/Kip1, members of the Cip/Kip family of cyclin-dependent kinase (CDK) inhibitory proteins, in balloon cells in surgical specimens of FCD IIb, TSC and HME taken from patients with epilepsy. Recent biological studies have provided evidence that these proteins play important roles in cell cycle regulation, proliferation, differentiation and migration of various types of cancer cells¹⁴ and of cortical precursors in the developing brain.¹⁵ We found that various proportions of balloon cells in the malformed brain tissue showed reactivity for p57/Kip2, but not for p27/Kip1.

MATERIALS AND METHODS

Subjects

The study was approved by the various institutional ethics committees, and all patients provided consent to use their resected tissues for research purposes. We examined surgical specimens taken from 26 patients with FCD IIb (14 male, 12 female: 15 right, 11 left: age at resection mean \pm SD = 16.4 \pm 12.9 years), 17 patients with TSC (nine male, eight female: seven right, 10 left: age 6.29 \pm 7.6 years) and six patients with HME (three male, three female: four right, two left: age 1.00 \pm 1.2 years), who had undergone resection of neocortical tissue because of intractable epilepsy (Table 1). Five of the patients with TSC were confirmed as harboring mutations in the *TSC1* or *TSC2* gene, as previously reported¹⁶ (Table 1). The surgical specimens were cut into slices and fixed with phosphate-buffered 20% formalin and embedded in paraffin wax. Serial 4- μ m-thick sections were then cut, and subjected to HE and KB staining. Diagnoses of FCD IIb,¹ cortical tubers of TSC² and HME,³ were made on the basis of histopathological features, clinical information, images and prognosis.

The term “balloon cells” is used for the abnormal cells observed in FCD IIb and HME, whereas “giant cells” is the term sometimes applied for those in cortical tubers. These

cells are morphologically indistinguishable. For clarity, the term “balloon cells” is used here for all cell populations.^{2,11}

Immunohistochemistry, cell counting and statistical analysis

The paraffin-embedded sections were processed by the avidin-biotin-peroxidase complex (ABC) method with a Vectastain ABC kit (Vector, Burlingame, CA, USA). As the primary antibodies, we used a rabbit polyclonal antibody against p57/Kip2 (Abcam, Cambridge, MA, USA; 1:200), and mouse monoclonal antibodies against p27/Kip1 (clone 57, BD Biosciences Pharmingen, Franklin Lakes, NJ, USA; 1:200) and CD34 (clone Qbend 10, Immunotech, Monrovia, CA, USA; 1:200). Pretreatment was performed by heat/autoclaving for 10 min at 121°C in 10 mmol/L sodium citrate buffer.

For cell counting, a single p57/Kip2-immunostained section from each case was used. The sections were observed under a light microscope (BX53, Olympus, Tokyo, Japan) and images were captured by a digital camera (DP73, Olympus). Balloon cells were identified as bizarre cells with abundant cytoplasm and eccentric nuclei (Fig. 1A). The numbers of the p57/Kip2-positive and -negative balloon cells in the images were counted manually using the “Count tool” of the Adobe Photoshop software package.

Statistical significance of differences in the frequency of p57/Kip2-positive balloon cells in any of the FCD IIb, TSC or HME cases was analyzed with nonparametric Kruskal-Wallis test and Mann-Whitney *U*-test at a significance level of $P < 0.01$. The results are shown as mean \pm SD. Data analysis was carried out using the IBM SPSS statistics version 20 software package (IBM SPSS Inc., Chicago, IL, USA).

Double immunofluorescence

A double-labeling immunofluorescence study was performed on several sections from eight patients with FCD IIb using the rabbit polyclonal anti-p57/Kip2 antibody (1:100) and the mouse monoclonal anti-CD34 antibody (1:100). The secondary antibodies used were Alexa Fluor 555 goat anti-mouse IgG and Alexa Fluor 488 goat anti-rabbit IgG (both Molecular Probes, Eugene, OR, USA; 1:1000). Slides were treated with Autofluorescence Eliminator Reagent (Millipore, Bellerica, MA, USA), and then mounted with glass coverslips using VECTAshield mounting medium with 4,6-diamidino-2-phenylindole (DAPI) nuclear stain (Vector Laboratories, Burlingame, CA, USA). A laser-scanning confocal microscope (Carl Zeiss LSM-700, Jena, Germany) was used to visualize immunoreactivity.

Table 1 Clinical and pathological profiles of the patients with FCD, TSC and HME

Case ID	Sex	Age (y)	Onset (y)	Location	Side	Pathology	Number of balloon cells	Number of p57/Kip2 positive cells	Percentages
1	F	2	1	T	R	FCD IIb	95	67	70.53
2	F	2	–	P	L	FCD IIb	69	50	72.46
3	M	3	0	F	L	FCD IIb	78	39	50.00
4	M	7	6	F	R	FCD IIb	51	50	98.04
5	M	8	5	F	R	FCD IIb	120	97	80.83
6	M	8	7	F	L	FCD IIb	65	42	64.62
7	F	8	4	F	L	FCD IIb	163	80	49.08
8	F	9	5	P	R	FCD IIb	13	11	84.62
9	M	10	1	F	R	FCD IIb	19	12	63.16
10	F	10	3	P	R	FCD IIb	85	64	75.29
11	F	10	0	F	L	FCD IIb	154	102	66.23
12	M	11	9	O	R	FCD IIb	21	16	76.19
13	M	11	5	P	L	FCD IIb	73	62	84.93
14	M	12	6	F	R	FCD IIb	33	5	15.15
15	M	12	5	F	L	FCD IIb	63	31	49.21
16	F	12	0	T	R	FCD IIb	157	73	46.50
17	F	17	7	F	L	FCD IIb	66	50	75.76
18	F	18	5	P	R	FCD IIb	81	66	81.48
19	M	20	10	O	L	FCD IIb	50	26	52.00
20	F	20	4	F	R	FCD IIb	58	39	67.24
21	F	23	7	P	R	FCD IIb	84	70	83.33
22	M	26	6	P	R	FCD IIb	109	94	86.24
23	M	34	10	F	R	FCD IIb	162	95	58.64
24	M	38	1	M	L	FCD IIb	42	36	85.71
25	F	41	5	P	R	FCD IIb	78	40	51.28
26	M	54	3	F	L	FCD IIb	31	21	67.74
27	F	0	0	F	L	TSC	340	1	0.29
28	F	0	0	F	R	TSC	140	0	0.00
29	M	1	–	F	R	TSC	70	18	25.71
30	M	2	0	F	L	TSC	71	2	2.82
31	M	2	0	F	R	TSC	18	6	33.33
32**	F	2	0	T	L	TSC	81	14	17.28
33	F	2	0	T	L	TSC	117	1	0.85
34	M	3	1	F	R	TSC	37	22	59.46
35	M	3	2	F	L	TSC	52	4	7.69
36	F	3	0	T	L	TSC	43	0	0.00
37	F	4	2	P	L	TSC	37	1	2.70
38	F	5	0	P	L	TSC	14	0	0.00
39*	F	9	0	F	L	TSC	10	1	10.00
40**	M	11	0	F	R	TSC	9	1	11.11
41	M	11	–	F	L	TSC	24	5	20.83
42*	M	24	10	F	R	TSC	18	15	83.33
43**	M	25	6	F	R	TSC	30	4	13.33
44	M	0	0	P	L	HME	23	4	17.39
45	M	0	0	F	L	HME	94	82	87.23
46	F	0	0	F	R	HME	58	30	51.72
47	M	1	0	F	R	HME	140	7	5.00
48	F	2	0	F	R	HME	31	18	58.06
49	M	3	0	T	R	HME	150	91	60.67

F, female; M, male; F, frontal; T, temporal; P, parietal; O, occipital; R, right; L, left; FCD, focal cortical dysplasia; TSC, tuberous sclerosis; HME, hemimegalencephaly; y, year(s). Mutations in * *TSC1* and ** *TSC2* genes.

Immunoelectron microscopy

The ultrastructural localization of p57/Kip2 was examined using surgical specimens taken from five patients with FCD IIb, employing the post-embedding method previously described.¹⁷ Small tissue blocks were prepared from

formalin-fixed tissue, and washed with PBS. The tissue blocks were then washed with gradually increasing concentrations of dimethylformamide, and embedded in LR White resin (London Resin Company, Berkshire, UK). Ultrathin sections were cut, incubated with the anti-p57/Kip2 antibody (1:25) for 36 h, and reacted with 15-nm gold

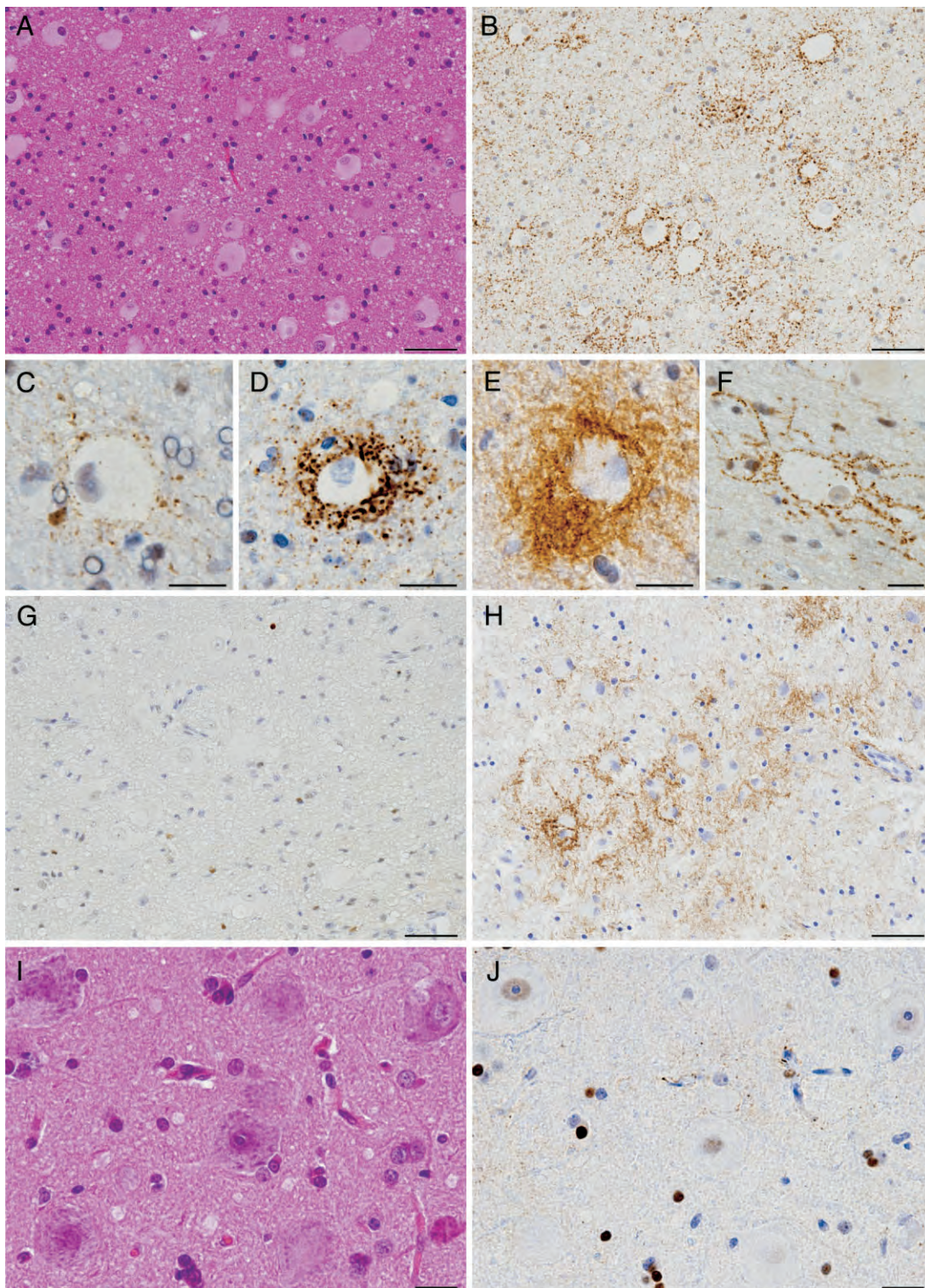


Fig. 1 p57/Kip2 immunohistochemical features. Balloon cells in focal cortical dysplasia (FCD) type IIb (A-F), tuberous sclerosis (TSC) (G), and hemimegalencephaly (HME) (H), and dysmorphic neurons in FCD type IIb (I, J). (A, B) Low-power magnification views of white matter of a sample demonstrating several balloon cells with abundant cytoplasm and eccentric nuclei (A), and dot-like immunoreactivity around the cytoplasm of the balloon cells (B). (C-F) Higher-magnification views of balloon cells showing faint (C), intense (D), reticular (E) and process-like (F) fashion. (G) No balloon cells with immunoreactivity are seen. (H) Many balloon cells showing similar immunoreactivity. (J) No dysmorphic neurons with immunoreactivity are seen. (A, I) Hematoxylin and eosin stain. (B-H, J) Immunostained and then counterstained with hematoxylin. Images of A and B, and those of I and J are taken from serial sections. Bars = 50 μ m for A, B, G and H, and 20 μ m for C-F, I and J.

colloidal particle-conjugated anti-rabbit IgG (British BioCell, Cardiff, UK, 1:30). The sections were then stained with lead citrate, and examined with a Hitachi H-7700 digital electron microscope at 75 kV.

RESULTS

p57/Kip2 immunohistochemistry

In FCD IIB, balloon cells showed characteristic p57/Kip2 immunoreactivity (Fig. 1B) in the form of dot-like profiles around the abundant cytoplasm, showing faint (Fig. 1C), intense (Fig. 1D), reticular (Fig. 1E) and process-like (Fig. 1F) patterns. These profiles appeared to be confined to the cytoplasmic membrane and proximal processes of the cells. No apparent immunoreactivity was evident within the perikaryon proper. Balloon cells with faint or intense p57/Kip2 immunoreactivity were found predominantly within the white matter, whereas those with the reticular and process-like patterns were scattered in deeper layers of the cortex and at its boundary with the white matter. Interestingly, a large proportion of balloon cells observed in TSC were p57/Kip2-negative (Fig. 1G). On the other hand, balloon cells in HME (Fig. 1H) showed immunoreactivity similar to that in FCD IIB.

The median frequencies of the p57/Kip2-positive balloon cells were 69.1% in FCD IIB (range, 51.8 to 81.9), 54.9% in HME (range, 17.4 to 60.7), and 10.0% in TSC (range, 0.9 to 20.8) (Table 1). The frequencies in FCD IIB and HME were higher than those in TSC (χ^2 (2, $n = 49$) = 22.9, $P < 0.001$). A post-hoc test revealed a significant difference between FCD IIB and TSC ($P < 0.001$), but not between HME and TSC.

We found no morphological differences between balloon cells with p57/Kip2 immunoreactivity and those without the immunoreactivity. No dysmorphic neurons (Fig. 1I) or other neurons with normal morphology showed reactivity for p57/Kip2 (Fig. 1J).

With regard to p27/Kip1, no labeling of balloon cells or dysmorphic neurons was evident in FCD IIB, TSC or HME (data not shown).

Double immunofluorescence

As the expression pattern of p57/Kip2 in balloon cells (Fig. 1B) appeared similar to that of CD34,⁹ we performed double immunofluorescence for detection of both p57/Kip2 and CD34. Surprisingly, we encountered no balloon cells that were immunoreactive with both of the antibodies used (Fig. 2).

Electron microscopy

Ultrastructurally, the balloon cells exhibited abundant cytoplasm containing numerous intermediate filaments,

and short cytoplasmic processes with abundant filaments (Fig. 3A, C), as previously reported.^{18,19} Immunogold labeling for p57/Kip2 was observed mainly on the filaments at the peripheral cytoplasm and proximal portion of the processes (Fig. 3B, D, E).

DISCUSSION

In the present study, for the first time, we have demonstrated the expression of p57/Kip2 in balloon cells (Fig. 1). The characteristic immunohistochemical features (Figs 1,3) suggest some significant role of the protein in the processes. Furthermore, we have shown that in comparison with balloon cells in FCD IIB and HME, those in TSC express p57/Kip2 much more rarely (Table 1), indicating that the roles of the protein in balloon cells may differ somewhat between FCD IIB/HME and TSC.

The CDK inhibitors of the Cip/Kip family, including p57/Kip2 and p27/Kip1, are known to regulate the cell cycle. Recent understanding of the roles of the family members in development of the CNS has been expanding, and it is now known to be involved in multiple aspects of neurogenesis through cell cycle arrest, specific cell-type differentiation and neuronal migration.^{15,20,21} Recently, it has been revealed that the members of this family differentially regulate neuroglial fate determination depending on environmental signals and developmental stage.²² Balloon cells are considered to be the consequence of aberrant differentiation of radial glial cells, a type of progenitor cell, to neurons and glia.⁵ Therefore, expression of p57/Kip2 in balloon cells may be associated with abnormal differentiation of the progenitor cells. It seems unlikely that the p57/Kip2 profiles observed in the present study reflected aberrant neurogenesis or neuronal migration, because neurons with normal or dysplastic morphologies were distributed irregularly within the cortex and white matter of FCD IIB/TSC/HME, but they showed no p57/Kip2 immunoreactivity.

It has been hypothesized that balloon cells may be arrested in cell cycle G1, based on the findings that they frequently express G1 markers in their nuclei.¹³ Concerning the cell cycle, a biological study demonstrated that p57/Kip2 was strongly expressed in association with the late G1 phase of developing cells of the CNS.²⁰ Therefore, the p57/Kip2 selected expression in the balloon cells in the present study appears compatible with the notion that they are arrested in G1. However, we could not consider close association between the p57/Kip2 expression and the cell cycle of the balloon cells, because G1 associated proteins usually localize within the nucleus, but p57/Kip2 was observed at the cytoplasmic processes, rather than the nucleus, of the balloon cells.

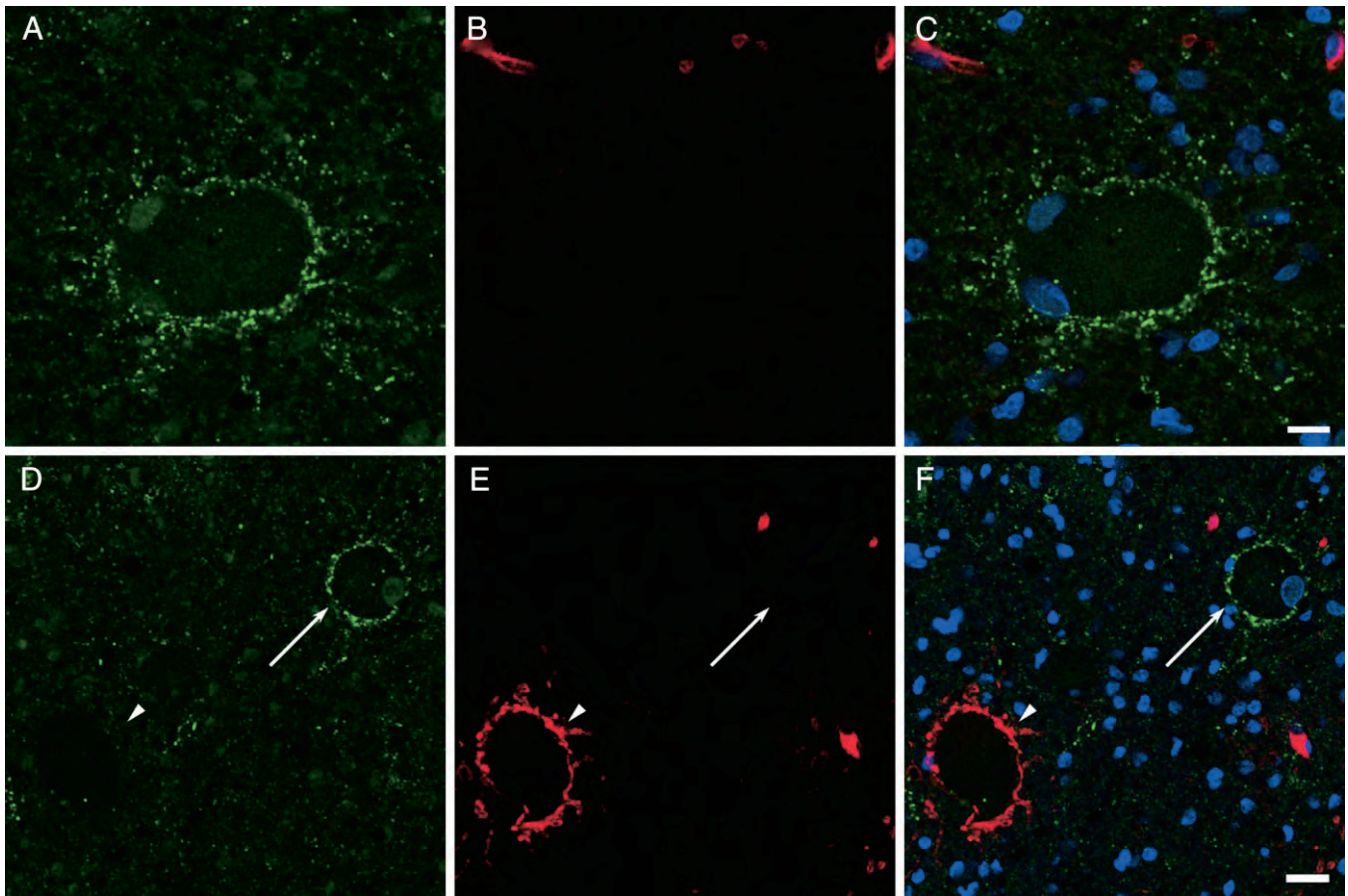


Fig. 2 Double immunofluorescence. Immunofluorescence with the p57/Kip2 (green, A, D) and CD34 (red, B, E) signals to demonstrate the spatial relationship of the two antigens. (C, F) Merged image of both signals. Nuclei are labeled with 4,6-diamidino-2-phenylindole (DAPI) (blue). High-power views demonstrating a single balloon cell with two nuclei (A-C) and lower-power views showing two cells (arrow and arrowhead) (D-F) in FCD type IIb. Note the cells show either signal. No co-localized signals are observed. Bars = 10 μ m for A-C, and 20 μ m for D-F.

TSC is an autosomal-dominant disease resulting from mutations of either *TSC1* or *TSC2*, encoding hamartin and tuberin, respectively. The TSC gene products form a functional heterodimer, which negatively regulates the activities of mammalian target of rapamycin (mTOR),²³ a serine/threonine kinase known to be a major effector of cell growth. In the CNS, activation of mTOR signaling may cause abnormal development of neurons and glia.²⁴ On the other hand, recent genetic studies have revealed somatic mutations in the *PIK3CA*, *AKT3* and *MTOR* genes in brain tissue of patients with HME, indicating aberrant activation of mTOR signaling.^{25,26} The molecular genetic mechanisms underlying FCD IIb have remained uncertain. FCD IIb, TSC and HME often share a number of histopathological features, including disruption of cortical cytoarchitecture, dysmorphic neurons and balloon cells. On the other hand, based on our experience of routine histopathological diagnoses of these developmental disorders, we have formed an impression that calcification and astrocytosis are much

more remarkable in TSC than in FCD IIb and HME. Moreover, the frequency of dysmorphic neurons appears to be much higher in HME than in FCD IIb and TSC. In a subset of patients with HME, balloon cells were not observed. Furthermore, a previous biochemical analysis demonstrated somewhat differential Pi3K-pathway activation in FCD IIb and TSC.²⁷ Another electrophysiological study demonstrated that FCD IIb and TSC display differences in the topography of abnormal cells, excitatory and inhibitory synaptic network properties, and GABA(A) receptor sensitivity.²⁸ Accordingly, certain differences in the pathomechanisms of these disorders may be associated with differences in the histological picture and expression of p57/Kip2 in balloon cells (Table 1). In the present study, we found no clear association between genetic profiles and the frequencies of p57/Kip2-positive balloon cells in patients with TSC. For example, the frequency in two patients with *TSC1* mutations (cases #39 and #42 in Table 1) were considerably differed.

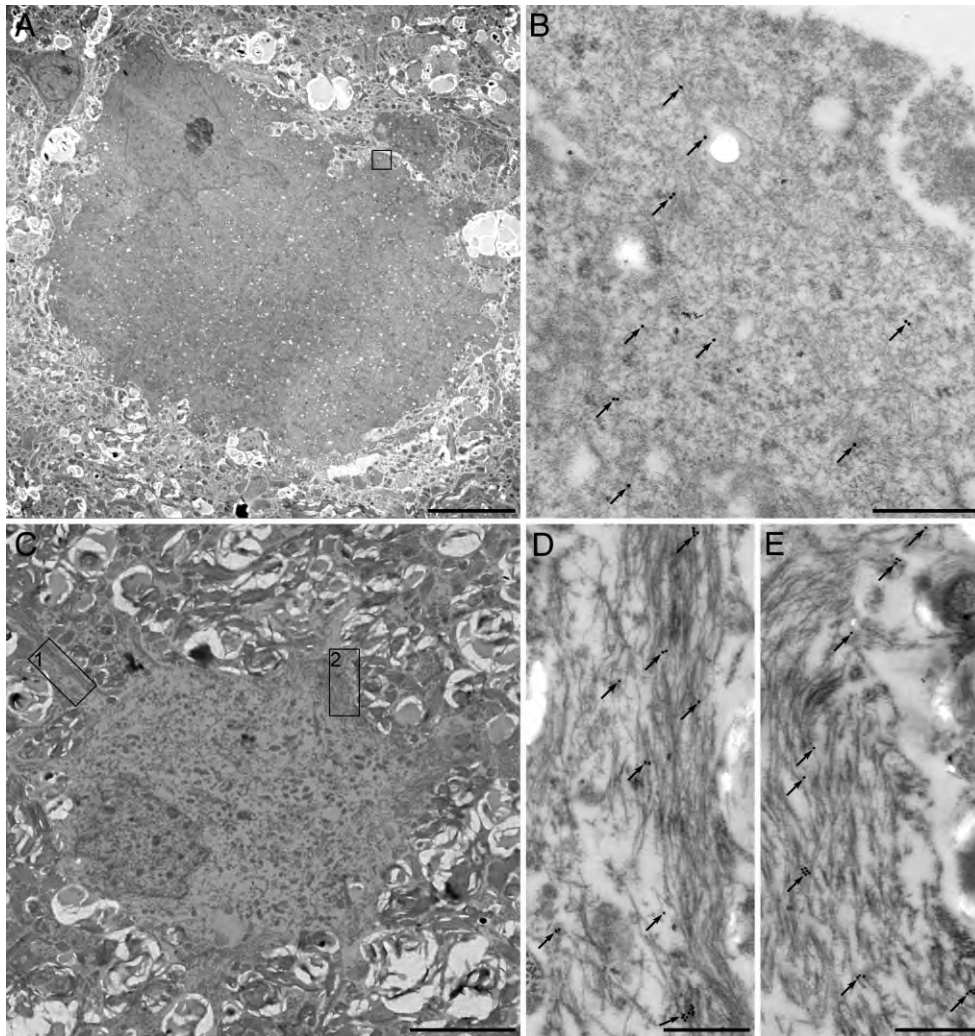


Fig. 3 Ultrastructural localization of p57/Kip2. (A) Low-power view of a balloon cell showing eccentric nucleus, abundant cytoplasm with filaments and cell organelle, and short cytoplasmic processes. (B) A higher magnification view of the short processes. The area indicated by a square in A. Note the immunoreactivity in the proximal portion of the cytoplasmic processes (arrows). (C-E) Another example of balloon cell with abundant intermediate filaments. (D, E) Higher magnification views of the areas indicated by square 1 rotated by 45° and square 2 in C, respectively, showing the immunoreactivity on the intermediate filaments. Bars = 10 μ m for A, 500 nm for B, D and E, and 5 μ m for C.

CD34, a stem cell/progenitor cell marker, is well known to be expressed in balloon cells in FCD IIb, TSC and HME, where the immunolabeled cells are exclusively located within the deep white matter or close to the gray matter boundary, but not in the cortex.⁹ In the present study, we also detected several CD34-labeled balloon cells; however, double-labeling immunofluorescence revealed distinct populations of balloon cells showing immunoreactivity for either CD34 or p57/Kip2 (Fig. 2). Even though these populations were located closely to each other within the white matter, we found no balloon cells that expressed both proteins (Fig. 2). CD34 is known to be expressed during neural tube formation.²⁹ Moreover, it has been reported that CD34-labeled progenitor-like cells are sometimes observed in ganglioglioma and other epilepsy-associated brain

tumors taken from patients with epilepsy.³⁰ However, the significance of CD34, and also p57/Kip2, in balloon cells has remained uncertain. It seems unlikely that certain cellular mechanisms would induce some sort of conflict in the expression of CD34 and p57/Kip2. Therefore, we speculate that the available evidence points to heterogeneity of the cells.

We were able to observe the ultrastructural localization of p57/Kip2 on intermediate filaments, presumably mainly vimentin filaments and possibly glial filaments as reported previously,¹⁹ in the proximal parts of the cytoplasmic processes (Fig. 3). This ultrastructural localization appeared to be compatible with the immunohistochemical picture (Fig. 1). In the perikarya of balloon cells, the intermediate filaments are loosely arranged and intermingled with

intracellular organelles, whereas in the proximal processes, the filaments show a tendency to be much more densely packed and aligned in the direction of extension of the processes (Fig. 3D, E). Up to now, the significance of p57/Kip2 localization in balloon cells has been uncertain. However, recent biochemical studies have provided evidence for a critical role of p57/Kip2 in the regulation of actin cytoskeletal dynamics, and thus migration ability, in cancer cells.³¹ Therefore, there is a possibility that p57/Kip2 may be involved in the intermediate filament assembly that is necessary for extension of the cytoplasmic processes of balloon cells.

In conclusion, we have reported aberrant expression of p57/Kip2 in balloon cells in various types of brain malformation. Our observations appear to be consistent with the notion that these cells represent abnormal differentiation of progenitor cells. Characteristically, the immunoreactivity appears to be localized in the proximal portion of cytoplasmic processes, implying that the protein has functional significance in the processes. The significant difference in the frequency of immunoreactive cells between FCD IIb and TSC suggests that the function of the protein may differ between these malformations.

ACKNOWLEDGMENTS

We thank Prof. Kouhei Akazawa, Department of Medical Informatics, University of Niigata, for statistical analysis.

DISCLAIMER

The authors report no conflicts of interest concerning the materials or methods used in this study or the findings presented.

REFERENCES

- Blümcke I, Thom M, Aronica E *et al.* The clinicopathologic spectrum of focal cortical dysplasias: a consensus classification proposed by an ad hoc Task Force of the ILAE Diagnostic Methods Commission. *Epilepsia* 2011; **52**: 158–174.
- Vinters HV, Miyata H. Chapter 9: tuberous sclerosis. In: Golden JA, Harding BN, eds. *Pathology & Genetics Developmental Neuropathology*. Basel: Neuropath Press, 2004; 79–87.
- Thom M. Chapter 8.1: hemimegalencephaly. In: Golden JA, Harding BN, eds. *Pathology & Genetics Developmental Neuropathology*. Basel: Neuropath Press, 2004; 67–72.
- Crino PB, Trojanowski JQ, Eberwine J. Internexin, MAP1B, and nestin in cortical dysplasia as markers of developmental maturity. *Acta Neuropathol* 1997; **93**: 619–627.
- Lamparello P, Baybis M, Pollard J *et al.* Developmental lineage of cell types in cortical dysplasia with balloon cells. *Brain* 2007; **130**: 2267–2276.
- Englund C, Folkerth RD, Born D, Lacy JM, Hevner RF. Aberrant neuronal-glial differentiation in Taylor-type focal cortical dysplasia (type IIA/B). *Acta Neuropathol* 2005; **109**: 519–533.
- Ying Z, Gonzalez-Martinez J, Tilelli C, Bingaman W, Najm I. Expression of neural stem cell surface marker CD133 in balloon cells of human focal cortical dysplasia. *Epilepsia* 2005; **46**: 1716–1723.
- Oh HS, Lee MC, Kim HS *et al.* Pathophysiological characteristics of balloon cells in cortical dysplasia. *Childs Nerv Syst* 2008; **24**: 175–183.
- Fausser S, Becker A, Schulze-Bonhage A *et al.* CD34-immunoreactive balloon cells in cortical malformations. *Acta Neuropathol* 2004; **108**: 272–278.
- Thom M, Martinian L, Sisodiya SM *et al.* Mcm2 labelling of balloon cells in focal cortical dysplasia. *Neuropathol Appl Neurobiol* 2005; **31**: 580–588.
- Yasin SA, Latak K, Becherini F *et al.* Balloon cells in human cortical dysplasia and tuberous sclerosis: isolation of a pathological progenitor-like cell. *Acta Neuropathol* 2010; **120**: 85–96.
- Cepeda C, André VM, Levine MS *et al.* Epileptogenesis in pediatric cortical dysplasia: the dysmature cerebral developmental hypothesis. *Epilepsy Behav* 2006; **9**: 219–235.
- Thom M, Martinian L, Sen A *et al.* An investigation of the expression of G₁-phase cell cycle proteins in focal cortical dysplasia type IIb. *J Neuropathol Exp Neurol* 2007; **66**: 1045–1055.
- Kavanagh E, Joseph B. The hallmarks of CDKN1C (p57, KIP2) in cancer. *Biochim Biophys Acta* 2011; **1816**: 50–56.
- Tury A, Mairet-Coello G, DiCicco-Bloom E. The multiple roles of the cyclin-dependent kinase inhibitory protein p57/Kip2 in cerebral cortical neurogenesis. *Dev Neurobiol* 2012; **72**: 821–842.
- Miyahara H, Natsumeda M, Shiga A *et al.* Suppressed expression of autophagosomal protein LC3 in cortical tubers of tuberous sclerosis complex. *Brain Pathol* 2013; **23**: 254–262.
- Tan CF, Yamada M, Toyoshima Y *et al.* Selective occurrence of TDP-43-immunoreactive inclusions in the lower motor neurons in Machado-Joseph disease. *Acta Neuropathol* 2009; **118**: 553–560.
- Alonso-Nanclares L, Garbelli R, Sola RG *et al.* Microanatomy of the dysplastic neocortex from epileptic patients. *Brain* 2005; **128**: 158–173.
- Garbelli R, Munari C, De Biasi S *et al.* Taylor's cortical dysplasia: a confocal and ultrastructural immunohistochemical study. *Brain Pathology* 1999; **9**: 445–461.

20. Gui H, Li S, Matisse MP. A cell-autonomous requirement for Cip/Kip cyclin-kinase inhibitors in regulating neuronal cell cycle exit but not differentiation in the developing spinal cord. *Dev Biol* 2007; **301**: 14–26.
21. Itoh Y, Masuyama N, Nakayama K, Nakayama KI, Gotoh Y. The cyclin-dependent kinase inhibitors p57 and p27 regulate neuronal migration in the developing mouse neocortex. *J Biol Chem* 2007; **282**: 390–396.
22. Tury A, Mairet-Coello G, Diccico-Bloom E. The cyclin-dependent kinase inhibitor p57Kip2 regulates cell cycle exit, differentiation, and migration of embryonic cerebral cortical precursors. *Cereb Cortex* 2011; **15**: 1343–1355.
23. Tee AR, Fingar DC, Manning BD, Kwiatkowski DJ, Cantley LC, Blenis J. Tuberous sclerosis complex-1 and -2 gene products function together to inhibit mammalian target of rapamycin (mTOR)-mediated downstream signaling. *Proc Natl Acad Sci U S A* 2002; **99**: 13571–13576.
24. Takei N, Nawa H. mTOR signaling and its roles in normal and abnormal brain development. *Front Mol Neurosci* 2014; **7**: 28. doi: 10.3389/fnmol.2014.00028. eCollection 2014.
25. Lee JH, Huynh M, Silhavy JL *et al.* De novo somatic mutations in components of the PI3K-AKT3-mTOR pathway cause hemimegalencephaly. *Nat Genet* 2012; **44**: 941–946.
26. Poduri A, Evrony GD, Cai X *et al.* Somatic activation of AKT3 causes hemispheric developmental brain malformations. *Neuron* 2012; **74**: 41–48.
27. Schick V, Majores M, Engels G *et al.* Differential Pi3K-pathway activation in cortical tubers and focal cortical dysplasias with balloon cell. *Brain Pathol* 2007; **17**: 165–173.
28. Cepeda C, André VM, Hauptman JS *et al.* Enhanced GABAergic network and receptor function in pediatric cortical dysplasia type IIB compared with tuberous sclerosis complex. *Neurobiol Dis* 2012; **45**: 310–321.
29. Lin G, Finger E, Gutierrez-Ramos JC. Expression of CD34 in endothelial cells, hematopoietic progenitors and nervous cells in fetal and adult mouse tissues. *Eur J Immunol* 1995; **25**: 1508–1516.
30. Blümcke I, Aronica E, Urbach H, Alexopoulos A, Gonzalez-Martinez JA. A neuropathology-based approach to epilepsy surgery in brain tumors and proposal for a new terminology use for long-term epilepsy-associated brain tumors. *Acta Neuropathol* 2014; **128**: 39–54.
31. Vlachos P, Joseph B. The Cdk inhibitor p57^{Kip2} controls LIM-kinase 1 activity and regulates actin cytoskeleton dynamics. *Oncogene* 2009; **28**: 4175–4188.

RESEARCH ARTICLE

p62 Deficiency Enhances α -Synuclein Pathology in Mice

Kunikazu Tanji^{1*}; Saori Odagiri^{2*}; Yasuo Miki¹; Atsushi Maruyama³; Yoshikazu Nikaido⁴; Junsei Mimura³; Fumiaki Mori¹; Eiji Warabi⁵; Toru Yanagawa⁵; Shinya Ueno⁴; Ken Itoh³; Koichi Wakabayashi¹

¹ Department of Neuropathology, ² Department of Stress Response Science, ³ Department of Neurophysiology, Hirosaki University Graduate School of Medicine, Hirosaki, ⁴ Department of Neuroanatomy, Cell Biology and Histology, ⁵ Majors of Medical Sciences, University of Tsukuba, Tsukuba, Japan.

Keywords

α -synuclein, Lewy body disease, p62/Sequestosome 1/SQSTM1, Parkinson's disease, proteolysis, stress.

Corresponding author:

Kunikazu Tanji, PhD, Department of Neuropathology, Hirosaki University Graduate School of Medicine, 5 Zaifu-cho, Hirosaki 036-8562, Japan (E-mail: kunikazu@cc.hirosaki-u.ac.jp)

Received 16 June 2014

Accepted 02 October 2014

Published Online Article Accepted 10 October 2014

* These authors contributed equally to the manuscript.

doi:10.1111/bpa.12214

Abstract

In Lewy body disease (LBD) such as dementia with LBs and Parkinson's disease, several lines of evidence show that disrupted proteolysis occurs. p62/SQSTM1 (p62) is highly involved with intracellular proteolysis and is a component of ubiquitin-positive inclusions in various neurodegenerative disorders. However, it is not clear whether p62 deficiency affects inclusion formation and abnormal protein accumulation. To answer this question, we used a mouse model of LBD that lacks p62, and found that LB-like inclusions were observed in transgenic mice that overexpressed α -synuclein (Tg mice) with or without the p62 protein. p62 deficiency enhanced α -synuclein pathology with regard to the number of inclusions and staining intensity compared with Tg mice that expressed p62. To further investigate the molecular mechanisms associated with the loss of p62 in Tg mice, we assessed the *mRNA* and protein levels of several molecules, and found that the neighbor of the *brca1* gene (*Nbr1*), which is functionally and structurally similar to p62, is increased in Tg mice without p62 compared with control Tg mice. These findings suggest that p62 and NBR1 affect the pathogenesis of neurodegenerative diseases through the cooperative modulation of α -synuclein aggregation.

INTRODUCTION

Lewy body disease (LBD) including dementia with LBs and Parkinson's disease (PD) is pathologically characterized by the presence of intracellular inclusions called LBs. α -Synuclein has been identified as a component of LBs (41), and the duplication and triplication of the α -synuclein gene are found in both sporadic and early onset forms of PD (40). Mutations (A30P and A53T) in the α -synuclein gene are linked to autosomal dominant forms of PD (20, 31). Originally, α -synuclein is a proteinase K (PK)-soluble protein that localizes at presynaptic terminals; however, α -synuclein becomes resistant to PK and widely deposited throughout the brain of patients with LBD (19, 42). These findings suggest that α -synuclein is significantly involved in the pathogenesis of both familial and sporadic cases of LBD.

α -Synuclein is physiologically processed by two intracellular degradation systems, including the ubiquitin–proteasome and autophagy–lysosome systems. In case of α -synuclein overload, the autophagy–lysosome system, including chaperone-mediated autophagy, predominantly aids in the degradation of excess α -synuclein (6, 22, 46). Thus, it is possible that dysfunction of intracellular degradation system results in the up-regulation of

α -synuclein expression and contributes to abnormal protein accumulation. Indeed, several lysosomal-related genes were identified as a causative mutation in familial PD, including leucine-rich repeat kinase 2 and adenosine-3-phosphate 13A2. Furthermore, PD has been genetically linked to rare lysosomal storage diseases, including Gaucher's disease (25) and Sanfilippo syndrome (47).

p62/SQSTM1/sequestosome 1 (referred to as p62) is a multifunctional protein that is strongly associated with the intracellular degradation system. P62 knockout (KO) mice exhibit mature-onset obesity, insulin and leptin resistance (37). Pathologically, loss of p62 results in the accumulation of hyperphosphorylated tau and insoluble K63-linked polyubiquitin chains (33, 48). p62 contains a ubiquitin-associated (UBA) domain at the C-terminus that enables its interaction with ubiquitinated and misfolded proteins. Additionally, p62 possesses a Phox and Bem1p (PB1) domain at the N-terminus and a LC3 interacting region, suggesting that p62 is able to interact with proteasome components and autophagosomal membranes (29, 38). Thus, it has been suggested that p62 can efficiently degrade ubiquitinated and misfolded proteins through the proteasome and autophagy–lysosome systems. It has been reported that p62 is an inducible protein that easily aggregates under several pathological conditions, such as oxidative

stress and neurodegeneration (1, 11, 27). Accordingly, dysfunction of the intracellular degradation systems induces p62 aggregation *in vivo* (2, 16). Furthermore, loss of p62 suppressed ubiquitin-positive inclusions in neurons of brain-specific autophagy-deficient mice (17). Additionally, ubiquitin- and p62-positive protein aggregates were abrogated in Atg8 and p62 double-mutant flies (26). These findings suggest that p62 may be responsible for the formation of cytoplasmic inclusions and abnormal protein accumulation.

In this study, we used transgenic (Tg) mice overexpressing α -synuclein with a A53T mutation as a model for LBD. We crossed the Tg mice with p62 KO mice to examine the involvement of p62 in abnormal α -synuclein pathology. Immunohistochemical analyses showed that p62 deficiency enhanced α -synuclein pathology, as shown by an increase in inclusion number and staining intensity. We assessed several genes and proteins related to stress response and proteolysis. These data revealed that the expression of neighbor of brca1 gene (NBR1), which is a functional homologue to p62, was increased in p62-deficient mice.

MATERIALS AND METHODS

Animals and experimental design

α -Synuclein Tg mice have been widely used as an animal model for LBD (7, 14, 21, 23, 24, 34, 36, 45). To create this LBD model in a p62-deficient background, we used mice overexpressing human α -synuclein with the A53T mutation under the prion promoter (Jackson Laboratories, Bar Harbor, ME, USA) (7) and p62 KO mice with exon 1–4 deleted as previously described (17). The p62 KO mice lacked abnormal tau pathology. α -Synuclein Tg and p62 KO mice were backcrossed with C57BL/6J mice for at least 10 generations. First, heterozygous α -synuclein Tg mice were bred with p62 KO mice to generate α -synuclein^{+/-}/p62^{+/-} mice. Second, α -synuclein^{+/-}/p62^{+/-} mice were inbred to generate wild type, p62 KO, α -synuclein^{+/-}/p62^{+/+} and α -synuclein^{+/-}/p62^{-/-} mice (Figure 1A). Hereafter, wild-type, p62 KO, α -synuclein^{+/-}/p62^{+/+} and α -synuclein^{+/-}/p62^{-/-} mice are simply referred to as WT, KO, Tg and Tg/KO mice, respectively. All comparisons were made

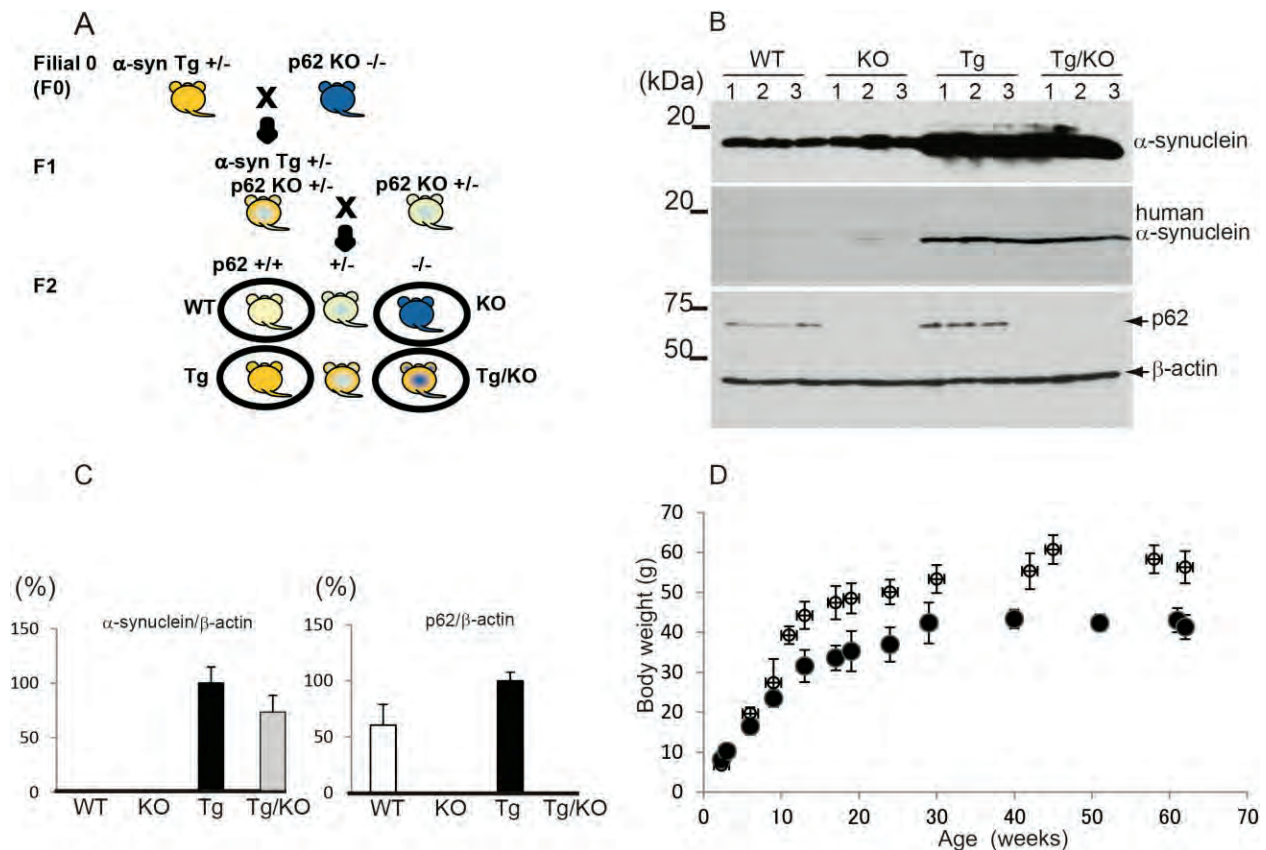


Figure 1. Characterization of p62 protein deficiency in an animal model of Lewy body disease. **A.** Breeding strategies to generate p62 deficiency in α -synuclein transgenic (Tg) mice. Initially, heterozygous α -synuclein Tg and homozygous p62-knockout (KO) mice were crossed. Next, littermates and heterozygous p62-deficient mice were mated to generate Tg mice without p62 (Tg/KO), of which four groups were used in this study (black circles). **B.** Immunoblot analysis confirmed that α -synuclein was overexpressed in Tg and Tg/KO mice and that p62

signals were diminished in KO and Tg/KO mice (9 weeks of age, n = 6 per group). The molecular mass is indicated on the left side of the panel. β -Actin was used as a loading control. **C.** A quantitative analysis shows that human α -synuclein is expressed in Tg and Tg/KO mice and that p62 is absent in KO and Tg/KO mice. The values of Tg mice are defined as 100%. **D.** The weight changes of Tg (black circle) and Tg/KO mice (grey circle) are shown (mean \pm standard deviation, n = 6–8 per group).

among littermates to minimize confounding effects by different genetic backgrounds. Mice were housed with a light/dark cycle of 12 h and were given food and water *ad libitum*. The experimental protocol was approved by the Institutional Animal Care and Use Committee at the Hiroshima University Graduate School of Medicine in Japan. Tg mice were genotyped using real-time polymerase chain reaction (PCR) analysis (forward primer, 5'-TGT AGG CTC CAA AAC CAA GG-3'; reverse primer, 5'-TAT GCC TGT GGA TCC TGA CA-3'), and verified by backcrossing. Conventional PCR was used for p62 genotyping (primer pair for wild type, forward, 5'-CTT ACG GGT CCT TTT CCC AAC-3'; reverse, 5'-TCC TCC TTG CCC AGA AGA TAG-3'; primer for p62 KO, forward; 5'-CTG CAT GTC TTC TCC CAT GAC-3'; reverse, 5'-TAG ATA CCT AGG TGA GCT CTG-3'). Mice were transcardially perfused with phosphate-buffered saline. The brain was removed, and the right hemisphere was fixed with 4% paraformaldehyde for 48 h. After dehydrating through a graded ethanol series, the right hemisphere was embedded in paraffin and cut into 4- μ m thick sections. The left hemisphere was frozen at -80°C for subsequent biochemical analyses.

Antibodies and immunohistochemistry

Rabbit antibodies against Keap1 (ProteinTech Group, Inc., Chicago, IL, USA), p62 (MBL, Nagoya, Japan), NBR1 (Sigma, St. Louis, MO, USA and Santa Cruz Biotechnology, Santa Cruz, CA, USA), NAD(P)H quinone oxidoreductase 1 (NQO1) (Sigma), LC3 (Sigma and MBL), ubiquitin (DAKO, Glostrup, Denmark), UBQLN1 (Lifespan Biosciences, Seattle, WA, USA), phosphorylated α -synuclein (Abcam, Cambridge, UK) and β -actin (Sigma) were used in this study. Mouse antibodies against p62 (BD Biosciences, Franklin Lakes, NJ, USA), SNAP25 (Chemicon, Temecula, CA, USA), synaptophysin (DAKO), human α -synuclein (LB509; Zymed, South San Francisco, CA, USA), human and mouse α -synucleins (4D6; GeneTex, Irvine, CA, USA) and phosphorylated α -synuclein (pSyn#64; Wako, Osaka, Japan) were also used.

The sections were dehydrated and pretreated with heat retrieval using an autoclave for 10 minutes in 10 mM citrate buffer (pH 6.0) for rabbit anti-Keap1 and anti-NBR1 antibodies. The sections were then subjected to immunohistochemical processing using the avidin-biotin-peroxidase complex method with diaminobenzidine (Sigma). In addition, the sections were counterstained with hematoxylin. For the staining of presynaptic PK-resistant α -synuclein, sections were pretreated with PK (Gibco BRL, Gaithersburg, MD, USA; 50 $\mu\text{g}/\text{mL}$) in a PK buffer containing 10 mM Tris-HCl, pH 7.8, 100 mM NaCl, 0.1% Nonidet-P40 at 37°C for 5 minutes. The total number of inclusions immunostained with anti-phosphorylated α -synuclein was quantified in contiguous sections. Immunohistochemical studies were performed at 9 weeks of age ($n = 6$ per group).

Quantitative reverse transcription-polymerase chain reaction (qRT-PCR)

Total RNA was extracted from the right hemisphere of the brain using the RNeasy lipid tissue mini kit (Qiagen, Hilden, Germany) at 9 weeks of age ($n = 3$ per group). cDNA was synthesized from 1 μg of total RNA using the PrimeScript[®] II first-strand cDNA

synthesis kit (Takara Bio Inc., Otsu, Japan). An aliquot of cDNA was used for gene expression analysis with the SYBR[®] Premix Ex Taq[™] II (Perfect Real Time) (Takara Bio Inc.) and CFX Real-Time PCR Detection System (Bio-Rad, Hercules, CA, USA) using the following primer sets: heme oxygenase-1 (*Ho-1*) (5'-CCA GCA ACA AAG TGC AAG ATT C-3'; 5'-TCA CAT GGC ATA AAG CCC TAC AG-3'), *Nqo1* (5'-GTC ATT CTC TGG CCA ATT CAG AGT-3'; 5'-TTC CAG GAT TTG AAT TCG GG-3'), glutamate-cysteine ligase catalytic subunit (*Gclc*) (5'-AAA ATG CGG AGG CAT CAA-3'; 5'-ATA TGC TGC AGG CTT GGA AT-3'), *p62* (5'-AGC TGC CTT GTA CCC ACA TC-3'; 5'-CAG AGA AGC CCA TGG ACA G-3'), *Cyclophilin A* (5'-ATG CTG GAC CCA ACA CAA AT-3'; 5'-TCT TTC ACT TTG CCA AAC ACC-3'), *Keap1* (5'-CAC AGC AGC GTG GAG AGA-3'; 5'-CAA CAT TGG CGC GAC TAG A-3'), *Lamp1* (5'-CCT ACG AGA CTG CGA ATG GT-3'; 5'-CCA CAA GAA CTG CCA TTT TTC-3'), *Cathepsin D* (5'-CCC TCC ATT CAT TGC AAG ATA C-3'; 5'-TGC TGG ACT TGT CAC TGT TGT-3'), *transcription factor EB (TfEB)* (5'-GAG CTG GGA ATG CTG ATC C-3'; 5'-GGG ACT TCT GCA GGT CCT T-3'), *Rab711* (5'-GCT GCA GCT CTG GGA TAG TG-3'; 5'-TAG TAG AGT CGT GTC ATG GAT GTG-3') and *Nbr1* (5'-TCA ACA GGA CTC GCA AAC AG-3'; 5'-ATG CTG CTC CCA TTG TGG-3'). *Cyclophilin A* was used for normalization.

Immunoblot analysis

Western blot analysis was performed as previously described (43). For total cell lysate, we used a lysis buffer with 4% sodium dodecyl sulfate (SDS; 75 mM Tris-HCl, pH 6.8, 4% SDS, 25% glycerol, 5% β -mercaptoethanol) and passed sample through 21 gauge needle attached on a 1 mL syringe. For an experiment using insoluble sample of detergent, samples were weighted and lysed with 10-fold volume of Tris-based buffer (pH 7.4) containing 0.1% Triton X-100 on ice. After homogenization with a pestle 20 times, they were passed 10 times through 21 gauge needle attached on a 1 mL syringe. Lysates were incubated for 5 minutes on ice, and centrifuged at $12\,000 \times g$ for 10 minutes. Supernatant was used as a soluble fraction. The pellets were resuspended with 8 M urea and sonicated (insoluble fraction). Signal detection was performed according to the protocol provided with the ECL or ECL prime detection systems (Amersham Pharmacia Biotech, Piscataway, NJ, USA). We performed each immunoblot analysis a minimum of three times, and all data were quantified and collected.

Animal behavioral testing

The Morris water maze

Spatial learning was assessed in a round tank of water (0.95 m in diameter) at 30°C . An escape platform (10 cm in diameter) was placed 1 cm below the water surface. A camera (Primetech Engineering Corp., Tokyo, Japan) was mounted above the maze and attached to a computer running the Smart software (Primetech Engineering Corp.). The training paradigm for the hidden platform version of the Morris water maze consisted of two trials per day for five consecutive days. The time taken to reach the platform (latency to escape) was recorded for each trial. The time limit was 120 s, and the intertrial interval was 1 h. If the animal could not

find the platform, it was placed on the platform for 20 s. After removing the platform, the probe trial was carried out 2 h after the completion of training on the fifth day. The latency to reach the former location of the platform and the percentage of total time spent in each quadrant were recorded.

Forced swim test

Immobility time was analyzed using a forced swim test. Animals were individually placed in a transparent acrylic cylindrical beaker (height: 25 cm, diameter: 18 cm) containing 4600 mL of clear water at $25 \pm 1^\circ\text{C}$ for 6 minutes. A mouse was judged to be immobile when it remained passively floating in the water for more than 2 s. Immobility time was quantified using a Forced Swim Scan software (Clever Sys Inc., Reston, VA, USA).

Quantitative analysis and statistical analysis

A semi-quantitative analysis of protein levels was performed using the ImageJ software provided by the NIH. All data were represented as the mean + standard deviation. The statistical significance was evaluated using one-way analysis of variance (ANOVA) with Bonferroni's post hoc test to analyze four genotypes and Student's *t*-test to analyze two genotypes. A probability value of less than 0.05 ($P < 0.05$) was considered to be significant.

RESULTS

Characterization of α -synuclein Tg mice with or without p62

To test the possibility that p62 is responsible for the formation of cytoplasmic inclusions and abnormal protein accumulation, we generated mice that overexpressed human α -synuclein (Tg) on a p62-deficient background (Figure 1A). First, we crossed Tg mice with p62 KO mice. Next, littermates with or without p62 and/or human α -synuclein were selected by genotyping and crossed to generate Tg mice lacking p62. Consequently, littermates with or without endogenous p62 and/or human α -synuclein expression were born at the expected Mendelian ratio. For our studies, we used WT, KO, Tg and Tg/KO mice.

We confirmed that α -synuclein was robustly expressed in the brains of Tg mice and Tg/KO mice (Figure 1B). We used a human α -synuclein-specific antibody, LB509, to confirm that human α -synuclein expression was present only in Tg and Tg/KO mice. There were no differences in the endogenous and human α -synuclein levels between the Tg and Tg/KO mice. We also confirmed that p62 protein levels were diminished in the brains of KO and Tg/KO mice. Interestingly, the amount of p62 was slightly higher in Tg mice than it was in WT mice (Figure 1C). An increase of p62 was also supported by immunohistochemical studies that showed an increase in p62 immunoreactivity in Tg mice compared with WT mice (Figure 2A). α -Synuclein expression was mainly observed in the presynapses in the brains of WT and p62 KO mice; however, additional staining of α -synuclein was observed in the cytoplasm and presynapses in the brains of Tg and Tg/KO mice (Figure 2B). Consistent with previous papers (28, 37), KO mice exhibited mature-onset obesity. As they aged, Tg/KO mice had a heavier average body weight than did Tg mice (Figure 1D). The

majority of Tg mice remained healthy until at least 70 weeks of age. Tg and Tg/KO mice were behaviorally indistinguishable and displayed lower food intake and activity at the end stage of the disease.

Tg/KO mice exhibit an increase in phosphorylated α -synuclein staining and inclusion number compared with Tg mice

Similar to the human pathological conditions, there are two types of abnormal α -synuclein in the brains of Tg mice (7, 42), including phosphorylated α -synuclein (P-syn) and PK-resistant α -synuclein (PK-syn). Immunohistochemical analyses showed that P-syn is observed in both Tg/KO and Tg mice (Figure 3A). We compared the number of P-syn-positive inclusions in the thalamus of Tg and Tg/KO mice. Quantitative data indicated that the number of inclusions was higher in Tg/KO mice compared with Tg mice (Figure 3B). Furthermore, the intensity of P-syn staining was increased in the hippocampus and cerebral cortex of Tg/KO mice compared with Tg mice (Figure 3C). Unlike human pathological conditions, p62 was not localized in the cytoplasmic inclusions in the brains of Tg mice. Immunohistochemical studies demonstrated that PK treatment abolished normal α -synuclein immunoreactivity, and PK-syn was found in the presynapses of the brain of both Tg and Tg/KO mice (Figure 3D). Western blot analysis verified that P-syn signal intensity was higher in Tg/KO than Tg mice using two kinds of antibodies against P-syn (Figure 3E). Furthermore, we fractionated samples of Tg and Tg/KO mice by buffer with 0.1% Triton X-100 detergent, and found that insoluble P-syn level was increased in Tg/KO compared with Tg mice (Figure 3F). Thus, p62 deficiency modulates α -synuclein pathology with regard to P-syn staining intensity, the number of P-syn inclusions and solubility.

Behavioral tests revealed a longer immobility time for p62-deficient mice

Given the presynaptic aggregation of PK-syn in the hippocampus of Tg and Tg/KO mice, we sought to determine whether memory function was also affected in these mice. We performed the Morris water maze test using mice at a younger age (9 weeks old) to exclude differences in body weight. The average weight was comparable between Tg and Tg/KO mice (21.1 g in Tg, 22.0 g in Tg/KO) at 9 weeks of age. During the training phase of the Morris water maze test, WT and Tg mice showed a gradual decrease in escape latency over time; however, KO and Tg/KO mice exhibited longer escape latencies (Supporting Information Video Clip S1 and S2). When the platform was removed, 80% of WT mice and 70% of Tg mice found the platform location. In contrast, less than 50% of KO and Tg/KO mice found the platform location. KO and Tg/KO mice took a longer time to reach to the platform location (Figure 4A) and spent less time in the target quadrant (Figure 4B) than did WT mice. The lower rate of platform crossing in the KO mice was due to their immobility (Figure 4C,D), which is consistent with previous results showing that KO mice exhibited immobility during training and probe trials (33). During only the first minute of a forced swim test, KO mice showed a significantly increased immobility that lasted longer than 2 s when compared with WT mice (Figure 4E,F). Thereafter, the time course for

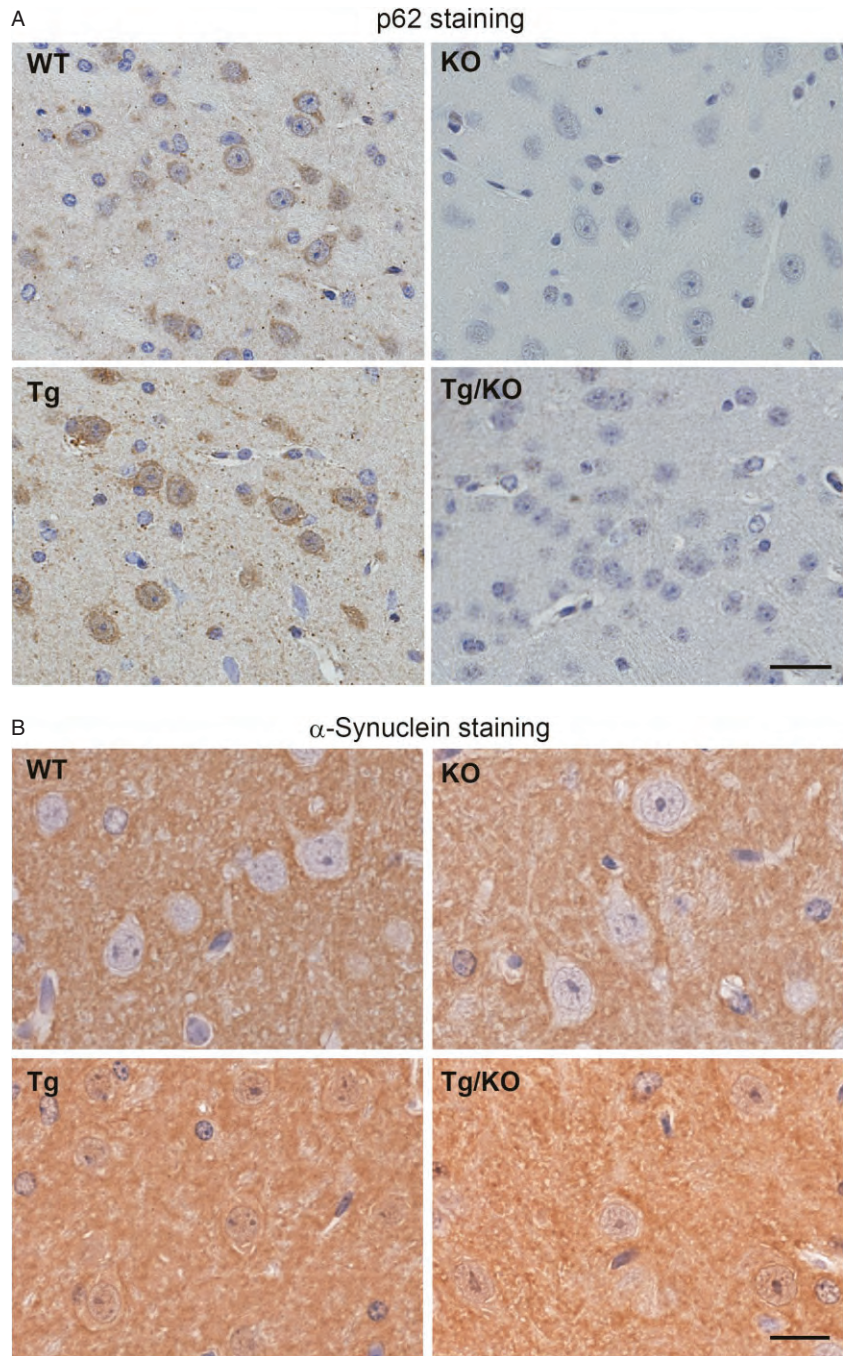


Figure 2. *p62* and α -synuclein staining in wild-type (WT), knockout (KO), Tg and Tg/KO mice. **A.** Immunohistochemical analysis shows that p62 immunoreactivity is observed in WT and Tg mice but not in KO mice (9 weeks of age, $n = 6$ per group). Bar = 20 μm . **B.** Human and mouse α -synuclein is strongly expressed in the presynapse and cytoplasm of cortical neurons in Tg and Tg/KO mice. Bar = 10 μm .

floating behavior (the percentage of immobility) was similar between groups. There was no significant difference between Tg/KO and WT mice. These results suggest that p62 plays a role in maintaining neurological functions, such as stress responses and motivation to escape.

Increased levels of the functional homologue, NBR1, in p62 KO and Tg/KO mice

To analyze the molecular mechanisms associated with the loss of p62 on Tg mice, we performed quantitative RT-PCR analysis using

primers for genes related to the stress response and proteolysis (Figure 5). Consistent with the genotype results, the *p62* mRNA level was diminished in KO and Tg/KO mice. Keap1 is a binding partner of p62 and functions as a sensor for noxious stimuli such as oxidants and electrophiles. The mRNA level of *Keap1* appeared to be different between the four groups; however, the data were not statistically significant ($P = 0.069$). Previous papers have reported that autophagy-deficient mice display a higher expression of detoxifying enzymes, such as *Ho-1*, *Nqo1* and *Gclc* (18). There were no differences in the mRNA levels of these enzymes among the four groups. Recent evidence indicates that α -synuclein

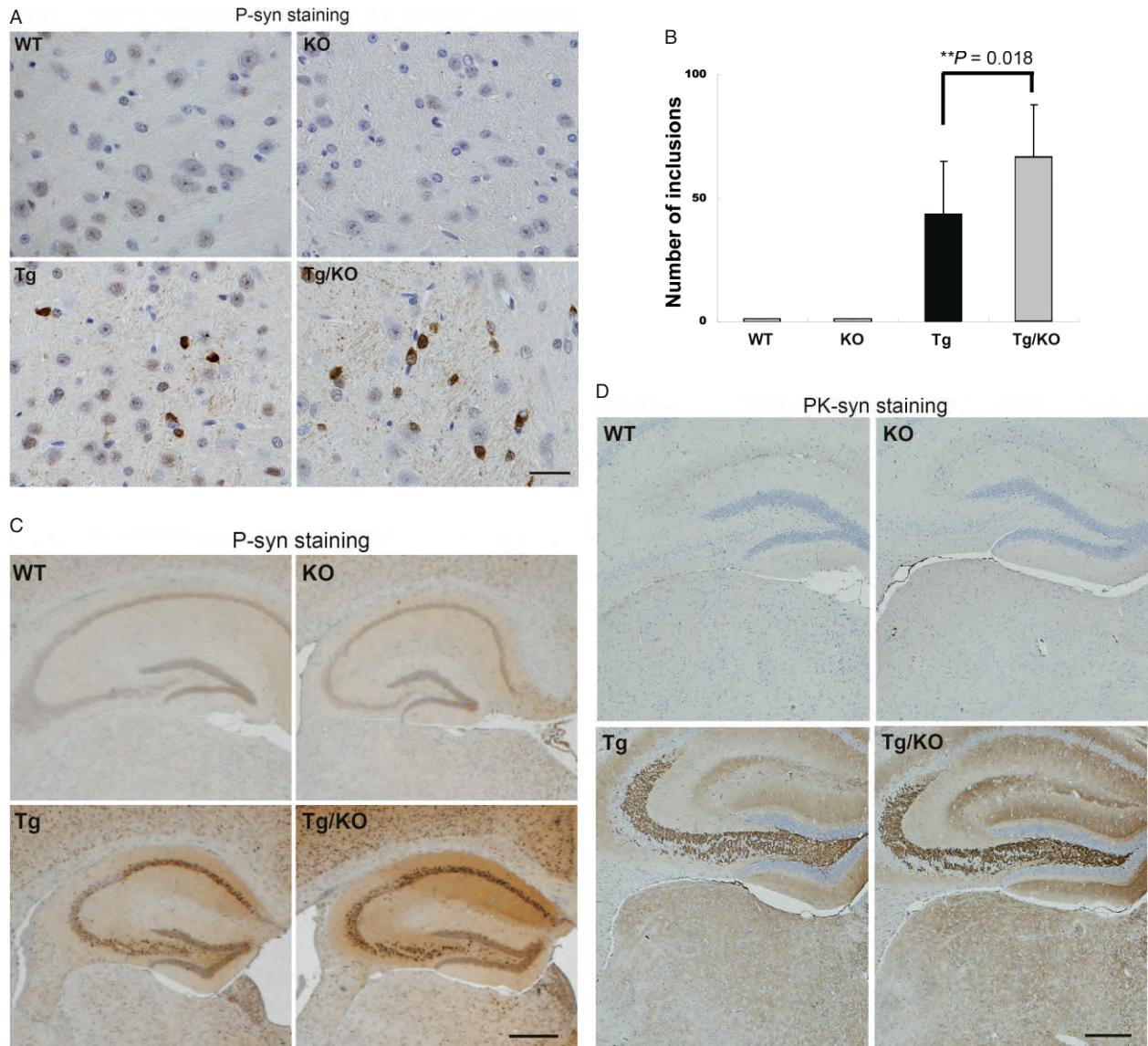


Figure 3. The effect of p62 deficiency on abnormal α -synuclein expression. **A.** Cytoplasmic inclusions are positive for phosphorylated α -synuclein (P-syn) in the thalamus of Tg and Tg/knockout (KO) mice. Bar = 20 μ m. **B.** A quantitative analysis shows that the number of cytoplasmic inclusions is significantly increased in Tg/KO mice when compared with Tg mice (9 weeks of age, $n = 6$ per group). The groups differed significantly [analysis of variance (ANOVA), $F(3, 11) = 160.81$, $P < 0.01$]. **C.** P-syn staining is observed in the neurons of the cerebral cortex and hippocampus in Tg and Tg/KO mice. An increased staining intensity is observed in Tg/KO mice compared with Tg mice. Bar = 500 μ m. **D.** No

obvious differences in proteinase K-resistant α -synuclein (PK-syn) are found between Tg and Tg/KO mice. Bar = 250 μ m. **E.** P-syn level is significantly increased in Tg/KO mice compared with Tg mice. Ratio of P-syn to β -actin was calculated, and the values of Tg mice are defined as 1.0. The groups differed significantly [ANOVA, $F(3, 11) = 147.1$, $P < 0.01$]. **F.** Triton X-100 soluble and insoluble samples were prepared from Tg and Tg/KO mice (9 weeks of age, $n = 2$ per Tg and Tg/KO groups). Insoluble P-syn level is increased in Tg/KO mice compared with Tg mice. P-syn levels were normalized by total synuclein, and the values of Tg mice were defined as 1.0 in a soluble or insoluble sample.

overexpression causes dynamic changes in the autophagy-lysosomal system. Therefore, we assessed levels of *TjEB*, a major transcriptional regulator for this system (39), lysosomal enzymes (*Lamp1* and *cathepsin D*), molecules responsible for membrane trafficking (*Rab711*) and selective autophagy markers (*Nbr1*). Among these genes, only the *Nbr1* mRNA levels were significantly different ($P < 0.01$) between the four groups. Consistent with this

result, the NBR1 protein levels were significantly increased in mice lacking p62 compared with mice with p62 ($P < 0.05$) (Figure 6A,B). Additionally, Keap1 protein levels were also significantly different among the four groups at the protein level. There were no alterations in NQO1, synaptic proteins and proteolysis-related molecules, such as ubiquitin and LC3, which are essential to autophagosomal formation (13). Based on the

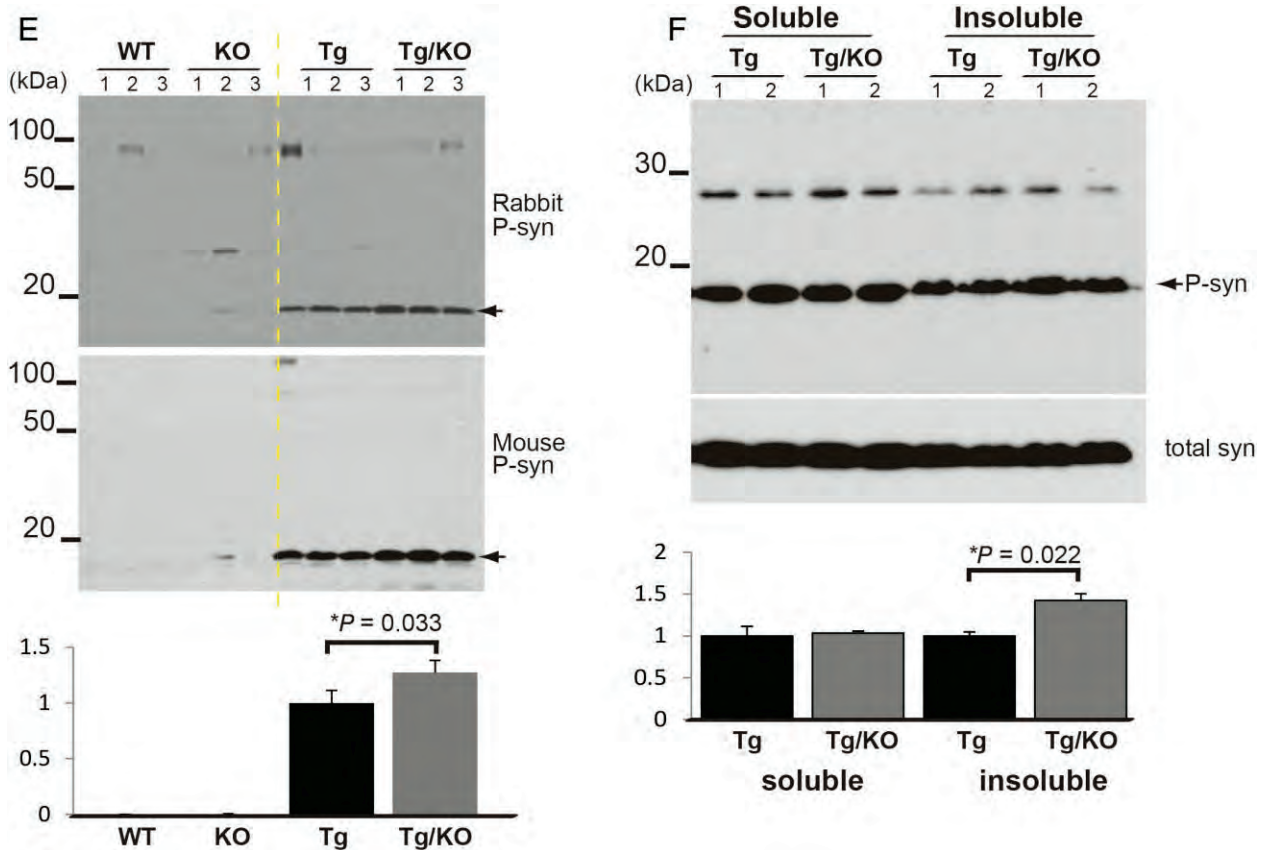


Figure 3. Continued.

increased NBR1 levels in mice lacking p62, we compared the distribution patterns of p62 and NBR1 in the mouse brain. Interestingly, immunoblotting showed that p62 and NBR1 are similarly distributed in distinct regions of the mouse brain (Figure 7A,B). NBR1 was mainly localized in the cytoplasm of neurons, and its intensity was higher in Tg/KO than in Tg mice (Figure 7C). These data are consistent with the qRT-PCR and immunoblotting analyses.

DISCUSSION

p62 is an inducible protein that easily aggregates under pathological conditions, such as oxidative stress and disrupted proteolysis, and it is localized in cytoplasmic inclusions in LBD and other neurodegenerative diseases, suggesting that p62 contributes to inclusion formation. Moreover, p62- and ubiquitin-positive inclusions in the neurons of brain-specific *Atg7*-deficient mice disappear with the loss of p62 (17). Based on these findings, we initially predicted that p62 deficiency would lead to a decrease in the number of inclusions in Tg mice that overexpressed α -synuclein. However, our data suggest that p62 deficiency results in an exaggeration of α -synuclein pathology with regard to P-syn staining intensity and inclusion number. Consistent with our findings, Doi *et al* demonstrated that a loss of p62 exacerbated neuropathological outcomes (5) in a mouse model of spinal and bulbar muscular atrophy, which is one of polyglutamine diseases. Our

pathological data showed that the number of P-syn-positive inclusion increased by 1.5-fold in Tg/KO mice compared with Tg mice. Consistently, this was supported by Western blot analyses showing that P-syn level was higher in Tg/KO mice than Tg mice using two kinds of antibodies against P-syn. Considering that increased P-syn is mainly resistant to detergent of Triton X-100, it is possible that biochemical property of α -synuclein is altered and leads to more aggregation in Tg/KO mice. Although it remains controversial whether the formation of cytoplasmic inclusions exerts a beneficial or toxic effect on cells, our findings strengthen the idea that p62 can modulate α -synuclein aggregation and the pathogenesis of diseases.

Consistent with previous results (28, 37), a p62 deficiency resulted in mature-onset obesity in mice. Recent evidence indicates that hyperphagia is the primary cause of obesity in p62-deficient mice due to the disruption of leptin signaling (9). Accordingly, p62 is highly expressed in hypothalamic neurons, including proopiomelanocortin (POMC) neurons in the arcuate nucleus (3, 9) that are responsible for the control of appetite and energy intake. Interestingly, lack of autophagic activity in POMC neurons caused higher post-weaning body weight and p62/ubiquitin aggregation (4, 32). Furthermore, leptin signaling is also disrupted in these mice. This may have broad implications for the pathophysiology of p62 KO mice. Because p62 helps shuttle insoluble and ubiquitinated proteins into autophagosomes, disruption of autophagic flux or loss of p62 gives rise to the accumulation

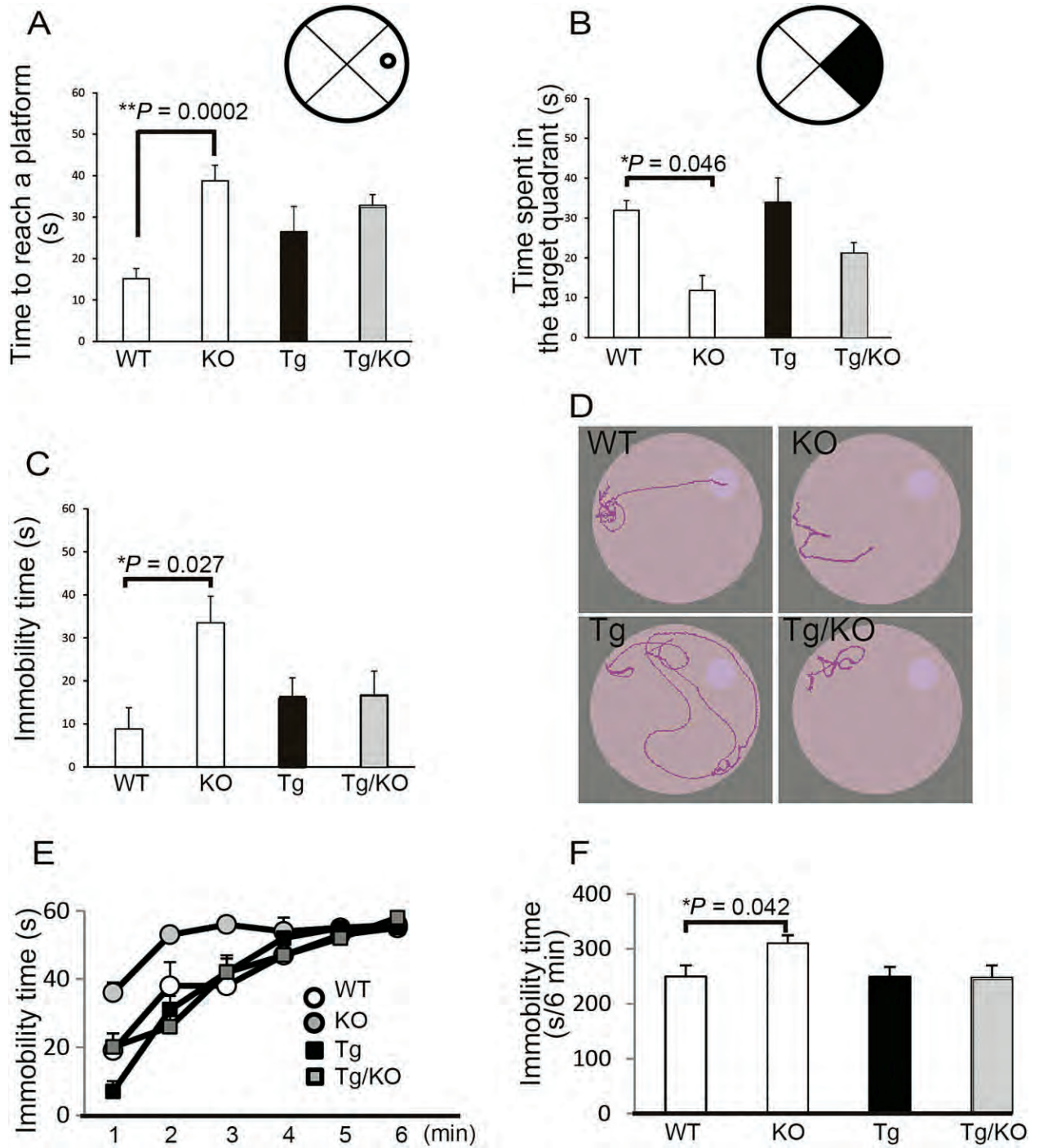


Figure 4. *p62*-deficient mice exhibit longer escape latencies due to lower activity. **A.** The probe trial was completed after 5 days of hidden platform training in the Morris water maze. Wild type (WT, $n = 10$), *p62* knockout (KO, $n = 11$), α -synuclein Tg (Tg, $n = 9$) and α -synuclein mice lacking *p62* (Tg/KO, $n = 9$) were tested at 9 weeks of age. KO mice take longer to reach the platform location. The groups differed significantly [analysis of variance (ANOVA), $F(3, 39) = 4.53$, $P < 0.01$]. **B.** The percentage of time spent in the target quadrant (black) during a 60 s probe trial of the Morris water maze test. KO mice spend less time in the target

quadrant. **C.** The immobility time of the Morris water maze. Longer immobility times are evident in KO mice. **D.** Representative path tracings are shown. Light pink indicates the position of the platform. **E.** A forced swim test was performed at 9–10 weeks of age ($n = 9$ –11 per group) and shows a significant difference in immobility latency, with KO mice lasting longer than 2 s and WT mice remaining mobile for the first 1 minute. **F.** KO mice exhibit higher immobility times for the first 6 minutes. The groups differed significantly [ANOVA, $F(3, 39) = 2.14$, $P < 0.05$]. $*P < 0.05$.

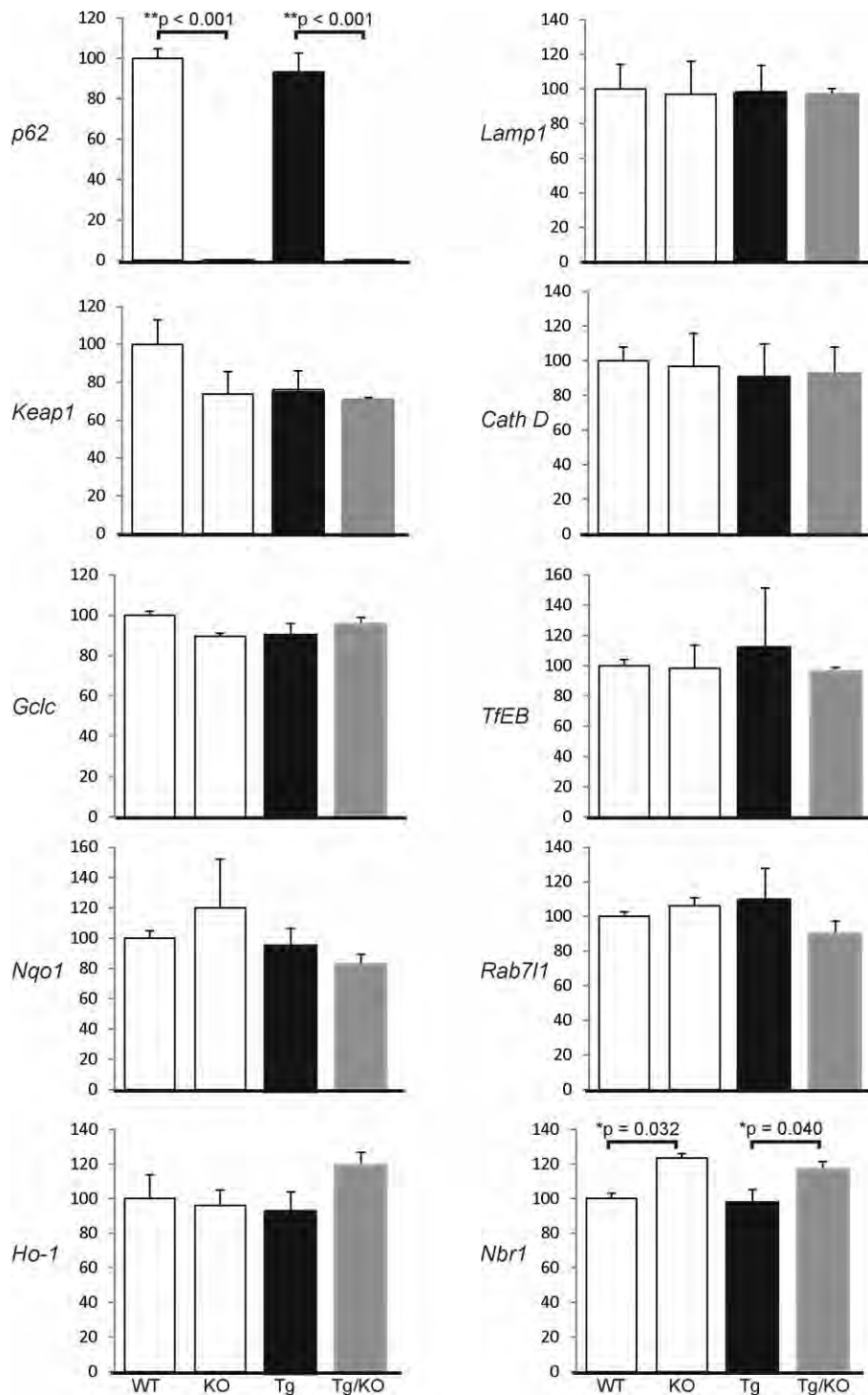


Figure 5. The effect of p62 deficiency on several kinds of genes. The mRNA levels of genes related to proteolysis and oxidative stress in the brains of WT, KO, Tg and TG/KO mice were determined at 9 weeks of age (n = 3 per group). mRNA was measured by quantitative reverse transcription-polymerase chain reaction (qRT-PCR) using the right hemisphere of the brain. Data are normalized by the *Cyclophilin A* mRNA level in each sample, and the average and standard deviation was calculated. qRT-PCR reveals that there is no significant difference in the

Keap1, glutamate-cysteine ligase catalytic subunit (*Gclc*), NAD(P)H quinone oxidoreductase 1 (*Nqo1*), heme oxygenase-1 (*Ho-1*), *Lamp1*, *Cathepsin D*, *TfEB* and *Rab71* levels among the four groups. In contrast, the mRNA level of p62 ($P < 0.01$) and *Nbr1* ($P < 0.05$) are significantly different. The groups differed significantly [analysis of variance, $F(3, 11) = 226.86$, $P < 0.01$ in p62 mRNA, $F(3, 11) = 14.15$, $P < 0.01$ in *Nbr1* mRNA]. The WT values are defined as 100%. * $P < 0.05$, ** $P < 0.01$.

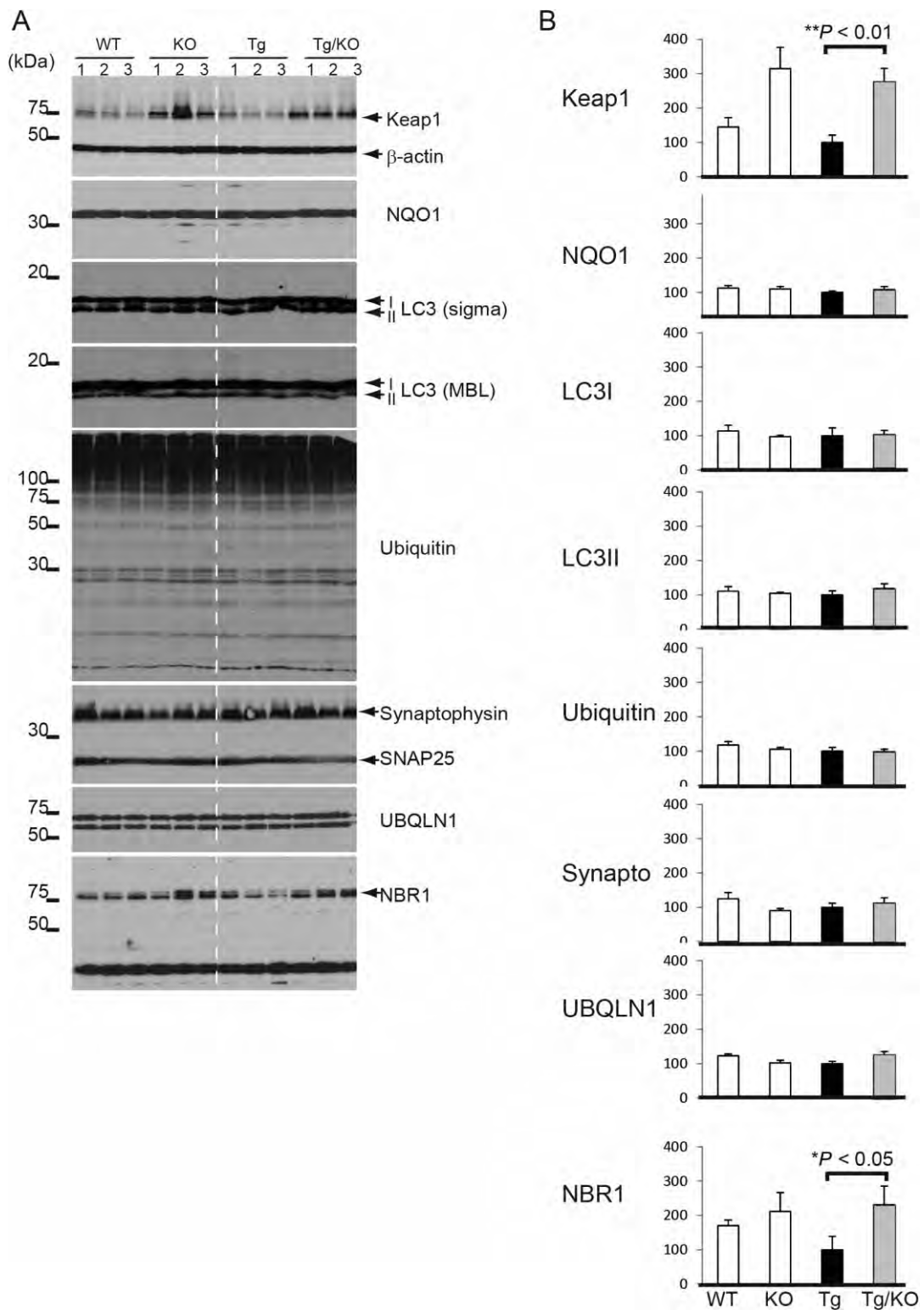


Figure 6. The effect of p62 deficiency on molecules related to proteolysis, oxidative stress and the synapse. **A.** Expression of Keap1 and NBR1 is significantly increased in Tg/KO mice compared with Tg mice. NAD(P)H quinone oxidoreductase 1 (NQO1), LC3, ubiquitin, synaptophysin and SNAP25 levels are not significantly different between the four groups (9 weeks of age, n = 6 per group). **B.** A

quantitative analysis indicates that the Keap1 and NBR1 levels are significantly increased in p62-deficient mice compared with mice with p62. The Tg values are defined as 100%. * $P < 0.05$, ** $P < 0.01$. The groups differed significantly [analysis of variance, $F(3, 11) = 7.44$, $P = 0.011$ in Keap1, $F(3, 11) = 4.27$, $P = 0.045$ in NBR1].

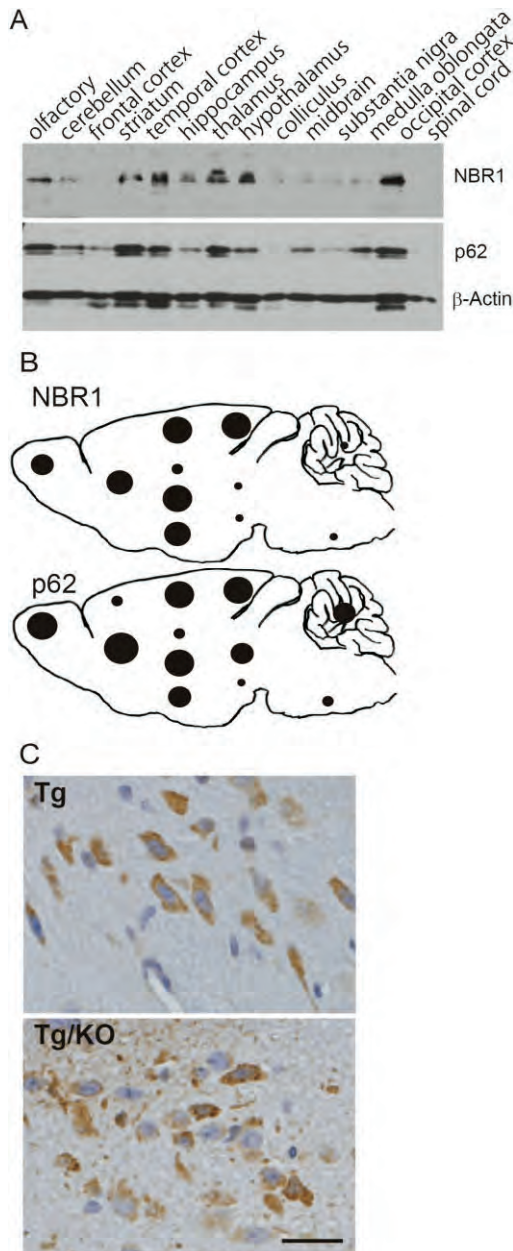


Figure 7. The spatial patterns of p62 and NBR1 in the mouse brain. **A.** Equal amounts of homogenates from the indicated regions were analyzed by immunoblotting (12 weeks of age, $n = 2$ in wild-type mice). Antibodies against NBR1 (upper) or p62 (bottom) were used to detect endogenous proteins. NBR1 is mainly expressed in the olfactory bulb, temporal and occipital cortices, striatum, thalamus and hypothalamus. The highest expression of p62 is observed in the olfactory bulb, striatum, temporal and occipital cortices, hippocampus, thalamus, hypothalamus and medulla oblongata. β -Actin is used as a loading control. **B.** Distribution patterns of NBR1 and p62 in the sagittal section of mice brains. NBR1 or p62 levels are normalized by β -actin. The circles represent the size of the expression level. **C.** NBR1 immunostaining in Tg and Tg/KO mice (9 weeks of age, $n = 6$ per group). NBR1 immunoreactivity is mainly detected in neurons of the thalamus of both Tg and Tg/KO mice. Note the increased intensity of NBR1 immunoreactivity in Tg/KO mice compared with Tg mice. Bar = 30 μ m.

of p62 target molecules. Accordingly, we revealed that P-syn level is increased in Triton X-100 insoluble fraction of Tg/KO mice compared with Tg mice. Thus, p62 dysfunction observed in autophagy-deficient POMC neurons or p62 KO mice might also affect intercellular environment through disturbance of p62 binding partners or substrates. One of p62 binding partners is known to be dopamine receptor (15). Because dopamine is widely involved in physiological conditions such as mood, cognition and motor control, it is possible that p62 modulates dopamine system, and p62 dysfunction may cause pathogenesis of PD.

Our immunoblot results confirmed that the hypothalamus is one of the regions with the highest p62 expression level. The hypothalamus is known to regulate various physiological functions, particularly the hypothalamus-pituitary-adrenal axis, which coordinates emotional, neuroendocrine and autonomic inputs in response to stress. Regarding behavioral abnormalities, we could not distinguish Tg mice from Tg/KO mice; however, p62-deficient mice exhibited less activity and depression-like behavior in the Morris water maze and forced swim test. This is consistent with previous results (33). It is conceivable that p62 deficiency affects the hypothalamus-pituitary-adrenal axis, leading to behavioral abnormalities in response to stress. The immobility rate of Tg/KO mice was comparable with that of normal control mice. Considering previous reports that mice overexpressing α -synuclein are hyperactive (8, 30, 44), we speculate that the degree of immobility in Tg/KO mice is recovered because of the hyperactivity of Tg mice. Taken together, p62 plays an important role in modulating multiple physiological responses, including nutritional, oxidative and water stressors.

We screened multiple protein and *mRNA* levels to study the molecular mechanisms associated with the loss of p62 in Tg mice. We found that NBR1 was significantly increased in Tg/KO mice compared with Tg mice at both the *mRNA* and protein levels. p62 and NBR1 contain an N-terminal PB1 domain, an intermediate LC3 binding region, and a C-terminal UBA domain, and they function as cargo adapters for the autophagic degradation of ubiquitinated substrates (10, 12, 29). Intriguingly, our immunoblotting results suggest that these molecules are similarly distributed in distinct regions of the mouse brain. This spatial pattern and functional similarity raise the possibility that NBR1 levels can be up-regulated to compensate for the loss of p62 protein. Therefore, the functional redundancy of NBR1 may mask the anticipated abnormalities of p62-deficient mice.

In conclusion, we have provided evidence that p62 is unnecessary for the formation of inclusions in an animal model that overexpresses α -synuclein. In addition, p62 deficiency enhanced α -synuclein pathology based on the number of inclusions and staining intensity of P-syn. In support of this finding, it is likely that p62 indirectly helps sequester abnormal molecules through its own oligomerization (35). Further analyses at the molecular level suggest that NBR1 plays a compensatory role for p62 in the central nervous system. NBR1 and p62 double KO mice would be a useful tool to test this hypothesis.

ACKNOWLEDGMENTS

This work was supported by JSPS KAKENHI grant numbers 26430050 (K.T.), 26860655 (Y.M.), 26430049 (F.M.), 24300131

(K.W.); Priority Research Grant for Young Scientists designated by the president of Hirosaki University (K.T., J.M.); Hirosaki University Institutional Research Grant (K.I., K.W.); grants-in-aid from the Research Committee for Ataxic Disease from the Ministry of Health, Labor and Welfare, Japan (K.W.); and an Intramural Research Grant (24-5) for Neurological and Psychiatric Disorders of NCNP (K.W.). The authors wish to express their gratitude to K. Saruta, T. Kon, M. Nakata and A. Ono for their technical assistance.

REFERENCES

- Bartlett BJ, Isakson P, Lewerenz J, Sanchez H, Kotzebue RW, Cumming RC *et al* (2011) p62, Ref(2)P and ubiquitinated proteins are conserved markers of neuronal aging, aggregate formation and progressive autophagic defects. *Autophagy* **7**:572–583.
- Bedford L, Hay D, Devoy A, Paine S, Powe DG, Seth R *et al* (2008) Depletion of 26S proteasomes in mouse brain neurons causes neurodegeneration and Lewy-like inclusions resembling human pale bodies. *J Neurosci* **28**:8189–8198.
- Braak H, Thal DR, Del Tredici K (2011) Nerve cells immunoreactive for p62 in select hypothalamic and brainstem nuclei of controls and Parkinson's disease cases. *J Neural Transm* **118**:809–819.
- Coupe B, Ishii Y, Dietrich MO, Komatsu M, Horvath TL, Bouret SG (2012) Loss of autophagy in pro-opiomelanocortin neurons perturbs axon growth and causes metabolic dysregulation. *Cell Metab* **15**:247–255.
- Doi H, Adachi H, Katsuno M, Minamiyama M, Matsumoto S, Kondo N *et al* (2013) p62/SQSTM1 differentially removes the toxic mutant androgen receptor via autophagy and inclusion formation in a spinal and bulbar muscular atrophy mouse model. *J Neurosci* **33**:7710–7727.
- Ebrahimi-Fakhari D, Cantuti-Castelvetri I, Fan Z, Rockenstein E, Masliah E, Hyman BT *et al* (2011) Distinct roles in vivo for the ubiquitin-proteasome system and the autophagy-lysosomal pathway in the degradation of alpha-synuclein. *J Neurosci* **31**:14508–14520.
- Giasson BI, Duda JE, Quinn SM, Zhang B, Trojanowski JQ, Lee VM (2002) Neuronal alpha-synucleinopathy with severe movement disorder in mice expressing A53T human alpha-synuclein. *Neuron* **34**:521–533.
- Graham DR, Sidhu A (2010) Mice expressing the A53T mutant form of human alpha-synuclein exhibit hyperactivity and reduced anxiety-like behavior. *J Neurosci Res* **88**:1777–1783.
- Harada H, Warabi E, Matsuki T, Yanagawa T, Okada K, Uwayama J *et al* (2013) Deficiency of p62/Sequestosome 1 causes hyperphagia due to leptin resistance in the brain. *J Neurosci* **33**:14767–14777.
- Ichimura Y, Kumanomidou T, Sou YS, Mizushima T, Ezaki J, Ueno T *et al* (2008) Structural basis for sorting mechanism of p62 in selective autophagy. *J Biol Chem* **283**:22847–22857.
- Ishii T, Itoh K, Takahashi S, Sato H, Yanagawa T, Katoh Y *et al* (2000) Transcription factor Nrf2 coordinately regulates a group of oxidative stress-inducible genes in macrophages. *J Biol Chem* **275**:16023–16029.
- Johansen T, Lamark T (2011) Selective autophagy mediated by autophagic adapter proteins. *Autophagy* **7**:279–296.
- Kabeya Y, Mizushima N, Yamamoto A, Oshitani-Okamoto S, Ohsumi Y, Yoshimori T (2004) LC3, GABARAP and GATE16 localize to autophagosomal membrane depending on form-II formation. *J Cell Sci* **117**:2805–2812.
- Kahle PJ (2008) alpha-Synucleinopathy models and human neuropathology: similarities and differences. *Acta Neuropathol* **115**:87–95.
- Kim OJ, Ariano MA, Namkung Y, Marinec P, Kim E, Han J, Sibley DR (2008) D2 dopamine receptor expression and trafficking is regulated through direct interactions with ZIP. *J Neurochem* **106**:83–95.
- Komatsu M, Waguri S, Chiba T, Murata S, Iwata J, Tanida I *et al* (2006) Loss of autophagy in the central nervous system causes neurodegeneration in mice. *Nature* **441**:880–884.
- Komatsu M, Waguri S, Koike M, Sou YS, Ueno T, Hara T *et al* (2007) Homeostatic levels of p62 control cytoplasmic inclusion body formation in autophagy-deficient mice. *Cell* **131**:1149–1163.
- Komatsu M, Kurokawa H, Waguri S, Taguchi K, Kobayashi A, Ichimura Y *et al* (2010) The selective autophagy substrate p62 activates the stress responsive transcription factor Nrf2 through inactivation of Keap1. *Nat Cell Biol* **12**:213–223.
- Kramer ML, Schulz-Schaeffer WJ (2007) Presynaptic alpha-synuclein aggregates, not Lewy bodies, cause neurodegeneration in dementia with Lewy bodies. *J Neurosci* **27**:1405–1410.
- Kruger R, Kuhn W, Muller T, Woitalla D, Graeber M, Kosel S *et al* (1998) Ala30Pro mutation in the gene encoding alpha-synuclein in Parkinson's disease. *Nat Genet* **18**:106–108.
- Lee MK, Stirling W, Xu Y, Xu X, Qui D, Mandir AS *et al* (2002) Human alpha-synuclein-harboring familial Parkinson's disease-linked Ala-53 \rightarrow Thr mutation causes neurodegenerative disease with alpha-synuclein aggregation in transgenic mice. *Proc Natl Acad Sci U S A* **99**:8968–8973.
- Mak SK, McCormack AL, Manning-Bog AB, Cuervo AM, Di Monte DA (2010) Lysosomal degradation of alpha-synuclein in vivo. *J Biol Chem* **285**:13621–13629.
- Masliah E, Rockenstein E, Veinbergs I, Mallory M, Hashimoto M, Takeda A *et al* (2000) Dopaminergic loss and inclusion body formation in alpha-synuclein mice: implications for neurodegenerative disorders. *Science* **287**:1265–1269.
- Matsuoka Y, Vila M, Lincoln S, McCormack A, Picciano M, LaFrancois J *et al* (2001) Lack of nigral pathology in transgenic mice expressing human alpha-synuclein driven by the tyrosine hydroxylase promoter. *Neurobiol Dis* **8**:535–539.
- Mazzulli JR, Xu YH, Sun Y, Knight AL, McLean PJ, Caldwell GA *et al* (2011) Gaucher disease glucocerebrosidase and alpha-synuclein form a bidirectional pathogenic loop in synucleinopathies. *Cell* **146**:37–52.
- Nezis IP, Simonsen A, Sagona AP, Finley K, Gaumer S, Contamine D *et al* (2008) Ref(2)P, the *Drosophila melanogaster* homologue of mammalian p62, is required for the formation of protein aggregates in adult brain. *J Cell Biol* **180**:1065–1071.
- Odagiri S, Tanji K, Mori F, Kakita A, Takahashi H, Wakabayashi K (2012) Autophagic adapter protein NBR1 is localized in Lewy bodies and glial cytoplasmic inclusions and is involved in aggregate formation in alpha-synucleinopathy. *Acta Neuropathol* **124**:173–186.
- Okada K, Yanagawa T, Warabi E, Yamastu K, Uwayama J, Takeda K *et al* (2009) The alpha-glucosidase inhibitor acarbose prevents obesity and simple steatosis in sequestosome 1/A170/p62 deficient mice. *Hepatology* **39**:490–500.
- Pankiv S, Clausen TH, Lamark T, Brech A, Bruun JA, Outzen H *et al* (2007) p62/SQSTM1 binds directly to Atg8/LC3 to facilitate degradation of ubiquitinated protein aggregates by autophagy. *J Biol Chem* **282**:24131–24145.
- Paumier KL, Sukoff Rizzo SJ, Berger Z, Chen Y, Gonzales C, Kaftan E *et al* (2013) Behavioral characterization of A53T mice reveals early and late stage deficits related to Parkinson's disease. *PLoS ONE* **8**:e70274.

31. Polymeropoulos MH, Lavedan C, Leroy E, Ide SE, Dehejia A, Dutra A et al (1997) Mutation in the alpha-synuclein gene identified in families with Parkinson's disease. *Science* **276**:2045–2047.
32. Quan W, Kim HK, Moon EY, Kim SS, Choi CS, Komatsu M et al (2012) Role of hypothalamic proopiomelanocortin neuron autophagy in the control of appetite and leptin response. *Endocrinology* **153**:1817–1826.
33. Ramesh Babu J, Lamar Seibenhener M, Peng J, Strom AL, Kempainen R, Cox N et al (2008) Genetic inactivation of p62 leads to accumulation of hyperphosphorylated tau and neurodegeneration. *J Neurochem* **106**:107–120.
34. Richfield EK, Thiruchelvam MJ, Cory-Slechta DA, Wuertzer C, Gainetdinov RR, Caron MG et al (2002) Behavioral and neurochemical effects of wild-type and mutated human alpha-synuclein in transgenic mice. *Exp Neurol* **175**:35–48.
35. Riley BE, Kaiser SE, Shaler TA, Ng AC, Hara T, Hipp MS et al (2010) Ubiquitin accumulation in autophagy-deficient mice is dependent on the Nrf2-mediated stress response pathway: a potential role for protein aggregation in autophagic substrate selection. *J Cell Biol* **191**:537–552.
36. Rockenstein E, Mallory M, Hashimoto M, Song D, Shults CW, Lang I, Masliah E (2002) Differential neuropathological alterations in transgenic mice expressing alpha-synuclein from the platelet-derived growth factor and Thy-1 promoters. *J Neurosci Res* **68**:568–578.
37. Rodriguez A, Duran A, Selloum M, Champy MF, Diez-Guerra FJ, Flores JM et al (2006) Mature-onset obesity and insulin resistance in mice deficient in the signaling adapter p62. *Cell Metab* **3**:211–222.
38. Seibenhener ML, Babu JR, Geetha T, Wong HC, Krishna NR, Wooten MW (2004) Sequestosome 1/p62 is a polyubiquitin chain binding protein involved in ubiquitin proteasome degradation. *Mol Cell Biol* **24**:8055–8068.
39. Settembre C, Di Malta C, Polito VA, Garcia Arencibia M, Vetrini F, Erdin S et al (2011) TFEB links autophagy to lysosomal biogenesis. *Science* **332**:1429–1433.
40. Singleton AB, Farrer M, Johnson J, Singleton A, Hague S, Kachergus J et al (2003) alpha-Synuclein locus triplication causes Parkinson's disease. *Science* **302**:841.
41. Spillantini MG, Schmidt ML, Lee VM, Trojanowski JQ, Jakes R, Goedert M (1997) Alpha-synuclein in Lewy bodies. *Nature* **388**:839–840.
42. Tanji K, Mori F, Mimura J, Itoh K, Kakita A, Takahashi H, Wakabayashi K (2010) Proteinase K-resistant alpha-synuclein is deposited in presynapses in human Lewy body disease and A53T alpha-synuclein transgenic mice. *Acta Neuropathol* **120**:145–154.
43. Tanji K, Zhang HX, Mori F, Kakita A, Takahashi H, Wakabayashi K (2012) p62/sequestosome 1 binds to TDP-43 in brains with frontotemporal lobar degeneration with TDP-43 inclusions. *J Neurosci Res* **90**:2034–2042.
44. Unger EL, Eve DJ, Perez XA, Reichenbach DK, Xu Y, Lee MK, Andrews AM (2006) Locomotor hyperactivity and alterations in dopamine neurotransmission are associated with overexpression of A53T mutant human alpha-synuclein in mice. *Neurobiol Dis* **21**:431–443.
45. van der Putten H, Wiederhold KH, Probst A, Barbieri S, Mistl C, Danner S et al (2000) Neuropathology in mice expressing human alpha-synuclein. *J Neurosci* **20**:6021–6029.
46. Webb JL, Ravikumar B, Atkins J, Skepper JN, Rubinsztein DC (2003) Alpha-Synuclein is degraded by both autophagy and the proteasome. *J Biol Chem* **278**:25009–25013.
47. Winder-Rhodes SE, Garcia-Reitböck P, Ban M, Evans JR, Jacques TS, Kempainen A et al (2012) Genetic and pathological links between Parkinson's disease and the lysosomal disorder Sanfilippo syndrome. *Mov Disord* **27**:312–315.
48. Wooten MW, Geetha T, Babu JR, Seibenhener ML, Peng J, Cox N et al (2008) Essential role of sequestosome 1/p62 in regulating accumulation of Lys63-ubiquitinated proteins. *J Biol Chem* **283**:6783–6789.

SUPPORTING INFORMATION

Additional Supporting Information may be found in the online version of this article at the publisher's web-site:

Video Clip S1. The Morris water maze test. A wild-type mouse successfully reaches the platform within 30 s on the fourth day of training course.

Video Clip S2. The Morris water maze test. A p62-knockout mouse does not take an action within 60 s, and end up failing on the fourth day of training course.

RESEARCH

Open Access

Filamentous aggregations of phosphorylated α -synuclein in Schwann cells (Schwann cell cytoplasmic inclusions) in multiple system atrophy

Keiko Nakamura^{1,2}, Fumiaki Mori^{1*}, Tomoya Kon³, Kunikazu Tanji¹, Yasuo Miki¹, Masahiko Tomiyama³, Hidekachi Kurotaki⁴, Yasuko Toyoshima⁵, Akiyoshi Kakita⁶, Hitoshi Takahashi⁵, Masahito Yamada² and Koichi Wakabayashi¹

Abstract

Background: The histological hallmark of multiple system atrophy (MSA) is the presence of filamentous aggregations of phosphorylated α -synuclein in oligodendrocytes, referred to as glial cytoplasmic inclusions (GCIs). Although GCIs can occur widely in the central nervous system, accumulation of phosphorylated α -synuclein in Schwann cells has not been reported in MSA. We immunohistochemically examined the cranial and spinal nerves, peripheral ganglia and visceral autonomic nervous system of patients with MSA ($n = 14$) and control subjects ($n = 20$).

Results: In MSA, accumulation of phosphorylated α -synuclein was found in the cytoplasm of Schwann cells. These Schwann cell cytoplasmic inclusions (SCCIs) were also immunopositive for ubiquitin and p62. SCCIs were found in 12 of 14 patients with MSA (85.7 %). They were most frequent in the anterior nerve of the sacral cord and, to a lesser extent, in the cranial nerves (oculomotor, glossopharyngeal-vagus and hypoglossal nerves), and spinal and sympathetic ganglia. SCCIs were rarely found in the visceral organs. Immunoelectron microscopy demonstrated that the SCCIs consisted of abnormal filaments, 15–20 nm in diameter. No such inclusions were found in controls.

Conclusion: The present findings indicate that Schwann cells are also involved in the disease process of MSA.

Keywords: α -synuclein, Multiple system atrophy, Peripheral nerve, Schwann cell, Schwann cell cytoplasmic inclusion, Ultrastructure

Introduction

Multiple system atrophy (MSA) is an adult-onset neurodegenerative disorder manifested clinically as a combination of parkinsonism, cerebellar ataxia and autonomic dysfunction. MSA is now divided into two clinical subtypes: MSA with predominant parkinsonian features (MSA-P) and MSA with predominant cerebellar dysfunction (MSA-C) [1]. MSA is characterized pathologically by any combination of coexisting olivopontocerebellar atrophy, striatonigral degeneration and preganglionic

autonomic lesions [2]. The histological hallmark of MSA is widespread glial cytoplasmic inclusions (GCIs) in the central nervous system [3–6]. These GCIs can be visualized by silver staining such as the Gallyas-Braak method [3], and ultrastructurally they consist of granule-associated filaments 20–30 nm in diameter [3, 4, 7]. The major component of GCIs is α -synuclein [8], which is phosphorylated at Serine 129 [9] and ubiquitinated [10]. Although primary oligodendroglial pathology is the main feature of MSA [11–13], accumulation of phosphorylated α -synuclein is also consistently found in the neuronal cytoplasm, processes and nuclei [14]. Similar neuronal inclusions are found less frequently in the peripheral sympathetic ganglia [13, 15].

* Correspondence: neuropal@hirosaki-u.ac.jp

¹Department of Neuropathology, Institute of Brain Science, Hirosaki University Graduate School of Medicine, 5 Zaifu-cho, Hirosaki 036-8562, Japan

Full list of author information is available at the end of the article



Although immunoreactivity of non-phosphorylated α -synuclein has been reported in normal and neoplastic Schwann cells in the peripheral nervous system of humans [16], accumulation of phosphorylated α -synuclein in Schwann cells of patients with MSA has not been described hitherto. Here we immunohistochemically examined the cranial and spinal nerves, peripheral ganglia and visceral autonomic nervous system of patients with MSA using antibodies against phosphorylated α -synuclein, and report for the first time that Schwann cells in these patients are also affected by filamentous aggregations of phosphorylated α -synuclein.

Materials and methods

Subjects

Thirty-four autopsy cases were included in this study. Fourteen of the patients (age 49–79 years, average = 64.6 years) had a clinical history of MSA, which was confirmed at autopsy by the presence of numerous GCIs (Table 1). All of the MSA cases lacked Lewy body pathology. The clinical and neuropathological features of early MSA (cases 2 and 12) have been reported previously [17, 18]. Twenty patients used as controls (age 40–84 years, average = 70.0 years) were clinically and histopathologically free of neurodegenerative disease. This study was approved by the Institutional Ethics Committee of Hirosaki University Graduate School of Medicine.

Immunohistochemistry

Immunohistochemical analysis was carried out using formalin-fixed, paraffin-embedded, 4- μ m-thick sections from the midbrain, upper pons, medulla oblongata, spinal cord (cervical, thoracic, lumbar and sacral segments), and dorsal root and paravertebral sympathetic ganglia. Oculomotor and trigeminal nerves were examined at the level of the midbrain and upper pons, respectively. Glossopharyngeal and vagus nerves were examined at the level of the dorsal vagal nucleus. Since it was difficult to differentiate glossopharyngeal nerve from vagus nerve on the sections, these two nerves were described as a whole. Hypoglossal nerves were examined at the level of the gracile nucleus. Paraffin sections were also cut from block samples of the esophagus, stomach, small intestine, colon, heart, lung, thyroid, liver, pancreas, kidney, adrenal gland and urinary bladder. The sections were subjected to immunohistochemical processing using the avidin-biotin-peroxidase complex method with diaminobenzidine as the chromogen. The primary antibodies used were mouse monoclonal antibodies against phosphorylated α -synuclein (#64; Wako, Osaka, Japan; 1:5,000), aggregated α -synuclein (5G4; EMD Millipore, Temecula, CA, USA; 1:1,000) [19] and ubiquitin (1B3; MBL, Nagoya, Japan; 1:2,000), rabbit monoclonal antibody against phosphorylated α -synuclein (EP1536Y;

Abcam, Cambridge, UK; 1:5,000), and rabbit polyclonal antibody against p62 (MBL; 1:1,000). #64 is a monoclonal antibody against a synthetic peptide corresponding to amino acid residues 124–134 of human α -synuclein with a phosphorylated Serine 129 residue. EP1536Y is also a monoclonal antibody against a synthetic peptide corresponding to residues surrounding phosphorylated Serine 129 of human α -synuclein.

In addition to routine immunohistochemical techniques, selected sections from the spinal cord of MSA patients were first stained using the modified Gallyas-Braak method [20]. The spinal nerve roots were observed under a $\times 40$ objective lens. After removing the cover glasses from the slides using xylene, the specimens were decolorized in alcohol, then immunostained with anti-phosphorylated α -synuclein (Wako; 1:5,000). The spinal nerve roots were then observed again under a $\times 40$ objective lens.

Semiquantitative assessment of inclusions in Schwann cells was performed in each region by anti-phosphorylated α -synuclein immunolabeling. The numbers of inclusions were estimated as: –, none; +, 1 to 5 inclusions; ++, >5 inclusions.

Double immunostaining

To characterize the inclusion-bearing cells, anti-S-100 was used as a marker of Schwann cells [21], anti-tubulin polymerization promoting protein (TPPP)/p25 α as a marker of oligodendroglia [22], and anti-phosphorylated neurofilament as a marker of axons [23]. TPPP/p25 α is also known to be a component of GCIs in MSA [24]. Double immunofluorescence analysis was also performed to detect overlapping expression of phosphorylated α -synuclein and ubiquitin. Paraffin sections from the spinal cord of patients with MSA ($n = 3$) were processed for double-label immunofluorescence. Deparaffinized sections were blocked with donkey serum and then incubated overnight at 4 °C with a mixture of the monoclonal anti-phosphorylated α -synuclein (Wako; 1:500) and polyclonal anti-S-100 (DAKO, Tokyo, Japan; 1:500), anti-TPPP/p25 α (Sigma-Aldrich Japan, Tokyo, Japan; 1:500) or anti-ubiquitin (DAKO; 1:200), or a mixture of the mouse monoclonal anti-phosphorylated neurofilament (SMI31; Cosmo Bio, Tokyo, Japan; 1:500) and rabbit monoclonal anti-phosphorylated α -synuclein (Abcam; 1:500). The sections were then rinsed and incubated for 1 h at 38 °C with anti-rabbit IgG tagged with Alexa Fluor 488 (Invitrogen, Carlsbad, CA, USA; 1:200) and anti-mouse IgG tagged with Alexa Fluor 594 (Invitrogen; 1:200), or anti-rabbit IgG tagged with Alexa Fluor 594 (Invitrogen; 1:200) and anti-mouse IgG tagged with Alexa Fluor 488 (Invitrogen; 1:200). The sections were examined using an Olympus BX63 fluorescence microscope (Olympus, Tokyo, Japan).

Table 1 Summary of clinical findings of patients with multiple system atrophy (MSA)

Case No.	Age at death (years)	Gender	Disease duration (years)	Clinical diagnosis	Pathological diagnosis	Initial symptoms	Symptoms	Parkinsonian signs	Cerebellar signs	OH	UD	Constipation	Dyshidrosis	Impotence
1	49	F	7	MSA-P	MSA-P	limping	+	+	-	-	+	+	+	-
2	57	F	1	spinocerebellar degeneration	MSA-C	ataxia	-	-	+	-	-	-	-	-
3	58	M	7	SDS	MSA-C	UD, constipation, impotence	+	+	+	+	+	+	-	+
4	61	M	7	MSA-P	MSA-P	UD	+	+	+	-	+	+	-	-
5	61	F	4.5	MSA-P	MSA-P	tremor	+	+	+	-	+	+	-	-
6	63	F	3	MSA-P	MSA-P	gait disturbance	+	+	-	+	+	-	-	-
7	65	M	7	MSA-C	MSA-C	gait disturbance	+	+	+	-	+	+	-	-
8	65	M	14	MSA-C	MSA-P	gait disturbance	+	+	+	+	+	-	-	-
9	66	M	9	SDS	MSA-P	UD	+	+	+	+	+	+	-	-
10	66	M	13	MSA-C	MSA-C	sensory disturbance	+	+	+	+	+	+	-	-
11	69	M	8	SDS	MSA-C	snoring	-	-	+	+	+	+	-	-
12	71	F	<1	neurologically normal	MSA-C	none	-	-	-	-	-	-	-	-
13	75	M	8	progressive supranuclear palsy	MSA-P	gait disturbance	+	+	+	+	+	-	-	-
14	79	M	4	SDS	MSA-C	unsteady gait	-	-	+	+	+	-	-	-

OH, orthostatic hypotension; UD, urogenital dysfunction; SDS, Shy-Drager syndrome; +, present; -, absent

Immunoelectron microscopy

The anterior spinal nerve roots from a case of MSA (case 1) were processed for immunoelectron microscopy. Fifty-micrometer-thick vibratome sections were cut from the formalin-fixed tissue. The sections were incubated with a rabbit monoclonal anti-phosphorylated α -synuclein antibody (Abcam; 1:500), followed by incubation with a biotinylated secondary anti-rabbit IgG (Vector, Burlingame, CA, USA; 1:200) and avidin-biotin-peroxidase complex (Vector; 1:200), and the reaction was developed with diaminobenzidine. The immunolabeled sections were post-fixed in 1 % glutaraldehyde and 1 % osmium tetroxide, dehydrated in ethanol, and then embedded in Poly/Bed 812 resin (Polysciences, Inc., Warrington, PA, USA). Ultrathin sections were cut and viewed with a JEOL1230 electron microscope (JEOL Ltd., Tokyo, Japan).

Results

Morphology and immunohistochemical features

Immunostaining with anti-phosphorylated and anti-aggregated α -synuclein antibodies as well as the modified Gallyas-Braak method demonstrated widespread occurrence of GCIs throughout the brain and spinal cord of patients with MSA, but not in control subjects. The immunostaining with two monoclonal anti-phosphorylated α -synuclein antibodies and a monoclonal anti-aggregated α -synuclein antibody revealed Schwann cell cytoplasmic inclusions (SCCIs) in the cranial and spinal nerves, peripheral ganglia and visceral autonomic nervous system of MSA patients (Fig. 1a–q). They appeared crescent-shaped, coil-like, or cigar-shaped (Fig. 1d–f). The SCCIs enveloped the axons (Fig. 1g) and extended their processes from the cytoplasm to the axons (Fig. 1h, i). Similar inclusions were detected with anti-ubiquitin and anti-p62 antibodies (Fig. 1r, s). The inclusions could not be visualized with hematoxylin and eosin, Klüver-Barrera or Bodian's method. GCIs appeared argyrophilic with the modified Gallyas-Braak method, whereas SCCIs were stained only weakly or partially (Fig. 1 t, u). No such inclusions were found in controls.

To further characterize the inclusion-bearing cells, anti-S-100 was used as a Schwann cell marker, anti-TPPP/p25 α as an oligodendroglia marker, and phosphorylated neurofilament as an axon marker. Double immunofluorescence analysis revealed co-localization of phosphorylated α -synuclein and S-100 (Fig. 2a–c), but not TPPP/p25 α (Fig. 2d–f) or phosphorylated neurofilament (Fig. 2g–i), in the inclusions. Phosphorylated α -synuclein and ubiquitin were also co-localized in the inclusions (Fig. 2 j–l).

Immunoelectron microscopy

Pre-embedding immunoelectron microscopy demonstrated phosphorylated α -synuclein-immunoreactive structures in the cytoplasm of Schwann cells (Fig. 3a). The SCCIs

consisted of randomly arranged, loosely packed, granule-coated fibrils, approximately 15–20 nm in diameter (Fig. 3b). Immunodeposition was also detected in the outer and inner loops of the myelinated axons, where fibril formation was not apparent (Fig. 3c).

Distribution and incidence

The distribution and semiquantitative assessment of SCCIs in patients with MSA are summarized in Table 2. SCCIs were present in the cranial nerves (oculomotor, glossopharyngeal-vagus and hypoglossal nerves) and the spinal nerve roots. In the spinal nerve roots, SCCIs were found in the anterior nerves at the levels of the cervical, thoracic, lumbar and sacral segments, as well as in the posterior nerves in all the segments, except at the cervical level. They were also seen in the dorsal root and sympathetic ganglia and visceral autonomic nervous system.

SCCIs were found in 12 of 14 patients with MSA (85.7 %). They were most frequent in the anterior nerves of the sacral cord (69.2 %) and tended to be more frequent in the anterior than in the posterior nerves at each level. In one case of MSA (case 1), we examined the proximal and distal portions of the sacral nerve roots, and found that SCCIs were more numerous in the proximal than in the distal portion. In the cranial nerves, the inclusions were more frequent in the glossopharyngeal-vagus nerves (46.2 %) than in the oculomotor (28.6 %) and hypoglossal (9.1 %) nerves. SCCIs were found in 66.7 % and 33.3 % of the dorsal root and sympathetic ganglia, respectively. A small number of SCCIs were also found in the visceral organs in 2 of 14 patients with MSA (14.3 %): the subserosal nerves of the stomach in one patient (case 1) and the adrenal gland and urinary bladder in the other (case 12). There appeared to be no relationship between the frequency of SCCIs and the disease duration or clinical phenotype (MSA-C vs MSA-P) of patients with MSA.

Several neuronal cytoplasmic inclusions were found in the dorsal root ganglia in 2 of 9 MSA patients (cases 5 and 13) (Fig. 1 v, w). No such inclusions were found in the sympathetic ganglia or visceral organs.

Discussion

In the present study, we have demonstrated for the first time that phosphorylated α -synuclein accumulates in the cytoplasm of Schwann cells in patients with MSA. These SCCIs were also immunopositive for aggregated α -synuclein, ubiquitin and p62, a ubiquitin-proteasome system-related protein. Thus, the immunohistochemical profile of SCCIs is similar to that of GCIs [3, 7, 9, 19, 25]. Ultrastructurally, SCCIs were composed of randomly arranged, loosely packed, granule-coated fibrils, approximately 15–20 nm in diameter. Both GCIs and neuronal cytoplasmic inclusions also consisted of granule-coated fibrils, approximately 20–

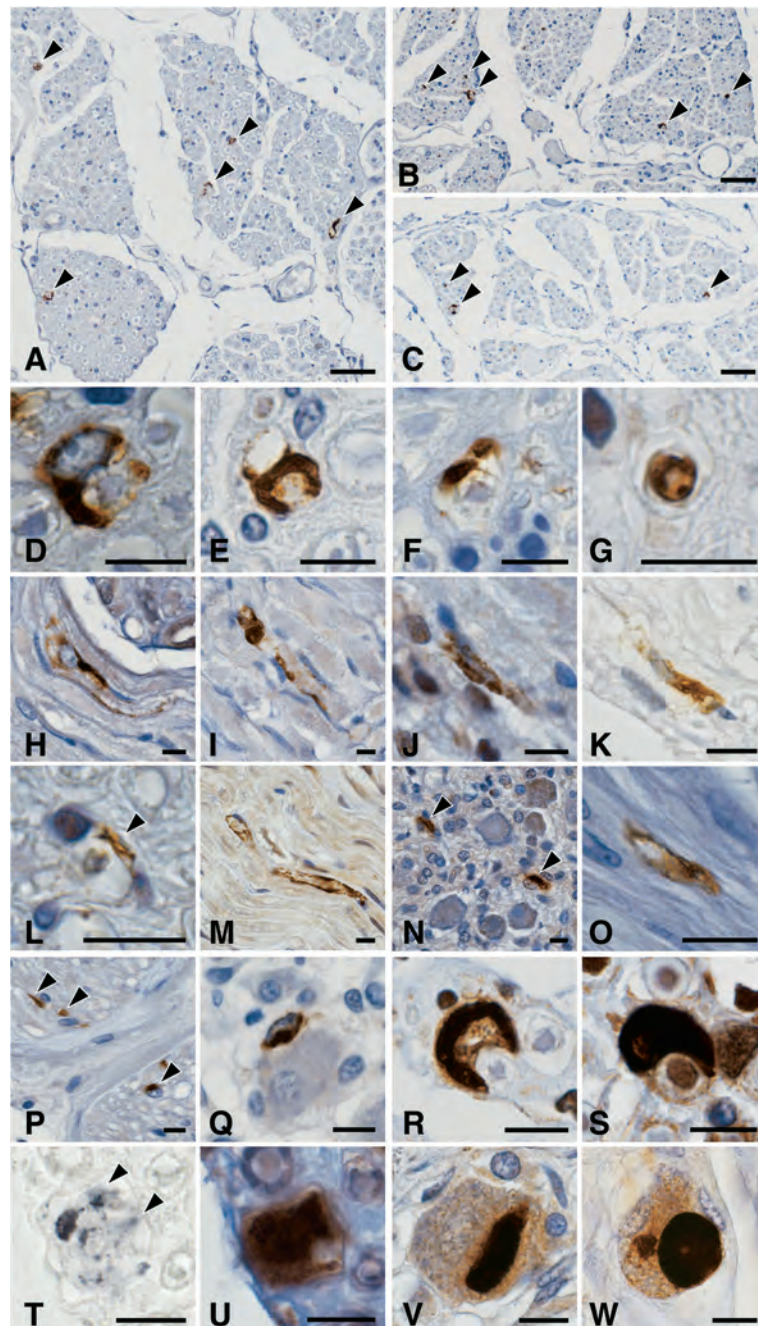
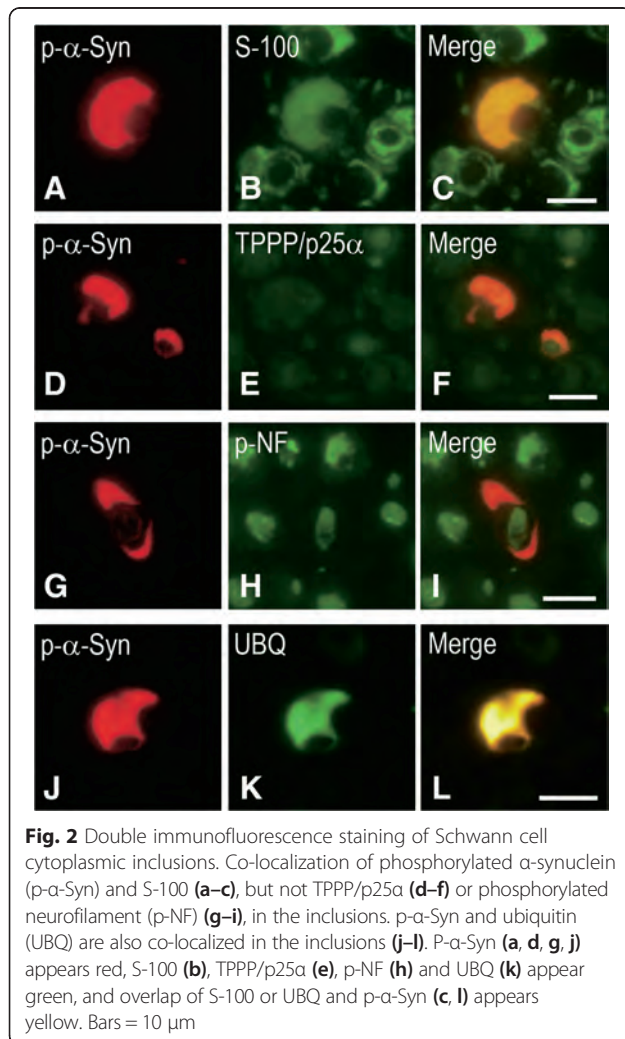


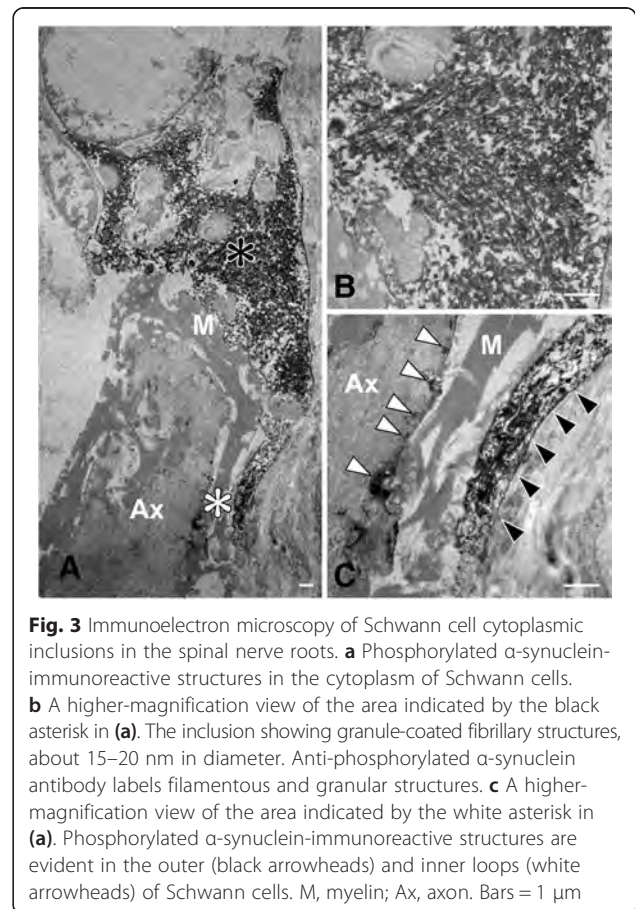
Fig. 1 Schwann cell (a–u) and neuronal (v, w) cytoplasmic inclusions stained with anti-phosphorylated α -synuclein (a, b, d–q, u–w), anti-aggregated α -synuclein (c), anti-ubiquitin (r), anti-p62 (s) and the Gallyas-Braak method (t). a–i Schwann cell cytoplasmic inclusions (SCCIs) (arrowheads) in the anterior spinal nerve roots. SCCIs displaying crescent-shaped (d), coil-like (e), or cigar-shaped morphology (f). SCCIs enwrapping the axons (g). SCCIs extending their processes to the axons (h, i). j–l SCCIs in the oculomotor (j), glossopharyngeal-vagus (k) and hypoglossal (l) nerves. m and n SCCIs in the dorsal root (m) and sympathetic (n) ganglia. o–q SCCIs in the stomach (o), adrenal gland (p) and urinary bladder (q). r and s SCCIs showing immunopositivity for ubiquitin (r) and p62 (s). t and u Sequential staining of the same sections of the spinal nerve with Gallyas-Braak (t) and anti-phosphorylated α -synuclein (u). SCCIs (arrowheads) are only weakly or partially stained with the Gallyas-Braak method. v and w Neuronal cytoplasmic inclusions in the dorsal root ganglia. Immunostaining with anti-phosphorylated α -synuclein antibodies (#64 for a, e, g–q, u–w; and EP1536Y for b, d, f). Bars = 50 μ m in a–c; 10 μ m in d–w



30 nm in diameter [3, 4, 7, 26–28]. These findings indicate that Schwann cells are also involved in the disease process of MSA.

SCCIs were found in 12 of 14 patients with MSA (85.7 %) in the present study. GCIs were consistently found in the brainstem and spinal cord in all of the MSA patients. By contrast, SCCIs were not observed in the cranial or spinal nerves in three patients (cases 2, 12 and 14), two of whom had early MSA [17, 18]. These findings suggest that the occurrence of GCIs precedes that of SCCIs in MSA.

Recently, expression of human α -synuclein has been reported in Schwann cells ensheathing the nerve fibers of the urinary bladder in a transgenic mouse model of MSA showing oligodendroglial overexpression of human α -synuclein under the control of the proteolipid protein promoter [29]. Urodynamic analysis revealed a less efficient and unstable urinary bladder in this MSA mouse model. In human MSA, widespread occurrence of GCIs in the central nervous system is a cardinal pathological



feature [3–6]. Moreover, neuronal cytoplasmic and nuclear inclusions have been observed in the inferior olivary and pontine nuclei, substantia nigra, putamen and cerebral cortex in patients with MSA [14, 28]. Filamentous aggregates of α -synuclein are also found in neurons in the sympathetic ganglia [14, 15]. In the present study, we further demonstrated that accumulation of phosphorylated α -synuclein occurs in the neuronal cytoplasm in the dorsal root ganglia. Sural nerve biopsy from patients with MSA shows a 23 % reduction of unmyelinated fibers (sensory afferent fibers and post-ganglionic sympathetic fibers) [30]. Mild degeneration of cardiac sympathetic nerves can occur in MSA [31]. Thus, MSA is a glio-neuronal α -synucleinopathy involving the central and peripheral nervous systems.

It is noteworthy that SCCIs tend to be more frequent in the peripheral nerves associated with autonomic function, i.e. glossopharyngeal-vagus nerves, and anterior spinal nerves of the thoracic and sacral cord. The vagus nerve is a mixed cranial nerve containing axons of branchiomeric motor neurons, parasympathetic preganglionic fibers, visceral afferent fibers, and somatic sensory afferent fibers. The glossopharyngeal nerve is related closely to the vagus nerve, sharing common medullary

Table 2 Distribution and frequency of Schwann cell cytoplasmic inclusions (SCCIs) in patients with multiple system atrophy

Case No.	Cranial nerves				Spinal nerves								DRG	SG	Visceral organs
	III	V	IX/X	XII	C		T		L		S				
					A	P	A	P	A	P	A	P			
1	NE	-	+	+	NE	NE	+	+	++	-	++	+	NE	NE	+(stomach)
2	-	-	-	-	-	-	-	-	-	-	-	-	-	-	-
3	-	NE	+	-	+	-	-	-	+	-	+	+	+	-	-
4	-	-	+	NE	NE	NE	+	-	+	-	+	-	NE	NE	-
5	+	NE	-	-	-	-	+	-	+	-	+	-	-	+	-
6	NE	NE	+	-	+	-	-	-	-	-	+	-	+	-	-
7	NE	NE	-	-	+	-	-	-	-	-	+	-	+	-	-
8	++	NE	+	NE	-	-	-	-	-	-	-	+	+	-	-
9	NE	-	+	NE	+	-	+	+	-	-	+	+	NE	NE	-
10	NE	NE	-	-	+	-	+	-	-	-	+	-	+	-	-
11	-	NE	-	-	-	-	-	-	-	+	+	-	-	+	-
12	-	-	-	-	-	-	-	-	-	-	-	-	NE	NE	+(adrenal, urinary bladder)
13	NE	NE	-	-	-	-	+	-	-	-	-	-	+	+	-
14	NE	-	NE	-	-	-	-	-	-	-	NE	NE	NE	NE	-
Percent positive for inclusions	28.6	0	46.2	9.1	41.7	0	42.9	14.3	28.6	7.1	69.2	30.8	66.7	33.3	14.3

DRG, dorsal root ganglia; SG, sympathetic ganglia; C, cervical; T, thoracic; L, lumbar; S, sacral; A, anterior; P, posterior. Semiquantitative assessment: -, none; +, 1 to 5 SCCIs per area; ++, more than 5 SCCIs per area; NE, not examined

nuclei and having similar functional components [32]. The sympathetic ganglia receive preganglionic fibers from the intermediolateral nucleus of the spinal cord through the anterior roots of all the thoracic and the upper two lumbar nerves [32]. The sacral preganglionic parasympathetic fibers exit from the sacral cord and go to the terminal ganglia of the pelvic plexuses, as well as to the myenteric and submucosal plexuses of the descending colon and rectum [32]. The widespread occurrence of SCCIs, at least in part, may play a role for the manifestation of a variety of autonomic symptoms in MSA.

Using the modified Gallyas-Braak method, GCIs were positive whereas SCCIs were stained only weakly or partially. Ultrastructurally, the constituent filaments of SCCIs (approximately 15–20 nm) appeared thinner than those of GCIs (approximately 20–30 nm) [3, 4, 7]. Phosphorylated α -synuclein-immunoreactive filamentous inclusions are also found in oligodendrocytes and astrocytes in the brains of patients with Parkinson’s disease and dementia with Lewy bodies [33–35] and are argyrophilic with the modified Gallyas-Braak method [36], suggesting that the process of α -synuclein aggregation in glial cells may differ somewhat between the central and peripheral nervous systems.

Cranial nerves are composed of myelinated and unmyelinated fibers in various proportions [37]. The nerve fibers of the anterior spinal nerve roots projecting to the autonomic ganglia are myelinated [38]. Both myelinated and unmyelinated fibers in the peripheral nervous

system are enveloped with Schwann cells. Although the number of samples was small, our immunoelectron microscopy examination demonstrated that inclusion-bearing Schwann cells, at least in part, ensheath the myelinated fibers. Considering that postganglionic sympathetic nerve fibers are unmyelinated [39] and a small number of SCCIs were observed in the visceral autonomic nervous system in MSA, SCCI formation may also occur in Schwann cells ensheathing the unmyelinated fibers. Moreover, immunodeposition was also found in the outer and inner loops of Schwann cells. In the central nervous system, constituent filaments of GCIs are not evident in the outer or inner loops of oligodendrocytes in MSA [7]. By contrast, tau- and Gallyas-positive filamentous structures are found in the outer and inner loops of oligodendrocytes in progressive supranuclear palsy and corticobasal degeneration [39–41]. These findings suggest that phosphorylated α -synuclein pathology develops both in the perikarya and distal processes of Schwann cells, whereas the perikarya is chiefly involved in oligodendrocytes in MSA.

It is unclear how aggregated α -synuclein in the cytoplasm of Schwann cells interacts with the axon, myelin and Schwann cell itself. Both oligodendrocytes and Schwann cells are essential for axonal function and integrity. These enwrapping glia support axonal growth and myelination by transfer of metabolic substrates and secretion of neurotrophic factors [42]. Glial cell line-derived neurotrophic factor (GDNF) is one of the

neurotrophic factors produced by oligodendrocytes [43] and Schwann cells [44]. The level of GDNF is significantly decreased in the frontal white matter and cerebellum of human MSA patients and in the brain of a MSA mouse model overexpressing human α -synuclein under the control of the myelin basic protein promoter [45]. Intraventricular infusion of GDNF improves behavioral deficits and ameliorates the neurodegenerative pathology in this MSA mouse model [45]. GDNF induces Schwann cell migration and axonal regeneration in the peripheral nervous system [46] and also prevents atrophy of facial motoneurons following axotomy [47]. Liver kinase B1 (LKB1) is also a crucial regulator of the major metabolic pathway in Schwann cells, which are central to axonal stability [48]. Deletion of LKB1 leads to energy depletion, mitochondrial dysfunction, abnormalities of lipid homeostasis and increased lactate release in Schwann cells [48]. The loss of viability in human neuroblastoma cells overexpressing wild-type α -synuclein is associated with reduced activation of intracellular energy sensors, including LKB1 [49]. α -Synuclein-overexpressing rat primary neurons also display lower LKB1 activity [49]. Based on the above findings, it is likely that overexpression of α -synuclein in Schwann cells impairs the activity of neurotrophic factors, leading to axonal destabilization in peripheral nerves.

The origin of α -synuclein in SCCIs is uncertain. Immunoreactivity of non-phosphorylated α -synuclein has been reported in normal and neoplastic Schwann cells in the peripheral nervous system of humans [16]. Therefore, it is possible to consider that overexpression of α -synuclein in Schwann cells would cause SCCI formation. As another possible mechanism, neuron-to-neuron transmission of α -synuclein fibrils through anterograde axonal transport has been demonstrated in primary cortical mouse neurons *in vitro* [50]. The fact that SCCIs tended to appear more frequently in the proximal than in the distal spinal nerve roots is appropriate for anterograde transport of α -synuclein. α -Synuclein in SCCIs could be derived from neurons. Future studies will be necessary to clarify the origin of α -synuclein in MSA Schwann cells.

Conclusion

In conclusion, we have provided for the first time evidence that filamentous aggregation of phosphorylated α -synuclein occurs in Schwann cells in patients with MSA. Similar inclusions are also observed in the oligodendrocytes and neurons of the central nervous system as well as in neurons of the peripheral ganglia. Both central and peripheral mechanisms may contribute to the neurodegeneration in MSA.

Competing interests

The authors declare that they have no competing interests.

Authors' contributions

KN, FM and KW designed the study and analyzed data. KN, FM, KT, HK, YT, AK, HT and KW performed the pathological observations and evaluations. TK, YM and MT performed the clinical evaluations. FM, MY and KW supervised the whole process of the study. KN, FM and KW wrote the manuscript. All authors read and approved the final manuscript.

Acknowledgements

The authors wish to express their gratitude to M. Nakata and A. Ono for technical assistance.

Funding

This work was supported by JSPS KAKENHI Grant Numbers 26430049 (F.M.), 26430050 (K.T.), 26860655 (Y.M.) and 24300131 (K.W.), a Grant for Hiroshima University Institutional Research (K.W.), the Collaborative Research Project (2014–2508) of the Brain Research Institute, Niigata University (F.M.), the Research Committee for Ataxic Disease (K.W.) from the Ministry of Health, Labour and Welfare, Japan, and an Intramural Research Grant (24–5) for Neurological and Psychiatric Disorders of NCNP (K.W.).

Author details

¹Department of Neuropathology, Institute of Brain Science, Hiroshima University Graduate School of Medicine, 5 Zaifu-cho, Hiroshima 036-8562, Japan. ²Department of Neurology and Neurobiology of Ageing, Kanazawa University Graduate School of Medical Science, Kanazawa, Japan. ³Department of Neurology, Aomori Prefectural Central Hospital, Aomori, Japan. ⁴Department of Pathology, Aomori Prefectural Central Hospital, Aomori, Japan. ⁵Department of Pathology, Brain Research Institute, University of Niigata, Niigata, Japan. ⁶Department of Pathological Neuroscience, Center for Bioresource-based Researches, Brain Research Institute, University of Niigata, Niigata, Japan.

Received: 26 March 2015 Accepted: 30 April 2015

Published online: 21 May 2015

References

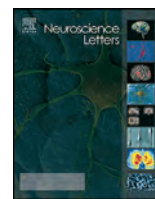
- Gilman S, Wenning GK, Low PA, Brooks DJ, Mathias CJ, Trojanowski JQ, Wood NW, Colosimo C, Dürr A, Fowler CJ, Kaufmann H, Klockgether T, Lees A, Poewe W, Quinn N, Revesz T, Robertson D, Sandroni P, Seppi K, Vidailhet M (2008) Second consensus statement on the diagnosis of multiple system atrophy. *Neurology* 71:670–676
- Graham JG, Oppenheimer DR (1969) Orthostatic hypotension and nicotine sensitivity in a case of multiple system atrophy. *J Neurol Neurosurg Psychiatr* 32:28–34
- Papp MI, Kahn JE, Lantos PL (1989) Glial cytoplasmic inclusions in the CNS of patients with multiple system atrophy (striatonigral degeneration, olivopontocerebellar atrophy and Shy-Drager syndrome). *J Neurol Sci* 94:79–100
- Nakazato Y, Yamazaki H, Hirato J, Ishida Y, Yamaguchi H (1990) Oligodendroglial microtubular tangles in olivopontocerebellar atrophy. *J Neuropathol Exp Neurol* 49:521–530
- Papp MI, Lantos PL (1994) The distribution of oligodendroglial inclusions in multiple system atrophy and its relevance to clinical symptomatology. *Brain* 117:235–243
- Ozawa T, Paviour D, Quinn NP, Josephs KA, Sangha H, Kilford L, Healy DG, Wood NW, Lees AJ, Holton JL, Revesz T (2004) The spectrum of pathological involvement of the striatonigral and olivopontocerebellar systems in multiple system atrophy: clinicopathological correlations. *Brain* 127:2657–2671
- Murayama S, Arima K, Nakazato Y, Satoh J, Oda M, Inose T (1992) Immunocytochemical and ultrastructural studies of neuronal and oligodendroglial cytoplasmic inclusions in multiple system atrophy. 2. Oligodendroglial cytoplasmic inclusions. *Acta Neuropathol* 84:32–38
- Wakabayashi K, Yoshimoto M, Tsuji S, Takahashi H (1998) α -Synuclein immunoreactivity in glial cytoplasmic inclusions in multiple system atrophy. *Neurosci Lett* 249:180–182
- Fujiwara H, Hasegawa M, Dohmae N, Kawashima A, Masliah E, Goldberg MS, Shen J, Takio K, Iwatsubo T (2002) α -Synuclein is phosphorylated in synucleinopathy lesions. *Nat Cell Biol* 4:160–164
- Hasegawa M, Fujiwara H, Nonaka T, Wakabayashi K, Takahashi H, Lee VM, Trojanowski JQ, Mann D, Iwatsubo T (2002) Phosphorylated α -synuclein is ubiquitinated in α -synucleinopathy lesions. *J Biol Chem* 277:49071–49076

11. Wenning GK, Stefanova N, Jellinger KA, Poewe W, Schlossmacher MG (2008) Multiple system atrophy: a primary oligodendroglialopathy. *Ann Neurol* 64:239–246
12. Fellner L, Stefanova N (2013) The role of glia in alpha-synucleinopathies. *Mol Neurobiol* 47:575–586
13. Jellinger KA (2014) Neuropathology of multiple system atrophy: new thoughts about pathogenesis. *Mov Disord* 29:1720–1741
14. Nishie M, Mori F, Fujiwara H, Hasegawa M, Yoshimoto M, Iwatsubo T, Takahashi H, Wakabayashi K (2004) Accumulation of phosphorylated α -synuclein in the brain and peripheral ganglia of patients with multiple system atrophy. *Acta Neuropathol* 107:292–298
15. Sone M, Yoshida M, Hashizume Y, Hishikawa N, Sobue G (2005) α -Synuclein-immunoreactive structure formation is enhanced in sympathetic ganglia of patients with multiple system atrophy. *Acta Neuropathol* 110:19–26
16. Mori F, Inenaga C, Yoshimoto M, Umezue H, Tanaka R, Takahashi H, Wakabayashi K (2002) α -Synuclein immunoreactivity in normal and neoplastic Schwann cells. *Acta Neuropathol* 103:145–151
17. Wakabayashi K, Mori F, Nishie M, Oyama Y, Kurihara A, Yoshimoto M, Kuroda N (2005) An autopsy case of early ("minimal change") olivopontocerebellar atrophy (multiple system atrophy-cerebellar). *Acta Neuropathol* 110:185–190
18. Kon T, Mori F, Tanji K, Miki Y, Wakabayashi K (2013) An autopsy case of preclinical multiple system atrophy (MSA-C). *Neuropathology* 33:667–672
19. Kovacs GG, Wagner U, Dumont B, Pikkarainen M, Osman AA, Streichenberger N, Leisser I, Verchère J, Baron T, Alafuzoff I, Budka H, Perret-Liaudet A, Lachmann I (2012) An antibody with high reactivity for disease-associated α -synuclein reveals extensive brain pathology. *Acta Neuropathol* 124:37–50
20. Wakabayashi K, Takahashi H (1996) Similarities and differences among progressive supranuclear palsy, corticobasal degeneration and Pick's disease. *Neuropathology* 16:262–268
21. Stefansson K, Wollmann RL, Moore BW (1982) Distribution of S-100 protein outside the central nervous system. *Brain Res* 234:309–317
22. Takahashi M, Tomizawa K, Fujita SC, Sato K, Uchida T, Imahori K (1993) A brain-specific protein p25 is localized and associated with oligodendrocytes, neuropil, and fiber-like structures of the CA3 hippocampal region in the rat brain. *J Neurochem* 60:228–235
23. Xiao J, Monteiro MJ (1994) Identification and characterization of a novel (115 kDa) neurofilament-associated kinase. *J Neurosci* 14:1820–1833
24. Kovács GG, László L, Kovács J, Jensen PH, Lindersson E, Botond G, Molnár T, Perczel A, Hudecz F, Mezo G, Erdei A, Tirián L, Lehotzky A, Gelpi E, Budka H, Ovádi J (2004) Natively unfolded tubulin polymerization promoting protein TPPP/p25 is a common marker of alpha-synucleinopathies. *Neurobiol Dis* 17:155–162
25. Kuusisto E, Kauppinen T, Alafuzoff I (2008) Use of p62/SQSTM1 antibodies for neuropathological diagnosis. *Neuropathol Appl Neurobiol* 34:169–180
26. Kato S, Nakamura H (1990) Cytoplasmic argyrophilic inclusions in neurons of pontine nuclei in patients with olivopontocerebellar atrophy: immunohistochemical and ultrastructural studies. *Acta Neuropathol* 79:584–594
27. Papp MI, Lantos PL (1992) Accumulation of tubular structures in oligodendroglial and neuronal cells as the basic alteration in multiple system atrophy. *J Neurol Sci* 107:172–182
28. Arima K, Murayama S, Mukoyama M, Inose T (1992) Immunocytochemical and ultrastructural studies of neuronal and oligodendroglial cytoplasmic inclusions in multiple system atrophy. 1. Neuronal cytoplasmic inclusions. *Acta Neuropathol* 83:453–460
29. Boudes M, Uvin P, Pinto S, Voets T, Fowler CJ, Wenning GK, De Ridder D, Stefanova N (2013) Bladder dysfunction in a transgenic mouse model of multiple system atrophy. *Mov Disord* 28:347–355
30. Kanda T, Tsukagoshi H, Oda M, Miyamoto K, Tanabe H (1996) Changes of unmyelinated nerve fibers in sural nerve in amyotrophic lateral sclerosis, Parkinson's disease and multiple system atrophy. *Acta Neuropathol* 91:145–154
31. Orimo S, Kanazawa T, Nakamura A, Uchihara T, Mori F, Kakita A, Wakabayashi K, Takahashi H (2007) Degeneration of cardiac sympathetic nerve can occur in multiple system atrophy. *Acta Neuropathol* 113:81–86
32. Parent A (1996) *Carpenter's human neuroanatomy*, 9th edn. Williams & Wilkins, Philadelphia
33. Wakabayashi K, Hayashi S, Yoshimoto M, Kudo H, Takahashi H (2000) NACP/ α -synuclein-positive filamentous inclusions in astrocytes and oligodendrocytes of Parkinson's disease brains. *Acta Neuropathol* 99:14–20
34. Hishikawa N, Hashizume Y, Yoshida M, Sobue G (2001) Widespread occurrence of argyrophilic glial inclusions in Parkinson's disease. *Neuropathol Appl Neurobiol* 27:362–372
35. Piao Y-S, Wakabayashi K, Hayashi S, Yoshimoto M, Takahashi H (2000) Aggregation of α -synuclein/NACP in the neuronal and glial cells in diffuse Lewy body disease: a survey of six patients. *Clin Neuropathol* 19:163–169
36. Wakabayashi K, Takahashi H (1996) Gallyas-positive, tau-negative glial inclusions in Parkinson's disease midbrain. *Neurosci Lett* 217:133–136
37. Takenoshita H (1987) Electron microscopic nerve fiber analysis of the cranial nerves in the rat. *Fukushima Igaku Zasshi* 37:223–243
38. Hillarp NA (1960) Peripheral autonomic mechanisms. In: Field J, Magoun HW, Hall VE (eds) *Handbook of physiology*. American Physiological Society, Washington DC
39. Ikeda K, Akiyama H, Haga C, Kondo H, Arima K, Oda T (1994) Argyrophilic thread-like structure in corticobasal degeneration and supranuclear palsy. *Neurosci Lett* 174:157–159
40. Arima K (1996) Tubular profile of the gallyas- and tau-positive argyrophilic threads in corticobasal degeneration: an electronmicroscopic study. *Neuropathology* 16:65–70
41. Arima K, Nakamura M, Sunohara N, Ogawa M, Anno M, Izumiya Y, Hirai S, Ikeda K (1997) Ultrastructural characterization of the tau-immunoreactive tubules in the oligodendroglial perikarya and their inner loop processes in progressive supranuclear palsy. *Acta Neuropathol* 93:558–566
42. Beirowski B (2013) Concepts for regulation of axon integrity by enwrapping glia. *Front Cell Neurosci* 7:256
43. Wilkins A, Majed H, Layfield R, Compston A, Chandran S (2003) Oligodendrocytes promote neuronal survival and axonal length by distinct intracellular mechanisms: a novel role for oligodendrocyte-derived glial cell line-derived neurotrophic factor. *J Neurosci* 23:4967–4974
44. Bär KJ, Saldanha GJ, Kennedy AJ, Facer P, Birch R, Carlstedt T, Anand P (1998) GDNF and its receptor component Ret in injured human nerves and dorsal root ganglia. *Neuroreport* 9:43–47
45. Ubhi K, Rockenstein E, Mante M, Inglis C, Adame A, Patrick C, Whitney K, Masliah E (2010) Neurodegeneration in a transgenic mouse model of multiple system atrophy is associated with altered expression of oligodendroglial-derived neurotrophic factors. *J Neurosci* 30:6236–6246
46. Chu TH, Wang L, Guo A, Chan VW, Wong CW, Wu W (2012) GDNF-treated acellular nerve graft promotes motoneuron axon regeneration after implantation into cervical root avulsed spinal cord. *Neuropathol Appl Neurobiol* 38:681–695
47. Henderson CE, Phillips HS, Pollock RA, Davies AM, Lemeulle C, Armanini M, Simpson LC, Moffet B, Vandlen RA, Koliatos VE, Rosenthal A (1994) GDNF: a potent survival factor for motoneurons present in peripheral nerve and muscle. *Science* 266:1062–1064
48. Beirowski B, Babetto E, Golden JP, Chen YJ, Yang K, Gross RW, Patti GJ, Milbrandt J (2014) Metabolic regulator LKB1 is crucial for Schwann cell-mediated axon maintenance. *Nat Neurosci* 17:1351–1361
49. Dulovic M, Jovanovic M, Xilouri M, Stefanis L, Harhaji-Trajkovic L, Kravic-Stevovic T, Paunovic V, Ardah MT, El-Agnaf OM, Kostic V, Markovic I, Trajkovic V (2014) The protective role of AMP-activated protein kinase in alpha-synuclein neurotoxicity in vitro. *Neurobiol Dis* 63:1–11
50. Freundt EC, Maynard N, Clancy EK, Roy S, Bousset L, Sourigues Y, Covert M, Melki R, Kirkegaard K, Brahm M (2012) Neuron-to-neuron transmission of α -synuclein fibrils through axonal transport. *Ann Neurol* 72:517–524



Contents lists available at ScienceDirect

Neuroscience Letters

journal homepage: www.elsevier.com/locate/neulet

Research paper

Sortilin-related receptor CNS expressed 2 (SorCS2) is localized to Bunina bodies in amyotrophic lateral sclerosis

Fumiaki Mori^{a,*}, Yasuo Miki^a, Kunikazu Tanji^a, Akiyoshi Kakita^b, Hitoshi Takahashi^c, Jun Utsumi^d, Hidenao Sasaki^d, Koichi Wakabayashi^a^a Department of Neuropathology, Institute of Brain Science, Hirosaki University Graduate School of Medicine, Hirosaki, Japan^b Department of Pathological Neuroscience, Center for Bioresource-based Researches, Brain Research Institute, University of Niigata, Niigata, Japan^c Department of Pathology, Brain Research Institute, University of Niigata, Niigata, Japan^d Department of Neurology, Hokkaido University Graduate School of Medicine, Sapporo, Japan

HIGHLIGHTS

- Amyotrophic lateral sclerosis (ALS) is one of the most devastating neurodegenerative disease.
- ALS-specific Bunina bodies are immunoreactive for SorCS2, a member of vacuolar protein sorting 10 family proteins (VPS10Ps).
- Immunoreactivity for VPS10Ps, sortilin and SorLA, is decreased in anterior horn cells of ALS patients.
- VPS10Ps may be involved in the pathomechanisms of ALS.

ARTICLE INFO

Article history:

Received 18 June 2015

Received in revised form 7 September 2015

Accepted 24 September 2015

Available online 28 September 2015

Keywords:

Amyotrophic lateral sclerosis

Bunina bodies

Immunohistochemistry

Sortilin-related receptor CNS expressed 2

Vacuolar protein sorting 10 family proteins

ABSTRACT

Sortilin-related receptor CNS expressed 2 (SorCS2) is one of the vacuolar protein sorting 10 family proteins (VPS10Ps) that have pleiotropic roles in protein trafficking and intracellular and intercellular signaling. Bunina bodies (BBs) are specifically detected in the lower motor neurons in patients with amyotrophic lateral sclerosis (ALS). BBs are immunolabeled with antibodies against cystatin C, transferrin and peripherin and are considered to originate from the endoplasmic reticulum, which is part of the protein sorting pathway. The present study investigated whether VPS10Ps are involved in the formation of BBs in ALS. We immunohistochemically examined the spinal cord from patients with ALS and control subjects using antibodies against VPS10Ps (sortilin, SorLA, SorCS1, SorCS2 and SorCS3). In normal controls, antibodies against VPS10Ps immunolabeled the cytoplasm of anterior horn cells in a fine granular pattern. In ALS, almost all BBs (95.1%) were strongly immunopositive for SorCS2, and immunoreactivity for sortilin and SorLA was decreased in anterior horn cells. These findings suggest that VPS10Ps may be involved in the disease process of ALS.

© 2015 Elsevier Ireland Ltd. All rights reserved.

1. Introduction

Sortilin-related receptor CNS expressed 2 (SorCS2) is a type I transmembrane glycoprotein receptor that belongs to the mammalian vacuolar protein sorting 10 protein (VPS10P) family [6,19]. VPS10Ps include sortilin, sorting protein-related receptor with A-type repeats (SorLA), SorCS1, SorCS2, and SorCS3 proteins. All SorCS proteins are expressed predominantly in the brain, especially

during development [6,8,19]. Interactions have been documented between VPS10Ps and retromer coat complex (VPS35 and VPS26), a key component of the intracellular trafficking apparatus that sorts cargo from the early endosome to the trans-Golgi network [9]. In recent years, it has been shown that a number of neurodegenerative diseases including Alzheimer's disease (AD), Parkinson's disease and frontotemporal lobar degeneration (FTLD) are characterized by the misprocessing and missorting of intracellular proteins (amyloid precursor protein, tau, α -synuclein, TDP-43, FUS) within endosomal-lysosomal pathways. Dysfunction within these pathways is proposed to be a major contributing factor to disease progression [9].

Bunina bodies (BBs) are small round eosinophilic inclusions, 1–5 μ m in diameter, observed in the lower motor neurons of

* Corresponding author at: Department of Neuropathology, Institute of Brain Science, Hirosaki University Graduate School of Medicine, 5 Zaifu-cho, Hirosaki 036-8562, Japan. Fax: +81 172 39 5132.

E-mail address: neuropal@hirosaki-u.ac.jp (F. Mori).

patients with amyotrophic lateral sclerosis (ALS), one of the most prevalent TDP-43 proteinopathies. BBs are immunolabeled with antibodies against cystatin C [16], transferrin [10] and peripherin [11]. BBs are considered to originate from the endoplasmic reticulum [21,23], which serves many general functions, including the folding of protein molecules in sacs called cisternae and the transport of synthesized proteins in vesicles to the Golgi apparatus. Our previous immunoelectron microscopy observations indicating that

cystatin C is localized to the vesicular membranous structures of BBs [13] prompted us to examine whether VPS10Ps are involved in the formation of BBs. Therefore, we immunohistochemically investigated the expression of VPS10Ps in spinal cord samples from patients with ALS and control subjects. Here we report that SorCS2 immunoreactivity is detectable in BBs in anterior horn cells (AHCs) and that immunoreactivity for sortilin and SorLA is decreased in AHCs of ALS patients in comparison to controls.

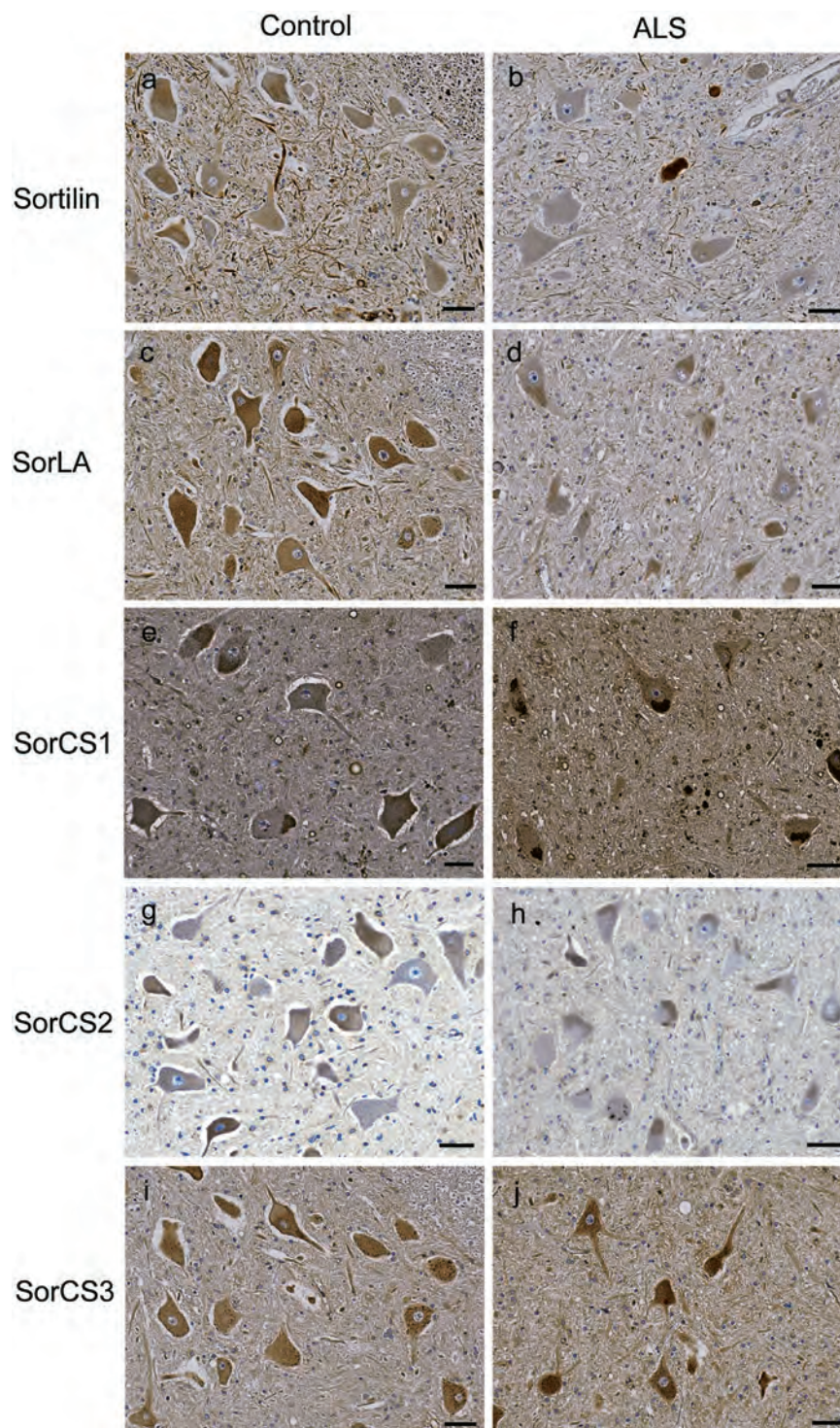


Fig. 1. Light micrographs of the anterior horn of the lumbar cord of normal controls (a,c,e,g,i) and patients with amyotrophic lateral sclerosis (ALS) (b,d,f,h,j), showing immunoreactivity for sortilin (a,b), sorting protein-related receptor with A-type repeats (SorLA) (c,d), sortilin-related receptor CNS expressed 1 (SorCS1) (e,f), SorCS2 (g,h), and SorCS3 (i,j). In ALS, immunoreactivity for sortilin and SorLA is decreased in anterior horn cells (b,d). Bars = 50 μ m.

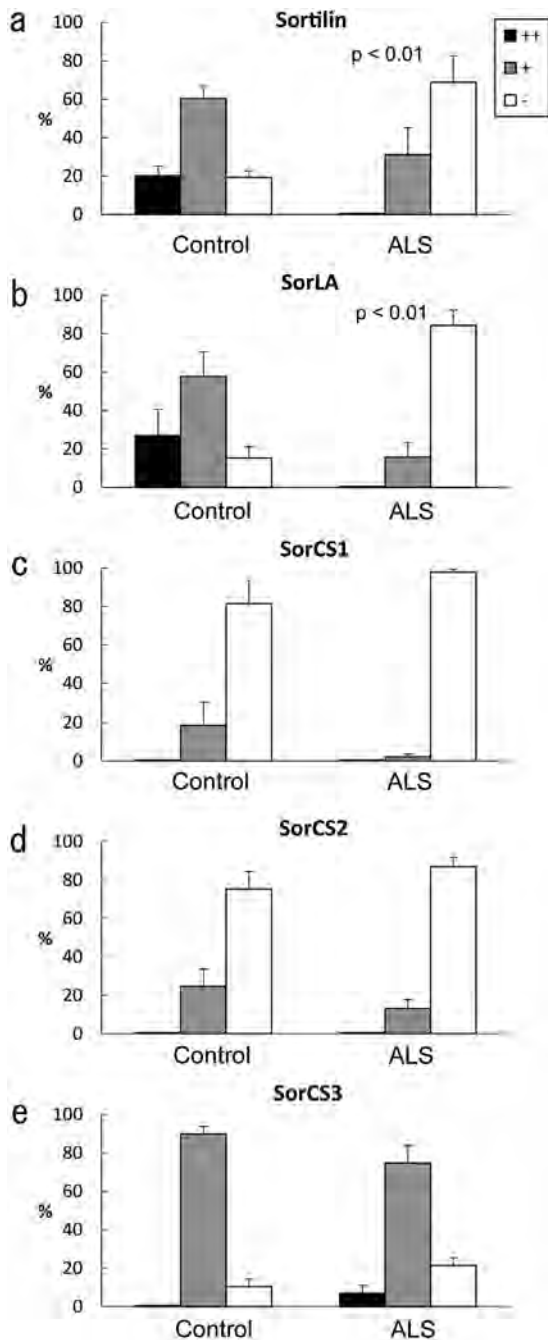


Fig. 2. Semi-quantification of immunoreactivity for sortilin (a), SorLA (b), SorCS1 (c), SorCS2 (d), and SorCS3 (e) of anterior horn cells in normal controls and ALS patients. The proportions of neurons with intense/moderate (++, black column), weak (+, gray column) or no immunostaining (-, white column) relative to the total number of neurons in the anterior horn are shown. Values are expressed as mean \pm standard error of the mean. Correlations at $p < 0.05$ were considered significant.

2. Materials and methods

2.1. Subjects

Twelve patients with sporadic ALS (aged 53–77 years, average 65.8 years) were studied. The diagnosis was confirmed both clinically and histopathologically. BBs were found in the AHCs in 8 of the 12 cases, and TDP-43-positive inclusions were evident in all the cases. We also examined five neurologically normal individuals (aged 53–84 years, average 67.8 years). For routine histological examination, 4- μ m-thick, formalin-fixed, paraffin-embedded

sections from multiple cortical and subcortical regions were stained with hematoxylin and eosin (H&E) or by the Klüver–Barrera method. We also examined the sections immunohistochemically using anti-TDP-43 antibody (10782-1-AP; ProteinTec Group, Inc., Chicago, IL, USA; 1:4000). This study was approved by the Institutional Ethics Committee of Hirosaki University Graduate School of Medicine.

2.2. Immunohistochemistry

Sheep polyclonal antibody against SorCS2 (AF4238; R&D Systems, Inc., Minneapolis, MN, USA; 1:40) and rabbit polyclonal antibodies against sortilin (HPA006889; Atlas Antibodies AB, Stockholm, Sweden; 1:50), SorLA (ab16642; Abcam, Cambridge, UK; 1:50), SorCS1 (23002-1-A1; ProteinTec Group, Inc.; 1:50) and SorCS3 (HPA049097; Atlas Antibodies AB; 1:500) were used in this study.

We identified BBs using H&E-stained sections. BBs were defined as small eosinophilic perikaryal inclusions, 1–5 μ m in diameter, which were sometimes clustered. Serial sections (4 μ m thick) were cut from paraffin blocks of the 4th lumbar segment in all cases and were first stained with H&E. Digital images of the anterior horn on both sides were captured by a virtual slide system (VS110-S1; Olympus, Tokyo, Japan). AHCs were defined as Nissl body-containing cells in Rexed VIII and IX, whose somal diameters were greater than 37 μ m [12]. AHCs with or without BBs were observed under a $\times 40$ objective lens, measured by a virtual slide system ($\times 600$ on a display) and numbered on enlarged prints ($\times 80$). When the same neuronal cell body was recognized on several contiguous sections, the same number was marked on the neuron. This approach ensured we avoided missing tiny BBs. After removing the cover glass from the slides in xylene, the specimens were decolorized in alcohol, subjected to heat retrieval using an autoclave for 10 min in 10 mM citrate buffer (pH 6.0), and immunostained with sheep antibody against SorCS2 (1:40) using a Vectastain ABC kit (Vector, Burlingame, CA, USA). Diaminobenzidine was used as the chromogen. The sections were counterstained with hematoxylin. Digital images of the anterior horn on both sides were captured by the virtual slide system again. The SorCS2 immunoreactivity of BBs was confirmed under a $\times 40$ objective lens in each neuron on a display.

Selected sections were double-immunolabeled with sheep polyclonal anti-SorCS2 (1:20) and rabbit polyclonal anti-cystatin C (A0541; DakoCytomation, Glostrup, Denmark; 1:500) antibodies. The secondary antibodies were Alexa Fluor 488 donkey anti-sheep IgG (A-11015; Invitrogen, Carlsbad, CA, USA; 1:200) and Alexa Fluor 594 donkey anti-rabbit IgG (A-21207; Invitrogen; 1:200). The sections were examined with an Olympus Provis fluorescence microscope (Olympus, Tokyo, Japan).

2.3. Semi-quantitative analysis

The numbers of neurons immunoreactive for sortilin, SorLA, SorCS1, SorCS2 and SorCS3 in control subjects and patients with ALS were assessed using a semi-quantitative rating scale: -, unstained; +, weakly stained; ++, moderately or intensely stained. The staining intensity was first graded as - or ++, and any intensity that was neither - nor ++ was defined as +. Three authors (FM, YM, KW), experienced neuropathologists, rated immunostained sections of ALS and control cases under blinded fashion. The proportions of sortilin, SorLA, SorCS1, SorCS2 and SorCS3-positive neurons relative to the total number of neurons were calculated in each case.

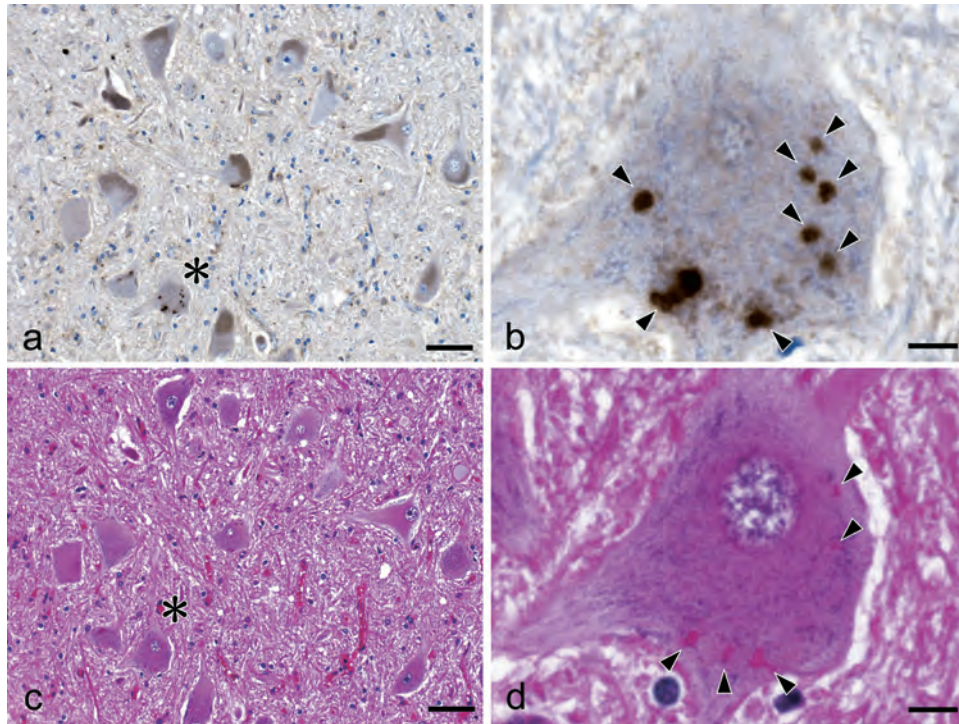


Fig. 3. Contiguous sections stained with anti-SorCS2 antibody (a,b) and hematoxylin and eosin (c,d). Higher-magnification view of the area indicated by the asterisks in a and c showing Bunina bodies (arrowheads) in the lumbar anterior horn of a patient with ALS (b,d). Bars in a and c = 50 μ m. Bars in b and d = 10 μ m.

2.4. Statistical analysis

Calculations were performed using Statcel software (OMS Publishing, Tokorozawa, Japan). Statistical comparison was performed with two-way factorial ANOVA. Values were expressed as mean \pm standard error of the mean. Correlations at $p < 0.05$ were considered significant. Good interrater reliability was achieved by three observers using the method, because the data from each rater showed the same significant result.

3. Results

In normal controls, antibodies against sortilin, SorLA and SorCS3 moderately immunolabeled the cytoplasm of AHCs in a diffuse granular pattern (Fig. 1a,c,i). With anti-SorCS1 and anti-SorCS2 antibodies, the cytoplasm of AHCs was barely immunolabeled, or was unstained (Fig. 1e,g). In ALS, immunoreactivity for sortilin and SorLA was decreased in the majority of AHCs (Fig. 1b,d). There was no apparent difference in staining intensity of the neuronal cytoplasm immunolabeled with anti-SorCS1, -SorCS2 or -SorCS3 between ALS patients and controls (Fig. 1f,h,j).

Semi-quantitative analysis showed that 20.2% of AHCs were moderately or intensely immunolabeled with anti-sortilin antibody and that 60.5% were weakly immunolabeled in normal controls (Fig. 2a, left). In ALS, 31.2% of AHCs showed weak immunoreactivity and 68.8% were unstained (Fig. 2a, right). Similarly, 27.0% of AHCs were moderately or intensely immunolabeled with anti-SorLA antibody and 57.7% were weakly immunolabeled in normal controls (Fig. 2b, left). In ALS patients, 15.6% of AHCs showed weak immunoreactivity and the rest were unstained (Fig. 2b, right). The differences in the staining intensity of AHCs immunolabeled with anti-sortilin or anti-SorLA between ALS patients and controls were statistically significant ($p < 0.01$). There were no significant differences in immunoreactivity for SorCS1, SorCS2 and SorCS3 between ALS patients and controls (Fig. 2c–e).

Although the cytoplasm of AHCs showed no or only weak immunoreactivity for SorCS2, BBs were intensely immunolabeled with anti-SorCS2 antibody (Fig. 3). Sequential staining of the same sections with H&E and anti-SorCS2 antibody revealed that almost all BBs were immunopositive for SorCS2 (90.9–100%, average 95.1%). No SorCS2-positive inclusions were observed in 4 cases of ALS, in which no BBs had been detected. No significant

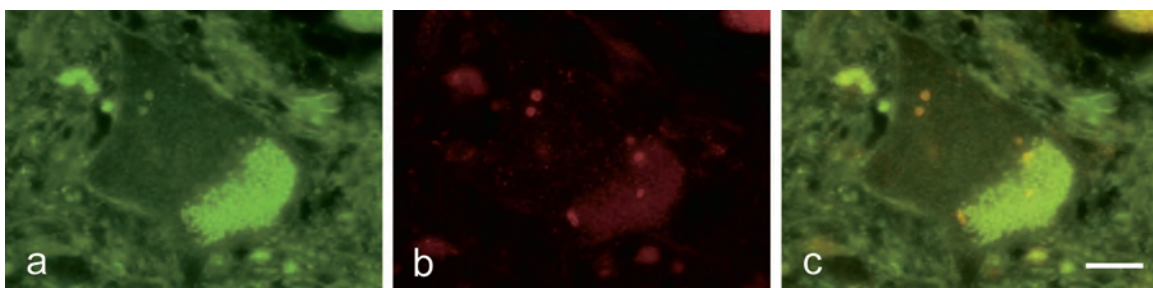


Fig. 4. Double-labeling immunofluorescence demonstrating co-localization of SorCS2 and cystatin C in Bunina bodies in spinal anterior horn cells of a patient with ALS. SorCS2 appears green (a) and cystatin C appears red (b). Overlap of SorCS2 and cystatin C appears yellow (c). Bars = 10 μ m.

immunoreactivity was detectable in sections from controls and ALS cases treated with phosphate-buffered saline solution or by pre-incubating the antibody (AF4238) with the corresponding synthetic protein (4238-SR; R&D Systems, Inc.) (data not shown).

Double-label immunofluorescence revealed co-localization of SorCS2 and cystatin C in BBs (Fig. 4). No significant immunoreactivity was detectable in negative reaction control sections incubated without the primary antibodies.

4. Discussion

A number of genome-wide association studies and biochemical studies have identified members of the VPS10Ps (sortilin, SorLA, SorCS1, SorCS2 and SorCS3) that regulate endosomal sorting as risk factors for neurodegenerative diseases [9]. In the present study, we demonstrated that immunoreactivity for sortilin and SorLA was significantly decreased in AHCs from patients with ALS and that BBs were immunoreactive for SorCS2, indicating that sortilin, SorLA and SorCS2 are linked to the pathomechanism of ALS.

Sortilin functions as a trafficking receptor for both Trk receptors and brain-derived neurotrophic factor through the secretory pathway. Progranulin is targeted to the endosomal–lysosomal pathway through a sortilin-dependent mechanism [9]. Haploinsufficiency of progranulin is a common genetic cause of FTLN with TDP-43 aggregates. Progranulin levels were sharply increased upon TDP-43 reduction and splicing of sortilin was altered [17]. TDP-43 is a major constituent of inclusions in motor and non-motor neurons in ALS and FTLN [1,14,22]. Decreased immunoreactivity for sortilin in AHCs of ALS might be associated with altered splicing of sortilin.

SorLA was the first member of the family of VPS10 proteins to be genetically linked with late-onset AD [20], and SorLA mutations have now also been suggested as causes of familial AD [18]. Subsequent *in vitro* and *in vivo* studies have shown that SorLA is indeed required for endosome to TGN trafficking of amyloid precursor protein [4,24]. Disruption of the VPS26 binding motif within the SorLA cytoplasmic tail results in increased localization of amyloid precursor protein to endosomal compartments and increased amyloidogenic processing of amyloid precursor protein to produce β -amyloid [4]. β -Amyloid has been reported to trigger ALS-associated TDP-43 pathology in AD models [7]. These findings suggest that decreased immunoreactivity for SorLA in AHCs of ALS might contribute to the pathomechanism of ALS.

We further demonstrated that BBs are immunoreactive for SorCS2, a member of the VPS10Ps which play various roles in membrane trafficking [9]. Our findings indicate that SorCS2 is another immunohistochemical marker for BBs in addition to cystatin C [16], which is a member of a super family of protease inhibitors, transferrin, which is an iron-binding plasma protein [10], and peripherin, which is a type III intermediate filament protein [11]. These three proteins show moderate to strong positive reactions in the cytoplasm in almost all neurons without BBs, suggesting that they might be incorporated into BBs. On the other hand, SorCS2 protein appears to be less detectable in the cytoplasm of AHCs without BBs, suggesting a different role of SorCS2 in the formation of BBs. SorCS2 is a member of the VPS10Ps, which have pleiotropic roles in protein trafficking and intra- and intercellular signaling in neuronal and non-neuronal cells [9]. Ultrastructurally, BBs are considered to originate from the endoplasmic reticulum [21,23], and cystatin C is localized to the vesicular structures of BBs [13]. These findings indicate that deposition of SorCS2 in BBs results from dysfunction of protein trafficking and intra- and intercellular signaling, leading to incorporation or mislocalization of cystatin C [16], transferrin [10] and peripherin [11] into BBs.

Sortilin is a sorting receptor that directs target proteins, such as growth factors, signaling receptors, and enzymes, to their destined

location in secretory or endocytic compartments of cells [2]. However, sortilin is not unique, and just one of five structurally related VPS10Ps including SorCS2 [25]. Emerging evidence suggests that VPS10Ps functionally cooperate, adding another level of complexity to the molecular network in which sortilin acts [15]. SorCS2 has been identified as a receptor that binds to pro-nerve growth factor, thereby mediating acute collapse of growth cones of hippocampal neurons [3]. SorCS2 has also been identified as a proneurotrophin receptor, mediating both trophic and apoptotic signals in conjunction with p75NTR [5]. These findings indicate that SorCS2 is involved in regressive changes of neuronal cells. In the present study, we have demonstrated that BBs, a specific hallmark of ALS, are strongly immunopositive for SorCS2. These findings indicate that, in ALS, SorCS2-positive BBs represent dysfunctional sorting of certain cellular proteins to their destined location in AHCs.

Acknowledgments

This work was supported by JSPS KAKENHI Grant Numbers 26430049 (F.M.), 26430050 (K.T.), 26860655 (Y.M.) and 24300131 (K.W.), a Grant for Hirosaki University Institutional Research (K.W.), the Collaborative Research Project (2015–2508) of the Brain Research Institute, Niigata University (F.M.), and Grants-in Aid from the Research Committee for Ataxic Disease, the Ministry of Health, Labour and Welfare, Japan (H.S., K.W.). The authors wish to express their gratitude to M. Nakata and A. Ono for their technical assistance.

References

- [1] T. Arai, M. Hasegawa, H. Akiyama, K. Ikeda, T. Nonaka, H. Mori, D. Mann, K. Tsuchiya, M. Yoshida, Y. Hashizume, T. Oda, TDP-43 is a component of ubiquitin-positive tau-negative inclusions in frontotemporal lobar degeneration and amyotrophic lateral sclerosis, *Biochem. Biophys. Res. Commun.* 351 (2006) 602–611.
- [2] A.S. Carlo, A. Nykjaer, T.E. Willnow, Sorting receptor sortilin—a culprit in cardiovascular and neurological diseases, *J. Mol. Med. (Berl.)* 92 (2014) 905–911.
- [3] K. Deinhardt, T. Kim, D.S. Spellman, R.E. Mains, B.A. Eipper, T.A. Neubert, M.V. Chao, B.L. Hempstead, Neuronal growth cone retraction relies on proneurotrophin receptor signaling through Rac, *Sci. Signal.* 4 (2011) ra82.
- [4] A.W. Fjorback, M. Seaman, C. Gustafsen, A. Mehmedbasic, S. Gokool, C. Wu, D. Millitz, V. Schmidt, P. Madsen, J.R. Nyengaard, T.E. Willnow, E.I. Christensen, W.B. Mobley, A. Nykjaer, O.M. Andersen, Retromer binds the FANSHY sorting motif in SorLA to regulate amyloid precursor protein sorting and processing, *J. Neurosci.* 32 (2012) 1467–1480.
- [5] S. Glerup, D. Olsen, C.B. Vaegter, C. Gustafsen, S.S. Sjoegaard, G. Hermey, M. Kjolby, S. Molgaard, M. Ulrichsen, S. Bogild, S. Skeldal, A.N. Fjorback, J.R. Nyengaard, J. Jacobsen, D. Bender, C.R. Bjarkam, E.S. Sorensen, E.M. Fuchtbauer, G. Eichele, P. Madsen, T.E. Willnow, C.M. Petersen, A. Nykjaer, SorCS2 regulates dopaminergic wiring and is processed into an apoptotic two-chain receptor in peripheral glia, *Neuron* 82 (2014) 1074–1087.
- [6] W. Hampe, M. Rezgaoui, I. Hermans-Borgmeyer, H.C. Schaller, The genes for the human VPS10 domain-containing receptors are large and contain many small exons, *Hum. Genet.* 108 (2001) 529–536.
- [7] A.M. Herman, P.J. Khandelwal, B.B. Stanczyk, G.W. Rebeck, C.E. Moussa, beta-amyloid triggers ALS-associated TDP-43 pathology in AD models, *Brain Res.* (2011).
- [8] G. Hermey, N. Plath, C.A. Hubner, D. Kuhl, H.C. Schaller, I. Hermans-Borgmeyer, The three sorCS genes are differentially expressed and regulated by synaptic activity, *J. Neurochem.* 88 (2004) 1470–1476.
- [9] R.F. Lane, P. St George-Hyslop, B.L. Hempstead, S.A. Small, S.M. Strittmatter, S. Gandy, VPS10 family proteins and the retromer complex in aging-related neurodegeneration and diabetes, *J. Neurosci.* 32 (2012) 14080–14086.
- [10] Y. Mizuno, M. Amari, M. Takatama, H. Aizawa, B. Mihara, K. Okamoto, Transferrin localizes in Bunina bodies in amyotrophic lateral sclerosis, *Acta Neuropathol.* 112 (2006) 597–603.
- [11] Y. Mizuno, Y. Fujita, M. Takatama, K. Okamoto, Peripherin partially localizes in Bunina bodies in amyotrophic lateral sclerosis, *J. Neurol. Sci.* 302 (2011) 14–18.
- [12] F. Mori, K. Tanji, Y. Miki, A. Kakita, H. Takahashi, K. Wakabayashi, Relationship between Bunina bodies and TDP-43 inclusions in spinal anterior horn in amyotrophic lateral sclerosis, *Neuropathol. Appl. Neurobiol.* 36 (2010) 345–352.
- [13] F. Mori, K. Tanji, Y. Miki, K. Wakabayashi, Decreased cystatin C immunoreactivity in spinal motor neurons and astrocytes in amyotrophic lateral sclerosis, *J. Neuropathol. Exp. Neurol.* 68 (2009) 1200–1206.

- [14] M. Neumann, L.K. Kwong, D.M. Sampathu, J.Q. Trojanowski, V.M. Lee, TDP-43 proteinopathy in frontotemporal lobar degeneration and amyotrophic lateral sclerosis: protein misfolding diseases without amyloidosis, *Arch. Neurol.* 64 (2007) 1388–1394.
- [15] A. Nykjaer, T.E. Willnow, Sortilin: a receptor to regulate neuronal viability and function, *Trends Neurosci.* 35 (2012) 261–270.
- [16] K. Okamoto, S. Hirai, M. Amari, M. Watanabe, A. Sakurai, Bunina bodies in amyotrophic lateral sclerosis immunostained with rabbit anti-cystatin C serum, *Neurosci. Lett.* 162 (1993) 125–128.
- [17] M. Polymenidou, C. Lagier-Tourenne, K.R. Hutt, S.C. Huelga, J. Moran, T.Y. Liang, S.C. Ling, E. Sun, E. Wancewicz, C. Mazur, H. Kordasiewicz, Y. Sedaghat, J.P. Donohue, L. Shiue, C.F. Bennett, G.W. Yeo, D.W. Cleveland, Long pre-mRNA depletion and RNA missplicing contribute to neuronal vulnerability from loss of TDP-43, *Nat. Neurosci.* 14 (2011) 459–468.
- [18] C. Pottier, D. Hannequin, S. Coutant, A. Rovelet-Lecrux, D. Wallon, S. Rousseau, S. Legallic, C. Paquet, S. Bombois, J. Pariente, C. Thomas-Anterion, A. Michon, B. Croisile, F. Etcharry-Bouyx, C. Berr, J.F. Dartigues, P. Amouyel, H. Dauchel, C. Boutoleau-Bretonniere, C. Thauvin, T. Frebourg, J.C. Lambert, D. Campion, High frequency of potentially pathogenic SORL1 mutations in autosomal dominant early-onset Alzheimer disease, *Mol. Psychiatry* 17 (2012) 875–879.
- [19] M. Rezzaoui, G. Hermey, I.B. Riedel, W. Hampe, H.C. Schaller, I. Hermans-Borgmeyer, Identification of SorCS2, a novel member of the VPS10 domain containing receptor family, prominently expressed in the developing mouse brain, *Mech. Dev.* 100 (2001) 335–338.
- [20] E. Rogaeva, Y. Meng, J.H. Lee, Y. Gu, T. Kawarai, F. Zou, T. Katayama, C.T. Baldwin, R. Cheng, H. Hasegawa, F. Chen, N. Shibata, K.L. Lunetta, R. Pardossi-Piquard, C. Bohm, Y. Wakutani, L.A. Cupples, K.T. Cuenco, R.C. Green, L. Pinessi, I. Rainero, S. Sorbi, A. Bruni, R. Duara, R.P. Friedland, R. Inzelberg, W. Hampe, H. Bujo, Y.Q. Song, O.M. Andersen, T.E. Willnow, N. Graff-Radford, R.C. Petersen, D. Dickson, S.D. Der, P.E. Fraser, G. Schmitt-Ulms, S. Younkin, R. Mayeux, L.A. Farrer, P. St George-Hyslop, The neuronal sortilin-related receptor SORL1 is genetically associated with Alzheimer disease, *Nat. Genet.* 39 (2007) 168–177.
- [21] H. Takahashi, E. Ohama, F. Ikuta, Are Bunina bodies of endoplasmic reticulum origin? An ultrastructural study of subthalamic eosinophilic inclusions in a case of atypical motor neuron disease, *Acta Pathol. Jpn.* 41 (1991) 889–894.
- [22] C.F. Tan, H. Eguchi, A. Tagawa, O. Onodera, T. Iwasaki, A. Tsujino, M. Nishizawa, A. Kakita, H. Takahashi, TDP-43 immunoreactivity in neuronal inclusions in familial amyotrophic lateral sclerosis with or without SOD1 gene mutation, *Acta Neuropathol.* 113 (2007) 535–542.
- [23] M. Tomonaga, M. Saito, M. Yoshimura, H. Shimada, H. Tohgi, Ultrastructure of the Bunina bodies in anterior horn cells of amyotrophic lateral sclerosis, *Acta Neuropathol.* 42 (1978) 81–86.
- [24] S.I. Vieira, S. Rebelo, H. Esselmann, J. Wiltfang, J. Lah, R. Lane, S.A. Small, S. Gandy, E.S.E.F. da Cruz, E.S.O.A. da Cruz, Retrieval of the Alzheimer's amyloid precursor protein from the endosome to the TGN is S65 phosphorylation state-dependent and retromer-mediated, *Mol. Neurodegener.* 5 (2010) 40.
- [25] T.E. Willnow, C.M. Petersen, A. Nykjaer, VPS10P-domain receptors—regulators of neuronal viability and function, *Nat. Rev. Neurosci.* 9 (2008) 899–909.

Case Report

Cortico-cortical activity between the primary and supplementary motor cortex: An intraoperative near-infrared spectroscopy study

Masafumi Fukuda, Tetsuro Takao, Tetsuya Hiraishi, Hiroshi Aoki, Ryosuke Ogura, Yosuke Sato, Yukihiro Fujii

Department of Neurosurgery, Brain Research Institute, University of Niigata, Niigata-City, Japan

E-mail: *Masafumi Fukuda - mfuku529@bri.niigata-u.ac.jp; Tetsuro Takao - takao@bri.niigata-u.ac.jp; Tetsuya Hiraishi - tetsuya_hiraishi@me.com; Hiroshi Aoki - aoki1123@bri.niigata-u.ac.jp; Ryosuke Ogura - oguryou@bri.niigata-u.ac.jp; Yosuke Sato - yosuke0420@hotmail.com; Yukihiro Fujii - yfujii@bri.niigata-u.ac.jp
*Corresponding author

Received: 18 August 14 Accepted: 02 January 15 Published: 24 March 15

This article may be cited as:Fukuda M, Takao T, Hiraishi T, Aoki H, Ogura R, Sato Y, et al. Cortico-cortical activity between the primary and supplementary motor cortex: An intraoperative near-infrared spectroscopy study. *Surg Neurol Int* 2015;6:44.Available FREE in open access from: <http://www.surgicalneurologyint.com/text.asp?2015/6/1/44/153872>

Copyright © 2015 Fukuda M. This is an open-access article distributed under the terms of the Creative Commons Attribution License, which permits unrestricted use, distribution, and reproduction in any medium, provided the original author and source are credited.

Abstract

Background: The supplementary motor area (SMA) makes multiple reciprocal connections to many areas of the cerebral cortices, such as the primary motor cortex (PMC), anterior cingulate cortex, and various regions in the parietal somatosensory cortex. In patients with SMA seizures, epileptic discharges from the SMA rapidly propagate to the PMC. We sought to determine whether near-infrared spectroscopy (NIRS) is able to intraoperatively display hemodynamic changes in epileptic network activities between the SMA and the PMC.

Case Descriptions: In a 60-year-old male with SMA seizures, we intraoperatively delivered a 500 Hz, 5-train stimulation to the medial cortical surface and measured the resulting hemodynamic changes in the PMC by calculating the oxyhemoglobin (HbO₂) and deoxyhemoglobin (HbR) concentration changes during stimulation. No hemodynamic changes in the lateral cortex were observed during stimulation of the medial surface corresponding to the foot motor areas. In contrast, both HbO₂ and HbR increased in the lateral cortex corresponding to the hand motor areas when the seizure onset zone was stimulated. In the premotor cortex and the lateral cortex corresponding to the trunk motor areas, hemodynamic changes showed a pattern of increased HbO₂ with decreased HbR.

Conclusions: This is the first reported study using intraoperative NIRS to characterize the epileptic network activities between the SMA and PMC. Our intraoperative NIRS procedure may thus be useful in monitoring the activities of cortico-cortical neural pathways such as the language system.

Key Words: Cortico-cortical activity, epilepsy, hemodynamic change, near-infrared spectroscopy, primary motor cortex, supplementary motor area

Access this article online**Website:**www.surgicalneurologyint.com**DOI:**

10.4103/2152-7806.153872

Quick Response Code:**INTRODUCTION**

Supplementary motor area (SMA) seizures are short in duration and characterized by abrupt, bilateral, tonic

posturing of the extremities, and vocalization without loss of consciousness.^[6] Epileptic discharges from the SMA can rapidly propagate through the primary motor cortex (PMC), anterior cingulate cortex (ACC),

and various parietal somatosensory areas, which form multiple reciprocal connections to the SMA.^[2,4] Better understanding of the mechanisms of SMA propagation can be achieved through improved methods to probe cortical network activities associated with epileptic discharges from the SMA. For example, an ictal single photon emission computed tomography study indicated that seizure-associated hyperperfusion areas did not localize within the SMA, but rather spread to adjacent cortical regions ipsilateral to epileptic foci, such as the ACC and PMC.^[1] Recently, we demonstrated using simultaneous transcranial near-infrared spectroscopy (NIRS) and electrocorticography (ECoG) recordings in a patient with SMA seizures that increased cerebral blood flow was observed from the epileptic discharges in the ipsilateral SMA and spread to the ipsilateral premotor cortex and PMC as well as the contralateral hemisphere.^[7]

In a patient with SMA seizure, we used a novel 4-probe device attached to the brain surface to conduct intraoperative NIRS from four probes to show increased blood flow in the PMC elicited by stimulation to the SMA. This is the first report to determine that intraoperative NIRS can reveal the cortico-cortical activities between the SMA and PMC. Moreover, by placing probes on the brain surface, we were able to obtain greater resolution than with transcranial NIRS methods. Our technique will thus allow improved mapping of cortico-cortical network activities intraoperatively.

CASE REPORT

A 60-year-old male presented with seizures a few months before admission to our hospital. His seizures were characterized by tonic posturing in the left extremities and occurred 3–4 times monthly. T2-weighted magnetic resonance (MR) imaging revealed a high intensity lesion in the medial surface of the right frontal lobe. The lesion was not enhanced by Gd on the T1-weighted MR images, and was suspected to be a low-grade glioma. In order to confirm the relationship between the lesion and the PMC corresponding to the lower extremities, subdural grid electrodes were placed to cover the lateral and medial surfaces adjacent to the PMC. Video-ECoG monitoring demonstrated seizure onset at the right medial surface corresponding to the SMA. The seizure activities rapidly propagated from the SMA to the lateral cortex, including the PMC.

Cortical electrical stimulation was performed for functional cortical mapping. A repetitive square wave with electrical currents of alternating polarity, a pulse width of 0.2 ms, and a frequency of 50 Hz were delivered for 5 s (Nihon Koden, Corporation, Japan). Two neighboring electrodes, with an intensity of 2–5 mA, were stimulated in a bipolar manner. Positive motor and sensory areas were identified by positive motor response (i.e. muscle

twitch) and subjective sensory sensation, respectively. To define the precise location of each electrode on the surface of the brain, subdural electrodes extracted from computed tomography (CT) images were co-registered to three-dimensional volume-rendered MR images (3.0 T) using image-analysis software (Zed-View, LEXI, Inc., Japan). The results of this functional cortical mapping are depicted in Figure 1. Cortical stimulation to the anterior and posterior areas of the seizure onset zone induced habitual seizures.

Before a partial resection of the lesion for pathology, intraoperative NIRS recording was performed upon stimulation of the placed subdural electrodes apparatus of the medial cortical surface. Constant current stimuli, consisting of five rectangular pulses with 2-ms interstimulus intervals, were generated and recorded with a Neuropac (Nihon Koden, Corporation, Japan). The cathode was positioned at Fz. Motor-evoked potentials were recorded from the abductor pollicis brevis and abductor hallucis brevis muscles through paired stainless-steel needle electrodes inserted subdermally. The band-pass filter was set to a range of 5–3000 Hz. The applied stimuli were adjusted to the supra-threshold intensity.

For NIRS monitoring, we developed a novel device comprising of four recording probes spaced 1.5 cm apart and equipped with fixable spatula retractors at the tip of each probe to enable attachment to the brain surface [Figure 2a and b]. The four probes were set to cover the lateral cortex, including the PMC [Figure 2c]. NIRS was carried out with a 695/830 nm spectrometer equipped to our novel monitoring device (ETG-7100; HITACHI Medical, Japan). Emitting light intensity was adjusted to 1 mW (approximately one-fourth

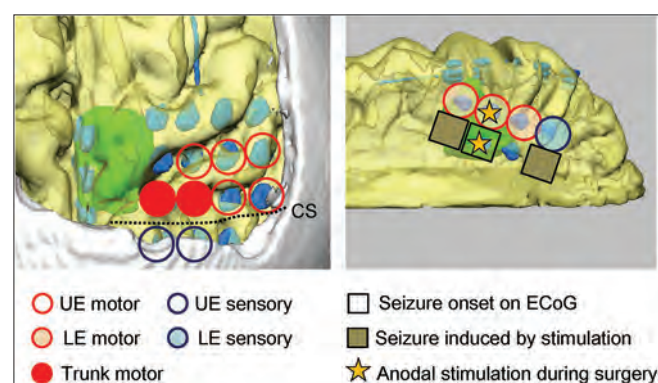


Figure 1: Results of video-electrocorticography (ECoG) monitoring and functional cortical mapping. 3D brain surface images showing recording electrodes (pale blue) and the brain tumor (green). The seizure onset zone (square) was confirmed to reside in the medial surface. The sites in which stimulation induced habitual seizures (closed square) were noted anterior and posterior to the seizure onset zone. Before partial tumor resection, both the foot motor area and seizure onset zone were stimulated for intraoperative NIRS study (stars). UE: Upper extremities, LE: Lower extremities, CS: Central sulcus

of scalp NIRS). The oxyhemoglobin (HbO₂) and deoxyhemoglobin (HbR) concentration changes corresponding to medial surface stimulation in each session were calculated for each segment, which consisted of a 30 s intervals comprising of a prestimulation block (10 s), a stimulation block, and a poststimulation block (20 s). Each session was repeated five times. The present study was approved by the Institutional Review Board Committee at the Niigata University School of Medicine, and informed consent was obtained from the patients (IRB#1559).

In the results, no hemodynamic changes were observed during stimulation of the medial surface corresponding to the foot motor areas at the intensity of 20 mA [Figure 3A]. In contrast, both HbO₂ and HbR increased in the lateral cortex corresponding to the hand motor areas when the seizure onset zone was stimulated at an intensity of 16 mA [b and c in Figure 3B]. In the lateral cortex corresponding to the trunk motor areas and the premotor cortex, hemodynamic changes showed a pattern of increased HbO₂ with decreased HbR [a and d in Figure 3B].

DISCUSSION

To our knowledge, this is the first report using intraoperative NIRS during cortical stimulation to demonstrate cortico-cortical activity between the SMA and PMC. We observed that stimulation of the foot motor area elicited no detectable hemodynamic responses in the lateral cortex, whereas stimulation to the seizure onset zone elicited hemodynamic responses at all four probes despite the stimulation intensity decreasing from 20 to 16 mA. These results likely reflected the epileptic network activities between the SMA and PMC.



Figure 2: (a) Our novel device for the intracranial setting of four NIRS probes. The inter-probe distance was 1.5 cm. (b) Four probes were equipped to the NIRS devices. (c) During surgery, the novel device and its four probes were wrapped by a sterilized cover. The device was fixed by spatula retractors at the tip of each probe for attachment to the brain surface. The probes were placed to cover the lateral cortex including the primary motor cortex

It should be noted that we used high frequency stimulation (5-trains, 500 Hz) in the present study, because we were concerned that 50 Hz-stimulation to the seizure onset zone during surgery and functional mapping might induce seizures. Previously, we characterized hemodynamic connectivity in the language system in a patient with temporal lobe epilepsy.^[8] In this study, 50 Hz-stimulation in the left superior temporal gyrus via subdural electrode contacts gave rise to hemodynamic increases in the inferior frontal gyrus, indicating a strong connection to the stimulation site. In a cortico-cortical evoked potential study,^[5] stimulation of the foot motor cortex elicited responses in the pre- and postcentral gyrus. Thus, 50 Hz-stimulation of the foot motor areas, rather than 500 Hz employed in our present experiments, might induce hemodynamic changes in the lateral cortex as well.

In this study, high frequency stimulation caused the hemodynamic changes characterized by increase in both HbO₂ and HbR in the lateral cortex corresponding to the hand motor areas. This phenomenon was also observed in a study of the language system of the frontal and temporal cortex using simultaneous NIRS and ECoG recordings during cortical stimulation.^[8] In contrast, in the areas corresponding to the trunk motor areas and premotor cortex, hemodynamic changes showed a pattern of increased HbO₂ with decreased HbR as is typical of task-evoked hemodynamic changes. In a previous NIRS study carried out simultaneously with cortical stimulation via subdural electrodes,^[3] 50 Hz-stimulation produced significant increases in both HbO₂ and HbR at the stimulation site and surrounding areas, while 5 Hz-stimulation produced a localized increase in HbO₂ and a decrease in HbR. An increase in HbO₂ with an

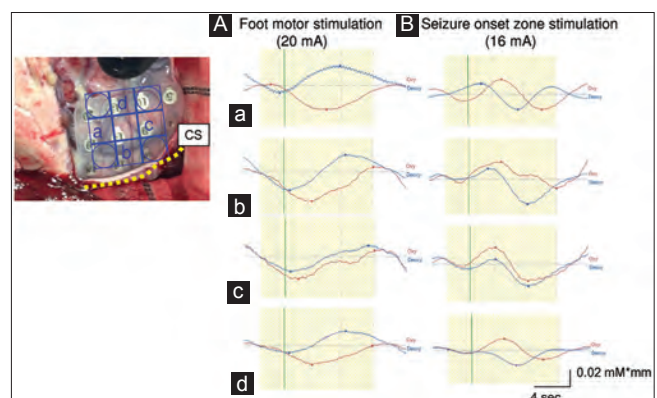


Figure 3: Time course changes of HbO₂ and HbR in the lateral cortex. The left picture shows the relationship between the sites of each of the four probes (circle) and subdural electrodes. Recording sites of NIRS were a, b, c, and d. CS: Central sulcus. (A) No hemodynamic changes were noted in any sites, when the foot motor area was stimulated at the intensity of 20 mA. (B) Both HbO₂ and HbR increased in the hand motor areas when the seizure onset zone was stimulated at an intensity of 16 mA (b and c). In the trunk motor areas (a) and the premotor cortex (d), hemodynamic changes showed a pattern of increased HbO₂ with decreased HbR

associated increase in HbR is thus indicative of higher levels of neural activity and indicates that oxygen consumption exceeds oxygen delivery via the blood supply.

These findings also suggest that stronger stimulations to the brain surface may likely induce increases in both HbO₂ and HbR not only in stimulation sites but also in remote areas that make strong neuronal connections to the stimulation sites. This implies that areas with robust connections are prone to seizure spread, even if remote, and that their connectivity will be reflected in the NIRS data. For instance, in the present study, hand motor cortex exhibited increases in both HbO₂ and HbR upon stimulation of the seizure onset zone. Oxygen consumption exceeded the rate of oxygen delivery, because the two areas had robust connections that lay within one of the epileptic networks. However, in the trunk motor and premotor cortex, which were conceivably not located within main epileptic networks and weakly connected to the seizure onset zone, the rate of oxygen consumption did not exceed the rate of delivery. Further studies are needed to clarify and extend the implications and relevance of such hemodynamic changes in resolving epileptic networks and more weakly connected surrounding areas.

In this study, we employed intraoperative NIRS from four probes to demonstrate that abnormal connectivity between regions of cortex characterizes epileptic network activities. Our results highlight the capability of intraoperative NIRS to provide us with useful information about the dynamics of cortico-cortical activity at high resolution and without artefacts due to scalp blood flow. This approach can thus expand on previous studies using NIRS scalp recordings, such as our description of hemodynamic connectivity between the superior temporal and inferior frontal cortex in the language system. The additional ability to make simultaneous electrical recording would enhance the level of information obtained through this approach. Recently, a thin flexible probe, with a probe head of 5.6×10 mm and the total thickness of 0.7 mm, was developed for simultaneous recording of NIRS and ECoG,^[9] by integrating near-infrared light-emitting diodes and photodiodes for NIRS measurement placed on the brain surface and ECoG electrodes. In their initial experimental study using this novel device, these researchers reported hemodynamic changes associated with both focal brain cooling and hyperventilation. If such small devices

were made widely available and applied in patients undergoing neurosurgery, it could be used to further our understanding of cortico-cortical projections and expand on intraoperative NRIS studies.^[8]

CONCLUSIONS

In a patient with SMA seizures, we employed intraoperative NIRS to demonstrate hemodynamic changes between the SMA, corresponding to the seizure onset zone, and the lateral PMC, corresponding to the seizure propagation areas. This is the first report to report that NIRS can reveal cortico-cortical activities from the brain surface intraoperatively. In the future, intraoperative NIRS will be useful in monitoring cortico-cortical activities such as in the language system and other cortical processes.

ACKNOWLEDGMENTS

This work was supported by JSPS KAKENHI Grant Number 25462246. The authors thank Akihiko Suzuki, Motohiro Soma, and Kiyoe Nonaka for their technical support.

REFERENCES

1. Fukuda M, Masuda H, Honma J, Fujimoto A, Kameyama S, Tanaka R. Ictal SPECT in supplementary motor area seizures. *Neuro Res* 2006;28:845-8.
2. Hatanaka N, Tokuno H, Hamada I, Inase M, Ito Y, Imanishi M, et al. Thalamocortical and intracortical connections of monkey cingulate motor areas. *J Comp Neurol* 2003;462:121-38.
3. Hoshino T, Sakatani K, Katayama Y, Fujiwara N, Murata Y, Kobayashi K, et al. Application of multichannel near-infrared spectroscopic topography to physiological monitoring of the cortex during cortical mapping: Technical case report. *Surg Neurol* 2005;64:272-5.
4. Luppino G, Matelli M, Camarda R, Rizzolatti G. Corticocortical connections of area F3 (SMA-proper) and area F6 (pre-SMA) in the macaque monkey. *J Comp Neurol* 1993;338:114-40.
5. Matsumoto R, Nair DR, LaPresto E, Bingaman W, Shibasaki H, Luders HO. Functional connectivity in human cortical motor system: A cortico-cortical evoked potential study. *Brain* 2007;130:181-97.
6. Morris HH 3rd, Dinner DS, Luders H, Wyllie E, Kramer R. Supplementary motor seizures: Clinical and electroencephalographic findings. *Neurology* 1988;38:1075-82.
7. Sato Y, Fukuda M, Oishi M, Shirasawa A, Fujii Y. Ictal near-infrared spectroscopy and electrocorticography study of supplementary motor area seizures. *J Biomed Opt* 2013;18:76022.
8. Sato Y, Oishi M, Fukuda M, Fujii Y. Hemodynamic and electrophysiological connectivity in the language system: Simultaneous near-infrared spectroscopy and electrocorticography recordings during cortical stimulation. *Brain Lang* 2012;123:64-7.
9. Yamakawa T, Inoue T, He Y, Fujii M, Suzuki M, Niwayama M. Development of an implantable flexible probe for simultaneous near-infrared spectroscopy and electrocorticography. *IEEE Trans Biomed Eng* 2014;61:388-95.

Limitations of Neuroendoscopic Treatment for Pediatric Hydrocephalus and Considerations from Future Perspectives

Kenichi NISHIYAMA,¹ Junichi YOSHIMURA,¹ and Yukihiro FUJII¹

¹Brain Research Institute, University of Niigata, Niigata, Niigata

Abstract

Neuroendoscopy has become common in the field of pediatric neurosurgery. As an alternative procedure to cerebrospinal fluid shunt, endoscopic third ventriculostomy has been the routine surgical treatment for obstructive hydrocephalus. However, the indication is still debatable in infantile periods. The predictors of late failure and how to manage are still unknown. Recently, the remarkable results of endoscopic choroid plexus coagulation in combination with third ventriculostomy, reported from experiences in Africa, present puzzling complexity. The current data on the role of neuroendoscopic surgery for pediatric hydrocephalus is reported with discussion of its limitations and future perspectives, in this review.

Key words: hydrocephalus, neuroendoscopy, cerebrospinal fluid, pediatric, shunt

Introduction

The cerebrospinal fluid (CSF) shunt has long been the classic treatment for pediatric hydrocephalus. It can resolve nearly all forms of hydrocephalus, regardless of the etiology. It is a simple procedure that can aid in having a relatively normal life. However, its failure rate is significant. The reported rate of shunt malfunction in the first year of placement is approximately 30%, and about 10% per year thereafter. The risk of infection is between 5% and 10%. In addition, the high rates of shunt complication such as slit ventricle syndrome are unacceptable by current standards. Children with shunts are dependent on surgical maintenance throughout their lives.^{1–8)} Therefore, the advent of neuroendoscopy was received with enthusiasm. Endoscopic third ventriculostomy (ETV) has been a routine surgical practice for the past two decades and provides an alternative to the CSF shunt. It is a straightforward procedure for diversion of the CSF and does not require placing devices in children's bodies. The utility and safety of ETV have been proven for obstructive hydrocephalus that occur secondary to aqueductal stenosis. However, for other indications, it is necessary to examine the anatomy and etiology, as well as the patient's age. During follow-up after

ETV, late failure can occur and may lead to rapid deterioration. The aim of this report is to review the current data on the use of neuroendoscopy in children and to discuss the limitations and future perspectives regarding this procedure.

Patient Selection and ETV in Infants

ETV has two main purposes: to restore CSF communication between the ventricle and subarachnoid space and to reduce transmantle pulsatile stress by increasing compliance of the ventricular wall.⁹⁾ Since the 1990s, patients with aqueductal stenosis have been considered ideal candidate for ETV.^{10,11)} ETV quietly developed into a common procedure, without any prospective randomized trials comparing its efficacy to that of the CSF shunt. In spite of strict patient selection, the overall ETV success rate does not exceed 80%.^{12–16)} However, as neuroendoscopic technology has evolved and pediatric neurosurgeons have gained experience with the procedure, the indications for ETV have broadened. For example, patients with hydrocephalus who had a previously failed shunt have become ETV candidates. The success rate of ETV for shunt malfunction is notable, around 80%.^{17–20)} In recent years, the use of ETV to treat many pathological conditions has been debated. These include myelomeningocele, Chiari type 1 malformation, Dandy-Walker malformation, and previous meningitis or hemorrhage.^{14,19,21,22)}

In infants, the benefits conferred by ETV may be considerable due to the high complication rate of CSF shunts. However, there are two concerns with the use of ETV in infants. The first is safety of the procedure, including the possibility of damage to the ventricular and cisternal structures during surgery, CSF leakage, or infection soon after surgery and late closure of the stoma with rapid deterioration. The second concern is that an infant successfully treated with ETV may be transformed from active hydrocephalus to an arrested type. These infants often have larger ventricles than children treated with CSF shunts. No study has attempted to correlate the larger ventricle size with any measurements of psychomotor development. According to reports from a multitude of international studies, the shunt independence rate ranges from 25% to 89%.^{23–28)} Two-thirds of the reports suggested that success rate is dependent on age of the infant at the time of ETV.^{29–34)} To increase ETV success rates, greater accuracy of appropriate patients would be advised. However, because of the high rate of shunt failure and complication, ETV is sometimes preferred as a first-line treatment. Further, the range of what is defined as failure in this age group is very wide. A multicenter prospective randomized study on infants up to 2 years of age with no flow at the level of the aqueduct, named the International Infant Hydrocephalus Study (IIHS) is now under way. This study focuses primarily on the neurodevelopmental outcomes associated with different treatment paradigms at 5 years, and includes a comprehensive assessment of relevant risks and benefits.³⁵⁾

Failed ETV and Its Management

ETV failure is a possible event. Although most failures from ETV occur in the early period, within a few days to 2 weeks following the procedure, late failure after many months may lead to rapid deterioration and even sudden death. A rapid increase in intracranial pressure caused by late obstruction of the stoma is typically regarded as the mechanism of failure.^{36–42)} Early failure is attributed to the incorrect surgical technique or different criteria in the selection of patients. However, the predictors of late failure are still unknown. Therefore, patients who have undergone successful ETV should be followed on an ongoing basis. Neurosurgeons should encourage patients and their parents to return as soon as possible if any adverse symptoms develop, because these may have severe consequences.⁴³⁾ Setting the CSF reservoir concurrently with ETV is one option for the treatment of emergencies, even though it means implantation of a foreign material. In Japan, a follow-up magnetic resonance imaging (MRI) examination

including sagittal T₂-weighted images, cine-MRI, or constructive interference in steady state (CISS) is often scheduled to detect the CSF flow across the stoma. However, there is currently no evidence regarding whether the patients with no flow on MRI following ETV may be at a greater risk to develop clinical symptoms. For these patients, a repeat ETV may be performed immediately rather than close observation. In the literature, repeat ETV has a good success rate.^{32,44–49)} Therefore, this is one option for patients with a failed ETV, and it provides a means of even avoiding the CSF shunt.

ETV vs. Aqueductoplasty

Endoscopic aqueductoplasty (EAP) is a means to restore the physiological CSF dynamics. This procedure provides an alternative to ETV, because it avoids the risk of severe arterial bleeding. EAP has been performed in cases with membranous or short segmental occlusion of the sylvian aqueduct. However, the long-term results of EAP have not been as successful as one would expect.^{50–54)} EAP has been shown to fail frequently. Schroeder et al. reported a re-closure rate of 50%, and proposed that one contributing factor to re-closure could be lower aqueductal CSF flow through the stoma than that following ETV.^{55,56)} In addition, aqueductoplasty is generally considered a riskier procedure due to the higher risk of injuring midbrain structures. It may lead to neurological deficits such as oculomotor or trochlear nerve palsy, Parinaud's syndrome, and periaqueductal syndrome. Therefore, ETV, which has higher long-term success rates and less risk, would be a better alternative for membranous, short segmental, and even tumor-related occlusion of the aqueduct.^{55,57)} However, the condition of isolated fourth ventricle (IFV) is an exception. Almost all patients with IFV have a medical history of hydrocephalus within first year of life, mostly post-infectious or post-hemorrhagic. Further, following shunt placement, they often experience complicated overdrainage with aqueductal stenosis. Aqueductoplasty could be a means of establishing CSF communication to the formerly isolated ventricular compartment; however, a stent is mandatory to keep this pathway open. EAP with a stent could be one choice in the endoscopic treatment of IFV.^{50,53,55,57,58)}

ETV vs. CSF Shunt in Children

As described above, ETV has been widely applied for pediatric hydrocephalus as an alternative to the CSF shunt mainly in an attempt to avoid foreign body implantation and to better simulate physiological

CSF dynamics. However, the results of CSF shunt have rarely been compared to ETV. According to the pediatric study by de Ribaupierre et al., the failure rate of ETV was 26% and that of ventriculoperitoneal (VP) shunt was 42% at 5 years follow-up. In a review of the literature, the same trend was seen in other studies.⁵⁹⁾ Kulkarni et al. reported that the relative risk of ETV failure is initially higher than that for the CSF shunt. However, the risk became progressively lower at approximately 3 months following the procedure, and was approximately half the risk of shunt failure at 2 years.⁶⁰⁾ The decrease in ventricle size is usually smaller and happens more slowly after ETV compared to shunt. Pediatric neurosurgeons are sometimes concerned about the relationship between these neuroimaging changes and neuropsychological outcomes. Hirsch reviewed that the postoperative intelligence quotient (IQ) was not significantly different in 70 patients with shunts vs. 44 who underwent percutaneous third ventriculostomy.⁶¹⁾ Other reports also have found similar results.^{62,63)} Recently, Kulkarni et al. reported that at 1 year following surgery, the quality of life and IQ scores were not significantly different between an ETV and a VP shunt group.^{64,65)}

Challenging Procedure of ETV + CPC

There has been a resurgence in the technique of choroid plexus coagulation (CPC) in combination with ETV ever since this procedure was performed for African children with hydrocephalus of various etiologies in 2005.^{66–73)} Warf and colleagues highlighted that hydrocephalus with shunt dependency is inadvisable in developing countries because of limited access to medical centers in the event of shunt malfunction. In 2005, Warf and colleagues reported the results of a combined ETV + CPC trial performed mainly in infant with post-infectious hydrocephalus and in those with myelomeningocele. A total of 266 patients underwent ETV + CPC, whereas ETV alone was performed in 284 patients. The results demonstrated that the ETV + CPC increased the success rate in infants from 47% to 66%.⁶⁶⁾ In 2008, they reported the long-term results of ETV + CPC in hydrocephalus with myelomeningocele. The intention-to-treat analysis showed a shunt independence rate of 76% in 338 infants, which was higher than the results of ETV alone reported in the literature.^{22,32,67)} Further analyses regarding ETV + CPC performed in patients with encephalocele, Dandy-Walker complex, and congenital aqueductal stenosis have been conducted using their database.^{70–72)} The success rates achieved were between 70% and 80%. However, all pediatric neurosurgeons should

Neurol Med Chir (Tokyo) 55, August, 2015

be cautious about the meaning of “success.” In these reports, success usually referred to controlling raised intracranial pressure and avoiding an extra-cranial CSF shunt. Cognitive function was not the main outcome index. In addition, all these results have been reported from Africa. In the coming years, the challenge will be to see whether these results from Africa can be extrapolated to developed countries.⁷⁴⁾ The main advantage of ETV + CPC was avoidance of a shunt in patients who were difficult to follow-up. In Africa, geographic and socioeconomic constraints reasons for poor follow-up. The low possibility of cognitive salvage or the high rate of shunt complications, such as holoprosencephaly or hydroanencephaly, may be further reasons in developed nations. Technically, Warf and colleagues used a steerable endoscope via a single burr hole, sometimes in combination with septostomy, and coagulated the bilateral choroid plexus from the foramen of Monro to the entrance of the temporal horn.^{66,73)} This procedure appeared to be safe in some cases of severely dilated ventricles. For Japanese neuroendoscopic surgeons, the flexible endoscope is more familiar than it is in other European nations. Nevertheless, almost all pediatric neurosurgeons still believe that the use of ETV + CPC in pediatric hydrocephalus needs further evaluation.

Conclusion

It is difficult to determine the best strategy for CSF diversion in pediatric hydrocephalus. ETV is one of the alternative procedures to the CSF shunt in conditions of obstructive hydrocephalus such as aqueductal stenosis. However, the preferred indications in infants have not been fully determined. The mechanisms and predictors of late ETV failure that might cause rapid deterioration are not still known. Recently, other clinical dilemmas, such as the use of ETV + CPC have arisen. Definition of the optimal indications, perfection of endoscopic techniques, developing strategies for follow-up, and considering socioeconomic constraints are required from pediatric neurosurgeons when selecting a surgical strategy in pediatric hydrocephalus.

Conflicts of Interest Disclosure

The authors declare that they have no conflicts of interest.

References

- 1) Aschoff A, Kremer P, Hashemi B, Kunze S: The scientific history of hydrocephalus and its treatment. *Neurosurg Rev* 22: 67–93; discussion 94–95, 1999

- 2) Hoppe-Hirsch E, Laroussinie F, Brunet L, Sainte-Rose C, Renier D, Cinalli G, Zerah M, Pierre-Kahn A: Late outcome of the surgical treatment of hydrocephalus. *Childs Nerv Syst* 14: 97–99, 1998
- 3) Kestle J, Drake J, Milner R, Sainte-Rose C, Cinalli G, Boop F, Piatt J, Haines S, Schiff S, Cochrane D, Steinbok P, MacNeil N: Long-term follow-up data from the Shunt Design Trial. *Pediatr Neurosurg* 33: 230–236, 2000
- 4) Kestle JR: Pediatric hydrocephalus: current management. *Neurol Clin* 21: 883–895, vii, 2003
- 5) Renier D, Sainte-Rose C, Pierre-Kahn A, Hirsch JF: Prenatal hydrocephalus: outcome and prognosis. *Childs Nerv Syst* 4: 213–222, 1988
- 6) Sainte-Rose C, Piatt JH, Renier D, Pierre-Kahn A, Hirsch JF, Hoffman HJ, Humphreys RP, Hendrick EB: Mechanical complications in shunts. *Pediatr Neurosurg* 17: 2–9, 1991
- 7) Simon TD, Riva-Cambrin J, Srivastava R, Bratton SL, Dean JM, Kestle JR; Hydrocephalus Clinical Research Network: Hospital care for children with hydrocephalus in the United States: utilization, charges, comorbidities, and deaths. *J Neurosurg Pediatr* 1: 131–137, 2008
- 8) Williams MA, McAllister JP, Walker ML, Kranz DA, Bergsneider M, Del Bigio MR, Fleming L, Frim DM, Gwinn K, Kestle JR, Luciano MG, Madsen JR, Oster-Granite ML, Spinella G: Priorities for hydrocephalus research: report from a National Institutes of Health-sponsored workshop. *J Neurosurg* 107: 345–357, 2007
- 9) Greitz D: Radiological assessment of hydrocephalus: new theories and implications for therapy. *Neurosurg Rev* 27: 145–165; discussion 166–167, 2004
- 10) Cinalli G, Sainte-Rose C, Chumas P, Zerah M, Brunelle F, Lot G, Pierre-Kahn A, Renier D: Failure of third ventriculostomy in the treatment of aqueductal stenosis in children. *J Neurosurg* 90: 448–454, 1999
- 11) Hellwig D, Grotenhuis JA, Tirakotai W, Riegel T, Schulte DM, Bauer BL, Bertalanffy H: Endoscopic third ventriculostomy for obstructive hydrocephalus. *Neurosurg Rev* 28: 1–34; discussion 35–38, 2005
- 12) Cinalli G, Cappabianca P, de Falco R, Spennato P, Cianciulli E, Cavallo LM, Esposito F, Ruggiero C, Maggi G, de Divitiis E: Current state and future development of intracranial neuroendoscopic surgery. *Expert Rev Med Devices* 2: 351–373, 2005
- 13) Goumnerova LC, Frim DM: Treatment of hydrocephalus with third ventriculocisternostomy: outcome and CSF flow patterns. *Pediatr Neurosurg* 27: 149–152, 1997
- 14) Jones RF, Stening WA, Brydon M: Endoscopic third ventriculostomy. *Neurosurgery* 26: 86–91; discussion 91–92, 1990
- 15) Kim S-K, Wang KC, Cho BK: Surgical outcome of pediatric hydrocephalus treated by endoscopic III ventriculostomy: prognostic factors and interpretation of postoperative neuroimaging. *Childs Nerv Syst* 16: 161–168; discussion 169, 2000
- 16) Tisell M, Edsbacke M, Stephensen H, Czornyka M, Wikkelso C: Elastance correlates with outcome after endoscopic third ventriculostomy in adults with hydrocephalus caused by primary aqueductal stenosis. *Neurosurgery* 50: 70–77, 2002
- 17) Bilginer B, Oguz KK, Akalan N: Endoscopic third ventriculostomy for malfunction in previously shunted infants. *Childs Nerv Syst* 25: 683–688, 2009
- 18) Boschert J, Hellwig D, Krauss JK: Endoscopic third ventriculostomy for shunt dysfunction in occlusive hydrocephalus: long-term follow up and review. *J Neurosurg* 98: 1032–1039, 2003
- 19) Cinalli G, Salazar C, Mallucci C, Yada JZ, Zerah M, Sainte-Rose C: The role of endoscopic third ventriculostomy in the management of shunt malfunction. *Neurosurgery* 43: 1323–1327; discussion 1327–1329, 1998
- 20) Nishiyama K, Mori H, Tanaka R: Changes in cerebrospinal fluid hydrodynamics following endoscopic third ventriculostomy for shunt-dependent noncommunicating hydrocephalus. *J Neurosurg* 98: 1027–1031, 2003
- 21) Siomin V, Cinalli G, Grotenhuis A, Golash A, Oi S, Kothbauer K, Weiner H, Roth J, Beni-Adani L, Pierre-Kahn A, Takahashi Y, Mallucci C, Abbott R, Wisoff J, Constantini S: Endoscopic third ventriculostomy in patients with cerebrospinal fluid infection and/or hemorrhage. *J Neurosurg* 97: 519–524, 2002
- 22) Teo C, Jones R: Management of hydrocephalus by endoscopic third ventriculostomy in patients with myelomeningocele. *Pediatr Neurosurg* 25: 57–63; discussion 63, 1996
- 23) Beems T, Grotenhuis JA: Is the success rate of endoscopic third ventriculostomy age-dependent? An analysis of the results of endoscopic third ventriculostomy in young children. *Childs Nerv Syst* 18: 605–608, 2002
- 24) Buxton N, Macarthur D, Mallucci C, Punt J, Vloeberghs M: Neuroendoscopy in the premature population. *Childs Nerv Syst* 14: 649–652, 1998
- 25) Garg A, Suri A, Chandra PS, Kumar R, Sharma BS, Mahapatra AK: Endoscopic third ventriculostomy: 5 years' experience at the All India Institute of Medical Sciences. *Pediatr Neurosurg* 45: 1–5, 2009
- 26) Idowu O, Doherty A, Tiamiyu O: Initial experience with endoscopic third ventriculostomy in Nigeria, West Africa. *Childs Nerv Syst* 24: 253–255; discussion 257, 2008
- 27) Koch D, Wagner W: Endoscopic third ventriculostomy in infants of less than 1 year of age: which factors influence the outcome? *Childs Nerv Syst* 20: 405–411, 2004
- 28) Sufianov AA, Sufianova GZ, Iakimov IA: Endoscopic third ventriculostomy in patients younger than 2 years: outcome analysis of 41 hydrocephalus cases. *J Neurosurg Pediatr* 5: 392–401, 2010
- 29) Baldauf J, Oertel J, Gaab MR, Schroeder HW: Endoscopic third ventriculostomy in children younger than 2 years of age. *Childs Nerv Syst* 23: 623–626, 2007
- 30) Drake JM: Endoscopic third ventriculostomy in pediatric patients: the Canadian experience. *Neurosurgery* 60: 881–886; discussion 881–886, 2007

- 31) Hopf NJ, Grunert P, Fries G, Resch KD, Perneczky A: Endoscopic third ventriculostomy: outcome analysis of 100 consecutive procedures. *Neurosurgery* 44: 795–804; discussion 804–806, 1999
- 32) Kadrian D, van Gelder J, Florida D, Jones R, Vonau M, Teo C, Stening W, Kwok B: Long-term reliability of endoscopic third ventriculostomy. *Neurosurgery* 56: 1271–1278; discussion 1278, 2005
- 33) Oertel JM, Baldauf J, Schroeder HW, Gaab MR: Endoscopic options in children: experience with 134 procedures. *J Neurosurg Pediatr* 3: 81–89, 2009
- 34) Warf BC: Hydrocephalus in Uganda: the predominance of infectious origin and primary management with endoscopic third ventriculostomy. *J Neurosurg* 102(1 Suppl 1): 1–15, 2005
- 35) Sgouros S, Kulkarni AV, Constantini S: The International Infant Hydrocephalus Study: concept and rationale. *Childs Nerv Syst* 22: 338–345, 2006
- 36) Drake J, Chumas P, Kestle J, Pierre-Kahn A, Vinchon M, Brown J, Pollack IF, Arai H: Late rapid deterioration after endoscopic third ventriculostomy: additional cases and review of the literature. *J Neurosurg* 105: 118–126, 2006
- 37) Fabiano AJ, Doyle K, Grand W: Delayed stoma failure in adult communicating hydrocephalus after initial successful treatment by endoscopic third ventriculostomy: case report. *Neurosurgery* 66: E1210–E1211; discussion E1211, 2010
- 38) Hader WJ, Drake J, Cochrane D, Sparrow O, Johnson ES, Kestle J: Death after late failure of third ventriculostomy in children. Report of three cases. *J Neurosurg* 97: 211–215, 2002
- 39) Javadpour M, May P, Mallucci C: Sudden death secondary to delayed closure of endoscopic third ventriculostomy. *Br J Neurosurg* 17: 266–269, 2003
- 40) Lipina R, Palecek T, Reguli S, Kovarova M: Death in consequence of late failure of endoscopic third ventriculostomy. *Childs Nerv Syst* 23: 815–819, 2007
- 41) Mobbs RJ, Vonau M, Davies MA: Death after late failure of endoscopic third ventriculostomy: a potential solution. *Neurosurgery* 53: 384–385; discussion 385–386, 2003
- 42) Nigri F, Telles C, Acioly MA: Late obstruction of an endoscopic third ventriculostomy stoma by metastatic seeding of a recurrent medulloblastoma. *J Neurosurg Pediatr* 5: 641–644, 2010
- 43) Kulkarni AV, Shams I, Cochrane DD, McNeely PD: Does treatment with endoscopic third ventriculostomy result in less concern among parents of children with hydrocephalus? *Childs Nerv Syst* 26: 1529–1534, 2010
- 44) Feng H, Huang G, Liao X, Fu K, Tan H, Pu H, Cheng Y, Liu W, Zhao D: Endoscopic third ventriculostomy in the management of obstructive hydrocephalus: an outcome analysis. *J Neurosurg* 100: 626–633, 2004
- 45) Hellwig D, Giordano M, Kappus C: Redo third ventriculostomy. *World Neurosurg* 79(2 Suppl): S22. e13–e20, 2013
- 46) Koch D, Grunert P, Filippi R, Hopf N: Re-ventriculostomy for treatment of obstructive hydrocephalus in cases of stoma dysfunction. *Minim Invasive Neurosurg* 45: 158–163, 2002
- 47) Mohanty A, Vasudev MK, Sampath S, Radhesh S, Sastry Kolluri VR: Failed endoscopic third ventriculostomy in children: management options. *Pediatr Neurosurg* 37: 304–309, 2002
- 48) Siomin V, Weiner H, Wisoff J, Cinalli G, Pierre-Kahn A, Saint-Rose C, Abbott R, Elran H, Beni-Adani L, Ouaknine G, Constantini S: Repeat endoscopic third ventriculostomy: is it worth trying? *Childs Nerv Syst* 17: 551–555, 2001
- 49) Surash S, Chumas P, Bhargava D, Crimmins D, Straiton J, Tyagi A: A retrospective analysis of revision endoscopic third ventriculostomy. *Childs Nerv Syst* 26: 1693–1698, 2010
- 50) Cinalli G, Spennato P, Savarese L, Ruggiero C, Aliberti F, Cuomo L, Cianciulli E, Maggi G: Endoscopic aqueductoplasty and placement of a stent in the cerebral aqueduct in the management of isolated fourth ventricle in children. *J Neurosurg* 104: 21–27, 2006
- 51) da Silva LR, Cavalheiro S, Zymberg ST: Endoscopic aqueductoplasty in the treatment of aqueductal stenosis. *Childs Nerv Syst* 23: 1263–1268, 2007
- 52) Erşahin Y: Endoscopic aqueductoplasty. *Childs Nerv Syst* 23: 143–150, 2007
- 53) Sagan LM, Kojder I, Poncyłjusz W: Endoscopic aqueductal stent placement for the treatment of a trapped fourth ventricle. *J Neurosurg* 105: 275–280, 2006
- 54) Schroeder HW, Oertel J, Gaab MR: Endoscopic aqueductoplasty in the treatment of aqueductal stenosis. *Childs Nerv Syst* 20: 821–827, 2004
- 55) Schroeder C, Fleck S, Gaab MR, Schweim KH, Schroeder HW: Why does endoscopic aqueductoplasty fail so frequently? Analysis of cerebrospinal fluid flow after endoscopic third ventriculostomy and aqueductoplasty using cine phase-contrast magnetic resonance imaging. *J Neurosurg* 117: 141–149, 2012
- 56) Schroeder HW, Schweim C, Schweim KH, Gaab MR: Analysis of aqueductal cerebrospinal fluid flow after endoscopic aqueductoplasty by using cine phase-contrast magnetic resonance imaging. *J Neurosurg* 93: 237–244, 2000
- 57) Fritsch MJ, Schroeder HW: Endoscopic aqueductoplasty and stenting. *World Neurosurg* 79(2 Suppl): S20.e15–e18, 2013
- 58) Fritsch MJ, Kienke S, Manwaring KH, Mehdorn HM: Endoscopic aqueductoplasty and interventriculostomy for the treatment of isolated fourth ventricle in children. *Neurosurgery* 55: 372–377; discussion 377–379, 2004
- 59) de Ribaupierre S, Rilliet B, Vernet O, Regli L, Villemure JG: Third ventriculostomy vs ventriculoperitoneal shunt in pediatric obstructive hydrocephalus: results from a Swiss series and literature review. *Childs Nerv Syst* 23: 527–533, 2007
- 60) Kulkarni AV, Drake JM, Kestle JR, Mallucci CL, Sgouros S, Constantini S; Canadian Pediatric Neurosurgery Study Group: Endoscopic third ventriculostomy vs cerebrospinal fluid shunt in the treatment of hydrocephalus

- in children: a propensity score-adjusted analysis. *Neurosurgery* 67: 588–593, 2010
- 61) Hirsch JF: Percutaneous ventriculocisternostomies in non-communicating hydrocephalus. *Monogr Neurol Sci* 8: 170–178, 1982
- 62) Sainte Rose C: Third ventriculostomy, in Manwaring KH, Crone KR (eds): *Neuroendoscopy*. New York, Mary Ann Liebert, pp 47–62, 1992
- 63) Tuli S, Alshail E, Drake J: Third ventriculostomy versus cerebrospinal fluid shunt as a first procedure in pediatric hydrocephalus. *Pediatr Neurosurg* 30: 11–15, 1999
- 64) Drake JM, Kulkarni AV, Kestle J: Endoscopic third ventriculostomy versus ventriculoperitoneal shunt in pediatric patients: a decision analysis. *Childs Nerv Syst* 25: 467–472, 2009
- 65) Kulkarni AV, Shams I, Cochrane DD, McNeely PD: Quality of life after endoscopic third ventriculostomy and cerebrospinal fluid shunting: an adjusted multivariable analysis in a large cohort. *J Neurosurg Pediatr* 6: 11–16, 2010
- 66) Warf BC: Comparison of endoscopic third ventriculostomy alone and combined with choroid plexus cauterization in infants younger than 1 year of age: a prospective study in 550 African children. *J Neurosurg* 103(6 Suppl): 475–481, 2005
- 67) Warf BC, Campbell JW: Combined endoscopic third ventriculostomy and choroid plexus cauterization as primary treatment of hydrocephalus for infants with myelomeningocele: long-term results of a prospective intent-to-treat study in 115 East African infants. *J Neurosurg Pediatr* 2: 310–316, 2008
- 68) Warf B, Ondoma S, Kulkarni A, Donnelly R, Ampeire M, Akona J, Kabachelor CR, Mulondo R, Nsubuga BK: Neurocognitive outcome and ventricular volume in children with myelomeningocele treated for hydrocephalus in Uganda. *J Neurosurg Pediatr* 4: 564–570, 2009
- 69) Warf BC, Campbell JW, Riddle E: Initial experience with combined endoscopic third ventriculostomy and choroid plexus cauterization for post-hemorrhagic hydrocephalus of prematurity: the importance of prepontine cistern status and the predictive value of FIESTA MRI imaging. *Childs Nerv Syst* 27: 1063–1071, 2011
- 70) Warf BC, Dewan M, Mugamba J: Management of Dandy-Walker complex-associated infant hydrocephalus by combined endoscopic third ventriculostomy and choroid plexus cauterization. *J Neurosurg Pediatr* 8: 377–383, 2011
- 71) Warf BC, Stagno V, Mugamba J: Encephalocele in Uganda: ethnic distinctions in lesion location, endoscopic management of hydrocephalus, and survival in 110 consecutive children. *J Neurosurg Pediatr* 7: 88–93, 2011
- 72) Warf BC, Tracy S, Mugamba J: Long-term outcome for endoscopic third ventriculostomy alone or in combination with choroid plexus cauterization for congenital aqueductal stenosis in African infants. *J Neurosurg Pediatr* 10: 108–111, 2012
- 73) Warf BC: Congenital idiopathic hydrocephalus of infancy: the results of treatment by endoscopic third ventriculostomy with or without choroid plexus cauterization and suggestions for how it works. *Childs Nerv Syst* 29: 935–940, 2013
- 74) Kulkarni AV, Riva-Cambrin J, Browd SR, Drake JM, Holubkov R, Kestle JR, Limbrick DD, Rozzelle CJ, Simon TD, Tamber MS, Wellons JC, Whitehead WE; Hydrocephalus Clinical Research Network: Endoscopic third ventriculostomy and choroid plexus cauterization in infants with hydrocephalus: a retrospective Hydrocephalus Clinical Research Network study. *J Neurosurg Pediatr* 14: 224–229, 2014

Address reprint requests to: Kenichi Nishiyama, MD, PhD,
Brain Research Institute, University of Niigata, 1-757
Asahimachi, Chuo-ku, Niigata, Niigata 951-8585,
Japan.
e-mail: nishiken@d4.dion.ne.jp

Multiple therapeutic effects of progranulin on experimental acute ischaemic stroke

Masato Kanazawa,^{1,*} Kunio Kawamura,^{1,*} Tetsuya Takahashi,¹ Minami Miura,¹ Yoshinori Tanaka,² Misaki Koyama,¹ Masafumi Toriyabe,¹ Hironaka Igarashi,³ Tsutomu Nakada,³ Masugi Nishihara,² Masatoyo Nishizawa¹ and Takayoshi Shimohata¹

See Zhao and Bateman (doi:10.1093/awv123) for a scientific commentary on this article.

*These authors contributed equally to this work.

In the central nervous system, progranulin, a glycoprotein growth factor, plays a crucial role in maintaining physiological functions, and progranulin gene mutations cause TAR DNA-binding protein-43-positive frontotemporal lobar degeneration. Although several studies have reported that progranulin plays a protective role against ischaemic brain injury, little is known about temporal changes in the expression level, cellular localization, and glycosylation status of progranulin after acute focal cerebral ischaemia. In addition, the precise mechanisms by which progranulin exerts protective effects on ischaemic brain injury remains unknown. Furthermore, the therapeutic potential of progranulin against acute focal cerebral ischaemia, including combination treatment with tissue plasminogen activator, remains to be elucidated. In the present study, we aimed to determine temporal changes in the expression and localization of progranulin after ischaemia as well as the therapeutic effects of progranulin on ischaemic brain injury using *in vitro* and *in vivo* models. First, we demonstrated a dynamic change in progranulin expression in ischaemic Sprague-Dawley rats, including increased levels of progranulin expression in microglia within the ischaemic core, and increased levels of progranulin expression in viable neurons as well as induction of progranulin expression in endothelial cells within the ischaemic penumbra. We also demonstrated that the fully glycosylated mature secretory isoform of progranulin (~88 kDa) decreased, whereas the glycosylated immature isoform of progranulin (58–68 kDa) markedly increased at 24 h and 72 h after reperfusion. *In vitro* experiments using primary cells from C57BL/6 mice revealed that the glycosylated immature isoform was secreted only from the microglia. Second, we demonstrated that progranulin could protect against acute focal cerebral ischaemia by a variety of mechanisms including attenuation of blood–brain barrier disruption, neuroinflammation suppression, and neuroprotection. We found that progranulin could regulate vascular permeability via vascular endothelial growth factor, suppress neuroinflammation after ischaemia via anti-inflammatory interleukin 10 in the microglia, and render neuroprotection in part by inhibition of cytoplasmic redistribution of TAR DNA-binding protein-43 as demonstrated in progranulin knockout mice (C57BL/6 background). Finally, we demonstrated the therapeutic potential of progranulin against acute focal cerebral ischaemia using a rat autologous thrombo-embolic model with delayed tissue plasminogen activator treatment. Intravenously administered recombinant progranulin reduced cerebral infarct and oedema, suppressed haemorrhagic transformation, and improved motor outcomes ($P = 0.007$, 0.038 , 0.007 and 0.004 , respectively). In conclusion, progranulin may be a novel therapeutic target that provides vascular protection, anti-neuroinflammation, and neuroprotection related in part to vascular endothelial growth factor, interleukin 10, and TAR DNA-binding protein-43, respectively.

1 Department of Neurology, Brain Research Institute, Niigata University, Niigata, Japan

2 Department of Veterinary Physiology, Graduate School of Agricultural and Life Sciences, The University of Tokyo, Tokyo, Japan

3 Department of Centre for Integrated Human Brain Science, Brain Research Institute, Niigata University, Niigata, Japan

Received September 19, 2014. Revised December 27, 2014. Accepted January 27, 2015. Advance Access publication April 2, 2015

© The Author (2015). Published by Oxford University Press on behalf of the Guarantors of Brain. All rights reserved.

For Permissions, please email: journals.permissions@oup.com

Correspondence to: Dr Takayoshi Shimohata,
Department of Neurology,
Brain Research Institute,
Niigata University,
1-757 Asahimachi-dori,
Chuoku, Niigata,
Niigata 951-8585,
Japan
E-mail: t-shimo@bri.niigata-u.ac.jp

Keywords: progranulin; cerebral ischaemia; VEGF; IL10; TDP-43

Abbreviations: FTLD-TDP = TAR DNA binding protein positive frontotemporal lobar degeneration; OGD = oxygen glucose deprivation; TDP-43 = TAR DNA-binding protein 43; TGF- β = transforming growth factor beta; TNF- α = tumor necrosis factor alpha; tPA = tissue plasminogen activator

Introduction

Progranulin (PGRN) is a secreted N-linked glycoprotein growth factor implicated in tissue regeneration, wound repair, and inflammation (He *et al.*, 2003a). Several *in vitro* studies have revealed that PGRN is classified into two isoforms according to its glycosylation status, the glycosylated immature isoform (58–68 kDa) and the fully glycosylated mature secretory isoform (~88 kDa) (Shankaran *et al.*, 2008; Naphade *et al.*, 2010; Alquézar *et al.*, 2014).

In the CNS, PGRN is considered to play a crucial role in maintaining physiological functions and in the survival of neurons for the following reasons: first, primary cortical neurons derived from *Pgrn* knockout mice showed reduced neuronal survival (Kleinberger *et al.*, 2010); second, PGRN has been shown to exhibit neurotrophic activity *in vitro* (Van Damme *et al.*, 2008) and *in vivo* (Laird *et al.*, 2010); and third, mutations in the *Pgrn* gene caused ubiquitin- and TAR DNA binding protein-positive frontotemporal lobar degeneration (FTLD-TDP), a progressive neurodegenerative disorder with an autosomal dominant inheritance pattern (Baker *et al.*, 2006; Cruts *et al.*, 2006).

Several studies raise the possibility that PGRN might be involved in ischaemic brain injury. First, PGRN might play a vascular protective role against focal cerebral ischaemia via suppression of blood–brain barrier disruption. Recent studies have demonstrated that intraventricular administration of recombinant PGRN could suppress cerebral oedema in a mouse transient focal cerebral ischaemia (suture model) (Egashira *et al.*, 2013), and that *Pgrn* knockout mice may prompt post-ischaemic blood–brain barrier disruption (Jackman *et al.*, 2013).

Second, PGRN has been shown to be involved in neuroinflammation after ischaemic brain injury. Previous studies have demonstrated that PGRN was induced in activated microglia after spinal cord injury (Naphade *et al.*, 2010) and traumatic brain injury (Tanaka *et al.*, 2013), indicating that the induction of PGRN reflects microglial responses. Similarly, in ischaemic brain injury, microglia have been shown to mediate expansion of the

infarct via inflammation in the acute phase (Mabuchi *et al.*, 2000; Yenari *et al.*, 2010), while it might also contribute to endogenous anti-inflammatory protection in the subacute phase (Faustino *et al.*, 2011). In this context, recent studies suggested that PGRN might suppress secretion of pro-inflammatory cytokines and recruitment of neutrophils associated with focal cerebral ischaemia (Tao *et al.*, 2012; Egashira *et al.*, 2013). However, a recent study showed that PGRN was not involved in neuroinflammation related to acute focal cerebral ischaemia (Jackman *et al.*, 2013). Therefore, the role of PGRN in neuroinflammation after ischaemic brain injury is controversial.

Third, PGRN might exhibit protective effects on neuronal cells after acute focal cerebral ischaemia based on analyses using transgenic mice expressing PGRN (Tao *et al.*, 2012) and *Pgrn* knockout mice (Jackman *et al.*, 2013), although the mechanism of neuroprotection remains unknown. We previously demonstrated that ischaemic neuronal injury might be caused in part by cleavage and cytoplasmic redistribution of TARDBP (previously known as TDP-43), a key protein in FTLD-TDP and amyotrophic lateral sclerosis (Kanazawa *et al.*, 2011b). Because PGRN can suppress the cleavage of TARDBP via inhibiting caspase 3 (Zhang *et al.*, 2007; Kanazawa *et al.*, 2011b), it raises the possibility that PGRN may prevent ischaemic neuronal injury via preservation of TARDBP functions.

Based on the abovementioned findings, we speculated that PGRN could exert a positive therapeutic effect via regulation of blood–brain barrier function, suppression of inflammation, and neuroprotection against acute focal cerebral ischaemia. Here, we investigated temporal changes in PGRN after focal cerebral ischaemia, including its cellular expression, glycosylation status, and sources of secretion. We also examined the role of PGRN in neuroinflammation after ischaemic brain injury and the mechanisms of neurovascular protective effects of PGRN. Moreover, we used a rat autologous thrombo-embolic model (Okubo *et al.*, 2007), which shows cerebral oedema and haemorrhagic transformation when tissue plasminogen activator (tPA) is administered beyond the therapeutic time window

(Kanazawa *et al.*, 2011a; Kawamura *et al.*, 2014) and demonstrated for the first time that intravenous administration of recombinant PGRN showed therapeutic effects on the volumes of cerebral infarct and oedema, haemorrhagic transformation, and prognosis.

Materials and methods

This study was carried out in strict accordance with the recommendations from the Guide for the Care and Use of Laboratory Animals of the National Institutes of Health. The protocol was approved by the Niigata University Administrative Panel on Laboratory Animal Care. All surgeries were performed under inhalation and intraperitoneal anaesthesia and according to the ARRIVE (Animal Research: Reporting of In Vivo Experiments) guidelines (Kilkenny *et al.*, 2010).

Focal cerebral ischaemia

Transient acute focal cerebral ischaemia was induced using the intraluminal filament in male Sprague-Dawley rats weighing 300–370 g and wild-type (C57BL/6) and *Pgrn* knockout mice (C57BL/6 background) weighing 22–28 g (Kanazawa *et al.*, 2011b). Briefly, anaesthesia was administered via inhalation of 1.5% halothane in a mixture of 70% nitrous oxide and 30% oxygen for rats and with intraperitoneal injection 10 mg/kg xylazine and 300 mg/kg chloral hydrate for mice. A nylon monofilament, with a diameter of 0.148 mm for rats and 0.074 mm for mice, was used for suturing. The tip of the nylon monofilament was rounded with heat. An 11-mm distal suture segment was coated with 0.350 mm diameter silicon for rats, and a 4-mm distal suture segment was coated with 0.185 mm diameter silicon for mice. Middle cerebral artery occlusion was performed by insertion of the suture via an external carotid artery into the internal carotid artery. After 90 min of ischaemia, the suture was withdrawn to restore blood flow. Body core temperature monitored with a rectal probe was maintained at $37.0 \pm 0.5^\circ\text{C}$, using a heating pad. To exclude the effects of anomalies of circle of Willis on the ischaemic size and oedema in *Pgrn* knockout mice, we investigated patterns of circle of Willis in both wild-type and *Pgrn* knockout mice using transcatheter perfusion with carbon black suspended in saline ($n \geq 7$) (Supplementary Fig. 1; Özdemir *et al.*, 1999). The sample size was calculated before performing the experiments. We calculated the sample size needed to detect the difference in the amount of cerebral haemorrhage or cerebral oedema volume between the tPA with the recombinant PGRN group and tPA with the control group with 80% power ($\alpha = 0.05$; one-sided analysis). Mice and rats were randomly assigned to various experimental groups, and analyses were performed by an investigator blinded to genotype and treatment.

Immunoblotting

The rats that survived for 10 min, 4 h, 10 h, 18 h, 24 h, and 72 h after reperfusion were euthanized with an overdose of halothane, followed by intracardiac perfusion with cold normal saline. We defined ischaemic penumbra as the region that was rescued by reperfusion, and the ischaemic core as the

region that was not rescued by reperfusion as described previously (Memezawa *et al.*, 1992; Kanazawa *et al.*, 2011b). The cortical tissues corresponding to the ischaemic core or penumbra were dissected for immunoblotting as described (Kanazawa *et al.*, 2011b). Cortical tissues from the sham-operated rats were also dissected as controls. For whole-cell extracts, proteins from brain tissues were extracted as described previously (Shimohata *et al.*, 2007). The proteins (50 μg) were subjected to tris-glycine sodium dodecyl sulphate polyacrylamide gel electrophoresis (SDS-PAGE).

For the whole-cell extracts *in vitro*, cells were harvested in cold cell lysis buffer (Cell Signaling Technology). Conditioned media were collected and concentrated ($30\times$) using Amicon Ultra-0.5 tubes (Millipore). Proteins (5 μg) in the samples were separated by tris-glycine SDS-PAGE and were probed with primary antibodies (Supplementary Table 1), followed by a secondary horseradish peroxidase-conjugated antibody (1:10 000). Signals were detected by an enhanced chemiluminescence (Millipore) and semiquantified by densitometry ($n = 5$). The membranes were stripped and probed with an anti- β -actin or an anti-transferrin antibody to confirm even loading of proteins.

Immunofluorescence staining and confocal microscopy

Rats and mice euthanized with an overdose inhalation of halothane or intraperitoneal injection of xylazine chloral hydrate were sacrificed by transcatheter perfusion with normal saline followed by perfusion with cold 4% paraformaldehyde in 0.1 M phosphate-buffered saline (PBS; pH 7.4) at 24 h and 72 h after reperfusion. We stained free-floating sections as described previously (Kanazawa *et al.*, 2011b) and mounted with Vectashield DAPI (Vector Laboratories). Information of the primary antibodies is described in Supplementary Table 1. The sections were examined under a confocal laser-scanning microscope (LSM510 META; Carl Zeiss). The results were confirmed in three independent samples.

Immunohistochemistry

Deeply anaesthetized rats and mice were perfused intracardially with cold 4% paraformaldehyde at 24 h and 72 h after reperfusion. The brains were removed and embedded in paraffin wax. Serial sections (4- μm thick) were cut from the paraffin blocks and stained using antibodies (Supplementary Table 1). The immunoreactive products were visualized using the ABC Vectastain kit (Vector Laboratories) and diaminobenzidine as the chromogen. The results were confirmed in three independent samples.

To measure immunoreactivity, we used ImageJ software 1.37r (National Institutes of Health, Bethesda, MD, USA) as described elsewhere (Krishnamurthy *et al.*, 2009). Briefly, images of the stained sections were visualized, examined blindly, and seven randomly chosen non-overlapping high-power fields ($\times 400$) covering the ischaemic cortex were analysed for both wild-type and *Pgrn* knockout mice ($n = 21$). For each image field, the total number of pixels was quantified on a grey scale (0–255). The levels of immunoreactivities were expressed as the average density (mean pixel value in an image field \pm SEM) for each experimental group.

Measurement of the volume of the cerebral infarct and oedema

At 24 h after reperfusion, the rats and mice were given highly concentrated halothane and deeply anaesthetized. After transcardial perfusion with saline, the brains were extracted. The brains were cut into 3-mm slices and stained with 2% 2, 3, 5-triphenyltetrazolium chloride solution (#264310; BD, Franklin Lakes). After staining, the slices were photographed with a scanner (CanoScan LiDE 50; Canon Inc), and cerebral infarct volume and cerebral oedema volume were measured with ImageJ software 1.37r (National Institutes of Health, Bethesda, MD, USA) according to the method described by Swanson *et al.* (1990). These values were expressed as a proportion of the cerebral hemisphere occupied. The analyses were performed by an investigator blinded to the genotype and treatment.

Neurological evaluations

Neurological evaluations were conducted at 24 h after reperfusion with a 6-point neurological scale (Zausinger *et al.*, 2000). Specifically, grade 5 indicated no neurological findings, grade 4 indicated an inability to move forward with the foot on the affected side, grade 3 indicated weak resistance to a force that was applied from the side on a level surface, grade 2 indicated turning to the affected side when pulled from behind on a level surface, grade 1 indicated spontaneously turning to the affected side, and grade 0 indicated an inability to move spontaneously or death.

Pgrn knockout mice

Pgrn knockout mice were produced by breeding heterozygous pairs in the Graduate School of Agricultural and Life Sciences, at the University of Tokyo, and genotyped using previously described protocols (Kayasuga *et al.*, 2007). Additionally, *Pgrn* knockout mice purchased from RIKEN BioResource Centre (Tsukuba, Japan) were bred and maintained in the Department of Comparative and Experimental Medicine, Brain Research Institute, Niigata University. We used only homozygous pairs to obtain *Pgrn* knockout pups. The mice were maintained under controlled light (lights on, 05:00–19:00), temperature ($23 \pm 1^\circ\text{C}$), and humidity ($55 \pm 10\%$) and given free access to food and water.

C6 cell culture and analysis of glycosylation

Rat C6 cells were grown in Opti-MEM[®] (Gibco/Invitrogen) with 10% foetal bovine serum (FBS) and 1% penicillin-streptomycin. Cells were grown in Opti-MEM[®] without FBS 24 h before the experiments. Cells were harvested in cell lysis buffer (Cell Signaling Technology) containing 1% Triton[™] X-100 and inhibitors for proteases and phosphatases (Sigma-Aldrich). After centrifugation at 14 000 rpm for 5 min (4°C), the supernatants were collected. Additionally, conditioned media were also obtained for immunoblotting. To analyse glycosylation of PGRN, cell lysates and media were digested at 37°C with peptide-N-glycosidase F (PNGase F; New England Biolabs) according to manufacturer's instructions, in triplicate.

Primary cell cultures

Primary murine neuronal cells were prepared from the neocortices of embryonic Day 17 C57Bl/6 mouse embryos (Takeuchi *et al.*, 2005). Briefly, cortical fragments were dissociated into single cells in a dissociation solution (Sumitomo Bakelite) and resuspended in nerve culture medium (Sumitomo Bakelite). Neurons were plated onto poly-D-lysine-coated (P7405, Sigma-Aldrich) six-well dishes (10×10^4 cells per well). The purity of these neuronal cultures was 95% as determined by NeuN-specific immunostaining (Takeuchi *et al.*, 2005).

Primary murine microglia and astrocytes were obtained as previously described (Milner *et al.*, 2008). Primary mixed glial cultures were established from the forebrains of postnatal C57Bl/6 mice by dissociating isolated cerebral cortices in papain and then growing the resulting cell suspension for 10 days in Dulbecco's modified Eagle medium (DMEM) supplemented with 10% FBS. After 10 days, the flasks were shaken for 15 min to remove the loosely attached microglia. The purity of these microglial cultures was 99% as determined by Mac-1 immunoreactivity in flow cytometry (Milner *et al.*, 2008). For astrocytes, the flasks were then shaken overnight to remove the microglia and oligodendrocyte precursors. The remaining monolayer was determined as >95% astrocytes by glial fibrillary acidic protein (GFAP) immunoreactivity (Milner *et al.*, 2008).

To investigate the effect of microglia and astrocytes on secretion of vascular endothelial growth factor (VEGF) from astrocyte after oxygen glucose deprivation (OGD), we cultured astrocytes with microglial conditioned media. Briefly, after we performed OGD using primary murine microglia, we collected the microglial low-glucose conditioned media. Then, we removed the astrocytic high-glucose conditioned media and washed thoroughly with PBS. We finally exchanged the PBS for the collected microglial low-glucose conditioned media. After overnight incubation under OGD condition, we measured the level of VEGF in the conditioned media using VEGF Quantikine[®] ELISA Kit (RRV00, R&D Systems), according to the manufacturer's instructions ($n = 6-7$). IL10 levels in the conditioned media from microglia were also determined by a sandwich ELISA using the IL10 Quantikine[®] ELISA Kit (M1000B, R&D Systems), according to the manufacturer's instructions ($n = 5-6$).

Oxygen-glucose deprivation

The standardized conditions for OGD have been described in detail elsewhere (Milner *et al.*, 2008). Briefly, before induction of OGD, serum-containing media was removed from the cell cultures by washing twice thoroughly with PBS before adding serum-free high glucose medium (4.5 mg/l, DMEM containing 4 mM L-glutamine, penicillin, and streptomycin, supplemented with N1 medium) or low-glucose medium (1.0 mg/l, supplemented with DMEM). The cultures containing low-glucose medium were placed in a hypoxia chamber (Billups-Rothenburg), which was flushed with a mixture of 95% N₂ and 5% CO₂ for 1 h, and then closed for 18 h or 24 h. Oxygen levels decreased to 0.1–0.4% at 4 h and was maintained throughout the experiment (del Zoppo *et al.*, 2012).

To determine the effects of PGRN under OGD, we added full-length recombinant mouse PGRN produced from HEK293 cells (AG-40A-0080, AdipoGen) into conditioned media. The recombinant PGRN is N-glycosylated, as determined by a

PNGase F assay (manufacturer's datasheet). Because a FLAG-tag was attached to the C-terminus of the recombinant PGRN protein, localization of exogenous recombinant PGRN protein was determined by immunohistochemical staining with an anti-FLAG antibody (Supplementary Table 1).

The survival of cells in culture exposed to OGD was determined by lactate dehydrogenase (LDH) release into the culture supernatant using a kit assay in six-well format (Roche Diagnostics), according to the manufacturer's instructions. The relative assessments of cytotoxicity were normalized by comparison with 100% cell damage ($n = 5$). The survival of neuronal cells in the culture exposed to OGD was determined using the propidium iodide method in which 33 $\mu\text{g}/\text{ml}$ propidium iodide solution (Sigma) was added to each well, followed by incubation for 5 min (Osada *et al.*, 2011).

Cell counting protocols

To determine the frequency of propidium iodide-positive neuronal cells after OGD conditions, we examined seven randomly chosen non-overlapping high-power fields ($\times 630$) of primary neuronal cells incubated under OGD conditions for 24 h ($n = 21$) (Kanazawa *et al.*, 2011b). To determine the frequency of microtubule-associated protein 2 (MAP2)-positive neurons with cytoplasmic redistribution of TARDBP, seven randomly chosen non-overlapping high-power fields ($\times 630$) of primary neuronal cells under normoxic or OGD conditions during 24 h were examined ($n = 7$) (Kanazawa *et al.*, 2011b). We also determined the appearance frequencies of microglia and neutrophils in the ischaemic tissue in wild-type and *Pgrn* knockout mice by examining seven randomly chosen non-overlapping high-power fields ($\times 400$) ($n = 21$). These analyses were conducted blinded to the sample information.

Reverse transcription polymerase chain reaction

Primary microglia were collected as pellets after centrifugation at 13 000 rpm for 10 min. Total RNA was isolated from the samples using NucleoSpin[®] RNA XS (U0902A, Takara Bio), and the first-strand cDNA was synthesized with ReverTra Ace (FSQ-101, TOYOBO). PCR reactions were performed with PrimeSTAR[®] Max DNA Polymerase (Takara Bio) and the following primers: TNF- α (forward, 5'- AAGAGGCACT CCCCAAAAG -3'; reverse, 5'- GCTACAGGCTTGTCACT CGAA -3'), TGF- β (forward, 5'- TGGAGCAACATGTGGA ACTC -3'; reverse, 5'- CAGCAGCCGGTTACCAAG -3'), IL-10 (forward, 5'- CTAACCGACTCCTTAATGCAG -3'; reverse, 5'- TTAAAATCACTCTTACCT -3'), and actin (forward, 5'- CATCCGTAAGACCTCTATGCCAAC -3'; reverse, 5'- ATGGAGCCACCGATCCACA -3'). The PCR reactions were carried out as follows: 35 cycles for amplification at 98°C for 10 s, 55°C for 5 s, and 72°C for 5 s. The genes of interest were normalized to actin ($n = 5-7$).

Quantitative real-time PCR

Primary microglia were collected as pellets after centrifugation at 13 000 rpm for 10 min. Total RNA was isolated from samples using NucleoSpin RNA XS (U0902A, Takara Bio), and first-strand cDNA was synthesized from total RNA by

ReverTra Ace (TOYOBO). Quantitative RT-PCR was performed with SYBR[®] Green Premix ExTaq on a TP-850 Real-Time PCR Detection system (Takara Bio). We designed primer pairs for IL10 as follows: (forward, 5'- ATTTGAATTCCCTGGGTGAGAAG -3'; reverse, 5'- CACAGGGGAGAAATCGATGACA -3'). PCR conditions were 30 s at 95°C for initial denaturing, followed by 40 cycles of 5 s at 95°C and 30 s at 60°C. Expression levels of the target gene relative to housekeeping enzyme (Takara Bio) were determined using the $\Delta\Delta\text{CT}$ method ($n = 3-4$).

Thrombolytic treatment with tissue plasminogen activator and PGRN

Cerebral ischaemia was created using a model of focal embolic ischaemia, in which the animals had their middle cerebral artery occluded by autologous thrombi (Okubo *et al.*, 2007; Kanazawa *et al.*, 2011a). tPA was administered intravenously in the form of alteplase (Mitsubishi Tanabe Pharma Co.) at a dose of 10 mg/kg per animal at 4 h after cerebral ischaemia, because we previously demonstrated that this condition caused cerebral oedema, haemorrhagic transformation, and severe prognosis (Kanazawa *et al.*, 2011a; Kawamura *et al.*, 2014). We demonstrated that cerebral cortical blood flow decreased by 40% from baseline after ischaemia and tPA treatment 4 h after ischaemia improved it by >70% from baseline in this thrombo-embolic model (Kanazawa *et al.*, 2011a). Immediately before tPA administration, 100 μg of FLAG-tagged recombinant PGRN or control protein (IgG; R5G10-048, OEM Concepts) was administered as a bolus through a catheter in the inguinal vein ($n = 6-7$). The volumes of the cerebral infarct and oedema, cerebral haemorrhage, neurological evaluations, and mortality ratio were examined. Cerebral infarct and oedema and cerebral haemorrhage measurements were performed in a randomized and blinded manner.

Statistical analyses

All data were presented as mean \pm SEM. Differences in the parameters were analysed using one-way or two-way ANOVA, followed by Bonferroni's *post hoc* test or unpaired *t*-test. Statistical analyses were performed using SPSS (ver.21; SPSS Inc.). Differences in the frequencies were assessed with Fisher's exact test or Mann-Whitney's U-test. All tests were considered statistically significant at a *P*-value < 0.05.

Results

Post-ischaemic changes of PGRN expression in neuronal cells, microglia and endothelial cells in rat cerebral cortex

To investigate the expression and localization of PGRN in the non-ischaemic cortex of Sprague-Dawley rats, we performed immunofluorescence staining using an anti-PGRN antibody. At first we tested specificity of the anti-PGRN antibody by immunoblotting and immunohistochemistry.

The cell lysates and brain tissue from *Pgrn* knockout mice did not show immunoreactivity against the antibody (Supplementary Fig. 1). Confocal microscopic studies revealed that the immunoreactivity for PGRN was detected only in cortical neurons (Fig. 1). PGRN was detected in a punctate pattern within neuronal cytoplasm, and double immunostaining revealed that PGRN was co-localized with marker proteins for the endoplasmic reticulum, Golgi apparatus, and lysosome [ERp57 (now known as PDIA3), Golgi-58k, and LAMP1, respectively]. We did not identify microglia or vessels that expressed PGRN.

We next investigated the effect of acute focal ischaemia on the expression and localization of PGRN using ischaemic Sprague-Dawley rats. Immunohistochemical analyses revealed that PGRN was not observed in the neurons from the ischaemic core (Fig. 2A), but observed in surviving neurons from the ischaemic penumbra (Fig. 2A). The expression pattern of PGRN in the surviving neurons from the ischaemic penumbra is diffused and strong, which is different from that of the non-ischaemic neurons (Fig. 2A). PGRN-positive microglia were increased at 24 h and markedly increased at 72 h after reperfusion, especially on the border of the ischaemic core and penumbra on the ischaemic core side (Fig. 2B). In addition, PGRN expression was observed in the von Willebrand factor-positive endothelial cells in the ischaemic penumbra at 24 h after reperfusion (Fig. 2C).

Temporal changes in PGRN expression and its glycosylated status in rat cerebral cortex after acute focal cerebral ischaemia

To investigate the effects of acute focal ischaemia on the expression and glycosylation status of PGRN, we next performed immunoblotting using whole-cell extracts of the ischaemic cortex of Sprague-Dawley rats. In the ischaemic core, the level of ~88 kDa PGRN gradually decreased after reperfusion, although it recovered at 72 h after reperfusion (Fig. 3A and B). On the other hand, the level of 58–68 kDa PGRN did not change until 18 h, but increased at 24 h and markedly increased at 72 h after reperfusion (Fig. 3A and B). In the ischaemic penumbra, the ~88-kDa PGRN decreased slightly, but not significantly, after reperfusion, while the 58–68 kDa PGRN moderately increased (Fig. 3A and B).

To confirm whether these two bands indicated secretory isoforms of PGRN, an *in vitro* study was performed. Cell lysates and conditioned media from rat C6 cells were subjected to immunoblotting, as this tumor cell line produces PGRN during growth (Liau *et al.*, 2000). We identified a low molecular-weight band (58–68 kDa) in the cell lysates and a high molecular-weight band (~88 kDa) in the conditioned media (Fig. 3C). In addition, after digestion with PNGase F, which cleaves all N-linked oligosaccharides,

the mobility of both bands from rat C6 cells changed to 58 kDa. A similar result was observed from an experiment using rat non-ischaemic brains (Fig. 3D). Therefore, it is considered that the high molecular-weight band (~88 kDa) was the secretory form of the fully glycosylated isoform of PGRN and that the low molecular-weight band (58–68 kDa) was the pre-secretory form of the glycosylated immature isoform of PGRN (Fig. 3D).

Production and secretion of the two isoforms of PGRN after OGD

To determine the potential cellular sources of the glycosylated immature isoform of 58–68 kDa PGRN, which markedly increased after reperfusion in ischaemic rats, immunoblot analyses of whole-cell extracts and conditioned media from primary murine neurons or microglia were performed. After 18 h incubation under OGD, both neurons and microglia were not dead as determined by the lack of change in LDH release from the cells (Fig. 4A). Under normoxic conditions, 58–68 kDa PGRN was observed in the neuronal cell extracts similar to C6 cell (Fig. 4B), and the ~88-kDa PGRN was observed in both neuronal and microglial conditioned media (Fig. 4C). We found that, after 18 h incubation under OGD, neurons produced ~88 kDa and 58–68 PGRN and secreted ~88 kDa PGRN, and the microglia produced ~88 kDa PGRN, and secreted both ~88 kDa and 58–68 kDa PGRN (Fig. 4C). Therefore, the glycosylated immature isoform of 58–68 kDa PGRN was secreted only from microglia.

Volumes of cerebral infarct and oedema, and outcome after ischaemia in *Pgrn* knockout mice

To investigate the roles of PGRN in acute focal cerebral ischaemia, we compared volumes of cerebral infarct and oedema between *Pgrn* knockout mice and wild-type mice, and evaluated the outcome by motor scale after middle cerebral artery occlusion. Before the comparison, we evaluated vascular anomaly of the circle of Willis (Özdemir *et al.*, 1999) of *Pgrn* knockout mice, and found no significant difference in vascular structure between wild-type and *Pgrn* knockout mice (Supplementary Fig. 2). There was also no significant difference in infarct size at 24 h after reperfusion between the two groups ($P = 0.12$) (Fig. 5A). However, cerebral oedema in the *Pgrn* knockout mice was larger than that in the wild-type mice at 24 h after reperfusion ($P = 0.048$) (Fig. 5B). In addition, motor scale at 24 h after reperfusion in *Pgrn* knockout mice was worse than that in the wild-type mice ($P = 0.02$) (Fig. 5C). There were no significant differences in cerebral oedema and motor scale at 72 h after reperfusion between the two groups ($P = 0.95$ and 0.75 , respectively).

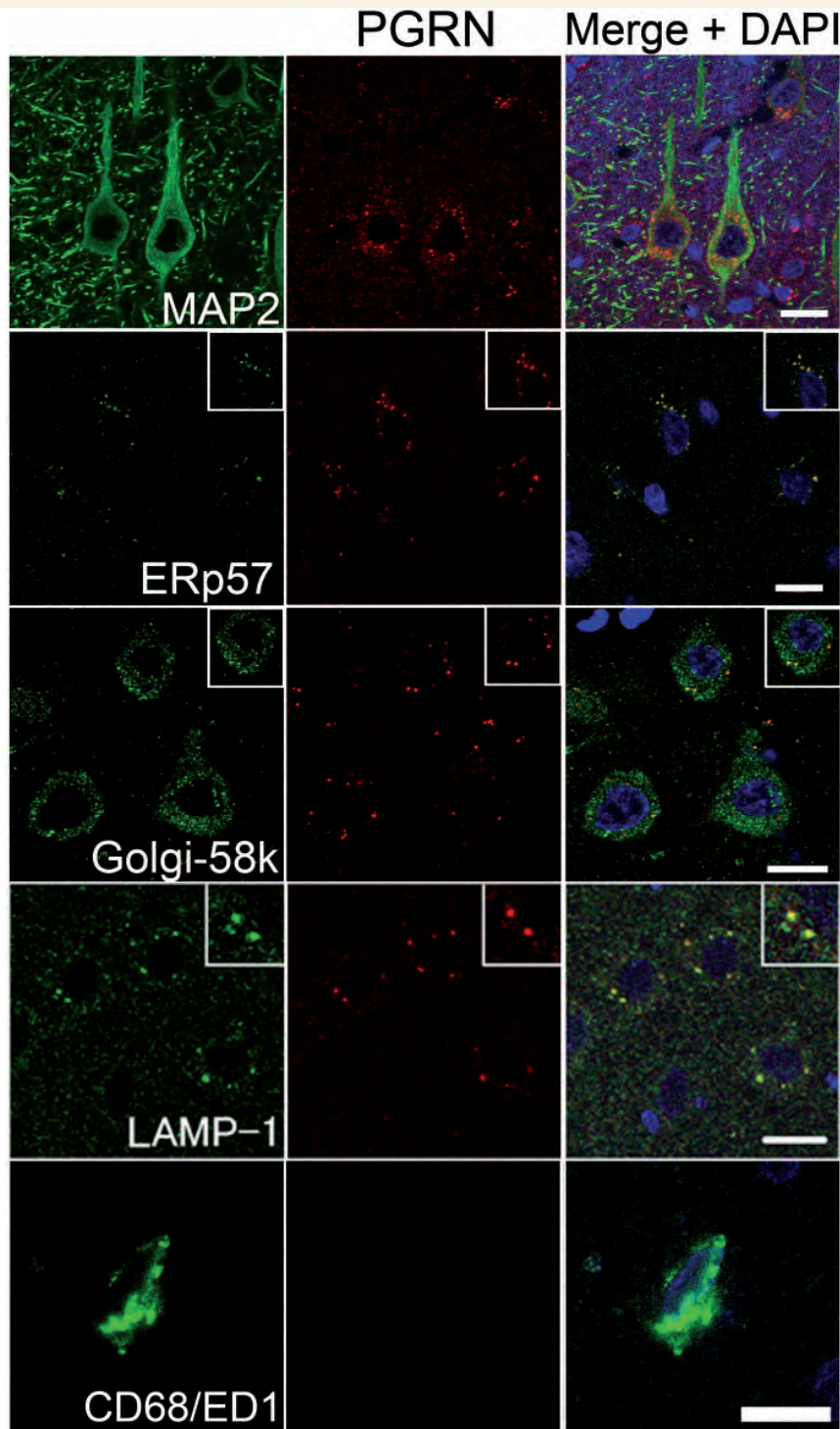


Figure 1 Analyses of PGRN expression in neuronal cells and microglia from rat non-ischaemic cerebral cortex. Microtubule-associated protein 2 (MAP2), endoplasmic reticulum stress protein 57 (ERp57, now known as PDIA3), Golgi-58k, lysosomal associated membrane protein 1 (LAMP-1), CD68/ED1 (green) / PGRN (red) / 4',6'-diamidino-2-phenylindole (DAPI; blue) triple labelling in the non-ischaemic cortices examined by confocal microscopy. MAP2, ERp57, Golgi-58k, LAMP1, and CD68/ED1 are markers for neuronal cells, endoplasmic reticulum, Golgi apparatus, lysosome, and microglia, respectively. Scale bars = 10 μ m.

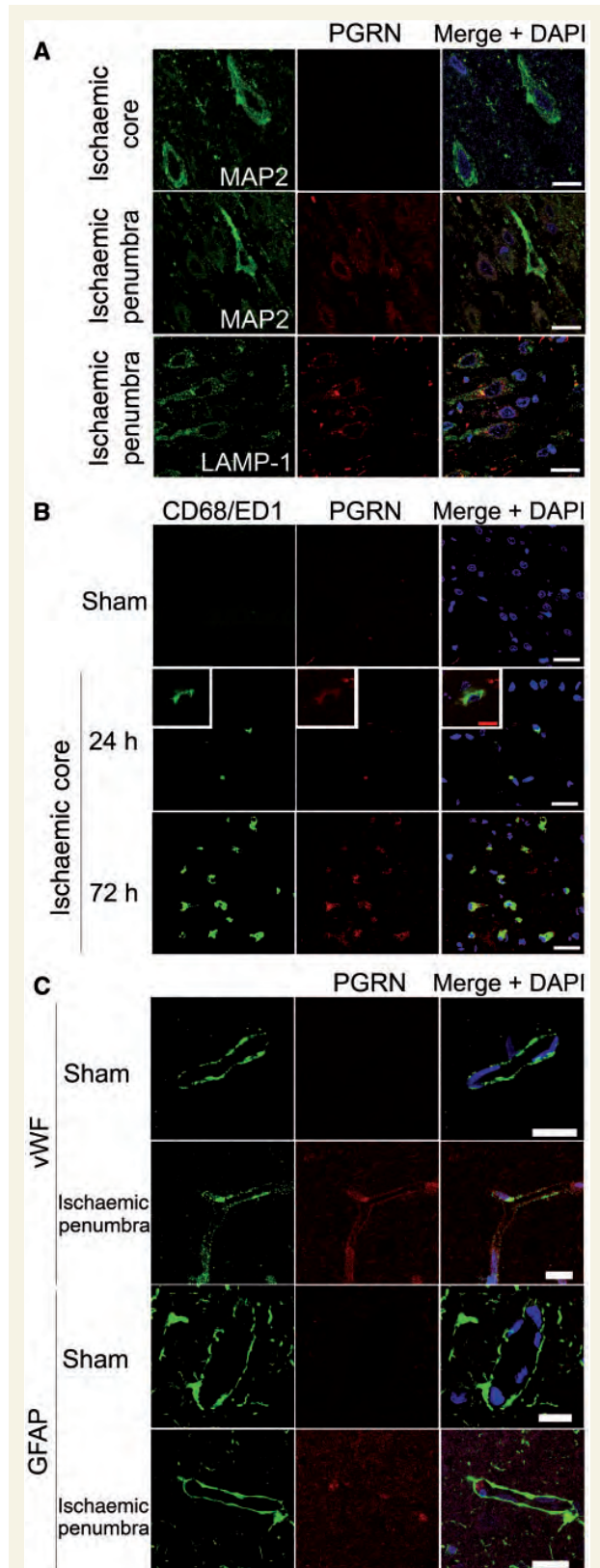


Figure 2 Post-ischaemic changes in PGRN expression in neuronal cells, microglia and endothelial cells in the rat cerebral cortex. (A) The absence of PGRN expression in the

Recruitment of neutrophils and microglia after ischaemia in *Pgrn* knockout mice

Because a recent study reported that recombinant PGRN treatment suppressed neutrophil recruitment into ischaemic mouse brain (Egashira *et al.*, 2013), we investigated whether cerebral oedema in *Pgrn* knockout mice is associated with neutrophil recruitment. Immunohistochemistry using an anti-myeloperoxidase antibody revealed that there were no significant differences in the numbers of myeloperoxidase-positive neutrophils between the ischaemic wild-type and *Pgrn* knockout mice at 24 h and 72 h after reperfusion (Supplementary Fig. 3). We also found that there were no significant differences in the numbers of IBA1 (now known as AIF1)-positive microglia in the border of the ischaemic core and penumbra between the wild-type and *Pgrn* knockout mice at 24 h and 72 h after reperfusion (Supplementary Fig. 4).

VEGF expression in *Pgrn* knockout mice after ischaemia

We next investigated the possibility that cerebral oedema in *Pgrn* knockout mice was caused by VEGF expression, because VEGF is a potent angiogenic factor that regulates vascular permeability after focal cerebral ischaemia (Zhang *et al.*, 2002). Additionally, a recent study, in which PDGF (platelet-derived growth factor) was used as an experimental agent to induce blood–brain barrier leakage, did not determine the VEGF protein level after ischaemia (Jackman *et al.*, 2013). Although VEGF expression was undetectable in brains of sham-operated wild-type and *Pgrn* knockout mice, VEGF expression was observed in the peri-infarct area from brains of ischaemic wild-type and *Pgrn* knockout mice 24 and 72 h after reperfusion. At 72 h after reperfusion, the expression was much more prominent in *Pgrn* knockout mice than in wild-type mice ($P < 0.001$) (Fig. 5D). VEGF expression was observed

Figure 2 Continued

ischaemic core and increased PGRN expression in the ischaemic penumbra at 24 h after reperfusion. MAP2, LAMP1 (green) / PGRN (red) / DAPI (blue) triple labelling in the ischaemic core and penumbra examined by confocal microscopy. Scale bars = 10 μ m. (B) Markedly increased PGRN-positive microglia at 72 h after reperfusion. CD68/ED1 (green) / PGRN (red) / DAPI (blue) triple labelling in the sham-operated or ischaemic cortex (ischaemic core) examined by confocal microscopy. Red scale bar = 10 μ m. White scale bars = 20 μ m. (C) PGRN expression in endothelial cells and astrocytic end-feet at 24 h after reperfusion. von Willebrand factor (vWF), glial fibrillary acidic protein (GFAP, green) / PGRN (red) / DAPI (blue) triple labelling in the sham-operated or ischaemic penumbra examined by confocal microscopy. von Willebrand factor is a marker for endothelial cells, and GFAP is a marker for astrocytes. Scale bars = 10 μ m.

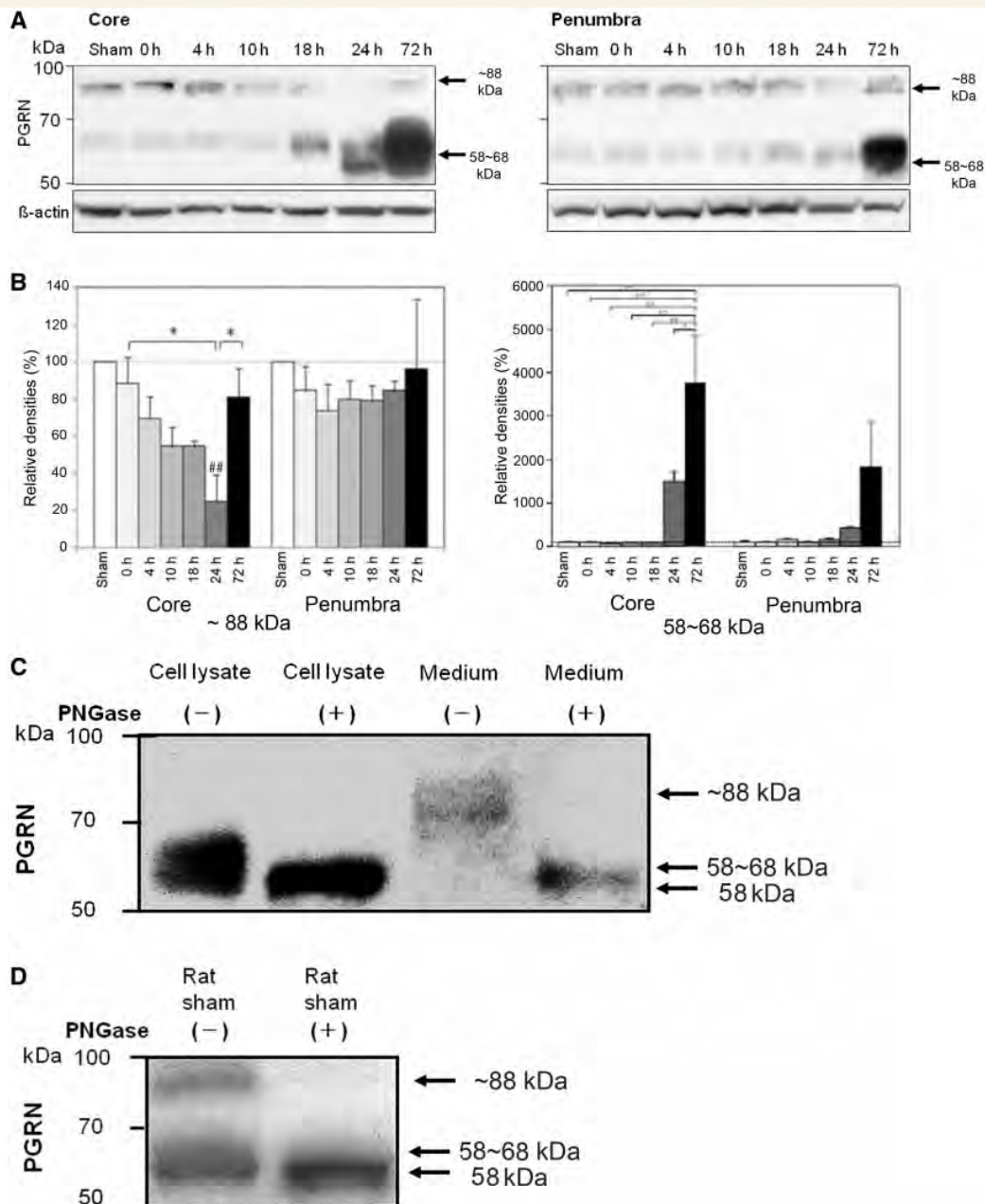


Figure 3 Temporal changes in PGRN expression in the rat cerebral cortex after focal cerebral ischaemia. **(A)** Representative PGRN protein bands of the rat cerebral cortex from the ischaemic core (*left*) and ischaemic penumbra (*right*). Two isoforms (~88 kDa and 58–68 kDa) were observed. β -actin confirmed equal loading of proteins. **(B)** Optical densitometry analyses for ~88 kDa (*left*) and 58–68 kDa isoforms (*right*) of PGRN. * $P < 0.05$, ** $P < 0.01$, ### $P < 0.01$ versus sham. Data represent relative optical densities of ischaemic brain samples compared to those of sham-operated samples. **(C)** Difference in glycosylation status in PGRN between cell lysates and conditioned media of rat C6 cells analysed by immunoblotting. Note that PGRN shows two isoforms (~88 kDa and 58–68 kDa), both of which change to 58 kDa after digestion with peptide-N-glycosidase F (PNGase F). All findings were confirmed in triplicate. **(D)** Difference in glycosylation status in PGRN from the rat non-ischaemic cortex analysed by immunoblotting. Similar to rat C6 cells, PGRN shows two isoforms (~88 kDa and 58–68 kDa), both of which change to 58 kDa after digestion with PNGase F. All findings were confirmed in triplicate.

mainly in astrocytes and endothelial cells (but not in microglia) within ischaemic mice (Supplementary Fig. 5).

To confirm the increased level of VEGF in ischaemic *Pgrn* knockout mice, we performed an *in vitro* study. We

first compared VEGF secretion after OGD from microglia and astrocytes between wild-type and *Pgrn* knockout mice (Fig. 5E). The levels of VEGF from microglia of *Pgrn* knockout mice were higher than those of wild-type mice

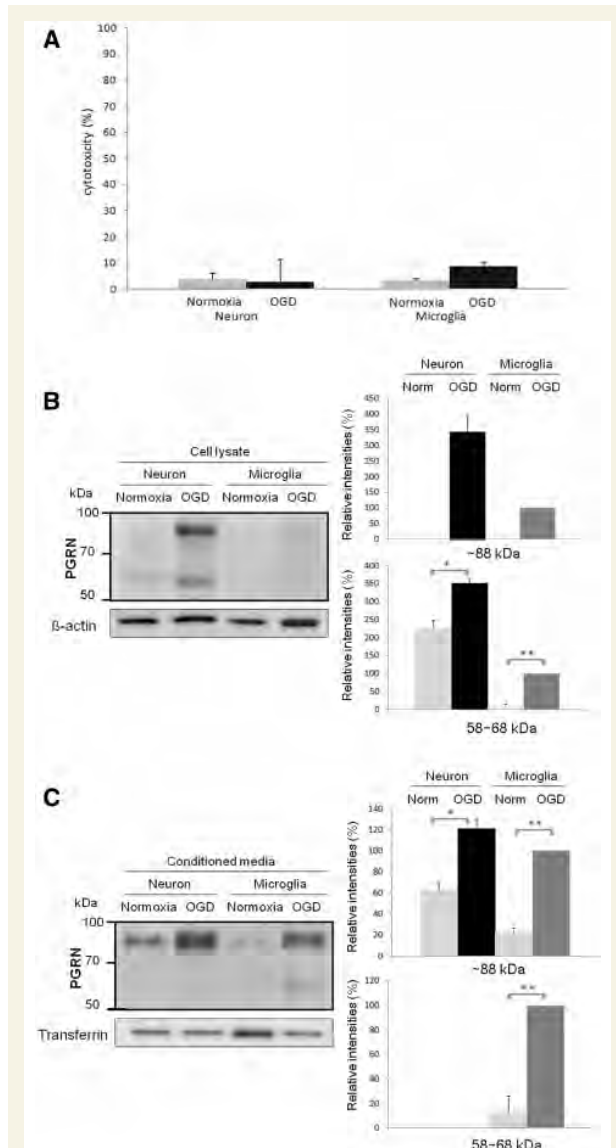


Figure 4 Effects of OGD on PGRN secretion from murine primary cultured neuronal and microglial cells. **(A)**

Cytotoxicity evaluated by lactate dehydrogenase assay between normoxia and OGD in neuronal cells and microglia ($n = 5$). **(B)** and **(C)** Representative PGRN protein bands in immunoblotting from whole-cell extracts **(B)** and conditioned media **(C)** of murine primary cultured cells (neurons and microglia) subjected to normoxia (norm) or OGD. After 18 h incubation under OGD condition, 58–68 kDa and ~88 kDa PGRN in the neuronal cell extracts as well as ~88 kDa PGRN in the neuronal conditioned media increased compared to those under normoxic condition ($P = 0.001$ and 0.011 , respectively). The ~88 kDa PGRN in the microglial conditioned media and the 58–68 kDa PGRN in the microglial cell extracts also increased compared to those under normoxic conditions ($P < 0.001$ and 0.0098 , respectively). Additionally, the 58–68 kDa PGRN in the microglial conditioned media markedly increased ($P < 0.001$). β -actin and transferrin confirmed equal loading of proteins. Optical densitometry analyses for PGRN are also shown. Data represent relative optical densities of each sample compared to microglial samples from OGD ($n = 5$). * $P < 0.05$. ** $P < 0.01$.

($P < 0.001$), although the levels of VEGF from astrocytes were not different between wild-type and *Pgrn* knockout mice ($P = 1.00$). To investigate the effect of microglia on VEGF secretion from astrocytes, microglial conditioned media of wild-type and *Pgrn* knockout mice were added to the astrocytes of wild-type and *Pgrn* knockout mice, respectively. Interestingly, the levels of VEGF from the astrocytes with microglial conditioned media of knockout mice was higher than that of wild-type under OGD ($P < 0.001$). In addition, the levels of VEGF from astrocytes with microglial conditioned media of knockout mice was higher than that from microglia alone ($P = 0.013$) or astrocytes alone ($P = 0.014$) of *Pgrn* knockout mice (Fig. 5E). These results suggest that lack of PGRN or unknown humoral factors from ischaemic microglia of *Pgrn* knockout mice might synergically promote VEGF secretion from the astrocytes.

The effects of VEGF expression by recombinant PGRN treatment after ischaemia *in vitro* and *in vivo*

To investigate the effect of recombinant PGRN on VEGF expression *in vitro*, we compared VEGF levels in astrocytes with microglial conditioned media for wild-type mice treated with vehicle controls and recombinant PGRN. The level of VEGF in astrocytes cultured in microglial conditioned media was decreased by recombinant PGRN ($10 \mu\text{g/ml}$) compared to vehicle treatment ($23.0 \pm 4.8\%$ reduction; $P = 0.046$, $n = 3-6$). We previously reported that delayed tPA treatment 4 h after ischaemia promoted expression of VEGF *in vivo* (Kanazawa *et al.*, 2011a). We investigated the effect of recombinant PGRN on VEGF expression using this thrombo-embolic model. For this purpose we administered $100 \mu\text{g}$ recombinant PGRN or vehicle along with tPA treatment 4 h after ischaemia. The co-administration of recombinant PGRN and tPA decreased the expression of VEGF compared to co-administration of vehicle and tPA ($P = 0.046$) (Supplementary Fig. 6).

Comparison of cytokine response of microglia between wild-type and *Pgrn* knockout mice after OGD

To investigate the effect of PGRN on neuroinflammation after acute ischaemia, we compared mRNA levels of several cytokines in microglia from wild-type and *Pgrn* knockout mice, under normoxic and OGD conditions, because the balance between pro-inflammatory and anti-inflammatory microglial phenotypes is considered to influence expansion of cerebral infarct (Hu *et al.*, 2012). We found that there were no differences in the mRNA levels of pro-inflammatory cytokines (TNF- α and TGF- β) between wild-type and *Pgrn* knockout mice, while the mRNA level of anti-inflammatory cytokine IL10 in the *Pgrn* knockout microglia was lower than that in the wild-type microglia after OGD

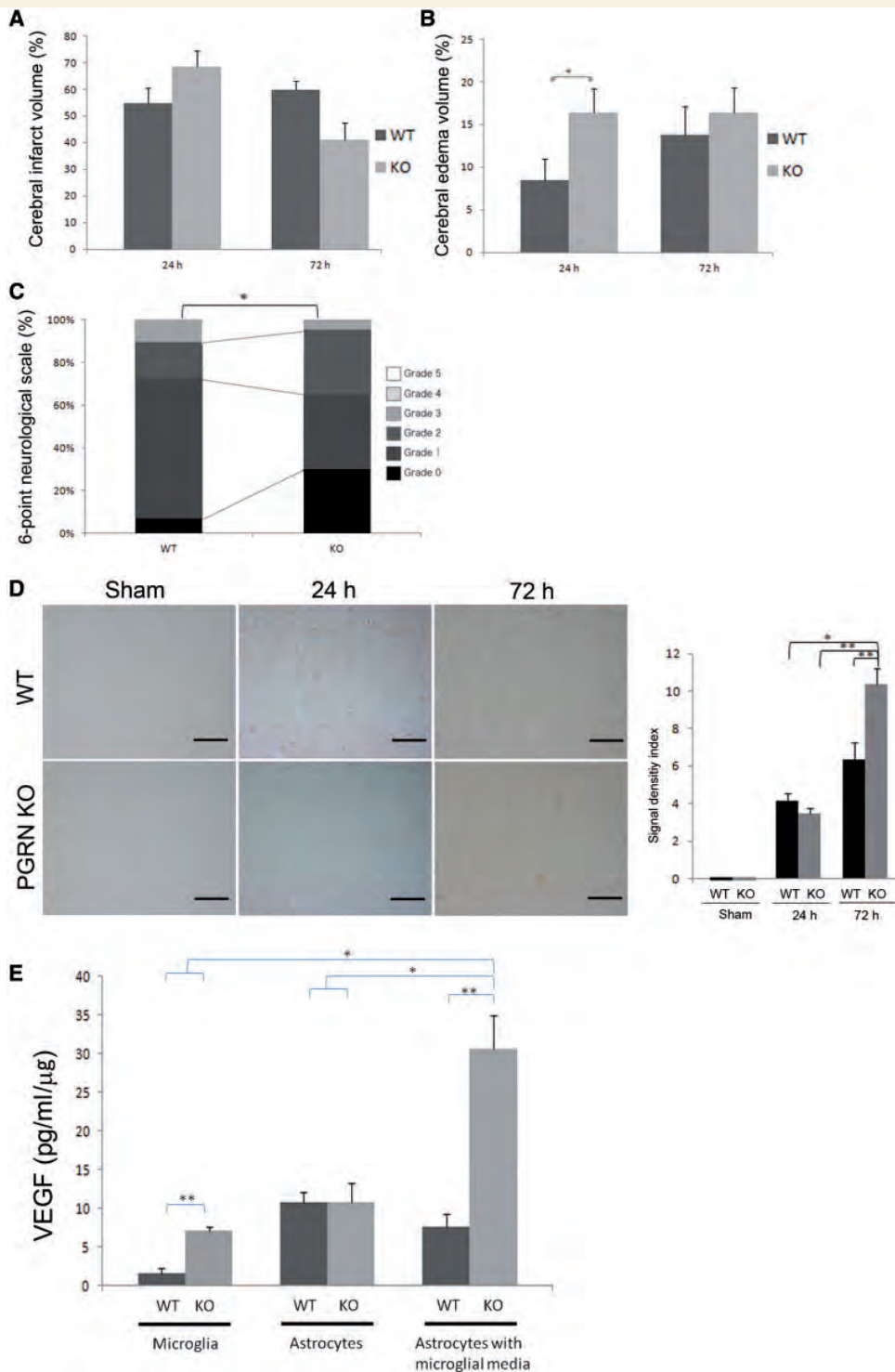


Figure 5 Comparison of ischaemic outcomes and VEGF expression between wild-type and *Pgrn* knockout mice. These panels show volumes of the cerebral infarct (**A**) and cerebral oedema (**B**) at 24 h and 72 h after reperfusion (all, $n \geq 9$), and outcome evaluated by a 6-point neurological scale score (**C**) at 24 h after reperfusion [wild-type (WT) $n = 29$, knockout (KO) $n = 22$]. Volumes of cerebral infarct and oedema are expressed as proportions on the ischaemic side of the cerebral hemisphere. $*P < 0.05$, $**P < 0.01$. (**D**) VEGF expression in the sham-operated and ischaemic brains (at 24 h and 72 h after reperfusion) from the wild-type and *Pgrn* knockout mice. The results were confirmed in triplicate. A secondary-only antibody control confirms that extracellular stainings of VEGF after ischaemia were not non-specific (data not shown). At 72 h after reperfusion, the expression of VEGF was higher in ischaemic brains of *Pgrn* knockout mice than in those of wild-type mice ($**P < 0.001$) ($n = 21$). Scale bars = 200 μm . (**E**) The levels of secretory VEGF from microglia, astrocytes, and astrocytes with microglial conditioned media of wild-type and *Pgrn* knockout mice after OGD ($n = 6-7$). $*P = 0.01$, $**P < 0.01$.

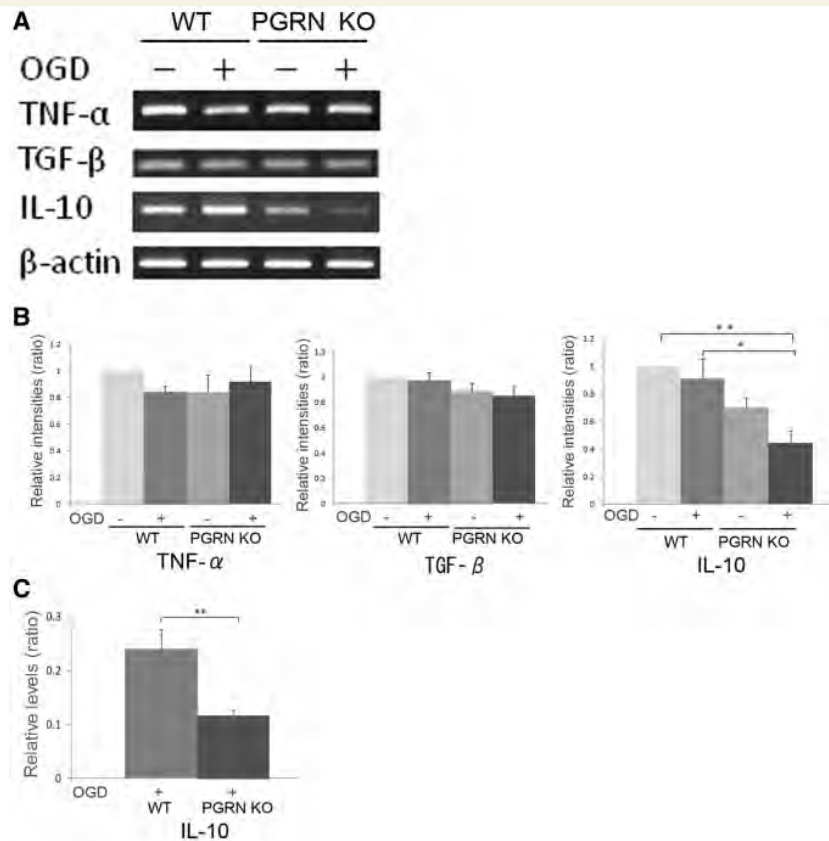


Figure 6 Comparison of cytokine response of microglia between wild-type and *Pgrn* knockout mice after OGD. (A) Representative cytokine mRNA bands from primary microglial cells of wild-type (WT) and *Pgrn* knockout (KO) under normoxic and OGD conditions. **(B)** Optical densitometry analyses for inflammatory cytokines such as TNF- α and transforming growth factor- β (TGF- β), and anti-inflammatory cytokines such as IL-10 ($n = 5-7$). Data represent relative optical densities of respective samples compared to samples from wild-type mice under normoxic conditions by one-way ANOVA. **(C)** Data represent relative *Il10* mRNA levels compared to samples from wild-type mice under normoxic conditions ($n = 3-4$). * $P < 0.05$, ** $P < 0.01$.

($P = 0.037$) (Fig. 6A and B). We also found that *Il10* mRNA levels in the *Pgrn* knockout microglia were lower than that in the wild-type microglia after OGD by real-time PCR ($P = 0.001$) (Fig. 6C). The level of *Il10* after 18 h incubation under OGD from microglial conditioned media of *Pgrn* knockout mice (10.3 ± 3.1 pg/ml) was lower than that from microglial conditioned media of wild-type mice (37.4 ± 12.2 pg/ml) ($P = 0.040$).

We also investigated the expression of TNF- α , TGF- β , and IL10 in brains from ischaemic wild-type and *Pgrn* knockout mice 24 and 72 h after reperfusion. Although the expressions of TNF- α and TGF- β in the ischaemic brains were not different between wild-type and *Pgrn* knockout mice ($P = 0.262$ and $P = 0.228$, respectively) (Supplementary Fig. 7A and B), IL10 expression was lower in the ischaemic brains of *Pgrn* knockout mice than in those of wild-type mice ($P < 0.001$) (Supplementary Fig. 7C). IL10 was expressed mainly in the extracellular parenchyma.

Effects of PGRN on neuronal cell death and cytoplasmic redistribution of TARDBP

We investigated the neuroprotective effect of PGRN on murine primary neuronal cells under OGD condition. Twenty-four hours incubation under OGD promoted neuronal cell death as evaluated by a lactate dehydrogenase assay (Fig. 7A), and the percentage of propidium iodide-positive neuronal cells after 24-h incubation under OGD was $8.4 \pm 3.7\%$ ($n = 21$) (Supplementary Fig. 8). The attached neuronal cells that showed cytoplasmic redistribution of TARDBP under the OGD conditions were confirmed to be living as they were propidium iodide-negative (Fig. 7B). However, we found that the recombinant PGRN ($5 \mu\text{g/ml}$) suppressed the neuronal cell death compared to the control ($P = 0.045$) (Fig. 7C). Immunocytochemistry confirmed that these surviving neurons incorporated the exogenously administered

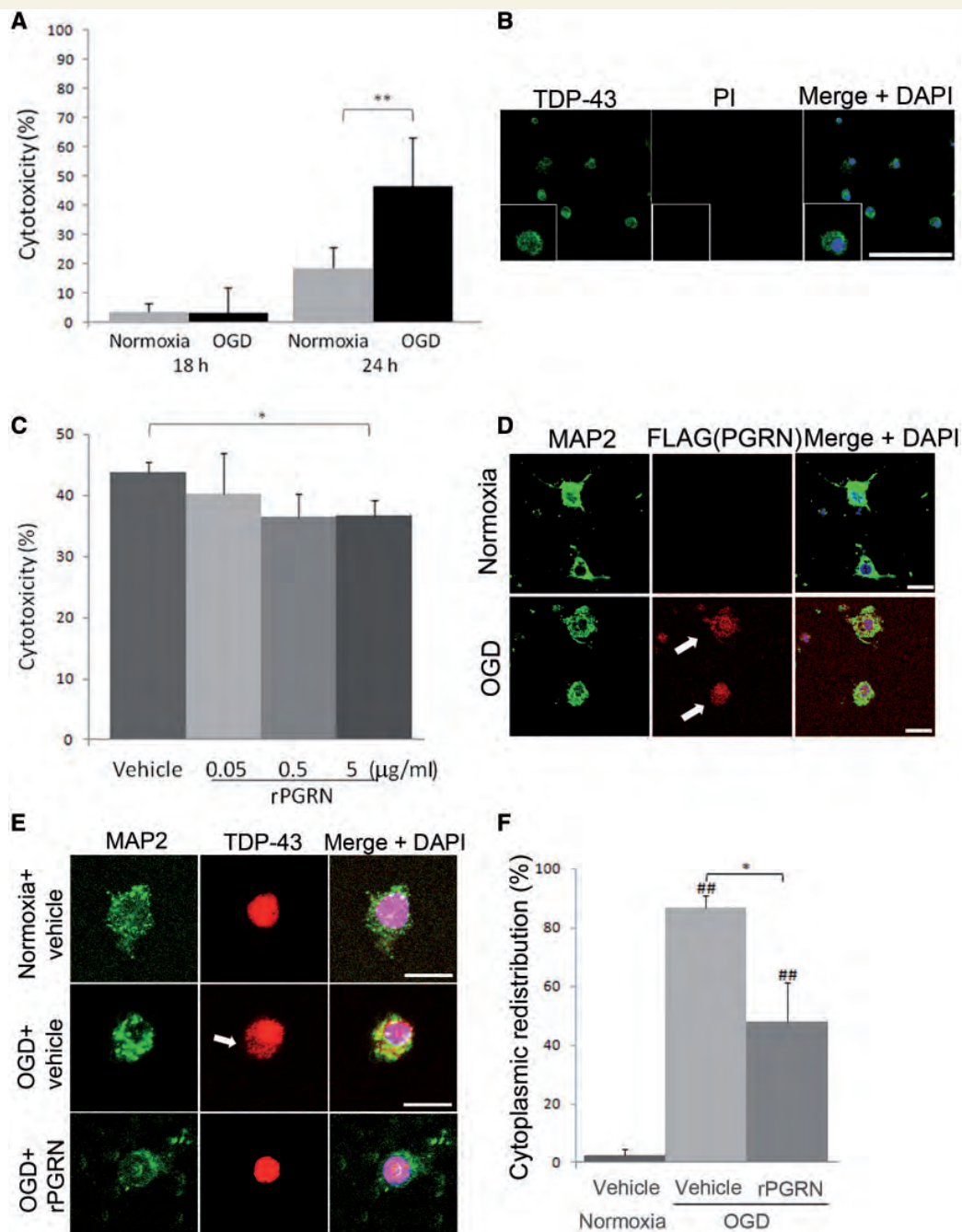


Figure 7 Suppression of neuronal cell death and cytoplasmic redistribution of TARDBP (TDP-43) under OGD conditions by recombinant PGRN. **(A)** Cytotoxicity of neuronal cells between normoxic and OGD conditions at 18 h and 24 h ($n = 5$). $**P < 0.01$. **(B)** Confocal microscopic observation of TDP-43 (now known as TARDBP, green)/propidium iodide (PI) (red)/DAPI (blue)-triple labelling in neuronal cells under OGD conditions. Magnification is double in the small inset. Cytoplasmic redistribution of TDP-43 was observed in surviving neurons under the OGD conditions. These neuronal cells were propidium iodide-negative. Scale bar = 50 μ m. **(C)** Recombinant PGRN (rPGRN) alleviated cytotoxicity at 24 h under OGD conditions ($n = 6$). $*P < 0.05$. **(D)** MAP2 (green)/FLAG (red) / DAPI (blue) triple labeling in neurons between normoxic and OGD conditions by confocal microscopy. FLAG-tagged recombinant PGRN was co-localized in surviving neurons under OGD condition (arrow). Scale bars = 20 μ m. **(E)** MAP2 (green)/TDP-43 (red)/DAPI (blue) triple labelling in neurons between normoxic and OGD conditions with or without recombinant PGRN treatment by confocal microscopy. Arrow indicates cytoplasmic redistribution of TARDBP at 24 h under OGD conditions. Scale bars = 20 μ m. **(F)** The frequencies cytoplasmic redistribution of TARDBP in MAP2-positive neuronal cells between normoxic and OGD conditions. recombinant PGRN blocked cytoplasmic redistribution of TARDBP at 24 h under OGD conditions. $*P < 0.05$, $###P < 0.01$ versus normoxic condition ($n = 7$).

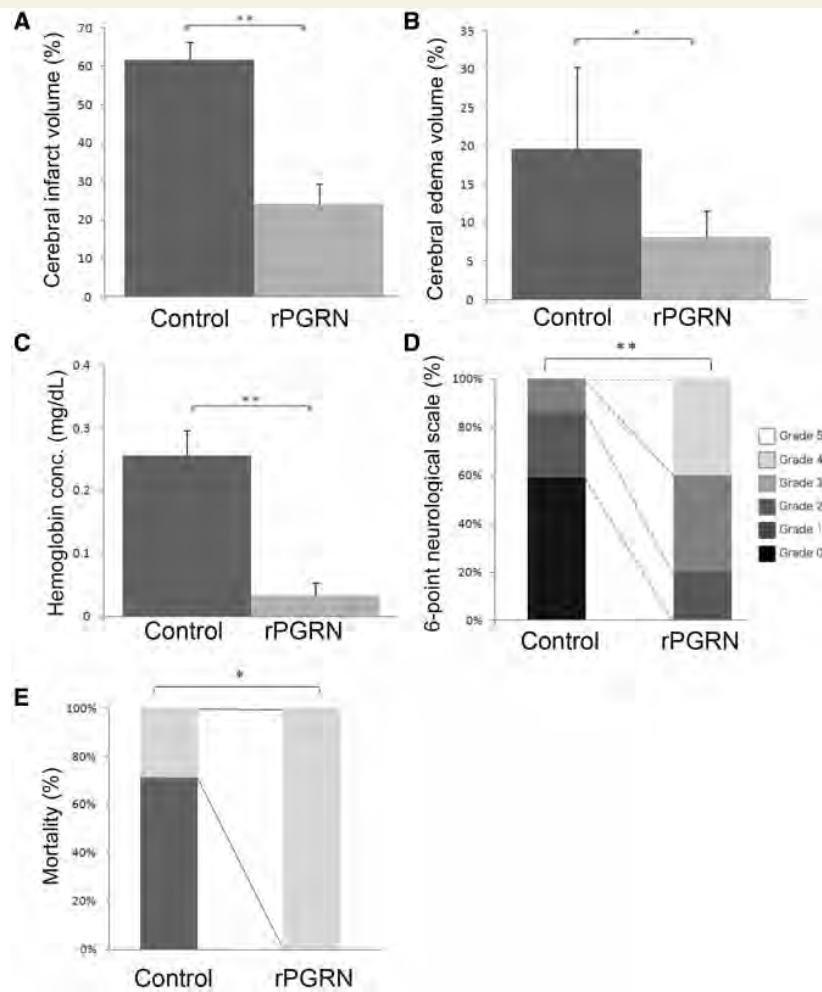


Figure 8 The improvements in ischaemic outcomes after delayed tPA treatment with recombinant PGRN. Quantification of volumes of cerebral infarct (A) and oedema (B), and haemoglobin concentrations of the lysates from the ischaemic hemisphere (C) at 24 h after reperfusion. Black bars: the tPA 4 h group treated with control protein; grey bars: the tPA 4 h group treated with recombinant PGRN (rPGRN) ($n = 5$). Six-point neurological scale (D) and mortality ratio (E) of the tPA 4 h group treated with control protein ($n = 7$) or recombinant PGRN ($n = 6$). * $P < 0.05$, ** $P < 0.01$.

FLAG-tagged recombinant PGRN (Fig. 7D). We also found that the neuronal cells, which incorporated the exogenous FLAG-tagged recombinant PGRN, showed a decrease in the cytoplasmic redistribution of TARDBP (Fig. 7E): the frequency of cytoplasmic redistribution of TARDBP in the neurons treated with recombinant PGRN under OGD was lower than that treated with the vehicle control ($48.0 \pm 35.4\%$ versus $86.9 \pm 10.4\%$; $P = 0.010$) (Fig. 7F).

Therapeutic effects of recombinant PGRN against delayed tPA treatment for acute focal cerebral ischaemia

Finally, we investigated therapeutic effects of recombinant PGRN using a rat autologous thrombo-embolic model (Okubo *et al.*, 2007), because this model shows cerebral

oedema and haemorrhagic transformation when tPA is administered beyond the therapeutic time window (4 h) (Kanazawa *et al.*, 2011a; Kawamura *et al.*, 2014). The group treated with tPA and intravenous administration of recombinant PGRN at 4 h after reperfusion showed therapeutic effects on the cerebral infarct volume (Fig. 8A), oedema volume (Fig. 8B), haemorrhage (Fig. 8C), motor scale (Fig. 8D), and mortality ratio (Fig. 8E) compared to the group treated with tPA and control ($P = 0.007$, 0.038, 0.007, 0.004 and 0.026, respectively).

Discussion

We demonstrated for the first time the dynamic changes in PGRN *in vivo* in the neurons, microglia, and endothelial cells after ischaemia, including decreased level of PGRN

expression in neurons within the ischaemic core, increased level of PGRN expression in the surviving neurons, as well as induction of PGRN expression in microglia and endothelial cells in the ischaemic penumbra. Immunoblot analyses demonstrated that the fully glycosylated mature secretory isoform (~88 kDa) decreased, while the glycosylated immature isoform (58–68 kDa) markedly increased after reperfusion. In addition, *in vitro* experiments revealed that the glycosylated mature isoform was secreted from neurons and microglia, and the glycosylated immature isoform was secreted only from microglia. Consistent with this finding, immunohistochemical analyses demonstrated a marked increase in PGRN-positive microglia at 72 h after reperfusion in ischaemic rats. These findings suggest that the marked increase in the glycosylated immature isoform of 58–68 kDa PGRN after reperfusion was caused by microglia.

We next demonstrated that PGRN has multiple therapeutic effects against ischaemic brain injury. First, we found that PGRN could attenuate blood–brain barrier disruption after acute focal cerebral ischaemia. We demonstrated for the first time that PGRN is expressed in the endothelial cells in the ischaemic penumbra. A previous report has shown that PGRN is induced in the capillary endothelium of wound granulation tissue and promotes the mitosis and migration of adult dermal microvascular cells (He *et al.*, 2003b), although PGRN is not expressed in the healthy endothelium (Daniel *et al.*, 2000). We speculated that the expression of PGRN in endothelial cells may be involved in the vascular protection or repair against ischaemic injury. Indeed, cerebral oedema volume in *Pgrn* knockout mice was larger than that in wild-type mice after focal cerebral ischaemia. Regarding the mechanism by which PGRN regulates vascular permeability, we considered that cerebral oedema is not caused by recruitment of neutrophils and microglia based on the findings from immunostainings using wild-type and *Pgrn* knockout mice. A very recent study demonstrated the involvement of the PDGF receptor pathway using *Pgrn* knockout mice (Jackman *et al.*, 2013). We proposed another possibility that PGRN might regulate vascular permeability via VEGF pathway, because we observed more prominent expression of VEGF in *Pgrn* knockout mice than in wild-type mice after focal cerebral ischaemia. In addition, *Pgrn* knockout microglia itself secreted VEGF and the conditioned media from *Pgrn* knockout microglia synergistically stimulated VEGF secretion from *Pgrn* knockout astrocytes after OGD. Although we could not identify the specific molecules that stimulate VEGF expression, a recent study demonstrated that PGRN might inhibit cerebral oedema via NF- κ B (Egashira *et al.*, 2013), which activates VEGF transcription (Yoshida *et al.*, 1998). PGRN may regulate vascular permeability by inhibiting microglial production of molecules that activate NF- κ B-VEGF signalling pathway.

In breast cancer, high levels of PGRN result in increased VEGF production (Tangkeangsirisin *et al.*, 2004), while in this study of ischaemia, depletion of PGRN increased

VEGF expression. Furthermore, we showed clear increases in PGRN expression in vessels of the penumbra (Fig. 2C), which is similar to what has been reported in peripheral wounds (He *et al.*, 2003b). Because elevated levels of PGRN have a significant biological effect on vessel growth that might be independent of VEGF (Toh *et al.*, 2013), some of the effects of *Pgrn* knockout on penumbral blood vessels might be mediated directly by PGRN loss rather than via increased VEGF expression (Jackman *et al.*, 2013). Further studies are needed to clarify the mechanism underlying PGRN-mediated vascular permeability.

Second, PGRN may suppress neuroinflammation after acute focal cerebral ischaemia via the anti-inflammatory cytokine, IL10. We demonstrated that the number of PGRN-positive microglia (CD68/ED1-positive cells) increased in the ischaemic core of Sprague-Dawley rats, and that the primary cultured-microglia from *Pgrn* knockout mice showed a decrease in the levels of IL10 under OGD, although levels of inflammatory cytokines such as TNF- α and TGF- β were not changed. Consistent with this finding, previous studies reported that the level of IL10 in glial cells from PGRN-overexpressing transgenic mice was higher than that from wild-type mice (Tao *et al.*, 2012), and that the macrophage/microglia from *Pgrn* knockout mice released less IL10 than from wild-type mice when exposed to bacterial lipopolysaccharide (Yin *et al.*, 2010). However, findings on pro-inflammatory cytokines are controversial and inconclusive. It has been demonstrated that levels of other pro-inflammatory cytokines (IL1B, IL6 and TNF- α) in glial cells from PGRN-overexpressing transgenic mice were lower than those from wild-type mice (Tao *et al.*, 2012), and that they were increased in the macrophage/microglia from *Pgrn* knockout mice compared to wild-type mice when mice exposed to bacterial lipopolysaccharide (Yin *et al.*, 2010). In contrast, a very recent study demonstrated that mRNA levels of *Il1b*, *Il6*, TNF- α (now known as *Tnf*), and TGF- β (now known as *Tgfb1*) (*Il10* not examined) after ischaemic brain injury were not associated with *Pgrn* knockout condition as seen in our results (Jackman *et al.*, 2013). We consider, based on our findings, that PGRN may suppress neuroinflammation via IL10 not by inhibiting pro-inflammatory cytokines.

Third, we confirmed that PGRN might play a neuroprotective role against acute focal cerebral ischaemia *in vitro* and *in vivo*. Neuronal PGRN decreased in the ischaemic core where neuronal death occurred, and increased in the ischaemic penumbra where neuronal survival occurred after acute focal cerebral ischaemia. *In vitro* studies demonstrated that the neuronal cells and microglia produced and secreted PGRN after ischaemia, and that exogenous recombinant PGRN could suppress neuronal cell death under OGD. Although PGRN has been shown to have neurotrophic effects, the exact mechanism remains unknown (Van Damme *et al.*, 2008; Laird *et al.*, 2010). We consider that the neurotrophic effects of PGRN might be explained in part by the inhibition of abnormal cytoplasmic

redistribution of nuclear TARDBP (Zhang *et al.*, 2007, 2009). Stated another way, the decreased level of PGRN might cause loss of function of TARDBP in neurons, resulting in neuronal damage.

Finally, we demonstrated that intravenously administered recombinant PGRN reduced volumes of cerebral infarct and oedema, suppressed haemorrhagic transformation, and improved motor outcome with delayed tPA treatment resulting in haemorrhagic transformation that is similar to human stroke, in a rat autologous embolic model (Kanazawa *et al.*, 2011a; Kawamura *et al.*, 2014). A previous study reported that intraventricular administration of recombinant PGRN reduced cerebral infarct and oedema in a mouse focal suture ischaemic model (Egashira *et al.*, 2013), although this model and injection route poorly reflected the clinical practice. Our findings indicate the possibility that recombinant PGRN could be used as a novel neurovascular protective drug with anti-inflammatory effect after delayed tPA treatment.

Because of the importance of protein glycosylation in mediating a wide range of biological processes, characterization of glycan structures is necessary to understand the structure–function relationship (Songsrirote *et al.*, 2010). Therefore, we chose the full-length glycosylated recombinant PGRN protein. We could not evaluate the impact of glycosylated status of the PGRN on neuronal cells because it is technically hard to use deglycosylated PGRN after PNGase assay because of reagent toxicities for cells. Further studies are needed to determine the impact of glycosylation status for recombinant PGRN on this effect.

In conclusion, we demonstrated dynamic changes of expression and localization of PGRN after acute focal cerebral ischaemia. PGRN may be a novel therapeutic target that provides vascular protection, anti-neuroinflammation, and neuroprotection related in part to VEGF, IL10 and TARDBP, respectively.

Acknowledgements

We thank Dr Riuko Ohashi (Department of Cellular Function, Division of Cellular and Molecular Pathology, Niigata University) for her support in the confocal imaging studies.

Funding

This work was supported by a Grant-in-Aid for Scientific Research, a grant from Naito Foundation, Takeda Science Foundation, Japan Cardiovascular Research Foundation, Japan Brain Foundation, Yujin Memorial Grant, Japan Medical Association (TS), and a Grant-in-Aid for Scientific Research, a grant from SENSHIN Medical Research Foundation, Uehara Memorial Foundation (MK).

Supplementary material

Supplementary material is available at *Brain* online.

References

- Alqu zar C, Esteras N, de la Encarnaci n A, Alzualde A, Moreno F, L pez de Munain A, et al. PGRN haploinsufficiency increased Wnt5a signaling in peripheral cells from frontotemporal lobar degeneration-progranulin mutation carriers. *Neurobiol Aging* 2014; 35: 886–98.
- Baker M, Mackenzie IR, Pickering-Brown SM, Gass J, Rademakers R, Lindholm C, et al. Mutations in progranulin cause tau-negative frontotemporal dementia linked to chromosome 17. *Nature* 2006; 442: 916–19.
- Cruts M, Gijselinck I, van der Zee J, Engelborghs S, Wils H, Pirici D, et al. Null mutations in progranulin cause ubiquitin-positive frontotemporal dementia linked to chromosome 17q21. *Nature* 2006; 442: 920–4.
- Daniel R, He Z, Carmichael KP, Halper J, Bateman A. Cellular localization of gene expression for progranulin. *J Histochem Cytochem* 2000; 48: 999–1009.
- del Zoppo GJ, Frankowski H, Gu YH, Osada T, Kanazawa M, Milner R, et al. Microglial cell activation is a source of metalloproteinase generation during hemorrhagic transformation. *J Cereb Blood Flow Metab* 2012; 32: 919–32.
- Egashira Y, Suzuki Y, Azuma Y, Takagi T, Mishiro K, Sugitani S, et al. The growth factor progranulin attenuates neuronal injury induced by cerebral ischemia-reperfusion through the suppression of neutrophil recruitment. *J Neuroinflammation* 2013; 10: 105.
- Faustino JV, Wang X, Johnson CE, Klibanov A, Derugin N, Wendland MF, et al. Microglial cells contribute to endogenous brain defenses after acute neonatal focal stroke. *J Neurosci* 2011; 31: 12992–3001.
- He Z, Bateman A. Progranulin (granulin-epithelin precursor, PC-cell-derived growth factor, acrogranin) mediates tissue repair and tumorigenesis. *J Mol Med (Berl)* 2003a; 81: 600–12.
- He Z, Ong CH, Halper J, Bateman A. Progranulin is a mediator of the wound response. *Nat Med* 2003b; 9: 225–9.
- Hu X, Li P, Guo Y, Wang H, Leak RK, Chen S, et al. Microglia/macrophage polarization dynamics reveal novel mechanism of injury expansion after focal cerebral ischemia. *Stroke* 2012; 43: 3063–70.
- Jackman K, Kahles T, Lane D, Garcia-Bonilla L, Abe T, Capone C, et al. Progranulin deficiency promotes post-ischemic blood–brain barrier disruption. *J Neurosci* 2013; 33: 19579–89.
- Kanazawa M, Igarashi H, Kawamura K, Takahashi T, Kakita A, Takahashi H, et al. Inhibition of VEGF signaling pathway attenuates hemorrhage after tPA treatment. *J Cereb Blood Flow Metab* 2011a; 31: 1461–74.
- Kanazawa M, Kakita A, Igarashi H, Takahashi T, Kawamura K, Takahashi H, et al. Biochemical and histopathological alterations in TAR DNA binding protein-43 after acute ischemic stroke in rats. *J Neurochem* 2011b; 116: 957–65.
- Kawamura K, Takahashi T, Kanazawa M, Igarashi H, Nakada T, Nishizawa M, et al. Effects of angiotensin-1 on hemorrhagic transformation and cerebral edema after tissue plasminogen activator treatment for ischemic stroke in rats. *PLoS One* 2014; 9: e98639.
- Kayasuga Y, Chiba S, Suzuki M, Kikusui T, Matsuwaki T, Yamanouchi K, et al. Alteration of behavioural phenotype in mice by targeted disruption of the progranulin gene. *Behav Brain Res* 2007; 185: 110–18.
- Kilkenny C, Browne W, Cuthill IC, Emerson M, Altman DG; National Centre for the Replacement, Refinement and Reduction of Animals in Research. Animal research: reporting in vivo experiments—the ARRIVE guidelines. *J Cereb Blood Flow Metab* 2010; 31: 991–3.

- Kleinberger G, Wils H, Ponsaerts P, Joris G, Timmermans JP, Van Broeckhoven C, et al. Increased caspase activation and decreased TDP-43 solubility in progranulin knockout cortical cultures. *J Neurochem* 2010; 115: 735–47.
- Krishnamurthy RG, Senut MC, Zemke D, Min J, Frenkel MB, Greenberg EJ, et al. Asiatic acid, a pentacyclic triterpene from *Centella asiatica*, is neuroprotective in a mouse model of focal cerebral ischemia. *J Neurosci Res* 2009; 87: 2541–50.
- Laird AS, Van Hoecke A, De Muyenck L, Timmers M, Van den Bosch L, Van Damme P, et al. Progranulin is neurotrophic in vivo and protects against a mutant TDP-43 induced axonopathy. *PLoS One* 2010; 5: e13368.
- Liau LM, Lallone RL, Seitz RS, Buznikov A, Gregg JP, Kornblum HI, et al. Identification of a human glioma-associated growth factor gene, granulin, using differential immuno-absorption. *Cancer Res* 2000; 60: 1353–60.
- Mabuchi T, Kitagawa K, Ohtsuki T, Kuwabara K, Yagita Y, Yanagihara T, et al. Contribution of microglia/macrophages to expansion of infarction and response of oligodendrocytes after focal cerebral ischemia in rats. *Stroke* 2000; 31: 1735–43.
- Memezawa H, Smith ML, Siesjö BK. Penumbra tissues salvaged by reperfusion following middle cerebral artery occlusion in rats. *Stroke* 1992; 23: 552–9.
- Milner R, Hung S, Wang X, Berg GI, Spatz M, del Zoppo GJ. Responses of endothelial cell and astrocyte matrix-integrin receptors to ischemia mimic those observed in the neurovascular unit. *Stroke* 2008; 39: 191–7.
- Naphade SB, Kigerl KA, Jakeman LB, Kostyk SK, Popovich PG, Kuret J. Progranulin expression is upregulated after spinal contusion in mice. *Acta Neuropathol* 2010; 119: 123–33.
- Okubo S, Igarashi H, Kanamatsu T, Hasegawa D, Orima H, Katayama Y. FK-506 extended the therapeutic time window for thrombolysis without increasing the risk of hemorrhagic transformation in an embolic rat stroke model. *Brain Res* 2007; 1143: 221–7.
- Osada T, Gu YH, Kanazawa M, Tsubota Y, Hawkins BT, Spatz M, et al. Interendothelial claudin-5 expression depends on cerebral endothelial cell-matrix adhesion by $\beta(1)$ -integrins. *J Cereb Blood Flow Metab* 2011; 31: 1972–85.
- Özdemir YG, Bolay H, Erdem E, Dalkara T. Occlusion of the MCA by an intraluminal filament may cause disturbances in the hippocampal blood flow due to anomalies of circle of Willis and filament thickness. *Brain Res* 1999; 822: 260–4.
- Tangkeangsirisin W, Serrero G. PC-cell derived growth factor (PCDGF/GP88) stimulates migration, invasiveness and VEGF expression in breast cancer cells. *Carcinogenesis* 2004; 25: 1587–92.
- Toh H, Cao M, Daniels E, Bateman A. Expression of the growth factor progranulin in endothelial cells influences growth and development of blood vessels: a novel mouse model. *PLoS One* 2013; 8: e64989.
- Shankaran SS, Capell A, Hruscha AT, Fellerer K, Neumann M, Schmid B, et al. Missense mutations in the progranulin gene linked to frontotemporal lobar degeneration with ubiquitin-immunoreactive inclusions reduce progranulin production and secretion. *J Biol Chem* 2008; 283: 1744–53.
- Shimohata T, Zhao H, Sung JH, Sun G, Mochly-Rosen D, Steinberg GK. Suppression of deltaPKC activation after focal cerebral ischemia contributes to the protective effect of hypothermia. *J Cereb Blood Flow Metab* 2007; 27: 1463–75.
- Songsrirote K, Li Z, Ashford D, Bateman A, Thomas-Oates J. Development and application of mass spectrometric methods for the analysis of progranulin N-glycosylation. *J Proteomics* 2010; 73: 1479–90.
- Swanson RA, Morton MT, Tsao-Wu G, Savalos RA, Davidson C, Sharp FR. A semiautomated method for measuring brain infarct volume. *J Cereb Blood Flow Metab* 1990; 10: 290–3.
- Takeuchi H, Mizuno T, Zhang G, Wang J, Kawanokuchi J, Kuno R, et al. Neuritic beading induced by activated microglia is an early feature of neuronal dysfunction toward neuronal death by inhibition of mitochondrial respiration and axonal transport. *J Biol Chem* 2005; 280: 10444–54.
- Tanaka Y, Matsuwaki T, Yamanouchi K, Nishihara M. Exacerbated inflammatory responses related to activated microglia after traumatic brain injury in progranulin-deficient mice. *Neuroscience* 2013; 250: 8–19.
- Tao J, Ji F, Wang F, Liu B, Zhu Y. Neuroprotective effects of progranulin in ischemic mice. *Brain Res* 2012; 1436: 130–6.
- Van Damme P, Van Hoecke A, Lambrechts D, Vanacker P, Bogaert E, van Swieten J, et al. Progranulin functions as a neurotrophic factor to regulate neurite outgrowth and enhance neuronal survival. *J Cell Biol* 2008; 181: 37–41.
- Yenari MA, Kauppinen TM, Swanson RA. Microglial activation in stroke: therapeutic targets. *Neurotherapeutics* 2010; 7: 378–91.
- Yin F, Banerjee R, Thomas B, Zhou P, Qian L, Jia T, et al. Exaggerated inflammation, impaired host defense, and neuropathology in progranulin-deficient mice. *J Exp Med* 2010; 207: 117–28.
- Yoshida A, Yoshida S, Khalil AK, Ishibashi T, Inomata H. Role of NF- κ B-mediated interleukin-8 expression in intraocular neovascularization. *Invest Ophthalmol Vis Sci* 1998; 39: 1097–106.
- Zausinger S, Hungerhuber E, Baethmann A, Reulen H, Schmid-Elsaesser R. Neurological impairment in rats after transient middle cerebral artery occlusion: a comparative study under various treatment paradigms. *Brain Res* 2000; 863: 94–105.
- Zhang YJ, Xu YF, Cook C, Gendron TF, Roettges P, Link CD, et al. Aberrant cleavage of TDP-43 enhances aggregation and cellular toxicity. *Proc Natl Acad Sci USA* 2009; 106: 7607–12.
- Zhang YJ, Xu YF, Dickey CA, Buratti E, Baralle F, Bailey R, et al. Progranulin mediates caspase-dependent cleavage of TAR DNA binding protein-43. *J Neurosci* 2007; 27: 10530–4.
- Zhang ZG, Zhang L, Tsang W, Soltanian-Zadeh H, Morris D, Zhang R, et al. Correlation of VEGF and angiopoietin expression with disruption of blood-brain barrier and angiogenesis after focal cerebral ischemia. *J Cereb Blood Flow Metab* 2002; 22: 379–92.

Clinicopathological Features in Anterior Visual Pathway in Neuromyelitis Optica

Mariko Hokari, MD,¹ Akiko Yokoseki, MD, PhD,¹ Musashi Arakawa, MD, PhD,¹
 Etsuji Saji, MD, PhD,¹ Kaori Yanagawa, MD, PhD,¹ Fumihiko Yanagimura, MD,¹
 Yasuko Toyoshima, MD, PhD,² Kouichirou Okamoto, MD, PhD,³
 Satoshi Ueki, MD, PhD,⁴ Tetsuhisa Hatase, MD, PhD,⁵ Riuko Ohashi, MD, PhD,⁶
 Takeo Fukuchi, MD, PhD,⁵ Kohei Akazawa, PhD,⁷ Mitsunori Yamada, MD, PhD,⁸
 Akiyoshi Kakita, MD, PhD,² Hitoshi Takahashi, MD, PhD,²
 Masatoyo Nishizawa, MD, PhD,¹ and Izumi Kawachi, MD, PhD¹

Objective: Neuromyelitis optica spectrum disorder (NMOsd) is an autoimmune disorder of the central nervous system characterized by aquaporin-4 (AQP4) autoantibodies. The aim of this study was to elucidate the characteristics of involvement of the anterior visual pathway (AVP) and neurodegeneration via glia–neuron interaction in NMOsd.

Methods: Thirty Japanese patients with serologically verified NMOsd were assessed with a neuro-ophthalmological study. Using 27 tissue blocks from 13 other cases of NMOsd, we performed neuropathological analysis of glial and neuroaxonal involvement in the AVP.

Results: The AVP involvement in NMOsd was characterized by the following, compared to multiple sclerosis: (1) longitudinally extensive optic neuritis (ON); (2) more severe visual impairment and worse prognosis for ON; (3) unique AQP4 dynamics, including loss of AQP4 immunoreactivity on astrocytes with complement activation in ON lesions, loss of AQP4 immunoreactivity on Müller cells with no deposition of complement in the retinas, and densely packed AQP4 immunoreactivity on astrocytes in gliosis of secondary anterograde/retrograde degeneration in the optic nerves and retinal nerve fiber layer (RNFL); and (4) more severe neurodegeneration, including axonal accumulation of degenerative mitochondria and transient receptor potential melastatin 4 channel with complement-dependent astrocyte pathology in ON lesions, mild loss of horizontal cells, and RNFL thinning and loss of ganglion cells with abundance of AQP4⁺ astrocytes, indicating secondary retrograde degeneration after ON.

Interpretation: Severe and widespread neuroaxonal damage and unique dynamics of astrocytes/Müller cells with alterations of AQP4 were prominent in the AVP and may be associated with poor visual function and prognosis in NMOsd.

ANN NEUROL 2016;79:605–624

Neuromyelitis optica (NMO) spectrum disorder (NMOsd)¹ and multiple sclerosis (MS) are the two main autoimmune, inflammatory, and demyelinating syndromes of the central nervous system (CNS). The serum NMO immunoglobulin G autoantibody targets

the water channel aquaporin-4 (AQP4) and is a specific marker of NMOsd.^{2,3} The anterior visual pathway (AVP), which includes the retinas and the pathway from the optic nerves to the lateral geniculate nuclei, is a frequent site of injury, as shown by the presence of optic

View this article online at wileyonlinelibrary.com. DOI: 10.1002/ana.24608

Received Aug 14, 2015, and in revised form Jan 28, 2016. Accepted for publication Jan 29, 2016.

Address correspondence to Dr Kawachi, Department of Neurology, Brain Research Institute, Niigata University, 1-757 Asahimachi, Chuo-ku, Niigata 951-8585, Japan. E-mail: ikawachi@bri.niigata-u.ac.jp

From the ¹Department of Neurology, Brain Research Institute, Niigata University, Niigata; ²Department of Pathology, Brain Research Institute, Niigata University, Niigata; ³Department of Neurosurgery, Brain Research Institute, Niigata University, Niigata; ⁴Center for Integrated Human Brain Science, Brain Research Institute, Niigata University, Niigata; ⁵Department of Ophthalmology, Niigata University, Niigata; ⁶Department of Pathology, Niigata University Medical and Dental Hospital, Niigata; ⁷Department of Medical Informatics, Niigata University Medical and Dental Hospital, Niigata; and ⁸Department of Brain Disease Research, Shinshu University School of Medicine, Matsumoto, Nagano, Japan.

Additional supporting information can be found in the online version of this article.

neuritis (ON) during the course of NMOsd. Compared to MS, ON in NMOsd is characterized as follows: (1) visual loss is generally more severe in NMOsd⁴; (2) the occurrence of bilateral simultaneous ON is more suggestive of NMOsd⁵; and (3) optic coherence tomography (OCT) assessment in NMOsd demonstrates a thinner retinal nerve fiber layer (RNFL), suggesting more widespread axonal injury.^{6,7}

In the optic nerves, chiasm, and tracts, expression of AQP4 is generally enriched in astrocytic endfoot membrane domains that face capillaries and the pia in the CNS.⁸ In the retinas, a striking feature of AQP4 expression is its polarized distribution in 2 types of retinal glia: (1) Müller cells, which are a specialized form of radial glia spanning the width of the retina from the inner limiting membrane to the outer limiting membrane, with the cell soma lying within the inner nuclear layer (INL); and (2) retinal astrocytes, which are mostly localized in the RNFL, which is composed predominantly of unmyelinated axons of retinal ganglion cells. However, little is known about the details of the pathology in the AVP, including the dynamics of AQP4 expression in Müller cells and astrocytes in NMOsd. Here we report that more severe and widespread neuroaxonal damage and unique dynamics of AQP4 in astrocytes/Müller cells was prominent in the AVP and may be associated with visual function and prognosis in NMOsd by using neuro-ophthalmological, radiological, and pathological assessments.

Patients and Methods

Neuro-ophthalmological and Neuroradiological Assessments

We retrospectively reviewed the medical records of 79 Japanese patients (67 women, 12 men; 30 patients with NMOsd, 49 patients with MS) between 2000 and 2013 at the MS/NMO clinic in the Department of Neurology at Niigata University Hospital. Patients were included in the study according to these ocular criteria: (1) intraocular pressure <20mmHg; (2) absence of current or previous history of other ocular diseases, including glaucoma, retinal detachment, early age-related macular degeneration, other macular degeneration, and retinal vascular diseases; and (3) adequate clinical data on follow-up (Supplementary Table 1). AQP4 autoantibodies were measured in the sera of all patients using the method described in our previous reports.^{9,10} We stringently defined the definite form of NMOsd as fulfilling all items of the 2006 NMO criteria,¹ and limited NMOsd to either: (1) ON and seropositivity for AQP4 autoantibodies but without spinal cord involvement or (2) myelitis with seropositivity for AQP4 autoantibodies but without optic nerve involvement. As a disease control, MS was defined as clinically definite MS according to the International Panel criteria for MS,¹¹ after excluding definite and limited NMOsd.

In NMOsd and MS patients, ON-affected eyes were defined as eyes with a previous clinical episode of ON or abnormalities in the AVP on magnetic resonance imaging (MRI) findings. ON-unaffected eyes were defined as eyes with no history of ON, no abnormalities in the AVP on MRI findings, and no abnormalities in the visual field (VF).

Visual function testing was performed using visual acuity (VA; Landolt broken ring chart), VF (automatic perimetry; Humphrey; Carl Zeiss Meditec, Jena, Germany), and visual-evoked potential (Neuropack X1; Nihon Kohden, Tokyo, Japan). OCT was performed on both eyes using Fourier/spectral-domain (F/SD)-OCT with an RTVue-100 instrument (Optovue, Fremont, CA) with software version A4.0.

To detect ON lesions with MRI, coronal-oblique fat-saturated dual echo fast spin-echo images with 3mm-thick slices, coronal-oblique 3-dimensional (3D) fast imaging employing steady-state acquisition with 0.8- to 1.0mm-thick slices, and coronal-oblique fat-saturated T1-weighted spin-echo images with 3mm-thick slices before and after administration of 0.1mmol/kg intravenous gadolinium were acquired using a 1.5T scanner (GE Medical Systems, Milwaukee, WI; Philips Achieve, Philips Medical Systems, Best, the Netherlands). The 3D double inversion recovery (DIR) images (repetition time = 5,500 milliseconds, echo time = 350 milliseconds, inversion time 1 (TI1) = 2,350 milliseconds; TI2 = 350 milliseconds, number of excitations = 2, echo train length = 208, measured voxel size = 1.30 × 1.31 × 1.30mm) were acquired using a 1.5T scanner.

The present study was approved by the institutional review board of the Niigata University School of Medicine, Niigata, Japan. Written informed consent was obtained from all patients or their guardians.

Neuropathological Assessments

This study was conducted on retina and optic nerve tissues from 13 patients with NMOsd (3 retinas, 13 optic nerves), 7 patients with MS (1 retina, 7 optic nerves), and 8 patients with other diseases (as controls; 4 retinas, 4 optic nerves; Supplementary Table 2). These individuals were different from those who underwent neuro-ophthalmological and neuroradiological assessments. One to 4 blocks of retinas and optic nerves were assessed per autopsy case. Four-micrometer-thick, paraffin-embedded sections were obtained and stained with hematoxylin and eosin, Klüver-Barrera staining, and Bodian silver impregnation. Selected sections were immunostained with polyclonal or monoclonal antibodies (Supplementary Table 3).^{9,12,13} All NMOsd and MS lesions were classified according to lesion activity.¹⁴ The area of Wallerian degeneration (Wld) was defined as an extensive loss of myelin and axons and profound gliosis with densely packed glial fibrillary acidic protein (GFAP) and AQP4 immunoreactivity (IR). For quantitative assessment, the content of mitochondria or channel proteins was determined as the volume occupied in axons using X-Y and X-Z confocal images, or as a percentage of the axonal volumes. Serial optical sections at intervals of 0.49 μ m in the Z dimension were captured by using a LSM510 or LSM710 laser

TABLE 1. Clinical Characteristics of Neuro-ophthalmological Assessment

Characteristic	NMOsd Patients, 25 Eyes, 28 Attacks	MS Patients, 22 Eyes, 25 Attacks
Episodes of anterior visual pathway involvement, No. ^a	1.1 ± 0.4	1.2 ± 0.4
Spherical equivalent, diopters ^a	-3.1 ± 2.1	-2.1 ± 2.5
Optic nerve head involvement at ON attacks, No. (%)	10/28 (36)	4/25 (16)
Visual acuity analysis		
Visual acuity, logMAR, at ON attacks, median [range]	1.52 [0.73–3.00] ^b	0.30 [0–1.35] ^b
Severe visual loss at ON attacks, No. (%) ^c	20/28 (71) ^b	9/25 (36) ^b
Severe visual loss at 6 months after ON attacks, No. (%) ^c	9/28 (32) ^b	0/25 (0) ^b
Chronic progressive visual disturbance, No. (%) ^d	7/28 (25)	2/25 (8)
Visual field defects at ON attacks		
MD, dB ^a	-16.4 ± 9.1 ^b	-8.4 ± 6.7 ^b
PSD, dB ^a	11.0 ± 3.8 ^b	6.0 ± 3.8 ^b
CPSD, dB ^a	10.6 ± 4.6 ^b	4.9 ± 2.7 ^b
I. Neurologic abnormalities, No. (%)	7/28 (25)	1/25 (4)
I.1. Vertical step	0 (0)	1 (4)
I.2. Quadrant	0 (0)	0 (0)
I.3. Partial hemianopia	0 (0)	0 (0)
I.4. Hemianopia	3 (11)	0 (0)
I.5. Three quadrant	4 (14) ^b	0 (0) ^b
II.1. Nerve fiber bundle abnormalities, No. (%)	5/28 (18)	3/25 (12)
II.1.a. Temporal wedge	0 (0)	0 (0)
II.1.b. Enlarged blind spot	0 (0)	1 (4)
II.1.c. Nasal step	1 (4)	0 (0)
II.1.d. Paracentral	1 (4)	0 (0)
II.1.e. Partial arcuate	0 (0)	0 (0)
II.1.f. Arcuate	0 (0)	2 (8)
II.1.g. Altitudinal	3 (11)	0 (0)
II.2. Diffuse abnormalities, No. (%)	0/28 (0)	6/25 (24)
II.2.a. Multiple foci	0 (0)	2 (8)
II.2.b. Widespread	0 (0)	4 (16)
II.3. Central abnormalities, No. (%)	4/28 (14) ^b	13/25 (52) ^b
II.3.a. Centrocecal	2 (7)	0 (0)
II.3.b. Central	2 (7) ^b	13 (52) ^b
II.4. Total loss of vision, No. (%)	12/28 (43) ^b	1/25 (4) ^b

TABLE 1: Continued

Characteristic	NMOsd Patients, 25 Eyes, 28 Attacks	MS Patients, 22 Eyes, 25 Attacks
Artifactual abnormalities, No. (%)	0/28 (0)	1/25 (4)
Normal, No. (%)	0/28 (0)	0/25 (0)
VEP analysis at ON attacks		
VEP abnormalities, No. (%)	12/13 (92)	15/16 (94)

^aMean \pm standard deviation.
^bStatistically significant difference between the linked values ($p < 0.05$).
^cSevere visual loss was defined as visual acuity worse than 20/200 (1.0 logMAR).
^dChronic visual disturbance was defined as progressive abnormalities of visual acuity ($+0.3$ logMAR or more) and/or visual field for >2 months.
CPSD = corrected pattern standard deviation; MD = mean deviation; MS = multiple sclerosis; NMOsd = neuromyelitis optica spectrum disorder; ON = optic neuritis; PSD = pattern standard deviation; VEP = visual evoked potential.

confocal microscope (Carl Zeiss, Gottingen, Germany), and Imaris software 7.6.4 (Bitplane, Zurich, Switzerland) was used to generate the 3D reconstructed images.¹⁵ Sections with long ($\geq 20\mu\text{m}$) axonal segments were identified based on an established morphological study and after minimizing identification of false-positive segments lacking mitochondrial elements because of the naturally discontinuous distribution of mitochondrial elements and the variability in the intermitochondrial distance within axons. To obtain these data, we quantified axonal morphology and the volume of mitochondria or channel proteins in 262 images ($\times 100$ objective) acquired from 2 to 6 fields of each area in 20 tissue blocks of the optic nerves from 8 NMOsd cases, 4 MS cases, and 5 controls.

Statistical Analyses

Data analyses were performed using GraphPad Prism 5 software (GraphPad Software, San Diego, CA), IBM SPSS 19 (IBM, Chicago, IL), and Stata 11 software (StataCorp, College Station, TX). Comparisons of medians and proportions between NMOsd and MS groups were performed using the Mann–Whitney U test or the Fisher exact test. Statistical tests among ≥ 3 subgroups were performed using analysis of variance, the Kruskal–Wallis H test, or the chi-square test. Multiple comparisons among subgroups were performed using the Bonferroni or Bonferroni–Dunn tests. Generalized estimating equation (GEE) models, accounting for the history of ON, age, and the effects of within-patient and intereye correlations, were used to determine the

TABLE 2. Clinical Characteristics of Neuroradiological Assessment: Contrast-Enhanced Magnetic Resonance Imaging Analysis of the Optic Nerves, Chiasma, and Tracts at the Time of ON Attack

Characteristic	NMOsd Patients, 21 Eyes, 28 Attacks	MS Patients, 18 Eyes, 21 Attacks
Optic perineuritis, No. (%)	13/28 (46)	6/21 (29)
Simultaneous bilateral involvement, No. (%)	5/28 (18)	2/21 (10)
Distribution of abnormal enhancement during ON attacks, No. (%)		
Nerve head segment involvement	0/28 (0)	0/21 (0)
Orbital segment involvement	24/28 (86) ^a	10/21 (48) ^a
Canalicular segment involvement	21/28 (75)	13/21 (62)
Intracranial segment involvement	9/28 (32)	6/21 (29)
Optic chiasm involvement	1/28 (4)	2/21 (10)
Optic tracts involvement	1/28 (4)	1/21 (5)

^aStatistically significant difference between the linked values ($p < 0.05$).
MS = multiple sclerosis; NMOsd = neuromyelitis optica spectrum disorder; ON = optic neuritis.

TABLE 3. Clinical Characteristics of Neuroradiological Assessment: Magnetic Resonance Imaging Double Inversion Recovery Analysis of the Optic Nerves, Chiasma, and Tracts in Remission

Distribution of Abnormal Intensity Lesion	NMOsd Patients, 13 Eyes, 36 Attacks	MS Patients, 18 Eyes, 41 Attacks
Nerve head segment involvement, No. (%)	0/13 (0)	0/18 (0)
Orbital segment involvement, No. (%)	13/13 (100)	17/18 (94)
Canalicular segment involvement, No. (%)	12/13 (92)	11/18 (61)
Intracranial segment involvement, No. (%)	10/13 (77) ^a	5/18 (28) ^a
Optic chiasm involvement, No. (%)	9/13 (69) ^a	3/18 (17) ^a
Optic tracts involvement, No. (%)	6/13 (46)	2/18 (11)

^aStatistically significant difference between the linked values ($p < 0.05$). MS = multiple sclerosis; NMOsd = neuromyelitis optica spectrum disorder.

relationship with clinical parameters, including neuro-ophthalmological and neuroradiological assessments (Tables 1–3; Fig 1). For all GEE analyses, age was controlled in the models, because this variable is an important factor in visual function and RNFL thickness.¹⁶ Cumulative probabilities of the follow-up visual performance as assessed with time to recovery of VA with 3 lines change from the nadir of ON attacks or to recovery of VA to 20/25 (0.1 logMAR) were estimated by the Kaplan–Meier method, and the significance test among curves of cumulative probabilities and survival rates was performed by the log-rank test. All statistical analyses were considered significant at p values of <0.05 .

Results

Neuro-ophthalmological Features of NMOsd at the Time of ON Attacks

Of the 158 eyes that met the inclusion criteria in the series, 31 of 60 eyes (20 of 30 patients, 67%, 56 attacks) with NMOsd and 41 of 98 eyes (26 of 49 patients, 53%, 57 attacks) with MS were diagnosed as having AVP involvement.

For the neuro-ophthalmological assessments at the time of ON attacks, eyes were excluded¹⁷ if the affected eyes had a prior ON attack and vision did not return to 20/20 (0 logMAR), mean deviation (MD) < -2.00 dB at a prior ON attack, or if optic disk pallor, a known baseline-corrected VA $< 20/40$ (>0.3 logMAR), or VF loss due to any other ophthalmic disorder was present, and then we evaluated each attack of ON-affected eyes with NMOsd (25 eyes, 28 attacks) and MS (22 eyes, 25 attacks; see Table 1). Among ON-affected eyes with NMOsd and MS, the mean (standard deviation [SD]) number of episodes of AVP involvement in eyes with NMOsd and MS was 1.1 (0.4) and 1.2 (0.4), respectively. In the VA analysis, the median VA (logMAR) at the time of ON attacks was significantly impaired. The frequency of eyes with

severe visual loss, which was defined as VA worse than 20/200 (1.0 logMAR), at onset was significantly higher in eyes with NMOsd compared with those with MS. In the VF analysis, the VF defects indicated by the average VF-MD, pattern SD, and corrected pattern SD were significantly impaired in eyes with NMOsd compared with those with MS. VF morphological analysis using the Optic Neuritis Treatment Trial classification¹⁸ demonstrated that “neurologic abnormalities (I)” and “total loss of vision (II.4)” were prominent in ON-affected eyes with NMOsd, whereas “central abnormalities (II.3)” were evident in those with MS. “Altitudinal abnormalities (II.1.g)” were present in 3 of 28 (11%) attacks with NMOsd, but 0 of 25 (0%) attacks with MS.

Intriguingly, 7 of 28 (25%) attacks in NMOsd and 2 of 25 (8%) attacks in MS were associated with chronic progressive visual deterioration, which was defined as progressive abnormalities in VA ($+0.3$ logMAR or more) and/or VF for >2 months.

Neuroradiological Features on Enhanced MRI in NMOsd at the Time of ON Attack

For the neuroradiological assessments at the time of ON attacks, we evaluated the AVP using enhanced T1-weighted images with fat suppression. Of 34 patients (17 patients with NMOsd; 17 patients with MS) who underwent MRI examination at ON attack, abnormal enhancement was present in 16 of 17 (94%) patients (21 eyes, 28 attacks) with NMOsd, and in 16 of 17 (94%) patients (18 eyes, 21 attacks) with MS (see Table 2; Fig 1). MRI findings demonstrated that the length of abnormally enhanced lesions in NMOsd patients was significantly longer than those in MS patients, suggesting that longitudinally extensive lesions were prominent in the optic nerves in NMOsd. During attacks, radiologic

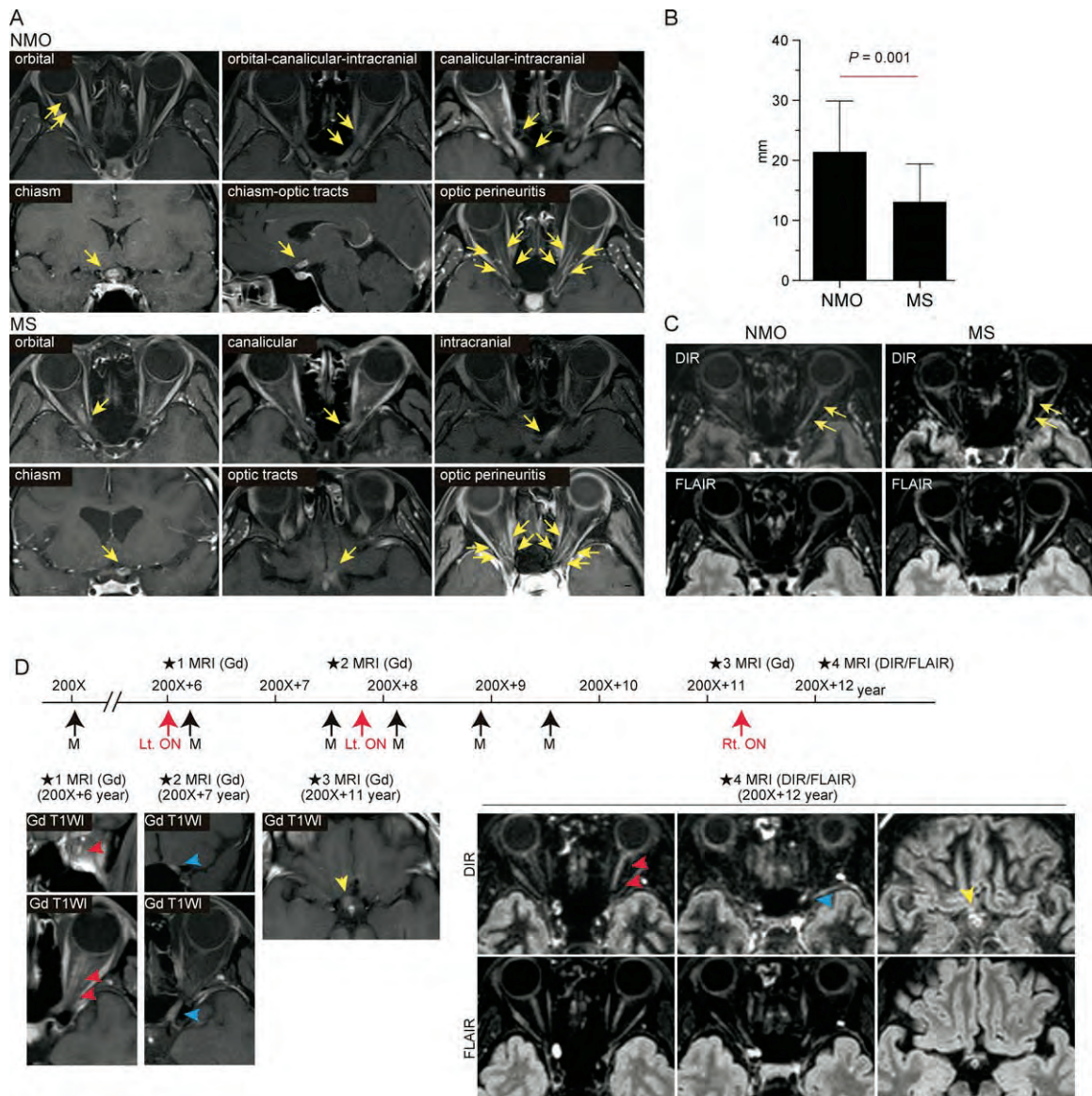


FIGURE 1: Radiological profiles of optic neuritis (ON) at the time of attacks in neuromyelitis optica (NMO) spectrum disorder (NMOsd) and multiple sclerosis (MS). Anterior visual pathways (AVP) during ON in NMOsd and MS were examined by using axial and coronal views of enhanced T1-weighted magnetic resonance images with fat suppression. (A) They were divided into 6 segments: head, orbital, canalicular, and intracranial segments of the optic nerves, the optic chiasm, and the optic tracts. Abnormal enhancement on fat-suppressed magnetic resonance imaging (MRI; arrows) was present in patients with NMOsd and MS. (B) The length of abnormally enhanced lesions in the AVP in NMOsd at the time of ON attacks ($n = 28$ events) was significantly longer than in MS attacks ($n = 21$ events). The pattern of abnormal enhancement in the AVP at the time of ON attacks was generally homogeneous in most NMOsd and MS patients (A). However, the pattern of optic nerve sheath enhancement, which is referred to as a “tram track sign” on axial views and a “doughnut sign” on coronal views, was also present in 46% of attacks in NMOsd patients and 29% of attacks in MS patients (A). This was defined as optic perineuritis (OPN).¹⁹ The pathologic evidence (see Fig 4) indicated that OPN was associated with more widespread meningeal and perineural inflammation around the optic nerves. (C, D) Three-dimensional (3D) double inversion recovery (DIR) MRI detected accumulation of archival ON lesions in NMOsd and MS. DIR MRI simultaneously suppresses the signals from white matter and cerebrospinal fluid (CSF). A substantial increase in cortical demyelinating lesions in patients with MS was found compared to more conventional sequences, including fluid-attenuated inversion recovery (FLAIR) imaging.⁴⁹ Therefore, not only cortical demyelinating lesions but also ON lesions, which usually contact the CSF, were detected with high sensitivity by using DIR imaging (C, arrows) compared to FLAIR imaging in ON lesions in NMOsd and MS. The distribution of abnormal intensity on 3D-DIR images showed accumulation of archival lesions through the disease course, based on longitudinally evaluated MRI data. A representative case is shown in D. A 38-year-old woman experienced 3 attacks of acute ON and 6 attacks of myelitis (M) during the 12 years after disease onset. The distribution of abnormal intensity on 3D-DIR images 12 years after disease onset (★4, red, blue, and yellow arrowheads) equaled the addition of each abnormally enhanced lesion in 3 attacks of ON (★1, red arrowheads, 6 years after onset; ★2, blue arrowheads, 7 years after onset; ★3, yellow arrowheads, 11 years after onset; D). Gd T1WI = gadolinium-enhanced T1-weighted image; Lt. = left eye; Rt. = right eye.

TABLE 4. Clinical Characteristics of OCT Assessment: OCT Analysis of the Retinas in Remission

Characteristic	NMOsd Patients		MS Patients	
	Unaffected Eyes, 14 Eyes	Affected Eyes, 8 Eyes	Unaffected Eyes, 18 Eyes	Affected Eyes, 8 Eyes
Mean RNFL thickness				
Mean RNFL, μm^a	95.9 \pm 9.4	63.9 \pm 10.2	96.5 \pm 9.7	78.9 \pm 9.5
Within normal limits, No. (%)	11/14 (79)	0/8 (0)	11/18 (61)	1/8 (13)
Borderline, No. (%)	1/14 (7)	0/8 (0)	5/18 (28)	0/8 (0)
Outside normal limits, No. (%)	2/14 (14)	8/8 (100)	2/18 (11)	7/8 (88)
16-sector RNFL analysis				
Average number of sectors with borderline or outside normal limits ^a	2.2 \pm 2.5	13.3 \pm 4.1	2.1 \pm 2.3	9.9 \pm 4.9
Mean GCC thickness				
Mean GCC, μm^a	87.3 \pm 12.5	60.4 \pm 11.0	89.2 \pm 5.8	70.1 \pm 7.9
Within normal limits, No. (%)	9/14 (64)	0/8(0)	13/18 (72)	0/8 (0)
Borderline, No. (%)	0/14 (0)	0/8 (0)	2/18 (11)	1/8 (13)
Outside normal limits, No. (%)	5/14 (36)	8/8 (100)	3/18 (17)	7/8 (88)

^aMean \pm standard deviation.
GCC = ganglion cell complex; MS = multiple sclerosis; NMOsd = neuromyelitis optica spectrum disorder; OCT = optical coherence tomography; RNFL = retinal nerve fiber layer.

characteristic features of optic perineuritis (OPN)¹⁹ were marked in NMOsd patients (13 of 28 [46%] attacks) compared to MS patients (6 of 21 [29%] attacks), but the difference was not significant. Some patients with NMOsd and MS retained abnormal enhancement with the OPN pattern for >4 weeks.²⁰ Five of 28 (18%) attacks in NMOsd and 2 of 21 (10%) attacks in MS simultaneously had bilateral optic nerve involvement.

Neuroradiological Features on 3D-DIR MRI in NMOsd in Remission

Based on longitudinally evaluated MRI data, the distribution of abnormal intensity on 3D-DIR images showed accumulation of archival lesions throughout the disease course (see Fig 1C, D). In remission, 3D-DIR MRI assessments were performed in 14 patients (28 eyes) with NMOsd and 28 patients (56 eyes) with MS. Thirteen of 28 (46%) eyes with NMOsd and 18 of 56 (32%) eyes with MS had abnormal intensities in the AVP. The numbers of segments with optic chiasma and intracranial involvement were significantly higher in NMOsd patients compared to MS patients (see Table 3).

OCT Analysis of Retinas with NMOsd in Remission

The cohort that underwent OCT assessment included 11 patients with NMOsd (4 with the definite form and 7

with the limited form; 22 eyes; 14 ON-unaffected eyes and 8 ON-affected eyes) and 13 patients with MS (26 eyes; 18 ON-unaffected eyes and 8 ON-affected eyes; Tables 4 and 5; Fig 2). In NMOsd and MS patients, the RNFL and ganglion cell complex (GCC) were significantly thinner in ON-affected eyes than in ON-unaffected eyes. For the ON-affected eyes, RNFL was significantly thinner in NMOsd patients than in MS patients.

When damage was classified as “borderline” and “outside normal limits” for the RNFL or GCC thickness, the frequency of ON-unaffected eyes with RNFL thinning was 21% in NMOsd patients and 39% in MS patients, and the frequency of ON-unaffected eyes with GCC thinning was 36% in NMOsd patients and 28% in MS patients (see Table 4). In patients with the limited form of NMOsd with myelitis but no history of ON, the frequency of ON-unaffected eyes with RNFL thinning was 30%, and the frequency of ON-unaffected eyes with GCC thinning was 40% (see Table 5). These data suggest that RNFL and GCC loss was evident in ON-affected and ON-unaffected eyes, and not only secondary retrograde changes after ON, but also in vivo primary neuroaxonal pathology, regardless of ON history, were present in retinas in NMOsd and MS.

TABLE 5. Clinical Characteristics of OCT Assessment: OCT Analysis of the Retinas in Limited Form of NMOsd with Myelitis Patients in Remission

Characteristic	Limited Form of NMOsd with Myelitis Patients, Unaffected Eyes, 10 Eyes
Mean RNFL thickness	
Mean RNFL, μm^a	94.0 \pm 10.4
Within normal limits, No. (%)	7/10 (70)
Borderline, No. (%)	1/10 (10)
Outside normal limits, No. (%)	2/10 (20)
16-sector RNFL analysis	
Average number of sectors with borderline or outside normal limits ^a	2.5 \pm 2.8
Mean GCC thickness	
Mean GCC, μm^a	87.3 \pm 11.2
Within normal limits, No. (%)	6/10 (60)
Borderline, No. (%)	0/10 (0)
Outside normal limits, No. (%)	4/10 (40)

^aMean \pm standard deviation.
GCC = ganglion cell complex; NMOsd = neuromyelitis optica spectrum disorder; OCT = optical coherence tomography; RNFL = retinal nerve fiber layer.

Follow-up Visual Performance in NMOsd

We evaluated the follow-up visual performance from the nadir of ON attacks in NMOsd and MS (Fig 3, Table 1). The frequency of eyes with severe visual loss, which was defined as VA worse than 20/200 (1.0 logMAR), at 6 months after ON onset was significantly higher in eyes with NMOsd compared with those with MS (see Table 1). Kaplan–Meier analysis of time to recovery of VA with 3 lines change from the nadir of ON attacks or to recovery of VA to 20/25 (0.1 logMAR) was performed. Patients with NMOsd developed a significantly worse outcome regarding visual performance over time than those with MS when we evaluated all cumulative attacks of ON in patients with NMOsd and MS or all first attacks of ON in each patient with NMOsd and MS (data not shown). Mean follow-up times between the ON onset and assessment were 11.5 months in NMOsd patients (25 attacks) and 9.2 months in MS patients (13 attacks) or 11.5 months in NMOsd patients (25 attacks)

and 9.4 months in MS patients (14 attacks). All patients with NMOsd and MS in the analysis were treated with methylprednisolone pulse treatment (1g per day) for 3 days and/or high-dose oral prednisolone treatment (1.0mg/kg per day) followed by prednisolone tapered to maintenance level. No patients in this study were treated with plasma exchange.

Astrocytopathy with Increased Meningeal Inflammation in Plaques of the Optic Nerves, Chiasm, and Tracts in NMOsd

Clinically, 85% (11 of 13) of NMOsd cases and 86% (6 of 7) of MS cases had a previous history of ON. Pathologically, all cases in NMOsd and MS had several plaques in the AVP (Fig 4). The pathology in the AVP in NMOsd cases was evaluated in 22 lesion areas, 13 areas of periplaque white matter (PPWM), 11 areas of normal-appearing white matter (NAWM), and 10 areas of Wld. Similarly, in cases with MS, we evaluated 14 lesion areas, 11 areas of PPWM, and 11 areas of NAWM. All plaques in the optic nerves in NMOsd cases showed hallmarks of NMO pathology, including pattern-specific loss of AQP4 IR with thickened hyalinized blood vessels.^{9,21} Moreover, thickening of the perioptic meninges with inflammatory infiltration including CD45RO⁺ T cells and Iba-1⁺ cells was prominent in the meninges adjacent to the plaques in NMOsd cases. The meningeal infiltrates also extended into the pial septa and parenchyma of the optic nerves (see Fig 4). Therefore, lesions in the AVP in NMOsd were pathologically defined as ON and/or OPN with meningeal inflammation, consistent with radiological findings (see Fig 1A).¹⁹

Severe axonal damage with abnormal mitochondrial dynamics and aberrant expression of the TRPM4 cation channel in the optic nerves, chiasm, and tracts in NMOsd

Axonal pathology was qualitatively and quantitatively assessed with Bodian silver impregnation, and immunohistochemistry for phosphorylated neurofilaments (SMI-31) and amyloid precursor protein. Axonal damage, including axonal loss, transections, swellings, and distorted axons, and axonal spheroids were evident in plaques and PPWM, and had accumulated toward the plaque center of the AVP in NMOsd and MS (Figs 5–7). The axonal damage was the most prominent in plaques and areas of Wld in NMOsd. The density of SMI-31⁺ axons was significantly reduced, and the percentages of swollen axons and axonal spheroids were significantly increased in plaques, PPWM, and Wld in NMOsd, and plaques, PPWM, and NAWM in MS compared to controls. Swollen axons and axonal spheroids with no significant reduction in axonal density were also present, even in the NAWM in NMOsd.

A. Affected optic neuritis eyes

B. Unaffected optic neuritis eyes with RNFL loss

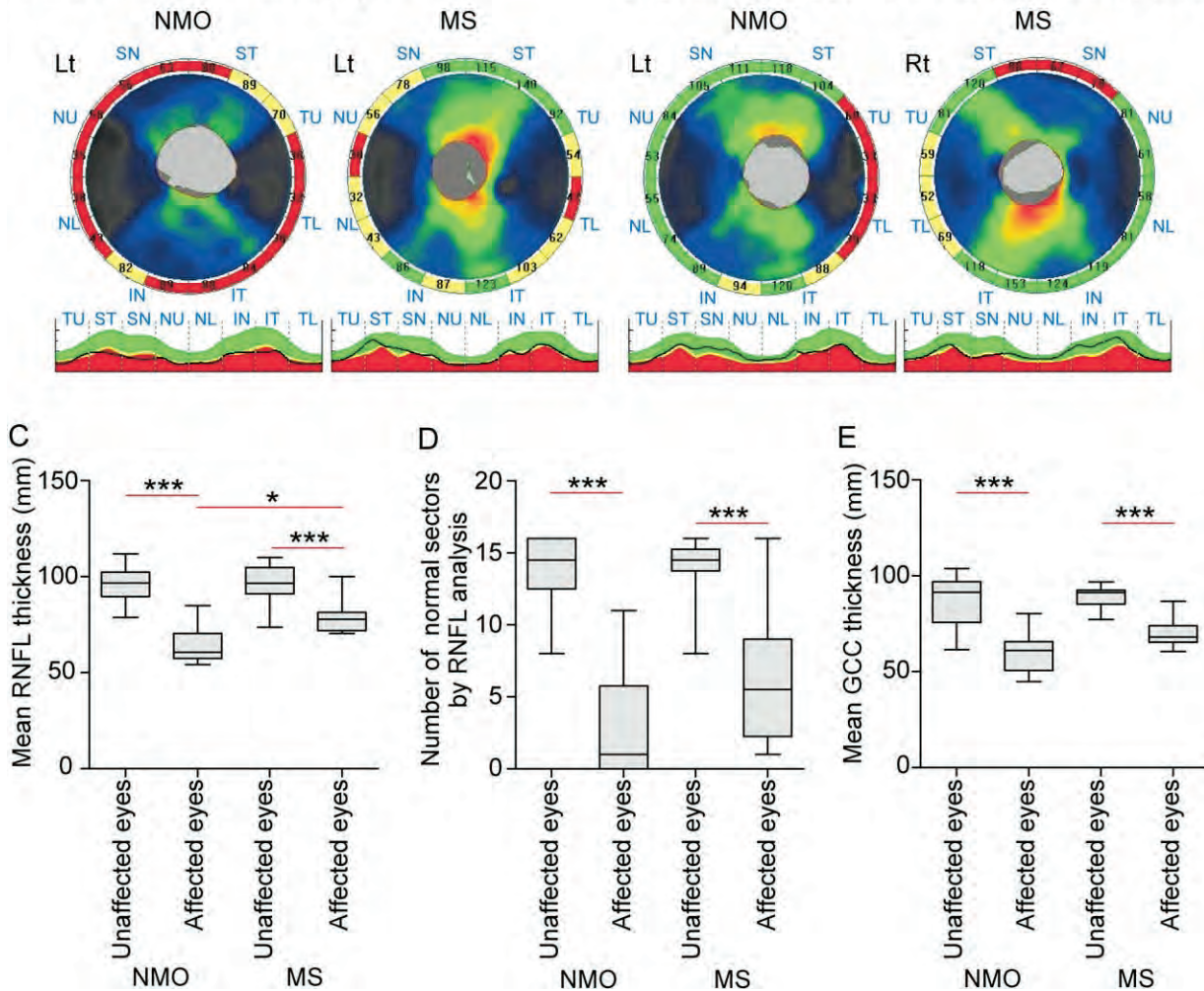


FIGURE 2: Optical coherence tomography (OCT) analysis in patients with neuromyelitis optica (NMO) spectrum disorder (NMOsd) and multiple sclerosis (MS). (A, B) The data shown are representative of optic neuritis (ON)-affected eyes with retinal nerve fiber layer (RNFL) thinning (A) and ON-unaffected eyes with RNFL thinning (B) in NMOsd and MS patients. In the 16-sector RNFL analysis, sectors with a classification of "within normal limits" (ie, sectors for which the probability of no damage $\geq 5\%$) are indicated in green, sectors with a "borderline" classification (probability < 5 but $\geq 1\%$) are indicated in yellow, and sectors with a classification of "outside normal limits" (probability $< 1\%$) are indicated in red. The 16-sector RNFL analysis (A) revealed that sectors with a classification of "outside normal limits" (red) and "borderline" (yellow) were present in the ON-affected eyes of NMOsd and MS patients. (C–E) The average thicknesses of the RNFL (C) and ganglion cell complex (GCC; E) were significantly decreased in the ON-affected eyes compared with the ON-unaffected eyes in patients with NMOsd and MS. The 16-sector RNFL analysis (D) revealed the average number of normal sectors with significantly decreased thickness in the ON-affected eyes compared with the ON-unaffected eyes in patients with NMOsd and MS. For the ON-affected eyes, RNFL was significantly thinner in NMOsd patients than in MS patients (C). Intriguingly, the 16-sector RNFL analysis (B) revealed that sectors with a classification of "outside normal limits" (red) and "borderline" (yellow) were present in the ON-unaffected eyes of NMOsd and MS patients. When damage was classified as "borderline" and "outside normal limits" for RNFL or GCC thickness, the frequency of ON-unaffected eyes with RNFL thinning was 21% in the NMOsd patients and 39% in the MS patients (see Table 4). The frequency of ON-unaffected eyes with GCC thinning was 36% in the NMOsd patients and 28% in the MS patients (see Table 4). These data suggest that RNFL and GCC loss is present and is independent of ON in NMOsd and MS. The peripapillary RNFL results were obtained based on Fourier/spectrum domain OCT using an RTVue-100 instrument in patients with NMOsd and MS. GCC scanning using the OCT system encompasses the following 3 layers in the retina: (1) the RNFL, which is composed of ganglion cell axons; (2) the ganglion cell layer, which is composed of ganglion cell bodies; and (3) the inner plexiform layer, which is composed of interlaced dendrites of ganglion cells and axons of bipolar cells with dendrites of amacrine cells (see Fig 8F). * $p < 0.05$, *** $p < 0.001$. IN = inferonasal; IT = inferotemporal; Lt = left eye; NL = nasal lower; NU = nasal upper; Rt = right eye; SN = superonasal; ST = superotemporal; TL = temporal lower; TU = temporal upper.

Mitochondrial dynamics is an important contributor to damage and loss of axons in several neurodegenerative disorders.²² We thus assessed the dynamics of

voltage-dependent anion channel (VDAC)/porin-labeled mitochondria located in SMI-31⁺ axons in NMOsd compared to mitochondria in MS and controls (see Fig

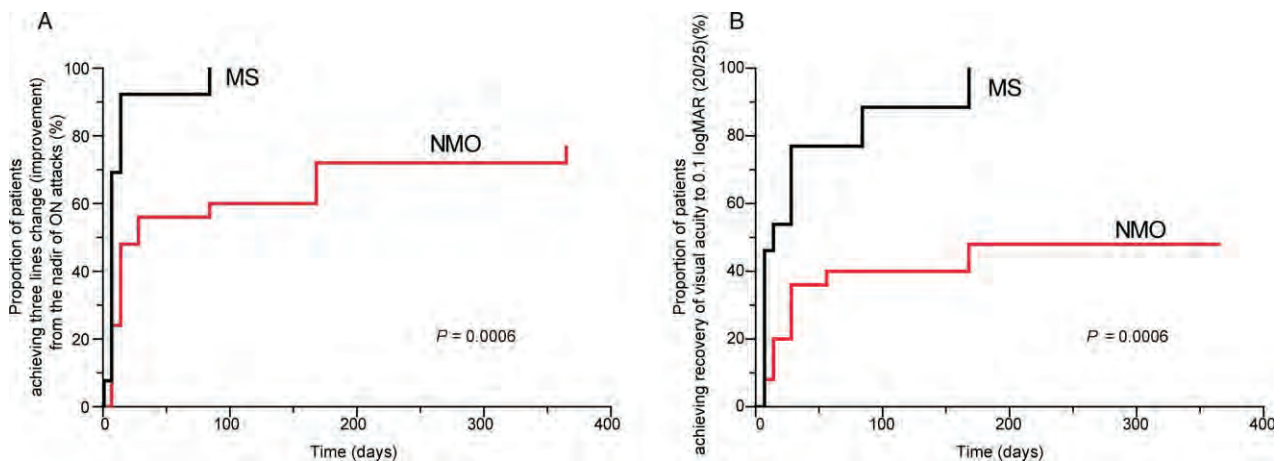


FIGURE 3: Follow-up visual performance in neuromyelitis optica (NMO) spectrum disorder (NMOsd) and multiple sclerosis (MS). We performed Kaplan–Meier analysis of time to (A) recovery of visual acuity (VA) with 3 lines change and (B) recovery of VA to 20/25 (0.1 logMAR) from the nadir of optic neuritis (ON) attacks in NMOsd and MS patients. Eyes were excluded if deterioration of VA with <3 lines change was present at presentation (A) or VA was >20/25 (<0.1 logMAR) at presentation (B). Patients with NMOsd developed significantly worse visual performance outcomes over time than those with MS, when we evaluated not only all accumulative attacks of ON in patients with NMOsd and MS, but also all first attacks of ON in each patient with NMOsd and MS (data not shown).

6). First, morphological analysis of VDAC-1⁺ mitochondria showed that shortened, fragmented, or swollen mitochondria, indicating extensive fission of mitochondria and mitochondrial degeneration, accumulated within axons in all areas including plaques, PPWM, NAWM, and Wld in NMOsd and MS compared to controls. Abnormal morphological changes were more evident in axons in NMOsd compared to those in MS, and were more prominent in swollen axons compared to nonswollen axons in NMOsd and MS. Second, compared to controls, quantitative analysis of the mitochondrial volume in axons demonstrated that the VDAC-1⁺ mitochondrial content in SMI-31⁺ axons was significantly increased in swollen axons of PPWM and NAWM and in areas of Wld in NMOsd, but not in these areas in MS. The VDAC-1⁺ mitochondrial content in the axons of active plaques (17.1%, 6.6; mean, SD) was increased compared to inactive plaques (6.1%, 3.4) in NMOsd. These qualitative and quantitative data suggest that the accumulation of mitochondria with abnormal morphology in axons was more extensive in NMOsd compared to MS and controls and was dependent on morphological changes in axons (swollen axons) and on the disease stage (active stage) from the lesion center to even NAWM in NMOsd (see Figs 5–7).

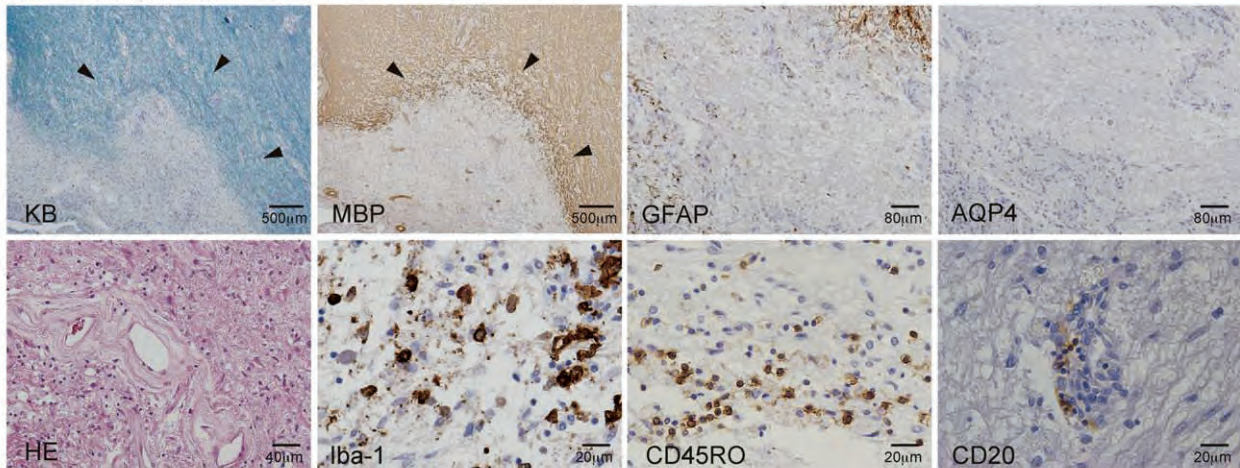
Consistent with the dynamics of degenerative mitochondria in axons, the axon-specific mitochondria docking protein, syntaphilin,²³ was also significantly increased in axons in plaques, PPWM, NAWM, and Wld in NMOsd and MS, suggesting immobile mitochondria or decreased mitochondrial movement within axons (see Fig 6C).

Next, to investigate the pathophysiological mechanisms of axonal damage in NMOsd, we assessed the transient receptor potential melastatin 4 (TRPM4). This protein crucially contributes to axonal damage, and pharmacological inhibition of TRPM4 using the antidiabetic drug glibenclamide reduces axonal degeneration in an animal model of MS, experimental autoimmune encephalomyelitis (EAE).²⁴ Quantification of axonal TRPM4 expression revealed significantly more TRPM4 IR in areas of plaques and Wld and in the swollen axons of PPWM and NAWM in NMOsd and MS compared to controls, in which we detected only a few TRPM4⁺ axons (see Figs 6B and 7D, E). TRPM4⁺ axons were more evident in swollen axons than in nonswollen axons in NMOsd and MS. Therefore, aberrant axonal accumulation of mitochondria with abnormal morphology and decreased movement, and abnormal axonal expression of TRPM4 extended over wider areas in NMOsd compared to MS.

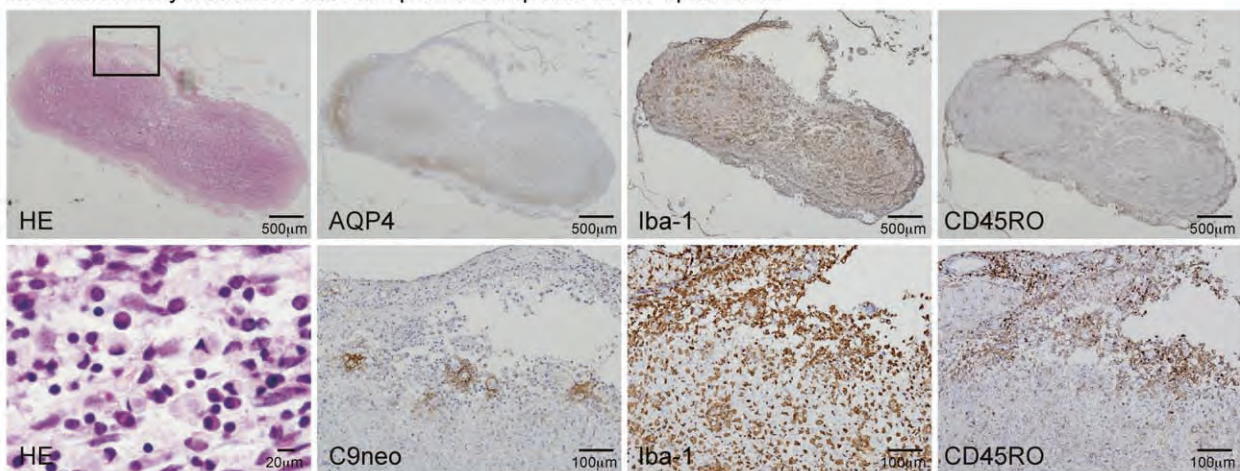
Neuroaxonal Damage with Müller Cell Pathology in the Retina in NMOsd

The retina is anatomically isolated and represents a unique unmyelinated model in which to study neurodegeneration and inflammation, as well as the distal effects of demyelination of optic nerves in inflammatory and demyelinating syndromes of the CNS. All retina samples from NMOsd autopsy cases showed severe RNFL thinning with an abundance of GFAP⁺ and AQP4⁺ astrocytes and neuronal loss of ganglion cells in the retina, suggesting the presence of secondary retinal retrograde degeneration after ON (Fig 8). The calcium-binding

A. Pattern-specific loss of AQP4 in the optic chiasma



B. Inflammatory infiltration with complement deposits in the optic nerve



C

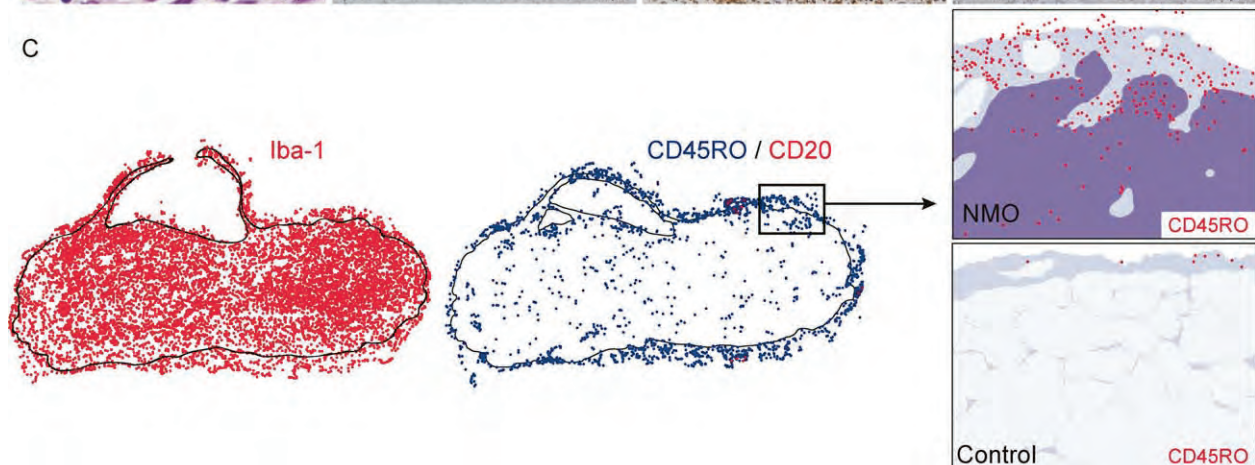


FIGURE 4: Characterization of typical pathological findings of neuromyelitis optica (NMO) spectrum disorder (NMOsd) in optic nerves including pattern-specific loss of aquaporin-4 (AQP4) immunoreactivity (IR) in inflammatory lesions. (A, B) All patients with NMOsd in this study had typical pathological findings of NMOsd in optic nerves (*arrowheads*), including pattern-specific loss of AQP4 and glial fibrillary acidic protein (GFAP) IR and immunoglobulin deposits colocalizing with a product of complement activation, C9neo, in a vasocentric pattern around thickened hyalinized vessels in inflammatory demyelinating lesions. Moreover, Iba-1⁺ microglia, CD45RO⁺ T cells, and CD20⁺ B cells were abundant in inflammatory demyelinating lesions. In particular, thickening of the perioptic meninges with inflammatory infiltration including CD45RO⁺ T cells and Iba-1⁺ cells was prominent in the meninges adjacent to the plaques in NMOsd patients. (C) The meningeal infiltrates also extended into the pial septa and parenchyma of the optic nerves. HE = hematoxylin and eosin; KB = Klüver-Barrera; MBP = myelin basic protein.

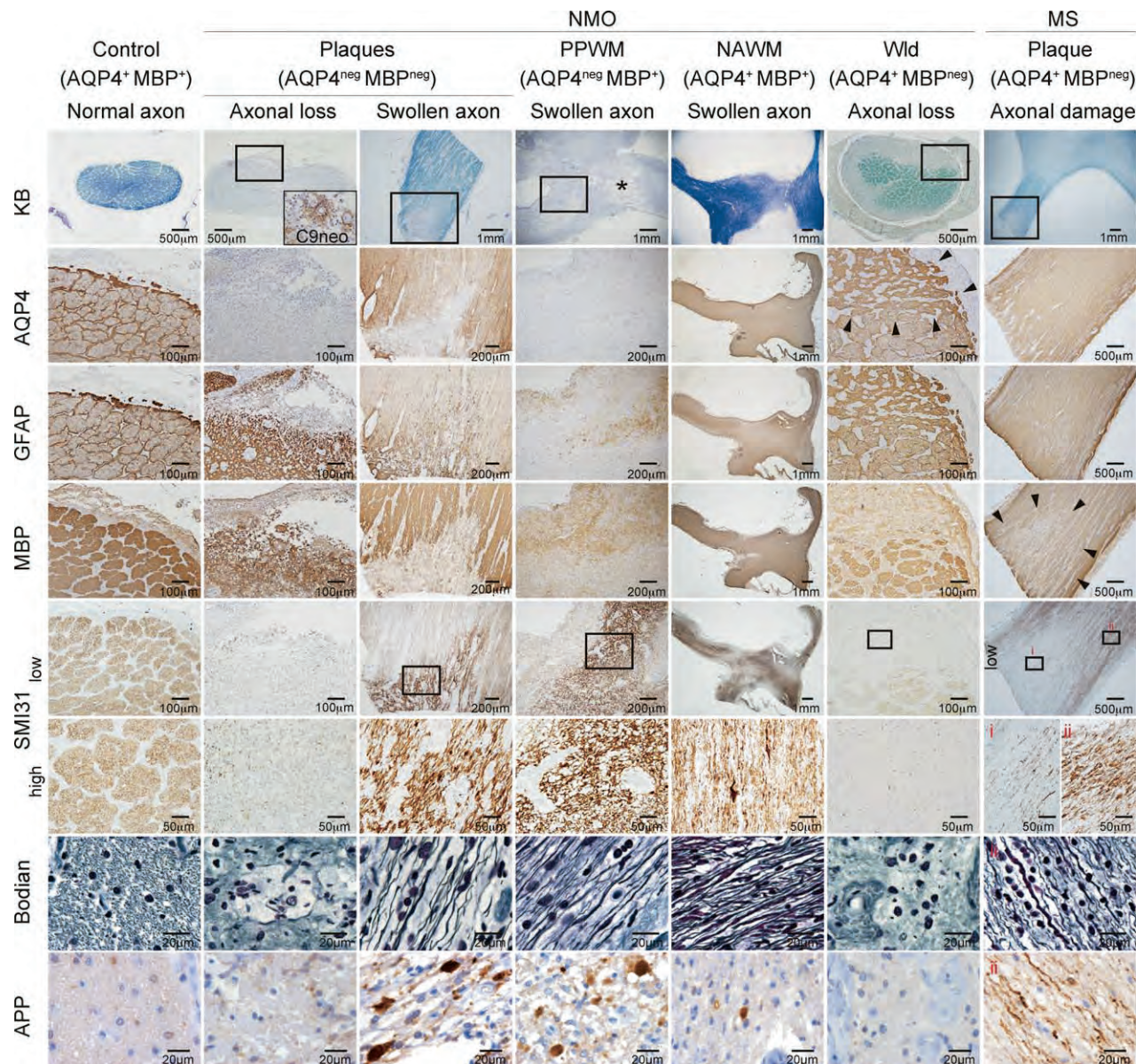


FIGURE 5: Severe axonal damage in the optic nerves in neuromyelitis optica (NMO) spectrum disorder (NMOsd). Axonal pathology of the optic nerves in NMOsd and multiple sclerosis (MS) was qualitatively assessed with Bodian silver impregnation, and immunohistochemistry for phosphorylated neurofilaments (SMI-31) and amyloid precursor protein (APP). Axonal damage, including axonal loss, transections, swellings, and distorted axons, and axonal spheroids were evident in plaques and periplaque white matter (PPWM) and had accumulated toward each plaque center in the optic nerves in NMOsd and MS compared to control. Areas of Wallerian degeneration (Wld), which were defined by an extensive loss of myelin and axons, and profound gliosis with densely packed glial fibrillary acidic protein (GFAP) and aquaporin-4 (AQP4) immunoreactivity (IR), were present in NMOsd. Axonal damage, including axonal loss, transections, swellings, and distorted axons, and axonal spheroids were most prominent in plaques and areas of Wld in NMOsd and MS. All NMO and MS lesions were classified according to lesion activity, as previously described.¹⁴ In brief, active plaques were characterized by macrophages with minor myelin products (cyclic nucleotide phosphodiesterase) or myelin basic protein (MBP) and profound inflammation, and inactive plaques were characterized by macrophages without minor or major myelin products within their cytoplasm. PPWM was defined as normal myelin, microglial activation, and few inflammatory infiltrates adjacent to the plaque. Additionally, PPWM in NMOsd included loss of AQP4 IR adjacent to the plaque.¹⁴ Normal-appearing white matter (NAWM) was defined as myelin integrity and at least 1 cm away from a plaque's edge.⁵⁰ Additionally, NAWM in NMOsd included preservation of AQP4 IR. *Plaque. KB = Klüber-Barrera; neg = negative.

protein calbindin is a known marker of cone photoreceptors, horizontal cells, and subpopulations of bipolar cells and amacrine cells in the human retina. In the retina in

NMOsd cases, we observed mild loss of calbindin⁺ horizontal cells in the INL and unique dynamics of Müller cells including scattered loss of AQP4 IR in Müller cells

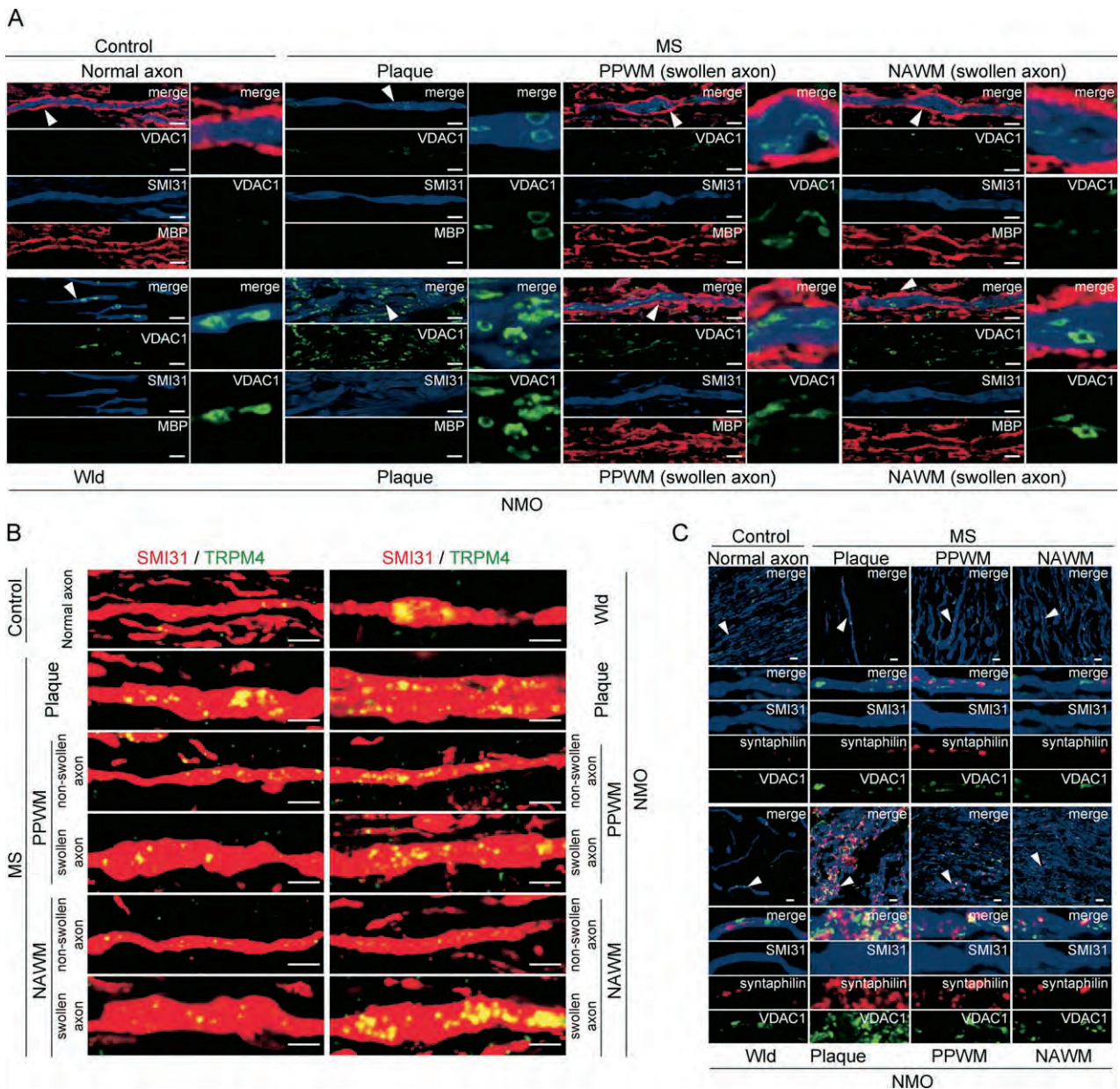


FIGURE 6: Abnormal axonal mitochondrial dynamics and aberrant axonal expression of transient receptor potential melastatin 4 (TRPM4) cation channel in the optic nerves in neuromyelitis optica (NMO) spectrum disorder (NMOsd). (A) We assessed the dynamics of mitochondria labeled with voltage-dependent anion channel (VDAC)/porin (green) located in SMI-31 (blue)⁺ axons in NMOsd compared to controls. Myelin basic protein (MBP; red)⁺ myelinated and MBP⁻ demyelinated axons were identified based on the lesion classification. Morphological analysis of VDAC-1⁺ mitochondria showed shortened, fragmented, or swollen mitochondria, indicating extensive fission of mitochondria and mitochondrial degeneration. These mitochondria accumulated within axons in all areas including plaques, periplaque white matter (PPWM), normal-appearing white matter (NAWM), and Wallerian degeneration (Wld) in NMOsd and multiple sclerosis (MS) compared to controls (arrowheads in A). (B) We then assessed the dynamics of the TRPM4 cation channel (green) in SMI-31 (red)⁺ axons in NMOsd and MS compared to controls. TRPM4⁺ axons were more evident in areas of plaques and Wld and in the swollen axons of PPWM and NAWM in NMOsd and MS compared to controls, in which we detected only a few TRPM4⁺ axons. (C) Consistent with the dynamics of degenerative mitochondria in axons (A), the axon-specific mitochondrial docking protein, syntaphilin (red), was also increased within SMI-31⁺ axons (blue) in plaques, PPWM, NAWM, and Wld in NMOsd and MS, suggesting immobile mitochondria or decreased mitochondrial movement within axons. Therefore, aberrant accumulation of mitochondria with abnormal morphology and with decreased movement in axons was evident in the optic nerves in NMOsd and MS. Scale bars = 50 μm.

and mild to moderate loss of glutamine synthetase (GS)⁺ Müller cell soma in the INL. Iba-1⁺ microglia were present in the inner retina in NMOsd cases; how-

ever, CD45RO⁺ T cells, CD20⁺ B cells, and perivascular deposition of complement, C9neo, were not observed in all retina samples from NMOsd cases (data not

shown). The retinas of MS cases showed severe RNFL thinning with an abundance of GFAP⁺ and AQP4⁺ astrocytes and neuronal loss of ganglion cells in the ganglion cell layer and calbindin⁺ horizontal cells in the INL. However, retinas from MS cases showed no changes in AQP4 or GS IR in Müller cells. Reported evidence supports the involvement of AQP4 in retinal inflammatory responses,²⁵ retinal swelling,²⁵ and light-induced retinal neurodegeneration.²⁶ Moreover, optic nerve

transection in animal models results in RNFL thinning and ganglion cell loss but not in atrophy or degeneration of deep retinal layers including the INL.²⁷ If this is the case in the eyes of NMO patients, the Müller cells with unique dynamics observed in NMO patients may be related to primary retinal degeneration. These data suggest that the characteristics of the retinal pathology observed in NMOs were strikingly distinct not only from the characteristics of the retinas in MS but also

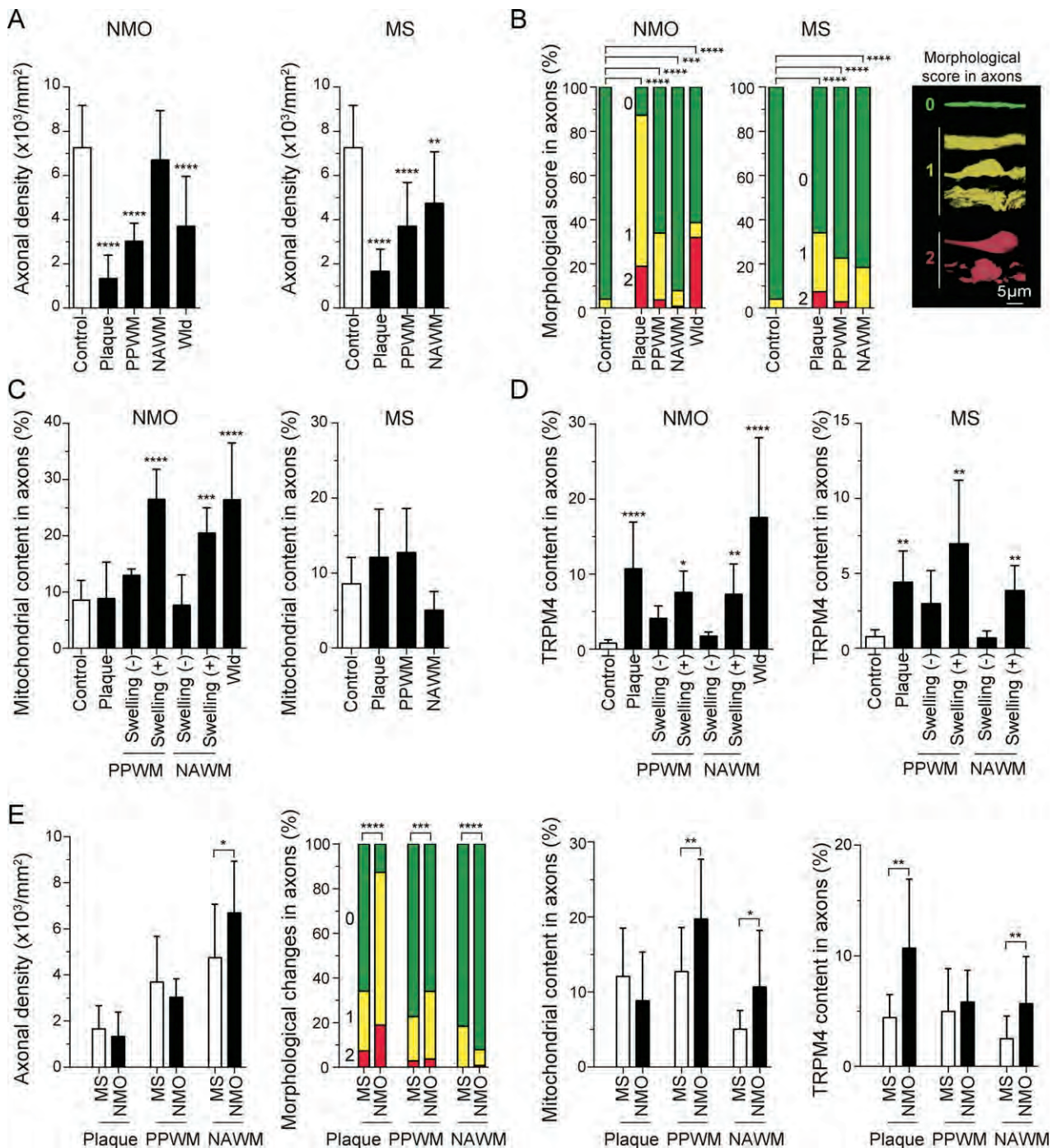


FIGURE 7.

from myelitis or ON in NMOsd (see Fig 4), and the retina of NMOsd cases was characterized by primary as well as secondary neuronal and axonal loss with unique dynamics of Müller cells.

Discussion

The optic nerves are the major site of involvement in NMOsd and have several distinguishing structures. First, the long, thin cylindrical dimension of the optic nerves with the cul-de-sac anatomy of the subarachnoid space may cause unique cerebrospinal fluid (CSF) dynamics, including restricted diffusion of proinflammatory elements (eg, AQP4 antibodies), retained inflammation, and limited clearance of myelin and axonal debris, followed by enhanced NMOsd lesion formation.^{28,29} We revealed prominent pathological meningeal thickening with inflammation (see Fig 4) and radiologically abnormal enhancement of the OPN pattern in NMOsd (see Fig 1). Inflammatory processes may contribute to the closing of the arachnoid apertures that drain CSF into the meningeal lymphatics, thus adding to CSF compartmentalization.²⁹ Second, the absence of classical blood-brain barrier (BBB) properties with nonspecific permeability of microvessels in the prelaminar region in the optic nerve head³⁰ may cause transmigration of AQP4 antibodies. Third, the unique structure of pial septa that partition each optic nerve fiber bundle from the adjoining glial limitans (a network of AQP4⁺ astrocytic foot processes) may form an immunological barrier that prevents immune cells from entering the CNS parenchyma. Penetration of this barrier by encephalitogenic T lymphocyte requires the activity of matrix metalloproteinases,

which are produced by myeloid cells in an EAE model.³¹ Thus, the presence of CD45RO⁺ T cells and Iba-1⁺ macrophages in the pial septa in NMOsd (see Fig 4) may increase the chance of breaking the barrier and promote effector responses for AQP4 on astrocytes. Finally, abundant large orthogonal arrays of particles (OAPs) in astrocytic endfeet of the optic nerves enhance binding of AQP4 antibodies and complement-dependent astrocyte damage.²⁸ These unique structures of the optic nerves may promote typical NMOsd lesions that show a pattern-specific loss of AQP4 with complement activation.

Importantly, we demonstrated that severe and widespread neurodegeneration with aberrant accumulation of degenerative mitochondria and TRPM4 channels was evident in the optic nerves in NMOsd. In the pathogenesis of MS, key elements that drive neurodegeneration and that can result in permanent clinical deficits³² include accumulation of axonal mitochondrial damage, ion channel dysfunction including TRPM4, and involvement of Wld in axons of the CNS as follows.^{24,33,34} First, axons are extremely susceptible to mitochondrial dysfunction, because the geometry of the neuron-axon unit presents a substantial challenge for efficient distribution of mitochondria and adenosine triphosphate (ATP) production within axons, which can reach 1m or more in length in humans.³³ “Fusion and fission” and an “increased number” of mitochondria play critical roles in maintaining functional mitochondria in the presence of environmental stress.²² These dynamics of mitochondria fine-tune fundamental cellular processes such as calcium homeostasis and the generation of ATP and reactive

FIGURE 7: Quantitative analysis of axonal damage in the optic nerves in neuromyelitis optica (NMO) spectrum disorder (NMOsd). (A–D) Axonal pathology in the optic nerves in NMOsd was quantitatively assessed by immunohistochemistry for SMI-31 (A, B), voltage-dependent anion channel -1 (VDAC-1; C), and transient receptor potential melastatin 4 (TRPM4; D). Axonal damage was classified as normal axons (score 0; green), swollen axons with or without spheroids (score 1; yellow), and fragmented axons (score 2; red), as modified from a previous report³⁵ (B). The density of SMI-31⁺ axons was significantly reduced (A), and percentages of swollen axons (score 1; yellow) and fragmented axons (score 2; red; B) were significantly increased in plaques and periplaque white matter (PPWM) in NMOsd and multiple sclerosis (MS) compared to controls. Swollen or fragmented axons with no significant reduction in axonal density were present in normal-appearing white matter (NAWM) in NMOsd, whereas both types of morphological changes and reduced axonal density were evident in NAWM in MS (A, B). Quantitative analysis of the mitochondrial volume in axons demonstrated that the VDAC-1⁺ mitochondrial content in SMI-31⁺ axons was significantly increased in swollen axons of PPWM and NAWM, and in areas of Wallerian degeneration (Wld) in NMOsd compared to controls (C). In contrast, quantitative analysis of the mitochondrial volume in axons demonstrated that the VDAC-1⁺ mitochondrial content in SMI-31⁺ axons was not increased in plaques, PPWM, or NAWM in MS (C). Quantification of axonal TRPM4 expression revealed significantly more TRPM4 immunoreactivity in areas of plaques and in swollen axons of PPWM and NAWM in NMOsd and MS compared to controls, in which we detected only a small proportion of TRPM4⁺ axons (D). TRPM4⁺ axons were more evident in swollen axons than in nonswollen axons in NMOsd and MS (D). (E) When the severity of axonal damage was compared between NMOsd and MS, more severe axonal damage, including swollen axons, increased axonal mitochondrial content, and aberrant TRPM4 cation channel expression, was prominent in plaques, PPWM, and NAWM in NMOsd compared to MS, except that reduced axonal density and swollen axons were more evident in NAWM in MS compared to NMOsd. These qualitative (see Figs 5 and 6) and quantitative (current figure) data suggest that the accumulation of mitochondria with abnormal morphology in the axons was more extensive in NMOsd compared to controls and depended on morphological changes in axons (swollen axons) and the disease stage (active stage) from the lesion center to NAWM in NMOsd. **p* < 0.05, ***p* < 0.01, ****p* < 0.001, *****p* < 0.0001; vs control in A–D, MS vs NMO in E.

oxygen species and consequently play important roles in apoptosis, mitophagy, and oxygen sensing.²² Intriguingly, in the EAE model, focal axonal degeneration/swelling

(FAD) with focal intra-axonal accumulation of dysmorphic and swollen mitochondria, but with intact myelin sheaths, is the earliest ultrastructural sign of damage,

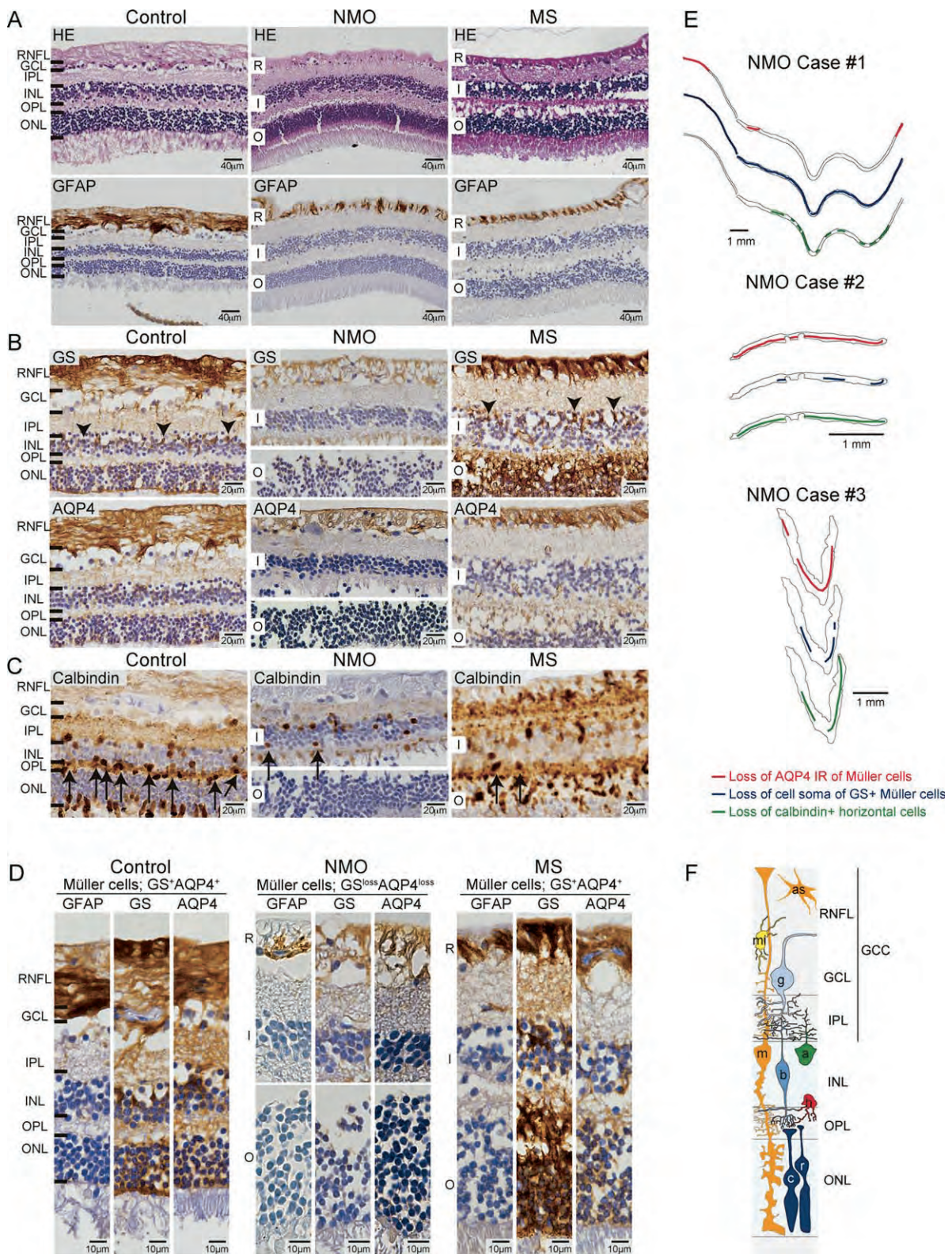


FIGURE 8.

which progresses to axonal fragmentation and demyelination.³⁵ These axonal changes that are consistent with FAD are present in acute MS lesions.³⁵ In addition, lack of mitochondrial respiratory chain complex IV activity in a proportion of Na^+/K^+ ATPase α -1⁺ demyelinated axons supports axonal dysfunction as a contributor to neurological impairment in MS.³⁶ Second, TRPM4 contributes crucially to inflammation-induced neurodegeneration including glutamate excitotoxicity, which is downstream of glutamatergic Ca^{2+} influx and depends on calcium-activated TRPM4-mediated inward currents. This excitotoxicity mediates axonal swelling and neuronal cell death in the EAE model and MS.²⁴ Third, Wld, which was traditionally thought to result from passive degeneration of axons due to a lack of cell body-derived nutrients,³⁷ is a prominent early feature of most neurodegenerative disorders, including amyotrophic lateral sclerosis. However, analysis of the slow Wallerian degeneration (*Wld^S*) mutant mouse has recently elucidated that Wld is mediated by an active autodestruction program via axon death signaling pathways, including the Toll-like receptor adaptor SARM1.³⁸ Early during Wld, mitochondria swell, fragments accumulate at paranodes, and mitochondria lose their membrane potential.³⁸ In the EAE model, *Wld^S* mutant mice show a modest attenuation of axonal loss, suggesting that EAE-associated axonal damage may

occur by a mechanism that is partially similar to Wld.³⁹ In early MS, Wld is a major component of axonal pathology in plaques and PPWM.³⁴ Collectively, degenerative mitochondria, accumulation of TRPM4, and Wld may be mutually interrelated and mediate processes of severe neurodegeneration in MS and EAE. In this study, we showed that more severe and widespread neurodegeneration, including Wld with accumulation of degenerative mitochondria and TRPM4 channels, was evident in NMOsd compared to MS. These factors may contribute to clinical features such as the profound and persistent visual loss and chronic progressive deterioration seen in ON in NMOsd.

We here propose that the pathogenesis of the AVP in NMOsd may be caused by several neurodegenerative processes, including not only secondary anterograde (Wld) or retrograde changes after ON, but also in vivo primary neuroaxonal pathology via AQP4 antibody-mediated pathology of astrocytes/Müller cells, regardless of ON history. The presence of neurodegeneration in AQP4-deficient regions including (1) myelin-preserved PPWM adjacent the optic nerve plaques and (2) the retina, which is physiologically devoid of myelin, in NMOsd may indicate that demyelination is not necessarily essential for processes of neurodegeneration in NMOsd. A marked reduction in the astrocytic Na^+ -

FIGURE 8: Retinal nerve fiber layer (RNFL) thinning and mild loss of calbindin⁺ horizontal cells with unique dynamics of Müller cells in the retina of neuromyelitis optica (NMO) spectrum disorder (NMOsd). (F) The retina consists of 2 major parts: the retinal pigment epithelium and the neural retina. The neural retina can be divided into 9 layers: (1) photoreceptors (rods [r] and cones [c]); (2) external limiting membrane (attachment sites of adjacent photoreceptors and Müller cells [m]); (3) outer nuclear layer (ONL; nuclei of photoreceptors); (4) outer plexiform layer (OPL; axonal extensions of photoreceptors), which contains the middle limiting membrane (desmosomelike attachments of photoreceptor synapse expansions); (5) inner nuclear layer (INL; nuclei of bipolar [b], horizontal [h], amacrine [a], and Müller cells); (6) inner plexiform layer (IPL; mostly synapses of bipolar cells, ganglion cells [g], and amacrine cells); (7) ganglion cell layer (GCL); (8) RNFL (axons of ganglion cells); and (9) internal limiting membrane (basement membrane of Müller cells). In addition to Müller cells, astroglial (as) and microglial cells (mi) are found in the inner retina. In normal conditions, aquaporin-4 (AQP4) water channels are expressed by astrocytes within the RNFL and by Müller cell membranes especially within the RNFL and OPL, and the cell soma of Müller cells lies within the INL. The calcium-binding protein calbindin is a known marker of cone photoreceptors, horizontal cells, and subpopulations of bipolar cells and amacrine cells in the human retina. The human retina is devoid of myelin. Ganglion cell complex (GCC) scanning using a Fourier/spectrum domain optical coherence tomography system encompasses the 3 layers, including the RNFL, GCL, and IPL in the retina. We uncovered 3 important findings in NMOsd retinas. (A) First, all NMOsd and multiple sclerosis (MS) autopsy cases showed severe thinning of the RNFL with an abundance of glial fibrillary acidic protein (GFAP)⁺ and AQP4⁺ astrocytes, and neuronal loss in the GCL in the retina, suggesting the presence of secondary retinal degeneration after optic neuritis (ON). (B, D) Second, we observed scattered loss of AQP4 immunoreactivity (IR) in the INL, OPL, and ONL of Müller cells and mild to severe reduction in Müller cell nuclei with glutamine synthetase (GS)-IR-rich cytoplasm in the INL of NMOsd cases. Conversely, the GS⁺ cell soma of Müller cells lay within the INL in control and MS retinas (arrowheads). (C) Third, all retinas in the NMOsd and MS patients showed mild loss of calbindin⁺ horizontal cells (arrows) in the INL. (E) Schematic lesion maps of the retina in each case with NMOsd are shown. Lesions with loss of AQP4 IR in Müller cells in the INL, OPL, and ONL are indicated in red, lesions with loss of soma of GS⁺ Müller cells in the INL are indicated in blue, and lesions with loss of calbindin⁺ horizontal cells in the INL are indicated in green. All NMOsd patients showed mild neuronal loss in the INL with unique dynamics in Müller cells. Iba-1⁺ microglia were present in the inner retina of NMOsd cases, but CD45RO⁺ T cells, CD20⁺ B cells, and perivascular deposition of complement, C9neo, were not observed (data not shown). These data suggest that the characteristics of the retinal pathology observed in NMOsd cases were strikingly distinct not only from those of the retina in MS cases but also from those of myelitis or ON in NMOsd cases (see Fig 4). Therefore, the retina in NMOsd cases was characterized by primary as well as secondary neuronal and axonal loss with unique dynamics of Müller cells. The data shown are representative of NMOsd, MS, and control retinas (A–D). HE = hematoxylin and eosin; I = INL; O = ONL; R = RNFL.

dependent excitatory amino acid transporter 2,^{40,41} and downregulation of the NMDA-receptor subunit NR1,⁴¹ are present in AQP4-deficient regions in NMOsd patients and a rat passive transfer model using AQP4 antibodies, even when myelin IR is preserved.⁴¹ These data suggest that disruption of glutamate homeostasis^{40,41} may play a role in primary neurodegeneration via glia–neuron interactions in NMOsd pathogenesis. Further research is required to investigate all aspects of NMOsd pathogenesis, including modulation of synaptic function/network activity and/or myelin maintenance caused by astrocytopathy in NMOsd.

The basic effector mechanisms of autoantibody binding to its cellular target may be: (1) functional block of the target, (2) target internalization, (3) complement-dependent cytotoxicity (CDC), and (4) antibody-dependent cell-mediated cytotoxicity (ADCC) in autoimmune disorders. Previous studies in rodent models and in vitro assays have shown indirect evidence that CDC,⁴² ADCC,⁴³ and internalization of AQP4 channels⁴⁴ may play important roles in NMOsd pathogenesis. CDC is the most important immune mechanism of AQP4 antibodies in NMOsd, because a hallmark of NMOsd pathology is pattern-specific loss of AQP4 IR on astrocytes with complement activation. This hallmark was prominent at 2 major sites, the optic nerves (see Fig 4) and spinal cord.^{9,21} Conversely, the pathology in the retina (see Fig 8) and cortical gray matter^{12,45} in NMOsd is distinct from that in the optic nerves and spinal cord. The retinal pathology in NMOsd was characterized by secondary retrograde degeneration of RNFL axons with gliosis (an abundance of AQP4⁺ astrocytes) following ON, loss of horizontal cells in the INL, and scattered loss of AQP4 IR on Müller cells, but no deposition of complement in situ. The cortical gray matter pathology in NMOsd is characterized by substantial cortical neuronal loss in layers II, III, and IV with nonlytic reaction of AQP4-negative astrocytes in layer I, but no cortical demyelination nor deposition of complement.¹² Thus, the pathological processes in the retina and cortical gray matter in NMOsd may consist of an entirely different mechanism than CDC or ADCC in the spinal cord and optic nerves. These region-specific pathologies in NMOsd may depend on the following factors: (1) anatomical structures, including the glial framework and BBB integrity; (2) the complement regulators CD46, CD55, and CD59, which protect the brain from complement-mediated damage⁴⁶; and (3) the cluster size of OAPs containing AQP4 tetramers, which is influenced by maturational differences in the ratio of the AQP4 M1 isoform to M23. OAPs contribute to effective complement activation on astrocytic membranes,⁴⁴ because OAP assemblies are required for

AQP4 antibodies to recognize AQP4.⁴⁷ The binding of AQP4 antibodies may cause incomplete internalization of AQP4 into the endolysosomal compartment in astrocytes, followed by disruption of water and/or glutamate homeostasis with excitotoxic consequences for neurons in the retina and cortical gray matter.

This study has some limitations. The subjects who were evaluated for neuro-ophthalmological assessments were different from those who were pathologically examined, and the cohort of individuals who were pathologically assessed was small. Our study has intrinsic limitations owing to the limited availability of autopsied samples and the partial postmortem detachment that occurs in the retina in NMOsd, similar to the situation in previous reports describing MS eyes.⁴⁸ In the future, prospective, long-term follow-up and large cohort studies are needed to further characterize NMOsd pathogenesis.

In summary, our findings are consistent with a new concept in which severe neurodegeneration via abnormal AQP4 dynamics in astrocytes/Müller cells is prominent in NMOsd pathogenesis. Based on this study, future therapeutic strategies designed to limit the deleterious effects of not only AQP4 antibodies and damage to astrocytes but also neurodegeneration via glia–neuron interactions (eg, mitochondrial protection and replenishment strategies for degenerative axonal mitochondria³³; TRPM4 inhibition strategies for accumulation of TRPM4²⁴; and *Wld^Δ*/nicotinamide mononucleotide adenylyltransferase-mediated axonal protection strategies for *Wld^Δ*) are worthy of further investigation.

Acknowledgment

This work was supported in part by JSPS KAKENHI (grant number 26461289, I.K.), and a Health and Labor Sciences Research Grant on Rare and Intractable Diseases (Evidence-Based Early Diagnosis and Treatment Strategies for Neuroimmunological Diseases) from the Ministry of Health, Labor, and Welfare of Japan (M.N.).

We thank S. Kawaguchi and M. Kaneko for technical assistance with assays for AQP4 autoantibodies, Dr. K. Tanaka for advice on neurological and immunological assessments, Dr. M. Tsujita and Dr. K. Sakimura for providing an AQP4 expression vector, and Dr. B. P. Morgan for providing the complement antibody.

Author Contributions

M.H. and A.Y. contributed equally to this work. Conception and design of the study: M.N., I.K. Acquisition and analysis of data: all authors. Drafting the text or preparing the figures: M.H., A.Y., M.A., E.S., K.Y., M.N., I.K.

Potential Conflicts of Interest

Nothing to report.

References

1. Wingerchuk DM, Lennon VA, Pittock SJ, et al. Revised diagnostic criteria for neuromyelitis optica. *Neurology* 2006;66:1485–1489.
2. Lennon VA, Wingerchuk DM, Kryzer TJ, et al. A serum autoantibody marker of neuromyelitis optica: distinction from multiple sclerosis. *Lancet* 2004;364:2106–2112.
3. Lennon VA, Kryzer TJ, Pittock SJ, et al. IgG marker of optic-spinal multiple sclerosis binds to the aquaporin-4 water channel. *J Exp Med* 2005;202:473–477.
4. Merle H, Olindo S, Bonnan M, et al. Natural history of the visual impairment of relapsing neuromyelitis optica. *Ophthalmology* 2007;114:810–815.
5. Wingerchuk DM, Weinshenker BG. Neuromyelitis optica: clinical predictors of a relapsing course and survival. *Neurology* 2003;60:848–853.
6. de Seze J, Blanc F, Jeanjean L, et al. Optical coherence tomography in neuromyelitis optica. *Arch Neurol* 2008;65:920–923.
7. Naismith RT, Tutlam NT, Xu J, et al. Optical coherence tomography differs in neuromyelitis optica compared with multiple sclerosis. *Neurology* 2009;72:1077–1082.
8. Verkman AS, Ruiz-Ederra J, Levin MH. Functions of aquaporins in the eye. *Prog Retin Eye Res* 2008;27:420–433.
9. Yanagawa K, Kawachi I, Toyoshima Y, et al. Pathologic and immunologic profiles of a limited form of neuromyelitis optica with myelitis. *Neurology* 2009;73:1628–1637.
10. Tanaka K, Tani T, Tanaka M, et al. Anti-aquaporin 4 antibody in selected Japanese multiple sclerosis patients with long spinal cord lesions. *Mult Scler* 2007;13:850–855.
11. Polman CH, Reingold SC, Banwell B, et al. Diagnostic criteria for multiple sclerosis: 2010 revisions to the McDonald criteria. *Ann Neurol* 2011;69:292–302.
12. Saji E, Arakawa M, Yanagawa K, et al. Cognitive impairment and cortical degeneration in neuromyelitis optica. *Ann Neurol* 2013;73:65–76.
13. Liu G, Amin S, Okuhama NN, et al. A quantitative evaluation of peroxidase inhibitors for tyramide signal amplification mediated cytochemistry and histochemistry. *Histochem Cell Biol* 2006;126:283–291.
14. Lassmann H. Review: the architecture of inflammatory demyelinating lesions: implications for studies on pathogenesis. *Neuropathol Appl Neurobiol* 2011;37:698–710.
15. Perego C, Fumagalli S, De Simoni MG. Three-dimensional confocal analysis of microglia/macrophage markers of polarization in experimental brain injury. *J Vis Exp* 2013(79).
16. Parikh RS, Parikh SR, Sekhar GC, et al. Normal age-related decay of retinal nerve fiber layer thickness. *Ophthalmology* 2007;114:921–926.
17. Kupersmith MJ, Alban T, Zeiffer B, Lefton D. Contrast-enhanced MRI in acute optic neuritis: relationship to visual performance. *Brain* 2002;125(pt 4):812–822.
18. Keltner JL, Johnson CA, Cello KE, et al. Visual field profile of optic neuritis: a final follow-up report from the optic neuritis treatment trial from baseline through 15 years. *Arch Ophthalmol* 2010;128:330–337.
19. Purvin V, Kawasaki A, Jacobson DM. Optic perineuritis: clinical and radiographic features. *Arch Ophthalmol* 2001;119:1299–1306.
20. Hickman SJ, Toosy AT, Jones SJ, et al. A serial MRI study following optic nerve mean area in acute optic neuritis. *Brain* 2004;127(pt 11):2498–2505.
21. Roemer SF, Parisi JE, Lennon VA, et al. Pattern-specific loss of aquaporin-4 immunoreactivity distinguishes neuromyelitis optica from multiple sclerosis. *Brain* 2007;130(pt 5):1194–1205.
22. Archer SL. Mitochondrial dynamics—mitochondrial fission and fusion in human diseases. *N Engl J Med* 2013;369:2236–2251.
23. Kang JS, Tian JH, Pan PY, et al. Docking of axonal mitochondria by syntaphilin controls their mobility and affects short-term facilitation. *Cell* 2008;132:137–148.
24. Schattling B, Steinbach K, Thies E, et al. TRPM4 cation channel mediates axonal and neuronal degeneration in experimental autoimmune encephalomyelitis and multiple sclerosis. *Nat Med* 2012;18:1805–1811.
25. Pannicke T, Wurm A, Landiev I, et al. Deletion of aquaporin-4 renders retinal glial cells more susceptible to osmotic stress. *J Neurosci Res* 2010;88:2877–2888.
26. Yuan S, Zhang W, Ding J, et al. Increased sensitivity to retinal light damage in aquaporin-4 knockout mice. *Exp Eye Res* 2009;89:119–122.
27. Levkovitch-Verbin H, Quigley HA, Kerrigan-Baumrind LA, et al. Optic nerve transection in monkeys may result in secondary degeneration of retinal ganglion cells. *Invest Ophthalmol Vis Sci* 2001;42:975–982.
28. Levin MH, Bennett JL, Verkman AS. Optic neuritis in neuromyelitis optica. *Prog Retin Eye Res* 2013;36:159–171.
29. Killer HE, Jaggi GP, Flammer J, et al. Cerebrospinal fluid dynamics between the intracranial and the subarachnoid space of the optic nerve. Is it always bidirectional? *Brain* 2007;130(pt 2):514–520.
30. Hofman P, Hoyng P, vanderWerf F, et al. Lack of blood-brain barrier properties in microvessels of the prelaminar optic nerve head. *Invest Ophthalmol Vis Sci* 2001;42:895–901.
31. Agrawal S, Anderson P, Durbeej M, et al. Dystroglycan is selectively cleaved at the parenchymal basement membrane at sites of leukocyte extravasation in experimental autoimmune encephalomyelitis. *J Exp Med* 2006;203:1007–1019.
32. Bjartmar C, Kidd G, Mork S, et al. Neurological disability correlates with spinal cord axonal loss and reduced N-acetyl aspartate in chronic multiple sclerosis patients. *Ann Neurol* 2000;48:893–901.
33. Mahad DH, Trapp BD, Lassmann H. Pathological mechanisms in progressive multiple sclerosis. *Lancet Neurol* 2015;14:183–193.
34. Dziejdzic T, Metz I, Dallenga T, et al. Wallerian degeneration: a major component of early axonal pathology in multiple sclerosis. *Brain Pathol* 2010;20:976–985.
35. Nikic I, Merkler D, Sorbara C, et al. A reversible form of axon damage in experimental autoimmune encephalomyelitis and multiple sclerosis. *Nat Med* 2011;17:495–499.
36. Mahad DJ, Ziabreva I, Campbell G, et al. Mitochondrial changes within axons in multiple sclerosis. *Brain* 2009;132(pt 5):1161–1174.
37. Osterloh JM, Yang J, Rooney TM, et al. dSarm/Sarm1 is required for activation of an injury-induced axon death pathway. *Science* 2012;337:481–484.
38. Conforti L, Gilley J, Coleman MP. Wallerian degeneration: an emerging axon death pathway linking injury and disease. *Nat Rev Neurosci* 2014;15:394–409.
39. Kaneko S, Wang J, Kaneko M, et al. Protecting axonal degeneration by increasing nicotinamide adenine dinucleotide levels in experimental autoimmune encephalomyelitis models. *J Neurosci* 2006;26:9794–9804.

40. Hinson SR, Roemer SF, Lucchinetti CF, et al. Aquaporin-4-binding autoantibodies in patients with neuromyelitis optica impair glutamate transport by down-regulating EAAT2. *J Exp Med* 2008;205:2473–2481.
41. Geis C, Ritter C, Ruschil C, et al. The intrinsic pathogenic role of autoantibodies to aquaporin 4 mediating spinal cord disease in a rat passive-transfer model. *Exp Neurol* 2015;265:8–21.
42. Bennett JL, Lam C, Kalluri SR, et al. Intrathecal pathogenic anti-aquaporin-4 antibodies in early neuromyelitis optica. *Ann Neurol* 2009;66:617–629.
43. Zhang H, Verkman AS. Eosinophil pathogenicity mechanisms and therapeutics in neuromyelitis optica. *J Clin Invest* 2013;123:2306–2316.
44. Hinson SR, Romero MF, Popescu BF, et al. Molecular outcomes of neuromyelitis optica (NMO)-IgG binding to aquaporin-4 in astrocytes. *Proc Natl Acad Sci U S A* 2012;109:1245–1250.
45. Popescu BF, Parisi JE, Cabrera-Gomez JA, et al. Absence of cortical demyelination in neuromyelitis optica. *Neurology* 2010;75:2103–2109.
46. Saadoun S, Papadopoulos MC. Role of membrane complement regulators in neuromyelitis optica. *Mult Scler* 2015;21:1644–1654.
47. Nicchia GP, Mastroianni M, Rossi A, et al. Aquaporin-4 orthogonal arrays of particles are the target for neuromyelitis optica autoantibodies. *Glia* 2009;57:1363–1373.
48. Green AJ, McQuaid S, Hauser SL, et al. Ocular pathology in multiple sclerosis: retinal atrophy and inflammation irrespective of disease duration. *Brain* 2010;133(pt 6):1591–1601.
49. Seewann A, Kooi EJ, Roosendaal SD, et al. Postmortem verification of MS cortical lesion detection with 3D DIR. *Neurology* 2012;78:302–308.
50. Allen IV, McKeown SR. A histological, histochemical and biochemical study of the macroscopically normal white matter in multiple sclerosis. *J Neurol Sci* 1979;41:81–91.

RESEARCH ARTICLE

Effects of Alda-1, an Aldehyde Dehydrogenase-2 Agonist, on Hypoglycemic Neuronal Death

Tetsuhiko Ikeda¹, Tetsuya Takahashi¹, Mika Tsujita², Masato Kanazawa¹, Masafumi Toriyabe¹, Misaki Koyama¹, Kosuke Itoh², Tsutomu Nakada², Masatoyo Nishizawa¹, Takayoshi Shimohata^{1*}

1 Department of Neurology, Brain Research Institute, Niigata University, Niigata, Japan, **2** Department of Center for Integrated Human Brain Science, Brain Research Institute, Niigata University, Niigata, Japan

* t-shimo@bri.niigata-u.ac.jp



CrossMark
click for updates

OPEN ACCESS

Citation: Ikeda T, Takahashi T, Tsujita M, Kanazawa M, Toriyabe M, Koyama M, et al. (2015) Effects of Alda-1, an Aldehyde Dehydrogenase-2 Agonist, on Hypoglycemic Neuronal Death. PLoS ONE 10(6): e0128844. doi:10.1371/journal.pone.0128844

Academic Editor: M.Faadiel Essop, Stellenbosch University, SOUTH AFRICA

Received: January 3, 2015

Accepted: April 30, 2015

Published: June 17, 2015

Copyright: © 2015 Ikeda et al. This is an open access article distributed under the terms of the [Creative Commons Attribution License](https://creativecommons.org/licenses/by/4.0/), which permits unrestricted use, distribution, and reproduction in any medium, provided the original author and source are credited.

Data Availability Statement: All relevant data are within the paper.

Funding: This work was supported by a grant from Grant for Promotion of Niigata University Research Projects.

Competing Interests: The authors have declared that no competing interests exist.

Abstract

Hypoglycemic encephalopathy (HE) is caused by a lack of glucose availability to neuronal cells, and no neuroprotective drugs have been developed as yet. Studies on the pathogenesis of HE and the development of new neuroprotective drugs have been conducted using animal models such as the hypoglycemic coma model and non-coma hypoglycemia model. However, both models have inherent problems, and establishment of animal models that mimic clinical situations is desirable. In this study, we first developed a short-term hypoglycemic coma model in which rats could be maintained in an isoelectric electroencephalogram (EEG) state for 2 min and subsequent hyperglycemia without requiring anti-seizure drugs and an artificial ventilation. This condition caused the production of 4-hydroxy-2-nonenal (4-HNE), a cytotoxic aldehyde, in neurons of the hippocampus and cerebral cortex, and a marked increase in neuronal death as evaluated by Fluoro-Jade B (FJB) staining. We also investigated whether *N*-(1,3-benzodioxole-5-ylmethyl)-2,6-dichlorobenzamide (Alda-1), a small-molecule agonist of aldehyde dehydrogenase-2, could attenuate 4-HNE levels and reduce hypoglycemic neuronal death. After confirming that EEG recordings remained isoelectric for 2 min, Alda-1 (8.5 mg/kg) or vehicle (dimethyl sulfoxide; DMSO) was administered intravenously with glucose to maintain a blood glucose level of 250 to 270 mg/dL. Fewer 4-HNE and FJB-positive cells were observed in the cerebral cortex of Alda-1-treated rats than in DMSO-treated rats 24 h after glucose administration ($P = 0.002$ and $P = 0.020$). Thus, activation of the ALDH2 pathway could be a molecular target for HE treatment, and Alda-1 is a potentially neuroprotective agent that exerts a beneficial effect on neurons when intravenously administered simultaneously with glucose.

Introduction

Transient hypoglycemic episodes occur during treatment of diabetes mellitus with insulin or oral hypoglycemic drugs and in cases involving insulinoma, alcoholism, anorexia nervosa, or

others. Although many patients recover with appropriate treatment, transient hypoglycemic episodes can result in coma, seizures, and myriad other global and focal neurological deficits [1–3]. In an analogy to hypoxic encephalopathy, this syndrome has been termed hypoglycemic encephalopathy (HE). The only treatment for HE is blood glucose (BG) correction by glucose administration, and no neuroprotective drugs have been developed as yet.

Studies on the pathogenesis of HE and the development of neuroprotective drugs have been conducted using animal models. There are two conventional animal models of HE: one in which an isoelectric electroencephalogram (EEG) is maintained for a long period (hypoglycemic coma model) [4, 5] and the other involving euthanization or glucose administration before the isoelectric EEG (hypoglycemic non-coma model) [6–8]. In the hypoglycemic coma model, the isoelectric EEG manifesting after the BG decrease is maintained for at least 30 min to ensure that the brains are in a state of severe hypoglycemia. However, once changes in the brain due to hypoglycemia become apparent, seizures and respiratory arrest that cause additional neuronal damage are unavoidable. Model animals must therefore be treated with an anti-seizure drug and an artificial ventilator beforehand. Regarding a prolonged, markedly hypoglycemic state with an anesthetic agent and an artificial ventilator use, the pathogenesis of HE in animal models may differ from that of human HE experienced in clinical practice. However, the hypoglycemic non-coma model can also be problematic in that the various indices used by researchers as alternatives to isoelectric EEG, to indicate degrees of severity and courses, vary considerably, reflecting differences in individual responses to hypoglycemic loads. Thus, in order to elucidate the pathogenesis of HE and develop neuroprotective drugs, there is a need to establish animal models using isoelectric EEG as a quantitative index of hypoglycemic loads, without the use of anti-seizure drugs and an artificial ventilation.

Regarding the pathological conditions of HE, neuronal death in animal models is reportedly induced by oxidative stress generated after glucose administration [5, 9, 10]. This phenomenon is termed “glucose reperfusion injury”, and its severity increases with higher BG levels after BG correction [10]. In this context, we recently confirmed higher BG levels after correction in 47 consecutive patients who experienced hypoglycemic episodes (271.1 ± 128.5 mg/dL) [3]. Therefore, an animal model that experiences hypoglycemia followed by similar higher BG levels is preferred.

Studies on the development of neuroprotective drugs for HE have aimed to improve hypometabolic conditions associated with hypoglycemia or to inhibit oxidative stress caused by glucose reperfusion injury. Among factors causing oxidative stress, 4-hydroxy-2-nonenal (4-HNE), a cytotoxic aldehyde that is a lipid oxidation product, has been intensively investigated in myocardial ischemia [11, 12]. It has been shown that 4-HNE is produced from ω -6 polyunsaturated fatty acids, such as arachidonic acid, and can cause mitochondrial disorders to potentially induce neuronal death [13]. Interestingly, *N*-(1,3-benzodioxole-5-ylmethyl)-2,6-dichlorobenzamide (Alda-1), an aldehyde dehydrogenase 2 (ALDH2) agonist that increases the activity of mitochondrial ALDH2, inhibits myocardial damage caused by 4-HNE after ischemia [12, 14]. Therefore, this raises the possibility that Alda-1 may inhibit oxidative stress caused by glucose reperfusion injury via suppression of 4-HNE levels.

Based on the aforementioned observations, this study had the following three objectives: (1) to establish a novel animal model of HE that can be maintained in an isoelectric EEG state for a short period without the use of anti-seizure drugs and an artificial ventilation, enabling the isoelectric EEG to be used as an index of HE (we termed this model “a short-term hypoglycemic coma model”), (2) to confirm whether oxidative stress and neuronal death occur in this model, and (3) to reveal whether Alda-1 exerts protective effects against neuronal death associated with glucose reperfusion injury thereby demonstrating its potential as a neuroprotective drug.

Materials and Methods

The study protocol was approved by the Niigata University Administrative Panel on Laboratory Animal Care. All operations concerning animals were performed according to ARRIVE (Animal Research: Reporting of In Vivo Experiments) guidelines [15]. All efforts were made to minimize the number of animals used and their suffering. Alda-1 and vehicle (dimethyl sulfoxide, DMSO) were coded and administered by a blinded observer.

EEG recordings

Male Sprague-Dawley rats (260–310 g, 8–10 weeks old, Charles River Japan, Inc.) were used. After sebum had been removed from both the shaved head and anterior neck regions by scrubbing with cotton balls soaked in alcohol, both areas were abraded with EEG abrasive gel (Skin Pure, Nihon Kohden Corporation). EEG disc electrodes (LEAD110A, BIOPAC Systems, Inc.) to which EEG disc electrode paste had been applied (Elefix, Nihon Kohden Corporation) were then attached to the forehead (near the nose) and the occiput (between the porus acusticus) of the rat, for use as EEG recording electrodes; the former served as the reference. Another disc electrode was also attached to the anterior neck to be used as the earth electrode. After the electrodes were attached, we confirmed with an alternating current (AC) resistance measuring instrument (Model 1089ES Checktrode, UFI Inc.) that the contact resistance between each electrode was 10 k Ω or less and that the variation in contact resistance at each electrode was 3 k Ω or less. An EEG amplifier (EEG100C, BIOPAC Systems, Inc.) was used for EEG amplification, and an analog-digital (A/D) converter (MP100System, BIOPAC Systems, Inc.) and waveform analysis software (AcqKnowledge, BIOPAC Systems, Inc., version 3.7.2) were used to collect and analyze the data. A bandpass of 0.1 to 100 Hz was used to filter the amplified EEG, and the sampling frequency of A/D conversion was 200 Hz.

Short-term hypoglycemic coma model

The aforementioned rats were used. Each rat was fed a restricted diet of 20 g/day [16] for at least three consecutive days and then fasted, being allowed only water, for one day before the operation. To prevent changes in food consumption due to stress caused by an increase or decrease in the number of rats in each cage [17], the number per cage was fixed at three. The remaining amount of food was measured once a day before feeding to confirm that there were no changes in food consumption.

Hypoglycemic loads were applied under anesthesia maintained with a mixed gas of 70% nitrous oxide and 30% oxygen with 1.0% to 1.5% halothane added while rectal temperature was monitored. The rectal temperature was maintained at $37.0 \pm 0.5^\circ\text{C}$ with a temperature control mat, a fan, and a heating lamp. Under direct visualization using a surgical microscope, the left inguinal region was incised to expose the left femoral vein. A polyethylene catheter (Clay Adams Intramedic polyethylene tube PE50, Becton Dickinson & Co.) filled with 1% heparinized saline was then placed in the vein and used to collect blood samples for BG measurement. A BG monitoring instrument (Ascensia BREEZE 2, Bayer Health Care) was used for BG measurement. Next, the left cervical region was incised to expose the left anterior facial vein. Another tube, as described above, was placed in the vein and used to administer glucose and experimental drugs. After a resting EEG had been recorded, rapid-acting insulin (Novolin R 100 IU/mL Injection, Novo Nordisk Pharma Co., Ltd.) was intraperitoneally administered at a dose of 15 IU/kg [5, 18], and blood samples were then collected every 15 min. If the EEG did not become isoelectric by more than 180 min after insulin administration, the experiment was discontinued. After 2 or 10 min of isoelectric EEG state, 50% glucose was intravenously injected at a dose of 0.2 mL (Fig 1A). Then, 50% glucose was intravenously infused at a rate of

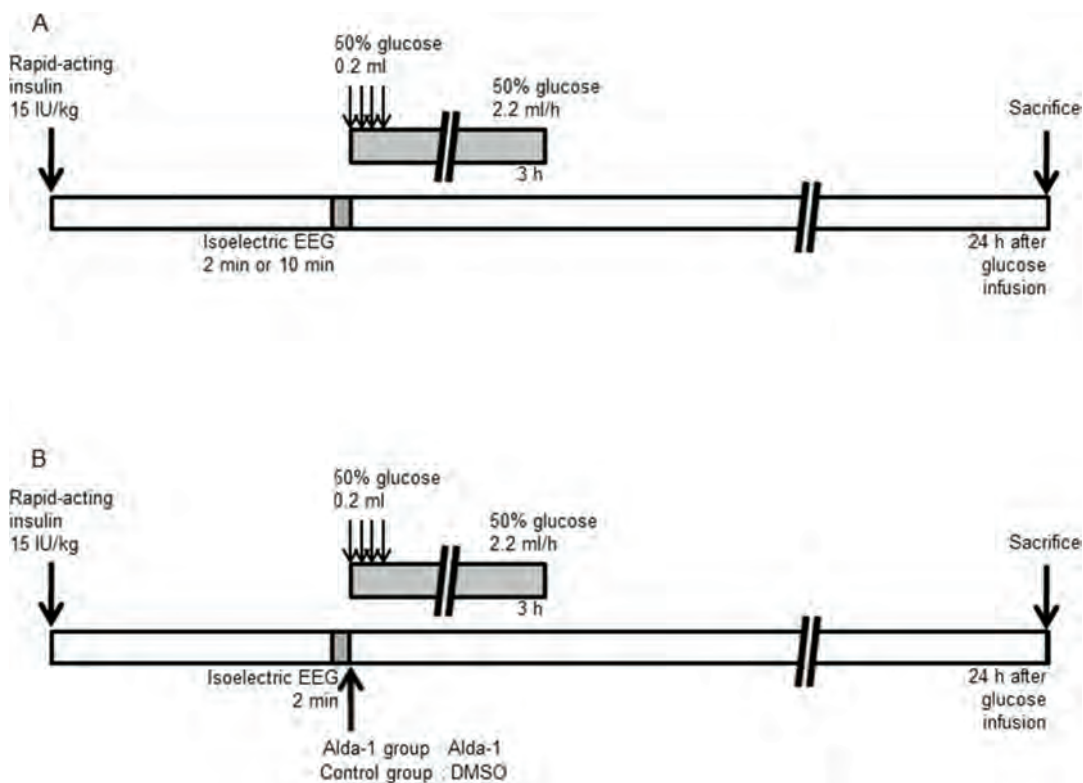


Fig 1. Short-term hypoglycemic coma model. (A) Protocol for hypoglycemic loading and induction of the hyperglycemic state. Rapid-acting insulin was intraperitoneally administered at a dose of 15 IU/kg. After 2 or 10 min of the presence of an isoelectric electroencephalogram (EEG), 50% glucose was intravenously injected at a dose of 0.2 mL and intravenously infused at a rate of 2.2 mL/h. Rats were sacrificed after 24 h of glucose reperfusion. (B) Alda-1 treatment protocol. After 2 min of an isoelectric EEG state, Alda-1 was administered intravenously at a dose of 8.5 mg/kg with 50% glucose (Alda-1 group) or the same dose of dimethyl sulfoxide (DMSO) was administered (control group).

doi:10.1371/journal.pone.0128844.g001

2.2 mL/h and again intravenously injected at a dose of 0.2 mL three times every 5 min. Furthermore, while blood samples were collected every 15 min, an additional 50% glucose solution was administered at doses of 0.2 mL if necessary, to maintain BG levels at the target of 250 to 270 mg/dL for 3 h to create a hyperglycemic state that would cause glucose reperfusion injury in HE. BG levels after correction by glucose administration were determined by reference to our clinical trials [3]. Disc electrodes and catheters were removed 3 h after the start of glucose administration.

Intravenous administration of an aldehyde dehydrogenase agonist

An ALDH2 agonist (Alda-1, Merck KGaA), an activator of aldehyde dehydrogenase, was dissolved in DMSO at a concentration of 15 mg/mL. At the end of the isoelectric EEG period, Alda-1 was administered to the Alda-1 group animals at a dose of 8.5 mg/kg with glucose into the left anterior facial vein, and the same dose of DMSO was administered to the control group (Fig 1B). The dose of Alda-1 was determined according to the optimal dosage described in previous reports of myocardial ischemia in rats [12, 14]. Alda-1 and DMSO were administered to randomly selected rats.

Immunostaining for 4-HNE, a lipid oxidation product

Rats were euthanized with halothane 24 h after glucose administration. The left ventricle was perfused with 200 mL of cold saline and 100 mL of 4% paraformaldehyde (PFA) [19]. Removed whole brains were fixed in 4% PFA at 4°C for 12 h [20]. After rinsing with 0.1 M phosphate buffered saline (PBS) at 4°C overnight, brains were immersed in 15% sucrose/0.1 M PBS at 4°C overnight and then 30% sucrose/0.1 M PBS at 4°C for 24 h. Four coronal sections were collected from each animal starting 4.0 mm posterior to Bregma. They were frozen in isopentane, embedded in optimal cutting temperature (OCT) compound (Tissue-Tek, Sakura Finetek Inc.), and stored at -80°C. Brain samples were cut with a cryostat (Cryotome E Electronic Cryostat, Thermo Electron Co.) into sections of 20 μm thickness, placed on slides, and dried for 2 h. Samples were immersed in 0.3% hydrogen peroxide dissolved in absolute methanol for 30 min to inhibit peroxidase activity. After rinsing with PBS, sections were incubated with mouse monoclonal anti-4-HNE antibody (HNEJ-2, JalCA, 1:50) at 4°C overnight. The secondary antibody (#BA-2000, Vector Laboratories, Inc.) was applied at room temperature for 2.5 h. After incubation with an ABC Elite kit (Vectastain ABC, Vector Laboratories, Inc.), sections were developed in 3,3'-diaminobenzidine. Cerebral cortices (hippocampus level) from each rat were viewed using a light microscope (Eclipse E600W, Nikon Co.). The number of 4-HNE-positive cells was counted in five non-overlapping areas of 0.25 mm^2 in both parietal and temporal cortical sections, and findings were confirmed in triplicate. Cells were counted in both hemispheres by a blinded observer.

Assessment of neuronal death by Fluoro-Jade B

The 25- μm sections were placed on slides, dried, then immersed in 0.1 M PBS, dried at 50°C or higher for 30 min, and immersed in 80% ethanol containing 1% sodium hydroxide. Next, samples were immersed in 70% ethanol solution for 2 min and in purified water for 2 min. After immersion in 0.06% potassium permanganate solution for another 10 min, samples were rinsed with purified water for 2 min. After immersion in degenerating neuron binding fluorescent derivative staining solution (Fluoro-Jade B [FJB], Histo-Chem Inc., 0.0004%) for 20 min, a 1-min rinse with purified water was repeated three times; samples were then dried at 50°C for 15 min. Next, samples were immersed in ethanol and xylene, dehydrated, and mounted with DPX (Fluka; Sigma-Aldrich Chemie GmbH, Deisenhofen, Germany). Cerebral cortices (hippocampus level) from each rat were observed with a fluorescence microscope (excitation wavelength, 480 nm; fluorescence wavelength, 525 nm). The number of FJB-positive cells was counted in five non-overlapping areas of 0.25 mm^2 in both parietal and temporal cortical sections, and findings were confirmed in triplicate. Cells were counted in both hemispheres by a blinded observer.

Statistical analysis

Results are expressed as means \pm standard deviation (SD). A *t*-test was used for statistical analyses. A *P* value < 0.05 was considered statistically significant.

Results

Changes in BG levels before and after insulin administration

We first measured BG levels of rats before and after insulin administration. The mean BG level before insulin administration was 112.4 ± 26.1 mg/dL (Fig 2). After insulin administration, BG levels gradually decreased and stabilized around 20 mg/dL 60 min after insulin administration. Since their EEGs did not become isoelectric more than 180 min after insulin administration,

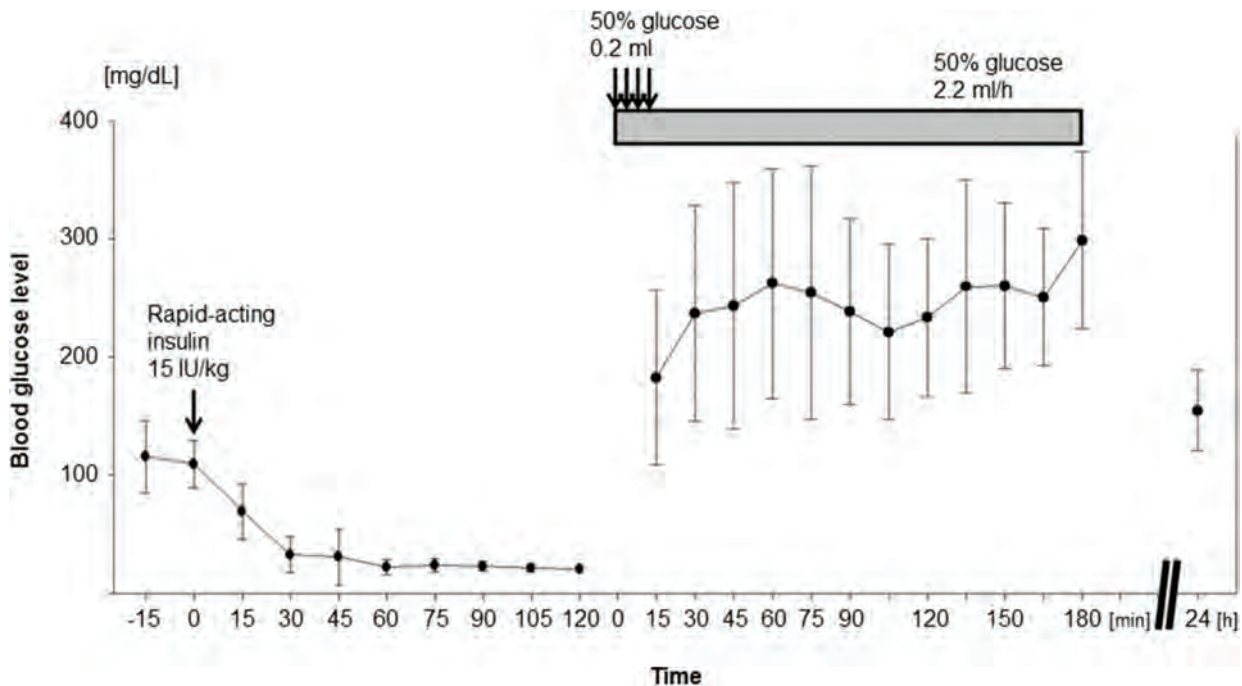


Fig 2. Temporal changes in blood glucose levels after administration of insulin and glucose. Blood glucose levels were measured every 15 min before and after injection of rapid-acting insulin (from -15 min to 120 min; $n = 48$) as well as after injection of 50% glucose (from 15 min to 180 min and 24 h; $n = 9$).

doi:10.1371/journal.pone.0128844.g002

the experiment was discontinued in 3 of 30 rats to which glucose was to be administered 2 min after an isoelectric EEG state was observed (2-min isoelectric EEG group) and 4 of 48 rats to which glucose was to be administered after 10 min of an isoelectric EEG state (10-min isoelectric EEG group). After glucose administration, BG levels immediately increased and remained in the 250 to 270 mg/dL range 30 min after the start of glucose administration and beyond.

Changes in EEG and neurological findings

We next investigated EEG findings and neurological signs associated with hypoglycemia and glucose reperfusion (Fig 3). Resting EEGs before insulin administration exhibited amplitudes of 10 to 50 μ V and a frequency range of 4 to 8 Hz. There were no pupil abnormalities, and the light reflex was rapid. High-amplitude slow waves (amplitude, 100–200 μ V; frequency, 0.1–4 Hz) occurred 69 ± 29 min after insulin administration. At this time, BG levels were 21.4 ± 4.9 mg/dL, pupil diameter was increased, and the light reflex was slow. Mean EEG amplitude and frequency then both gradually decreased, and the EEG became isoelectric 92 ± 33 min after insulin administration. At this time, BG levels were 18.3 ± 7.8 mg/dL, pupils were dilated, and the light reflex disappeared. When glucose was administered after isoelectric EEG, the appearance of the EEG was similar to that at rest (recovering EEG). Following glucose administration, BG levels were 245.8 ± 92.7 mg/dL, dilatation of the pupils disappeared, and the light reflex was rapid. Since pupil diameter and light reflexes were not maintained at a constant level during each phase, these findings were not suitable for predicting precise BG levels. Frequencies of seizure and subsequent death in the isoelectric EEG 2-min group were 6.7% (2/30) and 16.7% (5/30), respectively. By contrast, these were 100% (48/48) and 87.5% (42/48), respectively, in the 10-min isoelectric EEG group.

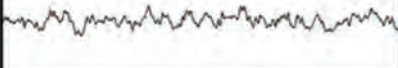
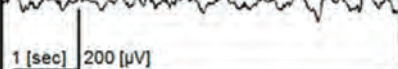
Time after insulin administration [min]	Blood glucose level [mg/dL]	EEG pattern	Neurological symptoms			
			Pupil size [mm]	Light reflex	Seizure %	
					Iso-EEG 2-min group	Iso-EEG 10-min group
N/A	112.4 ± 26.1	Resting EEG (Before insulin administration) 	1.5-2.5 (Normal)	Brisk	0	0
69 ± 29	21.4 ± 4.9	High amplitude and low frequency EEG (Blood glucose falling period) 	2.0-5.0	Sluggish	0	0
92 ± 33	18.3 ± 7.8	Isoelectric-EEG (Severe hypoglycemia) 	4.5-6.0 (Mydriasis)	Absent	6.7	100
117 ± 53	245.8 ± 92.7	Normalized EEG (After glucose infusion)  1 [sec] 200 [µV]	1.5-2.5 (Normal)	Brisk	0	22.9

Fig 3. Temporal changes in electroencephalogram findings and neurological signs. EEG; Electroencephalogram, N/A; not applicable. Data are means ± SD. Since pupil diameter and light reflexes were not maintained at a constant level during each phase, these findings were not suitable for predicting precise BG levels.

doi:10.1371/journal.pone.0128844.g003

Assessment of 4-HNE-positive cells in the short-term hypoglycemic coma model

The number of 4-HNE-positive cells was compared among the sham group (to which insulin was not administered), the 2-min isoelectric EEG group, and the 10-min isoelectric EEG group (Fig 4). There were no significant differences in body weight, food consumption, or BG levels before or after the experiment among the three groups. In the sham group, no 4-HNE-positive cells were detected in any of the brain regions examined. In the 2-min isoelectric EEG group, 4-HNE-positive cells were detected in the frontal to parietal-temporal cortex and in the hippocampus. The number of 4-HNE-positive cells in the hippocampus was less than that in the cerebral cortex. The frequency of 4-HNE-positive cells in the parietal-temporal cortex at the level of the hippocampus was significantly higher in the 10-min isoelectric EEG group than in the 2-min isoelectric EEG group (217.9 ± 27.1 cells/ 0.25 mm^2 vs. 104.8 ± 8.9 cells/ 0.25 mm^2 ; $P < 0.001$).

Assessment of FJB-positive cells in the short-term hypoglycemic coma model

The frequency of hypoglycemia-induced neuronal death, evaluated by FJB staining of the parietal-temporal cortex at the level of the hippocampus, was significantly higher in the 10-min isoelectric EEG without glucose reperfusion group than in the 2-min isoelectric EEG without glucose reperfusion group (109.9 ± 45.4 cells/ 0.25 mm^2 vs. 53.3 ± 15.9 cells/ 0.25 mm^2 ; $P = 0.009$, S1 Fig).

Next, the number of FJB-positive cells was compared among the sham, 2-min isoelectric EEG, and 10-min isoelectric EEG groups (Fig 5). In the sham group, there were no FJB-positive cells in any of the brain regions examined. In the 2-min isoelectric EEG group, FJB-positive

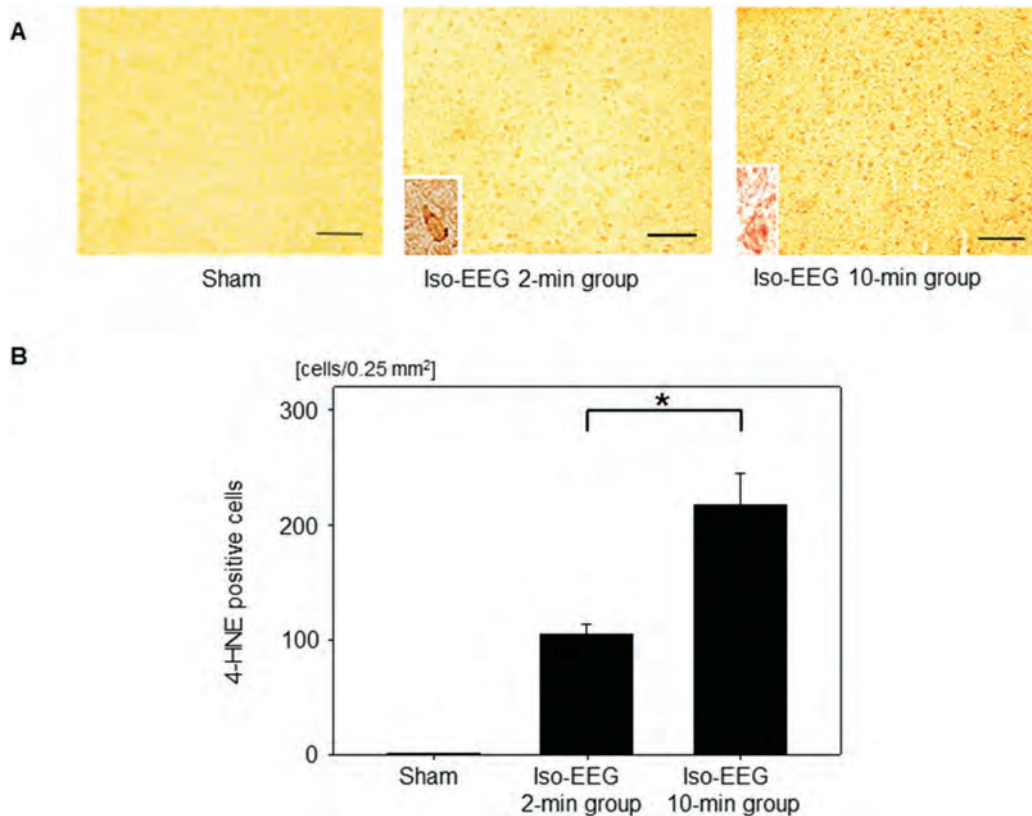


Fig 4. Distribution of 4-HNE-positive cells in the short-term hypoglycemic coma model. (A) Representative images of 4-HNE-positive cells in the sham group, the 2-min isoelectric EEG (iso-EEG) group, and the 10-min isoelectric EEG group. Higher magnification views of 4-HNE-positive cells are shown in the small frames. Scale bar: 100 μ m. (B) The number of 4-HNE-positive cells in the sham group, the 2-min isoelectric EEG group, and the 10-min isoelectric EEG group. Data are means \pm SD ($n = 15$ fields). * $P < 0.001$.

doi:10.1371/journal.pone.0128844.g004

cells were observed in the frontal to parietal-temporal cortex and hippocampus. The number of FJB-positive cells in the hippocampus was less than that in the cerebral cortex. The frequency of FJB-positive cells in the parietal-temporal cortex at the level of the hippocampus was significantly higher in the 10-min isoelectric EEG group than in the 2-min isoelectric EEG group (150.7 ± 19.8 cells/0.25 mm² vs. 89.9 ± 6.8 cells/0.25 mm²; $P < 0.001$).

Effects of Alda-1 on 4-HNE-positive cells

To examine the effects of Alda-1 on glucose reperfusion-associated 4-HNE expression, the number of 4-HNE-positive cells was examined in rats to which Alda-1 had been administered after 2 min of isoelectric EEG (Alda-1 group) and in rats to which DMSO, a solvent, had been administered (control group). There were no significant differences in body weight, food consumption, or BG levels between the two groups. The number of 4-HNE-positive cells was significantly lower in the Alda-1 group than in the control group (101.5 ± 5.6 vs. 92.9 ± 8.1 cells/0.25 mm²; $P = 0.002$) (Fig 6). We did not examine the effect of Alda-1 in the 10-min isoelectric EEG group because a large number of rats developed seizures before administration of glucose and Alda-1.

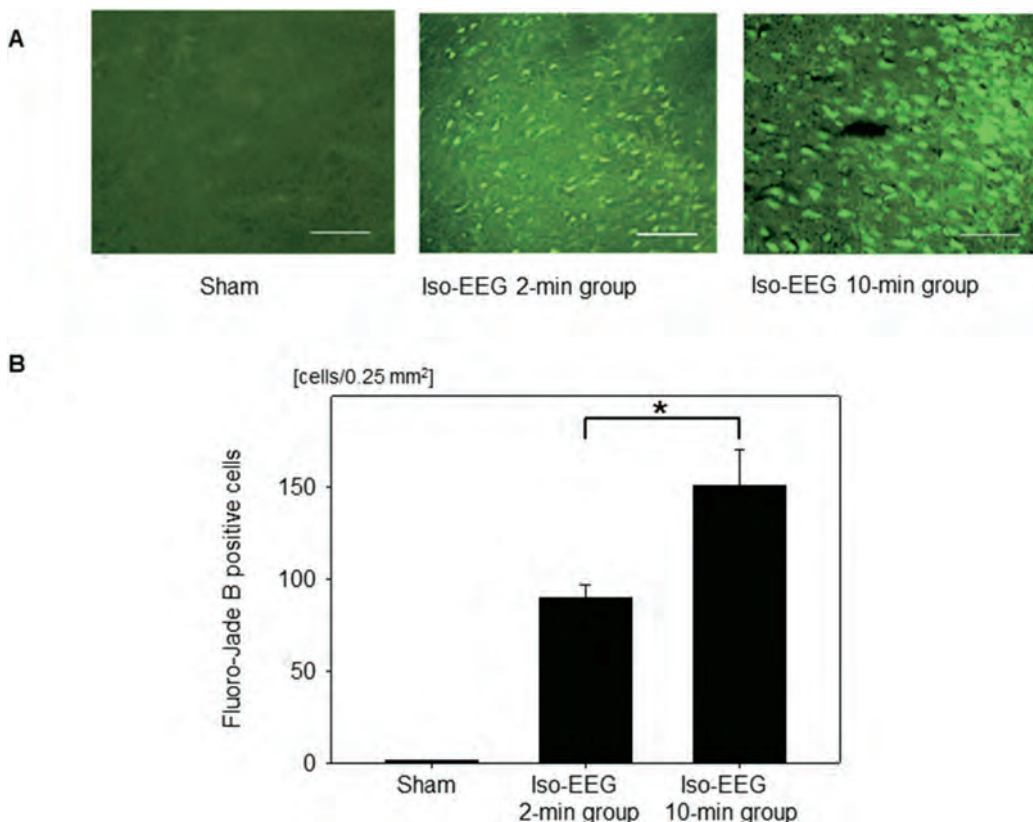


Fig 5. Fluoro-Jade B-positive cells in the short-term hypoglycemic coma model. (A) Representative images of Fluoro-Jade B-positive cells in the sham group, the 2-min isoelectric EEG (iso-EEG) group, and the 10-min isoelectric EEG group. Scale bar: 100 μ m. (B) The number of Fluoro-Jade B-positive cells in the sham group, the 2-min isoelectric EEG group, and the 10-min isoelectric EEG group. Data are means \pm SD ($n = 15$ fields). $*P < 0.001$.

doi:10.1371/journal.pone.0128844.g005

Effects of Alda-1 on FJB-positive cells

Finally, to ascertain whether Alda-1 exerts protective effects against glucose reperfusion-associated neuronal death, the number of FJB-positive cells was compared in the Alda-1 and control groups. Notably, the number of FJB-positive cells was significantly lower in the Alda-1 group than in the control group (50.9 ± 11.1 vs. 41.1 ± 6.3 cells/0.25 mm^2 ; $P = 0.020$) (Fig 7).

Discussion

In this study, we first attempted to develop a short-term hypoglycemic coma model that could be maintained in an isoelectric EEG state for a short period. The isoelectric EEG period was reduced from 30 min, which is the isoelectric period used in a conventional hypoglycemic coma model, to 2 min. We confirmed that seizures did not occur in this condition. The advantages of this model are as follows. (i) The degree of severity induced by the hypoglycemic load is relatively uniform, while measurements of the light reflex and pupil diameter lack objectivity and quantitativity. (ii) BG levels during the hyperglycemic state are determined on the basis of actual human clinical data [3]. (iii) This model does not require the use of anti-seizure drugs and an artificial ventilator. (iv) The severity of oxidative stress and neuronal death are quantifiable by measuring 4-HNE- and FJB-positive cells, respectively.

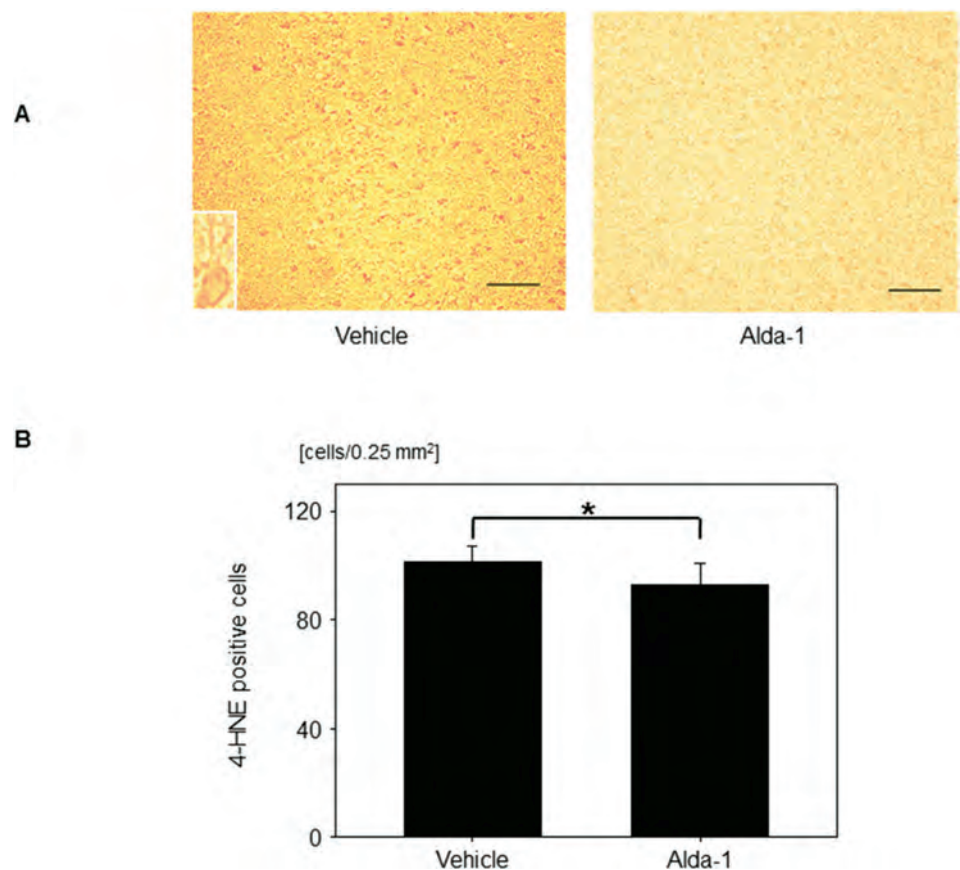


Fig 6. Effects of Alda-1 on 4-HNE-positive cells. (A) Representative images of 4-HNE-positive cells treated with vehicle (dimethyl sulfoxide; DMSO) or Alda-1. A higher magnification view of a 4-HNE-positive cell is shown in the small frame. Scale bar: 100 μ m. (B) Number of 4-HNE-positive cells in groups treated with vehicle (DMSO) or Alda-1. Data are means \pm SD ($n = 15$ fields). * $P = 0.002$.

doi:10.1371/journal.pone.0128844.g006

Next, we investigated the characteristics of glucose reperfusion injury using this model, and noted the following observations. (i) We found that the appearance of 4-HNE-positive cells in the brain even in the 2-min isoelectric EEG group. This suggests that the conditions present in the 2-min isoelectric EEG group are enough to cause glucose reperfusion injury. Since oxidative stress is not caused by hypoglycemic loads alone [7, 10], this raises the possibility that hyperglycemia associated with glucose administration causes glucose reperfusion injury. (ii) We observed fewer 4-HNE-positive cells in the 2-min isoelectric EEG group than in the 10-min isoelectric EEG group, although BG levels during the hyperglycemic state were similar. This finding suggests that the severity of glucose reperfusion injury may be influenced by the degree of severity of the hypoglycemic load-induced neuronal damage. However, to our knowledge, no reports have determined the effect of the severity of the hypoglycemic load on glucose reperfusion injury. Future studies need to address this issue. (iii) We observed fewer 4-HNE-positive cells in the hippocampus than in the cerebral cortex. Previous studies demonstrated similar findings in the non-coma model [7, 8], although the mechanism underlying the difference in 4-HNE production in different brain regions remains unknown.

Finally, we showed that administration of Alda-1 inhibits both the production of 4-HNE and neuronal death associated with glucose reperfusion injury, similar to previous reports in

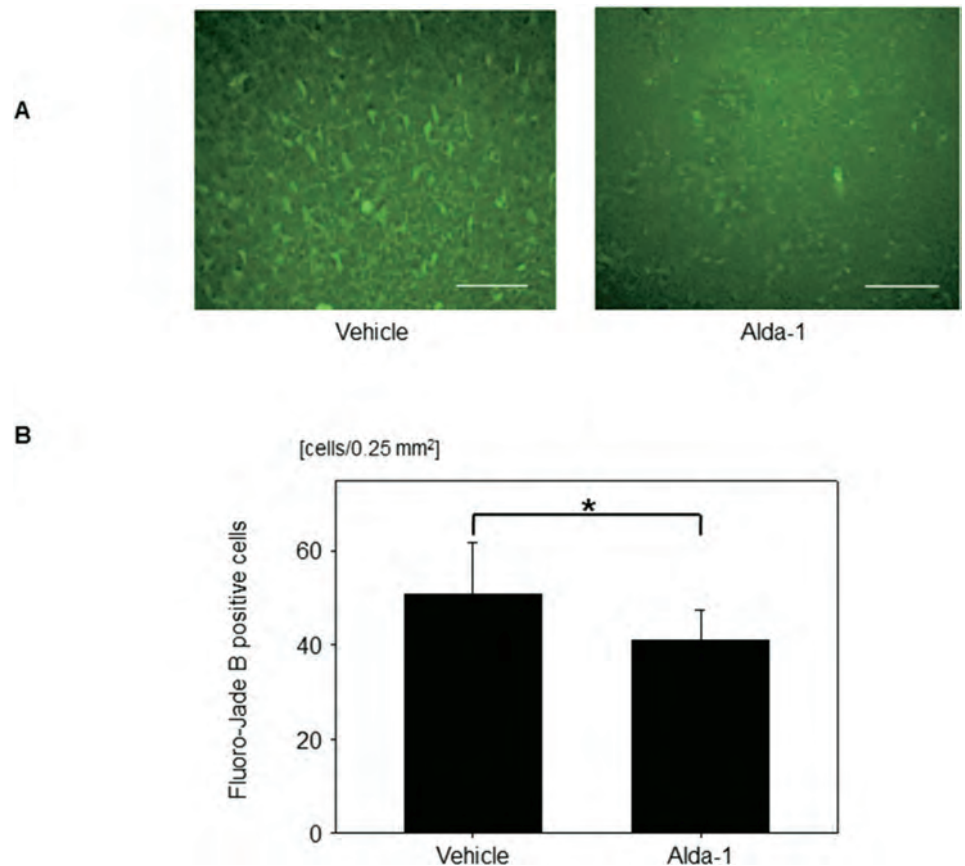


Fig 7. Effects of Alda-1 on Fluoro-Jade B-positive cells. (A) Representative images of Fluoro-Jade B-positive cells treated with vehicle (DMSO) or Alda-1. Scale bar: 100 μ m. (B) Number of Fluoro-Jade B-positive cells in groups treated with vehicle (DMSO) or Alda-1. Data are means \pm SD ($n = 15$ fields). * $P = 0.020$.

doi:10.1371/journal.pone.0128844.g007

which Alda-1 inhibits myocardial damage caused by 4-HNE after myocardial ischemia [12, 14]. Previous studies show that treatments devised to attenuate oxidative stress associated with glucose reperfusion injury may be therapeutic candidates, including therapeutic hypothermia [19], administration of nitric oxide synthase inhibitors [21], and nicotine adenine dinucleotide phosphate oxidase inhibitors [10]. In addition, Alda-1 may be a therapeutic candidate. Activation of ALDH2 by Alda-1 increases detoxification of reactive aldehydes, such as 4-HNE, a cytotoxic aldehyde that accumulates during glucose reperfusion injury as a by-product of ROS-induced lipid peroxidation [14]. Enhanced ALDH2 activity reduces 4-HNE protein adduct formation and increases cell survival. We suggest that activation of the ALDH2 pathway could be a molecular target for HE treatment, and that Alda-1 is a potentially neuroprotective agent that exerts a beneficial effect on neurons when intravenously administered simultaneously with glucose.

This study has a number of limitations. First, with regard to the FJB-positive cells in the 10-min isoelectric EEG group, the seizures associated with a prolonged hypoglycemic state may affect the results. Second, we did not investigate the effect of other neuroprotective drugs that inhibit oxidative stress on neuronal death. Future studies are required to determine the most suitable drug for treatment of glucose reperfusion injury.

In conclusion, we established a short-term hypoglycemic coma model. In this model, we confirmed both the appearance of 4-HNE-positive cells and neuronal death associated with glucose reperfusion injury. Furthermore, with this model we demonstrated that Alda-1 inhibits 4-HNE production and exerts a protective effect against neuronal death. Thus, Alda-1 may be a candidate neuroprotective agent for cases involving HE.

Supporting Information

S1 Fig. Hypoglycemia-induced neuronal death evaluated by Fluoro-Jade B staining. (A) Representative images of Fluoro-Jade B-positive cells in the sham group, the 2-min isoelectric EEG (iso-EEG) without glucose reperfusion group, and the 10-min isoelectric EEG without glucose reperfusion group. Scale bar: 100 μ m. (B) The number of Fluoro-Jade B-positive cells in the sham group, the 2-min isoelectric EEG without glucose reperfusion group, and the 10-min isoelectric EEG without glucose reperfusion group. Data are means \pm SD ($n = 15$ fields). * $P = 0.009$. (TIF)

Acknowledgments

The authors gratefully thank Prof. Hironaka Igarashi (Department of Center for Integrated Human Brain Science, Brain Research Institute, Niigata University) for his support.

Author Contributions

Conceived and designed the experiments: TI TT TS. Performed the experiments: TI TT M. Kanazawa M. Toriyabe M. Koyama. Analyzed the data: TI TT M. Kanazawa TS. Contributed reagents/materials/analysis tools: M. Tsujita KI TN. Wrote the paper: TI MN TS.

References

1. Fischer KF, Lees JA, Newman JH. Hypoglycemia in hospitalized patients. Causes and outcomes. *N Engl J Med.* 1986; 315(20):1245–50. Epub 1986/11/13. doi: [10.1056/NEJM198611133152002](https://doi.org/10.1056/NEJM198611133152002) PMID: [3534567](https://pubmed.ncbi.nlm.nih.gov/3534567/).
2. Seltzer HS. Drug-induced hypoglycemia. A review of 1418 cases. *Endocrinol Metab Clin North Am.* 1989; 18(1):163–83. Epub 1989/03/01. PMID: [2645125](https://pubmed.ncbi.nlm.nih.gov/2645125/).
3. Ikeda T, Takahashi T, Sato A, Tanaka H, Igarashi S, Fujita N, et al. Predictors of outcome in hypoglycemic encephalopathy. *Diabetes Res Clin Pract.* 2013. Epub 2013/07/04. doi: [10.1016/j.diabres.2013.05.007](https://doi.org/10.1016/j.diabres.2013.05.007) PMID: [23820485](https://pubmed.ncbi.nlm.nih.gov/23820485/).
4. Auer RN, Olsson Y, Siesjo BK. Hypoglycemic brain injury in the rat. Correlation of density of brain damage with the EEG isoelectric time: a quantitative study. *Diabetes.* 1984; 33(11):1090–8. Epub 1984/11/01. PMID: [6500189](https://pubmed.ncbi.nlm.nih.gov/6500189/).
5. Suh SW, Aoyama K, Chen Y, Garnier P, Matsumori Y, Gum E, et al. Hypoglycemic neuronal death and cognitive impairment are prevented by poly(ADP-ribose) polymerase inhibitors administered after hypoglycemia. *J Neurosci.* 2003; 23(33):10681–90. Epub 2003/11/25. doi: [23/33/10681](https://doi.org/10.1523/JNEUROSCI.2333-03.2003) [pii]. PMID: [14627653](https://pubmed.ncbi.nlm.nih.gov/14627653/).
6. Haces ML, Hernandez-Fonseca K, Medina-Campos ON, Montiel T, Pedraza-Chaverri J, Massieu L. Antioxidant capacity contributes to protection of ketone bodies against oxidative damage induced during hypoglycemic conditions. *Exp Neurol.* 2008; 211(1):85–96. Epub 2008/03/15. doi: [S0014-4886\(08\)00010-1](https://doi.org/10.1016/j.expneurol.2007.12.029) [pii] doi: [10.1016/j.expneurol.2007.12.029](https://doi.org/10.1016/j.expneurol.2007.12.029) PMID: [18339375](https://pubmed.ncbi.nlm.nih.gov/18339375/).
7. Haces ML, Montiel T, Massieu L. Selective vulnerability of brain regions to oxidative stress in a non-coma model of insulin-induced hypoglycemia. *Neuroscience.* 2010; 165(1):28–38. Epub 2009/10/13. doi: [S0306-4522\(09\)01643-1](https://doi.org/10.1016/j.neuroscience.2009.10.003) [pii] doi: [10.1016/j.neuroscience.2009.10.003](https://doi.org/10.1016/j.neuroscience.2009.10.003) PMID: [19818385](https://pubmed.ncbi.nlm.nih.gov/19818385/).
8. Tkacs NC, Pan Y, Raghupathi R, Dunn-Meynell AA, Levin BE. Cortical Fluoro-Jade staining and blunted adrenomedullary response to hypoglycemia after noncoma hypoglycemia in rats. *J Cereb Blood Flow Metab.* 2005; 25(12):1645–55. Epub 2005/05/20. doi: [9600152](https://doi.org/10.1038/sj.jcbfm.9600152) [pii] doi: [10.1038/sj.jcbfm.9600152](https://doi.org/10.1038/sj.jcbfm.9600152) PMID: [15902194](https://pubmed.ncbi.nlm.nih.gov/15902194/).

9. de Courten-Myers GM, Xi G, Hwang JH, Dunn RS, Mills AS, Holland SK, et al. Hypoglycemic brain injury: potentiation from respiratory depression and injury aggravation from hyperglycemic treatment overshoots. *J Cereb Blood Flow Metab.* 2000; 20(1):82–92. Epub 2000/01/05. doi: [10.1097/00004647-200001000-00012](https://doi.org/10.1097/00004647-200001000-00012) PMID: [10616796](https://pubmed.ncbi.nlm.nih.gov/10616796/).
10. Suh SW, Gum ET, Hamby AM, Chan PH, Swanson RA. Hypoglycemic neuronal death is triggered by glucose reperfusion and activation of neuronal NADPH oxidase. *J Clin Invest.* 2007; 117(4):910–8. Epub 2007/04/04. doi: [10.1172/JCI30077](https://doi.org/10.1172/JCI30077) PMID: [17404617](https://pubmed.ncbi.nlm.nih.gov/17404617/); PubMed Central PMCID: [PMC1838937](https://pubmed.ncbi.nlm.nih.gov/PMC1838937/).
11. Eaton P, Li JM, Hearse DJ, Shattock MJ. Formation of 4-hydroxy-2-nonenal-modified proteins in ischemic rat heart. *Am J Physiol.* 1999; 276(3 Pt 2):H935–43. Epub 1999/03/10. PMID: [10070077](https://pubmed.ncbi.nlm.nih.gov/10070077/).
12. Chen CH, Budas GR, Churchill EN, Disatnik MH, Hurley TD, Mochly-Rosen D. Activation of aldehyde dehydrogenase-2 reduces ischemic damage to the heart. *Science.* 2008; 321(5895):1493–5. Epub 2008/09/13. doi: [10.1126/science.1158554](https://doi.org/10.1126/science.1158554) PMID: [18787169](https://pubmed.ncbi.nlm.nih.gov/18787169/); PubMed Central PMCID: [PMC2741612](https://pubmed.ncbi.nlm.nih.gov/PMC2741612/).
13. Keller JN, Kindy MS, Holtsberg FW, St Clair DK, Yen HC, Germeyer A, et al. Mitochondrial manganese superoxide dismutase prevents neural apoptosis and reduces ischemic brain injury: suppression of peroxynitrite production, lipid peroxidation, and mitochondrial dysfunction. *J Neurosci.* 1998; 18(2):687–97. Epub 1998/02/07. PMID: [9425011](https://pubmed.ncbi.nlm.nih.gov/9425011/).
14. Perez-Miller S, Younus H, Vanam R, Chen CH, Mochly-Rosen D, Hurley TD. Alda-1 is an agonist and chemical chaperone for the common human aldehyde dehydrogenase 2 variant. *Nat Struct Mol Biol.* 2010; 17(2):159–64. Epub 2010/01/12. doi: [10.1038/nsmb.1737](https://doi.org/10.1038/nsmb.1737) [pii] doi: [10.1038/nsmb.1737](https://doi.org/10.1038/nsmb.1737) PMID: [20062057](https://pubmed.ncbi.nlm.nih.gov/20062057/); PubMed Central PMCID: [PMC2857674](https://pubmed.ncbi.nlm.nih.gov/PMC2857674/).
15. Kilkenny C, Browne W, Cuthill IC, Emerson M, Altman DG. Animal research: reporting in vivo experiments—the ARRIVE guidelines. *J Cereb Blood Flow Metab.* 2011; 31(4):991–3. Epub 2011/01/06. doi: [10.1038/jcbfm.2010.220](https://doi.org/10.1038/jcbfm.2010.220) PMID: [21206507](https://pubmed.ncbi.nlm.nih.gov/21206507/); PubMed Central PMCID: [PMC3070981](https://pubmed.ncbi.nlm.nih.gov/PMC3070981/).
16. Cathy A. Johnson-Delaney LH. *Exotic Companion Medicine Handbook for Veterinarians Zoological Education Network*; 1996 4/1. 500 p.
17. Hughes RN, Syme LA. The role of social isolation and sex in determining effects of chlordiazepoxide and methylphenidate on exploratory behaviour. *Psychopharmacologia.* 1972; 27(4):359–66. Epub 1972/01/01. PMID: [4648619](https://pubmed.ncbi.nlm.nih.gov/4648619/).
18. Suh SW, Aoyama K, Matsumori Y, Liu J, Swanson RA. Pyruvate administered after severe hypoglycemia reduces neuronal death and cognitive impairment. *Diabetes.* 2005; 54(5):1452–8. Epub 2005/04/28. doi: [10.2337/1452](https://doi.org/10.2337/1452) [pii]. PMID: [15855333](https://pubmed.ncbi.nlm.nih.gov/15855333/).
19. Shin BS, Won SJ, Yoo BH, Kauppinen TM, Suh SW. Prevention of hypoglycemia-induced neuronal death by hypothermia. *J Cereb Blood Flow Metab.* 2010; 30(2):390–402. Epub 2009/10/29. doi: [10.1038/jcbfm.2009.229](https://doi.org/10.1038/jcbfm.2009.229) PMID: [19861976](https://pubmed.ncbi.nlm.nih.gov/19861976/); PubMed Central PMCID: [PMC2949122](https://pubmed.ncbi.nlm.nih.gov/PMC2949122/).
20. Kawai H, Deguchi S, Deguchi K, Yamashita T, Ohta Y, Shang J, et al. Synergistic benefit of combined amlodipine plus atorvastatin on neuronal damage after stroke in Zucker metabolic rat. *Brain Res.* 2011; 1368:317–23. Epub 2010/10/26. doi: [10.1016/j.brainres.2010.10.046](https://doi.org/10.1016/j.brainres.2010.10.046) PMID: [20971084](https://pubmed.ncbi.nlm.nih.gov/20971084/).
21. Suh SW, Hamby AM, Gum ET, Shin BS, Won SJ, Sheline CT, et al. Sequential release of nitric oxide, zinc, and superoxide in hypoglycemic neuronal death. *J Cereb Blood Flow Metab.* 2008; 28(10):1697–706. Epub 2008/06/12. doi: [10.1038/jcbfm.2008.61](https://doi.org/10.1038/jcbfm.2008.61) PMID: [18545258](https://pubmed.ncbi.nlm.nih.gov/18545258/).

RESEARCH ARTICLE

Reduced CSF Water Influx in Alzheimer's Disease Supporting the β -Amyloid Clearance Hypothesis

Yuji Suzuki¹, Yukihiro Nakamura¹, Kenichi Yamada¹, Hironaka Igarashi¹, Kensaku Kasuga², Yuichi Yokoyama³, Takeshi Ikeuchi², Masatoyo Nishizawa⁴, Ingrid L. Kwee⁵, Tsutomu Nakada^{1,5*}

1 Center for Integrated Human Brain Science, Brain Research Institute, University of Niigata, Niigata, Japan, **2** Department of Molecular Genetics, Brain Research Institute, University of Niigata, Niigata, Japan, **3** Department of Psychiatry, Faculty of Medicine, University of Niigata, Niigata, Japan, **4** Department of Neurology, Brain Research Institute, University of Niigata, Niigata, Japan, **5** Department of Neurology, University of California Davis, Davis, California, United States of America

* tnakada@bri.niigata-u.ac.jp



 OPEN ACCESS

Citation: Suzuki Y, Nakamura Y, Yamada K, Igarashi H, Kasuga K, Yokoyama Y, et al. (2015) Reduced CSF Water Influx in Alzheimer's Disease Supporting the β -Amyloid Clearance Hypothesis. PLoS ONE 10 (5): e0123708. doi:10.1371/journal.pone.0123708

Academic Editor: Stephen D Ginsberg, Nathan Kline Institute and New York University School of Medicine, UNITED STATES

Received: October 12, 2014

Accepted: March 5, 2015

Published: May 6, 2015

Copyright: This is an open access article, free of all copyright, and may be freely reproduced, distributed, transmitted, modified, built upon, or otherwise used by anyone for any lawful purpose. The work is made available under the [Creative Commons CC0](https://creativecommons.org/licenses/by/4.0/) public domain dedication.

Data Availability Statement: All relevant data are within the paper and its Supporting Information files.

Funding: The study was supported by grants from the Ministry of Education, Culture, Sports, Science, and Technology (Japan) (TN).

Competing Interests: The authors have declared that no competing interests exist.

Abstract

Objective

To investigate whether water influx into cerebrospinal fluid (CSF) space is reduced in Alzheimer's patients as previously shown in the transgenic mouse model for Alzheimer's disease.

Methods

Ten normal young volunteers (young control, 21-30 years old), ten normal senior volunteers (senior control, 60-78 years old, MMSE \geq 29), and ten Alzheimer's disease (AD) patients (study group, 59-84 years old, MMSE: 13-19) participated in this study. All AD patients were diagnosed by neurologists specializing in dementia based on DSM-IV criteria. CSF dynamics were analyzed using positron emission tomography (PET) following an intravenous injection of 1,000 MBq [¹⁵O]H₂O synthesized on-line.

Results

Water influx into CSF space in AD patients, expressed as influx ratio, (0.755 ± 0.089) was significantly reduced compared to young controls (1.357 ± 0.185 ; $p < 0.001$) and also compared to normal senior controls (0.981 ± 0.253 , $p < 0.05$). Influx ratio in normal senior controls was significantly reduced compared to young controls ($p < 0.01$).

Conclusion

Water influx into the CSF is significantly reduced in AD patients. β -amyloid clearance has been shown to be dependent on interstitial flow and CSF production. The current study indicates that reduction in water influx into the CSF may disturb the clearance rate of β -amyloid, and therefore be linked to the pathogenesis of AD.

Trial Registration

UMIN Clinical Trials Registry [UMIN000011939](https://clinicaltrials.gov/ct2/show/study/UMIN000011939)

Introduction

The brain lacks conventional lymphatics for clearing interstitial fluid of solutes not absorbed across capillaries. The cerebrospinal flow (CSF) system has long been suggested to play a role equivalent to the systemic lymphatic system. Nevertheless, the role of CSF as the brain's lymphatic system has not received much attention. Recently, however, the classic CSF circulation theory where CSF is almost exclusively produced by choroid plexus is found to be incomplete. It is now understood that influx from the peri-capillary (Virchow-Robin) space into the CSF system, classically referred to as interstitial flow, plays a major role in CSF production [1–3]. Furthermore, a number of studies have now shown that this interstitial flow plays a critical role in the clearance of β -amyloid [4–8]. Prealbumin (transthyretin) in the CSF has been identified to play the role of chaperon to β -amyloid, and prevents β -amyloid's natural tendency to aggregate and form plaques [9]. It is highly conceivable, therefore, that disturbance of interstitial flow may play a significant role in the pathogenesis of senile plaque (SP) formation.

Water homeostasis of the Virchow-Robin space and, therefore, interstitial flow is regulated by aquaporin-4 (AQP-4) [2,3,10], an isoform of water channels abundant in the brain. Using JJ vicinal coupling proton exchange (JJVCPE) imaging [11,12], a novel non-invasive magnetic resonance imaging (MRI) method capable of tracing exogenously applied substrates in a manner similar to positron emission tomography (PET), we had previously demonstrated that water influx into the CSF system is significantly reduced in senile plaque bearing transgenic AD model mice to the extent similar to AQP-4 knockout mice [12,13]. Using PET, we confirmed in this study that water influx into CSF is also reduced in AD patients.

Materials and Methods

Subjects

Ten normal young volunteers (10 males, ages 21–30 years), ten normal senior volunteers (7 males and 3 females, ages 60–78 years), and ten Alzheimer's disease (AD) patients (6 males and 4 females, ages 59–84 years) participated in this study. Participant recruitment was completed between October 1, 2013, and April 4, 2014 (Fig 1). All volunteers were free of any significant medical conditions such as hypertension, diabetes, chronic pulmonary diseases, and were not taking any prescribed, over the counter, or herbal medications. AD patients were recruited from the Memory Clinic, Niigata University Hospital. The diagnosis of AD was determined based on DSM-IV criteria by neurologists specializing in dementia. The neurologists further determined whether the potential subject had decision making capacity to consent for the study. Age-matched senior volunteers were assessed to have no functional and no cognitive impairment (Mini-Mental State Examination (MMSE) score ≥ 29), and had no neurological disease. In compliance with the Institutional Review Board of University of Niigata, the study protocol was explained in detail to all potential subjects, or their proxy where appropriate. Written informed consent was obtained from all subjects or, where the Alzheimer's subject was deemed to have no decision making capacity to consent for the study, by his/her proxy. All imaging studies were performed between October 2013 and April 2014. The study was approved by the Ethics Review Board of the Internal Review Board of University of Niigata. The project



CONSORT 2010 Flow Diagram

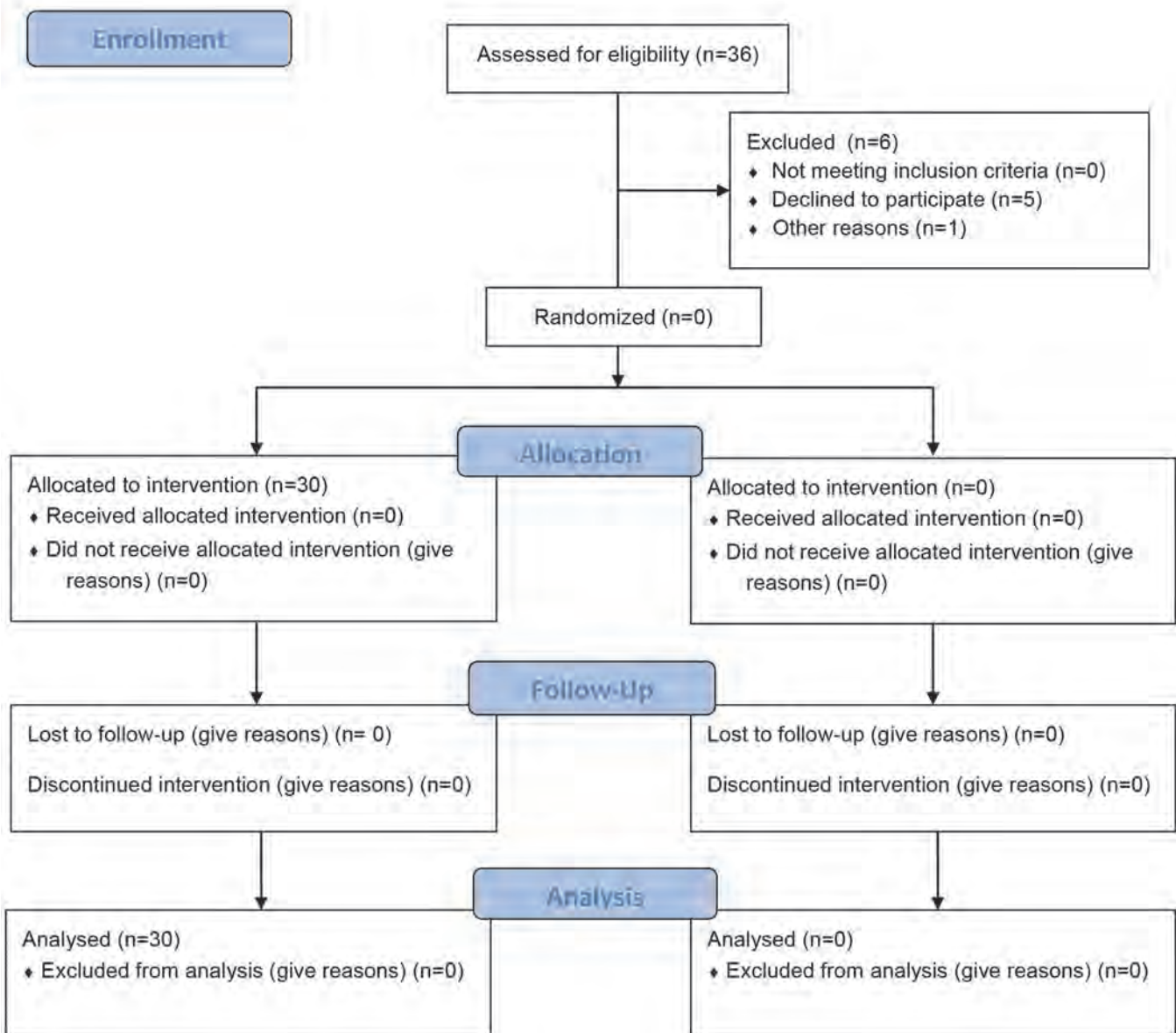


Fig 1. Consort Flow Diagram providing details of participant enrolment.

doi:10.1371/journal.pone.0123708.g001

was registered at the UMIN Clinical Trials Registry as UMIN000011939 (<http://www.umin.ac.jp/ctr/index.htm>). Participants were provided with contact names and telephone numbers in the event of any adverse event related to the study. All participants were followed up within one month of the study to further confirm the absence or occurrence of adverse events related to the study, not otherwise self-reported by the study participant or proxy to the study coordinator. Alzheimer's patients are additionally followed up annually at the Memory Clinic.

PET imaging

PET imaging was performed using a combined PET/CT scanner (Discovery ST Elite, GE Healthcare, Schenectady NY, USA) with a 15 cm field of view (FOV) positioned in the region of the cerebrum. To correct for photon attenuation, low-dose CT imaging was acquired in helical mode. The subject's head rested on a foam cushioned headrest. A head strap was applied to minimize head movement.

1000 MBq [^{15}O]H₂O, synthesized on-line ($[^{15}\text{O}]\text{CO}_2 + 4\text{H}_2 \rightarrow 2[^{15}\text{O}]\text{H}_2\text{O} + \text{CH}_4$) was injected intravenously into an antecubital vein via an automatic water injection system (AM WR01, JFE Technos, Yokohama, Japan). The system delivered a 10 ml bolus over 10 seconds at 1 ml/sec with both pre- and post- flush of an inert saline solution. Immediately after starting the administration, emission data were acquired over 20 minutes in three-dimensional list mode with a 25.6 cm axial FOV and sorted into 40 time frames (40 × 30 seconds).

All emission scans were normalized for detector inhomogeneity and corrected for random coincidences, dead time, scattered radiation, and photon attenuation. For optimization of image quality, the 40 frames of the dynamic emission scans were reconstructed using 3D-OSEM (Ordered-Subset Expectation Maximization) with 2 iterations and 28 subsets. The resultant image quality allowed manual identification of regions of interest (ROIs). For the reconstruction algorithms, the data were collected in a 128 × 128 × 47 matrix with a voxel size of 2.0 × 2.0 × 3.27mm.

Data Analysis

The CT and PET image data were transferred to a Xeleris 1.1 workstation (GE Healthcare) for PET data analysis. Manually defined ROIs on the attenuation corrected axial images and CT images (lateral and third ventricle, cortex of occipital lobe) were used to obtain the time-activity data of the scans of each subject. The tissue activity concentration in each ROI was expressed as the standardized uptake value (SUV, g/ml), corrected for the subject's body weight and administered dose of radioactivity. Each tissue time activity concentration was determined by fitting the data using the following equation:

$$y(t) = y_0 + ae^{-bt}$$

where y_0 is the baseline SUV. Subsequently, the ratio between SUVs of ventricle and cortex was defined as the influx ratio. The numerical data were subjected to the Mann-Whitney-Wilcoxon rank sum test for group analysis using IBM SPSS version 19.5 (IBM Corporation, Armonk, NY, USA).

Results

Results are shown in [Table 1](#) and summarized in [Fig 2](#). Water influx into CSF space in AD patients, expressed as influx ratio (0.755 ± 0.089), was significantly reduced compared to young controls (1.357 ± 0.185 , $p < 0.001$) and senior controls (0.981 ± 0.253 , $p < 0.05$). Furthermore, the influx ratio of senior controls compared to that of young controls was significantly reduced

Table 1.

	Age	Influx Ratio
Young	21	1.10620
	21	1.35608
	21	1.45009
	21	1.14260
	22	1.16180
	22	1.62079
	22	1.24990
	24	1.41213
	24	1.48959
	30	1.57873
Senior	60	0.68299
	63	0.92728
	63	1.03987
	63	1.05720
	65	1.44195
	68	0.94050
	68	1.27526
	69	0.81396
	74	1.03050
78	0.59892	
AD	59	0.69261
	61	0.79321
	63	0.86105
	63	0.62796
	71	0.70088
	71	0.73065
	73	0.74510
	79	0.66232
80	0.84389	
84	0.88935	

doi:10.1371/journal.pone.0123708.t001

($p < 0.01$) as well. The observed large range of influx ratio (0.599–1.442) in the senior controls suggested that the reduction in water influx into CSF represented an aging process.

Discussion

Fluid-filled canals surrounding perforating arteries and veins in the brain parenchyma were recognized in the early era of modern medicine. They became known as the Virchow Robin space, so named after the first two scientists who described the structure in detail, namely, Rudolph Virchow and Charles Philippe Robin [14,15]. It was soon recognized that fluid in the Virchow Robin space may play a role similar to systemic lymphatics [4–8,16]. Studies based on modern technologies disclosed some of the physiological roles of the Virchow Robin space and interstitial fluid flow, ranging from the regulation of regional blood flow to β -amyloid clearance during sleep [17–19].

The unique anatomical features of the brain's vascular system ensure a properly functioning blood brain barrier (BBB) and are a result of modification of the systemic circulation system. A critical property of the BBB is prevention of free water permeability across capillary walls (tight

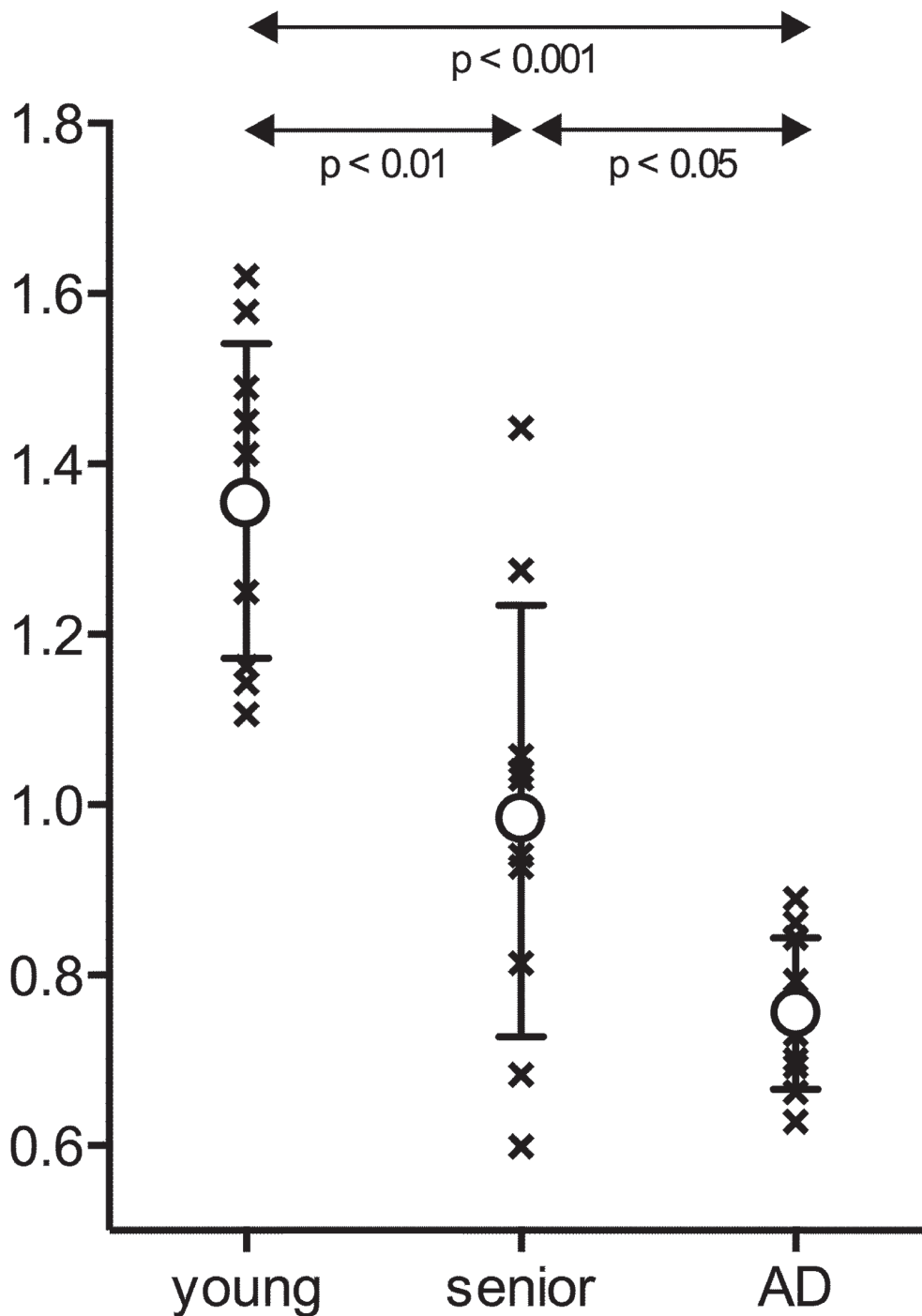


Fig 2. Schematic presentation of the results with mean (circle) and standard deviation (bar). Water influx into CSF space is expressed as influx ratio (IR): the ratio between the standardized uptake value (SUV, g/ml) of the ventricle to that of cortex. IR in Alzheimer's disease patients (AD) is significantly reduced compared to both young controls ($p < 0.001$) and senior controls ($p < 0.05$), Mann-Whitney-Wilcoxon rank sum test. Note that there is no overlap in data points between AD and young controls. Reduction of influx ratio in senior controls compared to that in young control is found to be significant ($p < 0.01$) as well. A large range of influx ratio in senior controls suggests that the observed reduction likely represents one of the aging processes.

doi:10.1371/journal.pone.0123708.g002

endothelium). This is in strong contrast to systemic capillaries which possess a leaky endothelium. The molecular basis of the tight endothelium is the formation of tight junctions. Various tight junction proteins such as claudin and occludin play the role of “gating control” of paracellular transport. Passive water movement across brain capillaries is strongly restricted by these tight junctions. In systemic capillaries, active water transport across endothelial cells is accomplished by the water channel aquaporin 1 (AQP-1). In brain capillaries, such water movement is totally abolished through the active suppression of AQP-1 [20]. Accordingly, water motion between capillary lumen into the peri-capillary Virchow Robin space is highly limited to restricted passive movement.

In contrast to the above situations, the peri-capillary Virchow Robin space receives constant water influx through AQP-4, another isoform of the aquaporin family, abundantly expressed in the perivascular endfeet of astrocytes [21]. Virchow Robin space water homeostasis and, hence, interstitial flow is primarily dependent on water influx through AQP-4 [2,3,10]. Accordingly, brain interstitial flow, which plays a role equivalent to the systemic lymphatic system, is now considered to be an AQP-4 dependent system [13]. The basic function of lymphatics is drainage of cellular debris that has been subjected to molecular scrutiny before being returned to venous circulation. β -amyloid has been shown to be essential for synaptic formation [22]. Disturbance in the proper clearance of β -amyloid, and negative balance between its clearance and production has been implicated to play a significant role in senile plaque formation and ultimately the pathogenesis of Alzheimer's disease. The various components of amyloid homeostasis have become a target of therapeutic strategies [23–25]. Since under physiological conditions interstitial flow plays a critical role in the clearance of β -amyloid [4–8], disturbance in AQP-4 functionality and resultant reduction in interstitial flow could cause significant β -amyloid accumulation. Transgenic mice lacking endothelial cell expression of Agrin are shown to have reduced AQP4 while BBB remained intact. These mice have significant accumulation of β -amyloid[26].

Although it is difficult to determine whether the observed reduction in water influx into the CSF system in AD patients is the primary abnormality or merely related to β -amyloid deposits in the brain, the clear cut differences between young normal volunteers and AD patients unequivocally indicated that AD patients have significant reduction in interstitial flow. Furthermore, the theoretical possibility of contribution by choroid plexus or the leptomeningeal vasculature to the water detected in the CSF compartment cannot be totally excluded. Nevertheless, the observed large range of influx ratios in senior controls without cognitive dysfunction, strongly suggests that reduction of water influx into the CSF itself is not a sufficient factor for the pathogenesis of AD, a situation similar to senile plaque formation. There must be additional factors that eventually lead to neural death and cortical dysfunction.

Drainage of β -amyloid by interstitial flow through the Virchow Robin space into CSF is essential for maintaining proper homeostasis between β -amyloid production and clearance. The balance between β -amyloid production and its clearance appears to be vital for maintaining proper neural function. Disruption in β -amyloid homeostasis may play a critical role in the pathogenesis of senile plaque formation, and, hence, the development of Alzheimer's disease. Assessment of the dynamic indices of production and clearance of β -amyloid in various cohort groups, including mild cognitive impairment (MCI), is warranted.

Supporting Information

S1 TREND Checklist.
(PDF)

Acknowledgments

The study in part was presented at the 66th AAN Annual Meeting of the American Academy of Neurology, April 2014, Philadelphia, USA and Alzheimer's Imaging Consortium, July 2014, Copenhagen, Denmark.

Author Contributions

Conceived and designed the experiments: TN. Performed the experiments: YS YN KY KK YY TI. Analyzed the data: YS HI MN ILK TN. Wrote the paper: YS ILK TN.

References

- Orešković D, Klarica M (2010) The formation of cerebrospinal fluid: Nearly a hundred years of interpretations and misinterpretations. *Brain Res. Rev* 64: 241–262. doi: [10.1016/j.brainresrev.2010.04.006](https://doi.org/10.1016/j.brainresrev.2010.04.006) PMID: [20435061](https://pubmed.ncbi.nlm.nih.gov/20435061/)
- Igarashi H, Tsujita M, Kwee IL, Nakada T (2014) Water Influx into Cerebrospinal Fluid (CSF) is Primarily Controlled by Aquaporin-4, not by Aquaporin-1: O-17 JVCPE MRI Study in Knockout Mice. *Neuroreport* 25: 39–43. doi: [10.1097/WNR.000000000000042](https://doi.org/10.1097/WNR.000000000000042) PMID: [24231830](https://pubmed.ncbi.nlm.nih.gov/24231830/)
- Haj-Yasein NN, Jensen V, Østby I, Omholt SW, Voipio J, Kaila K, et al. (2012) Aquaporin-4 regulates extracellular space volume dynamics during high-frequency synaptic stimulation: A gene deletion study in mouse hippocampus. *Glia* 60: 867–874. doi: [10.1002/glia.22319](https://doi.org/10.1002/glia.22319) PMID: [22419561](https://pubmed.ncbi.nlm.nih.gov/22419561/)
- Johnston M, Papaiconomou C (2002) Cerebrospinal fluid transport: a lymphatic perspective. *News Physiol Sci* 17: 227–230 PMID: [12433975](https://pubmed.ncbi.nlm.nih.gov/12433975/)
- Abott NJ (2004) Evidence for bulk flow of brain interstitial fluid: significance for physiology and pathology. *Neurochem Int* 45: 545–552 PMID: [15186921](https://pubmed.ncbi.nlm.nih.gov/15186921/)
- Weller RO, Djuanda E, Yow HY, Carare RO (2009) Lymphatic drainage of the brain and the pathophysiology of neurological disease. *Acta Neuropathol* 117: 1–14 doi: [10.1007/s00401-008-0457-0](https://doi.org/10.1007/s00401-008-0457-0) PMID: [19002474](https://pubmed.ncbi.nlm.nih.gov/19002474/)
- Iliff JJ, Wang M, Liao Y, Plogg BA, Peng W, Gundersen GA, et al. (2012) A paravascular pathway facilitates CSF flow through the brain parenchyma and the clearance of interstitial solutes, including amyloid β . *Sci Transl Med* 4: 147ra111
- Weller RO (1998) Pathology of cerebrospinal fluid and interstitial fluid of the CNS: significance for Alzheimer disease, prion disorders and multiple sclerosis. *J Neuropathol Exp Neurol* 57: 885–894 PMID: [9786239](https://pubmed.ncbi.nlm.nih.gov/9786239/)
- Xinyi L, Buxbaum JN (2011) Transthyretin and the brain re-visited: Is neuronal synthesis of transthyretin protective in Alzheimer's disease? *Mol Neurodegener* 6: 79. doi: [10.1186/1750-1326-6-79](https://doi.org/10.1186/1750-1326-6-79) PMID: [22112803](https://pubmed.ncbi.nlm.nih.gov/22112803/)
- Kitaura H, Tsujita M, Huber VJ, Kakita A, Shibuki K, Sakimura K, et al. (2009) Activity-dependent glial swelling is impaired in aquaporin-4 knockout mice. *Neurosci Res* 64: 208–212. doi: [10.1016/j.neures.2009.03.002](https://doi.org/10.1016/j.neures.2009.03.002) PMID: [19428702](https://pubmed.ncbi.nlm.nih.gov/19428702/)
- Suzuki K, Igarashi H, Huber VJ, Kitaura H, Kwee IL, et al. (In Press) Ligand based molecular MRI: O-17 JVCPE amyloid imaging in transgenic mice. *J. Neuroimag* 2014; 24:595–598.
- Igarashi H, Suzuki Y, Kwee IL, Nakada T (2014) Water Influx into cerebrospinal fluid is significantly reduced in senile plaque bearing transgenic mice, supporting β -Amyloid clearance hypothesis of Alzheimer's disease. *Neurol Res* 2014; 36:1094–1098 doi: [10.1179/1743132814Y.0000000434](https://doi.org/10.1179/1743132814Y.0000000434) PMID: [25082552](https://pubmed.ncbi.nlm.nih.gov/25082552/)
- Nakada T (2014) Review: Virchow-Robin space and aquaporin-4: New insights on an old friend. *Croatian Med J* 55: 328–336
- Virchow R (1851) Ueber die Erweiterung kleinerer Gefaesse. *Arch Pathol Anat Physiol Klin Med* 3: 427–462
- Robin C (1859) Recherches sur quelques particularites de la structure des capillaires de l'encephale. *J Physiol Homme Animaux* 2: 537–548
- Esiri MM, Gay D (1990) Immunological and neuropathological significance of the Virchow-Robin space. *J Neurol Sci* 100: 3–8 PMID: [2089138](https://pubmed.ncbi.nlm.nih.gov/2089138/)
- Nakada T (2015) The molecular mechanisms of neural flow coupling: A new concept. *J Neuroimaging* 2015 Feb 20. doi: [10.1111/jon.12219](https://doi.org/10.1111/jon.12219) [Epub ahead of print].

18. Lulu X, Kang H, Xu Q, Chen MJ, Liao Y, Thiyagarajan M, et al. (2013) Sleep drives metabolite clearance from the adult brain. *Science* 342: 373–377 doi: [10.1126/science.1241224](https://doi.org/10.1126/science.1241224) PMID: [24136970](https://pubmed.ncbi.nlm.nih.gov/24136970/)
19. Igarashi H, Tsujita M, Huber VJ, Kwee IL, Nakada T (2013) Inhibition of Aquaporin-4 significantly increases regional cerebral blood flow. *NeuroReport* 24: 324–328 doi: [10.1097/WNR.0b013e32835fc827](https://doi.org/10.1097/WNR.0b013e32835fc827) PMID: [23462267](https://pubmed.ncbi.nlm.nih.gov/23462267/)
20. Dolman D, Drndarski S, Abbott NJ, Rattray M (2005) Induction of aquaporin 1 but not aquaporin 4 messenger RNA in rat primary brain microvessel endothelial cells in culture. *J Neurochem* 93: 825–833 PMID: [15857386](https://pubmed.ncbi.nlm.nih.gov/15857386/)
21. Huber VJ, Tsujita M, Nakada T (2012) Aquaporins in drug discovery and pharmacotherapy. *Mol Aspects Med* 33: 691–703 doi: [10.1016/j.mam.2012.01.002](https://doi.org/10.1016/j.mam.2012.01.002) PMID: [22293138](https://pubmed.ncbi.nlm.nih.gov/22293138/)
22. Parihar MS, Brewer GJ (2010) Amyloid- β as a modulator of synaptic plasticity. *J Alzheimer's Dis* 22: 741–763
23. Wang Y-J, Zhou H-D, Zhou X-F (2006) Clearance of amyloid-beta in Alzheimer's disease: progress, problems and perspectives. *Drug Discovery Today* 11:931–938 PMID: [16997144](https://pubmed.ncbi.nlm.nih.gov/16997144/)
24. Muthuraj B, Hussaina S, Iyer PK (2013) A rapid and sensitive detection of ferritin at a nanomolar level and disruption of amyloid β fibrils using fluorescent conjugated polymer. *Polym Chem* 4:5096–5107
25. Deane R, Bell RD, Sagare A, Zlokovic BV (2009) Clearance of Amyloid- β peptide across the blood-brain barrier: Implication for therapies in Alzheimer's disease. *CNS Neurol Disord Drug Targets* 8:16–30 PMID: [19275634](https://pubmed.ncbi.nlm.nih.gov/19275634/)
26. Rauch SM, Huen K, Miller MC, Chaudry H, Lau M, Sanes JR, et al. (2011) Changes in brain β -amyloid deposition and aquaporin 4 levels in response to altered agrin expression in mice. *J Neuropathol Exp Neurol* 70: 1124–1137 doi: [10.1097/NEN.0b013e31823b0b12](https://doi.org/10.1097/NEN.0b013e31823b0b12) PMID: [22082664](https://pubmed.ncbi.nlm.nih.gov/22082664/)

The Molecular Mechanisms of Neural Flow Coupling: A New Concept

Tsutomu Nakada

From the Center for Integrated Human Brain Science, Brain Research Institute, University of Niigata, Niigata, Japan.

ABSTRACT

The phenomenon known as neural flow coupling (NFC) occurs at the capillary level where there are no known pressure controlling structures. Recent developments in advanced magnetic resonance imaging technologies have made possible in vivo direct investigations of water physiology that have shed new insight on the water dynamics of the cortical pericapillary space and their complex functionality in relation to NFC. Neural activities initiate a chain of events that ultimately affect NFC. First, neural activities generate extracellular acidification. Extracellular acidosis in turn produces inhibition of aquaporin-4 (AQP-4) located at the end feet of pericapillary astrocytes, the water channel which regulates water influx into the pericapillary space and, hence, interstitial flow. Reduction of pericapillary water pressure results in a negative balance between pericapillary and intraluminal capillary pressure, allowing for capillary caliber expansion. Proton permeability through the tight junctions of the blood brain barrier is significantly high owing to the Grotthuss proton “tunneling” mechanism and, therefore, carbonic anhydrase (CA) type IV (CA-IV) anchored to the luminal surface of brain capillaries functions as scavenger of extracellular protons. CA-IV inhibition by acetazolamide or carbon dioxide results in the accumulation of extracellular protons, causing AQP-4 inhibition and a secondary increase in rCBF.

Keywords: neuro flow coupling, aquaporin 4, interstitial flow, protons, neural activation.

Acceptance: Received December 10, 2014. Accepted for publication December 10, 2014.

Correspondence: Address correspondence to Tsutomu Nakada, MD, PhD, FAAN, FANA, Center for Integrated Human Brain Science, Brain Research Institute, University of Niigata, 1-757 Asahimachi, Niigata, 951-8585, Japan. E-mail: tnakada@bri.niigata-u.ac.jp.

J Neuroimaging 2015;25:861-865.

DOI: 10.1111/jon.12219

Introduction

Recent studies have shown that the classic circulation model of cerebrospinal fluid (CSF) is incomplete.¹ Production of CSF is not only dependent on choroid plexus but also on water flux in the pericapillary (Virchow Robin) space.^{2,3} Historically, CSF flow through the pericapillary space is known as interstitial flow, and is considered to play a role equivalent to the systemic lymphatic system.⁴⁻¹⁰ Advancements in modern magnetic resonance imaging (MRI) technologies have allowed for the *noninvasive* investigation of water flow in vivo. These studies revealed that water dynamics of the pericapillary space, ie, interstitial flow, is controlled by aquaporin-4 (AQP-4), the main subset of the aquaporin water channel family in the brain.¹¹⁻¹³ It has also been demonstrated that inhibition of AQP-4 is strongly coupled with an increase in regional cerebral blood flow (rCBF).¹⁴ These observations have led to a better understanding of the architectural significance and functionality of the cerebrovascular system.^{15,16} This article is a concise review of the modern concept of neural flow coupling (NFC) and its relationship to water dynamics in the pericapillary space.^{5-10,16}

Cerebral Autoregulation: Upstream Control

Cerebral autoregulation signifies an intrinsic ability of the cerebral vasculature to maintain cerebral blood flow at a relatively constant rate of approximately 50 ml per 100 g brain tissue per minute in the face of blood pressure changes.¹⁷⁻²²

Autoregulation generally functions between mean blood pressures of 60 to 150 mmHg. It is maintained in parasymphatically and/or sympathetically denervated animals,²¹ and the system is independent from extrinsic neural control. Instead, intrinsic neural nitric oxide (NO) control²² and release of vasoactive substrates by the brain are believed to play essential roles in maintaining constant cerebral perfusion.^{19,20} Perfusion is held constant by means of the cerebral vasculature smooth muscle that constricts and dilates in response to elevated and decreased systemic pressure, respectively.¹⁷⁻²² Although this “upstream” control of inflow pressure appears to be rather straightforward, the physiologic mechanisms underlying NFC, neural activity-associated rCBF increase, were until now poorly understood.

Virchow Robin Space and Interstitial Flow: Cerebral Lymphatic Equivalent

Fluid-filled canals surrounding perforating arteries and veins in the parenchyma of the brain were recognized in early modern medicine and described in detail by Rudolph Virchow and Charles Philippe Robin.^{23,24} The space is commonly referred to as the Virchow Robin space. It is now clearly understood that the fluid in the Virchow Robin space constitutes interstitial flow that drains into the CSF system (Fig 1). Virchow Robin interstitial flow is believed to play a role similar to systemic lymphatics.²⁻¹⁰

The basic function of systemic lymphatics is drainage of cellular debris subjected to molecular scrutiny before returning

This is an open access article under the terms of the Creative Commons Attribution-NonCommercial License, which permits use, distribution and reproduction in any medium, provided the original work is properly cited and is not used for commercial purposes.

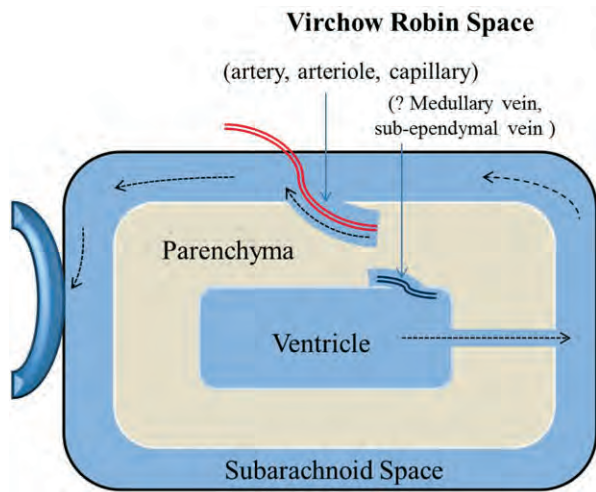


Fig 1. Virchow Robin space and interstitial flow. The ventricles and subarachnoid space represent the cerebrospinal fluid (CSF) space in the brain. The Virchow Robin space is a continuous canal surrounding penetrating vessels. Interstitial flow runs within the Virchow Robin space and drains into the subarachnoid space. Contrary to the classical concept of CSF flow, water CSF within the subarachnoid space is now believed to be dependent on interstitial flow in the Virchow Robin space. Although not as yet mainstream, the Virchow Robin space likely surrounds the medullary veins and subependymal veins as well. As shown in Figure 3, water influx from the systemic circulation into CSF is strongly dependent on interstitial flow in the Virchow Robin space through aquaporin-4 (AQP-4).

to the venous circulation. Although there is no conventional lymphatic system in the brain, interstitial flow of the Virchow Robin space constitutes its equivalent, and plays an essential role in clearing toxic proteins from brain parenchyma. Interstitial flow, and, hence, CSF circulation, eventually drains into the venous system through the cerebral dural sinuses (Pacchionian bodies), the latter playing a role similar to the thoracic duct of the systemic lymphatic system.

An important and intriguing example of interstitial flow protein clearance is β -amyloid clearance.^{3,5,7,8,14-16} β -amyloid is essential for synaptic formation.²⁵ Nonetheless, excess β -amyloid can result in aggregation of the protein and senile plaque formation. Drainage of β -amyloid by interstitial flow through the Virchow Robin space into CSF is likely critical for maintaining proper homeostasis of β -amyloid production and clearance. The role of prealbumin, abundant in CSF, as β -amyloid chaperon and in preventing β -amyloid's natural tendency to plaque formation, further supports the β -amyloid clearance hypothesis.²⁶

Pericapillary Water Dynamics and AQP-4

The aquaporin family is a large collection of integral membrane proteins that enable the movement of water across biological membranes. Three isoforms, namely AQP-1, AQP-4, and AQP-9, have been identified in brain in vivo. Expression of AQP-1 within CNS capillaries is actively suppressed, and AQP-1 in the brain is uniquely found in the choroid plexus epithelium. AQP-9 is only scarcely expressed in the CNS and is considered to have no significant role.^{12,27} By contrast, AQP-4 is expressed abundantly in the brain and has a specific distribution: the subpial and perivascular endfeet of astrocytes.^{2,10-14}

Active suppression of AQP-1 expression in brain capillaries is essential for proper maintenance of the blood brain barrier, preventing excessive movement of water across capillary walls.^{27,28} Active water influx into the CSF system from the blood stream has been shown to be regulated by AQP-4, not AQP-1, indicating that interstitial flow plays an important role in CSF dynamics.²

As cerebral equivalent of the systemic lymphatic system, interstitial flow dysfunction can be expected to result in reduction of β -amyloid clearance. Indeed, senile plaque bearing transgenic mice showed significant decline of water influx into the CSF system, to the extent similar to that found in AQP-4 knockout mice.²⁹ Positron emission tomography studies in AD patients have shown virtually identical results.¹⁴

NFC and rCBF

Increased rCBF associated with brain activation is a well-recognized phenomenon that is known as NFC. Since this is a micro-, rather than macroenvironmental event occurring within an area limited to 250 μm around the site of neural activity, the regulatory mechanism for NFC should be within the capillaries.³⁰

Considering blood flow to be steady, laminar flow within a long cylindrical pipe (Fig 2), the Hagen-Poiseuille equation gives volumetric blood flow, Φ , as

$$\Phi = \frac{\pi}{8\eta} \frac{\Delta P}{L} R^4$$

where ΔP is pressure loss (differences in inflow and outflow pressure), L is the length of the vessel tube, η is blood viscosity, and R is the radius of the vessel.³¹

Given that steady inflow pressure is rigorously controlled by upstream arterial autoregulation^{17,18} and constant venous pressure, under physiological conditions, cerebral blood flow is virtually determined by the radius of the vessel and increases parallel to its fourth power

$$\Phi \sim R^4$$

The relationship implies that even small changes in capillary caliber have significant effects on rCBF.

Capillaries are devoid of muscle and, hence, are not under neural control. The perforating vessels of the cerebral cortex are surrounded by a fluid-filled perivascular (Virchow Robin) space. At the capillary level, fluid pressure within the vessel lumen is directly opposed by pericapillary fluid pressure. Therefore, the parameter that determines capillary caliber is the pressure balance between luminal (intracapillary) and outer (pericapillary) fluid pressures. Since intracapillary pressure reflects the inner pressure of arterioles, and is therefore a function of upstream arterial autoregulation,^{17,18} it is the fluid pressure of the pericapillary space that inversely determines cerebral capillary caliber changes and, hence, rCBF, as follows:

$$\Phi \sim R^4 \sim 1/P_{\text{peri-capillary}}$$

AQP-4 controls the water dynamics of the pericapillary space in the brain.^{2,10,14} Therefore, AQP-4 activities play a role in controlling rCBF. Simply put, under physiological conditions, rCBF correlates inversely to AQP-4 activities.

$$rCBF \sim 1/AQP4 \text{ activities}$$

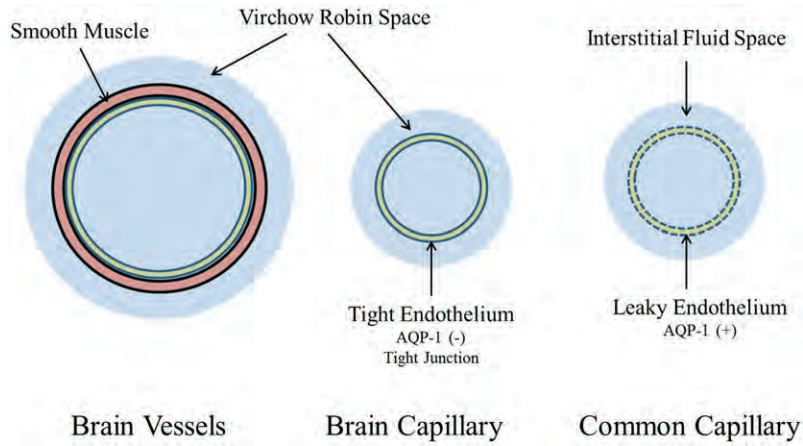


Fig 2. Vessel diameter is determined by tension of smooth muscle in artery, arteriole, venule, and vein (Brain Vessels). Capillaries are devoid of muscle and in capillaries with tight endothelium such as brain capillaries, capillary caliber is determined by the pressure balance between luminal and outer fluid pressures (Brain Capillary). For capillaries with leaky endothelium (Common Capillary), pressure balance is quickly equalized without capillary caliber changes.

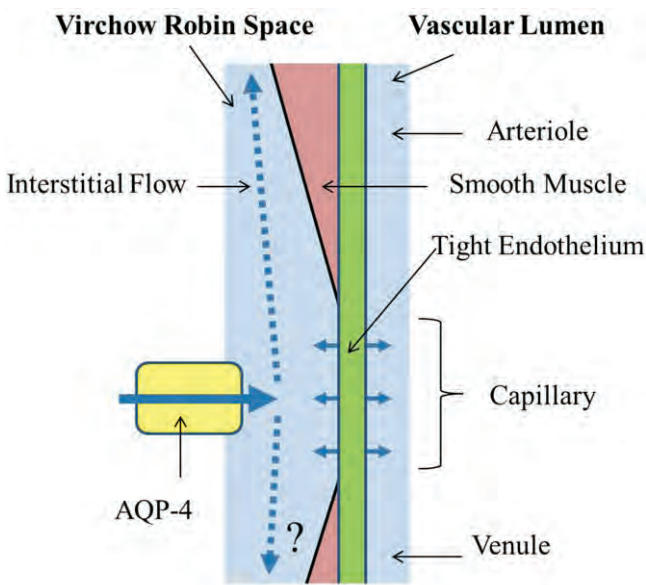


Fig 3. Pericapillary water dynamics. Water permeability of brain capillaries is restricted due to the tight endothelium, presence of tight junctions and active suppression of AQP-1. By contrast, significant water flow is present in the Virchow Robin space (interstitial flow) and is supported by active water inflow through AQP-4. Although it has not been clearly confirmed (?), interstitial flow may similarly be present along the medullary and subependymal veins.

Indeed, reduced AQP-4 activities by its inhibitor TGN-020 effectively increased rCBF in mice.¹³ Under physiological conditions, AQP-4 is believed to be inhibited by extracellular protons similar to other AQP isoforms.³² Therefore, rCBF is predicted to correlate with extracellular proton density (Figs 3 and 4).

$$rCBF \sim [H^+]_{extra}$$

The steps outlined above provide a fresh understanding of the underpinnings of NFC.

Neural Activities and Extracellular Acidosis

Since the original description by Urbanics et al³³ extracellular (interstitial) acidification associated with neural activities has been extensively studied by various investigators.³⁴⁻³⁶ Modern MRI technologies demonstrated unequivocally that regional neural activities in humans are accompanied by extracellular acidosis found in a virtually identical distribution as the neural activity-induced increase in rCBF detected by blood oxygenation level-dependent contrast.³⁷ Therefore, at least from a phenomenological stand point, neural activity-induced extracellular acidification plays a role in NFC. Although the precise underlying mechanisms remain to be elucidated, it appears clear that neural activity-induced interstitial acidification, and the resultant inhibition of AQP-4, is indeed a main mediator of neural activity-associated rCBF increase. Further support for this concept comes from the “Diamox effect.” Acetazolamide (Diamox) is a carbonic anhydrase (CA) inhibitor and a powerful agent for increasing rCBF. This “Diamox effect” is well known to be accompanied by interstitial acidosis in the brain.³⁸

Within the large CA family, CA type IV (CA-IV) represents the dominant CA in the cerebral cortex and is anchored to the luminal surface of cerebral capillaries.³⁹ It has been shown that interstitial CA activity in the brain is attributable to CA-IV.⁴⁰ The human NBC1 sodium bicarbonate cotransporter directly interacts with CA-IV. The tethering of intracellular CA type II (CA-II) and extracellular CA-IV in proximity to the NBC1 HCO₃⁻ transport site maximizes the transmembrane HCO₃⁻ gradient local to NBC1 and thereby activates the transport rate.⁴¹

Since proton permeability through the tight junctions is significantly higher than for other small molecules, owing to the Grothuss proton tunneling mechanism,⁴² capillary CA-IV with NBC1 and CA-II effectively function as scavenger of extracellular protons generated by neural activation (Fig 5). CA inhibition by acetazolamide or excess of carbon dioxide (CO₂) in capillary blood results in accumulation of extracellular protons which in turn inhibit water flux through AQP-4. The resultant negative pressure relation with respect to intraluminal capillary pressure affects capillary dilatation and an increase in rCBF.

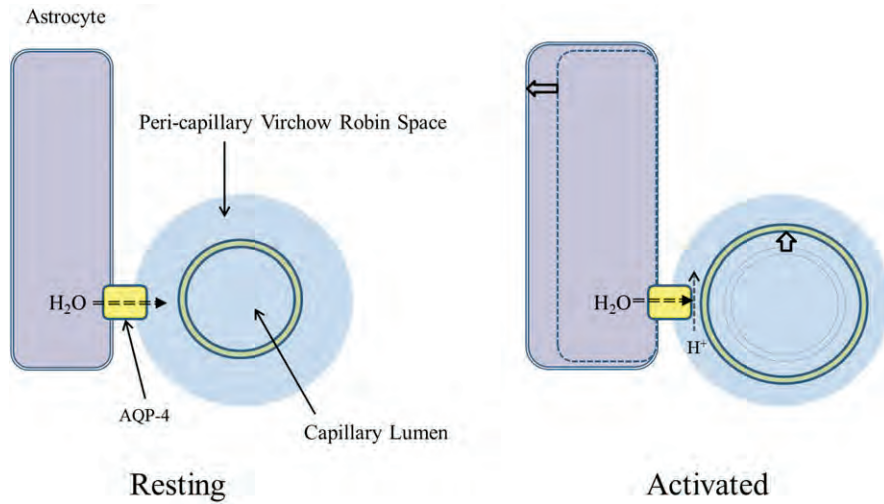


Fig 4. Neural activation. Neural activation produces extracellular acidification accompanied by increase in rCBF and astrocyte swelling. Proton inhibition of AQP-4 results in a reduction of water flow from astrocytes into the pericapillary Virchow Robin space, astrocyte swelling and capillary expansion due to reduction of pericapillary fluid pressure.

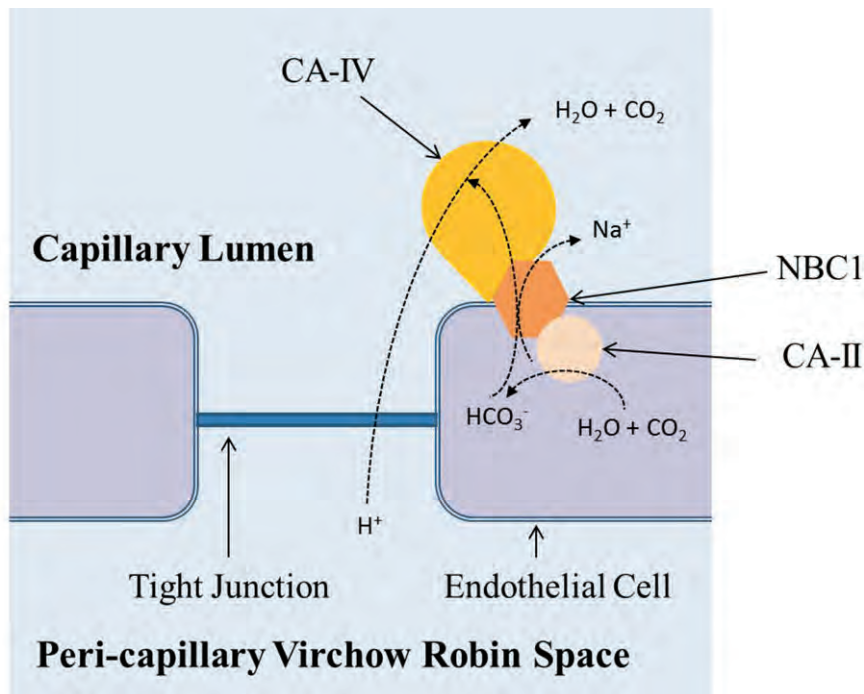


Fig 5. CA-IV system. Complex of CA-IV anchored to luminal surface of cerebral capillary, human NBC1 sodium bicarbonate cotransporter and intracellular CA-II. Their proximity maximizes the transmembrane HCO_3^- gradient local to NBC1 and thereby activates the transport rate. Because of the high proton permeability through tight junctions, capillary CA-IV with NBC1 and CA-II effectively function as scavenger of extracellular protons generated by neural activation. CA inhibition by acetazolamide or excess of CO_2 in capillary blood results in accumulation of extracellular protons.

Summary: A New Concept

Technological advancements, especially those in the field of MRI, have led to a new level of understanding of the physiologic underpinnings of neural activation-induced rCBF increase, a phenomenon known as NFC. The main player mediating NFC is the proton. Neural activities produce interstitial acidification. Excess protons inhibit AQP-4 activities in the pericapillary Virchow Robin space, resulting in a reduction in the pericapillary pressure. The negative balance between

pericapillary and intraluminal capillary pressure induces dilatation of capillaries and an increase in rCBF. Acetazolamide or excess CO_2 blocks active clearance of interstitial protons which are ordinarily highly permeable through the tight junctions and, similar to neural activities, causes interstitial acidification and an increase in rCBF.

The precise molecular mechanism of extracellular acidification associated with neural activities remains to be elucidated. Such acidification has been shown to be associated with

intracellular alkalization of astrocytes.³⁶ Active proton extrusion by astrocytes appears to be the most attractive explanation.^{14,36} The functional significance of NFC has been linked to elimination of heat production brought about by neural activities. A heat-sensitive voltage-gated proton channel similar to neutrophil Hv1 may play a role, although much remains to be investigated.^{14,43}

The work was supported by grants from the Ministry of Education, Culture, Sports, Science, and Technology (Japan).

References

- Oresković D, Klarica M. The formation of cerebrospinal fluid: nearly a hundred years of interpretations and misinterpretations. *Brain Res Rev* 2010;64:241-62.
- Igarashi H, Tsujita M, Kwee IL, et al. Water influx into Cerebrospinal fluid (CSF) is primarily controlled by aquaporin-4, not by aquaporin-1: O-17 JJVCPE MRI study in knockout mice. *Neuroreport* 2014;25:39-43.
- Iliff JJ, Wang M, Liao Y, et al. A paravascular pathway facilitates CSF flow through the brain parenchyma and the clearance of interstitial solutes, including amyloid. *Sci Transl Med* 2012;4:147ra111.
- Esiri MM, Gay D. Immunological and neuropathological significance of the Virchow-Robin space. *J Neurol Sci* 1990;100:3-8.
- Weller RO. Pathology of cerebrospinal fluid and interstitial fluid of the CNS: significance for Alzheimer disease, prion disorders and multiple sclerosis. *J Neuropathol Exp Neurol* 1998;57:885-94.
- Johnston M, Papaiconomou C. Cerebrospinal fluid transport: a lymphatic perspective. *News Physiol Sci* 2002;17:227-30.
- Abbott NJ. Evidence for bulk flow of brain interstitial fluid: significance for physiology and pathology. *Neurochem Int* 2004;45:545-52.
- Weller RO, Djuanda E, Yow HY, et al. Lymphatic drainage of the brain and the pathophysiology of neurological disease. *Acta Neuropathol* 2009;117:1-14.
- Weller RO, Kida S, Zhang ET. Pathways of fluid drainage from the brain – morphological aspects and immunological significance in rat and man. *Brain Pathol* 1992;2:277-84.
- Haj-Yasein NN, Jensen V, Østby I, et al. Aquaporin-4 regulates extracellular space volume dynamics during high-frequency synaptic stimulation: a gene deletion study in mouse hippocampus. *Glia* 2012;60:867-74.
- Kitaura H, Tsujita M, Huber VJ, et al. Activity-dependent glial swelling is impaired in aquaporin-4 knockout mice. *Neurosci Res* 2009;64:208-12.
- Huber VJ, Tsujita M, Nakada T. Aquaporins in drug discovery and pharmacotherapy. *Mol Aspects Med* 2012;33:691-703.
- Igarashi H, Tsujita M, Huber VJ, et al. Inhibition of Aquaporin-4 significantly increases regional cerebral blood flow. *NeuroReport* 2013;24:324-8.
- Nakada T. Virchow-Robin space and aquaporin-4: new insights on an old friend. *Croat Med J* 2014;55:328-36.
- Lulu X, Kang H, Xu Q, et al. Sleep drives metabolite clearance from the adult brain. *Science* 2013;342:373-7.
- Nakada T, Igarashi H, Suzuki Y, et al. Alzheimer patients show significant disturbance in water influx into CSF space strongly supporting β -amyloid clearance hypothesis. *American Academy of Neurology Annual Meeting* 2014;S58.001.
- Paulson OB, Strandgaard S, Edvinsson L. Cerebral autoregulation. *Cerebrovasc Brain Metab Rev* 1990;2:161-92.
- Heistad DD, Kontos HA. In: Berne RM, Sperelakis N, eds. *Handbook of Physiology. Chapter: The Cardiovascular System III*. Bethesda, MD: American Physiological Society; 1979:137-82.
- Mellander S. Functional aspects of myogenic vascular control. *J Hypertens* 1989;7:S21-30.
- Osol G, Brekke JF, McElroy-Yaggy K, et al. Myogenic tone, reactivity, and forced dilatation: a three-phase model of in vitro arterial myogenic behavior. *Am J Physiol Heart Circ Physiol* 2002;283:H2260-7.
- Busija EW, Heistad DD. Factors involved in the physiological regulation of the cerebral circulation. *Rev Physiol Biochem Pharmacol* 1984;101:161-211.
- Talman WT, Nitschke Dragon D. Neuronal nitric oxide mediates cerebral vasodilatation during acute hypertension. *Brain Res* 2007;1139:126-32.
- Virchow R. Ueber die Erweiterung kleinerer Gefaesse. *Arch Pathol Anat Physiol Klin Med* 1851;3:427-62.
- Robin C. Recherches sur quelques particularites de la structure des capillaires de l'encephale. *J Physiol Homme Animaux* 1859;2:537-48.
- Parihar MS, Brewer GJ. Amyloid- β as a modulator of synaptic plasticity. *J Alzheimers Dis* 2010;22:741-63.
- Li X, Buxbaum JN. Transthyretin and the brain re-visited: is neuronal synthesis of transthyretin protective in Alzheimer's disease? *Neurodegeneration* 2011;6:79.
- Nielsen S, Smith BL, Christensen EI, et al. Distribution of the aquaporin CHIP in secretory and resorptive epithelia and capillary endothelia. *Proc Natl Acad Sci USA* 1993;90:7275-9.
- Dolman D, Drndarski S, Abbott NJ, et al. Induction of aquaporin 1 but not aquaporin 4 messenger RNA in rat primary brain microvessel endothelial cells in culture. *J Neurochem* 2005;93:825-33.
- Igarashi H, Suzuki Y, Kwee IL, et al. Water influx into cerebrospinal fluid is significantly reduced in senile plaque bearing transgenic mice, supporting β -amyloid clearance hypothesis of Alzheimer disease. *Neurological Res* 2014;36:1094-8.
- Silver IA. Cellular microenvironment in relation to local blood flow. In: Elliott K, O'Connor M, eds. *Ciba Foundation Symposium 56 – Cerebral Vascular Smooth Muscle and Its Control*. Chichester, UK: John Wiley & Sons, 2008: Ch. 5.
- Faber TE. *Fluid Dynamics for Physicists*. Cambridge: Cambridge University Press, 1995.
- Frick A, Järvä M, Törnroth-Horsefield S. Structural basis for pH gating of plant aquaporins. *FEBS Letters* 2013;587:989-93.
- Urbanics R, Leniger-Follert E, Lübbers DW. Time course of changes of extracellular H⁺ and K⁺ activities during and after direct electrical stimulation of the brain cortex. *Pfluegers Arch* 1978;378:47-53.
- Kraig RP, Ferreira-Filho CR, Nicholson C. Alkaline and acid transients in cerebellar microenvironment. *J Neurophysiol* 1983;49:831-51.
- Chester M. Regulation and modulation of pH in the brain. *Physiol Rev* 2003;83:1183-221.
- Chester M, Kraig RP. Intracellular pH transients of mammalian astrocytes. *J Neurosci* 1989;9:2011-9.
- Magnotta VA, Heo HY, Dlouhy BJ, et al. Detecting activity-evoked pH changes in human brain. *Proc Natl Acad Sci* 2012;109:8270-3.
- Vorstrup S, Henriksen L, Paulson OB. Effect of acetazolamide on cerebral blood flow and cerebral metabolic rate for oxygen. *J Clin Invest* 1984;74:1634-9.
- Ghandour MS, Langley OK, Zhu XL, et al. Carbonic anhydrase IV on brain capillary endothelial cells: a marker associated with the blood-brain barrier. *Proc Natl Acad Sci USA* 1992;89:6823-7.
- Tong C-K, Brion LP, Suarez C, et al. Interstitial carbonic anhydrase (CA) activity in brain is attributable to membrane-bound CA type IV. *J Neurosci* 2000;20:8247-53.
- Alvarez BV, Loisel FB, Supuran CT, et al. Direct extracellular interaction between carbonic anhydrase IV and the human NBC1 sodium/bicarbonate co-transporter. *Biochemist* 2003;42:12321-9.
- Angelow S, Kim KJ, Yu ASL. Claudin-8 modulates paracellular permeability to acid and basic ions in MDCK II cells. *J Physiol* 2006;571.1:15-26.
- Fujiwara Y, Kurokawa T, Takeshita K, et al. The cytoplasmic coiled-coil mediates cooperative gating temperature sensitivity in the voltage-gated H⁺ channel Hv1. *Nat Commun* 2012;3:816.

REVIEW

N-acetylaspartate Decrease in Acute Stage of Ischemic Stroke: A Perspective from Experimental and Clinical Studies

Hironaka IGARASHI^{1*}, Yuji SUZUKI¹, Vincent J. HUBER¹, Masahiro IDA²,
and Tsutomu NAKADA¹

¹*Center for Integrated Human Brain Science, Brain Research Institute, University of Niigata
1-757 Asahimachi-dori, Chuo-ku, Niigata City 951-8585, Japan*

²*Department of Radiology, Tokyo Metropolitan Ebara Hospital*

(Received March 25, 2014; Accepted July 16, 2014; published online December 15, 2014)

N-acetylaspartate (NAA) appears in a prominent peak in proton magnetic resonance spectroscopy (¹H-MRS) of the brain. Exhibition by NAA of time-dependent attenuation that reflects energy metabolism during the acute stage of cerebral ischemia makes this metabolite a unique biomarker for assessing ischemic stroke. Although magnetic resonance (MR) imaging is a powerful technique for inspecting the pathological changes that occur during ischemic stroke, biomarkers that directly reflect the drastic metabolic changes associated with acute-stage ischemia are strongly warranted for appropriate therapeutic decision-making in daily clinical settings. In this review, we provide a brief overview of NAA metabolism and focus on the use of attenuation in NAA as a means for assessing the pathophysiological changes that occur during the acute stage of ischemic stroke.

Keywords: *brain, ischemia, magnetic resonance spectroscopy, N-acetylaspartate*

Introduction

N-acetylaspartate (NAA) is the acetylated derivative of L-aspartate¹ and the second most abundant amino acid-related metabolite in the mammalian brain after glutamate.^{2,3} Although the reason for its abundance in the brain remains to be elucidated, NAA exists mainly in neurons at sufficient concentrations to be visible in proton magnetic resonance spectra (¹H-MRS) of normal brain, where the methyl group of NAA shows a prominent peak at 2.01 ppm (Fig. 1). Furthermore, NAA levels attenuate in many of the pathological states relating to impaired cellular metabolism and neuronal loss. Pathological conditions characterized by acute failure of energy metabolism, i.e., ischemic stroke, hypoxia, and traumatic brain injury, exhibit drastic NAA attenuation from within minutes to hours following the specific initiating event.^{4,5} This attenuation during the acute stage may initially involve a deterioration of NAA synthesis, acceleration of NAA catabolism, or their combination. These pathologic conditions often lead

to a combination of brain tissue necrosis and neuronal loss within several days to a week following the ischemic event unless energy metabolism is resumed within the first several hours.

Ischemic stroke has been the most widely studied of pathological conditions that exhibit acute NAA attenuation in both animal models and humans, primarily because of its high worldwide incidence. ¹H-MRS is useful for visualizing the progression of those pathological conditions following severely compromised cerebral blood flow resulting from vascular occlusion. Lactate appears within minutes of the occlusion due to an acceleration of anaerobic glycolysis, which compensates for hampered mitochondrial oxidation. Because NAA synthesis is adenosine triphosphate (ATP)-dependent (energy-dependent),⁶ impaired energy availability initiates a continuous decline in levels of NAA, the rate of which depends in part on severity, within hours of the ischemic event. Although magnetic resonance (MR) imaging, especially diffusion-weighted images (DWI) and perfusion images (PI), is a powerful technique for visualizing pathological changes *in vivo* that can be applied to ischemic stroke, we believe observation of biomarkers that directly reflect

*Corresponding author, Phone: +81-25-227-0676, Fax: +81-25-227-0822, E-mail: higara@bri.niigata-u.ac.jp

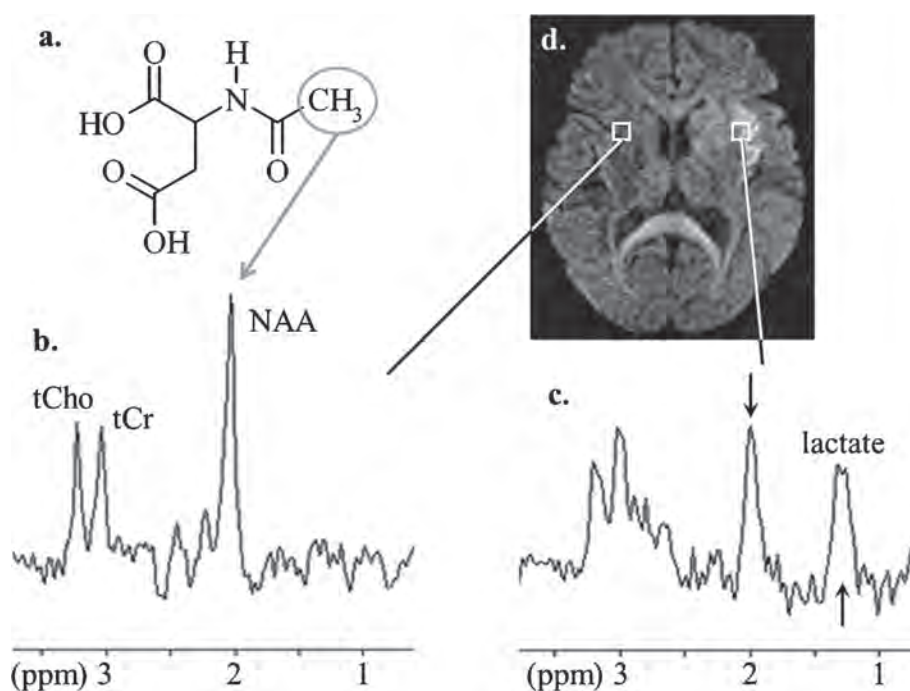


Fig. 1. Chemical structure of N-acetylaspartate (NAA) and representative proton magnetic resonance spectroscopy (^1H -MRS). The methyl group of NAA (a) shows the most prominent singlet peak at 2.01 ppm in ^1H -MRS of normal brain (b). NAA reduces and lactate appears (c) in the acute ischemic lesion delineated by diffusion-weighted imaging (DWI) (d). tCHO, total choline compounds; tCr, sum of creatine and phosphocreatine.

metabolic changes during the acute stage will be highly valuable for making the most appropriate therapeutic decisions. In this review, we present a brief overview of NAA metabolism with subsequent focus on the use of NAA visualization to assess pathophysiological changes during the acute stage of ischemic stroke.

Distribution, Biochemistry, and Functions

Distribution of NAA

Human studies using MRS show a relatively homogenous distribution of NAA throughout the brain, with slightly higher concentrations found in the occipital cortex, thalamus, and cerebellar hemisphere.^{7,8} These results agree with those of previous immunohistochemical studies using rodent brain.⁹ Additional immunohistochemical studies have demonstrated the presence of NAA predominately in neuronal cell bodies and their processes.^{4,9,10} Further confirmation of this distribution was obtained with high performance liquid chromatography (HPLC) and high resolution nuclear magnetic resonance (NMR) studies.^{11–13} Oligodendrocyte type-2 astrocyte progenitor cells (O-2A progenitors, NG2 cells)¹⁴ were also found to express NAA at easily detectable levels.^{12,13} NG2 cells in postnatal brain

have the potential to differentiate into oligodendroglia in gray and white matter¹⁵ and have been recently confirmed to make up about 5% of all cells in the adult central nervous system (CNS).¹⁶ Although the expression of NAA by NG2 cells in the adult brain has not been confirmed, some caution is warranted in interpreting changes in NAA concentration as a pure neuronal marker.

Tricellular compartment metabolism of NAA

NAA and its glutamate dipeptide derivative, N-acetylaspartylglutamate (NAAG), which supposedly works as a cotransmitter with glutamate and γ -aminobutyric acid (GABA),¹⁷ form the unique tricellular compartment metabolism involving neurons, oligodendrocytes, and astrocytes (Fig. 2).¹⁸ Both NAA and NAAG are synthesized in the neuron, but neither are catabolized in the neuron itself. NAA is either released from neurons or is transported to oligodendrocytes, where it is metabolized into acetate and aspartate by aspartoacylase (ASPA).¹⁹ NAA-derived acetate in the oligodendrocytes is converted to acetyl coenzyme A (acetyl CoA) with acetyl CoA synthetase, which serves primarily as a precursor in myelin lipid synthesis.^{20,21} NAAG is released from the axon terminal in response to neuronal activity, and most is subsequently hydrolyzed

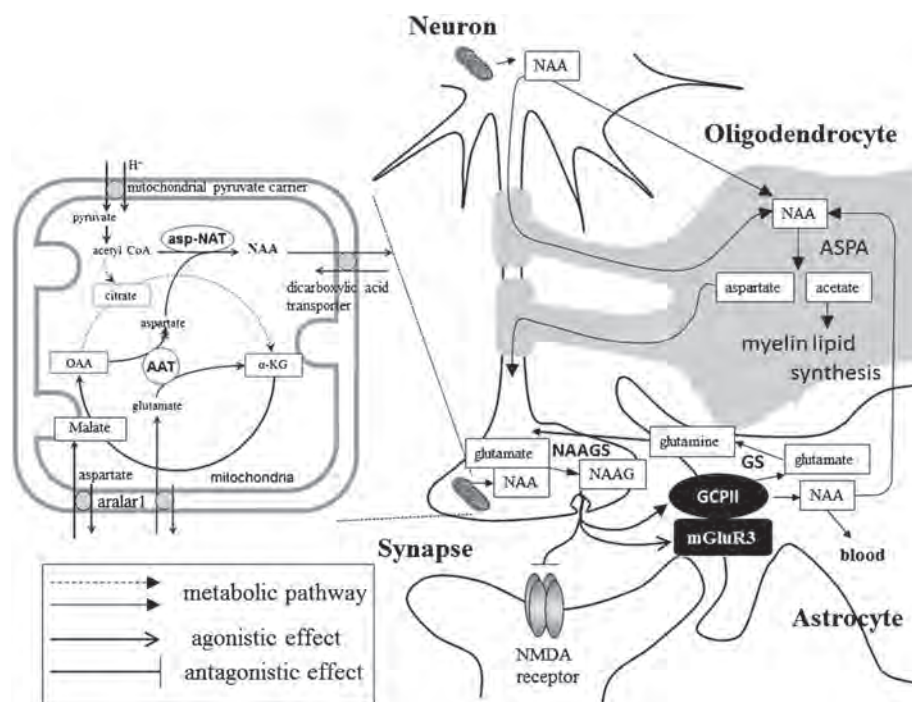


Fig. 2. Tricompartiment metabolism of N-acetylaspartate (NAA) and N-acetyl-aspartylglutamate synthetase (NAAG). Both NAA and NAAG are synthesized in neurons. NAA is mainly released from neurons or transported to oligodendrocytes, where it is metabolized into acetate and aspartate by aspartoacylase. NAA-derived acetate in oligodendrocytes is mainly used as a precursor of myelin lipid synthesis. NAAG is released from axonal terminals in concordance with neuronal activity, and most of them are hydrolyzed into NAA and glutamate with glutamate carboxypeptidase II (GCPII) at the surface of astrocytes. AAT, aspartate aminotransferase; acetyl CoA, acetyl coenzyme A; α -KG, α -keto glutarate; APSA, aspartoacylase; Asp-NAT, L-aspartate N-acetyltransferase; GS, glutamine synthetase; OAA, oxaloacetate.

into NAA and glutamate at the surface of the astrocyte membrane by glutamate carboxypeptidase II (GCPII).²²

Synthesis, catabolism, and functions

The majority of NAA is thought to be synthesized in neuronal mitochondria²³ from aspartate and acetyl-CoA.^{24,25} Aspartate is converted in the mitochondria from malate, which enters the mitochondria through the mitochondrial transporter, aralar1.²⁶ The conversion of malate to aspartate occurs via aspartate aminotransferase (AAT) and part of the tricarboxylic acid (TCA) cycle (Fig. 2).²⁷ Finally, NAA is synthesized by membrane-bound L-aspartate N-acetyltransferase (Asp-NAT)²⁸ in an energy-dependent manner.^{6,12,29} Partly because of that energy dependence and the involvement of the TCA cycle in the conversion of malate to aspartate in mitochondria, NAA biosynthesis is very susceptible to energy failure.⁶ Once synthesized, NAA is transported to the cytosol by the dicarboxylic acid transporter.³⁰ A recent report identified the synthesis of a small

but distinct amount of NAA in cytosol.^{31,32} In this secondary pathway, Asp-NAT in the cytosol is thought to utilize aspartate sequestered from the mitochondria through aralar1.³³ However, the significance of the 2 distinct NAA synthetic pathways remains unknown.

NAA synthesized in the neuron is transported to either the extracellular space (ECS) or oligodendroglia. Because it exists as a dianion at physiological pH, the nonspecific diffusion of NAA through the cell membrane is unlikely. No transporter of NAA has been identified, but Fujita and Ganapathy suggest that Na^+ /carboxylate cotransporter 3 (NaC3) is a likely candidate.³⁴ It has been estimated that approximately 5% of the total NAA in the CNS is excreted from the ECS into the blood presumably via putative NAA transporters in the astrocytes.³⁵

NAA is hydrolyzed by aspartoacylase, the distribution of which is restricted to oligodendrocytes.³⁶ Aspartoacylase activity is reported to increase in parallel with white matter myelination during development,³⁷ and NAA is hydrolyzed into aspartate

and acetate, the latter being an important component of myelin lipid. Therefore, it is believed that part of the NAA synthesized in the neuron serves as a source of building blocks for myelin synthesis in oligodendrocytes.^{20,21,38}

Other roles for NAA in the brain are still debated. However, there is evidence that NAA is important in maintaining the microenvironment of the brain parenchyma.⁴ Two tissues outside the CNS, peritoneal mast cells³⁹ and ocular lenses,⁴⁰ have been found to contain NAA, and in both examples, NAA appeared to play an important role in osmoregulation and the control of water distribution. Likewise, NAA is also thought to participate in controlling osmolality and water distribution in the CNS.⁴¹ In this context, Baslow claimed that NAA may be released from neurons in some controlled fashion, which can differ from that of neurotransmitters, and serve in intercellular signaling.¹⁹ A high concentration of NAA has also been considered to compensate for the anion deficit in the CNS.^{2,4} Nakada suggested that the negatively charged NAA in neuronal cytosol can facilitate passive diffusion of high energy phosphates from the mitochondria to the cell membrane to fulfill the high energy demands of neuronal cell membranes.^{42,43}

NAA Attenuation in Acute-stage Ischemic Stroke

Concept of experimental ischemic stroke

Experimental models of cerebral ischemia have been developed to assess pathophysiological changes resulting from ischemia. The universal feature of the various models is the interruption of cerebral blood flow that feeds a part of the brain, which, in turn, elicits a depletion of oxygen and glucose and disrupts tissue metabolism.⁴⁴ At present, rodent models are widely used because their preparation is convenient, and multiple means of analysis are available.⁴⁵

Rodent models of ischemia can be divided into 2 classes, global and focal. The global ischemia model is characterized by temporary pan-forebrain ischemia of relatively short duration, typically 5 to 30 min, that is induced by occlusion of the bilateral internal carotid arteries^{46,47} alone or with the simultaneous occlusion of the bilateral vertebral arteries.⁴⁸ This model elicits a profound ischemia of short duration over the forebrain, so it is considered to be a model of short-duration cardiac arrest or severe hypotension. Infarction is not the primary result of this insult, which instead leads within a week of the ischemic injury to patchy neuronal loss with several degrees of reactive gliosis in vulnera-

ble regions, such as the hippocampus, striatum and cortex.

Focal ischemia models are used to mimic clinical ischemic stroke. In these models, permanent (no reperfusion) or transient (reperfusion typically within several hours) ischemia are induced in a certain vascular territory, commonly that of the middle cerebral artery (MCA), by arterial occlusion using a silicon-coated suture, blood clot, or clipping. In this model, energy failure from severe blood cessation in the core of the circumscribed lesion (ischemic core) produces irreversible biological changes within a short time. Reduction of blood flow is relatively mild in the rim of the lesion, and that tissue can be salvaged if blood flow can be restored (reperfusion) within a few hours.⁴⁹ In this salvageable area, called the “penumbra” after the half-shaded area of an eclipse, blood flow is too low to maintain electric activity but remains sufficient to preserve the function of energy-dependent ion channels.⁵⁰ The term “penumbra” is now generally used to define ischemic but salvageable cerebral tissue that requires immediate reperfusion.⁵¹

MRS findings and gradual attenuation of NAA in the acute stage of ischemic stroke

Typical chronological changes visible by MRS during acute ischemic stroke have been identified in several animal studies^{52–55} and subsequently confirmed in human clinical studies.^{56–59} Typically, chronological changes of four MRS visible metabolites can be seen following cerebral ischemia, namely rise of lactate, and attenuations of NAA, creatine and phosphocreatine (Cr), and choline compounds (Cho). Lactate appears immediately after cerebral blood flow is compromised and usually reaches a concentration plateau within 24 hours depending on several factors, such as the severity of hypoperfusion and plasma glucose concentrations. Attenuation of NAA levels becomes evident within an hour and continues almost linearly during the first 24 hours (Fig. 3).^{54,56–59} After 24 hours, lactate tends to cover the entire topographical area of hypoperfusion, including the penumbra. Part of the “tissue at risk” can be identified as areas in which lactate is present but there is no attenuation of NAA (Fig. 3b).⁶⁰ Respective peaks caused by Cr and Cho begin to gradually fall after cell death begins, and tissue necrosis becomes obvious, typically several hours following ischemia.

The changes in relaxation affect the attenuations of metabolite peaks mainly in subacute to chronic stage of ischemia. In experimental study, van der Toorn and associates measured T_1 and T_2 of the metabolites and concluded that relaxations of NAA

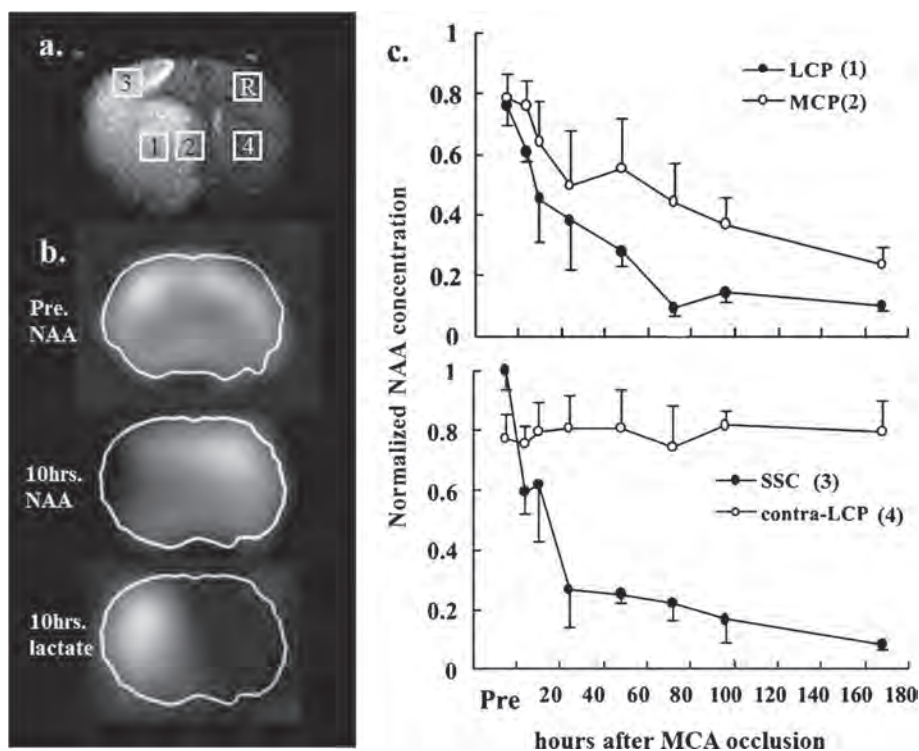


Fig. 3. Chronological changes in N-acetylaspartate (NAA) of rat brain with permanent focal ischemia. In a diffusion-weighted imaging (DWI)-delineated area of ischemia (a), NAA visually decreased on proton magnetic resonance spectroscopy (^1H -MRSI), and lactate appeared in the area at risk (b). NAA declined more steeply in the ischemic core (lateral caudo-putamen [LCP] and somatosensory cortex [SSC]) than the ischemic rim (MCS). MCP, medial caudo-putamen; R, reference area.

did not change within 24 hours after the induction of MCA occlusion in the ischemic core of the rat brain.⁶¹ These results agree with the clinical study which concluded that the T_2 of NAA decreased during the period between 5 and 20 days after the insult but did not change earlier.⁶²

Our laboratory confirmed a linear decrease in NAA levels within the ischemic core and rim in studies utilizing both rodent models and clinical cases.^{55,63} In both studies, no reperfusion was attempted at the point where MRS imaging (MRSI) was carried out. The observation of a steeper slope in the decline in NAA in the core than the penumbra (Figs. 3, 4) indicates that the rate of NAA attenuation in acute-stage ischemia depends in part on the severity of hypoperfusion. Some of the data in the human study deviated lower (open circle, Fig. 4), and most of those cases demonstrated hyperglycemia (>120 mg/dL), which adversely affects metabolic deterioration⁶⁴ and stroke outcome.⁶⁵ Therefore, we undertook a partial correlation of the normalized NAA concentration, time from stroke onset, and initial plasma glucose concentration. That correlation revealed that both the amount of time elapsed from the ischemic event and the plasma

concentration of glucose in the ischemic core contributed to the rate of NAA decline (Fig. 4b). The reason NAA declines faster in response to hyperglycemia remains unknown. However, hyperglycemia is thought to facilitate the release of cytoplasmic amino acids and their derivatives into the ECS during ischemia,⁶⁶ thereby raising the intracellular concentration of calcium ions, which can, in turn, activate aspartosylase.⁶⁷ These mechanisms may affect the acceleration of NAA decline.

In our human study, the rate of NAA attenuation was calculated as $0.67 \mu\text{g}/\text{kg}/\text{h}$; this included compensation from the concentration of plasma glucose in the brain tissue, which was calculated with an NAA concentration of $9.2 \text{ mmol}/\text{g}$ (Fig. 2b) revealed by ^{13}C -MRS study in human.⁶⁸ The result was somewhat larger than the rate of NAA synthesis in normal adult human brain ($0.55 \mu\text{g}/\text{kg}/\text{h}$) calculated from a human ^{13}C NMR study that measured the turnover of NAA in brain tissue.^{42,68} These results imply the occurrence of either NAA catabolism or its excretion and cleavage products, namely aspartate and acetate, during ischemic stroke, even if NAA production has failed completely. The ^{13}C NMR study in rats demonstrated that NAA syn-

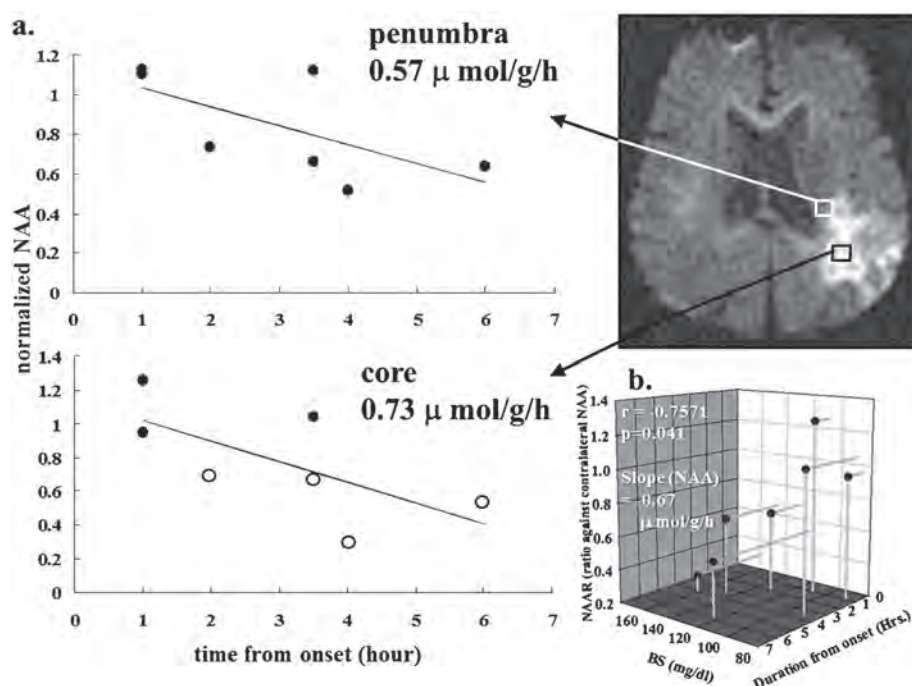


Fig. 4. Chronological changes in N-acetylaspartate (NAA) in clinical ischemic stroke. As observed in rat brain with permanent focal ischemia, NAA declines more steeply in the ischemic core than the ischemic rim (a). A closed circle shows the result from euglycemic cases (≤ 120 mg/dL), and an open circle denotes the results from hyperglycemic (> 120 mg/dL) cases in the ischemic core. NAA decline was partly determined with time and plasma glucose concentration in the ischemic core (b).

thesis continued within the ischemic core at 120 min after induction of the MCA occlusion, albeit at a significantly impaired level.⁶⁹ A massive NAA release into the ECS was observed in rat models of permanent focal ischemia, with the concentration of NAA in the ECS increasing to 10 times that of a normal rat. However, NAA was undetectable in the blood with ischemic stroke,⁷⁰ so the direct excretion of NAA into the residual blood flow within the ischemic core can be expected to play only a minor role on NAA attenuation in acute stage of ischemia. Furthermore, no rise in NAA levels were found in the CSF of rat models of focal ischemia^{71,72} despite its massive release into the ECS. These results suggest a previously unknown NAA catabolic pathway in brain tissue that is activated during ischemia. Indeed, complete global ischemia achieved by decapitation, in which there is a lack of residual blood flow, leads to a reciprocal accumulation of aspartate and acetate over NAA loss.⁷² Aspartacylase activated by Ca^{2+} accumulated in cytoplasm as a result of ischemia may play the dominant role in NAA catabolism in complete global ischemia.⁶⁸ Paradoxically, the levels of both aspartate and acetate decreased in the ischemic lesion during focal ischemia.^{72,73} One important difference between these 2

models of ischemia is the complete absence of blood flow in the global model and the maintenance of residual blood flow to the ischemic core of the focal model.⁷⁴ A massive amount of aspartate is also released into the ECS during ischemia.⁷⁵ Excretion of the aspartate from the ECS into the blood can occur through alanine-serine-cysteine transporter 2 (ASCT2) channels located on the basal membranes of the vascular epithelium, which are activated by ischemic acidosis.⁷⁶ Indeed, serum concentrations of aspartate were reported to rise during focal ischemia.⁷⁷ From these reports, we can ascertain that part of aspartate is released into residual blood flow from the CNS. Acetate may also be released into blood or further metabolized by surviving cells, possibly astrocytes that exclusively metabolize external acetate under normal physiological conditions.⁷⁸ Though the fate of acetate is unclear compared to that of aspartate, we confirmed that during focal ischemia, the NMR signal from acetate was detectable in the center of the ischemic core (Fig. 5a-c). In summary, attenuation of NAA during ischemic stroke can result from suppression of NAA synthesis, acceleration of NAA catabolism, excretion of NAA-related derivatives into blood, and further metabolism (Fig. 5d, e).

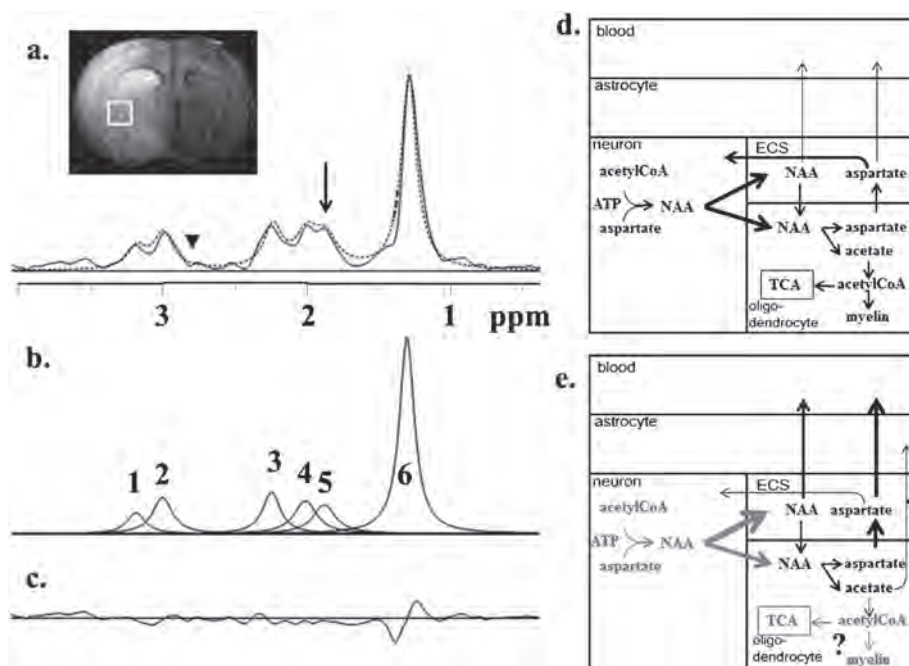


Fig. 5. Magnetic resonance spectroscopy (MRS) at 10 hours after induction of focal ischemia (a-c) and suspected metabolic state of N-acetylaspartate (NAA) and its derivatives (d,e). Proton MRS (¹H-MRS) (a, dashed line), fitted curve (a, solid line, and c) and fitted residual (d). An acetate peak was seen at 1.9 ppm (arrow), but a suspected aspartate peak (2.8 ppm) was absent (arrowhead). 1, total choline compounds (tCho); 2, creatine and phosphocreatine (Cr); 3, glutamate; 4, NAA; 5, acetate; 6, lactate. Reduction of NAA in ischemic stroke can result in the suppression of NAA synthesis, acceleration of NAA catabolism, release into blood of the derivatives, and further metabolism (d,e).

Association and Dissociation between NAA Attenuation and DWI Findings

Cross-sectional studies: topographical NAA concentration as a complement of DWI

Diffusion-weighted imaging is a powerful modality for visualizing focal ischemic lesions in acute ischemic stroke. It can be used to delineate the regional reduction of the apparent diffusion coefficient (ADC) of water, which can be calculated from several DWI images. Though energy failure from ischemia reduces both ADC and NAA, ADC is reduced primarily in the areas in which cellular structure is altered by Na⁺/K⁺ ATP pump failure, which may only reflect an indirect disruption of energy metabolism. On the other hand, a reduction of NAA directly reflects metabolic changes, specifically energy failure, in brain tissue during acute-stage ischemia. Based on that difference, we can expect NAA levels to reflect the condition of the ischemic area more sensibly than ADC. However, because NAA metabolism is comparatively slow, the delineation of the ischemic lesion based on NAA attenuation relating to metabolic energy failure lags behind the reduction of ADC. In clinical cases of

proximal MCA occlusion, Nicoli reported that within 7 hours from onset, MRSI could indicate a large heterogeneity in NAA concentration in ischemic areas showing even the lowest ADC values.⁷⁹ Moreover, some reports suggest a wide range of NAA concentrations, from 40 to more than 100% of the normal range, in acute-stage ischemic lesions having an unperturbed DWI.^{59,80} Although it is difficult at present to ascribe a threshold NAA concentration for making an accurate tissue prognosis, i.e., whether it will infarct or be salvageable, during the acute stages of ischemia, it has been suggested that salvageable areas might be characterized by the presence of lactate with no or only subtle NAA attenuation.⁸⁰ In cases with hemispheric transient ischemic attack (TIA), NAA was observed to attenuate about 10 to 15% in the acute stage, which recovered in 12 to 18 months after the incidents.⁸¹ Only the report of a case with occlusion of the brachiocephalic artery described the reversibility of NAA in the acute stage of ischemia, with the ratio of NAA to Cr attenuated 10% at the initial measurement normalized after recanalization.⁸² Though a larger study is warranted for confirmation, these reports suggest that NAA attenuation by less than 10

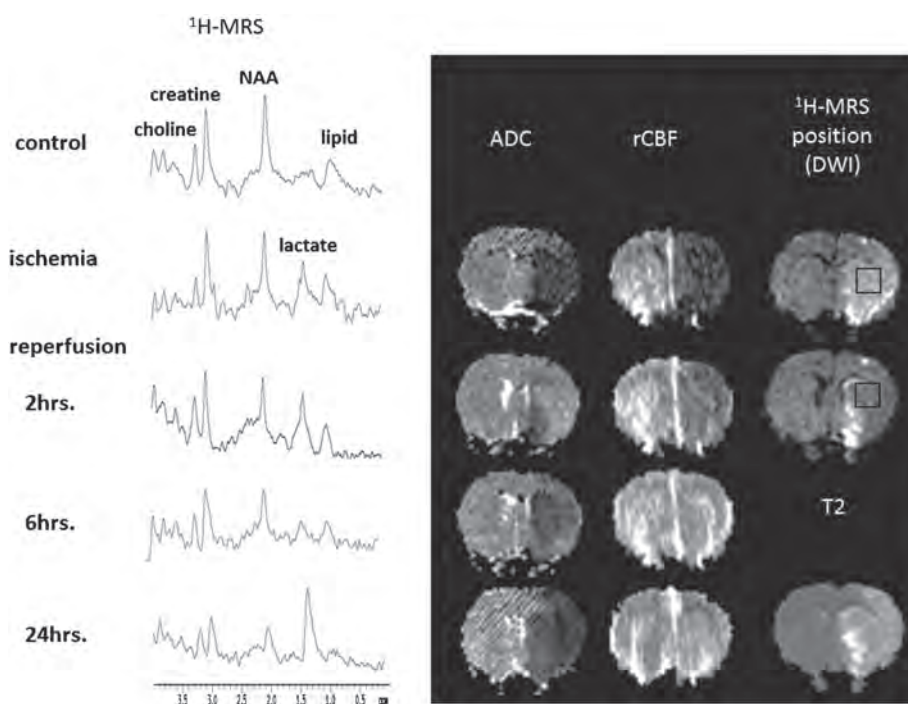


Fig. 6. Chronological changes of proton magnetic resonance spectroscopy (^1H -MRS), apparent diffusion coefficient (ADC) map, and regional cerebral blood flow (rCBF) map before, during, and after short-term focal ischemia.⁹² ADC restored at one hour after recirculation, but N-acetylaspartate (NAA) demonstrated continuous attenuation after the induction of ischemia. Open square delineates the region of interest for magnetic resonance spectroscopy (MRS).

to 15% may be reversible in the acute stage of cerebral ischemia.

Longitudinal studies: perpetual NAA attenuation against temporary restoration of ADC

NAA levels decline at an almost linear rate over time from the onset of ischemia. This time-dependent decline distinguishes NAA as a useful biomarker for the imaging of acute-stage ischemic stroke. Cvoro described a moderate correlation between the degree of NAA reduction and the time from onset.⁵⁹ Because the rate at which NAA levels decline is largely governed by the time from onset, residual blood flow and initial plasma glucose concentration, which are thought to be the most important factors determining the fate of ischemic tissue,⁸³ NAA levels can be used to predict the fate of tissue with an acute ischemic lesion independently. Combined DWI and PI studies may not be sufficient to predict tissue outcome successfully^{83,84} except in some limited situations.⁸⁵ Thus, a study combining DWI, PI, and MRSI can be expected to improve the prediction of tissue outcome, particularly given that NAA findings complement those of DWI and PI.⁸⁶

A representative situation in which dissociation between NAA and ADC is often observed is the case of transient ADC restoration following early

reperfusion in both experimental models^{87,88} and clinical^{89,90} settings. Following early reperfusion within a few hours of onset, DWI suggested resolution of the ischemia within several hours of reperfusion; however, the area re-emerged several hours later on DWI and became infarcted within 24 hours. We tested the chronological changes in NAA levels in a rat model of focal ischemia using 90-min MCA occlusion.⁹¹ Though ADC was restored to the normal range within one hour of reperfusion in the part of ischemic temporal cortex and lateral basal ganglia in which ischemic insult should be mild, NAA levels continued to show a decline in the same area (Fig. 6). The mechanism of NAA attenuation despite ADC resolution has not been solved in detail. However, one clue may be found in reports suggesting that energy restoration after recirculation could re-establish membrane potential (which is maintained by Na^+/K^+ ATP pump activity) to a marginally survivable level following ischemic insult and thereby normalize DWI. Nevertheless, energy production following reperfusion may not be sufficient to maintain other energy-dependent mechanisms, such as NAA synthesis, protein synthesis,⁹² and DNA repair via poly(ADP-ribose) polymerase (PARP),⁹³ at a level sufficient to ensure long-term cell survival.

Conclusion

Direct reflection of energy metabolism and near-linear time-dependency during acute-stage cerebral ischemia make NAA a unique biomarker for the clinical assessment of ischemic stroke. Despite the challenges remaining for the application of MRS(I) in the daily clinical setting, the levels of NAA with those of lactate measured in the CNS can provide one of the most promising biomarkers available for the assessment of pathophysiological changes that occur during acute-stage ischemic stroke.

Acknowledgements

This work was supported by grants from the Japanese Ministry of Education, Culture, Sports, Science, and Technology.

We would like to thank Professor Akiko Nishiyama, Department of Physiology and Neurobiology, University of Connecticut, for suggestive advice about NG2 cells.

References

1. Tallan HH, Moore S, Stein WH. N-acetyl-L-aspartic acid in brain. *J Biol Chem* 1956; 219:257–264.
2. Tallan HH. Studies on the distribution of N-acetyl-L-aspartic acid in brain. *J Biol Chem* 1957; 224:41–45.
3. Benarroch EE. N-acetylaspartate and N-acetylaspartylglutamate: neurobiology and clinical significance. *Neurology* 2008; 70:1353–1357.
4. Moffett JR, Ross B, Arun P, Madhavarao CN, Namboodiri AM. N-acetylaspartate in the CNS: from neurodiagnostics to neurobiology. *Prog Neurobiol* 2007; 81:89–131.
5. Duarte JM, Lei H, Mlynárik V, Gruetter R. The neurochemical profile quantified by *in vivo* ^1H NMR spectroscopy. *Neuroimage* 2012; 61:342–362.
6. Bates TE, Strangward M, Keelan J, Davey GP, Munro PM, Clark JB. Inhibition of N-acetylaspartate production: implications for ^1H MRS studies *in vivo*. *Neuroreport* 1996; 7:1397–1400.
7. Pouwels PJW, Frahm J. Regional metabolite concentrations in human brain as determined by quantitative localized proton MRS. *Magn Reson Med* 1998; 39: 53–60.
8. Baker EH, Basso G, Barker PB, Smith MA, Bonekamp D, Horská A. Regional apparent metabolite concentrations in young adult brain measured by (^1H) MR spectroscopy at 3 Tesla. *J Magn Reson Imaging* 2008; 27:489–499.
9. Moffett JR, Namboodiri MA. Differential distribution of N-acetylaspartylglutamate and N-acetylaspartate immunoreactivities in rat forebrain. *J Neurocytol* 1995; 24:409–433.
10. Simmons ML, Frondoza CG, Coyle JT. Immunocytochemical localization of N-acetyl-aspartate with monoclonal antibodies. *Neuroscience* 1991; 45:37–45.
11. Petroff OA, Burlina AP, Black J, Prichard JW. Quantitative analysis of rat synaptosomes and cerebrum using high-resolution ^1H magnetic resonance spectroscopy. *Clin Chim Acta* 1992; 206:137–146.
12. Urenjak J, Williams SR, Gadian DG, Noble M. Specific expression of N-acetylaspartate in neurons, oligodendrocyte-type-2 astrocyte progenitors, and immature oligodendrocytes *in vitro*. *J Neurochem* 1992; 59:55–61.
13. Bhakoo KK, Pearce D. *In vitro* expression of N-acetylaspartate by oligodendrocytes: implications for proton magnetic resonance spectroscopy signal *in vivo*. *J Neurochem* 2000; 74:254–262.
14. Richardson WD, Young KM, Tripathi RB, McKenzie I. NG2-glia as multipotent neural stem cells: fact or fantasy? *Neuron* 2011; 70:661–673.
15. Nishiyama A, Komitova M, Suzuki R, Zhu X. Polydendrocytes (NG2 cells): multifunctional cells with lineage plasticity. *Nat Rev Neurosci* 2009; 10:9–22.
16. Dawson MR, Polito A, Levine JM, Reynolds R. NG2-expressing glial progenitor cells: an abundant and widespread population of cycling cells in the adult rat CNS. *Mol Cell Neurosci* 2003; 24:476–488.
17. Neale JH, Bzdega T, Wroblewska B. N-acetylaspartylglutamate: the most abundant peptide neurotransmitter in the mammalian central nervous system. *J Neurochem* 2000; 75:443–452.
18. Baslow MH. Evidence that the tri-cellular metabolism of N-acetylaspartate functions as the brain's "operating system": how NAA metabolism supports meaningful intercellular frequency-encoded communications. *Amino acids* 2010; 39:1139–1145.
19. D'Adamo AF Jr, Smith JC, Woiler C. The occurrence of N-acetylaspartate amidohydrolase (aminoacylase II) in the developing rat. *J Neurochem* 1973; 20: 1275–1278.
20. Burri R, Steffen C, Herschkowitz N. N-acetyl-L-aspartate is a major source of acetyl groups for lipid synthesis during rat brain development. *Dev Neurosci* 1991; 13:403–411.
21. Mehta V, Namboodiri MA. N-acetylaspartate as an acetyl source in the nervous system. *Brain Res Mol Brain Res* 1995; 31:151–157.
22. Neale JH, Olszewski RT, Gehl LM, Wroblewska B, Bzdega T. The neurotransmitter N-acetylaspartylglutamate in models of pain, ALS, diabetic neuropathy, CNS injury and schizophrenia. *Trends Pharmacol Sci* 2005; 26:477–484.
23. Patel TB, Clark JB. Synthesis of N-acetyl-L-aspartate by rat brain mitochondria and its involvement in mitochondrial/cytosolic carbon transport. *Biochem J* 1979; 184:539–546.
24. Knizley H Jr. The enzymatic synthesis of N-acetyl-L-aspartic acid by a water-insoluble preparation of a cat brain acetone powder. *J Biol Chem* 1967; 242:4619–4622.

25. Goldstein FB. The enzymatic synthesis of N-acetyl-L-aspartic acid by subcellular preparations of rat brain. *J Biol Chem* 1969; 244:4257–4260.
26. Satrustegui J, Contreras L, Ramos M, et al. Role of aralar, the mitochondrial transporter of aspartate-glutamate, in brain N-acetylaspartate formation and Ca(2+) signaling in neuronal mitochondria. *J Neurosci Res* 2007; 85:3359–3366.
27. McKenna MC, Stevenson JH, Huang X, Hopkins IB. Differential distribution of the enzymes glutamate dehydrogenase and aspartate aminotransferase in cortical synaptic mitochondria contributes to metabolic compartmentation in cortical synaptic terminals. *Neurochem Int* 2000; 37:229–241.
28. Truckenmiller ME, Namboodiri MA, Brownstein MJ, Neale JH. N-acetylation of L-aspartate in the nervous system: differential distribution of a specific enzyme. *J Neurochem* 1985; 45:1658–1662.
29. Lu ZH, Chakraborty G, Ledeen RW, Yahya D, Wu G. N-acetylaspartate synthase is bimodally expressed in microsomes and mitochondria of brain. *Brain Res Mol Brain Res* 2004; 122:71–78.
30. Patel TB, Clark JB. Mitochondrial/cytosolic carbon transfer in the developing rat brain. *Biochim Biophys Acta* 1981; 677:373–380.
31. Arun P, Moffett JR, Namboodiri AM. Evidence for mitochondrial and cytoplasmic N-acetylaspartate synthesis in SH-SY5Y neuroblastoma cells. *Neurochem Int* 2009; 55:219–225.
32. Li S, Clements R, Sulak M, Gregory R, Freeman E, McDonough J. Decreased NAA in gray matter is correlated with decreased availability of acetate in white matter in postmortem multiple sclerosis cortex. *Neurochem Res* 2013; 38:2385–2396.
33. Jalil MA, Begum L, Contreras L, et al. Reduced N-acetylaspartate levels in mice lacking aralar, a brain- and muscle-type mitochondrial aspartate-glutamate carrier. *J Biol Chem* 2005; 280:31333–31339.
34. Ganapathy V, Fujita T. Identity of the high-affinity sodium/carboxylate cotransporter NaC₃ as the N-acetyl-L-aspartate transporter. *Adv Exp Med Biol* 2006; 576:67–76.
35. Sager TN, Thomsen C, Valsborg JS, Laursen H, Hansen AJ. Astroglia contain a specific transport mechanism for N-acetyl-L-aspartate. *J Neurochem* 1999; 73:807–811.
36. Madhavarao CN, Chinopoulos C, Chandrasekaran K, Namboodiri MA. Characterization of the N-acetyl-aspartate biosynthetic enzyme from rat brain. *J Neurochem* 2003; 86:824–835.
37. Kirmani BF, Jacobowitz DM, Namboodiri MA. Developmental increase of aspartoacylase in oligodendrocytes parallels CNS myelination. *Brain Res Dev Brain Res* 2003; 140:105–115.
38. Chakraborty G, Mekala P, Yahya D, Wu G, Ledeen RW. Intraneuronal N-acetylaspartate supplies acetyl groups for myelin lipid synthesis: evidence for myelin-associated aspartoacylase. *J Neurochem* 2001; 78:736–745.
39. Burlina AP, Ferrari V, Facci L, Skaper SD, Burlina AB. Mast cells contain large quantities of secretagogue-sensitive N-acetylaspartate. *J Neurochem* 1997; 69:1314–1317.
40. Baslow MH, Yamada S. Identification of N-acetylaspartate in the lens of the vertebrate eye: a new model for the investigation of the function of N-acetylated amino acids in vertebrates. *Exp Eye Res* 1997; 64:283–286.
41. Baslow MH. N-acetylaspartate in the vertebrate brain: metabolism and function. *Neurochem Res* 2003; 28:941–953.
42. Nakada T, Kwee IL, Igarashi H. Brain maturation and high-energy phosphate diffusivity: alteration in cytosolic microenvironment and effective viscosity. *Brain Res Dev Brain Res* 1994; 80:121–126.
43. Nakada T. Conversion of brain cytosol profile from fetal to adult type during the perinatal period: taurine-NAA exchange. *Proc Jpn Acad Ser B Phys Biol Sci* 2010; 86:630–642.
44. Jones TH, Morawetz RB, Crowell RM, et al. Thresholds of focal cerebral ischemia in awake monkeys. *J Neurosurg* 1981; 54:773–782.
45. Ginsberg MD, Busto R. Rodent models of cerebral ischemia. *Stroke* 1989; 20:1627–1642.
46. Kirino T. Delayed neuronal death in the gerbil hippocampus following ischemia. *Brain Res* 1982; 239:57–69.
47. Smith ML, Bendek G, Dahlgren N, Rosén I, Wieloch T, Siesjö BK. Models for studying long-term recovery following forebrain ischemia in the rat. 2. A 2-vessel occlusion model. *Acta Neurol Scand* 1984; 69:385–401.
48. Pulsinelli WA, Brierley JB. A new model of bilateral hemispheric ischemia in the unanesthetized rat. *Stroke* 1979; 10:267–272.
49. Memezawa H, Smith ML, Siesjö BK. Penumbra tissues salvaged by reperfusion following middle cerebral artery occlusion in rats. *Stroke* 1992; 23:552–559.
50. Astrup J, Symon L, Branston NM, Lassen NA. Cortical evoked potential and extracellular K⁺ and H⁺ at critical levels of brain ischemia. *Stroke* 1977; 8:51–57.
51. Ramos-Cabrer P, Campos F, Sobrino T, Castillo J. Targeting the ischemic penumbra. *Stroke* 2011; 42(1 Suppl):S7–S11.
52. Morikawa S, Inubushi T, Takahashi K, Ishii H, Shigemori S. Dissociation between lactate accumulation and acidosis in middle cerebral artery-occluded rats assessed by ³¹P and ¹H NMR metabolic images under a 2-T magnetic field. *Magn Reson Imaging* 1996; 14:1197–1204.
53. Higuchi T, Fernandez EJ, Maudsley AA, Shimizu H, Weiner MW, Weinstein PR. Mapping of lactate and N-acetyl-L-aspartate predicts infarction during acute focal ischemia: *in vivo* ¹H magnetic resonance spectroscopy in rats. *Neurosurgery* 1996; 38:121–130.
54. Dreher W, Kühn B, Gyngell ML, et al. Temporal and

- regional changes during focal ischemia in rat brain studied by proton spectroscopic imaging and quantitative diffusion NMR imaging. *Magn Reson Med* 1998; 39:878–888.
55. Igarashi H, Kwee IL, Nakada T, Katayama Y, Terashi A. ¹H magnetic resonance spectroscopic imaging of permanent focal cerebral ischemia in rat: longitudinal metabolic changes in ischemic core and rim. *Brain Res* 2001; 907:208–221.
 56. Gideon P, Henriksen O, Sperling B, et al. Early time course of N-acetylaspartate, creatine and phosphocreatine, and compounds containing choline in the brain after acute stroke. A proton magnetic resonance spectroscopy study. *Stroke* 1992; 23:1566–1572.
 57. Houkin K, Kamada K, Kamiyama H, Iwasaki Y, Abe H, Kashiwaba T. Longitudinal changes in proton magnetic resonance spectroscopy in cerebral infarction. *Stroke* 1993; 24:1316–1321.
 58. Liu YJ, Chen CY, Chung HW, et al. Neuronal damage after ischemic injury in the middle cerebral arterial territory: deep watershed versus territorial infarction at MR perfusion and spectroscopic imaging. *Radiology* 2003; 229:366–374.
 59. Cvorov V, Wardlaw JM, Marshall I, et al. Associations between diffusion and perfusion parameters, N-acetyl aspartate, and lactate in acute ischemic stroke. *Stroke* 2009; 40:767–772.
 60. Dani KA, An L, Henning EC, et al. Multivoxel MR spectroscopy in acute ischemic stroke: comparison to the stroke protocol MRI. *Stroke* 2012; 43:2962–2967.
 61. van der Toorn A, Dijkhuizen RM, Tulleken CA, Nicolai K. T₁ and T₂ relaxation times of the major ¹H-containing metabolites in rat brain after focal ischemia. *NMR Biomed* 1995; 8:245–252.
 62. Walker PM, Ben Salem D, Lalande A, Giroud M, Brunotte F. Time course of NAA T₂ and ADC(w) in ischaemic stroke patients: ¹H MRS imaging and diffusion-weighted MRI. *J Neurol Sci* 2004; 220:23–28.
 63. Igarashi H. [Proton magnetic resonance spectroscopy as a time clock measurement device in cerebral ischemia]. *Rinsho Shinkeigaku* 2011; 51:1178–1181. [Article in Japanese]
 64. Li PA, Siesjö BK. Role of hyperglycaemia-related acidosis in ischaemic brain damage. *Acta Physiol Scand* 1997; 161:567–580.
 65. Parsons MW, Barber PA, Desmond PM, et al. Acute hyperglycemia adversely affects stroke outcome: a magnetic resonance imaging and spectroscopy study. *Ann Neurol* 2002; 52:20–28.
 66. Guyot LL, Diaz FG, O'Regan MH, Song D, Phillis JW. The effect of streptozotocin-induced diabetes on the release of excitotoxic and other amino acids from the ischemic rat cerebral cortex. *Neurosurgery* 2001; 48:385–391.
 67. Moore RA, Le Coq J, Faehnle CR, Viola RE. Purification and preliminary characterization of brain aspartoacylase. *Arch Biochem Biophys* 2003; 413:1–8.
 68. Moreno A, Ross BD, Blüml S. Direct determination of the N-acetyl-L-aspartate synthesis rate in the human brain by (13)C MRS and [1-(13)C]glucose infusion. *J Neurochem* 2001; 77:347–350.
 69. Håberg A, Qu H, Haraldseth O, Unsgård G, Sonnewald U. *In vivo* injection of [1-13C]glucose and [1,2-13C]acetate combined with *ex vivo* 13C nuclear magnetic resonance spectroscopy: a novel approach to the study of middle cerebral artery occlusion in the rat. *J Cereb Blood Flow Metab* 1998; 18:1223–1232.
 70. Jung JY, Lee HS, Kang DG, et al. ¹H-NMR-based metabolomics study of cerebral infarction. *Stroke* 2011; 42:1282–1288.
 71. Wang Y, Wang Y, Li M, et al. ¹H NMR-based metabolomics exploring biomarkers in rat cerebrospinal fluid after cerebral ischemia/reperfusion. *Mol Biosyst* 2013; 9:431–439.
 72. Sager TN, Laursen H, Hansen AJ. Changes in N-acetyl-aspartate content during focal and global brain ischemia of the rat. *J Cereb Blood Flow Metab* 1995; 15:639–646.
 73. Nonaka M, Yoshimine T, Kumura E, Kohmura E, Wakayama A, Hayakawa T. Decrease in N-acetyl-aspartate without commensurate accumulation of acetate in focal cerebral ischemia in rat. *Neurol Res* 1999; 21:771–774.
 74. Katsura K, Takahashi K, Asoh S, et al. Combination therapy with transductive anti-death FNK protein and FK506 ameliorates brain damage with focal transient ischemia in rat. *J Neurochem* 2008; 106:258–270.
 75. Matsumoto K, Lo EH, Pierce AR, Halpern EF, Newcomb R. Secondary elevation of extracellular neurotransmitter amino acids in the reperfusion phase following focal cerebral ischemia. *J Cereb Blood Flow Metab* 1996; 16:114–124.
 76. Tetsuka K, Takanaga H, Ohtsuki S, Hosoya K, Terasaki T. The L-isomer-selective transport of aspartic acid is mediated by ASCT2 at the blood-brain barrier. *J Neurochem* 2003; 87:891–901.
 77. Gao J, Yang H, Chen J, et al. Analysis of serum metabolites for the discovery of amino acid biomarkers and the effect of galangin on cerebral ischemia. *Mol Biosyst* 2013; 9:2311–2321.
 78. Deelchand DK, Shestov AA, Koski DM, Uğurbil K, Henry PG. Acetate transport and utilization in the rat brain. *J Neurochem* 2009; 109 Suppl 1:S46–S54.
 79. Nicoli F, Lefur Y, Denis B, Ranjeva JP, Confort-Gouny S, Cozzzone PJ. Metabolic counterpart of decreased apparent diffusion coefficient during hyperacute ischemic stroke: a brain proton magnetic resonance spectroscopic imaging study. *Stroke* 2003; 34:e82–e87.
 80. Cvorov V, Marshall I, Armitage PA, et al. MR diffusion and perfusion parameters: relationship to metabolites in acute ischaemic stroke. *J Neurol Neurosurg Psychiatry* 2010; 81:185–191.
 81. Rutgers DR, Klijn CJ, Kappelle LJ, van der Grond J. Cerebral metabolic changes in patients with a symp-

- tomatic occlusion of the internal carotid artery: a longitudinal ^1H magnetic resonance spectroscopy study. *J Magn Reson Imaging* 2000; 11:279–286.
82. Cho YP, Lee JH, Kim GE. Metabolic changes after revascularization in a patient with innominate artery occlusion by localized *in vivo* proton magnetic resonance spectroscopy. *J Korean Med Sci* 2003; 18:267–271.
 83. Loh PS, Butcher KS, Parsons MW, et al. Apparent diffusion coefficient thresholds do not predict the response to acute stroke thrombolysis. *Stroke* 2005; 36:2626–2631.
 84. Rivers CS, Wardlaw JM, Armitage PA, et al. Do acute diffusion- and perfusion-weighted MRI lesions identify final infarct volume in ischemic stroke? *Stroke* 2006; 37:98–104.
 85. Purushotham A, Campbell BC, Straka M, et al. Apparent diffusion coefficient threshold for delineation of ischemic core. *Int J Stroke* 2013 Jun 27. doi: 10.1111/ijss.12068. [Epub ahead of print]
 86. Parsons MW, Li T, Barber PA, et al. Combined ^1H MR spectroscopy and diffusion-weighted MRI improves the prediction of stroke outcome. *Neurology* 2000; 55:498–505.
 87. van Lookeren Campagne M, Thomas GR, Thibodeaux H, et al. Secondary reduction in the apparent diffusion coefficient of water, increase in cerebral blood volume, and delayed neuronal death after middle cerebral artery occlusion and early reperfusion in the rat. *J Cereb Blood Flow Metab* 1999; 19:1354–1364.
 88. Li F, Silva MD, Liu KF, et al. Secondary decline in apparent diffusion coefficient and neurological outcomes after a short period of focal brain ischemia in rats. *Ann Neurol* 2000; 48:236–244.
 89. Ringer TM, Neumann-Haefelin T, Sobel RA, Moseley ME, Yenari MA. Reversal of early diffusion-weighted magnetic resonance imaging abnormalities does not necessarily reflect tissue salvage in experimental cerebral ischemia. *Stroke* 2001; 32:2362–2369.
 90. Kidwell CS, Saver JL, Starkman S, et al. Late secondary ischemic injury in patients receiving intraarterial thrombolysis. *Ann Neurol* 2002; 52:698–703.
 91. Kikuchi B. Mechanism of secondary deterioration after transient focal brain ischemia: ^1H -magnetic resonance spectroscopy study. *Niigata Med J* 2008; 122:271–279.
 92. Hermann DM, Kilic E, Hata R, Hossman KA, Mies G. Relationship between metabolic dysfunctions, gene responses and delayed cell death after mild focal cerebral ischemia in mice. *Neuroscience* 2001; 104:947–955.
 93. Strosznajder RP, Czubowicz K, Jesko H, Strosznajder JB. Poly(ADP-ribose) metabolism in brain and its role in ischemia pathology. *Mol Neurobiol* 2010; 41:187–196.
-

Reduced plasma desmosterol-to-cholesterol ratio and longitudinal cognitive decline in Alzheimer's disease

Yoshiaki Sato^a, Francois Bernier^a, Yasukazu Yamanaka^b, Ken Aoshima^a, Yoshiya Oda^c, Martin Ingelsson^d, Lars Lannfelt^d, Akinori Miyashita^e, Ryoza Kuwano^e, Takeshi Ikeuchi^{e,*}

^aEisai Co., Ltd., Tsukuba, Ibaraki, Japan

^bEIDIA Co., Ltd., Inashiki-gun, Ibaraki, Japan

^cEisai Inc., Andover, MA, USA

^dGeriatrics, Department of Public Health and Caring Sciences, Uppsala University, Uppsala, Sweden

^eDepartment of Molecular Genetics, Brain Research Institute, Niigata University, Niigata, Japan

Abstract

Background: We here examined whether plasma desmosterol-to-cholesterol ratio (DES/CHO) is decreased in patients with Alzheimer's disease (AD) and investigated the association between plasma DES/CHO and longitudinal cognitive decline.

Methods: Plasma DES/CHO of AD patients and age-matched controls in a Japanese cross-sectional cohort was determined. Plasma DES/CHO at baseline and follow-up visits was assessed in relation to cognitive decline in Japanese and Swedish longitudinal cohorts.

Results: Plasma DES/CHO was significantly reduced in Japanese AD patients and significantly correlated with Mini-Mental State Examination (MMSE) score. The longitudinal analysis revealed that plasma DES/CHO in AD patients shows a significant decrease at follow-up intervals. The decline in plasma DES/CHO is larger in the AD group with rapid progression than in that with slow progression. The changes in plasma DES/CHO significantly correlated with changes in the MMSE score.

Conclusion: Plasma DES/CHO is decreased in AD patients and may serve as a longitudinal surrogate marker associated with cognitive decline.

© 2015 The Alzheimer's Association. Published by Elsevier Inc. This is an open access article under the CC BY-NC-ND license (<http://creativecommons.org/licenses/by-nc-nd/4.0/>).

Keywords:

Alzheimer's disease; Mild cognitive impairment; Blood-based biomarker; Desmosterol; Longitudinal biomarker

1. Introduction

Alzheimer's disease (AD) is one of the most common and debilitating neurodegenerative disorders of the aging population. AD manifests itself as a progressive decline in memory accompanied by other cognitive and functional disabilities [1]. From the viewpoint of clinical practice and therapeutic clinical trials in AD, biomarkers are becoming increasingly important particularly when disease-modifying drugs will become available. Numerous studies have shown that tau, phosphorylated tau, and amyloid- β (A β) 42 in cerebrospinal

fluid (CSF) are reliable biomarkers for AD diagnosis [2–4]. However, the CSF examination of AD patients has not been broadly applied in general clinical practice because lumbar puncture to obtain CSF is relatively invasive and time consuming. Moreover, these CSF markers do not seem to be associated with longitudinal cognitive decline in patients with AD [5]. Thus, there is a compelling need to establish a noninvasive biomarker for AD that follows the disease progression. Efforts to find reliable blood-based biomarkers for AD have met with little success [6]. Several reports have been published describing altered levels of proteins, peptides, or metabolites in patients with AD, but those blood-based biomarkers have proven difficult to replicate in independent studies [6], highlighting the importance of multiple validations.

*Corresponding author. Tel.: +81-25-227-2343; Fax: +81-25-227-0793.

E-mail address: ikeuchi@bri.niigata-u.ac.jp

<http://dx.doi.org/10.1016/j.dadm.2014.11.009>

2352-8729/© 2015 The Alzheimer's Association. Published by Elsevier Inc. This is an open access article under the CC BY-NC-ND license (<http://creativecommons.org/licenses/by-nc-nd/4.0/>).

Table 1
Demographic characteristics of AD patients and age-matched cognitively normal controls in the Japanese cross-sectional cohort

Variable	Control (n = 201)	AD (n = 200)
Female (%)	72	75
Age, mean (SD)		
Age at examination (y)	77.6 (4.7)	77.6 (5.4)
Age at onset (y)	n/a	73.5 (5.0)
MMSE, mean (SD)	28.7 (1.5)	17.0 (5.2)**
APOE genotype		
2*3	15	6
2*4	2	1
3*3	151	71
3*4	32	99
4*4	1	23
DES/CHO (10^{-6}), mean (SD)	456 (119)	357 (134)**

Abbreviations: AD, Alzheimer's disease; n/a, not available; MMSE, Mini-Mental State Examination; DES/CHO, desmosterol-to-cholesterol ratio.

** $P < .01$.

In our previous report, we found that the plasma desmosterol-to-cholesterol ratio (DES/CHO) is significantly decreased in Caucasian patients with AD and subjects with mild cognitive impairment (MCI) [7]. Desmosterol is the most abundant precursor but rarely exceeds 1% of total brain sterols because the conversion from desmosterol to cholesterol is tightly regulated by the enzyme 3-hydroxysterol 24-reductase (DHCR24) [8]. A substantially higher desmosterol concentration in the hippocampus could be attributed to neurogenesis and synaptic plasticity that take place in the adult dentate gyrus [9]. Conversely, a decrease in desmosterol level in the hippocampus could at least in part correlate with the reduced number of progenitor cells differentiating into neurons [10]. These reports suggest an important role of desmosterol in the brain.

With this background, we here measured plasma DES/CHO of samples from a large Japanese cohort to extend our previous result that plasma DES/CHO is decreased in patients with AD in a different ethnic group. Furthermore, we

performed longitudinal studies to determine the association between plasma DES/CHO and cognitive decline in patients with AD over time.

2. Materials and methods

2.1. Subjects

For cross-sectional analysis, plasma samples of 200 patients with AD and 201 age-matched cognitively normal elderly individuals (older than 65 years) were collected from seven clinical institutions in Japan (Table 1). The diagnosis of AD was made on the basis of the criteria of the National Institute of Neurological and Communicative Disorders Association [11]. Each participant was asked to complete the Mini-Mental State Examination (MMSE) [12]. APOE genotyping was performed as previously reported [13].

For longitudinal analysis, we used 17 subjects with AD (Japanese longitudinal cohort collected at Niigata University Hospital) and 28 subjects (Swedish longitudinal cohort consisting of 6 control, 12 MCI, and 10 AD subjects collected at Uppsala University Hospital), whose blood was drawn at two different time points (Table 2). Additional longitudinal plasma samples of 30 subjects at least at 3 different time points were obtained from Uppsala University Hospital (AD, $n = 6$; MCI, $n = 6$; control, $n = 2$) or purchased from PrecisionMed, Inc. (AD, $n = 12$; control, $n = 4$) (San Diego, CA, USA). The criteria of Petersen et al. [14,15] were used for the diagnosis of MCI. To be considered as having MCI, the patients had to be free of significant underlying medical, neurologic, or psychiatric illness and meet the following criteria: (1) subjective memory complaint, (2) objective signs of decline in any cognitive domain, (3) intact activities of daily living, and (4) clinical features not fulfilling the DSM-IV/ICD-10 criteria for dementia [16]. The two AD/MCI groups with slow and rapid progression were classified on the basis of

Table 2
Demographic characteristics of subjects in the longitudinal study

Variable	Japanese cohort, AD (n = 17)	Swedish cohort			Combined cohort, MCI/AD (n = 39)
		Control (n = 6)	MCI (n = 12)	AD (n = 10)	
Female (%)	71	75	33	30	56
Age, mean (SD)	68 (8)	67 (9)	62 (8)	66 (10)	66 (9)
Follow-up time, y, mean (SD)	2.0 (1.0)	2.7 (0.8)	1.8 (0.9)	2.2 (0.9)	2.1 (1.0)
MMSE, mean (SD)					
Baseline	20 (5)	30 (1)	28 (2)	25 (3)	24 (6)
Follow-up	16 (7)	30 (0)	28 (2)	22 (3)	21 (7)
Δ MMSE	-4 (4)**	0 (1)	0 (2)	-3 (3)*	-2 (4)**
DES/CHO (10^{-6}), mean (SD)					
Baseline	329 (103)	654 (146)	660 (200)	556 (232)	489 (225)
Follow-up	290 (79)	661 (130)	607 (237)	487 (276)	438 (237)
% Change	-10 (14)*	1.7 (5.1)	-8.3 (21)	-18 (27)	-11 (20)**

Abbreviations: AD, Alzheimer's disease; MCI, mild cognitive impairment; MMSE, Mini-Mental State Examination; DES/CHO, desmosterol-to-cholesterol ratio.

* $P < .05$, ** $P < .01$.

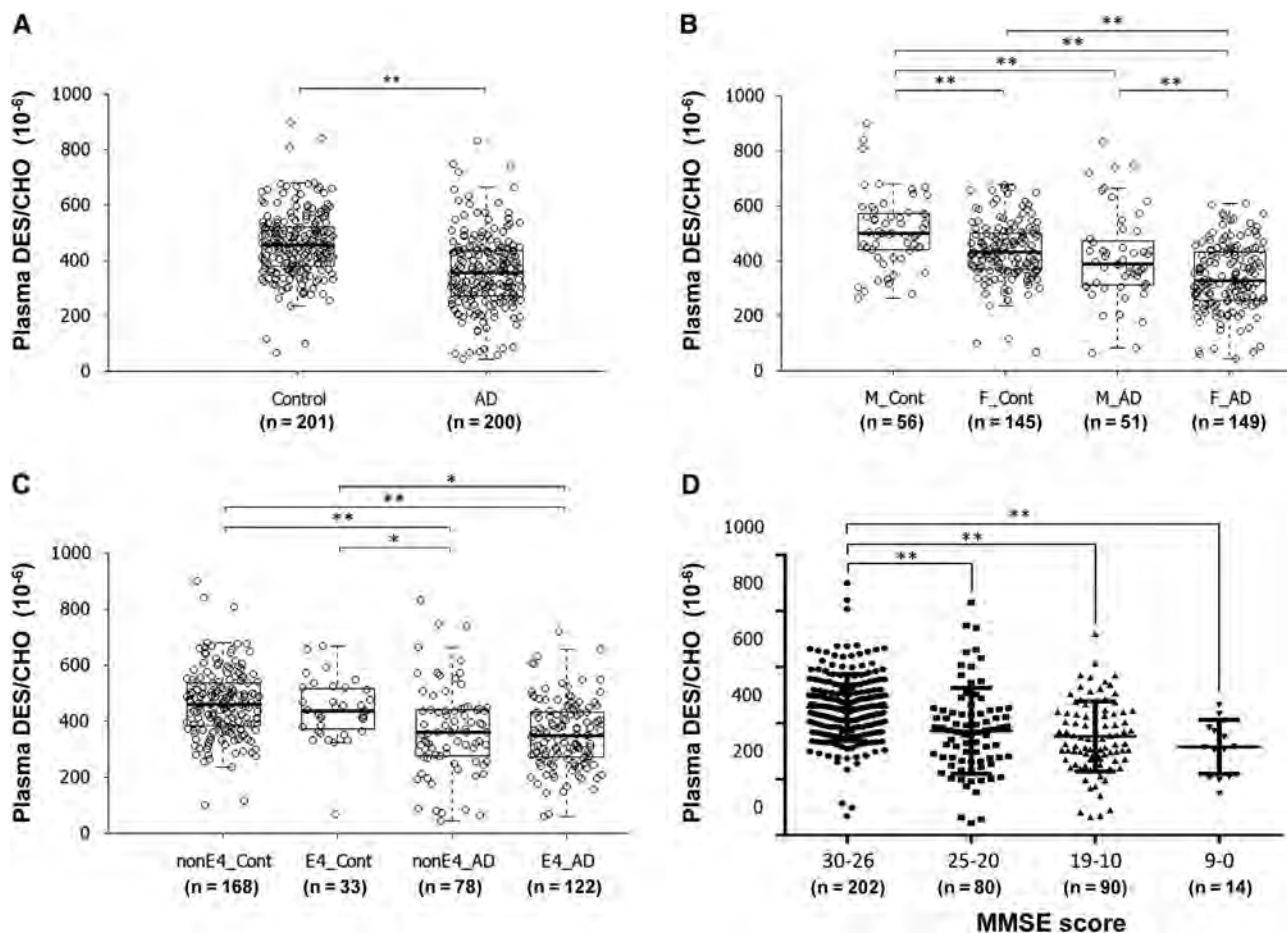


Fig. 1. Decreased plasma DES/CHO in patients with AD. (A) Comparison of plasma desmosterol-to-cholesterol ratio (DES/CHO) between 201 control and 200 AD subjects from a large Japanese cohort. (B) Comparison of plasma DES/CHO among male control (M_Cont), female control (F_Cont), male AD (M_AD), and female AD (F_AD) subjects. (C) Comparison of plasma DES/CHO between control subjects without *APOE* ϵ 4 (nonE4_Cont) and with *APOE* ϵ 4 (E4_Cont), and AD patients without *APOE* ϵ 4 (nonE4_AD) and with *APOE* ϵ 4 (E4_AD). (D) Comparison of plasma DES/CHO among groups classified as MMSE groups. * $P < .05$; ** $P < .01$.

the mean change in MMSE score (change from the baseline) as threshold. Written informed consent was obtained from each of the participants (or the respective legal guardian); the study was approved by the appropriate university, hospital, and company institutional ethics committees.

2.2. Blood sampling and laboratory measurement

Peripheral blood samples were obtained from each participant using the commercially available blood collection tubes (Terumo Venoject for Japanese cohort and BD Vacutainer for Swedish cohort) containing EDTA as the anticoagulant. Plasma was separated by centrifugation at 1500 g for 15 minutes at room temperature before being aliquoted and stored at -80°C until analysis.

The concentrations of desmosterol and cholesterol were measured with a liquid chromatography mass spectrometer (LC/MS), as described previously [7]. Briefly, 25 μL of plasma was spiked with cholesterol-25,26,26,26,27,27,27-D7 and desmosterol-26,26,26,27,27,27-D6 as internal standards. Fifty percent potassium hydroxide was then added to the solution, which was then mixed thoroughly and incu-

bated at 70°C for 60 minutes. After the incubation, 2 mL of hexane and 0.5 mL of phosphate-buffered saline (pH 6.8) were added and mixed well. The solution was centrifuged for 10 minutes at 2000 g , and the upper organic phase was transferred to a new tube. The lower layer was extracted with an additional 1 mL of hexane, which was also added to the organic-phase extract. The solvents were evaporated to dryness under a nitrogen gas stream at 40°C , and the obtained pellet was reconstituted in ethanol and the resulting solution was subjected to liquid chromatography/atmospheric pressure chemical ionization-mass spectrometer analysis as described previously [7].

2.3. Statistical analysis

Values are shown as mean \pm standard deviation. Correlations between different variables were assessed using the Pearson correlation coefficient on log-transformed data. The t test or analysis of variance was carried out to determine differences between two or more groups. Nonparametric tests (Mann-Whitney U test) were carried out when the variables were not normally distributed. The paired t test was

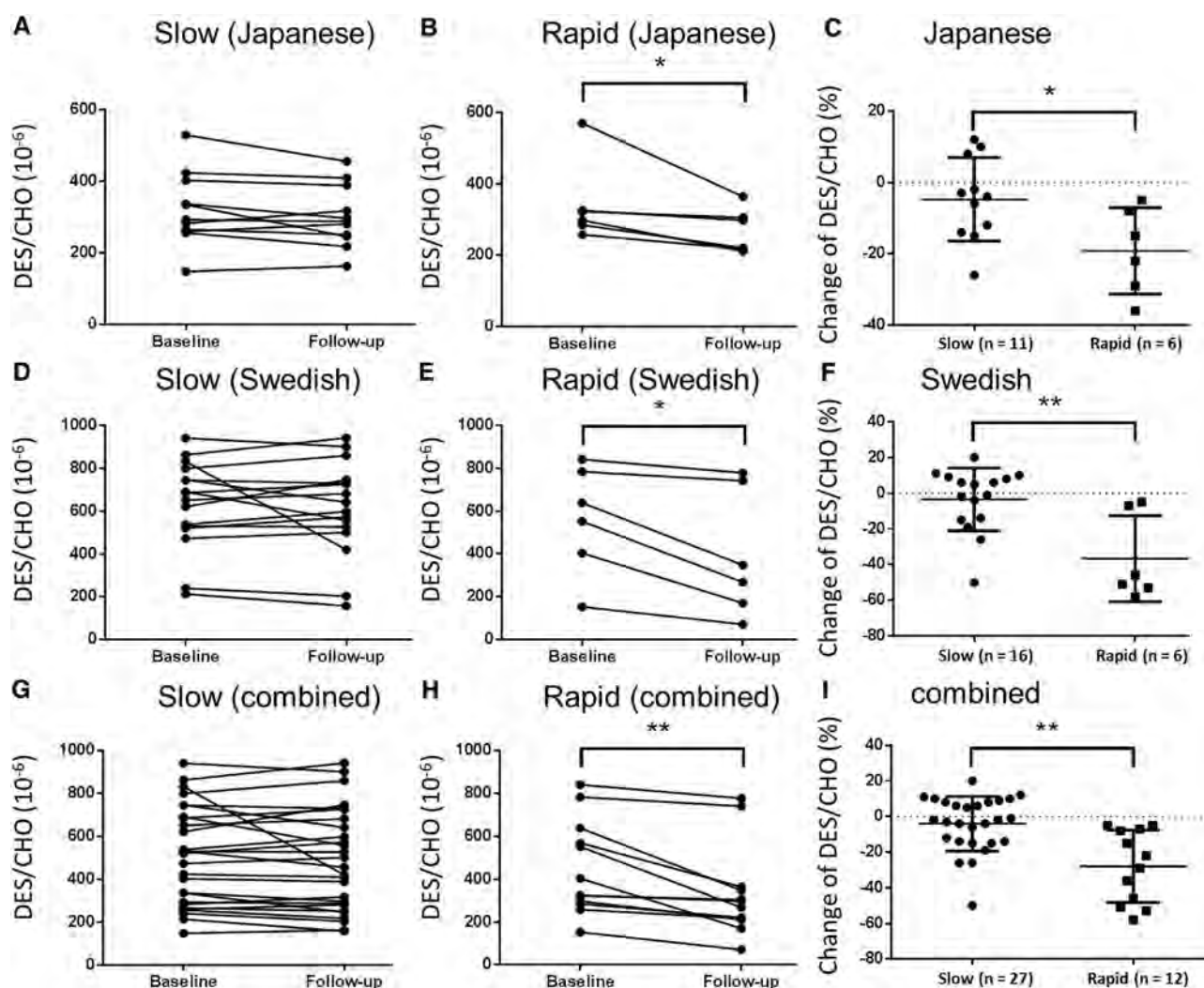


Fig. 2. Change in plasma DES/CHO between baseline and follow-up visits. AD/MCI subjects were classified into two groups, namely, those with slow progression (A, D, G) and those with rapid progression (B, E, H) on the basis of the mean Δ MMSE between baseline and follow-up visits in a Japanese cohort (A–C), a Swedish cohort (D–F), and a combined cohort (G–I). Plasma DES/CHO remains stable in the group with slow progression (A, D, G), whereas in the group with rapid progression, a significant decline over time was found (B, E, H). The change in plasma DES/CHO was significantly larger in the group with rapid progression than in the group with slow progression (C, F, I). * $P < .05$; ** $P < .01$.

carried out to see the difference in the individual values between baseline and follow-up visits. The statistical significance was set at $P < .05$.

3. Results

3.1. Cross-sectional study of plasma desmosterol

The characteristics of the AD and age-matched control subjects included in this cross-sectional study are listed in Table 1. A significant decline in plasma DES/CHO was observed in patients with AD compared with control subjects ($P < .01$; Fig. 1A). The decline in plasma DES/CHO in AD patients was significant regardless of gender or *APOE* $\epsilon 4$ status (Fig. 1B and C). There was a significant decline in plasma DES/CHO in AD patients with both the *APOE* $\epsilon 3/3$ and $\epsilon 3/4$ genotypes (data not shown; see Supplementary Fig. 1A and B for review). Plasma DES/

CHO of female subjects in both the AD and control groups was significantly lower than that of male subjects (Fig. 1B, $P < .01$). No significant correlation of plasma DES/CHO with age was observed (data not shown). A significant correlation between plasma DES/CHO and MMSE score in both males and females was observed (data not shown; see Supplementary Fig. 1C and D). We divided subjects of this cohort into four MMSE score groups: high MMSE score ($30 \geq \text{MMSE} \geq 26$), middle MMSE score ($25 \geq \text{MMSE} \geq 20$), low MMSE score ($19 \geq \text{MMSE} \geq 10$), and very low MMSE score ($9 \geq \text{MMSE} \geq 0$). We then compared DES/CHO among these groups. A significant difference between the high MMSE score group and the other MMSE score groups was observed (Fig. 1D). The linear trend analysis revealed that there was also a significant change showing that groups with lower MMSE scores had lower DES/CHO (trend t test: $P < .01$).

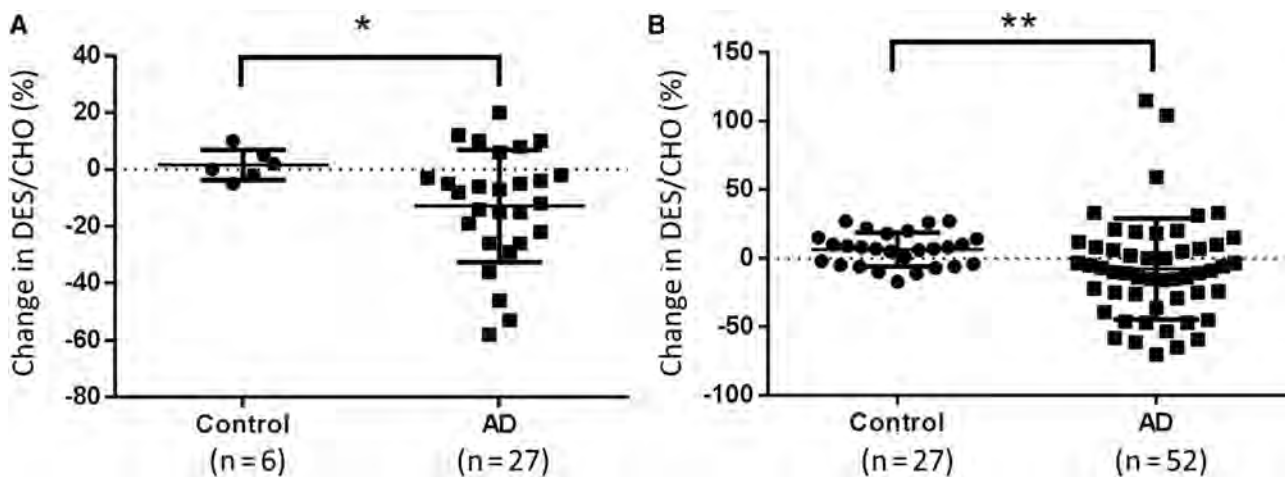


Fig. 3. Comparison of longitudinal change in plasma DES/CHO between control and AD subjects. (A) Longitudinal changes in plasma DES/CHO at two different points were compared between control subjects and AD patients from the combined cohort. * $P < .05$. (B) Longitudinal changes in plasma DES/CHO at multiple points were compared between control subjects and AD patients from the Swedish cohort and a commercially available resource. ** $P < .01$.

3.2. Longitudinal analysis

Longitudinal plasma samples were collected from two clinical institutes, namely, Niigata University Hospital (Japanese cohort) and Uppsala University Hospital Memory Clinic (Swedish cohort). Forty-seven participants composed of 17 subjects in the Japanese cohort and 30 subjects in the Swedish cohort were included, and the demographic characteristics of these subjects are listed in Table 2. At baseline, DES/CHO in Japanese AD patients was significantly lower than that of Swedish AD patients ($P < .01$).

In the Japanese longitudinal cohort, the average change in the MMSE score (Δ MMSE) between the baseline and follow-up visits was -4 ± 4 with a change in DES/CHO

of $-10 \pm 14\%$ (Table 2). Both MMSE score and plasma DES/CHO significantly decreased between the two visits in the Japanese cohort (paired t test, $P < .05$). In the Swedish cohort, the MMSE score (-3 ± 3) decreased significantly in AD patients between the baseline and follow-up visits ($P < .05$). However, in this cohort, there was no significant change in DES/CHO in both the AD patients and MCI subjects (Table 2). In the combined AD/MCI cohort, MMSE score (-2 ± 4) and plasma DES/CHO ($-11 \pm 20\%$) decreased significantly between the two visits (Table 2).

Next, we divided the AD/MCI subjects into two groups, namely, those with slow or rapid progression, on the basis of their mean Δ MMSE in the Japanese (cutoff score, -4) and Swedish cohorts (cutoff score, -2) and compared the longitudinal change in plasma DES/CHO between groups (Fig. 2). Although the AD/MCI group with slow progression did not show any significant change in plasma DES/CHO (Fig. 2A, D, and G), groups with rapid progression showed a significant decrease in plasma DES/CHO between the baseline and follow-up visits (Fig. 2B, E, and H). In addition, the change in plasma DES/CHO was significantly larger in the AD/MCI group with rapid progression than in the group with slow progression in the Japanese, Swedish, and combined cohorts (Fig. 2C, F, and I).

We further compared the longitudinal change in plasma DES/CHO in control subjects and AD patients (Fig. 3). The change in DES/CHO between the two visits was -12.8 ± 19.7 in the AD patients, which was significantly larger than that in the control subjects (1.7 ± 5.3 ; Fig. 3A). These results suggest that although plasma DES/CHO in normal subjects remained stable, plasma DES/CHO in AD patients tended to decline over time.

Finally, we performed another longitudinal study to determine the association between plasma DES/CHO and Δ MMSE in 30 participants, including 18 AD, 6 MCI, and 6 control subjects from either the Swedish cohort or from PrecisionMed. Blood samples were collected every year or

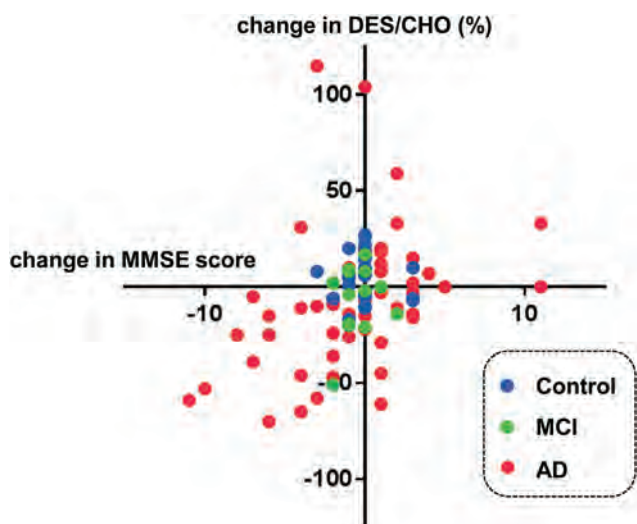


Fig. 4. Correlation between longitudinal changes in MMSE and plasma DES/CHO (%) in AD patients, MCI patients, and normal subjects. There were 122 points for blood collection, consisting of 30 baselines and 92 follow-ups (AD, 52 follow-ups; MCI, 13 follow-ups; and control, 27 follow-ups). There was a significant correlation between changes in MMSE and plasma DES/CHO ($r = 0.37$, $P < .01$).

every 6 months from the participants. There were 122 points for blood collection, consisting of 30 baselines and 92 follow-ups. The correlation between the Δ MMSE and the change in plasma DES/CHO (compared with baseline) determined using all 92 follow-up points is shown in Fig. 4. There was a significant correlation between the longitudinal Δ MMSE and the change in DES/CHO from the baseline ($P = .01$, $r = 0.37$). All the changes in MMSE score and plasma DES/CHO in each of the participants are shown (see Supplementary Fig. 2). In addition, AD patients showed a significant decrease in plasma DES/CHO at follow-up intervals ($-7.7 \pm 36.8\%$) compared with the control subjects ($6.4 \pm 12.3\%$) in this cohort (Fig. 3B).

4. Discussion

The present cross-sectional study using a Japanese cohort was undertaken to replicate our previous finding that plasma DES/CHO is decreased in Caucasian patients with AD. The following points were confirmed in the present Japanese and previously reported Caucasian cross-sectional cohorts: (1) plasma DES/CHO was decreased in patients with AD in comparison with control subjects, (2) the decrease in plasma DES/CHO in AD patients was independent of gender and *APOE* genotype, (3) female subjects tended to have a lower plasma DES/CHO than male subjects, and (4) plasma DES/CHO correlated significantly with the MMSE score. Taken together, the results suggest that plasma DES/CHO may be a potential diagnostic biomarker reflecting cognitive dysfunction in AD patients.

Recently, Popp et al. [17] have reported that the plasma desmosterol level does not change in AD patients. The discrepancy in finding between that and the present study may be explained by differences in the analytical methods used to determine the concentration of desmosterol. We previously showed that the LC/MS method that we used in the present study enables the purification of desmosterol in plasma more efficiently than the gas chromatography method used in the study by Popp et al. [7,17]. Thus, the LC/MS method is likely to be more suitable for the measurement of plasma desmosterol concentration.

Here, we determined for the first time the longitudinal change in plasma DES/CHO and examined a possible association with concurrent cognitive decline in AD/MCI patients. Our results revealed (1) that plasma DES/CHO was relatively stable over time in cognitively normal controls, whereas it significantly decreased in AD patients; (2) a more pronounced decline in plasma DES/CHO in the AD/MCI group with rapid progression than in the group with slow progression; and (3) that the longitudinal change in plasma DES/CHO positively correlated with the change in the MMSE score. These results suggest that the plasma DES/CHO change is associated with the cognitive decline in AD and might be used to monitor the progression of cognitive decline in patients with AD. It will be interesting to clarify the usefulness of monitoring plasma DES/CHO

as a surrogate marker for evaluating the effects of clinical drug trials in patients with AD.

Our longitudinal study suggests that the plasma DES/CHO changes before the appearance of clinical symptoms, as determined by MMSE in some cases (see Supplementary Fig. 2 for review; subjects A, C, and H). The result obtained from the subject with MCI that converted to AD (see Supplementary Fig. 2 for review; subject S) may suggest that plasma DES/CHO is useful as a progression marker to monitor the conversion from MCI to AD. In this connection, recent lipidomic analysis showed that the quantification of several lipid metabolites in plasma, such as phosphatidylcholine and acylcarnitine, is useful for predicting phenocconversion to amnesic MCI or AD in cognitively normal subjects [18].

There is now accumulating evidence that cholesterol metabolism may be relevant to the production and clearance of $A\beta$ and thus to the $A\beta$ -related toxicity in the pathogenesis of AD [19]. The strongest genetic risk factor for sporadic AD is the $\epsilon 4$ allele of *APOE*, which encodes apolipoprotein E (apoE), with a crucial role in cholesterol metabolism [20]. The presence of *APOE* $\epsilon 4$ may contribute to the pathologic accumulation and deposition of cerebral $A\beta$ at early preclinical disease stages [21]. A recent study has shown that CSF apoE levels are decreased in patients with AD and that MCI in subjects with a low CSF apoE level will more likely convert to AD [22]. An interaction between *APOE* genotype and plasma desmosterol level may be postulated because desmosterol is the immediate precursor of cholesterol. However, the plasma desmosterol level was not clearly associated with *APOE* genotype in this study.

It is of particular interest that the level of desmosterol in the AD brain was found to be lower than that of control brain [7,23]. It has been demonstrated that the levels of steroid hormones (e.g., progesterone, pregnenolone, and 17α OH-progesterone) that exhibit inhibitory activity against DHCR24 are decreased in the AD brain, particularly in the vicinity of plaques and neurofibrillary tangles [24]. Notably, the concentration of desmosterol is 100-fold higher in the rat brain than in the rat liver [25], which implies that most of the desmosterol in the blood might originate from the brain. Taken together, it could be speculated that brain desmosterol level may decrease with an increase in DHCR24 activity in the AD brain; this may subsequently result in a change in plasma DES/CHO. The question of why plasma DES/CHO decreases in patients with AD and is associated with longitudinal cognitive decline in the course of the disease warrants further investigation.

Although our findings, using samples from cross-sectional and longitudinal cohorts, are interesting, our study has some limitations. We did not analyze the samples from other types of dementia, including dementia with Lewy bodies, frontotemporal dementia, and vascular dementia. An additional cross-sectional study that includes samples from other types of dementia will be necessary. The number of samples from longitudinal cohorts in this study is relatively small. Longitudinal studies with a prospective design using a larger number

of samples should be performed to confirm the utility of plasma DES/CHO as a longitudinal biomarker. Moreover, it is important to understand how early plasma DES/CHO starts to decline using longitudinal samples from asymptomatic AD subjects with amyloid deposition confirmed by amyloid-positron emission tomography imaging. Although our findings need to be validated in independent cohorts, our data suggest that the use of plasma desmosterol as a blood biomarker can be useful in the diagnosis of AD and also in monitoring disease progression.

Acknowledgments

The authors would like to thank the subjects who participated in this study. We would like to thank Dr. Makoto Ogo and Mr. Mamoru Yanagimachi who provided valuable comments. Special thanks also go to Mr. Kentaro Matsuura and Mr. Masayuki Ikawa whose support and information have helped us throughout this study. This study was funded by grants from Eisai Co. Ltd., Japanese Society of Promotion of Science, Ministry of Health, Labour and Welfare, Japan, and Uppsala University.

Supplementary data

Supplementary data related to this article can be found at <http://dx.doi.org/10.1016/j.dadm.2014.11.009>.

RESEARCH IN CONTEXT

1. Systemic review: There is a compelling need to establish blood-based biomarker to diagnose Alzheimer's disease (AD) and monitor the disease progression. A previous study reported that plasma desmosterol-to-cholesterol ratio (DES/CHO) is significantly decreased in Caucasian patients with AD.
2. Interpretation: We found that plasma DES/CHO was significantly reduced in Japanese AD patients. The longitudinal study revealed (1) that plasma DES/CHO was relatively stable in normal controls, whereas it significantly decreased in AD patients; (2) a more pronounced decline in plasma DES/CHO in the AD/MCI group with rapid progression than in that with slow progression; and (3) that the longitudinal change in plasma DES/CHO positively correlated with the change in MMSE score.
3. Future directions: A future cross-sectional study that includes samples from other types of dementia and longitudinal studies with a prospective design using a larger number of samples need to be performed to confirm the utility of plasma DES/CHO.

References

- [1] Sperling RA, Aisen PS, Beckett LA, Bennett DA, Craft S, Fagan AM, et al. Toward defining the preclinical stages of Alzheimer's disease: recommendations from the National Institute on Aging-Alzheimer's Association workgroups on diagnostic guidelines for Alzheimer's disease. *Alzheimers Dement* 2011;7:280–92.
- [2] Blennow K, Hampel H. CSF markers for incipient Alzheimer's disease. *Lancet Neurol* 2003;2:605–13.
- [3] Jack CR Jr, Holtzman DM. Biomarker modeling of Alzheimer's disease. *Neuron* 2013;80:1347–58.
- [4] Sutphen CL, Fagan AM, Holtzman DM. Progress update: Fluid and imaging biomarkers in Alzheimer's disease. *Biol Psychiatry* 2014;75:520–6.
- [5] Rosen C, Hansson O, Blennow K, Zetterberg H. Fluid biomarkers in Alzheimer's disease—current concepts. *Mol Neurodegener* 2013;8:20.
- [6] Blennow K, Hampel H, Weiner M, Zetterberg H. Cerebrospinal fluid and plasma biomarkers in Alzheimer disease. *Nat Rev Neurol* 2010;6:131–44.
- [7] Sato Y, Suzuki I, Nakamura T, Bernier F, Aoshima K, Oda Y. Identification of a new plasma biomarker of Alzheimer's disease using metabolomics technology. *J Lipid Res* 2012;53:567–76.
- [8] Hinse CH, Shah SN. The desmosterol reductase activity of rat brain during development. *J Neurochem* 1971;18:1989–98.
- [9] Couillard-Despres S, Iglseider B, Aigner L. Neurogenesis, cellular plasticity and cognition: the impact of stem cells in the adult and aging brain—a mini-review. *Gerontology* 2011;57:559–64.
- [10] Jinno S. Decline in adult neurogenesis during aging follows a topographic pattern in the mouse hippocampus. *J Comp Neurol* 2011;519:451–466.
- [11] McKhann G, Drachman D, Folstein M, Katzman R, Price D, Stadlan EM. Clinical diagnosis of Alzheimer's disease: report of the NINCDS-ADRDA Work Group under the auspices of Department of Health and Human Services Task Force on Alzheimer's Disease. *Neurology* 1984;34:939–44.
- [12] Folstein MF, Folstein SE, McHugh PR. “Mini-mental state”. A practical method for grading the cognitive state of patients for the clinician. *J Psychiatr Res* 1975;12:189–98.
- [13] Kuwano R, Miyashita A, Arai H, Asada T, Imagawa M, Shoji M, et al. Dynamin-binding protein gene on chromosome 10q is associated with late-onset Alzheimer's disease. *Hum Mol Genet* 2006;15:2170–82.
- [14] Petersen RC, Morris JC. Mild cognitive impairment as a clinical entity and treatment target. *Arch Neurol* 2005;62:1160–3. discussion 7.
- [15] Petersen RC, Smith GE, Waring SC, Ivnik RJ, Tangalos EG, Kokmen E. Mild cognitive impairment: clinical characterization and outcome. *Arch Neurol* 1999;56:303–8.
- [16] Giedraitis V, Sundelof J, Irizarry MC, Garevik N, Hyman BT, Wahlund LO, et al. The normal equilibrium between CSF and plasma amyloid beta levels is disrupted in Alzheimer's disease. *Neurosci Lett* 2007;427:127–31.
- [17] Popp J, Meichsner S, Kolsch H, Lewczuk P, Maier W, Kornhuber J, et al. Cerebral and extracerebral cholesterol metabolism and CSF markers of Alzheimer's disease. *Biochem Pharmacol* 2013;86:37–42.
- [18] Mapstone M, Cheema AK, Fiandaca MS, Zhong X, Mhyre TR, MacArthur LH, et al. Plasma phospholipids identify antecedent memory impairment in older adults. *Nat Med* 2014;20:415–8.
- [19] Di Paolo G, Kim TW. Linking lipids to Alzheimer's disease: cholesterol and beyond. *Nat Rev Neurosci* 2011;12:284–96.
- [20] Bu G. Apolipoprotein E and its receptors in Alzheimer's disease: pathways, pathogenesis and therapy. *Nat Rev Neurosci* 2009;10:333–44.
- [21] Kok E, Haikonen S, Luoto T, Huhtala H, Goebeler S, Haapasalo H, et al. Apolipoprotein E-dependent accumulation of Alzheimer

- disease-related lesions begins in middle age. *Ann Neurol* 2009; 65:650–7.
- [22] Toledo JB, Da X, Weiner MW, Wolk DA, Xie SX, Arnold SE, et al. CSF Apo-E levels associate with cognitive decline and MRI changes. *Acta Neuropathol* 2014;127:621–32.
- [23] Wisniewski T, Newman K, Javitt NB. Alzheimer's disease: brain cholesterol levels. *J Alzheimers Dis* 2013;33:881–8.
- [24] Lindenthal B, Holleran AL, Aldaghtas TA, Ruan B, Schroepfer GJ Jr, Wilson WK, et al. Progestins block cholesterol synthesis to produce meiosis-activating sterols. *FASEB J* 2001;15:775–84.
- [25] Smiljanic K, Vanmierlo T, Djordjevic AM, Perovic M, Loncarevic-Vasiljkovic N, Tesic V, et al. Aging induces tissue-specific changes in cholesterol metabolism in rat brain and liver. *Lipids* 2013; 48:1069–77.

Supplementary Fig. 1. Sato et al. (for review)

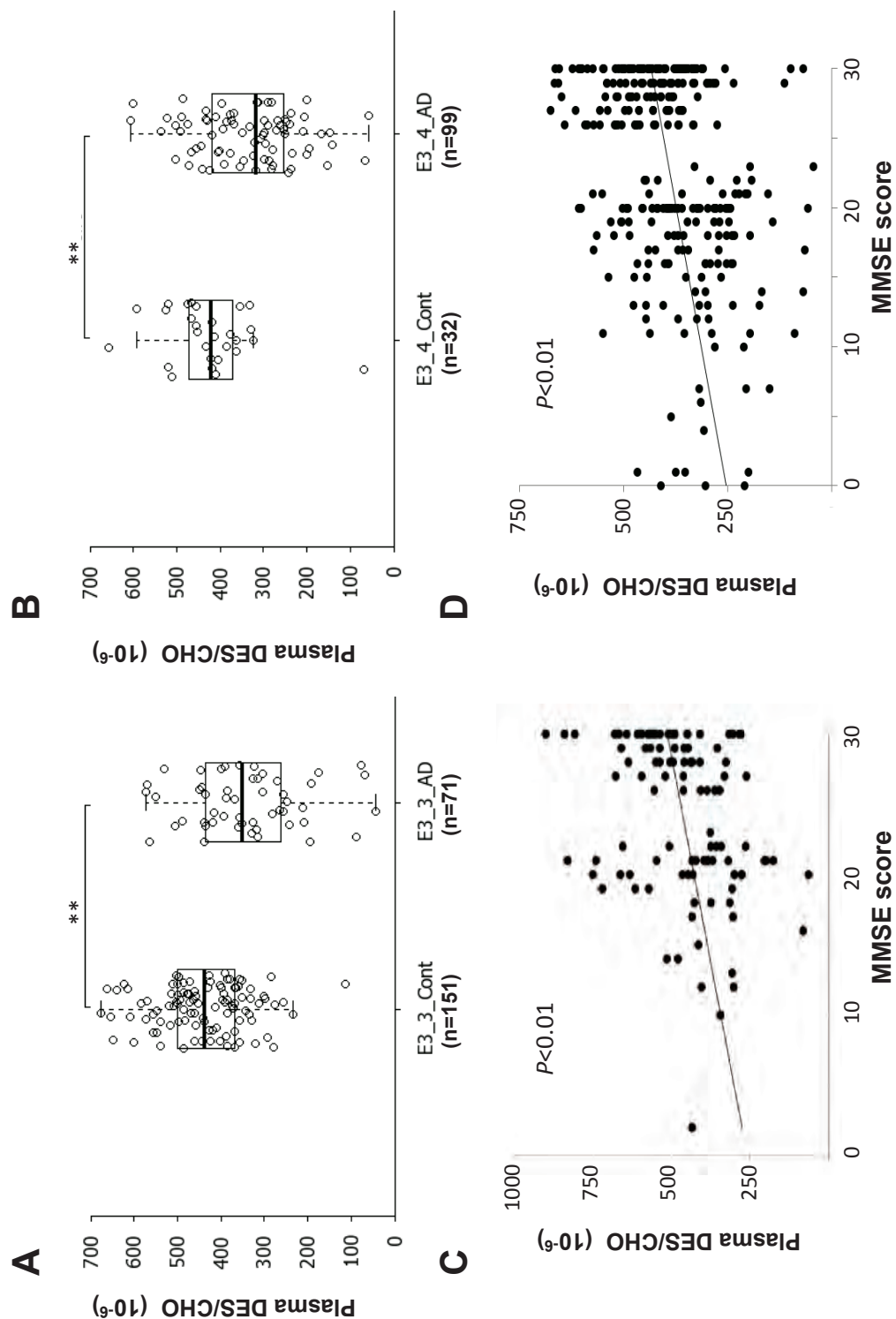


Figure legend Supplementary Fig. 1:

(A) Comparison of plasma DES/CHO between control subjects and AD patients with APOE $\epsilon 3/\epsilon 3$. **, $p < 0.01$.
 (B) Comparison of plasma DES/CHO between control subjects and AD patients with APOE $\epsilon 3/\epsilon 4$. **, $p < 0.01$.
 (C) Correlation between plasma DES/CHO and MMSE score in males (n=105).
 (D) Correlation between plasma DES/CHO and MMSE score in females (n=281).

Supplementary Fig. 2. Sato et al. (for review)

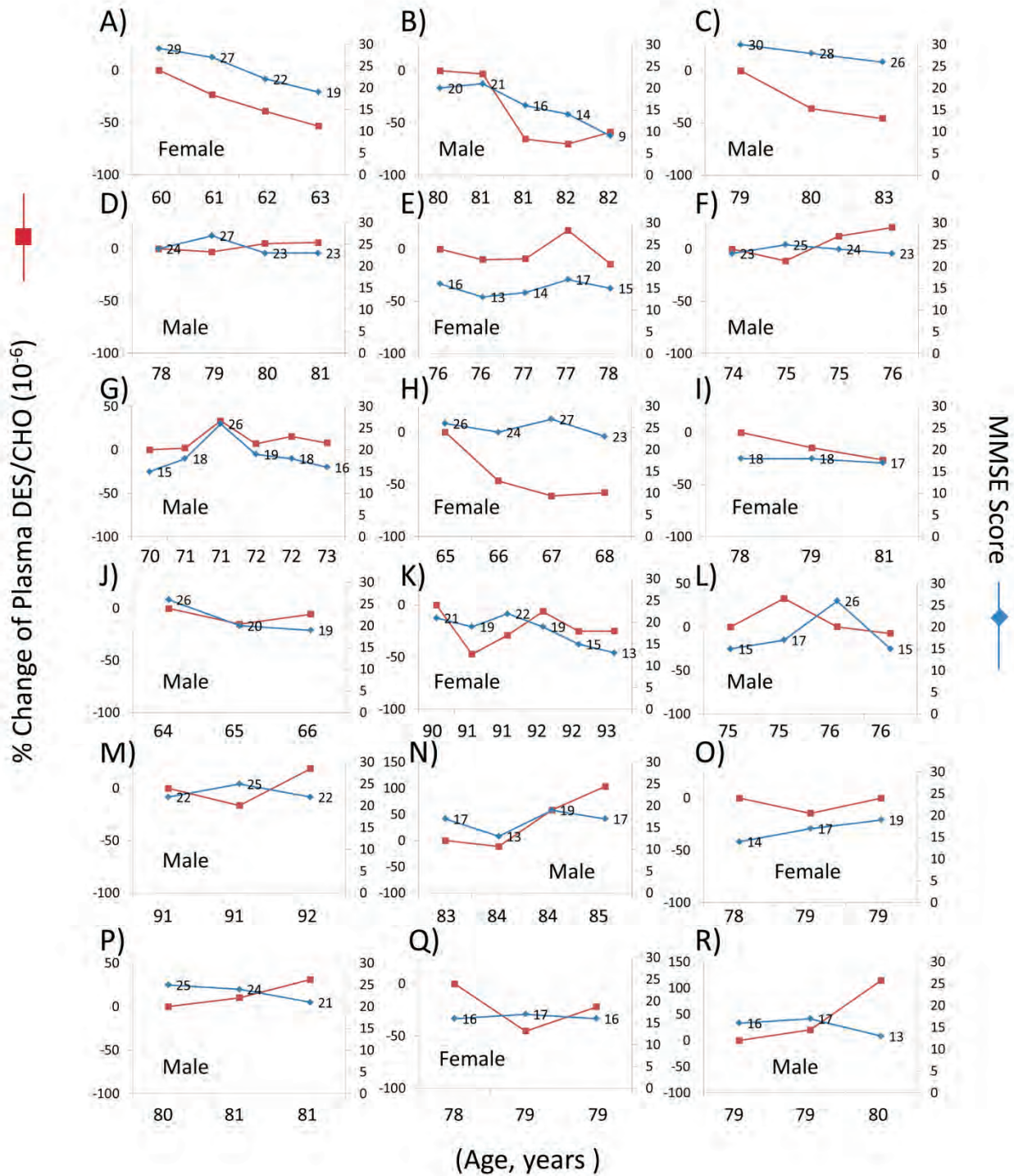
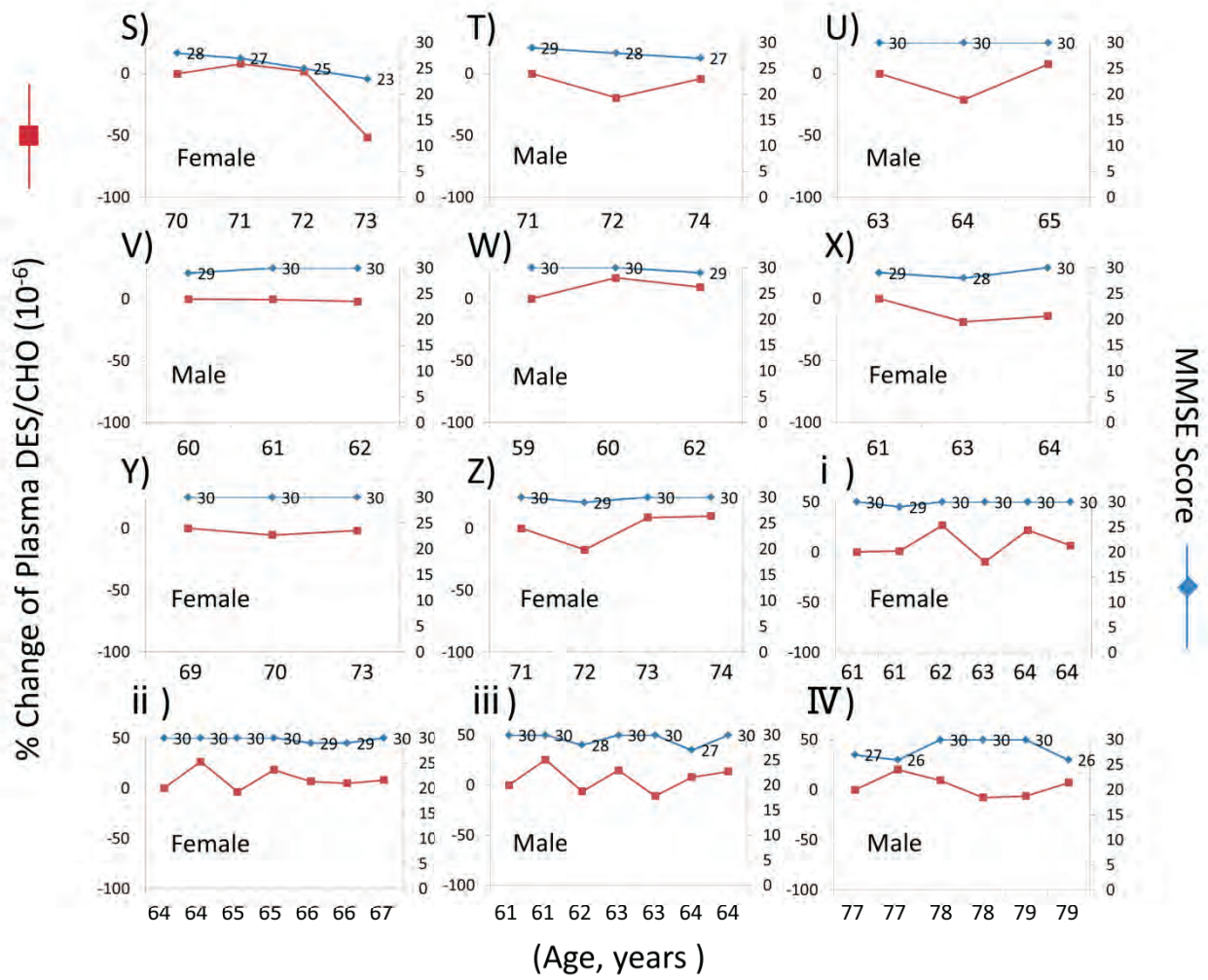


Figure legend for Supplementary Fig. 2:

Changes in plasma DES/CHO and MMSE scores in AD patients (A-R), MCI subjects (S-X), and normal subjects (Y-IV). The longitudinal change in plasma DES/CHO (red line) was compared with the baseline value. Longitudinal MMSE scores are shown in blue.

Supplementary Figure 2. Sato et al. (continued)



SHORT COMMUNICATION

Systematic review and meta-analysis of Japanese familial Alzheimer's disease and FTDP-17

Kensaku Kasuga^{1,2,6}, Masataka Kikuchi^{1,3,6}, Takayoshi Tokutake⁴, Akihiro Nakaya^{1,5}, Toshiyuki Tezuka⁴, Tamao Tsukie^{1,3}, Norikazu Hara¹, Akinori Miyashita¹, Ryoza Kuwano¹ and Takeshi Ikeuchi¹

Mutations in *APP*, *PSEN1* and *PSEN2* as the genetic causes of familial Alzheimer's disease (FAD) have been found in various ethnic populations. A substantial number of FAD pedigrees with mutations have been reported in the Japanese population; however, it remains unclear whether the genetic and clinical features of FAD in the Japanese population differ from those in other populations. To address this issue, we conducted a systematic review and meta-analysis of Japanese FAD and frontotemporal dementia with parkinsonism linked to chromosome 17 (FTDP-17) by literature search. Using this analysis, we identified 39 different *PSEN1* mutations in 140 patients, 5 *APP* mutations in 35 patients and 16 *MAPT* mutations in 84 patients. There was no *PSEN2* mutation among Japanese patients. The age at onset in Japanese FAD patients with *PSEN1* mutations was significantly younger than that in patients with *APP* mutations. Kaplan–Meier analysis revealed that patients with *MAPT* mutations showed a shorter survival than patients with *PSEN1* or *APP* mutations. Patients with mutations in different genes exhibit characteristic clinical presentations, suggesting that mutations in causative genes may modify the clinical presentations. By collecting and cataloging genetic and clinical information on Japanese FAD and FTDP-17, we developed an original database designated as Japanese Familial Alzheimer's Disease Database, which is accessible at <http://alzdb.bri.niigata-u.ac.jp/>.

Journal of Human Genetics (2015) 60, 281–283; doi:10.1038/jhg.2015.15; published online 19 February 2015

Mutations in *APP*, *PSEN1* and *PSEN2* as the genetic causes of familial Alzheimer's disease (FAD) have been found in various ethnic populations.^{1,2} In addition, patients with mutations in *MAPT* associated with frontotemporal dementia with parkinsonism linked to chromosome 17 (FTDP-17) have been shown to exhibit Alzheimer's disease (AD)-like phenotypes.^{3,4} Although a substantial number of FAD pedigrees have been reported in Japan, it is not yet clear whether the genetic and clinical features of FAD in the Japanese population differ from those in other ethnic populations. To characterize the genetic and clinical features of Japanese FAD and FTDP-17, we here performed a systematic review and meta-analysis, and developed an original database of Japanese FAD and FTDP-17.

To comprehensively review the previously reported Japanese FAD and FTDP-17 cases, we performed a systematic search for publications in PubMed and Ichushi, a bibliographic database of medical literature in Japanese. The terms 'familial Alzheimer', 'familial AD', 'FTDP-17', 'presenilin', '*PSEN1*', '*PSEN2*', '*APP*' and '*MAPT*' were used to search in PubMed, and the equivalent terms in Japanese were used to search in Ichushi. From the literature searches we found 60 English and 29 Japanese articles and/or abstracts that reported on Japanese FAD and FTDP-17 pedigrees bearing the causative mutations (Supplementary

Table 1). Using the information obtained by the systematic literature review, we developed an original database for Japanese FAD and FTDP-17 designated as Japanese Familial Alzheimer's Disease database (JFADdb). In the database, each of the mutations in *APP*, *PSEN1/2*, *MAPT* and *GRN* was described in accordance with the reference sequences.⁵ Information on age at onset, clinical manifestations, age at death and *APOE* genotype were included in the database (Supplementary Figure 1).

We identified 39 different *PSEN1* mutations in 140 patients, 5 *APP* mutations in 35 patients and 16 *MAPT* mutations in 84 patients (Table 1). Among them, 10 *PSEN1* mutations, 5 *APP* mutations and 11 *MAPT* mutations were not included in the well-known Alzheimer Disease and Frontotemporal Dementia Mutation database (<http://www.molgen.ua.ac.be/ADMutations/>).⁶ No *PSEN2* mutation has been found in Japanese FAD. The frequency of mutated genes in FAD patients in the Japanese population was not significantly different from those in other populations (χ^2 , $P=0.99$).⁶ Most FAD pedigrees show autosomal dominant inheritance; however, an *APP* $\Delta E693$ mutation was responsible for a recessively inherited FAD.⁷ Sporadic occurrences of mutations were observed: five patients with *PSEN1* mutations, one patient with *APP* mutation and two patients with *MAPT* mutations.

¹Department of Molecular Genetics, Brain Research Institute, Niigata University, Niigata, Japan; ²Center for Transdisciplinary Research, Niigata University, Niigata, Japan; ³Research Association for Biotechnology, Tokyo, Japan; ⁴Department of Neurology, Brain Research Institute, Niigata University, Niigata, Japan and ⁵Department of Genome Informatics, Graduate School of Medicine, Osaka University, Osaka, Japan

⁶These authors contributed equally to this work.

Correspondence: Dr T Ikeuchi, Department of Molecular Genetics, Brain Research Institute, Niigata University, 1-757 Asahimachi, Niigata 951-8585, Japan. E-mail: ikeuchi@bri.niigata-u.ac.jp

Received 7 November 2014; revised 7 January 2015; accepted 13 January 2015; published online 19 February 2015

Table 1 Summary of genetic features of Japanese FAD and FTDP-17

Disease	Genes	Number of mutations	Number of pedigrees	Number of patients
FAD	<i>PSEN1</i>	39	40	140
	<i>PSEN2</i>	0	0	0
	<i>APP</i>	5 ^a	13	35
FTDP-17	<i>MAPT</i>	16	29	84
	<i>GRN</i>	2	2	2

Abbreviations: FAD, familial Alzheimer's disease; FTDP-17, frontotemporal dementia with parkinsonism linked to chromosome 17.

^a*APP* duplication was included.

In our analysis, the majority of mutations (73%) was observed in a single small pedigree. Considering that novel mutations in FAD tend to be reported rapidly, note that there may be publication bias in the frequency of mutations in the database. Although rare, there were two *GRN* mutations in patients with primary progressive aphasia and frontotemporal lobar degeneration (FTLD).⁸ Because the number of *GRN* mutations was too small, the patients with *GRN* mutations were excluded from further meta-analysis.

The ages at onset were 44 ± 8 years (mean \pm s.d.) in patients with *PSEN1* mutations ($n=87$), 54 ± 9 years in *APP* mutations ($n=23$) and 45 ± 10 years in *MAPT* mutations ($n=51$). These ages at onset of FAD in our analysis are consistent with those reported in other ethnic populations.^{6,9} The age at onset in patients with *APP* mutations was significantly older than those in patients with *PSEN1* or *MAPT* mutations (Figure 1a). The clinical phenotypes of patients with *MAPT* mutations were classified into three subgroups: FTLD,¹⁰ AD-like^{3,4} and progressive supranuclear palsy (PSP) phenotypes.⁸ The age at onset in patients with the FTLD or PSP phenotype was significantly younger than that with the AD-like phenotype (Supplementary Figure 2). *APOE* genotypes did not significantly modify the age at onset in patients with causative mutations (Supplementary Figure 3). There was no significant difference in age at death among the patients with mutations in the three genes (Figure 1b). The disease duration from age at onset to death in patients with *MAPT* mutations was significantly shorter than that with *PSEN1* mutations (Figure 1c). The survival of patients after the onset was analyzed by Kaplan–Meier estimation, which revealed that patients with *MAPT* mutations showed a shorter survival than patients with *PSEN1* or *APP* mutations (Supplementary Figure 4).

The clinical diagnosis of AD before the genetic testing was performed in 96% of patients with *PSEN1* mutations and 97% of patients with *APP* mutations (Supplementary Table 2). Notably, only 57% of patients with *MAPT* mutations were clinically diagnosed as having FTLD; 19% and 12% of patients with *MAPT* mutations were clinically diagnosed as having AD and PSP, respectively (Supplementary Table 2). This finding suggests that mutational screening of clinically diagnosed FAD patients should not only include *APP* and *PSEN1/2* mutations but also include *MAPT* mutations.

We next analyzed the frequency of each of the clinical manifestations including psychiatric symptoms, mood disorders, spastic paraparesis, parkinsonism and epilepsy/seizure (Figure 2). As expected, the frequencies of psychiatric symptoms and parkinsonism were significantly higher in patients with *MAPT* mutations. Spastic paraparesis, which is a characteristic symptom of 'variant AD with cotton-wool plaque pathology'^{11,12} was observed in 15% of patients with *PSEN1* mutations, whereas none of the patients with *APP* mutations exhibited spastic paraplegia. Epilepsy/seizure was described in 8% of patients with *PSEN1* and 6% of patients with *APP* mutations,

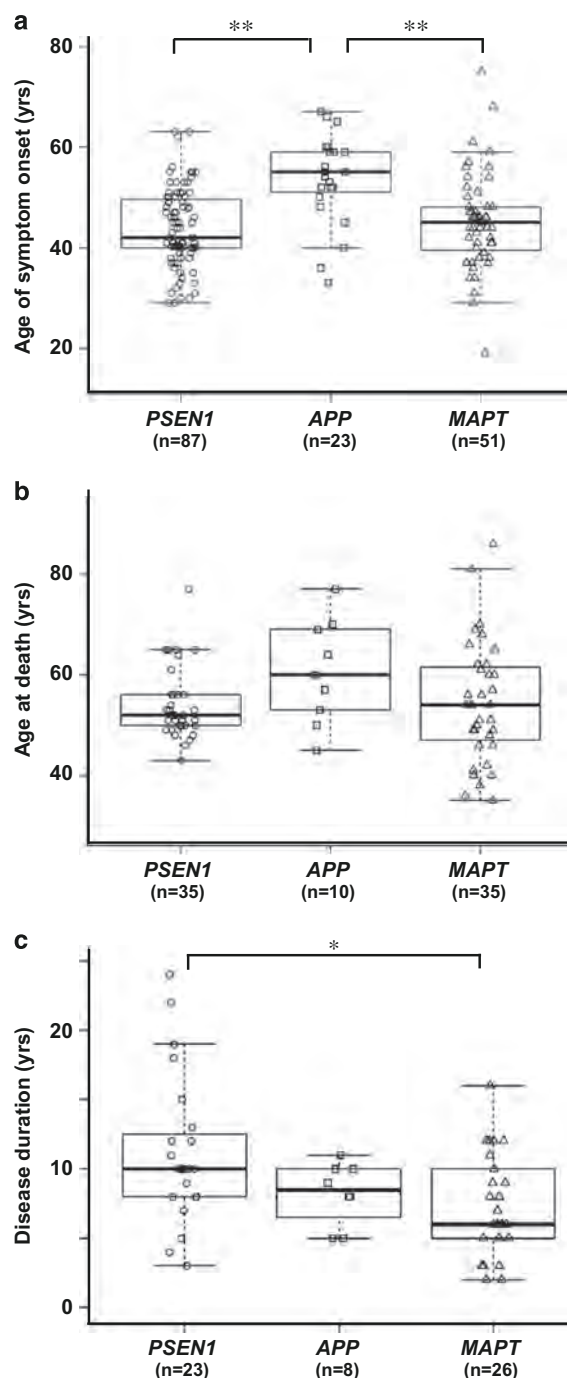


Figure 1 Age at onset and death, and disease duration in Japanese FAD and FTDP-17 patients. (a) Age at onset for patients grouped on the basis of *PSEN1*, *APP* and *MAPT* mutations. The horizontal line in the box indicates the median, the lower and upper boundaries of the box represent the lower and upper quartile boundaries, respectively, and whiskers are 1.5 times the interquartile range. Patients with *PSEN1* and *MAPT* mutation showed significantly younger age at onset than patients with *APP* mutations (** $P < 0.01$, ANOVA with *post hoc* Tukey's test). (b) Age at death of three groups with gene mutations. There was no significant difference in age at death among the groups. (c) Disease duration was defined as the period from age at onset to death. The disease courses of patients with *MAPT* mutations (7 ± 4 years, mean \pm s.d.) were significantly shorter than those with *PSEN1* mutations (11 ± 5) (* $P < 0.05$, ANOVA with *post hoc* Tukey's test). ANOVA, analysis of variance; FAD, familial Alzheimer's disease; FTDP-17, frontotemporal dementia with parkinsonism linked to chromosome 17.

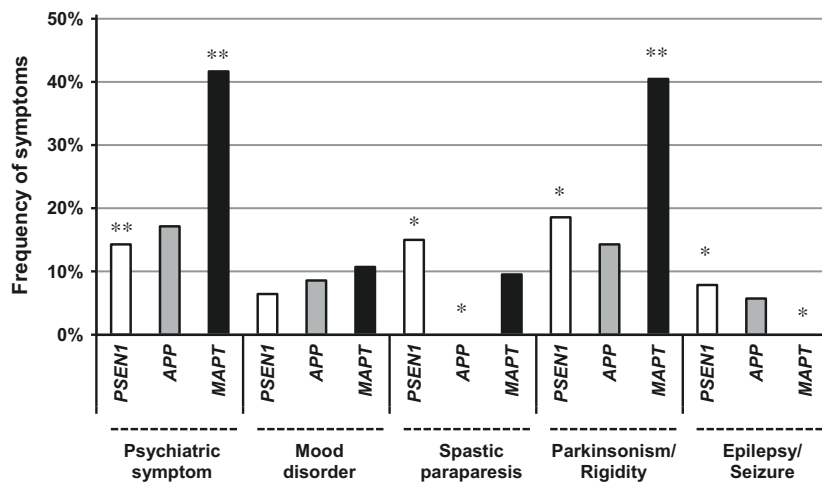


Figure 2 Frequency of each clinical manifestation in patients with Japanese FAD and FTDP-17. We investigated the presence or absence of psychiatric symptoms, mood disorders, spastic paraplegia, parkinsonism and epilepsy/seizure by careful reading of the original papers. We determined the frequency of each of the clinical manifestations by counting the number of patients for whom the presence of the manifestation was described in literature. In case there was no description of the manifestation, the patient was not counted as manifesting the manifestation. The observed frequencies of causative gene mutation were significantly different from the expected frequencies determined by residual analyses for χ^2 statistical analysis (* $P < 0.05$, ** $P < 0.01$). FAD, familial Alzheimer's disease; FTDP-17, frontotemporal dementia with parkinsonism linked to chromosome 17.

whereas none of the patients with *MAPT* mutations exhibited epilepsy/seizure. Previous studies showed that the frequency of seizure was relatively high in patients with early onset of AD,^{13,14} and low in patients with *MAPT* mutations.¹⁵ These findings suggest that epilepsy/seizure is closely associated with amyloid pathology, and that tauopathy alone may not be sufficient to cause epilepsy. Taken together, mutations in causative genes may modify the clinical presentations in patients with familial dementia.

In summary, we have comprehensively collected, cataloged and systematically meta-analyzed the data from currently available data on Japanese FAD and FTDP-17. We made all the results publicly available on the online database 'JFADdb'. The database may provide information useful for estimating the age at onset and the natural course of disease in future preventive or therapeutic trials of Japanese FAD.

CONFLICT OF INTEREST

The authors declare no conflict of interest.

ACKNOWLEDGEMENTS

This work is supported in part by Grants-in-Aid for scientific research from Japan Society of Promotion of Science, Japan (26870209 to KK, 23591234 and 20372469 to TI) and Grant-in-Aid from the Ministry of Health, Labour and Welfare of Japan. We are grateful to Dr Hasegawa and Ms Fukuami for their technical assistance.

- The role of *PSEN1* and *MAPT* R406W mutations. *Dement. Geriatr. Cogn. Disord.* **26**, 43–49 (2008).
- Pruitt, K. D., Brown, G. R., Hiatt, S. M., Thibaud-Nissen, F., Astashyn, A. & Ermolaeva, O. *et al.* RefSeq: an update on mammalian reference sequences. *Nucleic Acids Res.* **42**, D756–D763 (2014).
 - Cruts, M., Theuns, J. & Van Broeckhoven, C. Locus-specific mutation databases for neurodegenerative brain diseases. *Hum. Mutat.* **33**, 1340–1344 (2012).
 - Tomiyama, T., Nagata, T., Shimada, H., Teraoka, R., Fukushima, A. & Kanemitsu, H. *et al.* A new amyloid beta variant favoring oligomerization in Alzheimer's-type dementia. *Ann. Neurol.* **63**, 377–387 (2008).
 - Ogaki, K., Li, Y., Takanashi, M., Ishikawa, K., Kobayashi, T. & Nonaka, T. *et al.* Analyses of the *MAPT*, *PGRN*, and *C9orf72* mutations in Japanese patients with FTLD, PSP, and CBS. *Parkinsonism Relat. Disord.* **19**, 15–20 (2013).
 - Ryman, D. C., Acosta-Baena, N., Aisen, P. S., Bird, T., Danek, A. & Fox, N. C. *et al.* Symptom onset in autosomal dominant Alzheimer disease: a systematic review and meta-analysis. *Neurology* **83**, 253–260 (2014).
 - Foster, N. L., Wilhelmsen, K., Sima, A. A. F., Jones, M. Z. & D'Amato, C. J. *et al.* Frontotemporal dementia and parkinsonism linked to chromosome 17: a consensus conference. *Ann. Neurol.* **41**, 706–715 (1997).
 - Larner, A. J. & Doran, M. Clinical phenotypic heterogeneity of Alzheimer's disease associated with mutations of the presenilin-1 gene. *J. Neurol.* **253**, 139–158 (2006).
 - Tabira, T., Chui, D. H., Nakayama, H., Kuroda, S. & Shibuya, M. Alzheimer's disease with spastic paresis and cotton wool type plaques. *J. Neurosci. Res.* **70**, 367–372 (2002).
 - Noebels, J. A perfect storm: converging paths of epilepsy and Alzheimer's dementia intersect in the hippocampal formation. *Epilepsia* **52**, 39–46 (2011).
 - Vossel, K. A., Beagle, A. J., Rabinovici, G. D., Shu, H., Lee, S. E. & Naasan, G. *et al.* Seizures and epileptiform activity in the early stages of Alzheimer disease. *JAMA Neurol.* **70**, 1158–1166 (2013).
 - Sperfeld, A. D., Collatz, M. B., Baier, H., Palmbach, M., Storch, A. & Schwarz, J. *et al.* FTDP-17: an early-onset phenotype with parkinsonism and epileptic seizures caused by a novel mutation. *Ann. Neurol.* **46**, 708–715 (1999).



This work is licensed under a Creative Commons Attribution-NonCommercial-NoDerivs 3.0 Unported License. The images or other third party material in this article are included in the article's Creative Commons license, unless indicated otherwise in the credit line; if the material is not included under the Creative Commons license, users will need to obtain permission from the license holder to reproduce the material. To view a copy of this license, visit <http://creativecommons.org/licenses/by-nc-nd/3.0/>

- Karch, C. M., Cruchaga, C. & Goate, A. M. Alzheimer's disease genetics: from the bench to the clinic. *Neuron* **83**, 11–26 (2014).
- Guerreiro, R. J., Gustafson, D. R. & Hardy, J. The genetic architecture of Alzheimer's disease: beyond APP, PSENs and APOE. *Neurobiol. Aging* **33**, 437–456 (2012).
- Rademakers, R., Dermaut, B., Peeters, K., Cruts, M., Heutink, P. & Goate, A. *et al.* Tau (*MAPT*) mutation Arg406Trp presenting clinically with Alzheimer disease does not share a common founder in Western Europe. *Hum. Mutat.* **22**, 409–411 (2003).
- Ikeuchi, T., Kaneko, H., Miyashita, A., Nozaki, H., Kasuga, K. & Tsukie, T. *et al.* Mutational analysis in early-onset familial dementia in the Japanese population.

Supplementary Information accompanies the paper on Journal of Human Genetics website (<http://www.nature.com/jhg>)



Contents lists available at ScienceDirect

Biochemical and Biophysical Research Communications

journal homepage: www.elsevier.com/locate/ybbrc

ApoE-isoform-dependent cellular uptake of amyloid- β is mediated by lipoprotein receptor LR11/SorLA



Ryuji Yajima^a, Takayoshi Tokutake^a, Akihide Koyama^b, Kensaku Kasuga^{a,b,c}, Toshiyuki Tezuka^{a,c}, Masatoyo Nishizawa^a, Takeshi Ikeuchi^{c,*}

^a Department of Neurology, Brain Research Institute, Niigata University, Niigata, Japan

^b Center for Transdisciplinary Research, Niigata University, Niigata, Japan

^c Department of Molecular Genetics, Brain Research Institute, Niigata University, Niigata, Japan

ARTICLE INFO

Article history:

Received 7 November 2014

Available online 5 December 2014

Keywords:

Alzheimer's disease

LR11/SorLA

β -Amyloid

Apolipoprotein E

ABSTRACT

The formation of senile plaques composed of β -amyloid (A β) in the brain is likely the initial event in Alzheimer's disease (AD). Possession of the *APOE* ϵ 4 allele, the strong genetic factor for AD, facilitates the A β deposition from the presymptomatic stage of AD in a gene-dosage-dependent manner. However, the precise mechanism by which apoE isoforms differentially induce the AD pathology is largely unknown. LR11/SorLA is a type I membrane protein that functions as the neuronal lipoprotein endocytic receptor of apoE and the sorting receptor of the amyloid precursor protein (APP) to regulate amyloidogenesis. Recently, LR11/SorLA has been reported to be involved in the lysosomal targeting of extracellular amyloid- β (A β) through the binding of A β to the vacuolar protein sorting 10 (VPS10) protein domain of LR11/SorLA. Here, we attempted to examine the human-apoE-isoform-dependent effect on the cellular uptake of A β through the formation of a complex between an apoE isoform and LR11/SorLA. Cell culture experiments using Neuro2a cells revealed that the cellular uptake of secreted apoE3 and apoE4 was enhanced by the overexpression of LR11/SorLA. In contrast, the cellular uptake of apoE2 was not affected by the expression of LR11/SorLA. Co-immunoprecipitation assay revealed that apoE-isoform-dependent differences were observed in the formation of an apoE-LR11 complex (apoE4 > apoE3 > apoE2). ApoE-isoform-dependent differences in cellular uptake of FAM-labeled A β were further investigated by coculture assay in which donor cells secrete one of the apoE isoforms and recipient cells express FL-LR11. The cellular uptake of extracellular A β into the recipient cells was most prominently accentuated when cocultured with the donor cells secreting apoE4 in the medium, followed by apoE3 and apoE2. Taken together, our results provide evidence for the mechanism whereby human-apoE-isoform-dependent differences modulate the cellular uptake of A β mediated by LR11/SorLA.

© 2014 Elsevier Inc. All rights reserved.

1. Introduction

Alzheimer's disease (AD) has emerged as the most prevalent form of dementia in adults. The cardinal pathological features of AD brain are the loss of synapses and neurons as well as abnormal accumulation of misfolded proteins such as β -amyloid (A β) and

phosphorylated tau. The deposition of A β in the brain is considered to be the earliest event in AD [1] and is substantially affected by the *APOE* genotype, which has been shown to be a strong genetic risk factor for AD in various ethnic populations [2,3]. The presence of the *APOE* ϵ 4 allele markedly increases the risk of developing AD and decreases the age at onset by 10 to 15 years; in contrast, the ϵ 2 allele confers protection against AD development [4,5]. Although there have been numerous studies attempting to elucidate the mechanism underlying the increase or decrease in the risk of AD posed by different apoE isoforms [6], the exact mechanisms are still not completely understood. Thus, to address the differential effects of apoE isoforms on the amyloid pathology and A β metabolism is important in the elucidation of the AD pathogenic pathway.

LR11, also known as SorLA, is a type I membrane protein that has homology to members of the LDL receptor family and vacuolar

Abbreviations: AD, Alzheimer's disease; A β , amyloid- β ; APP, amyloid precursor protein; VPS10, vacuolar protein sorting 10; TACE, tumor necrosis factor- α -converting enzyme; FL, full-length; CSF, cerebrospinal fluid; PCR, polymerase chain reaction; GFP, green fluorescent protein; HEK, human embryonic kidney; SDS-PAGE, sodium dodecyl sulfate-polyacrylamide gel electrophoresis; co-IP, coimmunoprecipitation.

* Corresponding author at: Department of Molecular Genetics, Brain Research Institute, Niigata University, 1-757 Asahimachi, Niigata 951-8585, Japan. Fax: +81 25 227 0793.

E-mail address: ikeuchi@bri.niigata-u.ac.jp (T. Ikeuchi).

<http://dx.doi.org/10.1016/j.bbrc.2014.11.111>

0006-291X/© 2014 Elsevier Inc. All rights reserved.

protein sorting 10 (VPS10) protein family. LR11/SorLA is predominantly expressed on neurons in the cerebral cortex and hippocampus [7]. Reduced expression of LR11/SorLA in the brains of AD patients and subjects with mild cognitive impairment has been reported [8]. Furthermore, A β deposition is more prominent in LR11 knockout mice crossed with a mouse AD model [9]. These findings suggest the protective role of LR11/SorLA against AD pathology. In addition, some of the single-nucleotide polymorphisms (SNPs) in *SORL1* encoding LR11/SorLA were found to be associated with a risk of sporadic AD in various ethnic backgrounds [3]. Full-length (FL) LR11/SorLA is cleaved by tumor necrosis factor- α -converting enzyme (TACE) to generate soluble LR11 [10]. We previously reported that the level of soluble LR11/SorLA was significantly high in the cerebrospinal fluid (CSF) of patients with AD [11]. The *APOE* ϵ 4 carriers among AD patients showed higher levels of soluble LR11/SorLA than the ϵ 4 noncarriers [11]. This suggests that the level of soluble LR11/SorLA in CSF is associated with AD in an apoE-isoform-dependent manner.

LR11/SorLA functions as the neuronal lipoprotein endocytic receptor of ApoE [12] and the sorting receptor of the amyloid precursor protein (APP) to regulate amyloidogenesis in endosomal and Golgi compartments [13]. LR11/SorLA interacts with newly synthesized APP in the Golgi apparatus and prevents the trafficking of APP into the cellular compartment where secretases reside. Consequently, the overexpression of LR11/SorLA in cultured cells reduces amyloidogenic processing [14]. Very recently, a novel function of LR11/SorLA has been reported. Caglayan et al. reported that LR11/SorLA plays a role in the lysosomal targeting of newly generated A β through the binding of A β to the amino-terminal VPS10 protein domain of LR11 [15]. This binding enhances A β clearance in lysosomes by internalization of extracellular A β through the receptor LR11/SorLA. With this as a background, we here attempted to determine the apoE-isoform-dependent effects on the cellular uptake of A β through the formation of a complex between an apoE isoform and LR11/SorLA.

2. Materials and methods

2.1. cDNA cloning and construction of expression plasmids

Complementary DNA (cDNA) of human full-length LR11 was amplified by PCR using pCMV6 plasmid cDNA containing human LR11 (Origene, Rockville, USA) and cloned into the pcDNA3.1 vector (Life Technologies, Carlsbad, USA). Human *APOE* ϵ 3 cDNA was cloned and inserted into the pcDNA3.1 vector. We generated two allelic variants of human *APOE*, namely, *APOE* ϵ 2 and ϵ 4, by mutagenesis. Each isoform of *APOE* was cloned into the pEGFP vector (Clontech, Mountain View, USA). All constructs generated from PCR products were verified by DNA sequencing.

2.2. Cell culture and transfection

Mouse neuroblastoma Neuro2a (N2a) and human embryonic kidney (HEK)293T cells were cultured as previously described [16]. Transient transfection of plasmid DNA into cells was carried out by using Lipofectamine 2000 (Life Technologies). To generate stable cell lines, N2a cells transfected with cDNA encoding human apoE2, apoE3, apoE4 or FL-LR11 were selected using G418. Peptides of A β 40 were purchased from Wako (Tokyo, Japan) and FAM-labeled A β 40 from AnaSpec (Fremont, USA). They were dissolved in 1% ammonium hydroxide.

2.3. Coculture system

Coculture experiments were performed essentially as previously described [16]. Donor HEK293T cells transiently transfected

with cDNA encoding human apoE2, apoE3, apoE4, apoE2-GFP, apoE3-GFP, or apoE4-GFP were cultured on a dish with a 1.0 μ m filter insert (BD Bioscience, San Diego, USA) for 24 h. The donor HEK293T cells on the dish were placed in a six-well culture dish containing the recipient N2a cells mock-transfected or transiently transfected with the FL-LR11 cDNA construct. After 24 h of coculture, the lysate of the recipient cells and the medium were subjected to Western blot analysis.

2.4. Western blot analysis

The cells were solubilized using a lysis buffer (150 mM NaCl, 50 mM Tris-HCl, pH 7.4, 0.5% NP-40, 0.5% sodium deoxycholate, and 5 mM EDTA). The protein concentration of the detergent-extracted lysates was determined using a bicinchoninic acid protein assay kit (Pierce, Rockford, USA). Equal amounts of protein were boiled in Laemmli sample buffer and then subjected to Tris-glycine or Tris-tricine SDS-PAGE system. The separated proteins were transferred to a polyvinylidene difluoride membrane (Millipore, Billerica, USA) and then incubated with appropriate primary antibodies. FL-LR11 and sLR11 were detected using the monoclonal antibody 48/LR11 (BD Biosciences), which recognizes the extracellular domain of LR11. ApoE was visualized by the monoclonal antibody E6D7 (Sigma, St. Louis, USA). A β polypeptides were detected by the monoclonal antibody 6E10 (Covance, Berkeley, USA). GFP-fusion proteins were detected by the monoclonal antibody 1E4 (MBL, Japan). Actin was detected using the goat anti-actin antibody I-19 (Santa Cruz Biotechnology, Dallas, USA). Immunoreactive bands were detected using an Immobilon Western Chemiluminescent HRP substrate (Millipore). The band intensities were quantified using a LAS system (GE Healthcare, Pittsburgh, USA).

2.5. Co-immunoprecipitation assays

HEK293T cells were cotransfected with the cDNA encoding apoE2, apoE3, or apoE4 and with FL-LR11 cDNA. The cells were solubilized using co-IP buffer (1% CHAPS, 150 mM NaCl, 50 mM HEPES, pH 7.5). The supernatant was incubated with either an anti-LR11 antibody (48/LR11) or an anti-apoE antibody (AB947, Millipore) at 4 °C for 16 h. To immunoprecipitate the protein complex, 25 μ L of protein G Mag Sepharose beads (GE Healthcare) was added to the mixture, and the mixture was incubated on a rotator at 4 °C. The beads were collected on a magnetic stand and washed three times with the solubilization buffer. The immunoprecipitated proteins were released from the beads by incubation in Laemmli sample buffer. The obtained samples were analyzed by SDS-PAGE followed by Western blot analysis.

2.6. Fluorescence confocal laser scanning microscopy and image analysis

N2a cells treated with GFP-labeled apoE3 or FAM-labeled A β 40 were cultured. All images were obtained using an inverted microscope (TE-300NT, Nikon, Japan) and a confocal microscope (CSU-10, Yokogawa Electric Corp, Japan). The obtained images were further analyzed with a quantitative analysis system (AquaCosmos, Hamamatsu Photonics, Japan).

2.7. Statistical analyses

Data are shown as the mean \pm standard error of the mean (SEM). Statistical comparison between two groups was carried out by the Student *t*-test. For statistical comparison among several groups, we used one-way analysis of variance (ANOVA) followed

by the Tukey post hoc test. The statistical analyses were performed using SPSS ver. 12.0 J (SPSS Japan).

3. Results

3.1. Isoform-dependent change in level of secreted apoE by expression of LR11/SorLA

We first determined whether the expression of FL-LR11/SorLA affects the levels of apoE in the lysate and medium. N2a cells stably expressing human apoE3 were mock-transfected or transiently transfected with human FL-LR11 cDNA. The levels of apoE3 in the medium and lysate were determined using the anti-apoE antibody at different time points from 2 to 24 h after the medium was replaced. The level of apoE3 migrating at ~34 kDa and secreted into the medium increased after the medium replacement in a

time-dependent manner (Fig. 1A). The level of apoE3 in the medium was significantly lower in N2a cells transfected with FL-LR11 24 h after the medium change compared with mock-transfected cells, whereas the level of apoE in the lysate was comparable between the mock- and FL-LR11-transfected cells (Fig. 1B).

Next, we investigated whether apoE-isoform-dependent differences are observed in this study. N2a cells stably expressing human apoE2, apoE3, or apoE4, were mock-transfected or transiently transfected with FL-LR11, and the levels of apoE in the medium and lysate were determined by immunoblot analysis. The apoE ratio (medium/lysate) significantly decreased in apoE3- and E4-expressing cells that were transiently transfected with FL-LR11 (Fig. 1C and D), whereas the apoE ratio (medium/lysate) was unchanged in apoE2-expressing cells transfected with FL-LR11. These findings suggest that the effect of LR11/SorLA on apoE ratio (medium/lysate) is dependent on the apoE isoform.

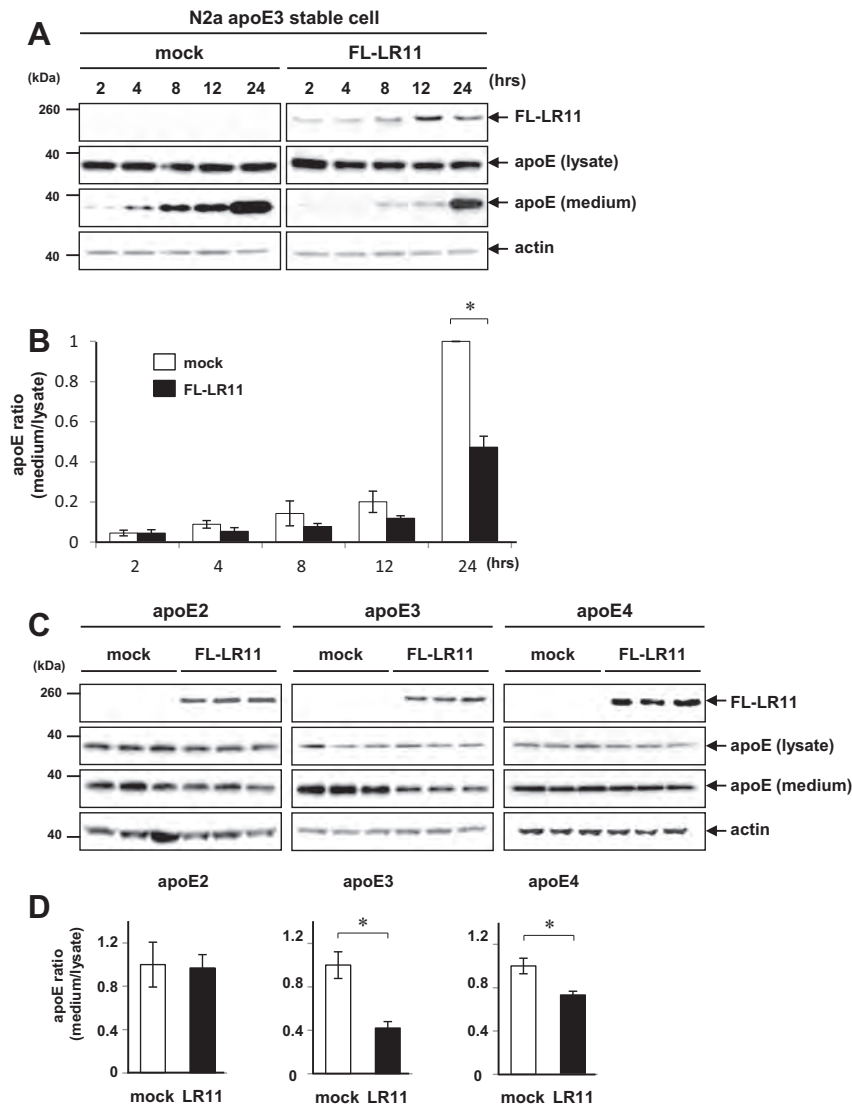


Fig. 1. Human-apoE-isoform-dependent differences in apoE ratio mediated by LR11/SorLA. (A) N2a cells stably expressing human apoE3 were mock-transfected or transiently transfected with human FL-LR11. The levels of apoE3 in the medium and cell lysate were determined by immunoblot analysis at different time points ranging from 2 to 24 h after the medium change. Note that the level of apoE in the medium of cells expressing FL-LR11 was decreased compared with mock-transfected cells. The equivalence of protein loading is shown in the β -actin blot. (B) Results of semiquantitative analysis by densitometry of apoE level. The apoE ratio (medium/lysate) was defined as the ratio of the level of apoE in the medium to that in the cell lysate. The apoE ratio (medium/lysate) significantly decreased 24 h after the medium change in cells transfected with FL-LR11 compared with mock-transfected cells. Results of three independent experiments are shown as mean \pm SEM. * $p < 0.05$ by Student t -test. (C) N2a cells stably expressing human apoE2, apoE3, or apoE4 were mock-transfected or transiently transfected with human FL-LR11. The levels of apoE in the medium and the lysate of cells expressing each of the apoE isoforms were determined 24 h after the medium change. (D) Results of semiquantitative analysis of the apoE ratio (medium/lysate). The apoE ratio (medium/lysate) was significantly decreased in apoE3- or apoE4-expressing cells transfected with FL-LR11, whereas the apoE ratio did not change in apoE2-expressing cells. * $p < 0.05$.

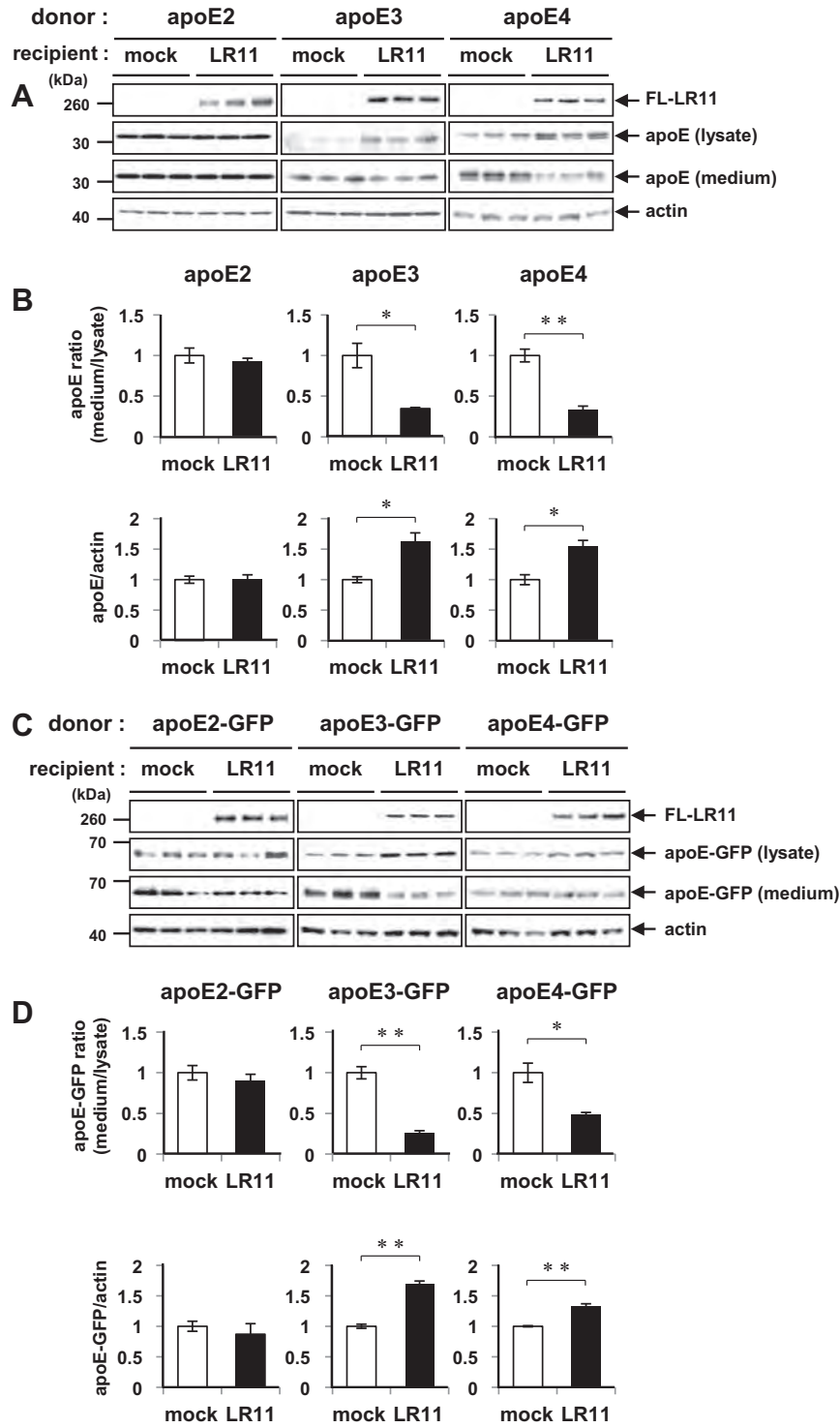


Fig. 2. ApoE isoform-dependent cellular uptake of apoE by LR11/SorLA in coculture system. (A) The recipient N2a cells mock-transfected or transiently transfected with FL-LR11 were cocultured with the donor HEK293T cells that were transiently transfected with apoE2, apoE3, or apoE4 for 24 h. Cellular uptake of secreted apoE from the medium into the recipient N2a cells was examined by Western blot analysis. (B) Results of semiquantitative analysis of cellular uptake of apoE are shown. The apoE ratio (medium/lysate) significantly decreased in the recipient cells transfected with FL-LR11 compared with the mock-transfected recipient cells when the recipient cells were cocultured with the donor HEK293T cells expressing apoE3 or apoE4 (upper panels). The apoE level normalized by β -actin level in the lysate of the recipient cells transfected with FL-LR11 showed a significant increase compared with that of mock-transfected recipient cells when the recipient cells were cocultured with the donor HEK293T cells expressing apoE3 or apoE4 (lower panels). * $p < 0.05$; ** $p < 0.01$. (C) The recipient N2a cells mock-transfected or transiently transfected with FL-LR11 were cocultured with the donor HEK293T cells that secreted apoE2-GFP, apoE3-GFP, or apoE4-GFP in the medium for 24 h. Cellular uptake of apoE from the medium into the recipient N2a cells was examined. (D) Results of semiquantitative analysis of cellular uptake of apoE-GFP are shown. The apoE ratios (medium/lysate) for the apoE isoforms are shown (upper panels). The levels of apoE-GFP normalized by β -actin level for the apoE isoforms are shown (lower panels). * $p < 0.05$; ** $p < 0.01$.

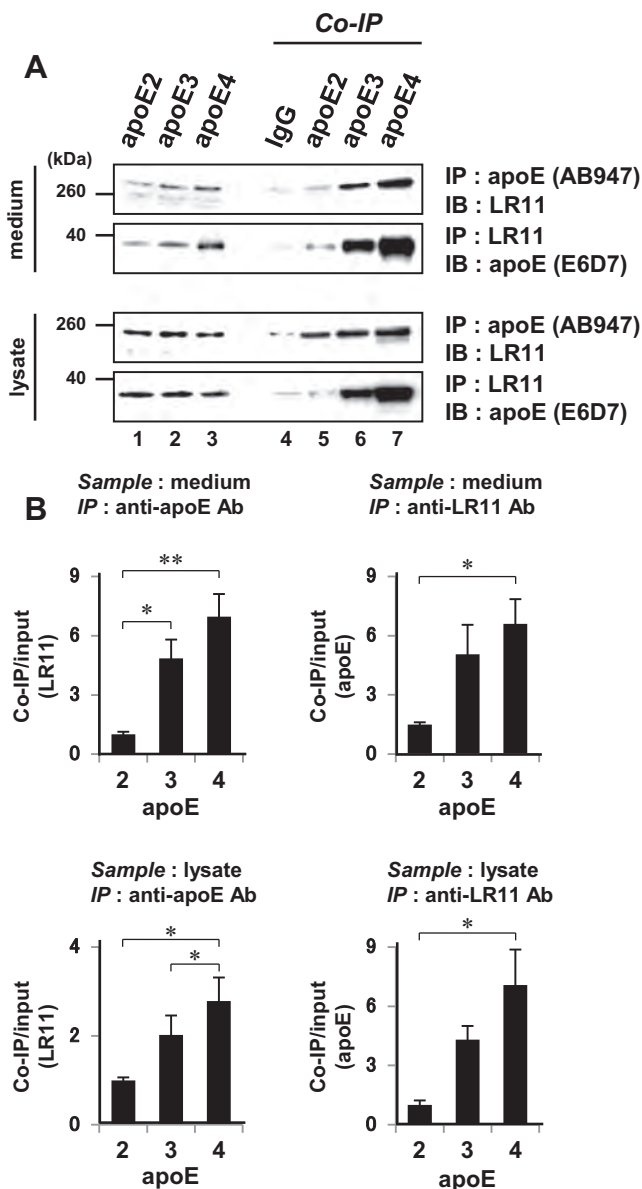


Fig. 3. Human-apoE-isoform-dependent differences in formation of complex between apoE and LR11/SorLA examined by co-IP assay. (A) HEK293T cells were cotransfected with each of the human apoE isoforms and human FL-LR11. The formed complex between apoE and LR11/SorLA was immunoprecipitated using the anti-apoE antibody (AB947) or anti-LR11 antibody (48/LR11), followed by immunoblot analysis. The lysates (lanes 1–3) and immunoprecipitated samples (lanes 4–7) were run on the same gel. (B) Results of semiquantitative analysis of immunoprecipitated apoE and LR11/SorLA. * $p < 0.05$; ** $p < 0.01$ by Tukey test following ANOVA.

3.2. Cellular uptake of apoE examined by fluorescence confocal laser microscopy

The finding that the level of apoE in the medium of cells transfected with FL-LR11 decreased raises the possibility that apoE in the medium was taken up into cells by the lipoprotein receptor LR11/SorLA. To explore this possibility, N2a cells were incubated with the medium prepared from cells that transiently expressed the apoE3-GFP fusion protein. Fluorescence confocal microscopy revealed apoE-GFP signals inside the cells transfected with FL-LR11 and incubated with the medium of cells expressing apoE3-GFP (Supplementary Fig. 1B). This finding suggests that the cellular uptake of apoE from the medium was enhanced by the expression of LR11/SorLA.

3.3. ApoE-isoform-dependent cellular uptake of apoE in coculture system

We next examined whether the enhanced uptake of apoE by FL-LR11 is modified by apoE isoforms using the coculture system. First, we attempted to confirm whether apoE3 and GFP-labeled apoE3 secreted from the donor HEK293T cells are taken up into the recipient cells. This experiment revealed that apoE3 and GFP-labeled apoE3 were detected in the lysate of the recipient cells (Supplementary Fig. 2B), whereas GFP alone without apoE was not detected in the recipient cells.

Having established that apoE secreted from the donor cells is taken up into the recipient cells, we next asked if isoforms of apoE differently affect the cellular uptake of apoE in the recipient N2a cells mock-transfected or transiently transfected with FL-LR11. The level of apoE taken up into the recipient N2a cells was determined by immunoblot analysis using the anti-apoE antibody (Fig. 2A). The cellular uptake levels of apoE3 and apoE4 were significantly higher in the recipient cells that express FL-LR11 compared with the mock-transfected cells (Fig. 2B). In a similar experiment using donor cells that express apoE2-GFP, apoE3-GFP, or apoE4-GFP, the cellular uptake levels of apoE3-GFP and apoE4-GFP were increased by the expression of FL-LR11 (Fig. 2C and D). These results suggest that FL-LR11 enhances the cellular uptake of apoE3 and apoE4 but not that of apoE2.

3.4. ApoE-isoform-dependent binding affinity to LR11/SorLA

We speculated that the differential cellular apoE uptake in the recipient cells may be explained by a difference in binding affinity between LR11/SorLA and each of the apoE isoforms. To test this hypothesis, we examined the ability of LR11/SorLA to form a complex with each of the apoE isoforms by co-immunoprecipitation (co-IP) assay. We collected the detergent-extracted lysate of HEK293T cells that were cotransfected with FL-LR11 and each of the apoE isoforms. Co-IP assay using the anti-apoE or anti-LR11 antibody was performed using the medium and cell lysate. This assay revealed that LR11/SorLA bound to each isoform of apoE with different efficiencies (Fig. 3A). ApoE4-expressing cells showed the highest level of the LR11-apoE complex, followed by apoE3- and apoE2-expressing cells (Fig. 3B).

3.5. ApoE-isoform-dependent cellular uptake of A β

Given the physical interaction between LR11/SorLA and apoE, we next considered the possibility that FL-LR11 may be involved in the cellular uptake of the apoE-A β complex, because apoE is known to form a complex with A β . To address this issue, N2a cells were incubated with FAM-labeled A β 40 at various concentrations of ranging from 0.5 to 3.0 μ M. By fluorescence confocal laser microscopy, we detected the cellular uptake of FAM-labeled A β at concentrations above 1.0 μ M (Supplementary Fig. 3A). We observed the cellular uptake of FAM-labeled A β at a low concentration of 0.25 μ M when the recipient cells were transfected with FL-LR11 and cocultured with the donor cells expressing apoE4 (Supplementary Figs. 3B, 4A and 4B). The finding suggests that the cellular uptake of A β was enhanced in the presence of both FL-LR11 and apoE.

We finally performed coculture experiments in which the recipient N2a cells mock-transfected or transiently transfected with FL-LR11 were cocultured with the donor cells expressing apoE2, E3, or E4 in the presence of the A β peptides at 0.25 μ M. The cellular uptake level of apoE and A β were highest when the recipient cells were cocultured with the donor cells expressing apoE4, followed by apoE3 and apoE2 (Fig. 4A and B).

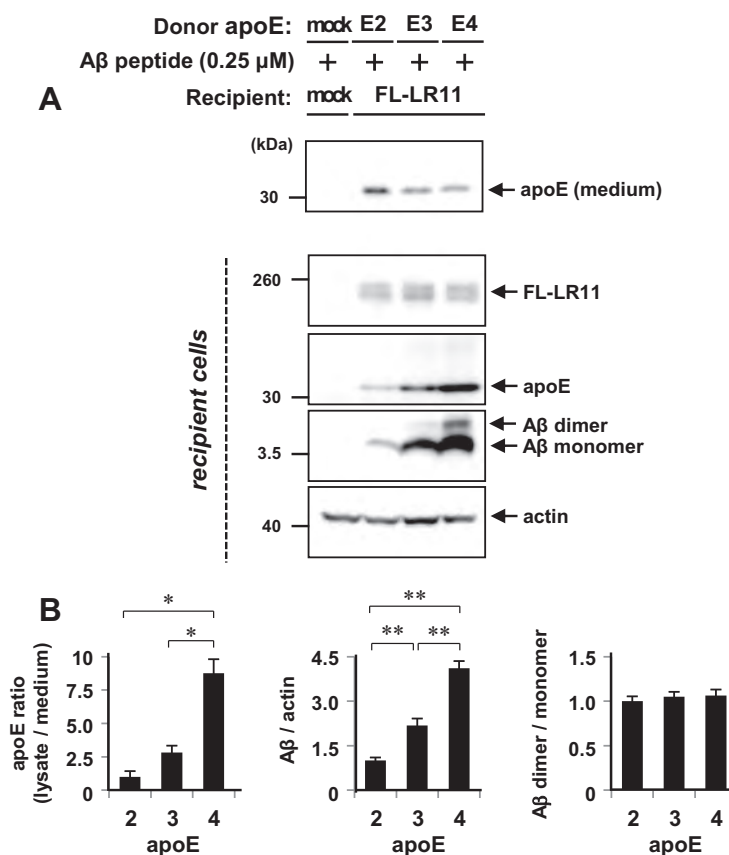


Fig. 4. ApoE-isoform-dependent differences in cellular uptake of A β in cells expressing LR11/SorLA. (A) Recipient N2a cells stably expressing human FL-LR11 were cocultured with donor N2a cells stably expressing human apoE2, apoE3, or apoE4 in the presence of A β 40 peptides at 0.25 μ M for 24 h. The cellular uptake of A β and apoE into the recipient cells was examined by Western blot analysis. (B) Results of semiquantitative analysis of cellular uptake of A β and apoE are shown as -fold increase compared with the apoE2 isoform. * p < 0.05; ** p < 0.01 by Tukey test following ANOVA.

4. Discussion

Despite significant advances in our understanding of the pathological events occurring in the AD brain, the factors leading to A β accumulation in sporadic AD patients are not well understood. A wealth of evidence has confirmed that APOE ϵ 4 is the strongest genetic risk factor for sporadic AD [2,3]. Although it is not fully understood how human apoE isoforms differentially affect the various pathogenic processes implicated in AD, several lines of evidence suggest that the effects of apoE on A β accumulation, aggregation, clearance, neurotoxicity, and neuroinflammation may play a role in AD pathogenesis [6]. Hence, understanding how each of the apoE isoforms differentially plays a pathophysiological role in AD is an important question to address. In this regard, this study provided new insights into how apoE isoforms differentially modify the AD pathogenic pathway with particular focus on the cellular uptake of A β via the lipoprotein receptor LR11/SorLA.

First, we demonstrated that the overexpression of LR11/SorLA enhanced the cellular uptake of apoE3 and apoE4. This finding suggests that LR11/SorLA functions as the apoE receptor. This notion was suggested by previous studies showing that FL-LR11 at the cell surface was capable of cellular uptake of apoE [12]. Importantly, we here showed that the cellular uptake of apoE is modified by different apoE isoforms. The cellular uptake of apoE4 and apoE3 was significantly enhanced by the expression of LR11/SorLA. In support of this notion, the co-IP assay revealed that the apoE-LR11/SorLA complex formation showed apoE-isoform-dependent differences in efficiencies, that is, apoE4 > apoE3 > apoE2. Major

apoE receptors belong to the LDL receptor family including the LDL receptor and LDLR-related protein (LRP1). Different efficiencies in the formation of complexes between the LDL receptor and the apoE isoforms were observed. Similar to our finding, the cellular uptake levels of apoE3 and apoE4 were previously found to be higher than that of apoE2 in cells expressing the LDL receptor [17].

Secondly, our cell culture experiments revealed that extracellular A β was taken up into cells overexpressing LR11/SorLA in an apoE-isoform-dependent manner. A recent study has shown that LR11/SorLA binds to A β directly through the VPS10 protein domain of LR11/SorLA [15]. Importantly, we demonstrated that the cellular uptake of extracellular A β was apoE-isoform-dependent, that is, apoE4 > apoE3 > apoE2. Although this finding is potentially interesting, how this finding is relevant to AD pathogenesis is not presently understood. Enhancement of cellular uptake of A β may have two different consequences. A harmful consequence would be that an increased intracellular A β concentration through the uptake of extracellular A β may provide seeds of A β oligomers, a toxic forms of A β [18]. Some studies suggested that intracellular A β oligomers may be a major cause of synaptic dysfunction [19]. On the other hand, a beneficial consequence would be that the cellular uptake of extracellular A β may enhance the clearance of A β in lysosomes [20]. Our finding favors the former possibility, that is, cellular uptake of A β may exert a detrimental effect on neurons because this phenomenon is most closely associated with the presence of apoE4. Further studies delineating the precise consequences of increased intracellular A β level caused by enhanced cellular uptake of A β will be required.

ApoE is predominantly generated by astrocytes and microglia in the brain and is subsequently lipidated by ABCA1 to form lipoprotein particles [21]. It has been demonstrated that lipoprotein receptors including LDLR and LRP on the neuronal surface are able to take apoE-A β complexes into neurons after apoE is lipidated [22]. The lipidation of apoE has been shown to influence its isoform-specific affinity to A β . The efficiency of complex formation between lipidated apoE and A β is in the order of apoE2 > apoE3 > apoE4 [23]. In addition, the variable levels of apoE oxidation may affect the properties of apoE binding to A β . In this study, we did not fully address the lipidation or oxidation status of apoE secreted from HEK293T cells, which should be taken into account when interpreting our results. To minimize confounding factors, it is desirable to use apoE prepared under conditions that preserve apoE lipidation and oxidation status found in the brain. Collectively, our study indicated that LR11/SorLA is capable of cellular uptake of A β in an apoE-isoform-dependent manner; however, its pathophysiological role requires further investigation.

Acknowledgments

This work is supported in part by JSPS KAKENHI (23591234 and 20372469 to T.I.) and a Grant-in-Aid from the Ministry of Health, Labour and Welfare of Japan.

Appendix A. Supplementary data

Supplementary data associated with this article can be found, in the online version, at <http://dx.doi.org/10.1016/j.bbrc.2014.11.111>.

References

- [1] C.R. Jack, D.M. Holtzman, Biomarker modeling of Alzheimer's disease, *Neuron* 80 (2013) 1347–1358.
- [2] J.C. Lambert, C.A. Ibrahim-Verbaas, D. Harold, et al., Meta-analysis of 74,046 individuals identifies 11 new susceptibility loci for Alzheimer's disease, *Nat. Genet.* 45 (2013) 1452–1458.
- [3] A. Miyashita, A. Koike, G. Jun, et al., SORL1 is genetically associated with late-onset Alzheimer's disease in Japanese, Koreans and Caucasians, *PLoS One* 8 (2013) e58618.
- [4] E.H. Corder, A.M. Saunders, W.J. Strittmatter, et al., Gene dose of apolipoprotein E type 4 allele and the risk of Alzheimer's disease in late onset families, *Science* 261 (1993) 921–923.
- [5] E.H. Corder, A.M. Saunders, N.J. Risch, et al., Protective effect of apolipoprotein E type 2 allele for late onset Alzheimer disease, *Nat. Genet.* 7 (1994) 180–184.
- [6] C.C. Liu, T. Kanekiyo, H. Xu, et al., Apolipoprotein E and Alzheimer disease: risk, mechanisms and therapy, *Nat. Rev. Neurol.* 9 (2013) 106–118.
- [7] Y. Motoi, T. Aizawa, S. Haga, et al., Neuronal localization of a novel mosaic apolipoprotein E receptor, LR11, in rat and human brain, *Brain Res.* 833 (1999) 209–215.
- [8] K.L. Sager, J. Wu, S.E. Leurgans, et al., Neuronal LR11/SorLA expression is reduced in mild cognitive impairment, *Ann. Neurol.* 62 (2007) 640–647.
- [9] S.E. Dodson, O.M. Andersen, V. Karmali, et al., Loss of LR11/SorLA enhances early pathology in a mouse model of amyloidosis: evidence for a proximal role in Alzheimer's disease, *J. Neurosci.* 28 (2008) 12877–12886.
- [10] M. Jiang, H. Bujo, K. Ohwaki, et al., Ang II-stimulated migration of vascular smooth muscle cells is dependent on LR11 in mice, *J. Clin. Invest.* 118 (2008) 2733–2746.
- [11] T. Ikeuchi, S. Hirayama, T. Miida, et al., Increased levels of soluble LR11 in cerebrospinal fluid of patients with Alzheimer disease, *Dement. Geriatr. Cogn. Disord.* 30 (2010) 28–32.
- [12] H. Yamazaki, H. Bujo, J. Kusunoki, et al., Elements of neural adhesion molecules and a yeast vacuolar protein sorting receptor are present in a novel mammalian low density lipoprotein receptor family member, *J. Biol. Chem.* 271 (1996) 24761–24768.
- [13] O.M. Andersen, J. Reiche, V. Schmidt, et al., Neuronal sorting protein-related receptor SorLA/LR11 regulates processing of the amyloid precursor protein, *Proc. Natl. Acad. Sci. U.S.A.* 102 (2005) 13461–13466.
- [14] A. Schmidt, M. Sporbert, M. Rohe, et al., SorLA/LR11 regulates processing of amyloid precursor protein via interaction with adaptors GGA and PACS-1, *J. Biol. Chem.* 282 (2007) 32956–32964.
- [15] S. Caglayan, S. Takagi-Niidome, F. Liao, et al., Lysosomal sorting of amyloid- β by the SorLA receptor is impaired by a familial Alzheimer's disease mutation, *Sci. Transl. Med.* 6 (2014). 223ra220.
- [16] T. Tokutake, K. Kasuga, R. Yajima, et al., Hyperphosphorylation of Tau induced by naturally secreted amyloid- β at nanomolar concentrations is modulated by insulin-dependent Akt-GSK3 β signaling pathway, *J. Biol. Chem.* 287 (2012) 35222–35233.
- [17] T. Simmons, Y.M. Newhouse, K.S. Arnold, et al., Human low density lipoprotein receptor fragment. Successful refolding of a functionally active ligand-binding domain produced in *Escherichia coli*, *J. Biol. Chem.* 272 (1997) 25531–25536.
- [18] X. Hu, S.L. Crick, G. Bu, et al., Amyloid seeds formed by cellular uptake, concentration, and aggregation of the amyloid-beta peptide, *Proc. Natl. Acad. Sci. U.S.A.* 106 (2009) 20324–20329.
- [19] P.N. Lacor, M.C. Buniel, P.W. Furlow, et al., A β oligomer-induced aberrations in synapse composition, shape, and density provide a molecular basis for loss of connectivity in Alzheimer's disease, *J. Neurosci.* 27 (2007) 796–807.
- [20] J. Li, T. Kanekiyo, M. Shinohara, et al., Differential regulation of amyloid- β endocytic trafficking and lysosomal degradation by apolipoprotein E isoforms, *J. Biol. Chem.* 287 (2012) 44593–44601.
- [21] S.E. Wahrle, H. Jiang, M. Parsadanian, et al., Overexpression of ABCA1 reduces amyloid deposition in the PDAPP mouse model of Alzheimer disease, *J. Clin. Invest.* 118 (2008) 671–682.
- [22] J. Kim, J.M. Basak, D.M. Holtzman, Overexpression of low-density lipoprotein receptor in the brain markedly inhibits amyloid deposition and increases extracellular A β clearance, *Neuron* 64 (2009) 632–644.
- [23] T. Tokuda, M. Calero, E. Matsubara, et al., Lipidation of apolipoprotein E influences its isoform-specific interaction with Alzheimer's amyloid beta peptides, *Biochem. J.* 348 (2000) 359–365.



ORIGINAL ARTICLE

Dopamine D1 Receptor-Mediated Transmission Maintains Information Flow Through the Cortico-Striato-Entopeduncular Direct Pathway to Release Movements

Satomi Chiken^{1,2,†}, Asako Sato^{3,4,†}, Chikara Ohta^{1,5}, Makoto Kurokawa⁵, Satoshi Arai³, Jun Maeshima³, Tomoko Sunayama-Morita^{4,6}, Toshikuni Sasaoka^{2,3,4,7}, and Atsushi Nambu^{1,2}

¹Division of System Neurophysiology, National Institute for Physiological Sciences, Okazaki 444-8585, Japan, ²School of Life Science, SOKENDAI (The Graduate University for Advanced Studies), Okazaki 444-8585, Japan, ³Department of Laboratory Animal Science, Kitasato University School of Medicine, Sagamihara 252-0374, Japan, ⁴National Institute for Basic Biology, Okazaki 444-8585, Japan, ⁵Department of Biological Sciences, Tokyo Metropolitan University, Tokyo 192-0397, Japan, ⁶Department of Life Sciences, Graduate School of Arts and Science, The University of Tokyo, Tokyo 153-8902, Japan and ⁷Department of Comparative and Experimental Medicine, Brain Research Institute, Niigata University, Niigata 951-8585, Japan

Address correspondence to Atsushi Nambu, Division of System Neurophysiology, National Institute for Physiological Sciences, 38 Nishigonaka, Myodaiji, Okazaki 444-8585, Japan. Email: nambu@nips.ac.jp; Toshikuni Sasaoka, Department of Comparative and Experimental Medicine, Brain Research Institute, Niigata University, Niigata 951-8585, Japan. Email: sasaoka@bri.niigata-u.ac.jp

[†]These authors contributed equally to this work.

Abstract

In the basal ganglia (BG), dopamine plays a pivotal role in motor control, and dopamine deficiency results in severe motor dysfunctions as seen in Parkinson's disease. According to the well-accepted model of the BG, dopamine activates striatal direct pathway neurons that directly project to the output nuclei of the BG through D1 receptors (D1Rs), whereas dopamine inhibits striatal indirect pathway neurons that project to the external pallidum (GPe) through D2 receptors. To clarify the exact role of dopaminergic transmission via D1Rs *in vivo*, we developed novel D1R knockdown mice in which D1Rs can be conditionally and reversibly regulated. Suppression of D1R expression by doxycycline treatment decreased spontaneous motor activity and impaired motor ability in the mice. Neuronal activity in the entopeduncular nucleus (EPN), one of the output nuclei of the rodent BG, was recorded in awake conditions to examine the mechanism of motor deficits. Cortically evoked inhibition in the EPN mediated by the cortico-striato-EPN direct pathway was mostly lost during suppression of D1R expression, whereas spontaneous firing rates and patterns remained unchanged. On the other hand, GPe activity changed little. These results suggest that D1R-mediated dopaminergic transmission maintains the information flow through the direct pathway to appropriately release motor actions.

Key words: basal ganglia, conditional knockdown, dopamine receptor, extracellular recording, mouse

Introduction

In the basal ganglia (BG), dopaminergic transmission plays a pivotal role in the control of voluntary movements and motor learning (Albin et al. 1989; DeLong 1990; Gerfen et al. 1990; Graybiel 2005; Joshua et al. 2009; Enomoto et al. 2011). Dopamine deficiency, as occurs in Parkinson's disease (PD), results in severe motor and nonmotor dysfunctions including bradykinesia, rigidity, tremor, autonomic abnormalities, cognitive dysfunction, and depression (Fahn et al. 2011; Seppi et al. 2011). Dopaminergic inputs from the substantia nigra pars compacta terminate in the striatum and are thought to differentially modulate the excitability of 2 types of striatal projection neurons through different receptors (Albin et al. 1989; DeLong 1990; Mallet et al. 2006) (Fig. 1A, left). One is excitatory effects through dopamine D1 receptors (D1Rs) on direct pathway neurons that directly project to the output nuclei of the BG, the entopeduncular nucleus (EPN), which is homologous to the internal segment of the globus pallidus (GPi) in primates, and substantia nigra pars reticulata (SNr). The other is inhibitory effects through D2 receptors (D2Rs) on indirect pathway neurons that project to the external

segment of the globus pallidus (GPe), which is also called the globus pallidus in rodents. Such differential effects of dopamine through D1Rs and D2Rs were originally proposed based on changes in gene expression, glucose utilization, and receptor binding in these pathways under conditions of dopamine depletion (Gerfen et al. 1990; Hirsch et al. 2000) and have been reinforced by recent in vitro electrophysiological studies (Surmeier et al. 2007; Day et al. 2008; Flores-Barrera et al. 2011; Gerfen and Surmeier 2011; Planert et al. 2013). The striato-EPN/SNr direct and striato-GPe-subthalamo (STN)-EPN/SNr indirect pathways play opposite roles in controlling movements. The signals through the direct pathway reduce activity of the EPN/SNr and increase thalamocortical activity via disinhibition, resulting in release of movements. In contrast, signals through the indirect pathway increase activity of the EPN/SNr, resulting in suppression of movements (Albin et al. 1989; DeLong 1990; Gerfen et al. 1990; Mink 1996; Nambu 2007; Kravitz et al. 2010; Sano et al. 2013). Thus, the loss of dopaminergic inputs to both pathway neurons is considered to increase firing rates of EPN/SNr neurons through the inhibitory striato-EPN/SNr direct and net excitatory

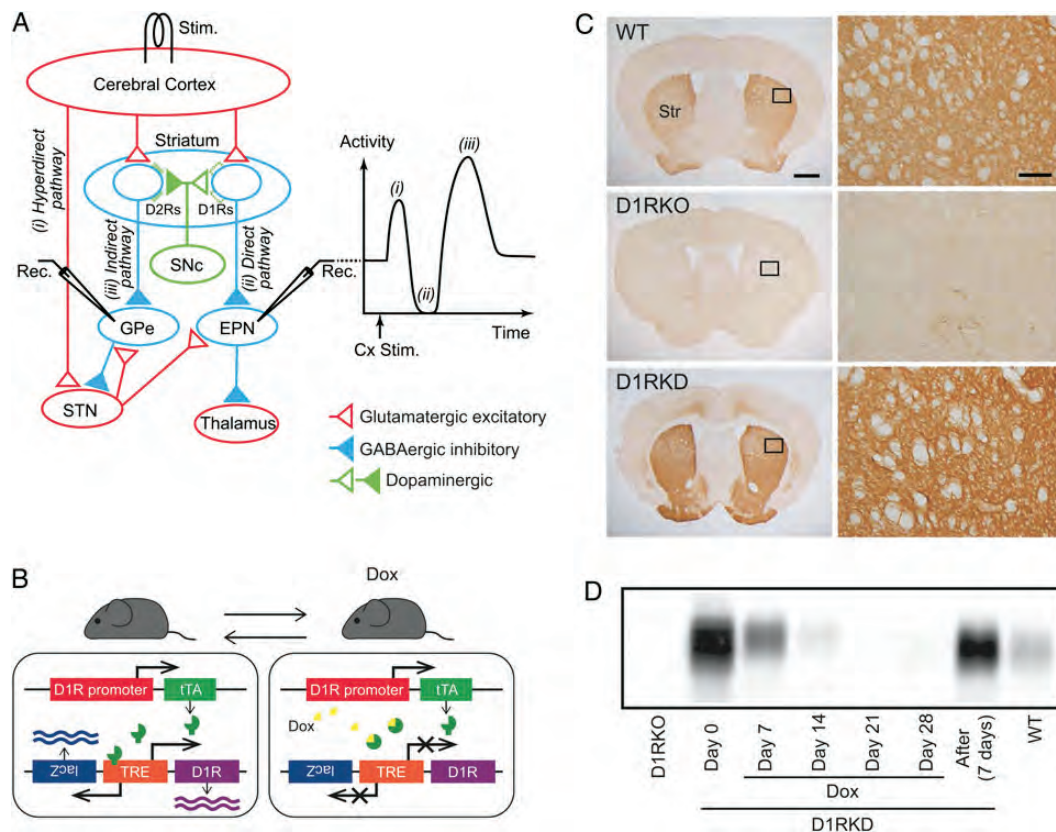


Figure 1. Dopamine D1 receptor (D1R) suppression in D1R knockdown (D1RKD) mice with doxycycline (Dox) treatment. (A) Schematic diagram showing the cortico-basal ganglia pathway and stimulating (Stim.) and recording (Rec.) sites in the electrophysiological experiments (left), along with a typical response pattern (right) in the entopeduncular nucleus (EPN) (homologous to the internal segment of the globus pallidus, GPi) to cortical stimulation (Cx Stim.) with early excitation, inhibition, and late excitation, which are mediated by the i) cortico-subthalamo (STN)-EPN hyperdirect, ii) cortico-striato-EPN direct, and iii) cortico-striato-external pallido (GPe)-STN-EPN indirect pathways, respectively. Red, blue, and green triangles represent glutamatergic excitatory, GABAergic inhibitory, and dopaminergic projections, respectively. D2Rs, dopamine D2 receptors; SNc, substantia nigra pars compacta. (B) Schematic diagram of Dox-regulated D1R expression in D1RKD mice. Before Dox treatment (left), tetracycline transactivator (tTA) binds to the tetracycline responsive element (TRE), and D1Rs and lacZ are transcribed. Dox treatment interferes with tTA binding to TRE (right), and suppresses D1R and lacZ expression (Tet-off system). (C) D1R immunoreactivity in the striatum (Str) of wild-type (WT, top), D1R knockout (D1RKO, middle), and D1RKD (before Dox treatment, bottom) mice shown in frontal sections. The pattern of D1R expression in D1RKD mice was similar to that in WT mice, whereas D1R immunoreactivity was not observed in D1RKO mice. The dorsolateral motor areas of the Str are defined by rectangles (left) and shown at higher magnification (right). Scale bars, 1 mm on the left, 100 μ m on the right. (D) Western blot analysis of D1R protein expression in the striatum of a D1RKO mouse ($n = 1$, number of mice used), D1RKD mice before, during, and after Dox treatment (Days 0, 7, 14, 21, 28, different days after starting Dox treatment; After, 7 days after cessation of Dox treatment for 14 days; $n = 3-4$ per condition), and WT mice ($n = 3$).

striato-GPe-STN-EPN/SNr indirect pathways, resulting in the decreased motor activity seen in PD (Albin et al. 1989; DeLong 1990).

However, the exact role of D1R-mediated dopaminergic transmission *in vivo* is not well understood. Contradicting results have been observed following D1R blockade. D1R knockout (KO) mice show increases in spontaneous locomotor activity, although pharmacological blockade of D1Rs induces locomotor suppression in agreement with the above explanation (Waddington et al. 2005). In the present study, we developed novel D1R knock-down (D1RKD) mice in which the D1Rs can be conditionally and reversibly regulated by doxycycline (Dox) treatment (Fig. 1B). The D1RKD mice enabled us to examine motor behaviors and neuronal activities in the cortico-BG pathways in the presence and absence of D1Rs in the same mice. The mice exhibited decreased spontaneous motor activity and impaired motor ability when D1R expression was suppressed, consistent with the pharmacological blockade study (Waddington et al. 2005). To examine the neural mechanism of the motor deficits, we next recorded neuronal activity in the EPN in awake mice, because the EPN is the main output nucleus of the BG to the thalamus and the target of D1R-expressing striatal neurons. Cortically evoked inhibition in the EPN, which is mediated by the cortico-striato-EPN direct pathway, was mostly lost during suppression of D1R expression, whereas spontaneous firing rates and patterns of EPN neurons remained unchanged. These results indicate that D1R suppression mostly blocks the information flow through the cortico-striato-EPN direct pathway and reduces spontaneous motor activity.

Materials and Methods

Animal protocols were approved by the Institutional Animal Care and Use Committee of National Institutes of Natural Sciences, Kitasato University and Niigata University, and were conducted according to the guidelines of the National Institutes of Health *Guide for the Care and Use of Laboratory Animals*. One to 5 mice were housed in each cage under a 12-h light-dark cycle (lights on at 8:00 AM) and given food and drinking water *ad libitum*.

Generation of Conditional and Reversible D1RKD Mice

We developed D1RKD mice in which D1Rs can be conditionally and reversibly regulated by Dox using the Tet-Off system after deletion of the endogenous D1Rs (Fig. 1B). To generate tetracycline transactivator-VP16 (tTA)-expressing mice using the D1R promoter (transactivator line), bacterial artificial chromosome (BAC) clones containing mouse D1R were modified with a 2-step Rec A strategy for BAC modification (Yang et al. 1997). A modification cassette that introduces the tTA into the endogenous D1R coding sequence was constructed (see Supplementary Fig. 1A). A DNA fragment (0.92 kb, A-arm) containing the upstream region of the translation initiation site of D1R was ligated to the DNA fragment (1.5 kb) containing the coding sequence of the tTA and the SV40 poly A signal (poly A) of the pTet-off vector (Clontech), and the resulting fragment was ligated to the DNA fragment (0.96 kb, B-arm) of exon 2 of D1R to generate D1Txx, the modification cassette (3.38 kb). Because the tTA and the SV40 poly A signal sequences were introduced at the initiation codon of D1R, the expression of endogenous D1R was disrupted. To generate the pSV1-RecA-D1T shuttle vector, the DNA fragment of D1Txx was inserted into the pSV1-RecA vector to facilitate homologous recombination in RecA⁻ *Escherichia coli*.

The BAC clone, BAC4-D1R (80 230 bp) (Research Genetics), was used (see Supplementary Fig. 1B). RecA⁻ *E. coli* carrying the original BAC clone were transformed with the pSV1-RecA-D1T shuttle

vector. The resulting clones were subjected to Southern analysis using either a 5' probe or tTA probe to confirm proper recombination (see Supplementary Fig. 1A). The BAC transgenic (Tg) construct, BAC4-tTA, was obtained (see Supplementary Fig. 1B).

The Tg construct, D1R-tetracycline responsive element (D1R-TRE), was generated for tetracycline operator (tetO)-target Tg mouse lines using the following DNA fragments (see Supplementary Fig. 1C): a 9.7-kb fragment including the entire D1R coding sequence, a 0.64-kb fragment encoding the TRE and bidirectional promoter from the pBI Tet vector (Clontech), a 3466-bp fragment encoding lacZ from the pBI-GL Tet vector (Clontech), a 0.98-kb fragment containing rabbit beta-globin poly A and SV40 poly A signals from the pBstN plasmid, and a 0.3-kb fragment encoding the chicken beta-globin insulator sequences from the plasmid pUC19 INS240-SNNS.

The BAC4-tTA and D1R-TRE DNAs (10 ng/ μ L each) were used for Tg mouse generation using standard techniques (Nagy et al. 2002). The BAC4-tTA and D1R-TRE DNAs were independently microinjected into fertilized mouse oocytes isolated from crosses of D1R homozygous knockout (D1RKO) female and male mice (Tran et al. 2008). Three Tg lines for BAC4-tTA and 15 Tg lines for D1R-TRE were independently generated. Each BAC4-tTA Tg line was crossed with each D1R-TRE Tg line. The progeny from crosses of BAC4-tTA and D1R-TRE Tg mice was subjected to analyses of Dox-controllable expression of lacZ using X-gal staining of brain sections using a standard method and expression of D1R in the striatum using western blotting with anti-D1R antibody (Sigma). Two Tg lines harboring BAC4-tTA and D1R-TRE (designated 442-43 and 442-112) were consistently found to exhibit distinct, comparable expression of lacZ in the region where endogenous D1R was expressed and Dox-controllable expression of lacZ and D1R. Therefore, the 442-112 line was used for further analyses as D1RKD mice.

Wild-type (WT) C57BL/6J and D1RKO (Tran et al. 2008) mice were also used for comparison in immunohistochemical, western blot, and behavioral analyses.

Dox Treatment

Dox (2.0 mg/mL) was mixed in drinking water containing 5% sucrose and delivered to the D1RKD and WT mice through a water bottle.

Immunohistochemistry

We used 4 D1RKD, 3 WT, and 1 D1RKO mice for immunohistochemical analysis. Mice were deeply anesthetized by injection of tribromoethanol (400 mg/kg body weight, *i.p.*) and perfused transcardially with 4% paraformaldehyde in phosphate buffer (PB, pH 7.4). The brains were postfixed overnight at 4°C, transferred to a 30% sucrose solution, immersed in OCT compound (Sakura Finetek), frozen, and stored at -80°C until use. Frontal sections were cut at 25- μ m thickness and stored in PBS at 4°C. Free-floating sections were incubated with 1% bovine serum albumin containing antibody for D1R (1:1000; Frontier Institute) overnight at 4°C. D1R antibody binding was visualized using the Vectastain Elite ABC System (Vector Laboratories) and 3, 3'-diaminobenzidine.

Western Blot Analysis

We used 19 D1RKD (3-4 in each condition, 0, 7, 14, 21, and 28 days after starting Dox treatment and 7 days after cessation of Dox treatment for 14 days), 3 WT, and 1 D1RKO mice for western

blot analysis as described previously (Tran et al. 2008) with minor modifications. Briefly, after euthanasia by cervical dislocation, the striatum was dissected and homogenized in lysis buffer. Total lysates were resolved with 10% SDS-PAGE and transferred to a polyvinylidene difluoride membrane (Millipore). The membrane was blocked with 5% skim milk and incubated with anti-D1R (1:5000; Sigma) or anti-actin (as a protein loading control; 1:500; Sigma) antibodies, followed by incubation with secondary antibodies conjugated to horseradish peroxidase (Sigma). Signals were developed with an ECL detection kit (GE Healthcare). The density of the bands was determined with CS Analyzer software (Atto).

Behavioral Analyses

D1RKD and age-matched WT male mice (7–28 weeks old) were used for behavioral analyses. D1RKD and WT mice were randomly divided into Dox-treated and untreated groups. All behavioral data are presented as the mean \pm SD.

Spontaneous Motor Activity

We assessed spontaneous motor activity of 9 Dox-treated D1RKD, 4 untreated D1RKD, and 5 Dox-treated WT mice. The mice were individually housed in an 11.8 cm (L) \times 20.8 cm (W) \times 14.5 cm (H) home cage, and movements of each mouse were detected before, during, and after Dox treatment with a pyroelectric infrared sensor installed above the cage (O'hara) as reported previously (Nakamura et al. 2014). Movements were continuously counted in 10-min bins, and spontaneous motor activity per day was calculated as the cumulative number of movements in 24 h beginning at 8:00 AM. The bedding was replaced every 7 days, and motor activity was increased after bedding replacement because of exploratory behavior. Thus, data on these days were excluded when calculating the mean weekly spontaneous motor activity. Spontaneous motor activity was classified into 3 levels based on counts per 10 min: inactive (≤ 9), low (10–199), and high (≥ 200). We also assessed spontaneous motor activity of another 4 Dox-treated D1RKD and 4 Dox-treated WT mice until 10 days after cessation of Dox treatment for 14 days.

Rotarod Test

We used another 13 Dox-treated D1RKD, 5 untreated D1RKD, 8 Dox-treated WT, and 15 untreated WT mice for the rotarod test. Dox treatment was started 35 days before the test and continued during the test periods for Dox-treated groups. Mice were placed on a rotating rod (32 mm diameter, O'hara), which initially rotated at 4 rpm, and then was accelerated at a constant rate from 4 to 40 rpm over 4 min, with the final speed maintained for 1 min. The time spent on the rotarod was measured in 3 trials every day between 1:00 PM and 7:00 PM and averaged.

Electrophysiology

Surgery

We used 4 D1RKD (mouse W, K, T, and O, 20–50 weeks old, males) and 3 age-matched WT mice for the electrophysiological experiments. Under anesthesia with ketamine hydrochloride (100 mg/kg, i.p.) and xylazine hydrochloride (4–5 mg/kg, i.p.), a small U-frame polyacetal head holder was fixed to the exposed skull of the mouse with transparent acrylic resin (for details, see Chiken et al. 2008; Sano et al. 2013). After recovery from the first surgery, under light anesthesia with ketamine hydrochloride (30–50 mg/kg, i.p.), a portion of the skull was removed to access the motor cortex, EPN, and GPe. Two pairs of bipolar stimulating electrodes

were chronically implanted into the caudal forelimb and orofacial regions of the motor cortex (for details, see Chiken et al. 2008).

Recording of Neuronal Activity in the Awake State

After full recovery from the second surgery, neuronal recording was started (for details, see Chiken et al. 2008; Sano et al. 2013). The awake mouse was kept quiet in a stereotaxic apparatus with its head restrained painlessly using the U-frame head holder. A glass-coated Elgiloy-alloy microelectrode was inserted vertically into the EPN/GPe through the dura mater. Unit activity was isolated and converted to digital pulses using a window discriminator. Spontaneous discharges and responses to the cortical stimulation (200- μ s duration, single pulse, 50- μ A strength) through the electrodes implanted in the motor cortex were recorded in the EPN/GPe from the same mouse in 3 conditions: before, during, and after Dox treatment. We first recorded neuronal activity before Dox treatment (“before” condition) and then started Dox treatment. Recording of neuronal activity was resumed 5 days after starting Dox treatment and continued till 22 days after starting Dox treatment (“during Dox” condition) when D1R expression was greatly suppressed and spontaneous motor activity was distinctly decreased (Figs 1D, 2A). Finally, we stopped Dox treatment and resumed recording 15 days after cessation of Dox treatment (“after” condition) when D1R expression and spontaneous motor activity had fully returned to the level prior to Dox treatment (Figs 1D and 2C). During the recording session, we carefully monitored vigilance state of the mouse by visual inspection.

Histology

In the final experiment, several sites of neuronal recording were marked by passing cathodal DC current (20 μ A for 30 s) through the recording electrodes. The mice were anesthetized deeply with sodium pentobarbital (120 mg/kg, i.p.) and perfused transcardially with 0.1 M PB (pH 7.3) followed by 10% formalin in 0.1 M PB, and then 0.1 M PB containing 10% sucrose. The brains were removed immediately and saturated with the same buffer containing 30% sucrose. They were cut into frontal 50- μ m-thick sections on a freezing microtome. The sections were mounted onto gelatin-coated glass slides, stained with 0.7% neutral red, dehydrated, and coverslipped. The sections were observed under a light microscope, and the recording sites were reconstructed according to the lesions made by current injection and traces of electrode tracks. The sites of stimulation in the motor cortex were also examined histologically.

Data Analysis

Spontaneous discharge rates were calculated from continuous digitized recordings for 50 s. The following parameters characterizing firing patterns were calculated from the first 30 s of the same recordings: the coefficient of variation (CV) of interspike intervals (ISIs), the burst index (Hutchison et al. 1998; Sano et al. 2013), and the percentage of spikes in bursts detected by the Poisson surprise method (Legéndy and Salcman 1985; Chiken et al. 2008; Sano et al. 2013) (Poisson surprise value ($-\log_{10} P$) ≥ 2.0 ; the minimum number of spikes during bursts was 3). Autocorrelograms (bin width of 0.5 ms) were constructed from continuous digitized recordings for 50 s.

Responses to cortical stimulation were examined by constructing peristimulus time histograms (PSTHs; bin width of 1 ms) for 100 stimulus trials. The mean value and SD of the discharge rate during the 100-ms period preceding the stimulation onset were calculated for each PSTH and considered as the

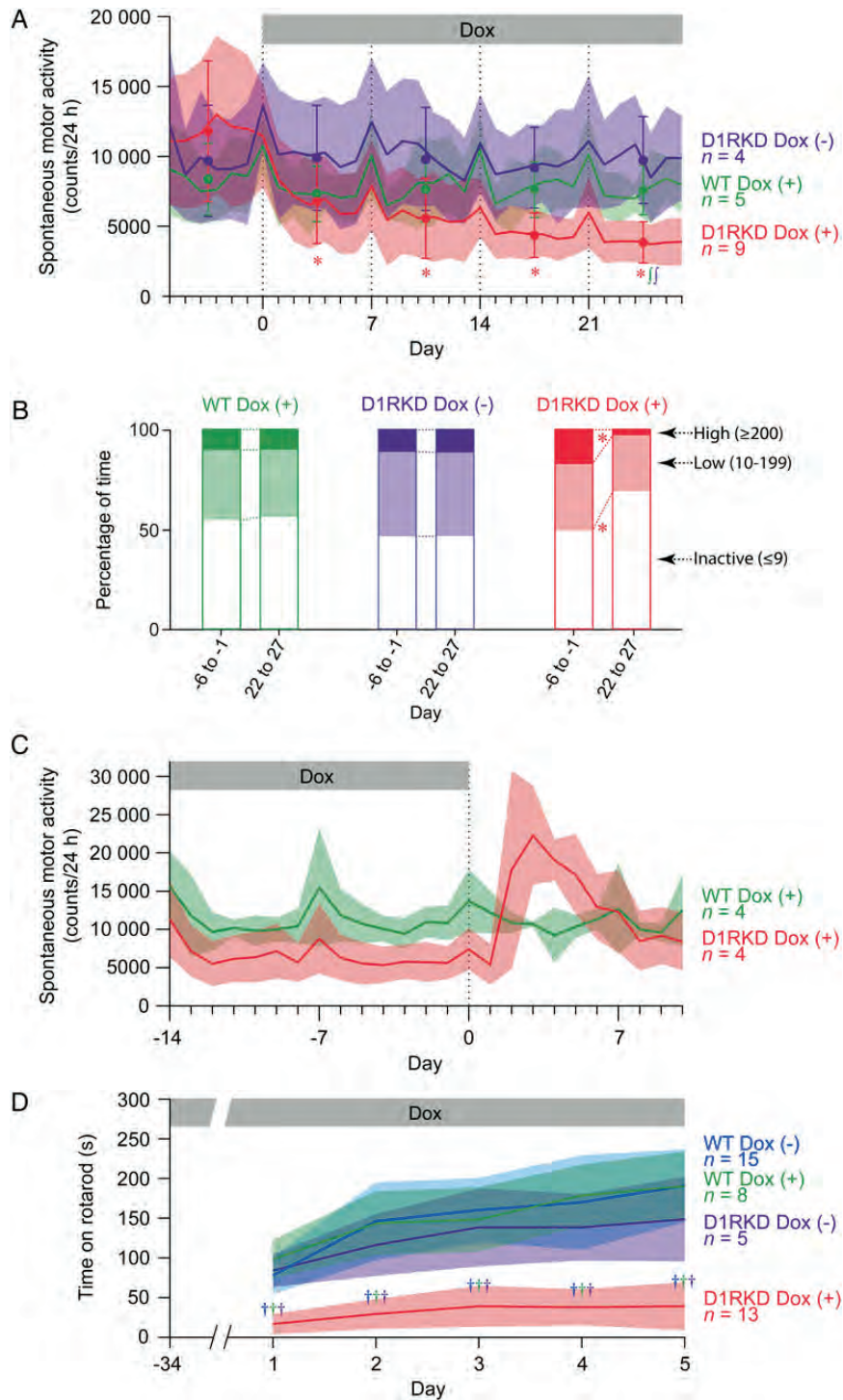


Figure 2. Spontaneous motor activity and rotarod performance during D1R suppression. (A) Spontaneous motor activity of Dox-treated D1RKD (D1RKD Dox (+)), untreated D1RKD (D1RKD Dox (-)), and Dox-treated WT (WT Dox (+)) mice in their home cages. Dox treatment was started on Day 0 and continued for 4 weeks for Dox-treated groups (gray bar). Daily changes in spontaneous motor activity during Dox treatment were observed. Bedding was replaced every 7 days (Days 0, 7, 14, and 21), and spontaneous motor activity was increased because of exploratory behavior. Thus, data on these days were excluded from further analyses. Colored lines and light-colored areas represent mean and \pm SD, and filled circles and whiskers represent mean weekly spontaneous motor activity and \pm SD. * $P < 0.05$; significantly different from before Dox treatment (Bonferroni test). $^{\dagger}P < 0.05$, significantly different from control (WT Dox (+) and D1RKD Dox (-) mice), which is indicated by the corresponding color (Bonferroni test). (B) Classifications of spontaneous motor activity of WT Dox (+), D1RKD Dox (-), and D1RKD Dox (+) mice before (Days -6 to -1) and during (Days 22-27) Dox treatment. Spontaneous motor activity was classified into 3 levels based on counts per 10 min: inactive (≤ 9), low (10-199), and high (≥ 200). *, the percentage of inactive (≤ 9) time significantly increased (χ^2 test with Bonferroni correction, $P = 0.008$), and that of high-active (≥ 200) time significantly decreased ($P = 0.0004$). (C) Spontaneous motor activity of D1RKD Dox (+) and WT Dox (+) mice after cessation of Dox treatment. The 2-week Dox treatment was stopped on Day 0. Bedding was replaced every 7 days (Days -14, -7, 0, and 7). (D) Rotarod performance of D1RKD Dox (+), D1RKD Dox (-), WT Dox (+), and untreated WT (WT Dox (-)) mice. Dox treatment was started 35 days before the rotarod test. $^{\dagger}P < 0.01$, significantly different from control, which is indicated by the corresponding color (Bonferroni test). The number of mice used for each experiment is indicated by n.

baseline discharge rate. Changes in neuronal activity in response to cortical stimulation were judged significant if the discharge rate during at least 2 consecutive bins (2 ms) reached a significance level of $P < 0.05$ (Nambu et al. 2000; Chiken et al. 2008; Tachibana et al. 2008; Sano et al. 2013). The latency of each response was defined as the time at which the first bin exceeded this level. The responses were judged to end when 2 consecutive bins fell below the significance level. The end point was determined as the time at which the last bin exceeded this level. The amplitude of each component of cortically evoked responses was defined as the number of spikes during the significant response minus that of the baseline discharge in the PSTH (i.e., the area of the response; positive and negative values indicate excitation and inhibition, respectively). If no significant changes were found, the amplitude was set to zero. For population PSTHs, the PSTH of each neuron with a significant response was averaged and filtered with a Gaussian filter ($\sigma = 1.6$ ms). All electrophysiological data are presented as the mean \pm SD.

Results

Biochemical Characteristics of D1RKD Mice

We developed D1RKD mice in which D1Rs were conditionally and reversibly regulated by Dox using the Tet-Off system (Fig. 1B, see also Materials and Methods). We first examined the distribution of D1Rs in D1RKD mice immunohistochemically (Fig. 1C) using D1R antibodies. The specificity of the antibodies was examined in WT C57BL/6J mice and D1RKO mice (Fig. 1C, WT and D1RKO). D1Rs were expressed at a high level in the striatum including the ventral striatum and at moderate levels in the cortex of D1RKD mice (Fig. 1C, D1RKD). The distribution of D1Rs was similar to that of WT mice (Fig. 1C, WT) and that reported previously (Freneau et al. 1991; Weiner et al. 1991; Gaspar et al. 1995). We next quantitatively evaluated D1R expression in the striatum of D1RKD mice before, during, and after Dox treatment using western blot analysis (Fig. 1D). Before Dox treatment, D1R expression in the striatum was 27-fold higher than that in WT mice (Fig. 1D, Day 0 of D1RKD and WT). Dox treatment rapidly and completely suppressed D1R expression (Day 7, $27.1 \pm 4.2\%$; Day 14, $3.1 \pm 1.4\%$; Days 21 and 28, undetectable). After cessation of Dox treatment, D1R expression recovered to the level prior to Dox treatment over 7 days (Fig. 1D, After).

Motor Behaviors During D1R Suppression

Before Dox treatment, D1RKD mice showed normal behaviors and similar spontaneous motor activity to WT mice (Days -6 to -1 in Fig. 2A), despite the higher D1R expression in D1RKD mice. Dox treatment significantly decreased spontaneous motor activity in D1RKD mice from the first week (Days 1–6 of D1RKD Dox (+) in Fig. 2A) and monotonically decreased their activity during the second, third, and fourth weeks. Dox had little effect on WT mice (WT Dox (+)), and spontaneous motor activity in untreated D1RKD mice (D1RKD Dox (–)) was also unchanged (repeated-measures 2-way ANOVA, $P = 0.0024$ for genotype–day interaction; Bonferroni test, $P = 0.013$ for Days 1–6, $P < 0.01$ for Days 8–13, 15–20 and 22–27). Finally, the difference in the spontaneous motor activity of D1RKD Dox (+) mice and that of WT Dox (+) and D1RKD Dox (–) mice became significant in the fourth week (Days 22–27) (Bonferroni test, $P < 0.01$). Decreased spontaneous motor activity in D1RKD Dox (+) mice was due to an increase in inactive time and a decrease in highly active time (Fig. 2B; χ^2 test with Bonferroni correction, $P = 0.008$); such changes in active

and inactive times were observed in neither WT Dox (+) nor D1RKD Dox (–) mice. After cessation of Dox treatment, spontaneous motor activity temporarily increased and then returned to the normal level over 7 days (Fig. 2C).

Motor ability was also impaired during Dox treatment as evidenced by the rotarod test. The time spent on the rotarod by D1RKD Dox (+) mice was significantly shorter than that for WT Dox (–), WT Dox (+), and D1RKD Dox (–) mice (Fig. 2D; repeated-measures 2-way ANOVA, $P < 0.0001$ for genotype–day interaction; Bonferroni test, $P < 0.01$).

Spontaneous Activity of EPN and GPe Neurons During D1R Suppression

To assess the mechanism of the decreased motor activity in D1RKD mice following D1R suppression, we examined neuronal activity in awake conditions in the motor-related area of the EPN (Chiken et al. 2008), which is the target of D1R-expressing striatal neurons and the main output nucleus of the BG to the thalamus (Fig. 1A). We first recorded spontaneous activity of 127 and 89 EPN neurons before and during Dox treatment, respectively, in 4 awake D1RKD mice. EPN neurons continuously and irregularly fired at a high discharge rate (53.9 ± 14.8 Hz) before Dox treatment (Table 1, Fig. 3A1) as observed in WT mice (Chiken et al. 2008). Dox treatment did not change either the firing rate (54.2 ± 13.5 Hz; Table 1; 1-way ANOVA, $P = 0.93$) or pattern (Table 1, Fig. 3A2). The CV of ISIs, the burst index, and percentage of spikes in bursts, which characterize firing patterns, also did not change. These results indicate that D1R suppression had little influence on the spontaneous activity of EPN neurons. More than 15 days after the cessation of Dox treatment, we recorded 36 EPN neurons and found that the firing rates and percentage of spikes in bursts remained unchanged, whereas the CV of ISIs and burst index were increased (Table 1; 1-way ANOVA with Tukey's post hoc test, $P < 0.001$ for the CV of ISIs and burst index).

For comparison, we also examined the activity of GPe neurons in the same 4 D1RKD mice, because striato-GPe neurons are assumed to express D2Rs, not D1Rs (Fig. 1A). We found no significant differences in the firing rate or pattern among the 3 conditions (Table 1; 1-way ANOVA, $P = 0.84$ for the firing rate,

Table 1 Spontaneous firing rates and patterns of EPN and GPe neurons before, during, and after Dox treatment in D1RKD mice

	Before	During Dox (5–22 days after starting Dox treatment)	After
EPN			
No. of neurons	127	89	36
Firing rate (Hz)	53.9 ± 14.8	54.2 ± 13.5	53.8 ± 19.0
CV of ISIs	$0.53 \pm 0.15^*$	$0.49 \pm 0.15^\#$	$0.65 \pm 0.19^{*,\#}$
Burst index	$1.33 \pm 0.36^*$	$1.23 \pm 0.30^\#$	$1.91 \pm 1.19^{*,\#}$
Spikes in bursts (%)	0.82 ± 2.02	0.69 ± 1.27	1.16 ± 1.70
GPe			
No. of neurons	120	100	38
Firing rate (Hz)	51.0 ± 15.8	51.1 ± 15.5	52.9 ± 16.4
CV of ISIs	0.63 ± 0.21	0.68 ± 0.24	0.69 ± 0.15
Burst index	1.61 ± 1.08	1.54 ± 0.47	1.69 ± 0.43
Spikes in bursts (%)	1.43 ± 3.17	1.12 ± 1.66	1.33 ± 1.80

* $\#P < 0.01$, significantly different from each other (1-way ANOVA with Tukey's post hoc test).

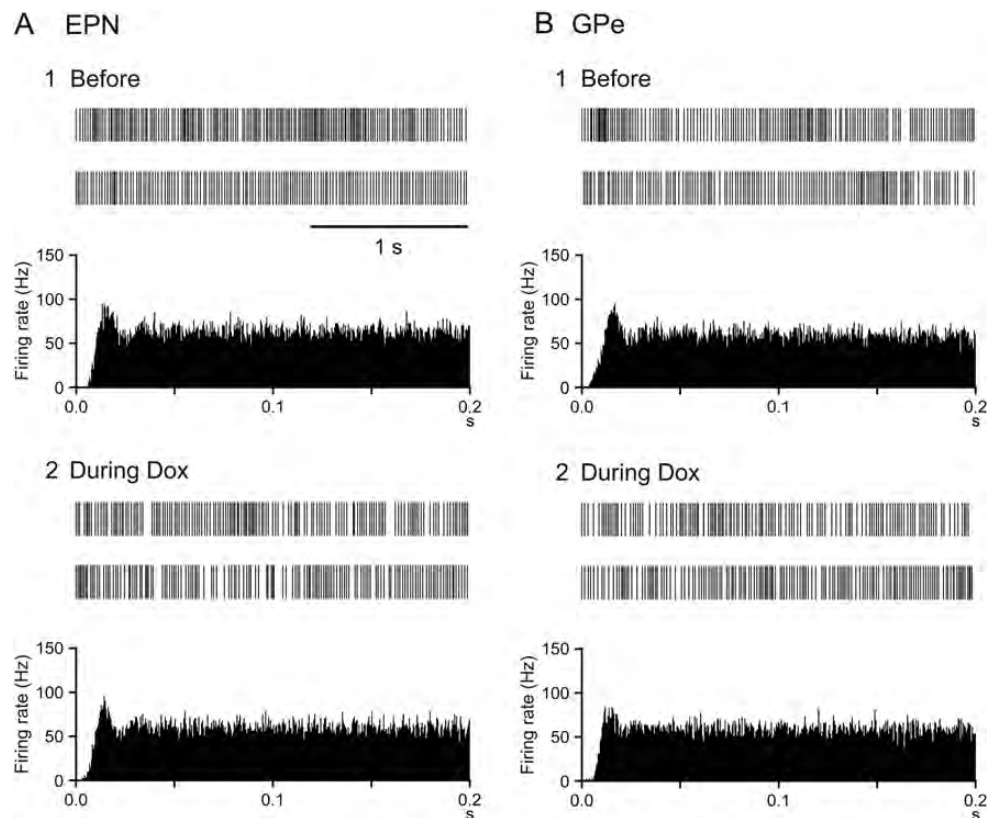


Figure 3. Spontaneous activity of EPN and GPe neurons during D1R suppression. Digitized spikes (top) and autocorrelograms (bottom) of spontaneous activity of EPN (A) and GPe (B) neurons before (1) and during (2) Dox treatment in D1RKD mice are shown.

$P = 0.26$ for the CV of ISIs, $P = 0.69$ for the burst index, $P = 0.73$ for the percentage of spikes in bursts; Fig. 3B).

Cortically Evoked Responses of EPN and GPe Neurons During D1R Suppression

After recording spontaneous activity of EPN neurons, we next examined the responses of these neurons to electrical stimulation of the forelimb and orofacial regions of the motor cortex (Chiken et al. 2008) (Fig. 4A), because cortical stimulation induces neuronal activity in the BG and mimics information processing during voluntary movements (Chiken et al. 2008; Tachibana et al. 2008; Sano et al. 2013). Before Dox treatment, 60% of EPN neurons (75/125 cells, Table 2) responded to stimulation of the motor cortex. The most common (64%) response was a triphasic response composed of early excitation, followed by inhibition and late excitation (ex-inh-ex) as observed in PSTHs (Fig. 4A1, left, see Supplementary Fig. 2A, Before), which is the typical response in WT mice (Chiken et al. 2008, see also Supplementary Fig. 3B). During Dox treatment, a similar percentage of neurons (72%, 63/88 cells, Table 2) responded to the motor cortical stimulation in the same area of the EPN (Fig. 5A); however, response patterns drastically changed. The inhibition was mostly lost (Fig. 4A2, left). The most common (65%) response was biphasic excitation consisting of early and late excitation, and the percentage of neurons exhibiting responses with inhibition, such as ex-inh-ex, ex-inh, inh-ex, and inh, was significantly decreased (before, 84%; during Dox, 24%; χ^2 test, $P < 0.0001$, see Supplementary Fig. 2A). These changes were also clearly observed in population PSTHs. The inhibition disappeared during Dox treatment (Fig. 4A1, A2, right).

The disappearance of the inhibition was already observed in the first half (5–14 days) of Dox treatment (see Supplementary Fig. 3A). Population PSTHs constructed for each mouse (Fig. 4B) evidenced that the disappearance of the inhibition was commonly observed in all 4 mice. Quantitative analysis showed that the duration and amplitude of the inhibition were markedly diminished during Dox treatment (Table 2; 1-way ANOVA with Tukey's post hoc test, $P < 0.001$ for the duration and amplitude). On the other hand, the latency, duration, and amplitude of the early excitation remained unchanged. The latency of the late excitation was decreased, and its amplitude was increased during Dox treatment ($P < 0.001$ for the duration, $P < 0.01$ for the amplitude), probably because the diminution of inhibition may unmask the late excitation. More than 15 days after the cessation of Dox treatment, a similar percentage of neurons (73%, Table 2) responded to the motor cortical stimulation, and the most common (58%) pattern was again triphasic, and was similar to that observed before Dox treatment (Fig. 4A3, left, see Supplementary Fig. 2A, After). Such recovery was also evident in population PSTHs (Fig. 4A3, right) and quantitative analyses (Table 2).

We also examined the cortically evoked responses of GPe neurons in the same 4 D1RKD mice for comparison. The most common cortically evoked response was triphasic with early excitation, followed by inhibition and late excitation throughout the 3 conditions (Fig. 4C, left; 67% before, 67% during, and 61% after Dox treatment, see Supplementary Fig. 2B); this is the typical response in WT mice (Chiken et al. 2008). In addition, population PSTHs (Fig. 4C, right) and the amplitude and duration of each component (Table 2; 1-way ANOVA; early excitation, $P = 0.51$ for the duration, $P = 0.42$ for the amplitude; inhibition, $P = 0.67$ for

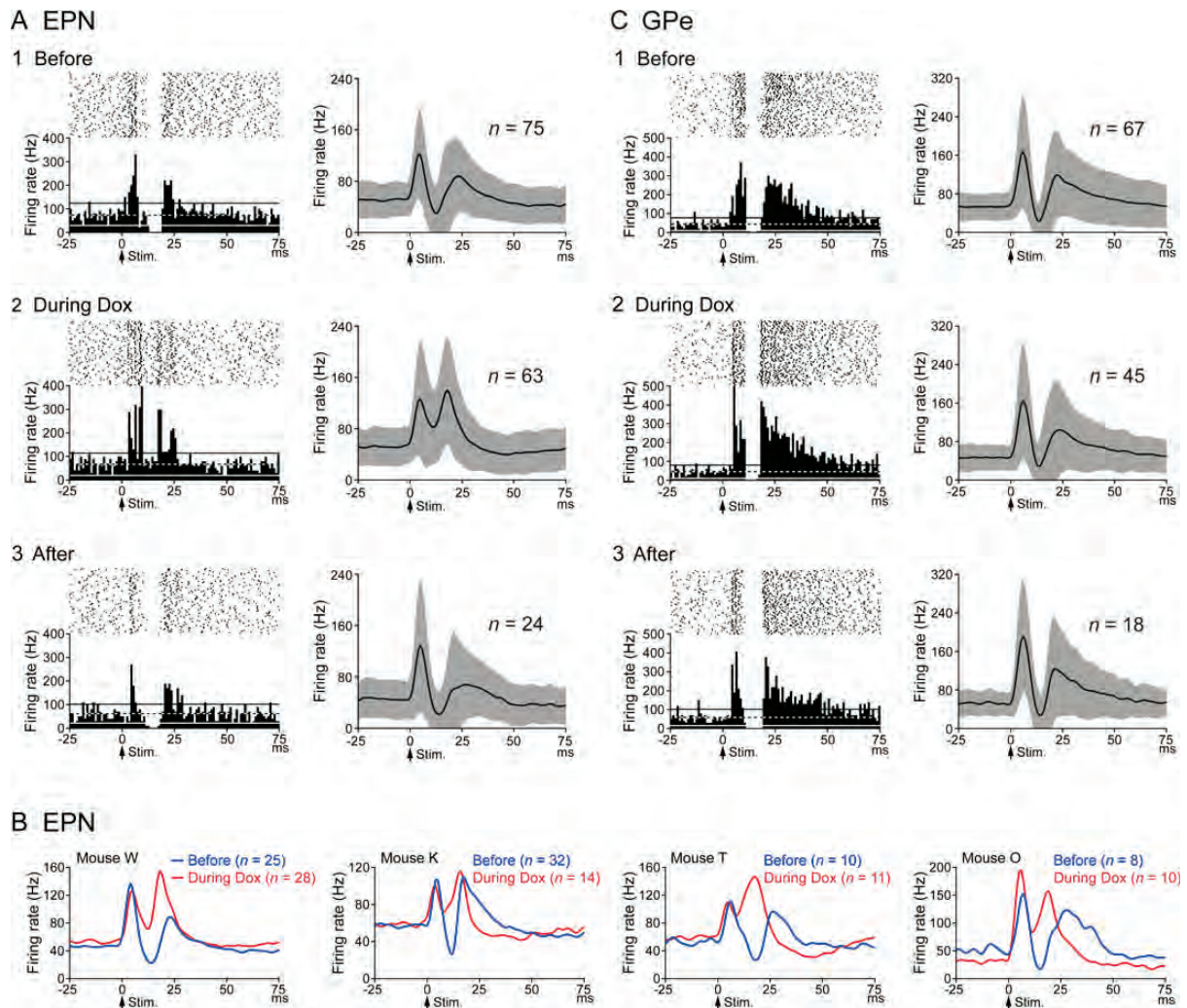


Figure 4. Cortically evoked responses of EPN and GPe neurons during D1R suppression. Cortically evoked responses of EPN (A) and GPe (C) neurons before (1), during (2), and after (3) Dox treatment in D1RKD mice. Raster and peristimulus time histograms (PSTHs; 100 trials; bin width, 1 ms) for typical examples (left) and population PSTHs (right, with Gaussian filter) are shown. Stimulation was delivered at time 0 (arrows). The mean firing rate and statistical levels of $P < 0.05$ (1-tailed t-test) are indicated in PSTHs by a black and white dashed line (mean) and black (upper limit) and white (lower limit) solid lines, respectively. The number of neurons used for population PSTHs is indicated by n , and the shaded areas represent \pm SD. (B) Population PSTHs (with Gaussian filter) of cortically evoked EPN responses constructed for each mouse (mouse W, K, T, and O). Blue and red lines represent before and during Dox treatment, respectively.

the duration, $P = 0.91$ for the amplitude; late excitation, $P = 0.72$ for the duration, $P = 0.83$ for the amplitude) were similar throughout the 3 conditions.

Finally, we examined whether the effects of Dox to EPN neurons described above were specifically observed in D1RKD mice, but not in WT mice. We recorded neuronal activity in the motor-related area of the EPN in 3 age-matched WT mice before and during Dox treatment. In WT mice, Dox treatment did not change the cortically evoked response in the EPN as observed in PSTHs and population PSTHs (see [Supplementary Fig. 3B](#)).

Location of Recorded Neurons

Recording sites in the EPN (mouse W) and GPe (mouse K) of D1RKD mice are shown in frontal sections using different symbols based on cortically evoked response patterns (Fig. 5). EPN neurons that responded to stimulation of the motor cortex were distributed throughout the middle and lateral parts of the EPN as

observed in WT mice ([Chicken et al. 2008](#)). The most common response before Dox treatment was a triphasic response composed of early excitation, followed by inhibition and late excitation (Fig. 5A1). During Dox treatment, cortically evoked responses in the same area mostly changed to biphasic excitation consisting of early and late excitation (Fig. 5A2). GPe neurons that responded to motor cortical stimulation were distributed in the middle and lateral parts of the GPe as observed in WT mice ([Chicken et al. 2008](#); [Sano et al. 2013](#)). The most common response was triphasic both before (Fig. 5B1) and during (Fig. 5B2) Dox treatment.

Discussion

The present study examined motor behaviors and neuronal activity of the BG in the presence and absence of D1Rs using novel D1RKD mice that we developed in which D1R expression can be conditionally and reversibly regulated by Dox treatment. Suppression of D1R expression by Dox treatment severely

Table 2 Cortically evoked responses of EPN and GPe neurons before, during, and after Dox treatment in D1RKD mice

	Before	During Dox (5–22 days after starting Dox treatment)	After
EPN			
No. of responded neurons/No. of tested neurons	75/125 (60%)	63/88 (72%)	24/33 (73%)
Early excitation			
Latency (ms)	3.7 ± 1.0	3.5 ± 0.9	3.4 ± 0.8
Duration (ms)	3.8 ± 2.5	4.5 ± 2.7	3.8 ± 2.6
Amplitude (spikes)	43.1 ± 30.2	58.1 ± 54.0	64.7 ± 56.4
Inhibition			
Latency (ms)	11.0 ± 2.5	10.5 ± 2.5	10.3 ± 3.2
Duration (ms)	6.1 ± 5.9*	0.8 ± 1.5* [#]	9.1 ± 6.2 [#]
Amplitude (spikes)	-27.4 ± 24.4*	-3.2 ± 7.7* [#]	-39.3 ± 33.9 [#]
Late excitation			
Latency (ms)	19.2 ± 3.8*	14.1 ± 3.2* [#]	21.0 ± 5.4 [#]
Duration (ms)	7.7 ± 5.9	9.8 ± 6.1	7.1 ± 7.4
Amplitude (spikes)	54.3 ± 54.2*	92.4 ± 79.3* [#]	51.2 ± 71.6 [#]
GPe			
No. of responded neurons/No. of tested neurons	67/114 (59%)	45/82 (55%)	18/30 (60%)
Early excitation			
Latency (ms)	3.9 ± 1.3	4.1 ± 1.0	4.0 ± 1.4
Duration (ms)	5.4 ± 2.7	6.0 ± 3.5	5.9 ± 1.9
Amplitude (spikes)	80.5 ± 48.7	83.5 ± 40.7	96.3 ± 42.8
Inhibition			
Latency (ms)	10.8 ± 2.4	11.2 ± 2.6	11.8 ± 1.9
Duration (ms)	6.1 ± 5.4	7.3 ± 6.7	6.6 ± 10.6
Amplitude (spikes)	-31.8 ± 30.6	-32.3 ± 24.9	-36.0 ± 74.7
Late excitation			
Latency (ms)	20.2 ± 4.2	19.9 ± 4.0	19.8 ± 3.8
Duration (ms)	21.6 ± 36.0	17.2 ± 25.1	17.5 ± 16.5
Amplitude (spikes)	196.1 ± 392.0	159.5 ± 292.7	162.5 ± 177.6

*[#]*P* < 0.01, significantly different from each other (1-way ANOVA with Tukey's post hoc test).

impaired motor behaviors in the mice. Cortically evoked inhibition in the EPN, which is mediated by the cortico-striato-EPN direct pathway, was mostly lost during suppression of D1R expression, whereas spontaneous firing rates and patterns of EPN neurons remained unchanged. These results suggest that D1R-mediated dopaminergic transmission maintains the information flow through the cortico-striato-EPN direct pathway to appropriately release motor actions.

Motor Behaviors and Spontaneous Activity of EPN and GPe Neurons

Based on the classical model of the BG, dopaminergic inputs exert excitatory effects on striatal direct pathway neurons through D1Rs (Albin et al. 1989; DeLong 1990; Gerfen et al.

1990). Thus, the loss of dopaminergic inputs through D1Rs would be expected to increase mean firing of EPN neurons and result in decreased motor activity. Increased mean firing rates were originally reported in the GPi (EPN in rodents) of primate models of PD (Miller and DeLong 1987; Fillion and Tremblay 1991; Boraud et al. 1998; Heimer et al. 2002; Wichmann et al. 2002). However, recent studies have failed to detect the expected firing rate increase in the GPi (Wichmann et al. 1999; Raz et al. 2000; Tachibana et al. 2011). Instead, abnormal firing patterns, such as bursts and oscillations, were recorded in the BG of PD animals and patients (Raz et al. 2000; Brown et al. 2001; Tachibana et al. 2011), and synchronous activation may disable the ability of individual neurons to process and relay motor-related information, resulting in failure of appropriate movements (Bergman et al. 1998; Brown 2007). The present study revealed that spontaneous motor activity in the mice was decreased during suppression of D1R expression (Fig. 2) without any prominent effects on spontaneous firing rates in either the EPN or GPe (Table 1, Fig. 3). The results indicate that the motor deficits during the absence of D1R-mediated dopaminergic transmission cannot be explained simply by changes in spontaneous firing rates in the EPN.

Cortically Evoked Responses of EPN and GPe Neurons

The BG receive inputs from a wide area of the cerebral cortex (Mink 1996; Nambu et al. 2002). The information is processed through the cortico-STN-EPN hyperdirect, cortico-striato-EPN direct, and cortico-striato-GPe-STN-EPN indirect pathways and reaches the EPN, the output station of the BG (Fig. 1A). During voluntary movements, neuronal signals originating in the cortex are considered to be transmitted through these pathways and reach the EPN. Thus, evaluating how neuronal signals originating in the motor cortex are transmitted through the BG is essential for assessing the mechanism of abnormal motor behaviors. Cortical stimulation induces neuronal activity in the BG mimicking information processing during voluntary movements and providing important clues for understanding the changes in information processing through the BG (Chiken et al. 2008; Tachibana et al. 2008; Sano et al. 2013). Cortically evoked responses in the BG are dramatically altered in hyper- and hypokinetic movement disorders (Chiken et al. 2008; Kita and Kita 2011; Nishibayashi et al. 2011).

Before Dox treatment, cortical stimulation induced a triphasic response composed of early excitation, followed by inhibition and late excitation in the EPN of D1RKD mice (Fig. 4A1); this is the typical response in WT mice (Chiken et al. 2008, see Supplementary Fig. 3B). D1RKD mice also showed normal behaviors and similar spontaneous motor activity to WT mice despite a high level of D1R expression, suggesting compensatory mechanisms, such as desensitization of D1Rs (Staunton et al. 1982) and decrease of dopamine release. Transient increase of spontaneous motor activity after cessation of Dox treatment (Fig. 2C) also suggests involvement of compensatory mechanisms, such as sensitization of D1Rs and increase of dopamine release. During suppression of D1R expression, cortically evoked inhibition in the EPN was mostly lost (Fig. 4A2, Table 2, see Supplementary Fig. 2A). On the other hand, cortical stimulation induced a triphasic response composed of early excitation, followed by inhibition and late excitation in the GPe that was not changed during D1R suppression (Fig. 4C, Table 2, see Supplementary Fig. 2B).

Many studies have revealed that cortically evoked early excitation, inhibition, and late excitation in the EPN/GPi are mediated by the hyperdirect, direct, and indirect pathways, respectively (Maurice et al. 1999; Nambu et al. 2000, 2002; Tachibana et al.

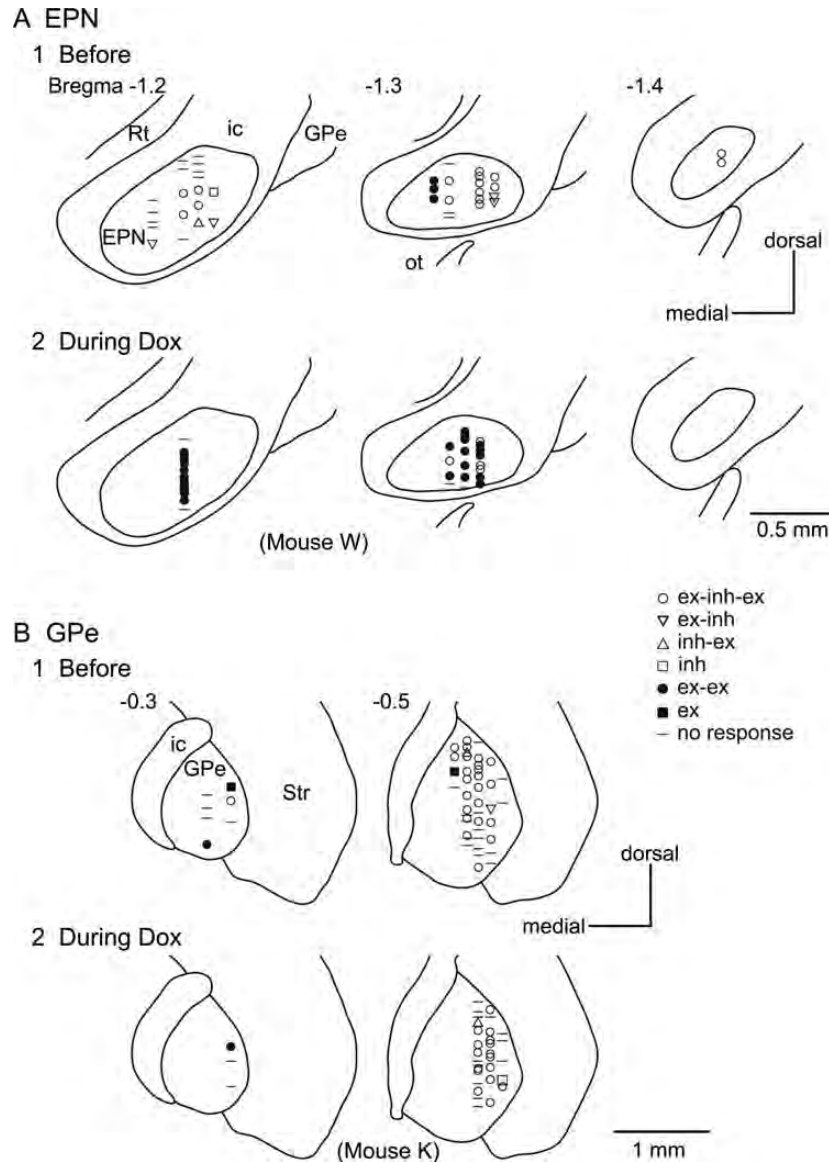


Figure 5. Recording sites in the EPN (A) (Mouse W) and GPe (B) (Mouse K) of D1RKD mice before (1) and during (2) Dox treatment. Frontal sections are arranged rostrocaudally from left to right, and the distance from bregma to each section is indicated. Locations of recorded neurons are indicated by different symbols based on cortically evoked response patterns. ex, excitation; ic, internal capsule; inh, inhibition; ot, optic tract; Rt, reticular thalamic nucleus; Str, striatum.

2008) (Fig. 1A). Thus, the loss of inhibition in the EPN during D1R suppression indicates that information flow through the cortico-striato-EPN direct pathway was strongly suppressed. Several possible mechanisms for this suppression can be considered. First, the excitability of striatal direct pathway neurons may be decreased during D1R suppression. The heads of dendritic spines of striatal projection neurons receive excitatory inputs from cortical neurons, with the neck of the spine receiving dopaminergic inputs through synapses and/or volume transmission (Hersch et al. 1995; Smith and Kiehl 2000; Arbuthnott and Wickens 2007). This spatial arrangement allows dopamine to modulate incoming excitatory glutamatergic drive. D1Rs are coupled to $G_{s/o1f}$, which activates adenylyl cyclase and facilitates intrinsic excitability and glutamate receptor-mediated responses in striatal neurons (Hervé et al. 1995; Surmeier et al. 2007; Gerfen and Surmeier 2011). D1R activation increases synaptic efficacy in

cortico-striatal synapses through long-term potentiation (Calabresi et al. 2007; Gerfen and Surmeier 2011). A significant loss of dendritic spines on striatal projection neurons in PD has also been reported (Villalba and Smith 2010). Second, other extrastriatal mechanisms can also be considered. A previous study (Kliem et al. 2007) revealed that D1Rs are also expressed in striatal axon terminals in the GPi, and their activation increases GABA release from the striato-GPi axon terminals. Decreased GABA release from the striato-EPN (homologous to GPi) terminals may contribute to loss of cortically evoked inhibition in the EPN. The EPN also receives GABAergic inhibitory inputs from the GPe. However, considering the fact that both spontaneous firing and the cortically evoked response in the GPe remained unchanged during D1R suppression (Fig. 3B, Fig. 4C, Tables 1 and 2, see Supplementary Fig. 2B), the GPe cannot be responsible for the attenuated cortically evoked inhibition in the EPN.

The cortically evoked triphasic response in the GPe is mediated sequentially by the cortico-STN-GPe, cortico-striato-GPe, and cortico-striato-GPe-STN-GPe pathways (Maurice et al. 1999; Nambu et al. 2000, 2002; Kita et al. 2004) (Fig. 1A). The maintained triphasic response in the GPe in the absence of D1Rs (Fig. 4C, Table 2, see Supplementary Fig. 2B) suggests that the excitability of these components, including the cortex, striatal indirect pathway neurons, GPe, and STN, remains unchanged despite the fact that D1Rs are also expressed at moderate levels in the cortex (Fig. 1C; Fremeau et al. 1991; Weiner et al. 1991; Gaspar et al. 1995). In situ hybridization study using a D2R-specific riboprobe followed by immunohistochemistry with Cre-specific antibody indicated that D1Rs may also be aberrantly expressed in striato-GPe indirect pathway neurons in transgenic mice expressing a Cre recombinase under the control of the D1R regulatory elements (Lemberger et al. 2007). However, neither spontaneous discharges nor cortically evoked responses of GPe neurons changed during D1R suppression in our current electrophysiological study (Figs 3B and 4C, Tables 1 and 2, see Supplementary Fig. 2B), suggesting that they are less functional.

Recent studies have shown conflicting results regarding the classical direct and indirect pathways model. Striatal neurons projecting to the EPN also have axon collaterals to the GPe, indicating no clear anatomical separation of the direct and indirect pathways (Graybiel 2005; Lévesque and Parent 2005; Fujiyama et al. 2011). Some striatal projection neurons express both D1Rs and D2Rs (Surmeier et al. 1996). However, the present results support the original notion that striatal projection neurons can be functionally separated into 2 groups, that is, one with D1Rs projecting to the EPN (GPi) and the other with D2Rs projecting to the GPe (Albin et al. 1989; DeLong 1990; Gerfen et al. 1990; Hersch et al. 1995; Sano et al. 2013). The axon terminals of striatal neurons that express D1Rs in the GPe may be minor or less functional compared with those with D2Rs.

D1R-Mediated Dopaminergic Transmission Maintains the Information Flow Through the Direct Pathway to Release Motor Actions

During D1R suppression, cortically evoked inhibition in the EPN was mostly lost (Fig. 4A,B), and motor behaviors were severely impaired (Fig. 2). Upon D1R re-expression, both the inhibition and motor behaviors were restored. This observation can explain the mechanism of reduced motor activity during D1R suppression (see Supplementary Fig. 4). Under normal D1R expression (see Supplementary Fig. 4, left), signals through the cortico-striato-EPN direct pathway induce inhibition in the EPN. The phasic inhibition in the EPN increases thalamocortical activity by disinhibitory mechanism and releases motor actions (Albin et al. 1989; DeLong 1990; Gerfen et al. 1990; Mink 1996; Hikosaka et al. 2000; Nambu et al. 2000, 2002; Nambu 2007; Kravitz et al. 2010). During D1R suppression (see Supplementary Fig. 4, right), signals through the cortico-striato-EPN direct pathway are strongly suppressed and fail to induce inhibition in the EPN, resulting in the reduced motor activity. Moreover, this observation suggests that the loss of the phasic inhibition in the EPN through the direct pathway, but not the firing rate or pattern changes, is a fundamental phenomenon in reduced motor activity during D1R suppression. The reduction of spontaneous motor activity was observed even in the first week of Dox treatment (Fig. 2A) when the level of D1R expression was still higher than that in WT mice (Fig. 1D). The loss of cortically evoked inhibition in EPN neurons was already observed in the first half (5–14 days) of Dox treatment (see Supplementary Fig. 3A). These results suggest that relative decrease of D1R expression would be responsible

for the changes in motor behavior and neuronal activity. Considering the fact that expression of D1Rs not only in the striatum but also outside the striatum was suppressed during Dox treatment in D1RKD mice (Fig. 1C), we cannot rule out the possibility that loss of extrastriatal D1Rs were also involved in their behavioral changes observed in the current study.

The present study revealed a crucial role for dopamine in maintaining the dynamics of the BG circuitry: D1R-mediated dopaminergic transmission maintains the information flow through the cortico-striato-EPN (GPi) direct pathway to appropriately release motor actions through disinhibitory mechanisms (see Supplementary Fig. 4). The present results also suggest that phasic activity changes in the EPN through the cortico-striato-EPN direct pathway are fundamental to both normal functions of the BG and the pathophysiology of movement disorders. Dopamine deficiency impairs phasic activation of the cortico-striato-EPN direct pathway and release of motor actions, and would be involved in the bradykinesia seen in PD.

Supplementary Material

Supplementary material can be found at: <http://www.cercor.oxfordjournals.org/>.

Funding

This study was supported by JSPS KAKENHI (#23115721, #21500378 and #25430021 to S.C.), JSPS KAKENHI (#22500343 and #26290029), the Collaborative Research Project (#2011-2221) of Brain Research Institute, Niigata University and the MEXT-Supported Program for the Strategic Research Foundation at Private Universities, 2011-2015 (to T.S.), and JSPS KAKENHI (#21240039, #26250009 and #15H05873), CREST, Strategic Japanese-German Cooperative Programme and the Takeda Science Foundation (to A.N.). Funding to pay the Open Access publication charges for this article was provided by the JSPS KAKENHI (#15H05873).

Notes

We thank M. Katsuki, A. Aiba, K. Nakamura, and K. Nakao for technical advice and critical discussion on generation of the D1RKD mice, K. Miyamoto, S. Sato, K. Awamura, H. Isogai, M. Goto, and members of the Department of Comparative and Experimental Medicine, Brain Research Institute, Niigata University for technical assistance. We also thank M. Kimura, Y. Kubo, and Y. Yamagata for comments on the manuscript. *Conflict of Interest*: None declared.

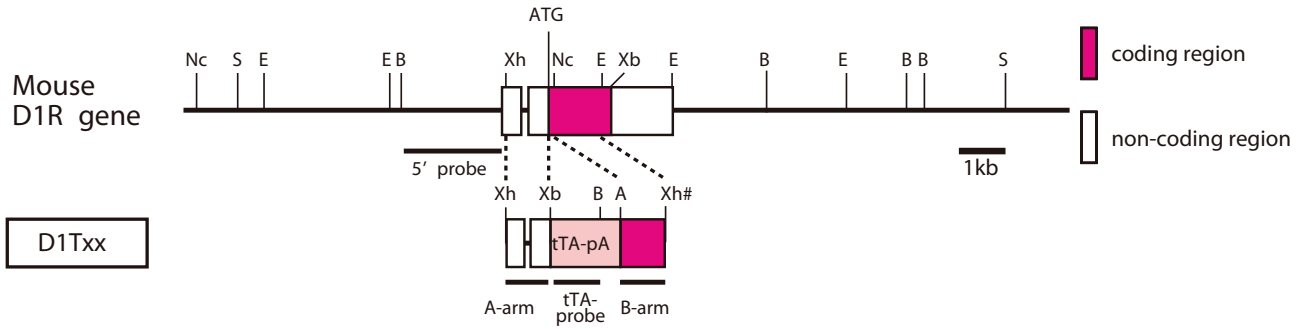
References

- Albin RL, Young AB, Penney JB. 1989. The functional anatomy of basal ganglia disorders. *Trends Neurosci.* 12:366–375.
- Arbuthnott GW, Wickens J. 2007. Space, time and dopamine. *Trends Neurosci.* 30:62–69.
- Bergman H, Feingold A, Nini A, Raz A, Slovin H, Abeles M, Vaadia E. 1998. Physiological aspects of information processing in the basal ganglia of normal and parkinsonian primates. *Trends Neurosci.* 21:32–38.
- Boraud T, Bezard E, Guehl D, Bioulac B, Gross C. 1998. Effects of L-DOPA on neuronal activity of the globus pallidus externalis (GPe) and globus pallidus internalis (GPi) in the MPTP-treated monkey. *Brain Res.* 787:157–160.
- Brown P. 2007. Abnormal oscillatory synchronisation in the motor system leads to impaired movement. *Curr Opin Neurobiol.* 17:656–664.

- Brown P, Oliviero A, Mazzone P, Insola A, Tonali P, Di Lazzaro V. 2001. Dopamine dependency of oscillations between subthalamic nucleus and pallidum in Parkinson's disease. *J Neurosci*. 21:1033–1038.
- Calabresi P, Picconi B, Tozzi A, Di Filippo M. 2007. Dopamine-mediated regulation of corticostriatal synaptic plasticity. *Trends Neurosci*. 30:211–219.
- Chiken S, Shashidharan P, Nambu A. 2008. Cortically evoked long-lasting inhibition of pallidal neurons in a transgenic mouse model of dystonia. *J Neurosci*. 28:13967–13977.
- Day M, Wokosin D, Plotkin JL, Tian X, Surmeier DJ. 2008. Differential excitability and modulation of striatal medium spiny neuron dendrites. *J Neurosci*. 28:11603–11614.
- DeLong MR. 1990. Primate models of movement disorders of basal ganglia origin. *Trends Neurosci*. 13:281–285.
- Enomoto K, Matsumoto N, Nakai S, Satoh T, Sato TK, Ueda Y, Inokawa H, Haruno M, Kimura M. 2011. Dopamine neurons learn to encode the long-term value of multiple future rewards. *Proc Natl Acad Sci USA*. 108:15462–15467.
- Fahn S, Jankovic J, Hallett M. 2011. Principles and practice of movement disorders. 2nd ed. Philadelphia: Elsevier Saunders.
- Filion M, Tremblay L. 1991. Abnormal spontaneous activity of globus pallidus neurons in monkeys with MPTP-induced parkinsonism. *Brain Res*. 547:142–151.
- Flores-Barrera E, Vizcarra-Chacon BJ, Vargas J, Tapia D, Galarraga E. 2011. Dopaminergic modulation of corticostriatal responses in medium spiny projection neurons from direct and indirect pathways. *Front Syst Neurosci*. 5:15.
- Freneau RT Jr, Duncan GE, Fornaretto MG, Deary A, Gingrich JA, Breese GR, Caron MG. 1991. Localization of D1 dopamine receptor mRNA in brain supports a role in cognitive, affective, and neuroendocrine aspects of dopaminergic neurotransmission. *Proc Natl Acad Sci USA*. 88:3772–3776.
- Fujiyama F, Sohn J, Nakano T, Furuta T, Nakamura KC, Matsuda W, Kaneko T. 2011. Exclusive and common targets of neostriatofugal projections of rat striosome neurons: a single neuron-tracing study using a viral vector. *Eur J Neurosci*. 33:668–677.
- Gaspar P, Bloch B, Le Moine C. 1995. D1 and D2 receptor gene expression in the rat frontal cortex: cellular localization in different classes of efferent neurons. *Eur J Neurosci*. 7:1050–1063.
- Gerfen CR, Engber TM, Mahan LC, Susel Z, Chase TN, Monsma FJ Jr, Sibley DR. 1990. D1 and D2 dopamine receptor-regulated gene expression of striatonigral and striatopallidal neurons. *Science*. 250:1429–1432.
- Gerfen CR, Surmeier DJ. 2011. Modulation of striatal projection systems by dopamine. *Annu Rev Neurosci*. 34:441–466.
- Graybiel AM. 2005. The basal ganglia: learning new tricks and loving it. *Curr Opin Neurobiol*. 5:638–644.
- Heimer G, Bar-Gad I, Goldberg JA, Bergman H. 2002. Dopamine replacement therapy reverses abnormal synchronization of pallidal neurons in the 1-methyl-4-phenyl-1,2,3,6-tetrahydropyridine primate model of parkinsonism. *J Neurosci*. 22:7850–7855.
- Hersch SM, Ciliax BJ, Gutekunst CA, Rees HD, Heilman CJ, Yung KK, Bolam JP, Ince E, Yi H, Levey AI. 1995. Electron microscopic analysis of D1 and D2 dopamine receptor proteins in the dorsal striatum and their synaptic relationships with motor corticostriatal afferents. *J Neurosci*. 15:5222–5237.
- Hervé D, Rogard M, Lévi-Strauss M. 1995. Molecular analysis of the multiple Golf alpha subunit mRNAs in the rat brain. *Brain Res Mol Brain Res*. 32:125–134.
- Hikosaka O, Takikawa Y, Kawagoe R. 2000. Role of the basal ganglia in the control of purposive saccadic eye movements. *Physiol Rev*. 80:953–978.
- Hirsch EC, Périer C, Orioux G, François C, Féger J, Yelnik J, Vila M, Levy R, Tolosa ES, Marin C, et al. 2000. Metabolic effects of nigrostriatal denervation in basal ganglia. *Trends Neurosci*. 23: S78–S85.
- Hutchison WD, Allan RJ, Opitz H, Levy R, Dostrovsky JO, Lang AE, Lozano AM. 1998. Neurophysiological identification of the subthalamic nucleus in surgery for Parkinson's disease. *Ann Neurol*. 44:622–628.
- Joshua M, Adler A, Bergman H. 2009. The dynamics of dopamine in control of motor behavior. *Curr Opin Neurobiol*. 19:615–620.
- Kita H, Nambu A, Kaneda K, Tachibana Y, Takada M. 2004. Role of ionotropic glutamatergic and GABAergic inputs on the firing activity of neurons in the external pallidum in awake monkeys. *J Neurophysiol*. 92:3069–3084.
- Kita T, Kita H. 2011. Cortical stimulation evokes abnormal responses in the dopamine-depleted rat basal ganglia. *J Neurosci*. 31:10311–10322.
- Kliem MA, Maidment NT, Ackerson LC, Chen S, Smith Y, Wichmann T. 2007. Activation of nigral and pallidal dopamine D1-like receptors modulates basal ganglia outflow in monkeys. *J Neurophysiol*. 98:1489–1500.
- Kravitz AV, Freeze BS, Parker PR, Kay K, Thwin MT, Deisseroth K, Kreitzer AC. 2010. Regulation of parkinsonian motor behaviours by optogenetic control of basal ganglia circuitry. *Nature*. 466:622–626.
- Legéndy CR, Salzman M. 1985. Bursts and recurrences of bursts in the spike trains of spontaneously active striate cortex neurons. *J Neurophysiol*. 53:926–939.
- Lemberger T, Parlato R, Dassel D, Westphal M, Casanova E, Turiault M, Tronche F, Schiffmann SN, Schutz G. 2007. Expression of Cre recombinase in dopaminergic neurons. *BMC Neuroscience*. 8:4.
- Lévesque M, Parent A. 2005. The striatofugal fiber system in primates: a reevaluation of its organization based on single-axon tracing studies. *Proc Natl Acad Sci USA*. 102:11888–11893.
- Mallet N, Ballion B, Le Moine C, Gonon F. 2006. Cortical inputs and GABA interneurons imbalance projection neurons in the striatum of parkinsonian rats. *J Neurosci*. 26:3875–3884.
- Maurice N, Deniau JM, Glowinski J, Thierry AM. 1999. Relationships between the prefrontal cortex and the basal ganglia in the rat: physiology of the cortico-nigral circuits. *J Neurosci*. 19:4674–4681.
- Miller WC, DeLong MR. 1987. Altered tonic activity of neurons in the globus pallidus and subthalamic nucleus in the primate MPTP model of parkinsonism. In: Carpenter MB, Jayaraman A, editors. *The basal ganglia II: structure and functions-current concepts*. New York: Plenum. p. 415–427.
- Mink JW. 1996. The basal ganglia: focused selection and inhibition of competing motor programs. *Prog Neurobiol*. 50:381–425.
- Nagy A, Gertsenstein M, Vintersten K, Behringer R. 2002. Manipulating the mouse embryo: a laboratory manual. 3rd ed. New York: Cold Spring Harbor Press.
- Nakamura T, Sato A, Kitsukawa T, Momiyama T, Yamamori T, Sasaoka T. 2014. Distinct motor impairments of dopamine D1 and D2 receptor knockout mice revealed by three types of motor behavior. *Front Integr Neurosci*. 8:56.
- Nambu A. 2007. Globus pallidus internal segment. *Prog Brain Res*. 160:135–150.

- Nambu A, Tokuno H, Hamada I, Kita H, Imanishi M, Akazawa T, Ikeuchi Y, Hasegawa N. 2000. Excitatory cortical inputs to pallidal neurons via the subthalamic nucleus in the monkey. *J Neurophysiol.* 84:289–300.
- Nambu A, Tokuno H, Takada M. 2002. Functional significance of the cortico-subthalamo-pallidal ‘hyperdirect’ pathway. *Neurosci Res.* 43:111–117.
- Nishibayashi H, Ogura M, Kakishita K, Tanaka S, Tachibana Y, Nambu A, Kita H, Itakura T. 2011. Cortically evoked responses of human pallidal neurons recorded during stereotactic neurosurgery. *Mov Disord.* 26:469–476.
- Planert H, Berger TK, Silberberg G. 2013. Membrane properties of striatal direct and indirect pathway neurons in mouse and rat slices and their modulation by dopamine. *PLoS One.* 8:e57054.
- Raz A, Vaadia E, Bergman H. 2000. Firing patterns and correlations of spontaneous discharge of pallidal neurons in the normal and the tremulous 1-methyl-4-phenyl-1,2,3,6-tetrahydropyridine vervet model of parkinsonism. *J Neurosci.* 20:8559–8571.
- Sano H, Chiken S, Hikida T, Kobayashi K, Nambu A. 2013. Signals through the striatopallidal indirect pathway stop movements by phasic excitation in the substantia nigra. *J Neurosci.* 33:7586–7594.
- Seppi K, Weintraub D, Coelho M, Perez-Lloret S, Fox SH, Katzenschlager R, Hametner EM, Poewe W, Rascol O, Goetz CG, et al. 2011. The movement disorder society evidence-based medicine review update: treatments for the non-motor symptoms of Parkinson’s disease. *Mov Disord.* 26 Suppl 3:S42–S80.
- Smith Y, Kieval JZ. 2000. Anatomy of the dopamine system in the basal ganglia. *Trends Neurosci.* 23:S28–S33.
- Staunton DA, Magistretti PJ, Koob GF, Shoemaker WJ, Bloom FE. 1982. Dopaminergic supersensitivity induced by denervation and chronic receptor blockade is additive. *Nature.* 299:72–74.
- Surmeier DJ, Ding J, Day M, Wang Z, Shen W. 2007. D1 and D2 dopamine-receptor modulation of striatal glutamatergic signaling in striatal medium spiny neurons. *Trends Neurosci.* 30:228–235.
- Surmeier DJ, Song WJ, Yan Z. 1996. Coordinated expression of dopamine receptors in neostriatal medium spiny neurons. *J Neurosci.* 16:6579–6591.
- Tachibana Y, Iwamuro H, Kita H, Takada M, Nambu A. 2011. Subthalamo-pallidal interactions underlying parkinsonian neuronal oscillations in the primate basal ganglia. *Eur J Neurosci.* 34:1470–1484.
- Tachibana Y, Kita H, Chiken S, Takada M, Nambu A. 2008. Motor cortical control of internal pallidal activity through glutamatergic and GABAergic inputs in awake monkeys. *Eur J Neurosci.* 27:238–253.
- Tran AH, Uwano T, Kimura T, Hori E, Katsuki M, Nishijo H, Ono T. 2008. Dopamine D1 receptor modulates hippocampal representation plasticity to spatial novelty. *J Neurosci.* 28:13390–13400.
- Villalba RM, Smith Y. 2010. Striatal spine plasticity in Parkinson’s disease. *Front Neuroanat.* 4:133.
- Waddington JL, O’Tuathaigh C, O’Sullivan G, Tomiyama K, Koshikawa N, Croke DT. 2005. Phenotypic studies on dopamine receptor subtype and associated signal transduction mutants: insights and challenges from 10 years at the psychopharmacology-molecular biology interface. *Psychopharmacology.* 181:611–638.
- Weiner DM, Levey AI, Sunahara RK, Niznik HB, O’Dowd BF, Seeman P, Brann MR. 1991. D1 and D2 dopamine receptor mRNA in rat brain. *Proc Natl Acad Sci USA.* 88:1859–1863.
- Wichmann T, Bergman H, Starr PA, Subramanian T, Watts RL, DeLong MR. 1999. Comparison of MPTP-induced changes in spontaneous neuronal discharge in the internal pallidal segment and in the substantia nigra pars reticulata in primates. *Exp Brain Res.* 125:397–409.
- Wichmann T, Kliem MA, Soares J. 2002. Slow oscillatory discharge in the primate basal ganglia. *J Neurophysiol.* 87:1145–1148.
- Yang XW, Model P, Heintz N. 1997. Homologous recombination based modification in *Escherichia coli* and germline transmission in transgenic mice of a bacterial artificial chromosome. *Nat Biotechnol.* 15:859–865.

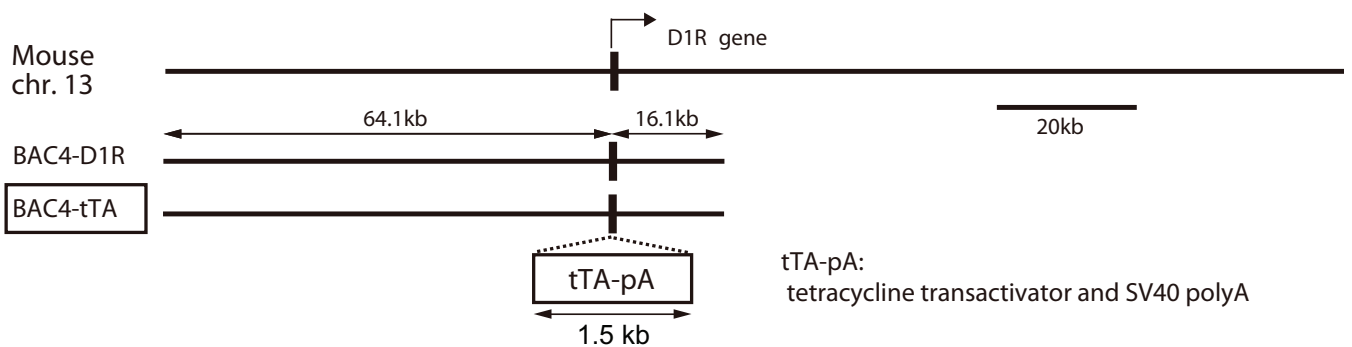
A Modification cassette construct



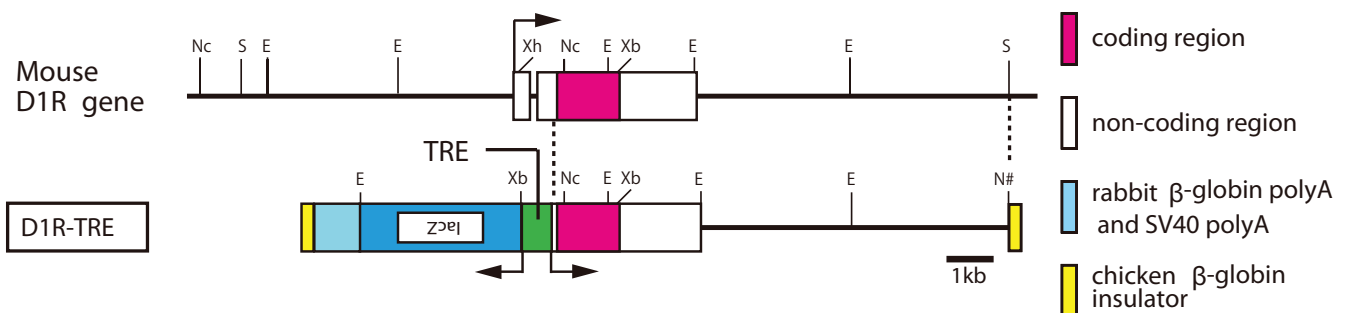
tTA-pA, tetracycline transactivator and SV40 polyA

A, Asc I; B, Bam HI; E, Eco RI; Nc, Nco I; S, Sau 3A; Xb, Xba I; Xh, Xho I; Xh#, Xho I (artificial)

B BAC4-tTA construct



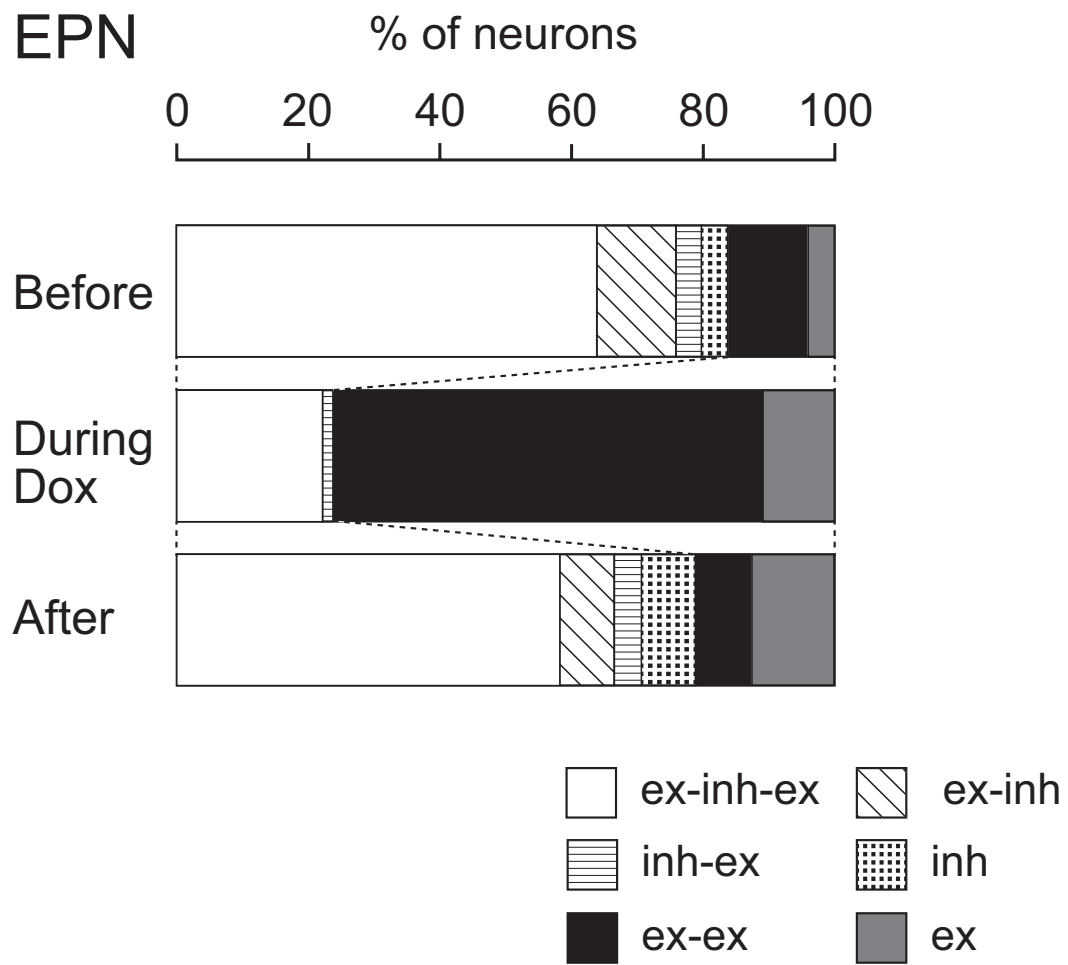
C D1R-TRE construct



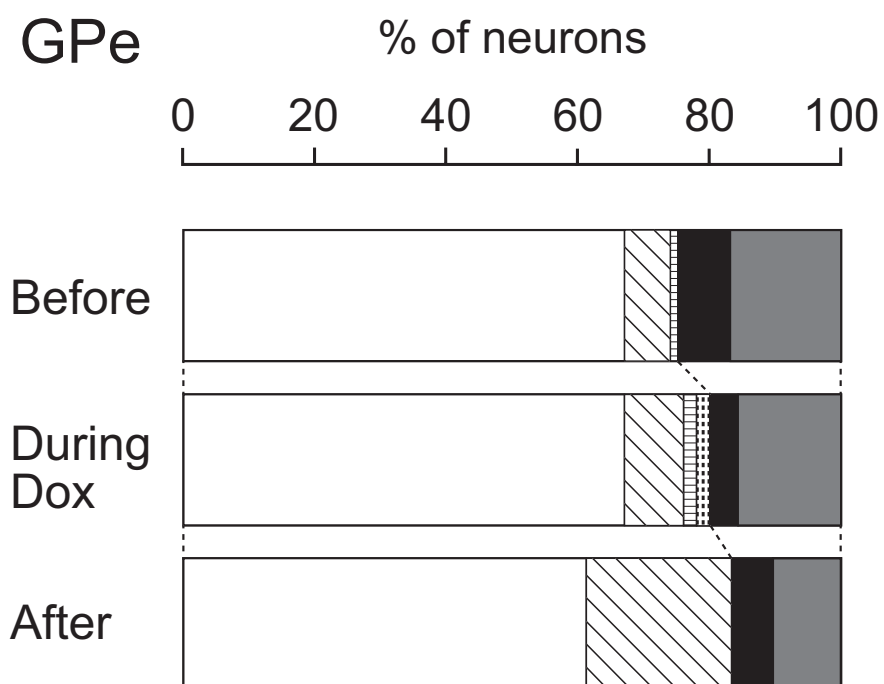
TRE, tetracycline responsive element and bidirectional promoter

E, Eco RI; Nc, Nco I; N#, Not I (artificial); S, Sau 3A; Xh, Xho I; Xb, Xba I

A EPN

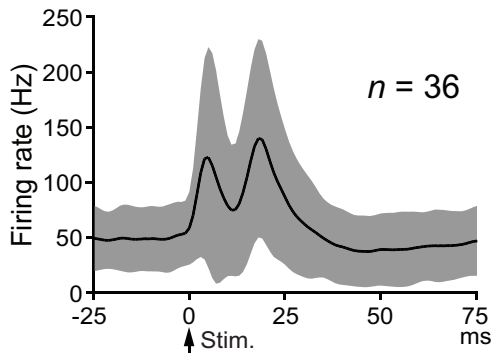


B GPe

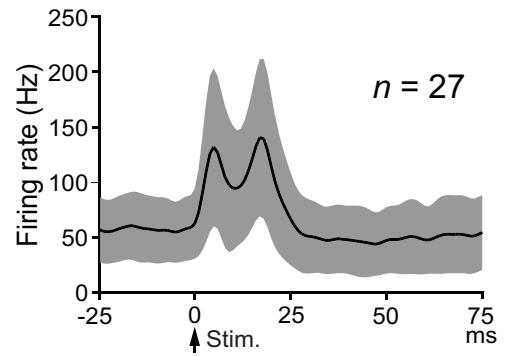


A D1RKD EPN

1 During Dox (5–14 days)

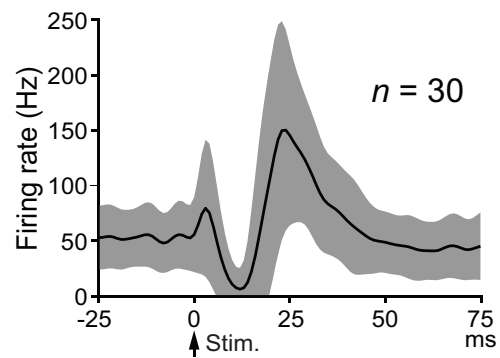
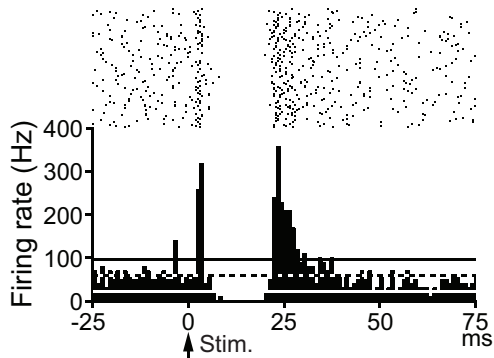


2 During Dox (15–22 days)

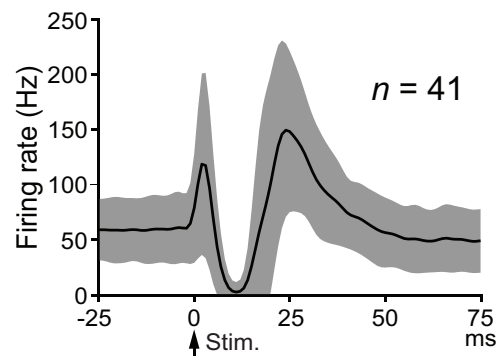
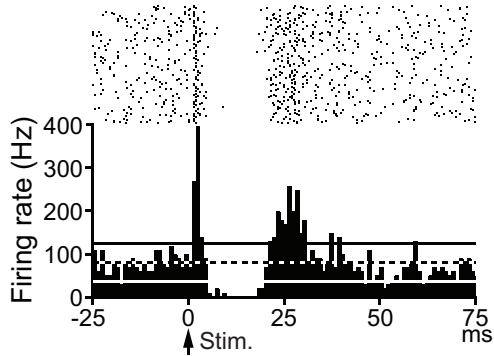


B WT EPN

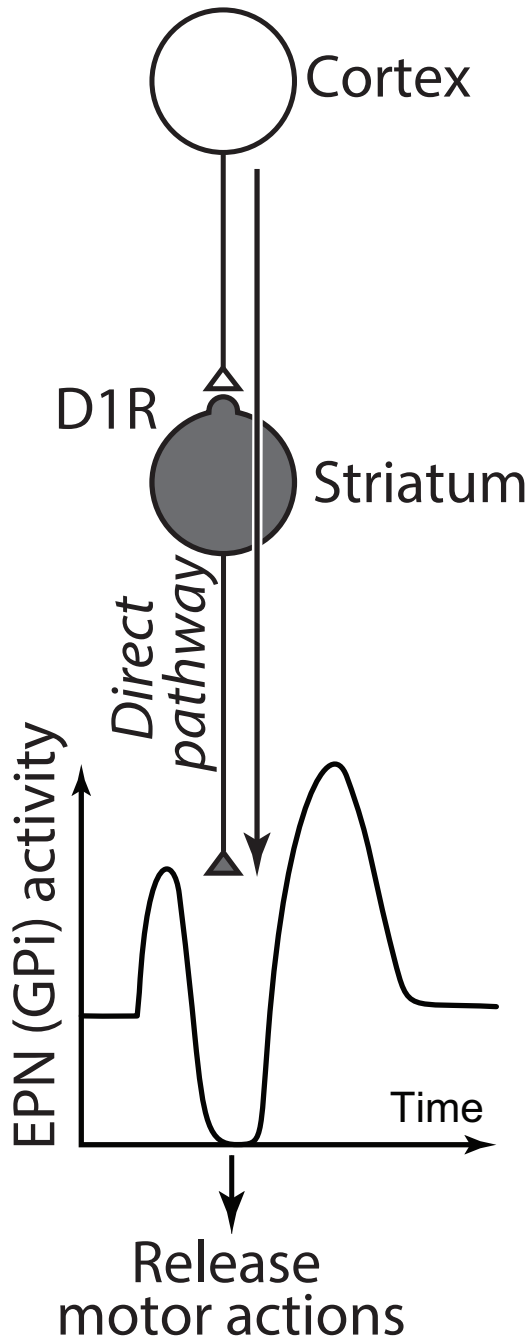
1 Before



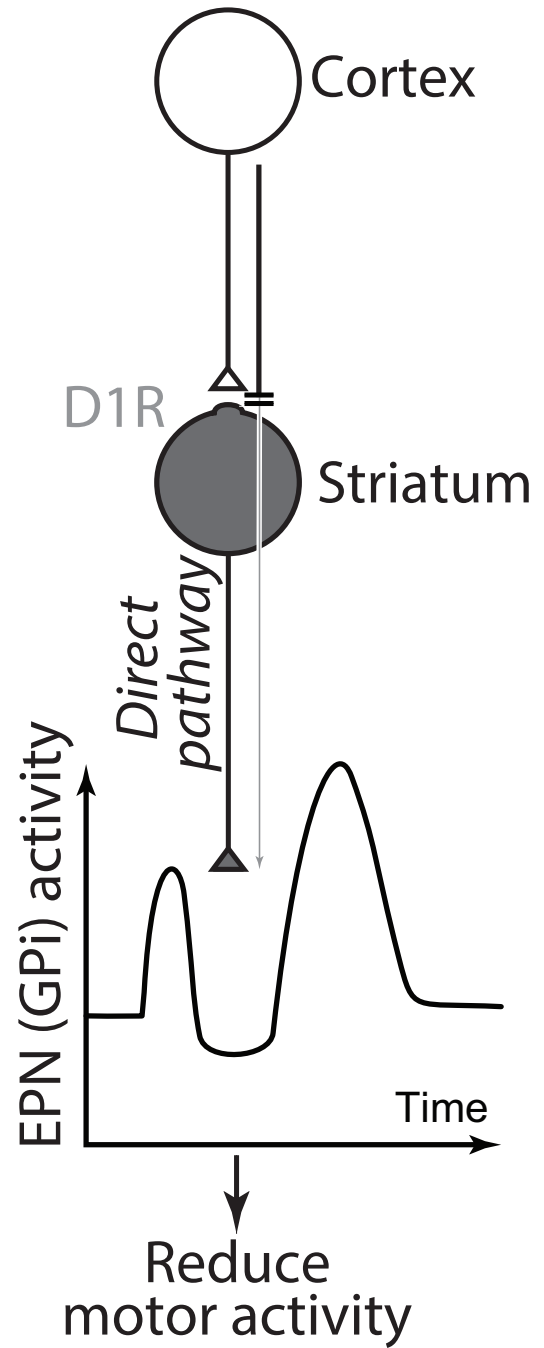
2 During Dox



Normal D1R



D1R suppression



Supplementary Figure 1. Construction of BAC4-tTA and D1R-TRE. (A) Schematic representation of mouse *DIR* and the modification cassette D1Txx for bacterial artificial chromosome (BAC) modification using a two-step Rec A strategy. The 5' probe, tTA probe, A-arm and B-arm were used for Southern analysis. (B) Schematic representation of the BAC clone containing mouse *DIR* and the construct for generation of tTA-expressing transgenic (Tg) mice. BAC4-D1R was modified using homologous recombination with the pSV1-RecA-D1T shuttle vector (see Materials and Methods) to generate BAC4-tTA. (C) Schematic representation of the D1R-TRE construct for the generation of tetracycline operator-target Tg mice. The bidirectional tetracycline-responsive promoter leads to simultaneous expression of both *DIR* and *lacZ* depending on the action of tTA.

Supplementary Figure 2. Proportions of neurons in the entopeduncular nucleus (EPN, A) and external pallidum (GPe, B) classified according to the cortically evoked response patterns before, during, and after doxycycline (Dox) treatment in Dopamine D1 receptor knockdown (D1RKD) mice. ex, excitation; inh, inhibition. Response patterns can be grouped into 2 groups: responses with inhibition, such as ex-inh-ex, ex-inh, inh-ex and inh, and responses without inhibition, such as ex-ex and ex.

Supplementary Figure 3. (A) Cortically evoked responses of EPN neurons in D1RKD mice in the first half (5–14 days after starting Dox treatment, 1) and in the latter half (15–22 days after starting Dox treatment, 2) of Dox treatment. Population peristimulus time histograms

(population PSTHs, with Gaussian filter) are shown. Stimulation was delivered at time 0 (arrows). The number of neurons is indicated by n , and the shaded areas represent \pm SD. (B) Cortically evoked responses of EPN neurons before (1) and during (2) Dox treatment in wild-type (WT) mice. Raster and PSTHs (100 trials; bin width, 1 ms) for typical examples (left) and population PSTHs are shown. The mean firing rate and statistical levels of $p < 0.05$ (one-tailed t-test) are indicated in PSTHs by a black and white dashed line (mean) and black (upper limit) and white (lower limit) solid lines, respectively.

Supplementary Figure 4. D1R-mediated dopaminergic transmission maintains the information flow through the cortico-striato-EPN (homologous to GPi) *direct* pathway to appropriately release motor actions. Under normal D1R expression (left), signals through the cortico-striato-EPN (GPi) *direct* pathway induce inhibition in the EPN (GPi) and release motor actions by disinhibiting the thalamus. During D1R suppression (right), the information flow through the cortico-striato-EPN (GPi) *direct* pathway is strongly suppressed and fails to induce inhibition in the EPN (GPi), resulting in the reduced motor activity. Open and shaded circles represent excitatory and inhibitory neurons, respectively.

Expression pattern of immediate early genes in the cerebellum of D1R KO, D2R KO, and wild type mice under vestibular-controlled activity

Toru Nakamura^{1,2,3}, Asako Sato^{4,5}, Takashi Kitsukawa^{1,3}, Toshikuni Sasaoka^{4,5,6} and Tetsuo Yamamori^{1,2,7*}

¹ Division of Brain Biology, National Institute for Basic Biology, Okazaki, Japan, ² Department of Basic Biology, Graduate University for Advanced Studies (SOKENDAI), Okazaki, Japan, ³ KOKORO-Biology Group, Laboratories for Integrated Biology, Graduate School of Frontier Biosciences, Osaka University, Suita, Japan, ⁴ Laboratory of Neurochemistry, National Institute for Basic Biology, Okazaki, Japan, ⁵ Department of Laboratory Animal Science, Kitasato University School of Medicine, Sagamihara, Japan, ⁶ Department of Comparative and Experimental Medicine, Brain Research Institute, Niigata University, Niigata, Japan, ⁷ Laboratory of Molecular Analysis for Higher Brain Function, RIKEN Brain Science Institute, Wako, Japan

OPEN ACCESS

Edited by:

Kathleen Dave,
St. Luke's University Health Network,
USA

Reviewed by:

William Wisden,
Imperial College London,
United Kingdom
Cathryn Kubera,
Monmouth University, USA

*Correspondence:

Tetsuo Yamamori,
RIKEN Brain Science Institute, Wako,
Saitama 351-0198, Japan
yamamori@nibb.ac.jp;
tetsuo.yamamori@riken.jp

Specialty section:

This article was submitted to
Systems Biology,
a section of the journal
Frontiers in Cell and Developmental
Biology

Received: 24 March 2015

Accepted: 01 June 2015

Published: 17 June 2015

Citation:

Nakamura T, Sato A, Kitsukawa T,
Sasaoka T and Yamamori T (2015)
Expression pattern of immediate early
genes in the cerebellum of D1R KO,
D2R KO, and wild type mice under
vestibular-controlled activity.
Front. Cell Dev. Biol. 3:38.
doi: 10.3389/fcell.2015.00038

We previously reported the different motor abilities of D1R knockout (KO), D2R KO and wild-type (WT) mice. To understand the interaction between the cerebellum and the striatal direct and indirect pathways, we examined the expression patterns of immediate early genes (IEG) in the cerebellum of these three genotypes of mice. In the WT naive mice, there was little IEG expression. However, we observed a robust expression of *c-fos* mRNA in the vermis and hemisphere after running rota-rod tasks. In the vermis, *c-fos* was expressed throughout the lobules except lobule 7, and also in crus 1 of the ansiform lobule (Crus1), copula of the pyramis (Cop) and most significantly in the flocculus in the hemisphere. *jun-B* was much less expressed but more preferentially expressed in Purkinje cells. In addition, we observed significant levels of *c-fos* and *jun-B* expressions after handling mice, and after the stationary rota-rod task in naive mice. Surprisingly, we observed significant expression of *c-fos* and *jun-B* even 30 min after single weighing. Nonetheless, certain additional *c-fos* and *jun-B* expressions were observed in three genotypes of the mice that experienced several sessions of motor tasks 24 h after stationary rota-rod task and on days 1 and 5 after rota-rod tasks, but no significant differences in expressions after the running rota-rod tasks were observed among the three genotypes. In addition, there may be some differences 24 h after the stationary rota-rod task between the naive mice and the mice that experienced several sessions of motor tasks.

Keywords: IEG, *c-fos*, *jun-B*, rota-rod, striatum

Introduction

We have recently reported the distinct motor impairments of congenic dopamine D1 and D2 receptor KO mice in their performance of three different types of motor behavioral tasks, that is, spontaneous motor activity tasks in the home cage, rota-rod tasks, and our own invented Step-Wheel task (Kitsukawa et al., 2011). In the Step-Wheel task, mice run as they adjust their steps on

foothold pegs to drink water (Nakamura et al., 2014). Durieux et al. (2012) showed that the ablation of D1R medium spiny neurons (MSNs) in the dorsolateral striatum (DLS) of mice corresponding to the primate putamen decreases the learning curve in rota-rod tasks. They also showed that the ablation of D2R MSN in the dorsomedial striatum (DMS) of mice corresponding to the primate caudate decreases the initial learning curve of the task. These results of local ablation are generally consistent with those of the entire striatal ablation of D1R and D2R neurons (Durieux et al., 2012) and the results of our behavioral experiments using general D1R and D2R KO mice, suggesting that DLS and DMS play major roles in rota-rod tasks. However, there are also differences in the results between local ablation and general D1R KO and D2R KO mice (Nakamura et al., 2014). The ablation of D1R MSNs in either DMS or the entire striatum reduced locomotion in the open field, which behavior is the reverse of general D1R KO mice. The ablation of D2R MSNs in either DMS or the entire striatum does not affect the late-phase performance (Durieux et al., 2012), whereas the general D2R KO mice showed poorer leaning than WT mice in the Step-Wheel tasks (Nakamura et al., 2014). These differences between local ablation of DRs and general KO suggest that the involvement and interaction between the striatum and other brain regions.

To explore this possibility further, in this study we employed the immediate early gene (IEG) mapping technique, with which the neuronal activity in the cerebellum is monitored on the basis of IEG expressions. Among eight IEGs we examined, *c-fos* and *jun-B* showed marked expression and specific induction, respectively, in the cerebellum immediately after the running rota-rod tasks. Interestingly, by examining *c-fos* and *jun-B* expressions in the vermis, Crus1, Cop and the flocculus in the cerebellar hemisphere, we found significant expressions of *c-fos* and *jun-B* 24 h after the stationary rota-rod tasks, during which time the mice did not perform any motor tasks but were allowed to move freely. We consider that this may be consistent with the idea that motor sequence learning and adaptation progress with time, through “consolidation” and “automatization” (Doyon et al., 2009).

We therefore examined in detail the expression patterns of *c-fos* and *jun-B* in the congenic D1R KO, D2R KO, and WT mice after the stationary and running rota-rod tasks in order to determine how cerebellar activities related to the D1R- and D2R-dependent pathways. Although we have not confirmed the alteration of *c-fos* expression patterns in the cerebellar flocculus on days 1 and 5 after the rotating rota-rod tasks among the three genotypes of mice, D1R KO, D2R KO, and WT mice, we found significant expressions of *c-fos* and *jun-B* not only immediately (30 min) after the mice ran on the rota-rod but also after handling them, and 30 min and unexpectedly even 24 h after the stationary rota-rod task. This observation led us to examine a series of examination for *c-fos* and *jun-B* expression patterns. We found that vestibular-controlled activities such as handling mice and weighing caused significant *c-fos* and *jun-B* expressions in cerebellar flocculus. However, there may be still some differences in expressions 24 h after the stationary rota-rod task between the naive and trained mice. Our results indicate that the analysis of

c-fos and *jun-B* expression patterns is a useful tool for studying cerebellar activity, which may play a role complementary to imaging studies such as functional MRI, because of the fine resolution at the cellular level, in understanding the sequential events of motor learning in the cerebellum.

Materials and Methods

The expression of eight IEGs was first examined in the cerebellum of naive WT mice, that is, mice that did not experience any motor tasks but were allowed to move freely. The IEG expression patterns were examined in the mice that performed a rota-rod task (Experiment 1). Next, we compared *c-fos* and *jun-B* mRNA expression levels, in the cerebellar hemisphere, especially the flocculus among the three genotypes of mice: D1R KO, D2R KO, and WT mice (Experiment 2). Additionally, we examined the expressions patterns of *c-fos* and *jun-B* in the mice 30 min and 24 h after the stationary rota-rod tasks and 1-week handling.

For Experiment 1, adult male mice (8–9 week old, $n = 5$, C57BL/6J, Charles river laboratories Japan Inc.) were purchased. For Experiment 2, mice lacking either D1R ($n = 7$) or D2R ($n = 9$) were generated in accordance with the protocol previously published (Yamaguchi et al., 1996; Tran et al., 2008) and backcrossed for up to 10 generations with C57BL/6J (CLEA Japan Inc.) mice. Their genotypes were determined by PCR analysis of genomic DNA extracted from the tail of each mouse. As a control, C57BL/6J WT mice were purchased. All mice were housed individually in a plastic cage under 12 h light/dark cycle (9:00–21:00) and given food (Rodent Diet CA-1, CE-2, CLEA Japan Inc.) and water *ad libitum*. To encourage food intake to maintain their health (Drago et al., 1994; McNamara et al., 2003), D1R KO mice were additionally given palatable food (Rodent Diet B-F, CLEA Japan Inc.) on the floor of their cages. All the experiments were performed in accordance with the guidelines of the National Institutes of Health and the Ministry of Education, Culture, Sports, Science and Technology (MEXT) of Japan, and were approved by the Institutional Animal Care and Use Committees of the National Institutes of Natural Sciences, Kitasato University School of Medicine, and Frontier Biosciences of Osaka University. We made all efforts to minimize the number of animals used and the incidence or severity of distress experienced by the animals.

Motor Behavior Tasks

In Experiment 1, WT naive mice were initially group housed for 1 week until they were segregated and individually housed during motor task training and testing as described in the Results. In Experiment 2, the same mice that experienced series of two types of motor tasks (rota-rod and Step-Wheel tasks) over a period of 4 months as described previously were used (Nakamura et al., 2014, detailed history is shown in **Figure 3** and Supplementary chart 1). In these series of experiments, the mice were divided into two groups for the rota-rod tasks: fast-slow (15–5 rpm) and slow-fast (5–15 rpm) groups (Nakamura et al., 2014). The mice were sacrificed at 10 months of age. We examined the expression patterns of *c-fos* and *jun-B* in the WT mice that did

not previously experience any motor task at 30 min ($n = 3$) and 24 h ($n = 3$) after the stationary (0 rpm) rota-rod task. The rota-rod apparatus (MK-660A, Muromachi Kikai Co., Ltd.) was used. The rod diameter was 3 cm and the rotation speed was 10 rpm (Experiment 1) or 5 rpm (Experiment 2). In the running rota-rod tasks, a trial was considered when any one of the following three events occurred: The mouse (1) fell, (2) remained on the rod up to 60 s (Experiment 1) or 120 s (Experiment 2), or (3) clung to the rod for two complete turns, in which the mouse was considered to have fallen. The duration (retention times) that the mouse remained on the rod was recorded as the score. Five trials (Experiment 1) or three trials (Experiment 2) per day were performed and the interval between the trials was set at 30–60 s, during which time, the mice were placed in their home cages. Presessions consisted of trials for 1 day (Experiment 1) or 3 days (Experiment 2), during which the mice were placed on a stationary rod for habituation to the apparatus. Following the presessions, the running experiments were started. In Experiment 1, the mice were sacrificed 30 min after the last trial on day 1 ($n = 2$). In Experiment 2, the mice were divided into 3 groups: Pre (WT, $n = 2$; D1R KO, $n = 2$; D2R KO, $n = 3$), day 1 (WT, $n = 3$; D1R KO, $n = 3$; D2R KO, $n = 3$), and day 5 (WT, $n = 3$; D1R KO, $n = 2$; D2R KO, $n = 3$) groups. The mice of the Pre group were sacrificed on day 1, that is, the next day after the presessions (24 h after riding on the stationary rod). For the days 1 and 5 groups, the mice were sacrificed 30 min after the last trial. The rota-rod tasks were performed during the light phase (13:00–19:00). For this series of experiments, we weighed 30 min before the decapitation except for naive mice in which no weighing was done at least for a week before sacrifice.

Handling

To investigate the effects of handling, WT mice ($n = 2$) that did not experience any motor tasks were handled for 1 week. The mice were placed on the palm of an experimenter for about 3 min per day. On the last day, the mice were decapitated 30 min after they were handled. On the other hand, the naive mice ($n = 2$) were fed *ad libitum*, and exposed to external factors as minimally as possible including experimenters and immediately decapitated.

In Situ Hybridization (ISH)

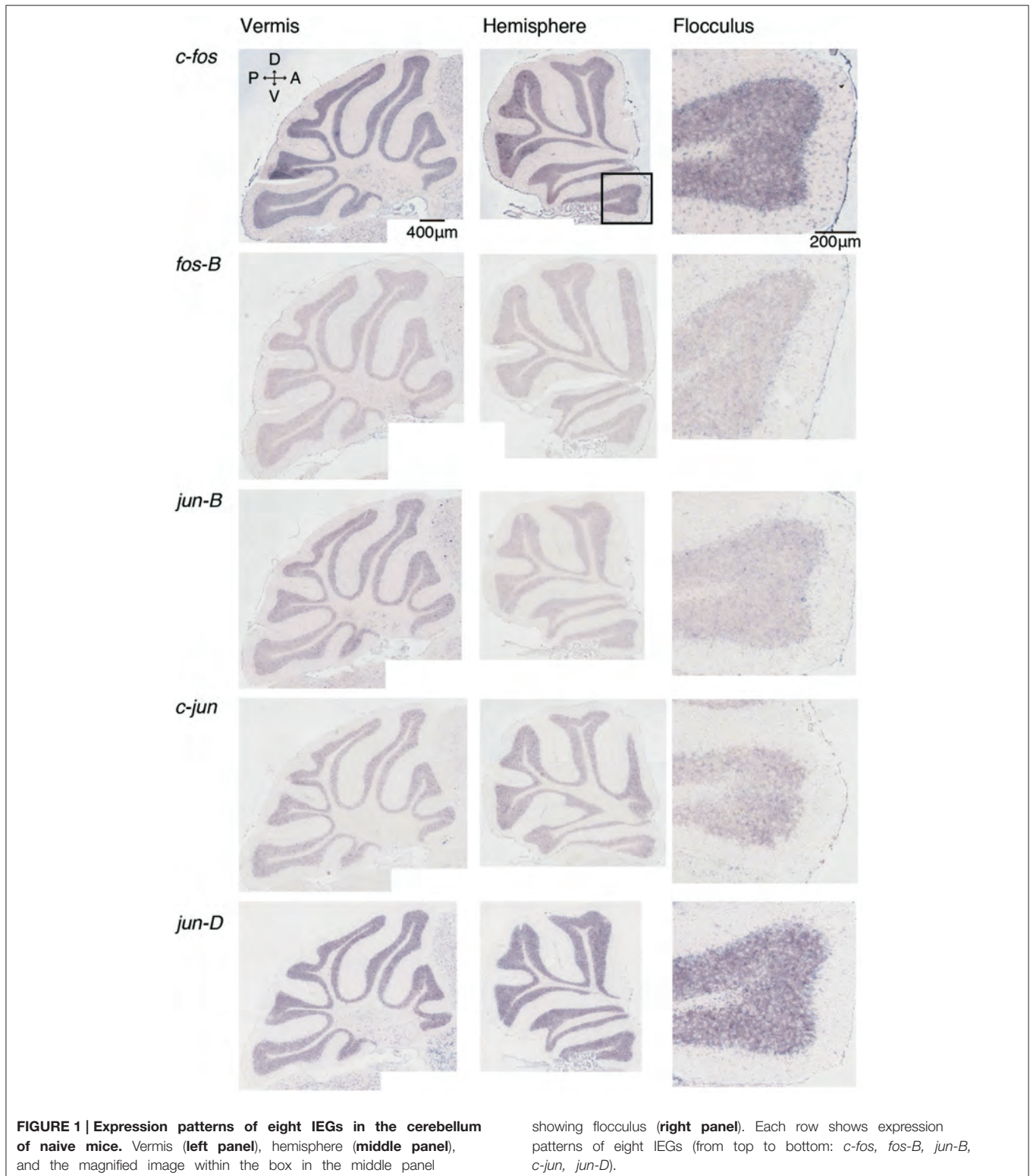
In situ hybridization (ISH) was performed as described previously (Schaeren-Wiemers and Gerfin-Moser, 1993; Liang et al., 2000; Komatsu et al., 2005) with some modifications. The mice were quickly decapitated. The brain was removed, embedded in O.C.T. compound (Sakura) and quickly frozen in isopentane cooled with liquid nitrogen. Sections (10 μ m thick) were cut on a cryostat (CM3050, Leica), thaw-mounted on slides (MAS coated glass slides, Matsunami), and air-dried. The sections were fixed in 4% paraformaldehyde (PFA) in 0.1 M phosphate buffer (PB, pH 7.3) for 15 min, washed three times in PBS, pH 7.4, acetylated for 10 min in 0.25% acetic anhydride in 0.1 M triethanolamine-HCl, pH 8.0, and washed three times with PBS. Prehybridization was performed using hybridization buffer [50% formamide, 5 \times SSC (20 \times SSC in 3 M NaCl, 0.3 M sodium citrate, pH 7.0), 5 \times Denhardt's, 250 μ g/ml yeast tRNA,

and 500 μ g/ml salmon sperm DNA] for 30 min. DIG-labeled cRNA probes were denatured for 2 min at 82°C and chilled on ice. The sections were covered with hybridization buffer containing 1 μ g/ml of the cRNA probes, added dropwise, and coverslipped. The information of each probes used in this study is shown in Supplementary Table 1. The slides were incubated overnight (14–18 h) at 72°C in a humidified chamber (50% formaldehyde, 5 \times SSC), washed three times with 0.2 \times SSC at 72°C, and then rinsed with TBS, pH 7.5 (100 mM Tris-HCl, pH 7.5, 150 mM NaCl). To detect the hybridized probes, the sections were blocked with 1 \times blocking solution (Roche) in TBS, pH 7.5, for 30 min, and then incubated in the blocking solution with an alkaline phosphatase (AP)-conjugated anti-DIG antibody (1:1000 dilution, Roche) overnight at 4°C. The sections were rinsed three times with TBS, pH 7.5, and equilibrated in TBS, pH 9.5 (100 mM Tris-HCl, pH 9.5, 100 mM NaCl, 50 mM MgCl₂). Enzymatic activity was visualized by staining with 0.2 mM 5-bromo-4-chloro-3-indolyl-phosphate, 0.2 mM nitroblue tetrazolium (NBT/BCIP) in TBS, pH 9.5, in the dark, until the signal reached a satisfactory intensity. After a brief wash in PBS and distilled water, the sections were dehydrated in a series of gradually increasing concentrations of ethanol solutions. After immersion in xylene, the sections were mounted in Entellan, a new rapid mounting medium (Merck).

Results

IEG Expression Patterns in the Cerebellum

We examined the IEG expression patterns in the cerebellum. In our previous study, we examined the expression patterns of IEGs including the *fos* and *jun* families in cerebellar slices without and with treatment with α -amino-3-hydroxy-5-methyl-4-isoxazole-propionate (AMPA) and/or 8-bromo-cGMP (8-Br-cGMP) (Nakazawa et al., 1993). That study showed that untreated slices express low levels of IEGs but slices treated with AMPA and 8-Br-cGMP express high levels of *c-fos*, *jun-B* and *zif-268* (*NGFI-A*). Following that study, we first examined IEG expression patterns in the cerebellum. Naive mice that were moving freely but doing no specific tasks were sacrificed, and the IEG expression patterns of the *fos* family (*c-fos*, *fos-B*), *jun* family (*jun-B*, *c-jun*, and *jun-D*), and other IEGs of *zif-268* (*egr 1*, *NGFI-A*), *krox 20* (*egr 2*, *NGFI-B*), and *arc* were examined immediately after the sacrifice (see Materials and Methods). Consistent with the previous results, we observed little expression of these eight IEGs in the cerebellum of naive mice (**Figures 1, 2**). We next examined the expression patterns of these IEGs immediately after the mice performed five trials of running rota-rod tasks (**Figure 3A**). The mice were sacrificed 30 min after the last trial and the IEG expression patterns in the cerebellum were examined (**Figures 4, 5**). Among the members of the *fos* and *jun* families, *c-fos* was expressed in almost all the lobules of the vermis (except lobule 7), and *Crus1*, *Cop* and most significantly in the flocculus in the hemisphere. It is strongly expressed in the granular and Purkinje layers, and some intense signals were observed in the molecular layer. *jun-B* was also expressed in the same regions as *c-fos* was expressed but more preferentially in Purkinje cells and some sparsely scattered intense signals



of *jun-B* were observed in the molecular layer. We observed some weak expression of *fos-B* in the flocculus as well. In the cerebellar slices, although we previously observed significant *zif-268* expression (Nakazawa et al., 1993), here we observed only

a generally moderate expression of *zif-268* under the present condition. *krox 20* was also expressed to some extent in the flocculus. Note that the adjacent external layer of the inferior colliculus expressed *arc* and *zif-268* at certain levels, which may

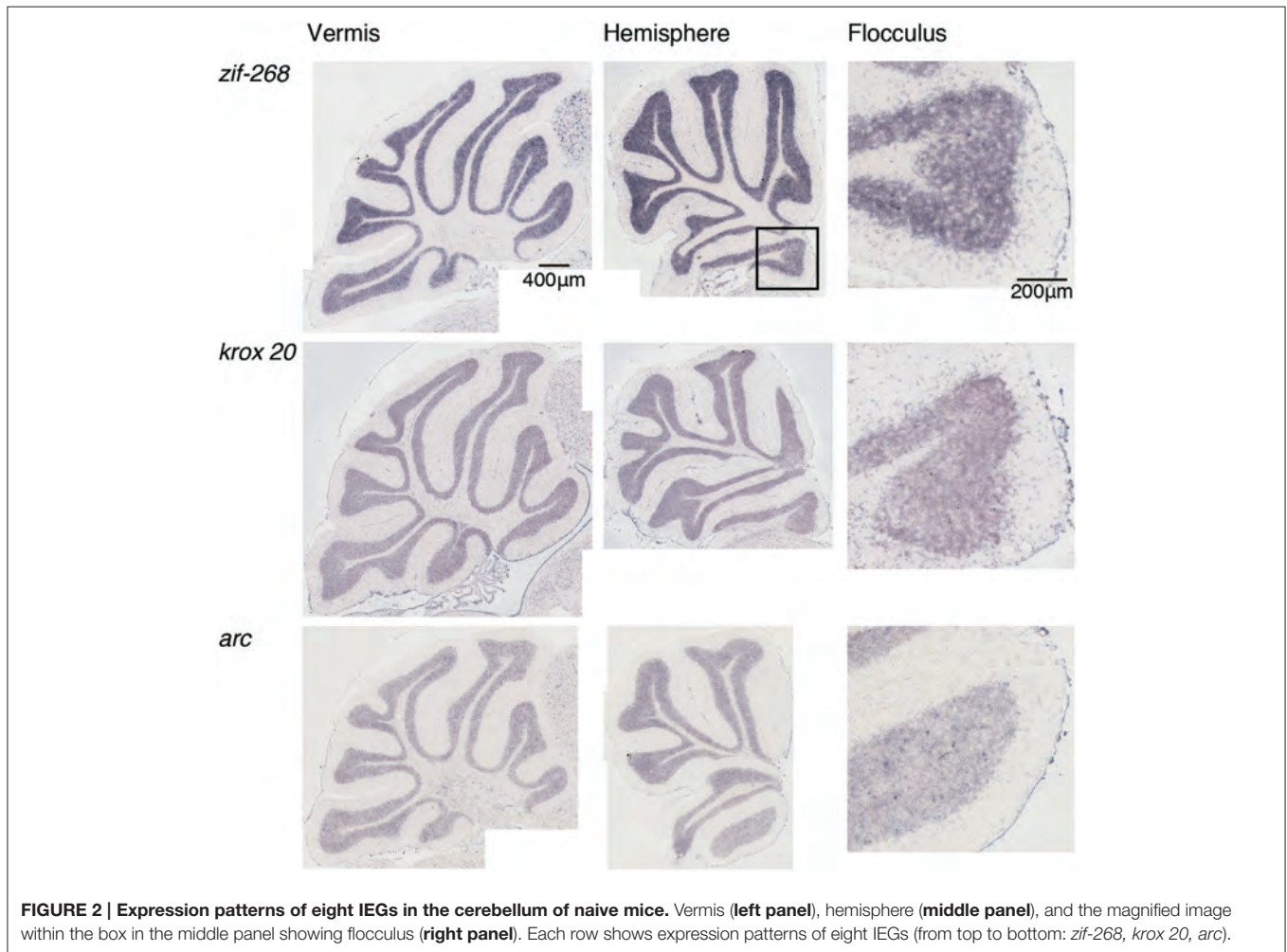


FIGURE 2 | Expression patterns of eight IEGs in the cerebellum of naive mice. Vermis (left panel), hemisphere (middle panel), and the magnified image within the box in the middle panel showing flocculus (right panel). Each row shows expression patterns of eight IEGs (from top to bottom: *zif-268*, *krox 20*, *arc*).

be used as internal controls for evaluating the IEG expression levels in the cerebellum. Overall, *c-fos* and *jun-B* among the IEGs examined in the flocculus showed most prominent expressions immediately (30 min) after the rota-rod running tasks. Therefore, hereinafter, we focused on the expression patterns of *c-fos* and *jun-B* in the flocculus.

***c-fos* and *jun-B* expression Patterns in Stationary Rota-Rod Task in Naive Mice**

As we mentioned in Introduction, we were interested in the functional relationship between the cerebellum and the striatum and explored a model experimental system. Dopamine receptors are distributed in certain brain regions (Gingrich and Caron, 1993). However, our previous studies demonstrated that D1R KO and D2R KO mice showed distinguished motor impairments (Nakamura et al., 2014). In the running rota-rod tasks, the impairments were largely similar to those resulting from local ablation of D1R neurons and D2R neurons in DLS and DMS (Durieux et al., 2012), respectively. These results suggest that when using D1R KO and D2R KO mice in the rota-rod tasks, the main target is the striatum. We therefore used D1R KO and D2R KO mice to examine the cerebellar flocculus

IEG (*c-fos* and *jun-B*) expression patterns and the relationship between the striatum and the cerebellum in relation to motor learning.

We first examined the expression patterns of *c-fos* and *jun-B* in the stationary rota-rod task. In this task, a mouse was placed on a non-rotating bar with a thickness about half the length of the mouse's body. This task was not too difficult for mice to perform, and not only WT mice but also D1R KO and D2R KO mice were able to stay for the time examined (Supplementary Figure 2). Nonetheless, this task requires mice to balance on the bar and therefore activates related brain regions. In parallel, we first examined the *c-fos* and *jun-B* expression patterns in the cerebellum of WT mice after they were handled for 1 week (Figure 6). Herein, from Figures 6–10 for all the ISH data, we examined 6–13 sections of the cerebellums of individual mice under each motor condition as described for each figure. We examined two to five sections of the vermis and four to nine sections of the hemisphere in each mouse, and here used the sections that showed the highest signal intensity of the IEG expression in the flocculus among the sections of the cerebellum under each condition. We were surprised to find high expression levels of *c-fos* and *jun-B* in the cerebellum immediately

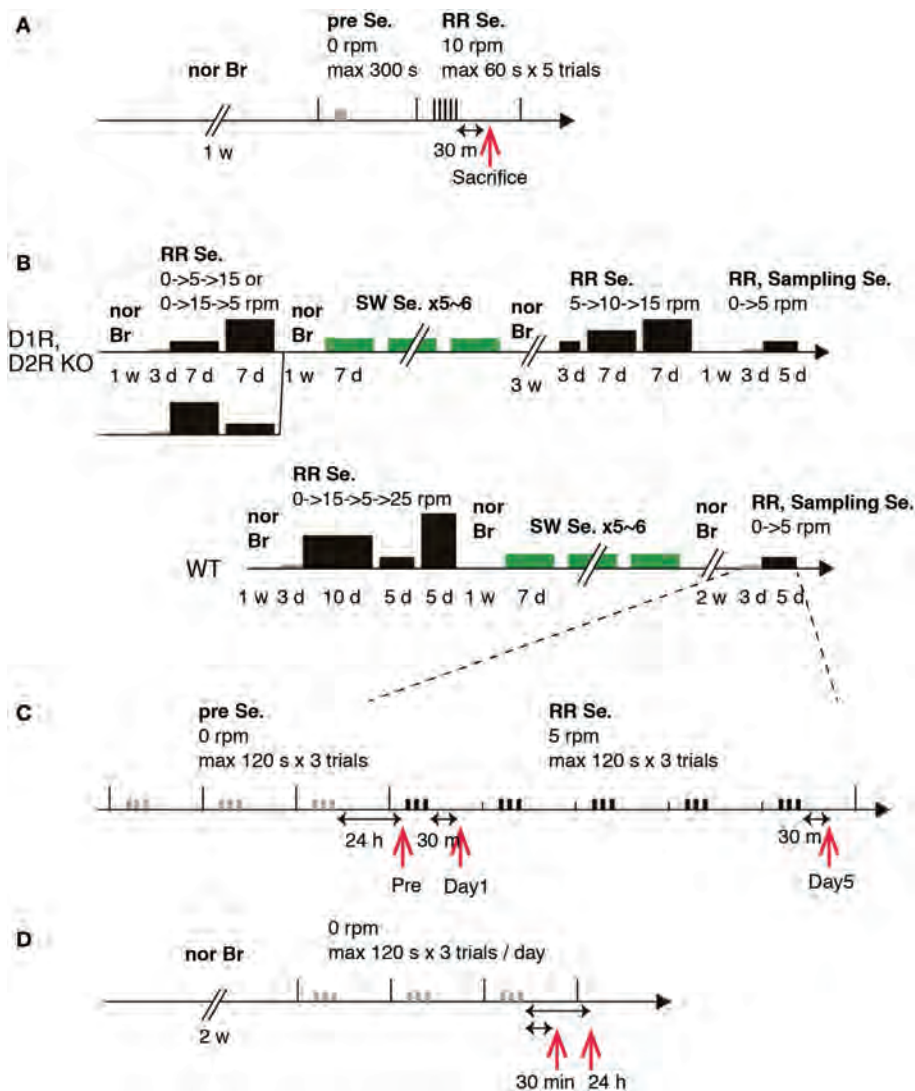


FIGURE 3 | Experimental schedules. Schematic experimental procedures for Experiments 1 and 2. **(A)** Experiment 1. **(B)** Experiment 2, WT, D1R KO, and D2R KO mice, training schedule. **(C)** Experiment 2, sampling schedule. **(D)** Experiment 2, 30 min and 24 h after stationary rota-rod task.

Abbreviations: nor Br, normal breeding; Se., session group; RR, rota-rod; SW, Step-Wheel; w, week; d, day; h, hour; m, minute; s, second. The width and height of the black bar represent task time and speed of rota-rod, respectively.

(30 min) after handling (**Figure 6**). In the hemisphere, we found moderately high expression levels in *Crus1*, and *Cop* and high expression levels in the flocculus. The expressions of *c-fos* and *jun-B* were probably induced by the attempts of mice to maintain their balance on the palm of the hand during the handling. The expression patterns of *c-fos* and *jun-B* appeared to be overall similar between the conditions (handling, stationary and running rota-rod), although there may have been some differences. We also found the expression of these genes not only immediately (30 min) after but also 24 h after the stationary rota-rod task for WT naive mice (**Figures 3D, 7A,B**) and for the same duration in the D1R KO, D2R KO, WT trained mice (**Figures 3B,C, 8**, three sessions as the trained mice). The expressions of *c-fos* and *jun-B* in the flocculus even 24 h after the stationary rota-rod task was unexpected because IEG expressions would not last for such a

long time. We weighed the mice 30 min prior to increase their sacrifice 24 h after the stationary rota-rod task. The weighing involved placing the mice on the scales of a balance, which may have activated the vestibular systems. It was indeed the case because we observed significant expression of *c-fos* and *jun-B* 30 min after only single weighing (Supplementary Figure 3A). We also examined the expression patterns of these two IEGs 24 h after the stationary rota-rod task in the mice that experienced several sessions of the wheel running and rota-rod tasks (rotating rota-rod and Step-Wheel tasks, see Materials and Methods for details, **Figure 8**). In the naive mice, which only experienced the stationary rota-rod task, the expression levels of *c-fos* and *jun-B* were reduced to some extent but were still significant. In the mice that experienced several sessions of motor tasks, the expressions, in particular that of *jun-B*, appeared to be more sustained

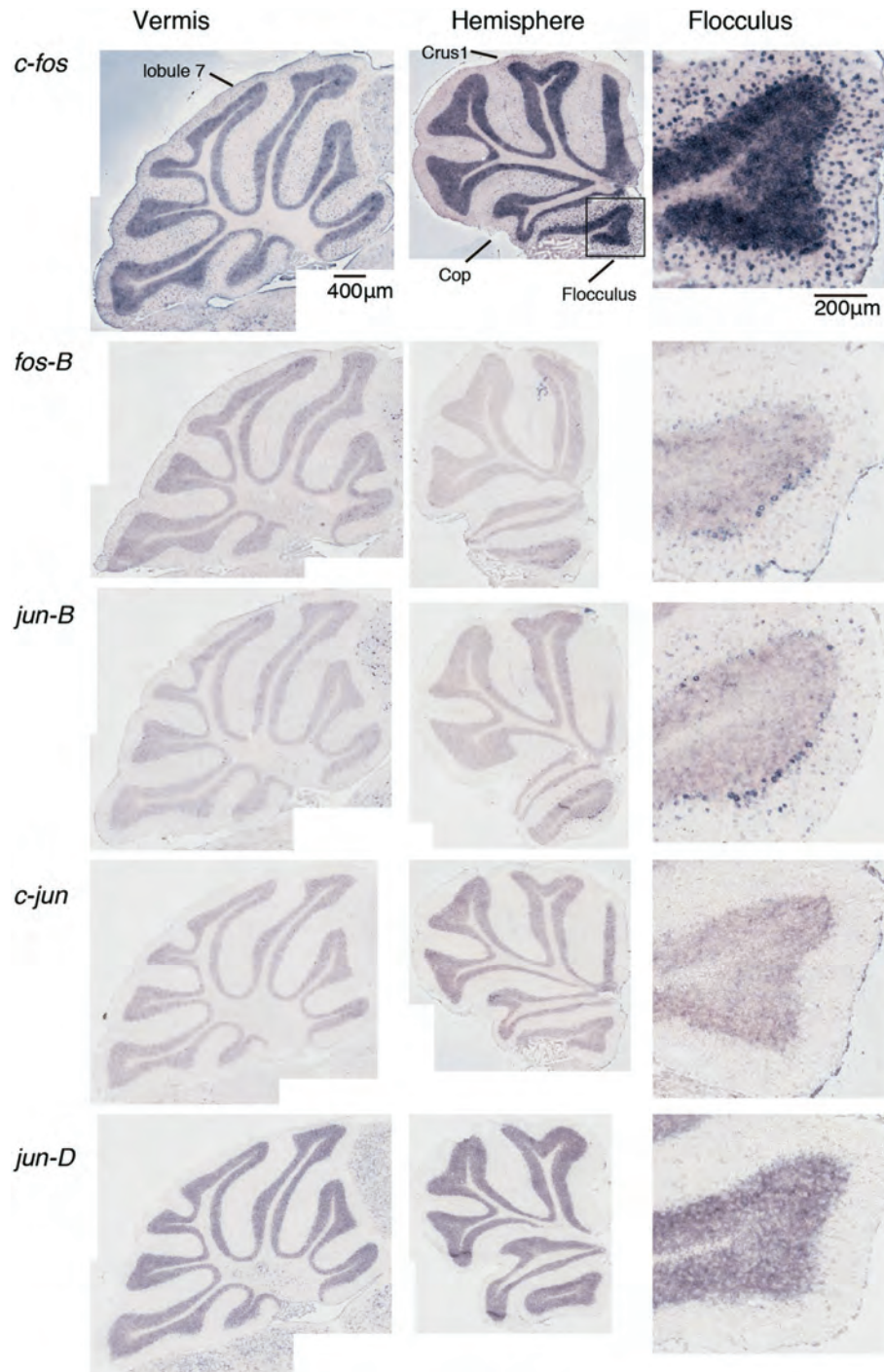
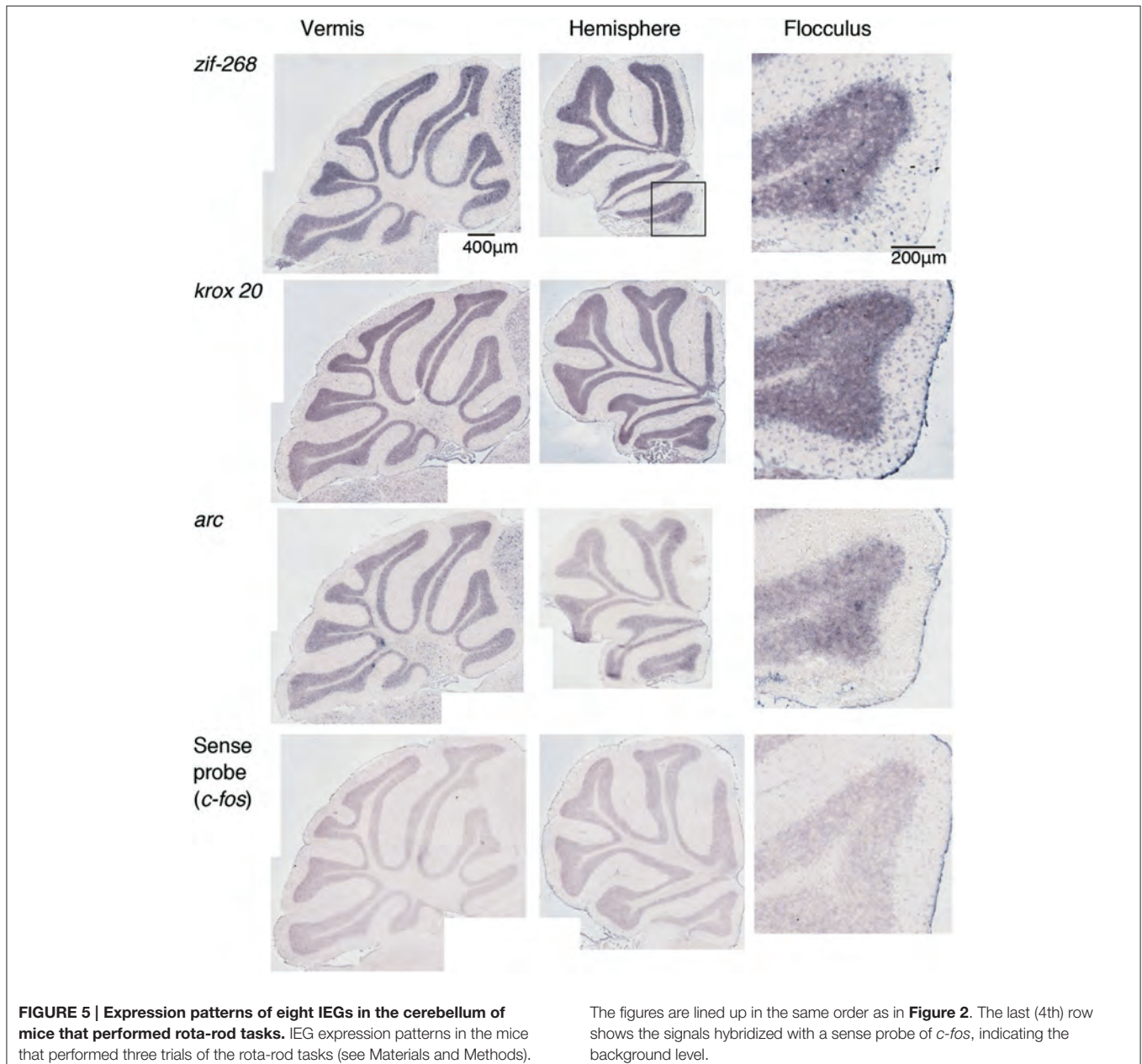


FIGURE 4 | Expression patterns of eight IEGs in the cerebellum of mice that performed rota-rod tasks. IEG expression patterns in the mice that performed three trials of the rota-rod tasks (see Materials and Methods). The figures are lined up in the same order as in **Figure 1**.

than those in the naive mice (**Figures 7, 8**). We also noticed that the expression pattern of *c-fos* and *jun-B* may be different between those of 30 min after only weighing in naive mice and 24 h after stationary rota-rod in trained mice (Supplementary **Figures 4, 5**).

***c-fos* and *jun-B* Expression Patterns in Stationary and Rotating Rota-Rod-Tasks In Trained Mice**

Doyon et al. (2009) proposed that the basal ganglia are functionally related to motor learning. They propose that motor sequence learning and adaptation progress with time through



the “consolidation” and “automatization” processes. During the course of these processes, the basal ganglia, cerebellum, hippocampus and cerebral cortex interact with each other, and, with time, the sites of plasticity are shifted to the cerebral cortex and striatum for motor sequence learning and the cerebral cortex and cerebellum for motor adaptation. We thus examined the cerebellar IEG expression patterns 24 h after the stationary rota-rod task in the mice that experienced several motor tasks (rotating rota-rod and Step-Wheel tasks, see Materials and Methods for details) in order to determine whether there are any differences in cerebellar activity among the three different genotypes of mice immediately (30 min) after they performed running rota-rod tasks on days 1 and 5 (**Figures 9, 10**).

Figures 9, 10 show the expression patterns of *c-fos* 24 h after the stationary rota-rod task in the three genotypes of mice after the rota-rod tasks on days 1 and 5, respectively. We observed significant expressions of *c-fos* in the hemisphere even 24 h after the stationary rota-rod task. Among the regions in the hemisphere, the expression in the flocculus was most significant. The *c-fos* expression is generally similar between days of 1 and 5. **Figures 9, 10** show cerebellar *jun-B* expression patterns in WT mice. *jun-B* was expressed in the cerebellar vermis, and Crus1 and Cop of cerebellar hemisphere. Although *jun-B* was expressed to some extent in the molecular layer and at a lower level in the granular layers, the expression was most prominent in Purkinje cells. *jun-B* expression in the Purkinje cells in the

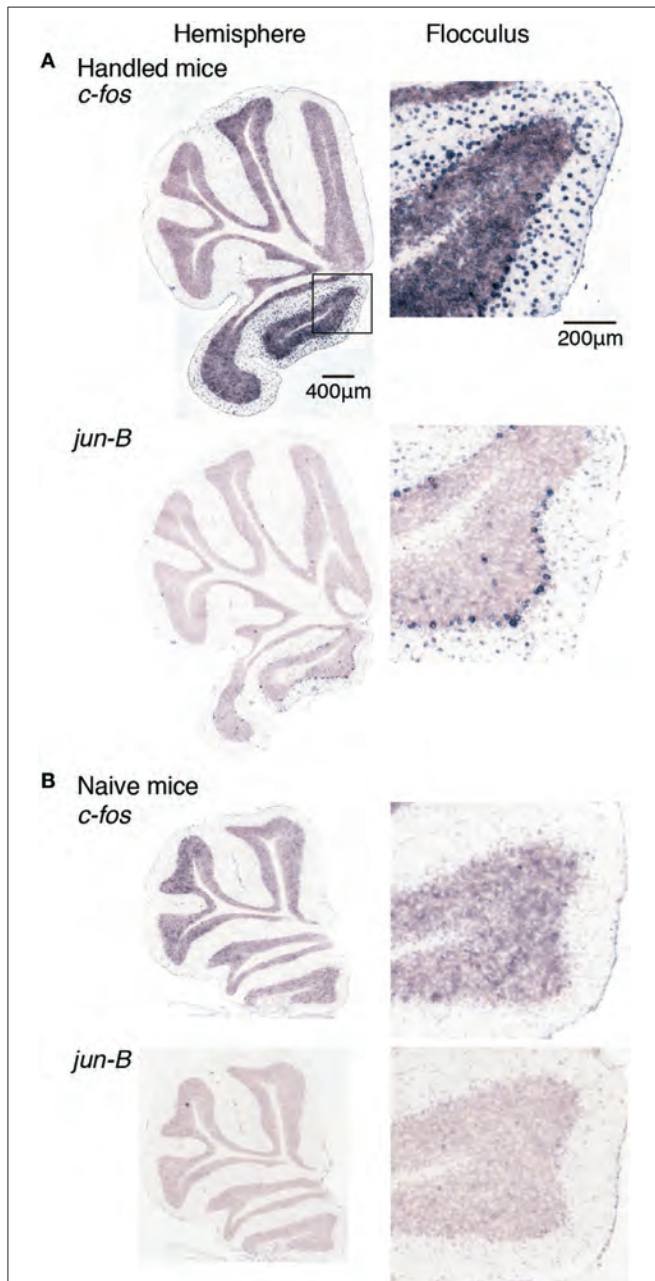


FIGURE 6 | Expression levels of *c-fos* and *jun-B* mRNAs in the cerebellum of mice handled for a week. (A) Mice handled for a week (see Materials and Methods). **(B)** Naive mice that were allowed to move freely but were not handled by humans. Sections of the hemisphere that showed the highest signal intensity for each gene are shown (left panel), Right panels show magnified images of floccular signals enclosed in a box in the top image of the left panel.

flocculus seemed to be similarly enhanced in the trained mice 24 h after the stationary rota-rod task in contrast to the naive mice, and immediately after the running rota-rod tasks on days 1 and 5.

D1R KO, D2R KO, and WT mice expressed *c-fos* in the cerebellar hemisphere, particularly in flocculus 24 h after the

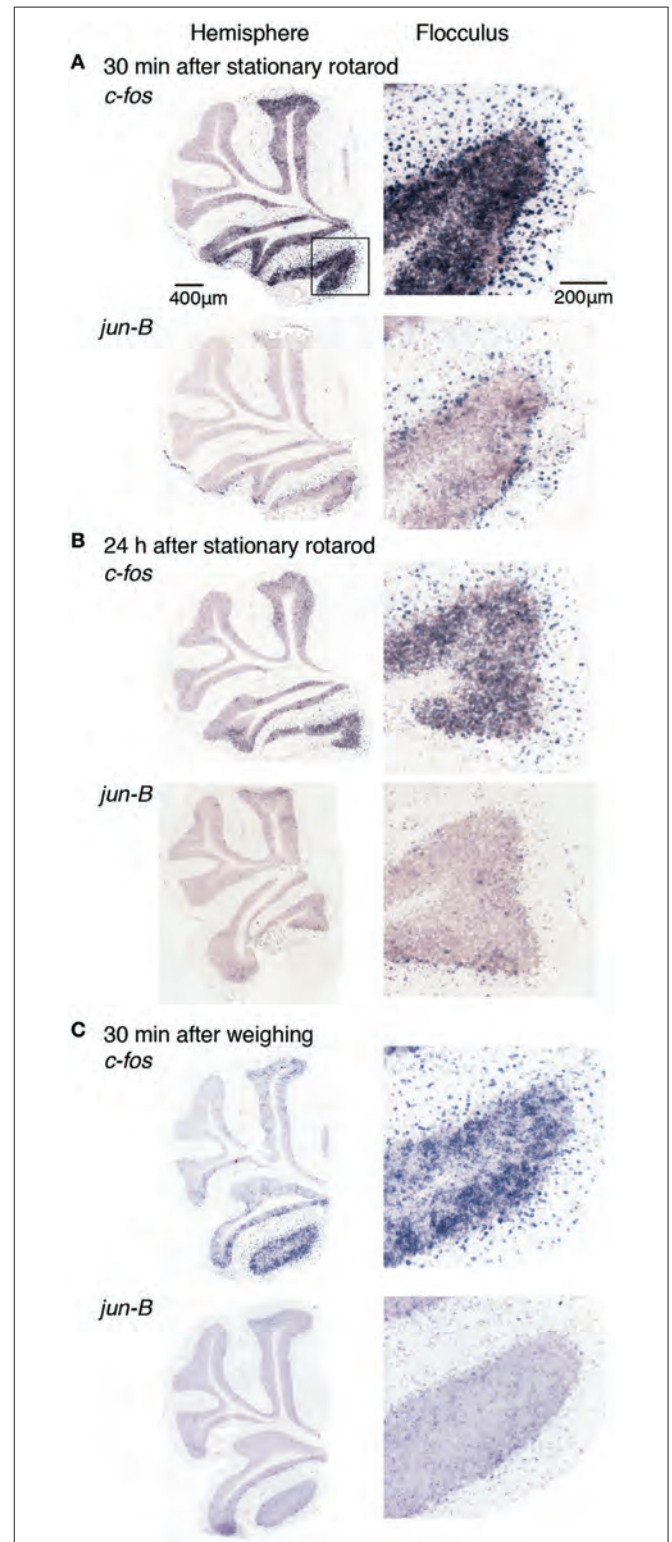
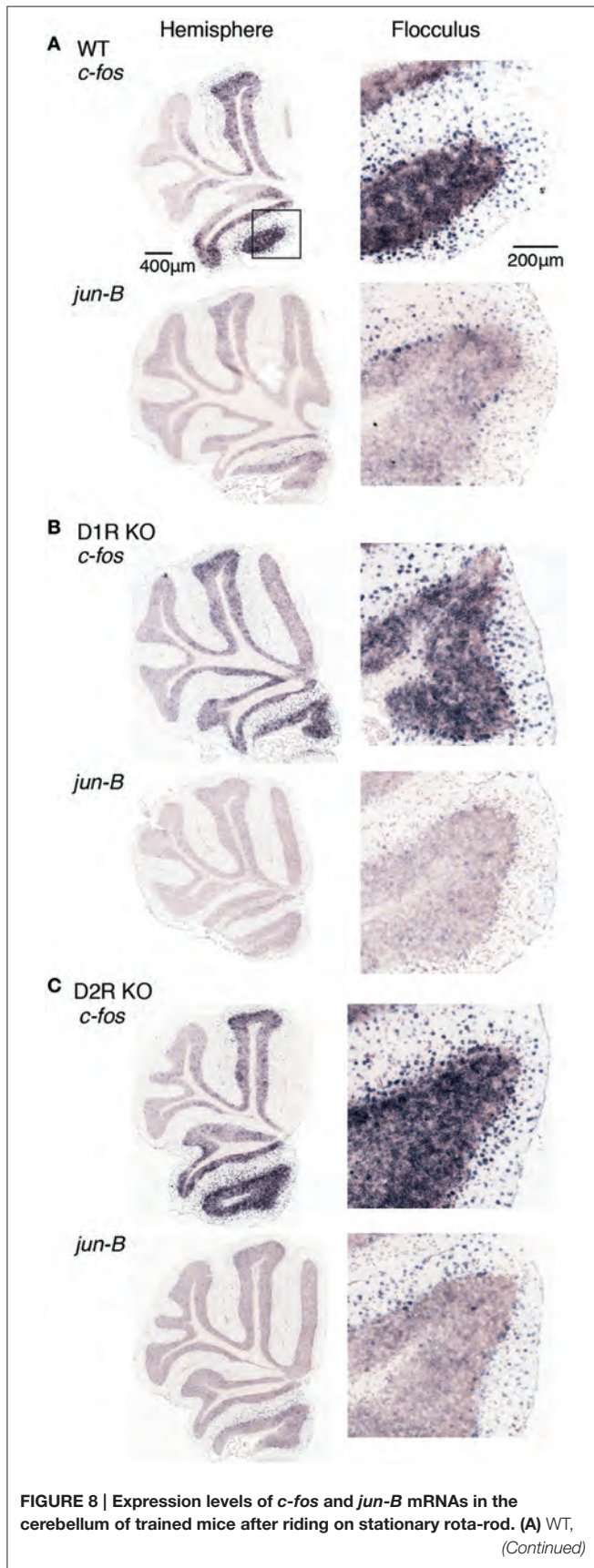


FIGURE 7 | Expression levels of *c-fos* and *jun-B* mRNAs in the cerebellum of mice after stationary rota-rod task or single weighing. Mice that did not experience any motor tasks (untrained) were sacrificed **(A)** 30 min, **(B)** 24 h after the stationary rod task (see Materials and Methods), or **(C)** 30 min after single weighing. Right panels show magnified images of floccular signals.

**FIGURE 8 | Continued**

(B) D1R KO, and (C) D2R KO mice were trained to perform a series of rota-rod and Step-Wheel tasks (see Materials and Methods). These mice were sacrificed 24 h after the stationary rota-rod task and designated as the Pre group for the running rota-rod tasks (see Materials and Methods). The left panels show the sections from the hemisphere that showed the highest signal intensity among the sections examined in each row. The right panels show the magnified images of the flocculus enclosed in a box in the first row of the left panel.

stationary rota-rod tasks and on days of 1 and 5 after the rotating rota-rod tasks. The expression levels of *c-fos* and *jun-B* 24 h after the stationary rota-rod task in D1R KO mice appeared lower than those in D2R KO and WT mice, but since we failed in the staining of ISH in one of D1R KO mice and we were unable to make a conclusion on the significance of this finding. The expression of *c-fos* in the granular layer of the flocculus of D2R KO mice might be more enhanced on day 1 after the running rota-rod tasks than under the other conditions (Figures 8–10). *jun-B* expression in D2R KO mice was also enhanced 24 h after stationary rota-rod and on days 1 and 5, and may be more enhanced on day 1. These observations, however, were not statistically confirmed any further owing to the lack of a sufficient number of mice of these three genotypes available for series of motor tasks.

Discussion

We examined cerebellar expression patterns of eight different IEGs in D1R KO, D2R KO, and WT mice following stationary and rotating rota-rod tasks. *c-fos* expression was enhanced in all the lobules of the vermis except lobule 7 and in Crus1, Cop and the flocculus in the hemisphere, whereas *jun-B* expression was only enhanced in some of the Purkinje cells in these regions. Furthermore, in this study we surprisingly found that *c-fos* and *jun-B* in the cerebellar vermis and flocculus were significantly expressed in mice after handling and 24 h after the stationary rota-rod task. We also found robust expressions of *c-fos* and *jun-B* after the running rota-rod tasks on days 1 and 5 in D1R KO, D2R KO, and WT mice.

IEG Expression Patterns in the Cerebellum

We examined the IEG expression patterns in the cerebellum. Among the eight IEGs we examined, *c-fos* was significantly expressed in all lobules of the cerebellar vermis except lobule 7 and in Crus1, Cop and the flocculus of the cerebellar hemisphere. *jun-B* was preferentially expressed in the Purkinje cells in these regions. *arc* is known to be induced by various types of neural activities including visual stimulation (e.g., Nakagami et al., 2013); there is virtually no induction in the cerebellum (Figure 5). *zif-268* is also known to be induced upon various neural activation, but was little induced in the cerebellum (Figure 5). One plausible reason why *arc* and *zif-268* are not induced in the cerebellum is that cerebellar Purkinje cells do not express functional NMDA receptors (Perkel et al., 1990; Llano et al., 1991). For example, *arc* transcription is regulated

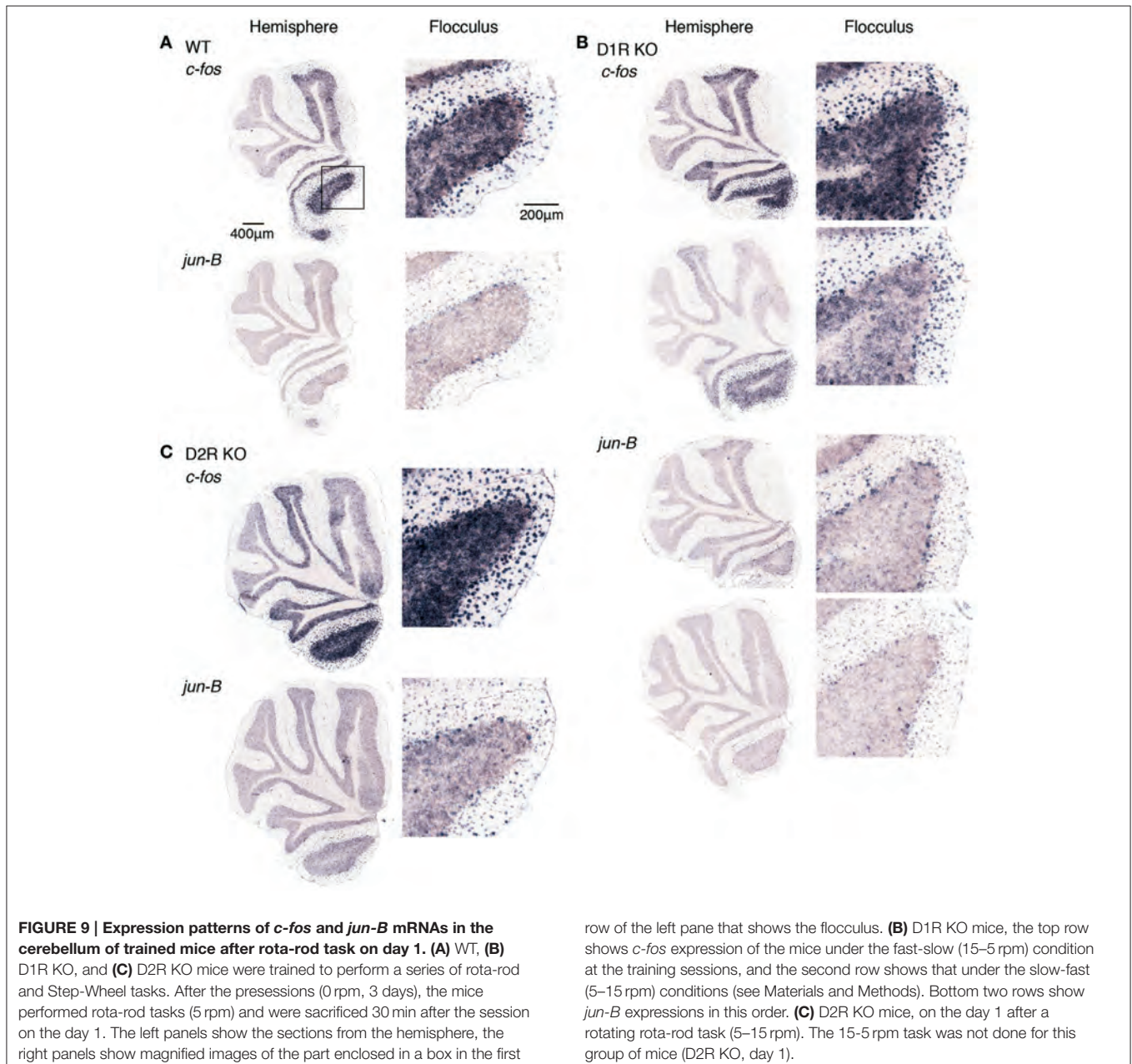


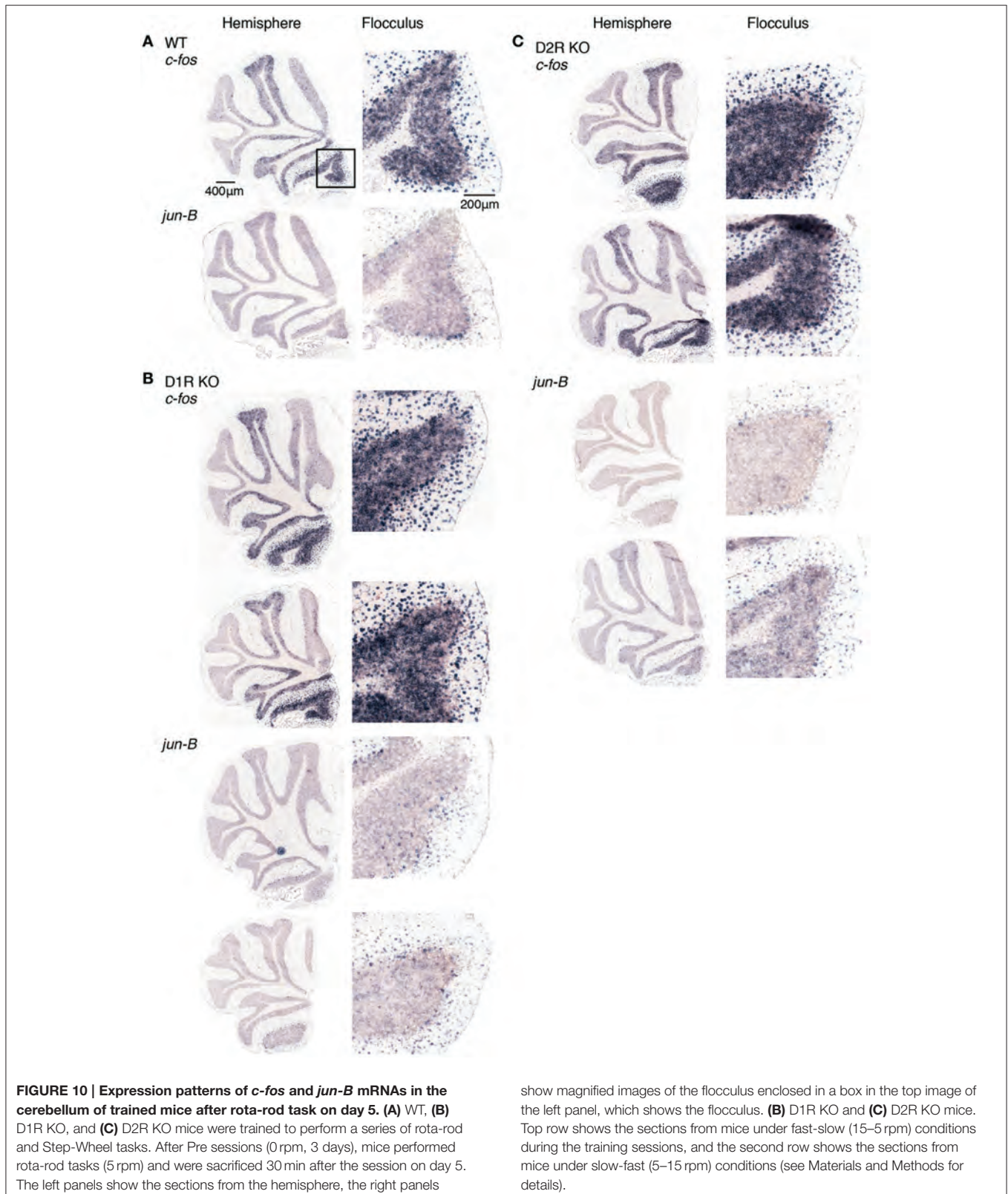
FIGURE 9 | Expression patterns of *c-fos* and *jun-B* mRNAs in the cerebellum of trained mice after rota-rod task on day 1. (A) WT, (B) D1R KO, and (C) D2R KO mice were trained to perform a series of rota-rod and Step-Wheel tasks. After the precessions (0 rpm, 3 days), the mice performed rota-rod tasks (5 rpm) and were sacrificed 30 min after the session on the day 1. The left panels show the sections from the hemisphere, the right panels show magnified images of the part enclosed in a box in the first

row of the left pane that shows the flocculus. (B) D1R KO mice, the top row shows *c-fos* expression of the mice under the fast-slow (15–5 rpm) condition at the training sessions, and the second row shows that under the slow-fast (5–15 rpm) conditions (see Materials and Methods). Bottom two rows show *jun-B* expressions in this order. (C) D2R KO mice, on the day 1 after a rotating rota-rod task (5–15 rpm). The 15–5 rpm task was not done for this group of mice (D2R KO, day 1).

by NMDA- or voltage-gated calcium channel (VGCC)- mediated membrane depolarization, cAMP-dependent pathways and brain-derived neurotrophic factor (BDNF)-mediated pathways (Zheng et al., 2009). However, the exact mechanisms underlying non-expression of arc in the cerebellum need to be elucidated in future studies.

c-fos mapping showed the regions activated immediately after the running rota-rod tasks. In the vermis, *c-fos* was moderately induced in all the lobules except lobule 7 throughout the cerebellar vermis. In the hemisphere, significant expressions of *c-fos* were observed in Crus1, Cop, and flocculus. This observation indicates that the cerebellar vermis plays a central role in visually guided movements (Edge et al., 2003) and receives limb

and visual inputs (see Edge et al., 2003 for reference). Crus1 also receives visuomotor inputs (Edge et al., 2003; Cerminara et al., 2005). Hindlimb stimulation primary activates the medial aspect of Cop (Santori et al., 1986). Our *c-fos* mapping results in this report well match those of the previous studies that examined the cerebellar areas activated by visuomotor inputs. One new observation in *c-fos* mapping may be the neuronal activation in the flocculus in the cerebellar hemisphere after the stationary and running rota-rod tasks. This is probably because the rota-rod tasks required mice to maintain their balance, which likely activated eye movements and the vestibular systems. The vestibular-ocular reflex presumably activates the flocculus (Ito, 1982).



***c-fos* and *jun-B* Expression Patterns after Stationary Rota-Rod Task**

We first examined the *c-fos* and *jun-B* expression patterns in the cerebellum immediately and 24 h after the mice performed the stationary rota-rod task in which mice were required to stay on the non-rotating (stationary) rota-rod. This is not a very difficult task for mice to perform, and both D1R KO and D2R KO mice were able to stay as long as WT mice did (Supplementary Figure 2). However, to our surprise, even 24 h after performing the stationary rota-rod task, we observed significant *c-fos* and *jun-B* expressions in the cerebellum. It was puzzling why the cerebellum was activated 24 h after the task, during which time the mice did not perform any specific tasks. One possible explanation for this would be as follows: there were other brain regions that were activated, which in turn activated the cerebellum. Interaction among the cerebellum, basal ganglia and cerebral cortex has been proposed (Doya, 2000; Hikosaka et al., 2002; Doyon et al., 2009; Bostan et al., 2013). It is therefore possible that the cerebellum was activated by other brain areas such as the basal ganglia. We therefore examined the *c-fos* and *jun-B* expression patterns in D1R KO and D2R KO mice after the running rota-rod tasks. We weighed the mice 30 min before sacrifice after 24 h after stationary rota-rod tasks. The weighing involved placing the mice on the scales of a balance, which may have activated the vestibular systems. It was indeed the case as shown in Supplementary Figure 3. However, the enhancement of *c-fos* and *jun-B* 24 h after the stationary rota-rod task in the mice that experienced several sessions of the motor tasks seems to be higher than that of 24 h after the stationary rota-rod for naive mice (Figures 7, 8). We also noticed the different IEG expression pattern between after only single weighing in naive mice and 24 h after stationary rota-rod in trained mice although both groups of mice were sacrificed 30 min after the last weighing (Supplementary Figures 4, 5). This difference may reflect the shift of cerebellar activation by forming internal model within the cerebellum (Bursztyn et al., 2006).

The expression of *c-fos* did not appear to be altered between days 1 and 5 after the running rota-rod tasks in D1R KO, D2R KO, and WT mice. However, there may be some difference in

jun-B expression under our conditions. Durieux et al. (2012) and Nakamura et al. (2014) demonstrated that D1R KO mice and mice with complete ablation of D1R neurons in the striatum showed decreased learning curve and performance after learning of the rota-rod tasks, whereas mice with ablated D2R neurons in the DMS and the entire striatum showed decreased initial performance of the rota-rod tasks. It has been reported that cerebellar activity reflects an acquired internal model (Imamizu et al., 2000). At the time when the impairment of striatal functions is severe, the cerebellar region works to compensate for the impairment and will presumably be most activated.

The expression of IEG and the downstream regulated genes in the striatum of D1R KO, D2R KO mice has been reported upon pharmacological stimulation (Drago et al., 1996; Aoyama et al., 2000; Welter et al., 2007). In D1R KO mice cocaine did not induce *c-fos* and *zif-268* expressions in the striatum (Drago et al., 1996). In D2R KO mice cocaine did not induce *c-fos* but induce *zif-268* in the striatum (Welter et al., 2007). In the striatum D1R is coexpressed with substance P (SP) and D2R is coexpressed with enkephalin (ENK). In D1R KO mice SP expression was reduced and ENK expression was unaltered. Cocaine induced SP but not ENK in the striatum of D1R KO mice. In D2 KO mice ENK expression was increased and SP expression was decreased (Aoyama et al., 2000). In D1R KO mice cocaine induced SP and but did not affect ENK expression (Drago et al., 1996). In D2 KO mice cocaine induced SP expression. Therefore, these previous studies indicated that by in large the direct (D1R) and indirect pathways (D2R) are affected as expected as we write in the Introduction in D1R KO and D2R KO mice in terms of the IEG expression. Compared to these previously reported results in the striatum where the D1R and D2R play direct roles in the regulation of IEGs, in the cerebellum there is little or only indirect effect in the IEG expression, if any, in D1R and D2R KO mice as we showed in this paper.

We have been using chemical methods for detecting ISH because of their high spatial resolution. However, for quantitative evaluation, chemical detection methods are not as quantitative

TABLE 1 | *c-fos* and *jun-B* expressions in cerebellar flocculus.

	WT		D1R KO		D2R KO	
	<i>c-fos</i>	<i>jun-B</i>	<i>c-fos</i>	<i>jun-B</i>	<i>c-fos</i>	<i>jun-B</i>
Naïve	–	–	NT	NT	NT	NT
Handling (for 1 week)	++	++	NT	NT	NT	NT
Stationary RR 30 min	+++	++	NT	NT	NT	NT
Stationary RR 24 h after (for naive mice)	++	+	NT	NT	NT	NT
Stationary RR 24 h (for trained mice)	+++	++	++*	+	+++	++
Running RR Day 1	+++	++	+++	++~+++**	+++	+++
Running RR Day 5	+++	++	+++	++	+++	++
Weighing	+~+++***	+++	NT	NT	NT	NT

Summary of the expression levels of *c-fos* and *jun-B* in the cerebellar flocculus are represented; –, background level; +, weak positive; ++, positive; +++, highly positive signal. *Only one mouse and somewhat weaker staining than other samples. **Some variations between two mice. ***Uneven expression within flocculus. NT: not tested. Note that all animals were sacrificed 30 min after final task except for the naive mice that were sacrificed without weighing. The evaluation was done subjectively with agreement of by two of authors (Toru Nakamura and Tetsuo Yamamori).

as radioisotope detection methods, in which the amount of radiation is strictly proportional to that of radioactive decay. Various conditions could affect chemical reactions; therefore, exact quantitation is difficult without an internal control. In this regard, our visual evaluation of *c-fos* expression in the flocculus on days 1 and 5 after the running rota-rod tasks in D1R KO and D2R KO mice should be more reliable because it enabled us to compare the expression with that in other lobules of the same section of the cerebellar hemisphere as an internal control.

It should be noted that *jun-B* was preferentially expressed in Purkinje cells after the rota-rod tasks. This expression pattern is quite in contrast to that of *c-fos*, which was particularly highly expressed in the granular layer and other layers as well. We previously reported that *jun-B* is selectively induced by conjunctive stimulation of climbing fibers and AMPA in the cerebellum, which mimics cerebellar LTD (Yamamori et al., 1995). *jun-B* expression level in the mice 24 h after the stationary rota-rod task may be higher in the mice that experienced several motor tasks than in the naive mice. However, these apparent differences should be examined by statistical analysis with a larger number of mice in future studies.

Implications of Studies of *c-fos* and *jun-B* Expression Patterns in the Cerebellum in D1R KO and D2R KO Mice

In this study, we applied techniques of IEG mapping in the cerebellum to detect the altered cerebellar neuronal activity after the stationary and running rota-rod tasks. We summarized the expression patterns of *c-fos* and *jun-B* in the flocculus in the cerebellum in **Table 1**. We consider that there are three main points in our studies reported in this paper. First, we found several different levels of expressions of *c-fos* and *jun-B* in the cerebellum in various conditions of weighing and handling,

30 min and 24 h after the stationary rota-rod task, and 30 min after running rota-rod on days 1 and 5. There may be some enhancement of *c-fos* and *jun-B* 24 h after the stationary rota-rod in the trained mice even considering the weighing effect for the expressions of *c-fos* and *jun-B*. Second, to further examine the interaction between the cerebellum and the striatum, we examined the *c-fos* and *jun-B* expressions in the cerebellum in D1R KO, D2R KO, and WT mice after the stationary and running rota-rod tasks. We did not observe significant differences among the three genotypes although this does not still exclude the possibility that there are some differences among them. To clarify whether there are indeed differences among the three genotypes, a larger number of mice need to be examined and statistical analysis should be conducted. Third, our results demonstrated the particular usefulness of *c-fos* and *jun-B* for examining expression patterns in the cerebellum, because other IEGs are little expressed in the cerebellum or not selectively expressed in Purkinje cells.

Acknowledgments

We thank Dr. Motoya Katsuki for scientific advice and critical discussion on the generation of D1R KO and D2R KO mice. This research is part of a project supported by a Grant-in-Aid for Scientific Research on Innovative Areas (Neocortical Organization) (#22123009 to T.Y.), a Grant-in-Aid for Scientific Research (B) (#26290029 to T.S.), and a Grant-in-Aid for Scientific Research (C) (#T25430009 to T.K.).

Supplementary Material

The Supplementary Material for this article can be found online at: <http://journal.frontiersin.org/article/10.3389/fcell.2015.00038/abstract>

References

- Aoyama, S., Kase, H., and Borrelli, E. (2000). Rescue of locomotor impairment in dopamine D2 receptor-deficient mice by an adenosine A2A receptor antagonist. *J. Neurosci.* 20, 5848–5852.
- Bostan, A. C., Dum, R. P., and Strick, P. L. (2013). Cerebellar networks with the cerebral cortex and basal ganglia. *Trends Cogn. Sci.* 17, 241–254. doi: 10.1016/j.tics.2013.03.003
- Bursztyn, L. L., Ganesh, G., Imamizu, H., Kawato, M., and Flanagan, J. R. (2006). Neural correlates of internal-model loading. *Curr. Biol.* 6, 2440–2445. doi: 10.1016/j.cub.2006.10.051
- Cerminara, N. L., Edge, A. L., Marple-Horvat, D. E., and Apps, R. (2005). The lateral cerebellum and visuomotor control. *Prog. Brain Res.* 148, 213–226. doi: 10.1016/s0079-6123(04)48018-2
- Doya, K. (2000). Complementary roles of basal ganglia and cerebellum in learning and motor control. *Curr. Opin. Neurobiol.* 10, 732–739. doi: 10.1016/S0959-4388(00)00153-7
- Doyon, J., Bellec, P., Amsel, R., Penhune, V., Monchi, O., Carrier, J., et al. (2009). Contributions of the basal ganglia and functionally related brain structures to motor learning. *Behav. Brain Res.* 199, 61–75. doi: 10.1016/j.bbr.2008.11.012
- Drago, J., Gerfen, C. R., Lachowicz, J. E., Steiner, H., Hollon, T. R., Love, P. E., et al. (1994). Altered striatal function in a mutant mouse lacking D1A dopamine receptors. *Proc. Natl. Acad. Sci. U.S.A.* 91, 12564–12568. doi: 10.1073/pnas.91.26.12564
- Drago, J., Gerfen, C. R., Westphal, H., and Steiner, H. (1996). D1 dopamine receptor-deficient mouse: cocaine-induced regulation of immediate-early gene and substance P expression in the striatum. *Neuroscience* 74, 813–823. doi: 10.1016/0306-4522(96)00145-5
- Durieux, P. F., Schiffmann, S. N., and de Kerchove d'Exaerde, A. (2012). Differential regulation of motor control and response to dopaminergic drugs by D1R and D2R neurons in distinct dorsal striatum subregions. *EMBO J.* 31, 640–653. doi: 10.1038/emboj.2011.400
- Edge, A. L., Marple-Horvat, D. E., and Apps, R. (2003). Lateral cerebellum: functional localization within crus I and correspondence to cortical zones. *Eur. J. Neurosci.* 18, 1468–1485. doi: 10.1046/j.1460-9568.2003.02873.x
- Gingrich, J. A., and Caron, M. G. (1993). Recent advances in the molecular biology of dopamine receptors. *Annu. Rev. Neurosci.* 16, 299–321. doi: 10.1146/annurev.ne.16.030193.001503
- Hikosaka, O., Nakamura, K., Sakai, K., and Nakahara, H. (2002). Central mechanisms of motor skill learning. *Curr. Opin. Neurobiol.* 12, 217–222. doi: 10.1016/S0959-4388(02)00307-0
- Imamizu, H., Miyauchi, S., Tamada, T., Sasaki, Y., Takino, R., Pütz, B., et al. (2000). Human cerebellar activity reflecting an acquired internal model of a new tool. *Nature* 403, 192–195. doi: 10.1038/35003194

- Ito, M. (1982). Cerebellar control of the vestibulo-ocular reflex—around the flocculus hypothesis. *Annu. Rev. Neurosci.* 5, 275–296. doi: 10.1146/annurev.ne.05.030182.001423
- Kitsukawa, T., Nagata, M., Yanagihara, D., Tomioka, R., Utsumi, H., Kubota, Y., et al. (2011). A novel instrumented multipeg running wheel system, Step-Wheel, for monitoring and controlling complex sequential stepping in mice. *J. Neurophysiol.* 106, 479–487. doi: 10.1152/jn.00139.2011
- Komatsu, Y., Watakabe, A., Hashikawa, T., Tochitani, S., and Yamamori, T. (2005). Retinol-binding protein gene is highly expressed in higher-order association areas of the primate neocortex. *Cereb. Cortex* 15, 96–108. doi: 10.1093/cercor/bhh112
- Liang, F., Hatanaka, Y., Saito, H., Yamamori, T., and Hashikawa, T. (2000). Differential expression of gamma-aminobutyric acid type B receptor-1a and -1b mRNA variants in GABA and non-GABAergic neurons of the rat brain. *J. Comp. Neurol.* 416, 475–495. doi: 10.1002/(SICI)1096-9861(20000124)416:4<475::AID-CNE5>3.0.CO;2-V
- Llano, I., Marty, A., Armstrong, C. M., and Konnerth, A. (1991). Synaptic- and agonist-induced excitatory currents of Purkinje cells in rat cerebellar slices. *J. Physiol.* 434, 183–213. doi: 10.1113/jphysiol.1991.sp018465
- McNamara, F. N., Clifford, J. J., Tighe, O., Kinsella, A., Drago, J., Croke, D. T., et al. (2003). Congenic D1A dopamine receptor mutants: ethologically based resolution of behavioural topography indicates genetic background as a determinant of knockout phenotype. *Neuropsychopharmacology* 28, 86–99. doi: 10.1038/sj.npp.1300008
- Nakagami, Y., Watakabe, A., and Yamamori, T. (2013). Monocular inhibition reveals temporal and spatial changes in gene expression in the primary visual cortex of marmoset. *Front. Neural Circuits* 7:43. doi: 10.3389/fncir.2013.00043
- Nakamura, T., Sato, A., Kitsukawa, T., Momiyama, T., Yamamori, T., and Sasaoka, T. (2014). Distinct motor impairments of dopamine D1 and D2 receptor knockout mice revealed by three types of motor behavior. *Front. Integr. Neurosci.* 8:56. doi: 10.3389/fnint.2014.00056
- Nakazawa, K., Karachot, L., Nakabeppu, Y., and Yamamori, T. (1993). The conjunctive stimuli that cause long-term desensitization also predominantly induce c-Fos and Jun-B in cerebellar Purkinje cells. *Neuroreport* 4, 1275–1278. doi: 10.1097/00001756-199309000-00017
- Perkel, D. J., Hestrin, S., Sah, P., and Nicoll, R. A. (1990). Excitatory synaptic currents in Purkinje cells. *Proc. Biol. Sci.* 241, 116–121. doi: 10.1098/rspb.1990.0074
- Santori, E. M., Der, T., and Collins, R. C. (1986). Functional metabolic mapping during forelimb II. Stimulation of forelimb muscles movement in rat. *J. Neurosci.* 6, 463–474.
- Schaeren-Wiemers, N., and Gerfin-Moser, A. (1993). A single protocol to detect transcripts of various types and expression levels in neural tissue and cultured cells: *in situ* hybridization using digoxigenin-labelled cRNA probes. *Histochemistry* 100, 431–440. doi: 10.1007/BF00267823
- Tran, A. H., Uwano, T., Kimura, T., Hori, E., Katsuki, M., Nishijo, H., et al. (2008). Dopamine D1 receptor modulates hippocampal representation plasticity to spatial novelty. *J. Neurosci.* 28, 13390–13400. doi: 10.1523/JNEUROSCI.2680-08.2008
- Welter, M., Vallone, D., Samad, T. A., Meziane, H., Usiello, A., and Borrelli, E. (2007). Absence of dopamine D2 receptors unmasks an inhibitory control over the brain circuitries activated by cocaine. *Proc. Natl. Acad. Sci. U.S.A.* 104, 6840–6845. doi: 10.1073/pnas.0610790104
- Yamaguchi, H., Aiba, A., and Nakamura, K. (1996). Dopamine D2 receptor plays a critical role in cell proliferation and proopiomelanocortin expression in the pituitary. *Genes Cells* 1, 253–268. doi: 10.1046/j.1365-2443.1996.d01-238.x
- Yamamori, T., Mikawa, S., and Kado, R. (1995). Jun-B expression in Purkinje cells by conjunctive stimulation of climbing fibre and AMPA. *Neuroreport* 6, 793–796. doi: 10.1097/00001756-199503270-00022
- Zheng, F., Luo, Y., and Wang, H. (2009). Regulation of brain-derived neurotrophic factor-mediated transcription of the immediate early gene Arc by intracellular calcium and calmodulin. *J. Neurosci. Res.* 87, 380–392. doi: 10.1002/jnr.21863

Conflict of Interest Statement: The authors declare that the research was conducted in the absence of any commercial or financial relationships that could be construed as a potential conflict of interest.

Copyright © 2015 Nakamura, Sato, Kitsukawa, Sasaoka and Yamamori. This is an open-access article distributed under the terms of the Creative Commons Attribution License (CC BY). The use, distribution or reproduction in other forums is permitted, provided the original author(s) or licensor are credited and that the original publication in this journal is cited, in accordance with accepted academic practice. No use, distribution or reproduction is permitted which does not comply with these terms.

ARTICLE

Received 25 Nov 2014 | Accepted 24 Feb 2015 | Published 13 Apr 2015

DOI: 10.1038/ncomms7745

G-CSF supports long-term muscle regeneration in mouse models of muscular dystrophy

Nozomi Hayashiji¹, Shinsuke Yuasa¹, Yuko Miyagoe-Suzuki², Mie Hara¹, Naoki Ito², Hisayuki Hashimoto¹, Dai Kusumoto¹, Tomohisa Seki¹, Shugo Tohyama¹, Masaki Kodaira¹, Akira Kunitomi¹, Shin Kashimura¹, Makoto Takei¹, Yuki Saito¹, Shinichiro Okata¹, Toru Egashira¹, Jin Endo¹, Toshikuni Sasaoka³, Shin'ichi Takeda² & Keiichi Fukuda¹

Duchenne muscular dystrophy (DMD) is a chronic and life-threatening disease that is initially supported by muscle regeneration but eventually shows satellite cell exhaustion and muscular dysfunction. The life-long maintenance of skeletal muscle homeostasis requires the satellite stem cell pool to be preserved. Asymmetric cell division plays a pivotal role in the maintenance of the satellite cell pool. Here we show that granulocyte colony-stimulating factor receptor (G-CSFR) is asymmetrically expressed in activated satellite cells. G-CSF positively affects the satellite cell population during multiple stages of differentiation in *ex vivo* cultured fibres. G-CSF could be important in developing an effective therapy for DMD based on its potential to modulate the supply of multiple stages of regenerated myocytes. This study shows that the G-CSF–G-CSFR axis is fundamentally important for long-term muscle regeneration, functional maintenance and lifespan extension in mouse models of DMD with varying severities.

¹Department of Cardiology, Keio University School of Medicine, 35-Shinanomachi Shinjuku-ku, Tokyo 160-8582, Japan. ²Department of Molecular Therapy, National Institute of Neuroscience, National Center of Neurology and Psychiatry, Tokyo 187-8502, Japan. ³Department of Comparative and Experimental Medicine, Brain Research Institute, Niigata University, Niigata 951-8585, Japan. Correspondence and requests for materials should be addressed to S.Y. (email: yuasa@a8.keio.jp).

Adult skeletal muscle has its own stem cell population known as satellite cells (SCs). After muscle injury, quiescent SCs are activated and then proliferate and differentiate into mature skeletal muscle to ensure that muscle function is recovered. SCs are at the top of the hierarchy of differentiating stages in adult myocytes, followed by myoblasts, immature myocytes and matured myocytes. Thus, maintaining the homeostasis of skeletal muscle function over the long term requires a well-preserved population of SCs. However, SCs are still heterogenic, and among the distinct differentiation stages, the satellite stem cell population must be maintained to preserve their stemness, that is, long-term self-renewal and differentiation abilities. Accumulating data indicate that SCs maintain their population by asymmetric cell division^{1–4}. The different differentiation stages of SCs are distinguishable by the expression of specific markers such as PAX7 and MYOD; PAX7 + /MYOD – cells are quiescent, PAX7 + /MYOD + cells are activated and PAX7 – /MYOD + cells are differentiating. Interestingly, some activated SCs exhibit asymmetric MYOD distribution within the cells, and each daughter cell is either PAX7 + /MYOD + or PAX7 + /MYOD –, the latter of which retains the quiescent state⁵. Such evidence indicated that asymmetric protein distribution produces asymmetric cell division, which has a critical role in maintaining the SC population. In our previous screen for myocyte differentiation-promoting factors^{6,7}, we noted markedly elevated expression of granulocyte colony-stimulating factor receptor (G-CSFR, encoded by *csf3r*) in the developing somite⁸. Furthermore, G-CSFR was transiently expressed in regenerating myocytes of adult injured skeletal muscle, and extrinsic G-CSF supported short-term muscle regeneration in cardiotoxin-induced skeletal muscle injury⁹ and crush injury¹⁰. However, although we found high G-CSFR expression in regenerating immature myocytes, whether G-CSFR would be expressed in SCs and whether G-CSF signalling would affect the SC population in skeletal muscle remain unclear.

Duchenne muscular dystrophy (DMD) is one of the most common inheritable muscle diseases in humans^{11,12}. It is an X-linked progressive disease that affects approximately one in 3,500 male live births¹³. DMD is caused by a mutation in the gene encoding *dystrophin*, which links the internal muscle cytoskeleton to the extracellular matrix, enabling the lateral transmission of force from within muscle cells to the surrounding matrix. Mutations in the *dystrophin* gene lead to dystrophin deficiency at the myofibre membrane and progressive muscle fibre degeneration^{14,15}. The absence of dystrophin increases the fragility of the sarcolemma, which is susceptible to even mild stress¹⁶. Subsequent injury results in myofibre necrosis, followed by repetitive degeneration and regeneration supported by innate SCs. In DMD, muscle regeneration initially supports the mutation-driven functional impairment; however, such regeneration is eventually attenuated due to stem cell exhaustion¹⁷. Therapy that induces effective long-term skeletal muscle regeneration is, therefore, crucially needed for DMD.

Long-term muscle regenerative therapy for conditions such as DMD relies on increasing the pool of functional myocytes and maintaining the pool of SCs. We showed that G-CSFR is asymmetrically distributed in activated SCs, and that G-CSF increases the population of SCs via the G-CSF–G-CSFR axis in *ex vivo* cultured myofibres. On the basis of this, we hypothesized that G-CSF could be important in developing an effective therapy for DMD based on its potential to modulate the supply of multiple stages of regenerated myocytes. It is surprising that haploinsufficiency of G-CSFR leads to early lethality in DMD model mice, indicating that dose reduction of the G-CSF/G-CSFR

system could not support the balance between degeneration and regeneration. We also showed that G-CSF administration in mice with severe DMD markedly improves the phenotype, including muscle pathology, functioning and lifespan. Together, our data suggested that the G-CSF–G-CSFR axis is fundamentally important for long-term muscle regeneration, functional maintenance and lifespan extension in DMD mouse models with varying severities.

Results

G-CSFR is expressed in activated SCs. To explore the precise expression pattern of G-CSFR in skeletal muscle, we examined the SCs on isolated myofibres from the extensor digitorum longus (EDL) muscles of wild-type mice. This model preserves the physiological behaviour of SCs through activation, proliferation and differentiation on myofibres. In the isolated myofibres, PAX7 + quiescent SCs showed no G-CSFR expression by immunostaining at the time of myofibre isolation (Fig. 1a). G-CSFR expression was observed in the PAX7 + cells after 6 h (Fig. 1a,c), when MYOD expression also appeared (Fig. 1b; Supplementary Fig. 1a). G-CSFR expression was still apparent at 48 h in the MYOGENIN + SCs, which are committed to differentiation (Supplementary Fig. 1b,c)¹⁸. By 24 and 48 h, the number of G-CSFR-expressing cells increased to ~94% of PAX7 + cells (Fig. 1c).

Asymmetrically expressed G-CSFR in activated SCs.

Unexpectedly, we found that G-CSFR is asymmetrically distributed within migrating SCs obtained from isolated myofibres at day 5 (Fig. 2a). This asymmetric distribution of G-CSFR was apparent in ~20% of PAX7 + SCs at 72 h (Fig. 2b). Syndecan-4 (SDC4) was expressed in the activated SCs until mature myocyte fusion occurred; thus, paired SDC4 + cells were characterized as the daughter cells of SC division^{19,20}. The majority of paired SDC4 + cells showed equivalent expression of G-CSFR (94.4%; Fig. 2c), but in the remaining 5.6% of paired SDC4 + cells, G-CSFR was detectable in only one daughter cell (Fig. 2d). Similarly, single SDC4 + SCs either express G-CSFR or not (Fig. 2e,f). In ~5% of paired PAX7 + /SDC4 + cells, one daughter cell highly expressed G-CSFR; in the other daughter cell, G-CSFR expression was not observed (Fig. 2g). In addition, in ~5% of paired PAX7 + cells, one G-CSFR + daughter cell highly expressed MYOD, whereas no MYOD expression observed in the other (Fig. 2h). These data suggested that G-CSFR is expressed from the activation of SCs through asymmetrical distribution during the first divisions but is not expressed in the self-renewing PAX7 + /MYOD – SCs (Supplementary Fig. 2).

G-CSF increases SCs via the G-CSF–G-CSFR axis. To elucidate whether G-CSFR signalling affects the populations of SCs, we examined the PAX7 + cell population in cultured myofibres from wild-type and G-CSFR-mutated (*csf3r*^{-/-}) mice. At 0 and 24 h, there was no significant difference in the number of PAX7 + cells between wild-type and *csf3r*^{-/-} mice; however, at 48 h, the *csf3r*^{-/-} mice showed a significantly smaller number of PAX7 + cells than that of wild-type mice (Fig. 3a,b). At 24 h, most PAX7 + cells express MYOD, are activated and thereafter proliferate and commit to differentiation^{21–23}. In the *csf3r*^{-/-} mice, the number of MYOD + /PAX7 + cells was significantly decreased in PAX7 + cells activated for 24 h (Fig. 3c,d), suggesting that the genetic ablation of G-CSFR signalling negatively affects the population of activated SCs. We then examined the direct role of G-CSF on SCs from wild-type mice. At 72 h, the subpopulation of activated SCs had lost MYOD expression *in vivo* and on cultured myofibres^{21–23}. Surprisingly,

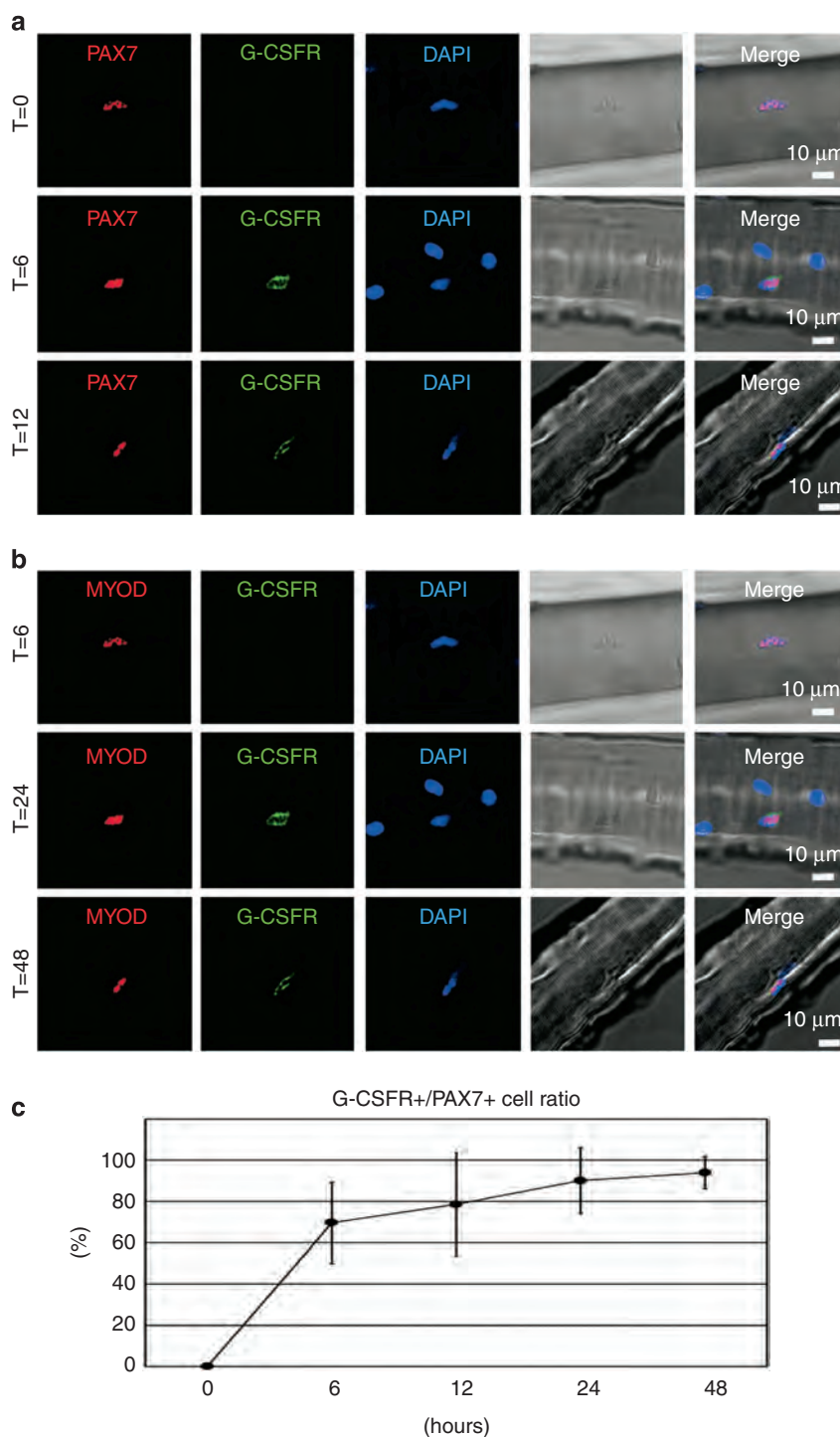


Figure 1 | G-CSFR is expressed in activated satellite cells. (a) Immunostaining of satellite cells on myofibres isolated from EDL muscles for PAX7 (red) and G-CSFR (green), including nuclei stained with DAPI (blue) and bright-field images, at 0 h ($T=0$), 6 h ($T=6$) and 12 h ($T=12$). Scale bar, 10 μm . (b) Immunostaining of satellite cells on myofibres for MYOD (red) and G-CSFR (green) at 6 h ($T=6$), 24 h ($T=24$) and 48 h ($T=48$). Scale bar, 10 μm . (c) The G-CSFR⁺/PAX7⁺ cell ratio at 0, 6, 12, 24 and 48 h ($T=0$: $n=53$; $T=6$: $n=73$; $T=12$: $n=45$; $T=24$: $n=41$; $T=48$: $n=297$; each myofibre: $n=20-30$). All myofibres were obtained from ~ 10 -week-old wild-type mice. Data are shown as mean \pm s.d. DAPI, 4',6-diamidino-2-phenylindole dihydrochloride.

G-CSF significantly increased the population of SCs throughout the differentiation stages, including self-renewal SCs, as shown by the PAX7⁺/MYOD⁻ cells at 72 h in wild-type mice; in addition, *csf3r*^{-/-} mice showed significantly decreased numbers of SCs throughout the differentiation stages (Fig. 3e,f; Supplementary Table 1). To elucidate the effect of G-CSF on the

population of PAX7⁺ cells *in vivo*, we examined SC behaviour in a cardiotoxin injury model (Fig. 3g). In the *csf3r*^{-/-} mice, the population of PAX7⁺-expressing cells was significantly decreased at 14 days after cardiotoxin injection (Fig. 3h,i), suggesting that genetic G-CSFR signal ablation negatively affects the population of PAX7⁺ cells *in vivo*.

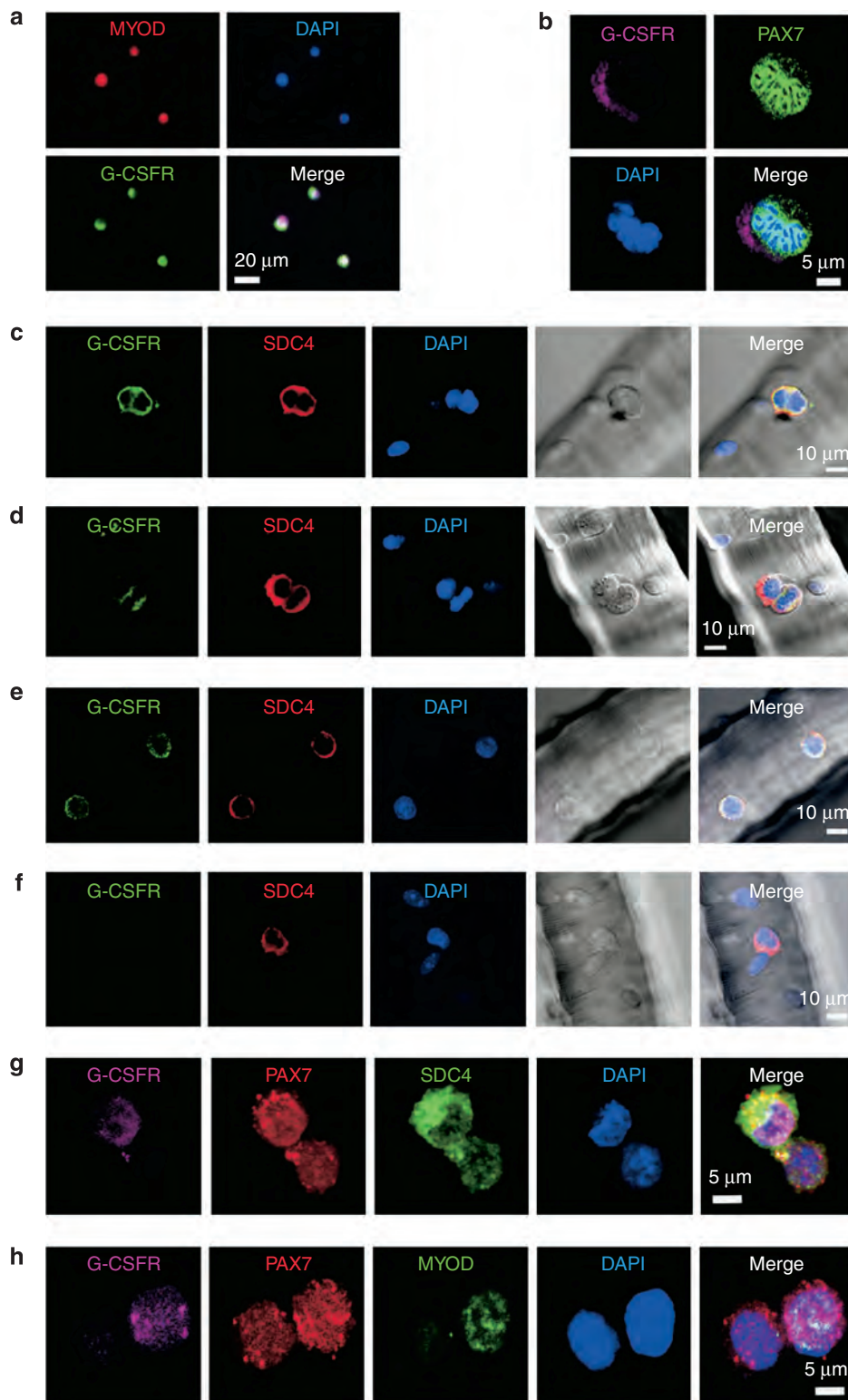


Figure 2 | G-CSFR is asymmetrically expressed in activated satellite cells. (a) Immunostaining of satellite cells for MYOD (red), G-CSFR (green) and DAPI (blue) at day 5. Scale bar, 20 μm . (b) Immunostaining of satellite cells for G-CSFR (purple), PAX7 (green) and DAPI (blue) at day 3. Scale bar, 5 μm . (c) Immunostaining of dividing satellite cells on myofibres for G-CSFR (green), SDC4 (red) and DAPI (blue), as well as bright-field (BF) images, at 48 h (satellite cells with symmetric G-CSFR expression: $n = 51$; satellite cells with asymmetric expression: $n = 3$). Scale bar, 10 μm . (d) Immunostaining of dividing satellite cells on myofibres for G-CSFR (green), SDC4 (red) and DAPI (blue), as well as BF images, at 48 h. Scale bar, 10 μm . (e,f) Immunostaining of satellite cells on myofibres for SDC4 (red), G-CSFR (green) and DAPI (blue), as well as BF images, at 48 h. Scale bar, 10 μm . (g) Immunostaining of cultured dividing satellite cells for G-CSFR (purple), PAX7 (red), SDC4 (green) and DAPI (blue). Scale bar, 5 μm . (h) Immunostaining of cultured dividing satellite cells for G-CSFR (purple), PAX7 (red), MYOD (green) and DAPI (blue) at day 3 (among 273 dividing satellite cells, dividing satellite cells with symmetric G-CSFR expression: $n = 5$; dividing satellite cells with asymmetric expression: $n = 268$). Scale bar, 5 μm . All myofibres were obtained from ~ 10 -week-old wild-type mice. DAPI, 4',6-diamidino-2-phenylindole dihydrochloride.

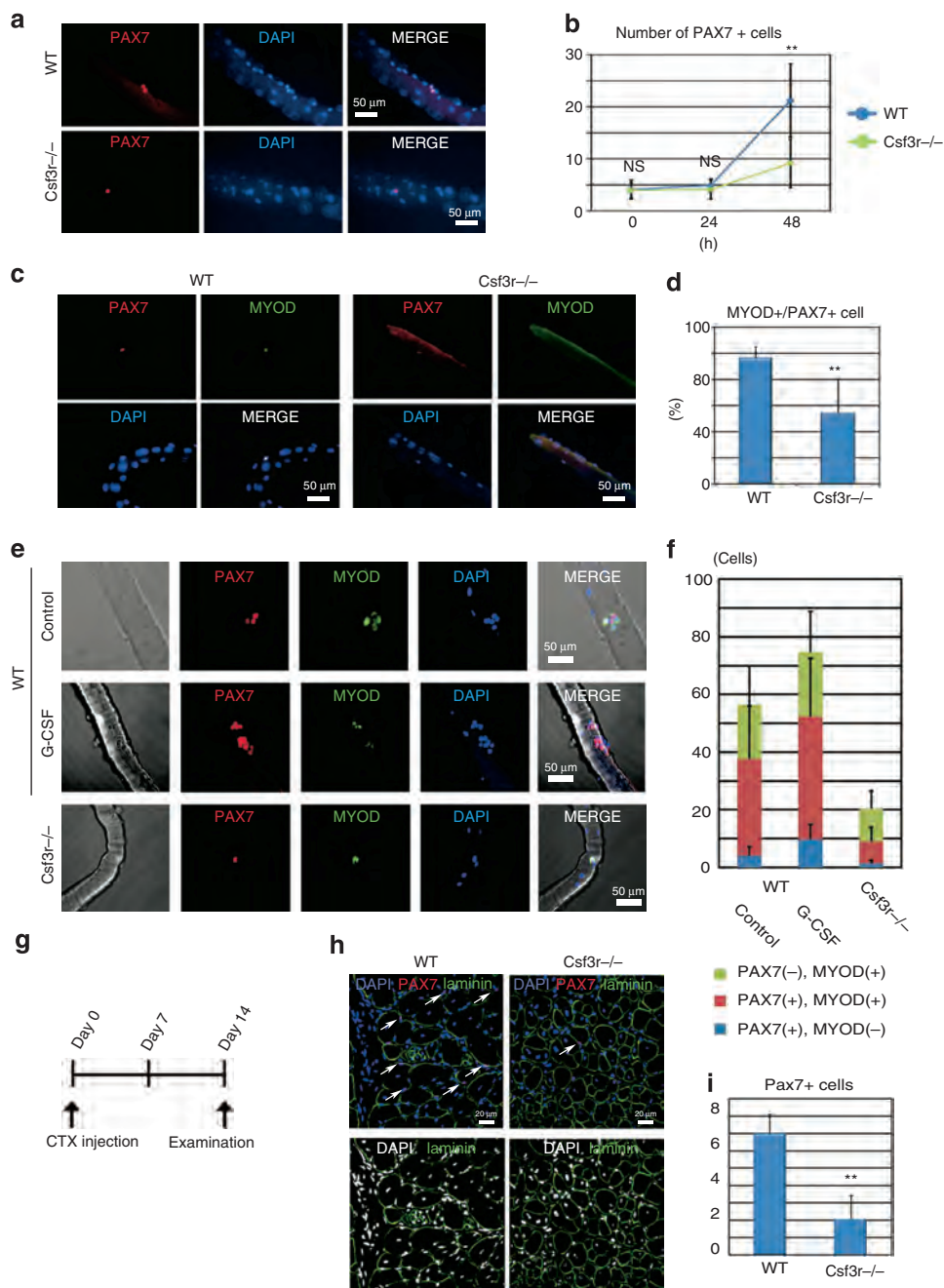


Figure 3 | G-CSF increases satellite cells in multiple differentiation stages. (a) Immunostaining of satellite cells on myofibres of ~10-week-old WT and *csf3r*^{-/-} mice for PAX7 (red) and DAPI (blue) at 48 h. Scale bar, 50 μ m. (b) Time course of the number of satellite cells (PAX7 +) at 0, 24 and 48 h per myofibre of WT and *csf3r*^{-/-} mice. Data are shown as mean \pm s.d. ***P* < 0.01; equal variance Student's *t*-test. Each fibre number: *n* = 20–29. (c) Immunostaining of satellite cells on myofibres of WT and *csf3r*^{-/-} mice for PAX7 (red), MYOD (green) and DAPI (blue) at 24 h. Scale bar, 50 μ m. (d) The percentage of MYOD + / PAX7 + satellite cells at 24 h. Data are shown as mean \pm s.d. ***P* < 0.01; unequal variance Student's *t*-test. Each fibre number: *n* = 29). (e) Immunostaining of satellite cells on myofibres of WT mice administered control and G-CSF and *csf3r*^{-/-} mice after being cultured for 72 h for PAX7 (red), MYOD (green) and DAPI (blue), as well as bright-field images. Scale bar, 50 μ m. (f) Quantification of the number of PAX7 - / MYOD + (green), PAX7 + / MYOD + (red) or PAX7 + / MYOD - (blue) satellite cells per myofibre. Data are shown as mean \pm s.d. One-way analysis of variance with Bonferroni's *post hoc* test. Quantification information in Supplementary Table 1. (g) Time course of cardiotoxin (CTX) injection and examination for 8-week-old WT and *csf3r*^{-/-} mice. (h) Immunostaining of cross-sections of TA muscle of WT and *csf3r*^{-/-} mice at 14 days after CTX injection for laminin, PAX7 and DAPI. Upper panel: merged with laminin (green), PAX7 (red) and DAPI (blue). Lower panel: merged with laminin (green) and DAPI (white). Arrows indicate PAX7 + / DAPI + cells. Scale bar, 20 μ m. (i) Number of PAX7 + / DAPI + cells per 100 myocytes of WT and *csf3r*^{-/-} mice. Data are shown as mean \pm s.d. ***P* < 0.01; unequal variance Student's *t*-test. *n* = 5–6 per group. DAPI, 4',6-diamidino-2-phenylindole; WT, wild type.

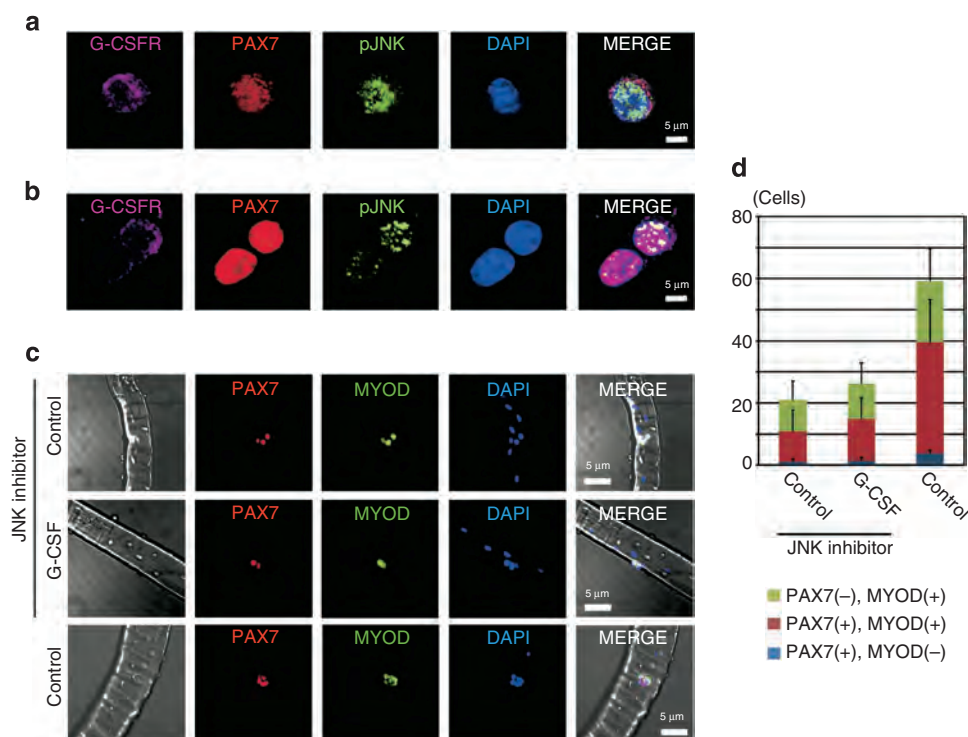


Figure 4 | G-CSF increases satellite cells through the G-CSF-G-CSFR-JNK axis. (a) Immunostaining of satellite cells for G-CSFR (purple), PAX7 (red), pJNK (green) and DAPI (blue) at day 3. Scale bar, 5 μ m. (b) Immunostaining of dividing satellite cells for G-CSFR (purple), PAX7 (red), pJNK (green) and DAPI (blue) at day 3. Scale bar, 5 μ m. (c) Immunostaining of satellite cells on myofibres of WT mice for PAX7 (red), MYOD (green) and DAPI (blue), as well as bright-field images, following JNK inhibitor administration with or without G-CSF at 72 h. Scale bar, 50 μ m. (d) Quantification of the number of PAX7⁻/MYOD⁺ (green), PAX7⁺/MYOD⁺ (red) or PAX7⁺/MYOD⁻ (blue) satellite cells per myofibre. Data are shown as mean \pm s.d. One-way analysis of variance with Bonferroni's *post hoc* test. Quantification information in Supplementary Table 1. DAPI, 4',6-diamidino-2-phenylindole dihydrochloride.

We previously showed that G-CSF apparently activates JNK and p38 signalling in cultured myoblasts⁹. Therefore, we examined whether these pathways are active in activated SCs. Immunostaining for pJNK and pp38 revealed that both JNK and p38 are activated in G-CSFR⁺ SCs (Fig. 4a; Supplementary Fig. 3a). The p38 pathway is required for SC activation and MYOD induction following proliferation²⁴; herein, p38 inhibition in single myofibres decreased the population of PAX7⁻/MYOD⁺ SCs with or without G-CSF (Supplementary Fig. 3b,c; Supplementary Table 1). Although JNK signalling is involved in myoblast differentiation²⁵, its role in SC behaviour remains unclear. In paired PAX7⁺ cells, the G-CSFR-expressing daughter cells highly expressed activated JNK, whereas the other daughter cells without G-CSFR expression did not (Fig. 4b). JNK inhibition also strongly reduced the number of PAX7⁺/MYOD⁻ and PAX7⁺/MYOD⁺ cells in single myofibres (Fig. 4c,d; Supplementary Table 1). These data indicated that G-CSF increases both activated and self-renewal SCs through the G-CSF-G-CSFR-JNK axis, suggesting that G-CSF could increase long-term regeneration in chronic skeletal muscle injury through maintenance of the SC pool.

G-CSF increases muscle regeneration in *mdx* mice. Patients with DMD show progressive physical impairment leading to the death by 20–30 years of age, whereas a mouse model of DMD (*mdx* mice) harbouring a *dystrophin* mutation has minimal physical impairment and a normal lifespan²⁶. Indeed, *mdx* mice appear grossly normal (Supplementary Fig. 4a). However, pathological analysis revealed apparent muscle degeneration and regeneration in these *mdx* mice from 3 to 5 weeks of age

(Supplementary Fig. 4b). Myocyte numbers in the tibialis anterior (TA) muscle were decreased at 3 weeks of age, but were thereafter recovered (Supplementary Fig. 4c). Generally, healthy myocytes have peripherally located nuclei, and regenerating and regenerated myocytes have central nuclei. The *mdx* mice myocytes showed central nuclei from 4 weeks of age and increased in number up to 12 weeks of age (Supplementary Fig. 4d). These data suggested initial injury to the muscle fibres with subsequent regeneration to an almost normal state in the *mdx* mice. The histological observation of TA muscle showed strong G-CSFR expression in regenerating myocytes (Supplementary Fig. 4e), implicating the possible role of G-CSF in the muscle regeneration process. We then examined whether G-CSF administration would improve skeletal muscle regeneration in *mdx* mice. We examined the gross appearance and functional differences following daily intraperitoneal (i.p.) G-CSF injections from 3 to 5 weeks of age (Fig. 5a). Immunostaining for laminin showed the typically fine cellular architecture of TA muscle (Fig. 5b). The number of myocytes with central nuclei significantly increased with G-CSF administration at 5 weeks of age (Fig. 5c). The BF-45 antibody recognizes myosin heavy chain present during embryonic and neonatal skeletal muscle development and in newly formed adult regenerating myocytes²⁷. Immunostaining for BF-45 in 4-week-old mice treated with G-CSF revealed significantly increased numbers of regenerating myocytes (Fig. 5d,e). Measuring the individual cross-sectional area of the myocytes further revealed a significantly increased proportion of small myocytes, indicating a substantial amount of newly formed regenerated myocytes at 5 weeks of age (Fig. 5f). Given that muscle size is a predictive value for muscle function, the demonstrated increase in the TA muscle

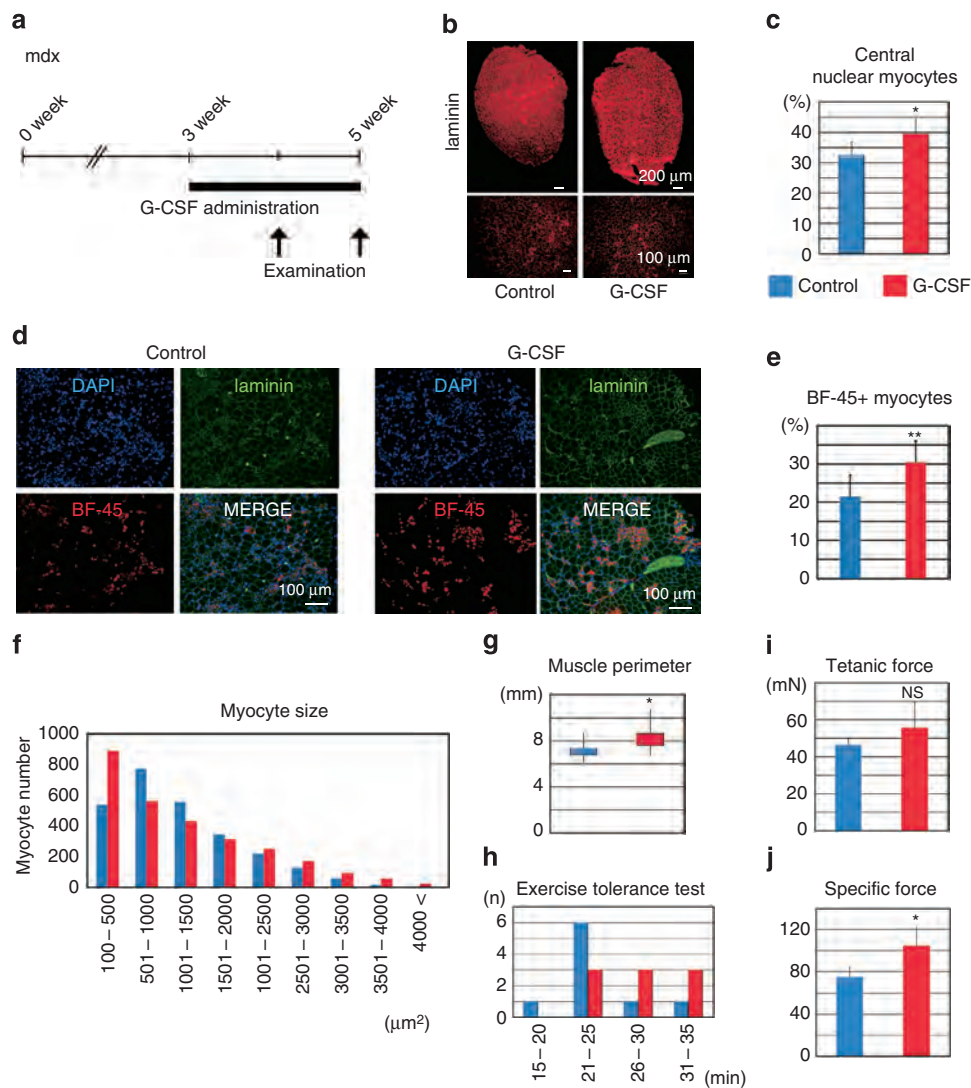


Figure 5 | G-CSF increases skeletal muscle regeneration in *mdx* mice. (a) Time course of G-CSF administration and examination in *mdx* mice. (b) Immunostaining of cross-sections of TA muscle for laminin at 5 weeks of age *mdx* mice. Scale bar, 200 μm (upper panel); 100 μm (lower panel). (c) The percentages of myocytes with central nuclei in cross-sections of TA muscle at 5 weeks of age. Data are shown as mean \pm s.d. * $P < 0.05$; equal variance Student's *t*-test. $n = 8$ per group. (d) Immunostaining of cross-sections of TA muscle for BF-45 (red), laminin (green) and DAPI (blue) at 4 weeks of age. Scale bar, 100 μm . (e) The percentages of BF-45-positive myocytes in cross-sections of TA muscle at 4 weeks of age. Data are shown as mean \pm s.d. ** $P < 0.01$; unequal variance Student's *t*-test. $n = 5$ per group. (f) The individual fibre cross-sectional area of individual myocytes in cross-sections of TA muscles at 5 weeks of age. Data are shown as mean. $n = 6$ per group. (g) Muscle perimeters of cross-sections of TA muscles at 5 weeks of age. Data are shown as box plot. Top, maximum; bottom, minimum. * $P < 0.05$; equal variance Student's *t*-test. $n = 8$ per group. (h) Exercise tolerance test results at 5 weeks of age. $n = 9$ per group. (i) Tetanic force examination of *ex vivo* EDL muscle tension at 5 weeks of age. Data are shown as mean \pm s.d. No significant difference; unequal variance Student's *t*-test; $n = 6$ per group. (j) Specific forces, which are the ratios of tetanic force to muscle size, measured at 5 weeks of age. Data are shown as mean \pm s.d. * $P < 0.05$; unequal variance Student's *t*-test. $n = 5$ per group. DAPI, 4',6-diamidino-2-phenylindole dihydrochloride; NS, not significant.

perimeter in G-CSF-treated mice at 5 weeks of age suggested enhanced muscle function recovery (Fig. 5g). G-CSF also significantly improved exercise capacity in the mice by 5 weeks of age based on *in vivo* exercise tolerance testing (Fig. 5h). In a pure muscle function test, *ex vivo* tetanic force measurements and specific force examinations showed significantly improved muscle tension in the treated mice at 5 weeks of age (Fig. 5i,j).

Next, we examined whether G-CSF treatment would accelerate the regeneration process following cardiotoxin injury in *mdx* mice (Fig. 6a). The number of myocytes with central nuclei significantly increased by G-CSF administration in cardiotoxin-injured *mdx* mice (Fig. 6b,c). The number of BF-45 + myocytes

was also significantly increased by G-CSF treatment (Fig. 6d,e). The TA muscle perimeter was also increased by G-CSF treatment in cardiotoxin-injured *mdx* mice (Fig. 6f). These data suggested that G-CSF significantly improves muscle function through myocyte regeneration in *mdx* mice.

Haploinsufficiency of G-CSFR induces lethality in *mdx* mice. To clarify the roles of G-CSF in DMD, we next used *csf3r*^{-/-} mice, which show a slight haematological disorder and a normal lifespan^{28,29}. We hypothesized that breeding G-CSFR homozygote-knockout *mdx* mice (*mdx/csf3r*^{-/-}) would produce

mice with severely impaired muscle regeneration and function. Surprisingly, G-CSFR heterozygote *mdx* (*mdx/csf3r*^{+/-}) mice showed early partial lethality after birth and late partial lethality

at 3–5 weeks of age (Fig. 7a). These striking data indicated the importance of proper G-CSF signalling in DMD. The *mdx*, *csf3r*^{+/-} and *mdx/csf3r*^{+/-} mice were of normal gross

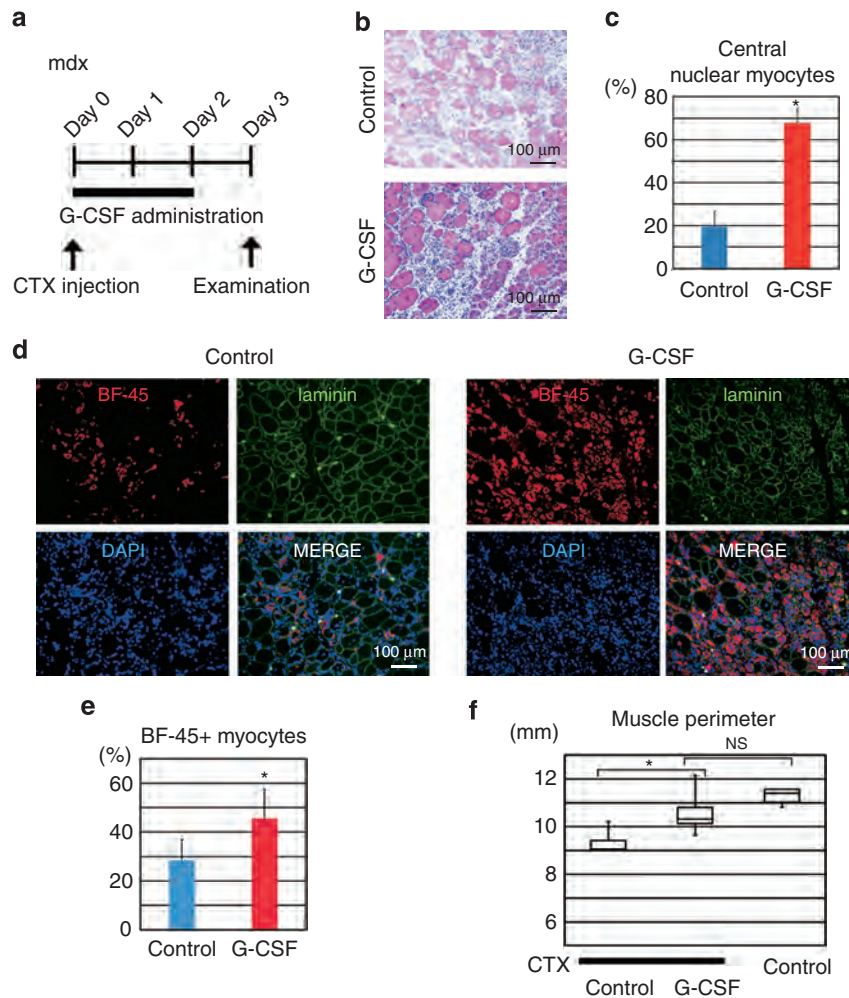
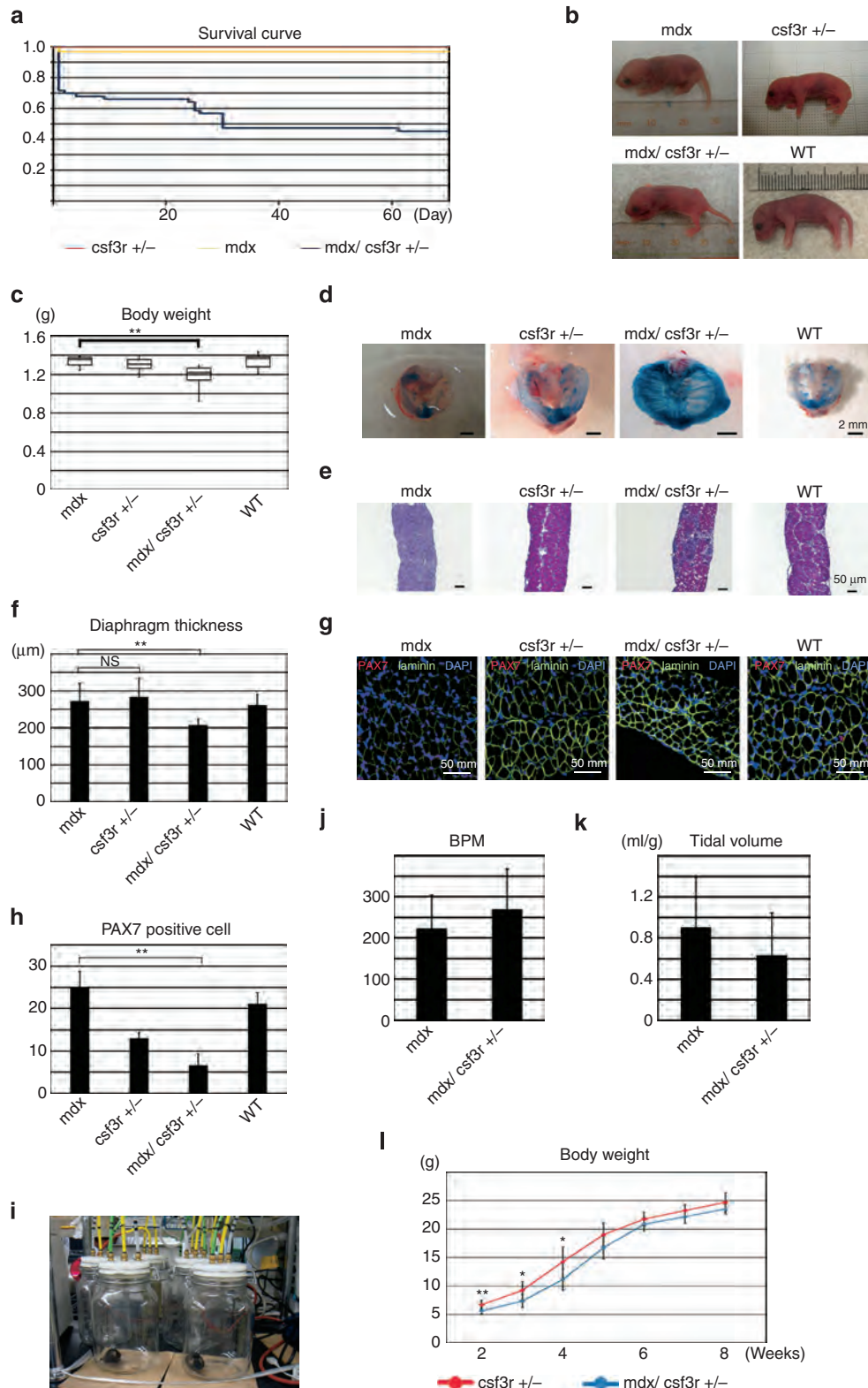


Figure 6 | G-CSF increases muscle regeneration in *mdx* mice after CTX injury. (a) Time course of CTX and G-CSF administration, and examination in 8-week-old *mdx* mice. (b) Haematoxylin and eosin staining of cross-sections of TA muscle at day 3 after CTX injection. Scale bar, 100 μ m. (c) The percentages of central nuclear myocytes in cross-sections of TA muscle at day 3 after CTX injection. Data are shown as mean \pm s.d. * P < 0.05; unequal variance Student's *t*-test. n = 4 per group. (d) Immunostaining of cross-sections of TA muscle for BF-45 (red), laminin (green) and DAPI (blue) at day 3 after CTX injection. Scale bar, 100 μ m. (e) The percentages of BF-45-positive myocytes in cross-sections of TA muscle at day 3 after CTX injection. Data are shown as mean \pm s.d. * P < 0.05; unequal variance Student's *t*-test. n = 5 per group. (f) Muscle perimeters of cross-sections of TA muscle at day 3 after CTX injection. Data are shown as box plot. Top, maximum; bottom, minimum. * P < 0.05; Student's *t*-test. n = 4–6 per group. CTX, cardiotoxin; DAPI, 4',6-diamidino-2-phenylindole dihydrochloride; NS, not significant.

Figure 7 | G-CSF signalling is essential for the survival in *mdx* mice. (a) Kaplan–Meier survival curve of *csf3r*^{+/-} (red, n = 50), *mdx* (yellow, n = 50) and *mdx/csf3r*^{+/-} (blue, n = 53) mice. (b) Gross appearance of *mdx*, *csf3r*^{+/-}, *mdx/csf3r*^{+/-} and WT mice at post-natal day 1. (c) Body weights of *mdx* (n = 7), *csf3r*^{+/-} (n = 9), *mdx/csf3r*^{+/-} (n = 11) and WT (n = 15) mice at post-natal day 1. Data are shown as box plot. Top, maximum; bottom, minimum. ** P < 0.01; unequal variance Student's *t*-test. (d) Evans blue staining of the diaphragm of *mdx*, *csf3r*^{+/-}, *mdx/csf3r*^{+/-} and WT mice at post-natal day 1. (e) Haematoxylin and eosin staining of the diaphragm of *mdx*, *csf3r*^{+/-}, *mdx/csf3r*^{+/-} and WT mice at post-natal day 1. Scale bar, 50 μ m. (f) Diaphragm thickness of *mdx*, *csf3r*^{+/-}, *mdx/csf3r*^{+/-} and WT mice at post-natal day 1 (n = 5 per group). Data are shown as mean \pm s.d. ** P < 0.01; Student's *t*-test; n = 5 per group. (g) Immunostaining of cross-sections of the diaphragm for PAX7 (red), laminin (green) and DAPI (blue) at post-natal day 1 of *mdx*, *csf3r*^{+/-}, *mdx/csf3r*^{+/-} and WT mice. Scale bar, 50 μ m. (h) Number of PAX7 + /DAPI + cells per 100 myocytes at post-natal day 1 of *mdx*, *csf3r*^{+/-}, *mdx/csf3r*^{+/-} and WT mice. Data are shown as mean \pm s.d. ** P < 0.01; Student's *t*-test; n = 5 per group. (i) Whole-body plethysmography to examine the respiratory function of individual mice. (j) Breath per min (BPM) in 8-week-old *mdx* and *mdx/csf3r*^{+/-} mice. Data are shown as mean \pm s.d. No significant difference; unequal variance Student's *t*-test; n = 4 per group. (k) Tidal volume of 8-week-old *mdx* and *mdx/csf3r*^{+/-} mice. Data are shown as mean \pm s.d. No significant difference; unequal variance Student's *t*-test; n = 4 per group. (l) Body weight growth curves of *csf3r*^{+/-} and *mdx/csf3r*^{+/-} mice from 2 to 8 weeks of age. Data are shown as mean \pm s.d. * P < 0.05, ** P < 0.01; unequal variance Student's *t*-test; n = 7 per group. DAPI, 4',6-diamidino-2-phenylindole dihydrochloride; NS, not significant; WT, wild type.

appearance at post-natal day (P) P1 (Fig. 7b); however, *mdx/csf3r*^{+/-} mice had significantly reduced body weights compared with *mdx* littermates (Fig. 7c). To elucidate the cause of early lethality, we examined the mice for gross appearance of the diaphragm and degenerative lesions by Evans blue staining. Lesions were largely absent from the *mdx*, *csf3r*^{+/-} and wild-type mice, whereas the *mdx/csf3r*^{+/-} mice showed

obvious degenerative lesions (Fig. 7d,e). Diaphragm thickness was also significantly decreased in *mdx/csf3r*^{+/-} mice compared with *mdx* littermates (Fig. 7f). The population of PAX7⁺ cells in diaphragm was also significantly decreased in *mdx/csf3r*^{+/-} mice (Fig. 7g,h). Whole-body plethysmography indicated that *mdx/csf3r*^{+/-} mice showed mildly impaired respiratory function (Fig. 7i-k). In addition, the surviving



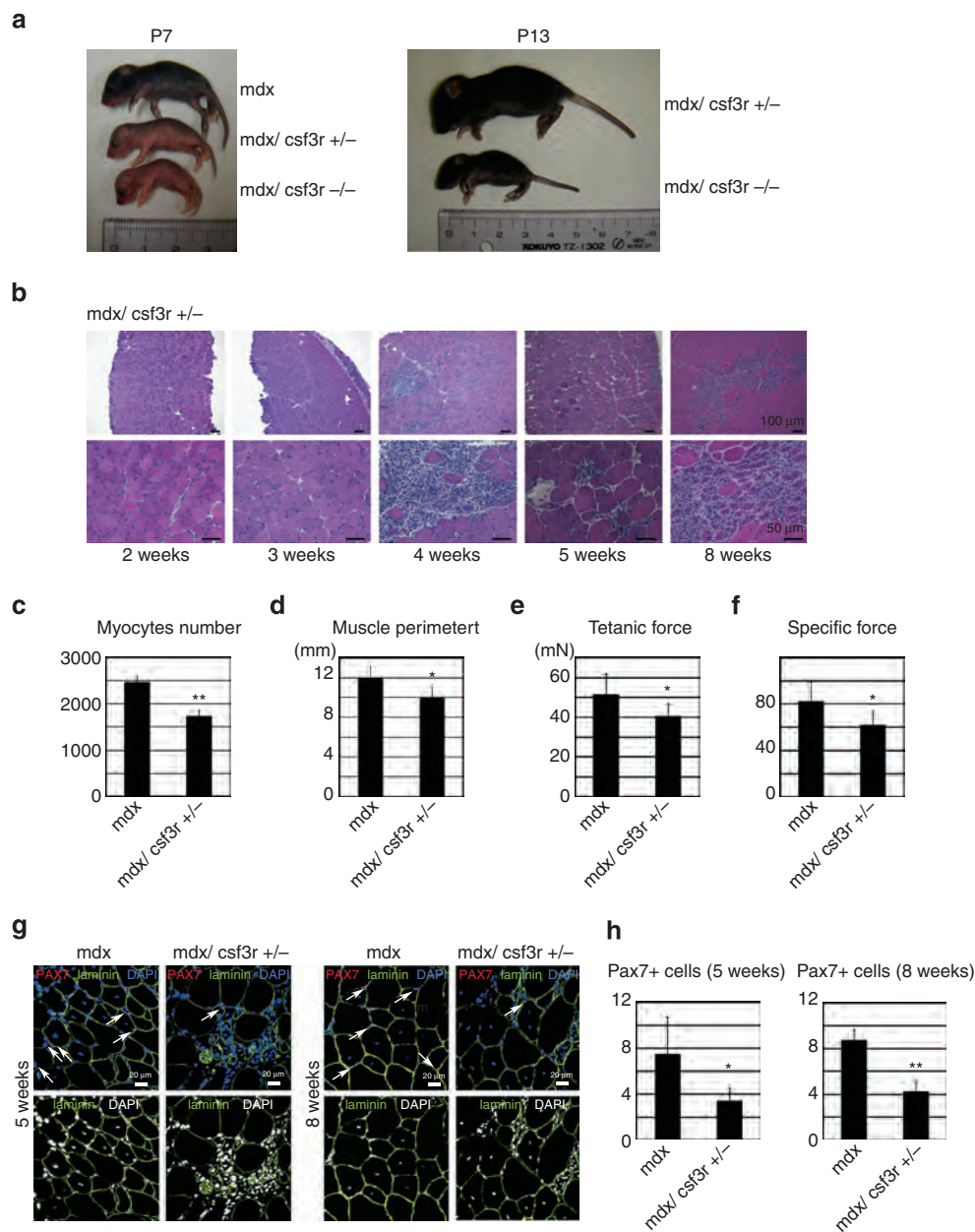


Figure 8 | Haploinsufficiency of G-CSFR reduces muscle regeneration in *mdx* mice. (a) Gross appearance analyses showing body size differences among *mdx*, *mdx/csf3r*^{+/-} and *mdx/csf3r*^{-/-} mice at post-natal day 7 (left panel) and between *mdx/csf3r*^{+/-} and *mdx/csf3r*^{-/-} mice at post-natal day 13 (right panel). (b) Haematoxylin and eosin staining of cross-sections of TA muscle from *mdx/csf3r*^{+/-} mice from 2 to 8 weeks of age are shown in the lower (upper panel) and higher (lower panel) magnified images. Scale bar, 100 μ m (upper panel); 50 μ m (lower panel). (c) The total numbers of myocytes in cross-sections of TA muscle at 8 weeks. Data are shown as mean \pm s.d. ** P < 0.01; unequal variance Student's *t*-test; n = 5 per group. (d) Perimeters of cross-sections of TA muscle at 8 weeks of age. Data are shown as mean \pm s.d. * P < 0.05; unequal variance Student's *t*-test; n = 5 per group. (e) Tetanic force examination of *ex vivo* EDL muscle tension at 8 weeks of age. Data are shown as mean \pm s.d. * P < 0.05; unequal variance Student's *t*-test; n = 5 per group. (f) Specific forces, represented by tetanic force per muscle size ratios, at 8 weeks of age. Data are shown as mean \pm s.d. * P < 0.05; unequal variance Student's *t*-test; n = 6 per group. (g) Immunostaining of cross-sections of TA muscle from *mdx* and *mdx/csf3r*^{+/-} mice at 5 and 8 weeks of age for laminin, PAX7 and DAPI. Upper panel: merged with laminin (green), PAX7 (red) and DAPI (blue). Lower panel: merged with laminin (green) and DAPI (white). Arrows indicate PAX7 +/DAPI + cells. Scale bar, 20 μ m. (h) Number of PAX7 +/DAPI + cells per 100 myocytes of *mdx* and *mdx/csf3r*^{+/-} mice at 5 and 8 weeks of age. Data are shown as mean \pm s.d. * P < 0.05, ** P < 0.01; unequal variance Student's *t*-test; n = 5 per group. DAPI, 4',6-diamidino-2-phenylindole dihydrochloride; NS, not significant; WT, wild type.

mdx/csf3r^{+/-} mice showed consecutive body weight loss compared with *csf3r*^{+/-} mice (Fig. 7i). Because most *mdx/csf3r*^{+/-} mice with a strong phenotype died before 5 weeks of age and relative healthy *mdx/csf3r*^{+/-} mice survive, the differences in body weight and respiratory function would be decreased thereafter.

In *mdx* mice, skeletal muscle degeneration and regeneration is prominent at 3–5 weeks of age. We therefore proposed that *mdx/csf3r*^{+/-} mice might show deteriorating muscle regeneration and function around that age. Gross examination revealed a smaller body size in *mdx/csf3r*^{+/-} and *mdx/csf3r*^{-/-} mice at P7, and apparently smaller body size in *mdx/csf3r*^{-/-} mice at

P13 (Fig. 8a). *Mdx/csf3r*^{+/-} mice that survived the initial early lethality prevalence showed significantly increased degeneration with decreased numbers of regenerating myocytes at ~4 weeks of age that remained at ~8 weeks of age (Fig. 8b). The myocyte number and TA muscle perimeter were also significantly decreased in *mdx/csf3r*^{+/-} mice at 8 weeks of age (Fig. 8c,d). *Ex vivo* muscle tension examination also indicated significantly decreased tetanic and specific forces in the *mdx/csf3r*^{+/-} mice compared with *mdx* mice (Fig. 8e,f). The population of PAX7+ cells was also significantly decreased in *mdx/csf3r*^{+/-} mice (Fig. 8g,h). These results confirmed that G-CSF signal is crucial for skeletal muscle regeneration in *mdx* mice.

G-CSF supports the survival of severe DMD model mice. The physically normal appearance of *mdx* mice could reflect a redundant function of the *utrophin* gene, a *dystrophin* paralogue. The *mdx/utrn*^{-/-} mice that express neither *dystrophin* nor *utrophin* manifest severe dystrophy resembling human DMD^{30,31}. These mice showed an apparently small body size compared with the *mdx* mice (Supplementary Fig. 5a), with prominent skeletal muscle degeneration that remained to a late stage of post-natal growth (Supplementary Fig. 5b). Total myocyte number in TA muscle was also decreased from 2 to 5 weeks of age in these *mdx/utrn*^{-/-} mice, and recovered thereafter (Supplementary Fig. 5c), and central nuclear myocytes

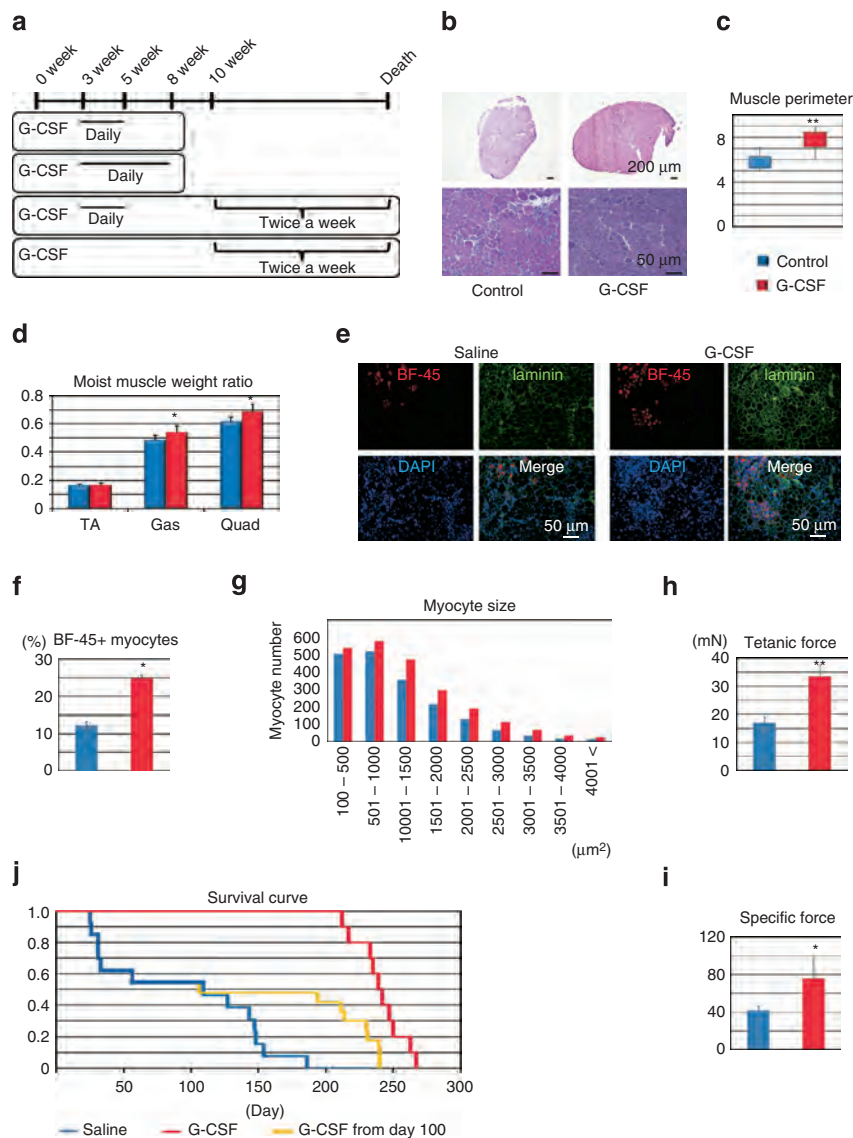


Figure 9 | G-CSF improves the survival of mice with severe muscular dystrophy. (a) Time course of G-CSF administration. (b) Haematoxylin and eosin staining of cross-sections of TA muscle from *mdx/utrn*^{-/-} mice at 5 weeks of age (left: control; right: G-CSF administration). Scale bar, 200 μm (upper panel); 50 μm (lower panel). (c) Perimeters of cross-sections of TA muscle at 5 weeks of age. Data are shown as box plot. Top, maximum; bottom, minimum. ***P*<0.01; unequal variance Student's *t*-test; *n*=6 per group. (d) Ratios of moist muscle weight to body weight at 5 weeks of age. Data are shown as mean ± s.d. **P*<0.05; equal variance Student's *t*-test; *n*=9 per group. (e) Immunostaining of cross-sections of TA muscle for BF-45 (red), laminin (green) and DAPI (blue) at 4 weeks of age. Scale bar, 50 μm. (f) The percentages of BF-45-positive myocytes in cross-sections of TA muscle at 4 weeks of age. Data are shown as mean ± s.d. ***P*<0.01; equal variance Student's *t*-test; *n*=5 per group. (g) The individual fibre cross-sectional areas of the myocytes in TA muscle at 5 weeks of age. Data are shown as mean; *n*=6 per group. (h) Tetanic force examination of *ex vivo* EDL muscle tension at 5 weeks of age is presented. Data are shown as mean ± s.d. ***P*<0.01; unequal variance Student's *t*-test; *n*=5 per group. (i) Specific force results, represented by tetanic force per muscle size ratios. Data are shown as mean ± s.d. **P*<0.05; unequal variance Student's *t*-test; *n*=5 per group. (j) Kaplan-Meier survival curve of *mdx/utrn*^{-/-} mice without G-CSF (*n*=13), with G-CSF (*n*=10) or with G-CSF administration starting at day 100 (*n*=9). DAPI, 4',6-diamidino-2-phenylindole dihydrochloride.

were apparent after 3 weeks (Supplementary Fig. 5d). G-CSFR was also expressed in regenerating myocytes in the *mdx/utrn*^{-/-} mice (Supplementary Fig. 5e).

To elucidate whether G-CSF improves skeletal muscle regeneration in these mice, we i.p. injected G-CSF using several schedules (Fig. 9a). After daily G-CSF injection from 3 to 5 weeks of age, muscle size was significantly increased in the G-CSF-treated animals at 5 weeks of age (Fig. 9b,c). G-CSF administration also significantly increased the moist muscle weight ratio of the gastrocnemius and quadriceps muscles in *mdx/utrn*^{-/-} mice (Fig. 9d), as well as the numbers of regenerated myocytes and total myocytes in TA muscle (Supplementary Fig. 6a,b; Fig. 9g). The number of BF-45⁺ myocytes was significantly increased by G-CSF treatment (Fig. 9e,f). The population of PAX7⁺ cell was also significantly increased by G-CSF treatment (Supplementary Fig. 6c,d). *Ex vivo* muscle functional analysis showed that tetanic and specific forces were significantly increased by G-CSF administration (Fig. 9h,i). These data suggested that G-CSF improves skeletal muscle regeneration and muscle function in *mdx/utrn*^{-/-} mice.

The *mdx/utrn*^{-/-} mice died at ~3 to 5 weeks of age and after 100 days of age, resulting in 100% lethality by 180 days (Fig. 9j, blue line). Finally, we showed that long-term G-CSF treatment could notably improve the survival of *mdx/utrn*^{-/-} mice, with G-CSF injected daily from 3 to 5 weeks of age and twice a week after 10 weeks of age (Fig. 9j, red line). It is clinically important to treat developed DMD; hence, the G-CSF was also injected from 10 weeks of age. G-CSF administration prolonged the survival of developed DMD model mice (Fig. 9j, yellow line). Whole-body plethysmography then indicated that G-CSF administration significantly increased respiratory function, measured by tidal volume (TV), in the *mdx/utrn*^{-/-} mice injected daily from 3 to 8 weeks of age (Supplementary Fig. 6e). The G-CSF-treated *mdx/utrn*^{-/-} mice also showed improved physical activity at 150 days of age (Supplementary Movie). Although cardiomyopathy is one of the fatal phenotypes of DMD, heart morphology is not affected by G-CSF treatment (Supplementary Fig. 6f,g). These data strongly suggested that G-CSF improves skeletal muscle regeneration and function, and supports the survival of DMD model mice.

Discussion

Research over many years has sought to understand the mechanism of skeletal muscle stem cell behaviour and elucidate the precise pathogenesis underlying DMD and, in turn, to develop effective therapies. Although many promising therapeutic strategies have been developed in animal experiments³², most human clinical trials failed to show significant efficacy in patients with DMD^{12,14,33–35}. In addition, with the exception of glucocorticoids, beneficial results with immunosuppressants were inconclusive^{36–39}. Indeed, the precise mechanism by which glucocorticoids increase muscle strength in DMD is not known and its clinical effects are generally not sufficient. Improved or additional therapies for DMD are therefore urgently needed. G-CSF is a well-known cytokine that recruits hematopoietic cells⁴⁰. The safety and side effects in humans were widely known from previously established clinical applications, which enable us to use G-CSF early in clinics. Our studies now highlight apparently encouraging the effects of G-CSF on DMD. In this work, we showed that G-CSFR is asymmetrically distributed in some activated SCs, and G-CSF successfully increases the population of SCs at the multi-differentiating stages. We successfully showed that G-CSF administration markedly improves the phenotype of DMD model mice.

The quiescent state in SC is required for the long-term maintenance of skeletal muscle⁴¹. We showed that G-CSF

increased the PAX7⁺/MYOD⁻ self-renewal SCs. There are quiescent SCs among PAX7⁺/MYOD⁻ SCs, but it remains unclear whether G-CSF would affect the quiescent SC population. Because G-CSFR is not expressed in PAX7⁺/MYOD⁻ SCs, G-CSF signalling would not be directly involved in the transition from activated SCs to PAX7⁺/MYOD⁻ SCs. Furthermore, it remains unclear how G-CSF signalling increases the population of PAX7⁺/MYOD⁻ SCs. And intrinsic differences among heterogenic satellite stem cells are still unclear and a practical marker to distinguish the subpopulations of satellite stem cells is still missing. Further precise elucidation of molecular mechanisms may directly facilitate control of the quiescent SC pool.

As a study limitation, we could not directly show that bone marrow cells would not be involved in the phenotype of DMD model. To determine whether bone marrow cells have a role in early lethality of haploinsufficiency for G-CSFR in the dystrophic background, we performed bone marrow transplantation using *mdx/csf3r*^{+/-} mice of ~3–4 weeks of age. There is no established method of bone marrow transplantation for pups earlier than those ages. We selected active *mdx/csf3r*^{+/-} mice of ~3–4 weeks of age and successfully performed bone marrow transplantation. One of eight *mdx/csf3r*^{+/-} mice died at 3 weeks after wild-type bone marrow transplantation by 8 weeks of age, which is similar to the survival rate of active *mdx/csf3r*^{+/-} mice without bone marrow transplantation. Although wild-type bone marrow cells could not rescue the lethality of *mdx/csf3r*^{+/-} mice, bone marrow transplantation would preferably be performed in *mdx/csf3r*^{+/-} mice 0 days of age; alternatively, skeletal muscle-specific G-CSFR-deficient mice would ideally be generated.

We confirmed that the G-CSF/G-CSFR system is critically involved in muscle regeneration during the course of DMD in several mouse models. Given our findings, it is surprising that haploinsufficiency of G-CSFR leads to early lethality in *mdx* mice, indicating that dose reduction of the G-CSF/G-CSFR system cannot support the balance between degeneration and regeneration in these mouse models. We also showed that G-CSF administration markedly improves the phenotype of *mdx/utrn*^{-/-} mice. Together, our data suggested that G-CSF could improve the phenotype of human DMD and could consequently form the basis of novel and effective therapies in the near future.

Methods

Mice. C57BL/6-background *mdx* mice were provided by Dr T. Sasaoka (Niigata University Niigata, Japan). The *utrophin*-knockout mice were a kind gift from Dr Kay E Davies (University of Oxford, Oxford, UK)³¹. The *dystrophin-utrophin* double-knockout male homozygous (*dystrophin*^{-Y} (*mdx*), *utrophin*^{-/-}) mice were obtained by crossing those heterozygous (*mdx*, *utrophin*^{+/-}) mice. The *csf3r*^{-/-} mice were kindly gifted by Dr Daniel C. Link (Washington University School of Medicine, St Louis)²⁸. Mice deficient in both *dystrophin* and *csf3r* were derived by the following breeding program: male *csf3r*-knockout (*csf3r*^{-/-}) mice were mated with female C57B/6 *mdx* (*dystrophin*^{-X}) mice, resulting in all F1-generation mice being heterozygous for *csf3r* (*csf3r*^{+/-}) and either heterozygous for the *mdx* mutation (*dystrophin*^{-X}, females) or hemizygous for the *mdx* mutation (*dystrophin*^{-Y}, males). All data were obtained from P1 to 20 weeks of age male mice. All experimental procedures and protocols were approved by the Animal Care and Use Committee of Keio University and conformed to the NIH Guidelines for the Care and Use of Laboratory Animals.

Genotyping. DNA was isolated from mouse tails using the Easy-DNA Kit (Invitrogen, CA, USA). PCR analysis to identify mutant dystrophin alleles used a forward primer complementary to mouse dystrophin (5'-CATAGTTATTAATG CATAGATATTCAG-3') and reverse primers complementary to the wild-type allele (5'-GTCACACTCAGATAGTTGAAGCCATTAG-3') or mouse mutant dystrophin allele (5'-GTCACACTCAGATAGTTGAAGCCATTAA-3'). PCR cycling conditions for both the reactions were as follows: 95 °C for 4 min; 34 cycles of 95 °C for 1 min, 55 °C for 1 min and 72 °C for 1 min, and 72 °C for 10 min. Each reaction yielded a 275-bp product. All PCR reactions were performed using the GoTaq DNA Polymerase kit (Promega, Madison, WI, USA). PCR analysis to assess the

utrophin-knockout status used a forward primer complementary to exon 7 of mouse utrophin (5'-GTGAAGGATGTCATGAAAG-3') and reverse primers complementary either to intron 7 (5'-TGAAGTCCGAAAGAGATACC-3') or to the PGK promoter located within the Neo-knockout cassette (5'-ACGAGACTAGT GAGACGTGC-3'). PCR reactions were carried out under the following conditions: 35 cycles of 94 °C for 30 s, 57 °C for 30 s and 72 °C for 25 s. PCR analysis to determine mutant *csf3r* alleles used a forward primer complementary to mouse *csf3r* (5'-AGTTCACCAGGAGGTGAGT-3') and reverse primers complementary to wild-type alleles (5'-GTAGGCTAGTTCATACCTG-3') or mouse mutant *csf3r* alleles (5'-TCCAGACTGCCTTGGGAAA-3'). The PCR cycling conditions for both reactions were as follows: 95 °C for 4 min, followed by 30 cycles of 95 °C for 30 sec, 60 °C for 30 sec and 72 °C for 45 sec. Each reaction yielded a 279-bp product for the wild-type allele and a 366-bp product for the mutant *csf3r* allele. All PCR reactions were conducted using the Taq DNA Polymerase kit (TaKaRa, Shiga, Japan).

G-CSF treatment. G-CSF (Neutrogin, 100 µg; Chugai, Tokyo, Japan) was diluted in 1 ml of saline (concentration of 100 µg ml⁻¹). Short-term treatment for *mdx* mice involved daily i.p. injections of 5 µg G-CSF from 3 to 5 weeks of age using a 27-gauge needle. Middle-term treatment for *mdx/utrn*^{-/-} mice involved daily i.p. injections from 3 to 8 weeks of age at 5 µg using a 27-gauge needle. Long-term treatment for *mdx/utrn*^{-/-} mice involved daily i.p. injections from 3 to 5 weeks of age and twice weekly from 10 weeks of age at 5 µg using a 27-gauge needle. Late treatment for *mdx/utrn*^{-/-} mice involved twice weekly i.p. injections from 10 weeks of age at 5 µg using a 27-gauge needle.

Histological analysis. Frozen section of TA muscle was stained by haematoxylin and eosin to measure the ratio of muscle regeneration. The fibre cross-sectional area was measured using software (BZ-H1C; Keyence, Osaka, Japan) from laminin-stained cross-sections of TA muscle. Micrographs were taken from each section at ×10 and ×20 magnification with a digital camera (BIOREVO; Keyence). Evans blue (Sigma-Aldrich, MO, USA) was dissolved in PBS (0.15 M NaCl, 10 mM phosphate buffer, pH 7.0). Mice were i.p. injected with 0.5 ml 0.1% Evans blue at P1 using a 27-gauge needle and were killed 3 h later.

Immunofluorescence. All immunofluorescence was carried out on 6-µm-thick frozen sections, myofibres and SCs. The frozen sections were fixed with acetone (WAKO, Osaka, Japan) for 20 min at -30 °C. Myofibres and SCs were fixed with 4% paraformaldehyde for 20 min at room temperature. All samples were incubated with 0.1% Triton X-100 for 5 min at room temperature, washed and then incubated with the following primary antibodies: anti-G-CSF receptor (sc-9173, 1:50; Santa Cruz Biotechnology, CA, USA; sc-323898, 1:100; Santa Cruz Biotechnology), anti-laminin 2 (L0663, 1:1000; Sigma-Aldrich), anti-laminin (L9393, 1:1000; Sigma-Aldrich), anti-BF-45 (1:30; Developmental Studies Hybridoma Bank, IA, USA), anti-MyoD (sc-32758, 1:200; mouse; sc-304, 1:200; Santa Cruz Biotechnology), anti-Pax7 (sc-81648, 1:100; 1:40; Santa Cruz Biotechnology), anti-myogenin (ab1835, 1:100; Abcam, Camb, UK; sc-576 1:100; Santa Cruz Biotechnology), anti-syndecan-4 (ab24511, 1:100; Abcam), anti-phospho-SAPK/JNK (#9251 1:100; rabbit, Cell Signaling Technology, MA, USA) and anti-phospho-p38 (sc-7973, 1:100; mouse, Santa Cruz Biotechnology). After overnight incubation, bound antibodies were visualized with a secondary antibody conjugated with Alexa 488, Alexa 546 or Alexa 633 (Life Technologies, CA, USA). Nuclei were stained with 4',6-diamidino-2-phenylindole dihydrochloride (Life technologies). For Pax7 staining, an M.O.M. kit (Vector Laboratories) was used to block the endogenous mouse IgG. The images were recorded using a confocal laser microscope system (Carl Zeiss, Jena, Germany) and BIOREVO (Keyence).

Muscle force measurements. EDL muscles were isolated and removed from 5-week-old mice. The muscles were carefully mounted in a chamber filled with PBS (95% O₂ and 5% CO₂) and maintained at 30 °C. One tendon of the muscle was attached to a steel hook in the chamber, and the other was tied to the lever arm of a dual-mode servomotor system (Electronic Stimulator; NIHON KOHDEN, Tokyo, Japan) via 5-0 surgical silk. The muscles were stretched to the length at which a single twitch and tetanic force showed the highest amplitude (optimal length; *L*_o). The corresponding tetanic force was then measured at 150 Hz over 5-s intervals for a total of 20 min, with a rest period of 120 s to change the buffer. The muscles were adjusted to the optimum length (*L*_o) before all force measurements. For comparative purposes, all force measurements were expressed per the total muscle unit cross-sectional area, which was calculated by dividing the muscle mass by the product of the length and the mammalian skeletal muscle density (1.056 mg mm⁻³). The specific force (N cm⁻²) was calculated with the muscle density assumed as 1.056 g cm⁻³.

Exercise tolerance tests. Mice were subjected to an exhaustion treadmill test by placing them on the belt of a one-lane motorized treadmill (MK-680S Treadmill for Rats & Mice; Muromachi Kikai, Tokyo, Japan). The test was started at an incline of 0 at 5 m min⁻¹ for 5 min; thereafter, the speed was increased by 1 m min⁻¹ every

minute. The end point of the test was when the mouse remained on the shocker plate for >20 s.

Whole-body plethysmography. Animals were placed in a free-moving chamber that was connected to a high-gain differential pressure transducer (Valdyne MP45, Valdyne, North Ridge, CA, USA). As the animal breathed, changes in the pressure were converted to signals representing the TV; these signals were amplified (BMA 830; CWE, Ardmore, PA, USA), recorded on a strip-chart recorder (Dash 10; Astro-Med, West Warwick, RI, USA) and stored in a computer with respiratory acquisition software for analysis. O₂ consumption and CO₂ production were measured by the open-circuit method using Beckman OM-14 and LB-2 analysers. The parameter TV was analysed in real time, then average values were calculated five times every 2 min for each serial 3-h period. The TV was normalized by dividing by the body weight.

Myofibre isolation and culture. Single myofibres were isolated from EDL muscles and digested in DMEM GltaMax (Gibco, CA, USA) with 0.2% type 1 collagenase at 37 °C for 90 min. Fibres were liberated by trituration in DMEM medium with Pasteur pipettes. Isolated myofibres were cultured in suspension in serum-coated dishes. The fibre medium contained 20% foetal bovine serum (Sigma-Aldrich), 1% chick embryo extract (US Biological, MA, USA) 1% penicillin-streptomycin (Gibco), and DMEM GltaMax (Gibco). Single myofibres were incubated at 37 °C with 5% CO₂ for the indicated times. For the treatments, G-CSF (Neutrogin; Chugai) was added to the fibre medium to a concentration of 0.375 ng ml⁻¹, p38 inhibitor (SB203580, CST) was added to the fibre medium at a concentration of 10 µM and JNK inhibitor (SP600125, Cell Signaling Technology) was added to the fibre medium at a concentration of 5 µM.

Isolation of SCs. We obtained SCs using single myofibre culture, during which the SCs began to migrate on Matrigel (BD Biosciences, CA, USA)-coated dishes. Single SCs were then placed in Matrigel-coated glass-base dishes (Asahi Glass, Tokyo, Japan) and were maintained in fibre medium at 37 °C with 5% CO₂ for 3 days to allow SCs to migrate off the fibre and onto the Matrigel-coated dishes.

Statistical analysis. Values are reported as the means ± s.d. The data were analysed using StatView J-4.5 software. Comparisons between the two groups were performed with Student's *t*-test. Comparisons among the groups were performed by one-way analysis of variance with Bonferroni's *post hoc* test. Scheffé's *F*-test was used to determine the level of significance. The probability level accepted for significance was **P*<0.05, ***P*<0.01.

References

- Rocheteau, P., Gayraud-Morel, B., Siegl-Cachedenier, I., Blasco, M. A. & Tajbakhsh, S. A Subpopulation of adult skeletal muscle stem cells retains all template DNA strands after cell division. *Cell* **148**, 112–125 (2012).
- Troy, A. *et al.* Coordination of satellite cell activation and self-renewal by Par-complex-dependent asymmetric activation of p38α/β MAPK. *Cell Stem Cell* **11**, 541–553 (2012).
- Kawabe, Y.-i., Wang, Y. u. X., McKinnell, I. W., Bedford, M. T. & Rudnicki, M. A. Carm1 regulates Pax7 transcriptional activity through MLL1/2 recruitment during asymmetric satellite stem cell divisions. *Cell Stem Cell* **11**, 333–345 (2012).
- Cheung, T. H. *et al.* Maintenance of muscle stem-cell quiescence by microRNA-489. *Nature* **482**, 524–528 (2012).
- Relaix, F. & Zammit, P. S. Satellite cells are essential for skeletal muscle regeneration: the cell on the edge returns centre stage. *Development* **139**, 2845–2856 (2012).
- Yuasa, S. *et al.* Transient inhibition of BMP signaling by Noggin induces cardiomyocyte differentiation of mouse embryonic stem cells. *Nat. Biotechnol.* **23**, 607–611 (2005).
- Yuasa, S. *et al.* Zac1 is an essential transcription factor for cardiac morphogenesis. *Circ. Res.* **106**, 1083–1091 (2010).
- Shimoji, K. *et al.* G-CSF promotes the proliferation of developing cardiomyocytes *in vivo* and in derivation from ESCs and iPSCs. *Cell Stem Cell* **6**, 227–237 (2010).
- Hara, M. *et al.* G-CSF influences mouse skeletal muscle development and regeneration by stimulating myoblast proliferation. *J. Exp. Med.* **208**, 715–727 (2011).
- Stratos, I., Rotter, R., Eipel, C., Mittlmeier, T. & Vollmar, B. Granulocyte-colony stimulating factor enhances muscle proliferation and strength following skeletal muscle injury in rats. *J. Appl. Physiol.* **103**, 1857–1863 (2007).
- Emery, A. E. H. The muscular dystrophies. *Lancet* **359**, 687–695 (2002).
- Bushby, K. *et al.* Diagnosis and management of Duchenne muscular dystrophy, part 1: diagnosis, and pharmacological and psychosocial management. *Lancet Neurol.* **9**, 77–93 (2010).
- Emery, A. E. H. Population frequencies of inherited neuromuscular diseases—a world survey. *Neuromuscul. Disord.* **1**, 19–29 (1991).

14. Muntoni, F., Torelli, S. & Ferlini, A. Dystrophin and mutations: one gene, several proteins, multiple phenotypes. *Lancet Neurol.* **2**, 731–740 (2003).
15. Hoffman, E. P. *et al.* Characterization of dystrophin in muscle-biopsy specimens from patients with Duchenne's or Becker's muscular dystrophy. *N. Engl. J. Med.* **318**, 1363–1368 (1988).
16. Petrof, B. J., Shrager, J. B., Stedman, H. H., Kelly, A. M. & Sweeney, H. L. Dystrophin protects the sarcolemma from stresses developed during muscle contraction. *Proc. Natl Acad. Sci. USA* **90**, 3710–3714 (1993).
17. Shi, X. & Garry, D. J. Muscle stem cells in development, regeneration, and disease. *Genes Dev.* **20**, 1692–1708 (2006).
18. Olguin, H. C., Yang, Z., Tapscott, S. J. & Olwin, B. B. Reciprocal inhibition between Pax7 and muscle regulatory factors modulates myogenic cell fate determination. *J. Cell Biol.* **177**, 769–779 (2007).
19. Bentzinger, C. F. *et al.* Fibronectin regulates Wnt7a Signaling and satellite cell expansion. *Cell Stem Cell* **12**, 75–87 (2013).
20. Tanaka, K. K. *et al.* Syndecan-4-expressing muscle progenitor cells in the SP engraft as satellite cells during muscle regeneration. *Cell Stem Cell* **4**, 217–225 (2009).
21. Zammit, P. S. *et al.* Muscle satellite cells adopt divergent fates: a mechanism for self-renewal? *J. Cell Biol.* **166**, 347–357 (2004).
22. Yablonka-Reuveni, Z., Day, K., Vine, A. & Shefer, G. Defining the transcriptional signature of skeletal muscle stem cells. *J. Anim. Sci.* **86**, E207–E216 (2008).
23. Siegel, A., Kuhlmann, P. & Cornelison, D. Muscle satellite cell proliferation and association: new insights from myofiber time-lapse imaging. *Skelet. Muscle* **1**, 7 (2011).
24. Jones, N. C. *et al.* The p38 α / β MAPK functions as a molecular switch to activate the quiescent satellite cell. *J. Cell Biol.* **169**, 105–116 (2005).
25. Alter, J., Rozentzweig, D. & Bengal, E. Inhibition of myoblast differentiation by tumor necrosis factor α is mediated by c-Jun N-terminal kinase 1 and leukemia inhibitory factor. *J. Biol. Chem.* **283**, 23224–23234 (2008).
26. Evans, N. P., Misyak, S. A., Robertson, J. L., Bassaganya-Riera, J. & Grange, R. W. Dysregulated intracellular signaling and inflammatory gene expression during initial disease onset in Duchenne muscular dystrophy. *Am. J. Phys. Med. Rehabil.* **88**, 502–522 (2009).
27. Schiaffino, S. *et al.* Embryonic and neonatal myosin heavy chain in denervated and paralyzed rat skeletal muscle. *Dev. Biol.* **127**, 1–11 (1988).
28. Richards, M. K., Liu, F., Iwasaki, H., Akashi, K. & Link, D. C. Pivotal role of granulocyte colony-stimulating factor in the development of progenitors in the common myeloid pathway. *Blood* **102**, 3562–3568 (2003).
29. Hermans, M. H. A. *et al.* Perturbed granulopoiesis in mice with a targeted mutation in the granulocyte colony-stimulating factor receptor gene associated with severe chronic neutropenia. *Blood* **92**, 32–39 (1998).
30. Grady, R. M. *et al.* Skeletal and cardiac myopathies in mice lacking utrophin and dystrophin: a model for Duchenne muscular dystrophy. *Cell* **90**, 729–738 (1997).
31. Deconinck, A. E. *et al.* Utrophin-dystrophin-deficient mice as a model for Duchenne muscular dystrophy. *Cell* **90**, 717–727 (1997).
32. Muntoni, F. & Wells, D. Genetic treatments in muscular dystrophies. *Curr. Opin. Neurol.* **20**, 590–594 (2007).
33. Bushby, K., Muntoni, F., Urtizberea, A., Hughes, R. & Griggs, R. Report on the 124th ENMC International Workshop. Treatment of Duchenne muscular dystrophy; defining the gold standards of management in the use of corticosteroids 2–4 April 2004, Naarden, The Netherlands. *Neuromuscul. Disord.* **14**, 526–534 (2004).
34. Drachman, D. B., Toyka, K. V. & Myer, E. Prednisone in Duchenne muscular dystrophy. *Lancet* **304**, 1409–1412 (1974).
35. Fairclough, R., Bareja, A. & Davies, K. Progress in therapy for Duchenne muscular dystrophy. *Exp. Physiol.* **96**, 1101–1113 (2011).
36. Ameen, V. & Robson, L. G. Experimental models of duchenne muscular dystrophy: relationship with cardiovascular disease. *Open Cardiovasc. Med. J.* **4**, 265–277 (2010).
37. Quinlan, J. G. *et al.* Evolution of the mdx mouse cardiomyopathy: physiological and morphological findings. *Neuromuscul. Disord.* **14**, 491–496 (2004).
38. Griggs, R. C. Duchenne muscular dystrophy: an important negative trial. *Lancet Neurol.* **9**, 1038–1039 (2010).
39. Sharma, K. R., Mynhier, M. A. & Miller, R. G. Cyclosporine increases muscular force generation in Duchenne muscular dystrophy. *Neurology* **43**, 527–532 (1993).
40. Cottler-Fox, M. H. *et al.* Stem cell mobilization. *Hematology Am. Soc. Hematol. Educ. Program* **1**, 419–437 (2003).
41. Wang, Y. X., Dumont, N. A. & Rudnicki, M. A. Muscle stem cells at a glance. *J. Cell. Sci.* **127**, 4543–4548 (2014).

Acknowledgements

This study was supported in part by research grants from The Ministry of Education, Science and Culture, Japan; The Program for Promotion of Fundamental Studies in Health Science of the National Institute of Biomedical Innovation; The Ministry of Health Labour and Welfare; Health Labour Sciences Research Grant; Nakatomi Foundation; Japan Heart Foundation/Novartis Grant for Research Award on Molecular and Cellular Cardiology; SENSHIN Medical Research Foundation; Kimura Memorial Heart Foundation Research Grant; Japan Intractable Diseases Research Foundation, Japan; The Cell Science Research Foundation; The Tokyo Biochemical Research Foundation; Suzuken Memorial Foundation; and The Japan Foundation for Applied Enzymology.

Author contributions

S.Y. designed the research, N.H., S.Y., Y.S., M.H., N.I., H.H., D.K., T.S., S.T., M.K., A.K., S.K., M.T., Y.S., S.O., T.E., J.E. and T.S. performed the research, N.H., S.Y., Y.S., S.T. and K.F. analysed the data and S.Y. wrote the paper.

Additional information

Supplementary Information accompanies this paper at <http://www.nature.com/naturecommunications>

Competing financial interests: The authors declare no competing financial interests.

Reprints and permission information is available online at <http://npg.nature.com/reprintsandpermissions/>

How to cite this article: Hayashiji, N. *et al.* G-CSF supports long-term muscle regeneration in mouse models of muscular dystrophy. *Nat. Commun.* **6**:6745 doi: 10.1038/ncomms7745 (2015).

Erratum: G-CSF supports long-term muscle regeneration in mouse models of muscular dystrophy

Nozomi Hayashiji, Shinsuke Yuasa, Yuko Miyagoe-Suzuki, Mie Hara, Naoki Ito, Hisayuki Hashimoto, Dai Kusumoto, Tomohisa Seki, Shugo Tohyama, Masaki Kodaira, Akira Kunitomi, Shin Kashimura, Makoto Takei, Yuki Saito, Shinichiro Okata, Toru Egashira, Jin Endo, Toshikuni Sasaoka, Shin'ichi Takeda & Keiichi Fukuda

Nature Communications 6:6745 doi: 10.1038/ncomms7745 (2015); Published 13 April 2015; Updated 18 Jun 2015.

The immunofluorescence images in Fig. 1b of the PDF version of this Article were inadvertently duplicated from Fig. 1a during the production process. The correct version of Fig. 1 appears below; the HTML version of the paper was correct from the time of publication.

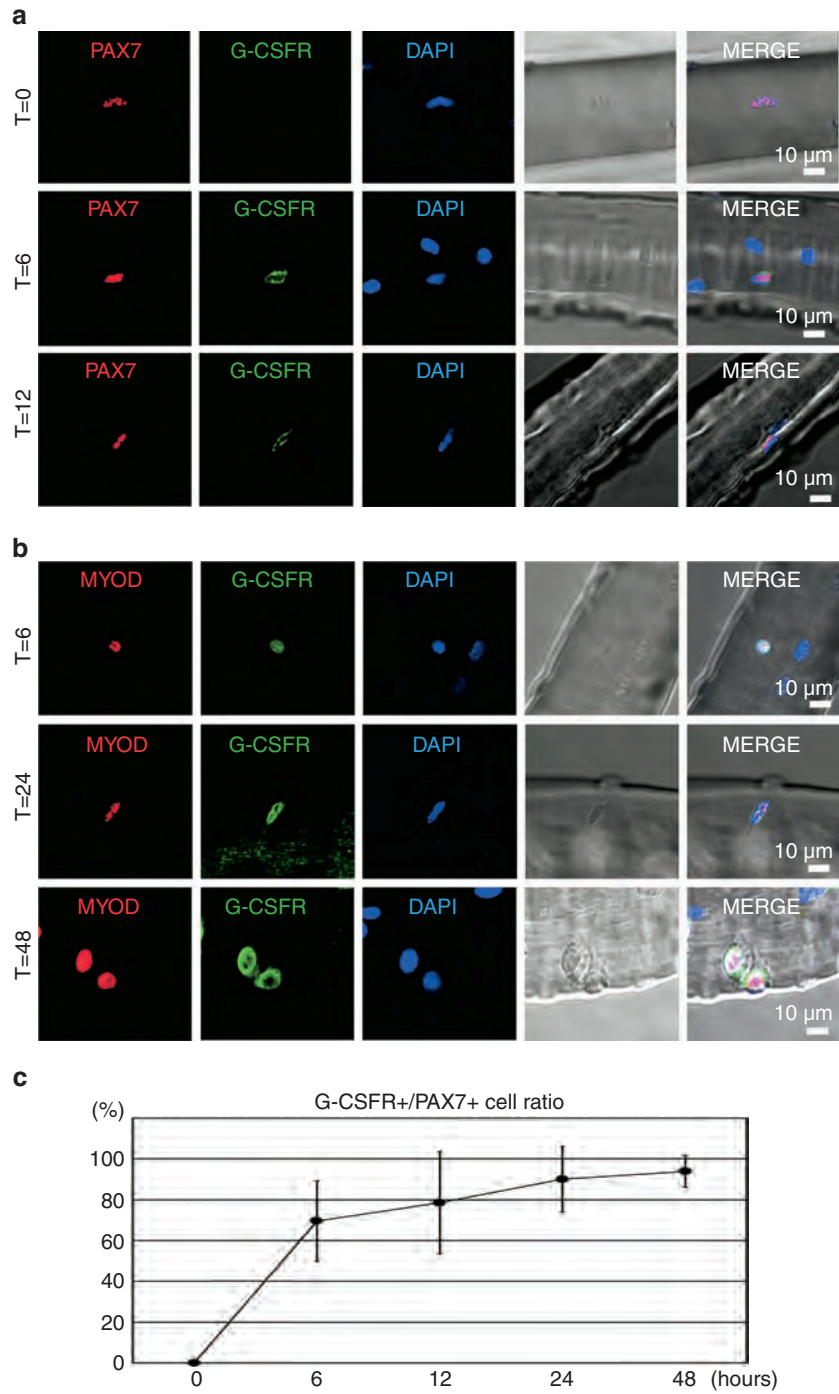


Figure 1

RESEARCH ARTICLE

Targeting Notch Signaling and Autophagy Increases Cytotoxicity in Glioblastoma Neurospheres

Manabu Natsumeda^{1,2}; Kosuke Maitani¹; Yang Liu¹; Hiroaki Miyahara¹; Harpreet Kaur¹; Qian Chu^{1,3}; Hongyan Zhang¹; Ulf D. Kahlert^{1,4}; Charles G. Eberhart¹

¹ Department of Pathology, Division of Neuropathology, Johns Hopkins Hospital, Baltimore, MD.

² Department of Neurosurgery, Brain Research Institute, Niigata University, Niigata, Japan.

³ Department of Oncology, Tongji Hospital, Wuhan, China.

⁴ Department of Neurosurgery, University Medical Center Düsseldorf, Düsseldorf, Germany.

Keywords

autophagy, chloroquine, combination treatment, gamma-secretase inhibitor, glioblastoma.

Corresponding author:

Manabu Natsumeda, MD, PhD, Department of Pathology, Division of Neuropathology, Johns Hopkins University School of Medicine, Ross Building 558, 720 Rutland Ave., Baltimore, MD 21205 (E-mail: mnatsumeda@bri.niigata-u.ac.jp)

Received 07 August 2015

Accepted 25 November 2015

Published Online Article Accepted

27 November 2015

doi:10.1111/bpa.12343

Abstract

Glioblastomas are highly aggressive tumors that contain treatment resistant stem-like cells. Therapies targeting developmental pathways such as Notch eliminate many neoplastic glioma cells, including those with stem cell features, but their efficacy can be limited by various mechanisms. One potential avenue for chemotherapeutic resistance is the induction of autophagy, but little is known how it might modulate the response to Notch inhibitors. We used the γ -secretase inhibitor MRK003 to block Notch pathway activity in glioblastoma neurospheres and assessed its effects on autophagy. A dramatic, several fold increase of LC3B-II/LC3B-I autophagy marker was noted on western blots, along with the emergence of punctate LC3B immunostaining in cultured cells. By combining the late stage autophagy inhibitor chloroquine (CQ) with MRK003, a significant induction in apoptosis and reduction in growth was noted as compared to Notch inhibition alone. A similar beneficial effect on inhibition of clonogenicity in soft agar was seen using the combination treatment. These results demonstrated that pharmacological Notch blockade can induce protective autophagy in glioma neurospheres, resulting in chemoresistance, which can be abrogated by combination treatment with autophagy inhibitors.

INTRODUCTION

Glioblastomas are the most common primary adult brain malignancy, comprising more than 50% of all gliomas (23). Despite some advances in therapeutic options, outcomes remain dismal with a median overall survival of 14.6 months and a 2-year survival rate of 26.5% (33). Treatment resistant stem-like glioma cells have been proposed as one reason for treatment failure (4, 8, 10, 25, 36, 38). We (3, 9) and others (30, 34) have demonstrated the efficacy of γ -secretase inhibitors (GSI), which block Notch pathway activity, using *in vitro* and *in vivo* glioma models. However, success has been limited in clinical trials using GSIs as a single agent in gliomas (17), and in other solid tumors alone (17, 35) or in combination with other drugs (5, 26, 29). We, therefore, examined if induction of autophagy might be limiting the therapeutic efficacy of Notch inhibitors.

Autophagy is a dynamic process by which cellular organelles and proteins are sequestered, delivered to lysosomes and digested (37). Induction of autophagy has been identified as a potential mechanism for resistance to chemotherapy (16) including temozolomide (14, 18, 19, 22, 42) as well as radiation treatment (13, 41), which represent the standard therapies for glioblastoma. Manipulation of autophagy has increasingly been explored as a treatment

strategy in many cancers (21). However, there is minimal data on the effects of the Notch pathway on autophagy in cancer (12). We examined if Notch pathway blockade using the GSI MRK003 would induce autophagy in glioma neurosphere lines, and found that it does. We next explored a therapeutic regimen using the late stage autophagy inhibitor, chloroquine (CQ), in conjunction with MRK003, and showed that the combination induced apoptosis and more effectively decreased cell growth, proliferation and clonogenicity.

MATERIALS AND METHODS

Cell culture conditions and drug preparation

HSR-GBM1 and JHH520 glioblastoma neurosphere lines were used, and their identity was authenticated at the Johns Hopkins Core Laboratory through short tandem repeat (STR) analysis. HSR-GBM1 was a kind gift from Dr. Angelo Vescovi, JHH520 from Dr. Gregory Riggins. The HSR-GBM1 is completely methylated at the MGMT locus but resistant to temozolomide *in vitro*, lacks mutation at the IDH1 and alterations in p53. For treatment studies, neurospheres were disassociated into single cell

suspensions using Accutase (Sigma Aldrich, St Louis, MO, USA), counted, plated and allowed to grow overnight in Neural Stem Cell medium supplemented with 20 ng/mL of human epidermal growth factor and 10 ng/mL of human fibroblast growth factor (Peprotech, Rocky Hill, NJ, USA). All cells were grown in a humidified atmosphere containing 5% CO₂ at 37°C. The next morning, GSI MRK003, generously provided by Merck Research Laboratories (Boston, MA, USA), dissolved in dimethyl sulfoxide (DMSO) (Sigma Aldrich, St Louis, MO, USA) at final concentrations of 0.5 to 5 μM, chloroquine diphosphate (CQ) (Sigma Aldrich, St Louis, MO, USA), dissolved in phosphate buffered saline (PBS) at a final concentration of 10 μM, or DMSO (1:1000 dilution) was added to the media. Bafilomycin A1 (BafA1) (Sigma-Aldrich, St Louis, MO, USA) was dissolved in DMSO at final concentrations of 0.5–5 nM. 3-methyladenine (3-MA) (Selleckchem, Houston, TX, USA) was diluted in DMEM at a final concentration of 10 mM.

Quantitative real-time PCR analyses

Cells were collected after treatment with 0–5 μL of MRK003 for 48 h. RNA extracted was performed using the RNeasy Mini Kit (Qiagen) with on-column DNA digestion to prevent amplification of genomic DNA. Reverse transcription into complementary DNA (cDNA) was performed. cDNA levels were analyzed by quantitative real-time PCR analysis with SsoAdvanced Universal SYBR Green Supermix (Bio-Rad, Hercules, CA, USA) on an iQ5 Multicolor real-time PCR detection system. Standard curves were used to determine expression levels and all values were normalized to β-actin. Statistical comparisons were between at least three biological replicates, each with triplicate technical replicates. Primer sequences were as follows: HES1 forward F: 5'-GTG-AAG-CAC-CTC-CGG-AAC-3', reverse R: 5'-CGT-TCA-TGC-ACT-CGC-TGA-3'; HES5 forward F: 5'-GTG-CCT-CCA-CTA-TGA-TCC-TTA-AA-3', reverse R: 5'-AGT-ACA-AAG-TCG-TGC-CCA-CA-3'; HEY1 forward F: 5'-TCT-GAG-CTG-AGA-AGG-CTG-GT-3', reverse R: 5'-CGA-AAT-CCC-AAA-CTC-CGA-TA-3'; β-actin forward F: 5'-CCC-AGC-ACA-ATG-AAG-ATC-AA-3', reverse R: 5'-CGA-TCC-ACA-CGG-AGT-ACT-TG-3'.

Western blot analysis

Proteins were extracted from HSR-GBM1 and JHH520 after treatment with MRK003 and/or CQ for 48–72 h, unless otherwise indicated. The cells were lysed in RIPA buffer containing protease inhibitor cocktail (Sigma-Aldrich, St Louis, MO, USA) and phosphatase inhibitors on ice for 10 minutes then centrifuged at 4°C and 14,000 rpm for 5 minutes to remove cellular debris. Protein quantification was done using the Bio-Rad protein assay (Bio-Rad, Hercules, CA, USA). Subsequently, protein separation was performed on 12% (for LC3B protein analysis) or 4%–12% (for analysis of other proteins) SDS-polyacrylamide gel, and transferred onto nitrocellulose membranes (Invitrogen, Carlsbad, CA, USA). Membranes were then probed with primary antibodies at 4°C overnight. The following primary antibodies were used: LC3B, P62/SQSTM1, phospho-AKT (Ser 473), AKT (C6E7), cleaved PARP, cleaved NOTCH1 (Val1744)(D3B8) (1:1000 dilution, Cell Signaling, Danvers, MA, USA), HES1 (1:800 dilution, Aviva Systems Biology, San Diego, CA, USA), β-actin (1:5000 dilution, Sigma-Aldrich, St Louis, MO, USA). Secondary antibodies conjugated to horseradish

peroxidase (KPL, Gaitersberg, MD, USA) were incubated for 1 h at room temperature and detected with a Western Lightning Plus ECL chemiluminescent kit (PerkinElmer, Waltham, MA). All blots were repeated at least three times and representative blots are shown. Densitometry was performed using Image J Ver. 1.440 software (<http://rsb.info.nih.gov/ij/>) (31).

Immunofluorescence and immunohistochemical analyses

HSR-GBM1 cells were treated with DMSO or 5 μM MRK003 for 48 h, or starved for 4 h in Earle's Basic Salt Solution (EBSS). The cells were subsequently pelleted, fixed in 10% formalin and embedded in paraffin. Antigen retrieval was performed by heating in a pressure cooker for 30 minutes in Target Retrieval Solution (Dako, Glostrup, Denmark). Sections were stained using anti-LC3B rabbit polyclonal antibodies (1:10,000 dilution, ab51520, Abcam, Cambridge, UK and 1:500 dilution, Cell Signaling, Danvers, MA, USA) at 4°C overnight. The sections were stained by avidin-biotin-peroxidase complex method (Vector, Burlingame, CA, USA) with secondary antibody incubation for 30 minutes at a dilution of 1:5000, diaminobenzidine as the chromogen and counterstained with hematoxylin.

For immunofluorescence staining, HSR-GBM1 and JHH520 cells were grown in 10% FBS DMEM in 12 well plates on coverslips. From the next day, the cells were treated with DMSO or 5 μM MRK003 for 48 h. The cells were subsequently fixed in 4% paraformaldehyde, permeabilized in ice cold (–20°C) methanol for 15 minutes, blocked for 30 minutes with 5% normal goat serum (NGS) with 0.3% Triton X solution. Sections were stained using anti-LC3B rabbit monoclonal antibody (1:2000 dilution, ab51520, Abcam, Cambridge, UK), which was added in 5% NGS with 0.3% Triton X solution at 4°C overnight. After washing with PBS, cells were incubated for 90 minutes at a dilution of 1:400 in Cy-3 (Jackson Immunoresearch Laboratories Inc., West Grove, PA, USA) conjugated secondary antibody. After washing with PBS, nuclei were counterstained with DAPI 4', 6-diamidino-2-phenylindole and coverslips were mounted on slides with antifade (Vectastain Elite, Vector Laboratories, Burlingame, CA, USA). Confocal imaging was done using the Fluoview 1000 (Olympus America, Melville, NY, USA).

Determination of cell growth

3-(4,5-dimethylthiazol-2-yl)-5-(3-carboxymethoxyphenyl)-2-(4-sulfophenyl)-2H-tetrazolium (MTS) assays were performed to determine growth in viable cell mass. Cells were dissociated and seeded into 96-well plates at a density of 5000 per well in 200 μL of medium and treated with DMSO, 5 μM MRK003 and/or 10 μM CQ and incubated in 5% CO₂ at 37°C. For the plate readings, 20 μL of MTS solution was added to each well after 0–96 h postplating and incubated for 1 h, protected from light. The optical density at 490 nm was subsequently measured by spectrophotometer. The experiments were repeated at least three times for each cell line.

Cell proliferation assay

Cells were treated with DMSO, 5 μM MRK003 and/or 10 μM CQ for 72 h. Cells were subsequently fixed and stained for Ki67 per

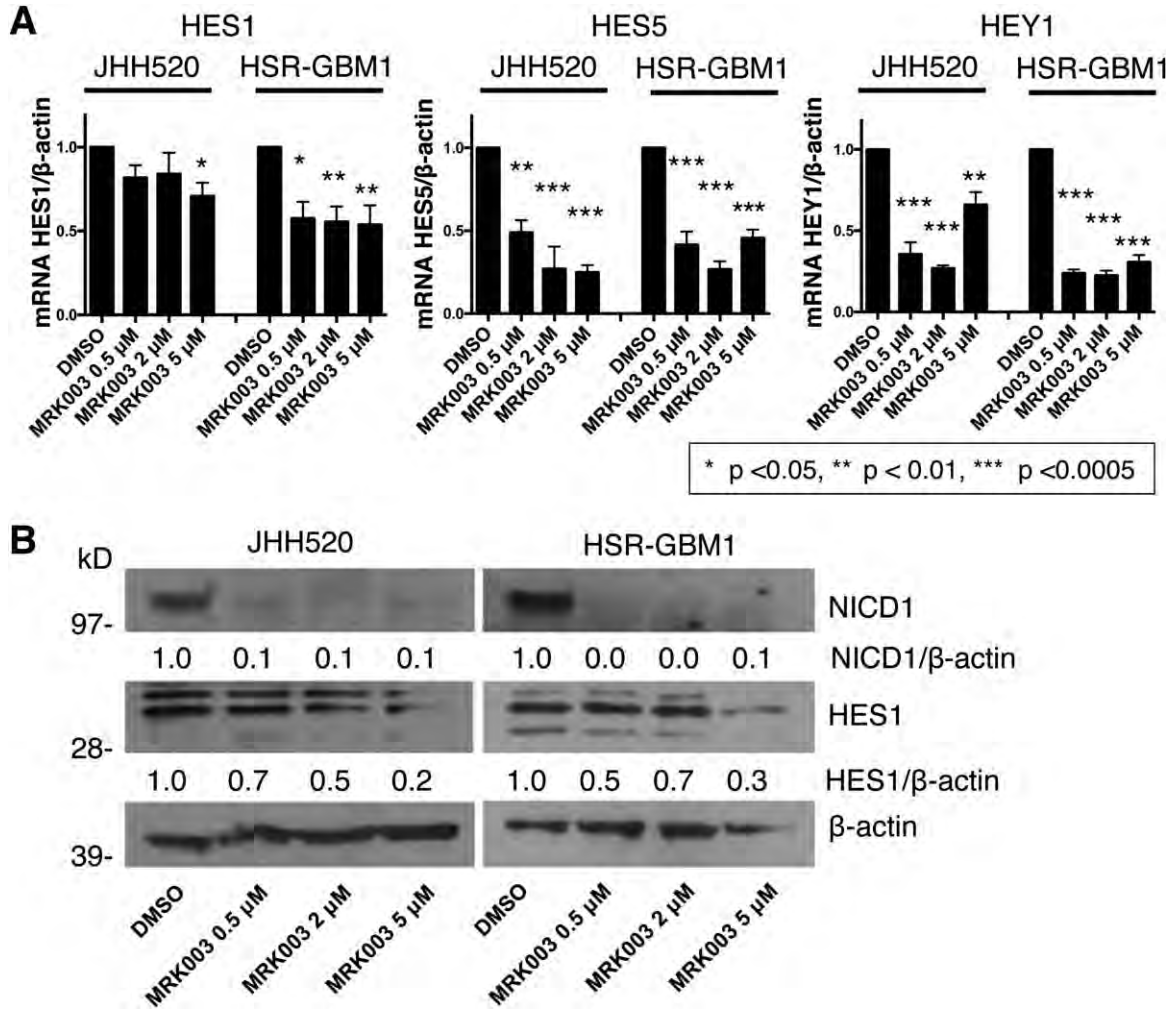


Figure 1. MRK003 inhibits Notch pathway. **A.** Treatment with MRK003 inhibited downstream Notch pathway transcription factors HES1, HES5, HEY1 in JHH520 and HSR-GBM1 lines at the mRNA level. A statistically significant up to 50% reduction of HES1 was seen after treatment with 5 μM MRK003. Likewise, an approximately 75% decrease of HES5 and approximately 80% decrease of HEY1

compared to DMSO control was seen after 2 μM MRK003 treatment in both lines. Stars denote *P* values vs. DMSO. **B.** Treatment with 0.5 μM MRK003 almost completely inhibited cleaved (active) Notch1 expression in JHH520 and HSR-GBM1 lines. Inhibition of HES1 was observed after treatment with 5 μM MRK003 in both cell lines.

manufacturer’s instructions using the Muse Ki67 Proliferation Assay (Millipore, Billerica, MA, USA). Cells incubated with IgG1 control in parallel were used to set the gates. The percentage of Ki67 positive cells was determined using the Muse Cell Analyzer. Analyses were repeated at least three separate times for each cell line.

Cell cycle analyses

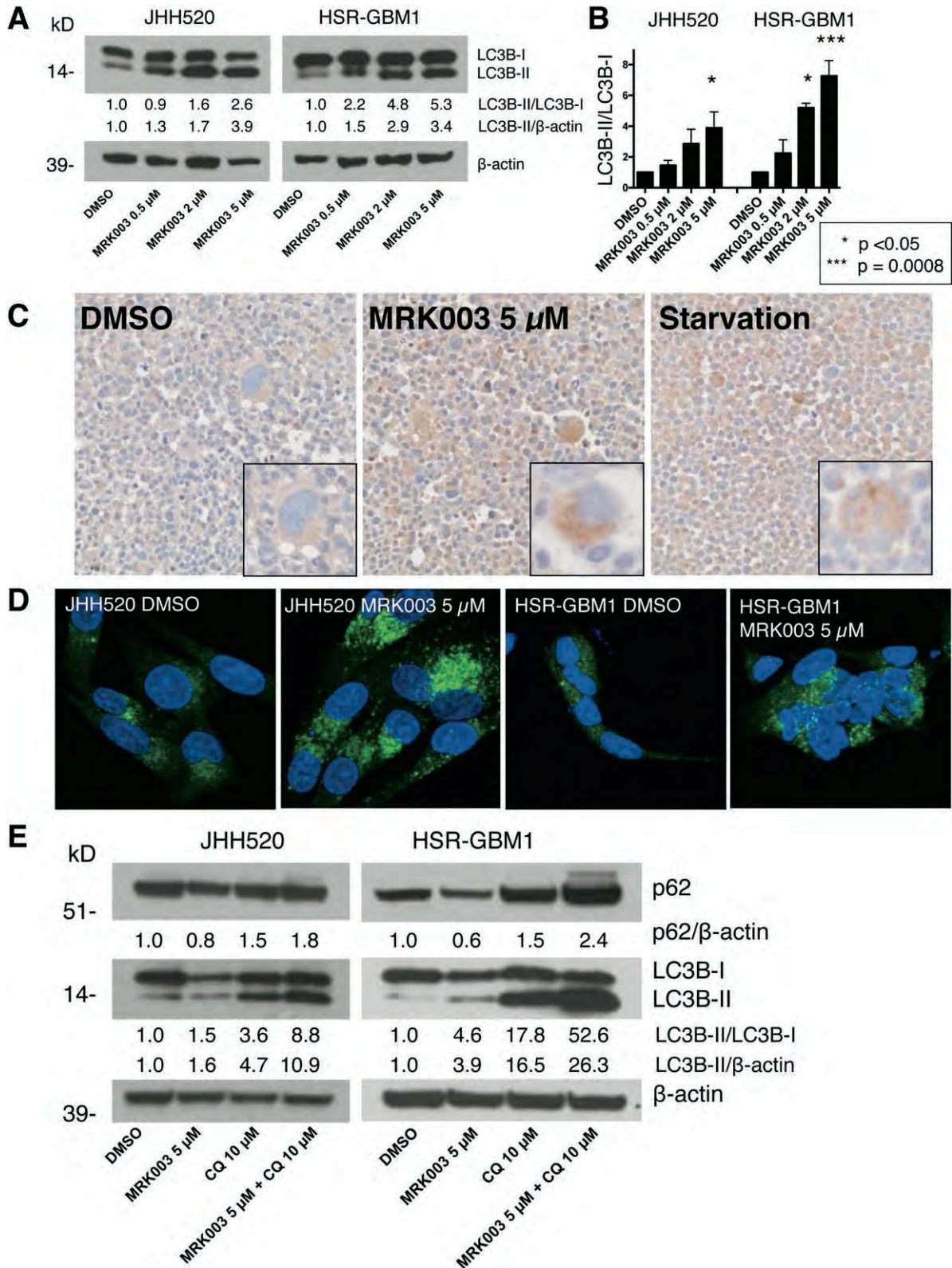
Cells were treated with DMSO, 5 μM MRK003 and/or 10 μM CQ for 72 h. Cells were then fixed with 70% ethanol for at least 3 h and stained with Muse Cell Cycle Reagent. Cell cycle analyses were performed using the Muse Cell Analyzer and percentages of sub-G1, G0/G1, S and G2/M populations were determined using FlowJo software. Analyses were repeated at least three separate times for each cell line.

Apoptosis assay

Apoptosis was measured using the Muse Annexin V and Dead Cell Assay per the manufacturer’s protocol. Neurospheres were treated with DMSO, 5 μM MRK003 and/or 10 μM CQ for 72 h. Cells were resuspended in DMEM/F12 without phenol red with 1% Bovine Serum Albumin (BSA) before analysis. Percentage of apoptotic and dead cells were analyzed using the Muse Cell Analyzer. Analyses were repeated at least three separate times for each cell line.

Clonogenic assays

Neurosphere media was mixed 3:1 with 4% agarose (Invitrogen, Carlsbad, CA, USA) to make the bottom layer, which was used to coat each well of a six-well plate. Neurospheres treated with DMSO, 2 μM MRK003 or a combination of 2 μM MRK003 and 10 μM CQ for 72 h were dissociated and added to 7:1 media and



agarose mixture at a concentration of 5000 cells per 2 mL to make the top layer. After the agarose gelled, 2 mL of fresh media and DMSO or drug were added to the top of each well. Media and drug

were changed every 1–4 days during the growth phase of the clonogenic assay. The cells were allowed to form colonies for 19–23 days. Colonies were visualized by staining with nitroblue

Figure 2. Autophagy is induced after MRK003 treatment *in vitro*. **A.** Western blot showed induction of autophagy as seen by the increase of the LC3B-II band after GSI treatment in JHH520 and HSR-GBM1 lines in a dose-dependent manner. **B.** Quantification of LC3B-II/LC3B-I from three separate blots. **C.** HSR-GBM1 cells were treated with DMSO, 5 μ M MRK003, or EBSS, then pelleted and stained for LC3B. Note the punctate staining of the cytoplasm of glioma cells after treatment with MRK003 and EBSS, but not DMSO (original magnification all \times 400). **D.** HSR-GBM1 and JHH520 cells were treated with DMSO

or 5 μ M MRK003 and stained for LC3B. Note the markedly increased punctate staining in the cytoplasm of glioma cells after treatment with MRK003 compared to DMSO by immunofluorescence analysis of LC3B (original magnification all \times 640). **E.** Accumulation (loss of clearance) of LC3B-II after treatment with chloroquine (CQ). A decrease in p62 after MRK003 treatment alone and increase of p62 was observed after combined treatment with MRK003 and CQ, suggesting inhibition of autophagy by CQ.

tetrazolium (NBT) in a tissue culture incubator overnight at 37°C after which they were imaged. Colonies greater than 50 μ m in diameter were scanned and counted using MCID Elite software (Cambridge, England, UK). For each well, at least three images were scanned and counted. Triplicates of each condition were plated and the experiment was repeated three times.

Statistical analyses

Differences between three or more groups were assessed using one way ANOVA test with post hoc Tukey's multiple comparison test. Error bars represent standard error of means. All statistical tests were performed using the GraphPad Prism 6 software (GraphPad Software, La Jolla, CA, USA). *P* values less than 0.05 were considered statistically significant.

RESULTS

MRK003 inhibits Notch pathway targets

Notch pathway activity was assessed using quantitative RT PCR to measure levels of the canonical Notch pathway transcriptional targets HES1, HES5 and HEY1 after 48-h treatment of glioblastoma neurospheres with MRK003. A statistically significant, dose dependent, up to 50% reduction of HES1 was seen after treatment with 5 μ M MRK003. Likewise, an approximately 75% decrease of HES5 and approximately 80% decrease of HEY1 was seen after 2 μ M MRK003 treatment in both cell lines (Figure 1A). Interestingly, the treatment with MRK003 at a high dose (5 μ M) resulted in a paradoxical increase in the mRNA levels of HES5 and HEY1. We have previously observed this paradoxical increase when blocking Notch activity in brain tumors with relatively high concentrations of GSI or arsenic trioxide, and speculated a feedback or resistance mechanism of cells surviving maximal therapy [(6) and unpublished data]. We next assessed the effects of MRK003 on Notch pathway activity at the protein level. Treatment with 0.5 μ M MRK003 almost completely inhibited cleaved (active) Notch1 expression in JHH520 and HSR-GBM1; inhibition of HES1 was also observed after treatment with 5 μ M MRK003 in both neurosphere lines (Figure 1B).

Notch inhibition induces autophagy in glioblastoma

Induction of autophagy, evidenced by a dose-dependent increase in LC3B-II/LC3B-I ratio, was seen after 48-h treatment with 0.5–5 μ M of MRK003 in both glioblastoma neurosphere lines (Figure 2A,B). In mature autophagosomes, LC3B-I undergoes a post-translational modification to LC3B-II increasing its hydrophobic

nature resulting in further migration on electrophoresis. A significant ($P < 0.05$) increase in LC3B-II/LC3B-I ratio averaging over threefold was seen after 5 μ M treatment with MRK003 in JHH520; likewise, over fourfold ($P < 0.05$) and sixfold ($P = 0.0008$) increases were seen after 2 and 5 μ M treatment in HSR-GBM1 (Figure 2B).

Having observed an induction of autophagy after treatment with MRK003 by western blotting, we next sought to determine if induction of autophagy could be confirmed by immunohistochemical analysis in HSR-GBM1 cells and by immunofluorescence analysis in both cell lines. Increased punctate staining of LC3B in the cytoplasm of HSR-GBM1 cells, suggesting mature autophagosomes, was observed after 48 h treatment with 5 μ M MRK003 and 4 h starvation in EBSS media, but not in DMSO control (Figure 2C). Immunofluorescence analysis showed markedly increased punctate staining for LC3B in the cytoplasm of tumor cells compared to DMSO control in both cell lines (Figure 2D).

Given the induction of potentially protective autophagy after treatment with MRK003, a combinatorial regimen using the late stage autophagy inhibitor CQ in conjunction with MRK003 was explored. CQ blocks LC3B clearance via lysosomal inhibition, causing its accumulation in tumor cells (1). Consistent with this mechanism, we saw a very strong induction of the LC3B-II band after CQ treatment in both lines, indicating in this context a blockade of late autophagy (Figure 2E). We chose a dosage of 5 μ M MRK003 for combination experiments, because maximal suppression of HES1 protein and induction of autophagy was seen at this level. An increase in LC3B-II/LC3B-I ratio was also seen after treatment with the two drugs in combination (Figure 2E). To help determine if this reflected an ongoing increase in autophagy or a late blockade of the process, we assessed expression of p62, which recognizes autophagic cargo and mediates formation of selective autophagy (27). p62 is known to be upregulated when autophagy is inhibited, resulting in intracellular waste accumulation. A 40% decrease in p62 was seen after induction of autophagy by MRK003 and was subsequently increased 2.4 fold after treatment with both 5 μ M MRK003 and 10 μ M CQ in HSR-GBM1, suggesting that the dominant process when both agents are used is inhibition of autophagy (Figure 2E). Interestingly, p62 was decreased by only 20% in JHH520 after treatment with 5 μ M MRK003, and the increase in p62 after combination MRK003 and CQ treatment was a modest 1.8-fold compared to DMSO control (Figure 2E). Likewise, a similar lack of p62 decrease after MRK003 treatment and only modest (1.6-fold compared to 3.9-fold for HSR-GBM1) increase of p62 was seen after combination MRK003 and BafA1 treatment in JHH520 (Supporting Information Figure 1B), suggesting a cell line dependent variability in effects.

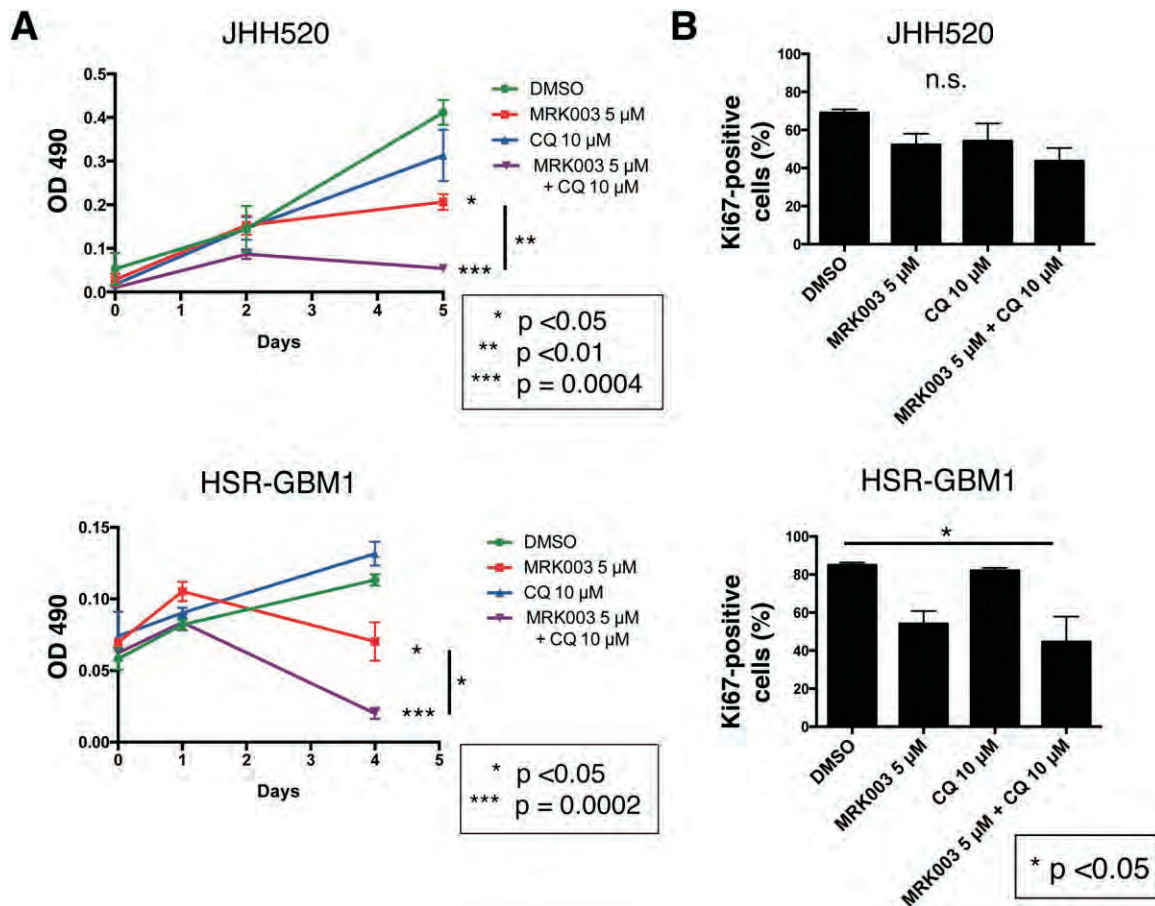


Figure 3. Combination treatment with MRK003 and chloroquine more effectively inhibits glioma neurosphere growth and proliferation. **A.** 5,000 JHH520 and HSR-GBM1 cells per well were plated in a 96-well plate and cell viability was assessed by MTS assay after treatment with DMSO, 5 μ M MRK003, 10 μ M CQ, and a combination of 5 μ M MRK003 and 10 μ M CQ at days 0–5 of treatment. Combination treatment markedly reduced growth compared to DMSO (JHH520;

$P = 0.0004$, HSR-GBM1; $P = 0.0002$) and MRK003 alone (JHH520; $P < 0.01$, HSR-GBM1; $P < 0.05$) in both neurosphere lines. Stars denote P values vs. DMSO unless otherwise specified. **B.** Ki67 MUSE assays were performed to assess effects on proliferation. A modest but significant decrease in the percentage of Ki67-positive cells was observed after combination treatment compared to DMSO control in the HSR-GBM1 line.

Combination treatment with MRK003 and chloroquine inhibits growth and proliferation

The effects of combination treatment with MRK003 and CQ on growth of the two glioblastoma neurosphere lines were examined using the MTS assay. In both lines, 10 μ M CQ did not have a significant effect on the viable cell mass, while Notch inhibition caused a moderate slowing ($P < 0.05$) in the glioma growth (Figure 3A). In both cell lines, culture growth was significantly reduced compared to DMSO controls (JHH520; $P = 0.0004$, HSR-GBM1; $P = 0.0002$) and MRK003 alone (JHH520; $P < 0.01$, HSR-GBM1; $P < 0.05$) when MRK003 treatment was paired with inhibition of autophagy (Figure 3A).

We sought to determine whether combination treatment of MRK003 with another late stage autophagy inhibitor, BafA1, would exhibit increased cytotoxicity. Combination treatment with 2 μ M of MRK003 and 0.5 μ M of BafA1 showed a drastic reduction of cell growth compared to DMSO (JHH520; $P < 0.0001$, HSR-GBM1; $P < 0.001$) (Supporting Information Figure 1A) after

5 days of treatment. However, while the addition of BafA1 to 2 μ M MRK003 resulted in fewer viable cells, this increase over the GSI alone was not statistically significant, perhaps because the anti-growth effects of MRK003 were particularly prominent in these studies. Similar effects were seen with combination of 2 μ M MRK003 and 5 μ M of BafA1 (data not shown). However, no reduction in p62 was noted in JHH520 cells after MRK003 treatment. Increases in LC3B-II/LCB-I ratio and p62 were seen after combination treatment with MRK003 and BafA1, suggesting inhibitory effects of BafA1 at the late stage of autophagy similar to CQ (Supporting Information Figure 1B).

A combination of 2 μ M MRK003 and 10 mM of the early stage autophagy inhibitor, 3-MA, showed significant reduction of cell growth compared to DMSO control (JHH520; $P = 0.002$, HSR-GBM1; $P = 0.002$) and MRK003 alone (JHH520; $P = 0.03$, HSR-GBM1; $P = 0.0009$) after 5 days of treatment (data not shown). Western blots showed a 50% decrease in p62 expression compared to DMSO after MRK003 treatment and a 3.2-fold increase in p62 after combination MRK003 and 3-MA treatment in HSR-GBM1

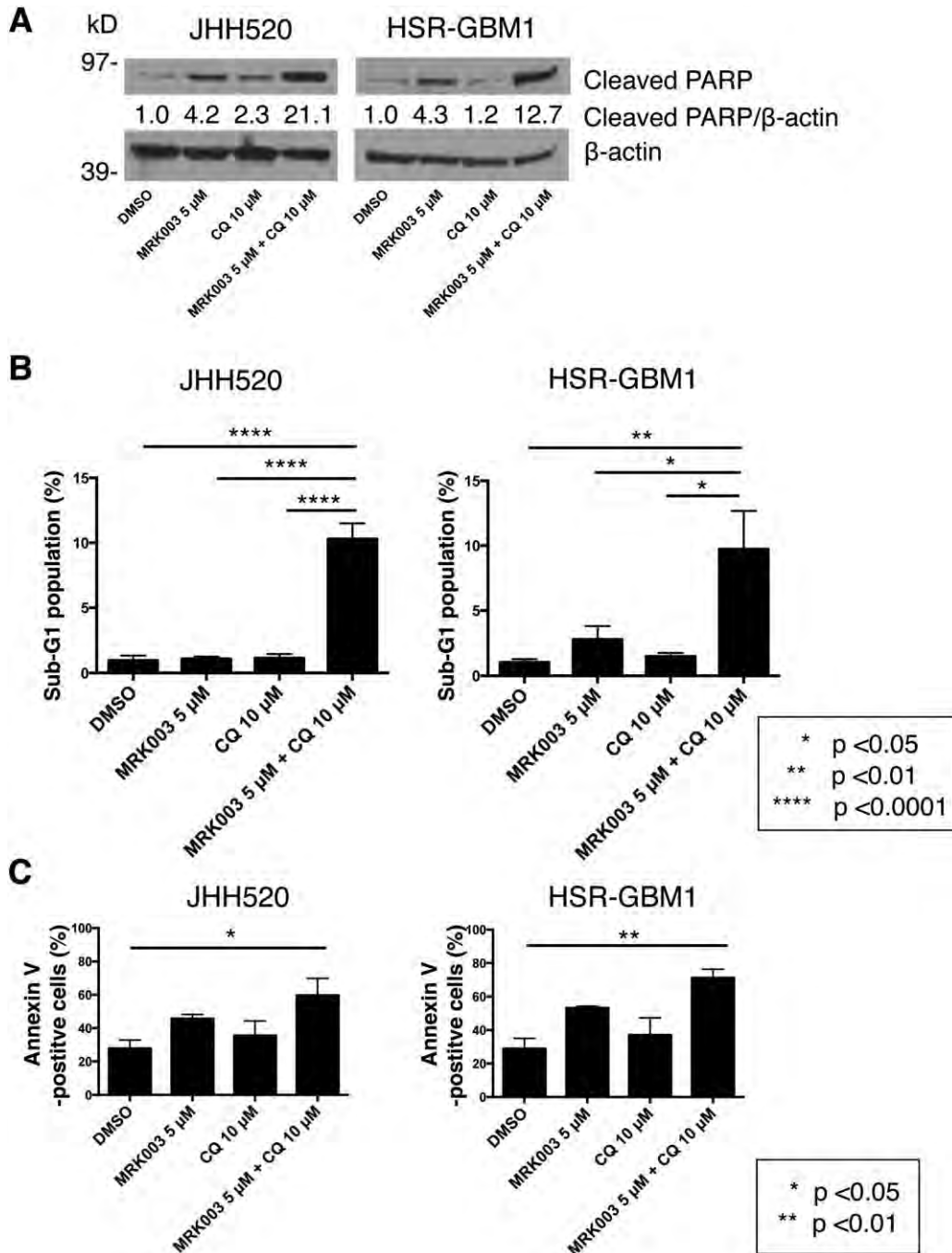


Figure 4. Induction of apoptosis is observed after combination treatment with MRK003 and chloroquine. **A.** Western blot showed approximately fourfold increase of cleaved PARP after 5 μ M MRK003 treatment compared to DMSO control and 12.7-fold to 21.1-fold increase after combination treatment compared to DMSO

control. **B.** Cell cycle analysis and **C.** Annexin V MUSE assays were performed to assess effects on apoptosis. An approximately 10-fold increase in percentage of sub-G1 population and modest but significant increase in percentage of Annexin V-positive cells were seen after combination treatment compared to DMSO control.

(Supporting Information Figure 2). A 40% reduction in LC3B-II/I ratio was seen after 10 mM 3-MA treatment compared to DMSO control and 30% decrease in LC3BII/I ratio was seen after combination MRK003 and 3-MA compared to MRK003 alone, suggesting the inhibition of early stage autophagy.

To determine if combination treatment altered the proliferation of glioblastoma neurospheres, the percentage of Ki67-positive cells was assessed using the MUSE Ki67 assay. A modest but significant reduction in the percentage of Ki67-positive cells was observed after combination treatment with 5 μ M MRK003 and 10 μ M CQ

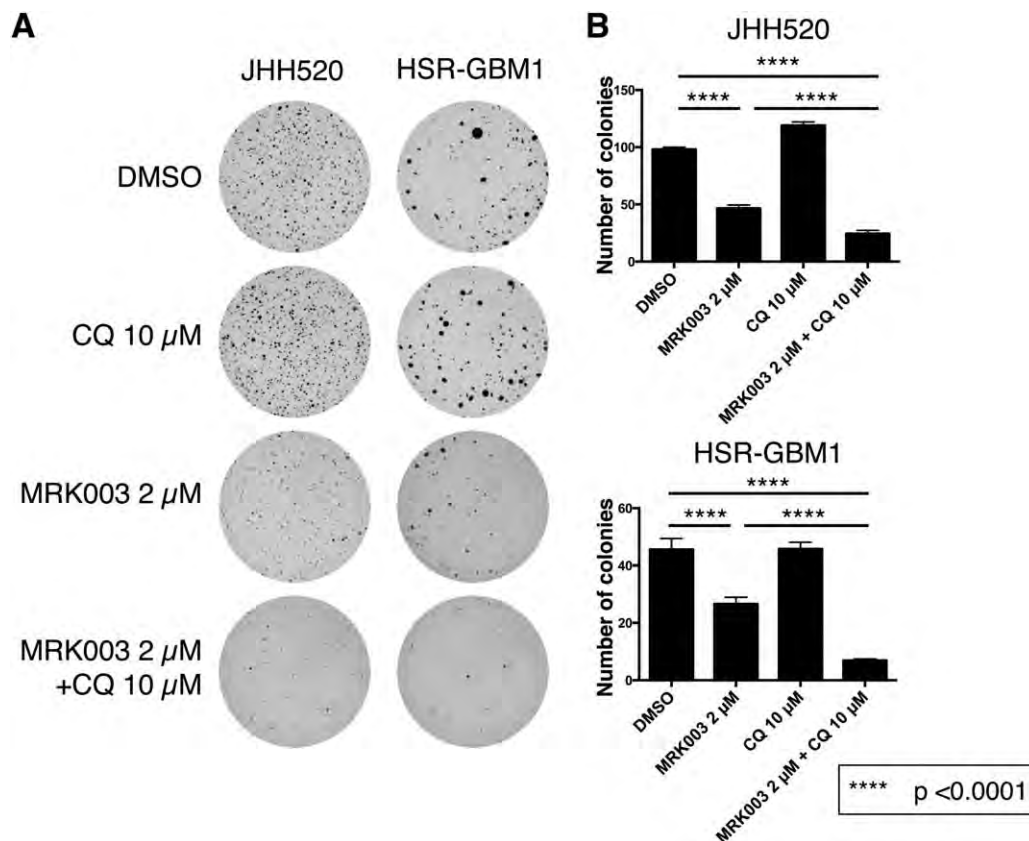


Figure 5. Combination treatment with MRK003 and chloroquine reduces clonogenicity in glioblastoma neurosphere lines. **A.** Representative images of nitroblue tetrazolium-stained colonies formed by JHH520 and HSR-GBM1 cells after treatment with DMSO,

2 μM MRK003, 10 μM CQ and combination MRK003 and CQ are shown. **B.** Quantification of number of colonies depicted in A, showing markedly reduced colony formation after combination therapy.

compared to DMSO control in the HSR-GBM1 line ($P < 0.05$) (Figure 3B). However, this reduction in proliferation following combination therapy was not significantly greater than noted after Notch inhibition alone, suggesting that it was not the only mechanism by which overall growth was affected.

Combination treatment with MRK003 and chloroquine induces apoptosis

Given the limited effect of combination treatment on proliferation, we examined changes in apoptosis. An approximately fourfold induction in the apoptotic mediator cleaved PARP was noted after 5 μM MRK003 treatment in both lines, with a lesser increase seen after pharmacological inhibition of autophagy (Figure 4A). In contrast, a dramatic 12-fold to 21-fold induction was seen after combination treatment. Only a minor, nonsignificant increase was observed in the percentage of sub-G1 population by cell cycle analysis after treatment with 5 μM of MRK003 compared to DMSO. In contrast, an 8.9-fold to 10.6-fold increase in percentage of sub-G1 population was observed after combination treatment (Figure 4B, Supporting Information Figure 2A,B).

With respect to other cell cycle alterations, no significant change in percentage of G0/G1, S, or G2/M population was noted after 72-h combination treatment of JHH520; a modest reduction of percent-

age of G0/G1 population was noted after 72-h combination treatment of HSR-GBM1 (Supporting Information Figure 2C). Although cell cycle arrest was not noted after 72-h combination treatment, G2/M arrest was seen after 48-h combination treatment in line (data not shown), suggesting that cells in G2/M arrest eventually undergo apoptosis. Finally, a significant but less pronounced increase in the percentage of total apoptotic cells was observed after combination treatment compared to DMSO control in both lines using the Annexin V assay (JHH520; $P < 0.05$, HSR-GBM1; $P < 0.01$) (Figure 4C). These data support the concept that induction of autophagy prevents apoptosis following Notch blockade in glioma cells, and that CQ can suppress this and increase the cytotoxicity of GSI.

Clonogenic capacity is reduced after combination treatment with MRK003 and chloroquine

Having confirmed the increase of apoptosis caused by inhibition of autophagy by CQ, we next looked at clonogenic capacity after monotherapy and combination treatment using the soft agar assay. These were performed using 2 μM rather than 5 μM MRK003, as the higher GSI dose resulted in too few colonies for an additive effect of the autophagy inhibitor to be examined. A representative

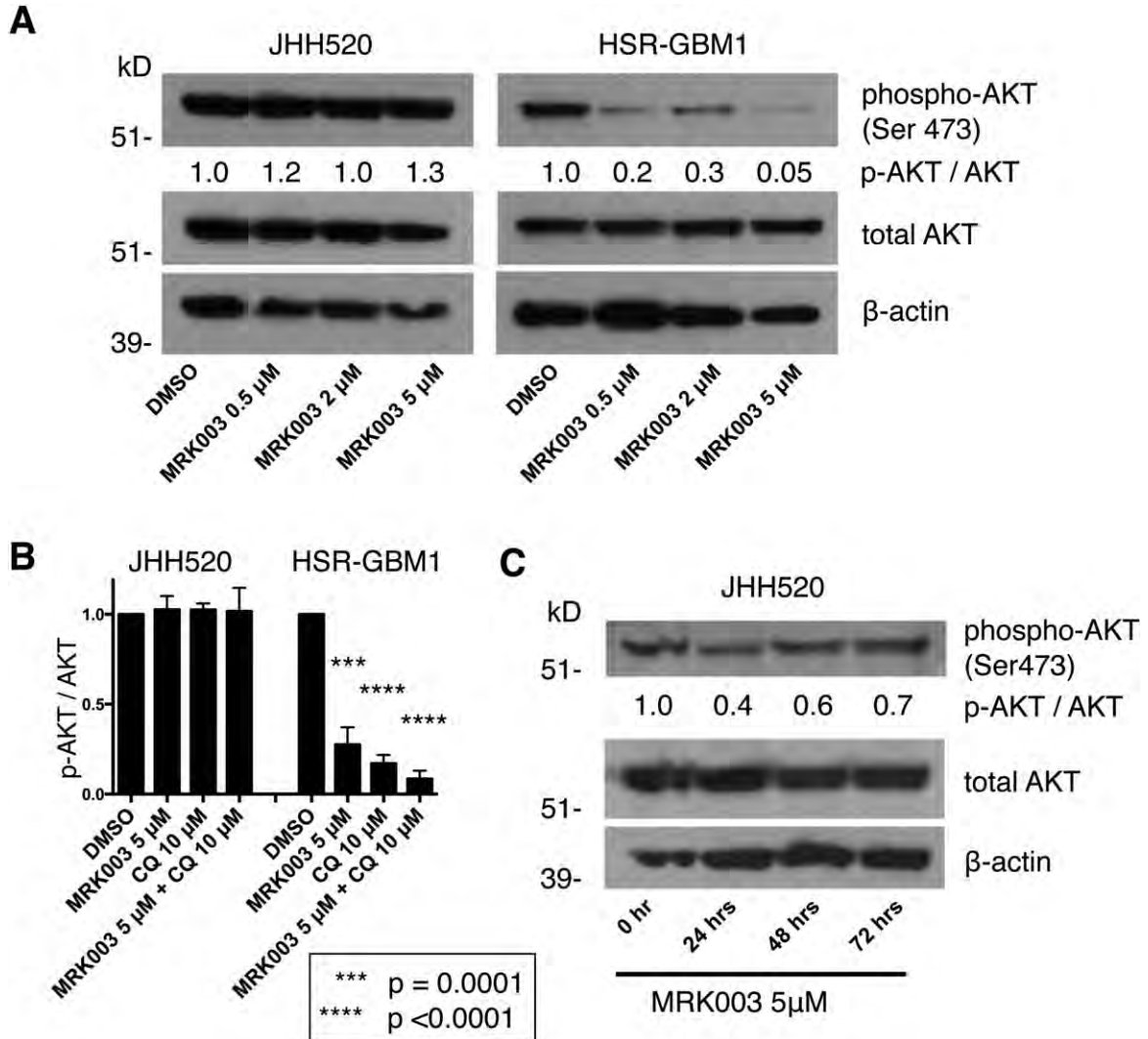


Figure 6. Phospho-AKT is inhibited by MRK003 and MRK003 induces autophagy *in vivo*. **A, B.** Phospho-AKT (Ser 473) was significantly inhibited by MRK003 after treatment with 0.5–5 μM MRK003 in HSR-GBM1 for 48 h ($P \leq 0.0001$). However, inhibition of phospho-AKT was

not seen in JHH520 after 5 μM MRK003 treatment for 48 h. **C.** Phospho-AKT was most inhibited by 5 μM MRK003 treatment for 24 h, but subsequently upregulated after 48–72 h treatment in JHH520 line.

experiment shows an approximately 40%–50% decrease in the number of colonies after treatment with 2 μM MRK003 alone compared to DMSO in both cell lines (Figure 5A,B). However, with combination therapy a 75%–85% reduction in clonogenicity was observed, and this was significantly more pronounced than the effect with 2 μM MRK003 alone (both $P < 0.0001$). The clonogenic assays were repeated three times for each cell line, and all of these experiments showed a significantly lower number of colonies for combination treatment than the GSI alone.

Inhibition of AKT following Notch inhibition

AKT activity is known to suppress autophagy (39), and is also modulated by Notch in cancers other than glioma (7, 24). We have previously shown that GSIs other than MRK003 can inhibit phosphorylation and activation of AKT (9) in glioblastoma. Using

MRK003, we found that phospho-AKT levels decreased dramatically 48 h after Notch inhibition at concentrations as low as 0.5 μM in HSR-GBM1 neurospheres (Figure 6A,B). JHH520 cells showed modest inhibition of AKT activity with greatest inhibition after 24 h treatment with 5 μM MRK003 (Figure 6C). However, further investigation is needed to elucidate whether autophagy after MRK003 treatment is mediated by mTORC2 inhibition.

DISCUSSION

Despite some recent advances in treatment, the prognosis for glioblastoma patients remains dismal. Induction of autophagy has been implicated as a potential resistance mechanism to general treatments in gliomas, and its manipulation has actively been investigated as a therapeutic strategy (15). However, little is known about

the role of Notch in regulating autophagy in gliomas, or the potential for autophagy to mediate resistance to pathway inhibitors such as GSIs. Increasing evidence suggests that the Notch pathway affects autophagosomal trafficking (2), and that inhibition of the Notch pathway induces autophagy in some types of cancer (12) and during differentiation of stem cells (32).

Our data provide initial evidence that pharmacological Notch pathway blockade can induce autophagy in gliomas. When neurosphere lines were treated with GSI, a dramatic several fold induction of the LC3B-II protein compared to LC3B-I was noted, as well as the emergence of punctate immunohistochemical LC3B staining in fixed cells, consistent with an increase in autophagic flux. However, a robust decrease in p62 following Notch blockade was only seen in one line, thus, clear induction of autophagy may be restricted to a subset of cases. Autophagy may also be present in a more complex *in vivo* treatment milieu, as analysis of orthotopic glioblastoma xenografts treated with the GSI from a prior study (3) has revealed focal punctate LC3B staining, but too little material was present for definitive conclusions to be drawn. Our findings are consistent with a very recent report demonstrating induction of autophagy after NOTCH1 knockdown by shRNA in a single glioma cell line (40).

The induction of autophagy is of potential clinical relevance, as combining the late stage autophagy inhibitor CQ with MRK003 resulted in a significant induction in apoptosis and reduction in growth and clonogenicity as compared to Notch inhibition alone. Similar growth changes were noted when combining Notch inhibition with the early stage autophagy inhibitor 3-MA. A few autophagy inhibitors have been clinically tested in gliomas. CQ is an antimalarial drug with lysosomotropic properties that inhibit lysosomal function. It is known to have central nervous system penetration and has been shown to effectively inhibit autophagy *in vitro* (28). A previous trial using radiation and carmustine with or without CQ in glioblastoma patients showed a trend toward increased median overall survival that was not significant (18). Hydroxychloroquine (HCQ), a derivative of CQ, shows equal potency to inhibit autophagy *in vitro* and has demonstrated less retinal toxicity. A trial of HCQ in conjunction with radiation therapy and temozolomide showed biological response caused by HCQ, but failed to improve overall survival in glioblastoma (28). New and more potent inhibitors of autophagy such as Lys05 (20) and VATG-027 (11) have been tested preclinically and await clinical validation.

We have demonstrated that pharmacological Notch blockade can induce protective autophagy in glioma neurospheres, which can be abrogated by combination treatment with CQ. Together, the two drugs efficiently induce apoptosis and decrease cell growth, proliferation and clonogenicity. A range of options for pharmacological inhibition of both Notch and autophagy exist, and combinatorial blockade of these two pathways represents a promising new treatment strategy for glioblastoma.

ACKNOWLEDGMENTS

We would like to acknowledge Dr. Jeff Mumm for assistance with the confocal microscope. The authors declare no conflict of interest. This study was funded by grant R01NS055089 to CGE.

REFERENCES

1. Amaravadi RK, Yu D, Lum JJ, Bui T, Christophorou MA, Evan GI *et al* (2007) Autophagy inhibition enhances therapy-induced apoptosis in a Myc-induced model of lymphoma. *J Clin Invest* **117**:326–336.
2. Barth JM, Kohler K (2014) How to take autophagy and endocytosis up a notch. *Biomed Res Int* **2014**:960803.
3. Chu Q, Orr BA, Semenkow S, Bar EE, Eberhart CG (2013) Prolonged inhibition of glioblastoma xenograft initiation and clonogenic growth following *in vivo* Notch blockade. *Clin Cancer Res* **19**:3224–3233.
4. Dean M, Fojo T, Bates S (2005) Tumour stem cells and drug resistance. *Nat Rev Cancer* **5**:275–284.
5. Diaz-Padilla I, Hirte H, Oza AM, Clarke BA, Cohen B, Reedjik M *et al* (2013) A phase Ib combination study of RO4929097, a gamma-secretase inhibitor, and temsirolimus in patients with advanced solid tumors. *Invest New Drugs* **31**:1182–1191.
6. Ding D, Lim K, Eberhart CG (2014) Arsenic trioxide inhibits Hedgehog, Notch and stem cell properties in glioblastoma neurospheres. *Acta Neuropathol Commun* **2**:31.
7. Efferson CL, Winkelmann CT, Ware C, Sullivan T, Giampaoli S, Tammam J *et al* (2010) Downregulation of Notch pathway by a gamma-secretase inhibitor attenuates AKT/mammalian target of rapamycin signaling and glucose uptake in an ERBB2 transgenic breast cancer model. *Cancer Res* **70**:2476–2484.
8. Eylar CE, Rich JN (2008) Survival of the fittest: cancer stem cells in therapeutic resistance and angiogenesis. *J Clin Oncol* **26**:2839–2845.
9. Fan X, Khaki L, Zhu TS, Soules ME, Talsma CE, Gul N *et al* (2010) NOTCH pathway blockade depletes CD133-positive glioblastoma cells and inhibits growth of tumor neurospheres and xenografts. *Stem Cells* **28**:5–16.
10. Frank NY, Schatton T, Frank MH (2010) The therapeutic promise of the cancer stem cell concept. *J Clin Invest* **120**:41–50.
11. Goodall ML, Wang T, Martin KR, Kortus MG, Kauffman AL, Trent JM *et al* (2014) Development of potent autophagy inhibitors that sensitize oncogenic BRAF V600E mutant melanoma tumor cells to vemurafenib. *Autophagy* **10**:1120–1136.
12. Hales EC, Taub JW, Matherly LH (2014) New insights into Notch1 regulation of the PI3K-AKT-mTOR1 signaling axis: targeted therapy of gamma-secretase inhibitor resistant T-cell acute lymphoblastic leukemia. *Cell Signal* **26**:149–161.
13. Ito H, Daido S, Kanzawa T, Kondo S, Kondo Y (2005) Radiation-induced autophagy is associated with LC3 and its inhibition sensitizes malignant glioma cells. *Int J Oncol* **26**:1401–1410.
14. Kanzawa T, Germano IM, Komata T, Ito H, Kondo Y, Kondo S (2005) Role of autophagy in temozolomide-induced cytotoxicity for malignant glioma cells. *Cell Death Differ* **11**:448–457.
15. Kaza N, Kohli L, Roth KA (2012) Autophagy in brain tumors: a new target for therapeutic intervention. *Brain Pathol* **22**:89–98.
16. Kondo Y, Kanzawa T, Sawaya R, Kondo S (2005) The role of autophagy in cancer development and response to therapy. *Nat Rev Cancer* **5**:726–734.
17. Krop I, Demuth T, Guthrie T, Wen PY, Mason WP, Chinnaiyan P *et al* (2012) Phase I pharmacologic and pharmacodynamic study of the gamma secretase (Notch) inhibitor MK-0752 in adult patients with advanced solid tumors. *J Clin Oncol* **30**:2307–2313.
18. Lee SW, Kim HK, Lee NH, Yi HY, Kim HS, Hong SH *et al* (2015) The synergistic effect of combination temozolomide and chloroquine treatment is dependent on autophagy formation and p53 status in glioma cells. *Cancer Lett* **360**:195–204.
19. Lin CJ, Lee CC, Shih YL, Lin TY, Wang SH, Lin YF, Shih CM (2012) Resveratrol enhances the therapeutic effect of temozolomide against malignant glioma *in vitro* and *in vivo* by inhibiting autophagy. *Free Radic Biol Med* **52**:377–391.
20. McAfee Q, Zhang Z, Samanta A, Levi SM, Ma X, Piao S *et al* (2012) Autophagy inhibitor Lys05 has single-agent antitumor activity and

- reproduces the phenotype of a genetic autophagy deficiency. *Proc Natl Acad Sci U S A* **109**:8253–8258.
21. Nagelkerke A, Bussink J, Geurts-Moespot A, Sweep FC, Span PN (2015) Therapeutic targeting of autophagy in cancer. Part II: pharmacological modulation of treatment-induced autophagy. *Semin Cancer Biol* **31**:99–105.
 22. Natsumeda M, Aoki H, Miyahara H, Yajima N, Uzuka T, Toyoshima Y *et al* (2011) Induction of autophagy in temozolomide treated malignant gliomas. *Neuropathology* **31**:486–493.
 23. Ohgaki H, Kleihues P (2005) Population-based studies on incidence, survival rates, and genetic alteration in astrocytic and oligodendroglial gliomas. *J Neuropathol Exp Neurol* **64**:479–489.
 24. Palomero T, Sulis ML, Cortina M, Real PJ, Barnes K, Ciofani M *et al* (2007) Mutational loss of PTEN induces resistance to NOTCH1 inhibition in T-cell leukemia. *Nat Med* **13**:1203–1210.
 25. Reya T, Morrison SJ, Clarke MF, Weissman IL (2001) Stem cells, cancer, and cancer stem cells. *Nature* **414**:105–111.
 26. Richter S, Bedard PL, Chen EX, Clarke BA, Tran B, Hotte SJ *et al* (2014) A phase I study of the oral gamma secretase inhibitor RO4929097 in combination with gemcitabine in patients with advanced solid tumors (PHL-078/CTEP 8575). *Invest New Drugs* **32**:243–249.
 27. Rogov V, Dotsch V, Johansen T, Kirkin V (2014) Interactions between autophagy receptors and ubiquitin-like proteins form the molecular basis for selective autophagy. *Mol Cell* **53**:167–178.
 28. Rosenfeld MR, Ye X, Supko JG, Desideri S, Grossman SA, Brem S *et al* (2014) A phase I/II trial of hydroxychloroquine in conjunction with radiation therapy and concurrent and adjuvant temozolomide in patients with newly diagnosed glioblastoma multiforme. *Autophagy* **10**:1359–1368.
 29. Sahebjam S, Bedard PL, Castonguay V, Chen Z, Reedijk M, Liu G *et al* (2013) A phase I study of the combination of ro4929097 and cediranib in patients with advanced solid tumours (PJC-004/NCI 8503). *Br J Cancer* **109**:943–949.
 30. Saito N, Fu J, Zheng S, Yao J, Wang S, Liu DD *et al* (2014) A high notch pathway activation predicts response to gamma secretase inhibitors in proneural subtype of glioma tumor-initiating cells. *Stem Cells* **32**:301–312.
 31. Schneider CA, Rasband WS, Eliceiri KW (2012) NIH Image to ImageJ: 25 years of image analysis. *Nature Methods* **9**:671–675.
 32. Song BQ, Chi Y, Li X, Du WJ, Han ZB, Tian JJ *et al* (2015) Inhibition of notch signaling promotes the adipogenic differentiation of mesenchymal stem cells through autophagy activation and PTEN-PI3K/AKT/mTOR pathway. *Cell Physiol Biochem* **36**:1991–2002.
 33. Stupp R, Hegi M, Mason W, van den Bent M, Taphoorn M, Janzer R *et al* (2009) Effects of radiotherapy with concomitant and adjuvant temozolomide versus radiotherapy alone on survival in glioblastoma in a randomised phase III study- 5-year analysis of the EORTC-NCIC trial. *Lancet Oncol* **10**:459–466.
 34. Tanaka S, Nakada M, Yamada D, Nakano I, Todo T, Ino Y *et al* (2015) Strong therapeutic potential of gamma-secretase inhibitor MRK003 for CD44-high and CD133-low glioblastoma initiating cells. *J Neurooncol* **121**:239–250.
 35. Tolcher AW, Messersmith WA, Mikulski SM, Papadopoulos KP, Kwak EL, Gibbon DG *et al* (2012) Phase I study of RO4929097, a gamma secretase inhibitor of Notch signaling, in patients with refractory metastatic or locally advanced solid tumors. *J Clin Oncol* **30**:2348–2353.
 36. Visvader JE, Lindeman GJ (2008) Cancer stem cells in solid tumours: accumulating evidence and unresolved questions. *Nat Rev Cancer* **8**:755–768.
 37. Wang CW, Klionsky DJ (2003) The molecular mechanism of autophagy. *Mol Med* **9**:65–76.
 38. Wicha MS, Liu S, Dontu G (2006) Cancer stem cells: an old idea—a paradigm shift. *Cancer Res* **66**:1883–1890; discussion 95–96.
 39. Yang Z, Klionsky DJ (2010) Mammalian autophagy: core molecular machinery and signaling regulation. *Curr Opin Cell Biol* **22**:124–131.
 40. Yao J, Zheng K, Li C, Liu H, Shan X (2015) Interference of Notch1 inhibits the growth of glioma cancer cells by inducing cell autophagy and down-regulation of Notch1-Hes-1 signaling pathway. *Med Oncol* **32**:610.
 41. Yao KC, Komata T, Kondo Y, Kanzawa T, Kondo S, Germano IM (2003) Molecular response of human glioblastoma multiforme cells to ionizing radiation- cell cycle arrest, modulation of the expression of cyclin-dependent kinase inhibitors, and autophagy. *J Neurosurg* **98**:378–384.
 42. Zhou Y, Wang HD, Zhu L, Cong ZX, Li N, Ji XJ *et al* (2013) Knockdown of Nrf2 enhances autophagy induced by temozolomide in U251 human glioma cell line. *Oncol Rep* **29**:394–400.

SUPPORTING INFORMATION

Additional Supporting Information may be found in the online version of this article at the publisher's web-site:

Figure 1. A Combination treatment with 2 μ M MRK003 and Bafilomycin A1 (BafA1) significantly decreased cell growth compared to DMSO in both cell lines. **B** Increase in LC3B-II/LC3B-I ratio expression and marked elevation of p62 is noted after treatment with BafA1, suggesting late stage inhibition of autophagy. Conversely, LC3B-II/LC3B-I ratio decreases and p62 increases after treatment with 3-MA, suggesting early stage autophagy inhibition.

Figure 2. A, B Representative cell cycle analysis data depicting marked increases in percentages of sub-G1 population in JHH520 (A) and HSR-GBM1 (B) lines after combination treatment with MRK003 and CQ. **C** Cell cycle arrest was not observed after 72-hour treatment with MRK003 and CQ.